

T. Pradeep

Publications 2020

# Contents

1. Publications.....	7
2. Lectures delivered.....	711
3. Patents/Technology.....	713
4. Media reports.....	715



# Journal Papers Published in 2020\*

## Publications from our group

1. A covalently integrated reduced graphene oxide-ion exchange resin electrode for efficient capacitive deionization, Md Rabiul Islam, Soujit Sen Gupta, Sourav Kanti Jana, Pillalamarri Srikrishnarka, Biswajit Mondal, Sudhakar Chennu, Tripti Ahuja, Amrita Chakraborty and Thalappil Pradeep, *Adv. Mater. Interfaces*, 2020. (Just Accepted)
2. New routes for multi-component atomically precise metal nanoclusters, Esma Khatun and Thalappil Pradeep, *ACS Omega*, 2020 (DOI: 10.1021/acsomega.0c04832) (Invited Perspective).
3. Reaction between  $\text{Ag}_{17}^+$  and acetylene outside the mass spectrometer: Dehydrogenation in the gas phase, Madhuri Jash, Rabin Rajan J. Methikkalam, Mohammad Bodiuzzaman, Ganesan Paramasivam and Thalappil Pradeep, *Chem. Commun.*, 56 (2020) 15623-15626 (DOI: 10.1039/d0cc05837h).
4. Microdroplet impact-induced spray ionization mass spectrometry (MISI MS) for online reaction monitoring and bacteria discrimination, Pallab Basuri, Subhashree Das, Shantha Kumar Jenifer, Sourav Jana and Thalappil Pradeep, *J. Am. Soc. Mass Spectrom.*, 2020 (DOI: 10.1021/jasms.0c00365).
5. Evaluating the impact of tailored water wettability on performance of  $\text{CO}_2$  capture, Adil Rather, Pillalamarri Srikrishnarka, Avijit Baidya, Arpita Shome, Thalappil Pradeep, Uttam Manna and Thalappil Pradeep, *ACS Appl. Energy Mater.*, 3 (2020) 10541-10549 (DOI: 10.1021/acsaem.0c01603).
6. Atom transfer between precision nanoclusters and polydispersed nanoparticles: A facile route for monodispersed alloy nanoparticles and their superstructures, Paulami Bose, Papri Chakraborty, Jyoti Sarita Mohanty, Nonappa, Angshuman Ray Chowdhuri, Esma Khatun, Tripti Ahuja, Ananthu Mahendranath and Thalappil Pradeep, *Nanoscale*, 12 (2020) 22116-22128 (DOI: 10.1039/D0NR04033A).

7. Dithiol-induced contraction in Ag<sub>14</sub> clusters and its manifestation in electronic structure, Mohammad Bodiuzzaman, Esma Khatun, Korath Shivan Sugi, Ganesan Paramasivam, Wakeel Ahmed Dar, Sudhadevi Antharjanam and Thalappil Pradeep, *J. Phys. Chem. C*, 124 (2020) 23426–23432 (DOI: 10.1021/acs.jpcc.0c07140).
8. Atomically precise noble metal cluster-assembled superstructures in water: Luminescence enhancement and sensing, Abhijit Nag, Papri Chakraborty, Athira Thacharon, Ganesan Paramasivam, Biswajit Mondal, Mohammad Bodiuzzaman and Thalappil Pradeep, *J. Phys. Chem. C*, 124 (2020) 22298–22303 (DOI: 10.1021/acs.jpcc.0c06770).
9. Smartphone-based fluoride-specific sensor for rapid and affordable colorimetric detection and precise quantification at sub-ppm levels for field applications, Sritama Mukherjee, Manav Shah, Kamalesh Chaudhari, Arijit Jana, Chennu Sudhakar, Pillalamarri Srikrishnarka, Md Rabiul Islam, Ligy Philip and Thalappil Pradeep, *ACS Omega*, 5 (2020) 25253–25263 (DOI: 10.1021/acsomega.0c03465).
10. Dual emitting Ag<sub>35</sub> nanocluster protected by 2-pyrene imine thiol, Arijit Jana, Papri Chakraborty, Wakeel Ahmed Dar, Sourov Chandra, Esma Khatun, M. P. Kannan, Robin H. A. Ras and Thalappil Pradeep, *Chem Commun.*, 56 (2020) 12550-12553 (DOI: 10.1039/d0cc03983g).
11. Co-crystals of atomically precise noble metal nanoclusters, Mohammad Bodiuzzaman, Wakeel Ahmed Dar and Thalappil Pradeep, *Small*, 2003981 (2020) (DOI: 10.1002/smll.202003981).
12. [Ag<sub>15</sub>H<sub>13</sub>(DPPH)<sub>5</sub>]<sup>2+</sup> and [Ag<sub>27</sub>H<sub>22</sub>(DPPB)<sub>7</sub>]<sup>3+</sup>: Two new hydride and phosphine co-protected clusters and their fragmentation leading to naked clusters, Ag<sub>13</sub><sup>+</sup> and Ag<sub>25</sub><sup>+</sup>, Madhuri Jash, Esma Khatun, Papri Chakraborty, Chennu Sudhakar and Thalappil Pradeep, *J. Phys. Chem. C*, 124(2020) 20569–20577 (DOI: 10.1021/acs.jpcc.0c05867).
13. Manifestation of structural differences of atomically precise cluster assembled solids in their mechanical properties, Korath Shivan Sugi, Payel Bandyopadhyay,

- Mohammad Bodiuzzaman, Abhijit Nag, Manjapoyil Hridya, Wakeel Ahmed Dar, Pijush Ghosh and Thalappil Pradeep, *Chem. Mater.*, 32 (2020) 7973–7984 (DOI: 10.1021/acs.chemmater.0c02905).
14. Non-stoichiometric copper sulfide nanostructures at the brass-rubber interface: Implications for rubber vulcanization temperature in the tire industry, M. P. Kannan, Anirban Som, Tripti Ahuja, Vidhya Subramanian, A. Sreekumaran Nair and Thalappil Pradeep, *ACS Appl. Nano Mater.*, 3 (2020) 7685–7694 (DOI: 10.1021/acsanm.0c01298).
  15. Accelerated microdroplet synthesis of benzimidazoles by nucleophilic addition to protonated carboxylic acids, Pallab Basuri, Louis Edwin Gonzalez, Nicolás Morato, Thalappil Pradeep and R. Graham Cooks, *Chem. Sci.*, 11 (2020) 12686–12694 (DOI: 10.1039/D0SC02467H).
  16. Probing subtle changes in molecular orientations using ambient electrospray deposition Raman spectroscopy (AESD RS), Atanu Ghosh, Tripti Ahuja, Kamallesh Chaudhari and Thalappil Pradeep, *J. Phys. Chem. C*, 124 (2020) 16644–16651 (DOI: 10.1021/acs.jpcc.0c04116).
  17. Entrapping atomically precise clusters in cyclodextrin-functionalized aminoclay sheets: Synthesis and enhanced luminescence, Mohd Azhardin Ganayee, C. K. Manju, Wakeel Ahmed Dar, Biswajit Mondal and Thalappil Pradeep, *Ind. Eng. Chem. Res.*, 59 (2020) 12737–12744 (DOI: 10.1021/acs.iecr.9b07018).
  18. Fullerene-mediated aggregation of  $M_{25}(SR)_{18}^-$  ( $M = Ag, Au$ ) nanoclusters, Papri Chakraborty, Abhijit Nag, Biswajit Mondal, Esma Khatun, Ganesan Paramasivam and Thalappil Pradeep, *J. Phys. Chem. C*, 124 (2020) 14891–14900 (DOI: 10.1021/acs.jpcc.0c03383).
  19. Clean water through nanotechnology: Needs, gaps, and fulfillment, Ankit Nagar and Thalappil Pradeep, *ACS Nano*, 14 (2020) 6420–6435 (DOI: 10.1021/acs.nano.9b01730).
  20. Enhanced capture of particulate matter by molecularly charged electrospun nanofibers, Pillalamarri Srikrishnarka, Vishal Kumar, Tripti Ahuja, Vidhya Subramanian, Arun Karthick Selvam, Paulami Bose, Shantha Kumar Jenifer,

- Ananthu Mahendranath, Mohd Azhardin Ganayee, Ramamurthy Nagarajan and Thalappil Pradeep, *ACS Sustain. Chem. Eng.*, 8 (2020) 7762–7773 (DOI: 10.1021/acssuschemeng.9b06853).
21. Iron assisted formation of CO<sub>2</sub> over condensed CO and its relevance to interstellar chemistry, Rabin Rajan J. Methikkalam, Jyotirmoy Ghosh, Radha Gobinda Bhuin, Soumabha Bag, Gopi Ragupathy, and Thalappil Pradeep, *Phys. Chem. Chem. Phys.*, 22 (2020) 8491-8498 (DOI: 10.1039/c9cp06983f).
  22. Arsenic toxicity: Carbonate's counteraction revealed, Swathy Jakka Ravindran, Shantha Kumar Jenifer, Jayashree Balasubramanyam, Sourav Jana, Subramanian Krishnakumar, Sailaja Elchuri, Ligy Philip, and Thalappil Pradeep, *ACS Sustain. Chem. Eng.*, 8 (2020) 5067-5075 (DOI: 10.1021/acssuschemeng.9b06850).
  23. Ligand structure and charge state-dependent separation of monolayer protected Au<sub>25</sub> clusters using non-aqueous reversed-phase HPLC, Korath Shivan Sugi, Shridevi Bhat, Abhijit Nag, Ganesan Paramasivam, Ananthu Mahendranath, and Thalappil Pradeep, *Analyst*, 145 (2020) 1337-1345 (DOI: 10.1039/c9an02043h).

### Publications with other groups

24. Self-assembly of precision noble metal nanoclusters: Hierarchical structural complexity, colloidal superstructures and applications, Jose V. Rival, Paloli Mymoona, Kavalloor Murali Lakshmi, Nonappa, Thalappil Pradeep, Edakkattuparambil Sidharth Shibu, *Small*, 2020. (Just accepted).
25. Ferrofluid microdroplet splitting for population-based microfluidics and interfacial tensiometry, Mika Latikka, Matilda Backholm, Avijit Baidya, Alberto Ballesio, Amandine Serve, Gregory Beaune, Jaakko V. I. Timonen, Thalappil Pradeep and Robin H. A. Ras, *Adv. Sci.*, 7 (2020) 2000359 (DOI: 10.1002/advs.202000359) (Early View).

26. Non-enzymatic glucose sensing using  $\text{Ni}_{60}\text{Nb}_{40}$  nanoglass, Soumabha Bag, Ananya Baksi, Sree Harsha Nandam, Di Wang, Xinglong Ye, Jyotirmoy Ghosh, Thalappil Pradeep, and Horst Hahn, *ACS Nano*, 14 (2020) 5543–5552 (DOI: 10.1021/acsnano.9b09778).
27. Ultrafast intersystem crossing in isolated  $\text{Ag}_{29}(\text{BDT})_{12}^{3-}$  probed by time-resolved pump-probe photoelectron spectroscopy, Aron Veenstra, Laurenz Monzel, Ananya Baksi, Joseph Czekner, Sergei Lebedkin, Erik Schneider, Thalappil Pradeep, Andreas-Neil Unterreiner, and Manfred Kappes, *J. Phys. Chem. Lett.*, 11 (2020) 2675-2681 (DOI: 10.1021/acs.jpcclett.0c00482).
28. Association of co-accumulation of arsenic and organophosphate insecticides with diabetes and atherosclerosis in a rural agricultural community, Ganesan Velmurugan, Krishnan Swaminathan, Sundaresan Mohanraj, Mani Dhivakar, Ganesh Veerasekar, Thomas Alexander, Mathew Cherian, Nalla G. Palaniswami, and Thalappil Pradeep, *Acta Diabetologica*, 57 (2020) 909 (DOI: 10.1007/s00592-020-01516-6).
29. Phosphorylated cellulose nanofibers exhibit exceptional capacity for uranium capture, Janika Lehtonen, Jukka Hassinen, Avula Anil Kumar, Leena-Sisko Johansson, Roni Mäenpää, Nikolaos Pahimanolis, Thalappil Pradeep, Olli Ikkala and Orlando J. Rojas, *Cellulose*, 27 (2020) 10719–10732 (DOI: 10.1007/s10570-020-02971-8).

\*Some of these papers will appear in 2021. Some were listed in publications of 2019 without page numbers, but appeared in 2020.

Publications from  
our group

# A Covalently Integrated Reduced Graphene Oxide–Ion-Exchange Resin Electrode for Efficient Capacitive Deionization

Md Rabiul Islam, Soujit Sen Gupta, Sourav Kanti Jana, Pillalamarri Srikrishnarka, Biswajit Mondal, Sudhakar Chennu, Tripti Ahuja, Amrita Chakraborty, and Thalappil Pradeep\*

Capacitive deionization (CDI) is an emerging, cost-effective alternative for energy-efficient desalination technology. Efficient electrode materials based on individual reduced graphene oxide (rGO) nanosheets are produced by functionalizing them with polystyrene (rGO–PS) through an in situ polymerization process involving rGO, styrene monomer, and divinylbenzene. The rGO–PS-integrated composite nanostructures are subsequently functionalized with sulfonate and quaternary amine functionalities to achieve positively and negatively charged electro-adsorbent ion-exchange resins (EAIERs), respectively. These EAIERs ‘molecular constructs’ are used to fabricate CDI electrodes, and deionization is performed to remove various ions. These molecular constructs promote faster charge transfer at the electrode–electrolyte interface and maintained the electrical conductivity of the active rGO. This leads to a high electroadsorption capacity of  $15.93 \text{ mg g}^{-1}$  of  $\text{Cl}^-$  using NaCl solution with a conductivity of  $802 \text{ }\mu\text{S}$  in laboratory batch experiments, which is approximately five times higher than the adsorption capacity of rGO electrodes reported earlier ( $\approx 2\text{--}3 \text{ mg g}^{-1}$ ) in comparable experimental conditions. No significant Faradaic redox reactions or chemical changes are observed on the electrode surface, which make these electrodes exhibit excellent electrochemical stability even after multiple adsorption/desorption cycles.

The availability of clean potable water at an affordable cost is a growing challenge for mankind. Recently, the drinking water crisis has reached alarming levels due to the increasing population, climate change, and contamination of various water sources.<sup>[1–7]</sup> To meet the growing demand for affordable drinking water, several technologies (such as reverse osmosis, ultrafiltration, adsorption, photocatalytic degradation, and distillation) are being utilized, some of which are highly expensive in

terms of equipment and energy consumption.<sup>[6,8–11]</sup> Capacitive deionization (CDI) is an emerging technology which involves adsorption and desorption of ions on the electrode surface by application of low potential difference ( $\approx 1.2\text{--}1.8 \text{ V}$ ) across a pair of porous carbon electrodes, thereby making it both energy and cost-efficient compared to other existing desalination methods. When a flowing water stream is passed across a CDI system, cations and anions move toward oppositely charged electrodes and get adsorbed on them, thereby generating deionized and ‘drinkable’ water, starting from brackish water. Subsequently, adsorbed ions can be removed from the electrode by reversing the polarity, thereby regenerating the electrode surface, ready for reuse for next adsorption cycle.<sup>[5]</sup> Thus, clean water can be produced continuously by repeating the adsorption and desorption cycles. CDI is a cost-effective, point-of-use method with a high theoretical desalination efficiency.<sup>[5]</sup> However, its practical applications for desalination are yet to be recognized at a

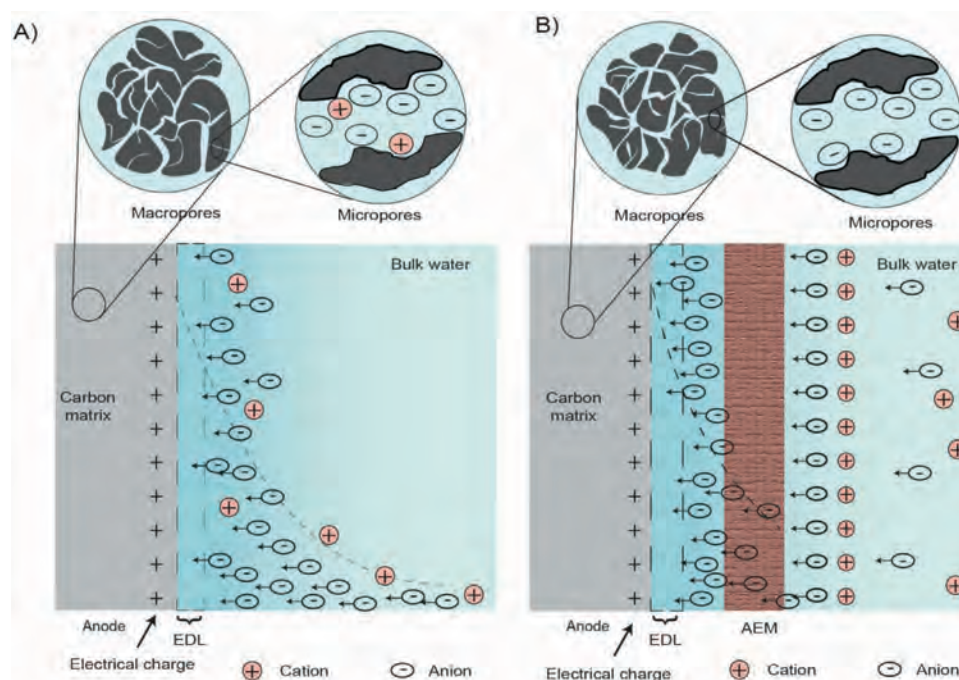
large scale, and research is being carried out to synthesize new materials with improved adsorption capacities.<sup>[5,12–14]</sup> Related technologies such as Faradaic deionization and the use of different 2D materials in CDI are also explored intensely.<sup>[15–17]</sup>

Various carbonaceous materials and their composites are being used as CDI electrodes because of their high salt adsorption capacities in the range of several  $\text{mg g}^{-1}$ .<sup>[18–25]</sup> Graphene, and graphene-derivatized materials, such as, graphene-like nanoflakes,<sup>[26]</sup> activated carbon,<sup>[27]</sup> activated carbon nanofiber (ACF),<sup>[28]</sup> reduced graphene oxide (rGO),<sup>[27,29]</sup> carbon nanotubes (CNT),<sup>[29]</sup> graphene–CNT composites,<sup>[29,30]</sup> rGO–ACF,<sup>[28]</sup> 3D macroporous graphene architectures,<sup>[31]</sup> sponge-templated graphene,<sup>[14]</sup> graphene– $\text{Fe}_3\text{O}_4$ ,<sup>[32]</sup> graphene chitosan– $\text{Mn}_3\text{O}_4$ ,<sup>[33]</sup> rGO–activated carbon composites,<sup>[27]</sup> and functionalized graphene nanocomposite,<sup>[34]</sup> have been used as CDI electrodes. The adsorption capacities of graphenic composites, such as graphene/carbon nanotube,  $\text{CO}_2$  activated rGO, sulfonic functional graphite nanosheets,  $\text{SO}_3\text{H}/\text{NH}_2$  graphene/activated carbon, MgAl–Ox/G nanohybrids, 3D-graphene architecture, and graphene sponge measured were 1.4, 6.26, 8.6, 10.3, 13.6,

M. R. Islam, S. S. Gupta, S. K. Jana, P. Srikrishnarka, B. Mondal, S. Chennu, T. Ahuja, A. Chakraborty, T. Pradeep  
DST Unit of Nanoscience (DST UNS)  
and Thematic Unit of Excellence (TUE)  
Department of Chemistry  
Indian Institute of Technology Madras  
Chennai 600 036, India  
E-mail: pradeep@iitm.ac.in

The ORCID identification number(s) for the author(s) of this article can be found under <https://doi.org/10.1002/admi.202001998>.

DOI: 10.1002/admi.202001998



**Scheme 1.** Ions adsorption mechanism for A) CDI and B) MCDI electrodes at the anode, where AEM denotes anion-exchange membrane. The corresponding process occurs at the cathode. (B) shows the enhanced electroadsorption in comparison to (A).

14.7, and 14.9 mg g<sup>-1</sup>, respectively, for an input of 500 ppm NaCl solution.<sup>[29,35–40]</sup>

The main objective of the CDI technology is to make a cost- and energy-efficient desalination process. Thus, synthesizing new materials and improving electrode architecture are the major tasks driving the progress of CDI technology. The electrode's performance largely depends upon the desalination capacity of the electrode materials and initial salt concentration. Mostly, carbon materials are utilized for electrode fabrication, but novel materials can also be integrated with carbon matrix to obtain enhanced electrode performance.<sup>[12]</sup> Electrode materials must have a high specific surface area, high electrical conductivity, and high electrochemical stability over different pH and voltage ranges (≈1.2–1.8 V). Additionally, electroadsorption capacity is also affected by total pore volume, pore size, and pore connectivity of the active electrode materials. Furthermore, suitable porosity of the electrode materials, excellent wetting behavior, and high bio-inertness to prevent biofouling are important factors for improving desalination performance. Besides electrode characteristics, input water flow rate, configuration of electrode stacks, lifetime of the electrodes, and the process's cost are other parameters that should be taken into account to design an efficient CDI technology.<sup>[12,41]</sup>

**Scheme 1** illustrates the adsorption mechanism of regular CDI and membrane CDI (MCDI) electrodes. In a regular CDI, when a voltage is applied across the electrodes, ions with opposite charges also referred to as counter-ions, move toward electrodes of opposite polarity (cations toward cathode and anions toward anode) and are adsorbed within the intraparticle porous network of the carbon electrode, while ions having the same charge (co-ions) are repelled from the electrodes of the same polarity (anions are repelled from cathode and cations are

repelled from anode). The co-ions present in the spacer channel, or separator (a gap between anode and cathode), further prevent the counter-ions from coming in contact with the electrode surface. Moreover, some of the co-ions, which may have accumulated in the micropores/macropores of the electrode, neutralize the adsorbed counter-ions, leading to a decrease in the adsorption capacity of the electrodes. In addition to the aforementioned drawbacks, poor electrochemical stability of regular CDI is another challenge. All of these have resulted in the invention of MCDI. In MCDI, ion-exchange membranes (IEMs, anion-exchange resin on the anode side, and vice versa) are incorporated in front of the carbon electrodes. Membranes containing covalently bound linkers, such as sulfonate or quaternary amine-containing IEMs, are typically used due to their high internal charge, which plays a significant role in selective transport of counter-ions. During MCDI, counter-ions are exchanged through the membrane (cations at cathode and anions at the anode, as the electrodes are coated with cation- and anion-exchange membranes, respectively). They can be adsorbed on the porous carbon surface, resulting in the formation of an electrical double layer (EDL) within the intraparticle nanostructures (micropores) of the porous carbon electrodes.<sup>[42]</sup> However, due to presence of a membrane on top of the electrodes, many counterions from the solution pass through the membrane to reach the active electrode surfaces. This movement of counter-ions results in the formation of an enhanced EDL at the electrodes. Moreover, counter-ions are also adsorbed on the respective membrane surfaces. Thus, the co-ions are blocked, and they reside in the vicinity of the membrane in the solution. Net effect is that IERs enhance the adsorption capacity of MCDI electrodes.<sup>[12,42–44]</sup> As the membrane is placed right over the carbon surface, the membrane layer extends well into the diffuse layer.



Thus, an MCDI system shows a higher salt removal rate or desalination performance. However, ion removal per unit energy consumption in MCDI is lower compared to regular CDI.<sup>[12,44]</sup> Although MCDI exhibits several advantages compared to conventional CDI, its major drawback is the weak adhesion between the electrode material and the IEM, leading to high charge transfer resistance at the electrode–electrolyte interface. Moreover, all the IEMs are hydrophobic and have poor wetting characteristics, which lead to low removal efficiency of the ions, even at low salt concentrations.<sup>[12]</sup>

In general, electroactive materials are printed on a stable conducting surface during CDI electrode fabrication. This usually requires the use of a non-conducting binder, such as polyvinylidene fluoride (PVDF) and polyvinyl alcohol, which reduces the available electrochemical surface area and conductivity of the electrode materials. This can be resolved by integrating electro-adsorbent materials with the ion-exchange resin via covalent linkages. Graphene and its derivatives have proved extremely advantageous in this context. Due to its large surface area, high electrical conductivity, and tunable functionality, it is possible to retain the electrodes' adsorption capacity even while maintaining proper covalent linkages. Selective functionalization of rGO with ion-permeable membranes by forming a single molecular construct enables the possibility of enhanced adsorption and ion permeation characteristics.<sup>[45]</sup>

In this work, CDI electrodes were prepared by forming covalent linkages between rGO and IERs, which were used for selective anion and cation permeation during the desalination process. This methodology also improves the adsorption capacity of the target ions (counter-ions) and the blocking of the co-ions, allowing rapid desalination of brackish water. By this process, the material retains its conductivity and wetting characteristics, unlike conventional MCDI. It is essential to point out that mixing graphene and ion-exchange resin without any covalent linkage does not produce the desired result.<sup>[46]</sup> In MCDI, IER is coated on electrode material through covalent linkages that decrease electrical conductivity of the electrode and simultaneously increase the charge transfer resistance at the electrode/electrolyte interface. However, this can be overcome by molecular constructs. Hence, our materials are expected to exhibit higher adsorption capacity and energy efficiency. Our technology has proved to be suitable for commercial implementation after the evaluation of its performance using various electrochemical and spectroscopic studies.

CDI electrode materials with molecular constructs were synthesized through in situ polymerization of styrene monomer in the presence of rGO. CDI electrodes were fabricated on bare graphite sheets, which were further characterized by different spectroscopic and microscopic techniques. Detailed synthesis and fabrication processes have been discussed in the Experimental Section. **Figure 1A** presents a schematic of the CDI cell integrated with electro-adsorbent ion-exchange resins (EAIERs) electrodes. The EAIERs were coated on graphite sheets, which act as current collectors, and a DC potential ( $\pm 1.5$  V) was applied to the electrodes to drive the counter-ions to the electrode surface from the input feed water. A spacer was placed between the two electrodes. An expanded view depicts the structure of the molecular construct of both +ve EAIERs and –ve EAIERs, namely cathode and anode, respectively. High-resolution

scanning electron microscopy (HRSEM) images of both the electrode materials are shown in an expanded view in **Figure 1A**. Electron microscopy images using HRSEM (magnified view in **Figure 1A**) and TEM (**Figure 1B,C**) confirmed that both the electrode materials had hierarchical structures with multiple rGO sheets arranged in a stacked manner. This structure shows a higher accessible surface area for a large number of ion adsorption/desorption cycles. Characterization of the starting materials is presented in the Supporting Information.

Fourier transform infrared (FT-IR) spectra, shown in **Figure 2** present the vibrational modes of different functional groups of electrode materials. The spectral features are assigned in **Table 1**. A discussion of these features is presented as part of Supporting Information. The aforementioned spectral features validate the covalent linkage between rGO and polystyrene (PS), in addition to the formation of anionic and cationic EAIERs.

Electrochemical adsorption and desorption behavior of both the electrodes was studied using cyclic voltammetry (CV) measurements in a conventional three-electrode configuration. A DC potential was applied at the working electrode (EAIERs coated graphite electrode) with respect to Ag/AgCl electrode, using 1 M NaCl solution, and the resulting capacitive current was measured between the working and platinum mesh counter electrodes. **Figure 3A,B** depicts the cyclic voltammograms obtained at different scan rates from 1 to 1000 mV s<sup>–1</sup> for cathode and anode, respectively. A noticeable change in the shape of the CV curve at higher scan rates was observed. At lower scan rates, the electrolyte penetrates within the pores of EAIERs unrestricted, which results in the formation of both an electrical double layer capacitance (EDLC) and diffusion capacitance at the interface of the hierarchical surfaces. However, at higher scan rates, ions do not have sufficient time to penetrate within the porous structures due to the ionic transport resistance, which affects the formation of diffusion capacitance at the electrode surface. Scan rate-dependent specific capacitance profiles of both +ve and –ve EAIERs are plotted in **Figure S5**, Supporting Information, demonstrating that electrodes exhibit higher specific capacitance at a lower scan rate and vice versa. This specific capacitance is the contribution of both EDLC and diffusion capacitance. EDLCs are formed at the interfaces due to the high surface charge density of the EAIERs electrodes. The formation of diffusion capacitance largely depends on the electrodes' porosity and the electrical potential applied to the electrodes.

Electrochemical impedance spectroscopy (EIS) was performed to understand the effect of the electrode materials' electronic conductivity on the interfacial (electrode/electrolyte) charge transport property and resulting electroadsorption behavior. EIS was carried out by applying a fixed AC signal of 10 mV at the CDI electrode, and the frequency of the motion was varied from 3 MHz to 5 mHz, simultaneously. The total impedance of the electrochemical cell (adopted with three-electrode configuration) was measured as a function of the applied frequency at the electrode. **Figure 3C,D** shows the Nyquist Plots of +ve and –ve EAIER electrodes (the expanded views are shown in inset), which depicts the variation of the imaginary part of the total impedance with the real part. Each plot is majorly constituted of two impedance regions, a small semicircle at the high-frequency region (3 MHz–1.5 KHz), followed by a straight line

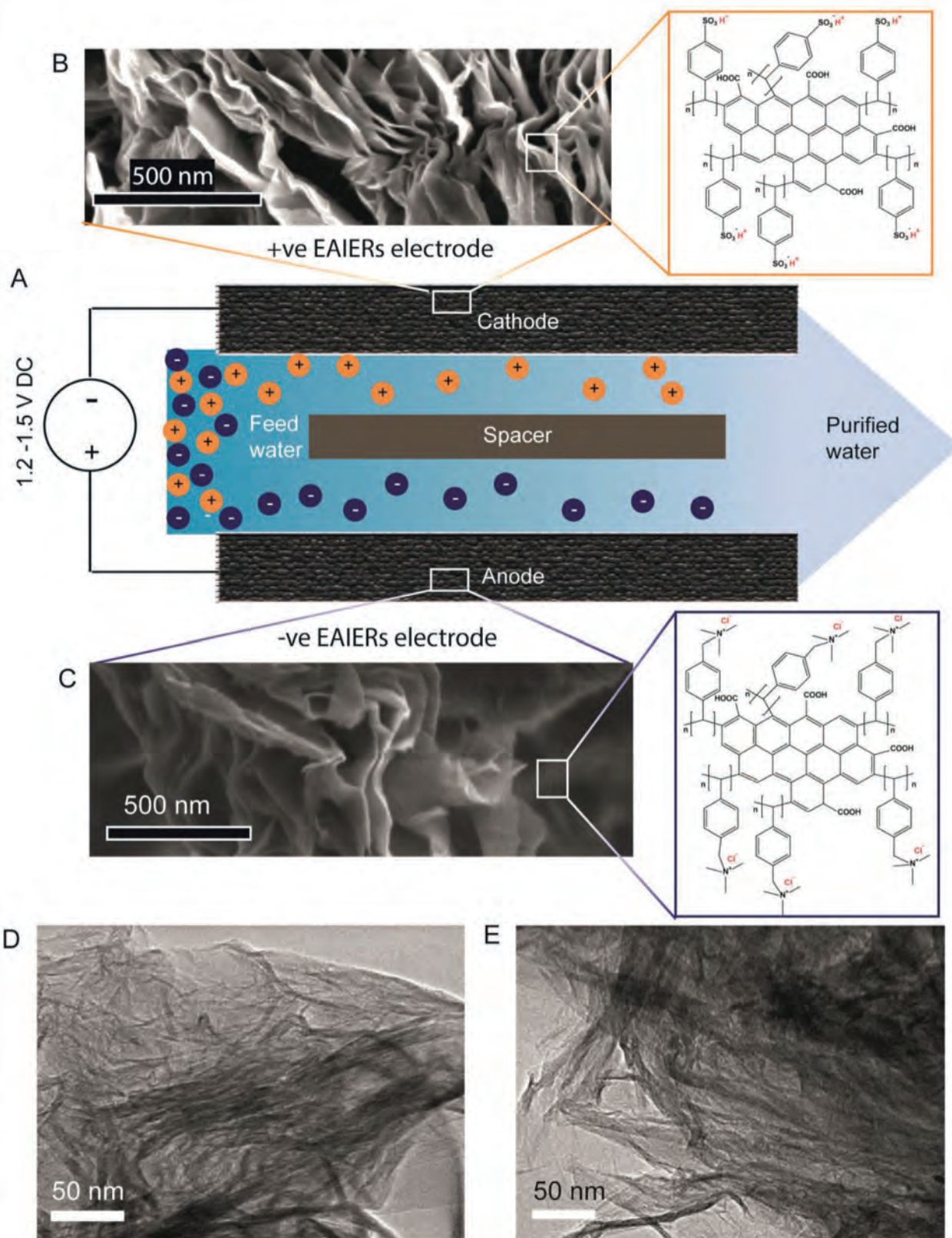


**Figure 1.** A) Schematic design of a cell with integrated EAIERs (molecular construct) for capacitive deionization (CDI). The rGO sheets have  $-\text{COOH}$  functionalization. Expanded views show the HRSEM images of +ve and -ve EAIERs, respectively. Corresponding molecular structures are also shown. TEM image of B) +ve EAIERs and C) -ve EAIERs materials. The scale bars are 500 and 50 nm for HRSEM and TEM, respectively.



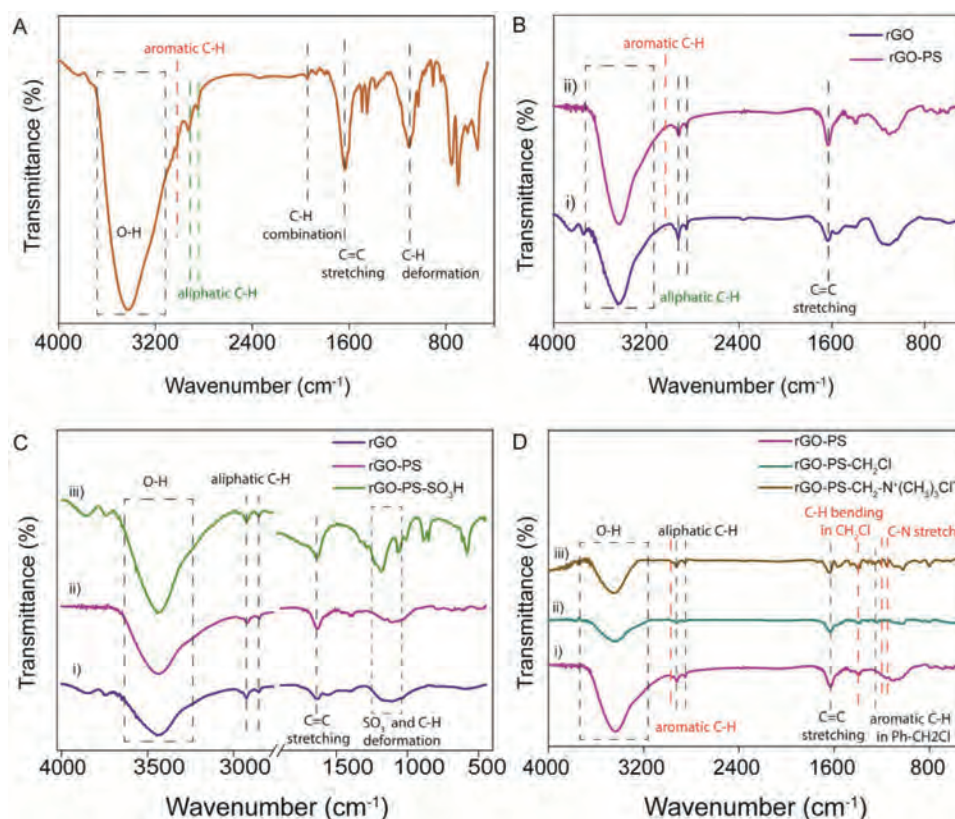


**Figure 2.** Fourier transform infrared (FT-IR) spectra of A) PS, B) rGO and rGO-PS, C) rGO, rGO-PS, and rGO-PS-SO<sub>3</sub>H (+ve EAIERs), and D) rGO-PS, rGO-PS-CH<sub>2</sub>Cl, and rGO-PS-CH<sub>2</sub>-N<sup>+</sup>(CH<sub>3</sub>)<sub>3</sub>Cl<sup>-</sup> (-ve EAIERs). Essential features are labeled. Chemical functionalization is evident.

in the low-frequency area (1.5 KHz–5 mHz). The first intercept of the semicircle (leftmost) is known as the equivalent series resistance (ESR), which is related to the combined effect of the material resistance of rGO-PS, the contact resistance between graphite sheet and the EAIERs coating, and the ionic resistance of the electrolyte ( $R_s$ ). Thus, the ESR value (1.56 ohm) confirms that the working electrode (EAIERs) retains the conductivity of bare rGO, even after covalent functionalization of rGO with PS. The quasi-semicircle with a small arc radius suggested a low charge transfer resistance at the electrode–electrolyte interface ( $R_{ct}$ ) for both the electrodes. High conductivity and enhanced surface charge density of EAIERs result in fast electroadsorption of ions. In the low-frequency region, the straight line implies the formation of an EDLC at the electrode–electrolyte interface. Moreover, the straight line parallel to the y-axis

(inset figure) also suggests fast ion diffusion to the electrodes, leading to a low Warburg diffusion resistance ( $W$ ). Thus, both +ve and -ve EAIERs electrodes have good accessibility for ions to/from an EDL at their surfaces. To sum up, the EAIERs electrodes possess low internal resistance because of the covalent interaction between rGO and PS. Therefore, low  $R_{ct}$  is retained in the composite material (rGO-PS), compared to bare rGO.<sup>[47]</sup> Figure S6A,B, Supporting Information, represents Bode plots for cathode and anode, respectively, which further confirm the capacitive nature of the electrode. Furthermore, the frequency-dependent phase angle of both the electrodes was determined from the EIS measurement, and these were maximum ( $\sim 75^\circ$ ) for both the electrodes in the low-frequency region. This confirmed the formation of EDL on the electrodes during the adsorption cycle.

**Table 1.** IR features of PS, rGO, rGO-PS, and -ve and +ve EAIERs, with assignments.

Wavenumber (cm <sup>-1</sup> )	Assigned vibrations	Wavenumber (cm <sup>-1</sup> )	Assigned vibrations
3450–3520	O–H stretching	1411	aliphatic C–H in chloromethyl –CH <sub>2</sub> Cl
2850–3035	aliphatic and aromatic C–H stretching	1261	aromatic C–H of Ph–CH <sub>2</sub> Cl groups
1740–1745	C=O stretching of a carboxylic acid group	1224 and 1180	S=O bond of SO <sub>3</sub> H
1631–1638	C=C stretching	1208 and 1154	C–N stretching frequencies of the tertiary amine group
1450	C–H deformation		

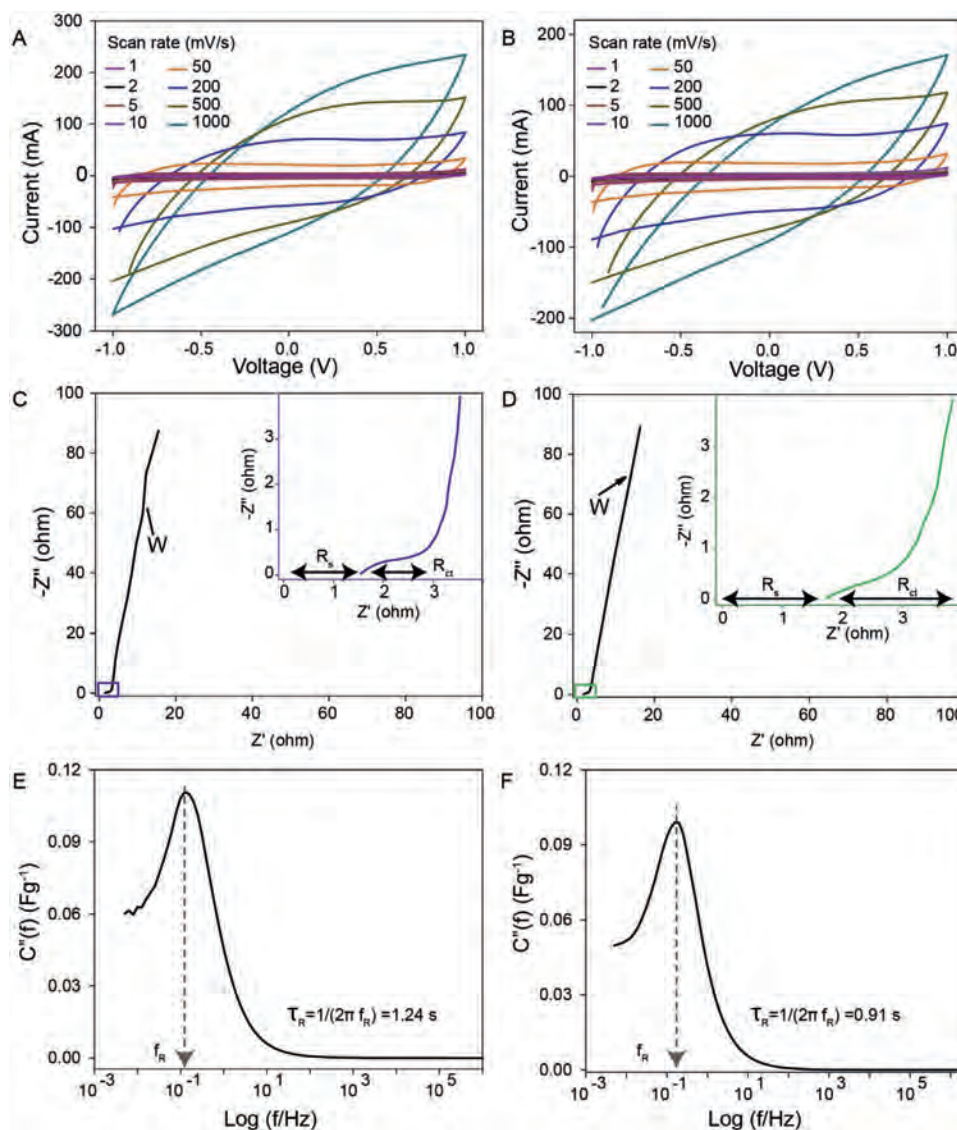


**Figure 3.** Cyclic voltammetry (CV) of A) +ve EAIERs electrode (cathode) and B) -ve EAIERs electrode (anode) at different scan rates; Nyquist Plots of C) +ve EAIERs electrode (the inset chart shows the magnified high-frequency region) and D) -ve EAIERs electrode (the inset chart shows the magnified high-frequency region); E,F) imaginary part of complex capacitance ( $C''$ ) versus frequency for cathode and anode, respectively, in 1 M NaCl electrolyte.

Electrochemical adsorption and desorption rates of the electrodes and the contribution of EDLC for desalination can be determined qualitatively through frequency-dependent interfacial capacitance analysis. In this context, frequency-dependent variations of both real ( $C'(f)$ ) and imaginary ( $C''(f)$ ) capacitances were calculated through EIS measurements for both the electrodes, and the resulting profiles are shown in Figure S6C,D, Supporting Information, and Figure 3E,F, respectively. Frequency-dependent imaginary capacitance profiles of both electrodes were calculated from Nyquist impedance plots. Figure S6C,D, Supporting Information, show  $C'(f)$  profiles were having three distinct regions. In the high-frequency region ( $1$  to  $2 \times 10^6$  Hz), the capacitance  $C'(f)$  becomes almost zero, which indicates that the electrode behaves like a resistor (R). However, in the low-frequency region, the capacitance is almost constant (within  $\pm 10\%$ ) up to a specific frequency ( $5$ – $100$  mHz),

indicating adsorption/desorption of ions occurred through physisorption, indicating pure capacitive behavior of the electrodes in this regime. In between high-frequency and low-frequency regions, that is,  $100$  mHz– $1$  Hz, the  $C'(f)$  decreases linearly with frequency, which indicates the loss of charge during the adsorption/desorption process. Furthermore,  $C''(f)$  profiles for both the electrodes shown in Figure 3E,F represent irreversible energy dissipation and ion relaxation process during adsorption/desorption.<sup>[48]</sup> Irreversible energy dissipation is related to loss of charges in the form of heat. It is well known that the adsorption/desorption kinetics of ions depends not only on the electrode's electronic conductivity but also on the electrode surface's structure and porosity.<sup>[25]</sup> Since HRSEM and TEM images (Figure 1) of our composite electrodes show a larger number of nanosheets assembled into a wrinkled microporous morphology, the ions which were adsorbed at the outward surface

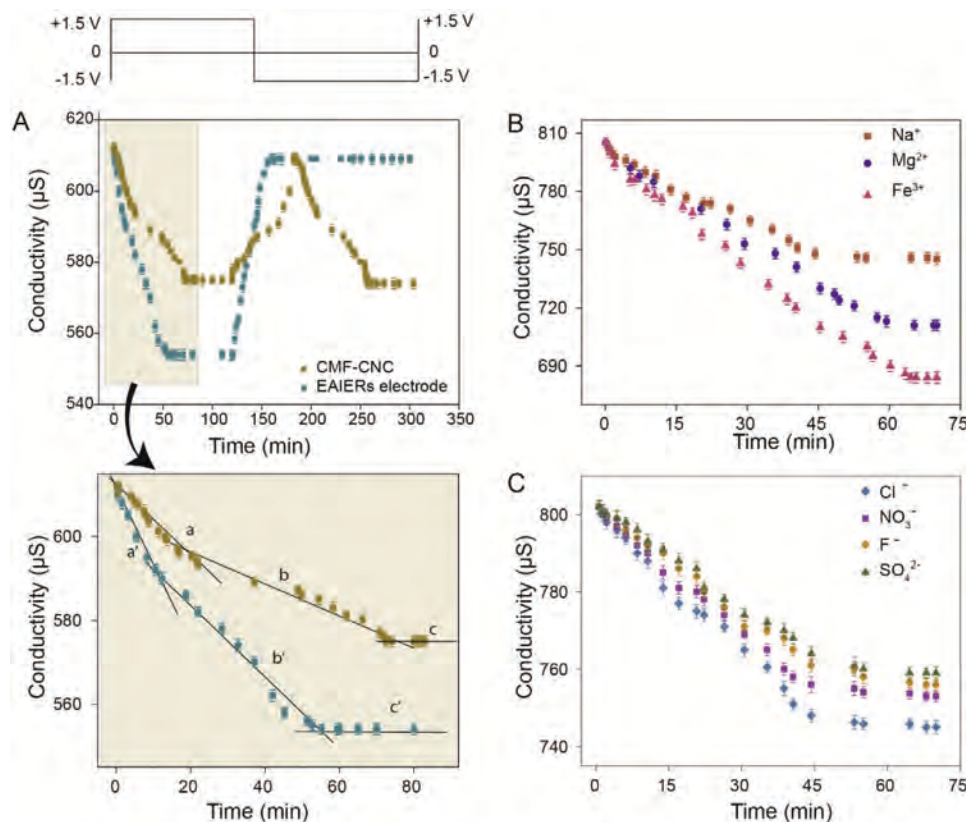


**Figure 4.** A) Comparison of CDI performance between covalently integrated EAIERs (rGO-PS functionalized) electrode and melamine-functionalized carbon nanocellulose (CMF-CNC) derived electrode in 610  $\mu\text{S}$  NaCl solutions. Electrosorption kinetics for both the integrated EAIERs and CMF-CNC electrodes are shown in the expanded views below. Three distinct regimes of adsorption are shown, marked with a, b, and c, and a', b', and c' for CMF-CNC and EAIERs electrode, respectively. Variation in the potential of the electrodes with time is shown on top of the (A). CDI performances of EAIERs electrodes using different B) cations ( $\text{Na}^+$ ,  $\text{Mg}^{2+}$ , and  $\text{Fe}^{3+}$ ) and C) anions ( $\text{Cl}^-$ ,  $\text{NO}_3^-$ ,  $\text{F}^-$ , and  $\text{SO}_4^{2-}$ ) with solution conductivity of 802  $\mu\text{S}$ . The operating potential was maintained at 1.5 V during the measurements.

(wrinkled sheets) of hierarchical structures come out with faster desorption kinetics. However, the ions that were adsorbed at the interlayer of the porous structure's nanosheets might not have had sufficient time to desorb entirely before the beginning of the next adsorption cycle.<sup>[49]</sup> In Figure 3E,F, the peak maximum represents the frequency at which ions were relaxed or released without facing any resistive barrier due to the contribution of both electronic and ionic conductivities. The relaxation time constant ( $\tau_R$ ) can be calculated from the peak frequency ( $f_R$ ), and this can be calculated using the equation,  $\tau_R = 1/(2\pi f_R)$ .<sup>[50]</sup> This time constant represents the minimum time required to discharge all the ions from the electrode surface. The value of  $\tau_R$  was found to be nearly the same for both the electrodes. These values were (1.24 and 0.91 s) comparable to the  $\tau_R$  value for other rGO based electrodes reported earlier.<sup>[48,50]</sup>

Figure S7, Supporting Information, shows a schematic representation of the experimental set-up for analyzing ions undergoing adsorption-desorption during CDI. A DC power source ( $\pm 1.5$  V) was connected to the electrodes that drive the ions present in the solution toward the electrodes (anions to anode and cations to cathode). A total-dissolved-solids meter was immersed in the solution to measure the time-dependent changes in the solution's conductivity during the adsorption/desorption processes. The adsorption/desorption performance

of EAIERs electrodes was compared with our previously reported work with conventional carbon-based CDI electrodes.<sup>[24]</sup> For that, carbon powder prepared from melamine functionalized nanocellulose (MF-CNC) was used for traditional CDI (CMF-CNC). The synthesis protocol of CMF-CNC was reported elsewhere.<sup>[51]</sup> A comparative adsorption/desorption study of EAIERs and CMF-CNC electrodes was carried out using an NaCl solution with ionic conductivity of 610  $\mu\text{S}$ . It is evident from Figure 4A that the EAIERs electrodes have higher adsorption capacity ( $\approx 15.86 \text{ mg g}^{-1}$ ) than CMF-CNC electrodes ( $\approx 7.45 \text{ mg g}^{-1}$ ) for  $\text{Cl}^-$  ions. In the EAIERs electrodes, the adsorption occurred for the first 58 min, leading to equilibrium. This adsorption equilibrium was allowed to continue up to 120 min. After 120 min, by reversing the applied potential's polarity to the electrodes, the desorption process was initiated. In this time interval, the conductivity of the solution approached an initial value of 610  $\mu\text{S}$ , as all the adsorbed ions were desorbed, and thus, adsorption sites were regenerated. The electroadsorption/desorption remained at equilibrium until the potential was reversed. Similarly, CMF-CNC electrodes were also tested for a comparative study of adsorption and desorption capacities with EAIERs electrodes.

CMF-CNC electrodes required  $\approx 73$  min to attain the adsorption equilibrium (Figure 4A). By reversing the polarity,



desorption started, and adsorption sites were regenerated at the electrode after 120 min. However, unlike EAIERs, the CMF-CNC electrodes started to adsorb ions before desorption of all the ions from the electrodes, which reflected in the desalination performance of CMC-CNC electrodes. This is the crucial difference between EAIERs and CMF-CNC electrodes in terms of desalination efficiency. Electroadsorption kinetics for the integrated EAIERs and CMF-CNC electrodes are shown as a zoomed-in view of Figure 4A, and the EAIERs electrodes show three distinct adsorption kinetics before reaching the equilibrium. Initially, the adsorption was fast in the first  $\approx 11$  min, and it was moderate within  $\approx 11$ –53 min; but in the final  $\approx 53$ –64 min, adsorption was very slow.

Similarly, CMF-CNC electrodes also showed three distinct kinetics; initially, faster adsorption in the first  $\approx 20$  min, followed by moderate adsorption during  $\approx 20$ –71 min, and finally, slower adsorption during  $\approx 71$ –80 min. These results revealed that EAIERs electrodes have more active adsorption sites than conventional CDI electrodes (CMF-CNC). Furthermore, the covalent linkage between rGO and IER (synthesized material), which maintained the electronic conductivity of the EAIERs electrodes compared to rGO, further reduces the charge transfer resistance at the electrode–electrolyte interface during adsorption/desorption processes. Thus, EAIERs electrodes exhibited faster adsorption/desorption rate at their surfaces, resulting in a higher desalination efficiency than standard MCDI electrodes. In MCDI, the presence of a membrane on top of the electrode surface increases the charge transfer resistance at the electrolyte interface, effectively reducing the overall adsorption capacity of active electrodes. However, high adsorption capacity with faster desorption kinetics was observed for EAIERs electrodes (Figure 4A). Therefore, synthesized materials, which would be more energy efficient (desalination per unit energy consumption,  $\text{mg g}^{-1} \text{ watt}^{-1}$ ) with higher adsorption capacity, could be utilized for developing future CDI electrodes. The comparison of desalination efficiency of different electrode materials in terms of their salt adsorption capacities, reported in the recent past, is shown in Table 2. It is clear that the synthesized EAIERs electrode materials are superior to the reported ones.

Other than surface porosity and electronic conductivity, the electrochemical adsorption capacity of the electrode materials also depends on i) hydrated ionic radii, ii) ionic charge, and iii) initial concentration of the solution. To determine the adsorption capacity, considering the above factors, a set of different cations ( $\text{Na}^+$ ,  $\text{Mg}^{2+}$ , and  $\text{Fe}^{3+}$ ) and anions ( $\text{NO}_3^-$ ,  $\text{F}^-$ ,  $\text{Cl}^-$ , and  $\text{SO}_4^{2-}$ ) were taken. Here,  $\text{Cl}^-$  ions were chosen as the common anion for all cations, and  $\text{Na}^+$  was the common cation for all anions. The electrochemical adsorption–desorption capacity of EAIERs electrodes and corresponding changes in the conductivity of the solution was monitored. Conductivity profiles of the electrolyte containing each of the aforementioned ions during the adsorption–desorption process are shown in Figures 4B,C, and Figures S8, S9, and S11, Supporting Information. A comparative study of the adsorption capacity of EAIERs electrodes was performed in the presence of different cations ( $\text{Fe}^{3+}$ ,  $\text{Mg}^{2+}$ , and  $\text{Na}^+$ ). Initial ionic conductivity of the solution with each of these ions was maintained as  $802 \mu\text{S}$ , as shown in Figure 4B. It is evident that the adsorption capacity of the

electrode corresponding to individual cations follows the trend,  $\text{Fe}^{3+} > \text{Mg}^{2+} > \text{Na}^+$ . It was noticed that the adsorption capacity of the EAIERs electrode increased with an increase in charge of the individual cation. Therefore, properties such as the ionic charge, ionic radii, and hydrated radii of different cations ( $\text{Na}^+$ ,  $\text{Mg}^{2+}$ , and  $\text{Fe}^{3+}$ ) and anions ( $\text{NO}_3^-$ ,  $\text{F}^-$ ,  $\text{Cl}^-$ , and  $\text{SO}_4^{2-}$ ) affect the adsorption capacity. In the case of cations, adsorption capacity increased with an increase in valency; however, the reverse trend was observed in the case of anions (with the same cation,  $\text{Na}^+$ ). The hydrated radius of  $\text{Fe}^{3+}$  is the largest, and  $\text{Na}^+$  is the smallest among these cations. Therefore, adsorption of cations should follow the order,  $\text{Na}^+ > \text{Mg}^{2+} > \text{Fe}^{3+}$ ; however, the reverse trend was observed experimentally. In the case of cations, the charge of the ion is the predominant factor than the hydrated radius. When a potential was applied at the electrodes, the cation with a higher charge should undergo higher adsorption than a lower charged cation. Therefore, trivalent  $\text{Fe}^{3+}$  was adsorbed at a faster rate than divalent  $\text{Mg}^{2+}$ , followed by monovalent  $\text{Na}^+$ .<sup>[52]</sup> However, in the case of anions, adsorption capacity decreases with an increase in the charge of anions. Adsorption capacities for all the anions are shown in Figure 4C. In the case of anions, hydrated radii are more important than their charges. The size of the hydrated radii of anions decreases as  $\text{SO}_4^{2-} > \text{F}^- > \text{NO}_3^- > \text{Cl}^-$ . Anions with the smallest hydrated radii would pass through the pores efficiently and reach the electrode surface at faster kinetics, and adsorption capacity follows the trend,  $\text{Cl}^- > \text{NO}_3^- > \text{F}^- > \text{SO}_4^{2-}$ .<sup>[3]</sup> Conductivity profiles of the solution after electroadsorption in the presence of cations and anions with initial ionic conductivity of 450 and  $610 \mu\text{S}$  are shown in Figure S8, Supporting Information.

Adsorption capacities of covalently integrated EAIERs electrodes using various solutions, each with different conductivity, are depicted in Figure S9A–C, Supporting Information. The adsorption capacity of EAIERs electrodes increased with an increase in the concentration of NaCl. The observed values of adsorption capacity were 14.45, 15.86, and  $15.93 \text{ mg g}^{-1}$  for  $\text{Cl}^-$  ions of NaCl, with ionic conductivities of 450, 610, and  $802 \mu\text{S}$ , respectively. The obtained adsorption capacities were much higher in comparison to pristine rGO or graphene-based CDI electrodes (Table 2).

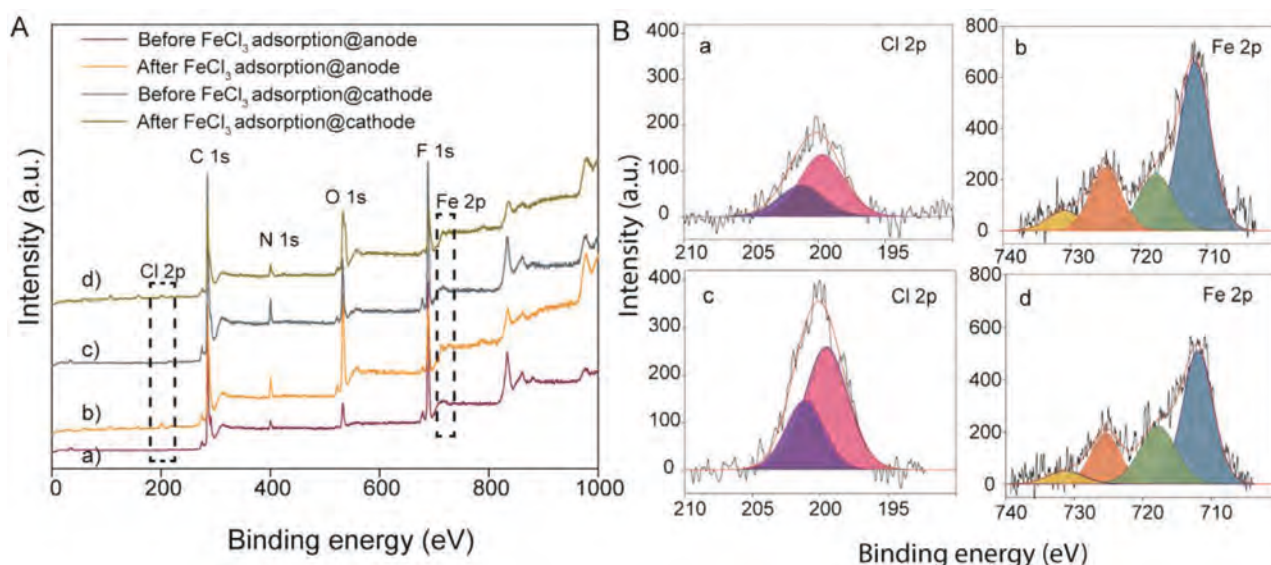
To investigate the reproducibility of the electrode's adsorption/desorption performance, it was carried out with the same measurement for 20 cycles. Four adsorption/desorption cycles were presented in Figure S9, Supporting Information. It was observed that adsorption–desorption efficiency (ratio between adsorption and desorption rate) was the same and remained constant even after 20 cycles (Figure S10, Supporting Information). There was no significant change observed in the desalination efficiency even if the electrode was run for a longer time more than 400 adsorption–desorption cycles. Stability of the electrode was assessed by performing the experiment repeatedly over a period of nearly a year. No noticeable effect in performance was observed. Due to high electrochemical stability of our electrodes during electrochemical cycles, they can be implemented in practical CDI technology.

Figure S11A–C, Supporting Information, shows the conductivity versus time plots upon varying the concentration of  $\text{MgCl}_2$  in solution. The adsorption capacities of  $\text{Mg}^{2+}$  ions were found to be 20.40, 23.51, and  $26.63 \text{ mg g}^{-1}$  for the input

Q6

**Table 2.** Comparison of electrode materials efficiency in terms of salt adsorption capacity in  $\text{mg g}^{-1}$  reported in the recent past.

Materials	Initial concentration ( $\text{mg L}^{-1}$ )	Adsorption capacity ( $\text{mg g}^{-1}$ )	Year of publication/Reference
Graphene	86.9	0.88	2012 <sup>[26]</sup>
Graphene	25	1.85	2009 <sup>[57]</sup>
rGO–CA composite	65	3.23	2012 <sup>[27]</sup>
rGO	65	1.8	
Activated carbon	65	1.51	
3D Macroporous graphene architectures	$\approx 52$	3.9	2013 <sup>[31]</sup>
Sulfonated graphite nanosheet	250	8.6	2012 <sup>[35]</sup>
Sponge-templated graphene	106	4.95	2014 <sup>[14]</sup>
rGO–activated carbon nanofiber (rGO–ACF)	400	7.2	2014 <sup>[28]</sup>
Graphene sponge	500	14.9	2015 <sup>[40]</sup>
Microporous graphene	$\approx 74$	11.86	2015 <sup>[58]</sup>
3D Porous graphene	300	18.43	2016 <sup>[59]</sup>
Graphene/carbon nanotube	500	1.4	2013 <sup>[29]</sup>
rGO–activated carbon composites	$\approx 25$	2.94	2012 <sup>[60]</sup>
rGO–resol (rGO–RF)/rGO–CA	40	3.47	2012 <sup>[61]</sup>
Graphene oxide/ZrO <sub>2</sub>	50	6.3	2016 <sup>[62]</sup>
MnO <sub>2</sub> -Nanorods@graphene	$\approx 50$	5.01	2014 <sup>[63]</sup>
Sulfonic functional graphite nanosheet	500 $\mu\text{S cm}^{-1}$	8.6	2012 <sup>[64]</sup>
Graphene–Fe <sub>3</sub> O <sub>4</sub> (E-Gr-Fe <sub>3</sub> O <sub>4</sub> )	300 $\mu\text{S cm}^{-1}$	10.3	2015 <sup>[65]</sup>
rGO	300 $\mu\text{S cm}^{-1}$	6.00	
Graphene–chitosan–Mn <sub>3</sub> O <sub>4</sub> composites	100 $\mu\text{S cm}^{-1}$	9.32	2015 <sup>[33]</sup>
	300 $\mu\text{S cm}^{-1}$	12.76	
	500 $\mu\text{S cm}^{-1}$	14.83	
3D Graphene architectures	500	14.7	2016 <sup>[38]</sup>
Anion-exchange polymer layered graphene composites (A-NRGS)	300 $\mu\text{S cm}^{-1}$	11.3	2017 <sup>[66]</sup>
N-doped rGO sponge composite (NRGS)	300 $\mu\text{S cm}^{-1}$	8.6	
rGO	300 $\mu\text{S cm}^{-1}$	6.2	
Few-layered graphene (HCG)	50 $\mu\text{S cm}^{-1}$	1.72	2015 <sup>[67]</sup>
Highly-crumpled N-doped graphene	50 $\mu\text{S cm}^{-1}$	1.96	
N-doped electrospun rGO–carbon nanofiber composite (NG–CNF)	$\approx 100 \mu\text{S cm}^{-1}$	3.91	2015 <sup>[68]</sup>
SO <sub>3</sub> H–graphene–carbon nanofibers	400	9.54	2015 <sup>[69]</sup>
SO <sub>3</sub> H/NH <sub>2</sub> graphene/activated carbon	500	10.3	2014 <sup>[36]</sup>
Hierarchical hole-enhanced 3D graphene	80	8.0	2018 <sup>[70]</sup>
Spherical macroporous	$0.5 \times 10^{-3} \text{ m}$	5.7	2018 <sup>[71]</sup>
3D intercalated graphene nanocomposite	500	22.09	2018 <sup>[72]</sup>
MgAl–Ox/G nanohybrids	500	13.6	2018 <sup>[37]</sup>
3D channel-structured graphene (CSG)	295	9.6	2019 <sup>[73]</sup>
CO <sub>2</sub> activated rGO(AGE)	500	6.26	2019 <sup>[39]</sup>
GO/hierarchical porous carbon	55.72	7.74	2018 <sup>[74]</sup>
SiO <sub>2</sub> activated GO (GR/NMC)	500	18.4	2018 <sup>[75]</sup>
p-phenylenediamine functionalized GO	$\approx 100 \mu\text{S cm}^{-1}$	7.88	2018 <sup>[76]</sup>
Mesoporous G@MC heterostructured	500	24.3	2018 <sup>[77]</sup>
Graphene/Co <sub>3</sub> O <sub>4</sub> composite	250	18.63	2018 <sup>[78]</sup>
N-doped graphitic carbon polyhedrons	500	17.77	2019 <sup>[79]</sup>
EAIERS	802 $\mu\text{S cm}^{-1}$	15.93	2020 (This work)



**Figure 5.** A) XPS survey spectra of the material after single adsorption, a) anode and c) cathode (before adsorption); b) anode and d) cathode (after  $\text{FeCl}_3$  adsorption), and B) deconvoluted XPS spectra of a) Cl 2p, b) Fe 2p of the cathode and c) Cl 2p, d) Fe 2p of anode after adsorption of  $\text{FeCl}_3$ . Peaks appearing at 717.35 eV (green) and 731.34 eV (yellow) are the satellite peaks of  $\text{Fe } 2p_{3/2}$  (blue) and  $2p_{1/2}$  (brown), respectively.

conductivities of 450, 610, and 802  $\mu\text{S}$ , respectively. Figure S11 D–F, Supporting Information, shows that for  $\text{Fe}^{3+}$ , the values were 28.9, 32.58, and 34.28  $\text{mg g}^{-1}$  for initial conductivities of 450, 610, and 802  $\mu\text{S}$ , respectively. It was observed that the adsorption capacities of EAIERs electrodes increased with an increase in the concentration of ions (Figure 4B,C, and Figures S8, S9, and S11, Supporting Information). The observed results, comparable with other reported graphenic composites, revealed that our material exhibited improved adsorption capacity than bare rGO (approximately five times higher than reported) (Table 2).

Further, change in morphology, and chemical composition of the electrode surface, after one electrochemical adsorption cycle was investigated by SEM energy dispersive spectroscopy (EDS) (Figure S12, Supporting Information) and X-ray photoelectron spectroscopy (XPS) analysis (Figure 5), respectively. Before performing these experiments, electrodes were kept in a solution containing  $\text{MgCl}_2$  and  $\text{FeCl}_3$  for a long time until adsorption equilibrium was achieved. Subsequently, they were washed with deionized water to remove the physisorbed ions. Elemental composition, after electroadsorption of  $\text{MgCl}_2$  on the electrode surface, was determined by EDS measurements, and the results are shown in Figure S12A,B, Supporting Information.  $\text{Mg}^{2+}$  and  $\text{Cl}^-$  were adsorbed on cathode and anode, respectively. The inset of Figure S12, Supporting Information, shows the EDS elemental mapping of the ions after physisorption.

Figure 5 shows the XPS survey spectra of both anodic and cathodic EAIERs electrodes before and after the adsorption of  $\text{FeCl}_3$ . In the XPS survey spectra, no significant changes were observed in the binding energies of carbon, nitrogen, oxygen, and fluorine of both cathode and anode, even after electrochemical adsorption. The XPS survey spectra (Figure 5A) and deconvoluted XPS spectra (Figure 5B) revealed the enhanced intensity of  $\text{Fe}^{3+}$  and  $\text{Cl}^-$  ions at cathode and anode, respectively.

However, small amounts of  $\text{Cl}^-$  on cathode and  $\text{Fe}^{3+}$  on anode were detected at the electrodes, which might be attributed to physisorption.

The electrode's stability during electrochemical measurements is crucial in CDI technology, as adsorption/desorption occurs continuously. Thus, a cyclability test was performed by measuring continuous CV in a 1 M NaCl solution at a scan rate of 50  $\text{mV s}^{-1}$ . Figure S13, Supporting Information, depicts CV cycles of +ve and -ve EAIERs electrodes, which revealed that the electrode's adsorption/desorption occurred at the same rate for 400 cycles. CV cycles of both the electrodes exhibited nearly the same current in the anodic and cathodic sweep, demonstrating the electrode's electrochemical stability. Therefore, it can be concluded that no leaching or corrosion occurred on the electrode surface during the desalination process.

The present work describes the preparation of CDI electrodes via in situ polymerization of styrene on rGO to create a single molecular construct for excellent electroadsorption and selective ion permeation. The functionalization of nanostructured rGO–PS composite resulted in positively and negatively charged EAIERs. These molecular constructs preserved the active composite material's electronic conductivity, comparable to bare rGO, thereby promoting faster non-Faradaic charge transfer at the electrode–electrolyte interface. The synthesized EAIERs molecular constructs were used as CDI electrodes for removal of different cations ( $\text{Fe}^{3+}$ ,  $\text{Mg}^{2+}$ , and  $\text{Na}^+$ ) and anions ( $\text{Cl}^-$ ,  $\text{NO}_3^-$ ,  $\text{F}^-$ , and  $\text{SO}_4^{2-}$ ). The electroadsorption capacity of EAIERs electrode was  $\approx 15.93 \text{ mg g}^{-1}$  for  $\text{Cl}^-$  using 802  $\mu\text{S}$  NaCl solution in lab-scale experiments, the highest observed so far in comparable situations. This occurs as the electrode material has a large electrochemical surface area with a hierarchically porous structure and low interfacial charge transfer resistance. These EAIERs electrodes also exhibited high electroadsorption performance, fast deionization rate, and good regeneration



capability. Thus, we believe that this electrode fabrication methodology could lead to improving the existing membrane-based CDI technology. Molecular construction gives new generation CDI electrodes with enhanced capacity for cost-effective brackish water desalination.

## Experimental Section

**Materials and Chemicals Used:** Natural graphite flakes (95% of carbon) were obtained from Active Carbon India Pvt. Ltd. Ammonia ( $\text{NH}_3$ , 30%), hydrazine hydrate ( $\text{N}_2\text{H}_4$ ), sulfuric acid ( $\text{H}_2\text{SO}_4$ , 95–98%), and hydrochloric acid ( $\text{HCl}$ , 36%) were procured from Rankem Chemicals Pvt. Ltd., India. Phosphorus pentoxide ( $\text{P}_2\text{O}_5$ , 95%), and hydrogen peroxide ( $\text{H}_2\text{O}_2$ , 98%), were purchased from SD Fine Chemicals Pvt. Ltd., India. Merck, India. Potassium permanganate ( $\text{KMnO}_4$ , 98.5%), and potassium peroxydisulfate ( $\text{K}_2\text{S}_2\text{O}_8$ , 98%), were procured from Sisco Research Laboratories Pvt. Ltd., India. Styrene monomer ( $\text{C}_8\text{H}_8$ ) was purchased from Avra Synthesis Pvt. Ltd., India. Nitric acid ( $\text{HNO}_3$ , 65–68%) and sodium hydroxide ( $\text{NaOH}$ ) were purchased from Merck, India. Acetone, sodium chloride ( $\text{NaCl}$ ), magnesium chloride ( $\text{MgCl}_2$ ), ferric chloride ( $\text{FeCl}_3$ ), sodium nitrate ( $\text{NaNO}_3$ ), sodium fluoride, and sodium sulfate were purchased from Loba Chemie, India.

All chemicals were of analytical grade and were used as received without further purification. Glassware was cleaned thoroughly with aqua regia ( $\text{HCl}:\text{HNO}_3$ , 3:1 vol%), rinsed with deionized water, and dried in an oven before use. Deionized water was used for the swelling. All solutions and suspensions were prepared in deionized water unless otherwise mentioned.

**Preparation of Graphene Oxide:** GO was synthesized from graphite powder using modified Hummer's method.<sup>[53]</sup> Graphite powder (2 g) was oxidized in a hot solution (100 °C) of concentrated  $\text{H}_2\text{SO}_4$  (25 mL) containing  $\text{K}_2\text{S}_2\text{O}_8$  (4 g) and  $\text{P}_2\text{O}_5$  (4 g). The resulting dark blue mixture was thermally isolated and slowly cooled to room temperature for 6 h. The mixture was diluted to 200 mL and filtrated subsequently with a Whatman filter paper, and finally, the filtrated product was dried overnight at 60 °C in an oven. The preoxidized graphite powder (2 g) was added to 92 mL of cold  $\text{H}_2\text{SO}_4$  (0 °C), to which  $\text{KMnO}_4$  (12 g) was added gradually under continuous stirring in an ice-bath. After 15 min,  $\text{NaNO}_3$  (2 g) was added to the mixture. The solution was further stirred for 2 h at 35 °C, and distilled water (200 mL) was added to it. The reaction was stopped after adding a solvent mixture containing 300 mL distilled water and 10 mL  $\text{H}_2\text{O}_2$  (30%). The product was washed with  $\text{HCl}$  (1:10) and further with water, and finally, suspended in distilled water. The brown dispersion was extensively dialyzed to remove residual metal ions and acids. Subsequently, the dispersion was sonicated (300 W) for 2 h, aiming for better exfoliation of GO sheets. However, unexfoliated graphite oxide was removed by centrifugation. UV–vis and Raman spectroscopy techniques were performed as spectroscopic characterization of GO, and it was studied further by high-resolution transmission electron microscopy (HRTEM).

**Preparation of Reduced Graphene Oxide:** At first, as-synthesized freeze-dried GO of 1 g was taken and dispersed in 1000 mL of deionized water. The GO solution was further mixed with a solvent mixture of ammonia and aqueous potassium hydroxide to adjust the alkalinity ( $\text{pH} \approx 10$ ) of the GO dispersion, and the resulting solution was kept under continuous ultrasonication for 1 h. Ultrasound created an exfoliation of the lamellar GO structure, and this further leads to electrostatic repulsion between the interlayers of the lamellar structure. By this process, stacked layers were peeled off, and the authors obtained a uniform or homogeneous dispersion of GO. Subsequently, 1 mL  $\text{N}_2\text{H}_4$  solution was added to the above dispersion under stirring conditions. Further, the solution was stirred in an oil-bath, where the temperature was set to 95 °C. The solution was refluxed overnight under this condition.<sup>[54]</sup> After completion of the reaction, the color of GO suspension was converted from brown to black, which suggested the formation of rGO. The resulting suspension was filtered and washed several times with deionized water. The washed

solid rGO was dried under a vacuum. A small amount of solid rGO was dispersed in deionized water by ultrasonication. Finally, this dispersion was used for the synthesis of the rGO–PS composite.

**Activation of Styrene:** Styrene ( $\text{C}_8\text{H}_8$ , chemically pure) was alternately washed thrice with 0.5 M  $\text{NaOH}$  and deionized water to remove the polymerization inhibitor. Activated styrene was further used for the polymerization process.

**Synthesis Protocol of an Integrated Electro-Adsorbent Ion-Exchange Resin Composite:** Detailed synthesis protocol of both GO and rGO is described in the Experimental Section. The characterization data of GO are shown in Figure S1, Supporting Information. Before starting the polymerization process, as-prepared rGO (1 g), activated styrene monomer, and divinylbenzene were taken in the ratio of 10:1:0.1 (in wt%) in 25 mL of deionized water, and the mixture was ultrasonicated for 10 min to obtain a uniform dispersion. The polymerization process was further carried out in an inert atmosphere (using  $\text{N}_2$  gas). Under this condition, the solution was stirred for 15 min, and 320 mg of  $\text{K}_2\text{S}_2\text{O}_8$  was added successively to the reaction mixture. Initially, the reaction mixture was stirred at room temperature for 30 min; after that, the temperature of the solution mixture was increased gradually to 70 °C and maintained at the same temperature for 1 h. The temperature was further increased to 80–85 °C and kept the solution for 12 h under the same condition. Finally, the temperature was raised again to 90–95 °C and kept there for another 2 h. After completion of the reaction, rGO–PS composite was washed with hot deionized water and dried overnight at 90 °C in a hot air oven.

For synthesizing anionic EAIERs (–ve EAIERs), anchoring of chloromethyl groups to the network of the polymer composite (rGO–PS) was essential. For this, the Friedel–Craft alkylation reaction was performed. Subsequently, the polymer composite (1 g) and chloromethylmethylether (3 mL) were mixed in 10 mL deionized water, and the mixture was allowed to stir for 2 h at room temperature. Afterward,  $\text{ZnCl}_2$  ( $\approx 380$  mg) was added to the reaction mixture, and the mixture was stirred for 12 h at 35–38 °C. The chloromethylated product was washed with acetone several times and dried at 60 °C overnight. The obtained product was allowed to swell by immersing in 1,2-dichloromethane for 2 h. Subsequently, trimethylamine hydrochloride (1 g) was added to the resultant mixture, and the reaction was continued for the next 6 h at room temperature. The final chloro-aminated product (rGO–PS– $\text{CH}_2\text{–N}^+(\text{CH}_3)_3\text{Cl}^-$  or –ve EAIERs) was dried overnight at 60 °C.<sup>[55]</sup>

To synthesize cationic EAIERs (+ve EAIERs), rGO–PS composite (1 g) was dispersed in 20 mL of 4 M  $\text{H}_2\text{SO}_4$ , and the dispersion was stirred for 24 h at 100 °C. After completion of this reaction, the rGO–PS– $\text{SO}_3^-\text{H}^+$  (+ve EAIERs) was formed, and the final product was dried in a hot air oven at 60 °C.<sup>[56]</sup>

**Preparation of Electrodes:** To fabricate the electrodes using as-prepared materials, EAIERs (300.3 mg) and 15 wt% of PVDF were dispersed in DMF, and the resulting solution was stirred to prepare a homogeneous viscous slurry. It was coated on a graphite sheet ( $\approx 250$   $\mu\text{m}$  thickness), and the electrode was kept in an electrode coater for curing. Finally, the coated sheet was immersed in DI water overnight. A lab-scale CDI batch experiment was performed using a single pair of oppositely charged EAIERs electrodes (size  $5 \times 3$   $\text{cm}^2$ ). Furthermore, the conventional CDI electrodes prepared using CMF–CNC (422.4 mg) as the carbon source were fabricated using the above procedure.

**Capacitive Deionization Set-Up:** A CDI set-up was prepared with a two-electrode configuration using –ve EAIER (anode) and +ve EAIER (cathode), and an interelectrode spacing of  $\approx 0.2$  mm was maintained with a nylon membrane. This two-electrode configuration was immersed in a 100 mL beaker containing 85 mL of saline water with different ions. The initial conductivity of the solution was maintained as 450, 610, and 802  $\mu\text{S}$ , in separate experiments. By applying a potential ( $\approx 1.2$ – $1.8$  V DC) to the electrodes, the cations and anions of the input feed water got adsorbed electrostatically on the cathode and anode, respectively. This process was continued until the electrodes become saturated, and the system attained equilibrium. The regeneration (desorption) was conducted by reversing the polarity of electrodes, where all the adsorbed

ions were desorbed. The same surface was used further for the next set of adsorption–desorption cycles. The maximum adsorption capacity of the material was calculated from the equilibrium adsorption curve. The temperature of the solution was maintained at  $\approx 23\text{--}25^\circ\text{C}$  during the adsorption and desorption process.

The electroadsorption capacity ( $Q$ ,  $\text{mg g}^{-1}$ ) of electrodes was calculated by using the formula:

$$Q = (C_i - C_f) \times V / m \quad (1)$$

where  $C_i$  and  $C_f$  were initial and final concentrations of the solution ( $\text{mg L}^{-1}$ ),  $V$  was the volume of the solution (mL), and  $m$  was the total mass of the electrodes (in g).

**Instrumentation:** Morphological studies of the electrode surface, elemental analysis, and elemental mapping were carried out using a scanning electron microscope equipped with energy dispersive analysis of X-rays (EDAX or EDS) (FEI Quanta 200). Also, HRSEM images of the electrode materials were obtained through Thermo Scientific Verios G4 UC SEM. The HRTEM images of the electrodes were obtained with JEOL 3010 (JEOL, Japan), which was operated at 200 keV and before HRTEM measurements, the samples were drop-casted on carbon-coated copper grids and allowed to dry under ambient conditions. XPS measurements were performed using ESCA Probe TPD of Omicron Nanotechnology with polychromatic Mg K $\alpha$  as the X-ray source ( $h\nu = 1253.6\text{ eV}$ ), and the binding energy was calibrated with respect to C 1s at 284.5 eV. Raman spectra were obtained with a WITec GmbH, Alpha-SNOM alpha 300 S confocal Raman microscope having a 532-nm laser as the excitation source. A PerkinElmer Lambda 25 spectrophotometer was used to measure the UV–vis spectral feature of the sample. Raman spectra of GO were collected by a confocal Raman spectroscopy (WITec GmbH CRM200). IR spectra of electrode materials were taken by PerkinElmer FT-IR spectrometer. The Eyela Freeze Dryer (Model No: FDU-1200) was used for drying the sample.

The Eutech Cyber scan PC650 multiparameter monitor (Thermo Scientific, India) was used for ionic conductivity measurement. The electrochemical capacitive behavior of EAIRs was determined by CV using CH Electrochemical Analyzer (CH 600A). The CV was performed at various scan rates ( $1\text{--}1000\text{ mV s}^{-1}$ ) in a potential range of  $-1.0$  to  $+1.0\text{ V}$ . The specific capacitance was calculated from the CV curve based on the following equation:

$$C_s = \left( \frac{1}{mR\Delta V} \right) \times \int I(V) dV \quad (2)$$

where  $C_s$  was the specific capacitance,  $m$  was the mass of the active material,  $R$  was the scan rate,  $dV$  was the potential window of scanning, and  $\int I(V) dV$  was the integral area under the CV curve. The electrochemical capacitive behavior of EAIRs was determined by CV. All electrochemical measurements were carried out at room temperature in a three-electrode cell with  $1\text{ M}$  aqueous NaCl solution. An electrochemical cell with three-electrode configuration was adopted with an rGO–PS-coated graphite sheet, Ag/AgCl, and Pt mesh used as working, reference, and counter electrode, respectively.

## Supporting Information

Supporting Information is available from the Wiley Online Library or from the author.

## Acknowledgements

The authors thank the Department of Science and Technology (DST) and Nano Mission of India's Government for constantly supporting their research program on nanomaterials. M.R.I. and A.C. thank the Council of Scientific & Industrial Research (CSIR) for research fellowships. P.S., B.M., S.C., and T.A. thank IIT Madras for their research fellowships.

## Conflict of Interest

The authors declare no conflict of interest.

## Keywords

capacitive deionization, desalination, ion-exchange resins, reduced graphene oxides, water purification

Received: November 16, 2020

Revised: December 25, 2020

Published online:

- [1] A. Y. Hoekstra, T. O. Wiedmann, *Science* **2014**, *344*, 1114.
- [2] J. Schewe, J. Heinke, D. Gerten, I. Haddeland, N. W. Arnell, D. B. Clark, R. Dankers, S. Eisner, B. M. Fekete, F. J. Colón-González, S. N. Gosling, H. Kim, X. Liu, Y. Masaki, F. T. Portmann, Y. Satoh, T. Stacke, Q. Tang, Y. Wada, D. Wisser, T. Albrecht, K. Frieler, F. Piontek, L. Warszawski, P. Kabat, *Proc. Natl. Acad. Sci. U. S. A.* **2014**, *111*, 3245.
- [3] N. Pugazhenthiran, S. Sen Gupta, A. Prabhath, M. Manikandan, J. R. Swathy, V. K. Raman, T. Pradeep, *ACS Appl. Mater. Interfaces* **2015**, *7*, 20156.
- [4] M. A. Shannon, P. W. Bohn, M. Elimelech, J. G. Georgiadis, B. J. Mariñas, A. M. Mayes, *Nature* **2008**, *452*, 301.
- [5] S. S. Gupta, M. R. Islam, T. Pradeep, in *Advances in Water Purification Techniques* (Ed: S. Ahuja), Elsevier, Amsterdam **2019**, p. 165.
- [6] A. Nagar, T. Pradeep, *ACS Nano* **2020**, *14*, 6420.
- [7] S. Kumar, R. R. Nair, P. B. Pillai, S. N. Gupta, M. A. R. Iyengar, A. K. Sood, *ACS Appl. Mater. Interfaces* **2014**, *6*, 17426.
- [8] A. A. Kumar, A. Som, P. Longo, C. Sudhakar, R. G. Bhui, S. S. Gupta, Anshup, M. U. Sankar, A. Chaudhary, R. Kumar, T. Pradeep, *Adv. Mater.* **2017**, *29*, 1604260.
- [9] K. G. Zhou, K. S. Vasu, C. T. Cherian, M. Neek-Amal, J. C. Zhang, H. Ghorbanfekr-Kalashami, K. Huang, O. P. Marshall, V. G. Kravets, J. Abraham, Y. Su, A. N. Grigorenko, A. Pratt, A. K. Geim, F. M. Peeters, K. S. Novoselov, R. R. Nair, *Nature* **2018**, *559*, 236.
- [10] Y. Han, Z. Xu, C. Gao, *Adv. Funct. Mater.* **2013**, *23*, 3693.
- [11] H. Wang, X. Mi, Y. Li, S. Zhan, *Adv. Mater.* **2020**, *32*, 1806843.
- [12] S. Porada, R. Zhao, A. van der Wal, V. Presser, P. M. Biesheuvel, *Prog. Mater. Sci.* **2013**, *58*, 1388.
- [13] N. R. Glavin, R. Rao, V. Varshney, E. Bianco, A. Apte, A. Roy, E. Ringe, P. M. Ajayan, *Adv. Mater.* **2020**, *32*, 1904302.
- [14] Z.-Y. Yang, L.-J. Jin, G.-Q. Lu, Q.-Q. Xiao, Y.-X. Zhang, L. Jing, X.-X. Zhang, Y.-M. Yan, K.-N. Sun, *Adv. Funct. Mater.* **2014**, *24*, 3917.
- [15] K. Xiao, D. Jiang, R. Amal, D.-W. Wang, *Adv. Mater.* **2018**, *30*, 1800400.
- [16] C. Zhang, B. Anasori, A. Seral-Ascaso, S.-H. Park, N. McEvoy, A. Shmeliov, G. S. Duesberg, J. N. Coleman, Y. Gogotsi, V. Nicolosi, *Adv. Mater.* **2017**, *29*, 1702678.
- [17] Q. Li, Y. Zheng, D. Xiao, T. Or, R. Gao, Z. Li, M. Feng, L. Shui, G. Zhou, X. Wang, Z. Chen, *Adv. Sci.* **2020**, *7*, 2002213.
- [18] H. Yin, S. Zhao, J. Wan, H. Tang, L. Chang, L. He, H. Zhao, Y. Gao, Z. Tang, *Adv. Mater.* **2013**, *25*, 6270.
- [19] A. C. Arulrajana, D. L. Ramasamy, M. Sillanpää, A. van der Wal, P. M. Biesheuvel, S. Porada, J. E. Dykstra, *Adv. Mater.* **2019**, *31*, 1806937.
- [20] J. Kim, M. S. Choi, K. H. Shin, M. Kota, Y. Kang, S. Lee, J. Y. Lee, H. S. Park, *Adv. Mater.* **2019**, *31*, 1803444.
- [21] J. Benson, I. Kovalenko, S. Boukhalfa, D. Lashmore, M. Sanghadasa, G. Yushin, *Adv. Mater.* **2013**, *25*, 6625.

- [22] M. Wang, X. Xu, J. Tang, S. Hou, M. S. A. Hossain, L. Pan, Y. Yamauchi, *Chem. Commun.* **2017**, 53, 10784.
- [23] S. Dutta, S.-Y. Huang, C. Chen, J. E. Chen, Z. A. Allothman, Y. Yamauchi, C.-H. Hou, K. C. W. Wu, *ACS Sustainable Chem. Eng.* **2016**, 4, 1885.
- [24] X. Xu, A. E. Allah, C. Wang, H. Tan, A. A. Farghali, M. H. Khedr, V. Malgras, T. Yang, Y. Yamauchi, *Chem. Eng. J.* **2019**, 362, 887.
- [25] Z. Wang, X. Xu, J. Kim, V. Malgras, R. Mo, C. Li, Y. Lin, H. Tan, J. Tang, L. Pan, Y. Bando, T. Yang, Y. Yamauchi, *Mater. Horiz.* **2019**, 6, 1433.
- [26] H. Wang, D. Zhang, T. Yan, X. Wen, L. Shi, J. Zhang, *J. Mater. Chem.* **2012**, 22, 23745.
- [27] Z. Wang, B. Dou, L. Zheng, G. Zhang, Z. Liu, Z. Hao, *Desalination* **2012**, 299, 96.
- [28] Q. Dong, G. Wang, B. Qian, C. Hu, Y. Wang, J. Qiu, *Electrochim. Acta* **2014**, 137, 388.
- [29] H. Li, S. Liang, J. Li, L. He, *J. Mater. Chem. A* **2013**, 1, 6335.
- [30] D. Zhang, X. Wen, L. Shi, T. Yan, J. Zhang, *Nanoscale* **2012**, 4, 5440.
- [31] H. Wang, D. Zhang, T. Yan, X. Wen, J. Zhang, L. Shi, Q. Zhong, *J. Mater. Chem. A* **2013**, 1, 11778.
- [32] H. Li, Z. Y. Leong, W. Shi, J. Zhang, T. Chen, H. Y. Yang, *RSC Adv.* **2016**, 6, 11967.
- [33] X. Gu, Y. Yang, Y. Hu, M. Hu, C. Wang, A. C. S. Sustain, *Chem. Eng.* **2015**, 3, 1056.
- [34] P. Liu, T. Yan, L. Shi, H. S. Park, X. Chen, Z. Zhao, D. Zhang, *J. Mater. Chem. A* **2017**, 5, 13907.
- [35] B. Jia, L. Zou, *Chem. Phys. Lett.* **2012**, 548, 23.
- [36] M. Lu, J.-Y. Liu, J. Cheng, S.-P. Wang, J.-M. Yang, *Wuli Huaxue Xuebao* **2014**, 30, 2263.
- [37] Q. Ren, G. Wang, T. Wu, X. He, J. Wang, J. Yang, C. Yu, J. Qiu, *Ind. Eng. Chem. Res.* **2018**, 57, 6417.
- [38] H. Wang, T. Yan, P. Liu, G. Chen, L. Shi, J. Zhang, Q. Zhong, D. Zhang, *J. Mater. Chem. A* **2016**, 4, 4908.
- [39] Y. Zhang, L. Chen, S. Mao, Z. Sun, Y. Song, R. Zhao, *J. Colloid Interface Sci.* **2019**, 536, 252.
- [40] X. Xu, L. Pan, Y. Liu, T. Lu, Z. Sun, D. H. C. Chua, *Sci. Rep.* **2015**, 5, 8458.
- [41] Y. Oren, *Desalination* **2008**, 228, 10.
- [42] P. M. Biesheuvel, R. Zhao, S. Porada, A. van der Wal, *J. Colloid Interface Sci.* **2011**, 360, 239.
- [43] P. M. Biesheuvel, Y. Fu, M. Z. Bazant, *Phys. Rev. E* **2011**, 83, 061507.
- [44] R. Zhao, P. M. Biesheuvel, A. van der Wal, *Energy Environ. Sci.* **2012**, 5, 9520.
- [45] H. Yang, J.-S. Li, X. Zeng, *ACS Appl. Nano Mater.* **2018**, 1, 2763.
- [46] N. Wu, X. She, D. Yang, X. Wu, F. Su, Y. Chen, *J. Mater. Chem.* **2012**, 22, 17254.
- [47] Y. Gong, D. Li, Q. Fu, C. Pan, *Prog. Nat. Sci.* **2015**, 25, 379.
- [48] J. H. Jang, S. Yoon, B. H. Ka, Y.-H. Jung, S. M. Oh, *J. Electrochem. Soc.* **2005**, 152, A1418.
- [49] S. Fletcher, V. J. Black, I. Kirkpatrick, *J. Solid State Electrochem.* **2014**, 18, 1377.
- [50] C.-W. Huang, C.-H. Hsu, P.-L. Kuo, C.-T. Hsieh, H. Teng, *Carbon* **2011**, 49, 895.
- [51] J. Cha, J. Kim, S. Ryu, S. H. Hong, *Composites, Part B* **2019**, 173, 106976.
- [52] R. Kumar, S. Sen Gupta, S. Katiyar, V. K. Raman, S. K. Varigala, T. Pradeep, A. Sharma, *Carbon* **2016**, 99, 375.
- [53] N. I. Zaaba, K. L. Foo, U. Hashim, S. J. Tan, W.-W. Liu, C. H. Voon, *Procedia Eng.* **2017**, 184, 469.
- [54] C. K. Chua, M. Pumera, *Chem. Soc. Rev.* **2014**, 43, 291.
- [55] Y. Li, F. Yu, W. He, W. Yang, *J. Appl. Polym. Sci.* **2015**, 132.
- [56] Y. Yao, L. Ji, Z. Lin, Y. Li, M. Alcoutlabi, H. Hamouda, X. Zhang, *ACS Appl. Mater. Interfaces* **2011**, 3, 3732.
- [57] H. Li, T. Lu, L. Pan, Y. Zhang, Z. Sun, *J. Mater. Chem.* **2009**, 19, 6773.
- [58] Z. Li, B. Song, Z. Wu, Z. Lin, Y. Yao, K.-S. Moon, C. P. Wong, *Nano Energy* **2015**, 11, 711.
- [59] A. G. El-Deen, R. M. Boom, H. Y. Kim, H. Duan, M. B. Chan-Park, J.-H. Choi, *ACS Appl. Mater. Interfaces* **2016**, 8, 25313.
- [60] H. Li, L. Pan, C. Nie, Y. Liu, Z. Sun, *J. Mater. Chem.* **2012**, 22, 15556.
- [61] Z. Wang, L. Yue, Z.-T. Liu, Z.-H. Liu, Z. Hao, *J. Mater. Chem.* **2012**, 22, 14101.
- [62] A. S. Yasin, H. O. Mohamed, I. M. A. Mohamed, H. M. Mousa, N. A. M. Barakat, *Sep. Purif. Technol.* **2016**, 171, 34.
- [63] A. G. El-Deen, N. A. M. Barakat, H. Y. Kim, *Desalination* **2014**, 344, 289.
- [64] B. Jia, L. Zou, *Carbon* **2012**, 50, 2315.
- [65] X. Gu, M. Hu, Z. Du, J. Huang, C. Wang, *Electrochim. Acta* **2015**, 182, 183.
- [66] X. Gu, Y. Deng, C. Wang, A. C. S. Sustain, *Chem. Eng.* **2017**, 5, 325.
- [67] A. Amiri, G. Ahmadi, M. Shanbedi, M. Savari, S. N. Kazi, B. T. Chew, *Sci. Rep.* **2015**, 5, 17503.
- [68] Y. Liu, X. Xu, T. Lu, Z. Sun, D. H. C. Chua, L. Pan, *RSC Adv.* **2015**, 5, 34117.
- [69] B. Qian, G. Wang, Z. Ling, Q. Dong, T. Wu, X. Zhang, J. Qiu, *Adv. Mater. Interfaces* **2015**, 2, 1500372/1.
- [70] J. Li, B. Ji, R. Jiang, P. Zhang, N. Chen, G. Zhang, L. Qu, *Carbon* **2018**, 129, 95.
- [71] H.-Y. Lian, S. Dutta, S. Tominaka, Y.-A. Lee, S.-Y. Huang, Y. Sakamoto, C.-H. Hou, W.-R. Liu, J. Henzie, Y. Yamauchi, K. C. W. Wu, *Small* **2018**, 14, 1702054.
- [72] Z. U. Khan, T. Yan, L. Shi, D. Zhang, *Environ. Sci.: Nano* **2018**, 5, 980.
- [73] L. Chang, Y. H. Hu, *J. Colloid Interface Sci.* **2019**, 538, 420.
- [74] J. Feng, Z. Yang, S. Hou, M. Li, R. Lv, F. Kang, Z.-H. Huang, *Colloids Surf., A* **2018**, 547, 134.
- [75] T. Yan, J. Liu, H. Lei, L. Shi, Z. An, H. S. Park, D. Zhang, *Environ. Sci.: Nano* **2018**, 5, 2722.
- [76] X. Zhang, K. Xie, J. Gao, S. Zhang, S. Wang, C. Ma, H. Song, *Desalination* **2018**, 445, 149.
- [77] O. Noonan, Y. Liu, X. Huang, C. Yu, *J. Mater. Chem. A* **2018**, 6, 14272.
- [78] G. Divyapriya, K. K. Vijayakumar, I. Nambi, *Desalination* **2019**, 451, 102.
- [79] T. Gao, Y. Du, H. Li, *Sep. Purif. Technol.* **2019**, 211, 233.

## Supporting Information

**A covalently integrated reduced graphene oxide-ion exchange resin electrode for efficient capacitive deionization**

*Md Rabiul Islam, Soujit Sen Gupta, Sourav Kanti Jana, Pillalamarri Srikrishnarka, Biswajit Mondal, Sudhakar Chennu, Tripti Ahuja, Amrita Chakraborty, and Thalappil Pradeep\**

**Table of Contents**

<b>SL.No</b>	<b>Description</b>	<b>Page</b>
1	Experimental section	2-7
2	IR features of PS, rGO, rGO-PS, and –ve and +ve EAIERs and Comparison of electrode materials efficiency in terms of salt adsorption capacity in mg/g reported in the recent past	8-9
3	Characterization of starting materials and FT-IR spectra of electrode materials in details	10-13
4	Characterization of GO using UV-Vis spectra, Raman spectrum, and TEM	14
5	UV-Vis absorption spectra of polystyrene (PS), rGO, rGO-PS composite and Raman spectra of PS, rGO, and rGO-PS composite	15
6	SEM EDS of rGO-PS functionalized ion exchange resin materials of +ve and –ve EAIERs	16
7	SEM EDS of anode and cathode (before adsorption)	17
8	Variation of specific capacitance vs. scan rate	18
9	Bode impedance for cathode and anode; complex capacitance vs. frequency plot: desorption rate determination for +ve and -ve EAIERs	19
10	Schematic representation of a CDI set-up	20
11	CDI performances of EAIERs electrodes using different cations ( $\text{Na}^+$ , $\text{Mg}^{2+}$ , and $\text{Fe}^{3+}$ ) and anions ( $\text{Cl}^-$ , $\text{NO}_3^-$ , $\text{F}^-$ and $\text{SO}_4^{2-}$ ) with a solution of different conductivities	21
12	The adsorption capacities of covalently integrated EAIERs with NaCl at different solution conductivities	22
13	Electrode repeatability was shown using NaCl solution	23
14	The adsorption capacities of covalently integrated EAIERs with $\text{MgCl}_2$ and $\text{FeCl}_3$ at different solution conductivities	24
15	SEM EDS of $\text{MgCl}_2$ adsorption after single adsorption cycle on cathode and anode	25
16	Cyclic voltammetry of +ve and –ve EAIERs electrode	26

## Experimental section

*Materials and Chemicals used:* Natural graphite flakes (95% of carbon) were obtained from Active Carbon India Pvt. Ltd. Ammonia ( $\text{NH}_3$ , 30%), hydrazine hydrate ( $\text{N}_2\text{H}_4$ ), sulfuric acid ( $\text{H}_2\text{SO}_4$ , 95–98%), and hydrochloric acid ( $\text{HCl}$ , 36%) were procured from Rankem Chemicals Pvt. Ltd., India. Phosphorus pentoxide ( $\text{P}_2\text{O}_5$ , 95%), and hydrogen peroxide ( $\text{H}_2\text{O}_2$ , 98%), were purchased from SD Fine Chemicals Pvt. Ltd., India. Merck, India. Potassium permanganate ( $\text{KMnO}_4$ , 98.5%), and potassium peroxydisulfate ( $\text{K}_2\text{S}_2\text{O}_8$ , 98%), were procured from Sisco Research Laboratories Pvt. Ltd., India. Styrene monomer ( $\text{C}_8\text{H}_8$ ) was purchase from Avra Synthesis Pvt. Ltd., India. Nitric acid ( $\text{HNO}_3$ ) (65–68%) and sodium hydroxide ( $\text{NaOH}$ ) were purchased from Merck, India. Acetone, sodium chloride ( $\text{NaCl}$ ), magnesium chloride ( $\text{MgCl}_2$ ), ferric chloride ( $\text{FeCl}_3$ ), sodium nitrate ( $\text{NaNO}_3$ ), sodium fluoride ( $\text{NaF}$ ), and sodium sulphate ( $\text{Na}_2\text{SO}_4$ ) were purchased from Loba Chemie, India.

All chemicals were of analytical grade and were used as received without further purification. Glassware was cleaned thoroughly with aqua regia ( $\text{HCl}:\text{HNO}_3$ , 3:1 vol%), rinsed with deionized water (DI) water, and dried in an oven before use. Deionized water was used for the swelling. All solutions and suspensions were prepared in deionized (DI) water unless otherwise mentioned.

*Preparation of Graphene oxide (GO):* GO was synthesized from graphite powder using modified Hummer's method.<sup>[49]</sup> Graphite powder (2 g) was oxidized in a hot solution ( $100^\circ\text{C}$ ) of concentrated  $\text{H}_2\text{SO}_4$  (25 mL) containing  $\text{K}_2\text{S}_2\text{O}_8$  (4 g) and  $\text{P}_2\text{O}_5$  (4 g). The resulting dark blue mixture was thermally isolated and slowly cooled to room temperature for 6 h. The mixture was diluted to 200 mL and filtrated subsequently with a Whatman filter paper, and finally, the filtrated product was dried overnight at  $60^\circ\text{C}$  in an oven. The pre-oxidized graphite powder (2 g) was added to 92 mL of cold  $\text{H}_2\text{SO}_4$  ( $0^\circ\text{C}$ ), to which  $\text{KMnO}_4$  (12 g) was added gradually under continuous stirring in an ice-bath. After 15 min,  $\text{NaNO}_3$  (2 g) was added to the mixture. The solution was further stirred for 2 h at  $35^\circ\text{C}$ , and distilled water (200 mL) was added to it.

The reaction was stopped after adding a solvent mixture containing 300 mL distilled water and 10 mL H<sub>2</sub>O<sub>2</sub> (30 %). The product was washed with HCl (1:10) and further with water, and finally, suspended in distilled water. The brown dispersion was extensively dialyzed to remove residual metal ions and acids. Subsequently, the dispersion was sonicated (300 W) for 2 h, aiming for better exfoliation of GO sheets. However, unexfoliated graphite oxide was removed by centrifugation. UV-vis and Raman spectroscopy techniques performed spectroscopic characterization of GO, and it was also studied by HRTEM.

*Preparation of reduced graphene oxide (rGO):* At first, as-synthesized freeze-dried GO of 1 g was taken and dispersed in 1000 mL of deionized water. The GO solution was further mixed with a solvent mixture of ammonia and aqueous potassium hydroxide to adjust the alkalinity (pH~10) of the GO dispersion, and the resulting solution was kept under continuous ultrasonication for 1 hour. Ultrasound created an exfoliation of the lamellar GO structure, and this further leads to electrostatic repulsion between the interlayers of the lamellar structure. By this process, stacked layers were peeled off, and we obtained a GO uniform or homogeneous dispersion. Subsequently, 1 mL hydrazine hydrate solution was added to the above dispersion under stirring conditions. Further, the solution was stirred in an oil bath, where the temperature was set to 95 °C. The solution was refluxed overnight under this condition.<sup>[50]</sup> After completion of the reaction, the color of GO suspension was converted from brown to black, which suggested the formation of rGO. The resulting suspension was filtered and washed several times with deionized water. The washed solid rGO was dried under a vacuum. A small amount of solid rGO was dispersed in deionized water by ultrasonication. Finally, this dispersion was used for the synthesis of the rGO-polystyrene composite.

*Activation of styrene (ST):* Styrene (C<sub>8</sub>H<sub>8</sub>, chemically pure) was alternately washed three times with 0.5 M sodium hydroxide (NaOH) and deionized water to remove the polymerization inhibitor. Activated styrene was further used for the polymerization process.



*Synthesis protocol of an integrated electro-adsorbent-ion exchange resin (EAIERs)*

*composites:* Detailed synthesis protocol of both GO and rGO is described in the experimental section. The characterization data of GO are shown in Figure S1. Before starting the polymerization process, as-prepared rGO (1 g), activated styrene (ST) monomer, and divinylbenzene (DVB) were taken in the ratio of 10:1:0.1 (in wt%) in 25 mL of DI water, and the mixture was ultrasonicated for 10 min to obtain a uniform dispersion. The polymerization process was further carried out in an inert atmosphere (using N<sub>2</sub> gas). Under this condition, the solution was stirred for 15 min, and 320 mg of K<sub>2</sub>S<sub>2</sub>O<sub>8</sub> was added successively to the reaction mixture. Initially, the reaction mixture was stirred at room temperature for 30 min; after that, the temperature of the solution mixture was increased gradually to 70 °C and maintained at the same temperature for 1 h. The temperature was further increased to 80–85 °C and kept the solution for 12 h under the same condition. Finally, the temperature was raised again to 90–95 °C and kept there for another 2 h. After completion of the reaction, rGO-PS composite was washed with hot DI water and dried overnight at 90 °C in a hot air oven.

For synthesizing anionic EAIERs (-ve EAIERs), anchoring of chloromethyl groups to the network of the polymer composite (rGO-PS) is essential. For this, the Friedel-Craft alkylation reaction was performed. Subsequently, the polymer composite (1 g) and chloromethylmethylether (3 mL) were mixed in 10 mL DI water, and the mixture was allowed to stir for 2 h at room temperature. Afterward, ZnCl<sub>2</sub> (~380 mg) was added to the reaction mixture, and the mixture was stirred for 12 h at 35–38 °C. The chloromethylated product was washed with acetone several times and dried at 60 °C overnight. The obtained product was allowed to swell by immersing in 1,2-dichloromethane (DCM) for 2 h. Subsequently, trimethylamine hydrochloride (1 g) was added to the resultant mixture, and the reaction was continued for the next 6 h at room temperature. The final chloro-aminated product (rGO-PS-CH<sub>2</sub>-N<sup>+</sup>(CH<sub>3</sub>)<sub>3</sub>Cl<sup>-</sup> or -ve EAIERs) was dried overnight at 60 °C.<sup>[51]</sup>

To synthesize cationic EAIERs (+ve EAIERs), rGO-PS composite (1 g) was dispersed in 20 mL of 4 M H<sub>2</sub>SO<sub>4</sub>, and the dispersion was stirred for 24 h at 100 °C. After completion of this reaction, the rGO-PS-SO<sub>3</sub><sup>-</sup>H<sup>+</sup> (+ve EAIERs) was formed, and the final product was dried in a hot air oven at 60 °C.<sup>[52]</sup>

*Preparation of electrodes:* To fabricate the electrodes using as-prepared materials, EAIERs (300.3 mg) and 15 wt% of PVDF were dispersed in DMF, and the resulting solution was stirred to prepare a homogeneous viscous slurry. It was coated on a graphite sheet (~250 µm thickness), and the electrode was kept in an electrode coater for curing. Finally, the coated sheet was immersed in DI water overnight. A laboratory-scale CDI batch experiment was performed using a single pair of oppositely charged EAIERs electrodes (size 5 x 3 cm<sup>2</sup>). Furthermore, the conventional CDI electrodes prepared using CMF-CNC (422.4 mg) as the carbon source were fabricated using the above procedure.

*Capacitive deionization set-up:* A CDI set-up was prepared with a two-electrode configuration using -ve EAIER (anode) and +ve EAIER (cathode), and an inter-electrode spacing of ~0.2 mm was maintained with a nylon membrane. This two-electrode configuration was immersed in a 100 mL beaker containing 85 mL of saline water with different ions. The initial conductivity of the solution was maintained as 450, 610, and 802 µS, in separate experiments. By applying a potential (~1.2-1.8 V DC) to the electrodes, the cations and anions of the input feed water got adsorbed electrostatically on the cathode and anode, respectively. This process was continued until the electrodes become saturated, and the system attained an equilibrium. The regeneration (desorption) was conducted by reversing the polarity of electrodes, where all the adsorbed ions were desorbed. The same surface was used further for the next set of adsorption-desorption cycles. The maximum adsorption capacity of the material was calculated from the equilibrium adsorption curve. The temperature of the solution was maintained at ~23-25 °C during the adsorption and desorption process.



The electroadsorption capacity ( $Q$ , mg /g) of electrodes was calculated by using the formula:

$$Q = (C_i - C_f) \times V/m \quad (1)$$

where  $C_i$  and  $C_f$  are initial and final concentrations of the solution (mg/L),  $V$  is the volume of the solution (mL), and  $m$  is the total mass of the electrodes (in g).

*Instrumentation:* Morphological studies of the electrode surface, elemental analysis, and elemental mapping were carried out using a scanning electron microscope equipped with energy dispersive analysis of X-rays (EDAX or energy dispersive spectroscopy, EDS) (FEI Quanta 200). Also, high-resolution scanning electron microscopy images of the electrode materials were obtained through ThermoScientific Verios G4 UC SEM. The high-resolution transmission electron microscopy (HRTEM) images of the electrodes were obtained with JEOL 3010 (JEOL, Japan), which was operated at 200 keV (and before HRTEM measurements, the samples were drop-casted on carbon-coated copper grids and allowed to dry under ambient conditions. X-ray photoelectron spectroscopy (XPS) measurements were performed using ESCA Probe TPD of Omicron Nanotechnology with polychromatic Mg  $K\alpha$  as the X-ray source ( $h\nu = 1253.6$  eV), and the binding energy was calibrated with respect to C 1s at 284.5 eV. Raman spectra were obtained with a WITec GmbH, Alpha-SNOM alpha 300 S confocal Raman microscope having a 532 nm laser as the excitation source. A PerkinElmer Lambda 25 spectrophotometer was used to measure the UV-vis spectral feature of the sample. Raman spectra of GO were collected by a confocal Raman spectroscopy (WiTec GmbH CRM200). IR spectra of electrode materials were taken by PerkinElmer Fourier transform infrared (FT-IR) spectrometer. The Eyela Freeze Dryer (Model No: FDU – 1200) was used for drying the sample.

The Eutech Cyber scan PC650 multiparameter monitor (Thermo Scientific, India) was used for ionic conductivity measurement. The electrochemical capacitive behavior of EAIERs was

determined by cyclic voltammetry (CV) using CH Electrochemical Analyzer (CH 600A). The CV was performed at various scan rates (1 mV/s to 1000 mV/s) in a potential range of -1.0 V to +1.0 V. The specific capacitance was calculated from the CV curve based on the following equation:

$$C_s = \left( \frac{1}{mR\Delta V} \right) \times \int I(V) dV \quad (2)$$

where  $C_s$  is the specific capacitance,  $m$  is the mass of the active material,  $R$  is the scan rate,  $dV$  is the potential window of scanning,  $\int I(V) dV$  which is the integral area under the CV curve. The electrochemical capacitive behavior of EAERs was determined by cyclic voltammetry (CV). All electrochemical measurements were carried out at room temperature in a three-electrode cell with 1 M aqueous NaCl solution. An electrochemical cell with three-electrode configuration was adopted with an rGO-PS-coated graphite sheet, Ag/AgCl, and Pt mesh used as working, reference, and counter electrode, respectively.

**Table 1.** IR features of PS, rGO, rGO-PS, and –ve and +ve EAIERs, with assignments.

Wavenumber (cm <sup>-1</sup> )	Assigned vibrations	Wavenumber (cm <sup>-1</sup> )	Assigned vibrations
3450-3520	O–H stretching	1411	aliphatic C–H in chloromethyl –CH <sub>2</sub> Cl
2850-3035	aliphatic and aromatic C–H stretching	1261	aromatic C–H of Ph–CH <sub>2</sub> Cl groups
1740-1745	C=O stretching of a carboxylic acid group	1224 and 1180	S=O bond of SO <sub>3</sub> H
1631-1638	C=C stretching	1208 and 1154	C–N stretching frequencies of the tertiary amine group
1450	C–H deformation		

**Table 2.** Comparison of electrode materials efficiency in terms of salt adsorption capacity in mg/g reported in the recent past.

Materials	Initial conc. (mg/L)	Ads. capacity (mg/g)	Year of publication/ Reference.
Graphene	86.9	0.88	2012 <sup>[22]</sup>
Graphene	25	1.85	2009 <sup>[53]</sup>
rGO-CA composite	65	3.23	2012 <sup>[23]</sup>
rGO	65	1.8	
AC	65	1.51	
3D Macroporous graphene architectures	~52	3.9	2013 <sup>[27]</sup>
Sulphonated graphite nanosheet	250	8.6	2012 <sup>[31]</sup>
Sponge-templated graphene	106	4.95	2014 <sup>[14]</sup>
rGO- activated carbon nanofiber (rGO-ACF)	400	7.2	2014 <sup>[24]</sup>
Graphene sponge	500	14.9	2015 <sup>[36]</sup>
Microporous graphene	~74	11.86	2015 <sup>[54]</sup>
3D Porous graphene	300	18.43	2016 <sup>[55]</sup>
Graphene/carbon nanotube	500	1.4	2013 <sup>[25]</sup>
rGO-AC composites	~25	2.94	2012 <sup>[56]</sup>
rGOresol (rGO-RF)/rGO-CA	40	3.47	2012 <sup>[57]</sup>
Graphene oxide/ZrO <sub>2</sub>	50	6.3	2016 <sup>[58]</sup>
MnO <sub>2</sub> -Nanorods@graphene	~50	5.01	2014 <sup>[59]</sup>
Sulphonic functional graphite nanosheet	500 µS/cm	8.6	2012 <sup>[60]</sup>
Graphene-Fe <sub>3</sub> O <sub>4</sub> (E-Gr-Fe <sub>3</sub> O <sub>4</sub> )	300 µS/cm	10.3	2015 <sup>[61]</sup>
rGO	300 µS/cm	6.00	
Graphene–chitosan–Mn <sub>3</sub> O <sub>4</sub> composites	100 µS/cm	9.32	2015 <sup>[29]</sup>
	300 µS/cm	12.76	
	500 µS/cm	14.83	
3D Graphene architectures	500	14.7	2016 <sup>[34]</sup>
Anion-exchange polymer layered Graphene composites (A-NRGS)	300 µS/cm	11.3	2017 <sup>[62]</sup>
N-doped rGO sponge composite (NRGS)	300 µS/cm	8.6	
rGO	300 µS/cm	6.2	
Few-layered graphene (HCG)	50 µS/cm	1.72	2015 <sup>[63]</sup>
Highly-crumpled N-doped graphene	50 µS/cm	1.96	

N-doped electrospun GO-carbon nanofiber composite (NG-CNF)	~100 $\mu\text{S}/\text{cm}$	3.91	2015 <sup>[64]</sup>
SO <sub>3</sub> H-graphene-carbon nanofibers	400	9.54	2015 <sup>[65]</sup>
SO <sub>3</sub> H/NH <sub>2</sub> graphene/AC	500	10.3	2014 <sup>[32]</sup>
Hierarchical hole-enhanced 3D graphene	80	8.0	2018 <sup>[66]</sup>
Spherical macroporous, 3D intercalated graphene nano-composite.	$0.5 \times 10^{-3}$ M	5.7	2018 <sup>[67]</sup>
MgAl-Ox/G nanohybrids	500	22.09	2018 <sup>[68]</sup>
3D channel-structured graphene (CSG)	500	13.6	2018 <sup>[33]</sup>
CO <sub>2</sub> activated rGO(AGE)	295	9.6	2019 <sup>[69]</sup>
GO/hierarchical porous carbon	500	6.26	2019 <sup>[35]</sup>
SiO <sub>2</sub> activated GO (GR/NMC)	55.72	7.74	2018 <sup>[70]</sup>
p-phenylenediamine functionalized GO	500	18.4	2018 <sup>[71]</sup>
Meso porous G@MC heterostructured Graphene/Co <sub>3</sub> O <sub>4</sub> composite	~100 $\mu\text{S}/\text{cm}$	7.88	2018 <sup>[72]</sup>
N-doped graphitic carbon polyhedrons	500	24.3	J2018 <sup>[73]</sup>
EAIERS	802 $\mu\text{S}/\text{cm}$	18.63	2018 <sup>[74]</sup>
		17.77	2019 <sup>[75]</sup>
		15.93	<b>2020 (This work)</b>

### Characterization of starting materials

Before starting the electrode fabrication method, graphene oxide (GO) was synthesized (detailed protocol has been provided in the experimental section), and it was characterized through spectroscopy (UV-vis and Raman) and transmission electron microscopy (TEM) techniques. Characterization results are shown in Figure S1. In the UV-vis spectrum, two characteristic features of GO were observed at  $\sim 310$  and  $235$  nm, which are ascribed to the  $\pi^*$  and  $\pi$ - $\pi^*$  resonances, respectively (Figure S1A). The Raman spectrum of the GO sample is shown in Figure S1B, which has two significant peaks at  $1350$  and  $1596\text{ cm}^{-1}$ , corresponding to the D- and G-bands, respectively. Usually, G- and D-bands signify  $\text{sp}^2$  hybridization (graphitic signature of carbon) and disorderiness of the  $\text{sp}^2$  hybridized hexagonal sheet of graphenic carbon, respectively. The G- and D-bands lie in the range of  $\sim 1500$ - $1600\text{ cm}^{-1}$  and  $\sim 1300$ - $1400\text{ cm}^{-1}$ , respectively. The D-band's peak intensity and line-width are larger than the G-band in GO, indicating higher disorder, which could be attributed to intense chemical treatments and/or increased amorphous carbon content (unreacted graphite powder). Thus, the Raman spectrum confirms the presence of a graphitic signature of carbon (in-plane  $\text{sp}^2$  carbon) and defects present in GO sheets ( $\text{sp}^3$  carbon). High-resolution TEM (HRTEM) images of GO at lower and higher magnifications are presented in Figure S1C and Figure S1D, respectively. The HRTEM images revealed a few-layered structure with nearly transparent, wrinkled, and folded GO sheets.

Chemical functionalization of rGO was confirmed using spectroscopic techniques such as UV-vis, Raman, and FT-IR. HRSEM and TEM investigated the electrode material. Energy-dispersive spectroscopy (EDS) analysis further confirmed the chemical composition of the electrode materials. UV-vis spectra of PS, rGO, and rGO-PS are shown in Figure S2A. The characteristic peaks of PS were observed at  $273$  and  $287$  nm, which could be attributed to the

isolated phenyl groups and interactions between them, respectively [Figure S2A(i)].<sup>[76]</sup> A significant peak appeared at 277 nm in Figure S2A(ii), which corresponds to the feature of pristine rGO.<sup>[77]</sup> However, two new prominent peaks at ~270 and ~290 nm were also witnessed for rGO-PS composite, indicating an interaction between rGO and PS. The presence of both rGO and PS features in the UV-vis spectra suggests the formation of the rGO-PS composite [Figure S2A(iii)]. Raman spectra of PS, rGO, and rGO-PS are shown in Figure S2B. Peaks at 846, 898, 980, 1063, 1192, and 1217  $\text{cm}^{-1}$  are similar to the Raman features of PS, as observed in Figure S2B(i).<sup>[78]</sup> The peaks at 980 and 1063  $\text{cm}^{-1}$  correspond to the aromatic C-C stretching of benzene rings of polystyrene. In contrast, mono-substituted benzene rings of polystyrene were confirmed by two peaks observed at 1192 and 1217  $\text{cm}^{-1}$ . Figure S2B(ii) shows the Raman spectrum of bare rGO depicting the characteristic features of G- (1580  $\text{cm}^{-1}$ ) and D- (1331  $\text{cm}^{-1}$ ) bands, which signifies  $\text{sp}^2$  hybridization of graphitic carbons and defect-induced disorder on the  $\text{sp}^2$  hybridized hexagonal sheets of carbon. In Figure S2B(iii), the Raman spectrum of the rGO-PS composite is shown with peaks at 973, 1007, 1105, 1141, 1317, and 1577  $\text{cm}^{-1}$ . In the same spectrum, no significant shift was observed in the peak position of the G-band of rGO-PS, while the position of the D-band showed a considerable change of 14  $\text{cm}^{-1}$  compared to that of pristine rGO. This could be due to the polymeric chains of PS attached to the oxygen-functionalized edges of rGO.

Elemental compositions of both +ve and -ve EAIERs are shown in Figure S3. The SEM EDS of +ve EAIERs confirms C, O, and S as the elements in it (Figure S3A), where the S peak is due to -SO<sub>3</sub> functionality that might be formed after the sulfonation of EAIERs. Similarly, Figure S3B shows the elemental mapping of -ve EAIERs, which confirms carbon and oxygen as the same electrode material's main constituents. The presence of trace amounts of N and Cl is due to the formation of the chloro-aminated product of -ve EAIERs.

The EDS spectra and corresponding elemental maps of both anode (-ve EAIERs) and cathode (+ve EAIERs) are shown in Figure S4A,B. Fluorine was evident in both electrodes due

to PVDF, which was used as a binder (~15 wt%) and active materials (EAIERs) during the fabrication of electrodes on graphite substrates. The presence of C, O, F, and a small amount of N and Cl in EDS confirmed the chemical composition of –ve EAIERs (Figure S4A). The presence of trace amounts of S along with C, O, and F confirmed the chemical composition of +ve EAIERs (Figure S4B). The presence of aluminium (Al) in the EDS spectrum is due to the SEM stub.

Surface charges of both +ve and –ve EAIERs were confirmed by zeta potential measurements. The zeta potential values for +ve and –ve EAIERs were found as -11.1 and -28.4 mV, respectively, and the zeta potential of bare rGO was measured as -24.5 mV. These values further confirm the selective functionalization of both the electrode materials.

### **FT-IR spectra of electrode materials in details**

FT-IR spectrum of PS (Figure 2A) shows a broad peak around 3450-3520  $\text{cm}^{-1}$  due to O–H's stretching, which indicates the presence of hydroxyl groups in the electrode materials. This O–H vibrational feature may be due to either (i) the moisture adsorbed on electrode materials or (ii) the presence of NaOH that was used for the activation of styrene during the polymerization process. A characteristic peak at 3035  $\text{cm}^{-1}$  was observed due to the aromatic C–H stretching vibration. The other signature peaks at 2925 and 2850  $\text{cm}^{-1}$  are ascribed to the asymmetric and symmetric stretching frequencies of aliphatic C–H, respectively. The peaks at 1632 and 1450  $\text{cm}^{-1}$  are due to C =C stretching and C–H deformation, respectively. In addition, the IR spectra of both rGO and rGO-PS are shown in Figure 2B. FT-IR spectrum of rGO has been reported earlier.<sup>[79]</sup> The peaks at 2924 and 2854  $\text{cm}^{-1}$  of rGO are assigned to asymmetric and symmetric stretching of C–H bonds, respectively. The peak at ~1740-1745  $\text{cm}^{-1}$  is associated with C=O stretching of the carboxylic acid group. The peak at ~1634  $\text{cm}^{-1}$  is due to the C=C stretching frequency of rGO. The spectrum of rGO-PS showed a peak at 2968  $\text{cm}^{-1}$ , assigned to aromatic C–H vibration. The characteristic peaks at 2922 and 2852  $\text{cm}^{-1}$  are due to asymmetric and

symmetric stretching of aliphatic C–H, respectively. The peak at  $1631\text{ cm}^{-1}$  is due to the C=C stretching of rGO-PS. A substantial increase in the peak intensity of C=C was observed in the rGO-PS composite, owing to the covalent linkage between rGO and PS, which confirms the rGO-PS composite formation. Figure 2C(iii) shows the FT-IR spectrum of rGO-PS-SO<sub>3</sub>H (+ve EAIERs). Peaks at  $2925$  and  $2852\text{ cm}^{-1}$  are the characteristic features of asymmetric and symmetric stretching frequencies of aliphatic C–H bond of +ve EAIERs, respectively, and the other two peaks at  $1224$  and  $1180\text{ cm}^{-1}$  are associated with the S=O bond of SO<sub>3</sub>H in the same electrode. Figure 2D(ii) displays the IR spectrum after chloromethylation of rGO-PS composite, which showed two peaks at  $2923$  and  $2851\text{ cm}^{-1}$  indicating the C–H stretching (asymmetric and symmetric, respectively) of rGO-PS-CH<sub>2</sub>Cl. The remaining two prominent peaks in the same spectrum at  $1411$  and  $1261\text{ cm}^{-1}$  are assigned to the bending vibrations of aliphatic C–H in chloromethyl –CH<sub>2</sub>Cl and aromatic C–H of Ph–CH<sub>2</sub>Cl groups, respectively. The FT-IR spectrum of rGO-PS-CH<sub>2</sub>–N<sup>+</sup>(CH<sub>3</sub>)<sub>3</sub>Cl<sup>–</sup> (–ve EAIERs) in Figure 2D(iii) has a peak at  $2962\text{ cm}^{-1}$  due to aromatic C–H whereas, peaks at  $2924$  and  $2851\text{ cm}^{-1}$  are due to asymmetric and symmetric vibrations of aliphatic C–H, respectively. The peaks at  $1638$  and  $1632\text{ cm}^{-1}$  confirm the C=C stretching frequency of both –ve EAIERs and rGO-PS-CH<sub>2</sub>Cl, respectively. After the chlorinated product's amination, two new peaks were observed at  $1208$  and  $1154\text{ cm}^{-1}$ , which are assigned to the C–N stretching frequencies of the tertiary amine group in -ve EAIERs.



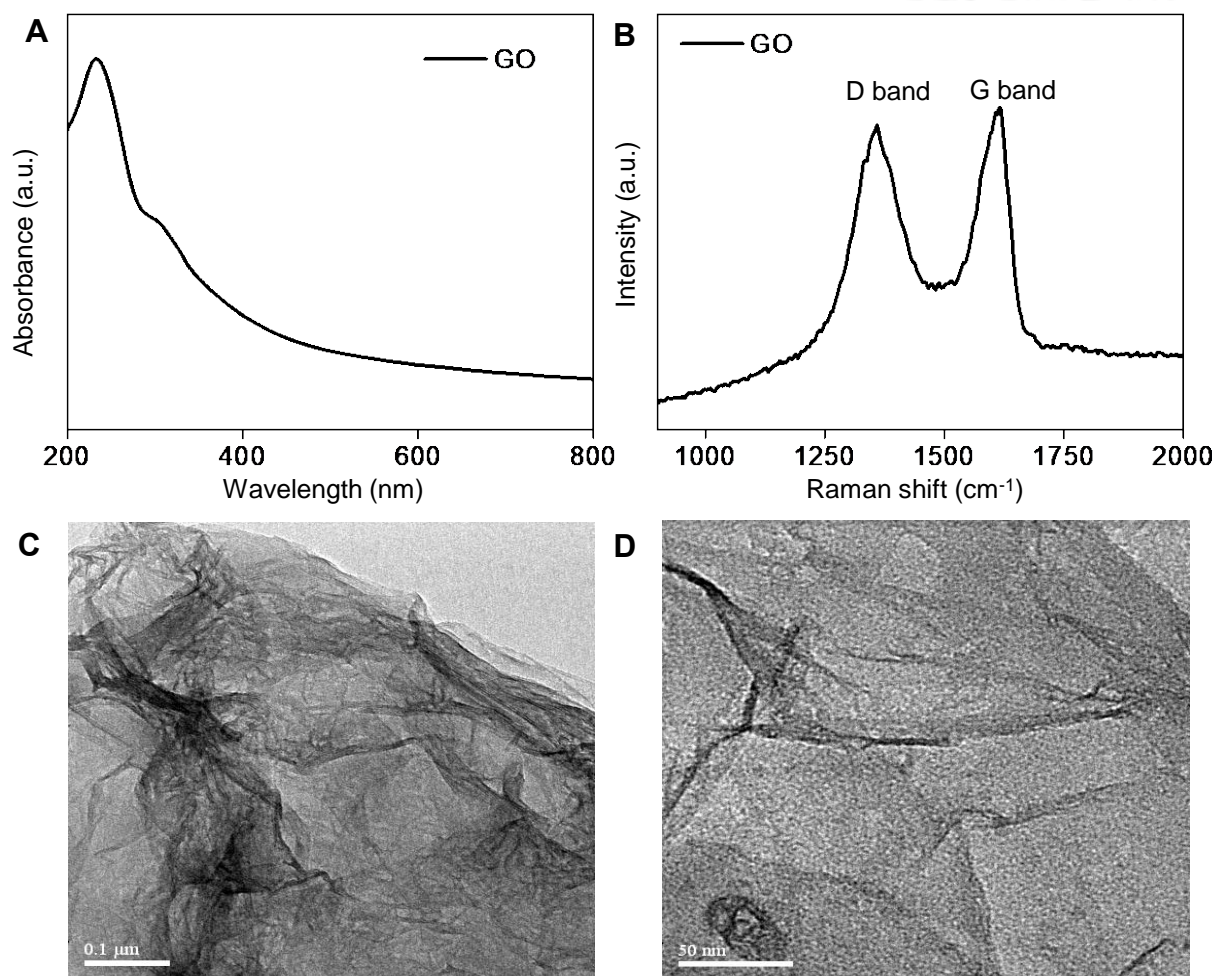


**Figure S1.** (A) UV-vis spectra of aqueous GO dispersions are presented, (B) Raman spectrum showing the presence of D, G bands, (C) and (D) TEM image of the GO at different magnifications (0.1 μm and 50 nm scale bar, respectively).

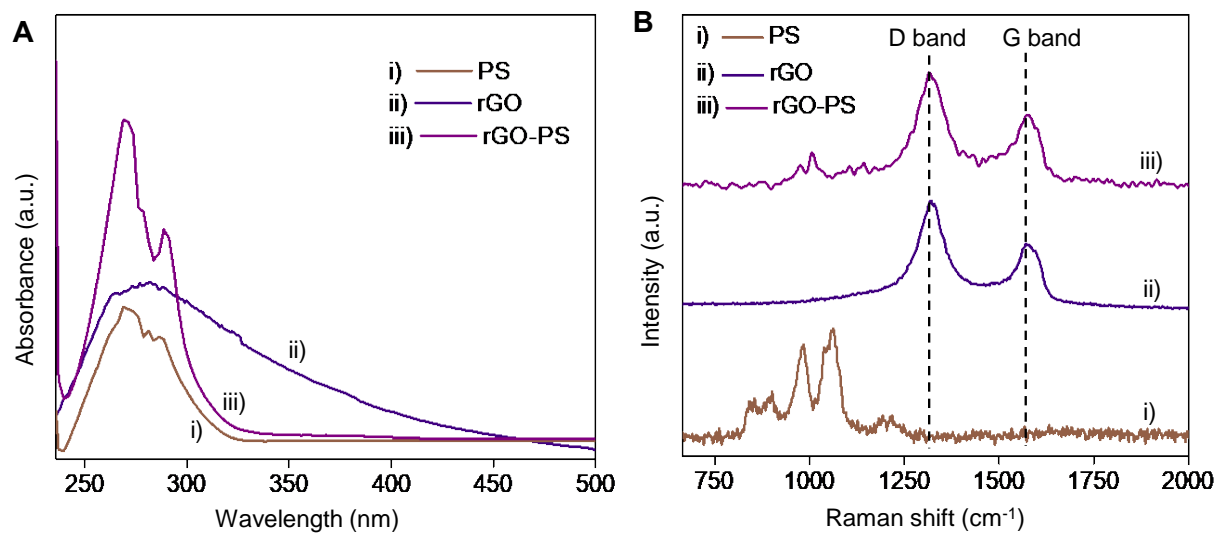


**Figure S2.** (A) UV-Vis absorption spectra of i) polystyrene (PS), ii) rGO, and iii) rGO-PS composite and (B) Raman spectra of i) PS, ii) rGO, and iii) rGO-PS composite.

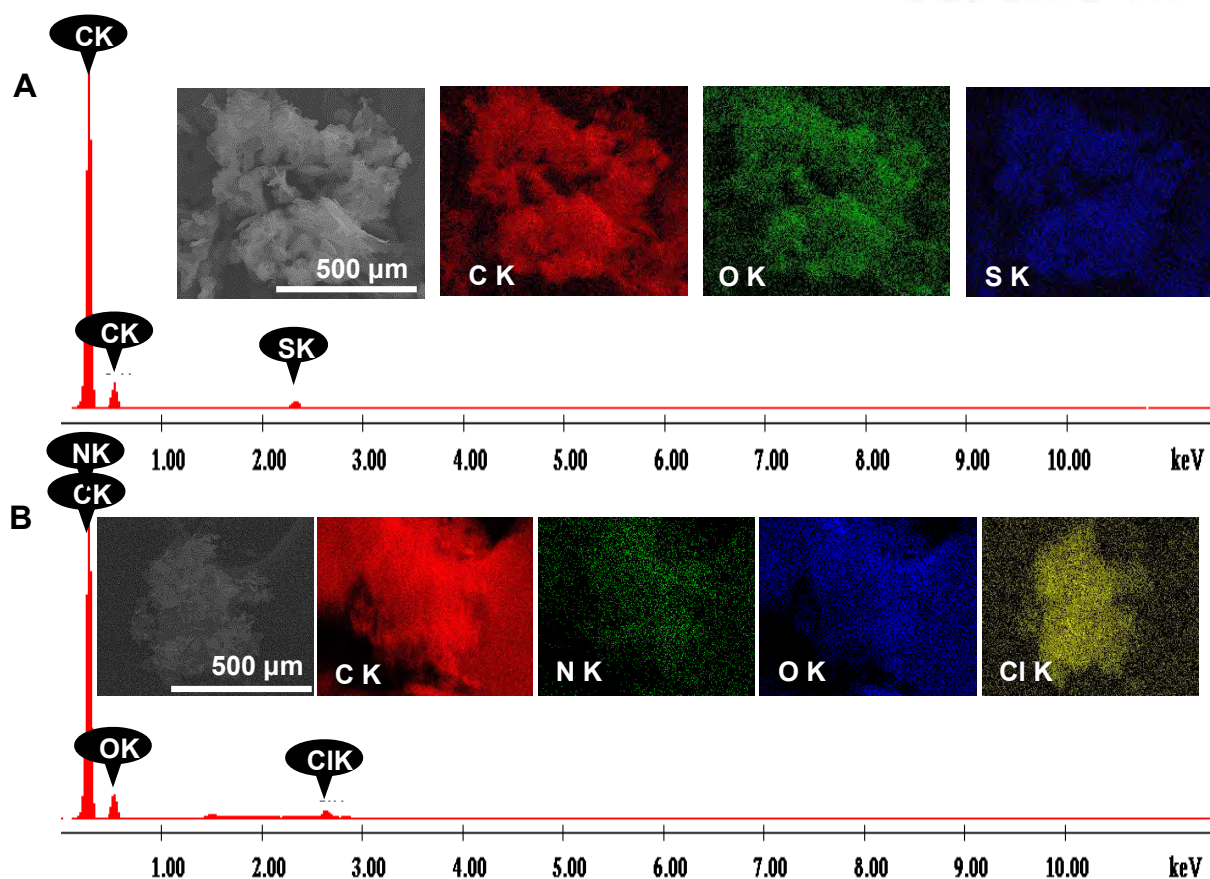


**Figure S3.** SEM EDS of rGO-PS functionalized ion exchange resin materials of (A) +ve EAIERs (cation EAIERs) and (B) -ve EAIERs (anion EAIERs). The corresponding SEM EDS and elemental mapping images are shown in the inset.

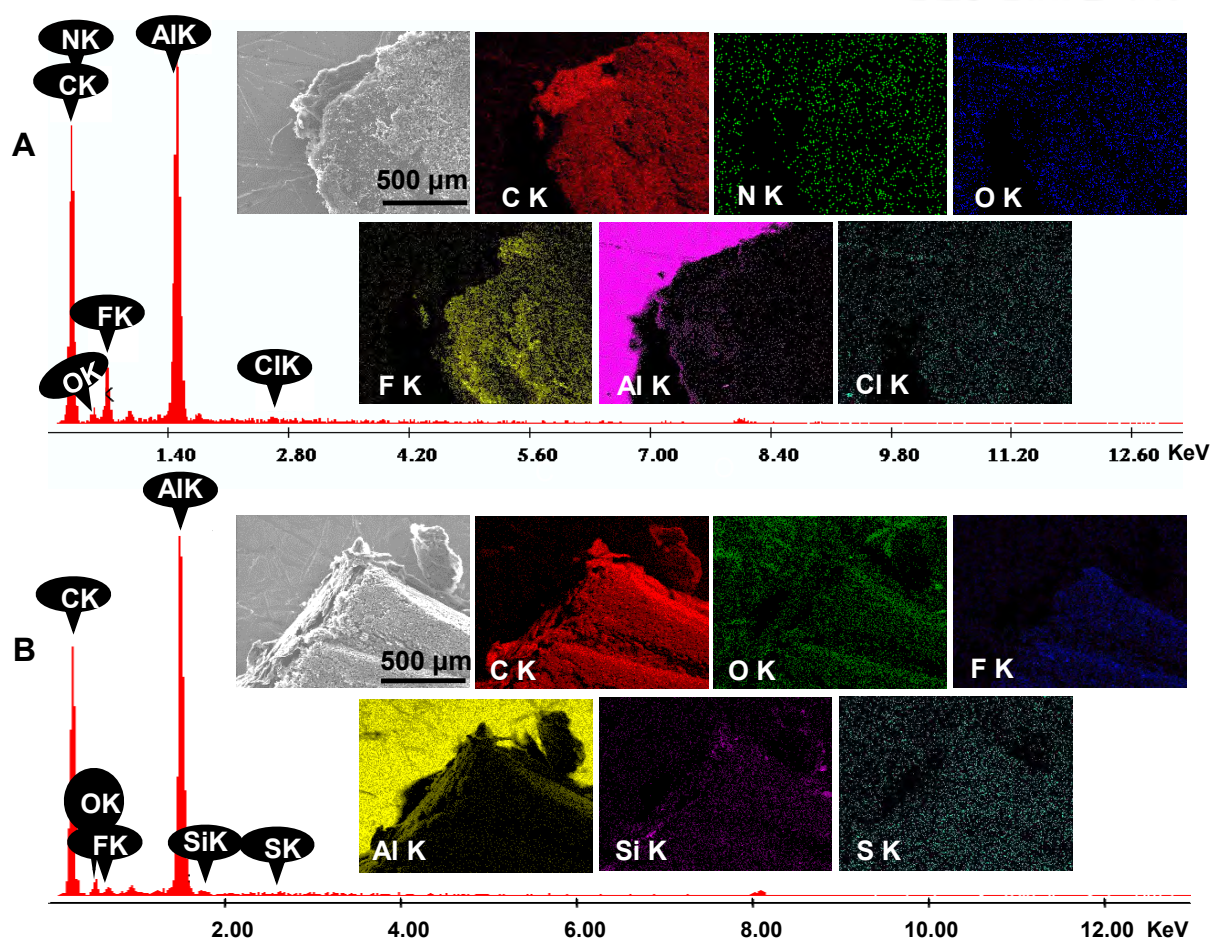


**Figure S4.** SEM EDS of (A) anode and (B) cathode (before adsorption). The SEM image and the corresponding elemental mapping images are shown in the insets. Aluminium is from the SEM stub.

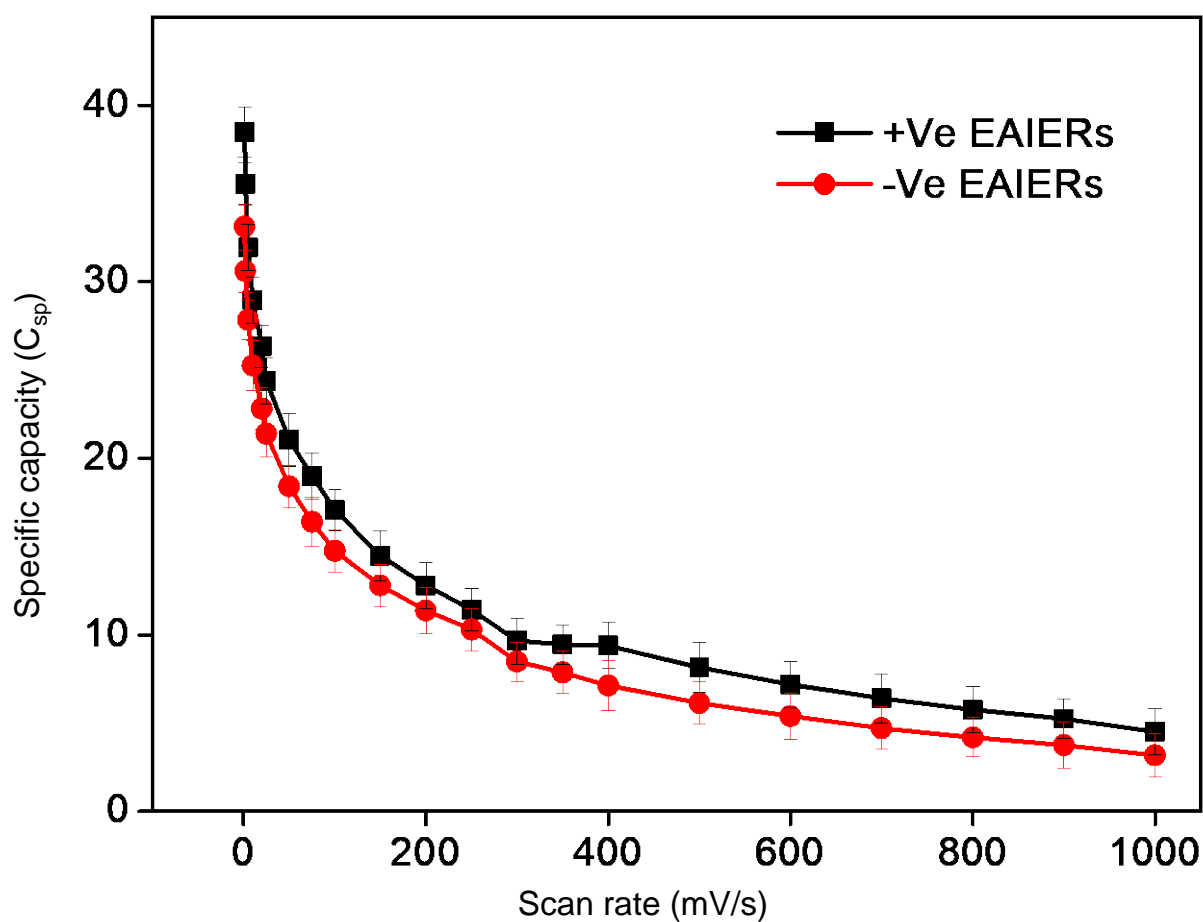


**Figure S5.** Specific capacitance vs. scan rate for both +ve and -ve EAIERs electrode materials in 1 M NaCl solution.

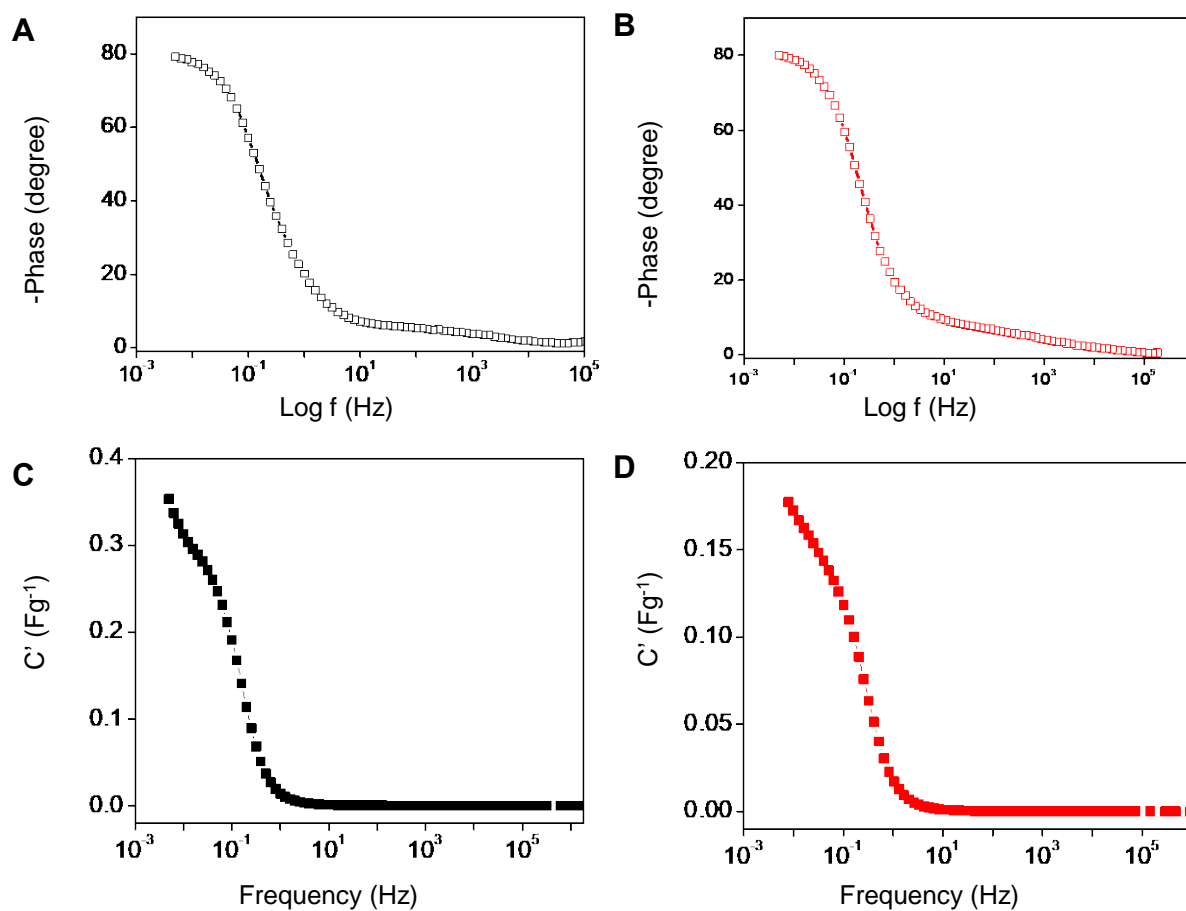


**Figure S6.** (A) and (B) are Bode impedance for cathode and anode, respectively; (C) and (D) real part of complex capacitance ( $C'$ ) vs. frequency for cathode and anode, respectively; in 1 M NaCl electrolyte.

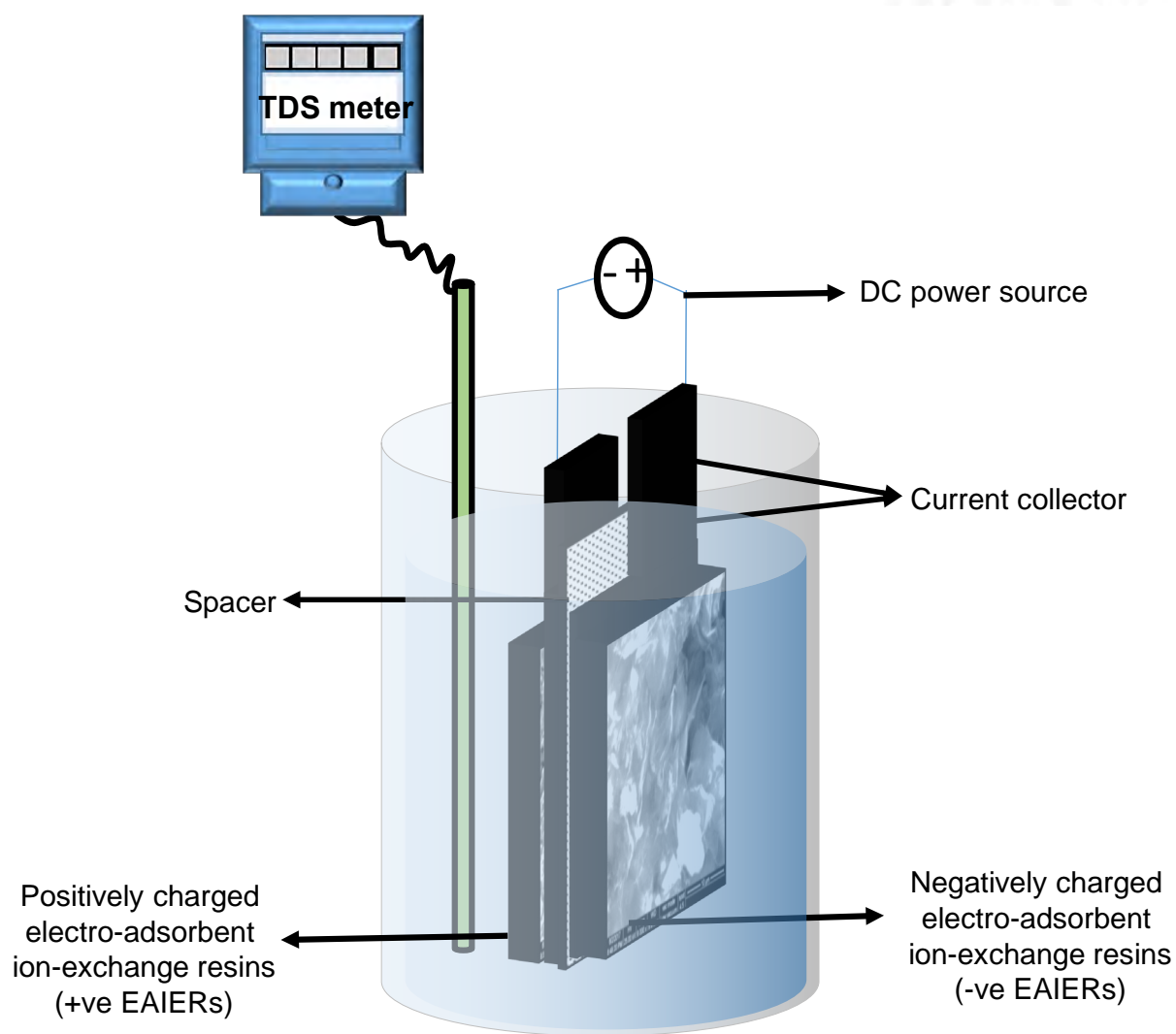


**Figure S7.** Schematic representation of a CDI set-up used for measuring CDI performance.

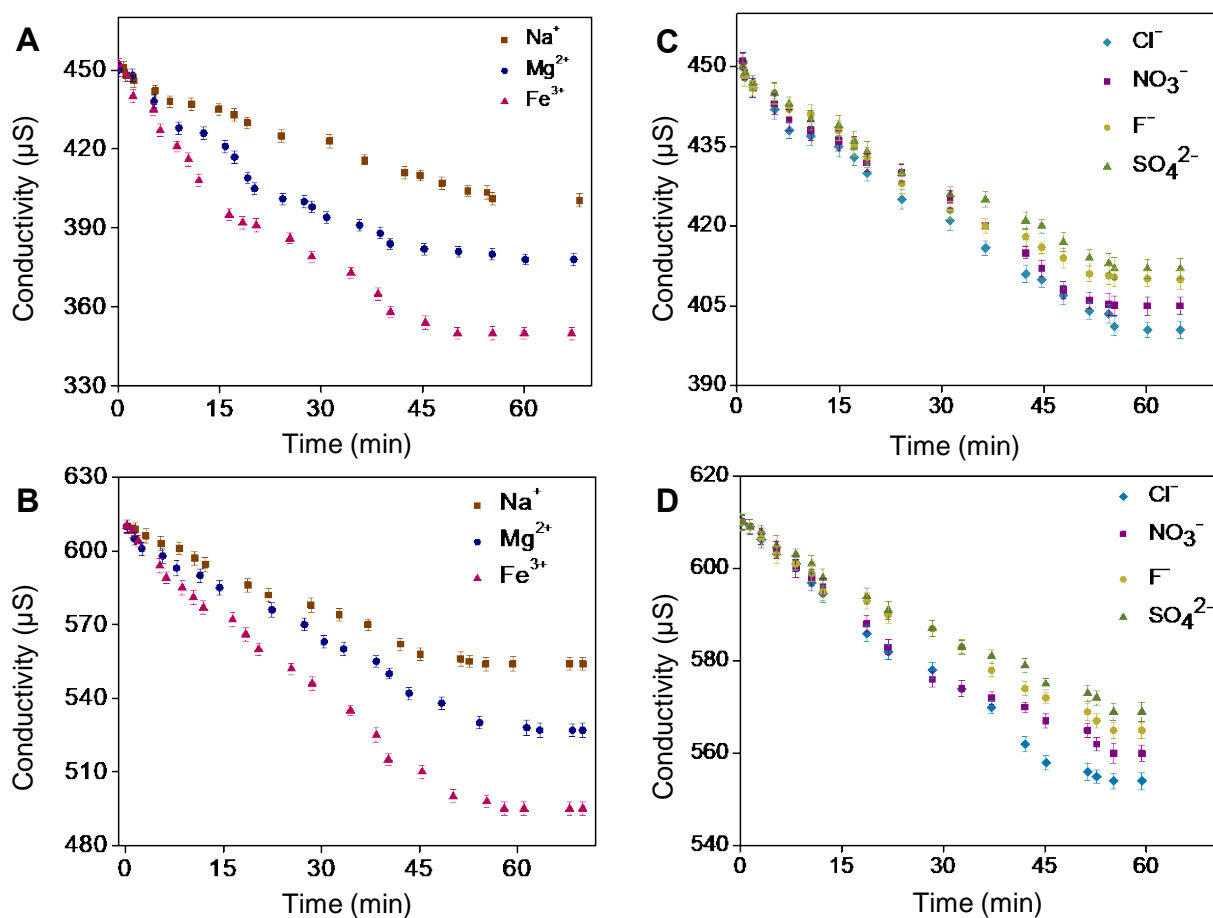


**Figure S8.** CDI performances of EAIERs electrodes using different cations ( $\text{Na}^+$ ,  $\text{Mg}^{2+}$ , and  $\text{Fe}^{3+}$ ) with solutions of different conductivities: (A) 450 and (B) 610  $\mu\text{S}$ . Similarly, anions ( $\text{Cl}^-$ ,  $\text{NO}_3^-$ ,  $\text{F}^-$  and  $\text{SO}_4^{2-}$ ) with solution of different conductivities: (C) 450 and (D) 610  $\mu\text{S}$ . The operating potential was maintained at 1.5 V during the measurements.



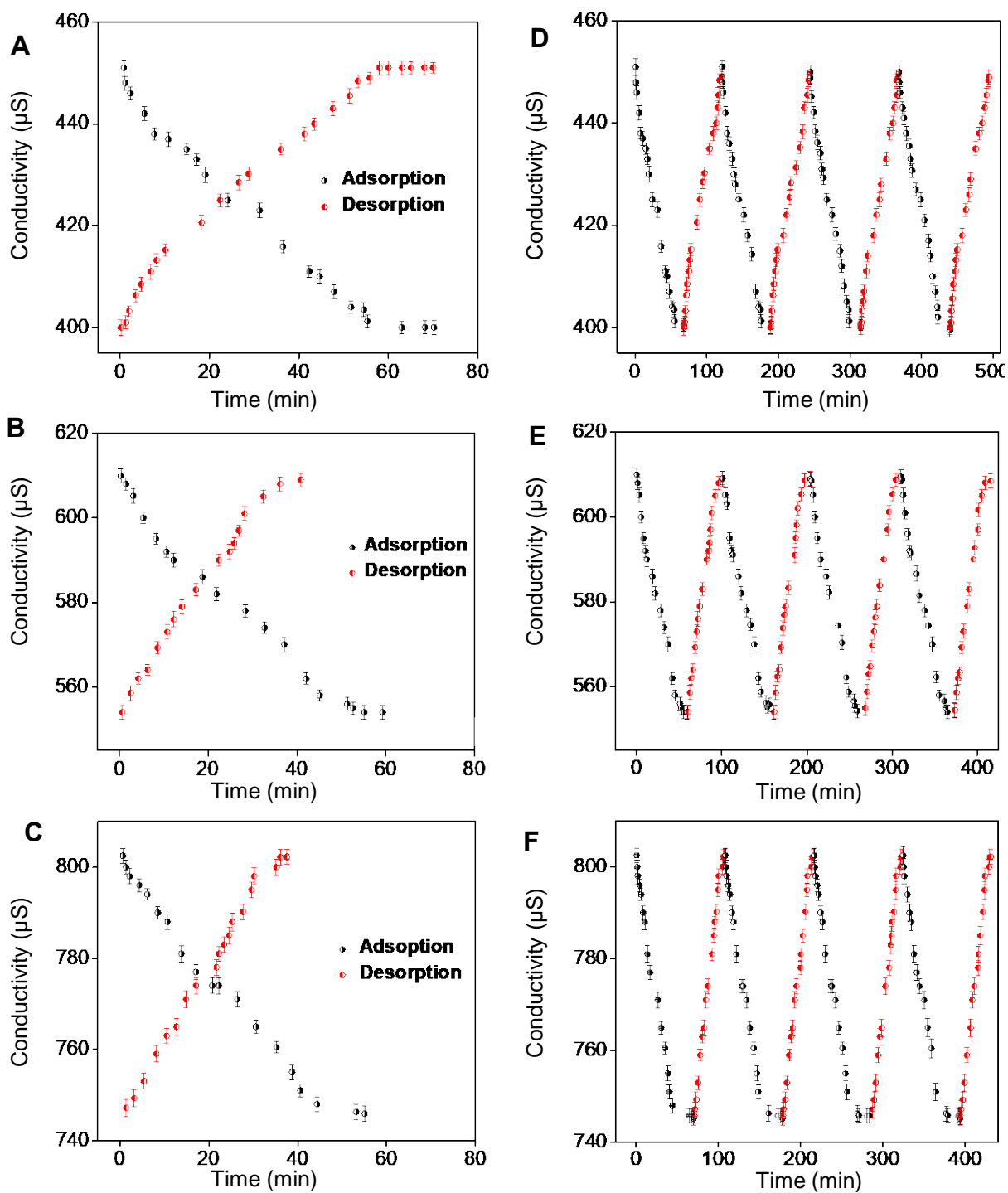


**Figure S9.** Adsorption capacities of covalently integrated EAIERs electrodes with NaCl solution of different conductivities: (A) 450, (B) 610 and (C) 802  $\mu\text{S}$ , as a function of time at an applied voltage of  $\pm 1.5$  V. Desorption starts after the adsorption cycle was complete, at an applied potential of  $\pm 1.5$  V. Four adsorption-desorption cycles are shown in (D), (E) and (F).

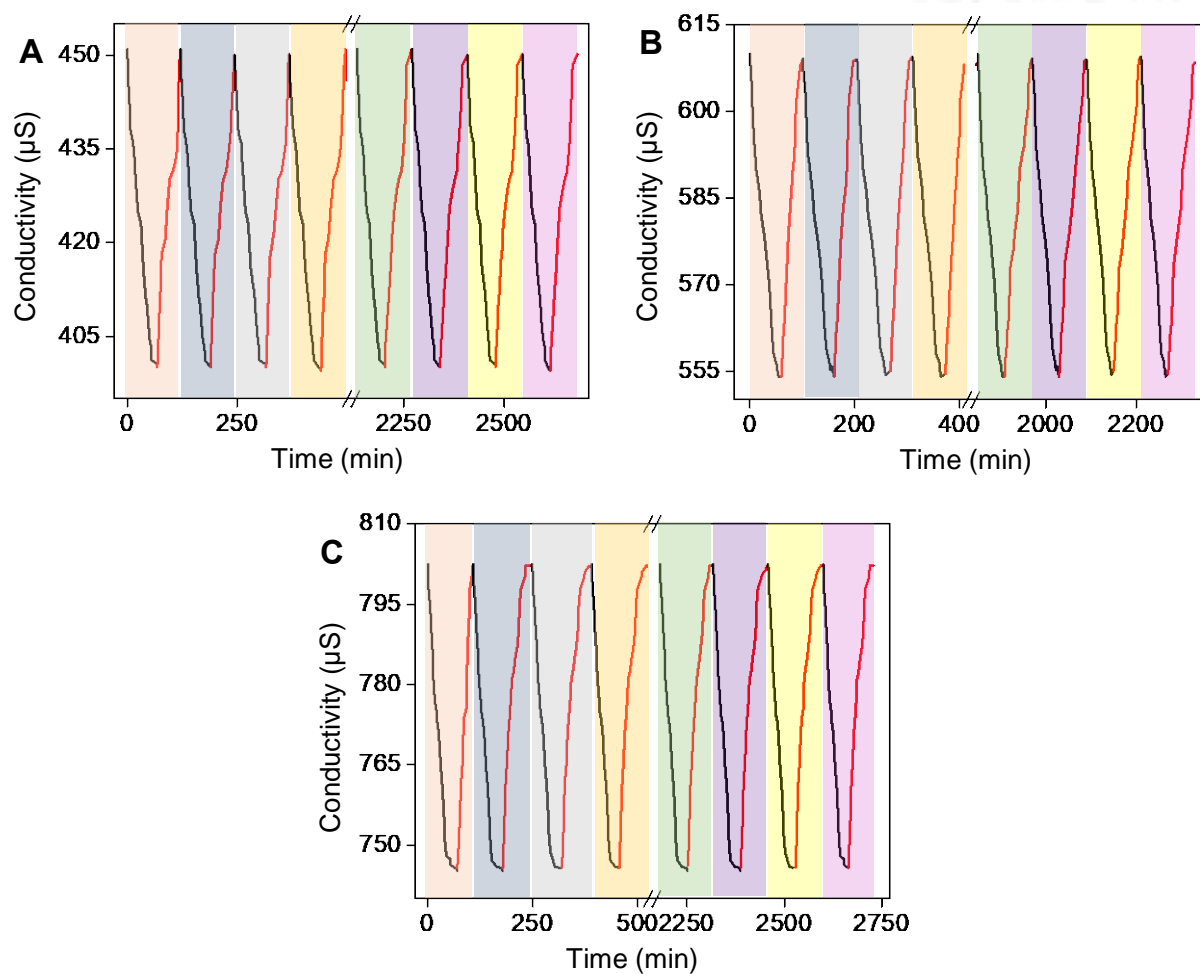


**Figure S10.** Electrode repeatability (20 cycles of adsorption-desorption) of a covalently integrated EAIERs electrode with different concentrations of NaCl solutions; (A) 450, (B) 610, and (C) 802  $\mu\text{S}$  at an applied voltage of  $\pm 1.5$  V.

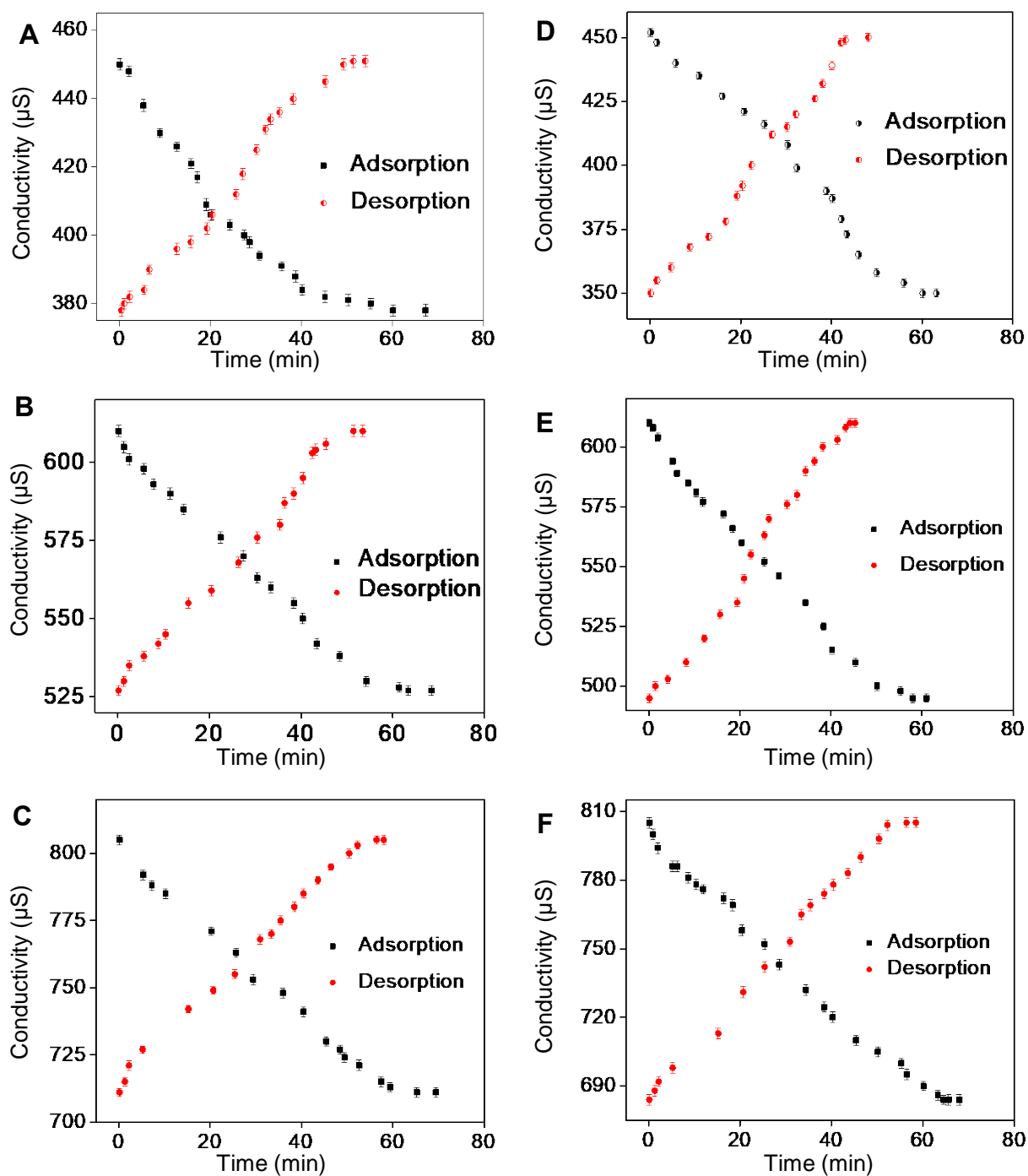


**Figure S11.** The adsorption and desorption rate of a covalently integrated EAIERs with  $\text{MgCl}_2$  and  $\text{FeCl}_3$  at different conductivities of 450 (A and D), 610 (B and E), and 802  $\mu\text{S}$  (C and F) as at an applied voltage of  $\pm 1.5$  V.

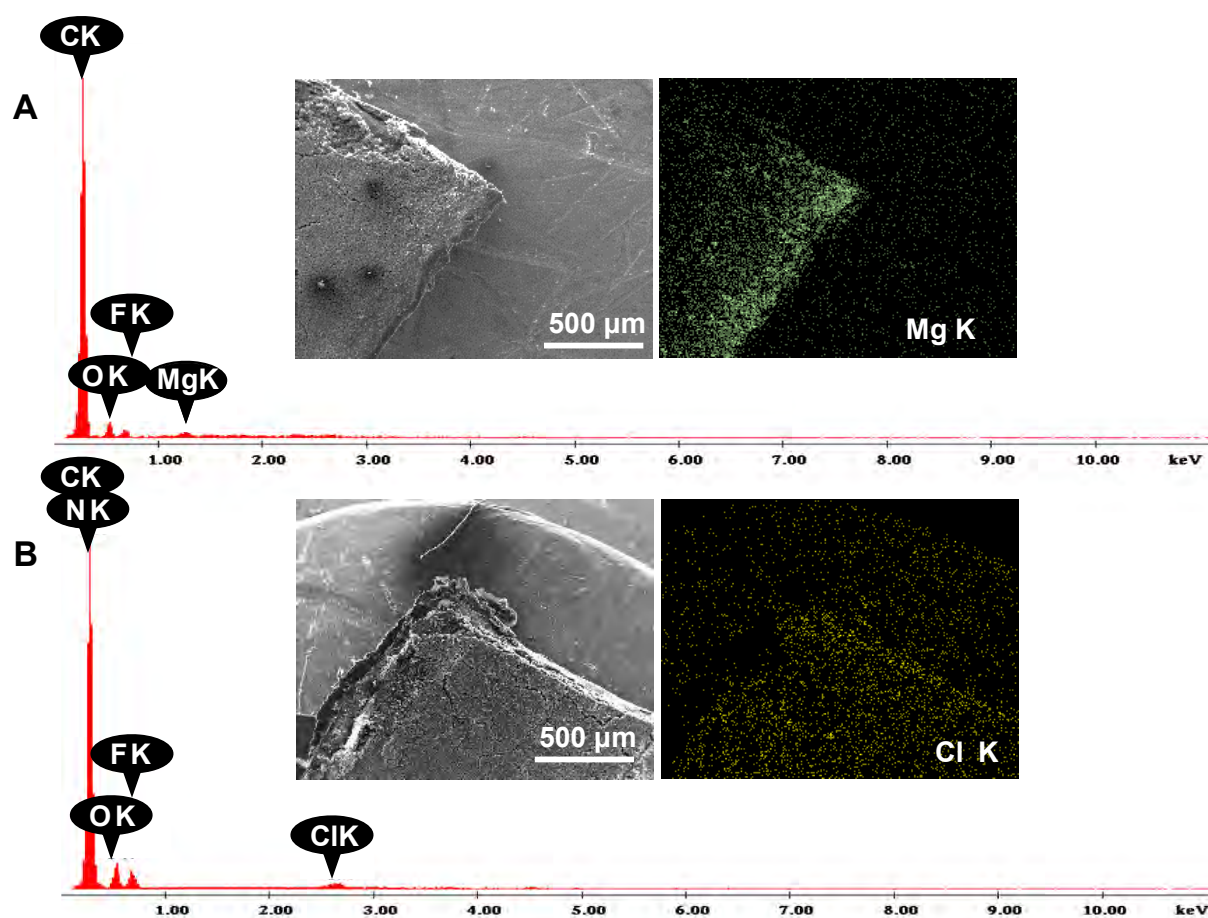


**Figure S12.** SEM EDS of  $\text{MgCl}_2$  adsorption after single adsorption on (A) cathode and (B) anode. The corresponding SEM EDS and elemental mapping images are shown in the insets.

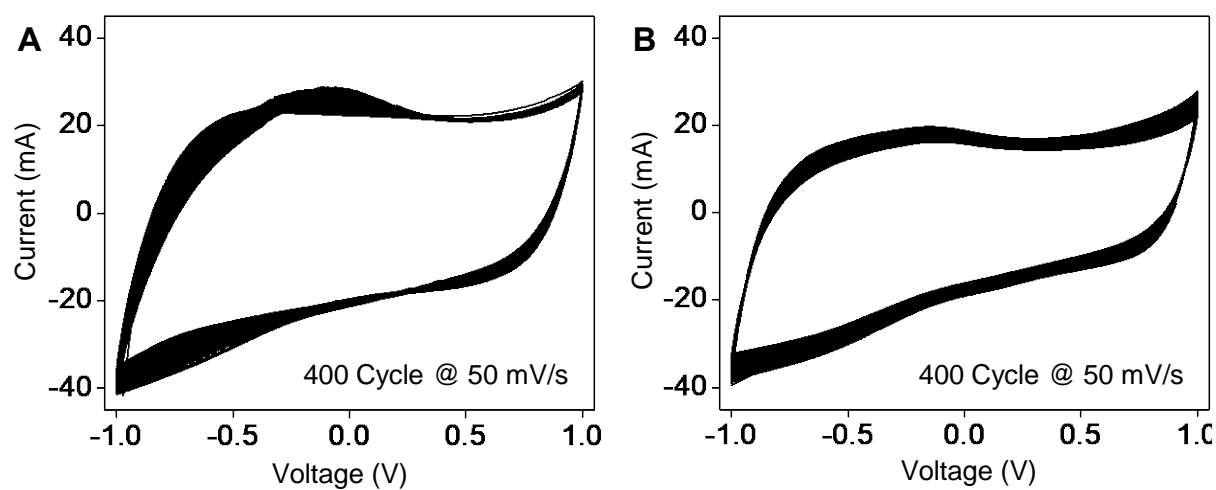


**Figure S13.** Cyclic voltammograms of (A) +ve and (B) -ve EAIERs electrodes and voltammetry was performed in 1 M NaCl at a fixed scan rate of 50 mV/s for 400 cycles.

# New Routes for Multicomponent Atomically Precise Metal Nanoclusters

Esma Khatun and Thalappil Pradeep\*



Cite This: <https://dx.doi.org/10.1021/acsomega.0c04832>



Read Online

ACCESS |

Metrics & More

Article Recommendations

**ABSTRACT:** Atomically precise metal nanoclusters (NCs), protected by a monolayer of ligands, are regarded as potential building blocks for advanced technologies. They are considered as intermediates between the atomic/molecular regime and the bulk. Incorporation of foreign metals in NCs enhances several of their properties such as catalytic activity, luminescence, and so on; hence, it is of high importance for tuning their properties and broadening the scope of applications. In most of the cases, enhancement in specific properties was observed upon alloying due to the synergistic effect. In the past several years, many alloy clusters have been synthesized, which show a tremendous change in the properties than their monometallic analogs. However, controlling the synthesis and tuning the structures of alloy NCs with atomic precision are major challenges. Various synthetic methodologies have been developed so far for the controlled synthesis of alloy NCs. In this perspective, we have highlighted those diverse synthetic routes to prepare alloys, which include co-reduction, galvanic reduction, antialgalvanic reduction, metal deposition, ligand exchange, intercluster reaction, and reaction of NCs with bulk metals. Advancement in synthetic procedures will help in the preparation of alloy NCs with the desired structure and composition. Future perceptions concerning the progress of alloy nanocluster science are also provided.



## 1. INTRODUCTION

There is a rich and fascinating history for metals and their alloys.<sup>1–3</sup> Alloys have been known from ancient times; bronze (90% Cu and 10% Sn) was the first to be invented circa BC 3500. Nanoscience has provided a new direction to the subject of metals and their alloys.<sup>4–6</sup> The famous Lycurgus cup known since the 4th century AD is one of the earliest known applications of nanotechnology.<sup>7</sup> It is found to be composed of nanoparticles of Ag, Au, and Cu of 50–100 nm in size, dispersed in a glass matrix.<sup>8</sup> The cup changes its color in different light, greenish in reflected light, and reddish in transmitted light. The nanoalloy particles of different sizes in the cup are responsible for this color change. Michael Faraday observed the unusual behavior of finely divided metal particles in their colloids in 1857.<sup>9</sup> Their optical properties are now known to be due to surface plasmon excitations. Nanoparticles with monolayer protection were prepared over a century later, enabling the synthesis of solid powders of such freely dispersible particles. They also show similar optical characteristics. Nanoclusters (NCs), which are atomically precised, are the smallest analogues of such ligand-protected nanoparticles and they exhibit unique optical, electronic, dielectric, magnetic, and chemical properties.<sup>10,11</sup> These properties are strongly dependent on the composition and geometric variations. The combination of two or more metals in NCs modify several of their properties, often leading to enhancement in the desired properties such as luminescence, catalysis, etc.<sup>12–14</sup> Therefore,

the main objective of multicomponent alloy NC science is to explore the rich variety of alloys and their interesting properties.

The synthesis of solution-phase Au NCs protected by phosphine ligands was started in 1969–1970 and a few phosphine-protected bi- and trimetallic NCs were also prepared.<sup>15–19</sup> After a long gap, in 2005, Shichibu *et al.* synthesized Au<sub>25</sub>(SG)<sub>18</sub> (SG = glutathione) by ligand exchange from phosphine-protected Au NCs.<sup>20</sup> Glutathione was used for the synthesis of gold nanoparticles by Whetten *et al.*<sup>21</sup> After that, many NCs have been prepared with ligand protection. More than 300 monometallic NCs of Au, Ag, and Cu have been synthesized by various synthetic methods. However, the number of multimetallic NCs is less.<sup>22–33</sup> Among them, the number of bimetallic NCs is higher than trimetallic and tetrametallic ones.<sup>34–42</sup>

During the synthesis of alloy NCs, mixtures of products get formed. For unambiguous characterization of the formed NC, it is important to purify or separate the as-synthesized NCs. Several separation techniques such as gel electrophoresis<sup>43</sup> and

Received: October 2, 2020

Accepted: December 8, 2020



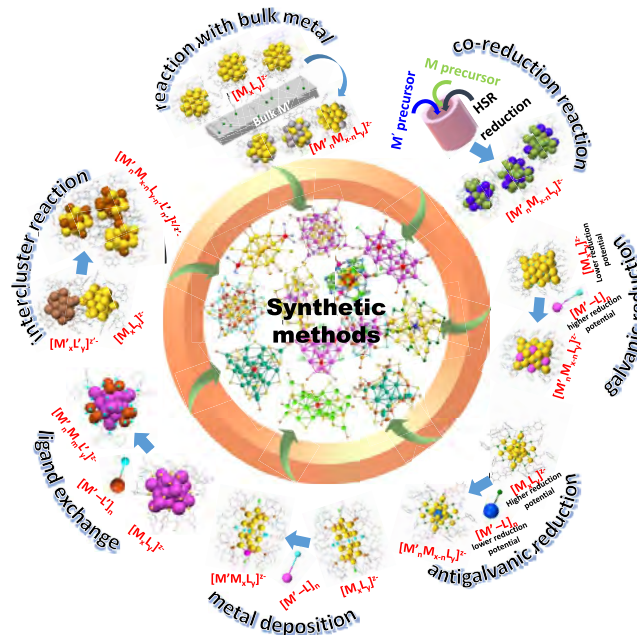


size exclusion chromatography (SEC)<sup>44</sup> have made tremendous contributions to the science of metal NCs and their alloys. In 2005, Tsukuda *et al.* separated the mixture of glutathione-protected Au NCs such as  $\text{Au}_{10}(\text{SG})_{10}$ ,  $\text{Au}_{15}(\text{SG})_{13}$ ,  $\text{Au}_{18}(\text{SG})_{14}$ ,  $\text{Au}_{22}(\text{SG})_{16}$ ,  $\text{Au}_{22}(\text{SG})_{17}$ ,  $\text{Au}_{25}(\text{SG})_{18}$ ,  $\text{Au}_{29}(\text{SG})_{20}$ ,  $\text{Au}_{33}(\text{SG})_{22}$ , and  $\text{Au}_{39}(\text{SG})_{24}$  using polyacrylamide gel electrophoresis (PAGE).<sup>45</sup> Other than SEC, high-performance liquid chromatography (HPLC) and thin-layer chromatography (TLC) are used widely for purification and separation of clusters. The composition of alloy NCs can be probed by high-resolution electrospray ionization (ESI) and matrix-assisted laser desorption ionization (MALDI) mass spectrometry (MS).<sup>42,46</sup> In 2005, compositions of a series of glutathione-protected Au NCs separated by PAGE technique were determined mass-spectrometrically. Later, Whetten *et al.* unambiguously assigned the composition of the most popular NC in this family,  $\text{Au}_{25}(\text{PET})_{18}$  (PET = 2-phenylethanethiol), through ESI MS in 2007.<sup>47</sup> Although the composition of alloy NCs can be examined by MS, the exact structure and position of dopants can be understood only by using single-crystal X-ray diffraction (SCXRD). The structure of  $\text{Au}_{25}(\text{PET})_{18}$  was solved in 2008 and, in 2014, the first X-ray crystal structure of  $\text{Ag}_x\text{Au}_{25-x}(\text{PET})_{18}$  was determined.<sup>22,47,48</sup> Recently, electron diffraction has been used to resolve the structures of those NCs for which crystallization is difficult.<sup>49</sup> In addition to the experimental methods, computation has also contributed significantly for understanding the structures and properties of these clusters.<sup>22,50–53</sup>

To understand the origin of optical and electronic properties of NCs, the substitution of metal atoms by another element is worthwhile. For example, the emission intensity of rod-like  $[\text{Au}_{25}(\text{PPh}_3)_{10}(\text{SR})_5\text{Cl}_2]^{2+}$  can be enhanced 200-fold by substituting 13 Au atoms with Ag.<sup>54</sup> The doped NC,  $[\text{Ag}_{13}\text{Au}_{12}(\text{PPh}_3)_{10}(\text{SR})_5\text{Cl}_2]^{2+}$ , having the same structure and nuclearity exhibits 40% photoluminescence quantum yield. An interesting change in the UV–vis spectrum of  $\text{Au}_{25}(\text{SR})_{18}$  was seen after single Pd/Pt doping.<sup>55–57</sup> The change in electronic structure upon doping with Pd/Pt led to the enhancement of catalytic efficiency toward hydrogen evolution reaction than with the undoped parent cluster,  $\text{Au}_{25}(\text{SR})_{18}$ . The stability of the NC was enhanced due to doping. Unlike Pd/Pt, multiple Au atoms were replaced by Ag atoms and, depending on the number of doped Ag atoms, the electronic and catalytic properties differ.<sup>58,59</sup> The silver analogue of  $\text{Au}_{25}(\text{SR})_{18}$ , namely,  $\text{Ag}_{25}(\text{SR})_{18}$ , also showed different optical and electronic properties upon doping with Pd, Pt, and Au atoms.<sup>60,61</sup> The yellow color of  $\text{Ag}_{25}(\text{SR})_{18}$  turned to greenish-yellow while being doped with Pd and the color turned dark green upon doping with Pt and Au. Also, the singly doped  $\text{Ag}_{25}(\text{SR})_{18}$  with Pd, Pt, and Au exhibited higher catalytic performance.<sup>62</sup> Doping can induce chirality in NCs. For example, the incorporation of three Ag atoms in  $\text{Au}_{18}(2,4\text{-DMBT})_{14}$  (DMBT = dimethylbenzenethiol) transformed the achiral NC into the chiral system.<sup>63,64</sup> Also, the doping of Ag in  $\text{Au}_{38}(\text{SR})_{24}$  induced chirality. Along with a significant change in circular dichroism (CD) spectrum,  $\text{Ag}_x\text{Au}_{38-x}(\text{SR})_{24}$  lowers the racemization temperature.<sup>36</sup> The doped foreign atoms prefer to occupy certain positions in the parent NC. Pd, Ni, Pt, and Cd atoms always prefer to occupy the center, whereas Ag and Au atoms can be doped in all the possible positions. But Cu atoms always prefer outer staple positions.<sup>65</sup> Hence, by proper combinations, more than one metal atom can be incorporated to make multicomponent alloy NCs.

In this perspective article, we focus on the various synthetic methods used for making multimetallic alloy NCs (Scheme 1).

**Scheme 1. Schematic Representation of Various Synthetic Methodologies of Alloy NCs<sup>a</sup>**



<sup>a</sup>Co-reduction, galvanic reduction, antigalvanic reduction, metal deposition, ligand exchange, intercluster reaction, and reaction of NCs with bulk metal are illustrated.

At first, we discuss the classical methods used for the preparation of alloy NCs such as co-reduction and galvanic and antigalvanic reduction methods. After that, we discuss the other emerging procedures for the formation of alloy NCs, which are metal deposition, ligand exchange, intercluster reactions, and reaction between NCs and bulk metals. In the case of co-reduction method, the structure and composition cannot be controlled, while galvanic and antigalvanic exchange reaction methods are used for making a large number of alloy NCs, keeping the structural integrity the same as that of the monometallic analogues. Metal deposition certainly changes the composition; however, the total structure of the parent cluster remains unaltered. Ligand exchange method, which is a well-established method for the preparation of noble metal NCs, is now being used for the synthesis of alloy NCs with new atomicity and properties. Other than galvanic and antigalvanic reduction methods, a new synthetic method has been discussed in detail where reaction involving two different NCs (named as intercluster reaction) leads to the formation of structure-conserved alloy NCs. Such intercluster reactions between Ag and Au NCs are illustrated here. Similar to the reaction between two NCs, NC was found to react with bulk metals also. For more detailed information about the structures and properties of NCs, we direct the readers to several recent review articles.<sup>13,61,66–70</sup>

## 2. CO-REDUCTION METHOD

Co-reduction is a kind of Brust–Schiffrin method where, instead of one metal precursor, several metal precursors are mixed with appropriate protective ligands and the reduction is performed with suitable reducing agents. The method is also known as the direct reduction method. With the help of this synthetic

Table 1. List of Alloy NCs, Their Method of Synthesis, and Characterization Methods Used

no	core	ligand	alloy cluster	focus	method of synthesis	reference
1	Au <sub>24</sub> Cd	phenylethylthiol	Au <sub>24</sub> Cd(PET) <sub>18</sub>	crystal structure	antigalvanic exchange	91,92
2	Au <sub>24</sub> Hg	phenylethylthiol	Au <sub>24</sub> Hg(PET) <sub>18</sub>	mass spectrometry	antigalvanic exchange	91,92
3	Au <sub>15</sub> Ag <sub>3</sub>	2,4-dimethylbenzenethiol	Au <sub>15</sub> Ag <sub>3</sub> (2,4-DMBT) <sub>14</sub>	crystal structure	antigalvanic exchange	63
4	Au <sub>9</sub> M <sub>4</sub> (M = Ag, Cu)	diphenylmethylphosphine	[Au <sub>9</sub> M <sub>4</sub> Cl <sub>4</sub> (PM <sub>6</sub> Ph <sub>2</sub> ) <sub>8</sub> ][C <sub>2</sub> B <sub>9</sub> H <sub>12</sub> ]-CH <sub>2</sub> Cl <sub>2</sub> (M = Ag, Cu)	FAB mass spectrometry	antigalvanic exchange	93
5	Au <sub>23-x</sub> Cu <sub>x</sub>	cyclohexanethiol	[Au <sub>23-x</sub> Cu <sub>x</sub> (CHT) <sub>16</sub> ] <sup>-</sup>	crystal structure	antigalvanic exchange	94
6	M <sub>1</sub> Ag <sub>5</sub> Au <sub>24-x</sub> (M = Cd/Hg)	phenylethanethiol	M <sub>1</sub> Ag <sub>5</sub> Au <sub>24-x</sub> (PET) <sub>18</sub> (M = Cd/Hg)	mass spectrometry	antigalvanic exchange	41
7	AgAu <sub>17</sub>	hexanethiol	AgAu <sub>17</sub> (HT) <sub>14</sub>	crystal structure	antigalvanic exchange	95
8	Au <sub>24-x-y</sub> Ag <sub>x</sub> Cu <sub>y</sub> Pd	1-dodecanethiol	Au <sub>24-x-y</sub> Ag <sub>x</sub> Cu <sub>y</sub> Pd(SC <sub>12</sub> H <sub>25</sub> ) <sub>18</sub>	mass spectrometry	antigalvanic exchange	96
9	Au <sub>38</sub> Cu <sub>1</sub>	2-phenylethanethiol	Au <sub>38</sub> Cu <sub>1</sub> (2-PET) <sub>24</sub>	mass spectrometry	antigalvanic exchange	97
10	(Ag-Au) <sub>144</sub>	phenylethanethiol	(Ag-Au) <sub>144</sub> (PET) <sub>60</sub>	mass spectrometry	co-reduction	83
11	Au <sub>144-x</sub> Cu <sub>x</sub>	hexanethiol	Au <sub>144-x</sub> Cu <sub>x</sub> (HT) <sub>60</sub>	mass spectrometry	co-reduction	82
12	Ag <sub>4</sub> Ni <sub>2</sub>	dimercaptosuccinic acid	Ag <sub>4</sub> Ni <sub>2</sub> (DMSA) <sub>4</sub>	mass spectrometry	co-reduction	80
13	Ag <sub>4</sub> Pt <sub>2</sub>	dimercaptosuccinic acid	Ag <sub>4</sub> Pt <sub>2</sub> (DMSA) <sub>4</sub>	mass spectrometry	co-reduction	98
14	Ag <sub>4</sub> Pd <sub>2</sub>	dimercaptosuccinic acid	Ag <sub>4</sub> Pd <sub>2</sub> (DMSA) <sub>4</sub>	crystal structure	co-reduction	99
15	Au <sub>13</sub> Cu <sub>x</sub> (x = 2, 4, 8)	pyridine-2-thiol, triphenylpyridine 4- <i>tert</i> -butylbenzenethiol pyridinediphenylphosphine	Au <sub>13</sub> Cu <sub>x</sub> (PPh <sub>3</sub> ) <sub>6</sub> (SPy) <sub>6</sub> <sup>+</sup> Au <sub>13</sub> Cu <sub>4</sub> (PPh <sub>3</sub> Py) <sub>4</sub> (SC <sub>6</sub> H <sub>4</sub> - <i>tert</i> -C <sub>4</sub> H <sub>9</sub> ) <sub>8</sub> <sup>+</sup> Au <sub>13</sub> Cu <sub>8</sub> (PPh <sub>3</sub> Py) <sub>12</sub> <sup>+</sup>	crystal structures	co-reduction	100
16	Ag <sub>28</sub> Cu <sub>12</sub>	2,4-dichlorobenzenethiol	[Ag <sub>28</sub> Cu <sub>12</sub> (2,4-DCBT) <sub>24</sub> ] <sup>-4</sup>	crystal structure	co-reduction	85
17	Au <sub>24</sub> Ag <sub>20</sub>	phenylalkynyl, 2-pyridylthiolate	Au <sub>24</sub> Ag <sub>20</sub> (2-Spy) <sub>4</sub> (PhC≡C) <sub>20</sub> Cl <sub>2</sub>	crystal structure	co-reduction	101
18	Ag <sub>24</sub> Pd	2,4-dichlorobenzenethiol	(PPh <sub>3</sub> ) <sub>2</sub> [Ag <sub>24</sub> Pd(2,4-DCBT) <sub>18</sub> ]	crystal structure	co-reduction	60
19	Ag <sub>24</sub> Pt	2,4-dichlorobenzenethiol	(PPh <sub>3</sub> ) <sub>2</sub> [Ag <sub>24</sub> -Pt <sub>2</sub> (2,4-DC) <sub>18</sub> ] (x = 1, 2)	crystal structure	co-reduction	60
20	Ag <sub>24</sub> Ni	2,4-dimethylbenzenethiol	(PPh <sub>3</sub> ) <sub>2</sub> [Ag <sub>24</sub> Ni(SR) <sub>18</sub> ]	mass spectrometry	co-reduction	89
21	Au <sub>80</sub> Ag <sub>30</sub>	phenylalkene	[Au <sub>80</sub> Ag <sub>30</sub> (PhC≡C) <sub>42</sub> Cl <sub>9</sub> ]	crystal structure	co-reduction	84
22	Au <sub>24</sub> Pd	phenylethanethiol	[Au <sub>24</sub> Pd(PET) <sub>18</sub> ] <sup>-1</sup>	crystal structure	co-reduction	57,102
23	Au <sub>24</sub> Pt	phenylethanethiol	[Au <sub>24</sub> Pt(PET) <sub>18</sub> ]	crystal structure	co-reduction	55,102
24	Au <sub>37</sub> Pd <sub>1</sub>	phenylethanethiol	Au <sub>37</sub> Pd <sub>1</sub> (PET) <sub>24</sub>	mass spectrometry	co-reduction	56
25	Au <sub>36</sub> Pd <sub>2</sub>	phenylethanethiol	Au <sub>36</sub> Pd <sub>2</sub> (PET) <sub>24</sub>	mass spectrometry	co-reduction	56,103
26	Ag <sub>4</sub> Au <sub>38-x</sub>	phenylethanethiol	Ag <sub>4</sub> Au <sub>38-x</sub> (PET) <sub>24</sub>	crystal structure	co-reduction	36
27	Ag <sub>6</sub> Au <sub>24</sub>	<i>tert</i> -butyl hydroperoxide	[Ag <sub>6</sub> Au <sub>24</sub> (TBHP) <sub>32</sub> ] <sup>2+</sup>	crystal structure	co-reduction	86
28	Au <sub>12</sub> Ag <sub>12</sub> Ni	hexafluoroantimonate, triphenylphosphine	[Au <sub>12</sub> Ag <sub>12</sub> Ni(PPh <sub>3</sub> ) <sub>10</sub> Cl <sub>7</sub> ][SbF <sub>6</sub> ]	crystal structure	co-reduction	18
29	Au <sub>12</sub> Ag <sub>12</sub> Pt	triphenylphosphine	[Au <sub>12</sub> Ag <sub>12</sub> Pt(PPh <sub>3</sub> ) <sub>10</sub> Cl <sub>7</sub> ]	crystal structure	co-reduction	18
30	Ag <sub>3</sub> Au <sub>12</sub>	diphenylmethylphosphine	(MePh <sub>2</sub> P) <sub>10</sub> Au <sub>12</sub> Ag <sub>12</sub> Br <sub>9</sub>	crystal structure	co-reduction	104
31	Au <sub>18</sub> Ag <sub>20</sub>	<i>para</i> -tolylphosphine	[( <i>p</i> -Tol <sub>3</sub> P) <sub>12</sub> Au <sub>18</sub> Ag <sub>20</sub> Cl <sub>14</sub> ]	crystal structure	co-reduction	7
32	Au <sub>22</sub> Ag <sub>24</sub>	triphenylphosphine	[(PPh <sub>3</sub> ) <sub>12</sub> Au <sub>22</sub> Ag <sub>24</sub> Cl <sub>10</sub> ]	crystal structure	co-reduction	74
33	AuAg <sub>9</sub>	<i>O,O</i> -disopropyl dithiophosphate	[AuAg <sub>9</sub> (S <sub>2</sub> P(O <sup>i</sup> Pr) <sub>2</sub> ) <sub>12</sub> ]	crystal structure	co-reduction	105
34	AuAg <sub>24</sub>	1,1-bis(diphenylphosphino)methane, cyclohexanethiol	[AuAg <sub>24</sub> (Dppm) <sub>3</sub> (CHT) <sub>17</sub> ] <sup>2+</sup>	crystal structure	co-reduction	106
35	Pt <sub>2</sub> Ag <sub>3</sub>	triphenylphosphine	[Pt <sub>2</sub> Ag <sub>3</sub> Cl <sub>7</sub> (PPh <sub>3</sub> ) <sub>10</sub> ]	crystal structure	co-reduction	107
36	AuAg <sub>16</sub>	<i>tert</i> -butylbenzenethiol	(TOA) <sub>3</sub> AuAg <sub>16</sub> (TBBT) <sub>12</sub>	crystal structure	co-reduction	87
37	Ag <sub>26</sub> Pt	2-ethylbenzenethiol	Ag <sub>26</sub> Pt(2-EBT) <sub>18</sub> (PPh <sub>3</sub> ) <sub>6</sub>	crystal structure	co-reduction	108
38	Au <sub>2</sub> Cu <sub>6</sub>	adamentanethiol, diphenylpyridinephosphine	Au <sub>2</sub> Cu <sub>6</sub> (S-Adm) <sub>6</sub> (PPh <sub>2</sub> Py) <sub>2</sub>	crystal structure	co-reduction	109
39	Au <sub>4</sub> Ag <sub>5</sub>	adamentanethiol, 1,1-bis(diphenylphosphino)methane	[Au <sub>4</sub> Ag <sub>5</sub> (dppm) <sub>2</sub> (SAdm) <sub>6</sub> ] <sup>+</sup>	crystal structure	co-reduction	110
40	Au <sub>4</sub> Ag <sub>23</sub>	1,1'-bis(diphenylphosphino)ferrocene, <i>tert</i> -butylalkynyl	[Au <sub>4</sub> Ag <sub>23</sub> (C≡CBut) <sub>10</sub> Cl <sub>7</sub> (dppf) <sub>4</sub> ] <sup>2+</sup>	crystal structure	co-reduction	39



Table 1. continued

no	core	ligand	alloy cluster	focus	method of synthesis	reference
41	Au <sub>3</sub> Ag <sub>24</sub>	1,1'-bis(diphenylphosphino)ferrocene, <i>tert</i> -butylbenzylInyl	[Au <sub>3</sub> Ag <sub>24</sub> (C≡CC <sub>6</sub> H <sub>4</sub> P <sup>+</sup> But) <sub>16</sub> (dppf) <sub>4</sub> Cl <sub>4</sub> ] <sup>3+</sup>	crystal structure	co-reduction	39
42	Au <sub>2</sub> Ag <sub>59-<i>x</i></sub>	1,3-benzenedithiol, triphenylphosphine	Au <sub>2</sub> Ag <sub>59-<i>x</i></sub> (BDT) <sub>12</sub> (PPh <sub>3</sub> ) <sub>4</sub>	crystal structure, mass spectrometry	co-reduction	35
43	Au <sub>23-<i>x</i></sub> Ag <sub>6<i>x</i></sub>	cyclohexanethiol	Au <sub>23-<i>x</i></sub> Ag <sub>6<i>x</i></sub> (S-Adm) <sub>16</sub>	crystal structure	co-reduction	111
44	Au <sub>19</sub> Cd <sub>2</sub>	cyclohexanethiol	[Au <sub>19</sub> Cd <sub>2</sub> (CHT) <sub>16</sub> ] <sup>+</sup>	crystal structure	co-reduction	94
45	Cu <sub>30</sub> Ag <sub>61</sub>	adamentanethiol, tetraphenylborate	[Cu <sub>30</sub> Ag <sub>61</sub> (SAdm) <sub>38</sub> S <sub>3</sub> ](BPh <sub>4</sub> )	crystal structure	co-reduction	112
46	Au <sub>4</sub> Cu <sub>4</sub>	adamentanethiol, 1,1-bis(diphenylphosphino)methane	[Au <sub>4</sub> Cu <sub>4</sub> (Dppm) <sub>2</sub> (SAdm) <sub>3</sub> ] <sub>2</sub> Br	crystal structure	co-reduction	113
47	Au <sub>8</sub> Ag <sub>57</sub>	1,3-bis(diphenylphosphino)propane, cyclohexanethiol	[Au <sub>8</sub> Ag <sub>57</sub> (Dppp) <sub>4</sub> (CHT) <sub>3</sub> Cl <sub>2</sub> ] <sub>2</sub> Cl	crystal structure	co-reduction	114
48	Pt <sub>1</sub> Ag <sub>9</sub>	tris(4-fluorophenyl)phosphine	Pt <sub>1</sub> Ag <sub>9</sub> [P(Ph-F) <sub>3</sub> ] <sub>3</sub> Cl <sub>3</sub>	crystal structure	co-reduction	115
49	Au <sub>130-<i>x</i></sub> Ag <sub>6<i>x</i></sub>	<i>tert</i> -butylbenzenethiol	Au <sub>130-<i>x</i></sub> Ag <sub>6<i>x</i></sub> (TBBT) <sub>55</sub>	crystal structure	co-reduction	116
50	Ag <sub>17</sub> Cu <sub>12</sub>	1,3-benzenedithiol, triphenylphosphine	Ag <sub>17</sub> Cu <sub>12</sub> (BDT) <sub>12</sub> (PPh <sub>3</sub> ) <sub>4</sub>	crystal structure	co-reduction	117
51	Au <sub>7</sub> Ag <sub>9</sub>	1,1'-bis(diphenylphosphino)ferrocene	[Au <sub>7</sub> Ag <sub>9</sub> (dppf) <sub>3</sub> (CF <sub>3</sub> CO <sub>2</sub> ) <sub>2</sub> BF <sub>4</sub> ] <sub>n</sub>	crystal structure	co-reduction	118
52	Ag <sub>20</sub> Cu <sub>12</sub>	2,4-dimethylbenzenethiol, 1,1-bis(diphenylphosphino)methane	[Ag <sub>20</sub> Cu <sub>12</sub> (2,4-DMBT) <sub>14</sub> (Dppm) <sub>6</sub> Br <sub>8</sub> ] <sub>2</sub> <sup>2+</sup>	crystal structure	co-reduction	119
53	Au <sub>9</sub> Ag <sub>12</sub>	1-adamantanethiol/ <i>tert</i> -butylmercaptopan, 1,1-bis(diphenylphosphino)methane	[Au <sub>9</sub> Ag <sub>12</sub> (SR) <sub>4</sub> (dppm) <sub>6</sub> ] <sub>3</sub> <sup>3+</sup>	crystal structure	co-reduction	120
54	PtAu <sub>8</sub>	triphenylphosphine	PtAu <sub>8</sub> (PPh <sub>3</sub> ) <sub>8</sub> (NO <sub>3</sub> ) <sub>2</sub>	crystal structure	co-reduction	121
55	Au <sub>12-<i>n</i></sub> Cu <sub>32</sub>	4-(trifluoromethyl)thiophenol	Au <sub>12-<i>n</i></sub> Cu <sub>32</sub> (SR) <sub>30-<i>m</i></sub> ] <sub>4</sub> <sup>4-</sup> ( <i>n</i> = 0, 2, 4, 6)	crystal structure	co-reduction	122
56	Cd <sub>1</sub> Au <sub>14</sub>	<i>tert</i> -butylthiol	Cd <sub>1</sub> Au <sub>14</sub> (S <sup>+</sup> Bu) <sub>12</sub>	crystal structure	co-reduction	123
57	Au <sub>8</sub> Ag <sub>3</sub>	triphenylphosphine	Au <sub>8</sub> Ag <sub>3</sub> (PPh <sub>3</sub> ) <sub>3</sub> Cl <sub>3</sub>	crystal structure	co-reduction	124
58	Au <sub>36-<i>x</i></sub> Ag <sub>6<i>x</i></sub>	<i>tert</i> -butylbenzenethiol	Au <sub>36-<i>x</i></sub> Ag <sub>6<i>x</i></sub> (SPh <sup>+</sup> Bu) <sub>24</sub>	mass spectrometry	co-reduction	125
59	Au <sub>38-<i>x</i></sub> Cu <sub>6<i>x</i></sub>	2,4-dimethylbenzenethiol	Au <sub>38-<i>x</i></sub> Cu <sub>6<i>x</i></sub> (2,4-DMBT) <sub>24</sub> ( <i>x</i> = 0–6)	crystal structure	co-reduction	126
60	Au <sub>19</sub> Cu <sub>30</sub>	3-ethynylthiophene/ethynylbenzene	[Au <sub>19</sub> Cu <sub>30</sub> (C≡C) <sub>22</sub> (Ph <sub>3</sub> P) <sub>6</sub> Cl <sub>2</sub> ]	crystal structure	co-reduction	127
61	Au <sub>3</sub> Ag <sub>38</sub>	phenylethanethiol	[Au <sub>3</sub> Ag <sub>38</sub> (PET) <sub>24</sub> X <sub>5</sub> ] <sub>2</sub> <sup>2-</sup> (X = Cl or Br)	crystal structure	co-reduction	128
62	Au <sub>4</sub> Pt <sub>2</sub>	phenylethanethiol	Au <sub>4</sub> Pt <sub>2</sub> (PET) <sub>8</sub>	crystal structure	co-reduction	129
63	Au <sub>4</sub> Pd <sub>2</sub>	phenylethanethiol	Au <sub>4</sub> Pd <sub>2</sub> (PET) <sub>8</sub>	crystal structure	co-reduction	130
64	Au <sub>24</sub> Cu <sub>6</sub>	<i>tert</i> -butyl benzenethiol	Au <sub>24</sub> Cu <sub>6</sub> (TBBT) <sub>22</sub>	crystal structure	co-reduction	131
65	Au <sub>36-<i>x</i></sub> Cu <sub>6<i>x</i></sub>	<i>m</i> -methylbenzenethiol	Au <sub>36-<i>x</i></sub> Cu <sub>6<i>x</i></sub> ( <i>m</i> -MBT) <sub>24</sub> ( <i>x</i> = 1–3)	crystal structure	co-reduction	132
66	Au <sub>13</sub> Cu <sub>2</sub>	1,3-bis(diphenylphosphino)propane, pyridine-2-thiol, (2 <i>r</i> ,4 <i>r</i> )/(2 <i>s</i> ,4 <i>s</i> )-2,4-bis(diphenylphosphino)pentane	Au <sub>13</sub> Cu <sub>2</sub> (DPPP) <sub>3</sub> (SPy) <sub>6</sub> , Au <sub>13</sub> Cu <sub>2</sub> ((2 <i>r</i> ,4 <i>r</i> )/(2 <i>s</i> ,4 <i>s</i> )-BDPP) <sub>3</sub> (SPy) <sub>6</sub>	crystal structure	co-reduction	81
67	PtAu <sub>7</sub>	triphenylphosphine	[Pt(H)(PPh <sub>3</sub> )(AuPPh <sub>3</sub> ) <sub>7</sub> ] <sub>2</sub> <sup>2+</sup>	crystal structure	co-reduction	90
68	Ag <sub>32</sub> Au <sub>12</sub>	fluorobenzenethiol	Ag <sub>32</sub> Au <sub>12</sub> (FTP) <sub>30</sub> ] <sub>4</sub> <sup>4-</sup>	crystal structure	co-reduction, intercluster reaction	31,133
69	Au <sub>21-<i>x</i></sub> Ag <sub>6<i>x</i></sub>	<i>tert</i> -butylthiol	Au <sub>21-<i>x</i></sub> Ag <sub>6<i>x</i></sub> (TBT) <sub>15</sub> ( <i>x</i> = 4–8)	crystal structure	co-reduction, ligand exchange	134
70	Au <sub>21-<i>x</i></sub> Cu <sub>6<i>x</i></sub>	<i>tert</i> -butylthiol	Au <sub>21-<i>x</i></sub> Cu <sub>6<i>x</i></sub> (TBT) <sub>15</sub> ( <i>x</i> = 0, 1), Au <sub>21-<i>x</i></sub> Cu <sub>6<i>x</i></sub> (TBT) <sub>15</sub> ( <i>x</i> = 2–5)	crystal structure	co-reduction, ligand exchange	134
71	Au <sub>25-<i>x</i></sub> Ag <sub>6<i>x</i></sub> ( <i>x</i> = 6–8)	phenylethanethiol	[Au <sub>25-<i>x</i></sub> Ag <sub>6<i>x</i></sub> (PET) <sub>18</sub> ]	crystal structure	co-reduction, antialgal exchange	48,76,92,135,136
72	Au <sub>25-<i>x</i></sub> Cu <sub>6<i>x</i></sub>	phenylethanethiol	[Au <sub>25-<i>x</i></sub> Cu <sub>6<i>x</i></sub> (PET) <sub>18</sub> ]	mass spectrometry	co-reduction, antialgal exchange	77,92,136
73	Ag <sub>25-<i>x</i></sub> Au <sub>6<i>x</i></sub>	2,4-dichlorobenzenethiol/2,4-dimethylbenzenethiol	(PPh <sub>4</sub> ) <sub>2</sub> [Ag <sub>25-<i>x</i></sub> Au <sub>6<i>x</i></sub> (SR) <sub>18</sub> ]	crystal structure, mass spectrometry	co-reduction, galvnic exchange, intercluster reaction	60,137,138
74	Ag <sub>7</sub> Au <sub>6</sub>	mercaptoposuccinic acid	Ag <sub>7</sub> Au <sub>6</sub> (H <sub>2</sub> MSA)	mass spectrometry	galvnic exchange	37
75	Au <sub>2</sub> Ag <sub>60-<i>x</i></sub>	<i>tert</i> -butyl benzylmercaptopan 1,1-bis(diphenylphosphino)methane	Au <sub>2</sub> Ag <sub>60-<i>x</i></sub> (DPPM) <sub>6</sub> (SR) <sub>30</sub> (R = TBBM)	crystal structure	galvnic exchange	139

Table 1. continued

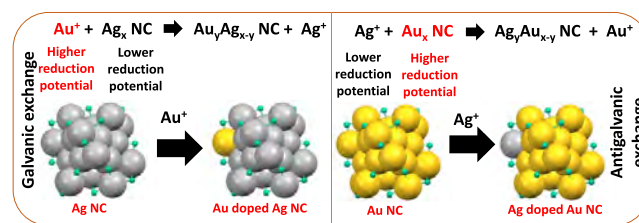
no	core	ligand	alloy cluster	focus	method of synthesis	reference
76	AuAg <sub>24</sub>	6-mercaptotetranedioic acid	AuAg <sub>24</sub> (MHA) <sub>18</sub>	mass spectrometry	galvanic exchange	140
77	Ag <sub>50</sub> Au/Ag <sub>24</sub> Au	2-ethylbenzenethiol	[Ag <sub>50</sub> Au(2-EBT) <sub>18</sub> (PPh <sub>3</sub> ) <sub>6</sub> ] <sup>7+</sup> /[Ag <sub>24</sub> Au(2-EBT) <sub>18</sub> ] <sup>7-</sup>	crystal structure	galvanic exchange	141
78	PtAg <sub>12</sub> Cu <sub>12</sub> Au <sub>4</sub>	adamentanethiol	PtAg <sub>12</sub> Cu <sub>12</sub> Au <sub>4</sub> (S-Adm) <sub>18</sub> (PPh <sub>3</sub> ) <sub>4</sub>	mass spectrometry	galvanic reduction	34
79	Au <sub>22</sub> Ir <sub>3</sub>	phenylethylthiol	Au <sub>22</sub> Ir <sub>3</sub> (PET) <sub>18</sub>	mass spectrometry	intercluster reaction	142
80	Au <sub>12</sub> Ag <sub>17</sub>	1,3-benzenedithiol, triphenylphosphine	Au <sub>12</sub> Ag <sub>17</sub> (BDT) <sub>12</sub> (PPh <sub>3</sub> ) <sub>4</sub>	mass spectrometry	intercluster reaction	89
81	MAu <sub>x</sub> Ag <sub>28-x</sub> (M = Ni/Pd/Pt)	1,3-benzenedithiol, triphenylphosphine	MAu <sub>x</sub> Ag <sub>28-x</sub> (BDT) <sub>12</sub> (PPh <sub>3</sub> ) <sub>4</sub> (M = Ni/Pd/Pt)	mass spectrometry	intercluster reaction	89
82	Au <sub>20</sub> Ag <sub>5</sub>	captropril	Au <sub>20</sub> Ag <sub>5</sub> (Capt) <sub>18</sub>	mass spectrometry	intercluster reaction	143
83	Ag <sub>51-x</sub> Au <sub>x</sub>	1,3-benzenedithiol	Ag <sub>51-x</sub> Au <sub>x</sub> (BDT) <sub>19</sub> (PPh <sub>3</sub> ) <sub>3</sub>	mass spectrometry	intercluster reaction	144
84	Ag <sub>13</sub> Au <sub>12</sub>	triphenylphosphine, phenylethanethiol	[Ag <sub>13</sub> Au <sub>12</sub> (PPh <sub>3</sub> ) <sub>10</sub> (SR) <sub>5</sub> Cl <sub>2</sub> ] <sub>2</sub> <sup>2+</sup>	crystal structure	ligand exchange	54
85	PtAg <sub>28</sub>	1,3-benzenedithiol, triphenylphosphine	PtAg <sub>28</sub> (BDT) <sub>12</sub> (PPh <sub>3</sub> ) <sub>4</sub>	crystal structure	ligand exchange	145,146
86	PdAg <sub>28</sub>	1,3-benzenedithiol, triphenylphosphine	PdAg <sub>28</sub> (BDT) <sub>12</sub> (PPh <sub>3</sub> ) <sub>4</sub>	mass spectrometry	ligand exchange	89
87	NiAg <sub>28</sub>	1,3-benzenedithiol, triphenylphosphine	NiAg <sub>28</sub> (BDT) <sub>12</sub> (PPh <sub>3</sub> ) <sub>4</sub>	mass spectrometry	ligand exchange	89
88	Au <sub>16</sub> Ag	adamentanethiol	[Au <sub>16</sub> Ag(S-Adm) <sub>13</sub> ]	crystal structure	ligand exchange	95
89	PtAg <sub>12</sub>	1,1-bis(diphenylphosphino)methane, 2,4-dimethylbenzenethiol	PtAg <sub>12</sub> (dppm) <sub>5</sub> (SPhMe <sub>2</sub> ) <sub>2</sub>	mass spectrometry	ligand exchange	147
90	Au <sub>4</sub> Cu <sub>5</sub>	cyclohexanethiol, 1,1-bis(diphenylphosphino)methane	[Au <sub>4</sub> Cu <sub>5</sub> (C <sub>6</sub> H <sub>11</sub> S) <sub>6</sub> (Dppm) <sub>2</sub> ](BPh <sub>4</sub> )	crystal structure	ligand exchange	113
91	Au <sub>8</sub> Ag <sub>55</sub>	1,3-bis(diphenylphosphino)propane, cyclohexanethiol, tetraphenylborate	[Au <sub>8</sub> Ag <sub>55</sub> (Dppp) <sub>4</sub> (C <sub>6</sub> H <sub>11</sub> S) <sub>3,4</sub> ](BPh <sub>4</sub> ) <sub>2</sub>	crystal structure	ligand exchange	114
92	PtAg <sub>28</sub>	adamentanethiol, triphenylphosphine	PtAg <sub>28</sub> (S-Adm) <sub>18</sub> (PPh <sub>3</sub> ) <sub>4</sub>	crystal structure	ligand exchange	148
93	Au <sub>14</sub> Ag <sub>22</sub>	adamentanethiol	[Au <sub>14</sub> Ag <sub>22</sub> (S-Adm) <sub>12</sub> ] <sub>3</sub> <sup>3+</sup>	crystal structure	ligand exchange	149
94	Au <sub>24-x</sub> Ag <sub>x</sub>	<i>tert</i> -butyl benzylmercaptant	Au <sub>24-x</sub> Ag <sub>x</sub> (TBBM) <sub>20</sub>	crystal structure	ligand exchange	150
95	PtAg <sub>28</sub>	hexanethiol	PtAg <sub>28</sub> (HT) <sub>18</sub> (PPh <sub>3</sub> ) <sub>4</sub>	crystal structure	ligand exchange	151
96	Ag <sub>2</sub> Au <sub>25</sub>	phenylethanethiol	Ag <sub>2</sub> Au <sub>25</sub> (PET) <sub>18</sub>	mass spectrometry	metal deposition	152
97	MAu <sub>24</sub> (M = Ag/Cu)	phenylethanethiol, triphenylphosphine	[MAu <sub>24</sub> (PPh <sub>3</sub> ) <sub>10</sub> (PET) <sub>5</sub> Cl <sub>3</sub> ] <sub>2</sub> <sup>2+</sup> (M = Ag/Cu)	crystal structure	metal deposition	153

procedure, a large number of bimetallic NCs and a few trimetallic NCs have been prepared. In 1984, the first phosphine-protected biicosahedral Au and Ag alloy NC was synthesized following co-reduction method by Teo and Keating. The obtained alloy NC contained 25 metal atoms with the molecular composition of  $[(PPh_3)_{12}Au_{13}Ag_{12}Cl_6]^{m+}$ .<sup>71</sup> This work was followed by the synthesis of  $[(Ph_3P)_{10}Au_{13}Ag_{12}Br_8]-(PF_6)$ .<sup>72</sup> Then, the same group found new triicosahedral and tetraicosahedral alloy NCs,  $[(p-Tol_3P)_{12}Au_{18}Ag_{20}Cl_{14}]$  and  $[(Ph_3P)_{12}Au_{22}Ag_{24}Cl_{10}]$ , respectively.<sup>73,74</sup> In 1994, Brust *et al.* reported the synthesis of thiolate-protected Au NCs, which showed more stability than their phosphine-protected analogs.<sup>75</sup> Among thiolate-protected NCs,  $Au_{25}(SR)_{18}$  is one of the most studied NCs due to its higher stability. In 2009, Murray *et al.* synthesized  $PdAu_{24}(PET)_{18}$ , which was found to have different electrochemical properties than its monometallic analog.<sup>57</sup> Ag, Cu, and Pt atoms were incorporated into  $Au_{25}(PET)_{18}$  to make  $Au_{25-x}Ag_x(PET)_{18}$ ,<sup>76</sup>  $Au_{25-x}Cu_x(PET)_{18}$ ,<sup>77</sup> and  $PtAu_{24}(PET)_{18}$ <sup>55</sup> via this method. Later,  $PdAu_{24}(DDT)_{18}$  (DDT = dodecanethiol) was purified by Negishi *et al.* using HPLC and the cluster was more stable than monometallic  $Au_{25}(DDT)_{18}$ .<sup>78</sup>  $Au_{25-x}Ag_x(DDT)_{18}$  was also prepared and the number of doped Ag atoms was dependent on the molar ratio of the precursor salts.<sup>79</sup> Ni-doped bi- and trimetallic clusters such as  $Ag_4Ni$  and  $Ag_{12}Au_{12}Ni$  were achieved by this method, which can exhibit interesting magnetic properties.<sup>18,80</sup> Various other alloys with interesting properties can be synthesized easily. Such an example is the chiral alloy NC,  $Au_{13}Cu_2((2R,4R)/(2S,4S)-BDPP)_3(SP_y)_6$ , which was synthesized using chiral ligand 2,4-bis(diphenylphosphino)pentane (BDPP).<sup>81</sup> In addition, alloys of larger-sized NCs were also obtained such as  $(Ag-Au)_{144}(PET)_{60}$ ,  $Au_{144-x}Cu_x(SC_6H_{13})_{60}$ ,  $[Au_{80}Ag_{30}(PhC\equiv C)_{42}Cl_9]Cl$ , etc.<sup>82–84</sup> A large number of Ag-rich alloy NCs were also synthesized such as  $[Ag_{46}Au_{24}(TBHP)_{32}]^{2+}$ ,  $(TOA)_3AuAg_{16}(TBBT)_{12}$ ,  $Au_{12}Ag_{32}(FTP)_{30}$ ,  $Ag_{28}Cu_{12}(2,4-DCBT)_{24}$ , etc.<sup>31,85–87</sup> Among various Ag NCs,  $Ag_{25}(DMBT)_{18}$  is one of the most studied Ag NCs due to its exceptional stability than other Ag NCs and it is structurally similar to  $Au_{25}(PET)_{18}$ . Different groups have synthesized its Pt-, Pd-, and Au-doped alloys such as  $PtAg_{24}(2,4-DMBT)_{18}$ ,  $PdAg_{24}(2,4-DMBT)_{18}$ , and  $Ag_xAu_{25-x}(PET)_{18}$ .<sup>60,88</sup> Our group has reported Ni-doped  $Ag_{25}$ ,  $NiAg_{24}(2,4-DMBT)_{18}$ .<sup>89</sup> Synthesis of alloy NCs using metal precursors having large differences in their redox potentials is difficult. Hence, the incorporation of Fe and Cd by co-reduction method is not possible.  $NaBH_4$  is the most used reducing agent during the synthesis of bi- and trimetallic NCs. However, other reducing agents were used such as  $H_2$ , which was used to prepare  $[Pt(H)(PPh_3)(AuPPh_3)_7]^{2+}$ .<sup>90</sup> A list of NCs prepared so far (until September 2020) is given in Table 1, which includes co-reduction method.

### 3. GALVANIC REDUCTION METHOD

The post-synthetic metal exchange reaction of a NC with a suitable metal precursor is one of the important methods for the preparation of alloy NCs. Among different metal exchange reactions, galvanic reduction reaction has become a very effective approach for making multimetallic alloy NCs as well as various anisotropic alloy nanoparticles. According to the classic galvanic theory, a metal ion of higher reduction potential in solution gets reduced and replaces a metal atom present in a material and the latter subsequently enters the solution after being oxidized. The process is explained in detail in Scheme 2. The metal activity sequence is  $Fe (-0.77 V) > Cd (-0.40 V) >$

**Scheme 2. Schematic Representation of Galvanic and Antigalvanic Exchange Reaction Processes Using Au and Ag as Examples**

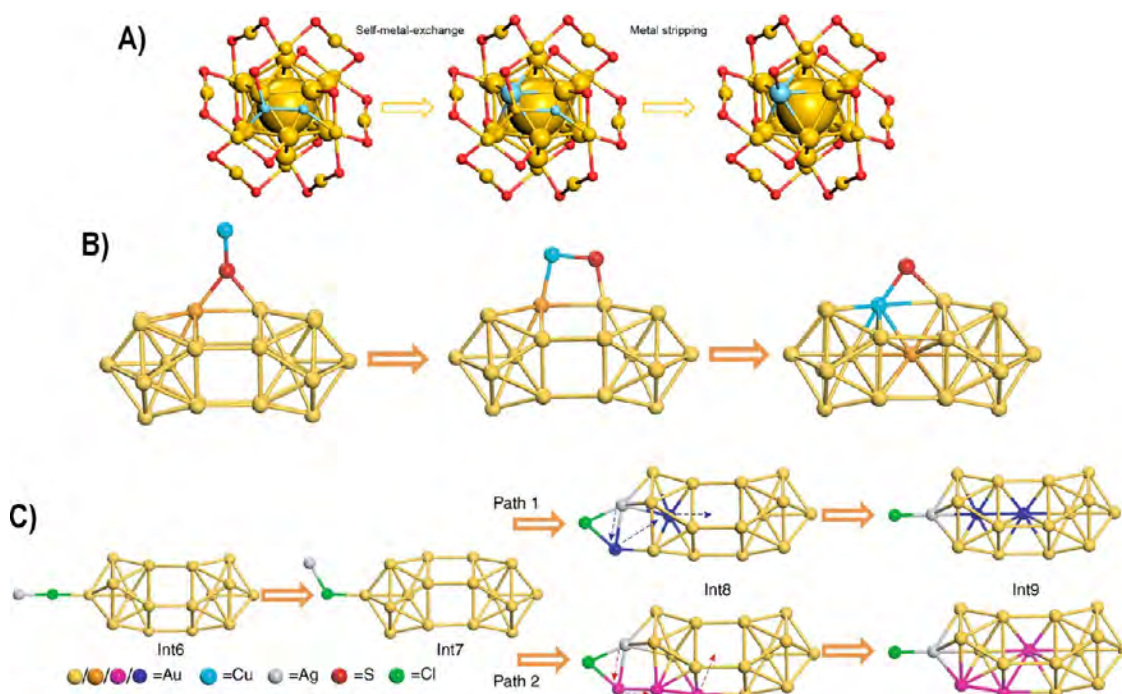


$Co (-0.28 V) > Ni (-0.25 V) > Cu (+0.34 V) > Hg (+0.79 V) > Ag (+0.80 V) > Pd (+0.95 V) > Pt (+1.2 V) > Au (+1.50 V)$ . Various metal atoms have been incorporated in the Ag NCs using galvanic replacement procedure to make silver-rich multimetallic alloy NCs. Such an example is the atomically precise doping of Au atom in  $Ag_{25}(DMBT)_{18}$  to make  $Ag_{24}Au(DMBT)_{18}$  (reduction potentials of  $Ag^+/Ag$  and  $Au^+/Au$  are 0.80 and 1.69 V, respectively).<sup>137</sup> It was found that co-reduction led to the synthesis of  $Ag_{25-x}Au_x(DMBT)_{18}$  (where  $x = 1-8$ ) and, therefore, it is difficult to make single crystals. The availability of single crystal will help in understanding the position of the dopant and, hence, synthesis of a single product is important, which can be achieved by this method.  $Ag_{24}Au(DMBT)_{18}$  exhibits higher stability and enhanced photoluminescence than monometallic  $Ag_{25}(DMBT)_{18}$ . For the synthesis of  $Ag_{24}Au(DMBT)_{18}$ , an already synthesized  $Ag_{25}(DMBT)_{18}$  was treated with  $AuClIPPh_3$ , which changed the color of the solution from brown to green. The product was characterized using ESI MS and SCXRD. The structure of bimetallic  $Ag_{24}Au(DMBT)_{18}$  is similar to the monometallic one. During galvanic exchange reaction, the structure of monometallic NC remains unaltered in their multimetallic analogue; however, Kang *et al.* reported shape-altered synthesis of alloy NCs using this method.<sup>40</sup> The incorporation of Au atoms in  $PtAg_{24}(DMBT)_{18}$  resulted in the formation of shape-unaltered trimetallic  $PtAu_xAg_{24-x}(DMBT)_{18}$  when Au-DMBT was used as the precursor, while the use of  $AuBrPPh_3$  led to the formation of shape-altered trimetallic  $Pt_2Au_{10}Ag_{13}(PPh_3)_{10}Br_7$ . In this case,  $Br^-$  peeled away the  $PtAg_{12}$  core from the staple motifs and transformed it into a biicosahedron, which was stabilized by  $PPh_3$  ligand instead of DMBT. Trimetallic  $PtCu_xAg_{28-x}(BDT)_{12}(PPh_3)_4$  and tetrametallic  $Pt_1Ag_{12}Cu_{12}Au_4(S-Adm)_{18}-(PPh_3)_4$  ( $S-Adm$  = adamantanethiol) NCs were synthesized by galvanic replacement procedure. Several bimetallic NCs have been prepared via this method, which are listed in Table 1.

### 4. ANTIGALVANIC EXCHANGE REACTION

Alloying or doping in  $Au_{25}(SR)_{18}$  was performed largely with different metals such as Ag, Cu, Pd, Pt, Ni, Cd, Hg, and Ir. According to the classic galvanic reduction method, Au NCs are unable to react with the less noble metal atoms such as Ag, Cu, Cd, etc. (reduction potentials of  $Au^+/Au$ ,  $Ag^+/Ag$ ,  $Cu^{2+}/Cu$ , and  $Cd^{2+}/Cd$  are +1.50, +0.80, +0.34, and  $-0.40 V$ , respectively). However, Murray *et al.* showed the reduction of Ag ions by Au NCs, which was followed by the replacement of Au atoms with Ag, leading to the formation of  $Ag_xAu_{25-x}(SR)_{18}$  alloy NCs.<sup>135</sup> This reaction was named as antigalvanic reduction, which is a unique property of Au and Ag NCs and nanoparticles of core size below 3 nm.<sup>136</sup> In 2012, Wu performed the reaction between  $Au_{25}(PET)_{18}$  and Ag ions and the formed bimetallic

**Scheme 3.** Mechanistic pathway of the conversion of  $\text{Ag}_2\text{Au}_{25}(\text{SR})_{18}$  to  $\text{AgAu}_{25}(\text{SR})_{18}$  and Proposed Mechanisms of Cu and Ag Atom Deposition in  $[\text{Au}_{24}(\text{PPh}_3)_{10}(\text{PET})_5\text{Cl}_2]^+$ .<sup>a</sup>



Adapted from refs 152 and 153. Copyright 2018 Nanomaterials and 2017 Nature.<sup>a</sup> (A) Mechanistic pathway of the conversion of  $\text{Ag}_2\text{Au}_{25}(\text{SR})_{18}$  to  $\text{AgAu}_{25}(\text{SR})_{18}$ . Color codes: red, yellow, and cyan colors denote S, Au, and Ag atoms, respectively. (B, C) Proposed mechanisms of Cu and Ag atom deposition in  $[\text{Au}_{24}(\text{PPh}_3)_{10}(\text{PET})_5\text{Cl}_2]^+$ , which resulted in the synthesis of  $[\text{MAu}_{24}(\text{PPh}_3)_{10}(\text{PET})_5\text{Cl}_2]^{2+}$  ( $\text{M} = \text{Cu}/\text{Ag}$ ). Color codes: yellow, orange, pink, and navy blue colors denote Au atoms, while cyan, gray, red, and green colors denote Cu, Ag, S, and Cl, respectively.

products were characterized using laser desorption ionization (LDI) MS. To prove that antialgal exchange reaction is not a unique property of  $\text{Au}_{25}(\text{PET})_{18}$  NC, approximately 2–3 nm nanoparticles were treated with  $\text{AgNO}_3$  solution. The incorporated Ag was detected by XPS and, after the reaction, the binding energy of Ag indicated the incorporation of neutral Ag, which confirmed the reduction of Ag ions by Au nanoparticles. A similar experiment was performed on 3 nm-sized Ag nanoparticles using Cu salt and incorporation of neutral Cu in Ag nanoparticles was observed using XPS. This proved that Cu ions can be reduced by more noble Ag atoms. Antialgal reduction reaction is feasible due to the enhanced reducing ability when the metal is in nanoscale form. One of the important driving factors for antialgal reduction is the protective ligands on the surface of nanoparticles or NCs. It was proposed that the partial negative charge present on the surface ligands plays a crucial role in the reduction of more reactive ions. This observation led Wu *et al.* to modify the sequence of metal activity as  $\text{Fe} > \text{Ni} > \text{Pd} > \text{Au} (\sim 3 \text{ nm}) > \text{Cu} > \text{Ag}$ .<sup>92,136</sup> After that, Zhu *et al.* showed the incorporation of monovalent Cu/Ag and bivalent Cd/Hg in  $\text{Au}_{25}(\text{SR})_{18}$  NCs.<sup>91</sup> Cd and Hg atoms were getting doped at the center of the icosahedral core, while Cu and Ag atoms were incorporated on the surface of the icosahedron. Similar to galvanic exchange reaction, in the case of antialgal exchange, dopants are mostly getting incorporated in the parent NCs without changing their structures and compositions. However, in some NC systems, the replacement with a foreign metal atom can lead to structural transformations. For example, the doping of Ag and Cu atoms in  $\text{Au}_{25}(\text{SR})_{18}$ ,  $\text{Au}_{38}(\text{PET})_{24}$ ,  $\text{Au}_{36}(\text{SR})_{24}$ ,  $\text{Au}_{144}(\text{PET})_{60}$ , etc., and doping of Cd and Hg in  $\text{Au}_{25}(\text{SR})_{18}$  resulted in the formation of alloy NCs

with preserved composition and structure.<sup>82,91,97,132</sup> On the other hand, doping of Ag atoms in  $\text{Au}_{23}(\text{CHT})_{16}$  (CHT = cyclohexylthiol) NCs first led to the formation of  $\text{Au}_{23-x}\text{Ag}_x(\text{CHT})_{16}$ , which then got converted to  $\text{Au}_{25-x}\text{Ag}_x(\text{CHT})_{18}$ .<sup>38,154</sup> The Au-rich trimetallic and tetrametallic NCs  $\text{M}_1\text{Ag}_x\text{Au}_{24-x}(\text{SR})_{18}$  ( $\text{M} = \text{Cd}/\text{Hg}$ )<sup>41</sup> have also been synthesized by this effective method. A list of multicomponent NCs made *via* antialgal reduction is presented in Table 1.

## 5. METAL DEPOSITION METHOD

The metal deposition or intramolecular metal exchange is one of the emerging alloying methods. Li *et al.* reported the synthesis of  $\text{Ag}_2\text{Au}_{25}(\text{SR})_{18}$  *via* reaction of  $\text{Au}_{25}(\text{SR})_{18}$  with  $\text{AgNO}_3$ <sup>152</sup> where Ag atoms occupied the outer staple. But, after treatment with excess ligand, Ag atoms diffused within the icosahedral core, which led to the formation of  $\text{AgAu}_{24}(\text{SR})_{18}$ . The reaction occurred in two steps as shown in Scheme 3A. The first step is the self-metal exchange, which is the intramolecular metal exchange. During the first step, one of the Ag atoms, which were in the outer staple (denoted in blue color in Scheme 3A), got exchanged with one of the icosahedral Au atoms. Thus, after exchange, one Ag atom was on the inner icosahedral surface and another one in the outer staple. This was followed by the second step where the surface Au and Ag atoms were detached from the surface of the cluster and resulted in the synthesis of  $\text{AgAu}_{24}(\text{SR})_{18}$ . This process was called the metal stripping process. The same process was observed by Zheng *et al.* in  $\text{AuAg}_{24}(\text{MHA})_{18}$  NCs.<sup>140</sup>

Using high-resolution ESI MS, they monitored real-time diffusion of Au atoms from the staple motif to the icosahedral surface and then to the center of the icosahedron to attain



thermodynamic stability. The metal deposition method can be extrapolated into a hollowing and refilling process where foreign metal atoms are incorporated to make alloy NCs. Single Cu and Ag atoms were added successfully by Wang *et al.* in  $[\text{Au}_{24}(\text{PPh}_3)_{10}(\text{PET})_5\text{Cl}_2]^+$ , which led to the synthesis of  $[\text{MAu}_{24}(\text{PPh}_3)_{10}(\text{PET})_5\text{Cl}_2]^{2+}$  ( $\text{M} = \text{Ag}/\text{Cu}$ ).<sup>153</sup> In this case, the  $-\text{SR}$  group and Cl atom played important roles. At first, a foreign atom got attached to the S/Cl atom present in the waist/apex positions, respectively. Due to this interaction, the Au–S/Au–Cl bond collapsed and the Au atom migrated to the central position, which reduced the energy of the system as shown in Scheme 3B,C. Mainly, the Ag atom was doped at the apex site, while Cu occupied both apex and waist positions as the Ag–Cl bond is stronger than Ag–SR, unlike that of Cu–Cl that has the same binding energy as of Cu–SR.

## 6. LIGAND EXCHANGE METHOD

Ligand exchange is an efficient method for the synthesis of atomically precise NCs in which one NC is converted to another, with the same or different nuclearity in the presence of foreign ligands.<sup>68</sup> The ligand exchange process where the structure of the starting NC undergoes structural conversion is named as ligand exchange-induced structural transformation (LEIST) by Jin's group.<sup>155</sup> This is a fast-evolving method in NC chemistry, which enhances the range of applications of NCs by introducing different functional ligands. LEIST method has been widely used for making a large number of monometallic NCs; however, it is now also being used for the preparation of multimetallic NCs. Biicosahedral  $\text{PtAg}_{23}(\text{PPh}_3)_{10}\text{Cl}_7$  was converted to monoicosahedral  $\text{PtAg}_{24}(\text{DMBT})_{18}$  and  $\text{PtAg}_{28}(\text{BDT})_{12}(\text{PPh}_3)_4$  on addition of DMBT and BDT ligands, respectively.<sup>145,147</sup>  $\text{PtAg}_{28}(\text{S-Adm})_{18}(\text{PPh}_3)_4$  was synthesized by the conversion of  $\text{PtAg}_{24}(\text{DMBT})_{18}$  after addition of Adm-SH and  $\text{PPh}_3$ .<sup>148</sup> Similarly,  $\text{MAG}_{28}(\text{BDT})_{12}(\text{PPh}_3)_4$  ( $\text{M} = \text{Ni}/\text{Pd}/\text{Pt}$ ) was synthesized *via* the LEIST method starting from  $\text{MAG}_{24}(\text{DMBT})_{18}$  ( $\text{M} = \text{Ni}/\text{Pd}/\text{Pt}$ ) (see Figure 1).<sup>89</sup> Ligand exchange method also helped make the *n*-hexanethiol (HT)-protected NC,  $\text{PtAg}_{28}(\text{HT})_{18}(\text{PPh}_3)_4$  from  $\text{PtAg}_{28}(\text{S-Adm})_{18}(\text{PPh}_3)_4$ , keeping the structure unaltered.<sup>151</sup> Moreover, Zhu *et al.* showed the synthesis of highly luminescent  $\text{Pt}_1\text{Ag}_{12}(\text{dppm})_5(\text{DMBT})_2$  from feebly luminescent  $\text{Pt}_2\text{Ag}_{23}(\text{PPh}_3)_{10}\text{Cl}_7$  by introducing dppm along with DMBT.<sup>147</sup> Further, Kang *et al.* reported a new alloy NC,  $\text{AgAu}_{16}(\text{S-Adm})_{13}$  starting from  $\text{AgAu}_{17}(\text{CHT})_{14}$  by this methodology.<sup>95</sup> Also,  $\text{Ag}_x\text{Au}_{24-x}(\text{TBBT})_{16}$  was synthesized from  $\text{Ag}_x\text{Ag}_{23-x}(\text{HT})_{16}$  upon treatment with TBBT. It has been proposed that the drastic change in the nuclearity of the NC is due to the change in the electron-withdrawing and electron-donating effect of ligands, which depends on the position of the functional groups. The noncovalent interactions and steric hindrance are also crucial factors for this transformation. However, the effect of ligand on the nuclearity and structure of the NC is unclear.

## 7. INTERCLUSTER REACTION METHOD

Besides various synthetic methods, the reaction between two NCs has become an emerging method to obtain multimetallic alloy NCs. We are discussing this method more elaborately than others as it has not been reviewed previously, in the context of alloy clusters. Krishnadas *et al.* found the chemical reaction between two atomically precise NCs, which resembles the reaction between two organic molecules. They first reported the

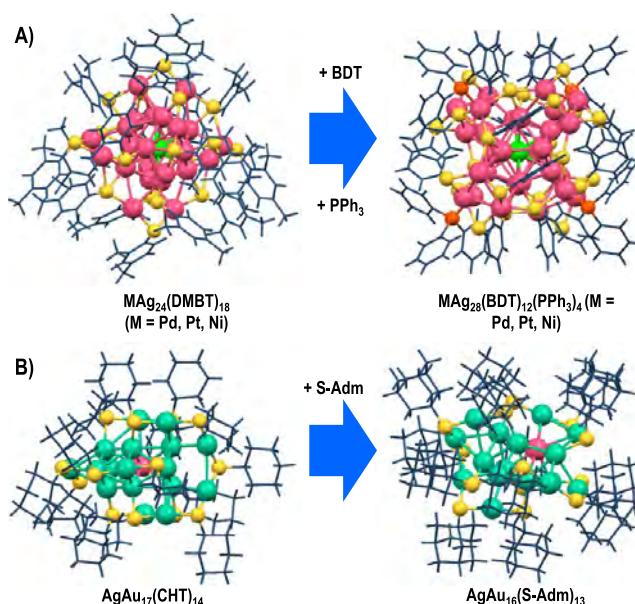


**Figure 1.** (A) Formation of  $\text{MAG}_{28}(\text{BDT})_{12}(\text{PPh}_3)_4$  from  $\text{MAG}_{24}(\text{DMBT})_{18}$  ( $\text{M} = \text{Pd, Pt, Ni}$ ) NCs. Green, pink, yellow, and orange denote M (Pd, Pt, Ni), Ag, S, and P atoms, respectively. Blue color denotes C and H atoms of thiol ligands. (B) Conversion of  $\text{AgAu}_{17}(\text{CHAT})_{14}$  to  $\text{AgAu}_{16}(\text{S-Adm})_{13}$ . The colors pink, green, and yellow denote Ag, Au, and S atoms, respectively. Blue color denotes C and H atoms of thiol ligands.

reaction between pure Ag and Au NCs,  $\text{Ag}_{44}(\text{FTP})_{30}$  and  $\text{Au}_{25}(\text{FTP})_{18}$ , respectively, which led to the formation of Au-doped  $\text{Ag}_{44}(\text{FTP})_{30}$  and Ag-doped  $\text{Au}_{25}(\text{FTP})_{18}$  bimetallic NCs.<sup>138</sup> These intercluster reactions are controlled by both kinetics and thermodynamics. The extent of reaction and its mechanism were studied in detail using MS. Negative-mode MALDI MS at two different reaction times at the  $\text{Au}_{25}(\text{FTP})_{18}$  side is shown in Figure 2. The blue spectrum corresponding to MALDI MS after 1 h of reaction showed the incorporation of up to 5 Ag atoms, which resulted in the formation of  $\text{Au}_{25-x}\text{Ag}_x(\text{FTP})_{18}$ , while the insertion of up to 13 Ag atoms was observed after 3 h of reaction (red spectrum). As both reacting NCs were protected by the same protecting ligand, no

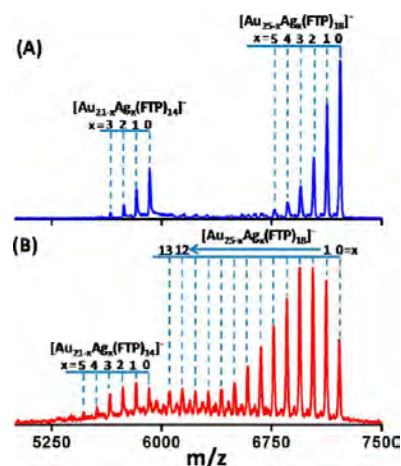


**Figure 2.** MALDI MS of reaction between  $\text{Au}_{25}(\text{FTP})_{18}$  and  $\text{Ag}_{44}(\text{FTP})_{30}$  in negative ion mode after (A) 1 h and (B) 3 h of the reaction at the  $\text{Au}_{25}$  region. Reprinted from ref 138. Copyright 2016 American Chemical Society.

ligand exchange was observed in the MS. The doping of Ag atoms into  $\text{Au}_{25}(\text{SR})_{18}$  was found to be more facile *via* this protocol where up to 20 Ag atoms can be incorporated. The total number of atoms and the overall charge state remain preserved in the formed alloy NCs during this kind of substitution reaction. Similar to the  $\text{Au}_{25}$  region, the reaction also occurred in the  $\text{Ag}_{44}$  region as shown in Figure 3.<sup>133</sup> At first, a mixture of bimetallic

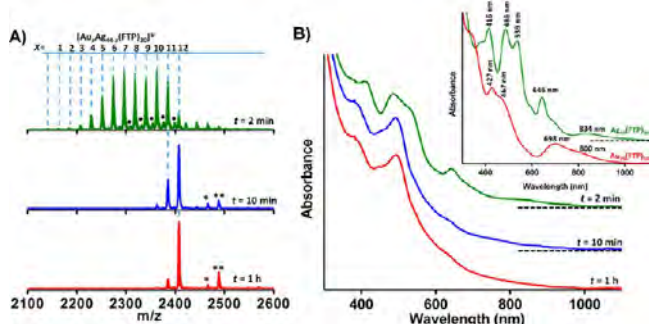


**Figure 3.** (A) Time-dependent ESI MS and (B) time-dependent UV–vis absorption spectra of the reaction between  $\text{Ag}_{44}(\text{FTP})_{30}$  and  $\text{Au}_{25}(\text{FTP})_{18}$  at the  $\text{Ag}_{44}$  region. Adapted from ref 133. Copyright 2017 American Chemical Society.

NCs was formed having the composition,  $\text{Au}_x\text{Ag}_{44-x}(\text{FTP})_{30}$  where  $x = 1–12$ . After 1 h, this mixture resulted in the formation of  $\text{Au}_{12}\text{Ag}_{32}(\text{FTP})_{30}$  exclusively (Figure 3A). The reaction was monitored by time-dependent UV–vis spectroscopy as shown in Figure 3B. It showed a significant spectral change with time and the final spectrum was completely different than that of  $\text{Ag}_{44}(\text{FTP})_{30}$  as well as  $\text{Au}_{25}(\text{FTP})_{18}$ , confirming the formation of the bimetallic NC  $\text{Au}_{12}\text{Ag}_{32}(\text{FTP})_{30}$ . Although tools like MS, UV–vis absorption spectroscopy, NMR, etc., help in understanding the extent of doping, the precise structural insight can be obtained only from X-ray crystallography. In the absence of a single crystal, one can understand the doping position by computations as the structures of the monometallic NCs remain preserved to a large extent in the multimetallic NCs during such reactions. The single-crystal X-ray structure of  $\text{Ag}_{44}(\text{FTP})_{30}$  consists of a  $\text{Ag}_{12}$  hollow icosahedron inside a  $\text{Ag}_{20}$  dodecahedron, which is covered by a  $\text{Ag}_{12}(\text{FTP})_{30}$  outer shell. On the other hand,  $\text{Au}_{25}(\text{FTP})_{18}$  is made up of a  $\text{Ag}_{13}$  central icosahedron protected by a  $\text{Ag}_{12}(\text{FTP})_{18}$  surface motif. In the case of the reaction involving  $\text{Ag}_{44}(\text{FTP})_{30}$  and  $\text{Au}_{25}(\text{FTP})_{18}$ , the total energy of the substituted product was found to be the most negative when Au and Ag atoms occupied the icosahedral surface of  $\text{Ag}_{44}(\text{FTP})_{30}$  and  $\text{Au}_{25}(\text{FTP})_{18}$ , respectively. Hence, it was concluded that the substitution of metal atoms during the intercluster reaction was an energy-driven process. It was proposed that the intercluster reaction proceeds through bond breaking due to metallophilic and noncovalent interactions between ligands or redox reactions. The fragments generated after bond breaking behaved as nucleophiles, which led to the incorporation of another metal atom similar to that of the metal exchange reactions. The formation of an adduct of two NCs (due to noncovalent interactions between ligands and metallophilic interactions) was observed in ESI MS during the reaction between two structurally similar Au and Ag NCs,  $\text{Au}_{25}(\text{PET})_{18}$  and  $\text{Ag}_{25}(\text{DMBT})_{18}$ , as shown in Figure 4.<sup>156</sup> The adduct vanished within 5 min of mixing and a series of peaks were observed due to the formation of  $\text{Au}_x\text{Ag}_y(\text{SR})_{18}$ . This adduct formation suggested that the intercluster reaction is

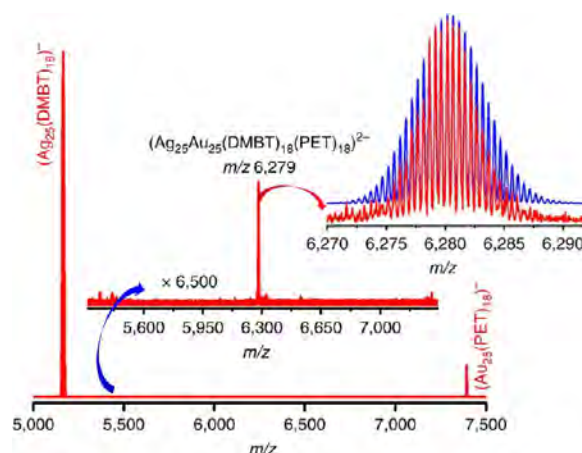


**Figure 4.** ESI MS of the mixture of  $[\text{Ag}_{25}(\text{DMBT})_{18}]^-$  and  $[\text{Au}_{25}(\text{PET})_{18}]^-$ , resulting in the formation of the intermediate adduct  $[\text{Ag}_{25}\text{Au}_{25}(\text{DMBT})_{18}(\text{PET})_{18}]^{2-}$  whose theoretical and experimental isotopic distributions match with each other. Reprinted from ref 156. Copyright 2016 Nature.

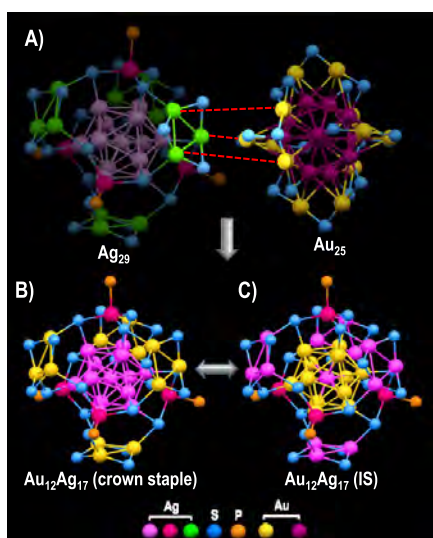
bimolecular. The structure of this adduct was calculated using DFT, which manifested that bond lengths of both NCs were longer than that of individual NCs. Also, the bond angles of staples of both NCs changed significantly in the adduct. Further chemical and structural transformation might occur during the reaction after adduct formation. In the alloy NCs  $\text{Au}_x\text{Ag}_y(\text{SR})_{18}$ , the number of doped Ag and Au atoms can be varied from 1 to 24 by varying the molar ratio of reactant NCs. Therefore, the desired number of dopants can be inserted using intercluster reaction. Similar to the previous reaction, in this case, the total number of metal and ligand in alloy NCs is identical with that of the unreacted NCs. Regarding the dopant position, the computational study revealed that the total energy of the reaction will be the most favorable when a Au atom occupies the central position of the icosahedron in  $\text{Ag}_{25}(\text{DMBT})_{18}$ , while a Ag atom occupies the icosahedral surface of  $\text{Au}_{25}(\text{PET})_{18}$ . Not only Ag but also Ir metal incorporation in  $\text{Au}_{25}(\text{SR})_{18}$  was obtained *via* intercluster reaction, which otherwise is difficult to achieve by other methods. Bhat *et al.* discussed the intercluster reaction between an Ir NC,  $\text{Ir}_9(\text{PET})_6$ , and a Au NC,  $\text{Au}_{25}(\text{PET})_{18}$ , which led to the formation of  $\text{Ir}_3\text{Au}_{22}(\text{PET})_{18}$ .<sup>142</sup> In this reaction, only one single product got formed, which was then separated from the unreacted NCs by thin-layer chromatography (TLC), and the purity was checked with ESI MS. The DFT study revealed that the Ir atoms occupy the center and surface of the icosahedral core.

In these reactions, the use of two monothiol-protected NCs also led to ligand exchange; although, the total number of thiol ligands remains the same. As DMBT and PET are of the same mass, no ligand exchange could be observed in ESI MS data but ligand exchange between FTP and PET was observed. Due to high mobility, ligands undergo spontaneous exchange. The mobility of ligands can be decreased by using bidentate ligands such as dithiols. Ghosh *et al.* showed the reactions of bidentate thiol-protected NCs,  $\text{Ag}_{51}(\text{BDT})_{19}(\text{PPh}_3)_3$  and  $\text{Ag}_{29}(\text{BDT})_{12}(\text{PPh}_3)_4$ , with  $\text{Au}_{25}(\text{PET})_{18}$  and noticed the exchange between Ag and Au atoms and no exchange occurred between the ligands.<sup>144</sup> The reaction rate was observed to be slow, which may be due to the presence of a rigid bidentate ligand that rigidifies the surface of the NC. They found the incorporation of three Au atoms in  $\text{Ag}_{51}(\text{BDT})_{19}(\text{PPh}_3)_3$  and



$\text{Ag}_{29}(\text{BDT})_{12}(\text{PPh}_3)_4$ . Later on, the reaction between  $\text{Ag}_{29}(\text{BDT})_{12}(\text{PPh}_3)_4$  and  $\text{Au}_{25}(\text{PET})_{18}$  was studied in detail, which showed the incorporation of a maximum of 12 Au atoms in  $\text{Ag}_{29}(\text{BDT})_{12}(\text{PPh}_3)_4$ , while only up to 7 Ag atoms were getting doped in  $\text{Au}_{25}(\text{PET})_{18}$ , unlike the previously mentioned intercluster reactions.<sup>89</sup> This was due to the use of a very high concentration of  $\text{Au}_{25}(\text{PET})_{18}$  (five times higher) in comparison to  $\text{Ag}_{29}(\text{BDT})_{12}(\text{PPh}_3)_4$  to increase the reaction rate, which was otherwise very slow due to the rigid surface. This proved that the rate of reactions strongly depends on the metal–ligand interface. The oligomeric  $\text{M}_x\text{L}_y$  surface staples were well defined in these NCs, and in some of these clusters, the oligomeric staple motifs formed interlocked rings as in  $\text{Ag}_{25}(\text{SR})_{18}$  and  $\text{Au}_{25}(\text{SR})_{18}$ . The structure of these kinds of NCs had been compared to the Borromean rings, as proposed by Natarajan *et al.*, and NCs were referred to as aspicules (meaning shielded molecules).<sup>157</sup> According to this structural alignment, breaking of one ring led to the destruction of the entire structure of these NCs, which resulted in the generation of  $\text{M}_x\text{L}_y$  fragments behaving as nucleophiles in the substitution reaction. This process led to the incorporation of 1–24 Ag and Au atoms in the respective NCs to make bimetallic ones. This was not the same in the case of dithiol-protected NCs such as in  $\text{Ag}_{29}(\text{BDT})_{12}(\text{PPh}_3)_4$ , which comprised two types of staples:  $\text{Ag}_3\text{S}_6$  and Ag–P, unlike that of the Borromean ring structure. These staples were difficult to break as they were stabilized by dithiol, and hence, it was proposed that  $\text{Au}_{25}(\text{SR})_{18}$  NCs were interacting with  $\text{Ag}_{29}(\text{BDT})_{12}(\text{PPh}_3)_4$  via weak van der Waal interactions at the less congested  $\text{Ag}_3\text{S}_6$  staples as shown in Scheme 4. This interaction assisted the metal exchange between two NCs at the outer staple, leading to the synthesis of bimetallic NCs. Then, the doped Ag and Au atoms underwent intramolecular galvanic

**Scheme 4. Proposed Interactions between Ag and Au Atoms of  $\text{Ag}_{29}(\text{BDT})_{12}(\text{PPh}_3)_4$  and  $\text{Au}_{25}(\text{PET})_{18}$  (A), Which Led to the Formation of Kinetically Controlled  $\text{Au}_{12}\text{Ag}_{17}(\text{BDT})_{12}(\text{PPh}_3)_4$  at the Outer Surface, Which Then Diffuses Inside the Icosahedron Core to Form a Thermodynamically Stable Structure.<sup>a</sup>**



Adapted with permission from ref 89. Copyright 2020 American Chemical Society <sup>a</sup>Color codes: Green and pink (both light and dark shades) denote Ag atoms, yellow and purple denote Au atoms, cyan denotes S atoms, and orange denotes P atoms.

and antialgal exchange to occupy the energetically most stable positions, which were the icosahedral surface positions.

Intercluster reaction was then expanded to make trimetallic NCs.<sup>89</sup> We showed the reaction of bimetallic  $\text{MAg}_{28}(\text{BDT})_{12}(\text{PPh}_3)_4$  (where  $\text{M} = \text{Ni}/\text{Pd}/\text{Pt}$ ) with monometallic  $\text{Au}_{25}(\text{PET})_{18}$ , which produced a mixture of trimetallic  $\text{MAu}_x\text{Ag}_{28-x}(\text{BDT})_{12}(\text{PPh}_3)_4$  and bimetallic  $\text{Ag}_x\text{Au}_{25-x}(\text{PET})_{18}$ . Unlike  $\text{Ag}_{29}(\text{BDT})_{12}(\text{PPh}_3)_4$ , the use of doped  $\text{Ag}_{29}(\text{BDT})_{12}(\text{PPh}_3)_4$  exhibited higher reactivity; however, it was slower as compared to the monothiol-protected ones. A time-dependent ESI MS of the reaction sequence between  $\text{PdAg}_{28}(\text{BDT})_{12}(\text{PPh}_3)_4$  and  $\text{Au}_{25}(\text{PET})_{18}$  (1:5 molar ratio) is shown in Figure 5, which manifests the extent of reaction with time. With increasing time, the number of doped Au atoms increased and it formed a stable single trimetallic NC  $\text{PdAu}_{12}\text{Ag}_{16}(\text{BDT})_{12}(\text{PPh}_3)_4$ , while doping up to 7 Ag atoms was seen in  $\text{Au}_{25}(\text{PET})_{18}$  forming a mixture of bimetallic  $\text{Ag}_x\text{Au}_{25-x}(\text{PET})_{18}$  (where  $x = 1-7$ ) clusters. Similar to  $\text{PdAu}_{12}\text{Ag}_{16}(\text{BDT})_{12}(\text{PPh}_3)_4$ , trimetallic  $\text{PtAu}_{12}\text{Ag}_{16}(\text{BDT})_{12}(\text{PPh}_3)_4$  NC too got formed by intercluster reaction between  $\text{PtAg}_{28}(\text{BDT})_{12}(\text{PPh}_3)_4$  and  $\text{Au}_{25}(\text{PET})_{18}$ . Also,  $\text{NiAu}_x\text{Ag}_{28-x}(\text{BDT})_{12}(\text{PPh}_3)_4$  was obtained by intercluster reaction between  $\text{NiAg}_{28}(\text{BDT})_{12}(\text{PPh}_3)_4$  and  $\text{Au}_{25}(\text{PET})_{18}$ . One important aspect to notice here was that the centrally doped Ni, Pd, and Pt atoms in  $\text{Ag}_{29}(\text{BDT})_{12}(\text{PPh}_3)_4$  did not get transferred to  $\text{Au}_{25}(\text{PET})_{18}$  to make corresponding bi- or trimetallic NCs. This observation supported the above mechanism, which depicted the involvement of metal–ligand interface during the intercluster reaction and not the central atom. Hence, based on this, we calculated the structure of trimetallic  $\text{MAu}_{12}\text{Ag}_{16}(\text{BDT})_{12}(\text{PPh}_3)_4$  ( $\text{M} = \text{Ni}/\text{Pd}/\text{Pt}$ ), where M atom was at the center of the icosahedral core and 12 Au atoms occupied the icosahedral surface positions.

There have been other attempts of intercluster reactions by other groups such as Xia *et al.*, who reported the synthesis of  $\text{Au}_{20}\text{Ag}_5(\text{Capt})_{18}$  by the reaction between  $\text{Au}_{25}(\text{Capt})_{18}$  and  $\text{Ag}_{30}(\text{Capt})_{18}$ .<sup>143</sup> The product was purified using polyacrylamide gel electrophoresis (PAGE). While both the reactant NCs were non-emissive, the alloy cluster exhibited intense red emission. MALDI MS was used to determine the composition of as-synthesized alloy NCs.

The reaction of nanocluster has also been observed with nanoparticles by Xia *et al.*<sup>143</sup> They found the doping of Cu atoms by the reaction of  $\text{Au}_{25}(\text{SR})_{18}$  with Cu nanoparticles of  $\sim 1.4$  nm. This gave a new turn of the reaction involving nanoclusters. Similarly, Bose *et al.* have observed doping of Ag atoms in atomically precise  $\text{Au}_{25}(\text{PET})_{18}$  nanoclusters using polydispersed Ag nanoparticles.<sup>158</sup>

## 8. NANOCUSTER-BULK REACTIONS

To understand the mechanism of intercluster reactions and the role of metal–ligand interfaces in greater detail, Kazan *et al.* conducted a reaction of NCs with surfaces of bulk metals.<sup>159</sup> They used  $\text{Au}_{25}(\text{PET})_{18}$  and  $\text{Au}_{38}(\text{PET})_{24}$  NCs to react with Ag, Cu, and Cd foils before and after functionalization with thiols. The doping rate was observed to be different for the treated and untreated foils. Treated Ag foils exhibited a faster reaction rate, which decreased with time, while the untreated one showed a lower reaction rate at first and slowly increased after a certain time. This observation indicated that pre-functionalized thiols on the foils play a crucial role in the reaction, which indeed emphasized the importance of metal–ligand interfaces during the reaction between NCs (the mechanism is shown in Scheme

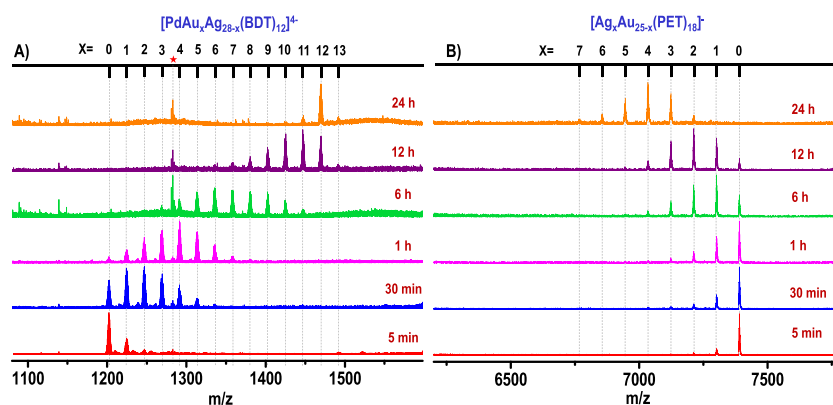
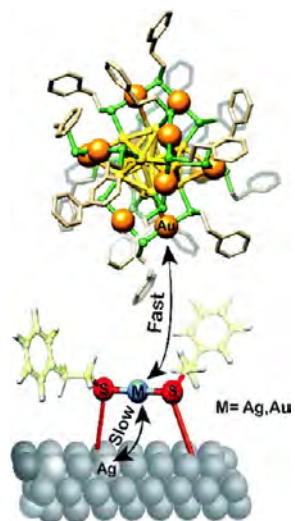


**Figure 5.** ESI MS of reaction between  $\text{PdAg}_{28}(\text{BDT})_{12}(\text{PPh}_3)_4$  and  $\text{Au}_{25}(\text{PET})_{18}$  (1:5 molar ratio) at different time intervals. (A) Reaction at the  $\text{PdAg}_{28}(\text{BDT})_{12}(\text{PPh}_3)_4$  side and (B) the reaction at the  $\text{Au}_{25}(\text{PET})_{18}$  side. The formed clusters are  $[\text{PdAu}_x\text{Ag}_{28-x}(\text{BDT})_{12}]^{4-}$  and  $[\text{Ag}_x\text{Au}_{25-x}(\text{PET})_{18}]^-$ . The charged species are not mentioned in the text for simplicity. The red asterisk in (A) is due to thiolates produced during the reaction. Adapted with permission from ref 89. Copyright 2020 American Chemical Society.

5).<sup>160</sup> In the case of Cu and Cd foils, the reaction did not occur with the bare metal foils. Insertion of a few Cu and Cd atoms can

**Scheme 5. Pictorial Illustration of the Reaction between  $\text{Au}_{25}(\text{PET})_{18}$  with Ag Foil. Adapted with permission from ref 159. Copyright 2019 Royal Society of Chemistry**



be seen during the reaction with the pre-treated foils. This new class of reactions of NCs with bulk metals opens up new opportunities for making different alloy NCs.

## 9. CONCLUSIONS AND FUTURE PERSPECTIVES

In the following, we list below several possibilities to expand this science.

**Diversity:** About 100 bimetallic alloy NCs are known till now; however, only about 10 alloy NCs with more than one heteroatom have been reported. To the best of our knowledge, only two tetrametallic NCs ( $[\text{Pt}_1\text{Ag}_{12}\text{Cu}_{12}\text{Au}_4(\text{S-Adm})_{18}(\text{PPh}_3)_4]$  and  $\text{Au}_{24-x-y}\text{Ag}_x\text{Cu}_y\text{Pd}(\text{SC}_{12}\text{H}_{25})_{18}$ ) have been reported. Hence, incorporation of more metals in a given cluster core, such as pentametallic and beyond, will be worth exploring. This may lead to high entropy alloy NCs, which might show improved properties, in areas such as catalysis. Finding some

methods to control the number of doped atoms in an alloy NC are also important.

The reaction of a NC with another NC of a different metal or even bulk metal is an efficient method for preparing bimetallic and trimetallic NCs. The reactions between a few NCs have been studied. There are more than 150 NCs whose structures have been solved and many more NCs are reported, whose structures are yet to be understood. Hence, intercluster reactions using these NCs can be studied to expand their chemistry. Reactions of NCs can be studied with other nanostructures and different bulk metals, which might give a new twist to the area.

**Structures and properties:** Over 100 multicomponent atomically precise alloy NCs comprising Au, Ag, Ni, Cu, Hg, Ir, Cd, Pd, and Pt have been synthesized till date using different synthesis methods. Most of these have been characterized with mass spectrometry, and about 50 have crystal structures. As a glaring gap, Fe and Co doping has not been accomplished yet in such clusters and these alloy clusters can be of potential interest due to their magnetic properties. Incorporation of lanthanides in NCs to make alloys will be an exciting study due to their interesting magnetic and photophysical properties. Even though Ni-doped NCs such as  $\text{NiAu}_{24}$ ,  $\text{NiAg}_{24}$ , and  $\text{NiAg}_{28}$  have been synthesized, their magnetic properties have not been studied so far. These alloy NCs can show multiple phenomena such as circularly polarized luminescence, magneto-fluorescence, etc., which will help to broaden their applications.

Structures of multimetallic NCs will provide details of their optical and electronic properties. Unlike bimetallic NCs, the structure of tri- and tetrametallic NCs are yet to be studied extensively. Mainly, two kinds of alloy NCs are observed, (i) keeping the structure and composition the same, a specific number of foreign atoms are doped and (ii) the structure and compositions are different and the extent of doping depends on the molar ratio of the precursors used. In both the cases, it is crucial to get a single product either by controlling the synthesis method or by isolating the cluster of interest. The isolation of a specific isomer will be highly interesting, which can induce the possibility of crystallization.



**Dynamics and mechanism:** The exchange of metal atoms and the ligands between two different NCs manifest the dynamic nature of the outer staple motifs of NCs and protecting ligands. The investigation of this chemical event will be interesting. Also, a detailed study of the metal–ligand interface by theoretical calculations can reveal important information. In addition, a mechanistic study of the interactions between two NCs in the transition state is essential to have a deeper understanding of intercluster reactions. Although interaction of clusters leading to dimers have been observed in mass spectrometry, these species have not been trapped. Cluster reactions go through such an intermediate and several such intermediates have been identified. However, none of them have been seen. With the advancements in cryo-electron microscopy, it might be possible to observe such species in solution. If that becomes possible, it will lead to a new understanding of atom transfer processes, how chemical bonds are modified, etc. The existence of Borromean rings may be understood from such studies.

**Bulk properties:** The availability of larger crystals will enable the measurements of various physical properties of NC solids such as electrical conductivity, mechanical properties, etc., which can open a new paradigm in NC-based research. A systematic effort in the properties of clusters has to occur. The mechanical response of a few monometallic NC solids has been studied; however, this new field need to be explored using various multimetallic NC solids.

**Assemblies and superstructures:** Supramolecular assemblies of NCs with different nanoparticles or molecules and NC-based metal–organic frameworks are emerging materials as they can be used as functional building blocks to make hierarchical frameworks with improved properties. Although a few assemblies have been made using monometallic NCs, the area is yet to be expanded to multimetallic alloy NCs, which can bring in several unprecedented properties.

While many of these will be pursued in the coming years, there are inherent challenges in this system. The principal one is related to the dynamics of atoms in this length scale. That would mean that stabilizing the cluster systems in the solution and solid state for extended periods would involve the use of specific ligands, which do not allow atom transfer to occur. However, in some other contexts, these dynamics may be advantageous also. The extent of dynamics may be the reason for their use in catalysis. Whatever be the case, understanding such processes will require a great amount of computational effort. As the size of the systems increases, these efforts will become increasingly demanding.

## AUTHOR INFORMATION

### Corresponding Author

**Thalappil Pradeep** – Department of Chemistry, DST Unit of Nanoscience (DST UNS) and Thematic Unit of Excellence (TUE), Indian Institute of Technology Madras, Chennai 600036, India; [orcid.org/0000-0003-3174-534X](https://orcid.org/0000-0003-3174-534X); Email: [pradeep@iitm.ac.in](mailto:pradeep@iitm.ac.in)

### Author

**Esma Khatun** – Department of Chemistry, DST Unit of Nanoscience (DST UNS) and Thematic Unit of Excellence

(TUE), Indian Institute of Technology Madras, Chennai 600036, India

Complete contact information is available at:  
<https://pubs.acs.org/10.1021/acsomega.0c04832>

## Notes

The authors declare no competing financial interest.

## ACKNOWLEDGMENTS

We thank the Department of Science and Technology, Government of India for constantly supporting our research program on nanomaterials. E.K. thanks the Indian Institute of Technology Madras for research and doctoral fellowships.

## REFERENCES

- (1) Acheson, L. A History of Metals. *Science* **1960**, *132*, 887–888.
- (2) Maddin, R. *The Beginning of the Use of Metals and Alloys*. The MIT Press, 1988.
- (3) Pradeep, T.; Anshup. Noble Metal Nanoparticles for Water Purification: A Critical Review. *Thin Solid Films* **2009**, *517*, 6441–6478.
- (4) Talapin, D. V.; Shevchenko, E. V. Introduction: Nanoparticle Chemistry. *Chem. Rev.* **2016**, *116*, 10343–10345.
- (5) Sajanalal, P. R.; Khatun, E.; Pradeep, T. *Gold Nanoparticles*; Kirk-Othmer Encyclopedia, 2019.
- (6) Haruta, M.; Editor; *Gold Nanotechnology: Fundamentals and Applications*; Shi Emu Shi Shuppan Co., Ltd. 2009.
- (7) *The British Museum*. [www.thebritishmuseum.ac.uk](http://www.thebritishmuseum.ac.uk).
- (8) Barber, D. J.; Freestone, I. C. An investigation of the origin of the Lyncurus Cup by analytical transmission electron spectroscopy. *Archaeometry* **1990**, *32*, 33–45.
- (9) Faraday, M. X. The Bakerian Lecture: -Experimental Relations of Gold (and Other Metals) to Light. *Philos. Trans. R. Soc. London* **1857**, *147*, 145–181.
- (10) Chakraborty, I.; Pradeep, T. Atomically Precise Clusters of Noble Metals: Emerging Link between Atoms and Nanoparticles. *Chem. Rev.* **2017**, *117*, 8208–8271.
- (11) Jin, R.; Zeng, C.; Zhou, M.; Chen, Y. Atomically Precise Colloidal Metal Nanoclusters and Nanoparticles: Fundamentals and Opportunities. *Chem. Rev.* **2016**, *116*, 10346–10413.
- (12) Ferrando, R.; Jellinek, J.; Johnston, R. L. Nanoalloys: From Theory to Applications of Alloy Clusters and Nanoparticles. *Chem. Rev.* **2008**, *108*, 845–910.
- (13) Wang, S.; Li, Q.; Kang, X.; Zhu, M. Customizing the Structure, Composition, and Properties of Alloy Nanoclusters by Metal Exchange. *Acc. Chem. Res.* **2018**, *51*, 2784–2792.
- (14) Hossain, S.; Niihori, Y.; Nair, L. V.; Kumar, B.; Kurashige, W.; Negishi, Y. Alloy Clusters: Precise Synthesis and Mixing Effects. *Acc. Chem. Res.* **2018**, *51*, 3114–3124.
- (15) McPartlin, M.; Mason, R.; Malatesta, L. Novel Cluster Complexes of Gold(0)–Gold(I). *J. Chem. Soc. D* **1969**, *7*, 334–334.
- (16) Boer, F. P.; Flynn, J. J.; Hecht, J. K. Crystal and Molecular Structure of Cis-1,2-Diacetyl-1,2,3,3-Tetra-Chlorocyclopropane. *J. Chem. Soc. B* **1970**, *4021*, 381.
- (17) Teo, B. K.; Zhang, H.; Shi, X. Design, Synthesis, and Structure of the Largest Trimetallic Cluster, [(Ph<sub>3</sub>P)<sub>10</sub>Au<sub>12</sub>Ag<sub>12</sub>PtCl<sub>7</sub>]Cl: The First Example of a Trimetallic Biicosahedral Supracluster and Its Implication for the Vertex-Sharing Polyicosahedral Growth of the Au/Ag/Pt Ternary Cluster. *J. Am. Chem. Soc.* **1993**, *115*, 8489–8490.
- (18) Teo, B. K.; Zhang, H.; Shi, X. Site Preference in Vertex-Sharing Polyicosahedral Supraclusters Containing Groups 10 and 11 Metals and Their Bonding Implications: Syntheses and Structures of the First Au-Ag-M (M = Pt, Ni) Biicosahedral Clusters [(Ph<sub>3</sub>P)<sub>10</sub>Au<sub>12</sub>Ag<sub>12</sub>PtCl<sub>7</sub>]Cl and [(Ph<sub>3</sub>P)<sub>10</sub>Au<sub>12</sub>Ag<sub>12</sub>NiCl<sub>7</sub>](SbF<sub>6</sub>). *Inorg. Chem.* **1994**, *33*, 4086–4097.
- (19) Teo, B. K.; Zhang, H.; Shi, X. Molecular Architecture of a Novel Vertex-Sharing Biicosahedral Cluster [(p-Tol<sub>3</sub>P)<sub>10</sub>Au<sub>13</sub>Ag<sub>12</sub>Br<sub>8</sub>](PF<sub>6</sub>)

Containing a Staggered-Staggered-Staggered Configuration for the 25-Atom Metal Framework. *Inorg. Chem.* **1990**, *29*, 2083–2091.

- (20) Shichibu, Y.; Negishi, Y.; Tsukuda, T.; Teranishi, T. Large-Scale Synthesis of Thiolated Au<sub>25</sub> Clusters via Ligand Exchange Reactions of Phosphine-Stabilized Au<sub>11</sub> Clusters. *J. Am. Chem. Soc.* **2005**, *127*, 13464–13465.
- (21) Whetten, R. L.; Khoury, J. T.; Alvarez, M. M.; Murthy, S.; Vezmar, I.; Wang, Z. L.; Stephens, P. W.; Cleveland, C. L.; Luedtke, W. D.; Landman, U. Nanocrystal Gold Molecules. *Adv. Mater.* **1996**, *8*, 428–433.
- (22) Zhu, M.; Aikens, C. M.; Hollander, F. J.; Schatz, G. C.; Jin, R. Correlating the Crystal Structure of A Thiol-Protected Au<sub>25</sub> Cluster and Optical Properties. *J. Am. Chem. Soc.* **2008**, *130*, 5883–5885.
- (23) Donkers, R. L.; Lee, D.; Murray, R. W. Synthesis and Isolation of the Molecule-like Cluster Au<sub>38</sub>(PhCH<sub>2</sub>CH<sub>2</sub>S)<sub>24</sub>. *Langmuir* **2004**, *20*, 1945–1952.
- (24) Li, J.; Ma, H. Z.; Reid, G. E.; Edwards, A. J.; Hong, Y.; White, J. M.; Mulder, R. J.; O'Hair, R. A. J. Synthesis and X-Ray Crystallographic Characterisation of Frustum-Shaped Ligated [Cu<sub>18</sub>H<sub>16</sub>(DPPE)<sub>6</sub>]<sup>2+</sup> and [Cu<sub>16</sub>H<sub>14</sub>(DPPA)<sub>6</sub>]<sup>2+</sup> Nanoclusters and Studies on Their H<sub>2</sub> Evolution Reactions. *Chem. - Eur. J.* **2018**, *24*, 2070–2074.
- (25) Cook, A. W.; Jones, Z. R.; Wu, G.; Scott, S. L.; Hayton, T. W. An Organometallic Cu<sub>20</sub> Nanocluster: Synthesis, Characterization, Immobilization on Silica, and “Click” Chemistry. *J. Am. Chem. Soc.* **2018**, *140*, 394–400.
- (26) Nimmala, P. R.; Yoon, B.; Whetten, R. L.; Landman, U.; Dass, A. Au<sub>67</sub>(SR)<sub>35</sub> Nanomolecules: Characteristic Size-Specific Optical, Electrochemical, Structural Properties and First-Principles Theoretical Analysis. *J. Phys. Chem. A* **2013**, *117*, 504–517.
- (27) Nimmala, P. R.; Dass, A. Au<sub>36</sub>(SPh)<sub>23</sub> Nanomolecules. *J. Am. Chem. Soc.* **2011**, *133*, 9175–9177.
- (28) Sakthivel, N. A.; Theivendran, S.; Ganeshraj, V.; Oliver, A. G.; Dass, A. Crystal Structure of Faradaurate-279: Au<sub>279</sub>(SPh<sup>t</sup>Bu)<sub>84</sub> Plasmonic Nanocrystal Molecules. *J. Am. Chem. Soc.* **2017**, *139*, 15450–15459.
- (29) Joshi, C. P.; Bootharaju, M. S.; Alhilaly, M. J.; Bakr, O. M. [Ag<sub>25</sub>(SR)<sub>18</sub>]<sup>−</sup>: The “Golden” Silver Nanoparticle Silver Nanoparticle. *J. Am. Chem. Soc.* **2015**, *137*, 11578–11581.
- (30) AbdulHalim, L. G.; Bootharaju, M. S.; Tang, Q.; Del Gobbo, S.; AbdulHalim, R. G.; Eddaoudi, M.; Jiang, D.; Bakr, O. M. Ag<sub>29</sub>(BDT)<sub>12</sub>(TPP)<sub>4</sub>: A Tetravalent Nanocluster. *J. Am. Chem. Soc.* **2015**, *137*, 11970–11975.
- (31) Yang, H.; Wang, Y.; Huang, H.; Gell, L.; Lehtovaara, L.; Malola, S.; Häkkinen, H.; Zheng, N. All-Thiol-Stabilized Ag<sub>44</sub> and Au<sub>12</sub>Ag<sub>32</sub> Nanoparticles with Single-Crystal Structures. *Nat. Commun.* **2013**, *4*, 2422.
- (32) Bootharaju, M. S.; Dey, R.; Gevers, L. E.; Hedhili, M. N.; Basset, J. M.; Bakr, O. M. A New Class of Atomically Precise, Hydride-Rich Silver Nanoclusters Co-Protected by Phosphines. *J. Am. Chem. Soc.* **2016**, *138*, 13770–13773.
- (33) Nguyen, T. A. D.; Jones, Z. R.; Goldsmith, B. R.; Buratto, W. R.; Wu, G.; Scott, S. L.; Hayton, T. W. A Cu<sub>25</sub> Nanocluster with Partial Cu(0) Character. *J. Am. Chem. Soc.* **2015**, *137*, 13319–13324.
- (34) Kang, X.; Wei, X.; Jin, S.; Yuan, Q.; Luan, X.; Pei, Y.; Wang, S.; Zhu, M.; Jin, R. Rational Construction of a Library of M<sub>29</sub> Nanoclusters from Monometallic to Tetrametallic. *Proc. Natl. Acad. Sci.* **2019**, *116*, 18834–18840.
- (35) Soldan, G.; Aljuhani, M. A.; Bootharaju, M. S.; AbdulHalim, L. G.; Parida, M. R.; Emwas, A.-H.; Mohammed, O. F.; Bakr, O. M. Gold Doping of Silver Nanoclusters: A 26-Fold Enhancement in the Luminescence Quantum Yield. *Angew. Chem., Int. Ed.* **2016**, *55*, 5749–5753.
- (36) Kumara, C.; Gagnon, K. J.; Dass, A. X-Ray Crystal Structure of Au<sub>38-x</sub>Ag<sub>x</sub>(SCH<sub>2</sub>CH<sub>2</sub>Ph)<sub>24</sub> Alloy Nanomolecules. *J. Phys. Chem. Lett.* **2015**, *6*, 1223–1228.
- (37) Udayabhaskararao, T.; Sun, Y.; Goswami, N.; Pal, S. K.; Balasubramanian, K.; Pradeep, T. Ag<sub>7</sub>Au<sub>6</sub>: A 13-Atom Alloy Quantum Cluster. *Angew. Chem., Int. Ed.* **2012**, *51*, 2155–2159.
- (38) Li, Q.; Wang, S.; Kirschbaum, K.; Lambright, K. J.; Das, A.; Jin, R. Heavily Doped Au<sub>25-x</sub>Ag<sub>x</sub>(SC<sub>6</sub>H<sub>11</sub>)<sub>18</sub><sup>−</sup> Nanoclusters: Silver Goes from the Core to the Surface. *Chem. Commun.* **2016**, *52*, 5194–5197.
- (39) Du, Y.; Guan, Z.-J.; Wen, Z.-R.; Lin, Y.-M.; Wang, Q.-M. Ligand-Controlled Doping Effects in Alloy Nanoclusters Au<sub>4</sub>Ag<sub>23</sub> and Au<sub>5</sub>Ag<sub>24</sub>. *Chem. Eur. J.* **2018**, *24*, 16029–16035.
- (40) Kang, X.; Xiong, L.; Wang, S.; Yu, H.; Jin, S.; Song, Y.; Chen, T.; Zheng, L.; Pan, C.; Pei, Y.; Zhu, M. Shape-Controlled Synthesis of Trimetallic Nanoclusters: Structure Elucidation and Properties Investigation. *Chem. Eur. J.* **2016**, *22*, 17145–17150.
- (41) Yang, S.; Wang, S.; Jin, S.; Chen, S.; Sheng, H.; Zhu, M. A Metal Exchange Method for Thiolate-Protected Tri-Metal M<sub>1</sub>Ag<sub>x</sub>Au<sub>24-x</sub>(SR)<sub>18</sub><sup>0</sup> (M = Cd/Hg) Nanoclusters. *Nanoscale* **2015**, *7*, 10005–10007.
- (42) Sharma, S.; Kurashige, W.; Nobusada, K.; Negishi, Y. Effect of Trimetallization in Thiolate-Protected Au<sub>24-n</sub>Cu<sub>n</sub>Pd Clusters. *Nanoscale* **2015**, *7*, 10606–10612.
- (43) Kimura, K.; Sugimoto, N.; Sato, S.; Yao, H.; Negishi, Y.; Tsukuda, T. Size Determination of Gold Clusters by Polyacrylamide Gel Electrophoresis in a Large Cluster Region. *J. Phys. Chem. C* **2009**, *113*, 14076–14082.
- (44) Knoppe, S.; Boudon, J.; Dolamic, I.; Dass, A.; Bürgi, T. Size Exclusion Chromatography for Semipreparative Scale Separation of Au<sub>38</sub>(SR)<sub>24</sub> and Au<sub>40</sub>(SR)<sub>24</sub> and Larger Clusters. *Anal. Chem.* **2011**, *83*, 5056–5061.
- (45) Negishi, Y.; Nobusada, K.; Tsukuda, T. Glutathione-Protected Gold Clusters Revisited: Bridging the Gap between Gold(I)–Thiolate Complexes and Thiolate-Protected Gold Nanocrystals. *J. Am. Chem. Soc.* **2005**, *127*, 5261–5270.
- (46) Chen, T.; Yao, Q.; Nasaruddin, R. R.; Xie, J. Electrospray Ionization Mass Spectrometry: A Powerful Platform for Noble-Metal Nanocluster Analysis. *Angew. Chem., Int. Ed.* **2019**, *58*, 11967–11977.
- (47) Heaven, M. W.; Dass, A.; White, P. S.; Holt, K. M.; Murray, R. W. Crystal Structure of the Gold Nanoparticle [N(C<sub>8</sub>H<sub>17</sub>)<sub>4</sub>]-[Au<sub>25</sub>(SCH<sub>2</sub>CH<sub>2</sub>Ph)<sub>18</sub>]. *J. Am. Chem. Soc.* **2008**, *130*, 3754–3755.
- (48) Kumara, C.; Aikens, C. M.; Dass, A. X-Ray Crystal Structure and Theoretical Analysis of Au<sub>25-x</sub>Ag<sub>x</sub>(SCH<sub>2</sub>CH<sub>2</sub>Ph)<sub>18</sub><sup>−</sup> Alloy. *J. Phys. Chem. Lett.* **2014**, *5*, 461–466.
- (49) Nannenga, B. L.; Gonen, T. MicroED: A Versatile CryoEM Method for Structure Determination. *Emerg. Top. Life Sci.* **2018**, *2*, 1–8.
- (50) Roduner, E. Superatom Chemistry: Promising Properties of near-Spherical Noble Metal Clusters. *Phys. Chem. Chem. Phys.* **2018**, *20*, 23812–23826.
- (51) Häkkinen, H. Atomic and Electronic Structure of Gold Clusters: Understanding Flakes, Cages and Superatoms from Simple Concepts. *Chem. Soc. Rev.* **2008**, *37*, 1847–1859.
- (52) Bertorelle, F.; Russier-Antoine, I.; Calin, N.; Comby-Zerbino, C.; Bensalah-Ledoux, A.; Guy, S.; Dugourd, P.; Brevet, P.-F.; Sanader, Ž.; Krstić, M.; et al. Au<sub>10</sub>(SG)<sub>10</sub>: A Chiral Gold Catenane Nanocluster with Zero Confined Electrons. Optical Properties and First-Principles Theoretical Analysis. *J. Phys. Chem. Lett.* **2017**, *8*, 1979–1985.
- (53) Weerawardene, K. L. D. M.; Häkkinen, H.; Aikens, C. M. Connections Between Theory and Experiment for Gold and Silver Nanoclusters. *Annu. Rev. Phys. Chem.* **2018**, *69*, 205–229.
- (54) Wang, S.; Meng, X.; Das, A.; Li, T.; Song, Y.; Cao, T.; Zhu, X.; Zhu, M.; Jin, R. A 200-Fold Quantum Yield Boost in the Photoluminescence of Silver-Doped Ag<sub>x</sub>Au<sub>25-x</sub> Nanoclusters: The 13<sup>th</sup> Silver Atom Matters. *Angew. Chem., Int. Ed.* **2014**, *53*, 2376–2380.
- (55) Suyama, M.; Takano, S.; Nakamura, T.; Tsukuda, T. Stoichiometric Formation of Open-Shell [PtAu<sub>24</sub>(SC<sub>2</sub>H<sub>4</sub>Ph)<sub>18</sub>]<sup>−</sup> via Spontaneous Electron Proportionation between [PtAu<sub>24</sub>(SC<sub>2</sub>H<sub>4</sub>Ph)<sub>18</sub>]<sup>2−</sup> and [PtAu<sub>24</sub>(SC<sub>2</sub>H<sub>4</sub>Ph)<sub>18</sub>]<sup>0</sup>. *J. Am. Chem. Soc.* **2019**, *141*, 14048–14051.
- (56) Huifeng, Q.; Ellen, B.; Zhu, Y.; Jin, R. Doping 25-Atom and 38-Atom Gold Nanoclusters with Palladium. *Acta Phys.-Chim. Sin.* **2011**, *27*, 513–519.
- (57) Fields-Zinna, C. A.; Crowe, M. C.; Dass, A.; Weaver, J. E. F.; Murray, R. W. Mass Spectrometry of Small Bimetal Monolayer-Protected Clusters. *Langmuir* **2009**, *25*, 7704–7710.



- (58) Kwak, K.; Choi, W.; Tang, Q.; Kim, M.; Lee, Y.; Jiang, D.-E.; Lee, D. A Molecule-like PtAu<sub>24</sub>(SC<sub>6</sub>H<sub>13</sub>)<sub>18</sub> Nanocluster as an Electrocatalyst for Hydrogen Production. *Nat. Commun.* **2017**, *8*, 14723.
- (59) Xie, S.; Tsunoyama, H.; Kurashige, W.; Negishi, Y.; Tsukuda, T. Enhancement in Aerobic Alcohol Oxidation Catalysis of Au<sub>25</sub> Clusters by Single Pd Atom Doping. *ACS Catal.* **2012**, *2*, 1519–1523.
- (60) Yan, J.; Su, H.; Yang, H.; Malola, S.; Lin, S.; Häkkinen, H.; Zheng, N. Total Structure and Electronic Structure Analysis of Doped Thiolated Silver [MAg<sub>24</sub>(SR)<sub>18</sub>]<sup>2-</sup> (M = Pd, Pt) Clusters. *J. Am. Chem. Soc.* **2015**, *137*, 11880–11883.
- (61) Jin, R.; Zhao, S.; Xing, Y.; Jin, R. All-Thiolate-Protected Silver and Silver-Rich Alloy Nanoclusters with Atomic Precision: Stable Sizes, Structural Characterization and Optical Properties. *CrystEngComm* **2016**, *18*, 3996–4005.
- (62) Liu, Y.; Chai, X.; Cai, X.; Chen, M.; Jin, R.; Ding, W.; Zhu, Y. Central Doping of a Foreign Atom into the Silver Cluster for Catalytic Conversion of CO<sub>2</sub> toward C–C Bond Formation. *Angew. Chem., Int. Ed.* **2018**, *57*, 9775–9779.
- (63) Kang, X.; Silalai, C.; Lv, Y.; Sun, G.; Chen, S.; Yu, H.; Xu, F.; Zhu, M. Au<sub>15</sub>Ag<sub>3</sub>(SPhMe<sub>2</sub>)<sub>14</sub> Nanoclusters – Crystal Structure and Insights into Ligand-Induced Variation. *Eur. J. Inorg. Chem.* **2017**, *2017*, 1414–1419.
- (64) Molina, B.; Tlahuice-Flores, A. Thiolated Au<sub>18</sub> Cluster: Preferred Ag Sites for Doping, Structures, and Optical and Chiroptical Properties. *Phys. Chem. Chem. Phys.* **2016**, *18*, 1397–1403.
- (65) Jin, R.; Nobusada, K. Doping and Alloying in Atomically Precise Gold Nanoparticles. *Nano Res.* **2014**, *7*, 285–300.
- (66) Kang, X.; Li, Y.; Zhu, M.; Jin, R. Atomically Precise Alloy Nanoclusters: Syntheses, Structures, and Properties. *Chem. Soc. Rev.* **2020**, *49*, 6443–6514.
- (67) Kawawaki, T.; Imai, Y.; Suzuki, D.; Kato, S.; Kobayashi, I.; Suzuki, T.; Kaneko, R.; Hossain, S.; Negishi, Y. Atomically Precise Alloy Nanoclusters. *Chem. Eur. J.* **2020**, 16145.
- (68) Kang, X.; Zhu, M. Transformation of Atomically Precise Nanoclusters by Ligand-Exchange. *Chem. Mater.* **2019**, *31*, 9939–9969.
- (69) Higaki, T.; Li, Y.; Zhao, S.; Li, Q.; Li, S.; Du, X.-S.; Yang, S.; Chai, J.; Jin, R. Atomically Tailored Gold Nanoclusters for Catalytic Application. *Angew. Chem., Int. Ed.* **2019**, *58*, 8291–8302.
- (70) Kang, X.; Zhu, M. Tailoring the Photoluminescence of Atomically Precise Nanoclusters. *Chem. Soc. Rev.* **2019**, *48*, 2422–2457.
- (71) Teo, B. K.; Keating, K. Novel Triicosahedral Structure of the Largest Metal Alloy Cluster: hexachlorododecakis(triphenylphosphine)-gold-silver cluster [(Ph<sub>3</sub>P)<sub>12</sub>Au<sub>13</sub>Ag<sub>12</sub>Cl<sub>6</sub>]<sup>M+</sup>. *J. Am. Chem. Soc.* **1984**, *106*, 2224–2226.
- (72) Teo, B. K.; Shi, X.; Zhang, H. Cluster Rotamerism of a 25-Metal-Atom Cluster [(Ph<sub>3</sub>P)<sub>10</sub>Au<sub>13</sub>Ag<sub>12</sub>Br<sub>8</sub>]<sup>+</sup> Monocation: A Molecular Rotary Unit. *J. Chem. Soc., Chem. Commun.* **1992**, *17*, 1195.
- (73) Teo, B. K.; Zhang, H.; Shi, X. Cluster of Clusters: A Modular Approach to Large Metal Clusters. Structural Characterization of a 38-Atom Cluster [(p-Tol<sub>3</sub>P)<sub>12</sub>Au<sub>18</sub>Ag<sub>20</sub>Cl<sub>14</sub>] Based on Vertex-Sharing Triicosahedra. *J. Am. Chem. Soc.* **1990**, *112*, 8552–8562.
- (74) Haggin, J. Illinois Scientists Synthesize Huge Cluster. *Chem. Eng. News Arch.* **1989**, *67*, 6.
- (75) Brust, M.; Walker, M.; Bethell, D.; Schiffrin, D. J.; Whyman, R. Synthesis of Thiol-Derivatized Gold Nanoparticles in a Two-Phase Liquid–Liquid System. *J. Chem. Soc., Chem. Commun.* **1994**, *0*, 801–802.
- (76) Kauffman, D. R.; Alfonso, D.; Matranga, C.; Qian, H.; Jin, R. A Quantum Alloy: The Ligand-Protected Au<sub>25-x</sub>Ag<sub>x</sub>(SR)<sub>18</sub> Cluster. *J. Phys. Chem. C* **2013**, *117*, 7914–7923.
- (77) Negishi, Y.; Munakata, K.; Ohgake, W.; Nobusada, K. Effect of Copper Doping on Electronic Structure, Geometric Structure, and Stability of Thiolate-Protected Au<sub>25</sub> Nanoclusters. *J. Phys. Chem. Lett.* **2012**, *3*, 2209–2214.
- (78) Negishi, Y.; Kurashige, W.; Niihori, Y.; Iwasa, T.; Nobusada, K. Isolation, Structure, and Stability of a Dodecanethiolate-Protected Pd<sub>1</sub>Au<sub>24</sub> Cluster. *Phys. Chem. Chem. Phys.* **2010**, *12*, 6219–6225.
- (79) Negishi, Y.; Iwai, T.; Ide, M. Continuous Modulation of Electronic Structure of Stable Thiolate-Protected Au<sub>25</sub> Cluster by Ag Doping. *Chem. Commun.* **2010**, *46*, 4713–4715.
- (80) Biltek, S. R.; Mandal, S.; Sen, A.; Reber, A. C.; Pedicini, A. F.; Khanna, S. N. Synthesis and Structural Characterization of an Atom-Precise Bimetallic Nanocluster, Ag<sub>4</sub>Ni<sub>2</sub>(DMSA)<sub>4</sub>. *J. Am. Chem. Soc.* **2013**, *135*, 20.
- (81) Deng, G.; Malola, S.; Yan, J.; Han, Y.; Yuan, P.; Zhao, C.; Yuan, X.; Lin, S.; Tang, Z.; Teo, B. K.; et al. From Symmetry Breaking to Unraveling the Origin of the Chirality of Ligated Au<sub>13</sub>Cu<sub>2</sub> Nanoclusters. *Angew. Chem., Int. Ed.* **2018**, *57*, 3421–3425.
- (82) Dharmaratne, A. C.; Dass, A. Au<sub>144-x</sub>Cu<sub>x</sub>(SC<sub>6</sub>H<sub>13</sub>)<sub>60</sub> Nanomolecules: Effect of Cu Incorporation on Composition and Plasmon-like Peak Emergence in Optical Spectra. *Chem. Commun.* **2014**, *50*, 1722.
- (83) Jensen, K. M. Ø.; Juhas, P.; Tofanelli, M. A.; Heinecke, C. L.; Vaughan, G.; Ackerson, C. J.; Billinge, S. J. L. Polymorphism in Magic-Sized Au<sub>144</sub>(SR)<sub>60</sub> Clusters. *Nat. Commun.* **2016**, *7*, 11859.
- (84) Zeng, J. L.; Guan, Z. J.; Du, Y.; Nan, Z. A.; Lin, Y. M.; Wang, Q. M. Chloride-Promoted Formation of a Bimetallic Nanocluster Au<sub>30</sub>Ag<sub>30</sub> and the Total Structure Determination. *J. Am. Chem. Soc.* **2016**, *138*, 7848–7851.
- (85) Yan, J.; Su, H.; Yang, H.; Hu, C.; Malola, S.; Lin, S.; Teo, B. K.; Häkkinen, H.; Zheng, N. Asymmetric Synthesis of Chiral Bimetallic [Ag<sub>28</sub>Cu<sub>12</sub>(SR)<sub>24</sub>]<sup>4-</sup> Nanoclusters via Ion Pairing. *J. Am. Chem. Soc.* **2016**, *138*, 12751–12754.
- (86) Wang, S.; Jin, S.; Yang, S.; Chen, S.; Song, Y.; Zhang, J.; Zhu, M. Total Structure Determination of Surface Doping [Ag<sub>46</sub>Au<sub>24</sub>(SR)<sub>32</sub>]- (BPh<sub>4</sub>)<sub>2</sub> Nanocluster and Its Structure-Related Catalytic Property. *Sci. Adv.* **2015**, *1*, No. e1500441.
- (87) Conn, B. E.; Atmagulov, A.; Yoon, B.; Barnett, R. N.; Landman, U.; Bigioni, T. P. Confirmation of a de Novo Structure Prediction for an Atomically Precise Monolayer-Coated Silver Nanoparticle. *Sci. Adv.* **2016**, *2*, No. e1601609.
- (88) Kauffman, D. R.; Alfonso, D.; Matranga, C.; Qian, H.; Jin, R. A Quantum Alloy: The Ligand-Protected Au<sub>25-x</sub>Ag<sub>x</sub>(SR)<sub>18</sub> Cluster. *J. Phys. Chem. C* **2013**, *117*, 7914–7923.
- (89) Khatun, E.; Chakraborty, P.; Jacob, B. R.; Paramasivam, G.; Boduazzaman, M.; Dar, W. A.; Pradeep, T. Intercluster Reactions Resulting in Silver-Rich Trimetallic Nanoclusters. *Chem. Mater.* **2020**, *32*, 611–619.
- (90) Kanters, R. P. F.; Bour, J. J.; Schlebos, P. P. J.; Bosman, W. P.; Behm, H.; Steggerda, J. J.; Ito, L. N.; Pignolet, L. H. Structure and Properties of the Hydride-Containing Cluster Ion hydrido-(triphenylphosphine)heptakis[(triphenylphosphine)gold]platinum-(2+). *Inorg. Chem.* **1989**, *28*, 2591–2594.
- (91) Wang, S.; Song, Y.; Jin, S.; Liu, X.; Zhang, J.; Pei, Y.; Meng, X.; Chen, M.; Li, P.; Zhu, M. Metal Exchange Method Using Au<sub>25</sub> Nanoclusters as Templates for Alloy Nanoclusters with Atomic Precision. *J. Am. Chem. Soc.* **2015**, *137*, 4018–4021.
- (92) Gan, Z.; Xia, N.; Wu, Z. Discovery, Mechanism, and Application of Antitigalvanic Reaction. *Acc. Chem. Res.* **2018**, *51*, 2774–2783.
- (93) Copley, R. C. B.; Mingos, D. M. P. Synthesis and Characterization of the Centred Icosahedral Cluster Series [Au<sub>9</sub>MIB<sub>4</sub>Cl<sub>4</sub>(PMePh<sub>2</sub>)<sub>8</sub>][C<sub>2</sub>B<sub>9</sub>H<sub>12</sub>], Where MIB = Au, Ag or Cu. *J. Chem. Soc. Dalton Trans.* **1996**, *4*, 491.
- (94) Li, Q.; Lambright, K. J.; Taylor, M. G.; Kirschbaum, K.; Luo, T. Y.; Zhao, J.; Mpourmpakis, G.; Mokashi-Punekar, S.; Rosi, N. L.; Jin, R. Reconstructing the Surface of Gold Nanoclusters by Cadmium Doping. *J. Am. Chem. Soc.* **2017**, *139*, 17779–17782.
- (95) Kang, X.; Xiong, L.; Wang, S.; Pei, Y.; Zhu, M. Combining the Single-Atom Engineering and Ligand-Exchange Strategies: Obtaining the Single-Heteroatom-Doped Au<sub>16</sub>Ag<sub>1</sub>(S-Adm)<sub>13</sub> Nanocluster with Atomically Precise Structure. *Inorg. Chem.* **2017**, *57*, 335–342.
- (96) Sharma, S.; Yamazoe, S.; Ono, T.; Kurashige, W.; Niihori, Y.; Nobusada, K.; Tsukuda, T.; Negishi, Y. Tuning the Electronic Structure of Thiolate-Protected 25-Atom Clusters by Co-Substitution with Metals Having Different Preferential Sites. *Dalton Trans.* **2016**, *45*, 18064–18068.

- (97) Kazan, R.; Zhang, B.; Bürgi, T.  $\text{Au}_{38}\text{Cu}_1(2\text{-PET})_{24}$  nanocluster: Synthesis, Enantioseparation and Luminescence. *Dalton Trans.* **2017**, 46, 7708–7713.
- (98) Biltek, S. R.; Sen, A.; Pedicini, A. F.; Reber, A. C.; Khanna, S. N. Isolation and Structural Characterization of a Silver–Platinum Nanocluster,  $\text{Ag}_4\text{Pt}_2(\text{DMSA})_4$ . *J. Phys. Chem. A* **2014**, 118, 8314–8319.
- (99) Liu, X.; Yuan, J.; Chen, J.; Yang, J.; Wu, Z. The Synthesis of Chiral  $\text{Ag}_4\text{Pd}_2(\text{SR})_8$  by Nonreplaced Galvanic Reaction. *Part. Part. Syst. Charact.* **2019**, 36, 1900003.
- (100) Yang, H.; Wang, Y.; Lei, J.; Shi, L.; Wu, X.; Mäkinen, V.; Lin, S.; Tang, Z.; He, J.; Häkkinen, H.; et al. Ligand-Stabilized  $\text{Au}_{13}\text{Cu}_x$  ( $x = 2, 4, 8$ ) Bimetallic Nanoclusters: Ligand Engineering to Control the Exposure of Metal Sites. *J. Am. Chem. Soc.* **2013**, 135, 9568–9571.
- (101) Wang, Y.; Su, H.; Xu, C.; Li, G.; Gell, L.; Lin, S.; Tang, Z.; Häkkinen, H.; Zheng, N. An Intermetallic  $\text{Au}_{24}\text{Ag}_{20}$  Superatom Nanocluster Stabilized by Labile Ligands. *J. Am. Chem. Soc.* **2015**, 137, 4324–4327.
- (102) Tian, S.; Liao, L.; Yuan, J.; Yao, C.; Chen, J.; Yang, J.; Wu, Z. Structures and Magnetism of Mono-Palladium and Mono-Platinum Doped  $\text{Au}_{25}(\text{PET})_{18}$  Nanoclusters. *Chem. Commun.* **2016**, 52, 9873–9876.
- (103) Negishi, Y.; Igarashi, K.; Munakata, K.; Ohgake, W.; Nobusada, K. Palladium Doping of Magic Gold Cluster  $\text{Au}_{38}(\text{SC}_2\text{H}_4\text{Ph})_{24}$ : Formation of  $\text{Pd}_2\text{Au}_{36}(\text{SC}_2\text{H}_4\text{Ph})_{24}$  with Higher Stability than  $\text{Au}_{38}(\text{SC}_2\text{H}_4\text{Ph})_{24}$ . *Chem. Commun.* **2012**, 48, 660–662.
- (104) Teo, B. K.; Dang, H.; Campana, C. F.; Zhang, H. Synthesis, Structure, and Characterization of  $(\text{MePh}_2\text{P})_{10}\text{Au}_{12}\text{Ag}_{13}\text{Br}$ : The First Example of a Neutral Bi-Icosahedral Au Ag Cluster with a Novel Seven-Membered Satellite Ring of Bridging Ligands. *Polyhedron* **1998**, 17, 617–621.
- (105) Lin, Y.-R.; Kishore, P. V. V. N.; Liao, J.-H.; Kahlal, S.; Liu, Y.-C.; Chiang, M.-H.; Saillard, J.-Y.; Liu, C. W. Synthesis, Structural Characterization and Transformation of an Eight-Electron Superatomic Alloy,  $[\text{Au}@\text{Ag}_{19}\{\text{S}_2\text{P}(\text{OPr})_2\}_{12}]$ . *Nanoscale* **2018**, 10, 6855–6860.
- (106) Li, Y.; Zhou, M.; Jin, S.; Xiong, L.; Yuan, Q.; Du, W.; Pei, Y.; Wang, S.; Zhu, M. Total Structural Determination of  $[\text{Au}_1\text{Ag}_{24}(\text{Dppm})_3(\text{SR})_{17}]^{2+}$  Comprising an Open Icosahedral  $\text{Au}_1\text{Ag}_{12}$  Core with Six Free Valence Electrons. *Chem. Commun.* **2019**, 55, 6457–6460.
- (107) Bootharaju, M. S.; Kozlov, S. M.; Cao, Z.; Harb, M.; Maity, N.; Shkurenko, A.; Parida, M. R.; Hedhili, M. N.; Eddaoudi, M.; Mohammed, O. F.; et al. Doping-Induced Anisotropic Self-Assembly of Silver Icosahedra in  $[\text{Pt}_2\text{Ag}_{23}\text{Cl}_2(\text{PPh}_3)_{10}]$  Nanoclusters. *J. Am. Chem. Soc.* **2017**, 139, 1053–1056.
- (108) He, L.; Yuan, J.; Xia, N.; Liao, L.; Liu, X.; Gan, Z.; Wang, C.; Yang, J.; Wu, Z. Kernel Tuning and Nonuniform Influence on Optical and Electrochemical Gaps of Bimetal Nanoclusters. *J. Am. Chem. Soc.* **2018**, 140, 3487–3490.
- (109) Kang, X.; Li, X.; Yu, H.; Lv, Y.; Sun, G.; Li, Y.; Wang, S.; Zhu, M. Modulating Photo-Luminescence of  $\text{Au}_2\text{Cu}_6$  Nanoclusters: Via Ligand-Engineering. *RSC Adv.* **2017**, 7, 28606–28609.
- (110) Jin, S.; Liu, W.; Hu, D.; Zou, X.; Kang, X.; Du, W.; Chen, S.; Wei, S.; Wang, S.; Zhu, M. Aggregation-Induced Emission (AIE) in Ag–Au Bimetallic Nanocluster. *Chem. Eur. J.* **2018**, 24, 3712–3715.
- (111) Liu, C.; Ren, X.; Lin, F.; Fu, X.; Lin, X.; Li, T.; Sun, K.; Huang, J. Structure of the  $\text{Au}_{23-x}\text{Ag}_x(\text{S-Adm})_{15}$  Nanocluster and Its Application for Photocatalytic Degradation of Organic Pollutants. *Angew. Chem., Int. Ed.* **2019**, 58, 11335–11339.
- (112) Zou, X.; Li, Y.; Jin, S.; Kang, X.; Wei, X.; Wang, S.; Meng, X.; Zhu, M. Doping Copper Atoms into the Nanocluster Kernel: Total Structure Determination of  $[\text{Cu}_{30}\text{Ag}_{61}(\text{SAdm})_{38}\text{S}_3](\text{BPh}_4)$ . *J. Phys. Chem. Lett.* **2020**, 11, 2272–2276.
- (113) Zhou, M.; Jin, S.; Wei, X.; Yuan, Q.; Wang, S.; Du, Y.; Zhu, M. Reversible Cu–S Motif Transformation and  $\text{Au}_4$  Distortion via Thiol Ligand Exchange Engineering. *J. Phys. Chem. C* **2020**, 124, 7531–7538.
- (114) Jin, S.; Zhou, M.; Kang, X.; Li, X.; Du, W.; Wei, X.; Chen, S.; Wang, S.; Zhu, M. Three-dimensional Octameric Assembly of Icosahedral  $\text{M}_{13}$  Units in  $[\text{Au}_8\text{Ag}_{57}(\text{Dppp})_4(\text{C}_6\text{H}_{11}\text{S})_{32}\text{Cl}_2]\text{Cl}$  and Its  $[\text{Au}_8\text{Ag}_{55}(\text{Dppp})_4(\text{C}_6\text{H}_{11}\text{S})_{34}][\text{BPh}_4]_2$  Derivative. *Angew. Chem.* **2020**, 132, 3919–3923.
- (115) Sun, W.; Jin, S.; Du, W.; Kang, X.; Chen, A.; Wang, S.; Sheng, H.; Zhu, M. Total Structure Determination of the  $\text{Pt}_1\text{Ag}_9[\text{P}(\text{Ph-F})_3]_7\text{Cl}_3$  Nanocluster. *Eur. J. Inorg. Chem.* **2020**, 2020, 590–594.
- (116) Higaki, T.; Liu, C.; Morris, D. J.; He, G.; Luo, T. Y.; Sfeir, M. Y.; Zhang, P.; Rosi, N. L.; Jin, R.  $\text{Au}_{130-x}\text{Ag}_x$  Nanoclusters with Non-Metallicity: A Drum of Silver-Rich Sites Enclosed in a Marks-Decahedral Cage of Gold-Rich Sites. *Angew. Chem., Int. Ed.* **2019**, 58, 18798–18802.
- (117) Kang, X.; Abroshan, H.; Wang, S.; Zhu, M. Free Valence Electron Centralization Strategy for Preparing Ultrastable Nanoclusters and Their Catalytic Application. *Inorg. Chem.* **2019**, 58, 11000–11009.
- (118) Wen, Z.-R.; Guan, Z.-J.; Zhang, Y.; Lin, Y.-M.; Wang, Q.-M.  $[\text{Au-Ag}_9(\text{Dppf})_3(\text{CF}_3\text{CO}_2)_7\text{BF}_4]_n$ : A Linear Nanocluster Polymer from Molecular  $\text{Au-Ag}_8$  Clusters Covalently Linked by Silver Atoms. *Chem. Commun.* **2019**, 55, 12992–12995.
- (119) Zou, X.; Jin, S.; Wang, S.; Zhu, M.; Jin, R. Tailoring the Structure of 32-Metal-Atom Nanoclusters by Ligands and Alloying. *Nano Futures* **2018**, 2, No. 045004.
- (120) Jin, S.; Xu, F.; Du, W.; Kang, X.; Chen, S.; Zhang, J.; Li, X.; Hu, D.; Wang, S.; Zhu, M. Isomerism in Au–Ag Alloy Nanoclusters: Structure Determination and Enantioseparation of  $[\text{Au}_9\text{Ag}_{12}(\text{SR})_4(\text{Dppm})_6\text{X}_6]^{3+}$ . *Inorg. Chem.* **2018**, 57, 5114–5119.
- (121) Bour, J. J.; Kanters, R. P. F.; Schlebos, P. P. J.; Bosman, W. P.; Behm, H.; Beurskens, P. T.; Steggerda, J. J. Hetero-Metallic Clusters. Synthesis and Characterization of  $[\text{PtAu}_8(\text{PPh}_3)_8](\text{NO}_3)_2$  and  $[\text{HPtAu}_7(\text{PPh}_3)_8](\text{NO}_3)_2$ . *Recl. des Trav. Chim. des Pays-Bas* **1987**, 106, 157–158.
- (122) Yang, H.; Wang, Y.; Yan, J.; Chen, X.; Zhang, X.; Häkkinen, H.; Zheng, N. Structural Evolution of Atomically Precise Thiolated Bimetallic  $[\text{Au}_{12+n}\text{Cu}_{32}(\text{SR})_{30+n}]^{4-}$  ( $n = 0, 2, 4, 6$ ) Nanoclusters. *J. Am. Chem. Soc.* **2014**, 136, 7197–7200.
- (123) Yang, S.; Chen, S.; Xiong, L.; Liu, C.; Yu, H.; Wang, S.; Rosi, N. L.; Pei, Y.; Zhu, M. Total Structure Determination of  $\text{Au}_{16}(\text{S-Adm})_{12}$  and  $\text{Cd}_4\text{Au}_{14}(\text{S}^t\text{Bu})_{12}$  and Implications for the Structure of  $\text{Au}_{15}(\text{SR})_{13}$ . *J. Am. Chem. Soc.* **2018**, 140, 10988–10994.
- (124) Qin, Z.; Zhao, D.; Zhao, L.; Xiao, Q.; Wu, T.; Zhang, J.; Wan, C.; Li, G. Tailoring the Stability, Photocatalysis and Photoluminescence Properties of Engineering. *Nanoscale Adv.* **2019**, 1, 2529–2536.
- (125) Theivendran, S.; Chang, L.; Mukherjee, A.; Sementa, L.; Stener, M.; Fortunelli, A.; Dass, A. Principles of Optical Spectroscopy of Aromatic Alloy Nanomolecules:  $\text{Au}_{36-x}\text{Ag}_x(\text{SPh}^t\text{Bu})_{24}$ . *J. Phys. Chem. C* **2018**, 122, 4524–4531.
- (126) Chai, J.; Lv, Y.; Yang, S.; Song, Y.; Zan, X.; Li, Q.; Yu, H.; Wu, M.; Zhu, M. X-Ray Crystal Structure and Optical Properties of  $\text{Au}_{38-x}\text{Cu}_x(2,4\text{-(CH}_3)_2\text{C}_6\text{H}_3\text{S})_{24}$  ( $x = 0\text{--}6$ ) Alloy Nanocluster. *J. Phys. Chem. C* **2017**, 121, 21665–21669.
- (127) Wan, X.-K.; Cheng, X.-L.; Tang, Q.; Han, Y.-Z.; Hu, G.; Jiang, D.-E.; Wang, Q.-M. Atomically Precise Bimetallic  $\text{Au}_{19}\text{Cu}_{30}$  Nanocluster with an Icosidodecahedral  $\text{Cu}_{30}$  Shell and an Alkynyl–Cu Interface. *J. Am. Chem. Soc.* **2017**, 139, 9451–9454.
- (128) Wang, Z.; Senanayake, R.; Aikens, C. M.; Chen, W.-M.; Tung, C.-H.; Sun, D. Gold-Doped Silver Nanocluster  $[\text{Au}_3\text{Ag}_{38}(\text{SCH}_2\text{Ph})_{24}\text{X}_5]^{2-}$  ( $\text{X} = \text{Cl}$  or  $\text{Br}$ ). *Nanoscale* **2016**, 8, 18905.
- (129) Hossain, S.; Imai, Y.; Motohashi, Y.; Chen, Z.; Suzuki, D.; Suzuki, T.; Kataoka, Y.; Hirata, M.; Ono, T.; Kurashige, W.; et al. Understanding and Designing One-Dimensional Assemblies of Ligand-Protected Metal Nanoclusters. *Mater. Horiz.* **2020**, 7, 796.
- (130) Chen, J.; Liu, L.; Liu, X.; Liao, L.; Zhuang, S.; Zhou, S.; Yang, J.; Wu, Z. Gold-Doping of Double-Crown Pd Nanoclusters. *Chem. Eur. J.* **2017**, 23, 18187–18192.
- (131) Chai, J.; Yang, S.; Lv, Y.; Chong, H.; Yu, H.; Zhu, M. Exposing the Delocalized Cu–S  $\pi$  Bonds on the  $\text{Au}_{24}\text{Cu}_6(\text{SPh}^t\text{Bu})_{22}$  Nanocluster and Its Application in Ring-Opening Reactions. *Angew. Chem., Int. Ed.* **2019**, 58, 15671–15674.
- (132) Rao, B.; Zhao, T.; Yang, S.; Chai, J.; Pan, Y.; Weng, S.; Yu, H.; Li, X.; Zhu, M. X-Ray Crystal Structure and Doping Mechanism of

Bimetallic Nanocluster  $\text{Au}_{36-x}\text{Cu}_x(\text{m-MBT})_{24}$  ( $x = 1-3$ ). *Dalton Trans.* **2018**, 47, 475–480.

(133) Krishnadas, K. R.; Baksi, A.; Ghosh, A.; Natarajan, G.; Pradeep, T. Manifestation of Geometric and Electronic Shell Structures of Metal Clusters in Intercluster Reactions. *ACS Nano* **2017**, 11, 6015–6023.

(134) Yang, S.; Chai, J.; Song, Y.; Fan, J.; Chen, T.; Wang, S.; Yu, H.; Li, X.; Zhu, M. In Situ Two-Phase Ligand Exchange: A New Method for the Synthesis of Alloy Nanoclusters with Precise Atomic Structures. *J. Am. Chem. Soc.* **2017**, 139, 5668–5671.

(135) Choi, J.-P.; Fields-Zinna, C. A.; Stiles, R. L.; Balasubramanian, R.; Douglas, A. D.; Crowe, M. C.; Murray, R. W. Reactivity of  $[\text{Au}_{25}(\text{SCH}_2\text{CH}_2\text{Ph})_{18}]^{1-}$  Nanoparticles with Metal Ions. *J. Phys. Chem. C* **2010**, 114, 15890–15896.

(136) Wu, Z. Anti-Galvanic Reduction of Thiolate-Protected Gold and Silver Nanoparticles. *Angew. Chem., Int. Ed.* **2012**, 51, 2934–2938.

(137) Bootharaju, M. S.; Joshi, C. P.; Parida, M. R.; Mohammed, O. F.; Bakr, O. M. Templated Atom-Precise Galvanic Synthesis and Structure Elucidation of a  $[\text{Ag}_{24}\text{Au}(\text{SR})_{18}]^{-}$  Nanocluster. *Angew. Chem., Int. Ed.* **2016**, 55, 824.

(138) Krishnadas, K. R.; Ghosh, A.; Baksi, A.; Chakraborty, I.; Natarajan, G.; Pradeep, T. Intercluster Reactions between  $\text{Au}_{25}(\text{SR})_{18}$  and  $\text{Ag}_{44}(\text{SR})_{30}$ . *J. Am. Chem. Soc.* **2016**, 138, 140–148.

(139) Du, W.; Jin, S.; Xiong, L.; Chen, M.; Zhang, J.; Zou, X.; Pei, Y.; Wang, S.; Zhu, M.  $\text{Ag}_{50}(\text{Dppm})_6(\text{SR})_{30}$  and Its Homologue  $\text{Au}_{50-x}\text{Ag}_{50-x}(\text{Dppm})_6(\text{SR})_{30}$  Alloy Nanocluster: Seeded Growth, Structure Determination, and Differences in Properties. *J. Am. Chem. Soc.* **2017**, 139, 1618–1624.

(140) Zheng, K.; Fung, V.; Yuan, X.; Jiang, D. E.; Xie, J. Real Time Monitoring of the Dynamic Intracuster Diffusion of Single Gold Atoms into Silver Nanoclusters. *J. Am. Chem. Soc.* **2019**, 141, 18977–18983.

(141) He, L.; Gan, Z.; Xia, N.; Liao, L.; Wu, Z. Alternating Array Stacking of  $\text{Ag}_{26}\text{Au}$  and  $\text{Ag}_{24}\text{Au}$  Nanoclusters. *Angew. Chem.* **2019**, 131, 10002–10006.

(142) Bhat, S.; Baksi, A.; Mudedla, S. K.; Natarajan, G.; Subramanian, V.; Pradeep, T.  $\text{Au}_{22}\text{Ir}_3(\text{PET})_{18}$ : An Unusual Alloy Cluster through Intercluster Reaction. *J. Phys. Chem. Lett.* **2017**, 8, 2787–2793.

(143) Xia, N.; Wu, Z. Doping  $\text{Au}_{25}$  Nanoparticles Using Ultrasmall Silver or Copper Nanoparticles as the Metal Source. *J. Mater. Chem. C* **2016**, 4, 4125–4128.

(144) Ghosh, A.; Ghosh, D.; Khatun, E.; Chakraborty, P.; Pradeep, T. Unusual Reactivity of Dithiol Protected Clusters in Comparison to Monothiol Protected Clusters: Studies Using  $\text{Ag}_{51}(\text{BDT})_{19}(\text{TPP})_3$  and  $\text{Ag}_{29}(\text{BDT})_{12}(\text{TPP})_4$ . *Nanoscale* **2017**, 9, 1068–1077.

(145) Bootharaju, M. S.; Kozlov, S. M.; Cao, Z.; Harb, M.; Parida, M. R.; Hedhili, M. N.; Mohammed, O. F.; Bakr, O. M.; Cavallo, L.; Basset, J.-M. Direct versus Ligand-Exchange Synthesis of  $[\text{PtAg}_{28}(\text{BDT})_{12}(\text{TPP})_4]^{4-}$  Nanoclusters: Effect of a Single-Atom Dopant on the Optoelectronic and Chemical Properties. *Nanoscale* **2017**, 9, 9529–9536.

(146) Bootharaju, M. S.; Kozlov, S. M.; Cao, Z.; Shkurenko, A.; El-Zohry, A. M.; Mohammed, O. F.; Eddaoudi, M.; Bakr, O. M.; Cavallo, L.; Basset, J.-M. Tailoring the Crystal Structure of Nanoclusters Unveiled High Photoluminescence via Ion Pairing. *Chem. Mater.* **2018**, 30, 2719–2725.

(147) Kang, X.; Xiong, L.; Wang, S.; Pei, Y.; Zhu, M. De-Assembly of Assembled  $\text{Pt}_1\text{Ag}_{12}$  Units: Tailoring the Photoluminescence of Atomically Precise Nanoclusters. *Chem. Commun.* **2017**, 53, 12564–12567.

(148) Kang, X.; Zhou, M.; Wang, S.; Jin, S.; Sun, G.; Zhu, M.; Jin, R. The Tetrahedral Structure and Luminescence Properties of Bi-Metallic  $\text{Pt}_1\text{Ag}_{28}(\text{SR})_{18}(\text{PPh}_3)_4$  Nanocluster. *Chem. Sci.* **2017**, 8, 2581–2587.

(149) Chen, S.; Du, W.; Qin, C.; Liu, D.; Tang, L.; Liu, Y.; Wang, S.; Zhu, M. Assembly of the Thiolated  $[\text{Au}_1\text{Ag}_{22}(\text{S-Adm})_{12}]^{3+}$  Superatom Complex into a Framework Material through Direct Linkage by  $\text{SbF}_6^-$  Anions. *Angew. Chem., Int. Ed.* **2020**, 59, 7542–7547.

(150) Li, Q.; Taylor, M. G.; Kirschbaum, K.; Lambright, K. J.; Zhu, X.; Mpourmpakis, G.; Jin, R. Site-Selective Substitution of Gold Atoms in the  $\text{Au}_{24}(\text{SR})_{20}$  Nanocluster by Silver. *J. Colloid Interface Sci.* **2017**, 505, 1202–1207.

(151) Kang, X.; Huang, L.; Liu, W.; Xiong, L.; Pei, Y.; Sun, Z.; Wang, S.; Wei, S.; Zhu, M. Reversible Nanocluster Structure Transformation between Face-Centered Cubic and Icosahedral Isomers. *Chem. Sci.* **2019**, 10, 8685–8693.

(152) Li, Y.; Chen, M.; Wang, S.; Zhu, M. Intramolecular Metal Exchange Reaction Promoted by Thiol Ligands. *Nanomaterials* **2018**, 8, 1070.

(153) Wang, S.; Abroshan, H.; Liu, C.; Luo, T.-Y.; Zhu, M.; Kim, H. J.; Rosi, N. L.; Jin, R. Shuttling Single Metal Atom into and out of a Metal Nanoparticle. *Nat. Commun.* **2017**, 8, 848.

(154) Li, Q.; Luo, T.-Y.; Taylor, M. G.; Wang, S.; Zhu, X.; Song, Y.; Mpourmpakis, G.; Rosi, N. L.; Jin, R. Molecular “Surgery” on a 23-Gold-Atom Nanoparticle. *Sci. Adv.* **2017**, 3, No. e1603193.

(155) Zeng, C.; Chen, Y.; Das, A.; Jin, R. Transformation Chemistry of Gold Nanoclusters: From One Stable Size to Another. *J. Phys. Chem. Lett.* **2015**, 6, 2976–2986.

(156) Krishnadas, K. R.; Baksi, A.; Ghosh, A.; Natarajan, G.; Pradeep, T. Structure-Conserving Spontaneous Transformations between Nanoparticles. *Nat. Commun.* **2016**, 7, 13447.

(157) Natarajan, G.; Mathew, A.; Negishi, Y.; Whetten, R. L.; Pradeep, T. A Unified Framework for Understanding the Structure and Modifications of Atomically Precise Monolayer Protected Gold Clusters. *J. Phys. Chem. C* **2015**, 119, 27768–27785.

(158) Bose, P.; Chakraborty, P.; Mohanty, J. S.; Nonappa; Chowdhuri, A. R.; Khatun, E.; Ahuja, T.; Mahendranath, A.; Pradeep, T. Atom transfer between precision nanoclusters and polydispersed nanoparticles: a facile route for monodisperse alloy nanoparticles and their superstructures. *Nanoscale* **2020**, 12, 22116–22128.

(159) Kazan, R.; Müller, U.; Bürgi, T. Doping of Thiolate Protected Gold Clusters through Reaction with Metal Surfaces. *Nanoscale* **2019**, 11, 2938–2945.

(160) Krishnadas, K. R.; Natarajan, G.; Baksi, A.; Ghosh, A.; Khatun, E.; Pradeep, T. Metal–Ligand Interface in the Chemical Reactions of Ligand-Protected Noble Metal Clusters. *Langmuir* **2019**, 35, 11243–11254.





Cite this: *Chem. Commun.*, 2020, 56, 15623

Received 1st September 2020,  
Accepted 19th November 2020

DOI: 10.1039/d0cc05837h

rsc.li/chemcomm

## Reaction between $\text{Ag}_{17}^+$ and acetylene outside the mass spectrometer: dehydrogenation in the gas phase†

Madhuri Jash, Rabin Rajan J. Methikkalam,  Mohammad Bodiuzzaman, Ganesan Paramasivam and Thalappil Pradeep \*

**We present the first example of acetylide protected silver clusters by a reaction between  $\text{Ag}_{17}^+$  and acetylene, conducted around atmospheric pressure. The products were obtained after dehydrogenation of acetylene in the gas phase. The observed reaction mechanism may be helpful to design new catalysts useful in organometallic chemistry.**

Atomically precise nanoclusters (NCs), being the link between atoms and bulk materials, show unique properties and represent one of the major pillars of current nanoscience.<sup>1</sup> Due to their electronic and geometric shell closing and quantum confinement, even a change of one atom can alter their physical and chemical properties.<sup>2</sup> Catalytic properties of most of the NCs are studied in the supported form after ligand desorption, although stabilizing clusters after ligand removal, in a specific size and shape, is of concern.<sup>3</sup> In contrast, gas phase studies of size-selected naked clusters give us molecular level understanding of their catalytic processes due to the absence of ligands and the stabilising medium.<sup>4–6</sup>

From an organometallic point of view, transition metal- $\pi$  complexes are crucial intermediates of several metal-mediated transformations.<sup>7,8</sup> This kind of metal-unsaturated hydrocarbon interaction can be varied by changing a single metal atom in a metal cluster.<sup>4,9</sup> The type of interaction can be ionic, covalent or weak ion- $\pi$  interaction, depending on the cluster's atomicity, valence electrons and ligands. Mass spectrometry,<sup>10</sup> photoelectron spectroscopy<sup>11</sup> and infrared spectroscopy<sup>12</sup> are different characterization tools for the investigation of such gas phase interactions along with quantum chemical calculations.

Gas phase reactivity and catalysis of cluster metal ions have been reported by various research groups, inside the mass spectrometer.<sup>4,5,13,14</sup> The first report of the formation of silver

clusters by electrospray ionization under atmospheric pressure was in 2013.<sup>15</sup> Later, we had shown that single gas phase species,  $\text{Ag}_{17}^+$  can be produced outside as well as inside a mass spectrometer, without mass selection.<sup>16,17</sup> Recently, it has also been shown that  $\text{Ag}_{17}^+$  reacts with acetylene under vacuum and formed  $-\text{C}_2\text{H}_5$  attached  $\text{Ag}_{17}^+$  within the ion trap.<sup>18</sup> However, interaction of such large sized clusters has not been studied before outside the mass spectrometer, under atmospheric pressure conditions. In this communication, we explored the interaction of acetylene with  $\text{Ag}_{17}^+$  outside a mass spectrometer where  $\text{Ag}_{17}^+$  forms adducts with 2, 4 and 6 acetylene molecules after dehydrogenation. Density functional theory (DFT) calculations elucidate the structure of these adducts along with the dehydrogenation mechanism.

Gas phase ion-molecule reaction experiments were conducted using a LTQ XL Linear Ion Trap Mass Spectrometer with an external home-built nano-electrospray ion source. Here, we have used  $[\text{Ag}_{18}\text{H}_{16}(\text{TPP})_{10}]^{2+}$  clusters as a precursor analyte, which was synthesized following a reported method<sup>19</sup> and details are presented in the Experimental section. All the characteristic features including their UV-Vis spectrum, high resolution ESI mass spectrum and formation of deuterated analogue,  $[\text{Ag}_{18}\text{D}_{16}(\text{TPP})_{10}]^{2+}$  (measured with a Synapt G2Si HDMS instrument) confirm the formation of the cluster and all these data are shown in Fig. S1A–D (ESI†). The electrosprayed cluster was passed through a heating tube by using  $\text{N}_2$  as the nebulizing gas to obtain a stream of the naked cluster. This flow of naked cluster ions was reacted with acetylene outside the mass spectrometer. Fig. 1 shows a schematic of the experimental set-up which consists of a coiled copper tube as the heater, a stainless steel union cross connector with external gas line and an LTQ mass spectrometer. Formation of naked clusters from  $[\text{Ag}_{18}\text{H}_{16}(\text{TPP})_{10}]^{2+}$  was presented in our previous report.<sup>16</sup> The end of the heating tube was connected to one inlet of the union cross connector. Another inlet was fixed to the acetylene gas channel, an outlet was directed to the mass spectrometer inlet and another port was blanked. The acetylene gas channel was made with a stainless-steel tube of 1.5 mm

DST Unit of Nanoscience (DST UNS) and Thematic Unit of Excellence (TUE), Department of Chemistry, Indian Institute of Technology Madras, Chennai 600 036, India. E-mail: pradeep@iitm.ac.in

† Electronic supplementary information (ESI) available. See DOI: 10.1039/d0cc05837h

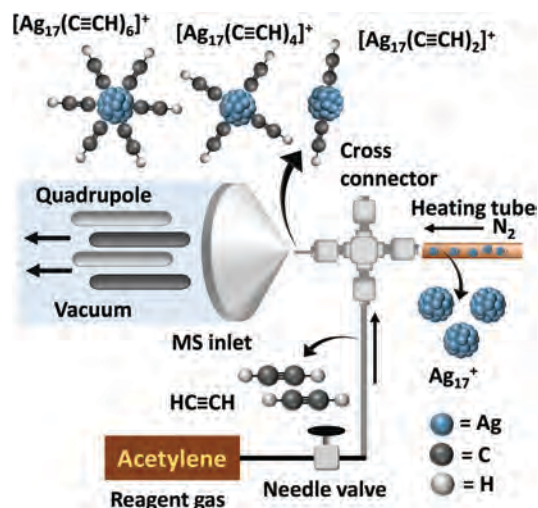


Fig. 1 Schematic diagram for an ion/molecule reaction between naked clusters and acetylene. Acetylene was crossed with the flowing naked clusters coming out from the heating tube and the products are detected with an LTO mass spectrometer.

outer diameter and 0.7 mm inner diameter, where the gas flow could be controlled with a needle valve. This set-up was kept in air, to make ion/molecule reactions feasible in air. The resulting ions, coming out from the cross connector enter the transfer capillary of the mass spectrometer and are analysed by the LTO mass spectrometer.

At first, naked clusters were made from electrospayed  $[\text{Ag}_{18}\text{H}_{16}(\text{TPP})_{10}]^{2+}$  in the absence of acetylene and the ESI mass spectrum obtained is shown in Fig. 2A. During this process, we get  $\text{Ag}_{17}^+$  ( $m/z$  1833) and  $\text{Ag}_{18}\text{H}^+$  ( $m/z$  1943) alone, without any mass selection. To study the ion/molecule reaction under ambient conditions, acetylene gas (from Rana Industrial Gases & Products, purity 99.99%) was introduced into the cross connector where the naked clusters enter from the heating tube along with  $\text{N}_2$ . During this reaction, the  $\text{N}_2$  gas flow was increased from 25 psi to 40 psi to obtain adequate ion signal in the mass spectrometer. Fig. 2B represents the ESI mass spectrum after introducing acetylene gas at a lower flow rate. Three adduct peaks of  $[\text{Ag}_{17}(\text{C}\equiv\text{CH})_2]^+$ ,  $[\text{Ag}_{17}(\text{C}\equiv\text{CH})_4]^+$  and  $[\text{Ag}_{17}(\text{C}\equiv\text{CH})_6]^+$  appeared at  $m/z$  1883, 1933 and 1983, respectively and the intensity of  $\text{Ag}_{17}^+$  got reduced. The isotopic distributions of  $\text{Ag}_{17}^+$  and the adducts matched well with their calculated spectra shown in Fig. S2 (ESI<sup>†</sup>). As acetylene pressure was increased in Fig. 2C, the intensities of the adduct peaks increased and the peak of  $\text{Ag}_{17}^+$  disappeared. Dehydrogenation of acetylene ( $\text{C}_2\text{H}_2$ ) to acetylide ( $-\text{C}_2\text{H}$ ) during adduct formation was confirmed by the mass shift of  $\Delta m/z = 2, 4$  and  $6$  in the case of  $[\text{Ag}_{17}(\text{C}\equiv\text{CH})_2]^+$ ,  $[\text{Ag}_{17}(\text{C}\equiv\text{CH})_4]^+$  and  $[\text{Ag}_{17}(\text{C}\equiv\text{CH})_6]^+$ , respectively (Fig. 2D–F). As always even mass shift was seen, which was suggested to be due to the loss of a hydrogen molecule ( $\text{H}_2$ ) during adduct formation, in our experimental conditions. Here the disappearance of  $\text{Ag}_{18}\text{H}^+$  with acetylene gas flow can be due to its very low abundance. Full range ESI mass spectra of this ion/molecule reaction are shown in Fig. S3 (ESI<sup>†</sup>). The reaction of  $\text{Ag}_{17}\text{H}_{14}^+$  was also conducted with acetylene, but it was inert due to the surface passivation by hydride ligands.

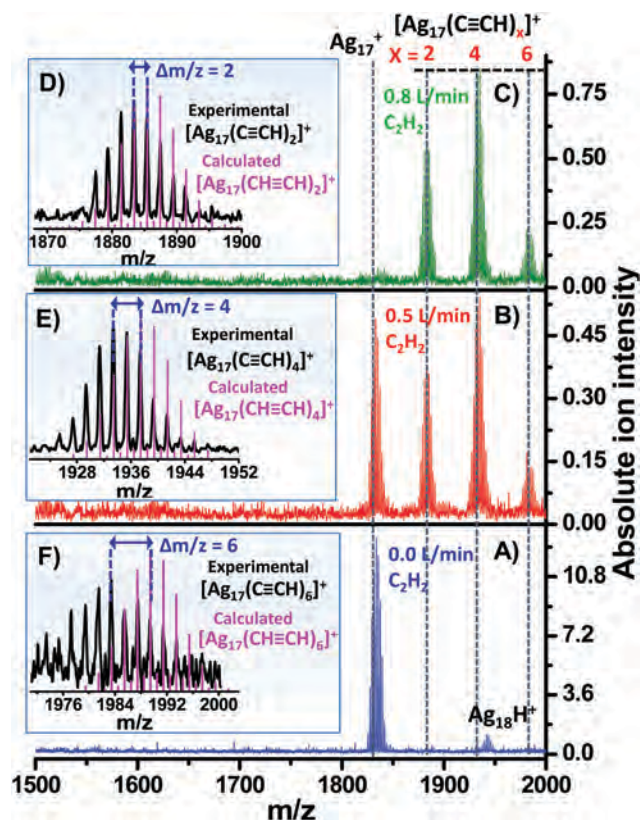
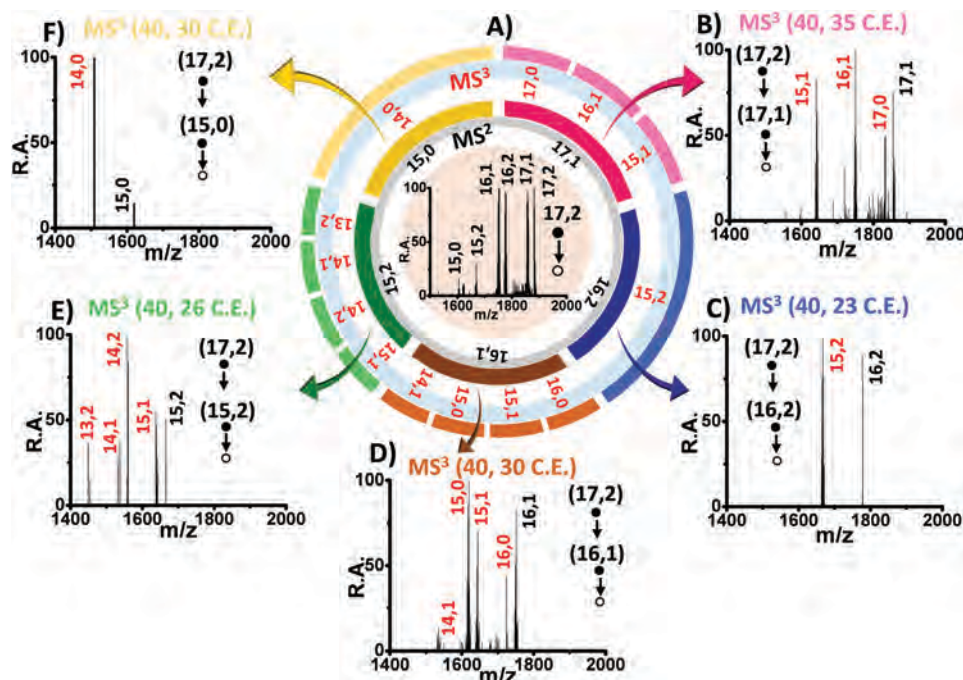


Fig. 2 (A) ESI mass spectrum of  $\text{Ag}_{17}^+$  and  $\text{Ag}_{18}\text{H}^+$  before the reaction with acetylene. (B and C) Are the ESI mass spectra after the reaction of  $\text{Ag}_{17}^+$  and acetylene, at different flow rates of acetylene. During this reaction, three adducts appeared as  $[\text{Ag}_{17}(\text{C}\equiv\text{CH})_2]^+$ ,  $[\text{Ag}_{17}(\text{C}\equiv\text{CH})_4]^+$  and  $[\text{Ag}_{17}(\text{C}\equiv\text{CH})_6]^+$ . The experimental (black) spectrum of (D)  $[\text{Ag}_{17}(\text{C}\equiv\text{CH})_2]^+$ , (E)  $[\text{Ag}_{17}(\text{C}\equiv\text{CH})_4]^+$  and (F)  $[\text{Ag}_{17}(\text{C}\equiv\text{CH})_6]^+$  show mass shifts of  $\Delta m/z = 2, 4, 6$  with the calculated spectrum (magenta) of  $[\text{Ag}_{17}(\text{CH}\equiv\text{CH})_2]^+$ ,  $[\text{Ag}_{17}(\text{CH}\equiv\text{CH})_4]^+$  and  $[\text{Ag}_{17}(\text{CH}\equiv\text{CH})_6]^+$ , respectively.

To get a clear idea about the structure and binding pattern of the adducts, collision induced dissociation (CID) experiments were performed. For a simpler representation, the adducts  $[\text{Ag}_{17}(\text{C}\equiv\text{CH})_2]^+$ ,  $[\text{Ag}_{17}(\text{C}\equiv\text{CH})_4]^+$  and  $[\text{Ag}_{17}(\text{C}\equiv\text{CH})_6]^+$  are denoted as (17,2), (17,4) and (17,6), respectively where the first number inside the bracket represents the atomicity of the silver core and the second number represents the number of acetylide ligands attached to it. The same notation is also followed for the CID fragments. Here all the adducts and their CID fragments are in +1 charge states which is not mentioned separately in the case of bracket notations. The fragmentation patterns ( $\text{MS}^2$  and  $\text{MS}^3$ ) of (17,2) are shown in Fig. 3A with two concentric rings. The full fragmentation patterns from  $\text{MS}^2$  to  $\text{MS}^6$  are shown as a flow chart and also in the form of five concentric rings in Fig. S4A and B (ESI<sup>†</sup>), respectively. In Fig. 3A, the inner ring, closer to the centre, shows the five different  $\text{MS}^2$  fragments of (17,2). The  $\text{MS}^2$  spectrum showing these fragmented peaks is given at the centre of that circle. Then, the next level fragmentation is shown in a lighter shade of the same colour. Here the second ring represents the  $\text{MS}^3$  fragmentation products of the five  $\text{MS}^2$  fragments. Fig. 3B–F are the  $\text{MS}^3$  spectra of (17,1), (16,2), (16,1), (15,2) and (15,0), respectively. As it was not possible to represent all the





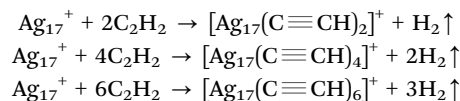
**Fig. 3** The CID fragments of  $[\text{Ag}_{17}(\text{C}\equiv\text{CH})_2]^+$  or (17,2) resulting from  $\text{MS}^2$  and  $\text{MS}^3$  experiments. (A) represents the  $\text{MS}^2$  spectrum of (17,2) at the centre of the circle and the  $\text{MS}^2$  and  $\text{MS}^3$  fragments with two individual concentric rings. (B–F) represent the  $\text{MS}^3$  spectrum of the corresponding (17,1), (16,2), (16,1), (15,2) and (15,0) fragments, respectively. The collision energies used are mentioned as  $\text{MS}^3$  (xx, yy C.E.) corresponding to  $\text{MS}^2$  and  $\text{MS}^3$  data and are in an instrumental unit.

mass spectra up to  $\text{MS}^6$  level in a single figure, we have plotted them separately. The different fragmentation pathways of (17,2), which proceed through (17,1), (16,2), (16,1) and (15,2) in  $\text{MS}^3$  level are presented in Fig. S5–S9 (ESI†). Whereas, the ion (15,0) does not reveal any fragmentation, probably due to low intensity.

For the (17,4) adduct, the overall fragmentation flowchart is shown in Fig. S10A (ESI†). In Fig. S10B (ESI†), the same fragmentation data are shown with two concentric rings. Fig. S11A (ESI†) shows the  $\text{MS}^2$  mass spectrum of (17,4) with three fragments, (17,3), (17,0) and (16,3). Fig. S11B–D (ESI†) are the  $\text{MS}^3$  mass spectra of (17,3), (17,0) and (16,3), respectively. For the third adduct (17,6), Fig. S12A (ESI†) represents the fragmentation flowchart whereas Fig. S12B (ESI†) represents it with one ring of  $\text{MS}^2$  fragments. The  $\text{MS}^2$  mass spectrum of (17,6) is shown in Fig. S13 (ESI†) with seven fragments. From all the fragmentation patterns of the three adducts, it is noticed that during the fragmentation process, the acetylide ligand can get knocked out from the cluster core with or without the silver atom. This result is very much unlike that from our previous report, fragmentation of the oxygen added peaks of  $\text{Ag}_{17}^+$ .<sup>16</sup> During the CID of oxygen added peaks, there was at first detachment of all oxygen atoms (ligands), forming intact  $\text{Ag}_{17}^+$ , which was further fragmented to smaller silver naked clusters with higher collision energy. From this result, we conclude that the fragmentation pattern of  $\text{Ag}_{17}^+$  adducts depends on the binding type of silver with the ligand. The experimental and calculated masses of all the assigned clusters in this experiment are summarized in Table S14 (ESI†).

The structures of  $\text{Ag}_{17}^+$  and adducts were optimised using density functional theory. The structure of  $\text{Ag}_{17}^+$  was optimized based on a previously reported method and then it was used for

further calculations.<sup>20</sup> The most stable structures of  $\text{Ag}_{17}^+$  and its adducts are shown in Fig. S15 (ESI†). In Fig. S16 (ESI†), their HOMO–LUMO gaps are also given. During the reaction, the increases in mass of the three adduct peaks were  $m/z$  50, 100 and 150 which are due to 2, 4 and 6  $-\text{C}_2\text{H}$  additions and desorption of 1, 2 and 3 hydrogen molecules, respectively as below:



To determine the actual mechanism of dehydrogenation, initially the interaction was calculated with one and two intact acetylene molecules over  $\text{Ag}_{17}^+$ , which show weak non-covalent cluster– $\pi$  interactions (Fig. S17, ESI†). According to a previous report, the dissociation threshold values for such larger cluster– $\pi$  moieties (for  $\text{Ag}_n^+$ , when  $n > 7$ ) is small, which makes them sufficiently unstable.<sup>21</sup> However, for  $[\text{Ag}_{17}(\text{HC}\equiv\text{CH})_2]^+$ , due to dehydrogenation of two acetylene molecules, we may have either one butadiyne ( $-\text{C}_4\text{H}_2$ ) or two acetylide ( $-\text{C}_2\text{H}$ ) attached  $\text{Ag}_{17}^+$  (Fig. S18, ESI†). The calculated total energies of these two structures are closer to each other but the binding energy values show that in  $[\text{Ag}_{17}(\text{C}\equiv\text{CH})_2]^+$ , the interaction of  $\text{C}_2\text{H}$  units with silver are stronger (covalent) than the butadiyne unit in  $[\text{Ag}_{17}\text{C}_4\text{H}_2]^+$  (non-covalent). Hence, the  $[\text{Ag}_{17}(\text{C}\equiv\text{CH})_2]^+$  structure, where the average bond distance of Ag–C was 2.25 Å, was considered for further calculation.

Possible mechanism for the formation of a hydrogen molecule after dehydrogenation of an even number of acetylenes interacting with  $\text{Ag}_{17}^+$ , was studied in detail. Fig. 4 shows the energy profile during the dehydrogenation of two acetylene over

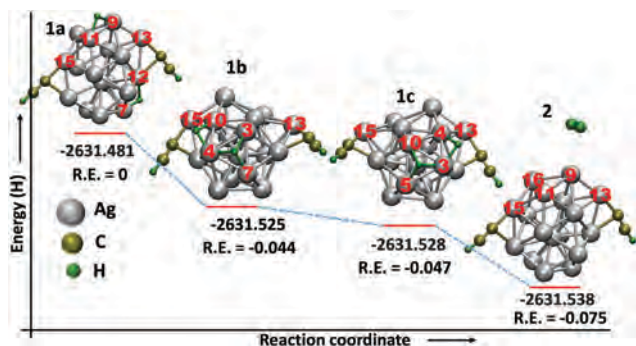


Fig. 4 Energy profile during the formation of  $[\text{Ag}_{17}(\text{C}\equiv\text{CH})_2]^+$  and a hydrogen molecule (**2**) starting from the intermediates (**1a–c**). During the optimization of the intermediate structure, there was mobility of bonded hydrogens with respect to silver atoms. The intermediates finally give the lower energy product after dehydrogenation. The total energy and relative energy values are in Hartree.

the surface of  $\text{Ag}_{17}^+$ . Here, like the previously reported  $[\text{Ag}_7^+\text{C}_2\text{H}_2]$  cluster, we have also calculated a competitive isomer (**1a** in Fig. 4) of  $[\text{Ag}_{17}(\text{HC}\equiv\text{CH})_2]^+$ , where one hydrogen from each of the acetylenes got dissociated and attached to the silver core transiently.<sup>21</sup> This competitive isomer was higher in energy ( $-2631.481$  H) compared to the normal  $[\text{Ag}_{17}(\text{HC}\equiv\text{CH})_2]^+$  ( $-2631.588$  H) and was considered as an intermediate structure for the next step. The attached hydrogens to silver, changed their positions with respect to the silver atoms during the optimization of the structure (**1a–c** in Fig. 4) and come out as a hydrogen molecule giving the final product,  $[\text{Ag}_{17}(\text{C}\equiv\text{CH})_2]^+$  (**2** in Fig. 4). The relatively lower energy of the product compared to the intermediates makes this reaction energetically favourable. Therefore, the formation of a hydrogen molecule is possible, which was observed in our experiments. Further detailed studies of binding of four and six acetylene molecules were also carried out which show the formation of hydrogen molecules and the products,  $[\text{Ag}_{17}(\text{C}\equiv\text{CH})_4]^+$  and  $[\text{Ag}_{17}(\text{C}\equiv\text{CH})_6]^+$ , respectively (Fig. S19 and S20, ESI<sup>†</sup>). Energy profile of the overall reaction is shown in Fig. S21 (ESI<sup>†</sup>). The dehydrogenation process also has been calculated for an odd (one) number of acetylenes but it gives only a higher energy intermediate, and not any stable product (Fig. S22, ESI<sup>†</sup>). Therefore, dehydrogenation or formation of a hydrogen molecule was successful only when an even number of acetylenes interacted with  $\text{Ag}_{17}^+$ . The calculated binding energies after dehydrogenation are listed in Table S23 (ESI<sup>†</sup>). Calculated structures of  $[\text{Ag}_{17}(\text{C}\equiv\text{CH})]^+$  and  $[\text{C}\equiv\text{CH}]$ , generated during the CID experiment of  $[\text{Ag}_{17}(\text{C}\equiv\text{CH})_2]^+$  are shown in Fig. S24 (ESI<sup>†</sup>). Electronic structures of  $[\text{Ag}_{17}(\text{C}\equiv\text{CH})_2]^+$ ,  $[\text{Ag}_{17}(\text{C}\equiv\text{CH})]^+$  and  $[\text{C}\equiv\text{CH}]$  have also been calculated and shown in Fig. S25–S27 (ESI<sup>†</sup>), respectively.

In conclusion, the naked cluster,  $\text{Ag}_{17}^+$  was formed outside a mass spectrometer and for the first time, its reactivity with acetylene was studied around atmospheric pressure. During the reaction, dehydrogenation of acetylene results in the formation

of acetylide attached  $\text{Ag}_{17}^+$ . Dehydrogenation occurred always for an even number of acetylenes, which also supports the dihydrogen molecule desorption. This study provides new insights into the binding mechanism of acetylene on  $\text{Ag}_{17}^+$  and gives new light on the reactivity of size-selected naked clusters. As these reactions were conducted near ambient conditions, it is possible to collect the product on a suitable substrate for further characterization. Similar studies with other molecules may lead to new directions in gas phase clusters. Potential application of this method will be in the understanding of catalytic processes in atomically precise materials.

We thank the Department of Science and Technology for supporting our research. M. J. thanks U. G. C. for her SRF fellowship.

## Conflicts of interest

There are no conflicts to declare.

## Notes and references

- I. Chakraborty and T. Pradeep, *Chem. Rev.*, 2017, **117**, 8208–8271.
- J. Zhang, Z. Li, J. Huang, C. Liu, F. Hong, K. Zheng and G. Li, *Nanoscale*, 2017, **9**, 16879–16886.
- M. Turner, V. B. Golovko, O. P. H. Vaughan, P. Abdulkin, A. Berenguer-Murcia, M. S. Tikhov, B. F. G. Johnson and R. M. Lambert, *Nature*, 2008, **454**, 981.
- Z. Luo, A. W. Castleman and S. N. Khanna, *Chem. Rev.*, 2016, **116**, 14456–14492.
- D. K. Boehme and H. Schwarz, *Angew. Chem., Int. Ed.*, 2005, **44**, 2336–2354.
- S. M. Lang, T. M. Bernhardt, R. N. Barnett, B. Yoon and U. Landman, *J. Am. Chem. Soc.*, 2009, **131**, 8939–8951.
- J.-M. Weibel, A. Blanc and P. Pale, *Chem. Rev.*, 2008, **108**, 3149–3173.
- M. Meldal and C. W. Tornøe, *Chem. Rev.*, 2008, **108**, 2952–3015.
- Z. Luo and A. W. Castleman, *Acc. Chem. Res.*, 2014, **47**, 2931–2940.
- M. J. Manard, P. R. Kemper, C. J. Carpenter and M. T. Bowers, *Int. J. Mass Spectrom.*, 2005, **241**, 99–108.
- W. Y. Lu, P. D. Kleiber, M. A. Young and K. H. Yang, *J. Chem. Phys.*, 2001, **115**, 5823–5829.
- T. B. Ward, A. D. Brathwaite and M. A. Duncan, *Top. Catal.*, 2018, **61**, 49–61.
- G. N. Khairallah and R. A. J. O'Hair, *Dalton Trans.*, 2007, 3149–3157, DOI: 10.1039/B700132K.
- P. B. Armentrout, *Annu. Rev. Phys. Chem.*, 2001, **52**, 423–461.
- M. Wlekinski, D. Sarkar, A. Hollerbach, T. Pradeep and R. G. Cooks, *Phys. Chem. Chem. Phys.*, 2015, **17**, 18364–18373.
- M. Jash, A. C. Reber, A. Ghosh, D. Sarkar, M. Bodiuzzaman, P. Basuri, A. Bakshi, S. N. Khanna and T. Pradeep, *Nanoscale*, 2018, **10**, 15714–15722.
- A. Ghosh, M. Bodiuzzaman, A. Nag, M. Jash, A. Bakshi and T. Pradeep, *ACS Nano*, 2017, **11**, 11145–11151.
- A. Bakshi, M. Jash, S. Bag, S. K. Mudedla, M. Bodiuzzaman, D. Ghosh, G. Paramasivam, V. Subramanian and T. Pradeep, *J. Phys. Chem. C*, 2019, **123**, 28494–28501.
- M. S. Bootharaju, R. Dey, L. E. Gevers, M. N. Hedhili, J.-M. Basset and O. M. Bakr, *J. Am. Chem. Soc.*, 2016, **138**, 13770–13773.
- M. Chen, J. E. Dyer, K. Li and D. A. Dixon, *J. Phys. Chem. A*, 2013, **117**, 8298–8313.
- M. Yang, H. Wu, B. Huang and Z. Luo, *J. Phys. Chem. A*, 2019, **123**, 6921–6926.

## Supporting Information

### Reaction between $\text{Ag}_{17}^+$ and acetylene outside the mass spectrometer: Dehydrogenation in the gas phase

Madhuri Jash, Rabin Rajan J. Methikkalam, Mohammad Bodiuzzaman, Ganesan Paramasivam, and Thalappil Pradeep\*

DST Unit of Nanoscience (DST UNS) and Thematic Unit of Excellence (TUE), Department of Chemistry, Indian Institute of Technology Madras, Chennai 600 036, India

\*To whom correspondence should be addressed. E-mail: [pradeep@iitm.ac.in](mailto:pradeep@iitm.ac.in)

### Table of Contents

Name	Description	Page No.
S1	Characterisation of $[\text{Ag}_{18}\text{H}_{16}(\text{TPP})_{10}]^{2+}$ and $[\text{Ag}_{18}\text{D}_{16}(\text{TPP})_{10}]^{2+}$ clusters	5
S2	Experimental and calculated spectra of $\text{Ag}_{17}^+$ , $[\text{Ag}_{17}(\text{C}\equiv\text{CH})_2]^+$ , $[\text{Ag}_{17}(\text{C}\equiv\text{CH})_4]^+$ and $[\text{Ag}_{17}(\text{C}\equiv\text{CH})_6]^+$	6
S3	Full range ESI mass spectra during the reaction between naked clusters and acetylene	7
S4	Total CID pattern of $[\text{Ag}_{17}(\text{C}\equiv\text{CH})_2]^+$	8-9
S5	CID mass spectra of $[\text{Ag}_{17}(\text{C}\equiv\text{CH})_2]^+$ through $[\text{Ag}_{17}(\text{C}\equiv\text{CH})_1]^+$ pathway	10
S6	CID mass spectra of $[\text{Ag}_{17}(\text{C}\equiv\text{CH})_2]^+$ through $[\text{Ag}_{16}(\text{C}\equiv\text{CH})_2]^+$ pathway	11
S7	CID mass spectra of $[\text{Ag}_{17}(\text{C}\equiv\text{CH})_2]^+$ through $[\text{Ag}_{16}(\text{C}\equiv\text{CH})_1]^+$ and followed by $[\text{Ag}_{15}(\text{C}\equiv\text{CH})_1]^+$ pathway	12
S8	CID mass spectra of $[\text{Ag}_{17}(\text{C}\equiv\text{CH})_2]^+$ through $[\text{Ag}_{16}(\text{C}\equiv\text{CH})_1]^+$ and followed by $[\text{Ag}_{15}]^+$ pathway	13
S9	CID mass spectra of $[\text{Ag}_{17}(\text{C}\equiv\text{CH})_2]^+$ through $[\text{Ag}_{15}(\text{C}\equiv\text{CH})_2]^+$ pathway	14
S10	Total CID pattern of $[\text{Ag}_{17}(\text{C}\equiv\text{CH})_4]^+$	15
S11	CID mass spectra of $[\text{Ag}_{17}(\text{C}\equiv\text{CH})_4]^+$ up to $\text{MS}^3$	16
S12	Total CID pattern of $[\text{Ag}_{17}(\text{C}\equiv\text{CH})_6]^+$	17
S13	CID mass spectrum of $[\text{Ag}_{17}(\text{C}\equiv\text{CH})_6]^+$ cluster for $\text{MS}^2$	18
S14	Comparison of experimental and calculated masses measured with the LTQ	19
S15	Most stable calculated structures of reactant and products	20
S16	HOMO-LUMO gap of reactant and products	21

S17	Calculated structure of $[\text{Ag}_{17}(\text{HC}\equiv\text{CH})]^+$ and $[\text{Ag}_{17}(\text{HC}\equiv\text{CH})_2]^+$	22
S18	Possibility of formation of $[\text{Ag}_{17}(\text{C}\equiv\text{CH})_2]^+$ and $[\text{Ag}_{17}\text{C}_4\text{H}_2]^+$	23
S19	Formation of $[\text{Ag}_{17}(\text{C}\equiv\text{CH})_4]^+$ and hydrogen molecule	24
S20	Formation of $[\text{Ag}_{17}(\text{C}\equiv\text{CH})_6]^+$ and hydrogen molecule	25
S21	Energy profile of overall reaction	26
S22	Possibility of formation of $[\text{Ag}_{17}(\text{C}\equiv\text{CH})]^+$	27
S23	Calculated binding energies	28
S24	Calculated structures of precursor and product ions during CID	29
S25	Electronic structure of $[\text{Ag}_{17}(\text{C}\equiv\text{CH})_2]^+$	30
S26	Electronic structure of $[\text{Ag}_{17}(\text{C}\equiv\text{CH})]^+$	31
S27	Electronic structure of $[\text{C}\equiv\text{CH}]$	32

## EXPERIMENTAL SECTION

### Reagents and Materials

Silver nitrate ( $\text{AgNO}_3$ ) was purchased from Rankem India, sodium borohydride ( $\text{NaBH}_4$ , 98%), sodium borodeuteride ( $\text{NaBD}_4$ , 98 atom% D) and triphenylphosphine (TPP) were purchased from Sigma-Aldrich. HPLC grade methanol ( $\text{MeOH}$ ) was from Finar chemicals and analytical grade chloroform ( $\text{CHCl}_3$ ) was from Rankem India. All the chemicals were used without further purification. Millipore water, with a resistivity of 18.2  $\text{M}\Omega\cdot\text{cm}$  was used for the synthesis purpose.

### Synthesis

The cluster  $[\text{Ag}_{18}\text{H}_{16}(\text{TPP})_{10}]^{2+}$  was synthesized by following our previous method, a modified method of a reported one. About 20 mg of  $\text{AgNO}_3$  was dissolved in 5 mL of  $\text{MeOH}$  followed by the addition of 70 mg of triphenylphosphine in 10 mL of chloroform, under stirring at room temperature. After 20 minutes of reaction, 6 mg of  $\text{NaBH}_4$  in 0.5 mL of ice cold water was added dropwise to the reaction mixture, which changed the color immediately from colorless to light yellow. Then the reaction was continued for three hours in dark condition to avoid any further oxidation of silver. The light yellow reaction mixture became dark green after three hours of continuous stirring, which indicated the formation of  $[\text{Ag}_{18}\text{H}_{16}(\text{TPP})_{10}]^{2+}$  cluster. The mixture of solvents was then vacuum evaporated and the excess silver precursor and  $\text{NaBH}_4$  were removed by washing with 20-22 mL of cold Millipore water. Then the solid material consisting of  $[\text{Ag}_{18}\text{H}_{16}(\text{TPP})_{10}]^{2+}$  cluster was extracted with 2 mL of methanol and centrifuged for 5 minutes at 5,000 rpm to remove the excess TPP ligand. The deep green  $[\text{Ag}_{18}\text{H}_{16}(\text{TPP})_{10}]^{2+}$  cluster solution was used for further characterizations like UV-Vis and ESI MS. For all of our mass spectrometric experiments in LTQ, the above mentioned green cluster solution was diluted to 10 times by using methanol. For synthesizing the  $[\text{Ag}_{18}\text{D}_{16}(\text{TPP})_{10}]^{2+}$ , in the synthesis procedure,  $\text{NaBH}_4$  was replaced by  $\text{NaBD}_4$ .

### Instrumentation

The optical absorption spectra of clusters were measured using a Perkin Elmer Lambda 25 UV-Vis spectrometer in the range of 200-1100 nm with a band pass filter of 1 nm. Waters Synapt G2Si HDMS instrument (abbreviated as G2Si subsequently) with electrospray ionization (ESI) source was used to record the high resolution mass spectra (HRMS) of  $[\text{Ag}_{18}\text{H}_{16}(\text{TPP})_{10}]^{2+}$  and  $[\text{Ag}_{18}\text{D}_{16}(\text{TPP})_{10}]^{2+}$  in positive ion mode. This mass spectrometer is equipped with electrospray source, quadrupole ion guide/trap, ion mobility cell and time of flight analyzer. For HRESI MS of the clusters, an optimized condition including a flow rate of 30  $\mu\text{L}/\text{min}$ , a capillary voltage of 2 kV, a cone voltage and source offset of 0 V was used. All other experiments, related to the naked clusters and their reactions with acetylene described in this paper were carried out by using Thermo Scientific LTQ XL Linear Ion Trap Mass Spectrometer (abbreviated as LTQ subsequently) with a home-built nano-ESI source. The instrumental set-up of LTQ with nano-ESI source was described in details in our previous publication. To obtain a well-resolved MS signal the optimized conditions were, flow rate: 3  $\mu\text{L}/\text{min}$ ; ionization spray voltage: 3 kV; capillary temperature: 250  $^\circ\text{C}$ ; capillary voltage (abbreviated as CV): 45 V and tube lens voltage (abbreviated as TV): 100 V. All the mass spectrometric measurements were done in the positive ion mode and 25 psi  $\text{N}_2$  was used as the nebulizing gas. In this LTQ, CID was done by selecting a ion with a specific mass to charge ratio ( $m/z$ ) by changing the radiofrequency (RF) and direct current, then colliding the ion with helium (He) gas inside the trap. Mass analysis of CID was done based on the ejected ions out of the trap. Multiple stages tandem mass spectrometry was also

performed in this instrument where a product ion, formed by CID experiment, was again selected for the next level CID experiment. These types of tandem mass spectrometry are also called MS<sup>n</sup> experiment, where n = number of product ion stages. During all the CID experiments, the following parameters were kept constant; injection time 300 ms, microscans 5, activation time 30 ms, activation Q value 0.25.

## COPUTATIONAL DETAILS

The ion/molecule reaction between acetylene and Ag<sub>17</sub><sup>+</sup> leads to dehydrogenation of acetylene and formation of hydrogen molecule/s and adducts such as [Ag<sub>17</sub>(C≡CH)<sub>2</sub>]<sup>+</sup>, [Ag<sub>17</sub>(C≡CH)<sub>4</sub>]<sup>+</sup> and [Ag<sub>17</sub>(C≡CH)<sub>6</sub>]<sup>+</sup>. All the structures were optimized using density functional theory (DFT) using the Gaussian 09 software.<sup>[1]</sup> Vibrational frequencies were calculated for all the optimized monocationic structures to ensure that it corresponds to a lower minimum. For the optimized structures of Ag<sub>17</sub><sup>+</sup>, [Ag<sub>17</sub>(C≡CH)<sub>2</sub>]<sup>+</sup>, [Ag<sub>17</sub>(C≡CH)<sub>4</sub>]<sup>+</sup> and [Ag<sub>17</sub>(C≡CH)<sub>6</sub>]<sup>+</sup>, HOMO-LUMO gaps were calculated. During the optimization of adduct structure [Ag<sub>17</sub>(C≡CH)<sub>2</sub>]<sup>+</sup>, other possible forms of acetylene adducts such as [Ag<sub>17</sub>(HC≡CH)]<sup>+</sup>, [Ag<sub>17</sub>(HC≡CH)<sub>2</sub>]<sup>+</sup>, [Ag<sub>17</sub>(C<sub>4</sub>H<sub>2</sub>)]<sup>+</sup> and [Ag<sub>17</sub>(C≡CH)]<sup>+</sup> have also been optimized along with their binding energy values to know their possibility of formation. The mechanism of formation of hydrogen molecule/s was studied computationally when even number of acetylene molecules react with Ag<sub>17</sub><sup>+</sup>. Whereas, for odd number of acetylene interaction, the intermediate does not end up with energetically favourable product or hydrogen molecule formation. We have also optimised the structures of [Ag<sub>17</sub>(C≡CH)]<sup>+</sup> and [C≡CH], generated during the CID experiments of [Ag<sub>17</sub>(C≡CH)<sub>2</sub>]<sup>+</sup>. The geometric optimization of the [Ag<sub>17</sub>(C≡CH)<sub>2</sub>]<sup>+</sup> cluster was done using restricted (closed electron shell) DFT in g09. The restricted occupancy of electrons allows 2 electrons for one MO. The calculated HOMO-LUMO gap of the cationic cluster is found to be 0.79 eV. The geometric optimization of [Ag<sub>17</sub>(C≡CH)]<sup>+</sup> fragment was done using unrestricted (open shell) DFT in g09 by keeping its spin multiplicity as 2. The unrestricted occupancy of electrons splits the MOs into alpha and beta MOs either with a single free spin-up or spin-down electron respectively. The calculated HOMO-LUMO gap of the cationic cluster is 0.21 eV. The [C≡CH] fragment exists in its neutral form having an odd electron system with spin multiplicity 2. The calculated HOMO-LUMO gap is 1.11 eV. The 1s electron of H atom contributes to the beta π-bonding orbital of beta MOs of C<sub>2</sub>H through sp<sup>2</sup> hybridization and the LUMO is made up of σ\* anti-bonding orbital of beta MOs.

The binding energies were calculated using the following equation,

$$\text{binding energy} = E_{\text{complex}} - [E_{\text{monomer1}} + E_{\text{monomer2}}]$$

where E<sub>complex</sub> is the energy of [Ag<sub>17</sub>(C≡CH)<sub>n</sub>]<sup>+</sup>, E<sub>monomer1</sub> is the energy of Ag<sub>17</sub><sup>+</sup>, and E<sub>monomer2</sub> is the energy of n number of (C≡CH), where n = 1, 2, 4 and 6. In other cases (without dehydrogenation of acetylene), E<sub>complex</sub> is the energy of [Ag<sub>17</sub>(HC≡CH)<sub>n</sub>]<sup>+</sup>, E<sub>monomer1</sub> is the energy of Ag<sub>17</sub><sup>+</sup>, and E<sub>monomer2</sub> is the energy of n number of (HC≡CH), where n = 1 and 2.

- [1] M. J. Frisch, G. W. Trucks, H. B. Schlegel, G. E. Scuseria, M. A. Robb, J. R. Cheeseman, G. Scalmani, V. Barone, B. Mennucci, G. A. Petersson, H. Nakatsuji, M. Caricato, X. Li, H. P. Hratchian, A. F. Izmaylov, J. Bloino, G. Zheng, J. L. Sonnenberg, M. Hada, M. Ehara, et al. *Gaussian 09*, Revision B.01. Gaussian 09, Revision B.01; Gaussian, Inc.: Wallingford, CT, 2009.



## Supporting information 1

### Characterisation of $[\text{Ag}_{18}\text{H}_{16}(\text{TPP})_{10}]^{2+}$ and $[\text{Ag}_{18}\text{D}_{16}(\text{TPP})_{10}]^{2+}$ clusters:

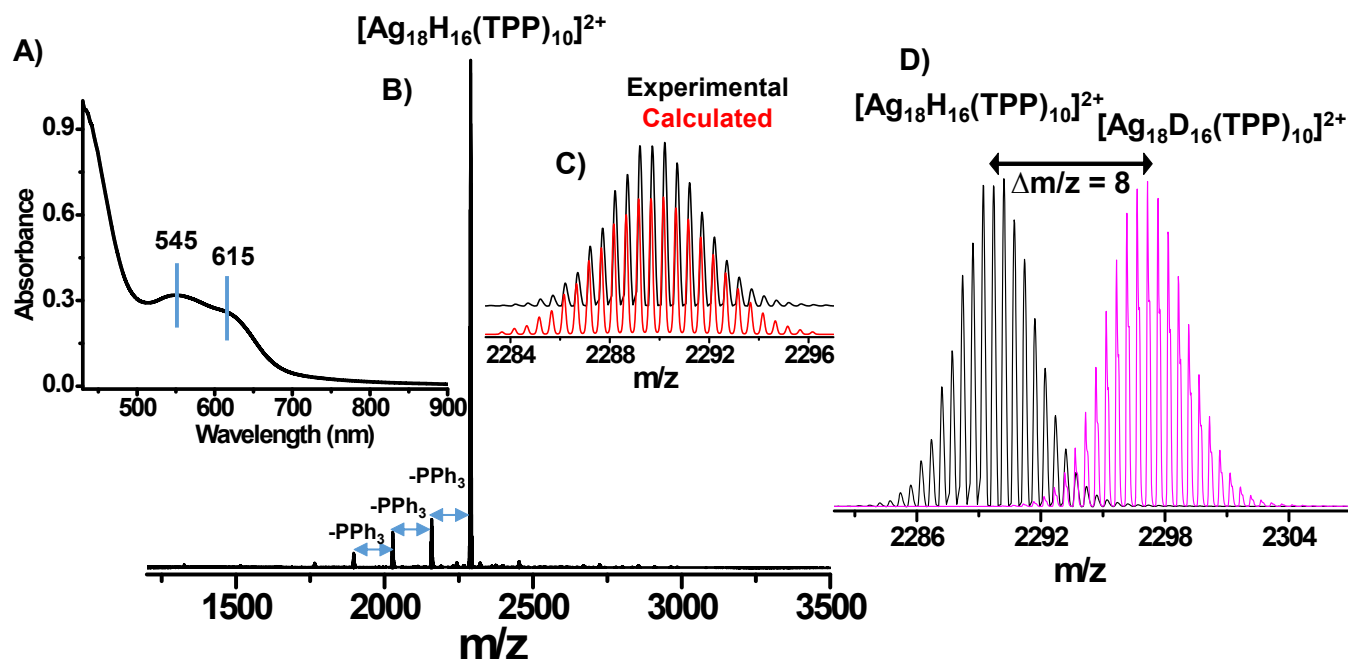


**Fig. S1** A) UV-Vis absorption spectrum of  $[\text{Ag}_{18}\text{H}_{16}(\text{TPP})_{10}]^{2+}$  in MeOH showing two peaks at 545 nm and 615 nm. The characteristic absorption features are marked. B) ESI mass spectrum of  $[\text{Ag}_{18}\text{H}_{16}(\text{TPP})_{10}]^{2+}$  in positive ion mode (using the G2Si) showing a sharp molecular ion peak at  $m/z$  2290 with 2+ charge state. Other small peaks arise due to  $\text{PPh}_3$  losses from molecular ion peak. C) Expanded view of the  $m/z$  2290 peak which shows the agreement between experimental and calculated isotopic patterns. D) ESI mass spectra of  $[\text{Ag}_{18}\text{H}_{16}(\text{TPP})_{10}]^{2+}$  and  $[\text{Ag}_{18}\text{D}_{16}(\text{TPP})_{10}]^{2+}$  clusters. The mass shift is  $\Delta m/z = 8$  which is due to the exchange of 16 hydride ions with deuteride ions in 2+ charge state.



## Supporting information 2

Experimental and calculated spectra of  $\text{Ag}_{17}^+$ ,  $[\text{Ag}_{17}(\text{C}\equiv\text{CH})_2]^+$ ,  $[\text{Ag}_{17}(\text{C}\equiv\text{CH})_4]^+$  and  $[\text{Ag}_{17}(\text{C}\equiv\text{CH})_6]^+$ :

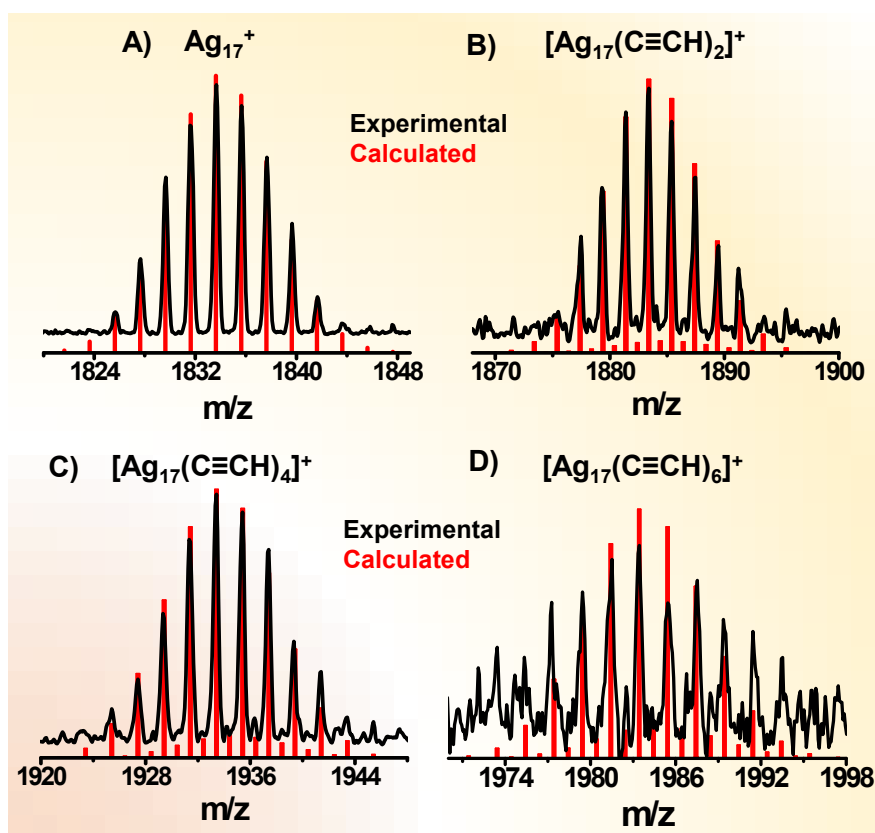


**Fig. S2** The isotopic distribution of experimental (black) mass spectrum of A)  $\text{Ag}_{17}^+$ , B)  $[\text{Ag}_{17}(\text{C}\equiv\text{CH})_2]^+$ , C)  $[\text{Ag}_{17}(\text{C}\equiv\text{CH})_4]^+$  and D)  $[\text{Ag}_{17}(\text{C}\equiv\text{CH})_6]^+$  matches well with their calculated (red) spectrum.

## Supporting information 3

### Full range ESI mass spectra during the reaction between naked clusters and acetylene:

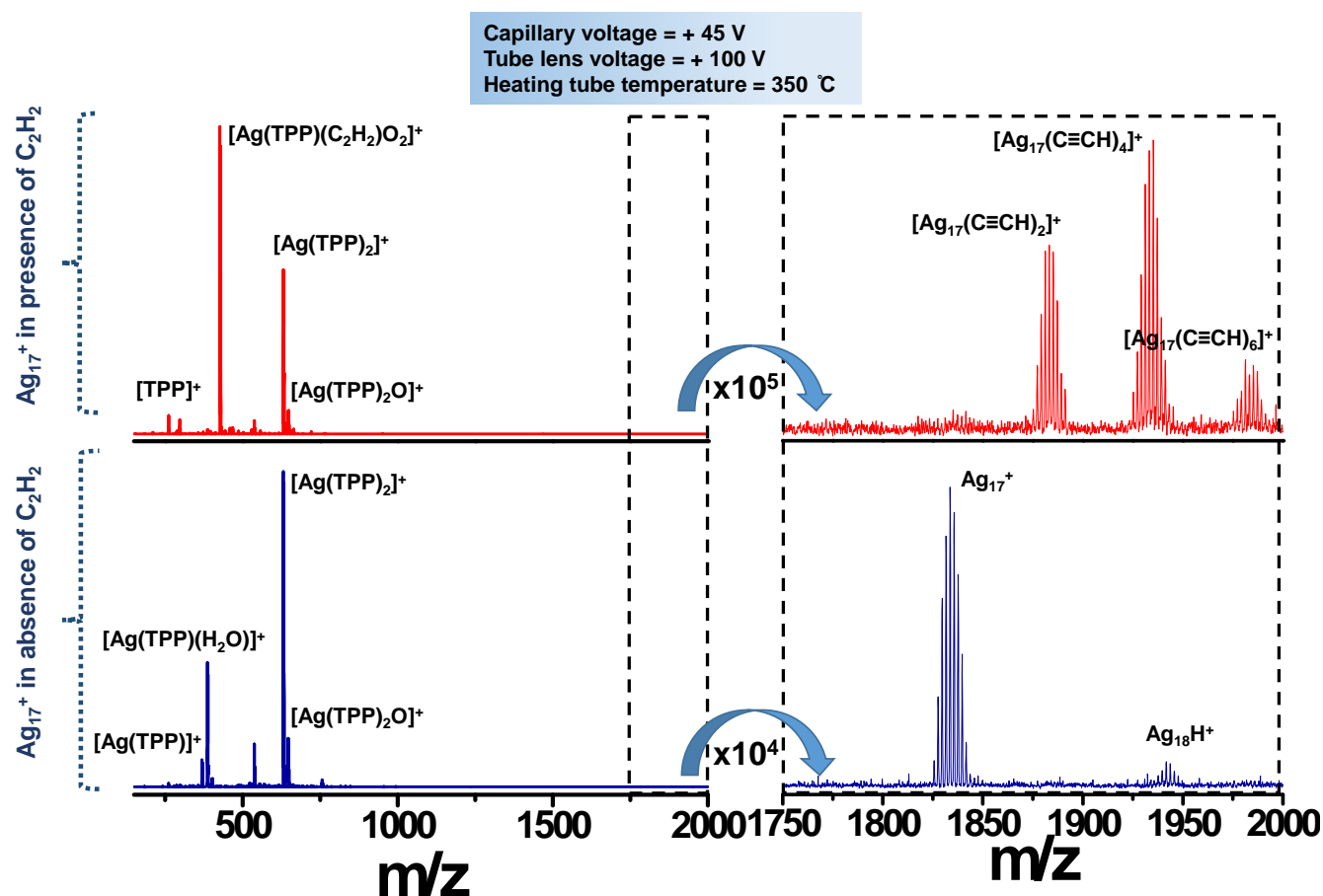


**Fig. S3** Full range (150-2000  $m/z$ ) ESI mass spectra of naked clusters in absence and presence of acetylene gas. In absence of acetylene, there were naked cluster peaks of Ag<sub>17</sub><sup>+</sup> and Ag<sub>18</sub>H<sup>+</sup> along with lower mass region peaks of [Ag(TPP)]<sup>+</sup>, [Ag(TPP)(H<sub>2</sub>O)]<sup>+</sup>, [Ag(TPP)<sub>2</sub>]<sup>+</sup> and [Ag(TPP)<sub>2</sub>O]<sup>+</sup>. In presence of acetylene, the lower mass peak [Ag(TPP)(H<sub>2</sub>O)]<sup>+</sup> converted to [Ag(TPP)(C<sub>2</sub>H<sub>2</sub>)O<sub>2</sub>]<sup>+</sup>, where acetylene (C<sub>2</sub>H<sub>2</sub>) addition was observed. Whereas, for higher mass region, Ag<sub>17</sub><sup>+</sup> resulted only acetylide (-C<sub>2</sub>H) addition peaks.

## Supporting information 4A

Total CID pattern of  $[\text{Ag}_{17}(\text{C}\equiv\text{CH})_2]^+$ :

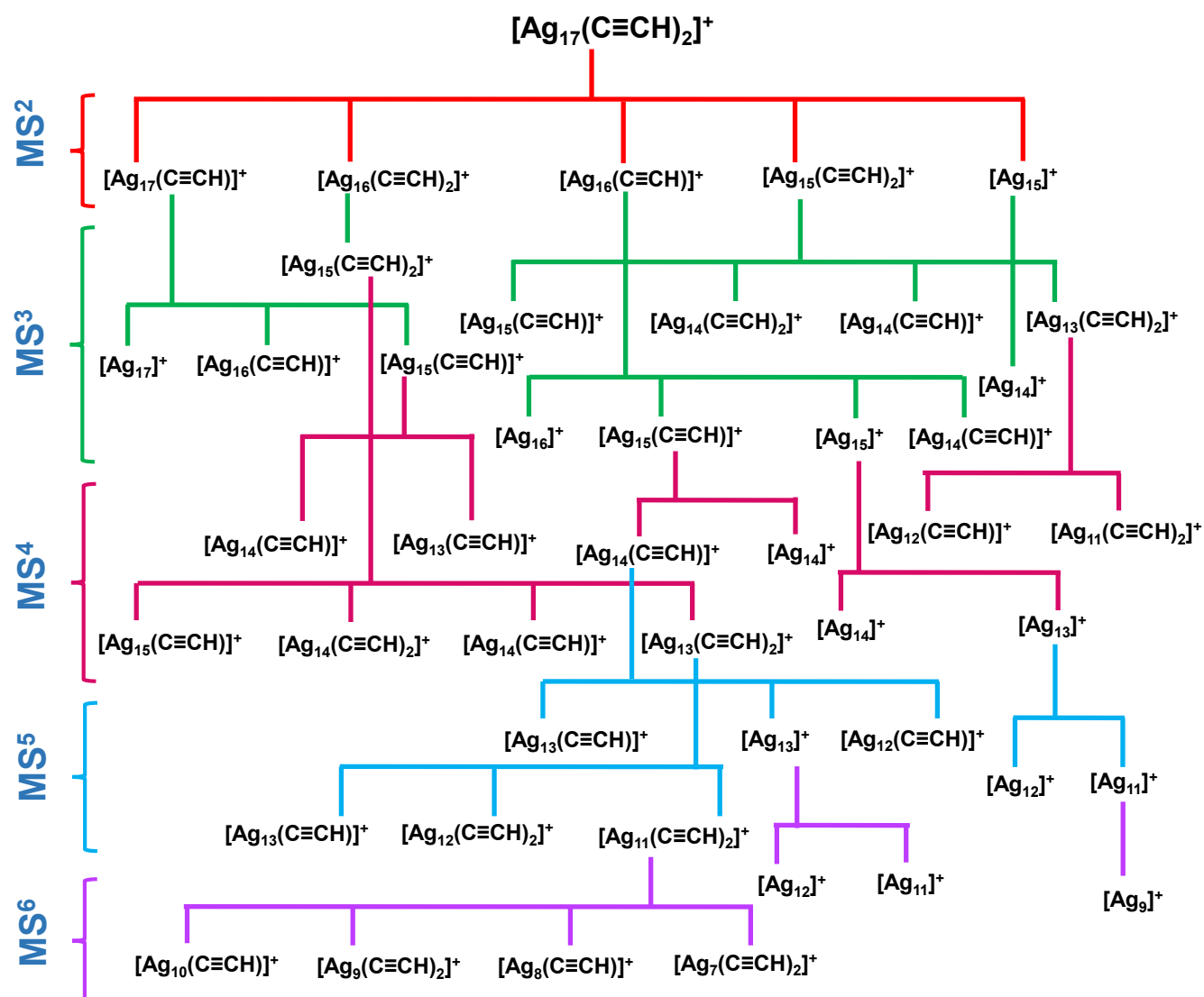


**Fig. S4A** Flow chart of the breaking pattern and fragments of the adduct  $[\text{Ag}_{17}(\text{C}\equiv\text{CH})_2]^+$ , which were resulted by MS<sup>2</sup> to MS<sup>6</sup> experiments.

## Supporting information 4B

### Total CID pattern of $[\text{Ag}_{17}(\text{C}\equiv\text{CH})_2]^+$ :

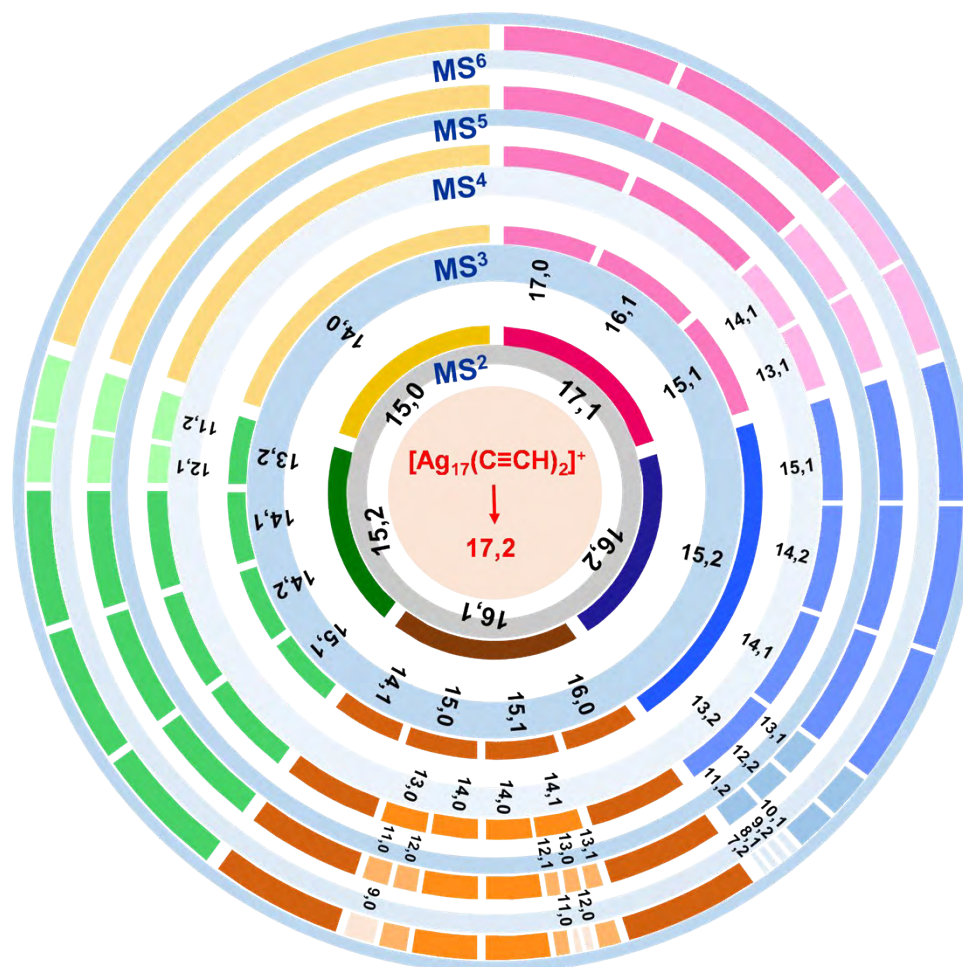


**Fig. S4B** The total CID fragments of  $[\text{Ag}_{17}(\text{C}\equiv\text{CH})_2]^+$  or (17,2), resulting from  $\text{MS}^2$  to  $\text{MS}^6$  experiments are presented with five individual concentric rings. The first number represents the atomicity of the silver core and the second number represents the number of acetylide ( $-\text{C}_2\text{H}$ ) ligands attached to it. The first level of fragmentation or  $\text{MS}^2$  is shown in inner most ring with five different fragments. Then the next level of fragmentation continues with lighter shade of the same colour, ending at  $\text{MS}^6$  level.

## Supporting information 5

CID mass spectra of  $[\text{Ag}_{17}(\text{C}\equiv\text{CH})_2]^+$  through  $[\text{Ag}_{17}(\text{C}\equiv\text{CH})_1]^+$  pathway:

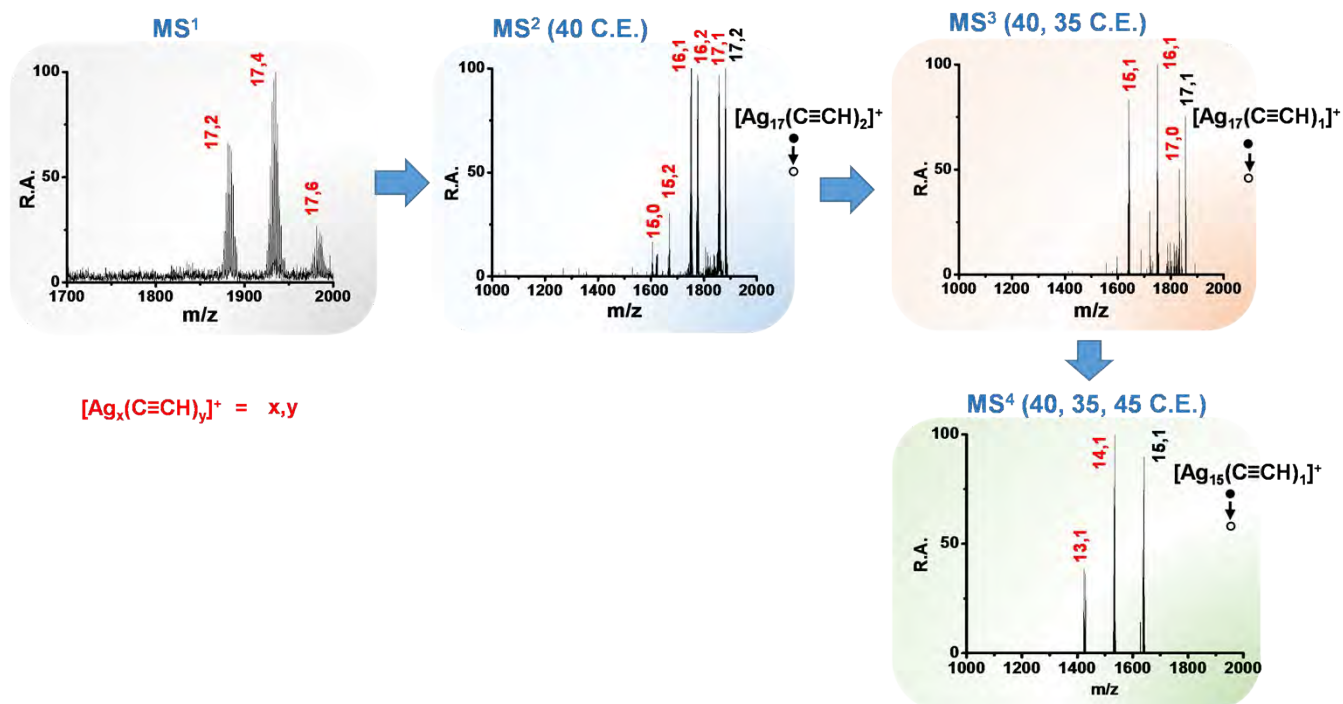


**Fig. S5** MS<sup>1</sup> to MS<sup>4</sup> mass spectra of  $[\text{Ag}_{17}(\text{C}\equiv\text{CH})_2]^+$  or (17,2) through the (17,1) and (15,1) fragmentation pathway. The collision energy required to get the particular CID mass spectrum are written at the top of every mass spectrum. RA refers to relative abundance.

## Supporting information 6

CID mass spectra of  $[\text{Ag}_{17}(\text{C}\equiv\text{CH})_2]^+$  through  $[\text{Ag}_{16}(\text{C}\equiv\text{CH})_2]^+$  pathway:

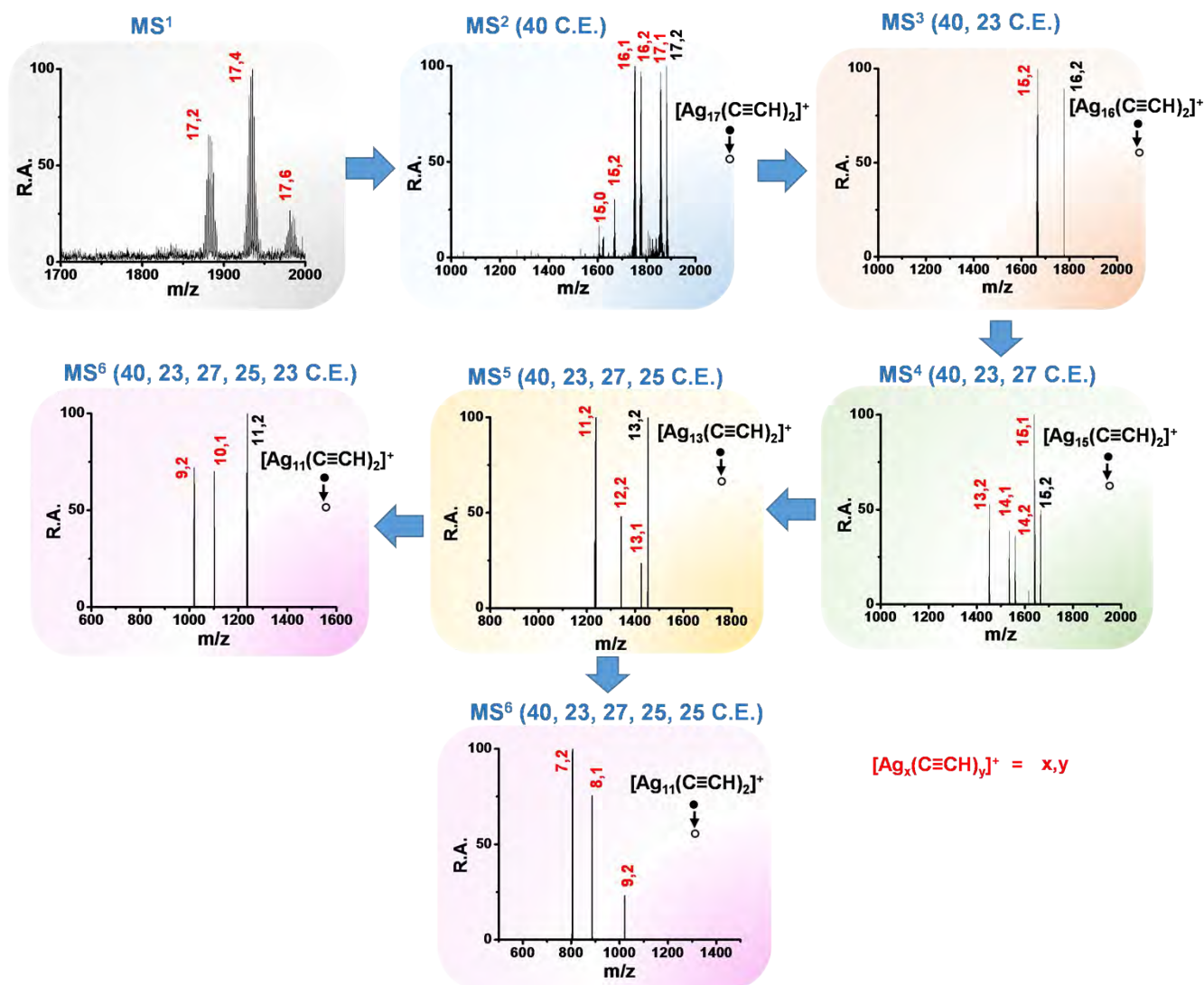


**Fig. S6**  $\text{MS}^1$  to  $\text{MS}^6$  mass spectra of  $[\text{Ag}_{17}(\text{C}\equiv\text{CH})_2]^+$  or (17,2) through the (16,2), (15,2), (13,2) and (11,2) fragmentation pathway. The collision energy required to get the particular CID mass spectrum are written at the top of every mass spectrum. At the last step of  $\text{MS}^6$ , collision energy was changed from 23 to 25 to get different fragments, shown in two different  $\text{MS}^6$  mass spectrum. RA refers to relative abundance.

## Supporting information 7

CID mass spectra of  $[\text{Ag}_{17}(\text{C}\equiv\text{CH})_2]^+$  through  $[\text{Ag}_{16}(\text{C}\equiv\text{CH})_1]^+$  and followed by  $[\text{Ag}_{15}(\text{C}\equiv\text{CH})_1]^+$  pathway:

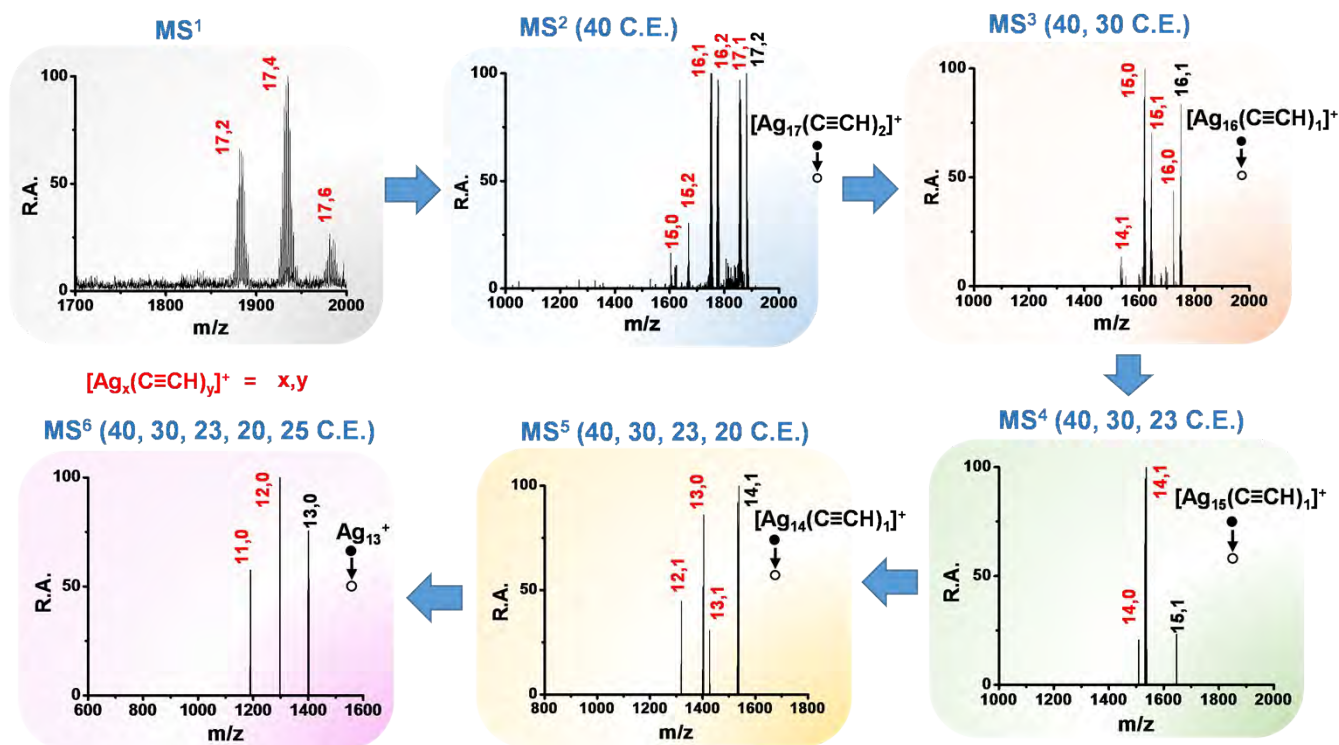


**Fig. S7** MS<sup>1</sup> to MS<sup>6</sup> mass spectra of  $[\text{Ag}_{17}(\text{C}\equiv\text{CH})_2]^+$  or (17,2) through the (16,1), (15,1), (14,1) and (13,0) fragmentation pathway. The collision energy required to get the particular CID mass spectrum are written at the top of every mass spectrum. RA refers to relative abundance.



## Supporting information 8

CID mass spectra of  $[\text{Ag}_{17}(\text{C}\equiv\text{CH})_2]^+$  through  $[\text{Ag}_{16}(\text{C}\equiv\text{CH})_1]^+$  and followed by  $[\text{Ag}_{15}]^+$  pathway:

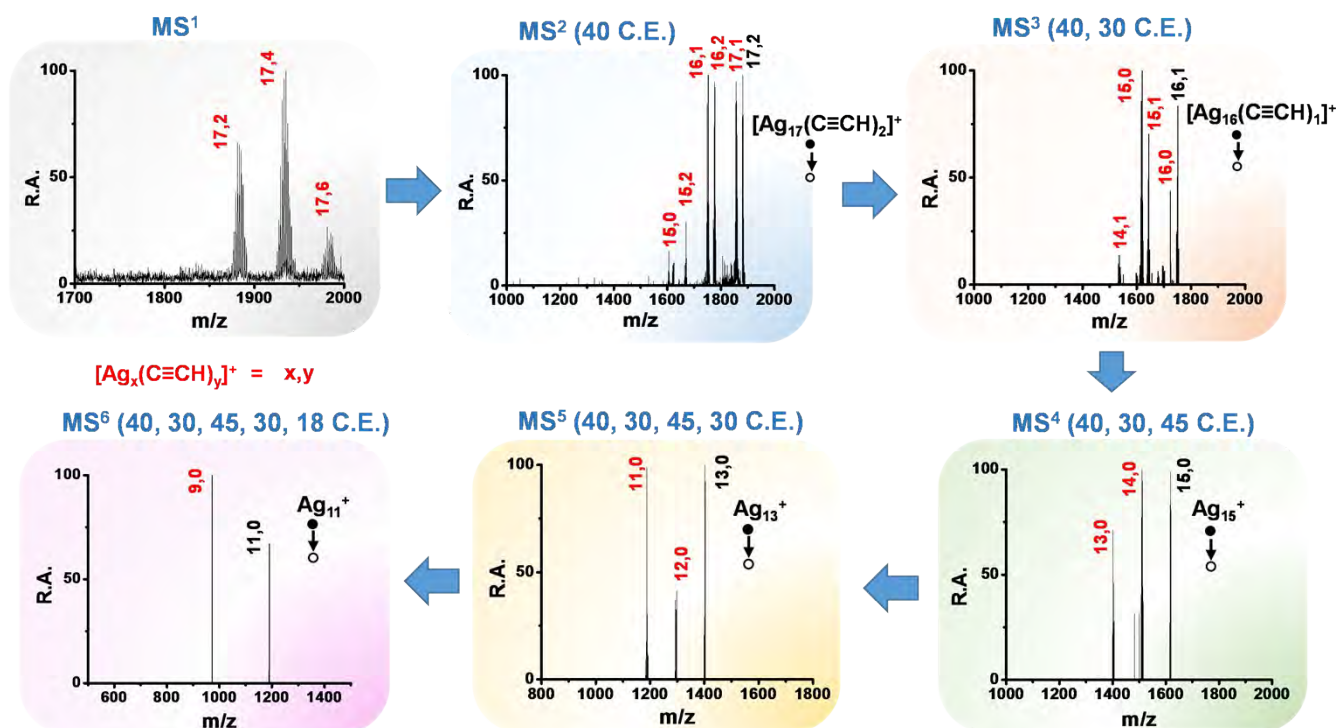


**Fig. S8** MS<sup>1</sup> to MS<sup>6</sup> mass spectra of  $[\text{Ag}_{17}(\text{C}\equiv\text{CH})_2]^+$  or (17,2) through the (16,1), (15,0), (13,0) and (11,0) fragmentation pathway. The collision energy required to get the particular CID mass spectrum are written at the top of every mass spectrum. RA refers to relative abundance.

## Supporting information 9

CID mass spectra of  $[\text{Ag}_{17}(\text{C}\equiv\text{CH})_2]^+$  through  $[\text{Ag}_{15}(\text{C}\equiv\text{CH})_2]^+$  pathway:

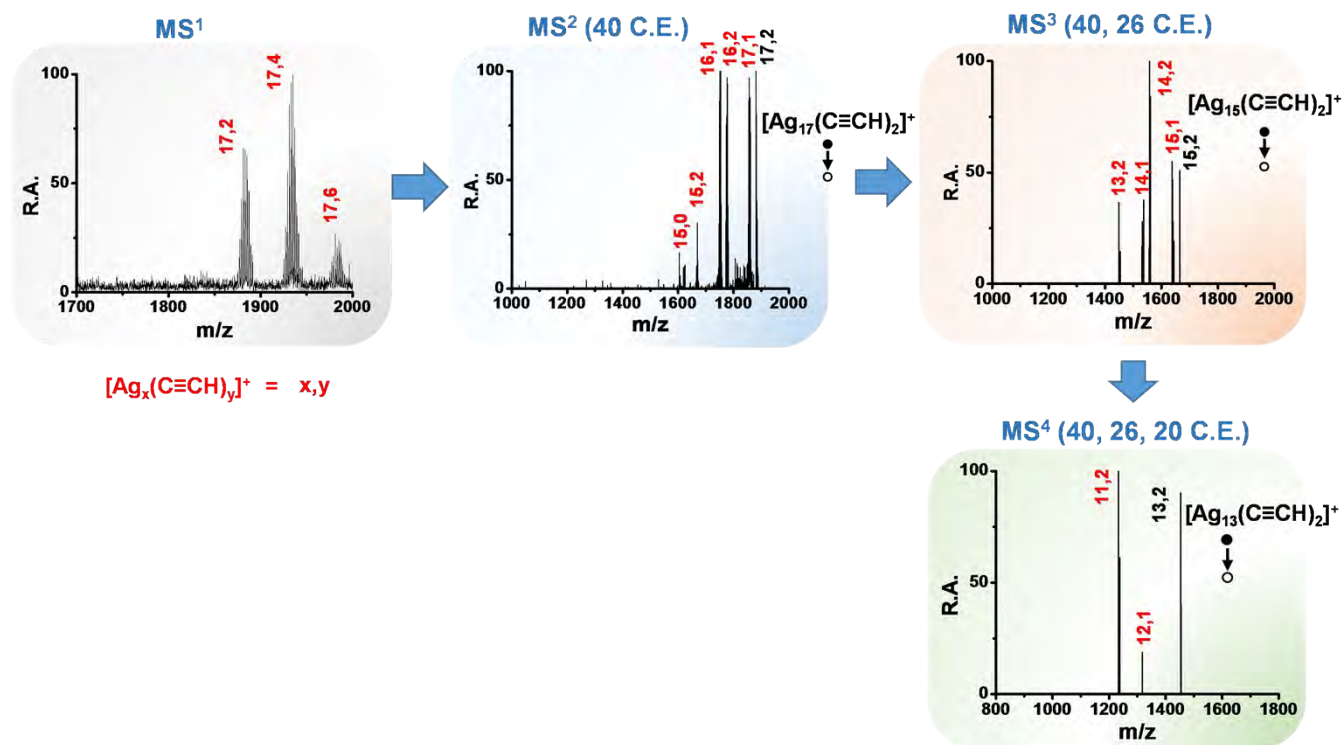


**Fig. S9** MS<sup>1</sup> to MS<sup>4</sup> mass spectra of  $[\text{Ag}_{17}(\text{C}\equiv\text{CH})_2]^+$  or (17,2) through the (15,2) and (13,2) fragmentation pathway. The collision energy required to get the particular CID mass spectrum are written at the top of every mass spectrum. RA refers to relative abundance.

## Supporting information 10

### Total CID pattern of $[\text{Ag}_{17}(\text{C}\equiv\text{CH})_4]^+$ :

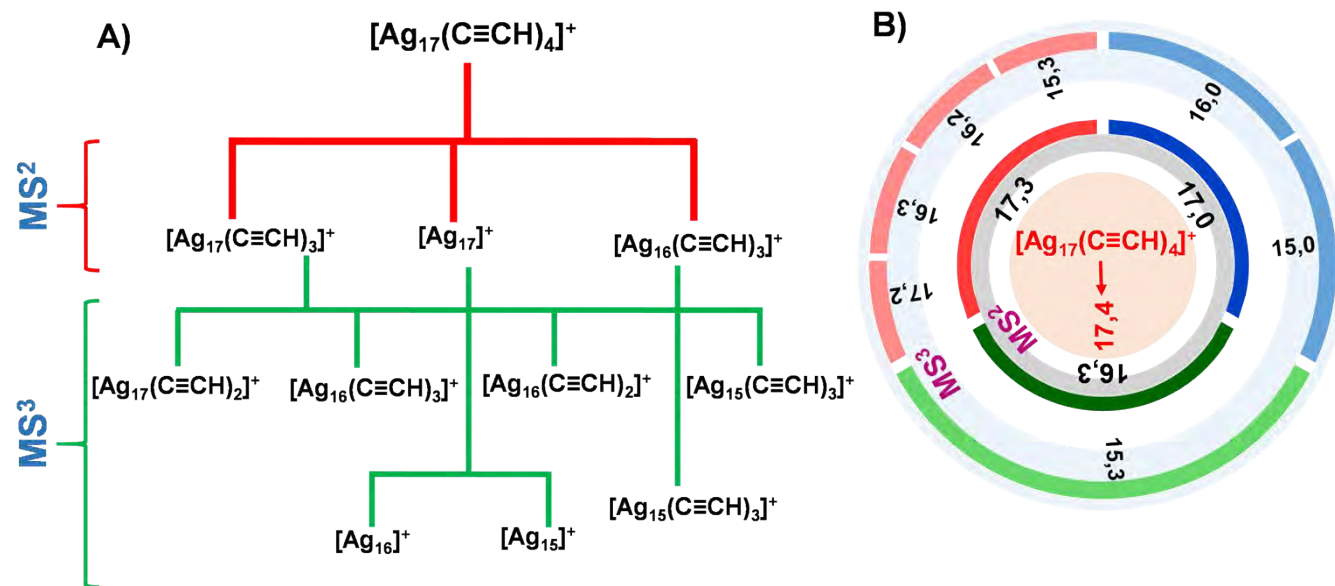


**Fig. S10** A) Flow chart of the breaking pattern and fragments of the adduct  $[\text{Ag}_{17}(\text{C}\equiv\text{CH})_4]^+$ , resulted from MS<sup>2</sup> and MS<sup>3</sup> experiments. B) The total CID fragments of  $[\text{Ag}_{17}(\text{C}\equiv\text{CH})_4]^+$  or (17,4) resulted from MS<sup>2</sup> and MS<sup>3</sup> experiments are presented with two individual concentric rings.

## Supporting information 11

### CID mass spectra of $[\text{Ag}_{17}(\text{C}\equiv\text{CH})_4]^+$ up to $\text{MS}^3$ :

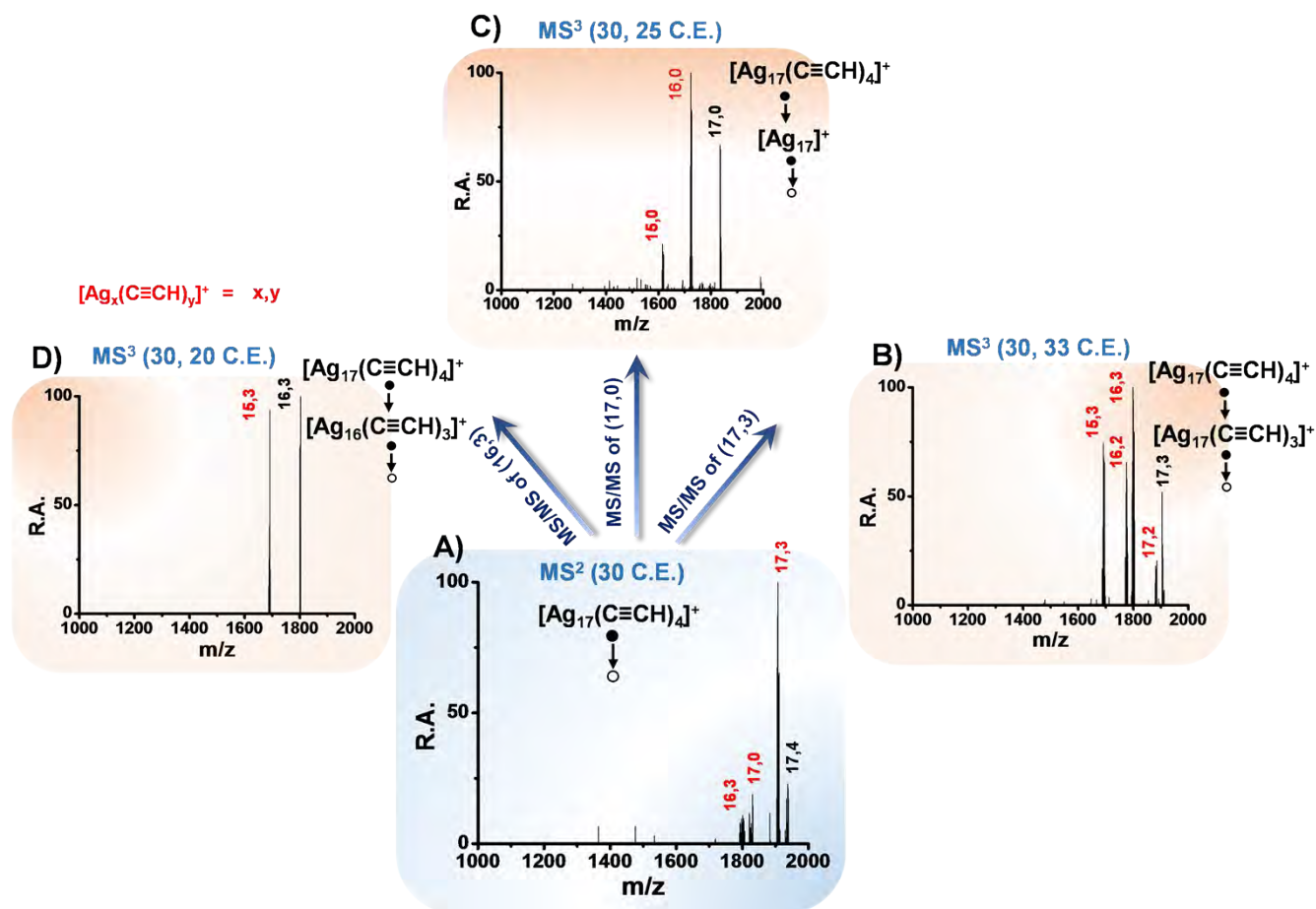


**Fig. S11** A)  $\text{MS}^2$  mass spectrum of  $[\text{Ag}_{17}(\text{C}\equiv\text{CH})_4]^+$  or (17,4), resulting three fragments of (17,3), (17,0) and (16,3).  $\text{MS}^3$  mass spectrum of (17,3), (17,0) and (16,3) are also shown in B), C) and D), respectively. The collision energy required to get the particular CID mass spectrum are written at the top of every mass spectrum. RA refers to relative abundance.

## Supporting information 12

### Total CID pattern of $[\text{Ag}_{17}(\text{C}\equiv\text{CH})_6]^+$ :

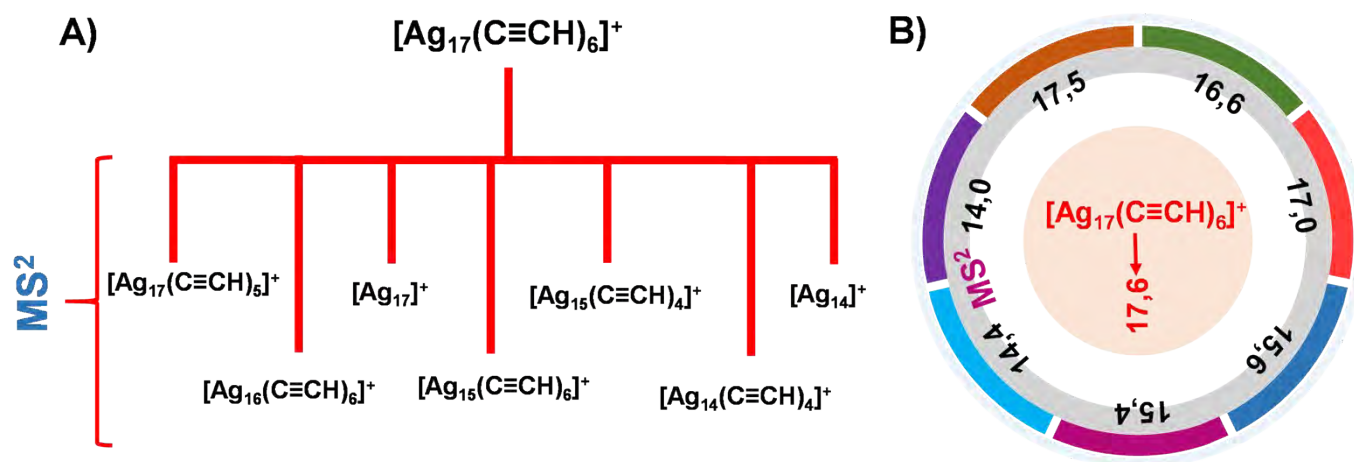


**Fig. S12** A) Flow chart of the breaking pattern and fragments of the adduct  $[\text{Ag}_{17}(\text{C}\equiv\text{CH})_6]^+$ , resulted from MS<sup>2</sup> experiment. B) The total CID fragments of  $[\text{Ag}_{17}(\text{C}\equiv\text{CH})_6]^+$  or (17,6) resulting from MS<sup>2</sup> experiment is presented with one ring.

## Supporting information 13

CID mass spectrum of  $[\text{Ag}_{17}(\text{C}\equiv\text{CH})_6]^+$  for MS<sup>2</sup>:

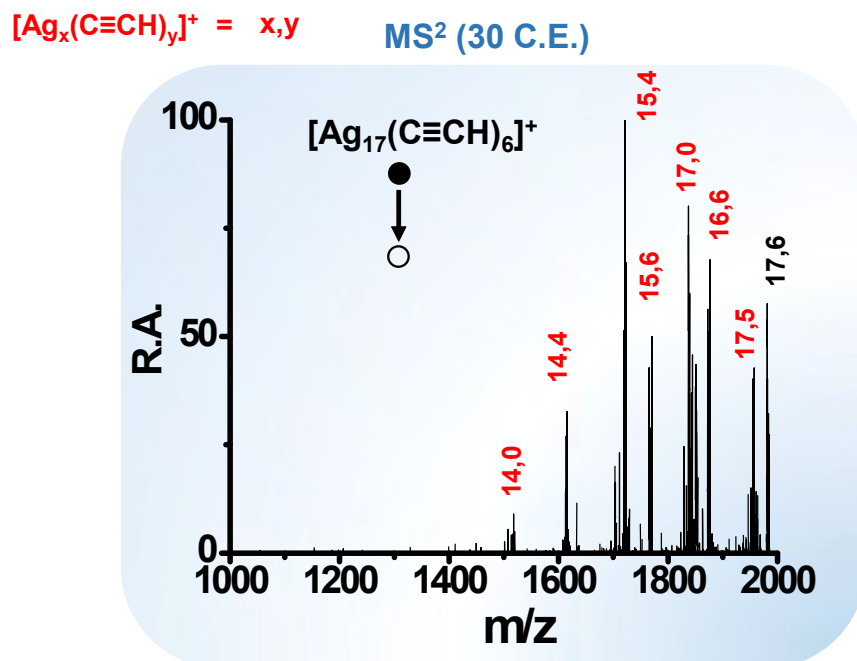


**Fig. S13** MS<sup>2</sup> mass spectrum of  $[\text{Ag}_{17}(\text{C}\equiv\text{CH})_6]^+$  or (17,6), resulting seven fragments of (17,5), (16,6), (17,0), (15,6), (15,4), (14,4) and (14,0). The collision energy required to get the particular CID mass spectrum is written at the top of the spectrum. RA refers to relative abundance.



**Table S14****Comparison of experimental and calculated masses measured with the LTQ:**

In the isotopic cluster, the most abundant peak is used to define the m/z value.

Experimental m/z	Calculated m/z	Assignment $[\text{Ag}_m(\text{PPh}_3)_n\text{H}_o(\text{H}_2\text{O})_p\text{O}_q(\text{C}_2\text{H}_2)_r(\text{C}_2\text{H})_s]^z+$							
		Ag (m)	PPh <sub>3</sub> (n)	H (o)	H <sub>2</sub> O (p)	O (q)	C <sub>2</sub> H <sub>2</sub> (r)	C <sub>2</sub> H (s)	Charge (z)
262.15	262.09		1						1
368.99	369.00	1	1						1
386.67	387.01	1	1		1				1
427.03	427.00	1	1			2	1		1
631.20	631.09	1	2						1
647.12	647.08	1	2			1			1
1833.12	1833.38	17							1
1883.30	1883.40	17						2	1
1933.33	1933.41	17						4	1
1983.33	1983.43	17						6	1
1943.41	1943.30	18		1					

## Supporting information 15

Most stable calculated structures of reactant and products:

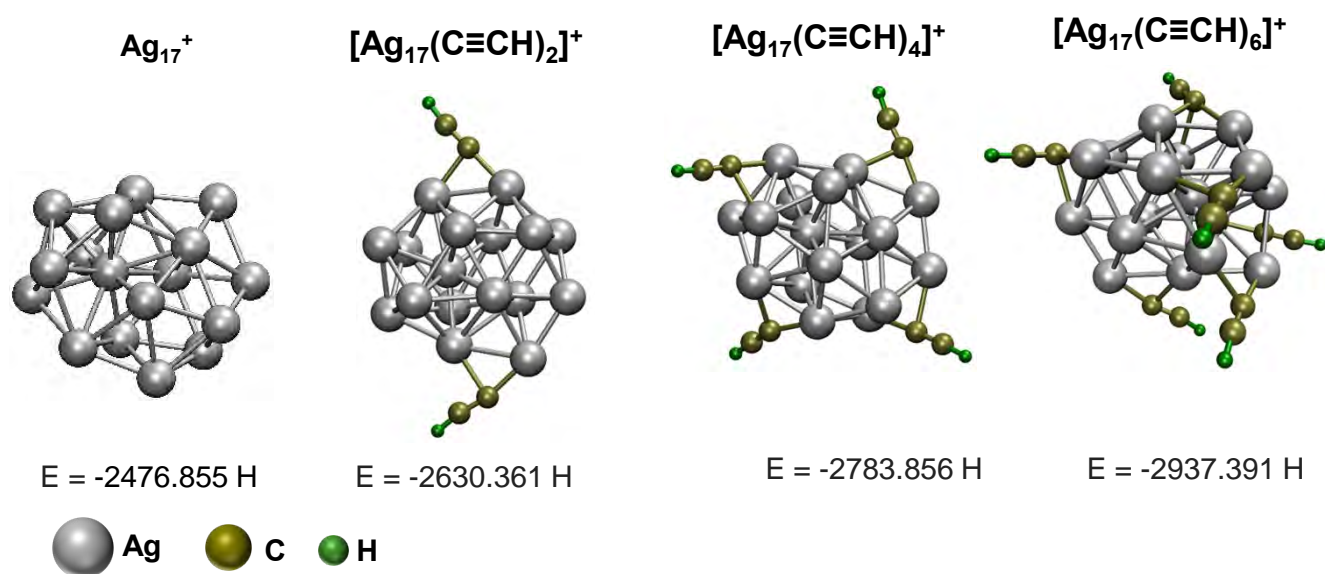


**Fig. S15** Calculated most stable structures of  $\text{Ag}_{17}^+$ ,  $[\text{Ag}_{17}(\text{C}\equiv\text{CH})_2]^+$ ,  $[\text{Ag}_{17}(\text{C}\equiv\text{CH})_4]^+$  and  $[\text{Ag}_{17}(\text{C}\equiv\text{CH})_6]^+$  with their calculated energy values. All the energy values are in Hartree.

## Supporting information 16

### HOMO-LUMO gap of reactant and products:

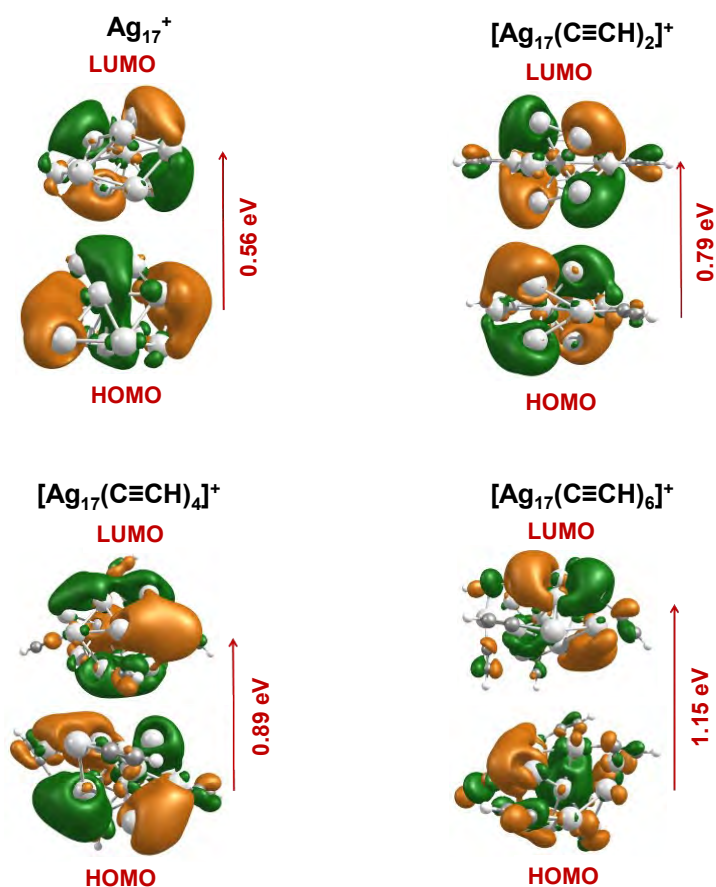


**Fig. S16** HOMO-LUMO gap ( $\Delta\text{HL}$ ) of most stable structures of  $\text{Ag}_{17}^+$ ,  $[\text{Ag}_{17}(\text{C}\equiv\text{CH})_2]^+$ ,  $[\text{Ag}_{17}(\text{C}\equiv\text{CH})_4]^+$  and  $[\text{Ag}_{17}(\text{C}\equiv\text{CH})_6]^+$ . With increasing the number of attached  $-\text{C}_2\text{H}$  unit to  $\text{Ag}_{17}^+$ ,  $\Delta\text{HL}$  value increases and for  $[\text{Ag}_{17}(\text{C}\equiv\text{CH})_6]^+$  it becomes highest, which makes it more resistive towards further reaction with acetylene.

## Supporting information 17

Calculated structure of  $[\text{Ag}_{17}(\text{HC}\equiv\text{CH})]^+$  and  $[\text{Ag}_{17}(\text{HC}\equiv\text{CH})_2]^+$ :

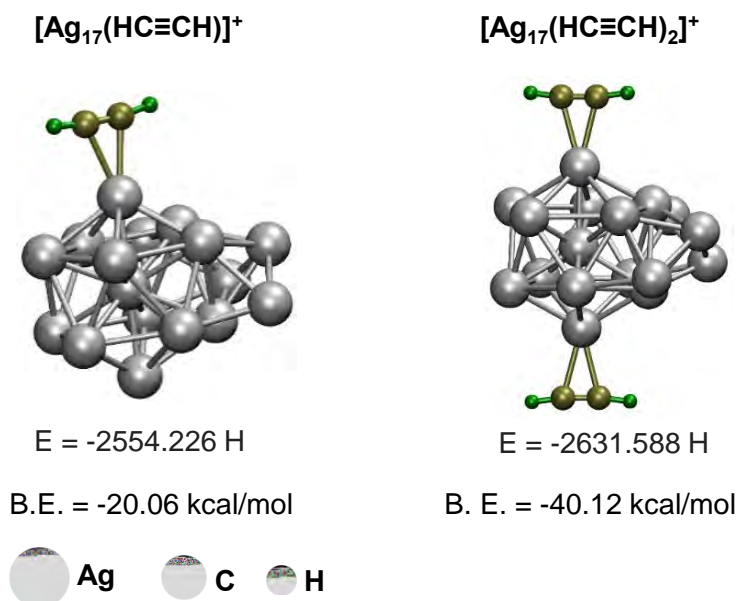


**Fig. S17** Most stable calculated structures of  $[\text{Ag}_{17}(\text{HC}\equiv\text{CH})]^+$  and  $[\text{Ag}_{17}(\text{HC}\equiv\text{CH})_2]^+$  with their energy and binding energy values. The higher binding energy of  $[\text{Ag}_{17}(\text{HC}\equiv\text{CH})_2]^+$  refers to the higher stability compared to  $[\text{Ag}_{17}(\text{HC}\equiv\text{CH})]^+$ . Energy values are in Hartree.

## Supporting information 18

Possibility of formation of  $[\text{Ag}_{17}(\text{C}\equiv\text{CH})_2]^+$  and  $[\text{Ag}_{17}\text{C}_4\text{H}_2]^+$ :

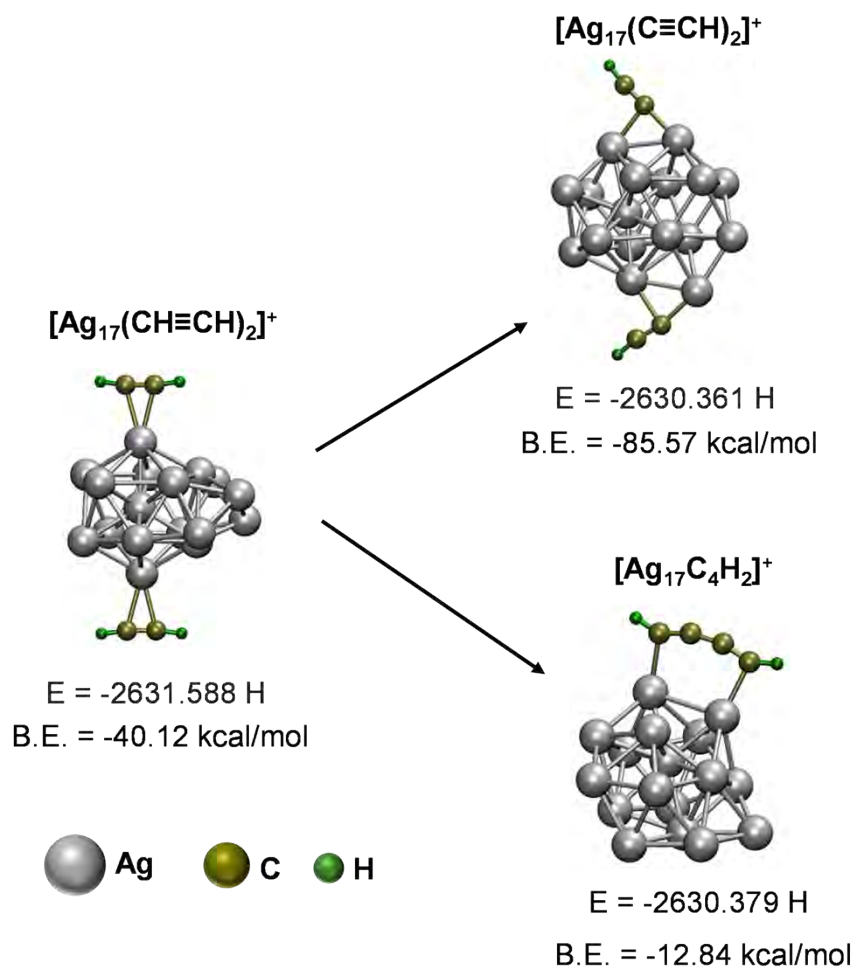


**Fig. S18** After dehydrogenation of  $[\text{Ag}_{17}(\text{HC}\equiv\text{CH})_2]^+$ , it can lead to the formation of either  $[\text{Ag}_{17}(\text{C}\equiv\text{CH})_2]^+$  or  $[\text{Ag}_{17}\text{C}_4\text{H}_2]^+$  which are of same energy. But as  $[\text{Ag}_{17}(\text{C}\equiv\text{CH})_2]^+$  is having higher binding energy compared to  $[\text{Ag}_{17}\text{C}_4\text{H}_2]^+$ , the chance of formation of later becomes minimal.



## Supporting information 19

### Formation of $[\text{Ag}_{17}(\text{C}\equiv\text{CH})_4]^+$ and hydrogen molecule:

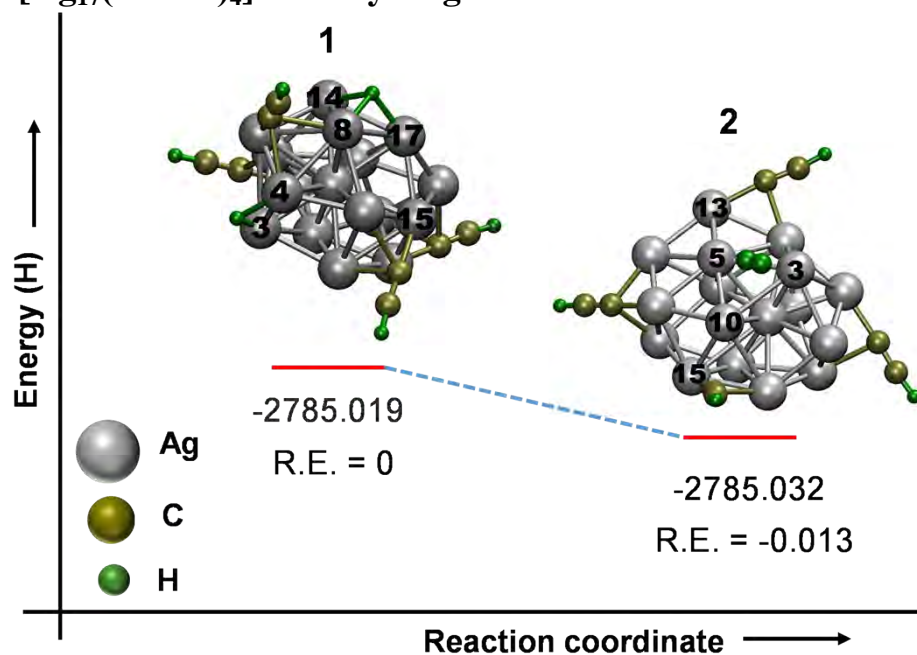


**Fig. S19** Energy profile during the formation of  $[\text{Ag}_{17}(\text{C}\equiv\text{CH})_4]^+$  and hydrogen molecule (2) starting from the intermediate (1) of higher energy. The energy difference between the product and intermediate is 0.013 H. The exact energy and relative energy values are in Hartree.

## Supporting information 20

### Formation of $[\text{Ag}_{17}(\text{C}\equiv\text{CH})_6]^+$ and hydrogen molecule:

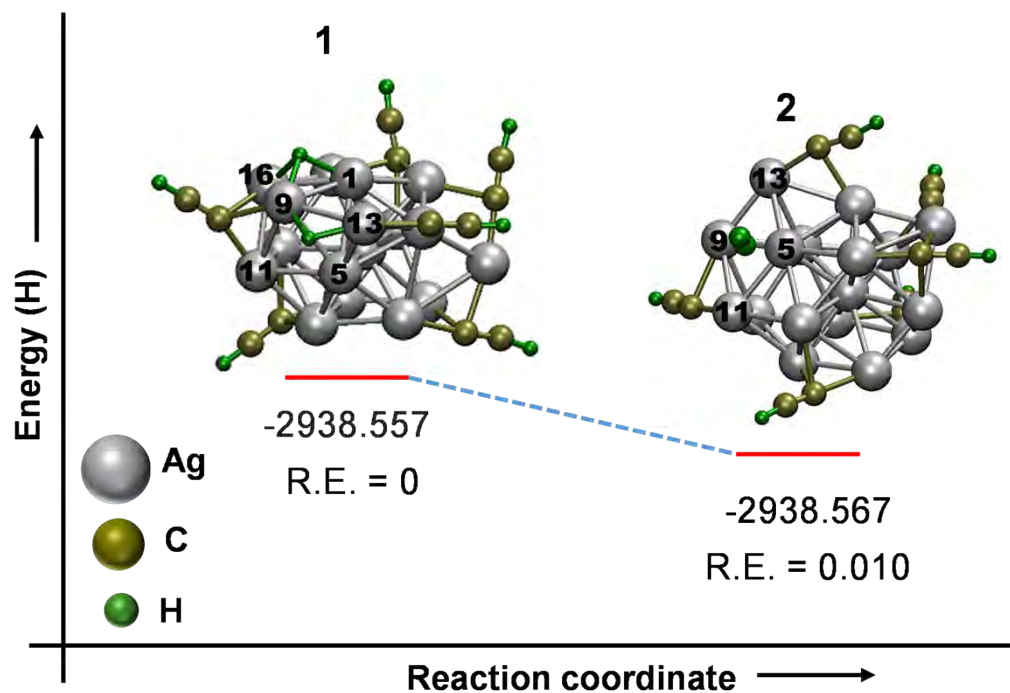


**Fig. S20** Energy profile during the formation of  $[\text{Ag}_{17}(\text{C}\equiv\text{CH})_6]^+$  and hydrogen molecule (2) starting from the intermediate (1) of higher energy. The energy difference between the product and intermediate is 0.010 H. The exact energy and relative energy values are in Hartree.

## Supporting information 21

### Energy profile of overall reaction:

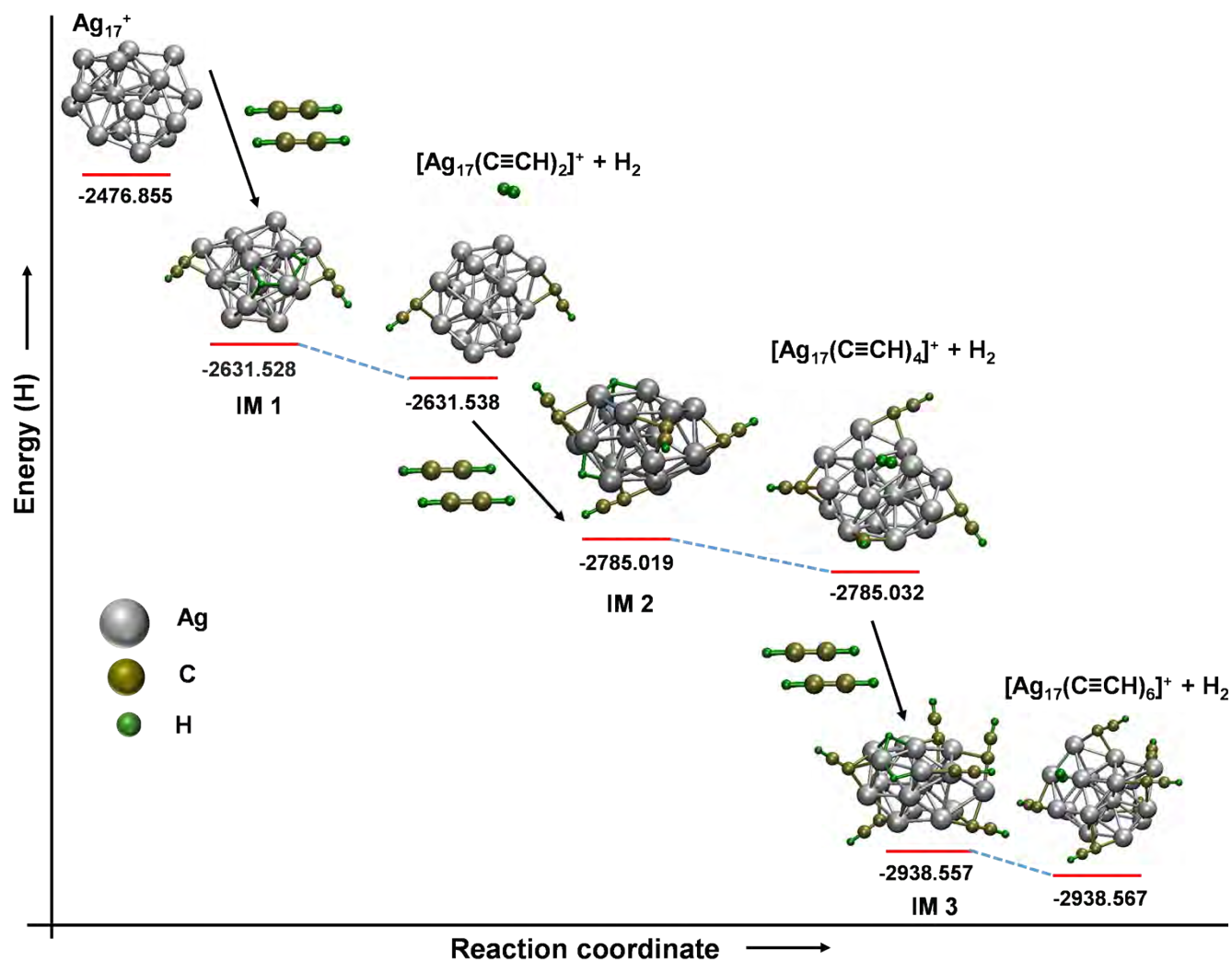


**Fig. S21** Energy profile during the overall reaction between  $\text{Ag}_{17}^+$  and acetylene. The exact energy of the reactant  $\text{Ag}_{17}^+$ , intermediates (IM) and products are in Hartree. This profile shows that with increasing the number of attached  $-\text{C}_2\text{H}$  unit to  $\text{Ag}_{17}^+$ , the energy got decreased starting from the free  $\text{Ag}_{17}^+$  to  $[\text{Ag}_{17}(\text{C}\equiv\text{CH})_6]^+$  consecutively.

## Supporting information 22

### Possibility of formation of $[\text{Ag}_{17}(\text{C}\equiv\text{CH})]^+$ :

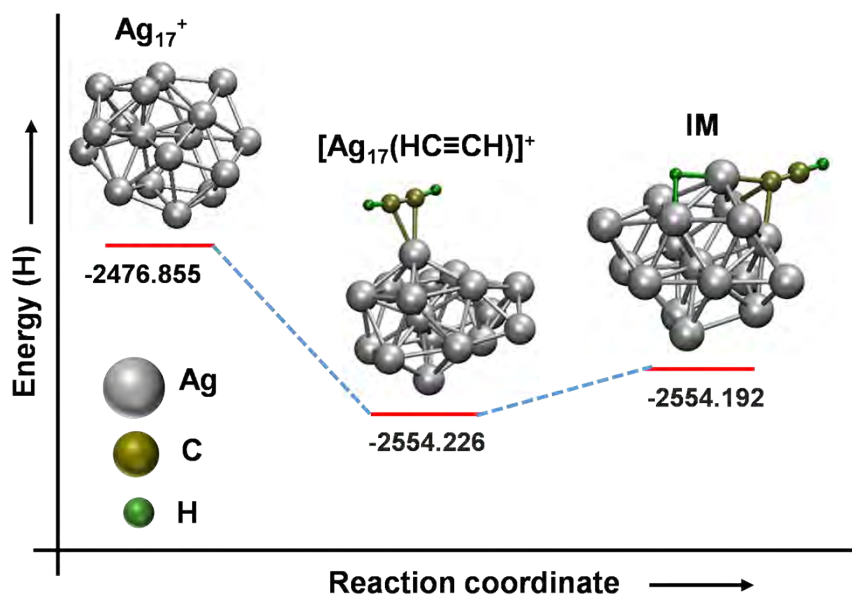


**Fig. S22** Energy profile during the formation of  $[\text{Ag}_{17}(\text{HC}\equiv\text{CH})]^+$  from  $\text{Ag}_{17}^+$  and its dehydrogenation, giving the higher energy intermediate (IM). The intermediate does not end up to any stable lower energy product in the case of odd (one) number of attached acetylene molecule. The energy values are in Hartree.

**Table S23****Calculated binding energies:**

<b>Cluster + C<sub>2</sub>H</b>	<b>Binding Energy (kcal/mol)</b>
[Ag <sub>17</sub> (C≡CH)] <sup>+</sup>	-79.90
[Ag <sub>17</sub> (C≡CH) <sub>2</sub> ] <sup>+</sup>	-85.57
[Ag <sub>17</sub> (C≡CH) <sub>4</sub> ] <sup>+</sup>	-83.04
[Ag <sub>17</sub> (C≡CH) <sub>6</sub> ] <sup>+</sup>	-86.43



## Supporting information 24

### Calculated structures of precursor and product ions during CID:

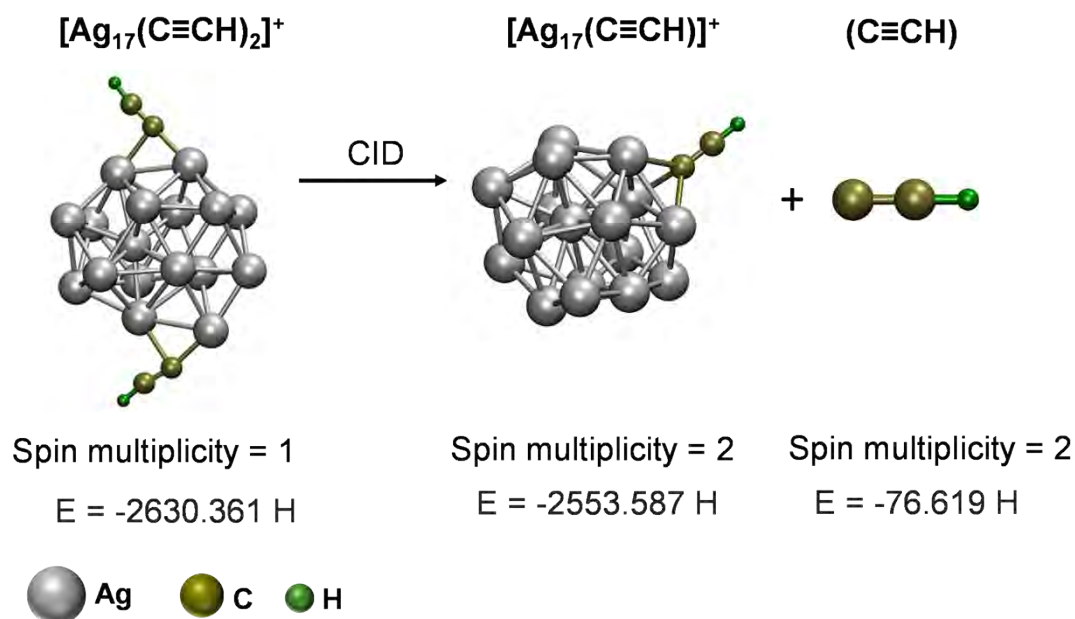


**Fig. S24** Structures of precursor and product ions during the CID event. Calculated structures of  $[\text{Ag}_{17}(\text{C}\equiv\text{CH})_2]^+$ ,  $[\text{Ag}_{17}(\text{C}\equiv\text{CH})]^+$  and  $[\text{C}\equiv\text{CH}]$  with their spin multiplicity and calculated energy values. All the energy values are in Hartree.

## Supporting information 25

### Electronic structure of $[\text{Ag}_{17}(\text{C}\equiv\text{CH})_2]^+$ :

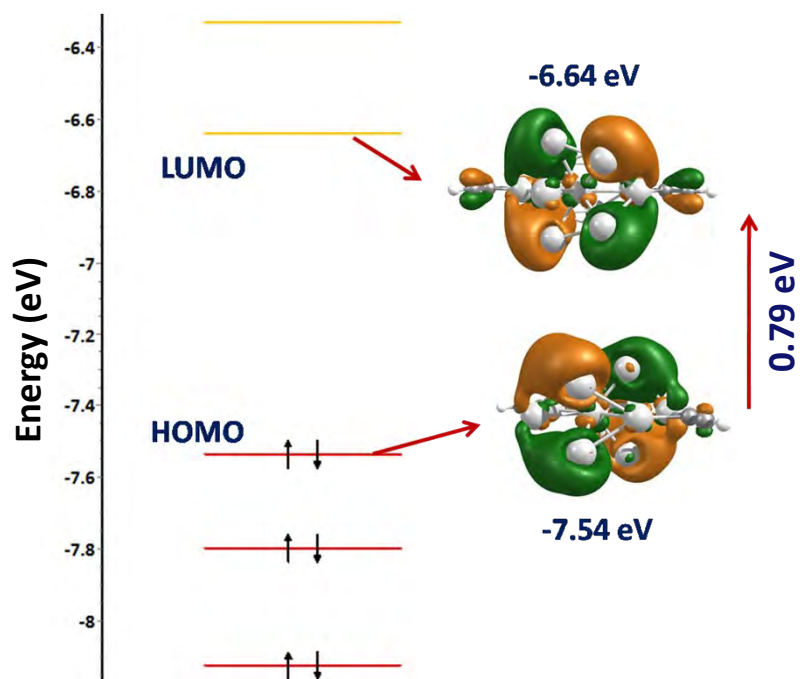


**Fig. S25** The electronic structure (closed-shell) and HOMO-LUMO gap of  $[\text{Ag}_{17}(\text{C}\equiv\text{CH})_2]^+$ . The electronic shell structure is  $|1\text{S}^2|1\text{P}^6|1\text{D}^6|$ .

## Supporting information 26

### Electronic structure of $[\text{Ag}_{17}(\text{C}\equiv\text{CH})]^+$ :

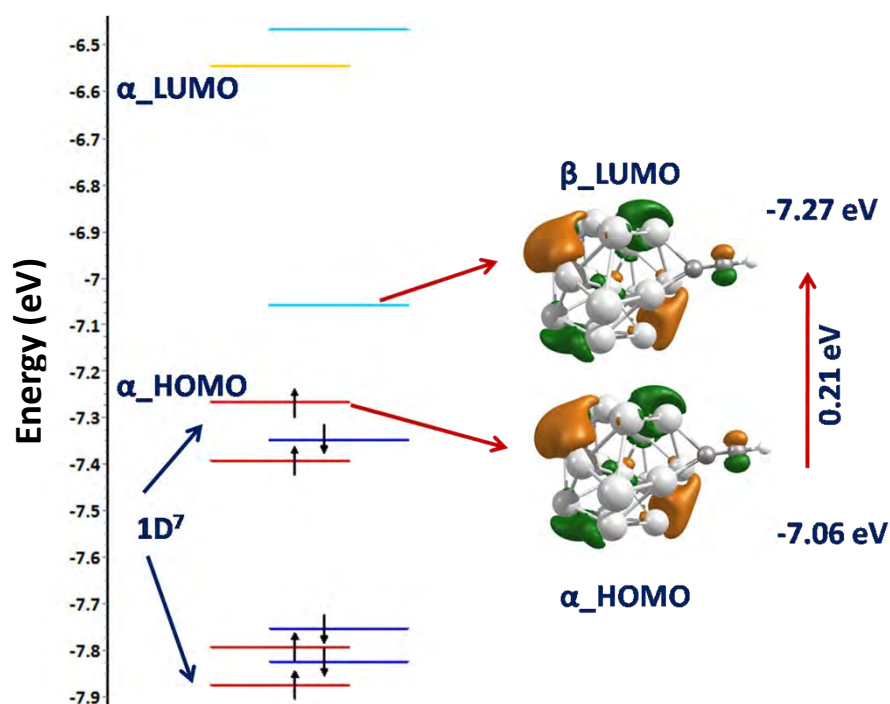


**Fig. S26** The electronic structure (open-shell) and HOMO-LUMO gap of  $[\text{Ag}_{17}(\text{C}\equiv\text{CH})]^+$ . The electronic shell structure is  $|1\text{S}^2|1\text{P}^6|1\text{D}^7|$ .

Electronic structure of  $[\text{C}\equiv\text{CH}]$ :

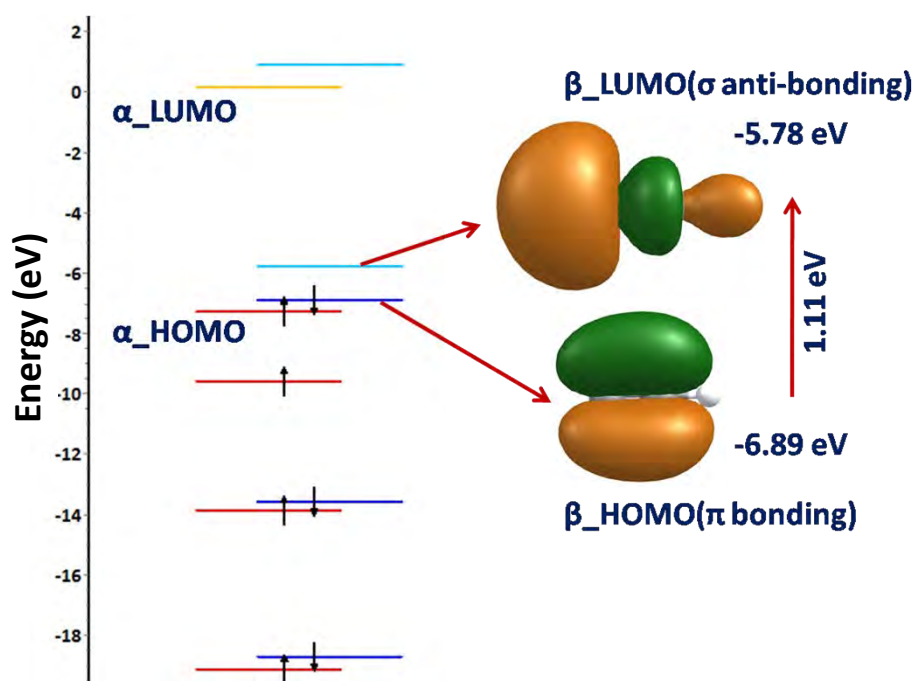


**Fig. S27** The electronic structure (open-shell) and HOMO-LUMO gap of  $[\text{C}\equiv\text{CH}]$ .

# Microdroplet Impact-Induced Spray Ionization Mass Spectrometry (MISI MS) for Online Reaction Monitoring and Bacteria Discrimination

Pallab Basuri, Subhashree Das, Shantha Kumar Jenifer, Sourav Kanti Jana, and Thalappil Pradeep\*



Cite This: <https://dx.doi.org/10.1021/jasms.0c00365>



Read Online

ACCESS |



Metrics & More

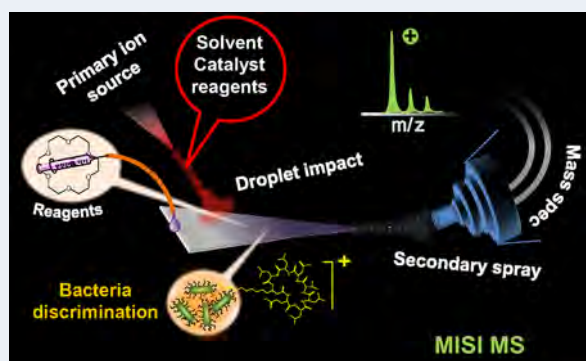


Article Recommendations



Supporting Information

**ABSTRACT:** Microdroplet impact-induced spray ionization (MISI) is demonstrated involving the impact of microdroplets produced from a paper and their impact on another, leading to the ionization of analytes deposited on the latter. This cascaded process is more advantageous in comparison to standard spray ionization as it performs reactions and ionization simultaneously in the absence of high voltage directly applied on the sample. In MISI, we apply direct current (DC) potential only to the terminal paper, used as the primary ion source. Charge transfer due to microdroplet/ion deposition on the flowing analyte solution on the second surface generates secondary charged microdroplets from it carrying the analytes, which ionize and get detected by a mass spectrometer. In this way, up to three cascaded spray sources could be assembled in series. We show the detection of small molecules and proteins in such ionization events. MISI provides a method to understand chemical reactions by droplet impact. The C–C bond formation reactions catalyzed by palladium and alkali metal ion encapsulation using crown ether were studied as our model reactions. To demonstrate the application of our ion source in a bioanalytical context, we studied the noninvasive in situ discrimination of bacteria samples under ambient conditions.



## INTRODUCTION

Electrospray ionization and its variations have grown phenomenally in recent years. Paper spray ionization (PSI) is one of them.<sup>1,2</sup> It has provided an easy and direct sampling method in the field of ambient ionization mass spectrometry. In a paper spray technique, a high DC potential is applied to achieve ionization from the tip of a paper in the form of charged microdroplets. However, additional factors such as heat,<sup>3</sup> ultrasonic sound,<sup>4</sup> chemical vapor,<sup>5</sup> solvent,<sup>6</sup> or laser<sup>7</sup> have also been used to assist ionization. Paper spray ionization and its other variants such as leaf spray,<sup>8</sup> spray from a polymer,<sup>9</sup> cloth,<sup>10</sup> cotton thread,<sup>11</sup> and glass<sup>12</sup> have also been used for the analysis of plant metabolites,<sup>13</sup> blood clots,<sup>14</sup> dyes,<sup>15</sup> bio fluids, etc. In all such cases, ion generation is mainly driven by the potential difference between the tip of the substrate and the inlet of the mass spectrometer (MS). Generally, potential on the order of a few kilovolts (kV), which produces a large electric field between the substrate and the inlet of MS, is required to facilitate the ionization process. In-source molecular fragmentation,<sup>16–19</sup> structural or conformational changes,<sup>20</sup> and biological damage of the analyte in large electric field<sup>21,22</sup> are undesired effects of such techniques. These limitations can be due to the generation of large electric field across the electrodes. However, ionization through nanomaterials has helped in reducing a few of the limitations.<sup>23</sup>

For example, a carbon nanotube-coated paper reduced the potential required from kilovolts to a few volts.<sup>24</sup> Nano- and microstructural super hydrophobic paper spray<sup>25,26</sup> helped in reaching a very low detection limit. But in comparison to kilovolt paper spray ionization (kVPSI), low voltage ionization is limited by its signal intensity and requires advanced materials for effective ionization.

Another interesting feature of a paper-based device is that a paper due to its inherent fibrous structure can be utilized in microfluidics. The capillarity-driven liquid transport on a paper surface makes it a unique reaction vessel in many cases. Examples include enzymatic reactions, immunoassays, bio-marker detection in biomedical applications, detection of heavy metal ions, pesticides, and volatile organic compounds (VOCs) in water for environmental applications and many more.<sup>27</sup> In most of the cases, the detection is performed either by direct colorimetric methods or coupling them with suitable detectors. Distance-based colorimetric detection is another

**Received:** September 30, 2020

**Revised:** October 31, 2020

**Accepted:** November 2, 2020



ACS Publications

© XXXX American Society for Mass Spectrometry. Published by American Chemical Society. All rights reserved.

A

<https://dx.doi.org/10.1021/jasms.0c00365>  
 J. Am. Soc. Mass Spectrom. XXXX, XXX, XXX–XXX

important feature of such paper microfluidics, in which colored product bands get generated during flow along the paper channel due to in situ reaction with predeposited reagents.<sup>28,29</sup> Reactive paper spray MS is being used for online monitoring of reactions on the paper surface, coupled with MS. In this technique, the reagents are being deposited/mixed over the paper surface to react in situ and products are analyzed using an MS, simultaneously. Many organic reactions such as reactions between isothiazolinones and cysteamine,<sup>30</sup> Suzuki-coupling,<sup>31</sup> haloform reaction,<sup>32</sup> quinone derivatization,<sup>33</sup> etc., have been investigated.

Herein, we introduce a new ambient ionization methodology, called microdroplet impact-induced spray ionization mass spectrometry (MISI MS). By this, we established a consecutive ionization process. In MISI, a primary ion source initiates a second paper spray by impinging desolvated ions and/or microdroplets on the latter. MISI provides ionization of analytes without directly applying a high potential to the sample. It supports analysis of live samples in real time. Several analytical methods have been developed for the detection and discrimination of bacteria. Many of them involve complex sample preparation processes such as extraction, purification, and preconcentration requiring expertise on sampling and instrumentation. Enzyme-linked immune assay (ELISA),<sup>34</sup> fluorescence microscopy,<sup>35</sup> polymerase chain reaction (PCR),<sup>36</sup> and biosensors<sup>37</sup> are a few examples of such analyses. However, techniques of this type are often time-consuming where the same sample cannot be measured repeatedly. Mass spectrometry-based detection methods, e.g., matrix-assisted laser desorption ionization (MALDI),<sup>38</sup> pyrolysis gas chromatography (Py GC),<sup>39</sup> electrospray ionization (ESI),<sup>40</sup> desorption electrospray ionization (DESI),<sup>41</sup> and paper spray ionization (PSI),<sup>42</sup> have also been employed in this context. However, most of the techniques are invasive and ineffective for direct live sample analyses.

MISI has been utilized as an online reaction monitoring system which can deliver reagents, catalysts, or solvents through microdroplets. We show that the mechanism of ionization is not due to the applied potential in the primary ion source but due to charge that transfer through interactions of the microdroplets/ions with the molecules on the paper surface during the flow of analyte solution. Many analytes have been ionized through MISI to show the applicability of the method. The technique provides molecular ionization in analytical situations which is often advantageous than standard ionization techniques such as electrospray ionization (ESI), nanoelectrospray ionization (nESI), desorption electrospray ionization (DESI) or kVPSI. We note that the relay mode of ionization (relay electrospray ionization; rESI), which generates secondary electrospray, was first demonstrated by Li et al. where they showed charge deposition onto an array of sample-loaded capillary.<sup>43</sup> They characterized the technique with a few biologically important molecules. Unlike glass capillaries used in rESI, employing a cascaded paper spray mode of ionization in MISI MS provides additional advantages. A few of them are demonstrated in this article and include ionization using immiscible solvents, Pd-catalyzed Suzuki–Miyaura cross-coupling reactions, monitoring ion encapsulation reactions in ambient conditions, controlling reaction dynamics, and discrimination of live bacterial samples in real time.

## MATERIALS AND METHODS

**Chemicals and sample preparation.** The chemicals were bought commercially and were used with no additional processing or purification. *p*-Nitrophenol, glucose, and malic acid were purchased from Avro. Benzothiophene, C<sub>60</sub>, indole, 18-crown-6, dibenzo-18-crown-6, rhodamine 6G, lysozyme, cytochrome c, and myoglobin were from Sigma-Aldrich. HPLC-grade methanol, toluene, and chloroform were from Sigma or Rankem. Luria–Bertani (LB) broth, nutrient agar, and Mackonkey agar for the culture of bacteria were obtained from HiMedia. *Bacillus subtilis* (ATCC 21331) was a gift from Prof. S. Gummadi (Department of Biotechnology, IITM). *Escherichia coli* (MTCC 443) and *Pseudomonas putida* (MTCC 2467) were obtained from the Microbial Type Culture Collection and Gene Bank. LIVE/DEAD BacLight bacterial viability kit was purchased from Molecular Probes, Eugene, OR.

**MISI MS.** To build a MISI source, we used a kV PSI technique as the primary ion source, and the charged microdroplets were then impacted to the next paper, as shown in the schematic of Figure 1, to induce a second paper

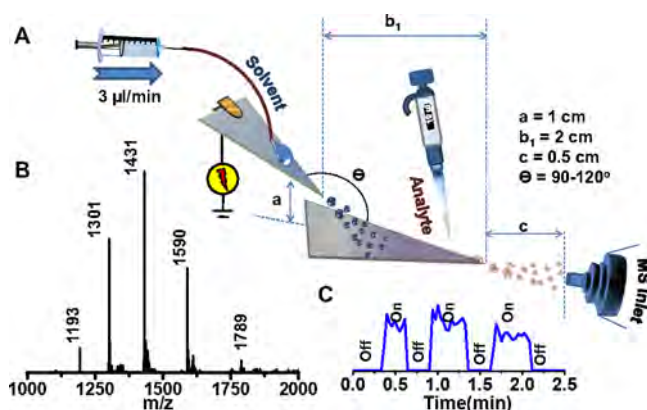


**Figure 1.** (A) Schematic representation of microdroplet impact-induced spray ionization mass spectrometry (C1), (B) mass spectrum of lysozyme, and (C) chronogram of primary ion source in on/off conditions. The chronogram is for the selected ion at  $m/z$  1431. “On/Off” in the chronogram describes on/off of the primary spray, respectively.  $a$ ,  $b$ , and  $c$  represent the distance between the planes of the two paper, tip-to-tip, and tip-to-inlet distance as shown in the schematic of the setup, respectively.

spray ionization. This paper spray couple is termed as cascade 1 (abbreviated as C1). The overall setup is then held in front of a mass spectrometer in such a way that the tip of the second triangular paper is pointed toward the inlet of the spectrometer. The primary ion source can be of any ambient ionization method such as, ESI, nESI or kVPSI, etc. We used kVPSI for our setup. Figure S1 presents the optical image of the setup. In a similar way, cascade 2 (C2) can be fabricated by placing a third paper below the second. This series can continue until the ion generation at the last paper becomes extremely poor. Shape and dimensions of the paper were chosen to be isosceles triangle of 50 mm<sup>2</sup> average area, with 10 mm base length. In the primary paper spray ion source, we ionize solvent molecules such as methanol or water. However, any solvent which can easily generate an electrospray plume is sufficient. Solvents were infused through a fused silica capillary with a preferred flow rate. The flow was driven by a syringe pump. The sample was pipetted on to the second paper and



analyzed immediately while it was still wet. Variable parameters used in MISI MS are the potential used in the primary ion source, the vertical gap between the two papers (termed as “ $a$ ” taken as 1 cm), the horizontal distance between the two paper tips (termed as “ $b_i$ ”,  $i = 1, 2, 3$ ) ( $b_1 = 2$  cm, as in Figure 1A), the distance between the tip of the final paper to the MS inlet (termed as “ $c$ ”, set to 1–8 mm), and the angle between the papers ( $\theta$ , set to  $120^\circ$ ), as shown in Figure 1A. The parameters mentioned were used in most experiments and changes, if any, are mentioned.

A Thermo LTQ XL mass spectrometer was used for all the mass spectrometric experiments. Capillary and tube lens voltages were set to  $\pm 35$  and  $\pm 139$  V, respectively, to obtain maximum ion intensity for the corresponding positive and negative analysis modes during most of the experiments. The capillary temperature was tuned to  $275^\circ\text{C}$ . The sheath gas flow rate was set to zero.

**Online Monitoring of Ion Encapsulation Reactions In-Flow.** Chemical reactions involving encapsulation of deposited ions in solution were investigated. We used reagents in the primary ion source instead of solvents alone, and the corresponding dryions or the charged microdroplets containing the solvated ions of the reagent were deposited on other reagent molecules, flowing continuously on the second paper. It is noted that for highly volatile solvents with sufficient flight time these primary microdroplets can desolvate to release and deposit dry ions. In both the cases, the reaction occurs in-flow after the impact of the charged microdroplets/ions in the second paper. Products of the reaction were analyzed in cascade mode using mass spectrometry. To demonstrate such an interaction of the deposited ions with the neutral molecules in-flow, alkali metal ion encapsulation reactions using crown ethers were performed. We used an aqueous solution containing equal concentrations of chlorides of Na, K, Rb, and Cs in the primary ion source. The individual ion concentration of each salt in the mixture was  $10\ \mu\text{M}$ . In the second paper, we used  $10\ \mu\text{M}$  solutions of two different crown ethers, namely 18-crown-6 and dibenzo-18-crown-6. We drop casted  $30\ \mu\text{L}$  of crown ether solution on the paper. The measurement was done in C1 mode. We have also recorded the mass spectrum of the bulk reaction in which the metal salts and the crown ether were mixed in a vial and stored for 30 min before measurement by kVPSI.

The kinetics of a reaction in any microfluidics system is measured by varying the reaction time either by changing the travel distance of the liquid, keeping the flow rate constant or by changing the flow rate for a constant travel distance.<sup>44–46</sup> Ratio of the travel distance and the flow velocity corresponds to the time of mixing or the reaction time. The reaction kinetics is then understood by plotting the relative intensity of the product with time. We have also monitored the kinetics of the alkali metal ion encapsulation in crown ethers using MISI. The experiment was conducted by infusing crown ether continuously on the paper. The mass spectrum was recorded by varying the distance,  $b_1$ . The relative intensity ratio of the potassiumated and the sodiumated peaks were plotted against the distance,  $b_1$ . The average terminal velocity of the fluid over the paper surface was also measured by taking the time taken for the liquid front to move a unit distance at a fixed flow rate of  $100\ \mu\text{L}/\text{min}$  from a syringe pump.

**Onsite Delivery of Active Catalyst for C–C Bond Formation in MISI.** Palladium-catalyzed C–C, C–O, and C–N bond formation reactions have been of interest to synthetic

organic chemistry.<sup>47</sup> Suzuki coupling is one such example where C–C coupling occurs between arylboronic acid and aryl halide in the presence of a catalyst and base.<sup>48</sup> One of the tricky parts of the reaction mechanism is to activate the precatalyst using base for the reaction to proceed further.<sup>49</sup> Research in this area shows different ways to perform such reactions.<sup>50</sup> Online reaction monitoring through mass spectrometry opens new possibilities to understand the chemistry of the catalyst during the reaction. Literature shows that the base eliminates the ligands from the catalyst to activate it. Chen et al. performed a Buchwald coupling reaction using liquid DESI, where the activated catalyst was mixed through channels to the reagent solution before electrospray detection.<sup>51</sup> We utilized MISI as a system to deliver such activated catalyst efficiently to the reagent mixture flowing on a paper surface through droplets. For this we used nESI as our primary ion source which contains the base and the catalyst. The solution was then subjected to spray over the flowing reaction mixture on the paper surface. The flowing reaction mixture contained the base, arylboronic acid, and aryl halide. It should be noted that MISI was used as a preparative tool rather than an analytical method.

We used xphos-Pd-G3 ( $0.1\ \text{mM}$  in ethanol) as our model catalyst. As reagents, we used 4-hydroxyboronic acid, 4-pyridineboronic acid, 6-bromoquinoline, and 4-iodoanisole and saw product formation both in positive and negative modes. Each reagent and base were prepared in ethanol in 1 and 2 mM concentrations. As the microdroplets from the primary spray impacted with the activated catalyst, the reaction was started in-flow and the products finally ended up in the secondary spray and were detected by the mass spectrometer.

**In Situ Detection of Bacterial Lipid at Ambient Conditions.** Fresh cultures of *B. subtilis*, *E. coli*, and *P. putida* were prepared from their respective stocks by inoculating  $0.1\ \text{mL}$  in  $10\ \text{mL}$  of LB broth and culturing at  $37^\circ\text{C}$ , with 210 rpm shaking, to reach late exponential phase. About  $100\ \mu\text{L}$  of the culture was drop casted on top of a triangularly cut sterile filter paper. In situ MISI MS was performed by directly placing the bacteria-containing paper in front of the inlet of the mass spectrometer (in C1 mode). Sterile water containing 10% methanol was sprayed on the paper, and it was used along with nutrient solution in the primary ion source. This was then electrosprayed at a potential of 3 kV. The mass spectra in both positive- and negative-ion modes were recorded, each for 1–2 min. The measurements were repeated after 10 min. We have continued this process at least 5 times and checked the viability of the bacteria after the analysis in MISI. In a supportive experiment, *B. subtilis* containing papers were placed on a nutrient agar plate after analysis for replica plating from the filter paper and the colonial growth of viable cells was observed visually.

## ■ RESULT AND DISCUSSION

**Characterization of the System.** One of the major advantages of doing MISI over other spray-based ionization methods is that there is no direct application of high voltage to the analyte. This allows one to bring the paper tip as close as possible ( $\sim 0.1\ \text{mm}$ ) to the inlet of the mass spectrometer without causing arc discharge, whereas ESI or PSI requires a minimum distance from the MS inlet to avoid discharge. Lowering the distance resulted in better coupling of the source with the spectrometer. Initial characterization of MISI MS was done with  $30\ \mu\text{L}$  of  $10\ \mu\text{M}$  aqueous solution of lysozyme. We

used methanol in the primary ion source to generate kVPSI because methanol can be electrosprayed comparatively at a lower kV (1.5–2 kV). We used 2 kV for most of the experiments. The experiment was done in C1 mode. Figure 1B represents the MISI mass spectrum collected using a 3 mm tip to inlet distance ( $c = 3$  mm). The cascade phenomenon was tested by switching on/off the primary ion source. As the primary ion source was switched off, the cascade process got stopped, which inhibits the ionization subsequently. In Figure 1C, we show the spray on/off signal of the chronogram of MISI. A few more protein samples were also analyzed to see the applicability of the setup toward different proteins. Figure S2 presents the MISI mass spectrum of cytochrome c and myoglobin.

We use a similar methodology to show that MISI in C1 mode can ionize a large variety of molecules having different functionalities. We have chosen a few small molecules, such as indole, malic acid, and  $C_{60}$ , as shown in Figure 2. In Figure

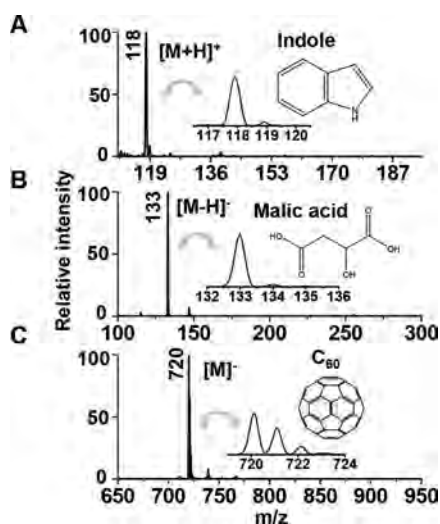


**Figure 2.** MISI mass spectra of (A) indole, (B) malic acid, and (C)  $C_{60}$  in positive- and negative-ion modes. Insets show isotopic distributions of the corresponding mass peaks and the molecular structures of the analytes.

2A,B, we observed the protonated and the deprotonated peaks of indole and malic acid at  $m/z$  118 and 133 in positive- and negative-ion modes, respectively, while a peak at  $m/z$  720 (Figure 2C) is due to the molecular ionization of  $C_{60}$  in negative-ion mode. Inset shows the molecular structure and the isotopic distribution of the corresponding analytes. Figure S3 similarly represents MISI MS of nitrophenol, glucose and benzothiophene. Assignments of the mass peaks were made by understanding their  $MS^2$  spectrum. Figure S4 represents the  $MS/MS$  spectrum of the corresponding ions of indole, malic acid, and nitrophenol. In an experiment, we demonstrated the cascade behavior of our setup as discussed in Supporting Information 1.

In MISI, ionization occurred through charge transfer from microdroplets to the neutral molecules. The cascade configuration was arranged in such a way (seen in Figure S6) that the microdroplets which are generated at the tip of the first paper impact on the second paper and ionize the analyte present on it. These charged droplets are also formed at the tip of the second paper, which promotes further droplet generation through Coulomb fission at the tip of the same

paper, and subsequently, they impact on the next paper in the cascade arrangement.  $C_{60}$  in toluene requires 3.5–4 kV to ionize in a standard PSI experiment (Figure 3A). At the same

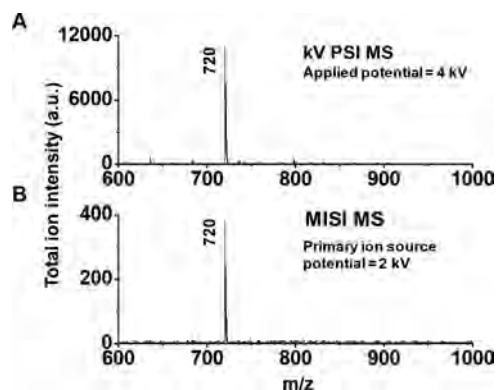


**Figure 3.** Comparative mass spectra of kVPSI and MISI. (A) kVPSI mass spectrum of  $C_{60}$  in toluene (20  $\mu$ L of 10  $\mu$ M) at 4 kV in negative-ion mode. (B) MISI mass spectrum of  $C_{60}$  in toluene (20  $\mu$ L of 10  $\mu$ M) in C1 mode using 2 kV in the primary ion source in which methanol was taken as the solvent. We observed  $\sim$ 30-fold difference in intensity between the two techniques.

time, MISI required only 1.5–2 kV to generate the electrospray plume in the primary ion source which subsequently ionized  $C_{60}$  as shown in Figure 3B. It is noted that any solvent in the primary ion source is suitable to deposit the charge to the second paper. It has also been noticed that the intensity of the  $C_{60}$  peak in MISI is 1 order of magnitude less in comparison to kVPSI. To understand the reason behind it, we measured ion current upon droplet impact at each paper in the cascade arrangement. We found that the current due to the secondary spray was less than the primary spray (Figure S9), measured by a picoammeter, connected as shown in the inset of the Figure. This clearly tells that a fraction of charge generated by the primary ion source gets transferred into the liquid, flowing on the subsequent paper due to the charged microdroplets/ions impact. Such charge loss is expected under ambient conditions. The ionization of the analytes flowing on subsequent papers in MISI is then caused by charge transfer occurring on the paper surface by the impact of charged microdroplets/ions with the solution. Loss of charge during deposition also explains the reduction in ion intensity in cascade, as shown previously.

The detection limit of the setup in C1 mode turned out to be 10 nM, measured using R6G in methanol. Figure S10 shows the calibration curve.

**MISI MS Monitoring of Suzuki–Miyaura Cross-Coupling Reactions.** The catalytic cycle of Suzuki reaction (Figure 4A) shows that NaOEt participates in reductive elimination of carbazole from the  $xphos-Pd-G3$  precatalyst, resulting in the activation of the catalyst. In this step, the success of the Suzuki reaction relies on the rapid delivery of the activated catalyst to the reaction mixture. The activation of the catalyst was done in the primary ion source as shown by the shaded area in Figure 4A. Finally, droplet impact and transport of matter through the fibers of the paper help the reaction to progress. We performed two different reactions as shown in the insets of Figure 4B,D. In the absence of the catalyst in the primary ion source, we observed a peak corresponding to deprotonated 4-hydroxyphenylboronic acid (Figure 4B) at  $m/z$  137 in the negative-ion mode for the first reaction. Similarly,

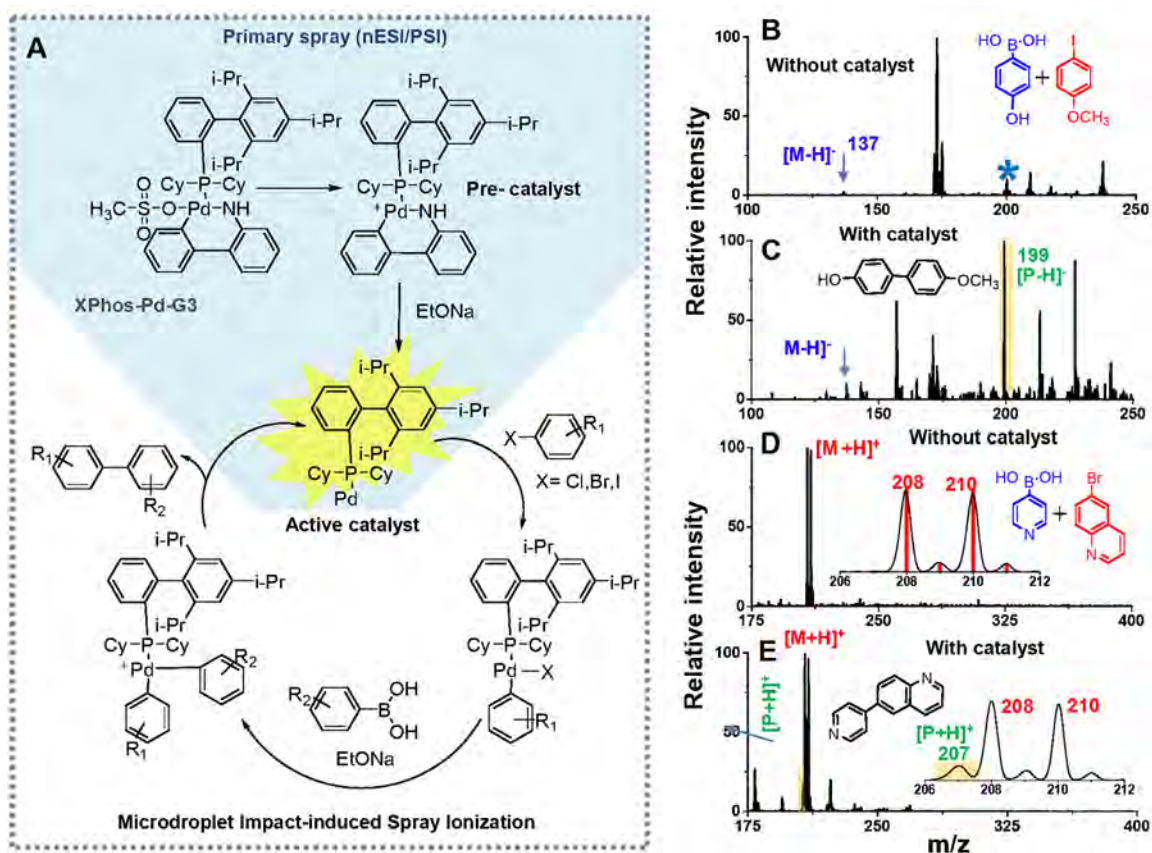


**Figure 4.** Microdroplet delivery of activated catalyst for online monitoring of Suzuki cross-coupling reaction by MISI MS. (A) Scheme of the catalytic cycle of the reaction using xphos-Pd-G3 catalyst. The sky blue shaded area represents the activation of the catalyst in the primary ion source. The primary ion source can either be nESI or PSI. (B, C) Mass spectra during the reaction between 4-hydroxyboronic acid and 4-iodoanisole in negative-ion mode in the absence and presence of the catalyst. (D, E) Mass spectra for the reaction between 4-pyridinboronic acid and 6-bromoquinoline in positive-ion mode in absence and presence of catalyst. Molecular structure of the reagents and the products are shown at the inset of the respective figure.

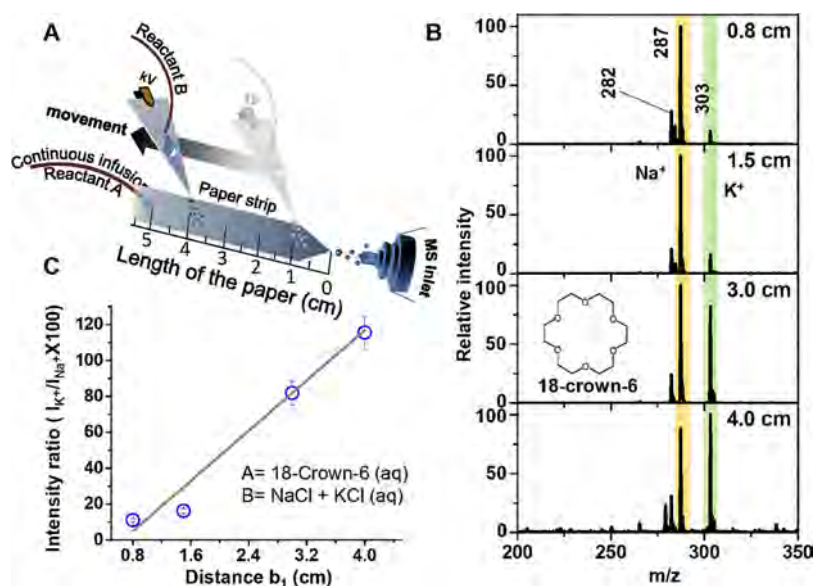


**Figure 5.** (A) Schematic representation of cascade 1 setup for encapsulation of alkali metal ions in the host, 18-crown-6. (B) MISI mass spectrum of  $Na^+$  and  $K^+$  addition in 18-C-6. Inset: molecular structure of 18-C-6. The yellow shaded area represents the peak for  $Na^+$  added crown ether at  $m/z$  287. Similarly, the green highlighted area shows the signal for the  $K^+$  added crown ether at  $m/z$  303. (C) Intensity ratio of  $K^+$  to  $Na^+$  added peaks vs distance.



the molecular ion peak of 6-bromoquinoline in positive-ion mode at  $m/z$  208 was seen for the second reaction. However, for both the reactions, we observed product peaks when the active catalyst was sprayed. The first reaction between 4-hydroxybromic acid and 4-iodoanisole gives a deprotonated cross-coupling product at  $m/z$  199 as the base peak (Figure 4C) along with a peak at  $m/z$  137 in negative-ion mode. In the second reaction, between 4-pyridinebromic acid and 6-bromoquinoline, we observed a protonated product at  $m/z$  207 (Figure 4E) along with a peak at  $m/z$  208 in the positive-ion mode. All the peaks were confirmed by their MSMS data as shown in Figure S11 and S12.

**Ion-Encapsulation Reactions.** MISI was utilized as a tool to investigate ion encapsulation reactions in situ in solution. This is because in MISI primary charged microdroplets/ions are impacting with molecules that are flowing on another paper surface. To give an example, we have conducted alkali metal ion encapsulation reactions with crown ethers. Figure S13A shows the MISI mass spectrum of the reaction between cations of Na, K, Rb, and Cs with 18-crown-6 in C1 mode. We found a sodiated peak of the crown ether at  $m/z$  287 as the base peak and a peak at  $m/z$  303 for  $K^+$  encapsulation. However, the bulk reaction shows different distribution of the peaks in which addition of all of the metal ions was observed. Figure S13B shows the mass spectrum of the same reaction done in bulk. We found the potassiated peak of the crown ether at  $m/z$  303 as the base peak in addition to the other peaks at  $m/z$  287, 349, and 397 for  $Na^+$ ,  $Rb^+$ , and  $Cs^+$  added crown ether, respectively. Generally, the equilibrium constant of 18-crown ethers for  $K^+$  selection is higher than  $Na^+$  selection for bulk reaction in water.<sup>52</sup> This hints at the fact that the encapsulation products during MISI measurement do not undergo thermodynamic equilibrium. Rather, it may be kinetically controlled. We have also demonstrated a similar phenomenon with another crown ether. The MISI and kVPSI mass spectra using dibenzo-18-crown-6 are presented in Figure S14. In Figure S14A, we see the mass spectrum of the bulk reaction which shows a different distribution than the ion molecule reaction in MISI, as shown in Figure S14B. The scanning electron microscopy images of the triangularly cut paper, in Figure S15, show that the fibers of the paper make a microfluidic system in which liquid transport is driven by capillary force. The reaction might occur during liquid transport through the capillaries of the paper by mixing of the reagents. Hence, if we increase the travel time of the liquid by lengthening the paper, we can increase the reaction time. To do so, we have changed the geometry of the paper. Figure 5A schematically presents such a setup. We have also put a scale on the paper by making pencil marks (which do not interfere with the reaction). Figure S16 shows an optical image of the setup. When we increase the travel distance (or time) by moving the primary spray head toward the base of the labeled paper (or increasing the  $b$  value), we see changes in the mass spectrum. For this, we have used equal concentration of sodium and potassium chlorides in the primary ion source. In Figure 5B, we observed that upon increasing  $b$  from 0.8 to 4 cm the intensity ratio between the potassiated ( $[K(18-C-6)]^+$  at  $m/z$  303) and the sodiated peaks ( $[Na(18-C-6)]^+$  at  $m/z$  287) increase and finally make a distribution like bulk (Figure S17). A plot of intensity ratio vs distance is shown in Figure 5C, which essentially suggests that the ion encapsulation reaction dynamics change linearly from kinetically controlled to thermodynamically controlled, as the reaction time was increased. In Supporting Information 2, we present the details

of terminal velocity calculation. Images taken during the experiment are also shown in Figure S18. The intensity ratio of potassiated and sodiated peaks of 18-crown-6 with respect to the calculated travel time shows similar change in the reaction dynamics with increasing time (Figure S19).

**In Situ Monitoring of Live Bacterial Lipid.** Having established that molecules over the paper surface experience negligible amount of potential in MISI, we tried to see the compatibility of the setup toward the analysis of live biological samples. For this, we have chosen three different bacterial samples. These were Gram-positive *B. subtilis*, Gram-negative *E. coli*, and *P. putida*.

A high electric field has a lethal effect on bacteria due to the rupture of cell membranes.<sup>22,53,54</sup> PSI is known to produce a large electric field ( $\sim 10^8$  V/cm) between the fibers of the paper as the gap between the fibers are in the micrometer range.<sup>55</sup> Such high electric fields can cause cell death. But MISI provides a noninvasive methodology to discriminate bacteria based on their lipid distribution as there is no high voltage applied directly on the sample. The signal intensity was quite similar to other ambient ionization processes such as electrospray or PSI, as discussed earlier. Figure 6A schemati-

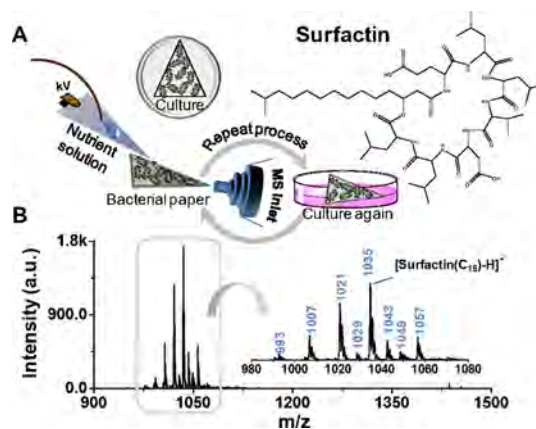


**Figure 6.** Noninvasive detection of bacterial lipid. (A) Schematic diagram of the experiment. Inset of the figure also shows the molecular structure of surfactin. (B) MISI mass spectrum of the bacterial lipid in negative-ion mode. *B. subtilis* was cultured over a triangularly cut filter paper. Inset shows the zoomed in view of the selected mass range. Deprotonated surfactin (C15) peak is at  $m/z$  1035. The other lipid peaks are indicated on the blue trace which are homologues of surfactin (C15).

cally illustrates the process of analysis in C1 mode using a bacterial sample deposited on a paper. Figure 6B presents the MISI mass spectrum collected in negative-ion mode using *B. subtilis*. The inset shows the lipids in a selected mass range, in which a peak at  $m/z$  1035 is identified as the signature deprotonated peak of surfactin (C15) for this species. This was confirmed using the MS/MS spectrum as shown in Figure S20. Figure 7 shows the lipidomic discrimination of three different bacteria in positive-ion mode. The paper after analysis was kept on saline water medium for controlled growth of bacteria. The entire measurement took place in 1–2 min. The paper was then measured again after 10 min, and similar signals were achieved. This suggests the noninvasiveness of the analysis. The same procedure was repeated at least five times.

Additionally, there were no tedious sample preparation steps involved in this technique. We found that the bacterial cells

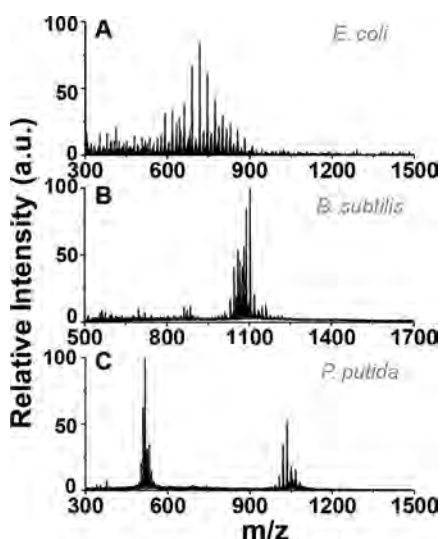


**Figure 7.** Discrimination of bacteria based on their lipid distribution in the positive-ion mode. MSI mass spectra of (A) *E. coli*, (B) *B. subtilis*, and (C) *P. putida*.

had a viability of 98% after the first analysis. The bacterial cells which were analyzed five times under MSI showed 89% viability, as shown in Figure S21. However, there is a significant reduction in the bacterial count after a single kVPSI experiment according to the replica plating experiment. Similarly, *B. subtilis* cells were also observed to grow on agar plates after they were transferred from the filter paper onto agar plates by placing the paper on the freshly prepared agar plates after analysis (Figure S22). We ensured that the bacteria subjected to MSI were studied for viability.

## CONCLUSION

We introduce the method of microdroplet impact-induced spray ionization mass spectrometry (MSI MS), which is more advantageous in comparison to standard kVPSI in terms of absence of high voltage directly applied on the sample. We show that the ionization is due to charge transfer by impact of charged microdroplets on flowing solutions. We have demonstrated three different modes of MSI, termed as C1, C2, and C3. The detection limit of the setup in C1 mode turned out to be 10 nM, measured using R6G in methanol. MSI paved a new way to perform reactions online. The Suzuki coupling reaction is shown as a model example, where the catalyst activation was performed, and the activated catalyst was delivered on the reactant. In this way, many reactions can be performed and monitored online, where the primary spray can be used as a source of catalyst/reagents either by synthesizing them or by delivering them using microdroplets. We have also shown that MSI can help in the noninvasive *in situ* detection of live bacterial samples. We have discriminated three bacterial species based on their lipid profiles. We have shown that the ionization causes no harm to the bacteria even after five analysis cycles. This indicates that our system can detect metabolites in live samples without electrical field-induced biological changes. Such unique aspects make MSI a novel ambient ionization method to investigate chemical and/or biological transformations in future.

## ASSOCIATED CONTENT

### Supporting Information

The Supporting Information is available free of charge at <https://pubs.acs.org/doi/10.1021/jasms.0c00365>.

Experimental data including optical images of the technique, SEM image of the normal paper, MS<sup>n</sup> data of the analytes, and mass spectra of other bacterial samples (PDF)

## AUTHOR INFORMATION

### Corresponding Author

Thalappil Pradeep – DST Unit of Nanoscience (DST UNS) and Thematic Unit of Excellence (TUE), Department of Chemistry, Indian Institute of Technology Madras, Chennai 600036, India; [orcid.org/0000-0003-3174-534X](https://orcid.org/0000-0003-3174-534X); Phone: +91-44-22574208; Email: [pradeep@iitm.ac.in](mailto:pradeep@iitm.ac.in); Fax: +91-44-2257 0509/0545

### Authors

Pallab Basuri – DST Unit of Nanoscience (DST UNS) and Thematic Unit of Excellence (TUE), Department of Chemistry, Indian Institute of Technology Madras, Chennai 600036, India

Subhashree Das – DST Unit of Nanoscience (DST UNS) and Thematic Unit of Excellence (TUE), Department of Chemistry, Indian Institute of Technology Madras, Chennai 600036, India

Shantha Kumar Jenifer – DST Unit of Nanoscience (DST UNS) and Thematic Unit of Excellence (TUE), Department of Chemistry, Indian Institute of Technology Madras, Chennai 600036, India

Sourav Kanti Jana – DST Unit of Nanoscience (DST UNS) and Thematic Unit of Excellence (TUE), Department of Chemistry, Indian Institute of Technology Madras, Chennai 600036, India; [orcid.org/0000-0001-5772-7022](https://orcid.org/0000-0001-5772-7022)

Complete contact information is available at: <https://pubs.acs.org/doi/10.1021/jasms.0c00365>

### Notes

The authors declare no competing financial interest.

## ACKNOWLEDGMENTS

We thank the Department of Science and Technology, Government of India, for equipment support through the Nano Mission. P.B. acknowledges IIT Madras for providing an Institute Doctoral Fellowship.

## REFERENCES

- (1) Wang, H.; Liu, J.; Cooks, R. G.; Ouyang, Z. Paper Spray for Direct Analysis of Complex Mixtures Using Mass Spectrometry. *Angew. Chem., Int. Ed.* **2010**, *49* (5), 877–880.
- (2) Liu, J.; Wang, H.; Manicke, N. E.; Lin, J.-M.; Cooks, R. G.; Ouyang, Z. Development, Characterization, and Application of Paper Spray Ionization. *Anal. Chem.* **2010**, *82* (6), 2463–2471.
- (3) Huang, H.; Wu, Q.; Zeng, L.; Wan, L.; Lai, S.; Yin, X.; Huang, J.; Yang, B.; Liu, J. Heating paper spray mass spectrometry for enhanced detection of propranolol in dried blood samples. *Anal. Methods* **2017**, *9* (29), 4282–4287.
- (4) Banks, J. F.; Shen, S.; Whitehouse, C. M.; Fenn, J. B. Ultrasonically assisted electrospray ionization for LC/MS determination of nucleosides from a transfer RNA digest. *Anal. Chem.* **1994**, *66* (3), 406–414.

- (5) Li, Z.; Li, L. Chemical-Vapor-Assisted Electrospray Ionization for Increasing Analyte Signals in Electrospray Ionization Mass Spectrometry. *Anal. Chem.* **2014**, *86* (1), 331–335.
- (6) Zhang, J.-T.; Wang, H.-Y.; Zhu, W.; Cai, T.-T.; Guo, Y.-L. Solvent-Assisted Electrospray Ionization for Direct Analysis of Various Compounds (Complex) from Low/Nonpolar Solvents and Eluents. *Anal. Chem.* **2014**, *86* (18), 8937–8942.
- (7) Basuri, P.; Sarkar, D.; Paramasivam, G.; Pradeep, T. Detection of Hydrocarbons by Laser Assisted Paper Spray Ionization Mass Spectrometry (LAPSI MS). *Anal. Chem.* **2018**, *90* (7), 4663–4668.
- (8) Liu, J.; Wang, H.; Cooks, R. G.; Ouyang, Z. Leaf Spray: Direct Chemical Analysis of Plant Material and Living Plants by Mass Spectrometry. *Anal. Chem.* **2011**, *83* (20), 7608–7613.
- (9) Song, X.; Chen, H.; Zare, R. N. Conductive Polymer Spray Ionization Mass Spectrometry for Biofluid Analysis. *Anal. Chem.* **2018**, *90* (21), 12878–12885.
- (10) Silva, L. C. d.; Pereira, I.; Carvalho, T. C. d.; Allochio Filho, J. F.; Romão, W.; Gontijo Vaz, B. Paper spray ionization and portable mass spectrometers: a review. *Anal. Methods* **2019**, *11* (8), 999–1013.
- (11) Jackson, S.; Swiner, D. J.; Capone, P. C.; Badu-Tawiah, A. K. Thread spray mass spectrometry for direct analysis of capsaicinoids in pepper products. *Anal. Chim. Acta* **2018**, *1023*, 81–88.
- (12) Jiang, J.; Zhang, H.; Li, M.; Dulay, M. T.; Ingram, A. J.; Li, N.; You, H.; Zare, R. N. Droplet Spray Ionization from a Glass Microscope Slide: Real-Time Monitoring of Ethylene Polymerization. *Anal. Chem.* **2015**, *87* (16), 8057–8062.
- (13) Freund, D. M.; Sammons, K. A.; Makunga, N. P.; Cohen, J. D.; Hegeman, A. D. Leaf spray mass spectrometry: a rapid ambient ionization technique to directly assess metabolites from plant tissues. *J. Visualized Exp.* **2018**, No. 136, No. e57949.
- (14) Bills, B. J.; Manicke, N. E. Development of a prototype blood fractionation cartridge for plasma analysis by paper spray mass spectrometry. *Clinical Mass Spectrometry* **2016**, *2*, 18–24.
- (15) Guo, T.; Zhang, Z.; Yannell, K. E.; Dong, Y.; Cooks, R. G. Paper spray ionization mass spectrometry for rapid quantification of illegal beverage dyes. *Anal. Methods* **2017**, *9* (44), 6273–6279.
- (16) Gu, J.; Hiraga, T.; Wada, Y. Electrospray ionization mass spectrometry of pyridylaminated oligosaccharide derivatives: Sensitivity and in-source fragmentation. *Biol. Mass Spectrom.* **1994**, *23* (4), 212–217.
- (17) Xue, J.; Domingo-Almenara, X.; Guijas, C.; Palermo, A.; Rinschen, M. M.; Isbell, J.; Benton, H. P.; Siuzdak, G. Enhanced In-Source Fragmentation Annotation Enables Novel Data Independent Acquisition and Autonomous METLIN Molecular Identification. *Anal. Chem.* **2020**, *92* (8), 6051–6059.
- (18) Gathungu, R. M.; Larrea, P.; Sniatynski, M. J.; Marur, V. R.; Bowden, J. A.; Koelmel, J. P.; Starke-Reed, P.; Hubbard, V. S.; Kristal, B. S. Optimization of Electrospray Ionization Source Parameters for Lipidomics To Reduce Misannotation of In-Source Fragments as Precursor Ions. *Anal. Chem.* **2018**, *90* (22), 13523–13532.
- (19) Xu, Y. F.; Lu, W.; Rabinowitz, J. D. Avoiding misannotation of in-source fragmentation products as cellular metabolites in liquid chromatography-mass spectrometry-based metabolomics. *Anal. Chem.* **2015**, *87* (4), 2273–81.
- (20) Kostyukevich, Y.; Kononikhin, A.; Popov, I.; Nikolaev, E. Conformational changes of ubiquitin during electrospray ionization as determined by in-ESI source H/D exchange combined with high-resolution MS and ECD fragmentation. *J. Mass Spectrom.* **2014**, *49* (10), 989–994.
- (21) Li, D.; Jia, S.; Zhang, L.; Wang, Z.; Pan, J.; Zhu, B.; Luo, Y. Effect of using a high voltage electrostatic field on microbial communities, degradation of adenosine triphosphate, and water loss when thawing lightly-salted, frozen common carp (*Cyprinus carpio*). *J. Food Eng.* **2017**, *212*, 226–233.
- (22) Zimmermann, U.; Pilwat, G.; Riemann, F. Dielectric breakdown of cell membranes. *Biophys. J.* **1974**, *14* (11), 881–899.
- (23) Narayanan, R.; Basuri, P.; Jana, S. K.; Mahendranath, A.; Bose, S.; Pradeep, T. In situ monitoring of electrochemical reactions through CNT-assisted paper cell mass spectrometry. *Analyst* **2019**, *144*, 5404.
- (24) Narayanan, R.; Sarkar, D.; Cooks, R. G.; Pradeep, T. Molecular Ionization from Carbon Nanotube Paper. *Angew. Chem.* **2014**, *126* (23), 6046–6050.
- (25) Damon, D. E.; Davis, K. M.; Moreira, C. R.; Capone, P.; Cruttenden, R.; Badu-Tawiah, A. K. Direct Biofluid Analysis Using Hydrophobic Paper Spray Mass Spectrometry. *Anal. Chem.* **2016**, *88* (3), 1878–1884.
- (26) Basuri, P.; Baidya, A.; Pradeep, T. Sub-Parts-per-Trillion Level Detection of Analytes by Superhydrophobic Preconcentration Paper Spray Ionization Mass Spectrometry (SHPPSI MS). *Anal. Chem.* **2019**, *91* (11), 7118–7124.
- (27) Yang, Y.; Noviana, E.; Nguyen, M. P.; Geiss, B. J.; Dandy, D. S.; Henry, C. S. Paper-Based Microfluidic Devices: Emerging Themes and Applications. *Anal. Chem.* **2017**, *89* (1), 71–91.
- (28) Cate, D. M.; Noblitt, S. D.; Volckens, J.; Henry, C. S. Multiplexed paper analytical device for quantification of metals using distance-based detection. *Lab Chip* **2015**, *15* (13), 2808–2818.
- (29) Cate, D. M.; Dungchai, W.; Cunningham, J. C.; Volckens, J.; Henry, C. S. Simple, distance-based measurement for paper analytical devices. *Lab Chip* **2013**, *13* (12), 2397–2404.
- (30) Choi, S.; Cha, S. Investigation of Reactions Between Isothiazolinones and Cysteamine by Reactive Paper Spray Ionization Mass Spectrometry (Reactive PSI MS). *Bulletin of the Korean Chemical Society* **2020**, *41* (1), 48–53.
- (31) Banerjee, S.; Basheer, C.; Zare, R. N. A Study of Heterogeneous Catalysis by Nanoparticle-Embedded Paper-Spray Ionization Mass Spectrometry. *Angew. Chem., Int. Ed.* **2016**, *55* (41), 12807–12811.
- (32) Bain, R. M.; Pulliam, C. J.; Raab, S. A.; Cooks, R. G. Chemical Synthesis Accelerated by Paper Spray: The Haloform Reaction. *J. Chem. Educ.* **2016**, *93* (2), 340–344.
- (33) Zhou, X.; Pei, J.; Huang, G. Reactive paper spray mass spectrometry for in situ identification of quinones. *Rapid Commun. Mass Spectrom.* **2015**, *29* (1), 100–106.
- (34) Boccatto, E.; Santos, S. A. d.; Mazieri, N. A. O.; Andrade, D. R. d.; Carrazza, F. R.; Yanaguita, R. M. Evaluation of a Rapid Screening Assay for Bacterial Identification (DOT-ELISA) in Fecal Samples from Children. *Rev. Inst. Med. Trop. Sao Paulo* **1997**, *39*, 21–28.
- (35) Krause, M.; Rösch, P.; Radt, B.; Popp, J. Localizing and Identifying Living Bacteria in an Abiotic Environment by a Combination of Raman and Fluorescence Microscopy. *Anal. Chem.* **2008**, *80* (22), 8568–8575.
- (36) Athamanolap, P.; Hsieh, K.; Chen, L.; Yang, S.; Wang, T.-H. Integrated Bacterial Identification and Antimicrobial Susceptibility Testing Using PCR and High-Resolution Melt. *Anal. Chem.* **2017**, *89* (21), 11529–11536.
- (37) Ahmed, A.; Rushworth, J. V.; Hirst, N. A.; Millner, P. A. Biosensors for Whole-Cell Bacterial Detection. *Clin. Microbiol. Rev.* **2014**, *27* (3), 631.
- (38) Yang, Y.; Lin, Y.; Qiao, L. Direct MALDI-TOF MS Identification of Bacterial Mixtures. *Anal. Chem.* **2018**, *90* (17), 10400–10408.
- (39) Snyder, A. P.; Dworzanski, J. P.; Tripathi, A.; Maswadeh, W. M.; Wick, C. H. Correlation of Mass Spectrometry Identified Bacterial Biomarkers from a Fielded Pyrolysis-Gas Chromatography-Ion Mobility Spectrometry Biotector with the Microbiological Gram Stain Classification Scheme. *Anal. Chem.* **2004**, *76* (21), 6492–6499.
- (40) Hsu, C.-C.; ElNaggar, M. S.; Peng, Y.; Fang, J.; Sanchez, L. M.; Mascuch, S. J.; Möller, K. A.; Alazzeh, E. K.; Pikula, J.; Quinn, R. A.; Zeng, Y.; Wolfe, B. E.; Dutton, R. J.; Gerwick, L.; Zhang, L.; Liu, X.; Månsson, M.; Dorrestein, P. C. Real-Time Metabolomics on Living Microorganisms Using Ambient Electrospray Ionization Flow-Probe. *Anal. Chem.* **2013**, *85* (15), 7014–7018.
- (41) Meetani, M. A.; Shin, Y.-S.; Zhang, S.; Mayer, R.; Basile, F. Desorption electrospray ionization mass spectrometry of intact bacteria. *J. Mass Spectrom.* **2007**, *42* (9), 1186–1193.
- (42) Hamid, A. M.; Jarmusch, A. K.; Pirro, V.; Pincus, D. H.; Clay, B. G.; Gervasi, G.; Cooks, R. G. Rapid Discrimination of Bacteria by



Paper Spray Mass Spectrometry. *Anal. Chem.* **2014**, *86* (15), 7500–7507.

(43) Li, A.; Hollerbach, A.; Luo, Q.; Cooks, R. G. On-Demand Ambient Ionization of Picoliter Samples Using Charge Pulses. *Angew. Chem., Int. Ed.* **2015**, *54* (23), 6893–6895.

(44) Bringer, M. R.; Gerdts, C. J.; Song, H.; Tice, J. D.; Ismagilov, R. F. Microfluidic systems for chemical kinetics that rely on chaotic mixing in droplets. *Philos. Trans. R. Soc., A* **2004**, *362* (1818), 1087–1104.

(45) Haven, J. J.; Zaquen, N.; Rubens, M.; Junkers, T. The Kinetics of n-Butyl Acrylate Radical Polymerization Revealed in a Single Experiment by Real Time On-line Mass Spectrometry Monitoring. *Macromol. React. Eng.* **2017**, *11* (4), 1700016.

(46) Shastry, M. C. R.; Luck, S. D.; Roder, H. A Continuous-Flow Capillary Mixing Method to Monitor Reactions on the Microsecond Time Scale. *Biophys. J.* **1998**, *74* (5), 2714–2721.

(47) Beccalli, E. M.; Brogini, G.; Martinelli, M.; Sottocornola, S. C-C, C-O, C-N Bond Formation on sp<sup>2</sup> Carbon by Pd(II)-Catalyzed Reactions Involving Oxidant Agents. *Chem. Rev.* **2007**, *107* (11), 5318–5365.

(48) Miyaura, N.; Yamada, K.; Suzuki, A. A new stereospecific cross-coupling by the palladium-catalyzed reaction of 1-alkenylboranes with 1-alkenyl or 1-alkynyl halides. *Tetrahedron Lett.* **1979**, *20* (36), 3437–3440.

(49) Melvin, P. R.; Balcells, D.; Hazari, N.; Nova, A. Understanding Precatalyst Activation in Cross-Coupling Reactions: Alcohol Facilitated Reduction from Pd(II) to Pd(0) in Precatalysts of the Type ( $\eta^3$ -allyl)Pd(L)(Cl) and ( $\eta^3$ -indenyl)Pd(L)(Cl). *ACS Catal.* **2015**, *5* (9), 5596–5606.

(50) Fedick, P. W.; Iyer, K.; Wei, Z.; Avramova, L.; Capek, G. O.; Cooks, R. G. Screening of the Suzuki Cross-Coupling Reaction Using Desorption Electrospray Ionization in High-Throughput and in Leidenfrost Droplet Experiments. *J. Am. Soc. Mass Spectrom.* **2019**, *30* (10), 2144–2151.

(51) Zheng, Q.; Liu, Y.; Chen, Q.; Hu, M.; Helmy, R.; Sherer, E. C.; Welch, C. J.; Chen, H. Capture of Reactive Monophosphine-Ligated Palladium(0) Intermediates by Mass Spectrometry. *J. Am. Chem. Soc.* **2015**, *137* (44), 14035–14038.

(52) Inokuchi, Y.; Ebata, T.; Ikeda, T.; Haino, T.; Kimura, T.; Guo, H.; Furutani, Y. New insights into metal ion-crown ether complexes revealed by SEIRA spectroscopy. *New J. Chem.* **2015**, *39* (11), 8673–8680.

(53) Sale, A. J. H.; Hamilton, W. A. Effects of high electric fields on microorganisms: I. Killing of bacteria and yeasts. *Biochim. Biophys. Acta, Gen. Subj.* **1967**, *148* (3), 781–788.

(54) Pillet, F.; Formosa-Dague, C.; Baaziz, H.; Dague, E.; Rols, M.-P. Cell wall as a target for bacteria inactivation by pulsed electric fields. *Sci. Rep.* **2016**, *6* (1), 19778.

(55) Espy, R. D.; Muliadi, A. R.; Ouyang, Z.; Cooks, R. G. Spray mechanism in paper spray ionization. *Int. J. Mass Spectrom.* **2012**, *325–327*, 167–171.

# Supporting Information

## **Microdroplet Impact-Induced Spray Ionization Mass Spectrometry (MISI MS) for Online Reaction Monitoring and Bacteria Discrimination**

**Pallab Basuri, Subhashree Das, Shantha Kumar Jenifer, Sourav Kanti Jana and Thalappil Pradeep\***

*DST Unit of Nanoscience (DST UNS) and Thematic Unit of Excellence,  
Department of Chemistry, Indian Institute of Technology Madras,  
Chennai 600036, India.*

\*E-mail: [pradeep@iitm.ac.in](mailto:pradeep@iitm.ac.in),

Fax: 91-44-2257 0545

## Table of contents

Number	Description	Page Number
Figure S1	Optical image of the MISI MS in C1 mode	S3
Figure S2	MISI mass spectra of A) cytochrome c, and B) myoglobin in C1 mode	S4
Figure S3	MISI mass spectra of A) nitrophenol, B) glucose and C) benzothiophene in C1 mode	S5
Figure S4	Fragmentation spectra of A) malic acid, B) indole, C) nitrophenol, and D) glucose	S6
Supporting information 1	Demonstration of cascaded mode of ionization	S7
Figure S5	MISI MS of R6G	S7
Figure S6	Optical images of MISI in C1, C2 and C3 mode	S8
Figure S7	Fragmentation spectrum of R6G	S9
Figure S8	MISI mass spectrum of R6G in C1-3 mode	S10
Figure S9	Ion current measurement using picoammeter	S11
Figure S10	Calibration curve using R6G in C1 mode	S12
Figure S11	MSMS spectra of $m/z$ 137 and 199 in negative-ion mode	S13
Figure S12	MSMS spectra of $m/z$ 208 and 207 in positive-ion mode	S14
Figure S13	MISI and kVPSI mass spectra of crown ether	S15
Figure S14	Comparative MISI and kVPSI mass spectra of ion encapsulation reaction	S16
Figure S15	SEM images of the paper	S17
Figure S16	Optical images of the setup for the measurement of encapsulation kinetics	S18
Figure S17	kVPSI mass spectrum of the bulk reaction between NaCl and KCl 1:1 mixture and 18-crown-6	S19
Supporting information 2	The fluid terminal velocity experiment and calculation	S20
Figure S18	Optical images during fluid terminal velocity measurement	S20
Figure S19	Reaction dynamics in time frame.	S21
Figure S20	Fragmentation spectrum of surfactin in negative and positive-ion modes	S22
Figure S21	Bacterial viability test	S23
Figure S22	Optical images of bacterial growth after MISI	S24

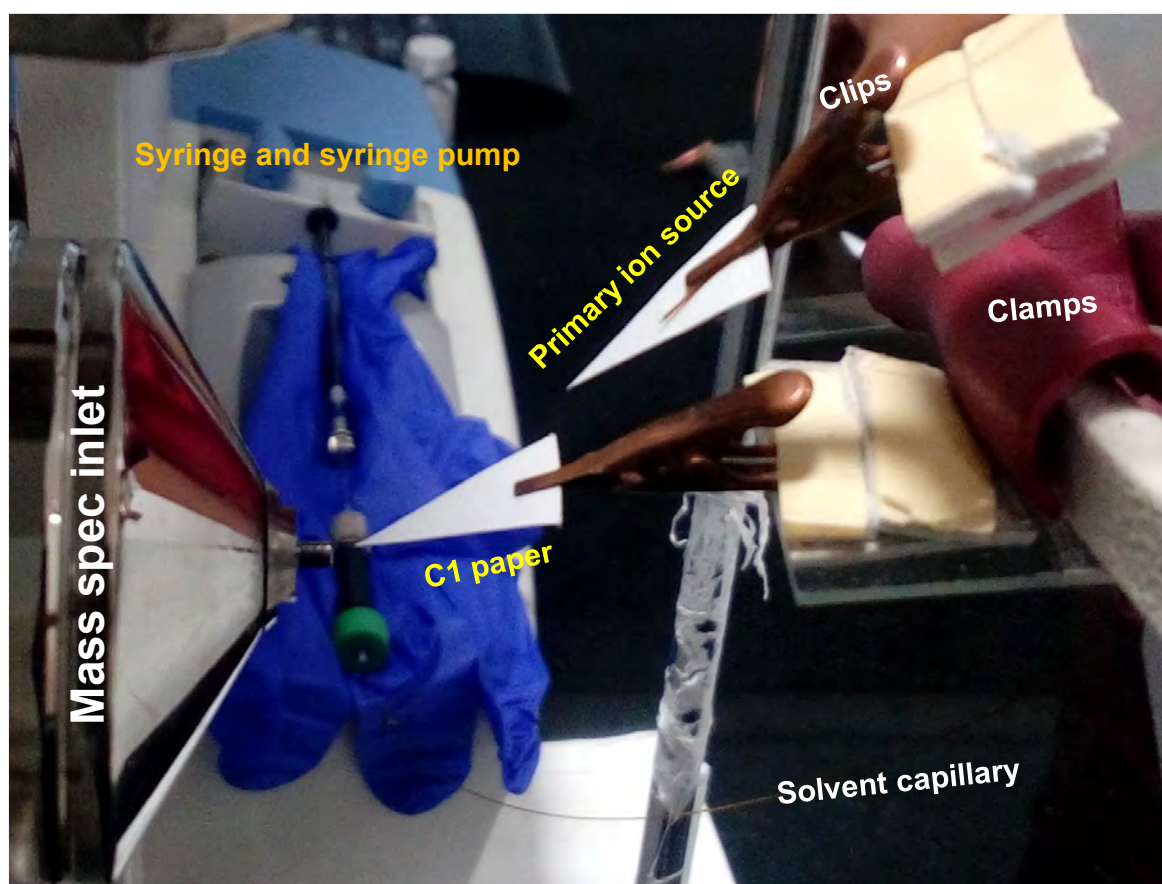


**Figure S1.** Optical image of the MISI MS in C1 mode. The primary ion source, paper in C1 mode, solvent capillary, mass spec inlet, clamp and clip are indicated in the picture.

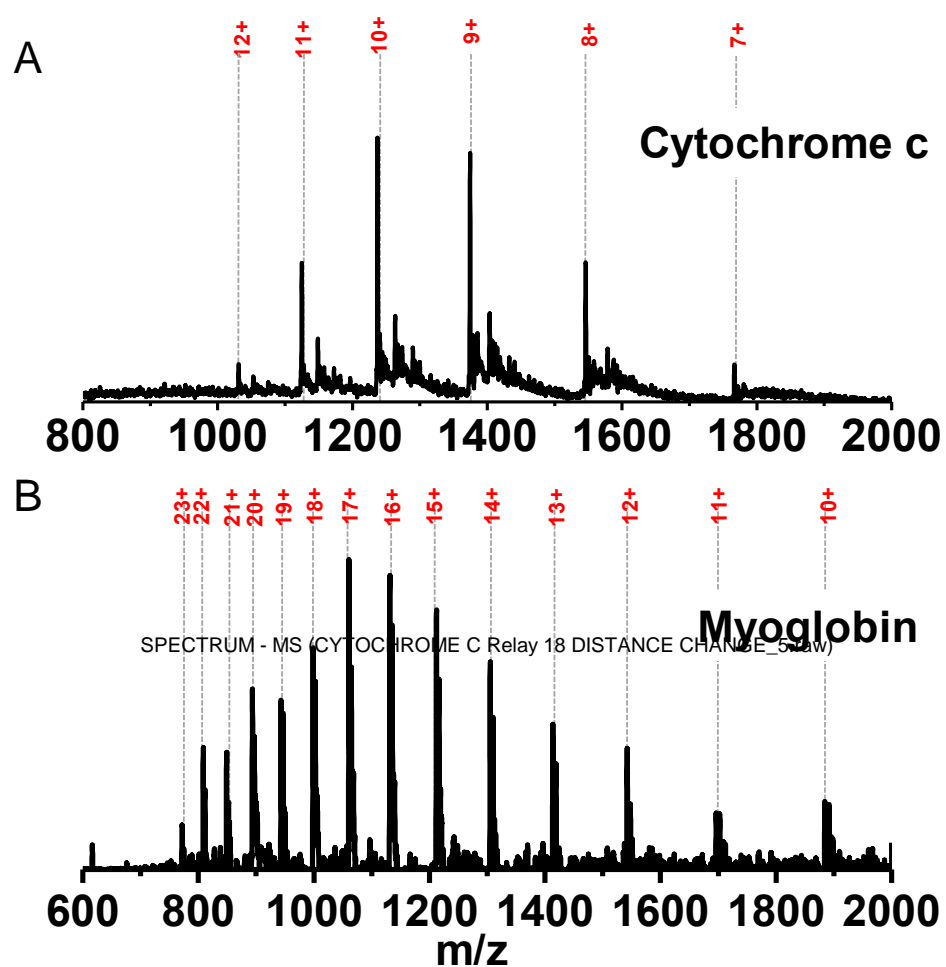


**Figure S2.** MSI mass spectra of A) cytochrome c, and B) myoglobin in C1 mode. The charge states of all the peaks for both the protein mass spectra are indicated in red. The solutions (0.1 mg/ml) were made in deionized water.



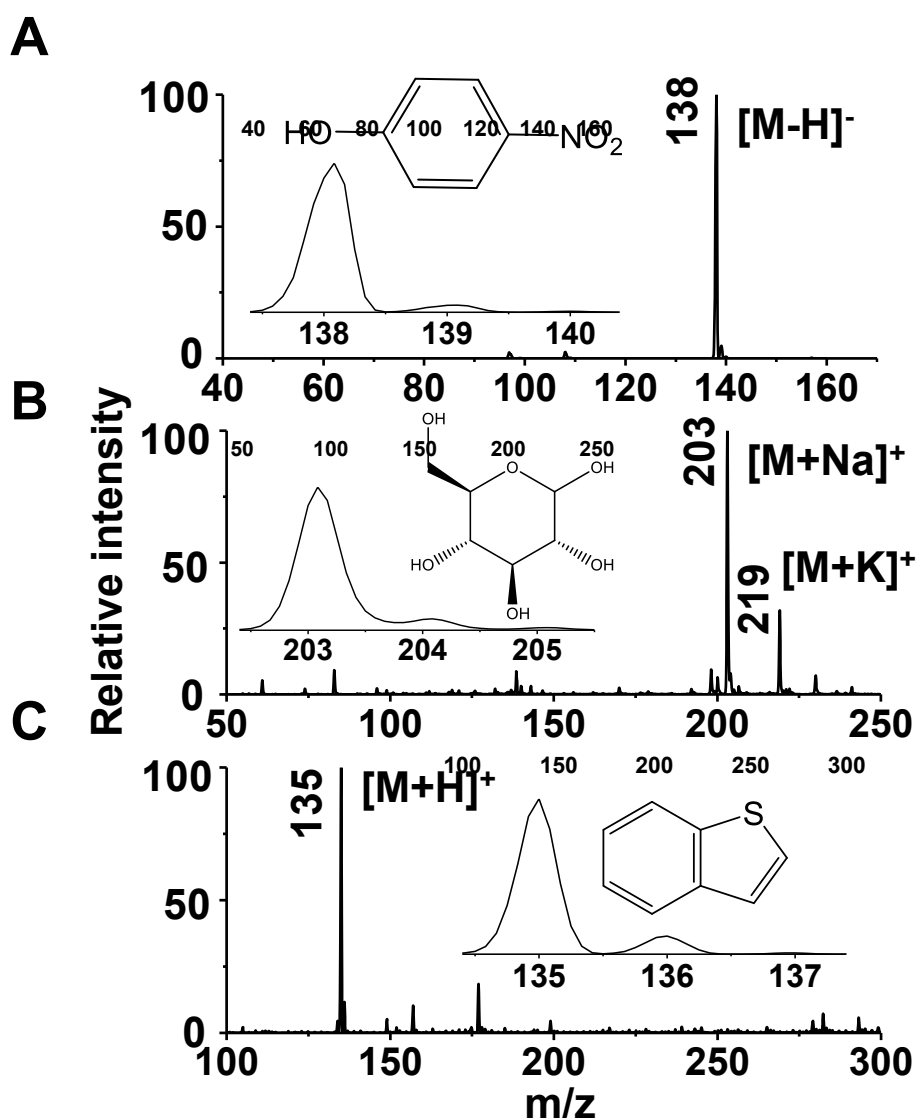


**Figure S3.** MSI mass spectra of A) nitrophenol, B) glucose and C) benzothiophene in C1 mode. Insets of each figure show the isotopic distribution of the corresponding peak as well as the molecular structure of the analyte used for the experiment.

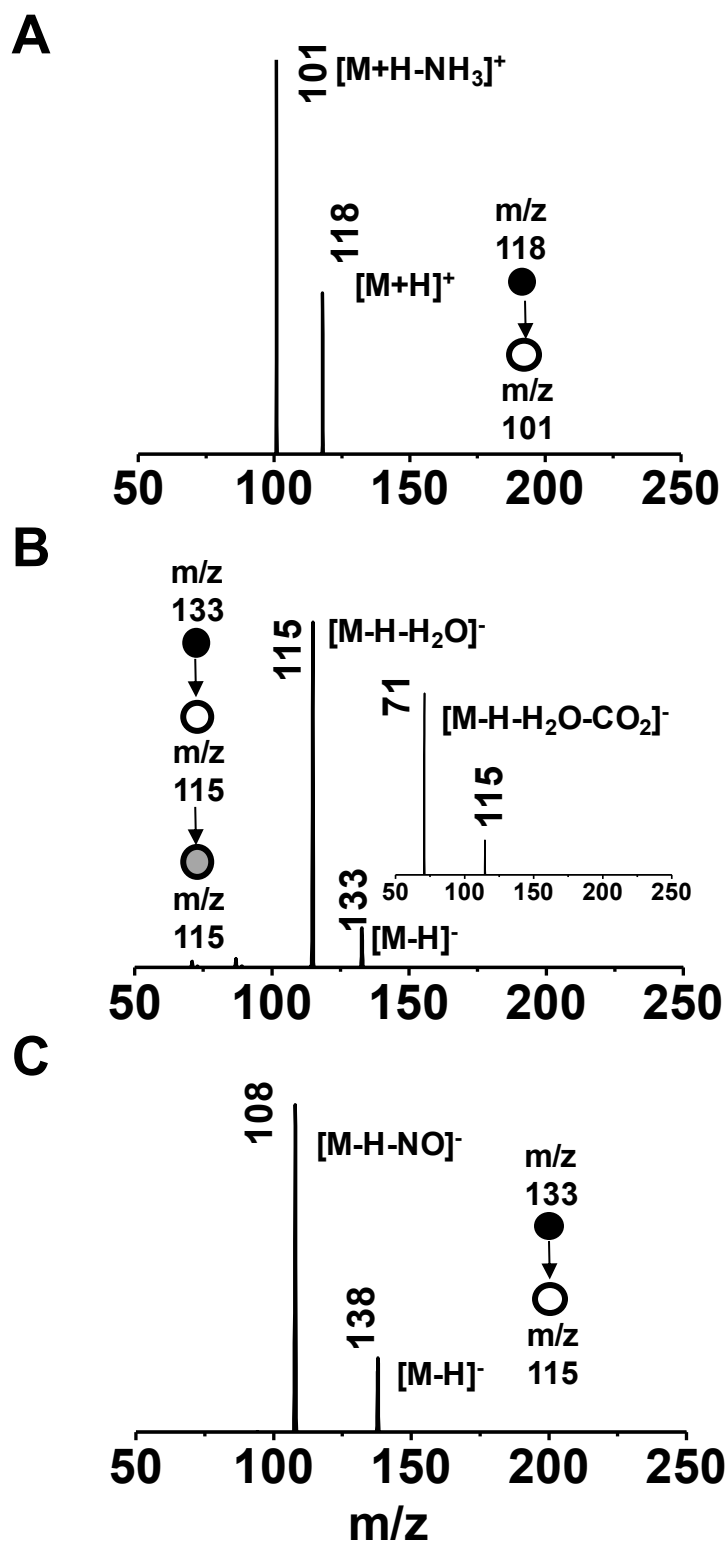


**Figure S4.** MS/MS spectrum of A) indole, B) malic acid, and C) p-nitrophenol in negative-ion mode. Inset of Figure B shows the MS<sup>3</sup> spectrum of the mass selected peak at  $m/z$  115. The peak assignments are based on the neutral loss during the fragmentation of peaks.

## Supporting information 1.

### Cascaded mode of ionization-

To demonstrate the cascaded behavior, rhodamine 6G (20  $\mu\text{L}$  of 10  $\mu\text{M}$ ) was chosen as an analyte. Figure S5A schematically represents the setup for cascade 1, 2 and 3 (C1, C2 and C3). The optical image of the setup is shown in Figure S6. The MSI mass spectrum of R6G in C3 mode is shown in Figure S5B. In it, we see a peak at  $m/z$  443 which corresponds to the protonated ion. This was further confirmed by the  $\text{MS}^2$  spectrum (Figure S7). Figure S8 presents the mass spectra of R6G for C1 to C3 modes where we see a gradual decrease in the absolute intensity. The absolute intensities of the selected peak at  $m/z$  443 in C1-3 modes of ionization are presented in Figure S5D.

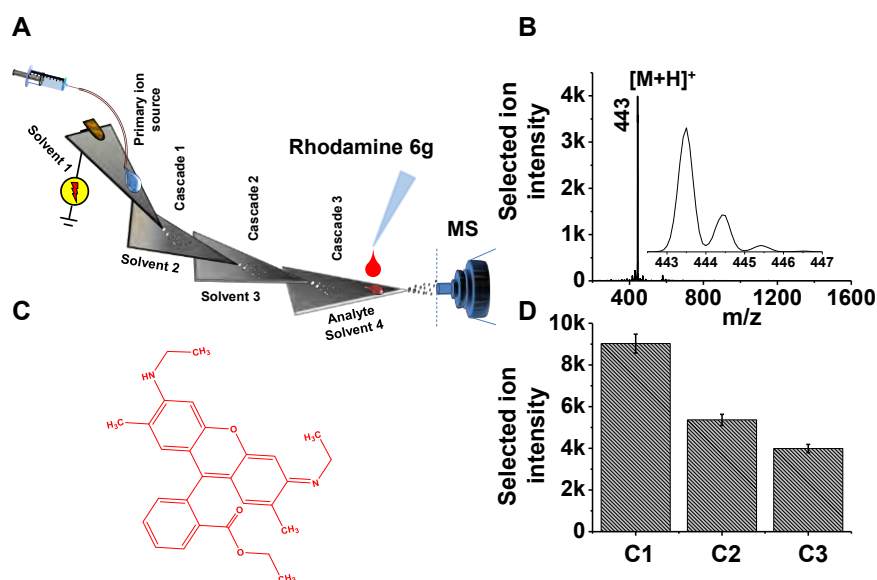


**Figure S5.** A) Schematic representation of cascade 1, 2 and 3. B) MSI mass spectrum of Rhodamine 6G in C3 mode. Inset represents the isotopic pattern of the peak at  $m/z$  443 and the molecular structure of R6G. C) Molecular structure of rhodamine 6G. D) Ion intensity of the selected ion at  $m/z$  443 for different cascade modes.

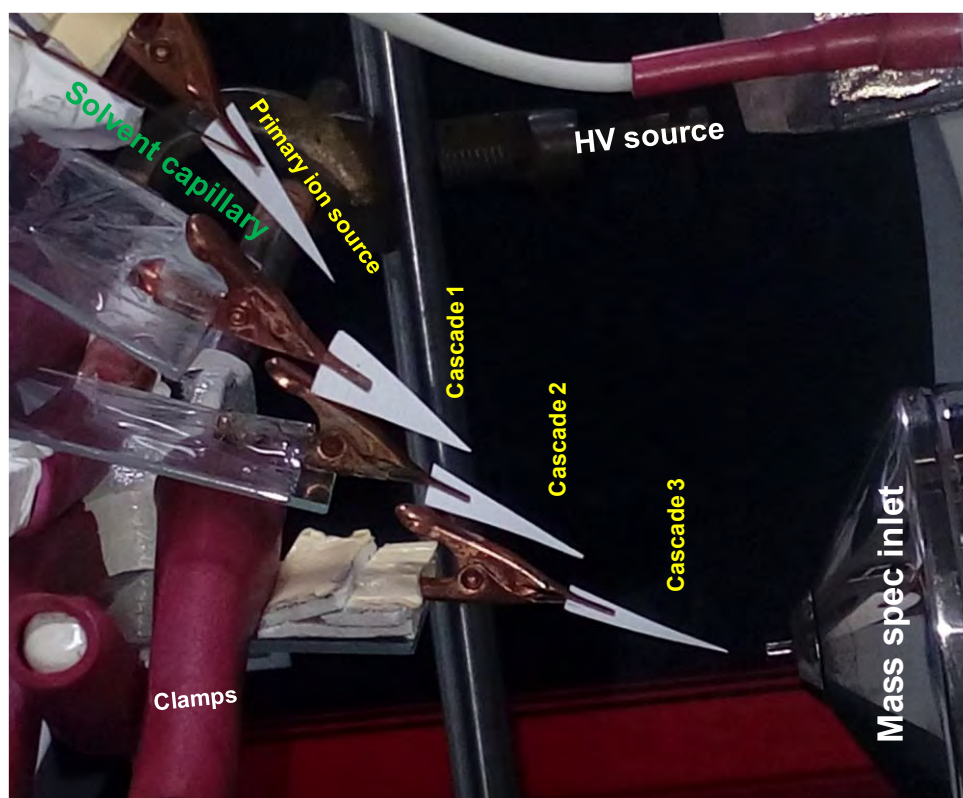


**Figure S6.** Optical image of MSI MS in C3 mode. the yellow traces indicate that the modes can be switched by removing or adding another paper triangle into the setup.

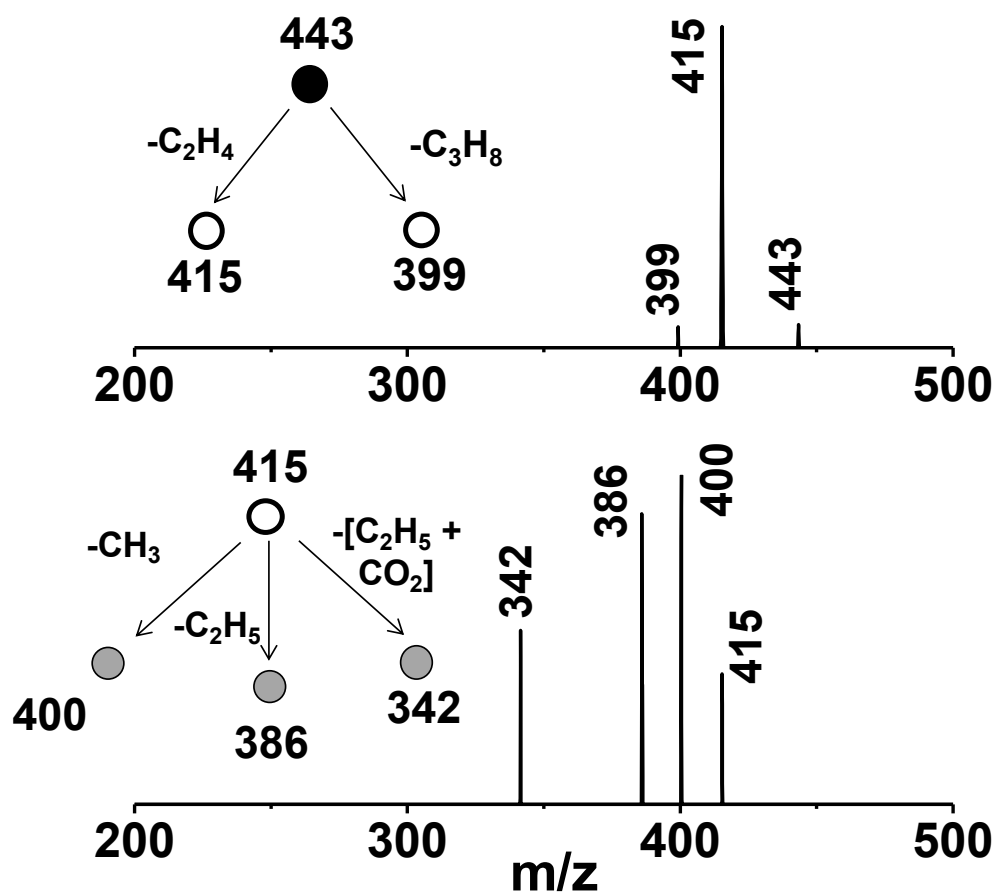


**Figure S7.** MS/MS spectra of the peak at  $m/z$  443 corresponding to the protonated peak of R6G. The above spectrum presents the MS<sup>2</sup> fragmentation of the mass selected peak at  $m/z$  443 whereas the bottom spectrum presents the MS<sup>3</sup> spectrum of the mass selected peak at  $m/z$  415.

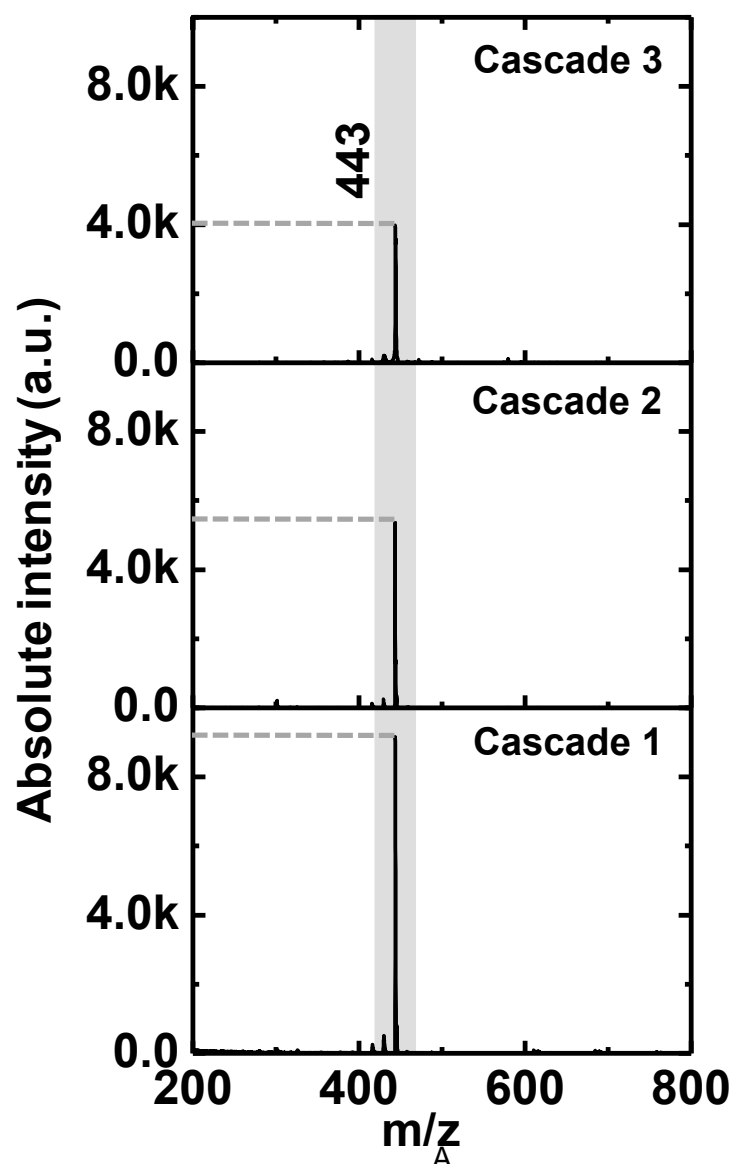


**Figure S8.** MISI mass spectrum of R6G in C1-3 mode. The intensity variation of the shaded peak at  $m/z$  443 is shown. The intensity loss during the cascaded process may due to the charge loss.



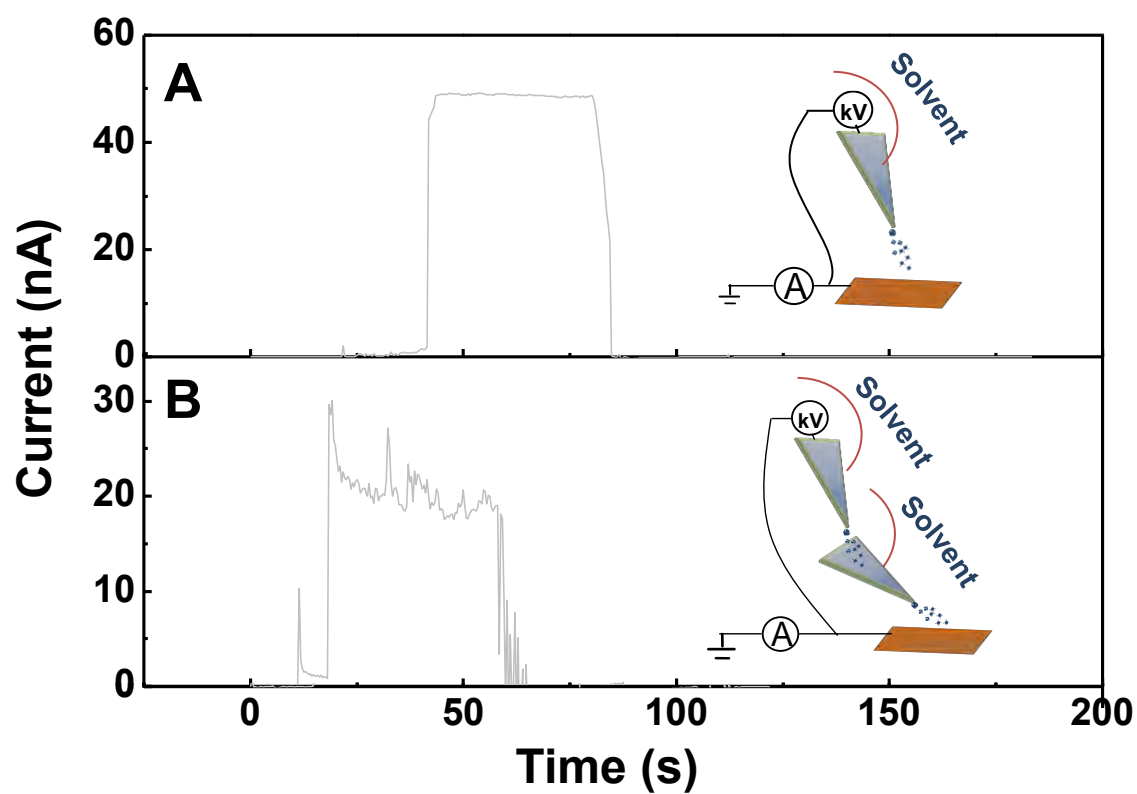


**Figure S9.** Spray current measurement in A) kVPSI, B) MISI. Inset of each trace presents the arrangements used for the measurement. The intensity fluctuations in the latter two spectra are probably due to the cascaded process in which the charges are also lost during the charge transfer processes over the surface.

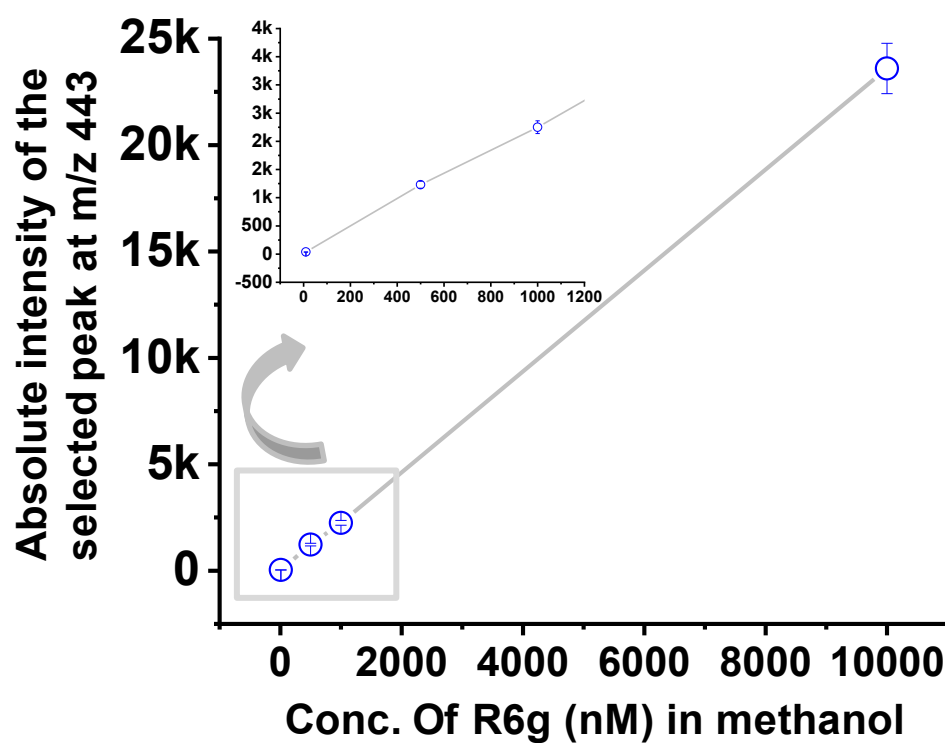


**Figure S10.** Intensity vs concentration plot using R6G as the analyte. The inset shows the zoomed-in view of the low concentration regime.

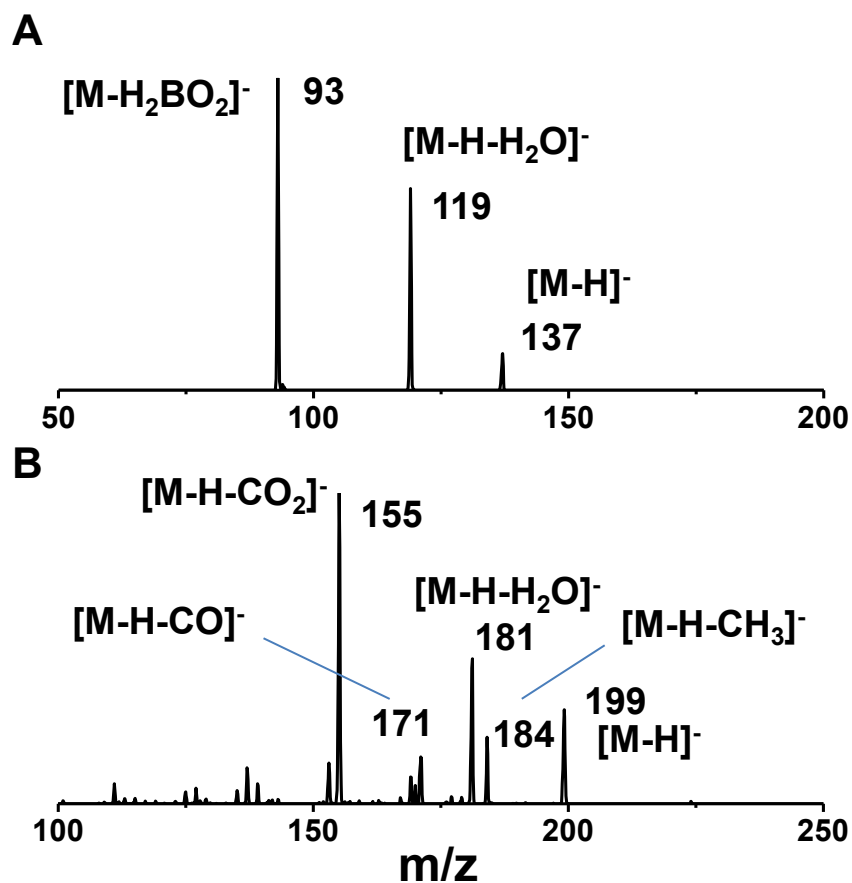


**Figure S11.** MSMS spectra of deprotonated 4-hydroxyboronic acid and product peak at  $m/z$  A) 137 and B) 119 in the negative-ion mode.

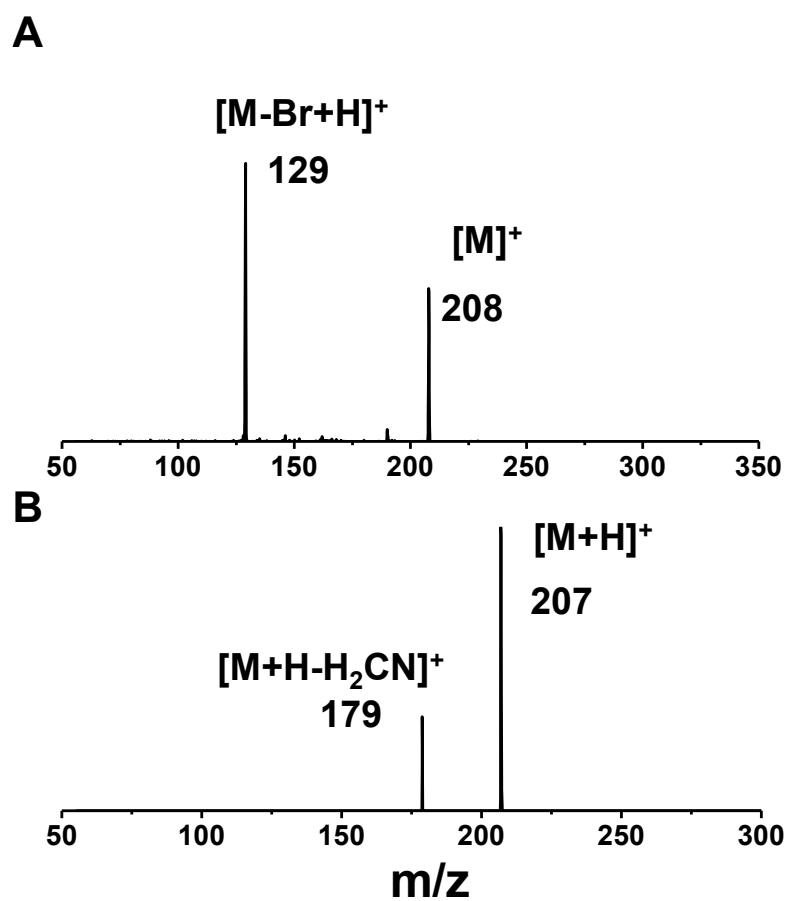


**Figure S12.** MSMS spectra of 6-bromoquinoline and product peak at  $m/z$  A) 208 and B) 207 in the positive-ion mode.

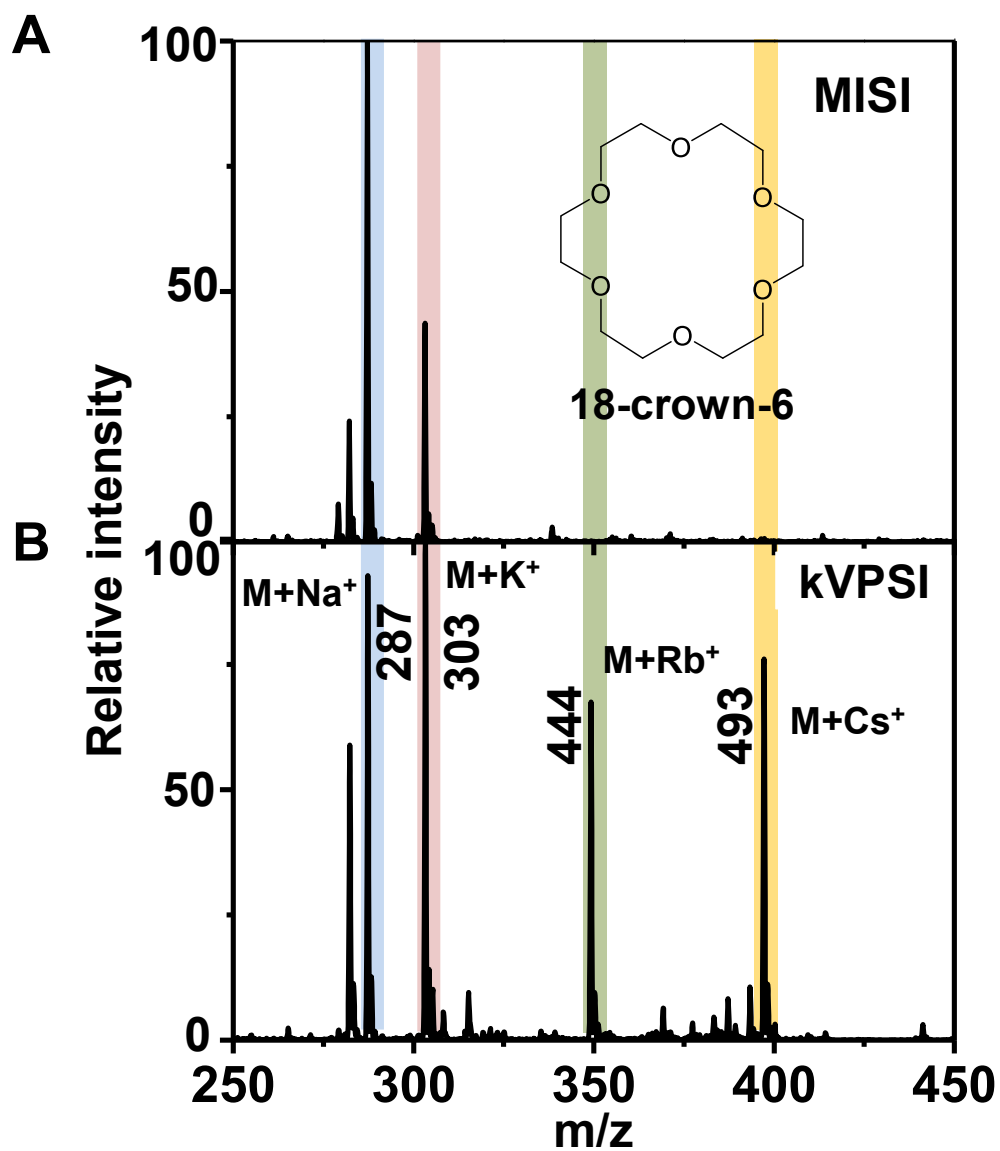


**Figure S13.** Comparative mass spectrum using A) MISI and B) kVPSI of ion encapsulation reaction between alkali metal ions with 18-crown-6. The kVPSI mass spectrum is recorded for the bulk reaction. Inset of Figure A shows the molecular structure of crown ether.

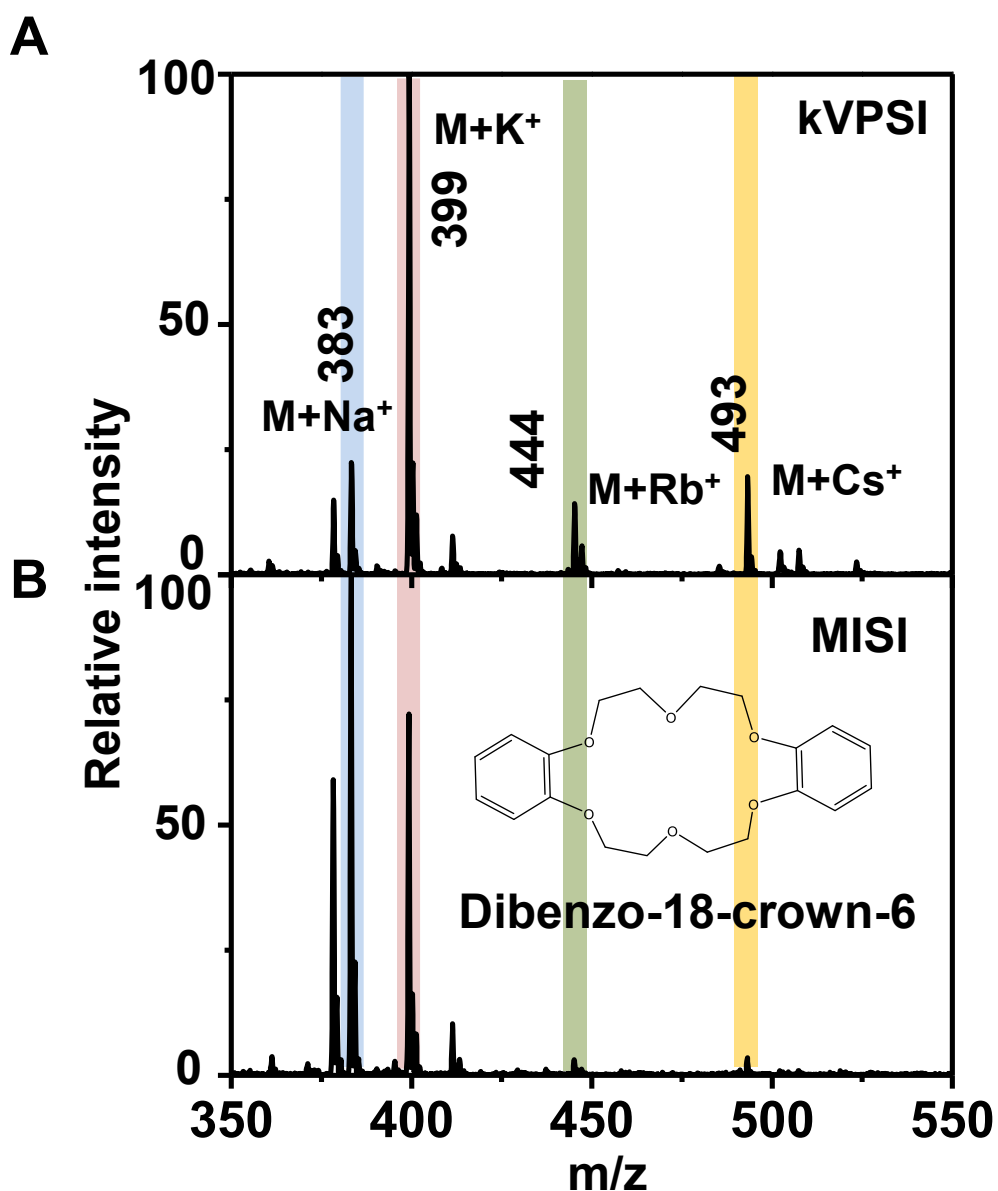


**Figure S14.** Comparative mass spectrum using A) kVPSI and B) MISI of ion encapsulation reaction between alkali metal ions with dibenzo-18-crown-6. The kVPSI mass spectrum is recorded for the bulk reaction. Inset of Figure B shows the molecular structure of the crown ether.



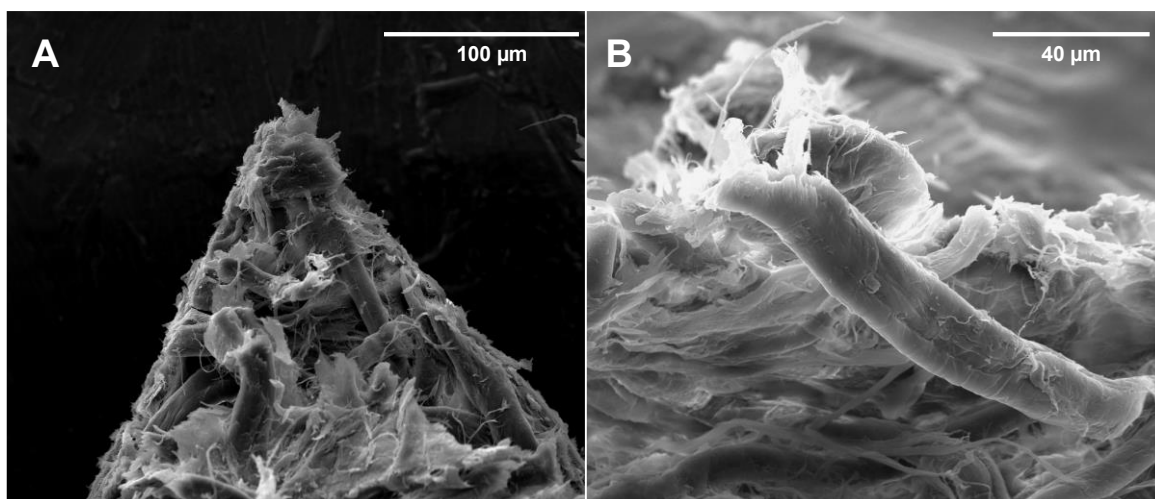


**Figure S15.** SEM images of paper surface. The scale bar is shown at the top of the images.

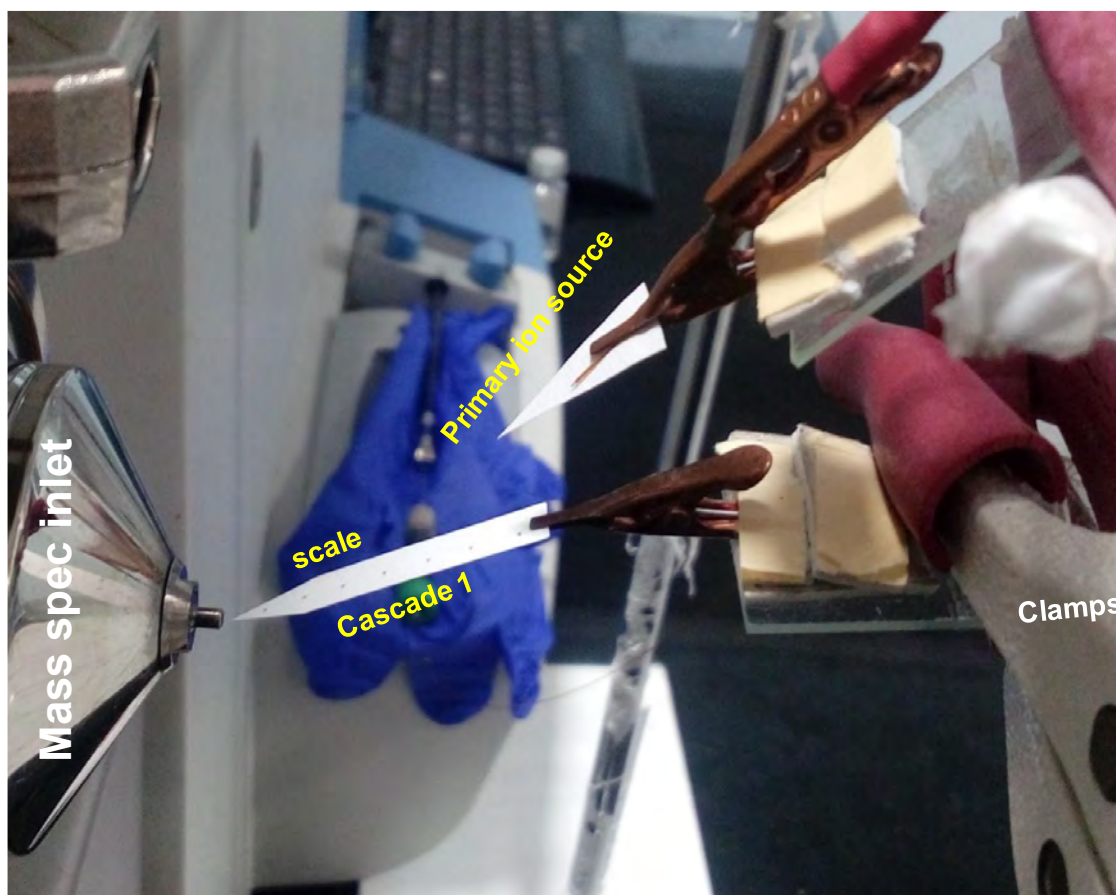


**Figure S16.** Photograph of the setup for the measurement of encapsulation kinetics. Marks over the second paper are to provide a measure of scale.

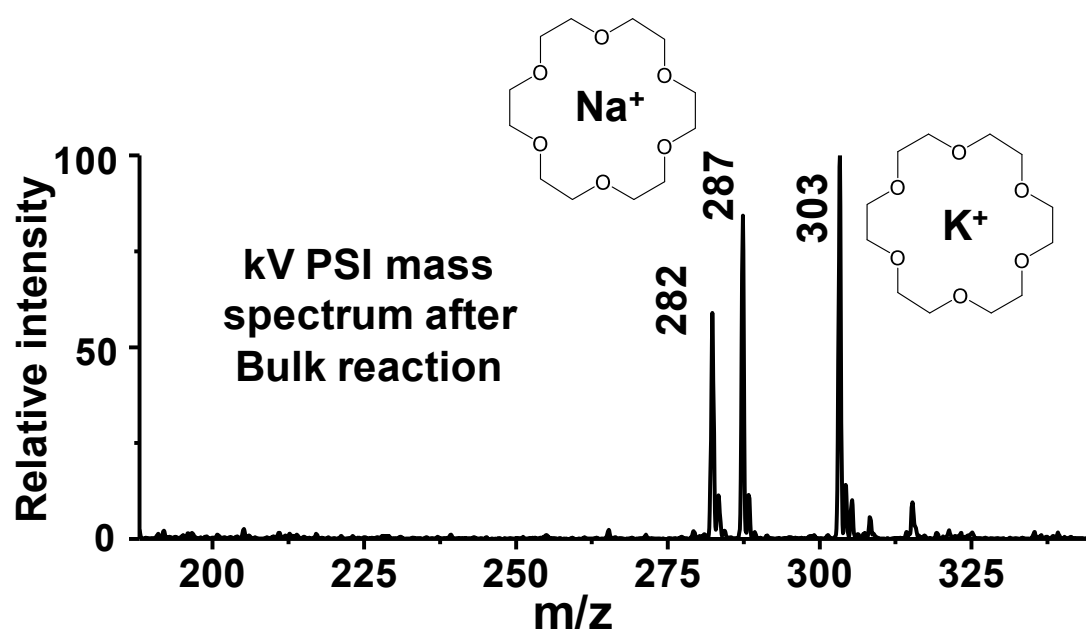


**Figure S17.** kVPSI mass spectrum of the bulk reaction. Intensity ratio of peak at  $m/z$  303 and 287 is 119 %. The final concentration of each reagent was 10  $\mu\text{M}$  in water. The reaction mixture was kept at room temperature for 15 min before the mass spectrometric measurement.

## Supporting information 2.

### Fluid terminal velocity-

**Experimental details-** The fluid terminal velocity over the paper surface was measured by measuring the time to flow a liquid due to the capillary action of the paper. The experiment was conducted on a labelled paper, as shown in Figure S18. The pencil marks do not interfere with the fluid flow. The flow was initiated using a fused silica capillary by flowing methanol containing some R6G in it. R6G was added to visualise the system. The flow rate was set to 100  $\mu\text{L}/\text{min}$  using a syringe and a pump. Three independent experiments gave time as 2.54, 2.60 and 3.20 s to travel a distance of 1 cm. The average time taken was 2.78 s. The velocity was found to be 0.36 cm/s.

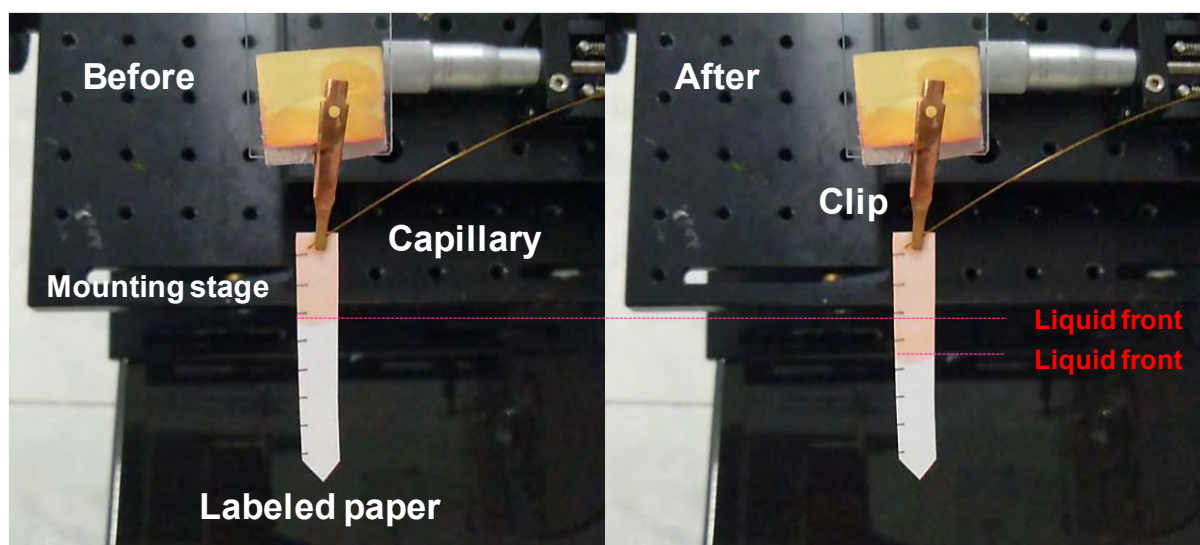


**Figure S18.** Optical images of the fluid terminal velocity experiment. The change in the liquid front is clearly visible and indicated in red trace. The paper has marks to indicate to scale. each gap in the paper corresponds to 1 cm. The flow rate is set to 100  $\mu\text{L}/\text{min}$ . The average terminal velocity of three measurements was 0.36 cm/s.

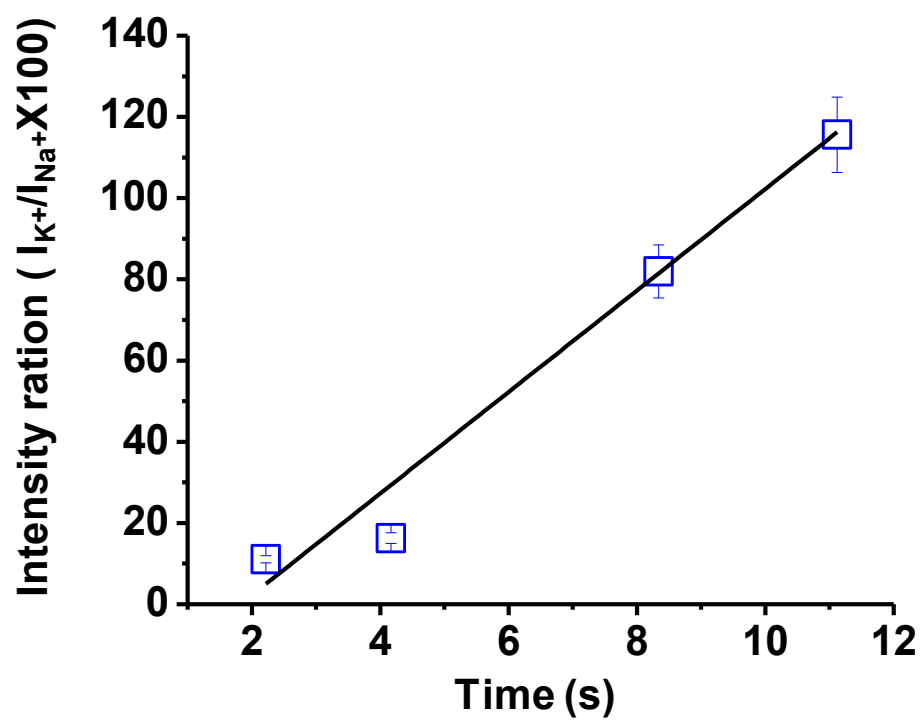


**Figure S19.** Mass spectral intensity ratio of  $K^+$  to  $Na^+$  added peaks of 18-crown-6 vs time.

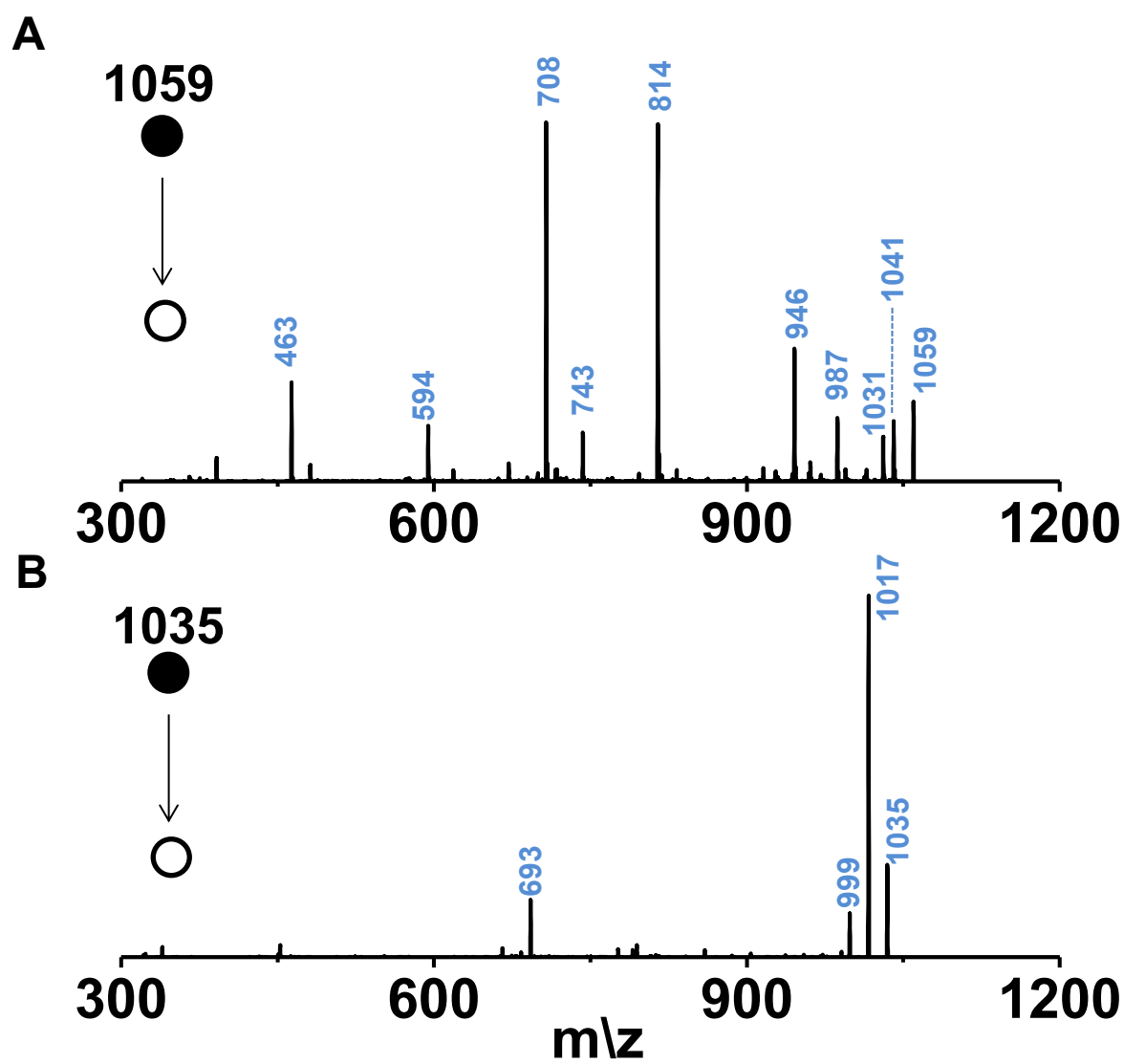


**Figure S20.** MS/MS spectrum of the peaks: A)  $m/z$  1059 in positive-ion mode and B)  $m/z$  1035 in negative-ion mode. The peaks are labeled in blue.



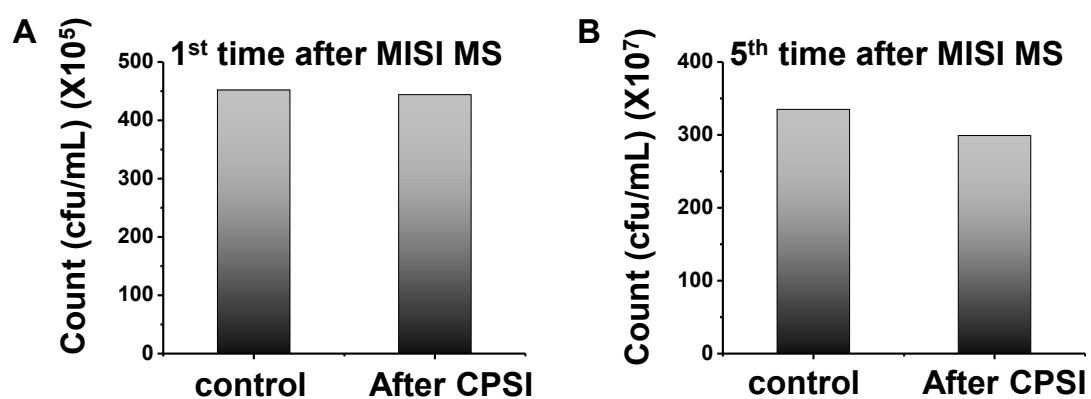


**Figure S21.** Effect of MISI on bacterial viability after A) 1st time and B) 5th time measurements. Bars represents the colony-forming units of the bacteria over the paper surface in control vs MISI-measured sample. Each measurement was conducted for 1-2 min and the paper was held for 10 min at rest in between the mass spec measurements.



**Figure S22.** Optical image of the petri dish containing three triangularly cut filter papers after 5-time measurements of bacterial lipids using MISI MS. Samples were incubated for 24 hrs after MISI measurements. Bacteria used for this image was *B. subtilis*.

# Evaluating the Impact of Tailored Water Wettability on Performance of CO<sub>2</sub> Capture

Adil Majeed Rather,<sup>†</sup> Pillalamarri Srikrishnarka,<sup>†</sup> Avijit Baidya, Arpita Shome, Thalappil Pradeep,\* and Uttam Manna\*



Cite This: <https://dx.doi.org/10.1021/acsaem.0c01603>



Read Online

ACCESS |



Metrics & More



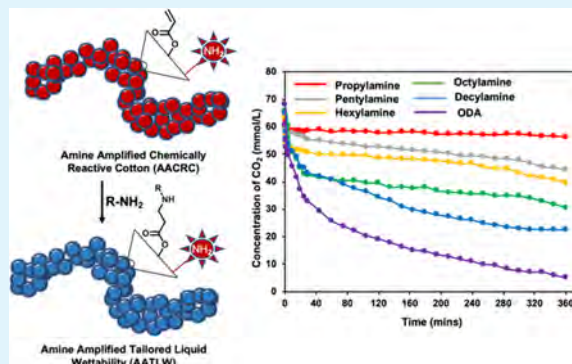
Article Recommendations



Supporting Information

**ABSTRACT:** The growing emission of CO<sub>2</sub> is a severe cause of concern due to its adverse impact on the environment and climate change worldwide. In the past, various approaches, including synthesis of porous materials and amino modifications, were adopted for efficient and direct separation of CO<sub>2</sub> from flue gas. Recently, hydrophobicity has been introduced to protect some of the highly potent porous materials and membranes from high humidity and aqueous exposures. While these approaches remained successful in removing CO<sub>2</sub> from flue gas, the exact role of hydrophobicity towards CO<sub>2</sub> separation is not yet validated in the literature. In this current study, an amine-amplified chemically reactive coating on fibrous cotton has been unprecedentedly developed for facile tailoring of different water wettability through the 1,4-conjugate addition reaction under ambient conditions. Further, these amine-amplified interfaces having tailored water wettability were extended to investigate independently the role of: (a) amine amplification and (b) hydrophobicity on the performance of CO<sub>2</sub> separation at room temperature and atmospheric pressure. The increased hydrophobicity on the amine-amplified interface played an important role in improving the CO<sub>2</sub> uptake from 24 mmol/L (water contact angle (WCA) of 86°) to 63 mmol/L (WCA of 151°). However, superhydrophobic coating that lacked the amine amplification process displayed a poor (7 mmol/L) CO<sub>2</sub> separation performance. Thus, controlled amalgamation of amine amplification and bioinspired superhydrophobicity in fibrous cotton lead to a synergistic impact towards efficient CO<sub>2</sub> separation at ambient temperature and pressure, irrespective of the level of humidity present during the course of the experiments. Thus, this current study would allow to design a more potent CO<sub>2</sub> removal material by strategic association of porosity, amine modulation, and liquid wettability.

**KEYWORDS:** reactive superhydrophobicity, amine amplification, chemically reactive, CO<sub>2</sub> separation, tailored wettability



## INTRODUCTION

Industrial revolution remains instrumental for the advancement of human civilization; however, the uncontrolled management of different forms of industrial wastes leads to various severe environmental pollutions, which has an adverse impact on climate and different ecosystems. For example, the rapidly growing emission of CO<sub>2</sub> due to excessive burning of fossil fuels, deforestation, vehicular and industrial exhausts, etc., has an immense catastrophic impact on the environment and climate.<sup>1,2</sup> In the past, various approaches were adopted to combat this existing severe challenge.<sup>3–6</sup> However, the direct capture of CO<sub>2</sub> from flue gas appears to be a more practical and promising approach.<sup>6</sup> In this process, different porous organic/inorganic nanomaterials were commonly decorated with amines for increasing the efficiency of CO<sub>2</sub> removal from air due to the strong and inherent affinity of the amines towards CO<sub>2</sub> gas.<sup>7–12</sup> However, the performance of many such materials varied depending on the level of humidity present during the proof of concept demonstrations.<sup>9–11</sup> In fact, the

amine modifications rendered the reported materials highly hydrophilic, which is likely to promote condensation of humid air in the reported material. Thus, the performance of CO<sub>2</sub> separation is expected to vary depending on the humidity in the surroundings.<sup>12–14</sup> For instance, a humidity-dependent swing in the CO<sub>2</sub> capture has been reported in the literature.<sup>15</sup> Thus, the design of a material for direct capture of CO<sub>2</sub> at ambient pressure and temperature, irrespective of the level of humidity, would be important for practical applications.

In the past, the design of highly porous materials remained an obvious strategy to separate CO<sub>2</sub> from flue air.<sup>16–19</sup> In this context, metal–organic frameworks (MOFs), which are

Received: July 7, 2020

Accepted: October 5, 2020

developed by integrating water-sensitive coordination bonds, emerged as a prospective approach for capturing CO<sub>2</sub> at high pressure.<sup>16–19</sup> However, the poor durability of such materials under humid conditions and other practically relevant circumstances is a major concern.<sup>13,14</sup> Recently, few special designs were introduced to improve the stability of the MOF, where hydrophobicity was adopted following modification of ligands and depositing a protective layer on top.<sup>20–29</sup> Another important material, that is, a CO<sub>2</sub> capturing membrane,<sup>30–35</sup> has been rationally decorated with bioinspired superhydrophobicity to prevent unwanted blocking of active absorption sites, where the extreme water repellence restricted the wetting of membranes by liquid water even in the presence of high humidity.<sup>30–35</sup> However, a detailed and systematic investigation of (a) amine modification and (b) tailoring hydrophobicity on the CO<sub>2</sub> separation performance is unprecedented in the literature. Moreover, such comprehensive investigation is likely to pave the way for designing a sustainable and eco-friendly approach for direct and unperturbed capture of CO<sub>2</sub> at ambient temperature and pressure, irrespective of the level of relative humidity.

Recently, a clay-based superhydrophobic coating was introduced on a fibrous filter paper, where 3-(2-aminoethylaminopropyltrimethoxysilane) was used to decorate the coating with residual amine groups.<sup>36</sup> The adsorption capacity was found to be around 10.90 mmol/L/g after 8 h of CO<sub>2</sub> exposure under ambient conditions; however, this separation performance varied depending on the level of humidity during the course of the experiment.<sup>36</sup> In this current study, a naturally abundant fibrous substrate, that is, cotton ball, has been decorated with a porous and chemically reactive polymeric coating to tune the water wettability through the 1,4-conjugate addition reaction between amine and residual acrylate moieties under ambient conditions. The chemically reactive coating (CRC) loaded with residual acrylate groups was first treated with the polymer, i.e. branched polyethylenimine (BPEI) for amine amplification, prior to treat with primary amine-containing small molecules (e.g. propylamine, pentylamine, hexylamine, octylamine, decylamine, and octadecylamine), where the length of the hydrocarbon tail of primary amine-containing small molecules allowed to tune the water wettability in the synthesized material. The amine-amplified chemically reactive coating (AACRC) that was post-modified with octadecylamine (ODA) yielded amine-amplified superhydrophobic cotton (AASHC). The synthesized AASHC lowered the CO<sub>2</sub> level with an adsorption capacity of 63 mmol/L over 6 h at room temperature and pressure. Interestingly, a very similar superhydrophobic cotton that lacked the amine amplification process displayed poor CO<sub>2</sub> separation performance under the same experimental conditions. Thereafter, the controlled tailoring of water wettability on the amine-amplified interface through the 1,4-conjugate addition reaction allowed to examine the impact of hydrophobicity on CO<sub>2</sub> separation performance under ambient conditions. The efficiency of CO<sub>2</sub> separation was compromised on lowering the hydrophobicity. Moreover, the CO<sub>2</sub> separation performances for hydrophobic and superhydrophobic amine-amplified cotton were noticed to be completely different at high humidity. Furthermore, the CO<sub>2</sub> separation ability of amine-amplified superhydrophobic cotton remained independent of the initial concentration of CO<sub>2</sub> present in the model flue air.

## ■ EXPERIMENTAL SECTION

**Materials.** Branched polyethylenimine (PEI; MW ≈ 25 kDa), dipentaerythritol penta-acrylate (5Acl, MW = 524.21 g/mol), propylamine, pentylamine, hexylamine, octylamine, decylamine, and octadecylamine were purchased from Sigma-Aldrich (Bangalore, India). Absolute ethyl alcohol (CAS 64-17-5; lot 1005150) was purchased from Tedia Company (United States of America). Reagent-grade THF was purchased from RANKEM (Maharashtra). Methylene blue was acquired from Sigma-Aldrich (Bangalore, India). A Lab Companion vacuum desiccator, UV blocking (Amber 6 L) was purchased from Tarson (India). CO<sub>2</sub> concentration was measured using a CO<sub>2</sub> meter Chauvin Arnoux (C.A 1510, Air Quality Measurement). Cotton was obtained from a local medical shop in Guwahati City (Assam, India). Milli-Q grade water was used for all experiments.

**General Considerations.** Glass vials that were used for preparing the polymer solutions were washed with acetone and ethanol prior to use. FTIR spectra were recorded using a PerkinElmer instrument under ambient condition by preparing the KBr pellets. Scanning electron microscopy images were obtained using a Sigma Carl Zeiss scanning electron microscope (samples were coated with a thin layer of gold prior to imaging). The water contact angles were measured using a KRÜSS drop shape analyzer-DSA25 instrument with an automatic liquid dispenser under ambient conditions. Change in the CO<sub>2</sub> concentration was measured using a CO<sub>2</sub> meter. Digital pictures were acquired using a Canon PowerShot SX420 IS digital camera.

**Preparation of Amine-Amplified Superhydrophobic Cotton.** First of all, the naturally abundant medical cotton (1 gram) was rinsed with ethanol and acetone to remove the deposited contaminants. Next, the precleaned cotton was placed in BPEI solution (10 mg/mL ethanol) for 2 h. Afterward, the BPEI-modified cotton was placed in the chemically reactive nanocomplex (CRNC) solution, which was prepared by mixing ethanolic solutions of 5-Acl (132.5 mg/mL) and BPEI (50 mg/mL) with an appropriate composition (5Acl/BPEI = 10:3) for 1 h. The deposition of the CRNC on the fibrous cotton yielded a chemically reactive coating (CRC). Next, the CRC was washed with ethanol to remove the unreacted and loosely bound nanocomplexes and was dried under ambient conditions. Thereafter, the CRC was post-modified with BPEI for amine amplification. The BPEI-treated CRC is denoted as amine-amplified chemically reactive coating (AACRC). Finally, the AACRC was exposed to solution (5 mg/mL in THF) of octadecylamine (ODA) for 8 h for adopting superhydrophobicity. After the ODA treatment, the synthesized material was washed thoroughly with THF for 1 h to remove the unreacted ODA molecules and allowed to air-dry under ambient conditions. Then, the water wettability of the as-modified cotton pieces was examined with digital images and contact angle measurement. This post-covalent modification of AACRC provided the amine-amplified superhydrophobic cotton (AASHC).

Similarly, AACRC was post-modified with lower analogues of ODA, including propylamine, pentylamine, hexylamine, octylamine, and decylamine for tailoring water wettability. After post-modification with these selected amine-containing small molecules, cotton pieces were rinsed with THF for 1 h and were dried under ambient conditions. After successful post-modification with different amines, the wettability of the cotton pieces was examined by measuring the water contact angle. Meanwhile, in the absence of the amine amplification process, the direct post-covalent modification of CRC with octadecylamine yielded another superhydrophobic interface, which is labeled as without amine-amplified superhydrophobic cotton (WOAASHC).

**Carbon Dioxide (CO<sub>2</sub>) Separation.** To understand the CO<sub>2</sub> adsorption capability of the AASHC, a Tarson 6 L desiccator was taken in which 1 g of uncoated and modified cotton along with the CO<sub>2</sub> sensor was placed. Thereafter, a desired amount of 99% pure CO<sub>2</sub> was introduced into the desiccator using a syringe and the change in CO<sub>2</sub> concentration was monitored using a CO<sub>2</sub> sensor for 24 h. These changes were recorded using a data logger present inside



**Scheme 1.** (A) Chemical Reaction of the 1,4-Conjugate Addition Reaction between Representative Amine and Acrylate Groups. (B) Chemical Structure of Branched Polyethylenimine (BPEI). (C) Schematic Illustration of Chemically Reactive Nanocomplex (CRPNC) Loaded with Residual Acrylate, Which Was Synthesized by Mixing BPEI and Dipentaerythritol Penta-acrylate (5Acl). (D, E) Illustrating the Deposition of CRPNC on the Fibrous Cotton That Yielded The Chemically Reactive Coating (CRC). (E, F) Schematic Representation Depicting the Amine Amplification Process of CRC through the 1,4-Conjugate Addition Reaction for Achieving Amine-Amplified Chemically Reactive Coating (AACRC; F). (G) Post-Covalent Modification of AACRC with Octadecylamine (ODA) Yielded Amine-Amplified Superhydrophobic Cotton (AASHC). (E, H) Post-Modification of CRC (E) with ODA Provided Superhydrophobic Coating that Lacked the Amine Amplification Step, and Such a Material Is Denoted as Without Amine-Amplified Superhydrophobic Cotton (WOAASHC, H)

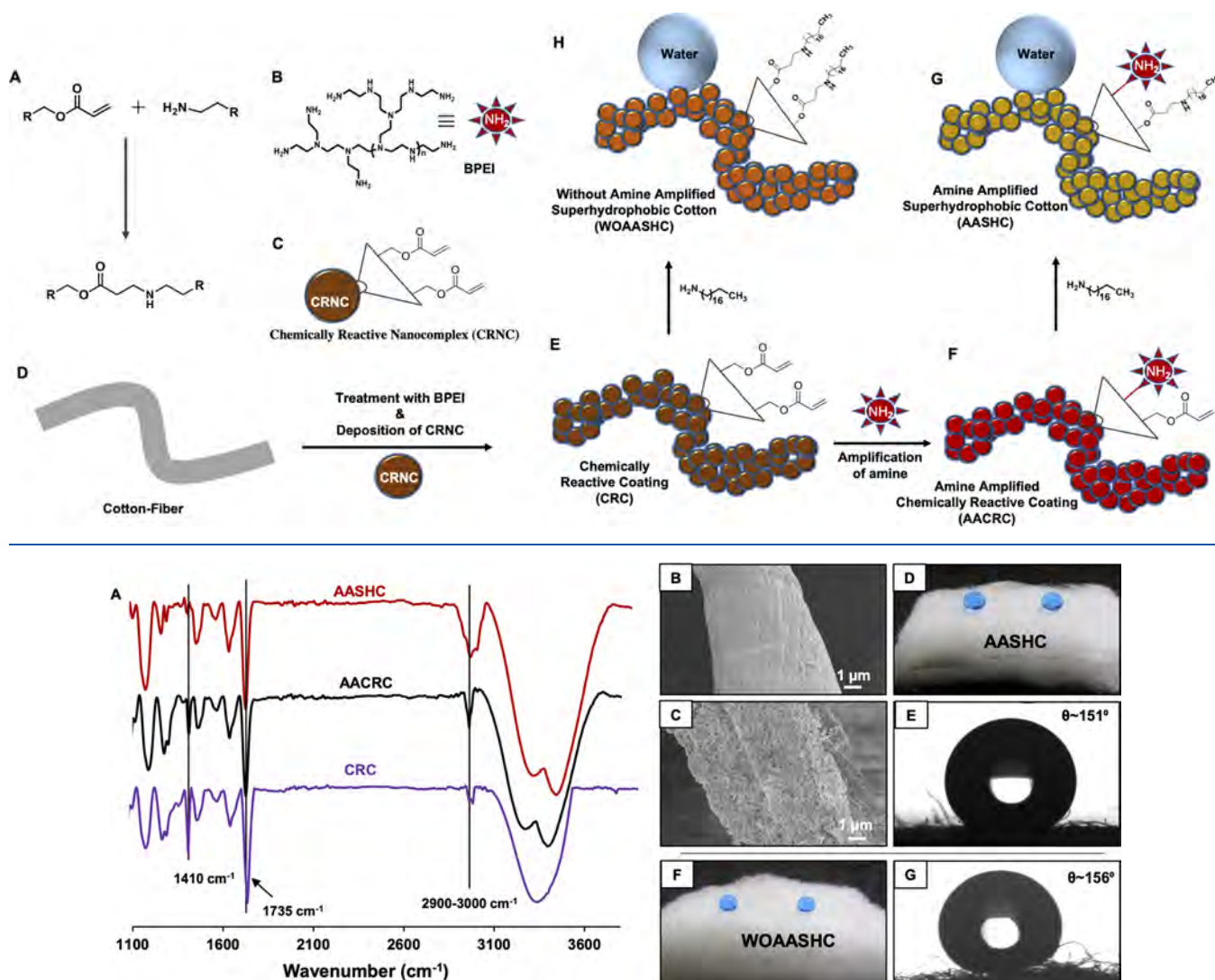


**Figure 1.** (A) FTIR spectra of chemically reactive coating (CRC: violet), amine-amplified chemically reactive coating (AACRC: black), and amine-amplified superhydrophobic cotton (AASHC: red). The peaks at 1409 and 1735 cm<sup>-1</sup> correspond to symmetric deformation for the C–H bond of the β-carbon of the vinyl group and the carbonyl stretching, respectively. (B, C) FESEM images of pristine cotton (B) and chemically reactive coating (C) on fibrous cotton. (D–G) Digital images (D, F) and contact angle images (E, G) of amine-amplified superhydrophobic cotton (AASHC; D, E) and without amine-amplified superhydrophobic cotton (WOAASHC; F, G) respectively.

the sensor and later transferred to PC. Afterwards, this cotton piece was placed at 60 °C in a conventional oven for 2 h for desorption of the adsorbed CO<sub>2</sub> gas. Moreover, the CO<sub>2</sub> separation studies for other cotton pieces including pristine cotton and superhydrophobic cotton were performed in a similar manner.

## RESULTS AND DISCUSSION

**Synthesis of Amine-Amplified Chemically Reactive Coating (AACRC).** In the recent past, interfaces consisting of residual amine groups were found to be an effective approach

for separating CO<sub>2</sub> from flue air.<sup>16–19</sup> In this context, branched polyethylenimine (BPEI) has been widely used for modifying various metal oxides and zeolites for demonstrating the CO<sub>2</sub> separation performance.<sup>16–19</sup> However, the controlled tailoring of hydrophobicity on amine-modified interfaces and its impact on the CO<sub>2</sub> separation process at practically relevant settings are rare in the literature. In our current design, an amine-amplified chemically reactive coating has been introduced for (a) tailoring of water wettability and (b) investigating its impact on CO<sub>2</sub> separation performance. In the recent past, our

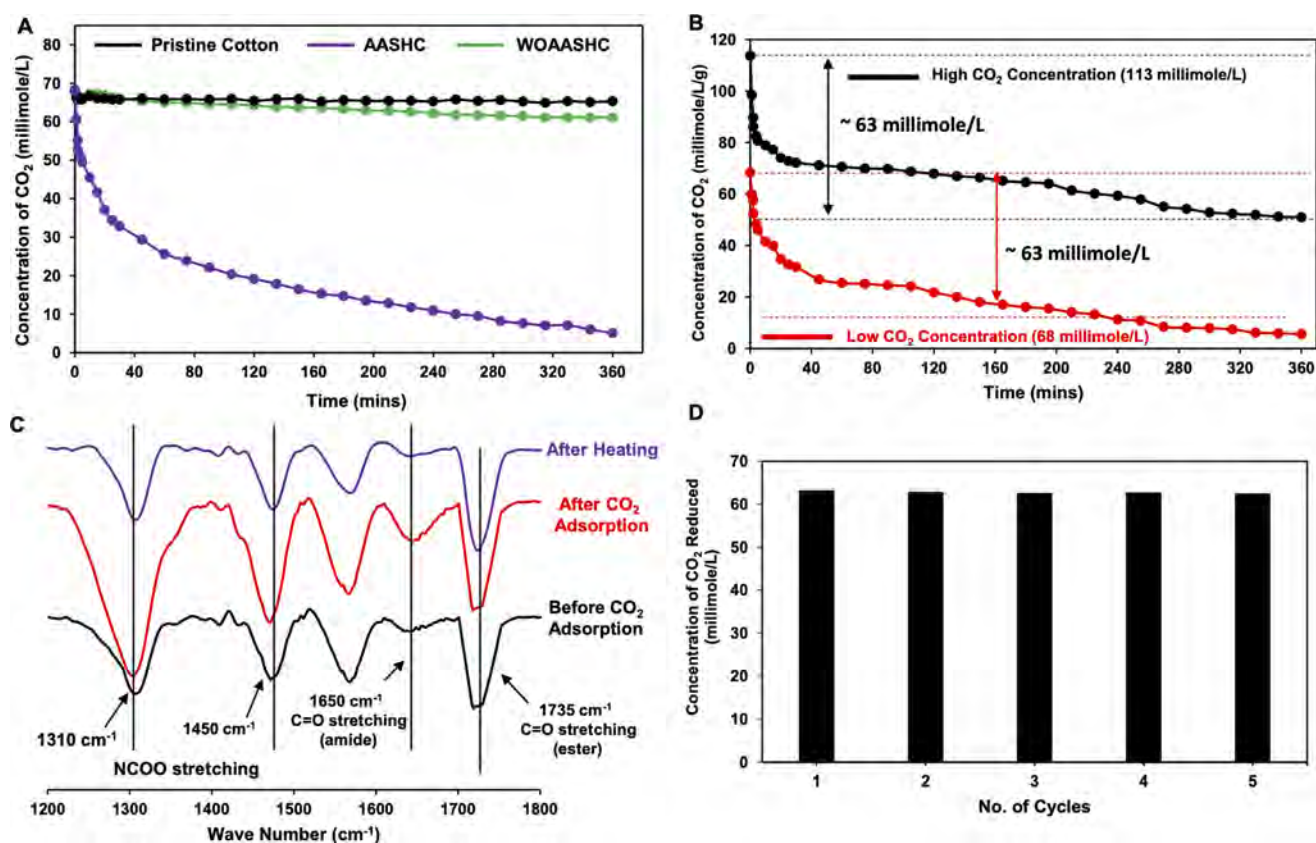


**Figure 2.** (A) Plot illustrating the reduction in the concentration of CO<sub>2</sub> by pristine cotton (black), without amine-amplified superhydrophobic cotton (WOAASHC: green), and amine-amplified superhydrophobic coating (AASHC: violet). (B) Plot displaying the CO<sub>2</sub> separation performance using AASHC at high (black) and low (red) concentrations of CO<sub>2</sub>. (C) FTIR spectra of amine-amplified superhydrophobic cotton before (black) and after (red) performing CO<sub>2</sub> separation, whereas the violet curve accounts for the IR spectrum after desorption (violet) of CO<sub>2</sub> at 60 °C for 2 h. (D) Plot illustrating the recyclability of AASHC in separating CO<sub>2</sub> for five consecutive cycles.

research group has extended the 1,4-conjugate addition reaction (Scheme 1A) between BPEI (Scheme 1B) and dipentaerythritol penta-acrylate (5AcI) to synthesize chemically reactive polymeric nanocomplex (CRPNC, Scheme 1C) loaded with residual acrylate group.<sup>37,38</sup> In the past, the spray deposition and layer-by-layer deposition of this CRPNC provided chemically reactive coatings for customizing different water and oil wettability through appropriate post-covalent modification with the selected small molecules.<sup>39–42</sup> Further, this CRPNC was successfully deposited on fibrous cotton to develop a chemically reactive coating (CRC, Scheme 1D,E), where the post-covalent modification of the coating with octadecylamine (ODA) provided durable superhydrophobicity, which was extended for remediation of oil spillages following an environment-friendly selective absorption and filtration approach.<sup>43</sup> In contrast to these earlier designs, a facile and covalent amine amplification process has been integrated to this CRPNC-derived chemically reactive coating through post-covalent modification with BPEI polymer (Scheme 1E,F). This coating is labeled as AACRC in the rest of the text. Next, the synthesized AACRC was modified with a hydrophobic small molecule (i.e. ODA) through the 1,4-conjugate addition reaction, to achieve amine-amplified superhydrophobic cotton (AASHC, Scheme 1G). The deposition of CRPNC on a fibrous substrate followed by the amine amplification process prior to ODA treatment was characterized through FESEM and FTIR analysis, as shown in Figure 1A–C and Figure S2. The characteristic IR peaks at

1410 cm<sup>-1</sup> and 1735 cm<sup>-1</sup> represent the symmetric deformation of the  $\beta$ -carbon of the vinyl group and the carbonyl stretching, respectively, revealing the presence of residual acrylate groups in the CRPNC deposited cotton, as shown in Figure 1A (violet spectrum). Further, the FESEM images of the uncoated (Figure 1B) and coated (Figure 1C) fibrous cotton confirmed the successful deposition of CRPNC, where the random aggregation of granular domains in CRC provided the essential hierarchical topography to achieve the bioinspired water wettability. The residual acrylate groups in the CRC further allowed the covalent immobilization of BPEI polymer, as confirmed with FTIR analysis. After the treatment of CRC with BPEI polymer, a significant change in the IR peak was observed in the region of 3200–3600 cm<sup>-1</sup>, where two prominent humps indicate the inclusion of primary amines from BPEI. Further, the IR peak intensity at 1410 cm<sup>-1</sup>, which corresponded to the symmetric deformation of the  $\beta$ -carbon of the vinyl group, decreased significantly with respect to the normalized carbonyl stretching at 1735 cm<sup>-1</sup>, as shown in Figure 1A (black spectrum). During this amine amplification process, ~28% of the total residual acrylate groups in CRC is consumed on the reaction with the amines of BPEI polymer through the 1,4-conjugate addition reaction. The remaining acrylate groups in AACRC were post-modified with selected small molecules for adopting the desired extreme water repellency. The FTIR analysis after the reaction of AACRC with ODA revealed the significant depletion of the IR signature for the  $\beta$ -carbon of the vinyl group at 1409 cm<sup>-1</sup> with respect



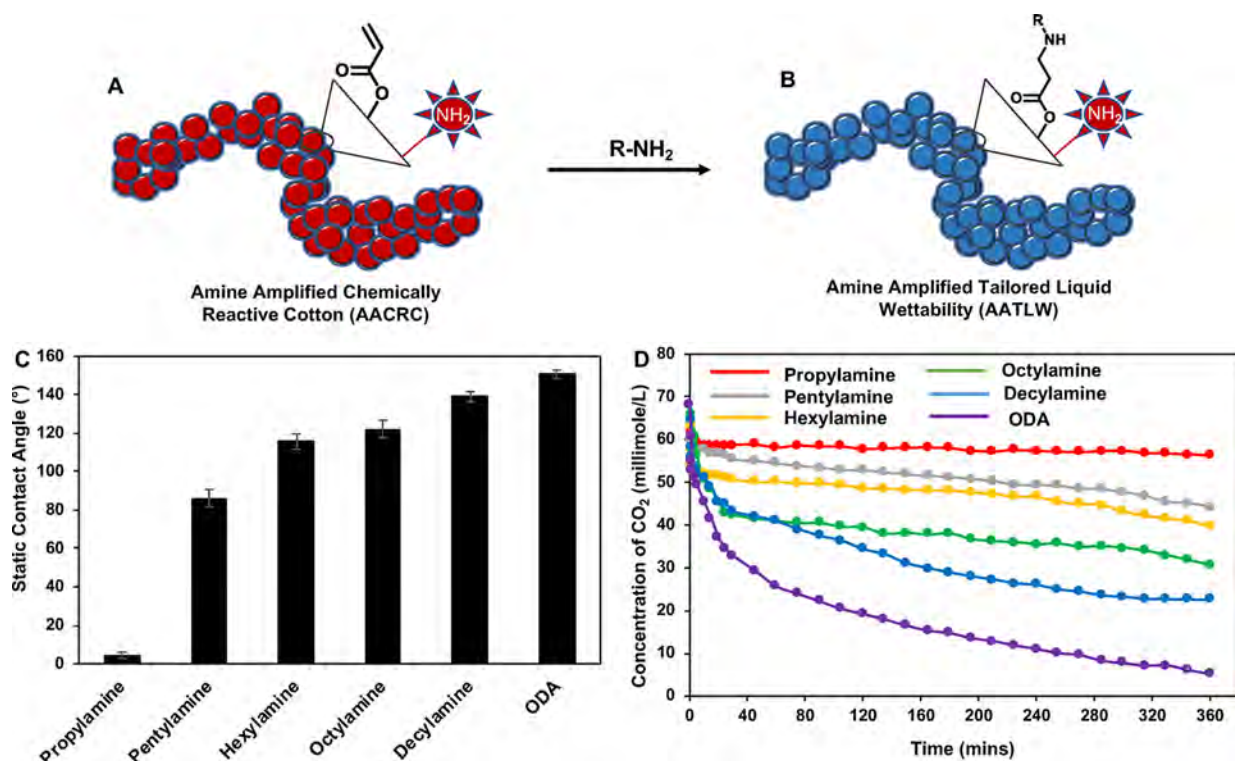


**Figure 3.** (A, B) Schematic illustration of amine-amplified chemically reactive cotton (AACRC; A) that was post-modified with amine-containing small molecules (B) through the 1,4-conjugate addition reaction for tailoring water wettability. (C) Plot displaying the static contact angle of beaded water droplets on amine-amplified chemically reactive coating after post-modification with different amine-containing small molecules including propylamine, pentylamine, hexylamine, octylamine, decylamine, and ODA. (D) Plot accounting for the CO<sub>2</sub> separation performance of AACRC after post-modification with different amine-containing small molecules including propylamine (red), pentylamine (gray), hexylamine (yellow), octylamine (green), decylamine (blue), and ODA (violet).

to the normalized carbonyl stretching at  $1735\text{ cm}^{-1}$ . This simple study confirmed the successful post-chemical modification of AACRC with selected small molecules, as shown in Figure 1A (red spectrum). The water wettability was monitored at each step, and AACRC remained superhydrophilic with a water contact angle of  $0^\circ$  as similar to uncoated cotton, as shown in Figure S1. However, after ODA treatment, the same AACRC displayed superhydrophobicity, where water droplets were beaded with a contact angle of  $151^\circ$ , as shown in Figure 1D,E. This coating on fibrous cotton will be denoted as amine-amplified superhydrophobic cotton (AASHC) for further discussion. During this amine amplification process, CRC was exposed to different concentrations of BPEI, prior to treatment with ODA. Beyond a certain concentration ( $125\text{ mg/mL}$ ) of BPEI treatment, AACRC failed to display superhydrophobicity, as shown in Figure S3. The amine amplification was performed with  $125\text{ mg/mL}$  concentration of BPEI polymer solution for the rest of the CO<sub>2</sub> separation experiments. As expected, after ODA treatment, the as-synthesized CRC, without any amine amplification, also displayed superhydrophobicity with a water contact angle of  $\sim 156^\circ$ , as shown in Figure 1F,G; and this coating on fibrous cotton was denoted as without amine-amplified superhydrophobic cotton (WOAASHC).

**Investigation on CO<sub>2</sub> Separation Performances by AASHC and WOAASHC.** In this current study, two distinct superhydrophobic coatings with (AASHC) and without (WOAASHC) amine amplification were extended to examine the role of embedded biomimicked superhydrophobicity on the performance of CO<sub>2</sub> separation. For direct comparison,

uncoated cotton, WOAASHC, and AASHC, with the same weight ( $1\text{ g}$ ), were individually exposed to a constant concentration ( $68\text{ mmol/L}$ ) of CO<sub>2</sub> gas at a relative humidity of 40% and ambient temperature and pressure. Over time, AASHC gradually lowered the concentration of CO<sub>2</sub> in the experimental system, and after 6 h, the concentration of CO<sub>2</sub> reduced from 68 to  $5\text{ mmol/L}$  (Figure 2A). However, under similar experimental conditions, both uncoated cotton and WOAASHC failed to perform, as evident from Figure 2A. Further, the CO<sub>2</sub> separation performance of AASHC was compared at settings having different initial concentrations of CO<sub>2</sub>. As a proof of concept demonstration, AASHC was separately exposed to two different concentrations of CO<sub>2</sub> including 68 and  $113\text{ mmol/L}$ . After 6 h of exposure, AASHC lowered the CO<sub>2</sub> concentration with equal efficiency ( $63\text{ mmol/L}$ ), irrespective of differences in the initial concentration of CO<sub>2</sub>, as shown in Figure 2B. Further, AASHC continued to separate CO<sub>2</sub> over 24 h, in contrast to WOAASHC, as shown in Figure S4. After 24 h, the reduction values in the concentration of CO<sub>2</sub> by WOAASHC and AASHC were 10 and  $87\text{ mmol/L}$ , respectively. To understand the mechanism of the efficient separation of CO<sub>2</sub> by AASHC, an FTIR analysis was performed on AASHC before and after conducting the CO<sub>2</sub> capture, as shown in Figure 2C. With respect to the normalized IR signature at  $1735\text{ cm}^{-1}$  for the ester carbonyl stretching, prominent appearance of IR peaks for the C–N ( $1310\text{ cm}^{-1}$ ) and amide C=O stretching ( $1650\text{ cm}^{-1}$ ) revealed chemisorption of CO<sub>2</sub> on AASHC through a mutual reaction between the residual amine and CO<sub>2</sub> gas. Further, these intense IR signatures for the C–N ( $1310\text{ cm}^{-1}$ )

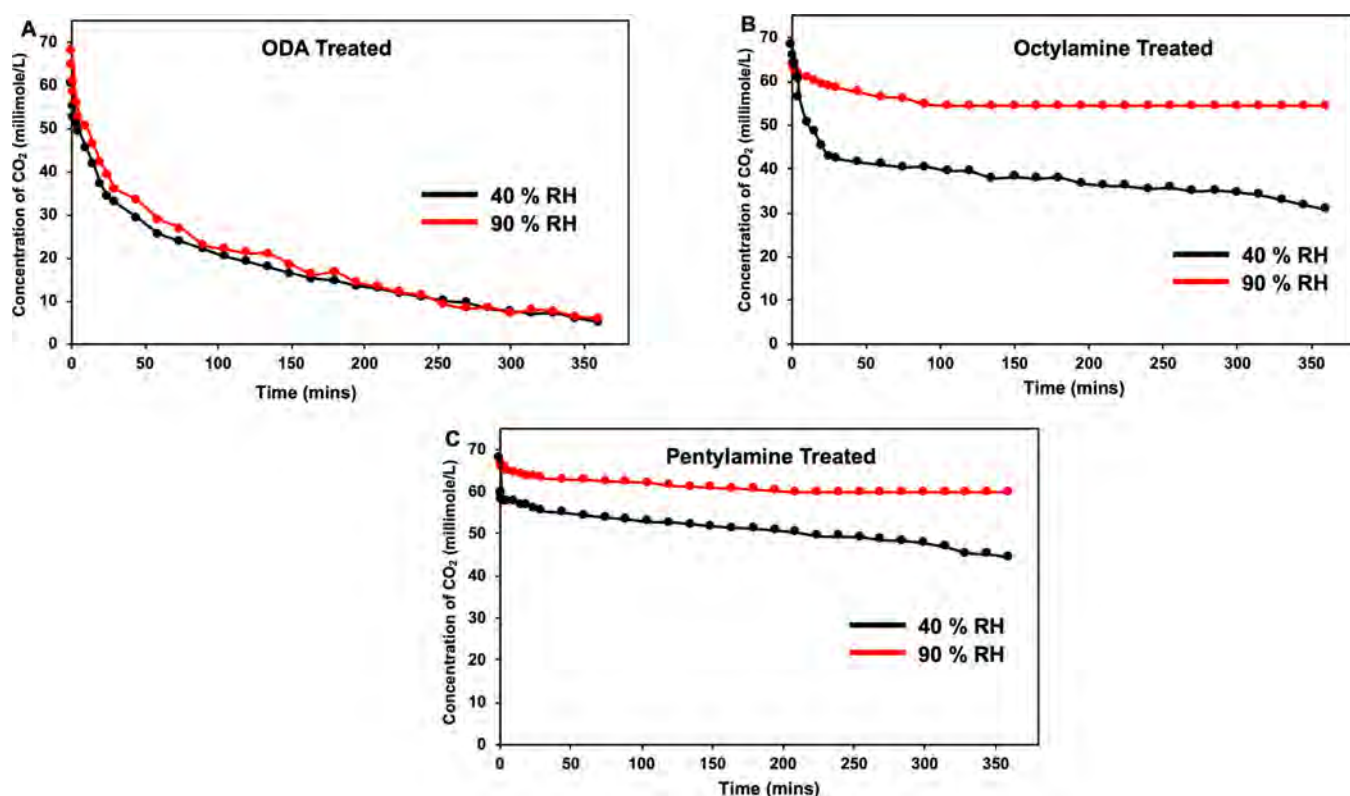


**Figure 4.** (A–C) Plots illustrating the reduction in the concentration of CO<sub>2</sub> in different humid conditions including 40% (black) and 90% (red) for amine-amplified chemically reactive coatings (AACRC) that were post-modified with ODA (A), octylamine (B), and pentylamine (C).

and amide C=O stretching depleted significantly with respect to the ester carbonyl stretching at  $1735\text{ cm}^{-1}$  after heating cotton at  $60\text{ }^{\circ}\text{C}$  for 2 h (violet spectrum; Figure 2C). This study suggested the successful desorption of CO<sub>2</sub> from AASHC. Interestingly, the same AASHC was successfully and repetitively used for separating CO<sub>2</sub> for five consecutive cycles, as shown in Figure 2D, without compromising its separation performance. At the end of each cycle, the AASHC was treated at  $60\text{ }^{\circ}\text{C}$  for 2 h for the desorption of CO<sub>2</sub> gas. Further, this repetitive adsorption and desorption of CO<sub>2</sub> has no impact on the integrity and antiwetting property of the AASHC. Hence, this study implies that the as-synthesized AASHC could be a potential candidate for practical applications owing to its highly durable and recyclable property.

**Effect of Change in Water Wettability on CO<sub>2</sub> Separation Performance.** In the past, few reports have focused on the extremely liquid-repellent interfaces to improve the CO<sub>2</sub> separation performance, where the extreme water repellence emphasized on protecting the CO<sub>2</sub> separating interface from unwanted wetting by the liquid phase.<sup>30–35</sup> However, the impact of different liquid wettability on CO<sub>2</sub> separation performance is yet to be demonstrated in the literature. The residual acrylate groups in the amine-amplified chemically reactive cotton (AACRC) allowed to tailor the liquid wettability by post-modification with various alkyl amines through the 1,4-conjugate addition reaction, as shown in Figure 3A,B. The extent of hydrophobicity was tailored by selecting appropriate alkylamines (i.e., propylamine, pentylamine, hexylamine, octylamine, decylamine, and octadecylamine). The water contact angle gradually enhanced on increasing the hydrocarbon chain length in the selected

alkylamine, as shown in Figure 3C. Afterward, these amine-amplified interfaces having different water wettability were explored for examining the CO<sub>2</sub> separation performance. Interestingly, the CO<sub>2</sub> separation ability significantly compromised on decreasing the hydrophobicity in the amine-amplified interface. For instance, the propylamine-treated AACRC, which is extremely hydrophilic, reduced the concentration of CO<sub>2</sub> by 12 mmol/L over 6 h, whereas the octylamine-treated AACRC, which displayed moderate hydrophobicity with a water contact angle of  $122^{\circ}$ , reduced the concentration of CO<sub>2</sub> by 38 mmol/L over the same time duration (6 h), under an identical experimental setup. However, under similar experimental conditions, the concentration of CO<sub>2</sub> was depleted significantly (63 mmol/L) by AASHC (ODA-treated AACRC) that embedded with biomimicked superhydrophobicity, as shown in Figure 3D. The initial concentration (68 mmol/L) of CO<sub>2</sub> and relative humidity (40%) were kept identical for examining the performance of CO<sub>2</sub> separation by amine-amplified cotton (1 g each) with tailored water wettability. Thus, the reduction in the concentration of CO<sub>2</sub> significantly changed with variation in the water wettability (Figure 3D). Therefore, this study affirms that the change in water wettability indeed has a significant impact on the CO<sub>2</sub> adsorption capability for the amine-amplified interface.

When evaluating CO<sub>2</sub> separation performance for flue gases, the presence of water vapor cannot be overlooked. In the past, various materials including zeolites, ionic liquids, carbon-based materials, and MOFs were explored for CO<sub>2</sub> adsorption. However, many synthesized materials explored in the past for CO<sub>2</sub> adsorption failed to perform on exposure under moist/humid conditions. The adsorption of water vapors into the adsorbent material is known to reduce the CO<sub>2</sub> adsorption

capacity under humid conditions. Therefore, the CO<sub>2</sub> separation performance of AASHC derived from AACRC was compared under low (RH: 10%; Figure S5), moderate (RH: 40%), and high (RH: 90%) humid conditions. The CO<sub>2</sub> separation ability of AASHC at three distinct RH values was found to remain unperturbed, as shown in Figure 4A and Figure S5. However, the same AACRC, that is, post-modified with octylamine, displayed moderate hydrophobicity and became inefficient for separating CO<sub>2</sub> at high relative humidity (RH: 90%), as shown in Figure 4B. Moreover, such depletion of the CO<sub>2</sub> separation performance was observed for pentylamine-treated AACRC (that is, embedded with an even lower WCA  $\approx$  86°) at high relative humidity (RH: 90%), as shown in Figure 4C. Hence, under a highly humid environment, the CO<sub>2</sub> separation performance is tremendously affected on decreasing the hydrophobicity in the amine-amplified interfaces. Such compromise of CO<sub>2</sub> separation at high humidity is likely due to the easy penetration of moisture in the less and moderately hydrophobic amine-amplified cotton; however, the long hydrocarbon tail of the covalently immobilized ODA in the AASHC restricts the condensation of moisture. Thus, the embedded superhydrophobicity merely has any impact on separation of CO<sub>2</sub> (see Figure 2A), but this extreme water repellence displayed an immense impact on the CO<sub>2</sub> uptake—once it is integrated with the amine-amplified interface. Further, the AASHC continued to perform under practically relevant high humid conditions. Therefore, the coexistence of bioinspired superhydrophobicity and amine amplification is important for efficient and uninterrupted CO<sub>2</sub> separation at practically relevant diverse settings.

## CONCLUSIONS

In conclusion, an amine-amplified chemically reactive cotton (AACRC) has been introduced through strategic use of the 1,4-conjugate addition reaction between residual acrylate of CRC and amines of BPEI polymer. The residual acrylate groups in CRC provided facile basis for both (i) associating amine amplification and (ii) tailoring various water wettability, including bioinspired superhydrophobicity. The performance of CO<sub>2</sub> separation was compared for amine-amplified coating that embedded with different water wettability. The CO<sub>2</sub> separation performance was observed to improve with increasing hydrophobicity in the amine-amplified interface, where AASHC that displayed superhydrophobicity was found to be the most efficient in separating CO<sub>2</sub> at ambient temperature and pressure. Thus, improved hydrophobicity on the amine-amplified interface has a positive impact on CO<sub>2</sub> uptake. However, without amine amplification, the superhydrophobicity has merely any impact on CO<sub>2</sub> uptake. Further, this CO<sub>2</sub> separation performance of AASHC remained unperturbed at high relative humidity, irrespective of the initial concentration of CO<sub>2</sub> present in the experimental system. Such a material would be useful in developing a more effective green house facility. Further association of AASHC with an appropriate catalytic component would allow to convert the separated CO<sub>2</sub> to useful chemicals.

## ASSOCIATED CONTENT

### Supporting Information

The Supporting Information is available free of charge at <https://pubs.acs.org/doi/10.1021/acsaem.0c01603>.

Digital images and contact angle images of pristine cotton and amine-amplified superhydrophobic cotton; FESEM images of uncoated cotton, WOAASHC, and AASHC at lower and higher magnifications; digital images and contact angle images of amine-amplified reactive coating after ODA treatment with different concentrations of BPEI; plots illustrating the decrease in concentration of CO<sub>2</sub> by WOAASHC and AASHC over 24 h; and plots illustrating the decrease in concentration of CO<sub>2</sub> by AASHC in different humid conditions (PDF)

## AUTHOR INFORMATION

### Corresponding Authors

**Thalappil Pradeep** – Department of Chemistry, DST Unit of Nanoscience (DST UNS) and Thematic Unit of Excellence (TUE), Indian Institute of Technology Madras, Chennai 600036, India; [orcid.org/0000-0003-3174-534X](https://orcid.org/0000-0003-3174-534X); Email: [pradeep@iitm.ac.in](mailto:pradeep@iitm.ac.in)

**Uttam Manna** – Department of Chemistry and Centre for Nanotechnology, Indian Institute of Technology-Guwahati, Guwahati, Assam 781039, India; [orcid.org/0000-0003-3204-158X](https://orcid.org/0000-0003-3204-158X); Email: [umanna@iitg.ac.in](mailto:umanna@iitg.ac.in)

### Authors

**Adil Majeed Rather** – Department of Chemistry, Indian Institute of Technology-Guwahati, Guwahati, Assam 781039, India

**Pillalamarri Srikrishnarka** – Department of Chemistry, DST Unit of Nanoscience (DST UNS) and Thematic Unit of Excellence (TUE), Indian Institute of Technology Madras, Chennai 600036, India; [orcid.org/0000-0001-5187-6879](https://orcid.org/0000-0001-5187-6879)

**Avijit Baidya** – Department of Chemistry, DST Unit of Nanoscience (DST UNS) and Thematic Unit of Excellence (TUE), Indian Institute of Technology Madras, Chennai 600036, India; [orcid.org/0000-0001-5215-2856](https://orcid.org/0000-0001-5215-2856)

**Arpita Shome** – Department of Chemistry, Indian Institute of Technology-Guwahati, Guwahati, Assam 781039, India

Complete contact information is available at: <https://pubs.acs.org/doi/10.1021/acsaem.0c01603>

### Author Contributions

<sup>†</sup>A.M.R. and P.S. contributed equally to this work. The manuscript was written through contributions of all authors. All authors have given approval to the final version of the manuscript.

### Notes

The authors declare no competing financial interest.

## ACKNOWLEDGMENTS

We acknowledge the financial support from Board of Research in Nuclear Sciences (BRNS) (34/20/31/2016-BRNS, DAE-YSRA) and Ministry of Electronics and Information Technology (grant no. 5(9)/2012-NANO), Government of India. We thank CIF and Department of Chemistry, Indian Institute of Technology-Guwahati, for their generous assistance in executing various experiments and for the infrastructure. A.S. thanks the institute for the Ph.D. scholarship. P.S. thanks IIT Madras for his Ph.D. fellowship.



## REFERENCES

- (1) Anderegg, W. R. L.; Prall, J. W.; Harold, J.; Schneider, S. H. Expert credibility in climate change. *Proc. Natl. Acad. Sci. U. S. A.* **2010**, *107*, 12107–12109.
- (2) Hansen, J.; Ruedy, R.; Sato, M.; Lo, K. Global Surface Temperature Change. *Rev. Geophys.* **2010**, *48*, RG4004.
- (3) Nielsen, C. J.; Herrmann, H.; Weller, C. Atmospheric chemistry and environmental impact of the use of amines in carbon capture and storage (CCS). *Chem. Soc. Rev.* **2012**, *41*, 6684–6704.
- (4) Sanz-Pérez, E. S.; Murdock, C. R.; Didas, S. A.; Jones, C. W. Direct Capture of CO<sub>2</sub> from Ambient Air. *Chem. Rev.* **2016**, *116*, 11840–11876.
- (5) Wang, S.; Li, X.; Wu, H.; Tian, Z.; Xin, Q.; He, G.; Peng, D.; Chen, S.; Yin, Y.; Jiang, Z.; Guiver, M. D. Advances in high permeability polymer-based membrane materials for CO<sub>2</sub> separations. *Energy Environ. Sci.* **2016**, *9*, 1863–1890.
- (6) Bui, M.; Adjiman, C. S.; Bardow, A.; Anthony, E. J.; Boston, A.; Brown, S.; Fennell, P. S.; Fuss, S.; Galindo, A.; Hackett, L. A.; Hallett, J. P.; Herzog, H. J.; Jackson, G.; Kemper, J.; Krevor, S.; Maitland, G. C.; Matuszewski, M.; Metcalfe, I. S.; Petit, C.; Puxty, G.; Reimer, J.; Reiner, D. M.; Rubin, E. S.; Scott, S. A.; Shah, N.; Smit, B.; Trusler, J. P. M.; Webley, P.; Wilcox, J.; Mac Dowell, N. Carbon capture and storage (CCS): the way forward. *Energy Environ. Sci.* **2018**, *11*, 1062–1176.
- (7) Chaikittisilp, W.; Kim, H.-J.; Jones, C. W. Mesoporous Alumina-Supported Amines as Potential Steam-Stable Adsorbents for Capturing CO<sub>2</sub> from Simulated Flue Gas and Ambient Air. *Energy Fuels* **2011**, *25*, 5528–5537.
- (8) Dutcher, B.; Fan, M.; Russell, A. G. Amine-Based CO<sub>2</sub> Capture Technology Development from the Beginning of 2013—A Review. *ACS Appl. Mater. Interfaces* **2015**, *7*, 2137–2148.
- (9) Flaig, R. W.; Popp, T. M. O.; Fracaro, A. M.; Kapustin, E. A.; Kalmutzki, M. J.; Altamimi, R. M.; Fathieh, F.; Reimer, J. A.; Yaghi, O. M. The Chemistry of CO<sub>2</sub> Capture in an Amine-Functionalized Metal–Organic Framework under Dry and Humid Conditions. *J. Am. Chem. Soc.* **2017**, *139*, 12125–12128.
- (10) Zhao, X.; Yuan, Y.; Li, P.; Song, Z.; Ma, C.; Pan, D.; Wu, S.; Ding, T.; Guo, Z.; Wang, N. A polyether amine modified metal organic framework enhanced the CO<sub>2</sub> adsorption capacity of room temperature porous liquids. *Chem. Commun.* **2019**, *55*, 13179–13182.
- (11) Lashaki, M. J.; Khiavi, S.; Sayari, A. Stability of amine-functionalized CO<sub>2</sub> adsorbents: a multifaceted puzzle. *Chem. Soc. Rev.* **2019**, *48*, 3320–3405.
- (12) Brandani, F.; Ruthven, D. M. The Effect of Water on the Adsorption of CO<sub>2</sub> and C<sub>3</sub>H<sub>8</sub> on Type X Zeolites. *Ind. Eng. Chem. Res.* **2004**, *43*, 8339–8344.
- (13) Liu, J.; Wang, Y.; Benin, A. I.; Jakubczak, P.; Willis, R. R.; LeVan, M. D. CO<sub>2</sub>/H<sub>2</sub>O Adsorption Equilibrium and Rates on Metal–Organic Frameworks: HKUST-1 and Ni/DOBDC. *Langmuir* **2010**, *26*, 14301–14307.
- (14) Bien, C. E.; Chen, K. K.; Chien, S.-C.; Reiner, B. R.; Lin, L.-C.; Wade, C. R.; Ho, W. S. W. Bioinspired Metal–Organic Framework for Trace CO<sub>2</sub> Capture. *J. Am. Chem. Soc.* **2018**, *140*, 12662–12666.
- (15) Yang, H.; Singh, M.; Schaefer, J. Humidity-swing mechanism for CO<sub>2</sub> capture from ambient air. *Chem. Commun.* **2018**, *54*, 4915–4918.
- (16) Hu, Z.; Wang, Y.; Shah, B. B.; Zhao, D. CO<sub>2</sub> Capture in Metal–Organic Framework Adsorbents: An Engineering Perspective. *Adv. Sustainable Syst.* **2019**, *3*, 1800080.
- (17) Espallargas, G. M.; Coronado, E. Magnetic functionalities in MOFs: from the framework to the pore. *Chem. Soc. Rev.* **2018**, *47*, 533–557.
- (18) Zhao, X.; Wang, Y.; Li, D.-S.; Bu, X.; Feng, P. Metal–Organic Frameworks for Separation. *Adv. Mater.* **2018**, *30*, 1705189.
- (19) Ding, M.; Flaig, R. W.; Jiang, H.-L.; Yaghi, O. M. Carbon capture and conversion using metal–organic frameworks and MOF-based materials. *Chem. Soc. Rev.* **2019**, *48*, 2783–2828.
- (20) Jasuja, H.; Huang, Y.-g.; Walton, K. S. Adjusting the Stability of Metal–Organic Frameworks Under Humid Conditions by Ligand Functionalization. *Langmuir* **2012**, *28*, 16874–16880.
- (21) Ding, M.; Cai, X.; Jiang, H.-L. Improving MOF stability: approaches and applications. *Chem. Sci.* **2019**, *10*, 10209–10230.
- (22) Nguyen, J. G.; Cohen, S. M. Moisture-Resistant and Superhydrophobic Metal–Organic Frameworks Obtained via Post-synthetic Modification. *J. Am. Chem. Soc.* **2010**, *132*, 4560–4561.
- (23) Sun, Q.; He, H.; Gao, W.-Y.; Aguila, B.; Wojtas, L.; Dai, Z.; Li, J.; Chen, Y.-S.; Xiao, F.-S.; Ma, S. Imparting amphiphobicity on single-crystalline porous materials. *Nat. Commun.* **2016**, *7*, 13300.
- (24) Fukushima, T.; Horike, S.; Kobayashi, H.; Tsujimoto, M.; Isoda, S.; Foo, M. L.; Kubota, Y.; Takata, M.; Kitagawa, S. Modular Design of Domain Assembly in Porous Coordination Polymer Crystals via Reactivity-Directed Crystallization Process. *J. Am. Chem. Soc.* **2012**, *134*, 13341–13347.
- (25) DeCoste, J. B.; Denny, M. S., Jr.; Peterson, G. W.; Mahle, J. J.; Cohen, S. M. Enhanced aging properties of HKUST-1 in hydrophobic mixed-matrix membranes for ammonia adsorption. *Chem. Sci.* **2016**, *7*, 2711–2716.
- (26) Qian, X.; Sun, F.; Sun, J.; Wu, H.; Xiao, F.; Wu, X.; Zhu, G. Imparting surface hydrophobicity to metal–organic frameworks using a facile solution-immersion process to enhance water stability for CO<sub>2</sub> capture. *Nanoscale* **2017**, *9*, 2003–2008.
- (27) Chen, Y.; Li, S.; Pei, X.; Zhou, J.; Feng, X.; Zhang, S.; Cheng, Y.; Li, H.; Han, R.; Wang, B. A Solvent-Free Hot-Pressing Method for Preparing Metal–Organic-Framework Coatings. *Angew. Chem., Int. Ed.* **2016**, *55*, 3419–3423.
- (28) Zhang, W.; Hu, Y.; Ge, J.; Jiang, H.-L.; Yu, S.-H. A Facile and General Coating Approach to Moisture/Water-Resistant Metal–Organic Frameworks with Intact Porosity. *J. Am. Chem. Soc.* **2014**, *136*, 16978–16981.
- (29) Yang, S.; Peng, L.; Sun, D. T.; Asgari, M.; Oveisi, E.; Trukhina, O.; Bulut, S.; Jamali, A.; Queen, W. L. A new post-synthetic polymerization strategy makes metal–organic frameworks more stable. *Chem. Sci.* **2019**, *10*, 4542–4549.
- (30) Lv, Y.; Yu, X.; Jia, J.; Tu, S.-T.; Yan, J.; Dahlquist, E. Fabrication and characterization of superhydrophobic polypropylene hollow fiber membranes for carbon dioxide absorption. *Appl. Energy* **2012**, *90*, 167–174.
- (31) Hou, J.; Ji, C.; Dong, G.; Xiao, B.; Ye, Y.; Chen, V. Biocatalytic Janus membranes for CO<sub>2</sub> removal utilizing carbonic anhydrase. *J. Mater. Chem. A* **2015**, *3*, 17032–17041.
- (32) Yu, X.; An, L.; Yang, J.; Tu, S.-T.; Yan, J. CO<sub>2</sub> capture using a superhydrophobic ceramic membrane contactor. *J. Membrane Sci.* **2015**, *496*, 1–12.
- (33) Geyer, F.; Schönecker, C.; Butt, H.-J.; Vollmer, D. Enhancing CO<sub>2</sub> Capture using Robust Superomphobic Membranes. *Adv. Mater.* **2016**, *29*, 1603524.
- (34) Lin, Y.-F.; Wang, W.-W.; Chang, C.-Y. Environmentally sustainable, fluorine-free and waterproof breathable PDMS/PS nanofibrous membranes for carbon dioxide capture. *J. Mater. Chem. A* **2018**, *6*, 9489–9497.
- (35) Wu, X.; Zhao, B.; Wang, L.; Zhang, Z.; Li, J.; He, X.; Zhang, H.; Zhao, X.; Wang, H. Superhydrophobic PVDF membrane induced by hydrophobic SiO<sub>2</sub> nanoparticles and its use for CO<sub>2</sub> absorption. *Sep. Purif. Technol.* **2018**, *190*, 108–116.
- (36) Baidya, A.; Yatheendran, A.; Ahuja, T.; Sudhakar, C.; Das, S. K.; Ras, R. H. A.; Pradeep, T. Waterborne Fluorine-Free Superhydrophobic Surfaces Exhibiting Simultaneous CO<sub>2</sub> and Humidity Sorption. *Adv. Mater. Interfaces* **2019**, *6*, 1901013.
- (37) Rather, A. M.; Manna, U. Facile Synthesis of Tunable and Durable Bulk Superhydrophobic Material from Amine “Reactive” Polymeric Gel. *Chem. Mater.* **2016**, *28*, 8689–8699.
- (38) Rather, A. M.; Manna, U. Stretchable and durable superhydrophobicity that acts both in air and under oil. *J. Mater. Chem. A* **2017**, *5*, 15208–15216.
- (39) Parbat, D.; Manna, U. Synthesis of ‘reactive’ and covalent polymeric multilayer coatings with durable superoleophobic and

superoleophilic properties under water. *Chem. Sci.* **2017**, *8*, 6092–6102.

(40) Maji, K.; Manna, U. Hierarchically featured and substrate independent bulk-deposition of ‘reactive’ polymeric nanocomplexes for controlled and strategic manipulation of durable biomimicking wettability. *J. Mater. Chem. A* **2018**, *6*, 6642–6653.

(41) Das, S.; Das, A.; Parbat, D.; Manna, U. Catalyst-Free and Rapid Chemical Approach for in Situ Growth of “Chemically Reactive” and Porous Polymeric Coating. *ACS Appl. Mater. Interfaces* **2019**, *11*, 34316–34329.

(42) Das, A.; Maji, K.; Naskar, S.; Manna, U. Facile optimization of hierarchical topography and chemistry on magnetically active graphene oxide nanosheets. *Chem. Sci.* **2020**, *11*, 6556–6566.

(43) Rather, A. M.; Jana, N.; Hazarika, P.; Manna, U. Sustainable polymeric material for the facile and repetitive removal of oil-spills through the complementary use of both selective-absorption and active-filtration processes. *J. Mater. Chem. A* **2017**, *5*, 23339–23348.

## Supporting Information

### Evaluating the Impact of Tailored Water Wettability on Performance of CO<sub>2</sub>-Capture

Adil Majeed Rather,<sup>§,a,d</sup> Pillalamarri Srikrishnarka,<sup>§,b</sup> Avijit Baidya,<sup>b</sup> Arpita Shome,<sup>a</sup> Thalappil Pradeep\*,<sup>b</sup> and Uttam Manna<sup>\*,a,c</sup>

<sup>a</sup>Department Department of Chemistry, Indian Institute of Technology-Guwahati, Kamrup, Assam 781039, India

<sup>b</sup>Department of Chemistry, DST Unit of Nanoscience (DST UNS) and Thematic Unit of Excellence (TUE), Indian Institute of Technology Madras, Chennai 600036, India

E-mail: [pradeep@iitm.ac.in](mailto:pradeep@iitm.ac.in)

<sup>c</sup>Centre for Nanotechnology, Indian Institute of Technology-Guwahati, Kamrup, Assam 781039, India

E-mail: [umanna@iitg.ac.in](mailto:umanna@iitg.ac.in)

<sup>d</sup>Present Address (A.M.R): Department of Chemical and Biomolecular Engineering The Ohio State University, Columbus, USA- 43210

§ Author Contributions: A.M. R. and P. S. contributed equally



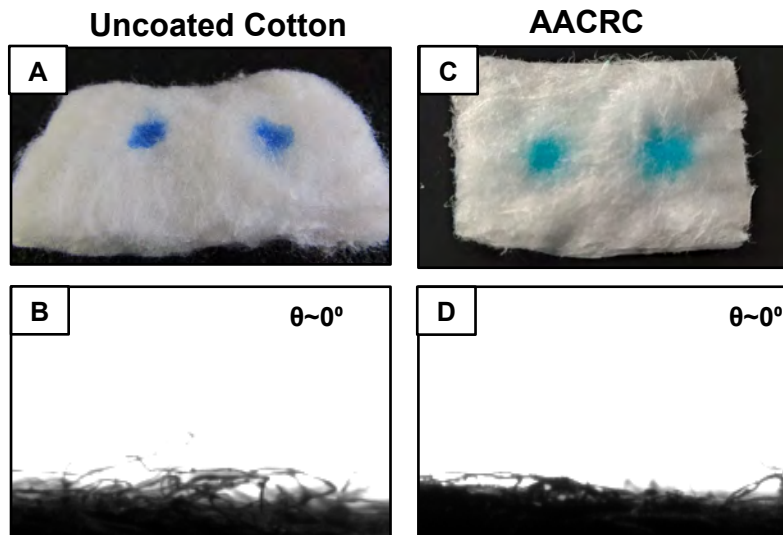


**Figure S1.** (A-D) Digital images (A, C) and contact angle images (B, D) of pristine cotton (A, B) and amine amplified

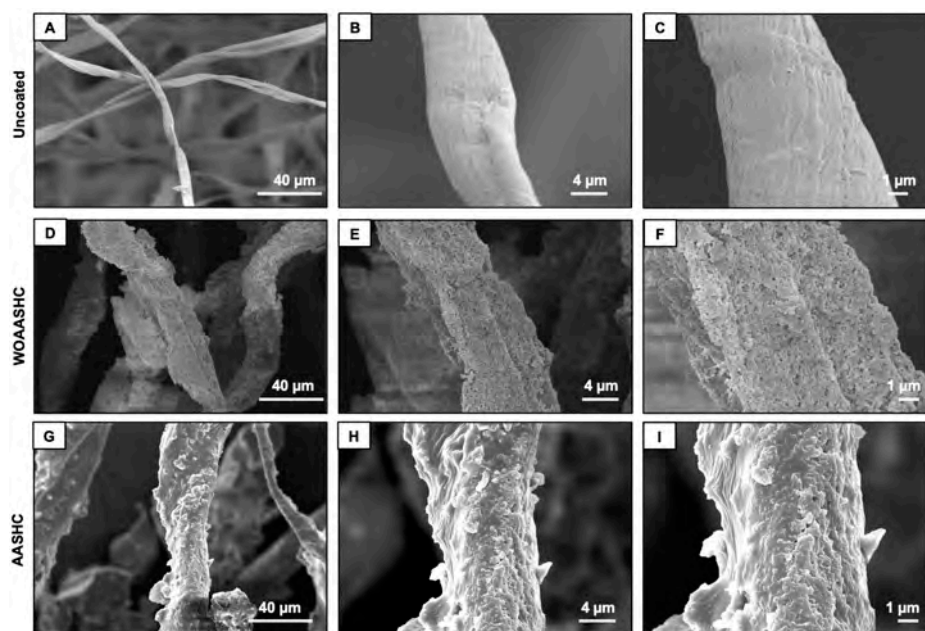


**Figure S2.** (A-I) FESEM images of uncoated cotton (A-C) and WOAASHC (D-F) and AASHC (G-I) at lower (A, D,G) and higher (B-C, E-F and H-I) magnifications.

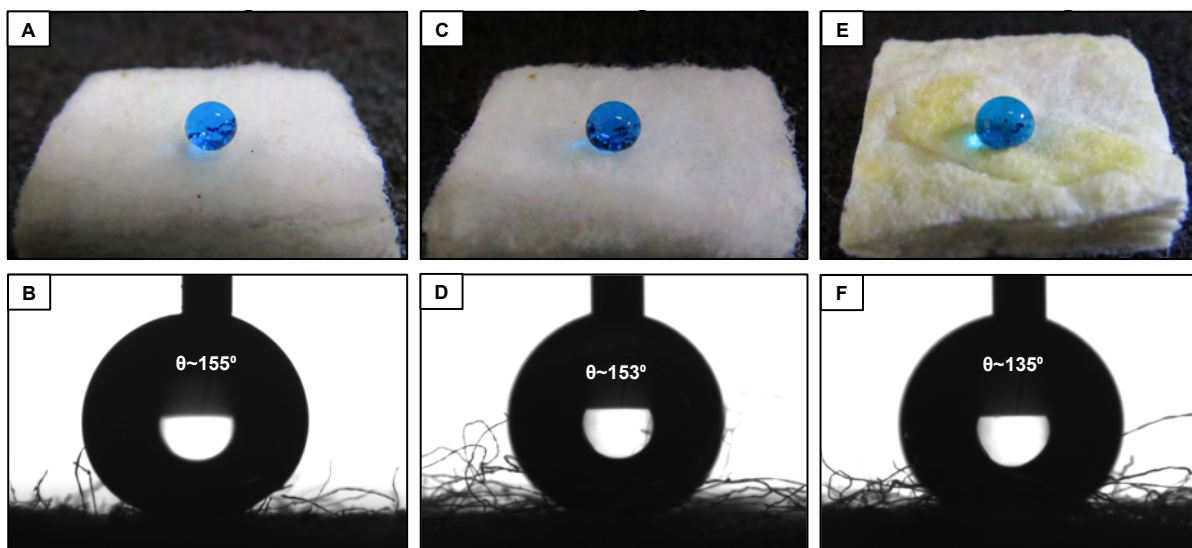


**Figure S3.** (A-F) Digital images (A, C, E) and contact angle images (B, D, F) of amine amplified reactive coating after ODA treatment with different concentrations of BPEI including 50 mg/ml (A, B), 125 mg/ml (C, D) and 250 mg/ml (E, F) respectively.

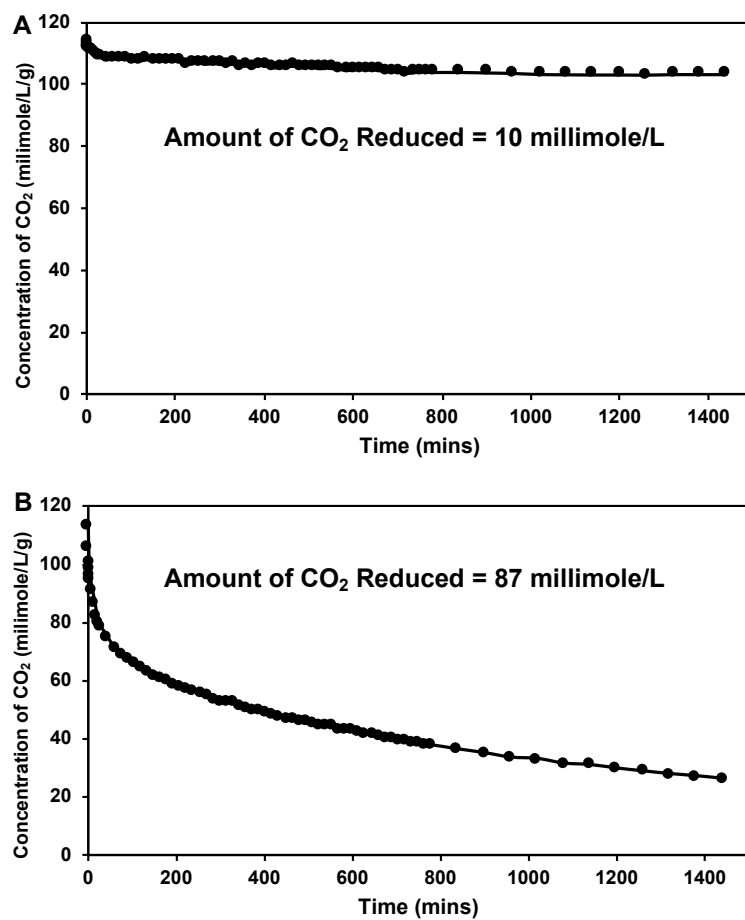


**Figure S4.** (A-B) Plots illustrating the decrease in concentration of CO<sub>2</sub> by WOAASHC (A) and AASHC (B) over 24 hours.

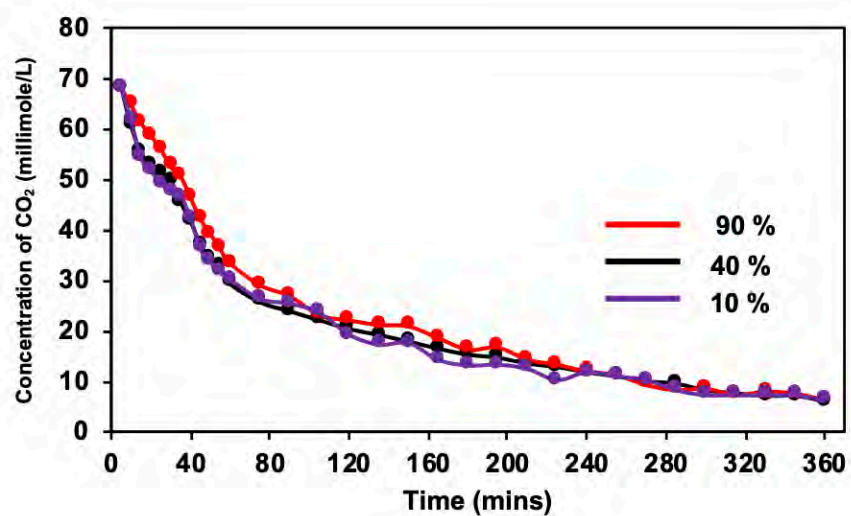


**Figure S5.** Plots illustrating the decrease in concentration of CO<sub>2</sub> by AASHC in different humid conditions including 10% (purple), 40% (black) and 90% (red).



Cite this: *Nanoscale*, 2020, **12**, 22116

# Atom transfer between precision nanoclusters and polydispersed nanoparticles: a facile route for monodisperse alloy nanoparticles and their superstructures†

Paulami Bose,<sup>a</sup> Papri Chakraborty,<sup>‡a</sup> Jyoti Sarita Mohanty,<sup>‡a</sup> Nonappa,<sup>id b</sup> Angshuman Ray Chowdhuri,<sup>a</sup> Esma Khatun,<sup>a</sup> Tripti Ahuja,<sup>a</sup> Ananthu Mahendranath<sup>a,c</sup> and Thalappil Pradeep<sup>id \*a</sup>

Reactions between atomically precise noble metal nanoclusters (NCs) have been studied widely in the recent past, but such processes between NCs and plasmonic nanoparticles (NPs) have not been explored earlier. For the first time, we demonstrate spontaneous reactions between an atomically precise NC, Au<sub>25</sub>(PET)<sub>18</sub> (PET = 2-phenylethanethiol), and polydispersed silver NPs with an average diameter of 4 nm and protected with PET, resulting in alloy NPs under ambient conditions. These reactions were specific to the nature of the protecting ligands as no reaction was observed between the Au<sub>25</sub>(SBB)<sub>18</sub> NC (SBB = 4-(*tert*-butyl)benzyl mercaptan) and the very same silver NPs. The mechanism involves an interparticle exchange of the metal and ligand species where the metal–ligand interface plays a vital role in controlling the reaction. The reaction proceeds through transient Au<sub>25–x</sub>Ag<sub>x</sub>(PET)<sub>n</sub> alloy cluster intermediates as observed in time-dependent electrospray ionization mass spectrometry (ESI MS). High-resolution transmission electron microscopy (HRTEM) analysis of the resulting dispersion showed the transformation of polydispersed silver NPs into highly monodisperse gold–silver alloy NPs which assembled to form 2-dimensional superlattices. Using NPs of other average sizes (3 and 8 nm), we demonstrated that size plays an important role in the reactivity as observed in ESI MS and HRTEM.

Received 26th May 2020,  
Accepted 29th September 2020  
DOI: 10.1039/d0nr04033a  
[rsc.li/nanoscale](http://rsc.li/nanoscale)

## Introduction

Well-defined plasmonic metal nanoparticles (NPs) are crucial in nanotechnology due to their unique roles as catalysts in fuel cells,<sup>1–3</sup> electrochemical reduction of CO<sub>2</sub>,<sup>4,5</sup> green chemistry,<sup>6,7</sup> etc. and as probes in biomedical diagnosis<sup>8,9</sup> and therapy.<sup>10,11</sup> These and related applications bring in challenges for synthetic methods that can offer fine control over NP size dispersity. Substantial progress has been made in developing recipes to synthesize metal NPs that could address

the issue of polydispersity as well as shape selectivity at the same time.<sup>12–17</sup> Efforts have been made to optimize synthetic methodologies for the size and shape-selective preparation of monodisperse spherical metal NPs, nanorods,<sup>18–21</sup> nanowires,<sup>22</sup> nanotriangles,<sup>23,24</sup> nanocubes<sup>25</sup> and other polygonal structures. Most of the available literature is limited to the synthesis of monodisperse particles of either gold (Au) or silver (Ag). It is well established that bimetallic Au–Ag alloys have enhanced catalytic and plasmonic performance.<sup>26,27</sup> Ultrafine bimetallic alloy NPs often suffer from inhomogeneous alloying and aggregation due to their high surface energy and phase separation at the atomic level.<sup>27</sup> There are still challenges to develop strategies to synthesize ultrafine well-alloyed NPs that can offer concurrent control over size homogeneity and crystallinity. Size dispersity of NPs can significantly alter their self-assembling behavior,<sup>28–30</sup> material properties,<sup>31</sup> and device performance.<sup>32,33</sup> Therefore, methods have been developed to enhance their monodispersity, including solvent-selective precipitation,<sup>34,35</sup> centrifugation,<sup>36</sup> size-exclusion chromatography,<sup>37,38</sup> and electrophoresis.<sup>39,40</sup> Anti-galvanic reactions (AGR) have recently been gaining popularity particularly in the preparation of atomically monodisperse bimetallic

<sup>a</sup>DST Unit of Nanoscience (DST UNS) and Thematic Unit of Excellence (TUE), Department of Chemistry, Indian Institute of Technology Madras, Chennai 600 036, India. E-mail: [pradeep@iitm.ac.in](mailto:pradeep@iitm.ac.in)

<sup>b</sup>Faculty of Engineering and Natural Sciences, Tampere University, P.O. Box 541, FI-33101 Tampere, Finland.

<sup>c</sup>Department of Metallurgical and Materials Engineering, Indian Institute of Technology Madras, Chennai 600036, India

†Electronic supplementary information (ESI) available: Concentration calculations, ESI MS, UV-Vis, HRTEM, MALDI MS, STEM-EDS, and Raman spectra. See DOI: 10.1039/d0nr04033a

‡These authors contributed equally.

NPs where NP size is less than 3 nm. AGR studies are mostly limited to atomically precise ultrasmall NPs of less than 3 nm in size, referred to as nanoclusters (NCs).<sup>41</sup> To the best of our knowledge, extensive studies of AGR involving larger NPs are rare. Available techniques<sup>27,42</sup> for ultrafine bimetallic alloy NPs are co-reduction,<sup>43</sup> seed-mediated growth,<sup>44</sup> laser ablation,<sup>45</sup> and galvanic replacement.<sup>46</sup>

In recent years, atomically precise noble metal nanoclusters (NCs) have emerged as a new family of nanomaterials with precise composition and structure, and exhibit well-defined physical, chemical and electronic properties.<sup>47–50</sup> Over a hundred well-defined NCs have been characterized in the recent past, and many of their properties have been examined in detail.<sup>51–53</sup> Of these, 2-phenylethanethiol (PET)-protected gold NC, Au<sub>25</sub>(PET)<sub>18</sub>, is one of the most studied NC systems, and has been used in the present investigation.<sup>54–57</sup>

Extensive studies on various properties of NCs showed that they are indeed molecules.<sup>58,59</sup> An essential characteristic of the NC is its chemical reactivity and sensitivity towards atomic exchange. It has been demonstrated that reactions between NCs (*i.e.* intercluster reactions), conserving composition and structure, involving atom exchange between two different types of NCs are possible.<sup>60</sup> An intercluster reaction was first reported for the NC systems comprising Au<sub>25</sub>(PET)<sub>18</sub> and Ag<sub>44</sub>(FTP)<sub>30</sub>, where FTP refers to 4-fluorothiophenol.<sup>61</sup> Later on, similar reactions were observed for Au<sub>25</sub>(PET)<sub>18</sub> with various other NC systems, such as Ag<sub>25</sub>(DMBT)<sub>18</sub>,<sup>60</sup> Ag<sub>51</sub>(BDT)<sub>19</sub>(TPP)<sub>3</sub>, and Ag<sub>29</sub>(BDT)<sub>12</sub>(TPP)<sub>4</sub>,<sup>62</sup> where DMBT, BDT, and TPP refer to 2,4-dimethylbenzenethiol, 1,3-benzene-dithiol, and triphenylphosphine, respectively. In a few cases, such intercluster reactions were employed to make new NC products as well.<sup>63</sup> For instance, Au<sub>25</sub>(PET)<sub>18</sub> reacts with Ir<sub>9</sub>(PET)<sub>6</sub> to give a completely new alloy NC, Au<sub>22</sub>Ir<sub>3</sub>(PET)<sub>18</sub> as the product, which was not synthesized earlier using the conventional synthetic protocols.<sup>64</sup> Metal exchanges were seen between Au<sub>25</sub>(PET)<sub>18</sub> and Au<sub>38</sub>(PET)<sub>24</sub> NCs with bulk metallic silver.<sup>65</sup>

In an effort to achieve monodispersity in NPs, a method called digestive ripening was proposed by Klabunde and Sorensen,<sup>66</sup> which demonstrated positive results for highly polydispersed dodecanethiol-ligated gold NPs. This method was extended to other metal systems and was explored extensively by several researchers over the years.<sup>67–70</sup> Digestive ripening is a post-synthetic size modification method that makes highly polydispersed particles to attain monodispersity, typically in the case of noble metal NPs, without employing any other size-separation techniques. This method is assumed to be driven by ligand-mediated surface etching of larger NPs along with the dissolution of smaller NPs, followed by the growth of the remaining NPs as they come in contact with the etched species. Both two-dimensional (2D) and three-dimensional (3D) superlattices have been prepared using this approach.<sup>71,72</sup> Despite its success in enhancing monodispersity, the mechanism involved has not been understood clearly. The binding strength between the NPs and the ligand, ligand-

solvent compatibility and temperature were already identified as the main parameters affecting digestive ripening.<sup>73–78</sup>

Previously, it has been shown that tellurium nanowires decorated with Ag<sub>44</sub>(*p*MBA)<sub>30</sub> NCs (where *p*MBA refers to *para*-mercaptobenzoic acid) form crossed bilayer assemblies driven by inter-NC hydrogen bonding.<sup>79</sup> Similarly, when *p*MBA-coated gold nanorods were interacted with Ag<sub>44</sub>(*p*MBA)<sub>30</sub> NCs, well-defined core-shell structures were formed.<sup>80</sup> It is important to note that in the above examples, the interaction between the NCs and NPs led to supramolecular assemblies directed purely *via* hydrogen bonding between the surface ligands and no metallic atom transfer reactions were involved. Therefore, the intrinsic properties of the individual components were retained in the superstructures. However, it is relevant to investigate the feasibility of chemical reactions between atomically precise NCs and plasmonic NPs. In this paper, we present the first example of a chemical reaction between Au NCs and polydispersed Ag NPs offering a unique route towards the preparation of well-defined highly monodisperse hybrid Au–Ag alloy NPs. The resulting alloy NPs further self-assemble spontaneously to a higher order superstructure. This study gives a better insight into the reaction pathways and intermediate species involved colloidal state reactions. Compared to other AGR reported to date, the merit of this method is that it allows modification in order to achieve fine control over the size and composition of bimetallic NPs and their assembly with reproducibility. The properties of the resulting NPs can be altered by simply modifying the reaction with different protecting ligands. We chose PET-protected polydispersed silver NPs (Ag@PET) and the Au<sub>25</sub>(PET)<sub>18</sub> NC as model systems to investigate NC–NP reactions.

We show that when gold NCs were mixed with polydispersed silver NPs, the NC–NP reactions led to highly monodisperse thermodynamically stable Ag–Au bimetallic NPs. Importantly, the newly formed monodisperse NPs underwent a higher order assembly resulting in a 2D superlattice. The transient NC species formed in the course of the reaction are alloys that have been characterized by mass spectrometry (MS). A host of microscopic and spectroscopic studies confirmed the compositional change in both the systems. We also observed that the composition of the alloy clusters formed in the process goes through time-dependent changes, suggesting the details of the mechanism involved. We propose that the atomic transfer between NCs and NPs during interparticle reactions is one of the plausible routes leading to digestive ripening. Our study also shows that such reactions are more facile with smaller NPs than with larger ones.

## Experimental

### Materials

Silver nitrate (AgNO<sub>3</sub>, 99.9%) was purchased from Rankem Chemicals. 2-PET, 4-(*tert*-butyl)benzyl mercaptan (BBSH), sodium borohydride (NaBH<sub>4</sub>, 98%), and tetraoctylammonium



bromide (TOABr) were purchased from Sigma-Aldrich. Tetrachloroauric acid ( $\text{HAuCl}_4 \cdot 3\text{H}_2\text{O}$ ) was prepared in the laboratory starting from pure gold. All the solvents (dichloromethane, methanol, and tetrahydrofuran) used were of HPLC grade and were used without further purification. Millipore-produced deionized water ( $\sim 18.2 \text{ M}\Omega$ ) was used throughout the experiments.

### Synthesis of Ag@PET nanoparticles

The synthesis of Ag@PET NPs was carried out by modifying the traditional preparation methods of silver NPs.<sup>81–83</sup> Different sizes of Ag NPs were obtained by varying the amount of the reducing agent used in the course of the reaction. In a typical synthesis, 50 mg of  $\text{AgNO}_3$  was dissolved in 0.5 mL water and added to 58  $\mu\text{L}$  of PET in 30 mL methanol. Subsequently, silver was reduced to the zero-valent state by slow addition of the freshly prepared aqueous  $\text{NaBH}_4$  solution (0.3 M, 0.2 M, and 0.1 M), made in 8 mL ice-cold water. The reaction mixture was kept under reflux at 333 K with vigorous stirring for 12 h. The resulting precipitate was collected and repeatedly washed with methanol by centrifugal precipitation. Finally, the Ag@PET NPs formed were extracted as dark brown precipitate, soluble in DCM and DMF. High-speed centrifugation at 8000 rpm for 20 min was used to separate larger-sized particles. The particles were found to be stable for weeks when stored in a refrigerator under dark conditions but the stability decreased to 3–4 days under ambient conditions. During the optimization process, it was observed that the amount of the reducing agent plays a key role in defining the size of the NPs. When the molar concentration of  $\text{NaBH}_4$  was increased in the reaction mixture, smaller Ag NPs were obtained. Apart from this, temperature was found to be a crucial factor in tuning the shape of the NPs, and hence the reaction temperature was set at 333 K. Fig. S1† shows the detailed characterization of the Ag NPs using HRTEM and UV-Vis spectroscopy, where characteristic plasmonic peaks were observed at 454, 442, and 453 nm for particles with mean sizes of  $3.17 \pm 1.5$ ,  $4.37 \pm 2.3$  and  $8.45 \pm 6.3 \text{ nm}$  NPs, respectively, which are referred to as 3, 4 and 8 nm particles subsequently. The sizes of the particles refer to the core diameter measured by high-resolution transmission electron microscopy (HRTEM).

### Synthesis of the $\text{Au}_{25}(\text{PET})_{18}$ NC

The synthesis of the NC was performed following the reported protocol.<sup>84,85</sup> A solution containing 40 mg of  $\text{HAuCl}_4 \cdot 3\text{H}_2\text{O}$  and 7.5 mL of THF was prepared, and to that 65 mg of TOABr was added. The mixture was stirred for 15 min until the solution turned orange red. Subsequently, 68  $\mu\text{L}$  of PET was added and the mixture was allowed to stir for 1 h. The as-formed Au-PET thiolate was reduced by adding a solution containing 39 mg  $\text{NaBH}_4$  in ice-cold water as the color of the reaction mixture changed from yellow to orange. Now, the solution was stirred for another 5 h for complete reduction and size focusing in order to achieve high yields of the intended NC. After 5 h, the crude NC was dried using a rotavapor and it was sub-

jected to a methanol wash to get rid of free thiols and excess thiolates. The process was repeated multiple times to obtain a clean NC. The NC was extracted in acetone and centrifuged, the supernatant was collected, and the precipitate containing larger NCs was discarded. The supernatant, composed of the size-focused clean NC in acetone, was vacuum dried. Finally, the NC was dissolved in DCM, followed by centrifugation at 10 000 rpm, and the supernatant comprising pure NC was collected. The purified NC was characterized using UV-Vis spectroscopy and ESI MS (Fig. S2†).

### Reaction of Ag@PET NPs with the $\text{Au}_{25}(\text{PET})_{18}$ NC

For the NP-NC reaction, about 7.5 mg of Ag@PET NPs were dissolved in 3 mL DCM ( $\sim 9.05 \mu\text{M}$ ) and about 0.9 mg of the  $\text{Au}_{25}(\text{PET})_{18}$  NC was dissolved in 300  $\mu\text{L}$  of DCM ( $\sim 7.67 \mu\text{M}$ , concentration in the final reaction mixture), separately. Concentrations mentioned are in terms of the metal present. The two dispersions were mixed at room temperature and after 15 min, about 100  $\mu\text{L}$  of the reaction mixture was taken and further diluted in 0.5 mL of DCM. The solution was characterized using HRTEM and UV-Vis spectroscopy. Allowing the reaction to continue for a longer time (of the order of hours) resulted in slow precipitation (black in color) with the supernatant turning colorless. The concentration calculations are presented in the ESI.†

### Sample preparation for ESI MS experiments

First, about  $75.99 \mu\text{M}$  solution of the NC was prepared by dissolving 8.1 mg of  $\text{Au}_{25}(\text{PET})_{18}$  in 3 mL of DCM. Another Ag@PET NP dispersion of  $\sim 9.05 \mu\text{M}$  was prepared with 7.5 mg of NPs in 3 mL DCM. Then, to the NC solution, 300  $\mu\text{L}$  of Ag NP ( $\sim 0.82 \mu\text{M}$ , concentration in the final reaction mixture) dispersion was added. The reaction was monitored using a stopwatch which was started immediately as the NP was added. After 2 min of the reaction, 0.25 mL of the reaction mixture was pipetted out and diluted with 0.25 mL of DCM, and was cooled in an ice-bath. The time interval specified is the time at which the pipetted out reaction mixture was dipped in the ice-cold conditions. The cooling down of the reaction mixture slowed down the reaction rate but did not quench it completely. The reaction mixture was then centrifuged and the supernatant was studied using ESI MS. The same process was repeated at 3, 4, 5, 7, and 10 min intervals. After 15 min, the left-over reaction mixture was centrifuged and the black precipitate was subjected to HRTEM imaging.

### Synthesis of the $\text{Au}_{25}(\text{SBB})_{18}$ NC

The NC was synthesized according to our already reported protocol.<sup>86</sup> In a round bottom flask, about 10 mL of  $\text{HAuCl}_4 \cdot 3\text{H}_2\text{O}$  (14.5 mM in THF) was taken and then 15 mL of 4-(*tert*-butyl) benzyl mercaptan (BBSH) (89.2 mM in THF) was added while stirring at 400 rpm at room temperature. The solution turned colorless after 15 min, indicating the formation of  $\text{Au(I)SBB}$  thiolate. This was followed by a rapid addition of 2.5 mL aqueous solution of  $\text{NaBH}_4$  (0.4 M) to the reaction mixture under vigorous stirring (1100 rpm). The color of the solution

changed from colorless to black, indicating the formation of NCs. The reaction mixture was allowed to stir for 3 h under ambient conditions and then for another 3 h at 318 K for complete conversion. The solution was left overnight for size focusing. The product was vacuum dried and the residue was washed repeatedly with 1:1 water:methanol mixture to remove excess BBSh and other side products. The  $\text{Au}_{25}(\text{SBB})_{18}$  NC was then precipitated, dried and used for further experiments.

## Results and discussion

### Characterization of the starting materials

To study the interparticle reaction between polydispersed silver NPs and atomically precise gold NCs,  $\text{Ag}@\text{PET}$  NPs and the  $\text{Au}_{25}(\text{PET})_{18}$  NC were chosen as model systems initially. Stability of the mentioned systems made us select them for the study. Initially, three differently sized  $\text{Ag}@\text{PET}$  NPs were synthesized using the protocol discussed in the Experimental section. The  $\text{Ag}@\text{PET}$  NPs were characterized using optical absorption spectroscopy (UV-Vis) and HRTEM (Fig. S1A–C†). Three discrete sets of the synthesized Ag NPs of average diameters 3, 4, and 8 nm showed plasmonic features in UV-Vis at 454, 442, and 453 nm, respectively (Fig. S1D†) (see the Experimental section for more details).

The atomically precise  $\text{Au}_{25}(\text{PET})_{18}$  NC was characterized using UV-Vis which showed the characteristic peaks at 675 and 450 nm (Fig. S2A†) and ESI MS measurements showed the molecular peak at  $m/z$  7391 (Fig. S2B†). The characteristic iso-

topic distribution further confirmed the composition of the NC.

### Reaction between $\text{Ag}@\text{PET}$ NPs and the $\text{Au}_{25}(\text{PET})_{18}$ NC

The reaction between  $\text{Ag}@\text{PET}$  NPs and the  $\text{Au}_{25}(\text{PET})_{18}$  NC was achieved by mixing known volumes of the respective solutions in DCM at room temperature (see the Experimental section). To monitor the progress of the reaction, after 15 min, the reaction product was analyzed under a HRTEM. These micrographs showed that the NP and the NC mixture resulted in highly monodisperse NPs (Fig. 1B), compared to the initial polydispersed  $\text{Ag}@\text{PET}$  NPs (Fig. 1A). More large area images from HRTEM are provided in Fig. S3† and the corresponding UV-Vis spectra in Fig. S4†. The UV-Vis spectrum of the reaction product shows clearly a red-shifted surface plasmon resonance (SPR) peak at 480 nm which happens to be a characteristic feature of bimetallic Au–Ag NPs (details are provided in the latter part of the manuscript).<sup>43</sup> The particle size distribution (Fig. S5†) also underwent a transformation from  $4.37 \pm 2.3$  nm (Fig. S5A†) in the case of parent silver NPs to  $3.45 \pm 1.2$  nm (Fig. S5B†) after the reaction. This can be correlated to the changes that usually happen during high temperature annealing of particles in the digestive ripening process.<sup>67</sup>

Both the parent NP and the NC were initially dispersed in DCM, and upon mixing, the assembly of NPs occurred spontaneously, and the reaction product underwent slow precipitation when left undisturbed. The product dispersed in DCM was dropcast on a copper grid for HRTEM studies. The reacted NPs were self-assembled into a hexagonal close-packed (hcp) 2D superlattice with an interparticle distance (denoted by “ $a$ ”)

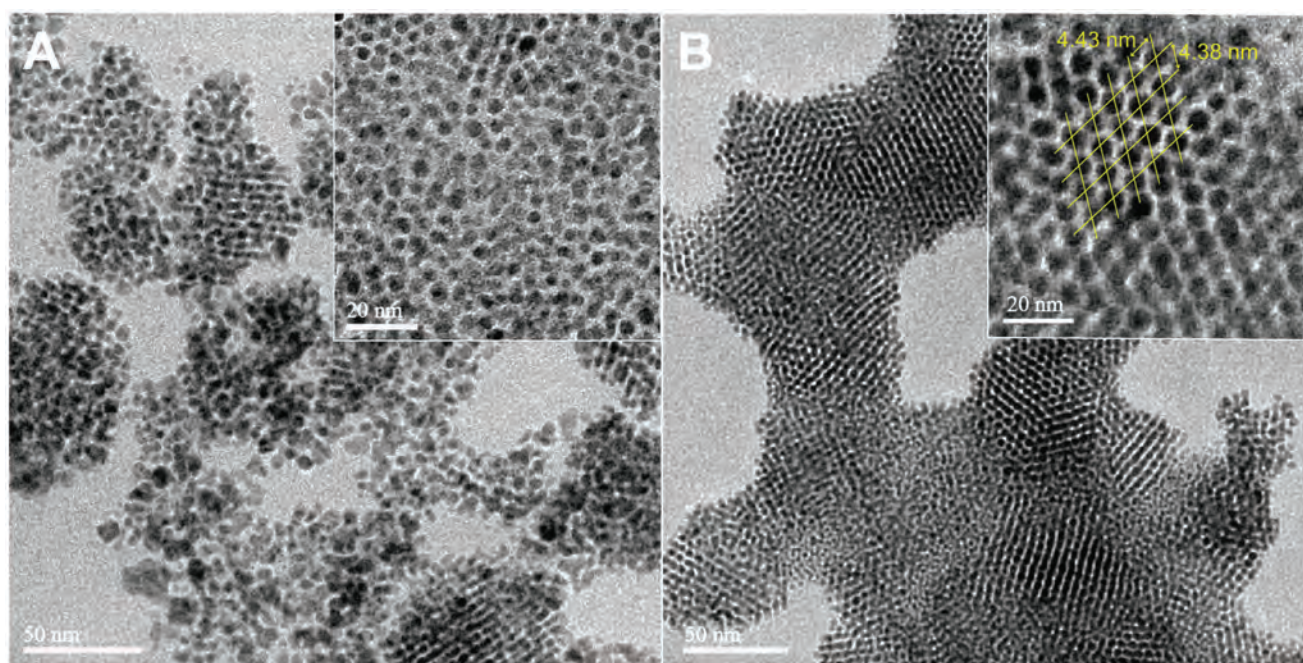


**Fig. 1** HRTEM micrographs of (A) 4 nm silver NPs protected by 2-PET, and (B) spontaneously assembled NPs after the parent NPs were subjected to react with the  $\text{Au}_{25}(\text{PET})_{18}$  NC.



of 4.48 nm and a periodicity (denoted by “ $d$ ”) of 4.23 nm (calculated using the formula,  $d = \sqrt{3}/2a$ ).<sup>87</sup> While the parameters “ $a$ ” and “ $d$ ” include the monolayers, particle diameters determined from HRTEM refer only to the core. The parent Ag@PET NPs had a lattice fringe of 2.1 Å which corresponds to the (111) plane of silver. Upon reaction, the lattice fringe remained unaltered at 2.1 Å accompanied by the altered size of the NP. Ag@PET NPs were characterized by Raman spectroscopy before and after the reaction. All the peaks of the spectra were assigned with the help of the literature which confirmed the presence of PET ligand before and after the reaction of Ag NPs.<sup>88</sup> Spectral peak assignments are presented in Fig. S6.† Reduced signal intensity of the 1586 cm<sup>−1</sup> peak (from 120 to 30 counts) was an indication of the reduced surface enhanced Raman activity of the reacted particles. Reduction in size led to reduced plasmonic nature of NPs which was evident from the HRTEM images. The composition was changed as well. A similar pattern of hcp superlattices in the case of crystalline Ag NPs was reported by Whetten *et al.*<sup>89</sup> Moreover, there exist reports on gold NPs organizing to form hcp superlattices.<sup>70</sup>

To analyse a reaction from the perspective of the nanoparticle, there are a few *in situ* characterization techniques, like *in situ* scanning transmission electron microscopy (STEM)<sup>90</sup> and *in situ* small-angle X-ray scattering (SAXS),<sup>91</sup> which can monitor the NP nucleation and growth, and which can also provide mechanistic insights. The main challenges with these measurements are their limited time resolution, short observation time, damage arising from the electron beam and high experimental cost. However, in order to avoid such complications, we attempted to understand the chemical changes during the reaction using different mass spectrometric techniques. However, initial experiments with MALDI MS were not successful because there was no NC left in the reaction medium when monitored after 2 min of the reaction (Fig. S7†). This was attributed to the fact that the NC concentration was low and it was consumed completely during the reaction. Therefore, to monitor the changes occurring to the NC during the reaction, the initial composition (NPs : NCs = 9.05 μM : 7.67 μM, in terms of the metal) was altered with a higher concentration of NCs and a lower concentration of NPs (NCs : NPs = 75.99 μM : 0.82 μM, in terms of the metal). Subsequent ESI MS measurements were carried out using this composition (Fig. 2). As described above in the Experimental section, after 15 min of the reaction, the solution was centrifuged and the black precipitate was subjected to HRTEM studies. HRTEM micrographs suggested that upon changing the composition of the reaction (refer to the Experimental section), no significant changes were seen in the product morphology (Fig. S8†). The arrangement of the reacted particles was slightly disturbed as a result of centrifugation in the process of separating the product from the excess NC. The reacted NPs showed an average size of 3.45 nm in the precipitate which is in agreement with the initial experiments. We also conducted a concentration-dependent experiment (Fig. S9†) where the concentration of Ag@PET NPs was kept

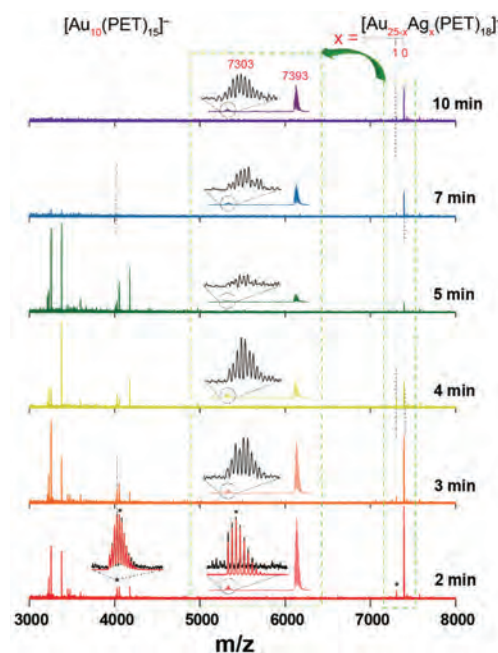


Fig. 2 Time-dependent ESI MS spectra of the reaction product identified the intermediate species, Au<sub>24</sub>Ag(PET)<sub>18</sub> along with the evolution of the parent NC, Au<sub>25</sub>(PET)<sub>18</sub> at  $m/z$  7303 and 7393, respectively. Calculated (red) and experimental (black) high-resolution isotopic distribution patterns (marked in \*) of Au<sub>24</sub>Ag(PET)<sub>18</sub> and Au<sub>10</sub>(PET)<sub>15</sub> ( $m/z$  4027) are provided for the 2 min interval spectrum. The spectral region of  $m/z$  7280–7410 is expanded as the inset.

constant, while the overall concentration of the Au<sub>25</sub>(PET)<sub>18</sub> NC was varied. First, stock solutions of 75.99 μM Au<sub>25</sub>(PET)<sub>18</sub> NC and 9.05 μM Ag@PET NPs were prepared (as mentioned in the Experimental section). To the Ag@PET NP dispersion, aliquots of 300 μL NC solution were added, and analyzed with HRTEM (Fig. S9A–C†) and UV-Vis spectroscopy (Fig. S9D†). Upon addition of the first aliquot of 300 μL NC, the UV-Vis spectrum (Fig. S9D,† red trace) mimicked the initial observations (Fig. S4,† blue trace), and the HRTEM micrographs (Fig. S9A†) appeared similar to the initial particles (Fig. 1B). As the volume of the NC was increased in the reaction mixture, HRTEM micrographs (Fig. S9B and C†) showed the presence of a superlattice and NC in a decreasing and increasing trend, respectively. Similarly, in the UV-Vis spectrum (Fig. S9D†), the reaction mixture was similar to that of the Au<sub>25</sub>(PET)<sub>18</sub> NC (Fig. S2A†). This observation led to the conclusion that the reaction was stoichiometric (all concentrations are in terms of the metal) in nature. From the above observations, it can be assumed that the reacted NP superlattices were formed when the reactants were mixed in a stoichiometric ratio (NCs : NPs = 1 : 1.18, in terms of the metal) and in the presence of excess Au<sub>25</sub>(PET)<sub>18</sub>, NC remained unreacted in the medium.

To understand the mechanistic details of the reaction, time-dependent ESI MS was performed for the reaction of 4 nm Ag@PET NPs with the Au<sub>25</sub>(PET)<sub>18</sub> NC (refer to the Experimental section). All the mass spectrometric parameters were kept constant throughout the experiment to analyze the

compositional variation of the reaction mixture with time. As shown in Fig. 2,  $\text{Au}_{24}\text{Ag}(\text{PET})_{18}$  ( $m/z$  7303) along with a few peaks ( $m/z$  3000–4500) corresponding to other intermediate species started to appear as early as 2 min (the corresponding UV-Vis spectrum is in Fig. S10†). The intensity of  $\text{Au}_{24}\text{Ag}(\text{PET})_{18}$  was observed to have a fluctuating trend.  $\text{Au}_{24}\text{Ag}$  was found to have a maximum lifetime in the reaction medium owing to its enhanced stability compared to other intermediate species.<sup>92</sup> The parent  $\text{Au}_{25}(\text{PET})_{18}$  NC ( $m/z$  7393) showed continuous reduction in signal intensity until 5 min, followed by regeneration. Changes in the intensity of the  $\text{Au}_{25}(\text{PET})_{18}$  NC can be correlated to one of the intermediates,  $\text{Au}_{10}(\text{PET})_{15}$  ( $m/z$  4027), the generation of this species might have happened at the cost of the  $\text{Au}_{25}(\text{PET})_{18}$  NC. Such short-lived species suggested that the dissociation of the  $\text{Au}_{25}(\text{PET})_{18}$  NC occurred in the presence of  $\text{Ag@PET}$  NPs. A time-dependent plot of signal intensity (Fig. S11†) of the intermediate species such as  $\text{Au}_{10}(\text{PET})_{15}$  and  $\text{Au}_{24}\text{Ag}(\text{PET})_{18}$ , in comparison to that of the  $\text{Au}_{25}(\text{PET})_{18}$  NC, suggested that the reaction proceeded through alloy-cluster intermediates in conjunction with NC dissociation. Occurrences of a few more thiolate intermediates were seen in the course of the reaction. Thus, all the fragments including the alloy NCs generated in the course of the reaction finally coalesce to form monodisperse alloy particles.

The particle size was already known as one of the primary variables of NPs, capable of modulating their chemical and physical properties.<sup>93–96</sup> The surface area of NPs has an inverse

proportional relationship with the particle size. Smaller metallic particles have a large fraction of atoms exposed, which in turn enhances their catalytic ability.<sup>97,98</sup> In Fig. 3 we showed that as the size of the parent Ag NP decreases, the interparticle reaction proceeds faster. The estimated time required for the 3, 4, and 8 nm Ag NPs to react and self-assemble was around 5, 15, and 30 min, respectively. Monodisperse 3 nm sized  $\text{Ag@PET}$  NPs (Fig. 3A) underwent a rapid self-assembly (Fig. 3B) upon reaction with the  $\text{Au}_{25}(\text{PET})_{18}$  NC. In this case, there was a slight increase in the size ( $\sim 3.5$  nm) of the NPs post reaction (particle size distribution in Fig. S24A†). To study the effect of size and polydispersity on the interparticle reactions, a batch of highly polydispersed  $\text{Ag@PET}$  NPs (Fig. 3C) with sizes ranging between 2 and 20 nm were used. When this polydispersed sample was mixed with the  $\text{Au}_{25}(\text{PET})_{18}$  NC, the reaction was relatively slower compared to monodisperse NPs of other two sizes. HRTEM analysis of the reaction mixture after 30 min revealed that NPs transformed into two different kinds of arrangements (Fig. S12†), one comprised of the reacted NPs of mostly 3.7 nm (Fig. 3D) and another a disc-shaped assembly extending over a diameter of about 240 nm, composed of nearly 2 nm reacted particles (Fig. S12C†). The particle size distribution of the post-reaction samples depicted that there was a transformation of Ag NPs from high polydispersity of  $8.45 \pm 6.3$  nm (Fig. S13A†) to monodispersity of  $3.73 \pm 1.0$  nm (Fig. S13B†). This transformation of NPs from  $8.45 \pm 6.3$  nm to  $3.73 \pm 1.0$  nm appears strange in terms of mass balance; however, we note that the number of particles has changed significantly in the course of the reaction. The reacted 3 and 8 nm Ag NPs were characterized using HRTEM (Fig. 3) and UV-Vis spectroscopy (Fig. S25†). A slightly shifted SPR peak was observed in the case of reaction of 3 nm Ag NPs (Fig. S25A†); this may be attributed to the highly reactive Ag atoms at the surface of NPs, which readily exchange with Au atoms of NCs, attaining rapid thermodynamic equilibrium (see below). On the other hand, in the case of 8 nm Ag NPs, there was a very prominent red-shifted broad SPR peak of the reaction product, centred at 556 nm (Fig. S25B†). Broad SPR peaks are in agreement with the formation of a higher order assembly of the reacted NPs. It is widely accepted that the SPR wavelength increases with the NP size for a fixed chemical composition.<sup>99,100</sup> However, it has been shown that the SPR position is expressed as second-order and third-order polynomial expressions with the composition and size-dependent coefficients, respectively. Therefore, the small shift observed for alloy NPs for 3 nm Ag NPs after the reaction is presumably due to low Au content, unlike alloys from 4 (discussed earlier in Fig. S4†) and 8 nm Ag NPs. Elemental compositions of the self-assembled superstructures were analyzed by energy-dispersive X-ray spectroscopy (EDS) using a scanning transmission electron microscope (STEM) (Fig. 4). Elemental mapping confirmed the presence of gold, silver, sulphur and carbon in the superstructure. More importantly, the uniform distribution of gold, silver and sulphur throughout superstructures suggested that the structures that resulted from the reaction were complex gold–silver hybrids.

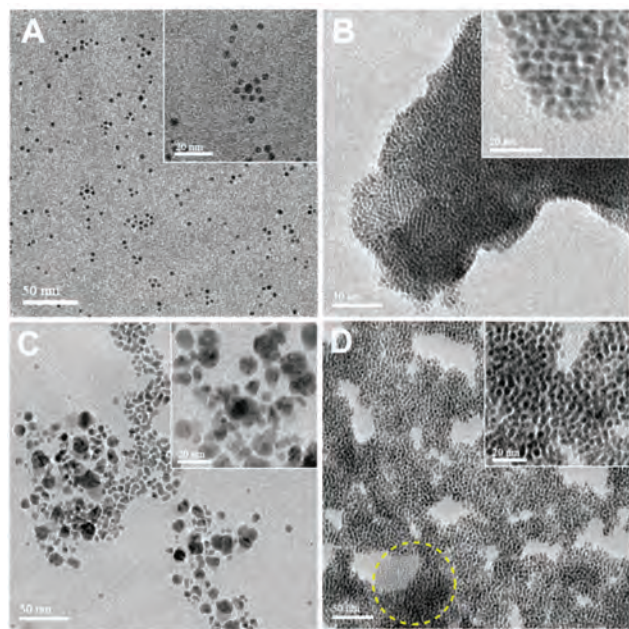


**Fig. 3** Size dependence of silver NPs on the spontaneous assembly. HRTEM images (left to right) showing  $\text{Ag@PET}$  NPs before and after reaction. Silver NPs with an average size of (A) highly uniform 3 nm, (B) assembly of post reacted particles, and (C) highly polydispersed 8 nm particles followed by (D) assembly post reaction. A second kind of assembly was observed in D (yellow circle); more images are presented in the ESI (Fig. S12C†). Higher magnification images of representative areas are in the respective insets.



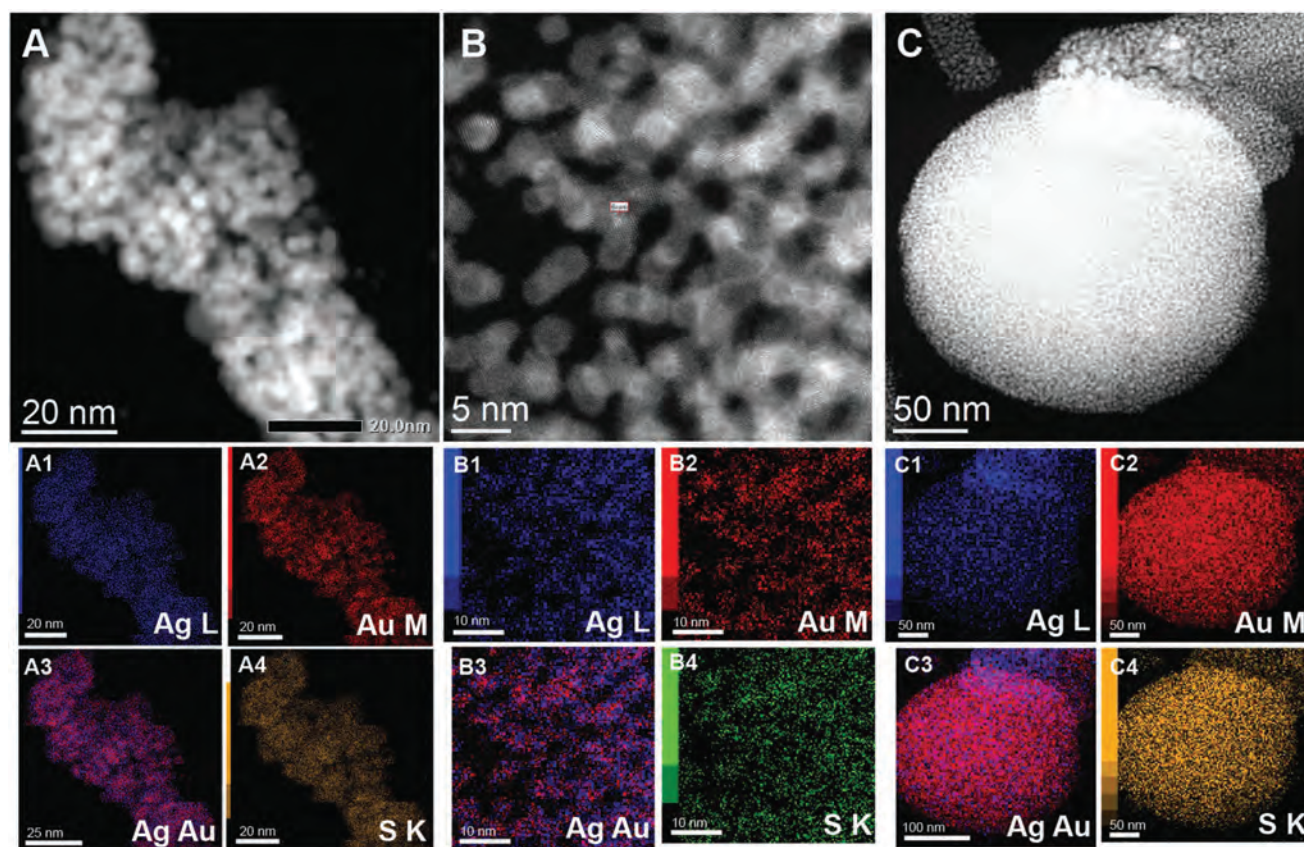


**Fig. 4** Scanning transmission electron micrographs (STEM) for the (A) assembly of the reacted 4 nm Ag@PET NPs and the reacted 8 nm Ag@PET NPs arranged in (B) a planar assembly and (C) a disc-shaped assembly. The corresponding STEM-EDS maps of Ag, Au, Ag–Au overlay, and S are given below the STEM micrographs.

Therefore, spot EDS analysis was performed for the reacted particles, as shown in Fig. 4A, obtained from parent 4 nm Ag@PET NPs, which confirmed the presence of gold (~29%) and silver (~71%) (refer to the spot EDS spectrum in Fig. S14†). The difference in ratios of Au and Ag between the initial mixing (Au NC : Ag NP = 1 : 1.18) and final resulting NPs (Au : Ag = 1 : 2.45) may be due to the experimental limitation where EDS mapping was attempted on a few particles in a selected area against the entire range of particles including byproducts, and therefore it is only a semi-qualitative method in the present case.<sup>101–103</sup> Then, a similar compositional analysis was performed on the self-assembled reacted particles obtained from polydispersed 8 nm Ag@PET NPs. The planar assembly showed alloy particles (Fig. 4B) with the presence of gold (~30%) and silver (~70%) (refer to the spot EDS spectrum in Fig. S15†). The disc-shaped assembly also confirmed to be a hybrid assembly of gold (~42%) and silver (~58%) (Fig. 4C) alloy NPs (refer to the spot EDS spectrum in Fig. S16†).

Fig. 5 shows the reactivity of three differently sized NPs as the progress of the reaction was monitored with ESI MS and UV-Vis spectroscopy (Fig. S17†) for the same period of time; in this case, at 2 min intervals, while all experimental conditions and parent substrate concentrations were kept constant.

Before the mass spectral investigation, the reactions were quenched by lowering the temperature to ice-cold conditions. For 3 nm Ag NPs (Fig. 5D),  $\text{Ag}_x\text{Au}_{25-x}$  particles were seen for  $x = 1, 2, 3$ , and 4, while for 8 nm Ag NPs (Fig. 5B) it was limited to  $x = 1$ . This reduced reactivity was reflected in all samples with a larger size and greater polydispersity, consequently such samples required comparatively more time to get mono-dispersed. Comparative HRTEM images of the progress of the reaction for 8 nm Ag@PET NPs with time are presented in Fig. S23.†

The reactions discussed above were extremely rapid and spontaneous in nature. Reactivity of the system was enhanced with the decreasing size of parent Ag NPs. Since the intermediates were short-lived, ESI MS peak intensities varied depending on the time at which the reaction was quenched. In an attempt to capture the intermediates, we performed the same time-dependent reaction of 4 nm Ag@PET NPs with the  $\text{Au}_{25}(\text{PET})_{18}$  NC under ice-cold conditions (Fig. S18A†). The reaction was found to proceed even at a lower temperature of 273 K but at a much slower rate. The reaction mixture was subjected to ESI MS measurements from 3 min until 6 h. The intermediates continued to exist until 6 h under the ice-cold conditions (Fig. S18A†), which was usually 5 min for the same reaction at room temperature (Fig. S18B†). In view of such reactivity, the

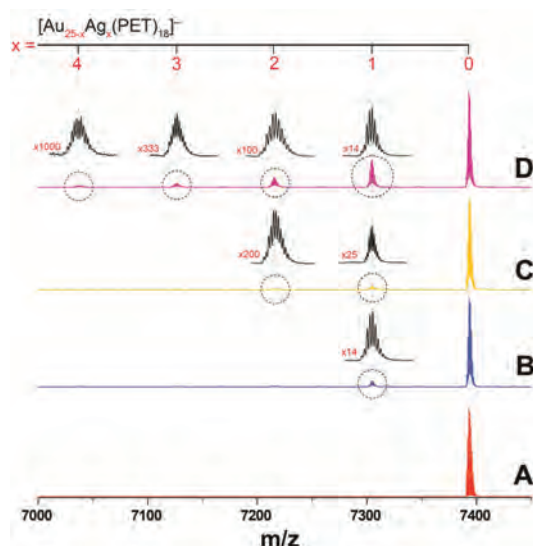


**Fig. 5** Size-dependent reactivity monitored using ESI MS, keeping the reaction and mass spectrometric conditions constant. The reaction was allowed for 2 min and quenched under ice-cold conditions. The rate of reaction was found to vary with the size of silver NPs. Spectra monitored after 2 min of reaction with (B) 8 nm, (C) 4 nm, and (D) 3 nm particles, and the extent of exchange was compared with the spectrum of the parent (A)  $\text{Au}_{25}(\text{PET})_{18}$  NC. Spectra were normalized with the corresponding  $\text{Au}_{25}(\text{PET})_{15}$  peak intensity for visual comparison.

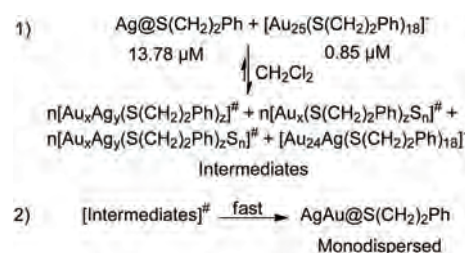
reported intermediate signal intensities would vary slightly from the true values for a given time interval of the reaction (observed under ambient conditions).

Owing to the spontaneous nature of the NP–NC reaction, we are assuming that the NP–NC reaction is driven towards a thermodynamically stable state. A monodisperse Au-doped Ag NP with an equilibrium size is thermodynamically more stable over its polydisperse pure monometallic state, under the reaction conditions. A thermodynamic equilibrium size of a metal NP depends on the specific protecting ligand and temperature of the reaction.<sup>69,104,105</sup> A thermodynamic equilibrium size is a critical size that possesses an optimum surface energy allowing a ligand coverage in order to protect the core of a metal NP from further reaction. We observed that upon interparticle reaction, when 3 nm Ag NPs were used, the resulting alloy NPs showed an increase in their size to 3.5 nm. However, when the reaction was carried out using 5 and 8 nm Ag NPs, a decrease in the size of the alloy NPs to 3.45 and 3.7 nm, respectively, was seen. Hence, we can say that, at room temperature, for PET-protected Au–Ag bimetallic NPs, the equilibrium sizes of the NPs range between 2 and 5 nm with an average of  $\sim 3.5$  nm (Fig. S24†). The effects of polydispersity in the shapes of Ag NPs (as evident from Fig. S1C†) were reflected in the nature of the intermediates. It may be said that greater the diversity in the shapes and sizes of parent Ag NPs, larger will be the number of intermediates, as observed in ESI MS (Fig. S19B†). Now, irrespective of the sizes of the parent Ag NPs, the reacted NPs get spontaneously resized to  $\sim 3.5$  nm due to the reaction pathway which involves complete fragmentation and exchange

of metal atoms between the particles. The process continues until a thermodynamically stable state is achieved. Digestive ripening implies the modification of both smaller and larger NPs until a preferred size is achieved. On similar lines, we are suggesting that the NP–NC reaction can be considered as one of the plausible routes of digestive ripening. Similarly, here we conclude that the smaller particles, *i.e.* NCs can drive particle fragmentation leading to monodispersity. This can be supported from the ESI MS experiment where a number of low mass fragments were seen in addition to alloy NCs in the initial stages of the reaction. From all this, we propose a reaction scheme (Scheme 1).

Monolayers on the surface of NPs have a contribution towards their chemical reactivity. We examined their influence with ESI MS (Fig. S20†) as we replaced the original NC with the  $\text{Au}_{25}(\text{SBB})_{18}$  NC. Here also, keeping all the experimental conditions similar, we allowed the NC to react for a span of 2 min and collected the mass spectra, where no new peaks were seen (Fig. S20A and C†). Again, HRTEM (Fig. S20B and D†) showed no change even after 30 min of the reaction (experimental conditions as mentioned in the previous case). We failed to find any notable changes in the reaction medium unlike the one observed in the case of the  $\text{Au}_{25}(\text{PET})_{18}$  NC. The results therefore suggested that the ligand also played a crucial role in such interparticle reactions. For a facile and effective reaction between a NC and a NP, the metal–ligand interface played an important role as the reaction was expected to occur through the exchange of surface atoms or metal–ligand fragments.<sup>106–108</sup> The failure of the reaction can be attributed to a possible steric hindrance between the bulky terminal *tert*-butyl group of SBB and the benzene ring of PET ligands restricting the closer approach of NC to the NP surface required to initiate the reaction.

From the previous discussion, it was evident that the reacted particles were arranging themselves in a specific pattern depending on the size of the reacting NPs. To gain further insights into packing of the resulting NP assemblies, inverse fast Fourier transforms (IFFT) of the selected images of assemblies corresponding to 4 and 8 nm Ag@PET NPs were



**Scheme 1** Proposed chemical pathway for the reaction between Ag@PET NPs and the  $\text{Au}_{25}(\text{PET})_{18}$  NC. Steps: (1) Ag@PET NPs initiating alloying and fragmentation of the  $\text{Au}_{25}(\text{PET})_{18}$  NC giving rise to intermediates, where  $x = 25, 24, 23, \dots$ , and  $y = 0, 1, 2, 3, \dots$ , and (2) finally the intermediates undergo mutual coalescence as well as with unreacted NPs, the reaction continues until complete consumption of the  $\text{Au}_{25}(\text{PET})_{18}$  NC, and resulting in monodisperse gold–silver alloy NPs.



performed. 3D structural reconstructions of assemblies were carried out using electron tomography. Accordingly, a series of 2D projections were collected by tilting the sample from  $+69^\circ$  to  $-69^\circ$  with an increment angle of  $2-3^\circ$ . The tilt series were then subjected to image processing to obtain the final 3D reconstruction. As shown in Fig. 6A, a superlattice assembly of the reacted 4 nm Ag@PET NPs showed an hcp array of particles, with an interparticle distance of  $\sim 4.5$  nm (refer to a square lattice in Fig. S21A†). On the other hand, for the first

kind of assembly derived from 8 nm Ag@PET NPs, the planar assembly (Fig. 6B) displayed a square lattice with an interparticle distance of  $\sim 4.0$  nm (refer to a square lattice in Fig. S21B†). However, due to complex 3D multilayered assemblies (Fig. 6B), unambiguous interpretation of the assemblies based on 2D projections remained inconclusive. The second kind of assembly (Fig. S22†) resulting from the same NPs turned out to be a circular disc, densely filled with the reacted particles. The tilt series and 3D reconstructions for the assemblies corres-

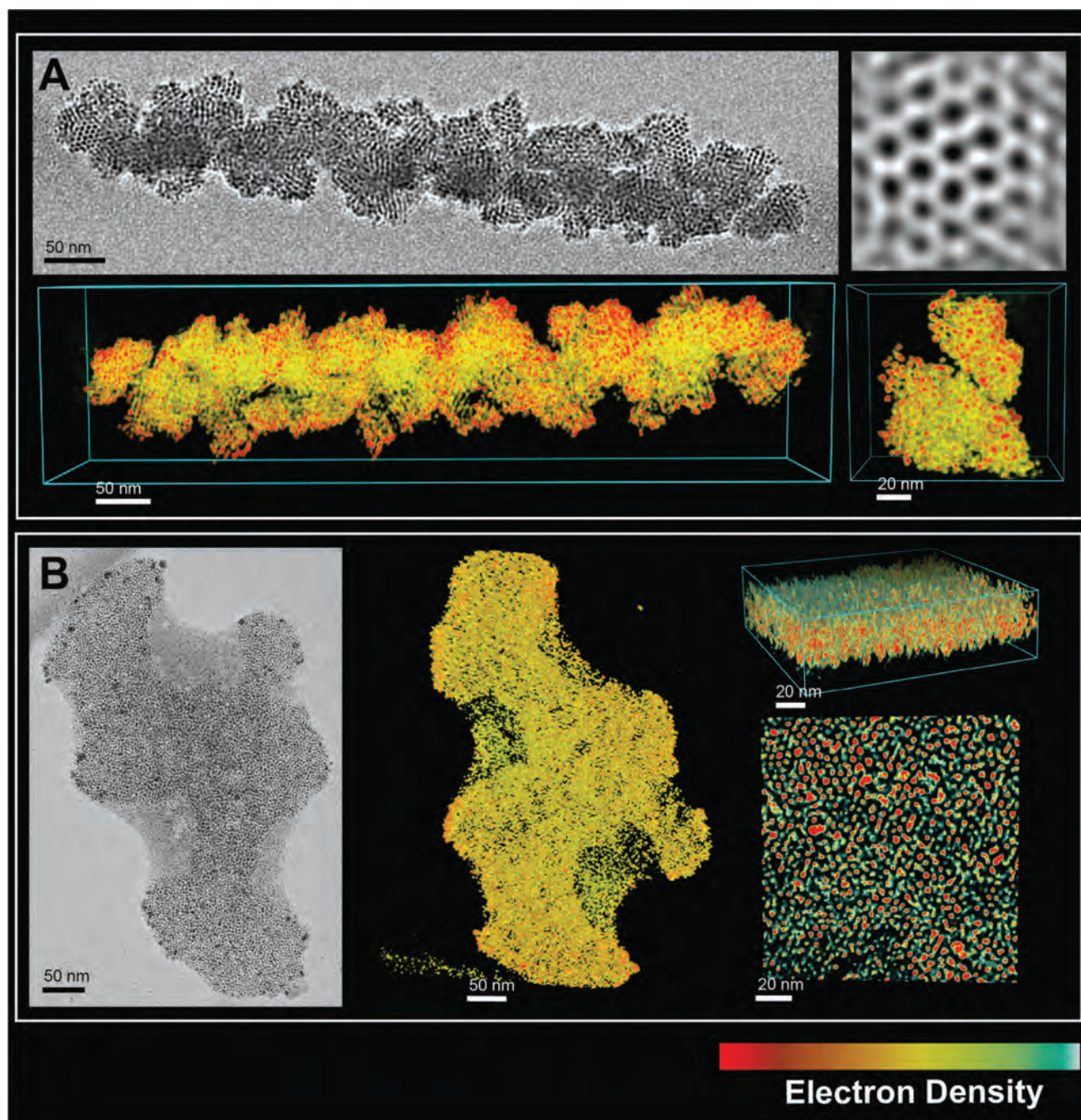


**Fig. 6** Electron tomography and 3D reconstruction: 2D projection followed by its corresponding 3D reconstruction for (A) the superlattice assembly of the reacted 4 nm Ag@PET NPs and IFFT image of the hcp assembly, and (B) a planar assembly of the reacted 8 nm Ag@PET NPs.

ponding to the reacted 4 nm Ag NPs (Fig. 6A) are provided in the ESI as Videos V1 and V2,<sup>†</sup> respectively. Also, tilt series and 3D reconstructions for the planar assembly of the reacted 8 nm Ag NPs (Fig. 6B) are provided in the ESI as Videos V3 and V4,<sup>†</sup> respectively.

We propose a mechanism for the reaction between Ag@PET NPs and the Au<sub>25</sub>(PET)<sub>18</sub> NC. The reaction can be hypothesized to proceed through a series of events like (i) interparticle approach, (ii) adduct formation, (iii) atomic exchange, and (iv) attaining monodispersity and consequent equilibrium. The metallophilic interaction of the Ag NPs and Au NCs might initiate their approach toward each other. The NC–NP reaction can be presumed to follow a host–guest reaction model similar to the enzyme–substrate model, where the NP host forms adducts with the NC guest. The flexibility of the protecting ligands on both the substrates plays a major role in allowing the adduct formation. Adduct formation apparently facilitates Au–Ag atomic exchange between the two species. It was already reported that the exchange of Au–PET and Ag–PET units is facile in the case of isolobal fragments.<sup>61</sup> Unlike dithiols, where only metal exchange is reported, for monothiol, the metal–ligand transfer is feasible.<sup>62</sup> The Au<sub>25</sub>(PET)<sub>18</sub> NC undergoes atomic exchange with Ag@PET NPs to form Au<sub>24</sub>Ag(PET)<sub>18</sub> with Ag at the center of the M<sub>13</sub> core (M = metal, in this case Au) which happens to be an exceptionally stable structure.<sup>109,110</sup> ESI MS measurements of the ongoing reaction suggested the presence of both multiple doped NCs as well as dissociated NC species. It can be assumed that extensive interparticle atomic exchange leads to multiple doping of the NCs, which eventually destabilized the system. In order to release this geometric strain, the NC system may undergo dissociation. The newly formed species (alloy–NC intermediates, dissociated NCs, and other low-mass fragments) in the reaction medium can now undergo coalescence mutually as well as with unreacted NPs until the system attains a stable equilibrium size. As the reactants were mixed in a ratio of NCs : NPs = 1 : 1.18 (in terms of the metal), the above process continues until complete consumption of Au<sub>25</sub>(PET)<sub>18</sub> occurs.

Apart from this, the phenomenon of digestive ripening can also occur. The driving force for digestive ripening is the decrease of interfacial free energy. In a study by Hwang *et al.*<sup>111</sup> on digestive ripening, the phenomenon was explained using a modified Gibbs–Thomson equation by the introduction of an electrostatic energy factor. The equation mainly relates interfacial free energy as one of the most important factors to other physical properties, like chemical potential, particle size, and curvature factor.<sup>112</sup> In the case of binary systems, the chemical potentials of both Au and Ag are important in resulting monodispersity. According to the phase diagram of an Au/Ag binary system,<sup>113,114</sup> Au and Ag are isomorphous with face-centered cubic (FCC) structure, and therefore it is assumed that Au and Ag NPs behave like an ideal binary solid solution. At equilibrium, the Gibbs free energy is the minimum for spherical Au–Ag binary particles compared to their pure states. The Au–Ag atomic exchange between the NPs contributes to the decrease in total Gibbs free energy. The

size and compositional change due to atomic exchange between the NPs is governed by the chemical potential, which finally contributes to the minimization of the total Gibbs free energy. According to reports, solid–gas interface free energies of Ag<sup>115</sup> and Au<sup>116</sup> are 1.25 J m<sup>−2</sup> and 1.2 J m<sup>−2</sup>, respectively, at their melting point. Interface free energies of Au, Ag, and Au/Ag solid solution in the colloidal form are assumed to have a value of 0.3 J m<sup>−2</sup>. The chemical potential of Au is always higher in Au NPs than in Ag NPs. Similarly, the chemical potential of Ag is higher in Ag NPs than in Au NPs. Therefore, simultaneous diffusion of Ag from Ag NPs to Au NPs and Au from Au NPs to Ag NPs minimizes the total free energy producing monodisperse alloy NPs. We can say that doped Au or Ag NPs are thermodynamically more stable compared to their monometallic state. Inter-ligand interaction plays an important role in the formation of superlattices.<sup>117–119</sup> During the self-assembly of metallic NPs, the presence of strong van der Waals forces between the metallic cores brings the particles closer and at the same time the ligands (dominantly the alkyl groups) introduce an opposing interparticle steric repulsion.<sup>120</sup> The inter-ligand steric repulsion balanced by strong interparticle van der Waals attraction can result in a superlattice arrangement. The strong van der Waals attraction usually contributes to the ligand interdigitation between adjacent particles.<sup>121–123</sup>

## Conclusions

In summary, we have explored the reaction of Ag NPs with atomically precise Au NCs resulting in monodisperse Au–Ag alloy NPs. Interparticle reactions are key initiators in the formation of the resulting 2D superlattice assemblies. Such interparticle reactions can be proposed as one of the methods contributing to the digestive ripening of NPs. Reactions were studied for the Au<sub>25</sub>(PET)<sub>18</sub> NC with differently sized Ag@PET NPs where we observed that the reactivity of the system was enhanced upon decreasing the size of the NPs. From our ESI MS measurements, it was evident that gold–silver alloying in the case of interparticle reactions proceeded through an alloy–nanocluster intermediate followed by atomic exchange between them and subsequent NC detachment. The proposed methodology was found to contribute to achieving the highest control over NP size distribution in solutions at room temperature. The nanocluster–nanoparticle reactions can open up an entirely new method of generating uniform alloy NPs with tunable optoelectronic properties. The method may be extended to other transition metals like Ni and Fe in order to introduce properties like magnetism. Similar studies could be conducted between NPs and NCs of the same metal, resulting in monodisperse NPs without change in composition, although the present investigation was conducted with Ag NPs and Au NCs in view of the feasibility in exploring the reaction by mass spectrometry, observing the changes by EDS and STEM. In the absence of stable PET-protected Ag NCs, it was not possible to extend this study presently to reaction between



Au@PET and Ag NCs. Further studies are progressing to understand the corresponding processes with other transition metal NPs, which will be reported in due course.

## Conflicts of interest

There are no conflicts to declare.

## Acknowledgements

P. B., E. K., A. M., and T. A. thank IIT Madras for their research fellowships. P. C. and A. R. C. thank the Department of Science and Technology (DST) for providing a postdoctoral fellowship. J. S. M. thanks the Council of Scientific and Industrial Research (CSIR) for her fellowships. We thank C. K. Manju for her help in the MALDI MS measurements, Ganesan Paramasivam for contributing with the NP and NC structures, Amrita Chakraborty, Amoghavarsha Kini, Srikrishnarka Pillalamarri and Vishal Kumar for valuable inputs in relation to this work. The Academy of Finland's Centre of Excellence in Molecular Engineering of Biosynthetic Hybrid Materials (HYBER, 2014–2019), Photonics Research and Innovation (PREIN) Flagship and Aalto University Nanomicroscopy Centre (Aalto-NMC) are acknowledged for providing access to their microscopy facilities.

## Notes and references

- M. Muzzio, J. Li, Z. Yin, I. M. Delahunty, J. Xie and S. Sun, *Nanoscale*, 2019, **11**, 18946–18967.
- F. J. Perez-Alonso, D. N. McCarthy, A. Nierhoff, P. Hernandez-Fernandez, C. Strebel, I. E. L. Stephens, J. H. Nielsen and I. Chorkendorff, *Angew. Chem., Int. Ed.*, 2012, **51**, 4641–4643.
- H. J. Yin, J. H. Zhou and Y. W. Zhang, *Inorg. Chem. Front.*, 2019, **6**, 2582–2618.
- P. T. Smith, E. M. Nichols, Z. Cao and C. J. Chang, *Acc. Chem. Res.*, 2020, **53**, 575–587.
- M. G. Kim, J. Jeong, Y. Choi, J. Park, E. Park, C. H. Cheon, N. K. Kim, B. K. Min and W. Kim, *ACS Appl. Mater. Interfaces*, 2020, **12**, 11890–11897.
- P. Sudarsanam, E. Peeters, E. V. Makshina, V. I. Parvulescu and B. F. Sels, *Chem. Soc. Rev.*, 2019, **48**, 2366–2421.
- C. Yu, X. Guo, M. Shen, B. Shen, M. Muzzio, Z. Yin, Q. Li, Z. Xi, J. Li, C. T. Seto and S. Sun, *Angew. Chem., Int. Ed.*, 2018, **57**, 451–455.
- D. Ni, E. B. Ehlerding and W. Cai, *Angew. Chem., Int. Ed.*, 2019, **58**, 2570–2579.
- Y. Ju, H. Zhang, J. Yu, S. Tong, N. Tian, Z. Wang, X. Wang, X. Su, X. Chu, J. Lin, Y. Ding, G. Li, F. Sheng and Y. Hou, *ACS Nano*, 2017, **11**, 9239–9248.
- L. Zhang, Q. Chen, Y. Ma and J. Sun, *ACS Appl. Bio Mater.*, 2020, **3**, 107–120.
- Z. Shen, M. P. Nieh and Y. Li, *Polymers*, 2016, **8**, 1–18.
- H. M. Ashberry, J. T. L. Gamler, R. R. Unocic and S. E. Skrabalak, *Nano Lett.*, 2019, **19**, 6418–6423.
- P. Qiu, B. Ma, C. Te Hung, W. Li and D. Zhao, *Acc. Chem. Res.*, 2019, **52**, 2928–2938.
- J. Mosquera, Y. Zhao, H. J. Jang, N. Xie, C. Xu, N. A. Kotov and L. M. Liz-Marzán, *Adv. Funct. Mater.*, 2020, **30**, 1–17.
- C. Martín-Sánchez, A. Sánchez-Iglesias, P. Mulvaney, L. M. Liz-Marzán and F. Rodríguez, *J. Phys. Chem. C*, 2020, **124**, 8978–8983.
- A. Vivien, M. Guillaumont, L. Meziane, C. Salzemann, C. Aubert, S. Halbert, H. Gérard, M. Petit and C. Petit, *Chem. Mater.*, 2019, **31**, 960–968.
- Y. Yan, J. S. Du, K. D. Gilroy, D. Yang, Y. Xia and H. Zhang, *Adv. Mater.*, 2017, **29**, 1605997.
- G. González-Rubio, P. Díaz-Núñez, A. Rivera, A. Prada, G. Tardajos, J. González-Izquierdo, L. Bañares, P. Llombart, L. G. Macdowell, M. Alcolea Palafox, L. M. Liz-Marzán, O. Peña-Rodríguez and A. Guerrero-Martínez, *Science*, 2017, **358**, 640–644.
- C. Martín-Sánchez, G. González-Rubio, P. Mulvaney, A. Guerrero-Martínez, L. M. Liz-Marzán and F. Rodríguez, *J. Phys. Chem. Lett.*, 2019, **10**, 1587–1593.
- W. Ye, K. Krüger, A. Sánchez-Iglesias, I. García, X. Jia, J. Sutter, S. Celiksoy, B. Foerster, L. M. Liz-Marzán, R. Ahijado-Guzmán and C. Sönnichsen, *Chem. Mater.*, 2020, **32**, 1650–1656.
- H. H. Chang and C. J. Murphy, *Chem. Mater.*, 2018, **30**, 1427–1435.
- C. Jia, Z. Lin, Y. Huang and X. Duan, *Chem. Rev.*, 2019, **119**, 9074–9135.
- L. Scarabelli, M. Coronado-Puchau, J. J. Giner-Casares, J. Langer and L. M. Liz-Marzán, *ACS Nano*, 2014, **8**, 5833–5842.
- C. Kuttner, M. Mayer, M. Dulle, A. Moscoso, J. M. López-Romero, S. Förster, A. Fery, J. Pérez-Juste and R. Contreras-Cáceres, *ACS Appl. Mater. Interfaces*, 2018, **10**, 11152–11163.
- S. Zhou, J. Li, K. D. Gilroy, J. Tao, C. Zhu, X. Yang, X. Sun and Y. Xia, *ACS Nano*, 2016, **10**, 9861–9870.
- M. Rebello Sousa Dias and M. S. Leite, *Acc. Chem. Res.*, 2019, **52**, 2881–2891.
- D. Tan, S. Tu, Y. Yang, S. Patskovsky, D. Rioux and M. Meunier, *J. Phys. Chem. C*, 2016, **120**, 21790–21796.
- D. García-Lojo, S. Núñez-Sánchez, S. Gómez-Graña, M. Grzelczak, I. Pastoriza-Santos, J. Pérez-Juste and L. M. Liz-Marzán, *Acc. Chem. Res.*, 2019, **52**, 1855–1864.
- Nonappa and O. Ikkala, *Adv. Funct. Mater.*, 2018, **28**, 1–14.
- T. Udayabhaskararao, T. Altantzis, L. Houben, M. Coronado-Puchau, J. Langer, R. Popovitz-Biro, L. M. Liz-Marzán, L. Vukovic, P. Král, S. Bals and R. Klajn, *Science*, 2017, **358**, 514–518.
- M. A. Boles, M. Engel and D. V. Talapin, *Chem. Rev.*, 2016, **116**, 11220–11289.
- J. Langer, D. J. de Aberasturi, J. Aizpurua, R. A. Alvarez-Puebla, B. Auguie, J. J. Baumberg, G. C. Bazan,

- S. E. J. Bell, A. Boisen, A. G. Brolo, J. Choo, D. Cialla-May, V. Deckert, L. Fabris, K. Faulds, F. J. G. de Abajo, R. Goodacre, D. Graham, A. J. Haes, C. L. Haynes, C. Huck, T. Itoh, M. Käll, J. Kneipp, N. A. Kotov, H. Kuang, E. C. Le Ru, H. K. Lee, J. F. Li, X. Y. Ling, S. A. Maier, T. Mayerhöfer, M. Moskovits, K. Murakoshi, J. M. Nam, S. Nie, Y. Ozaki, I. Pastoriza-Santos, J. Perez-Juste, J. Popp, A. Pucci, S. Reich, B. Ren, G. C. Schatz, T. Shegai, S. Schlücker, L. L. Tay, K. George Thomas, Z. Q. Tian, R. P. van Duyne, T. Vo-Dinh, Y. Wang, K. A. Willets, C. Xu, H. Xu, Y. Xu, Y. S. Yamamoto, B. Zhao and L. M. Liz-Marzán, *ACS Nano*, 2020, **14**, 28–117.
- 33 Z. Wang, S. Zong, L. Wu, D. Zhu and Y. Cui, *Chem. Rev.*, 2017, **117**, 7910–7963.
- 34 B. Kowalczyk, I. Lagzi and B. A. Grzybowski, *Curr. Opin. Colloid Interface Sci.*, 2011, **16**, 135–148.
- 35 K. Dey, S. Kunjattu, H. A. M. Chahande and R. Banerjee, *Angew. Chem.*, 2020, **59**, 1161–1165.
- 36 P. Li, A. Kumar, J. Ma, Y. Kuang, L. Luo and X. Sun, *Sci. Bull.*, 2018, **63**, 645–662.
- 37 S. Süß, V. Michaud, K. Amsharov, V. Akhmetov, M. Kaspereit, C. Damm and W. Peukert, *J. Phys. Chem. C*, 2019, **123**, 16747–16756.
- 38 X. X. Zhou, J. F. Liu and G. Bin Jiang, *Environ. Sci. Technol.*, 2017, **51**, 3892–3901.
- 39 A. Hlaváček, M. J. Mickert, T. Soukka, S. Lahtinen, T. Tallgren, N. Pizúrová, A. Król and H. H. Gorris, *Anal. Chem.*, 2019, **91**, 1241–1246.
- 40 B. Behdani, S. Monjezi, M. J. Carey, C. G. Weldon, J. Zhang, C. Wang and J. Park, *Biomicrofluidics*, 2018, **12**, 51503.
- 41 Z. Gan, N. Xia and Z. Wu, *Acc. Chem. Res.*, 2018, **51**, 2774–2783.
- 42 K. Loza, M. Heggen and M. Epple, *Adv. Funct. Mater.*, 2020, **30**, 1909260.
- 43 M. P. Mallin and C. J. Murphy, *Nano Lett.*, 2002, **2**, 1235–1237.
- 44 D. Rioux and M. Meunier, *J. Phys. Chem. C*, 2015, **119**, 13160–13168.
- 45 R. Intartaglia, G. Das, K. Bagga, A. Gopalakrishnan, A. Genovese, M. Povia, E. Di Fabrizio, R. Cingolani, A. Diaspro and F. Brandi, *Phys. Chem. Chem. Phys.*, 2013, **15**, 3075–3082.
- 46 X. Xia, Y. Wang, A. Ruditskiy and Y. Xia, *Adv. Mater.*, 2013, **25**, 6313–6333.
- 47 R. Jin, C. Zeng, M. Zhou and Y. Chen, *Chem. Rev.*, 2016, **116**, 10346–10413.
- 48 A. Mathew and T. Pradeep, *Part. Part. Syst. Charact.*, 2014, **31**, 1017–1053.
- 49 A. Baksi, P. Chakraborty, S. Bhat, G. Natarajan and T. Pradeep, *Chem. Commun.*, 2016, **52**, 8397–8400.
- 50 Q. Yao, X. Yuan, T. Chen, D. T. Leong and J. Xie, *Adv. Mater.*, 2018, **30**, 1–23.
- 51 I. Chakraborty and T. Pradeep, *Chem. Rev.*, 2017, **117**, 8208–8271.
- 52 T. Chen, Q. Yao, R. R. Nasaruddin and J. Xie, *Angew. Chem., Int. Ed.*, 2019, **58**, 11967–11977.
- 53 P. Chakraborty and T. Pradeep, *NPG Asia Mater.*, 2019, **11**, 48.
- 54 A. C. Templeton, W. P. Wuelfing and R. W. Murray, *Acc. Chem. Res.*, 2000, **33**, 27–36.
- 55 M. Zhu, C. M. Aikens, F. J. Hollander, G. C. Schatz and R. Jin, *J. Am. Chem. Soc.*, 2008, **130**, 5883–5885.
- 56 Z. Luo, V. Nachammai, B. Zhang, N. Yan, D. T. Leong, D. E. Jiang and J. Xie, *J. Am. Chem. Soc.*, 2014, **136**, 10577–10580.
- 57 J. Hassinen, P. Pulkkinen, E. Kalenius, T. Pradeep, H. Tenhu, H. Häkkinen and R. H. A. Ras, *J. Phys. Chem. Lett.*, 2014, **5**, 585–589.
- 58 C. M. Aikens, *J. Phys. Chem. Lett.*, 2011, **2**, 99–104.
- 59 A. Fernando, K. L. D. M. Weerawardene, N. V. Karimova and C. M. Aikens, *Chem. Rev.*, 2015, **115**, 6112–6216.
- 60 K. R. Krishnadas, A. Baksi, A. Ghosh, G. Natarajan and T. Pradeep, *Nat. Commun.*, 2016, **7**, 13447.
- 61 K. R. Krishnadas, A. Ghosh, A. Baksi, I. Chakraborty, G. Natarajan and T. Pradeep, *J. Am. Chem. Soc.*, 2016, **138**, 140–148.
- 62 A. Ghosh, D. Ghosh, E. Khatun, P. Chakraborty and T. Pradeep, *Nanoscale*, 2017, **9**, 1068–1077.
- 63 E. Khatun, P. Chakraborty, B. R. Jacob, G. Paramasivam, M. Bodiuzzaman, W. A. Dar and T. Pradeep, *Chem. Mater.*, 2020, **32**, 611–619.
- 64 S. Bhat, A. Baksi, S. K. Mudedla, G. Natarajan, V. Subramanian and T. Pradeep, *J. Phys. Chem. Lett.*, 2017, **8**, 2787–2793.
- 65 R. Kazan, U. Müller and T. Bürgi, *Nanoscale*, 2019, **11**, 2938–2945.
- 66 X. M. Lin, C. M. Sorensen and K. J. Klabunde, *J. Nanopart. Res.*, 2000, **2**, 157–164.
- 67 B. L. V. Prasad, S. I. Stoeva, C. M. Sorensen and K. J. Klabunde, *Langmuir*, 2002, **18**, 7515–7520.
- 68 J. R. Shimpi, D. S. Sidhaye and B. L. V. Prasad, *Langmuir*, 2017, **33**, 9491–9507.
- 69 D. Jose, J. E. Matthiesen, C. Parsons, C. M. Sorensen and K. J. Klabunde, *J. Phys. Chem. Lett.*, 2012, **3**, 885–890.
- 70 S. I. Stoeva, B. L. V. Prasad, S. Uma, P. K. Stoimenov, V. Zaikovski, C. M. Sorensen and K. J. Klabunde, *J. Phys. Chem. B*, 2003, **107**, 7441–7448.
- 71 P. Sahu and B. L. V. Prasad, *Langmuir*, 2014, **30**, 10143–10150.
- 72 S. Stoeva, K. J. Klabunde, C. M. Sorensen and I. Dragieva, *J. Am. Chem. Soc.*, 2002, **124**, 2305–2311.
- 73 S. P. Bhaskar, M. Vijayan and B. R. Jagirdar, *J. Phys. Chem. C*, 2014, **118**, 18214–18225.
- 74 P. Sahu and B. L. V. Prasad, *Nanoscale*, 2013, **5**, 1768–1771.
- 75 P. Sahu and B. L. V. Prasad, *Chem. Phys. Lett.*, 2012, **525–526**, 101–104.
- 76 J. R. Shimpi, V. R. Chaudhari and B. L. V. Prasad, *Langmuir*, 2018, **34**, 13680–13689.
- 77 D. S. Sidhaye and B. L. V. Prasad, *New J. Chem.*, 2011, **35**, 755–763.

- 78 B. L. V. Prasad, S. I. Stoeva, C. M. Sorensen and K. J. Klabunde, *Chem. Mater.*, 2003, **15**, 935–942.
- 79 A. Som, I. Chakraborty, T. A. Maark, S. Bhat and T. Pradeep, *Adv. Mater.*, 2016, **28**, 2827–2833.
- 80 A. Chakraborty, A. C. Fernandez, A. Som, B. Mondal, G. Natarajan, G. Paramasivam, T. Lahtinen, H. Häkkinen, Nonappa and T. Pradeep, *Angew. Chem., Int. Ed.*, 2018, **57**, 6522–6526.
- 81 J. Kimling, M. Maier, B. Okenve, V. Kotaidis, H. Ballot and A. Plech, *J. Phys. Chem. B*, 2006, **110**, 15700–15707.
- 82 A. Mari, P. Imperatori, G. Marchegiani, L. Pilloni, A. Mezzi, S. Kaciulis, C. Cannas, C. Meneghini, S. Mobilio and L. Suber, *Langmuir*, 2010, **26**, 15561–15566.
- 83 T. Dadosh, *Mater. Lett.*, 2009, **63**, 2236–2238.
- 84 Z. Wu, J. Suhan and R. Jin, *J. Mater. Chem.*, 2009, **19**, 622–626.
- 85 S. Bhat, R. P. Narayanan, A. Baksi, P. Chakraborty, G. Paramasivam, R. R. J. Methikkalam, A. Nag, G. Natarajan and T. Pradeep, *J. Phys. Chem. C*, 2018, **122**, 19455–19462.
- 86 A. Mathew, G. Natarajan, L. Lehtovaara, H. Häkkinen, R. M. Kumar, V. Subramanian, A. Jaleel and T. Pradeep, *ACS Nano*, 2014, **8**, 139–152.
- 87 Nonappa, T. Lahtinen, J. S. Haataja, T. R. Tero, H. Häkkinen and O. Ikkala, *Angew. Chem., Int. Ed.*, 2016, **55**, 16035–16038.
- 88 E. Lee, S. S. Yi, M. S. Kim and K. Kim, *J. Mol. Struct.*, 1993, **298**, 47–54.
- 89 S. A. Harfenist, Z. L. Wang, M. M. Alvarez, I. Vezmar and R. L. Whetten, *J. Phys. Chem.*, 1996, **100**, 13904–13910.
- 90 A. Hutzler, T. Schmutzler, M. P. M. Jank, R. Branscheid, T. Unruh, E. Spiecker and L. Frey, *Nano Lett.*, 2018, **18**, 7222–7229.
- 91 S. Mozaffari, W. Li, M. Dixit, S. Seifert, B. Lee, L. Kovarik, G. Mpourmpakis and A. M. Karim, *Nanoscale Adv.*, 2019, **1**, 4052–4066.
- 92 K. Zheng, V. Fung, X. Yuan, D. E. Jiang and J. Xie, *J. Am. Chem. Soc.*, 2019, **141**, 18977–18983.
- 93 M. A. El-Sayed, *Acc. Chem. Res.*, 2001, **34**, 257–264.
- 94 W. P. Halperin, *Rev. Mod. Phys.*, 1986, **58**, 533–606.
- 95 C. Burda, X. Chen, R. Narayanan and M. A. El-Sayed, *Chemistry and Properties of Nanocrystals of Different Shapes*, 2005, vol. 36.
- 96 X. Mao, C. Liu, M. Hesari, N. Zou and P. Chen, *Nat. Chem.*, 2019, **11**, 687–694.
- 97 X. Zhou, W. Xu, G. Liu, D. Panda and P. Chen, *J. Am. Chem. Soc.*, 2010, **132**, 138–146.
- 98 P. Suchomel, L. Kvitek, R. Prucek, A. Panacek, A. Halder, S. Vajda and R. Zboril, *Sci. Rep.*, 2018, **8**, 1–11.
- 99 S. W. Verbruggen, M. Keulemans, J. A. Martens and S. Lenaerts, *J. Phys. Chem. C*, 2013, **117**, 19142–19145.
- 100 L. M. Liz-Marzán, *Langmuir*, 2006, **22**, 32–41.
- 101 G. Kothleitner, M. J. Neish, N. R. Lugg, S. D. Findlay, W. Grogger, F. Hofer and L. J. Allen, *Phys. Rev. Lett.*, 2014, **112**, 1–5.
- 102 Z. Chen, M. Weyland, X. Sang, W. Xu, J. H. Dycus, J. M. LeBeau, A. J. D'Alfonso, L. J. Allen and S. D. Findlay, *Ultramicroscopy*, 2016, **168**, 7–16.
- 103 P. G. Kotula, D. O. Klenov and H. S. von Harrach, *Microsc. Microanal.*, 2012, **18**, 691–698.
- 104 S. Zhang, L. Zhang, K. Liu, M. Liu, Y. Yin and C. Gao, *Mater. Chem. Front.*, 2018, **2**, 1328–1333.
- 105 P. Peljo, H. H. Girault, J. A. Manzanares, P. Peljo and H. H. Girault, *J. Phys. Chem. C*, 2017, **121**, 13405–13411.
- 106 L. G. AbdulHalim, M. S. Bootharaju, Q. Tang, S. Del Gobbo, R. G. AbdulHalim, M. Eddaoudi, D. E. Jiang and O. M. Bakr, *J. Am. Chem. Soc.*, 2015, **137**, 11970–11975.
- 107 P. Chakraborty, A. Nag, A. Chakraborty and T. Pradeep, *Acc. Chem. Res.*, 2019, **52**, 2–11.
- 108 K. R. Krishnadas, G. Natarajan, A. Baksi, A. Ghosh, E. Khatun and T. Pradeep, *Langmuir*, 2019, **35**, 11243–11254.
- 109 Q. Li, S. Wang, K. Kirschbaum, K. J. Lambright, A. Das and R. Jin, *Chem. Commun.*, 2016, **52**, 5194–5197.
- 110 X. Kang, S. Chen, S. Jin, Y. Song, Y. Xu, H. Yu, H. Sheng and M. Zhu, *ChemElectroChem*, 2016, **3**, 1261–1265.
- 111 D. K. Lee, S. Il Park, J. K. Lee and N. M. Hwang, *Acta Mater.*, 2007, **55**, 5281–5288.
- 112 *Handbook of Nanophysics*, ed. K. Sattler, CRC Press, Boca Raton, 2010.
- 113 D. K. Lee and N. M. Hwang, *Scr. Mater.*, 2009, **61**, 304–307.
- 114 A. B. Smetana, K. J. Klabunde, C. M. Sorensen, A. A. Ponce and B. Mwale, *J. Phys. Chem. B*, 2006, **110**, 2155–2158.
- 115 D. S. Dessau, Z.-X. Shen, B. O. Wells, W. E. Spicer, R. S. List, A. J. Arko, R. J. Bartlett, C. G. Olson, D. B. Mitzi, C. B. Eom, A. Kapitulnik and T. H. Geballe, *J. Vac. Sci. Technol., A*, 1991, **9**, 383–389.
- 116 D. R. H. Jones, *J. Mater. Sci.*, 1974, **9**, 1–17.
- 117 L. Xu, W. Ma, L. Wang, C. Xu, H. Kuang and N. A. Kotov, *Chem. Soc. Rev.*, 2013, **42**, 3114–3126.
- 118 M. Boterashvili, T. Shirman, R. Popovitz-Biro, Q. Wen, M. Lahav and M. E. Van Der Boom, *Chem. Commun.*, 2016, **52**, 8079–8082.
- 119 A. Guerrero-Martínez, J. Pérez-Juste, E. Carbó-Argibay, G. Tardajos and L. M. Liz-Marzán, *Angew. Chem., Int. Ed.*, 2009, **48**, 9484–9488.
- 120 K. J. Si, Y. Chen, Q. Shi and W. Cheng, *Adv. Sci.*, 2018, **5**, 1700179.
- 121 X. M. Lin, H. M. Jaeger, C. M. Sorensen and K. J. Klabunde, *J. Phys. Chem. B*, 2001, **105**, 3353–3357.
- 122 J. He, P. Kanjanaboos, N. L. Frazer, A. Weis, X. M. Lin and H. M. Jaeger, *Small*, 2010, **6**, 1449–1456.
- 123 J. C. Love, L. A. Estroff, J. K. Kriebel, R. G. Nuzzo and G. M. Whitesides, *Chem. Rev.*, 2005, **105**, 1103–1170.

## ELECTRONIC SUPPLEMENTARY INFORMATION

### Atom Transfer between Precision Nanoclusters and Polydispersed Nanoparticles: A Facile Route for Monodispersed Alloy Nanoparticles and their Superstructures

Paulami Bose,<sup>a</sup> Papri Chakraborty,<sup>‡a</sup> Jyoti Sarita Mohanty,<sup>‡a</sup> Nonappa,<sup>b</sup> Angshuman Ray Chowdhuri,<sup>a</sup> Esma Khatun,<sup>a</sup> Tripti Ahuja,<sup>a</sup> Ananthu Mahendranath,<sup>a,c</sup> and Thalappil Pradeep<sup>\*a</sup>

<sup>a</sup>DST Unit of Nanoscience (DST UNS) and Thematic Unit of Excellence (TUE), Department of Chemistry, Indian Institute of Technology Madras, Chennai 600 036, India.

<sup>b</sup> Faculty of Engineering and Natural Sciences, Tampere University, P.O. Box 541, FI-33101 Tampere, Finland.

<sup>c</sup>Department of Metallurgical and Materials Engineering, Indian Institute of Technology Madras, Chennai 600036, India.

\*E-mail: [pradeep@iitm.ac.in](mailto:pradeep@iitm.ac.in)

‡ Authors contributed equally.

#### TABLE OF CONTENT

Fig.	Description	Page
SI 1	Instrumentation	2
Fig. S1	Characterization of 2-PET-capped silver NPs	6
Fig. S2	Characterization of Au <sub>25</sub> (PET) <sub>18</sub>	7
Fig. S3	HRTEM micrographs of reacted 4 nm Ag@PET NPs	8
Fig. S4	Changes in UV-Vis spectra in the course of the reaction	9
Fig. S5	Size distribution for reaction of 4 nm Ag@PET NPs	10
Fig. S6	Raman spectra of parent and reacted NPs	11
Fig. S7	MALDI MS studies	12
Fig. S8	HRTEM micrographs of the precipitate	13
Fig. S9	Concentration dependent study	14
Fig. S10	Kinetic study of the reaction using UV-Vis spectroscopy	15
Fig. S11	Intensity pattern of intermediates	16
Fig. S12	HRTEM images of reacted polydispersed 8 nm set	17
Fig. S13	Size distribution of polydispersed 8 nm NPs	18
Fig. S14	Spot EDS details of Fig. 4A	19
Fig. S15	Spot EDS details of Fig. 4B	20
Fig. S16	Spot EDS details of Fig. 4C	21
Fig. S17	Size effect of Ag@PET NP using UV-Vis spectroscopy	22



Fig. S18	Low temperature reaction monitoring	23
Fig. S19	Size dependent ESI-MS intermediates in m/z 2000-3000	24
Fig. S20	Role of ligand in the inter-particle reaction	25
Fig. S21	IFFT and Profile of Fig. 6A,B	26
Fig. S22	Electron Tomography and 3D reconstruction of disc shaped assembly	27
Fig. S23	HRTEM imaging of the progress of the reaction of 8 nm Ag NPs	28
Fig. S24	Effect of NP-NC reaction on the particle size distribution	29
Fig. S25	UV-Vis reaction for 3 and 8 nm Ag NPs	29
Video V1	Tilt series of Fig. 6A	Attached
Video V2	3D construction of Fig. 6A	Attached
Video V3	Tilt series of Fig. 6B	Attached
Video V4	3D construction of Fig. 6B	Attached
Video V5	Tilt series of Fig. S22	Attached
Video V6	3D construction of Fig. S22	Attached
SI 27	References	30

## Instrumentation

**UV-Vis Spectroscopy:** Perkin Elmer Lambda 25 instrument was used for optical absorption spectra recording having a range of 200 – 1100 nm with a band pass filter of 1 nm.

**HRTEM:** High-resolution transmission electron microscopy (HRTEM) imaging was carried out on a JEOL 3010, 300 kV instrument with a UHR polepiece. Energy dispersive analysis (EDS) was performed using an Oxford EDAX connected to the HRTEM. A Gatan 794 multiscan CCD camera was used to capture the images. Samples were prepared by dropcasting the dispersion on carbon coated copper grids (spi Supplies, 3530C-MB) and dried at ambient conditions.

**MALDI MS:** Matrix Assisted Laser Desorption Ionization Mass Spectrometer (MALDI MS) data were collected using Voyager-DE PRO Biospectrometry Workstation from Applied Biosystems.

A solution in 0.5 mL of dichloromethane (DCM) was made with about 6.2 mg of Trans-2-[3-(4-tertbutylphenyl)-2-methyl-2-propenylidene]malononitrile (DCTB, > 98%) matrix and it

was used for the MALDI MS measurements. Roughly 1 part of sample dissolved in DCM and 2 parts of the prepared DCTB matrix solution were mixed thoroughly and spotted on the sample plate and was left to dry at ambient conditions. In order to minimize fragmentation of the sample, all the measurements were carried out at the laser fluence. Desorption and ionization was carried out with a 337 nm Nitrogen laser. Mass spectra were recorded in linear positive ion and/or negative ion mode and were averaged for nearly 250 shots. Accelerating voltage was kept at 20 kV.

**ESI MS:** All the mass spectrometric measurements were carried out in a Waters SYNAPT G2-Si instrument. The instrument is well equipped with electrospray ionization, and all spectra were measured in the negative ion and resolution mode. The instrument has the capability of measuring ESI MS with high-resolution up to the orders of 50,000 (m/Dm). NaI was used for calibrating the instrument. The measurement conditions were optimized to a capillary voltage of 3 kV, a cone voltage of 20 V, a desolvation gas flow of 400 liters/hour, a source temperature of 100°C, a desolvation temperature of 150°C, and a sample infusion rate of 30 ml/hour.

All the mass spectrometric measurements were done in a Waters SYNAPT G2-Si instrument. The instrument is well equipped with ESI, and all spectra were measured in the negative ion and resolution mode. The instrument is capable of measuring ESI MS with high-resolution touching orders of 50,000 (m/Dm). The instrument was calibrated using NaI. An optimized condition involving a capillary voltage of 3 kV, a cone voltage of 20 V, a desolvation gas flow of 400 liters/hour, a source temperature of 100°C, a desolvation temperature of 150°C, and a sample infusion rate of 30 ml/hour was used for all measurements.

**Raman Spectroscopy:** Raman measurements were carried out using a WITec GmbH alpha300S confocal Raman equipped with a 532 nm laser as the excitation source. Measurements involved a 20× objective (Plan-Apochromat, Zeiss), 600 grooves/mm grating for 1 s acquisition time. A laser power of ~800 μW was maintained on the sample throughout the measurement.

**Serial EM and Electron Tomography Reconstruction:** The transmission electron microscopy (TEM) images were collected using JEM 3200FSC field emission microscope (JEOL) operated at 300 kV in bright field mode with Omega-type Zero-loss energy filter. The images were

acquired with Gatan digital micrograph software while the specimen temperature was maintained at -187°C. For transmission electron tomographic reconstruction, tilt series of 2D projections were acquired with the SerialEM-software package.<sup>1,2</sup> Specimen was tilted between  $\pm 69^\circ$  angles with 2-3° increment steps under low dose mode.<sup>3</sup> The acquired raw stack of images was first subjected for a series of pre-processing, coarse alignment, final alignment and further aligned using IMOD software package.<sup>4</sup> The final aligned file was then utilized for 3D reconstruction with custom made maximum entropy method (MEM) program with a regularization parameter value of  $\lambda = 1.0 \text{ e}^{-3}$  on MacPro.<sup>5,6</sup> The 3D isosurface and solid colored images were produced using UCSF Chimera.

**Scanning Transmission Electron Microscopy and EDS mapping:** The STEM imaging was performed using JEOL JEM-2800 high throughput electron microscope equipped with Schottky type field emission gun operated at 200 kV with simultaneous bright field (BF) and dark field (DF) STEM imaging. For elemental mapping energy dispersive X-ray mapping and spectra were collected using dual silicon drift detectors.

**Concentration calculation\* for 4 nm Ag@PET nanoparticles case (Fig. 1 A)**

Average size of Ag NP (HRTEM),  $2R = 4.37 \text{ nm}$

Volume of 1 Ag NP (sphere),  $V = \frac{4}{3}\pi R^3 = 43.69 \text{ nm}^3$

Density of Ag NPs,  $\rho = 10.5 \frac{\text{g}}{\text{cm}^3} = 1.05 \frac{\text{mg}}{\text{nm}^3}$

Mass of 1 Ag NPs,  $m = V\rho = 4.58 \times 10^{-16} \text{ mg}$

Weight of Ag NPs (dry weight of the sample),  $W = 7.5 \frac{\text{mg}}{3 \text{ mL}} = 2.5 \frac{\text{mg}}{\text{L}}$

Number of NPs in the sample,  $N = \frac{W}{m} = 5.45 \times 10^{18} \frac{\text{particles}}{\text{L}}$

Particle molarity of Ag@PET NPs =  $\frac{N}{N_A} = 9.05 \text{ } \mu\text{M}$

**Concentration calculation\* for 1.8 nm Au<sub>25</sub>(PET)<sub>18</sub> nanocluster**

Average size of gold nanocluster (HRTEM),  $2R = 1.8 \text{ nm}$

Volume of 1 gold nanocluster (sphere),  $V = \frac{4}{3}\pi R^3 = 3.05 \text{ nm}^3$

Density of gold nanoparticles,  $\rho = 19.32 \frac{\text{g}}{\text{cm}^3} = 1.93 \times 10^{-17} \frac{\text{mg}}{\text{nm}^3}$

Mass of 1 gold nanocluster,  $m = V\rho = 5.89 \times 10^{-17} \text{ mg}$

Weight of gold nanocluster (dry weight of the sample),  $W = 0.9 \frac{\text{mg}}{0.3 \text{ mL}} = 3000 \frac{\text{mg}}{\text{L}}$

Number of particles in the sample,  $N = \frac{W}{m} = 5.08 \times 10^{19} \frac{\text{particles}}{\text{L}}$

Particle molarity of gold nanocluster =  $\frac{N}{N_A} = 84.4 \mu\text{M}$

Using,  $M_1V_1 = M_2V_2$

Particle molarity ( $M_2$ ) when 0.3 mL cluster diluted in 3.3 mL DCM =  $7.67 \mu\text{M}$

Weight of gold nanocluster (dry weight of the sample),  $W = 8.1 \frac{\text{mg}}{3 \text{ mL}} = 2700 \frac{\text{mg}}{\text{L}}$

Number of particles in the sample,  $N = \frac{W}{m} = 4.57 \times 10^{19} \frac{\text{particles}}{\text{L}}$

Particle molarity of gold nanocluster =  $\frac{N}{N_A} = 75.99 \mu\text{M}$

\* For simplicity of calculation, the concentration was calculated in terms of the metal present.

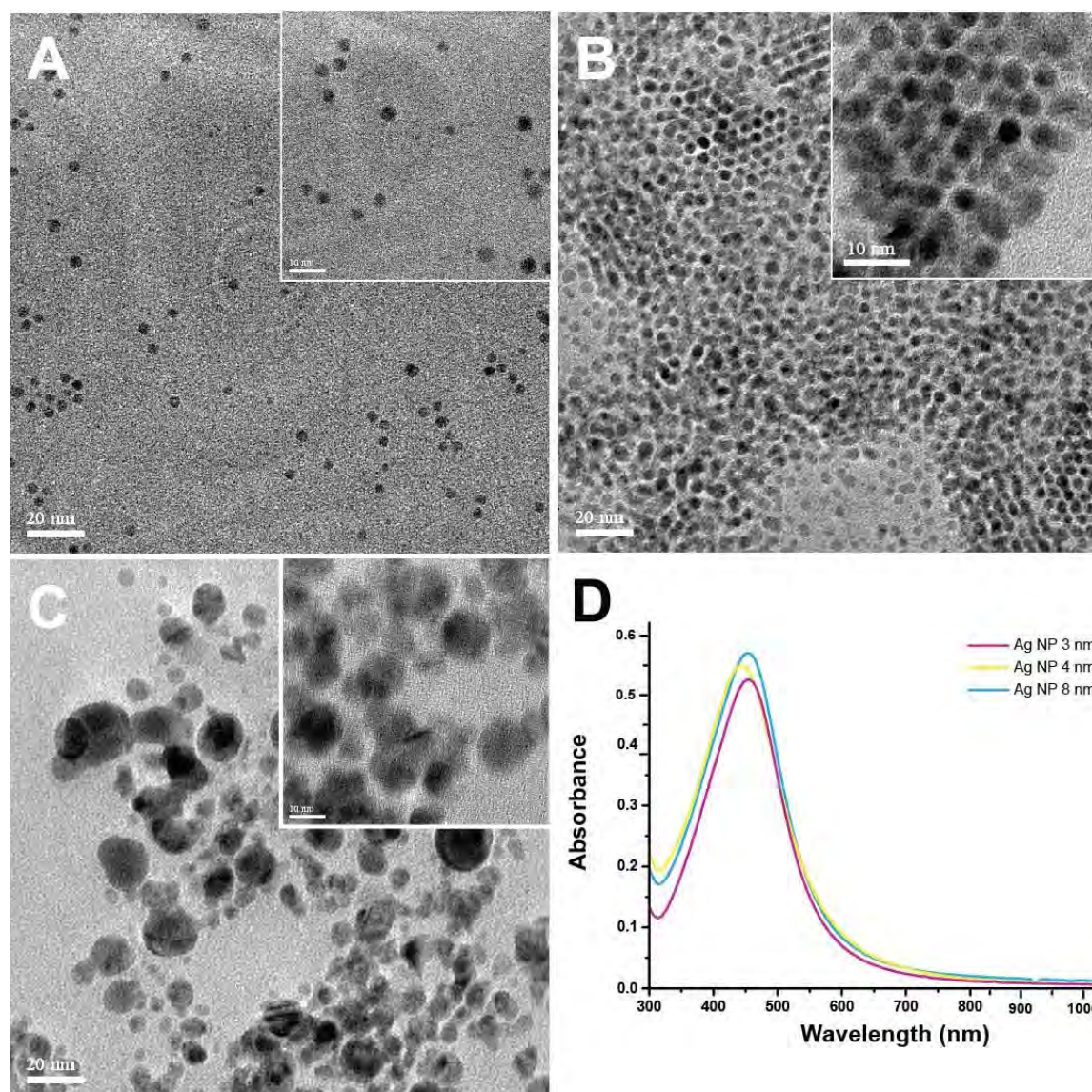


**Fig. S1** HRTEM micrographs of Ag@PET NPs of sizes, (A) 3 nm, (B) 4 nm, (C) polydispersed 8 nm, and (D) the corresponding UV-Vis spectra. The mentioned size indicates the most probable diameter of the metallic core of the particle.



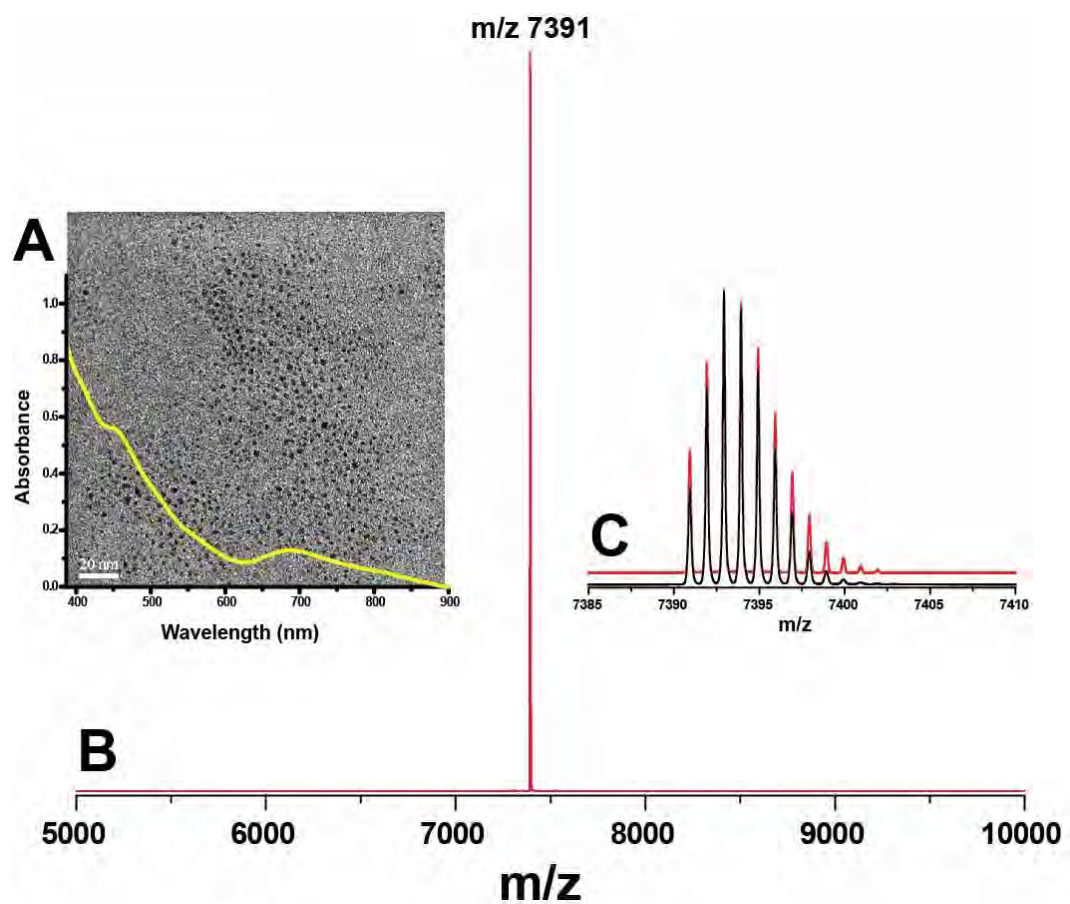


**Fig. S2** Characterization of  $\text{Au}_{25}(\text{PET})_{18}$  NC, (A) HRTEM micrograph and (inset) UV-Vis spectra with characteristic peaks at 397, 445, 552, 683, and 796 nm, (B) ESI MS spectrum of  $[\text{Au}_{25}(\text{PET})_{18}]^-$  NC having a molecular peak at  $m/z$  7391, (C) Experimental (black), and calculated (red) matching for high resolution isotopic distribution of the molecular ion peak. This is in agreement with already reported ESI MS spectra of  $\text{Au}_{25}(\text{PET})_{18}$  NC.<sup>7,8</sup>

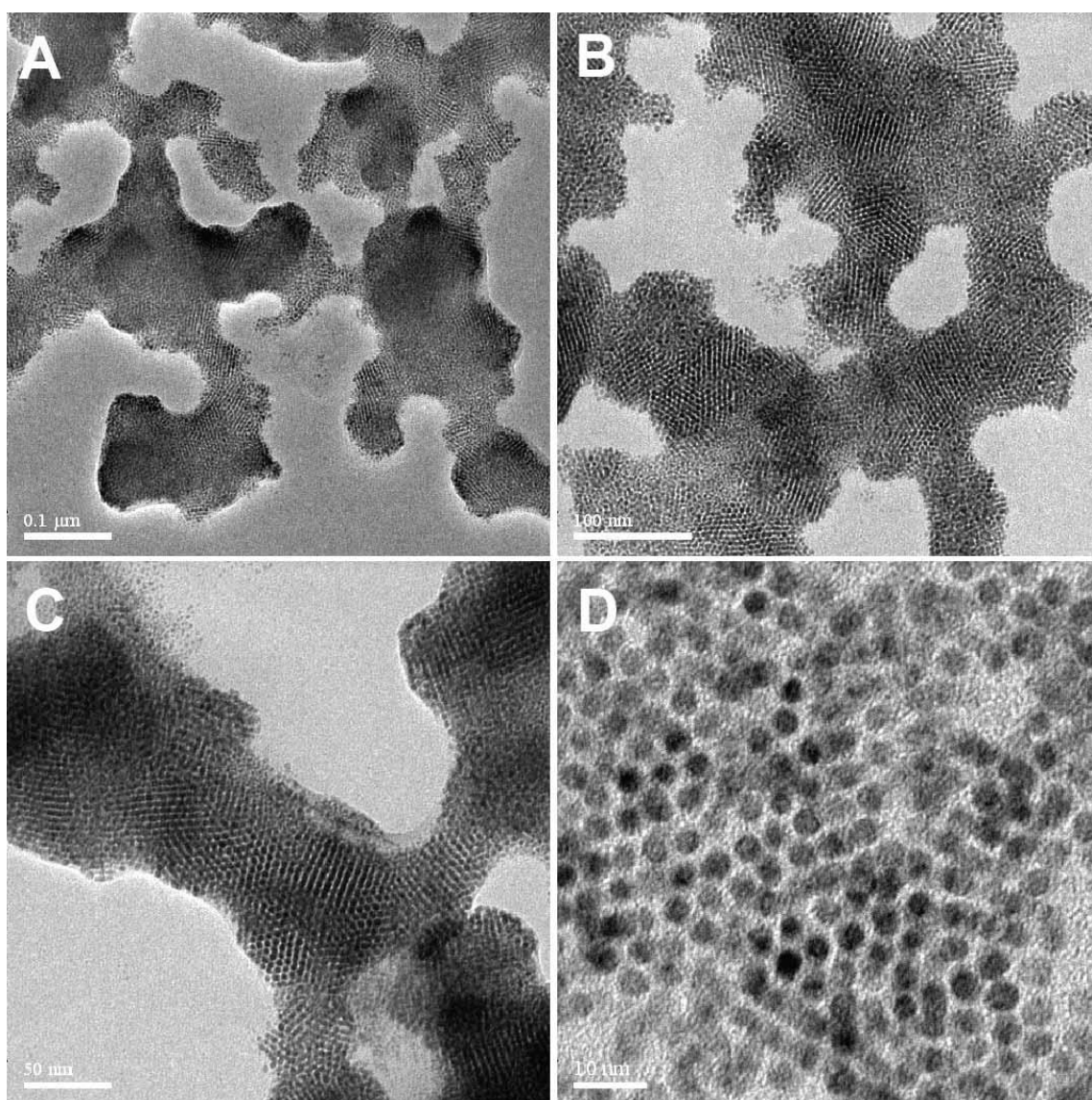


**Fig. S3** HRTEM micrographs of the spontaneous assembly formed after the reaction of 4 nm Ag@PET NPs captured at different magnifications, (A) 0.1  $\mu\text{m}$ , (B) 100 nm, (C) 50 nm, and (D) 10 nm. The NPs resulted in the reaction are approximately 3.45 nm.

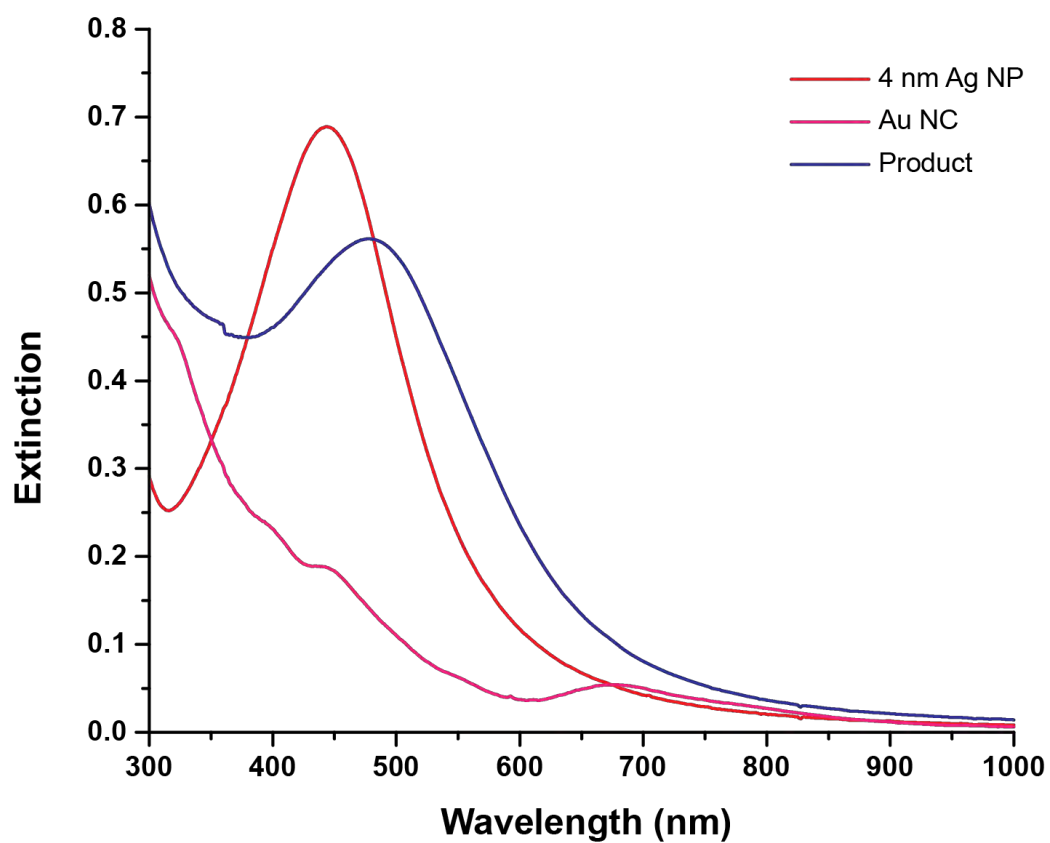


**Fig. S4** UV-Vis spectra of 4 nm Ag@PET NPs (red trace),  $\text{Au}_{25}(\text{PET})_{18}$  NC (magenta trace), and the reaction product (blue trace). The corresponding HRTEM micrographs from the same reaction mixture are already discussed in Fig. 1.

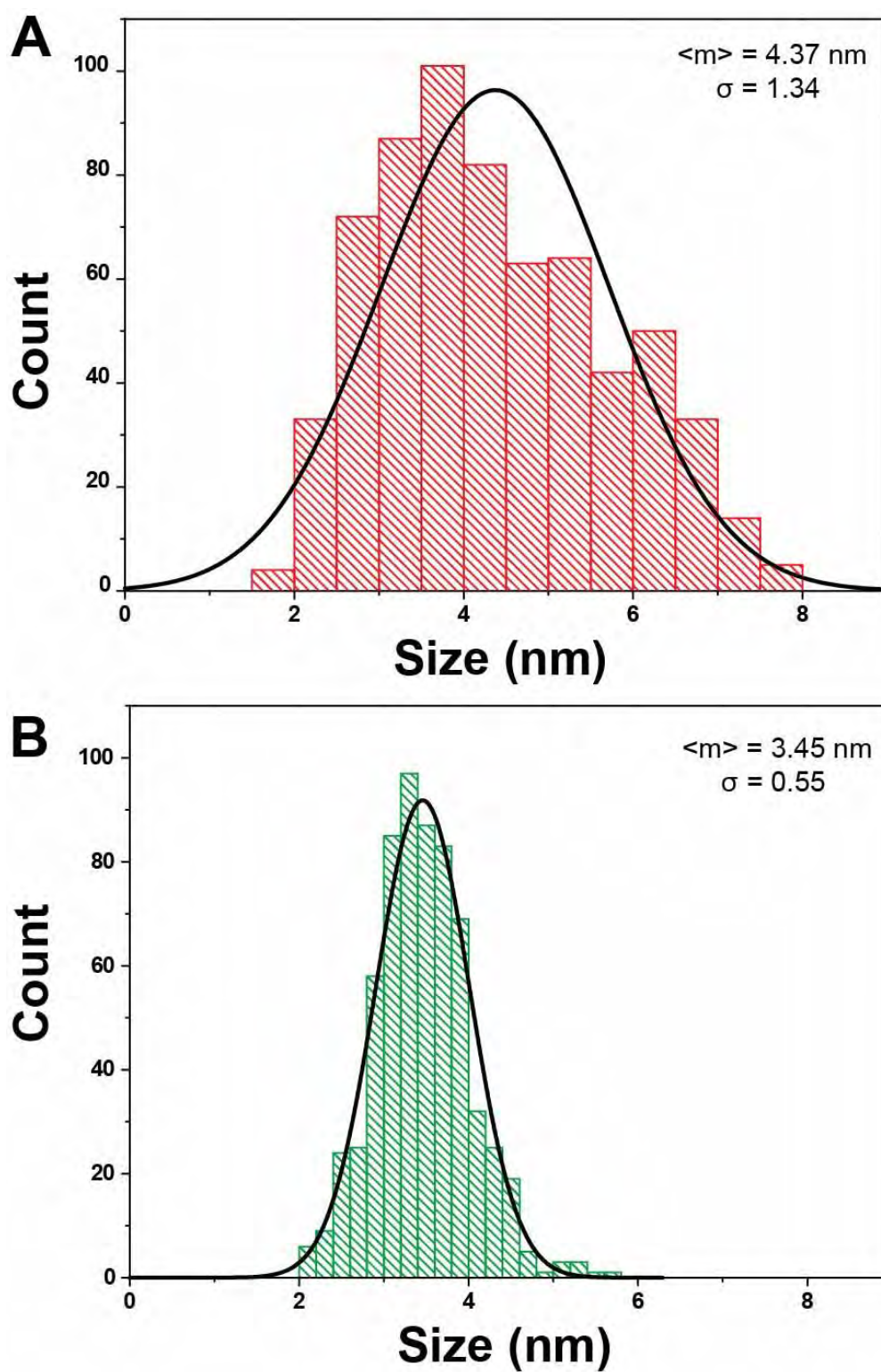


**Fig. S5** Particle size distribution of the 4 nm Ag@PET NP reaction case for the (A) parent NPs was  $4.37 \pm 2.3 \text{ nm}$ , and (B) reacted NPs was  $3.45 \pm 1.2 \text{ nm}$ , where  $\langle m \rangle$  and  $\sigma$  are the notations used for mean size and standard deviation, respectively.

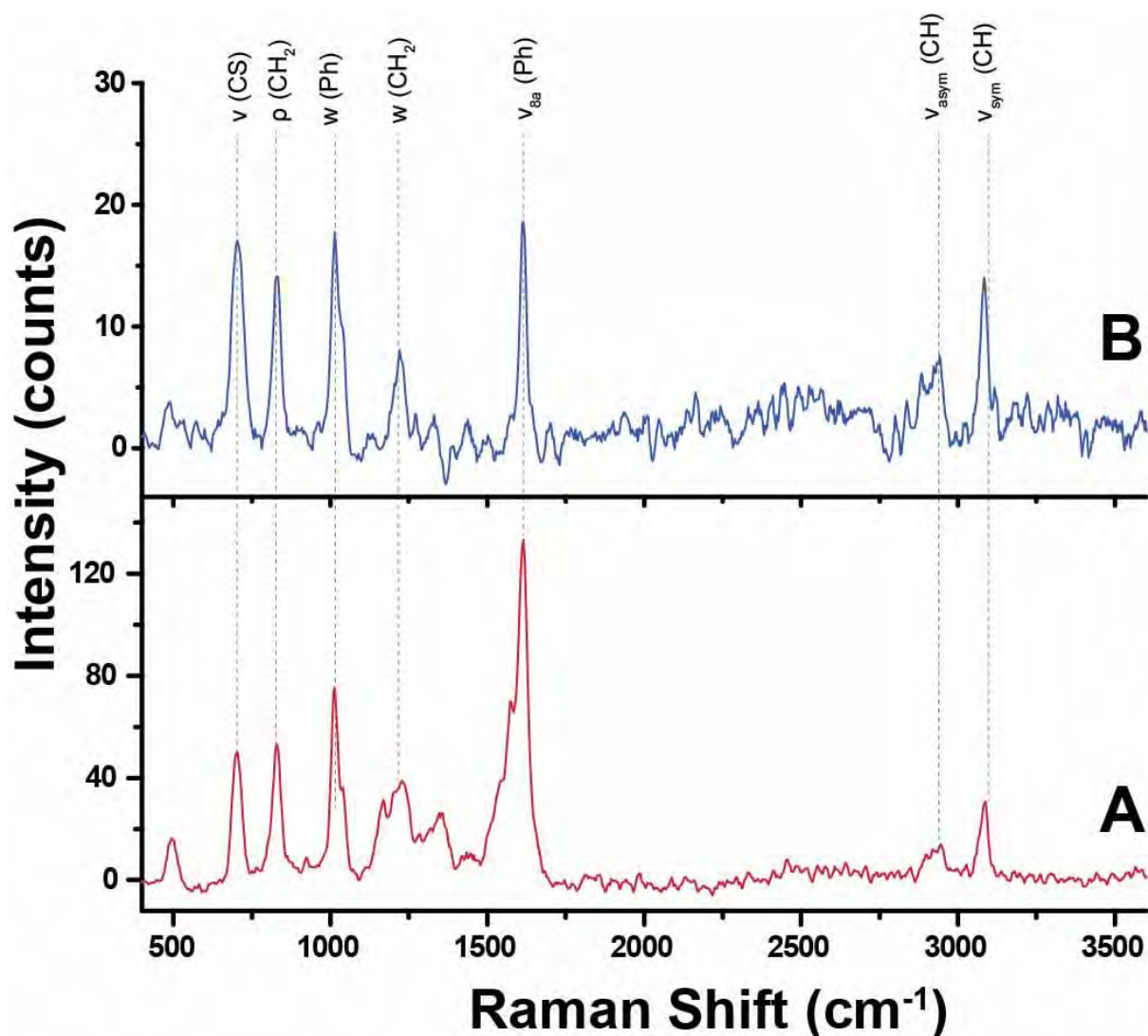


**Fig. S6** Raman Spectroscopic analysis of 4 nm Ag@PET NPs (A) before reaction, and (B) after reaction with  $\text{Au}_{25}(\text{PET})_{18}$  NC (reaction mixture was centrifuged followed by washing with DCM). Here, only the capping agent (2-PET) is Raman active.

**Spectral analysis of 2-PET:**  $699\text{ cm}^{-1}$  (CS symmetric stretch due to *trans* conformation of 2-PET),  $823\text{ cm}^{-1}$  ( $\text{CH}_2$  rocking),  $1005\text{ cm}^{-1}$  (In plane vibration of phenyl ring),  $1209\text{ cm}^{-1}$  ( $\text{CH}_2$  wag),  $1600\text{ cm}^{-1}$  (8a In a plane vibration of phenyl ring),  $2944\text{ cm}^{-1}$  (CH asymmetric stretch), and  $3071\text{ cm}^{-1}$  (CH symmetric stretch)



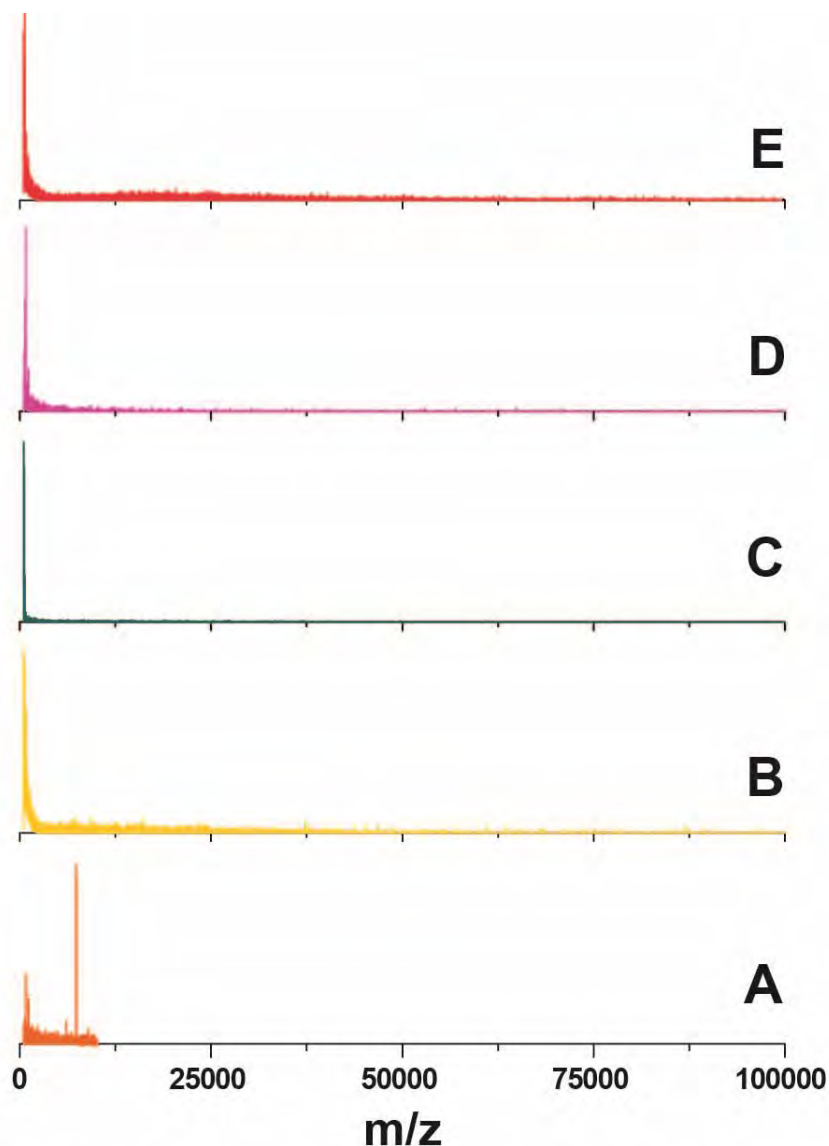


**Fig. S7** MALDI MS spectral analysis of the reactants, including, (A)  $\text{Au}_{25}(\text{PET})_{18}$  NC giving a molecular peak at  $m/z$  7407 in the negative ion mode, 4 nm Ag@PET NPs measured in (B) negative ion mode, and (C) positive ion mode. In case of the Ag NPs, in both the modes signals were absent. Then, the reactants were mixed and allowed to react for 15 min, following which the reaction mixture was subjected to centrifugation and the MALDI MS spectra was collected for both (D) supernatant, and (E) precipitate in the negative ion mode. The absence of peak at  $m/z$  7407 indicates the complete consumption of  $\text{Au}_{25}(\text{PET})_{18}$  NC during the reaction resulting in the alloy NPs.

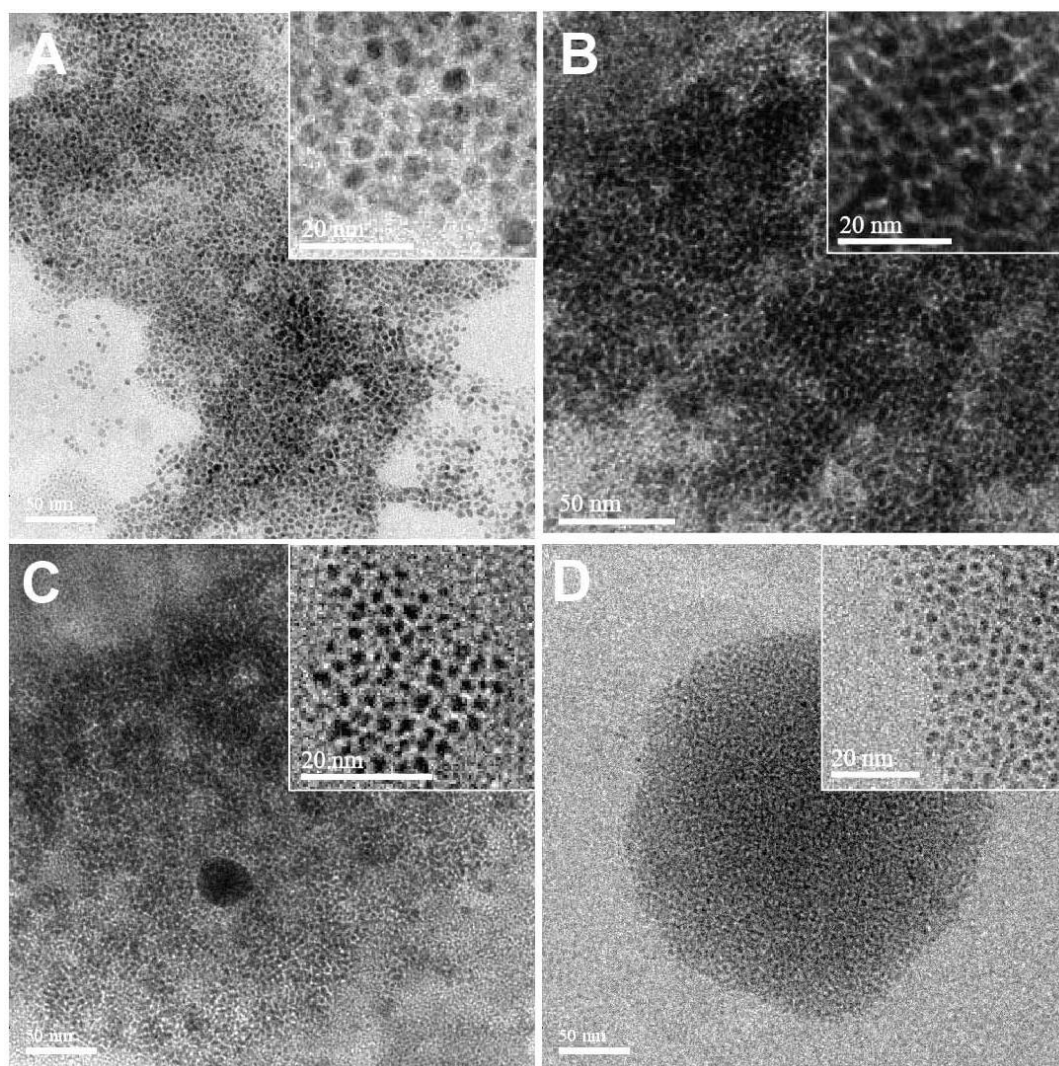


**Fig. S8** HRTEM micrographs of the precipitate collected on centrifugation after 15 min from the reaction mixture used for carrying out the ESI MS measurements. Precipitate images on the reaction with (A, B) 4 nm Ag@PET NPs, and (C, D) polydispersed 8 nm Ag@PET NPs. In both the cases, the precipitate HRTEM micrographs are similar to our initial findings in Fig. 1 A, and 3 D.

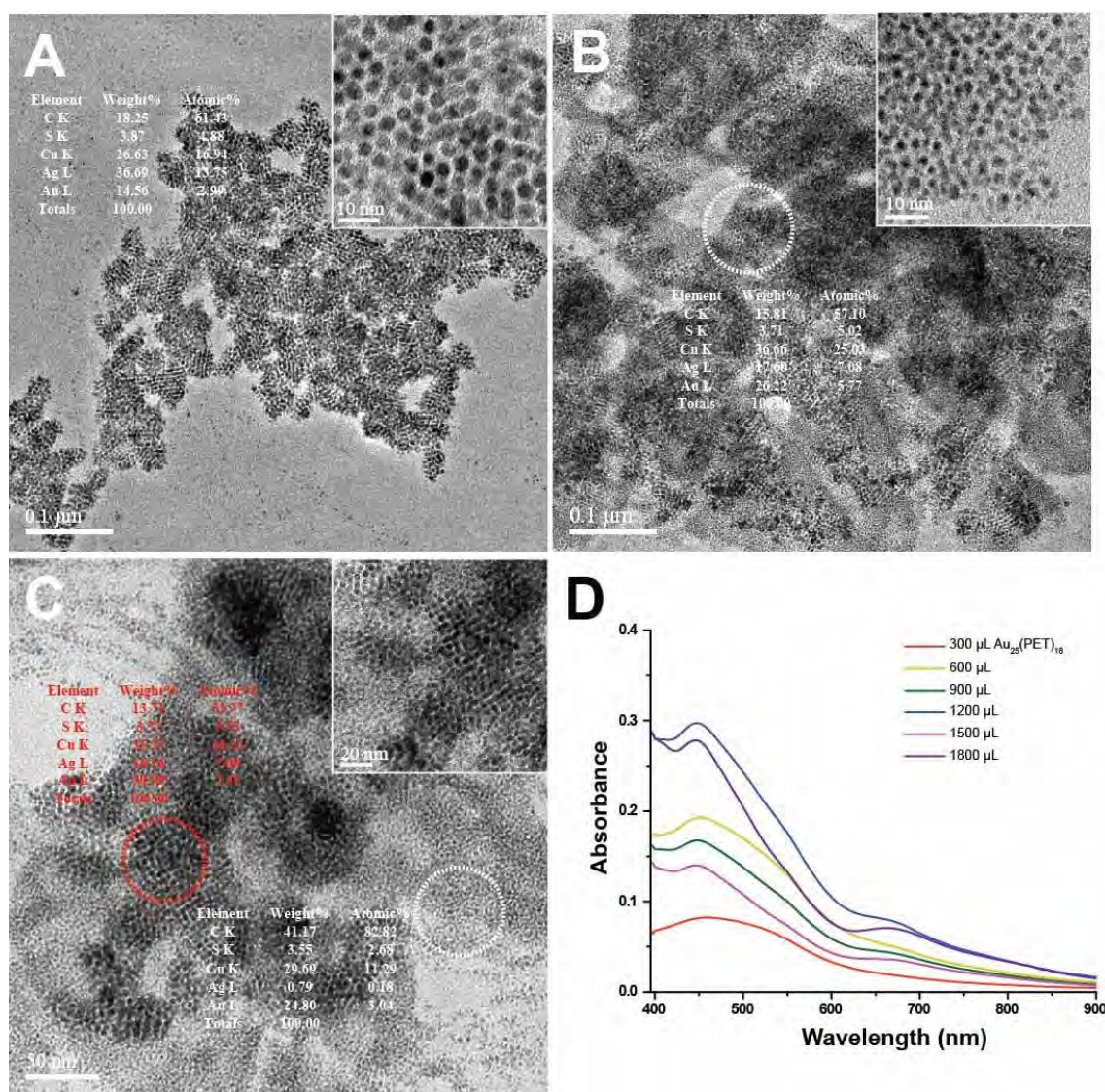


**Fig. S9** The concentration dependence of  $\text{Au}_{25}(\text{PET})_{18}$  NC in the reaction was studied using HRTEM and UV-Vis spectroscopy. The reaction mixture was monitored after adding each 300  $\mu\text{L}$  of  $\text{Au}_{25}(\text{PET})_{18}$  NC, HRTEM micrographs corresponding to the total cluster added to the reaction mixture, like, (A) 300  $\mu\text{L}$ , (B) 600  $\mu\text{L}$ , and (C) 900  $\mu\text{L}$ . (D) UV-Vis spectra showing the  $\text{Au}_{25}(\text{PET})_{18}$  NC features getting dominant as the amount of the cluster increases in the reaction medium. Concentrations mentioned in the experimental section.

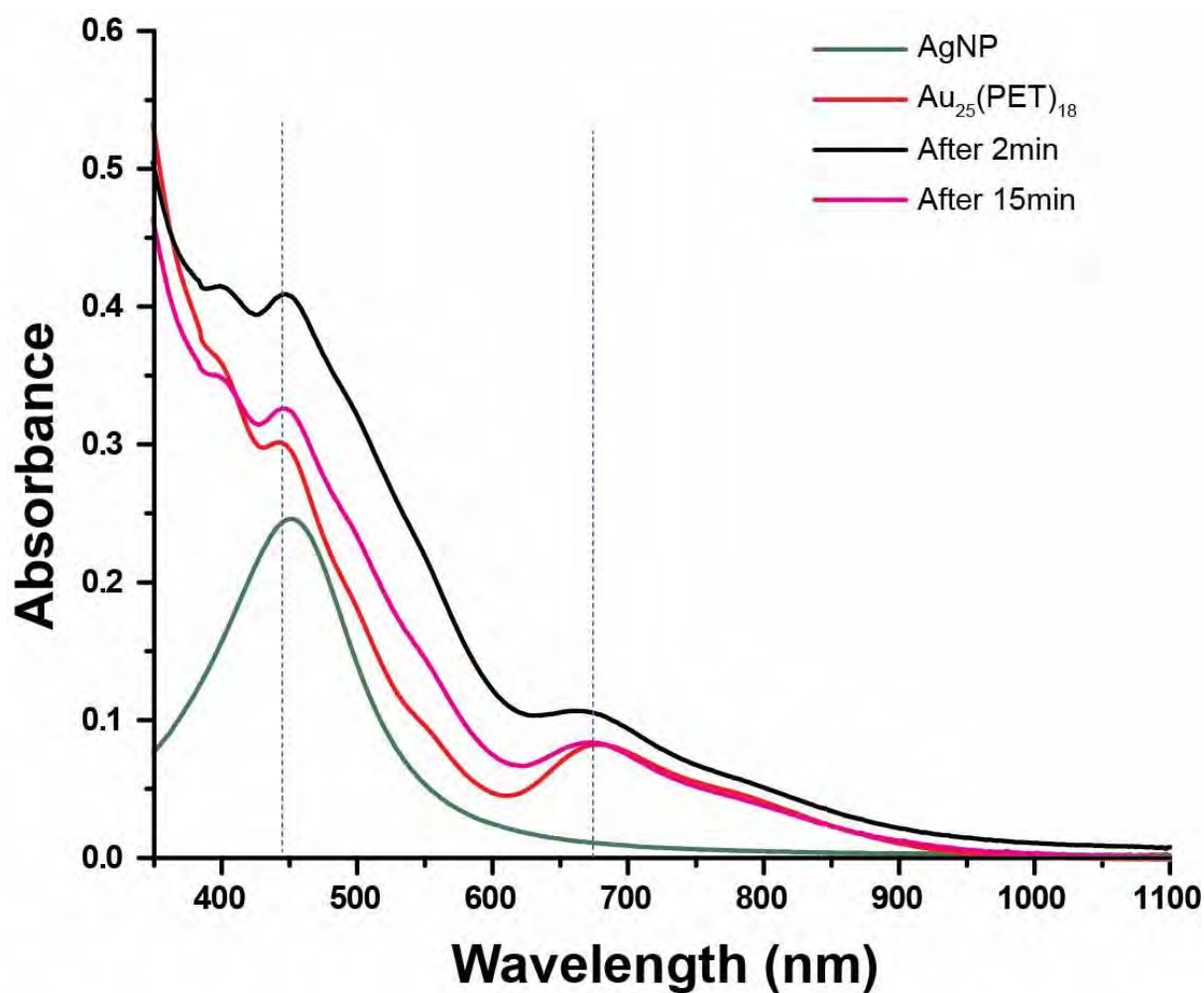


**Fig. S10** Kinetic study of the reaction of 4 nm Ag@PET NPs using UV-Vis spectroscopy, Ag@PET NPs (olive trace), Au<sub>25</sub>(PET)<sub>18</sub> (red trace), reaction mixture after 2 min (black trace) and 15 min (magenta trace). The blue shift (blue dotted lines) was observed after 2 min (black trace) and after 15 min the spectrum goes back to the original cluster (red trace) like feature. The shift in the UV-Vis spectrum at the 2 min interval suggests generation of new species in the reaction mixture.



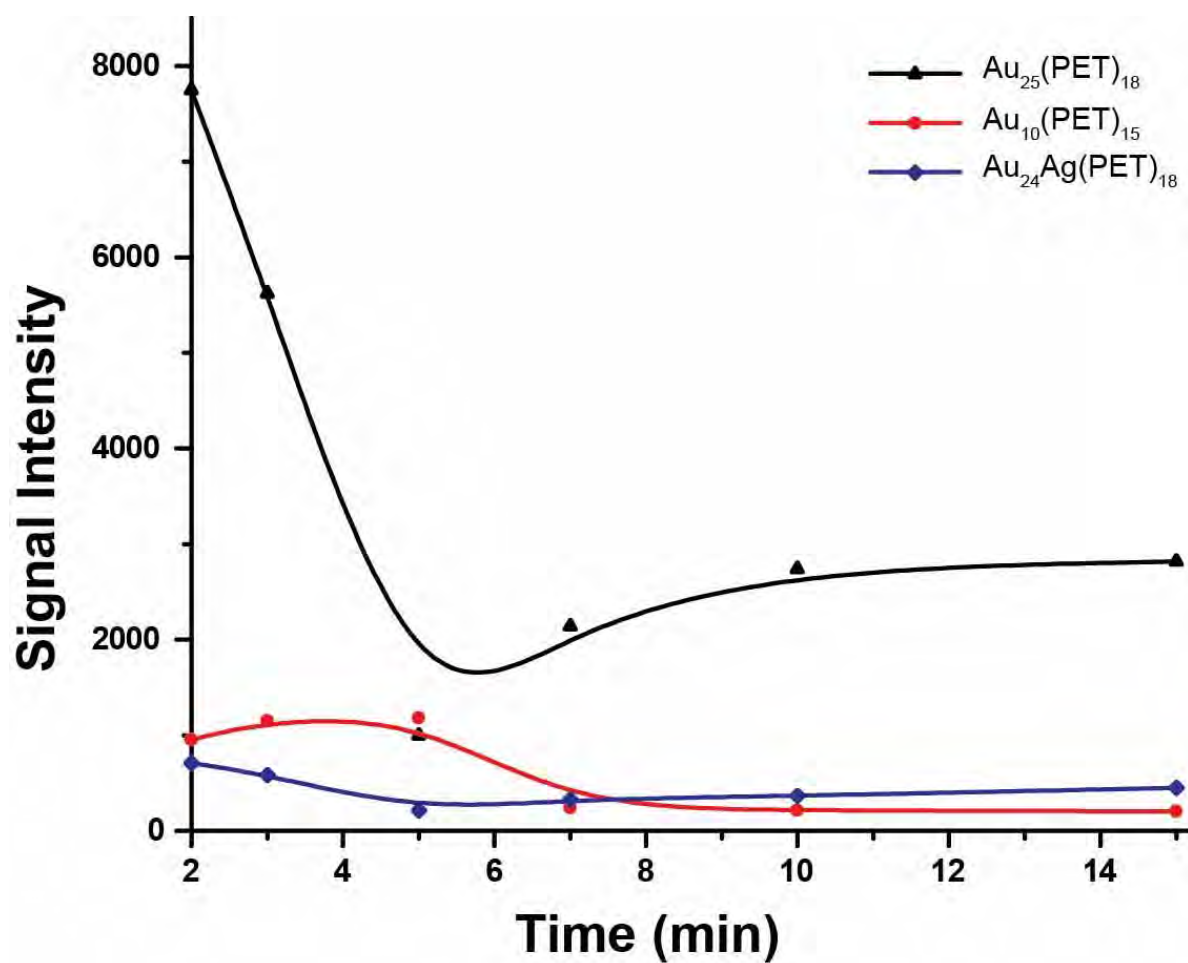


**Fig. S11** The evolution of the intermediate species  $\text{Au}_{24}\text{Ag}(\text{PET})_{18}$  and  $\text{Au}_{10}(\text{PET})_{15}$  can be observed in comparison to the parent  $\text{Au}_{25}(\text{PET})_{18}$  NC from the plot of signal intensities versus time.



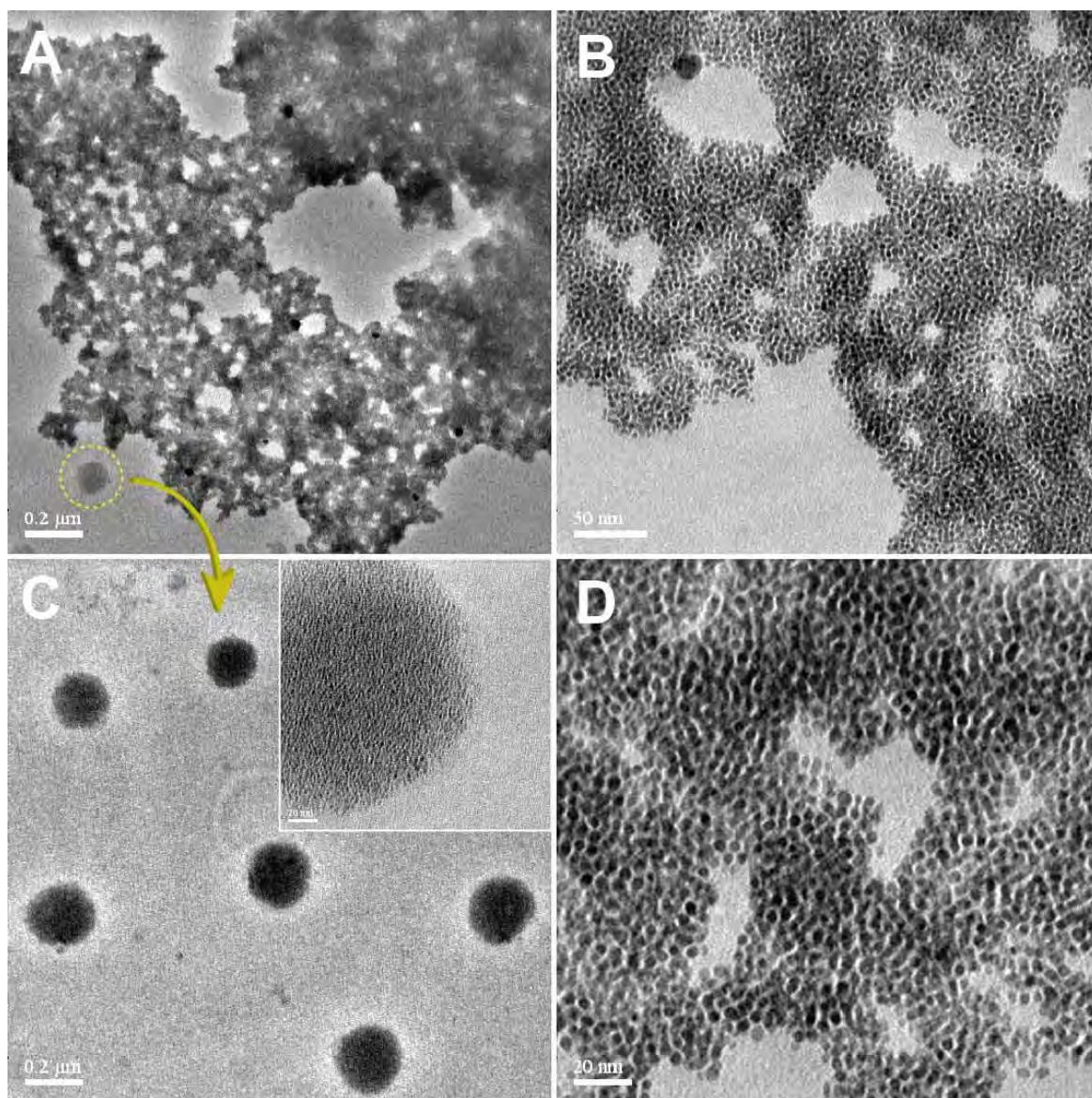


**Fig. S12** HRTEM micrographs of the spontaneous assembly formed after the reaction of 8 nm Ag@PET NPs captured at different magnifications, (A) 0.2  $\mu\text{m}$ , it comprises of two kinds of assemblies which further captured at (B) 50 nm, and (C) 0.2  $\mu\text{m}$  (yellow, inset) (D) 20 nm. The NPs resulted in the reaction are approximately 3.73 and 2 nm.

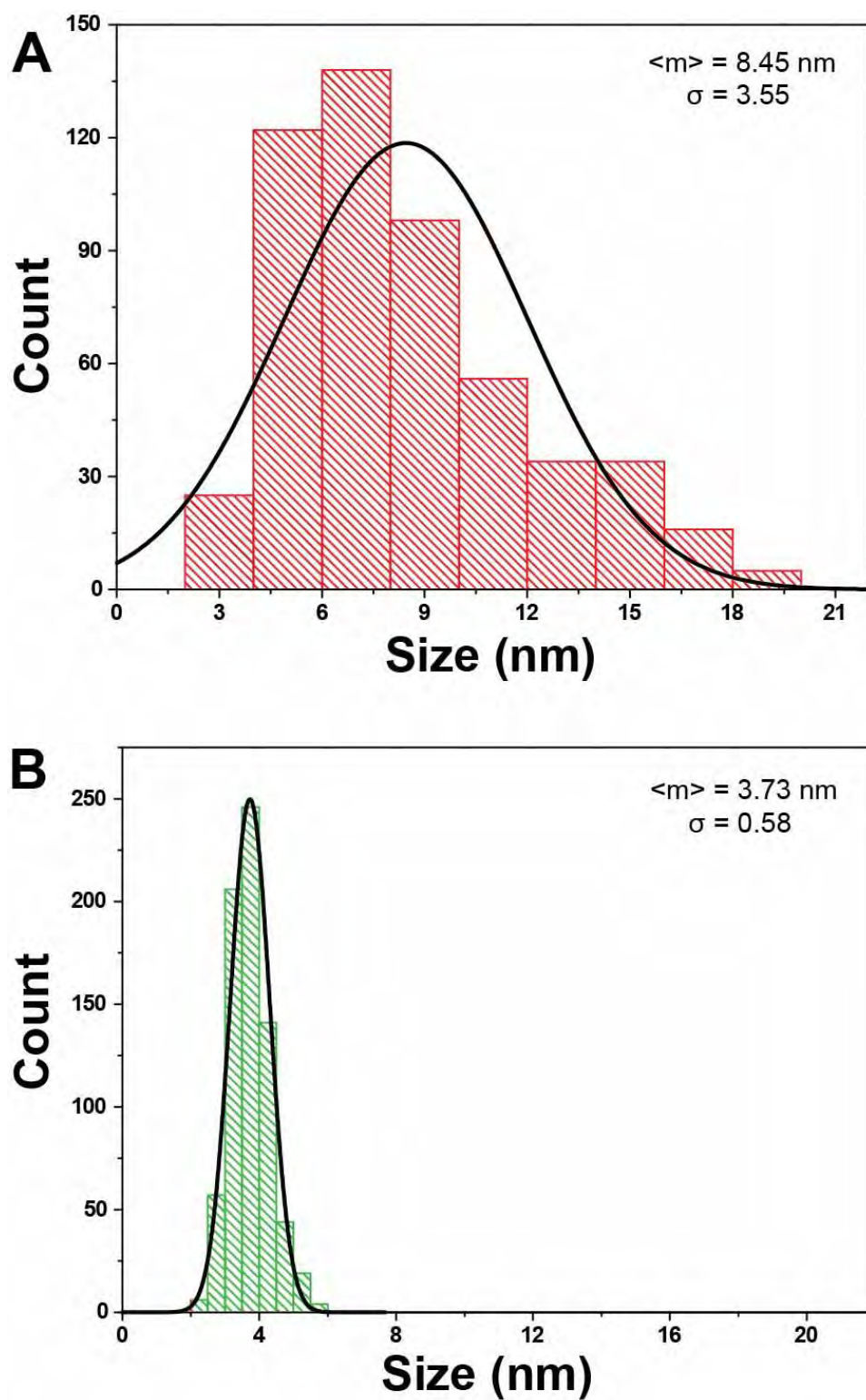
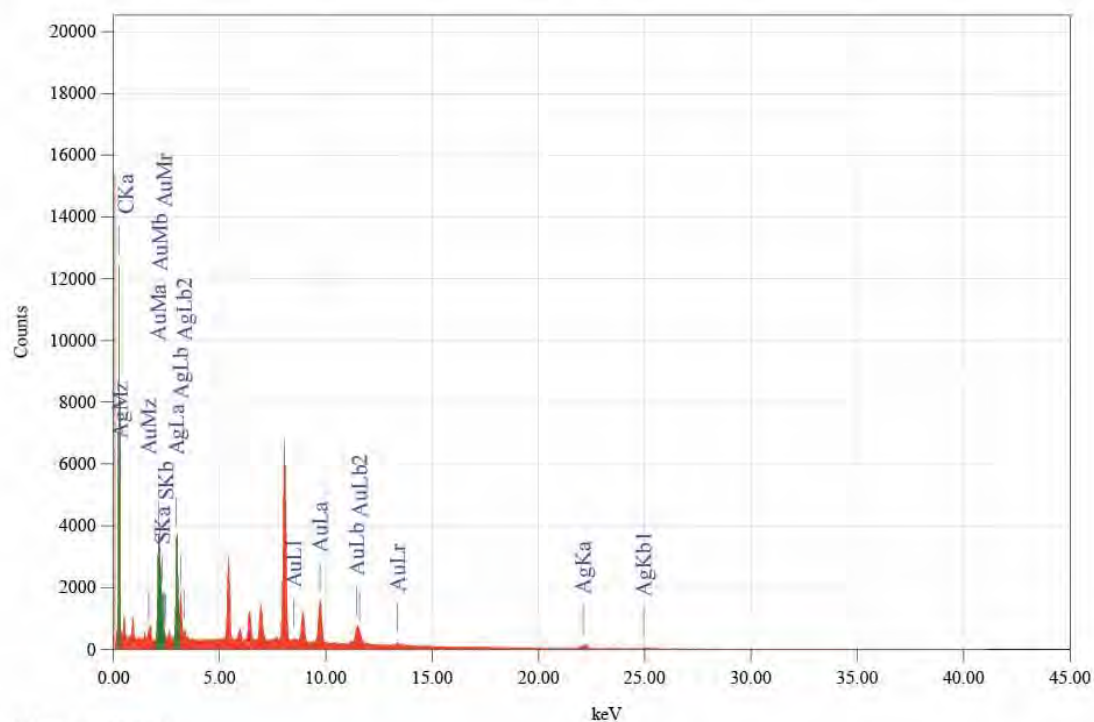


**Fig. S13** Particle size distribution of the polydispersed 8 nm reaction case for the (A) parent NPs was  $8.45 \pm 6.3 \text{ nm}$ , and (B) reacted NPs was  $3.73 \pm 1.0 \text{ nm}$ , where  $\langle m \rangle$  and  $\sigma$  are the notations used for mean size and standard deviation, respectively.



File: Untitled  
 Specimen ID:  
 Date: 12/21/2019 9:03:00 PM

## Acquisition Parameter

Acc. Voltage	: 200.0 kV	Probe Current	: 1.00000 nA
Real Time	: 539.20 sec	Dead Time	: 2 %
Live Time	: 524.26 sec	Counting Rate	: 1654 Counts/sec
Preset	: Off		
Energy Range	: 0 - 40 keV	PHA Mode	: T3

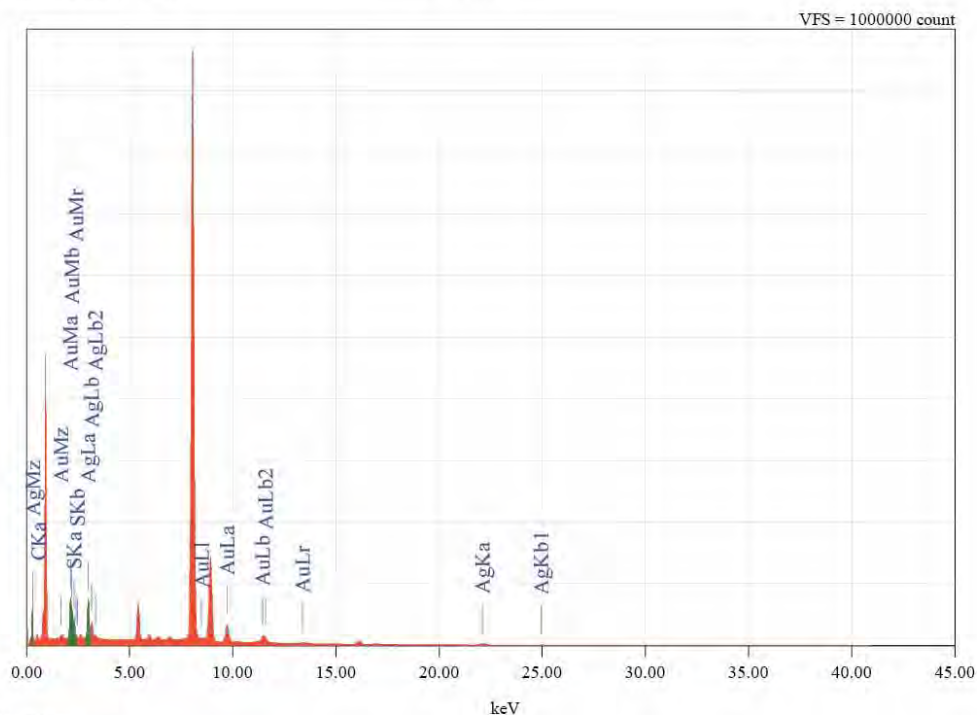
## Thin Film Standardless Standardless Quantitative Analysis

Fitting Coefficient : 0.6465

Element	(keV)	Mass%	Counts	Sigma	Atom%	Compound	Mass%	Cation	K
H *									
C K* (Ref.)	0.277	48.24	80092.55	0.16	88.76				1.0000
S K !	2.307	5.11	14664.02	0.09	3.52				0.5790
Ag L	2.984	26.78	51228.97	0.19	5.49				0.8679
Au M	2.120	19.86	36503.52	0.19	2.23				0.9032
Total		100.00			100.00				

**Fig. S14** Spot EDS spectrum of the reacted particle (Fig. 4A). Elemental composition was quantified for the presence of Sulfur (S), Silver (Ag), and Gold (Au) present in the superlattice.





File: Untitled

Specimen ID:

Date: 12/23/2019 3:25:44 PM

## Acquisition Parameter

Acc. Voltage	: 200.0 kV	Probe Current	: 1.00000 nA
Real Time	: 2125.89 sec	Dead Time	: 64 %
Live Time	: 524.11 sec	Counting Rate	: 102273 Counts/sec
Preset	: Off		
Energy Range	: 0 - 40 keV	PHA Mode	: T3

## Thin Film Standardless Standardless Quantitative Analysis

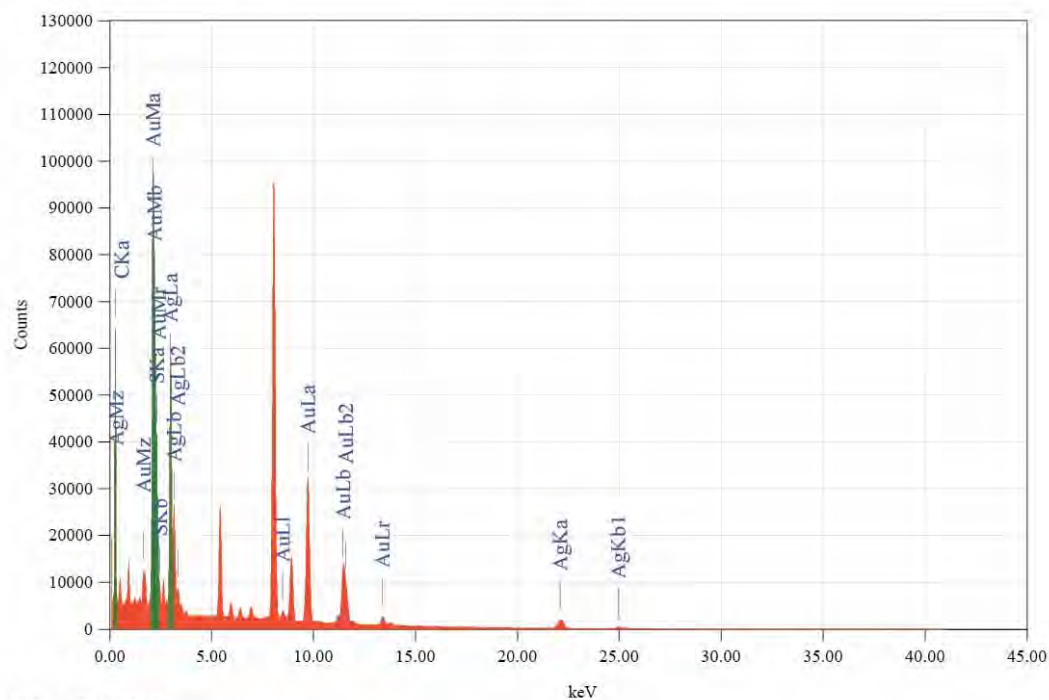
Fitting Coefficient : 0.9559

Element	(keV)	Mass%	Counts	Sigma	Atom%	Compound	Mass%	Cation	K
H K									
C K	0.277	17.42	326407.28	0.03	66.89				1.1522
S K	2.307	4.45	314464.25	0.02	6.41				0.3059
Ag L (Ref.)	2.984	43.43	937777.94	0.08	18.57				1.0000
Au M	2.120	34.70	720079.94	0.08	8.13				1.0407
Total		100.00			100.00				

**Fig. S15** Spot EDS spectrum of the reacted particle (Fig. 4B). Elemental composition was quantified for the presence of Sulfur (S), Silver (Ag), and Gold (Au) present in the layer-by-layer planar assembly.

Print:12/23/2019 2:57:38 PM

Untitled



File: Untitled  
Specimen ID:  
Date: 12/23/2019 2:30:33 PM

#### Acquisition Parameter

Acc. Voltage	: 200.0 kV	Probe Current	: 1.00000 nA
Real Time	: 672.69 sec	Dead Time	: 22 %
Live Time	: 524.22 sec	Counting Rate	: 23270 Counts/sec
Preset	: Off		
Energy Range	: 0 - 40 keV	PHA Mode	: T3

#### Thin Film Standardless Standardless Quantitative Analysis

Fitting Coefficient : 0.5976

Element	(keV)	Mass%	Counts	Sigma	Atom%	Compound	Mass%	Cation	K
H *									
C K	0.277	19.29	403043.19	0.03	70.70				1.1072
S K	2.307	4.53	356276.50	0.02	6.21				0.2939
Ag L	2.984	32.83	790207.94	0.06	13.40				0.9609
Au M (Ref.)	2.120	43.36	1002878.75	0.08	9.69				1.0000
Total		100.00			100.00				

**Fig. S16** Spot EDS spectrum of the reacted particle (Fig. 4C). Elemental composition was quantified for the presence of Sulfur (S), Silver (Ag), and Gold (Au) present in the disc-shaped assembly.



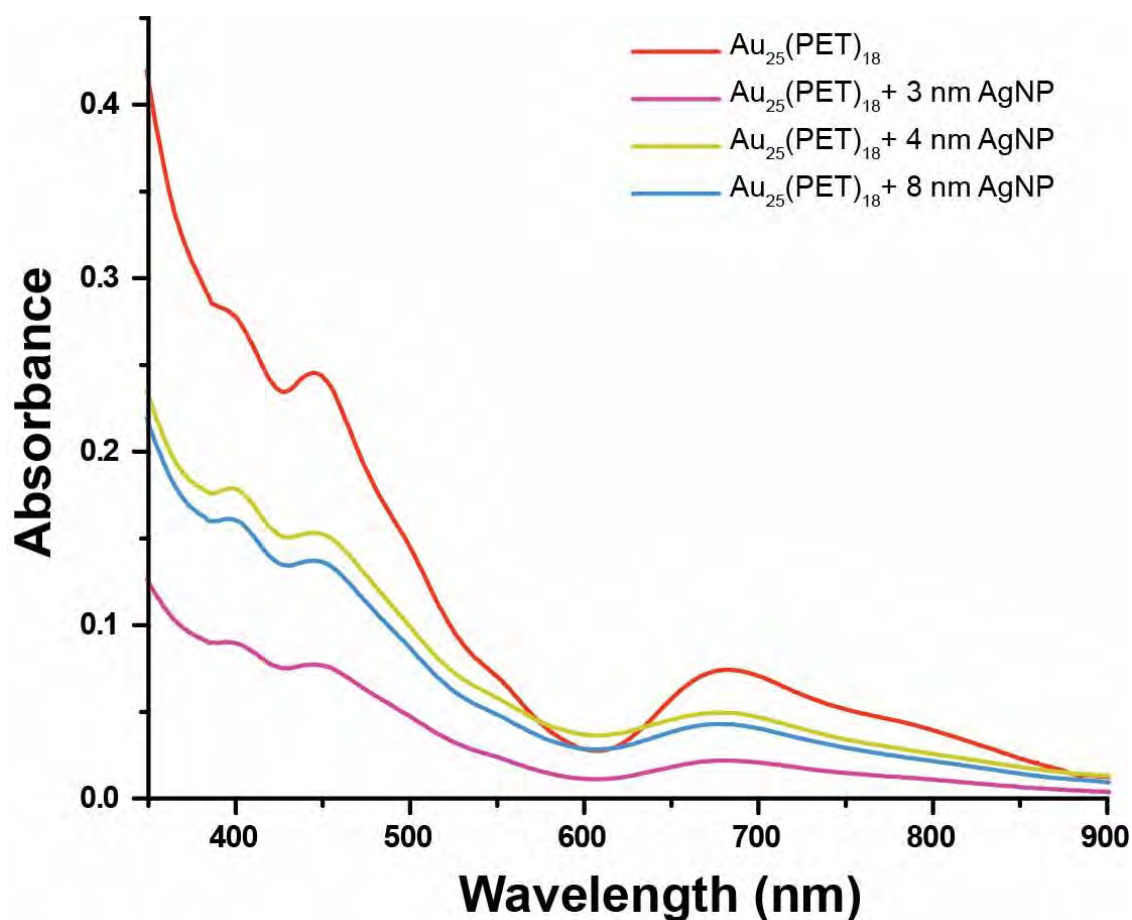


**Fig. S17** The reaction mixture was monitored at the 2 min interval using UV-Vis spectroscopy, in ESI MS experimental condition (Fig. 4), for differently sized Ag@PET NPs, polydispersed 8 (blue trace, Fig. 4 B), 4 (yellow trace, Fig. 4 C), 3 nm (magenta trace, Fig. 4 D), and the parent NC (red trace, Fig. 4 A). The shifts are present in all the cases that confirms the generation of new species in all the three case at the particular time.

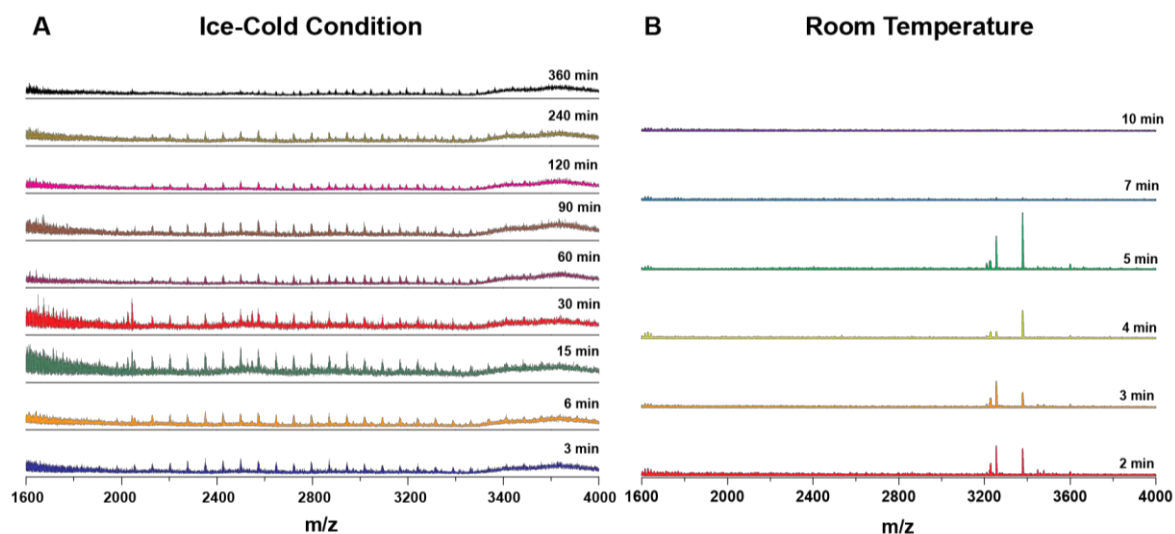


**Fig. S18** Time dependent low temperature reaction monitoring of 4 nm Ag@PET NPs with  $\text{Au}_{25}(\text{PET})_{18}$  at two temperatures, namely ice-cold condition and room temperature. (A) Reaction mixture was analysed in ESI MS at ice-cold condition for 3, 6, 15, 30, 60, 90, 120, 240 and 360 min. (B) The reaction was monitored at room temperature. Spectral region of  $m/z$  1600-4000 is plotted to compare evolution of the thiolate intermediates under two different conditions.

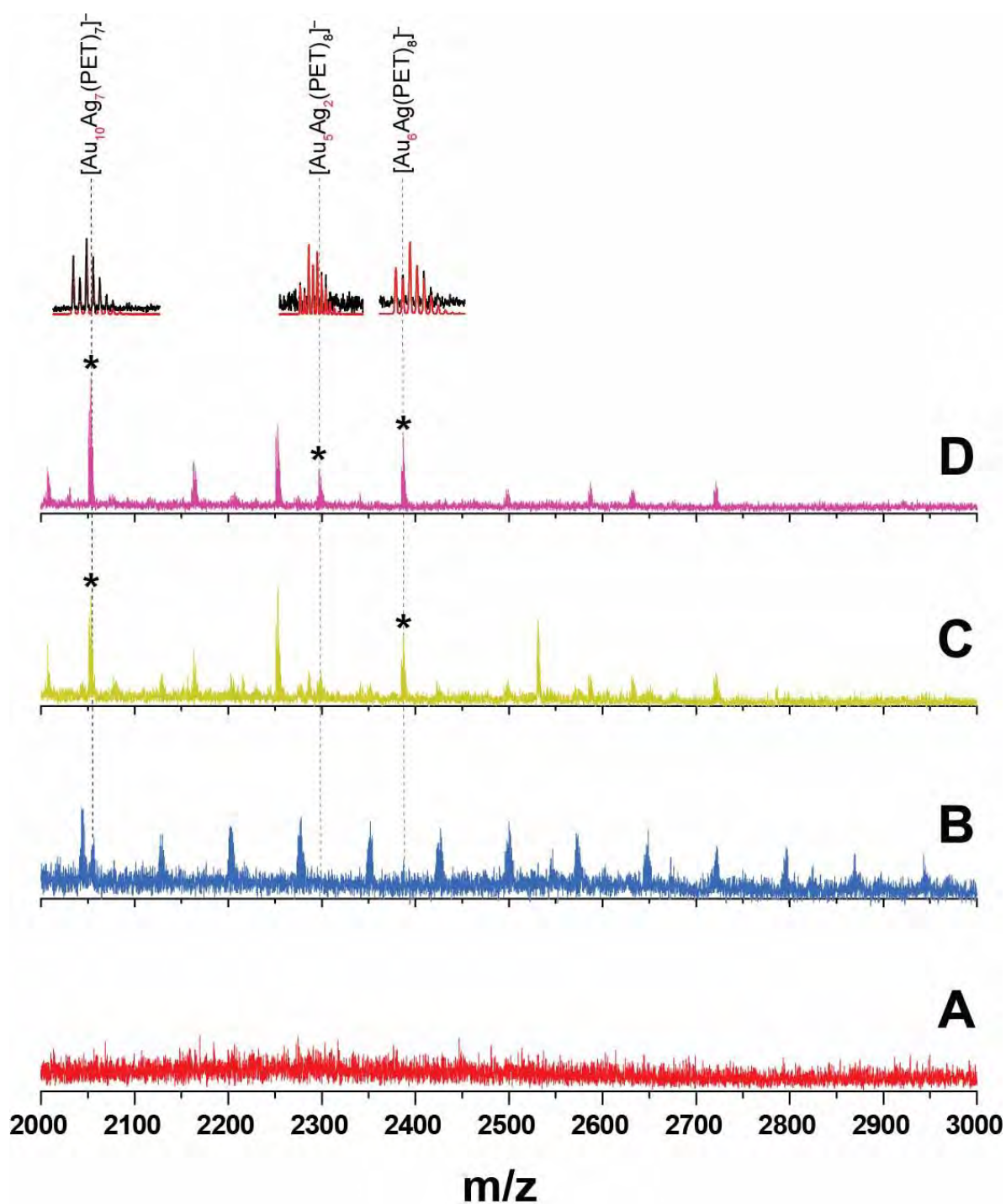


**Fig. S19** Size dependent reactivity monitored using ESI MS (Fig. 4), expanded region  $m/z$  2000-3000. The reaction fragments were found to vary for Ag@PET NPs for different sizes, (B) polydispersed 8 nm, (B) 4 nm, and (D) 3 nm. The exchange was compared with the (A) parent  $\text{Au}_{25}(\text{PET})_{18}$  cluster. Each spectrum is normalised w.r.t its corresponding  $\text{Au}_{25}(\text{PET})_{18}$  peak intensity for visual comparison.

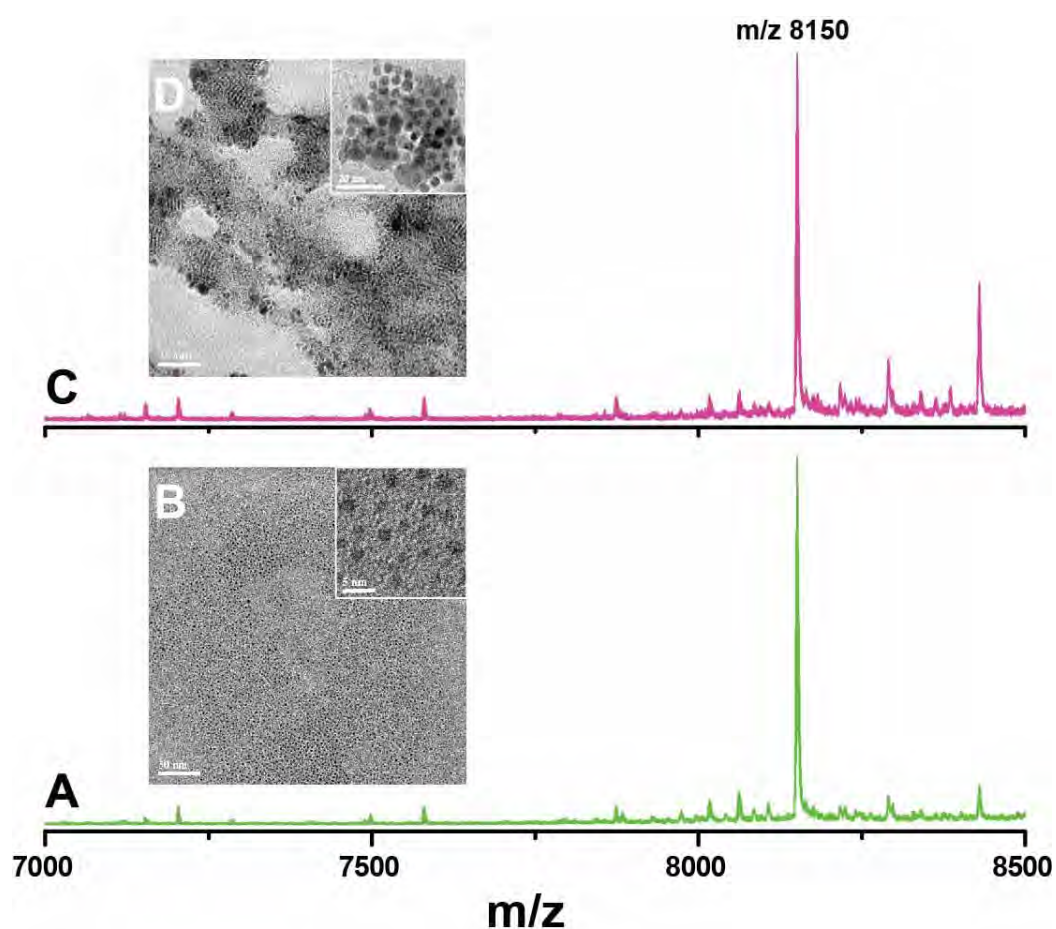


**Fig. S20** Ligand specificity in the discussed reaction was explored on reacting 4 nm Ag@PET NPs with  $\text{Au}_{25}(\text{SBB})_{18}$  NC. The pure  $\text{Au}_{25}(\text{SBB})_{18}$  NC was characterized using (A) ESI MS, molecular peak at  $m/z$  8150, and (B) HRTEM micrographs, at 50 nm and 5 nm (inset) magnifications. The reaction mixture was analysed after 2 min using (C) ESI MS, showed absence of new peaks, (D) HRTEM micrograph, no new morphology was observed unlike the previous cases (Fig. 1, 3). All the spectra were plotted to its original intensities.

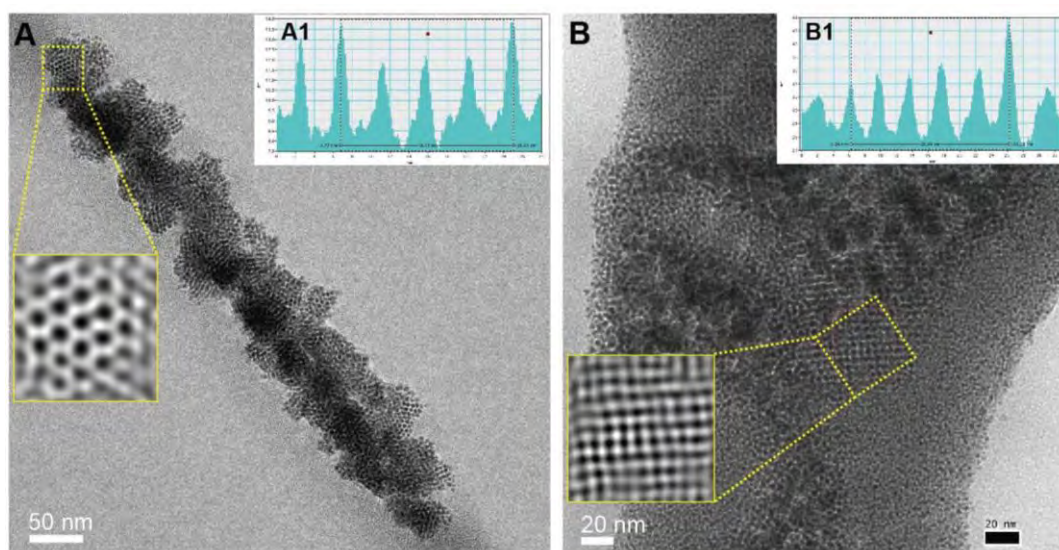


**Fig. S21** Inverse fast Fourier transform (IFFT) for (A) superlattice of the reacted 4 nm Ag@PET NP, (A1) profile, and (B) layer-by-layer of the reacted 8 nm Ag@PET NP, (B1) profile.



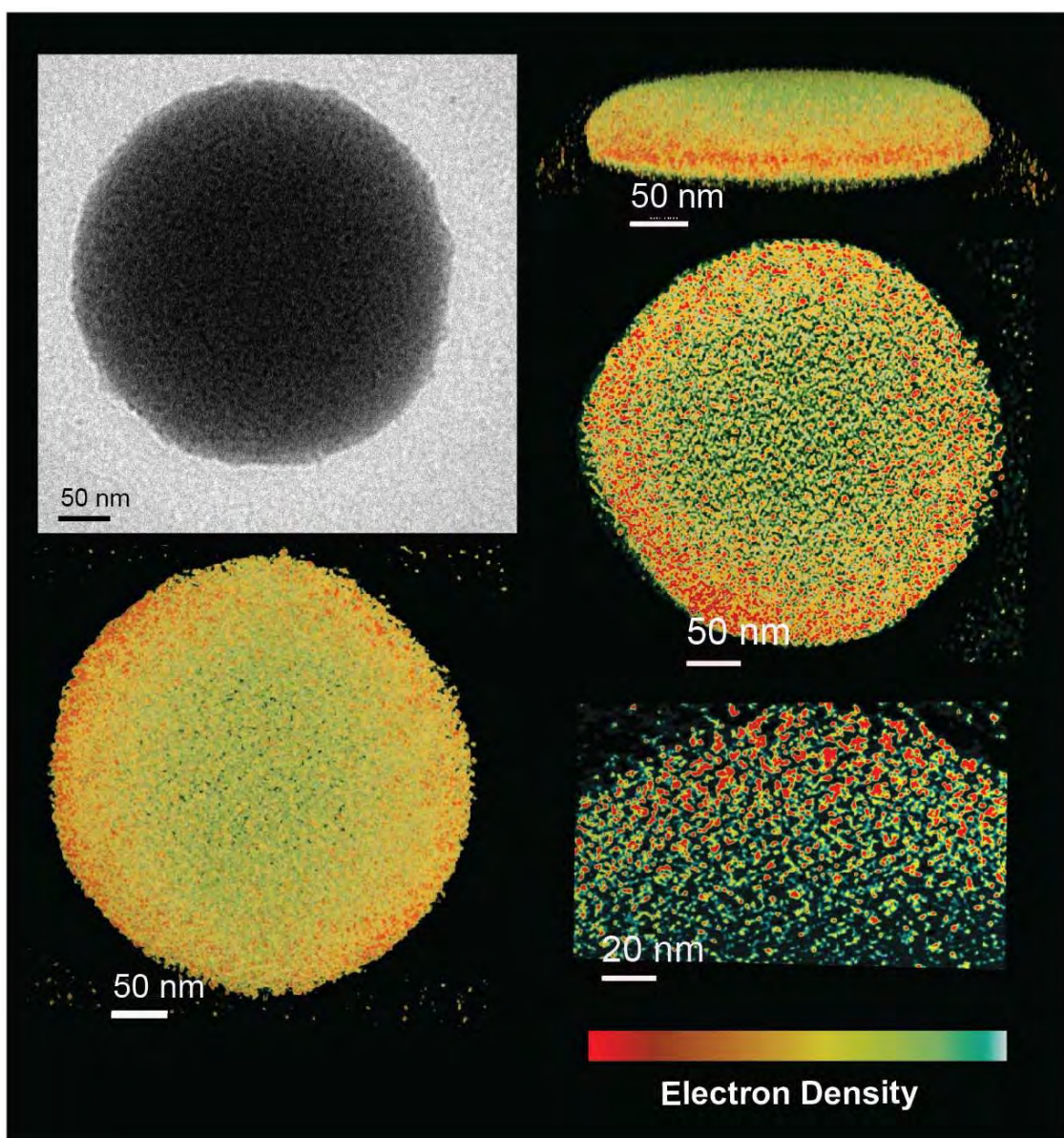


**Fig. S22** Electron Tomography and 3D reconstruction a disc-shaped assembly: 2D projection followed by its corresponding 3D reconstruction for the reacted 8 nm Ag@PET NPs assembled as disc densely filled with particles. The tilt series and 3D reconstruction for the assembly is provided as Video V5, and Video V6, respectively.

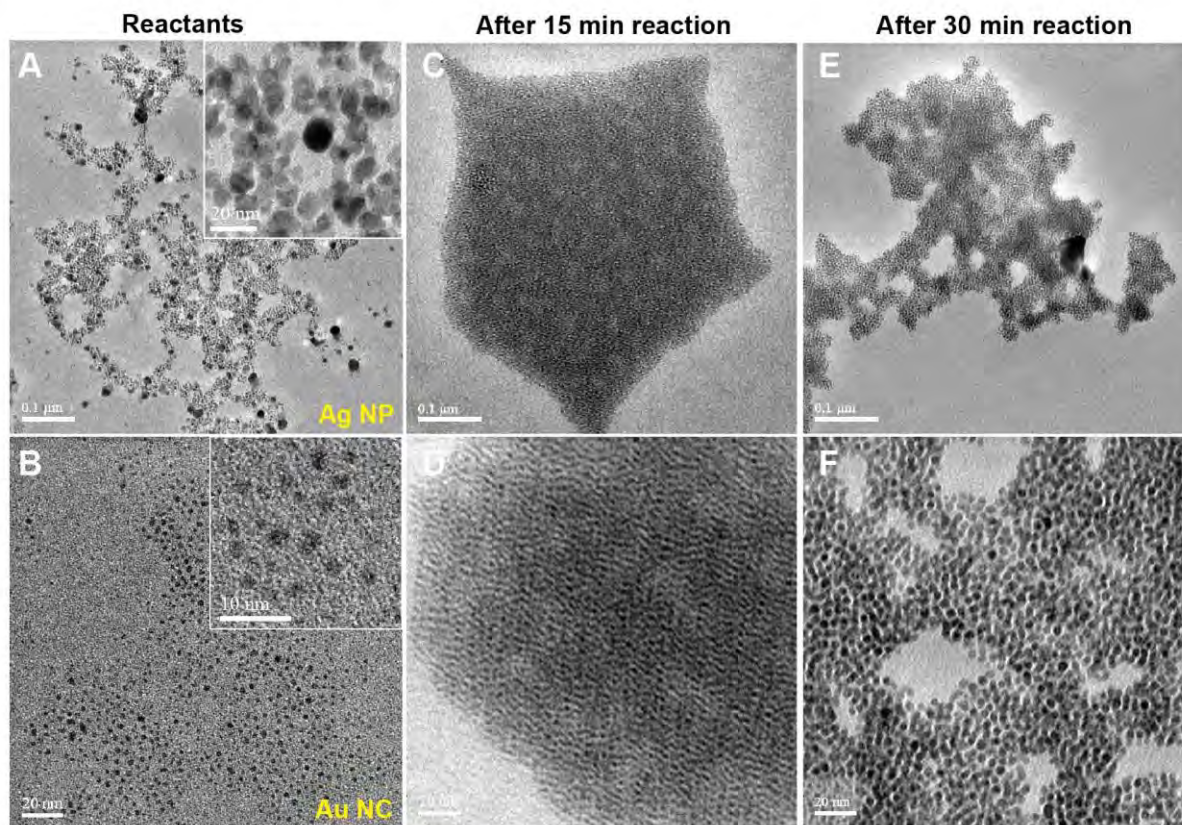


**Fig. S23** HRTEM micrographs of the reaction progress for a reaction between parent 8 nm Ag@PET NP (A), and Au<sub>25</sub>(PET)<sub>18</sub> NC (B). The products of the reaction after 15 (C, D) and 30 (E, F) min of reaction are also shown.

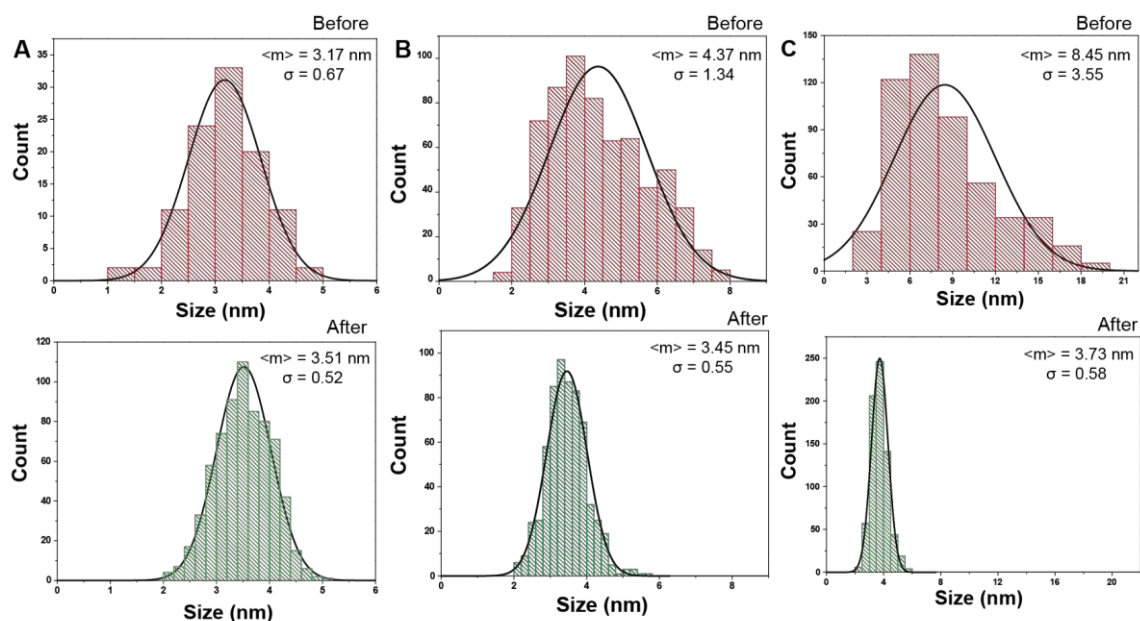


**Fig. S24** Effect of NP-NC reaction on the particle size distribution. Before and after reaction with Ag NPs with average size of (A) 3, (B) 4 and (C) 8 nm, where  $\langle m \rangle$  and  $\sigma$  are the notations used for mean size and standard deviation, respectively.

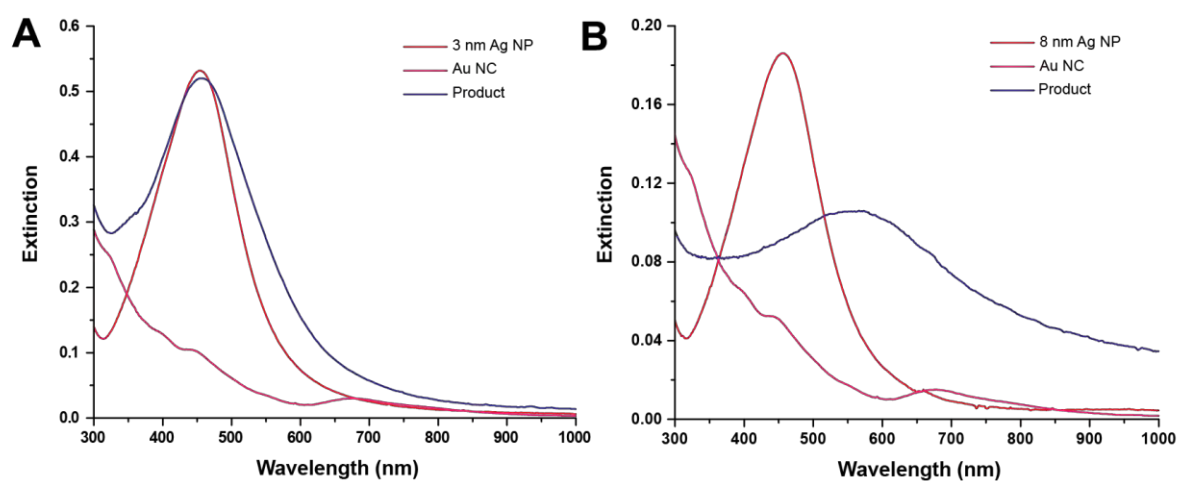


**Fig. S25** UV-Vis spectra of NP-NC reaction for (A) 3 and 8 nm Ag@PET NPs. Spectra are due to Ag NP (red trace),  $\text{Au}_{25}(\text{PET})_{18}$  NC (magenta trace), and the reaction product (blue trace). The broadening of the peak upon reaction is in agreement with the gradual formation of an assembly of the reacted NPs. Also see HRTEM micrographs of the reaction products for 3 and 8 nm Ag NPs in Fig. 3B and D.

## REFERENCES

- 1 D. N. Mastronarde, *J. Struct. Biol.*, 2005, **152**, 36–51.
- 2 D. N. Mastronarde, *Microsc. Microanal.*, 2003, **9**, 1182–1183.
- 3 N. Nonappa and P. Engelhardt, *Imaging Microsc.*, 2019, **21**, 22–24.
- 4 J. R. Kremer, D. N. Mastronarde and J. R. McIntosh, *J. Struct. Biol.*, 1996, **116**, 71–76.
- 5 P. Engelhardt, in *Electron Microscopy: Methods and Protocols*, ed. J. Kuo, Humana Press, Totowa, NJ, 2007, pp. 365–385.
- 6 P. Engelhardt, *Electron Tomography of Chromosome Structure*, 2006.
- 7 K. R. Krishnadas, A. Ghosh, A. Baksi, I. Chakraborty, G. Natarajan and T. Pradeep, *J. Am. Chem. Soc.*, 2016, **138**, 140–148.
- 8 A. Baksi, P. Chakraborty, A. Nag, D. Ghosh, S. Bhat and T. Pradeep, *Anal. Chem.*, 2018, **90**, 11351–11357.



# Dithiol-Induced Contraction in Ag<sub>14</sub> Clusters and Its Manifestation in Electronic Structures

Mohammad Bodiuzzaman, Esma Khatun, Korath Shivan Sugi, Ganesan Paramasivam, Wakeel Ahmed Dar, Sudhadevi Antharjanam, and Thalappil Pradeep\*

Cite This: *J. Phys. Chem. C* 2020, 124, 23426–23432

Read Online

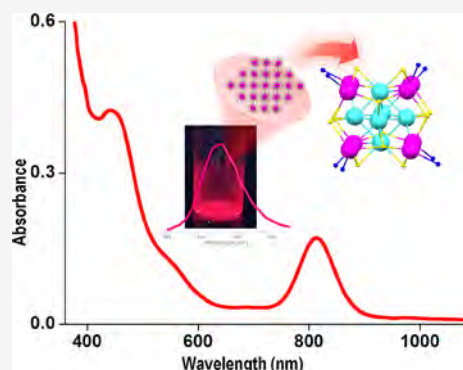
ACCESS |

Metrics & More

Article Recommendations

Supporting Information

**ABSTRACT:** We report a dithiol-protected silver cluster, Ag<sub>14</sub>(BDT)<sub>6</sub>(PPh<sub>3</sub>)<sub>8</sub> (BDT = 1,2-benzene dithiol), abbreviated as Ag<sub>14</sub>DT, which exhibits distinctly different optical properties than the analogous monothiol-protected Ag<sub>14</sub>(SC<sub>6</sub>H<sub>3</sub>F<sub>2</sub>)<sub>12</sub>(PPh<sub>3</sub>)<sub>8</sub>, abbreviated as Ag<sub>14</sub>MT. Replacement of monothiol by dithiol, keeping the composition constant, has not been possible so far. The inner cores of both Ag<sub>14</sub>DT and Ag<sub>14</sub>MT are composed of octahedral Ag<sub>6</sub>, but because of the presence of dithiol, the outer cubic Ag<sub>8</sub> shell became distorted in the former. Consequently, Ag<sub>14</sub>DT showed a unique absorption in the near-infrared (NIR) region, which is mainly due to transitions derived from ligands. It exhibits dual visible/NIR emission, at around 680 and 997 nm. Ag<sub>14</sub>DT exhibited greater thermal stability because of the rigidity provided by dithiol ligands. The clusters with NIR absorption and emission open up a possibility for their application in solar thermal conversion and medical imaging. NIR luminescence in the range of 1000 nm in ultrasmall clusters is very new.



## INTRODUCTION

Surface ligands play a pivotal role in directing the structures of atomically precise nanoclusters (NCs).<sup>1–6</sup> For years, researchers have been studying the effect of surface ligands on tuning the structure and properties of silver clusters. The availability of single crystal structures provides us with opportunities to study the structure–property relationships in greater detail, and such studies are further enriched by computations.<sup>7–11</sup>

The use of different ligands resulted in the formation of varying silver NCs of different atomicity, namely, Ag<sub>25</sub>(SPhMe<sub>2</sub>)<sub>18</sub>, Ag<sub>29</sub>(BDT)<sub>12</sub>(TPP)<sub>4</sub> (BDT = 1,3-benzene dithiol), Ag<sub>44</sub>(SR)<sub>30</sub> (SR = *p*-fluorothiophenol, *p*-mercaptobenzoic acid), and so forth.<sup>12–16</sup> Sometimes, the same ligand results in the formation of different NCs depending on the synthetic conditions, such as Ag<sub>29</sub>(BDT)<sub>12</sub>(TPP)<sub>4</sub> and Ag<sub>51</sub>(BDT)<sub>19</sub>(TPP)<sub>3</sub>, which were coprotected by BDT and TPP(PPh<sub>3</sub>) ligands.<sup>17</sup> A small change in the structure of the ligand can change the nuclearity of NCs.<sup>18</sup> For example, two isomers of DCBT (dichlorobenzenethiol), namely, 2,4-dichlorobenzenethiol and 2,5-dichlorobenzenethiol, resulted in two different NCs, Ag<sub>44</sub>(2,4-DCBT)<sub>30</sub> and Ag<sub>59</sub>(2,5-DCBT)<sub>32</sub>, respectively, under similar conditions.<sup>19</sup> Also, our recent report showed the formation of a single silver cluster, Ag<sub>46</sub>(SPhMe<sub>2</sub>)<sub>24</sub>(TPP)<sub>8</sub>, using 2,5-DMBT (DMBT = dimethylbenzenethiol), while the isomeric thiol, 2,4-DMBT produced a cocrystal, composed of Ag<sub>40</sub>(DMBT)<sub>24</sub>(PPh<sub>3</sub>)<sub>8</sub> and Ag<sub>46</sub>(DMBT)<sub>24</sub>(PPh<sub>3</sub>)<sub>8</sub>.<sup>20</sup> The origin of properties of NCs has been studied for long, among which the evolution of photoluminescence (PL) has

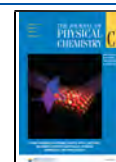
been studied extensively.<sup>6,21–23</sup> Among the silver NCs reported so far, Ag<sub>14</sub>(SC<sub>6</sub>H<sub>3</sub>F<sub>2</sub>)<sub>12</sub>(TPP)<sub>8</sub> is the first crystallized silver NC as per previous references to journals and books.<sup>8,24,25</sup> Interestingly, it exhibits yellow emission (with a peak maximum at 536 nm).<sup>25</sup> The cluster contains an octahedral Ag<sub>6</sub> metal core. Recently, Ag<sub>14</sub> was used as a building block to create cluster-based metal–organic frameworks (MOFs).<sup>26</sup>

Increase in denticity of the ligands increases the structural rigidity of inorganic complexes, which enhances their stability. Replacement of monothiol by dithiols in NCs can enhance the electronic confinement which would be reflected in optical properties. Ligand reconstruction also promoted the formation of NC-based MOFs, which exhibit interesting properties.<sup>27</sup> Furthermore, the change in the protecting ligand can vary the properties of NCs keeping their structures unaltered as in the case of Au<sub>22</sub>(SG)<sub>18</sub>. Surface engineering of this cluster resulted in 60% enhancement in PL quantum yield.<sup>28</sup> Other properties such as chirality, catalytic activity, and reactivity can also be tuned via surface ligand modifications.<sup>29–34</sup>

Received: August 4, 2020

Revised: September 27, 2020

Published: September 28, 2020





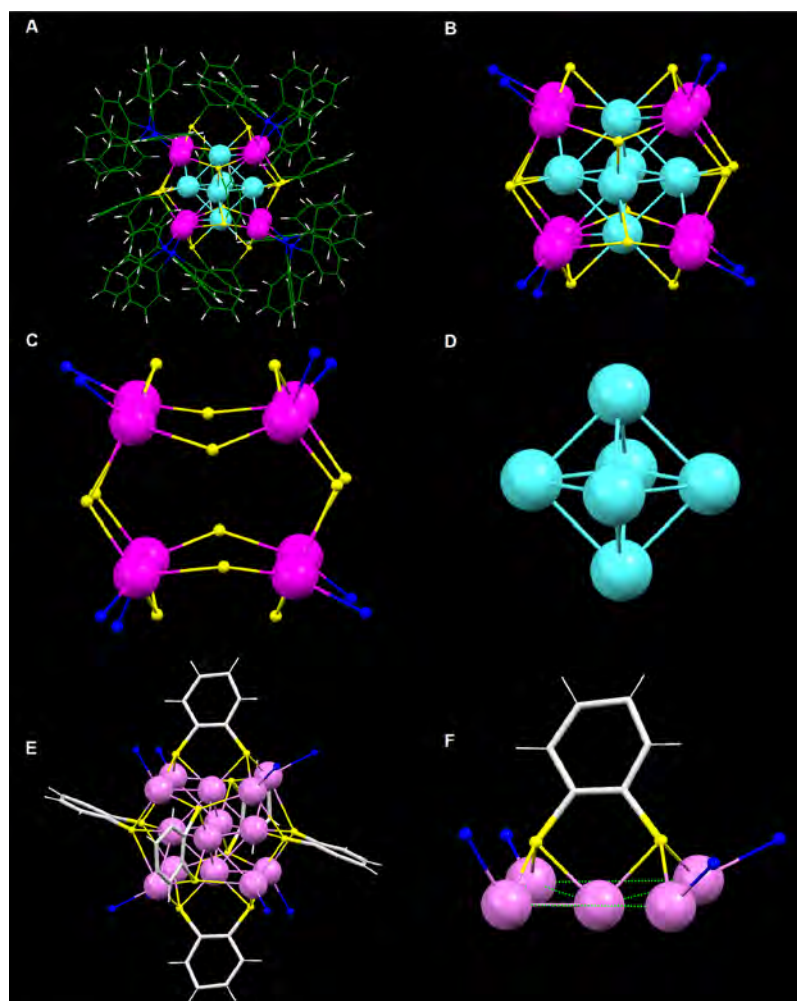


**Figure 1.** Structural anatomy of Ag<sub>14</sub>DT clusters. (A) Full structure of Ag<sub>14</sub>DT. (B) Structure of Ag<sub>14</sub>S<sub>12</sub>P<sub>8</sub> and (C) cubic shell of Ag<sub>8</sub>S<sub>12</sub>P<sub>8</sub>. (D) Octahedral Ag<sub>6</sub> inner core. (E) Structure of the unit, Ag<sub>14</sub>(BDT)<sub>6</sub>P<sub>8</sub>. Six faces cover the inner core. One such face is shown in (F). Color code: cyan, magenta, and violet, silver; yellow, sulfur; blue, phosphorous; green, carbon; and grey, hydrogen.

In this paper, we investigate the structure–property relationship between dithiol and monothiol protection in a given cluster core, namely, Ag<sub>14</sub>(BDT)<sub>6</sub>(TPP)<sub>8</sub> and Ag<sub>14</sub>(SC<sub>6</sub>H<sub>3</sub>F<sub>2</sub>)<sub>12</sub>(TPP)<sub>8</sub>, labeled as Ag<sub>14</sub>DT and Ag<sub>14</sub>MT, respectively. We observed that the dithiol (BDT) changes the outer cubic shell structure of the NC and further confines the inner Ag<sub>6</sub> octahedral core. This structural confinement leads to the improvement in optical properties. Introduction of dithiols convert singly emissive Ag<sub>14</sub>MT to dual emissive Ag<sub>14</sub>DT. Ligands of this kind can be handy to enhance photophysical properties of many clusters. Incorporation of such ligands enables strong supramolecular interactions, such as  $\pi\cdots\pi$  stacking, which were absent in the previously reported Ag<sub>14</sub> cluster.<sup>25</sup> The structure of Ag<sub>14</sub>DT was determined by single crystal X-ray diffraction (SCXRD), and the composition was confirmed by scanning electron microscopy (SEM)/energy-dispersive analysis (EDS) and elemental analysis measurements. New electronic properties were observed as evidenced from the calculations. A density functional theory (DFT) calculation was performed to obtain deep insights into the electronic structures of Ag<sub>14</sub>DT. Partial density of states (PDOS) was calculated to analyze the origin of electronic transitions. Further, superatomic orbital calculation revealed that the cluster is a 2e superatom with the electronic

configuration, 1S<sup>2</sup>. Our findings will enhance activities in the area of dithiol-protected NCs leading to their diversity in properties.

## EXPERIMENTAL SECTION

**Materials.** Silver nitrate was bought from Rankem. Sodium borohydride and 1,2-benzene dithiol (BDT) were bought from Sigma-Aldrich. Triphenylphosphine (TPP) was bought from Spectrochem Chemicals. Dichloromethane (DCM), methanol (MeOH), *n*-hexane, and chloroform (CHCl<sub>3</sub>) were bought from Rankem and are of analytical grade. Milli-Q water was used for the synthesis.

**Instrumentation.** Optical absorption measurements were performed in a PerkinElmer Lambda 25 UV–vis spectrophotometer.

A Horiba Jobin Yvon Nanolog spectrometer was used for the PL measurements. The excitation and the emission band pass were set at 3 nm.

SEM and EDS were performed using an FEI QUANTA-200.

SCXRD were measured using a Bruker Kappa APEX III CMOS diffractometer. Mo K $\alpha$  ( $\lambda = 0.71073$  Å) was used as a source of radiation. Indexing was done by APEX III.

Elemental analysis was done by LECO CS744 and LECO ONH 836 analyzers.

**Synthesis and Purification of  $[\text{Ag}_{18}\text{H}_{16}(\text{TPP})_{10}]^{2+}$ .** It was prepared by a known method.<sup>35,36</sup> 20 mg of silver nitrate was taken in 5 mL of methanol by sonication, and 10 mL of  $\text{CHCl}_3$  was added. Then, 70 mg of TPP was mixed to the reaction mixture under stirring condition. After 20 min of stirring, 5.5 mg of cold aqueous solution of sodium borohydride was added. On addition of the reducing agent, the color of the reaction mixture became yellow. The reaction was carried out for 3 h. After 3 h of stirring, it became dark green that confirms the production of the material. Solvents were evaporated under reduced pressure. The solid green material was cleaned several times with water. Then, it was extracted by MeOH to avoid excess phosphine. This green colored material was used for characterization and further reaction.

**Synthesis and Purification of  $[\text{Ag}_{14}(\text{BDT})_6(\text{PPh}_3)_8]$ .** The cluster was synthesized by a ligand exchange induced size/structural transformation methodology.<sup>20,37</sup> Here,  $[\text{Ag}_{18}(\text{PPh}_3)_{10}\text{H}_{16}]^{2+}$  was used as a precursor and reacted with 1,2-BDT. 5 mg of  $[\text{Ag}_{18}(\text{PPh}_3)_{10}\text{H}_{16}]^{2+}$  was taken in MeOH as a precursor. 1  $\mu\text{L}$  of 1,2-BDT was mixed to the methanolic solution. After adding dithiol, it became brown, and the reaction was continued for 6 h. The reaction mixture was centrifuged, and in the centrifugate, a brown color precipitate was observed. The precipitate was cleaned 2–3 times with MeOH and dissolved in DCM. This solution in DCM was used for further characterizations.

**Crystallization Technique.** Cleaned 20–30 mg of the material was taken in distilled DCM and filtered by 0.22  $\mu\text{m}$  syringe filter paper. Then, it was layered by distilled hexane (1:1) and kept at 4  $^\circ\text{C}$ . After approximately one week, square shape reddish yellow crystals were observed which were suitable for single crystal X-ray crystallography.

**Computational Methods.** The structural, electronic, and optical properties of the  $\text{Ag}_{14}$  cluster were investigated computationally by DFT as implemented in the GPAW (grid-based projector-augmented wave method) software package.<sup>38,39</sup> The chosen GPAW PAW-setups for each element of the cluster's constituent atoms had the valence electronic configurations given in brackets as follows, Ag ( $4d^{10}5s^1$ ), S ( $3s^23p^4$ ), P ( $3s^23p^3$ ), C ( $2s^22p^2$ ), and H ( $1s^1$ ), and scalar-relativistic effects were included for the Ag atoms.

The simulation cell was a cubic box of side 22  $\text{\AA}$ , and a grid spacing of 0.2  $\text{\AA}$  was used in real-space finite-difference mode of GPAW. The geometry optimization was carried out with the convergence condition that the forces acting on atoms should be less than 0.05 eV/ $\text{\AA}$  and without imposing any symmetry constraints. All calculations were performed using the Perdew–Burke–Ernzerhof exchange–correlation functional.<sup>40</sup> The initial geometry of the  $\text{Ag}_{14}$  cluster for the ground-state optimization was extracted from the atomic coordinates of the unit cell of the crystal structure, and the optimization was performed with complete ligands. The ground-state electronic structure of the optimized cluster structure was characterized by calculating and plotting the molecular orbitals (MOs). The total density of states (TDOSs) and PDOSs were calculated and plotted, and the superatom character of the MOs was analyzed on the basis of the PDOS and also the influence of ligand atomic orbitals (AOs) on the overall electronic structure of the cluster. The absorption spectrum was calculated using linear response time-dependent density functional theory (LR-TDDFT), and the corresponding ground state MOs involved in the optical transitions were identified and plotted.

## RESULTS AND DISCUSSION

The cluster was crystallized in a trigonal unit cell with the space group,  $R\bar{3}$ . Structural refinement showed that the  $R_{\text{int}}$  value is higher than that of usual small molecule structures. This is due to weak diffraction of the crystals, and the conclusions drawn are meaningful. The molecule is having an inversion and a 3-fold rotational symmetry. SCXRD showed that the molecular formula of the cluster is  $[\text{Ag}_{14}(\text{BDT})_6(\text{PPh}_3)_8]$ . The full structure of  $\text{Ag}_{14}\text{DT}$  is presented in Figure 1A. Figure 1B shows the structure after removal of C and H. The structural anatomy suggests its atomic structure to consist of an inner octahedral ( $\text{Ag}_6$ ) core, in which H is surrounded by a distorted cubic ( $\text{Ag}_8$ ) shell. This cubic shell and inner octahedral core are presented in Figure 1C,D, respectively. The Ag–Ag distance in the  $\text{Ag}_6$  core is 2.7  $\text{\AA}$  and the same for the  $\text{Ag}_8$  cube is 4.5  $\text{\AA}$  as they are linked through S. This indicates that the interactions of silver atoms in the inner core are stronger than in the shell. The six faces of the cubic shell are protected by dithiol moieties (Figure 1E). One such face is shown in Figure 1F. Dithiol ligands pull the corner atoms of the cubic  $\text{Ag}_8$  shell closer. Due to this, the edge length and the diagonal distances of the cube get shortened compared to  $\text{Ag}_{14}\text{MT}$ . The centroids of benzene groups of dithiol can be seen as they are placed at the six vertices of an octahedron, as shown in Figure S1A. The edges of the octahedron are shown in green dotted lines. Along with the primary protecting layer, the vertex of the cube is connected by eight  $\text{PPh}_3$  ligands. The distortion in the cubic shell is due to the strain on the sulfur atoms. The presence of dithiol ligands shortened the S–Ag–S bond angle. In the case of  $\text{Ag}_{14}\text{DT}$ , the bonding of the  $\text{Ag}_6$  core and the sulfur atoms showed an S–Ag–S bond angle of  $91.03^\circ$ , whereas in the case of  $\text{Ag}_{14}\text{MT}$ , it is  $119.7^\circ$  (Figure S1B). This change in bond angle makes a distortion in the cubic shell. The inner-shell silver atoms are coordinated to two thiolates, but in the outer-shell, some of the silver atoms are coordinated with two and the rest are coordinated with three thiolates. These different environments of silver atoms are presented in Figure S2. Hence, the inner-shell silver atoms are strongly interacting with sulfur atoms with an average Ag–S bond length of 2.50  $\text{\AA}$ , and it is shorter by 0.17  $\text{\AA}$  than the previous report.<sup>25</sup> In contrast, the 2-coordinated Ag–S distances are between 2.55 and 2.66  $\text{\AA}$ , and it is longer by 0.10  $\text{\AA}$  than the inner shell. Further, the 3-coordinated Ag atoms with sulfur have an average distance of 2.89  $\text{\AA}$  which shows weaker interactions. As a result of this, the interaction of the  $\text{PPh}_3$  ligands is anisotropic on the vertices of the  $\text{Ag}_8$  cube. The average Ag–P bond distance is 2.47  $\text{\AA}$ . Phosphine ligands bound at 3-coordinated silver atoms is shorter than those bound with 2-coordinated silver atoms. The packing arrangement of  $\text{Ag}_{14}\text{DT}$  shows that there are two molecules in a unit cell. A comparison of unit cell parameters of  $\text{Ag}_{14}\text{DT}$  and  $\text{Ag}_{14}\text{MT}$  is shown in Figure S3. In  $\text{Ag}_{14}\text{DT}$ , the clusters are connected by  $\pi\cdots\pi$  interactions of the BDT ligands (Figure S4). As Figure S4 showed, these interactions can also be looked as zigzag structures. The distances between these interactions are ranging from 2.9 to 3.2  $\text{\AA}$ . Due to the interlocking of the ligands, the interparticle distance got reduced to 1.7 nm, whereas the overall size of the cluster is 1.9 nm.<sup>41</sup> The octahedron formed by the centroids of the benzene dithiol groups clearly shows the direction of  $\pi\cdots\pi$  interactions (red dotted lines in Figure S5A). On the other hand, in  $\text{Ag}_{14}\text{MT}$ , the  $\pi\cdots\pi$  interactions are observed in a cluster, and

the clusters have C–H $\cdots\pi$  interactions in the unit cell. Hence, the nature of ligands whether it is dithiol or monothiol is crucial in dictating the nature of supramolecular interactions which determine the packing of the crystal. Along the (001) plane (view from the Z axis), Ag<sub>14</sub>DT is arranged in a hexagonal lattice where a 3-fold rotational axis passes through the center of the cluster. Along the (100) and (010) planes (viewed from X and Y axes, respectively), NCs are arranged in a rectangular lattice. Moreover, along the Z axis, NCs are assembled along two parallel (00–1) and (001) planes. Every NC on these planes possesses a center of symmetry.

To confirm the elements present in the cluster, SEM/EDS was performed. It showed the presence of Ag, S, P, and C which is consistent with the single crystal X-ray structure. In order to check the homogeneity of the elements in the crystal, EDS mapping was performed, as shown in Figure S6. CHS elemental analysis was also performed to confirm the composition (Table S3), and it showed good agreement with calculation. Electrospray ionization was carried out in both the ion modes to get the molecular ion peak, but unfortunately, no peak was observed. This indicates the neutral charge of the cluster which was further supported by SCXRD as no counter ion was observed. The cluster solution in DCM showed molecule-like transitions in the UV–vis spectrum. The most intense peak was observed at 425 nm with a broad hump around 600 nm. Along with these features, it had a strong absorption in the near-infrared (NIR) region, centered on 860 nm (Figure 2). The Ag<sub>14</sub>DT cluster showed dual visible/NIR

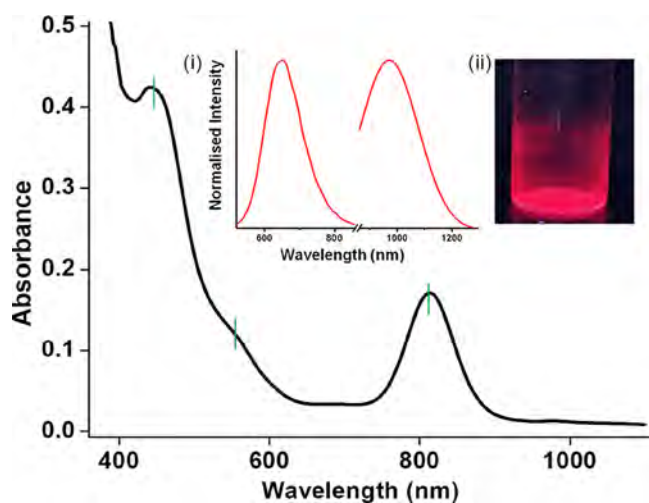


**Figure 2.** Optical absorption spectrum of Ag<sub>14</sub>DT dissolved in DCM. Inset (i) shows the PL spectrum of Ag<sub>14</sub>DT. It exhibits dual visible/NIR emission. The visible and NIR spectra were taken with two detectors, with the same sample. Inset (ii) the photograph of the crystals of Ag<sub>14</sub>DT under UV light.

PL. These emissions were around 680 and 997 nm, upon excitation at 365 and 860 nm, respectively (inset (i) of Figure 2). Ag<sub>14</sub>MT was reported with yellow PL at 530 nm. It is worthy to note that the PL of Ag<sub>14</sub>MT was stable for a few hours, but Ag<sub>14</sub>DT was stable for a few days at room temperature. The difference in the optical properties of monothiol- and dithiol-protected Ag<sub>14</sub> clusters is likely to be due to the change in the ligand shell. The modification of the primary ligand shell alters the electronic structure of the cluster which resulted in new optical properties. Ag<sub>14</sub>DT and Ag<sub>14</sub>MT had comparable thermal stability at 40 °C, and their absorption

spectra were recorded as a function of time. After 1 h of heating, the UV–vis features of Ag<sub>14</sub>MT started to change, and they disappeared almost completely after 2 h, whereas for Ag<sub>14</sub>DT, there was a slight decrease in the absorbance but no change in the peak shape (Figure S7). This observation implied that Ag<sub>14</sub>DT is thermally more robust than Ag<sub>14</sub>MT. This is due to the presence of dithiol which provides more rigidity to the ligand shell.

The electronic and optical properties of Ag<sub>14</sub>DT were computed by taking the atomic coordinates from the crystal structure as the starting point. The optimized structure of Ag<sub>14</sub>DT cluster in the reduced form is presented in Figure S8. Bader charge analysis (Table S1) showed that silver atoms in the inner shell accumulate lower positive charges (0.170e) than in the outer shell (0.294e). This analysis proved that the inner shell silver atoms are more confined than the outer shell. The optical absorption spectrum of [Ag<sub>14</sub>(BDT)<sub>6</sub>(P(CH<sub>3</sub>)<sub>3</sub>)<sub>8</sub>] cluster was calculated using LR-TDDFT. A reduced ligand structure was used in the calculations. Theoretical and experimental UV–vis spectra are compared in Figure 3A. The theoretical spectrum shows two distinct peaks at 720 and 471 nm along with a shoulder at 545 nm. There are some shifts between the calculated and measured optical spectra. These shifts between theoretical and experimental spectra might be due to lack of exact coordinates for calculating the spectra of the cluster.<sup>42</sup> The appearance or disappearance of some peaks might be due to the presence of distortions and intracuster interactions (between the organometallic complexes (AgS<sub>3</sub>PPh<sub>3</sub>) on the surface of the cluster) in the structure which may not have been properly accounted for in the computations.<sup>12</sup> Another reason for this discrepancy could be due to polymorphism and structural isomers in the solutions.

The new peak at 720 nm is due to the interaction of BDT ligands with the cluster which was not present in Ag<sub>14</sub>MT. The MOs responsible for ground state electronic structures are plotted which showed the respective MOs for each optical transition. The TDOS and PDOS were also calculated to study the influence of ligand AOs on the overall electronic structure of the cluster. The calculated highest-occupied molecular orbital (HOMO)–lowest-unoccupied molecular orbital (LUMO) gap was 1.72 eV. The peak at 720 nm arises from the transitions of HOMO – 1 and HOMO – 2 to LUMO. PDOS spectra showed that HOMO – 1 is mainly contributed by the 3p AOs of S, 4d AOs of Ag, and 2p AOs of (C), which contribute to some extent. Similarly, the LUMO is also made up of 3p (S), 4d (Ag), and 2p (C) (Figure 3B,C). Hence, the frontier orbitals are mainly influenced by the thiolate ligands, and therefore, the optical absorption is red-shifted than in Ag<sub>14</sub>MT. The transition for the peak at 545 nm is taking place from HOMO – 8 to LUMO, and this transition is well buried into the valence band. HOMO – 8 is highly dominated by 3p (S) and 2p (C). Finally, the transition at 471 nm takes place from HOMO – 5 to LUMO + 2. HOMO – 5 is mainly contributed by 3p (S), 5s (Ag), 4d (Ag), and 2p (C), while the LUMO + 2 is dominated by 5s (Ag).

In order to understand the contribution of the inner core and outer shell atoms to the optical properties, we have calculated PDOSs of the inner core and outer shell of the Ag<sub>14</sub> cluster. This helped us to identify the MOs responsible for optical properties. It is evident from Figure S9 that the MOs responsible for transitions are populated mainly from the outer shell. Thus, the outer shell which is composed of the Ag<sub>8</sub>S<sub>12</sub> framework is responsible for the optical transition. Introduc-



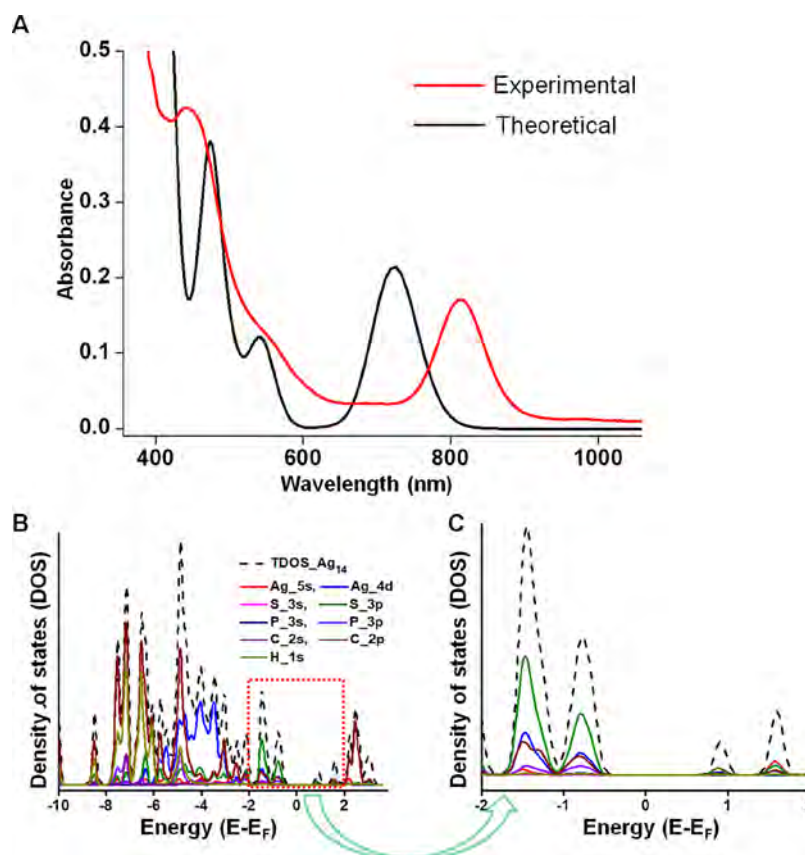


**Figure 3.** (A) Comparison of the experimental UV-vis spectrum (red trace) with the predicted one (black trace). Inset shows theoretical and experimental PL spectra. (B) TDOSs and PDOSs. HOMO–LUMO gap was kept at zero energy. (C) Expanded view of the selected region of (B).

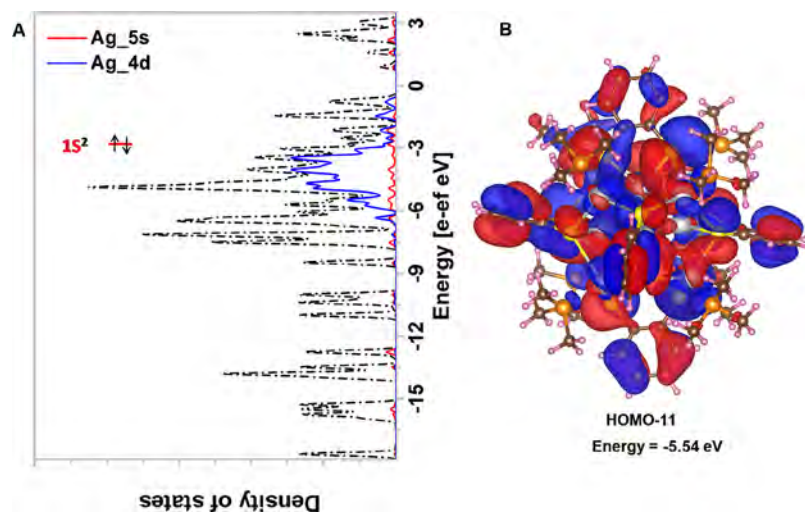


**Figure 4.** (A) Plot of density of states vs energy of Ag<sub>14</sub>DT. Dotted lines correspond to the total density of states. Blue and red solid lines indicate the density of states of Ag<sub>5s</sub> and Ag<sub>4d</sub>, respectively. (B) Isosurface of the superatomic orbital (1S) and its energy.

tion of benzenedithiol enhances intraligand interactions. Seemingly, there are possibilities of ligand–metal and metal–ligand charge transfer during excitation which affects the emission property.

According to the electron counting rule, the number of free electrons in the cluster is given by  $14 - 12 = 2$ , which is a superatom configuration. The superatom character of Ag<sub>14</sub> cluster is shown in Figure 4. The configuration is 1S<sup>2</sup>, and the superatomic orbital is made up of HOMO – 11 which has S character with the delocalized electron density. It is noted that

the 1P superatomic orbital is empty. Therefore, the optical transition takes place between 1S and 1P superatomic orbitals.

## CONCLUSIONS

In summary, we present a structural analogue of Ag<sub>14</sub>MT, namely, Ag<sub>14</sub>DT, composed of a core of the same nuclearity, protected with monothiol and dithiol, respectively. Structural details of Ag<sub>14</sub>DT were obtained by SCXRD which revealed the effect of ligands in the optical properties of NCs having

similar structures and compositions. Unlike the case of  $\text{Ag}_{14}\text{MT}$  which was reported previously,  $\text{Ag}_{14}\text{DT}$  possesses NIR absorption and emission which could be useful in various applications. DFT and PDOS calculations helped us to understand the electronic structures of  $\text{Ag}_{14}\text{DT}$  in greater detail. The large changes in optical properties are brought about by the subtle changes in ligands. Such changes can be very much useful for a whole range of cluster systems which are known now. This study shows the possibility of synthesizing clusters protected by new dithiols with exciting properties. We believe that dithiol-protected clusters can create a new avenue in cluster-assembled solids, and new explorations leading to new properties are likely from future research.

## ■ ASSOCIATED CONTENT

### Supporting Information

The Supporting Information is available free of charge at <https://pubs.acs.org/doi/10.1021/acs.jpcc.0c07140>.

Additional measurements of optical spectroscopy, SEM, elemental analysis, Bader charge analysis, and crystal structure refinement (PDF)

Crystallographic data for  $\text{Ag}_{14}\text{-3}$  (CIF)

## ■ AUTHOR INFORMATION

### Corresponding Author

**Thalappil Pradeep** – Department of Chemistry, DST Unit of Nanoscience (DST UNS) and Thematic Unit of Excellence (TUE), Indian Institute of Technology Madras, Chennai 600 036, India; [orcid.org/0000-0003-3174-534X](https://orcid.org/0000-0003-3174-534X); Email: [pradeep@iitm.ac.in](mailto:pradeep@iitm.ac.in)

### Authors

**Mohammad Bodiuzzaman** – Department of Chemistry, DST Unit of Nanoscience (DST UNS) and Thematic Unit of Excellence (TUE), Indian Institute of Technology Madras, Chennai 600 036, India

**Esma Khatun** – Department of Chemistry, DST Unit of Nanoscience (DST UNS) and Thematic Unit of Excellence (TUE), Indian Institute of Technology Madras, Chennai 600 036, India

**Korath Shivan Sugi** – Department of Chemistry, DST Unit of Nanoscience (DST UNS) and Thematic Unit of Excellence (TUE), Indian Institute of Technology Madras, Chennai 600 036, India

**Ganesan Paramasivam** – Department of Chemistry, DST Unit of Nanoscience (DST UNS) and Thematic Unit of Excellence (TUE), Indian Institute of Technology Madras, Chennai 600 036, India

**Wakeel Ahmed Dar** – Department of Chemistry, DST Unit of Nanoscience (DST UNS) and Thematic Unit of Excellence (TUE), Indian Institute of Technology Madras, Chennai 600 036, India

**Sudhadevi Antharjanam** – Sophisticated Analytical Instruments Facility, Indian Institute of Technology Madras, Chennai 600 036, India

Complete contact information is available at: <https://pubs.acs.org/doi/10.1021/acs.jpcc.0c07140>

### Notes

The authors declare no competing financial interest.

## ■ ACKNOWLEDGMENTS

We want to acknowledge DST, India, for supporting our research project. M.B. thanks U.G.C. for his research fellowship.

## ■ REFERENCES

- (1) Krishnadas, K. R.; Natarajan, G.; Baksi, A.; Ghosh, A.; Khatun, E.; Pradeep, T. Metal–Ligand Interface in the Chemical Reactions of Ligand-Protected Noble Metal Clusters. *Langmuir* **2019**, *35*, 11243–11254.
- (2) Yan, J.; Teo, B. K.; Zheng, N. Surface Chemistry of Atomically Precise Coinage–Metal Nanoclusters: From Structural Control to Surface Reactivity and Catalysis. *Acc. Chem. Res.* **2018**, *51*, 3084–3093.
- (3) Guan, Z.-J.; Zeng, J.-L.; Nan, Z.-A.; Wan, X.-K.; Lin, Y.-M.; Wang, Q.-M. Thiacalix[4]arene: New protection for metal nanoclusters. *Sci. Adv.* **2016**, *2*, No. e1600323.
- (4) Rambukwella, M.; Sakthivel, N. A.; Delcamp, J. H.; Sementa, L.; Fortunelli, A.; Dass, A. Ligand Structure Determines Nanoparticles' Atomic Structure, Metal-Ligand Interface and Properties. *Front. Chem.* **2018**, *6*, 330.
- (5) Aljuhani, M. A.; Bootharaju, M. S.; Sinatra, L.; Basset, J.-M.; Mohammed, O. F.; Bakr, O. M. Synthesis and Optical Properties of a Dithiolate/Phosphine-Protected  $\text{Au}_{28}$  Nanocluster. *J. Phys. Chem. C* **2017**, *121*, 10681–10685.
- (6) Wu, Z.; Jin, R. On the ligand's role in the fluorescence of gold nanoclusters. *Nano Lett.* **2010**, *10*, 2568.
- (7) Chai, J.; Yang, S.; Lv, Y.; Chen, T.; Wang, S.; Yu, H.; Zhu, M. A Unique Pair:  $\text{Ag}_{40}$  and  $\text{Ag}_{46}$  Nanoclusters with the Same Surface but Different Cores for Structure–Property Correlation. *J. Am. Chem. Soc.* **2018**, *140*, 15582–15585.
- (8) Chakraborty, I.; Pradeep, T. Atomically precise clusters of noble metals: Emerging link between atoms and nanoparticles. *Chem. Rev.* **2017**, *117*, 8208.
- (9) Jin, R.; Zeng, C.; Zhou, M.; Chen, Y. Atomically Precise Colloidal Metal Nanoclusters and Nanoparticles: Fundamentals and Opportunities. *Chem. Rev.* **2016**, *116*, 10346.
- (10) Zhu, M.; Aikens, C. M.; Hollander, F. J.; Schatz, G. C.; Jin, R. Correlating the Crystal Structure of A Thiol-Protected  $\text{Au}_{25}$  Cluster and Optical Properties. *J. Am. Chem. Soc.* **2008**, *130*, 5883–5885.
- (11) Häkkinen, H.; Walter, M.; Grönbeck, H. Divide and Protect: Capping Gold Nanoclusters with Molecular Gold–Thiolate Rings. *J. Phys. Chem. B* **2006**, *110*, 9927.
- (12) Joshi, C. P.; Bootharaju, M. S.; Alhilaly, M. J.; Bakr, O. M.  $[\text{Ag}_{25}(\text{SR})_{18}]^-$ : The “Golden” Silver Nanoparticle. *J. Am. Chem. Soc.* **2015**, *137*, 11578–11581.
- (13) Yang, H.; Wang, Y.; Huang, H.; Gell, L.; Lehtovaara, L.; Malola, S.; Häkkinen, H.; Zheng, N. All-thiol-stabilized  $\text{Ag}_{44}$  and  $\text{Au}_{12}\text{Ag}_{32}$  nanoparticles with single-crystal structures. *Nat. Commun.* **2013**, *4*, 2422.
- (14) AbdulHalim, L. G.; Bootharaju, M. S.; Tang, Q.; Del Gobbo, S.; AbdulHalim, R. G.; Eddaoudi, M.; Jiang, D.-e.; Bakr, O. M.  $\text{Ag}_{29}(\text{BDT})_{12}(\text{TPP})_4$ : A Tetravalent Nanocluster. *J. Am. Chem. Soc.* **2015**, *137*, 11970–11975.
- (15) Desiredy, A.; Conn, B. E.; Guo, J.; Yoon, B.; Barnett, R. N.; Monahan, B. M.; Kirschbaum, K.; Griffith, W. P.; Whetten, R. L.; Landman, U.; et al. Ultrastable silver nanoparticles. *Nature* **2013**, *501*, 399–402.
- (16) Harkness, K. M.; Tang, Y.; Dass, A.; Pan, J.; Kothalawala, N.; Reddy, V. J.; Cliffel, D. E.; Demeler, B.; Stellacci, F.; Bakr, O. M.; McLean, J. A.  $\text{Ag}_{44}(\text{SR})_{30}^{4+}$ : a silver-thiolate superatom complex. *Nanoscale* **2012**, *4*, 4269.
- (17) Ghosh, A.; Ghosh, D.; Khatun, E.; Chakraborty, P.; Pradeep, T. Unusual reactivity of dithiol protected clusters in comparison to monothiol protected clusters: studies using  $\text{Ag}_{51}(\text{BDT})_{19}(\text{TPP})_3$  and  $\text{Ag}_{29}(\text{BDT})_{12}(\text{TPP})_4$ . *Nanoscale* **2017**, *9*, 1068.



- (18) Chen, Y.; Zeng, C.; Kauffman, D. R.; Jin, R. Tuning the Magic Size of Atomically Precise Gold Nanoclusters via Isomeric Methylbenzenethiols. *Nano Lett.* **2015**, *15*, 3603.
- (19) Khatun, E.; Ghosh, A.; Ghosh, D.; Chakraborty, P.; Nag, A.; Mondal, B.; Chennu, S.; Pradeep, T.  $[\text{Ag}_{59}(\text{2,5-DCBT})_{32}]^{3-}$ : A new cluster and a precursor for three well-known clusters. *Nanoscale* **2017**, *9*, 8240.
- (20) Bodiuzzaman, M.; Ghosh, A.; Sugi, K. S.; Nag, A.; Khatun, E.; Varghese, B.; Paramasivam, G.; Antharjanam, S.; Natarajan, G.; Pradeep, T. Camouflaging Structural Diversity: Co-crystallization of Two Different Nanoparticles Having Different Cores But the Same Shell. *Angew. Chem., Int. Ed.* **2019**, *58*, 189–194.
- (21) Yang, T.-Q.; Peng, B.; Shan, B.-Q.; Zong, Y.-X.; Jiang, J.-G.; Wu, P.; Zhang, K. Origin of the photoluminescence of metal nanoclusters: from metal-centered emission to ligand-centered emission. *Nanomaterials* **2020**, *10*, 261.
- (22) Díez, I.; Ras, R. H. A. Fluorescent silver nanoclusters. *Nanoscale* **2011**, *3*, 1963–1970.
- (23) Wen, X.; Yu, P.; Toh, Y.-R.; Ma, X.; Huang, S.; Tang, J. Fluorescence origin and spectral broadening mechanism in atomically precise  $\text{Au}_8$  nanoclusters. *Nanoscale* **2013**, *5*, 10251–10257.
- (24) Choi, S.; Yu, J. Recent development in deciphering the structure of luminescent silver nanodots. *APL Mater.* **2017**, *5*, 053401.
- (25) Yang, H.; Lei, J.; Wu, B.; Wang, Y.; Zhou, M.; Xia, A.; Zheng, L.; Zheng, N. Crystal structure of a luminescent thiolated Ag nanocluster with an octahedral  $\text{Ag}_6^{4+}$  core. *Chem. Commun.* **2013**, *49*, 300–302.
- (26) Wang, Z.-Y.; Wang, M.-Q.; Li, Y.-L.; Luo, P.; Jia, T.-T.; Huang, R.-W.; Zang, S.-Q.; Mak, T. C. W. Atomically Precise Site-Specific Tailoring and Directional Assembly of Superatomic Silver Nanoclusters. *J. Am. Chem. Soc.* **2018**, *140*, 1069–1076.
- (27) Du, X.-S.; Yan, B.-J.; Wang, J.-Y.; Xi, X.-J.; Wang, Z.-Y.; Zang, S.-Q. Layer-sliding-driven crystal size and photoluminescence change in a novel SCC-MOF. *Chem. Commun.* **2018**, *54*, 5361–5364.
- (28) Pyo, K.; Thanthirige, V. D.; Yoon, S. Y.; Ramakrishna, G.; Lee, D. Enhanced luminescence of  $\text{Au}_{22}(\text{SG})_{18}$  nanoclusters via rational surface engineering. *Nanoscale* **2016**, *8*, 20008–20016.
- (29) Farrag, M.; Tschurl, M.; Heiz, U. Chiral Gold and Silver Nanoclusters: Preparation, Size Selection, and Chiroptical Properties. *Chem. Mater.* **2013**, *25*, 862–870.
- (30) Dolamic, I.; Knoppe, S.; Dass, A.; Bürgi, T. First enantioseparation and circular dichroism spectra of  $\text{Au}_{38}$  clusters protected by achiral ligands. *Nat. Commun.* **2012**, *3*, 798.
- (31) Liu, C.; Li, T.; Abroshan, H.; Li, Z.; Zhang, C.; Kim, H. J.; Li, G.; Jin, R. Chiral  $\text{Ag}_{23}$  nanocluster with open shell electronic structure and helical face-centered cubic framework. *Nat. Commun.* **2018**, *9*, 744.
- (32) Du, Y.; Sheng, H.; Astruc, D.; Zhu, M. Atomically Precise Noble Metal Nanoclusters as Efficient Catalysts: A Bridge between Structure and Properties. *Chem. Rev.* **2019**, *120*, 526–622.
- (33) Ren, L.; Yuan, P.; Su, H.; Malola, S.; Lin, S.; Tang, Z.; Teo, B. K.; Häkkinen, H.; Zheng, L.; Zheng, N. Bulky Surface Ligands Promote Surface Reactivities of  $[\text{Ag}_{141}\text{X}_{12}(\text{S-Adm})_{40}]^{3+}$  ( $\text{X} = \text{Cl}, \text{Br}, \text{I}$ ) Nanoclusters: Models for Multiple-Twinned Nanoparticles. *J. Am. Chem. Soc.* **2017**, *139*, 13288–13291.
- (34) Bootharaju, M. S.; Joshi, C. P.; Alhilaly, M. J.; Bakr, O. M. Switching a nanocluster core from hollow to nonhollow. *Chem. Mater.* **2016**, *28*, 3292.
- (35) Bootharaju, M. S.; Dey, R.; Gevers, L. E.; Hedhili, M. N.; Basset, J.-M.; Bakr, O. M. A New Class of Atomically Precise, Hydride-Rich Silver Nanoclusters Co-Protected by Phosphines. *J. Am. Chem. Soc.* **2016**, *138*, 13770–13773.
- (36) Ghosh, D.; Bodiuzzaman, M.; Som, A.; Raja, S.; Baksi, A.; Ghosh, A.; Ghosh, J.; Ganesh, A.; Samji, P.; Mahalingam, S.; Karunakaran, D.; Pradeep, T. Internalization of a Preformed Atomically Precise Silver Cluster in Proteins by Multistep Events and Emergence of Luminescent Counterparts Retaining Bioactivity. *J. Phys. Chem. C* **2019**, *123*, 29408–29417.
- (37) Jin, R.; Qian, H.; Wu, Z.; Zhu, Y.; Zhu, M.; Mohanty, A.; Garg, N. Size Focusing: A Methodology for Synthesizing Atomically Precise Gold Nanoclusters. *J. Phys. Chem. Lett.* **2010**, *1*, 2903–2910.
- (38) Enkovaara, J.; Rostgaard, C.; Mortensen, J. J.; Chen, J.; Dulak, M.; Ferrighi, L.; Gavnholt, J.; Glinzvad, C.; Haikola, V.; Hansen, H. A.; et al. Electronic structure calculations with GPAW: a real-space implementation of the projector augmented-wave method. *J. Phys.: Condens. Matter* **2010**, *22*, 253202.
- (39) Mortensen, J. J.; Hansen, L. B.; Jacobsen, K. W. Real-space grid implementation of the projector augmented wave method. *Phys. Rev. B: Condens. Matter Mater. Phys.* **2005**, *71*, 035109.
- (40) Walter, M.; Häkkinen, H.; Lehtovaara, L.; Puska, M.; Enkovaara, J.; Rostgaard, C.; Mortensen, J. J. Time-dependent density-functional theory in the projector augmented-wave method. *J. Chem. Phys.* **2008**, *128*, 244101.
- (41) Nag, A.; Chakraborty, P.; Bodiuzzaman, M.; Ahuja, T.; Antharjanam, S.; Pradeep, T. Polymorphism of  $\text{Ag}_{29}(\text{BDT})_{12}(\text{TPP})_4^{3-}$  cluster: interactions of secondary ligands and their effect on solid state luminescence. *Nanoscale* **2018**, *10*, 9851–9855.
- (42) Aikens, C. M. Origin of Discrete Optical Absorption Spectra of  $\text{M}_{25}(\text{SH})_{18}^-$  Nanoparticles ( $\text{M} = \text{Au}, \text{Ag}$ ). *J. Phys. Chem. C* **2008**, *112*, 19797–19800.

## Supporting Information

### Dithiol-Induced Contraction in Ag<sub>14</sub> Clusters and Its Manifestation in Electronic Structure

Mohammad Bodiuzzaman<sup>a</sup>, Esma Khatun<sup>a</sup>, Korath Shivan Sugi<sup>a</sup>, Ganesan Paramasivam<sup>a</sup>, Waakel Ahmed Dar<sup>a</sup>, Sudhadevi Antharjanam<sup>b</sup> and Thalappil Pradeep<sup>a\*</sup>

*E-mail: [pradeep@iitm.ac.in](mailto:pradeep@iitm.ac.in)*

a. Department of Chemistry, DST Unit of Nanoscience (DST UNS) and Thematic Unit of Excellence (TUE), Indian Institute of Technology Madras, Chennai 600036, India

b. Sophisticated Analytical Instruments Facility, Indian Institute of Technology Madras, Chennai 600036, India

Name	Description	Page no.
		1
Table S1	Bader charge analysis	2
Table S2	Crystal data and structure refinement	3
Table S3	Elemental analysis	4
Figure S1	Structure of octahedron formed by the centroids of the benzene rings	5
Figure S2	Different environments of silver atoms in Ag <sub>14</sub> DT	6
Figure S3	Unit cell dimensions of Ag <sub>14</sub> DT and Ag <sub>14</sub> MT	7
Figure S4	$\pi \dots \pi$ stacking interactions in Ag <sub>14</sub> DT	8
Figure S5	Supramolecular interactions of Ag <sub>14</sub> MT and Ag <sub>14</sub> DT	9
Figure S6	SEM EDS of a single crystal	10
Figure S7	Thermal stability of Ag <sub>14</sub> MT and Ag <sub>14</sub> DT	11
Figure S8	Optimized structure of Ag <sub>14</sub> DT	12
Figure S9	Density of states of inner core and outer shell of Ag <sub>14</sub> cluster	13

Table S1. Bader charges for Ag, S and P atoms in Ag<sub>14</sub>DT cluster

Ag <sub>6</sub> Inner Shell	Bader Charges (e)
Ag <sub>2</sub>	0.171
Ag <sub>5</sub>	0.179
Ag <sub>7</sub>	0.158
Ag <sub>9</sub>	0.170
Ag <sub>12</sub>	0.184
Ag <sub>14</sub>	0.157
Average	0.170
Ag <sub>8</sub> Outer Shell	
Ag <sub>1</sub>	0.303
Ag <sub>3</sub>	0.276
Ag <sub>4</sub>	0.304
Ag <sub>6</sub>	0.307
Ag <sub>8</sub>	0.303
Ag <sub>10</sub>	0.253
Ag <sub>11</sub>	0.303
Ag <sub>13</sub>	0.302
Average	0.294
Sulfur atoms	
S <sub>15</sub>	-0.282
S <sub>16</sub>	-0.295
S <sub>17</sub>	-0.280
S <sub>18</sub>	-0.279
S <sub>19</sub>	-0.282
S <sub>20</sub>	-0.298
S <sub>21</sub>	-0.281
S <sub>22</sub>	-0.283
S <sub>23</sub>	-0.289
S <sub>24</sub>	-0.294
S <sub>25</sub>	-0.288
S <sub>26</sub>	-0.295
Average	-0.287
Phosphorus	
P <sub>27</sub>	1.550
P <sub>28</sub>	1.563
P <sub>29</sub>	1.532
P <sub>30</sub>	1.537
P <sub>31</sub>	1.523
P <sub>32</sub>	1.576
P <sub>33</sub>	1.505
P <sub>34</sub>	1.555
Average	1.543

Table S2. Crystal data and structure refinement for Ag14-3.

Identification code	AG14-3	
Empirical formula	C198 H159 Ag14 P9 S12	
Formula weight	4711.87	
Temperature	296(2) K	
Wavelength	0.71073 Å	
Crystal system	Trigonal	
Space group	R-3	
Unit cell dimensions	a = 23.9695(12) Å	$\gamma = 90^\circ$ .
	b = 23.9695(12) Å	$\beta = 90^\circ$ .
	c = 28.297(2) Å	$\gamma = 120^\circ$ .
Volume	14079.6(18) Å <sup>3</sup>	
Z	3	
Density (calculated)	1.667 Mg/m <sup>3</sup>	
Absorption coefficient	1.685 mm <sup>-1</sup>	
F(000)	6996	
Crystal size	0.150 x 0.120 x 0.100 mm <sup>3</sup>	
Theta range for data collection	3.485 to 18.033°.	
Index ranges	-20 ≤ h ≤ 20, -20 ≤ k ≤ 20, -24 ≤ l ≤ 24	
Reflections collected	46201	
Independent reflections	2151 [R(int) = 0.3070]	
Completeness to theta = 18.033°	99.3 %	
Absorption correction	multi-scan	
Max. and min. transmission	0.74 and 0.64	
Refinement method	Full-matrix least-squares on F <sup>2</sup>	
Data / restraints / parameters	2151 / 493 / 379	
Goodness-of-fit on F <sup>2</sup>	1.020	
Final R indices [I > 2σ(I)]	R1 = 0.0606, wR2 = 0.1184	
R indices (all data)	R1 = 0.1234, wR2 = 0.1455	
Extinction coefficient	n/a	
Largest diff. peak and hole	0.595 and -0.426 e.Å <sup>-3</sup>	

Table S3. Results of elemental analysis of Ag<sub>14</sub>

Sample	C <sub>Exp.</sub> (content %)	C <sub>cal.</sub> (content %)	H <sub>Exp.</sub> (content %)	H <sub>Cal.</sub> (content %)	S <sub>Exp.</sub> (content %)	S <sub>cal</sub> (content %)
Ag <sub>14</sub>	48.91	48.54	3.52	3.24	9.11	8.64



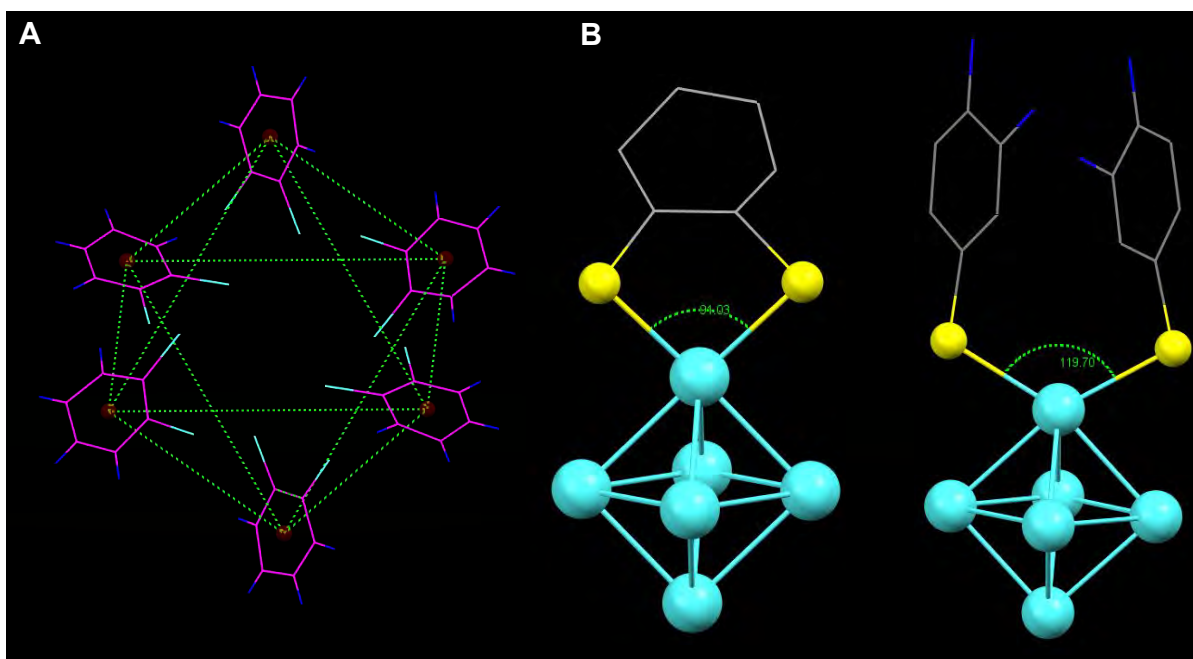


Figure S1 (A) The orientation of the primary ligands in a cluster. Centroids of the six benzenedithiol ligands form an octahedron. Green dotted lines are drawn to show the octahedron. (B) The comparison of the S-Ag-S bond angles in  $\text{Ag}_{14}\text{DT}$  and  $\text{Ag}_{14}\text{MT}$ .

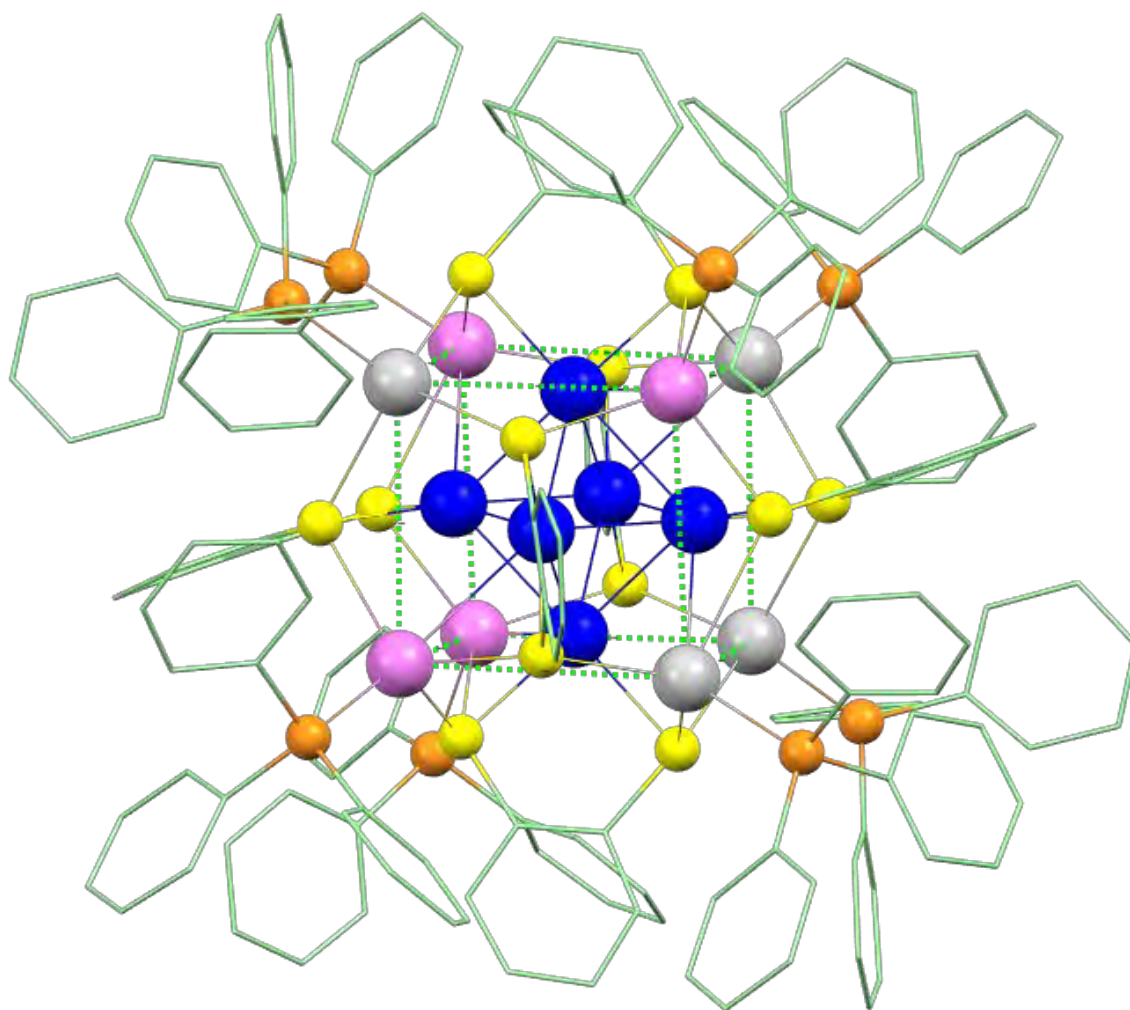


Figure S2 Different environments of silver in Ag<sub>14</sub> are noted in different colors. Blue shows the inner shell atoms and in outer shell, there are two types of silver atoms as shown in violet and grey.

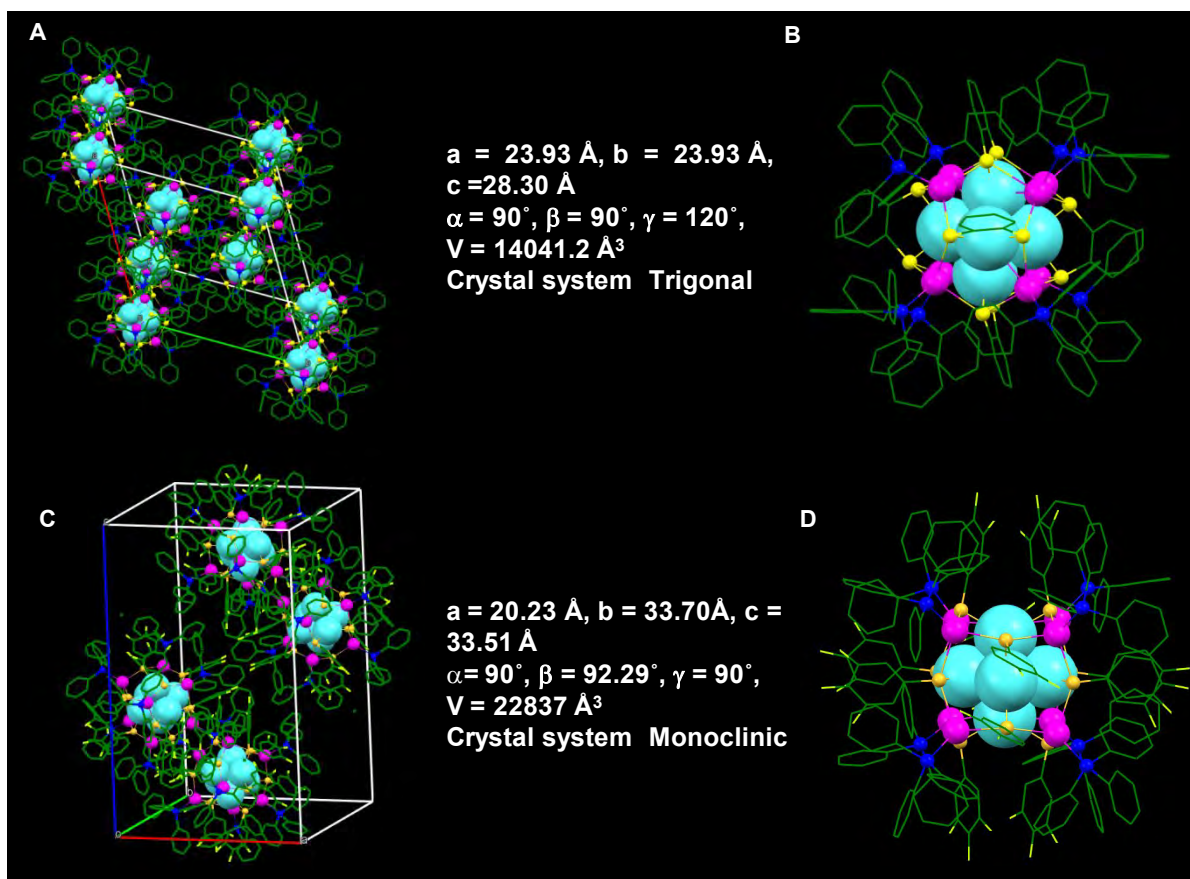


Figure S3 Comparison of crystal structures of  $\text{Ag}_{14}$  clusters. (A) and (C) Unit cell representations of both the clusters. The number of molecules in a unit cell is not same as evident from the packing. (B) and (D) Full structures of  $[\text{Ag}_{14}(\text{BDT})_6(\text{PPh}_3)_8]$  and  $[\text{Ag}_{14}(\text{SPhF}_2)_6(\text{PPh}_3)_8]$ , respectively. The octahedral core is shown in space filling and carbon atoms in wireframe model. Hydrogen atoms are omitted for clarity.

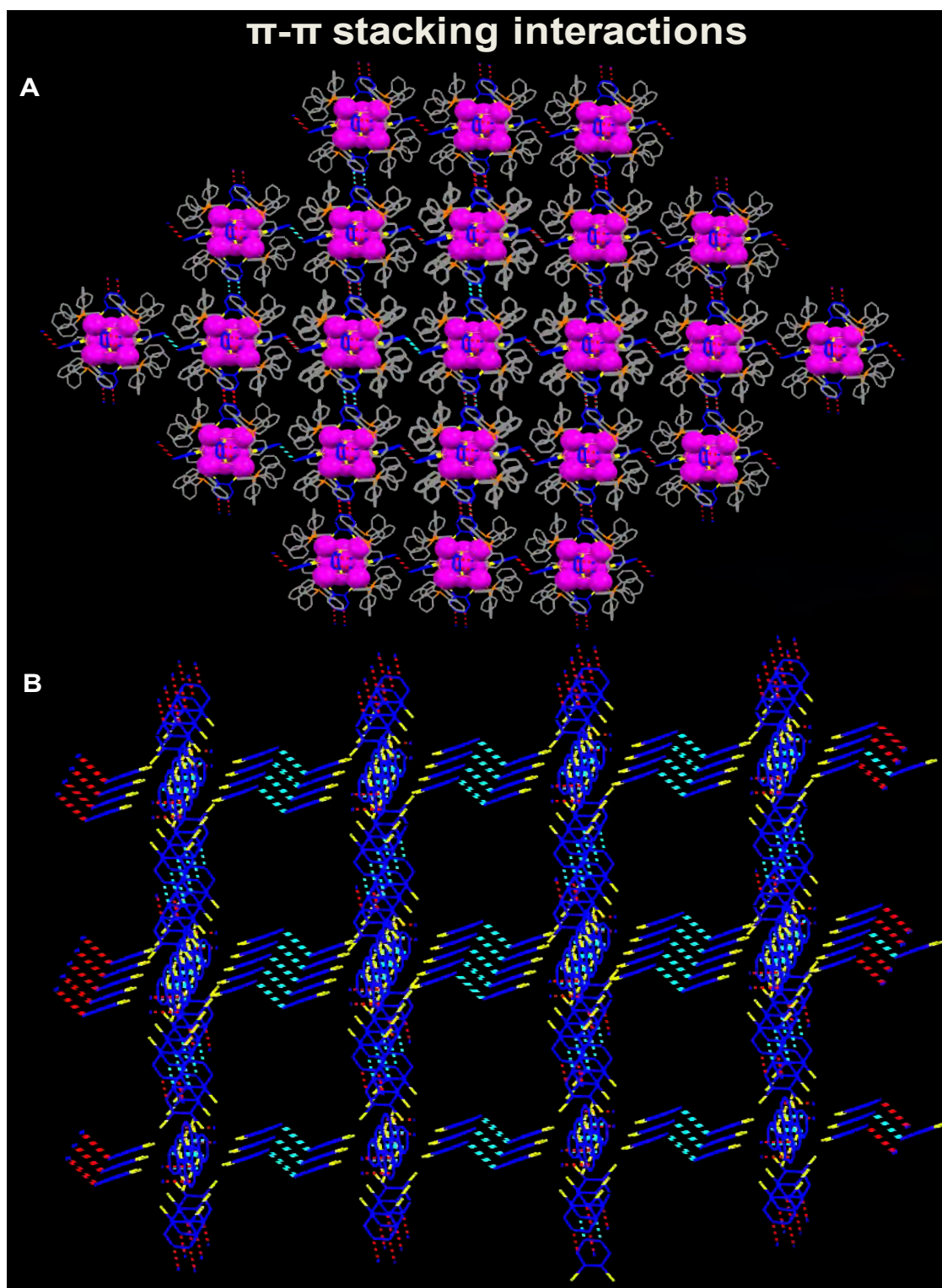


Figure S4 (A)  $\pi$ ... $\pi$  interactions between the benzene rings. BDT are shown in blue. (B)  $\pi$ ... $\pi$  interactions result in the zigzag structure.

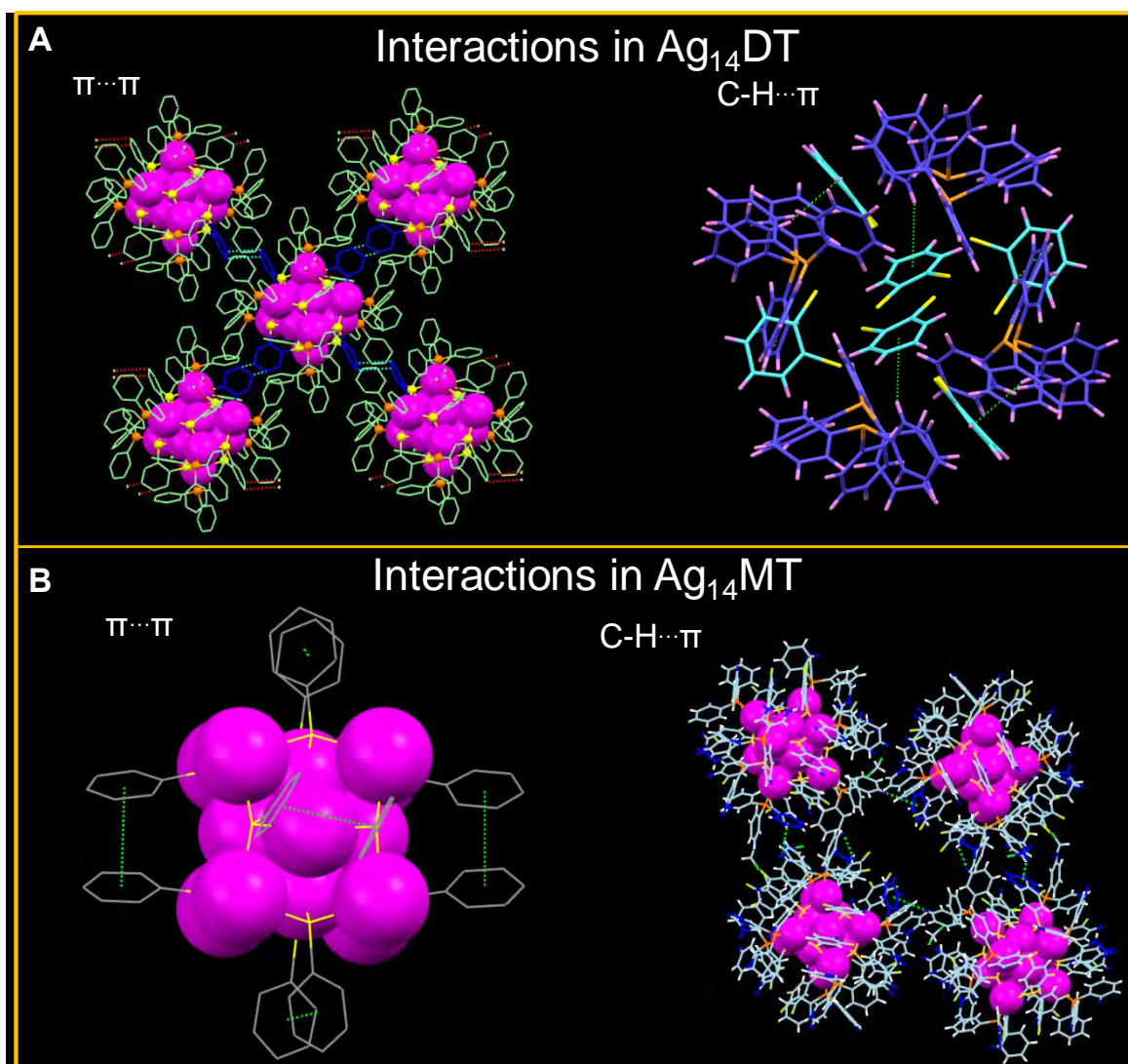


Figure S5 (A) Supramolecular interactions between the clusters. Interactions between the electrons of benzene rings are shown in blue. Intracuster interactions in  $\text{Ag}_{14}\text{DT}$  where  $\text{C-H} \cdots \pi$  interactions are shown by green dotted lines. (B) Intercluster interactions in  $\text{Ag}_{14}\text{MT}$ .  $\text{H} \cdots \text{H}$  vdw forces and  $\text{C-H} \cdots \pi$  interactions are shown by green dotted lines. In  $\text{Ag}_{14}\text{MT}$   $\pi \cdots \pi$  interactions are observed in the cluster. The nature of surface structure dictates the supramolecular interactions.



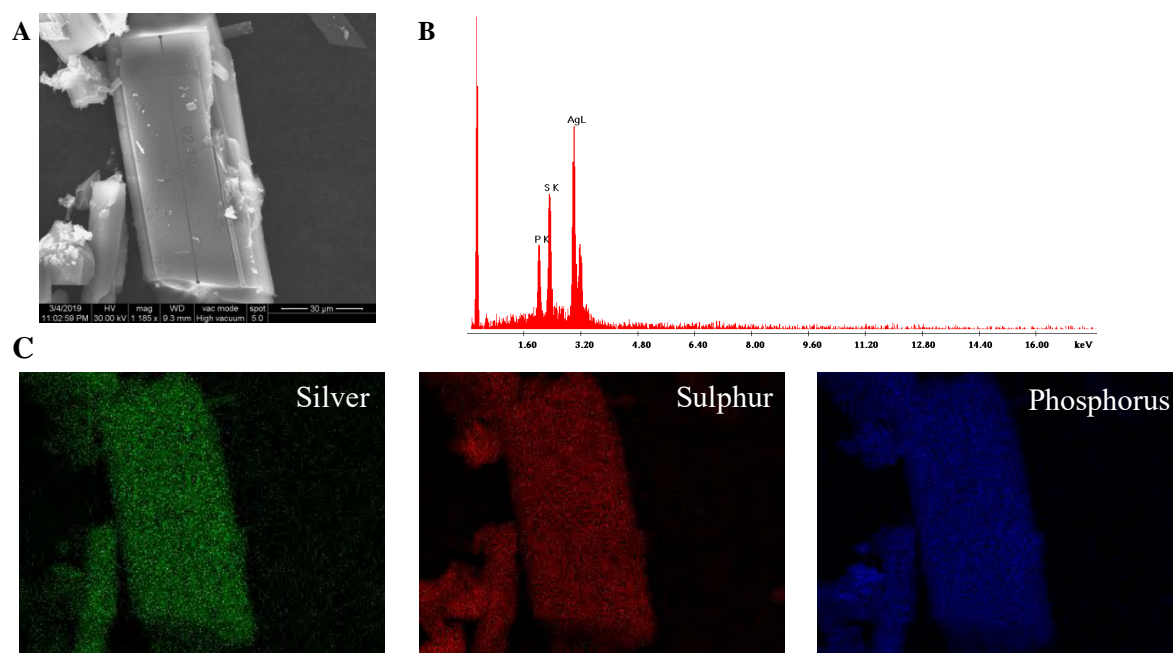


Figure S6 (A) SEM image of the single crystal. (B) SEM EDS shows the presence of Ag, S, and P as major elements. (C) Elemental mapping of the crystal which shows the uniformity of the elements in the crystal.

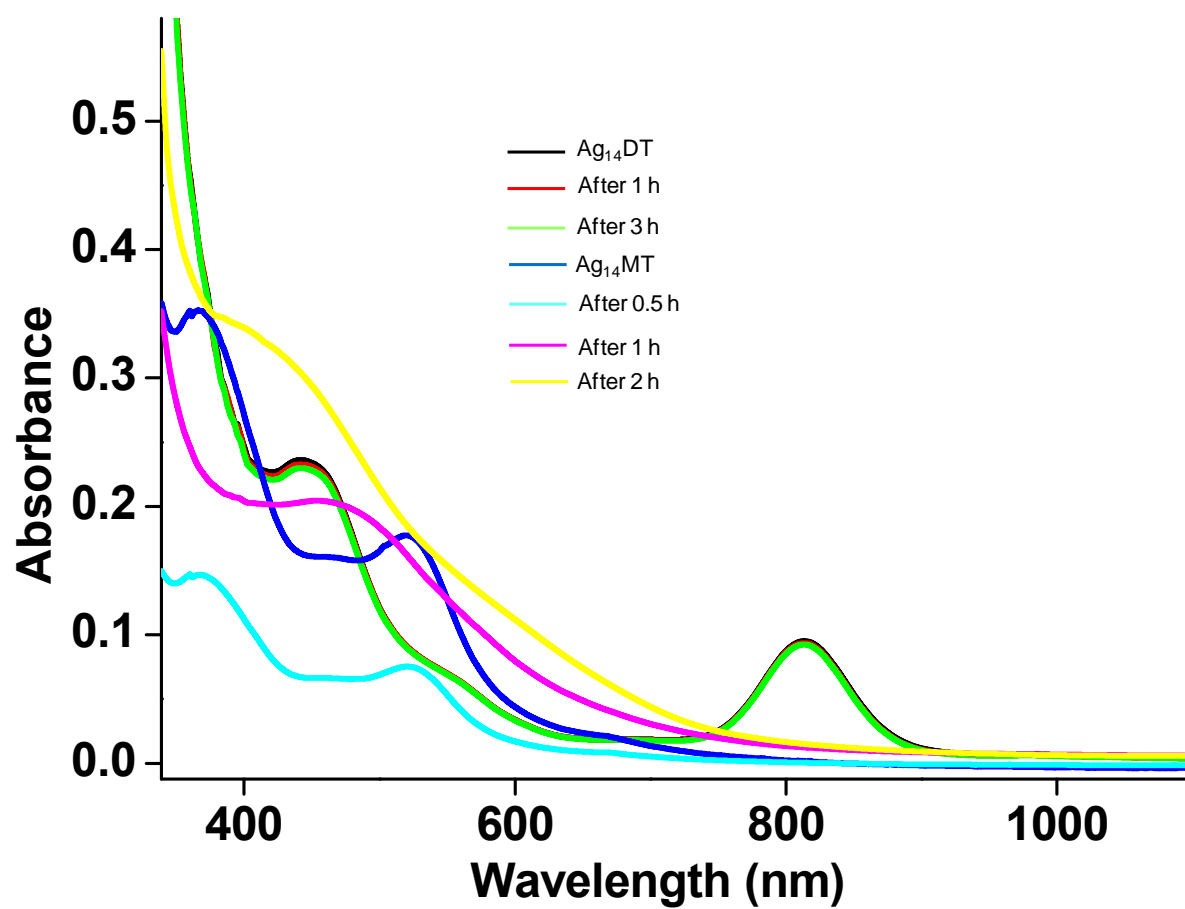


Figure S7 Comparison of thermal stability of Ag<sub>14</sub>DT and Ag<sub>14</sub>MT by time-dependent UV/Vis spectroscopy.

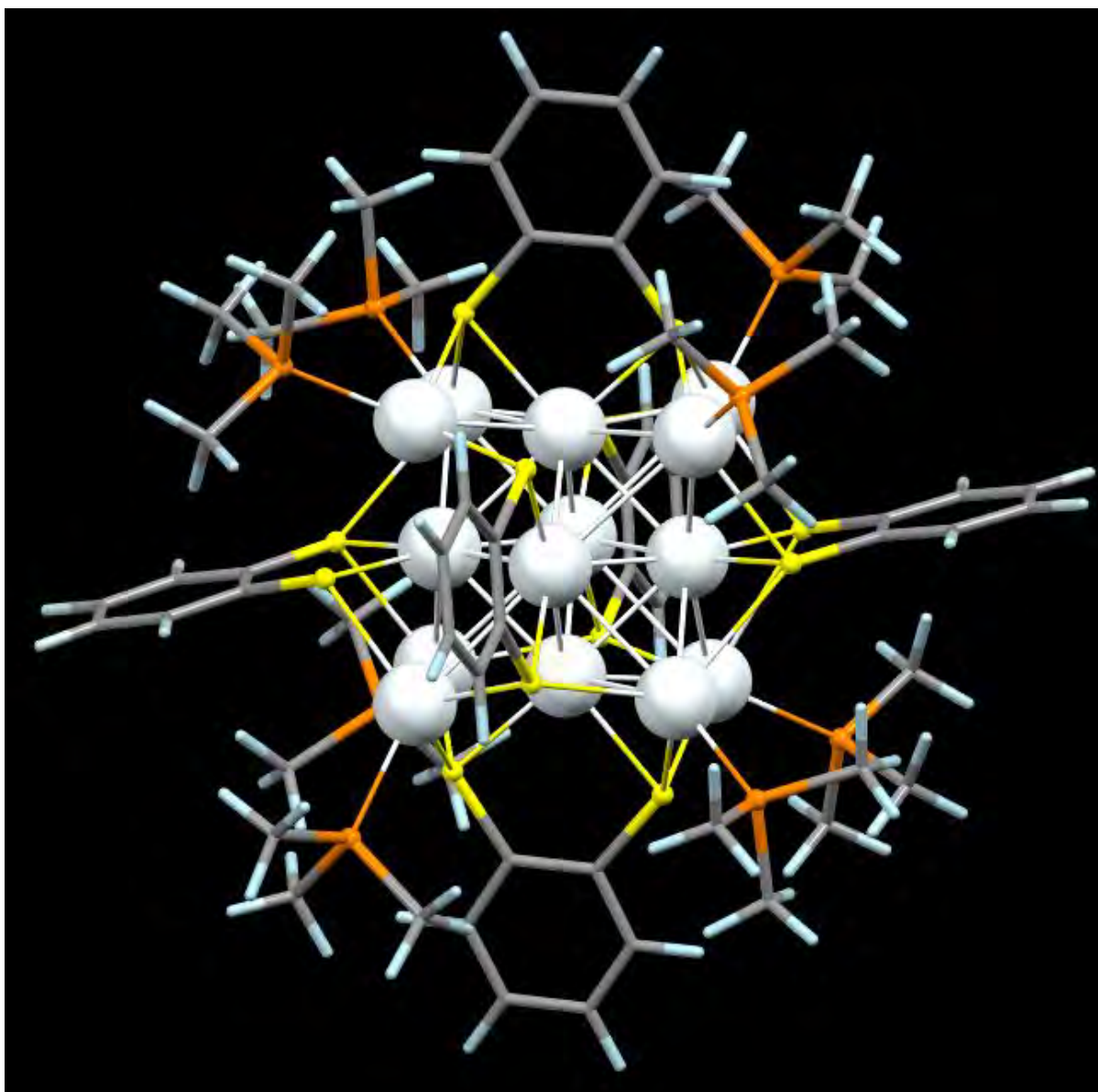


Figure S8 Optimized structure of  $\text{Ag}_{14}\text{DT}$  in reduced ligands. Phenyl rings of the  $\text{PPh}_3$  were reduced to  $\text{P}(\text{CH}_3)_3$ .

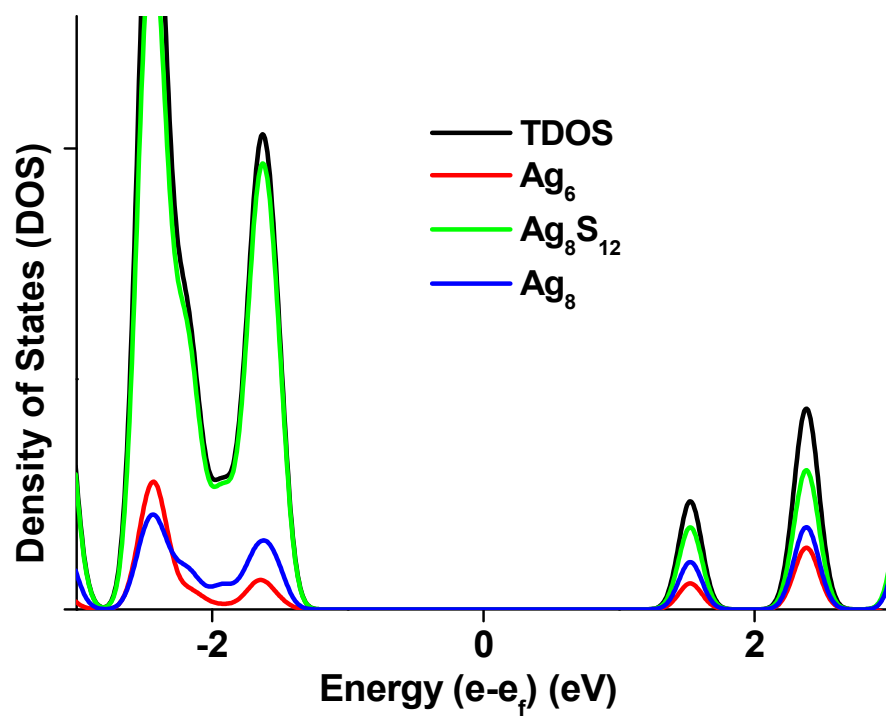


Figure S9 Density of states of inner core and outer shell of Ag<sub>14</sub> cluster.

# Atomically Precise Noble Metal Cluster-Assembled Superstructures in Water: Luminescence Enhancement and Sensing

Abhijit Nag, Papri Chakraborty, Athira Thacharon, Ganesan Paramasivam, Biswajit Mondal, Mohammad Bodiuzzaman, and Thalappil Pradeep\*

Cite This: *J. Phys. Chem. C* 2020, 124, 22298–22303

Read Online

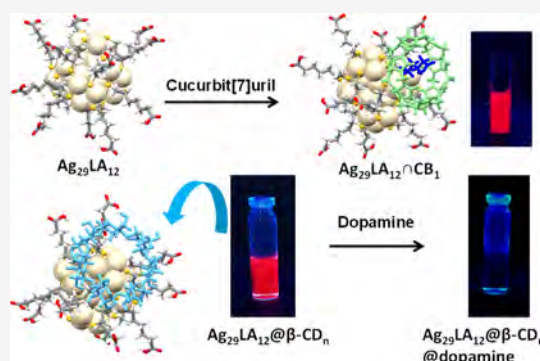
ACCESS |

Metrics & More

Article Recommendations

Supporting Information

**ABSTRACT:** We present an example of host–guest complexes of atomically precise noble metal nanoparticles with cucurbit[7]uril (CB) in water, specifically concentrating on  $\text{Ag}_{29}(\text{LA})_{12}$  (where LA is  $\alpha$ -lipoic acid), a well-known red luminescent silver cluster. Such host–guest interactions resulted in enhanced luminescence of about 1.25 times for the modified system, compared to the parent cluster. We extended our study to cyclodextrins (CDs), where about 1.5 times enhanced luminescence was estimated compared to the parent cluster. The formation of supramolecular complexes was confirmed using high-resolution electrospray ionization mass spectrometry (HRESI MS) and nuclear magnetic resonance spectroscopy. Molecular docking and density functional theory calculations supported our experimental results and showed that while CB formed inclusion complexes by encapsulation of one of the LA ligands of the cluster, CD formed supramolecular adducts by interaction with the cavity built by the ligands on the cluster surface. The complexation was favored by geometrical compatibility. Consequently, these superstructures are labeled as  $\text{Ag}_{29}\text{LA}_{12}\cap\text{CB}_n$  and  $\text{Ag}_{29}\text{LA}_{12}@\text{CD}_n$  ( $n = 1–3$ ), where  $\cap$  and  $@$  indicate the inclusion complex and supramolecular adduct, respectively. Solution-phase  $\text{Ag}_{29}\text{LA}_{12}@\text{CD}_n$  complexes were employed to detect dopamine (10 nM). Luminescent  $\text{Ag}_{29}\text{LA}_{12}@\text{CD}_n$  and  $\text{Ag}_{29}\text{LA}_{12}\cap\text{CB}_n$  complexes in water could be potential candidates for organic pollutant sensing and biomedical applications.



## INTRODUCTION

Noble metal nanoclusters (NMCs) have emerged as new functional nanomaterials<sup>1–3</sup> because of their wide range of applications including biomedical imaging,<sup>4</sup> sensing,<sup>5</sup> catalysis,<sup>6,7</sup> energy conversion,<sup>8</sup> and so forth. Various properties of NMCs like catalysis, chirality, and photoluminescence (PL) are controlled by not only the central metal core but also the ligands.<sup>2,9,10</sup> Diverse organic ligands including thiolates,<sup>11–13</sup> phosphines,<sup>14–17</sup> and alkynes<sup>18,19</sup> have been used for the synthesis of NMCs.

Supramolecular chemistry involves chemical methods to build complex structures from simple molecular building blocks via noncovalent interactions. Noncovalent interactions include ion–ion, hydrogen bonding,  $\pi$ – $\pi$  stacking, and van der Waals (vdWs) interactions.<sup>20,21</sup> Such interactions of nanoparticles resulted in self-assembled superstructures.<sup>22</sup> As the nanoclusters are protected by organic ligands, supramolecular complexation is possible for NMCs also.<sup>20</sup> Cyclodextrins (CDs) and cucurbit[7]uril (CB) were used in supramolecular chemistry because of their encapsulation activity.<sup>23</sup> Recently, Mathew et al. reported the host–guest complexation of  $[\text{Au}_{25}(\text{SBB})_{18}]^-$  with  $\beta$ -CD.<sup>24</sup> Moussawi et al. synthesized and crystallized a supramolecular hybrid complex of a polyoxometalate  $[\text{P}_2\text{W}_{18}\text{O}_{62}]^{6-}$ ,  $\gamma$ -CD, and  $[\text{Ta}_6\text{Br}_{12}(\text{H}_2\text{O})_6]^{2+}$ ,

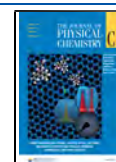
where CD acted as a linker between polyoxometalate and the cluster.<sup>25</sup> Recently, our group reported isomerism in  $\text{Ag}_{29}\text{BDT}_{12}\cap\beta\text{-CD}_n$  (where BDT is 1,3-benzenedithiol;  $n = 2–4$ ) complexes.<sup>26</sup> The supramolecular complexes of  $[\text{Ag}_{29}(\text{BDT})_{12}]^{3-}$  with fullerenes ( $\text{C}_{60}$  and  $\text{C}_{70}$ ) were also studied.<sup>27</sup> The crystal structure of the supramolecular complexes of crown ethers with  $\text{Ag}_{29}\text{BDT}_{12}$  was resolved, and the driving forces for such complexation were seen to be noncovalent interactions.<sup>28</sup> Such supramolecular interactions could assemble them in crystalline superstructures because of the strong noncovalent interactions. CB belongs to a family of host molecules which could form assemblies with NMCs. The supramolecular complexation of luminescent clusters with CDs and CB in water could be highly useful for biomedical applications.

A supramolecular adduct is one in which molecular interactions bring two species together. An inclusion complex

Received: July 28, 2020

Revised: September 16, 2020

Published: September 16, 2020





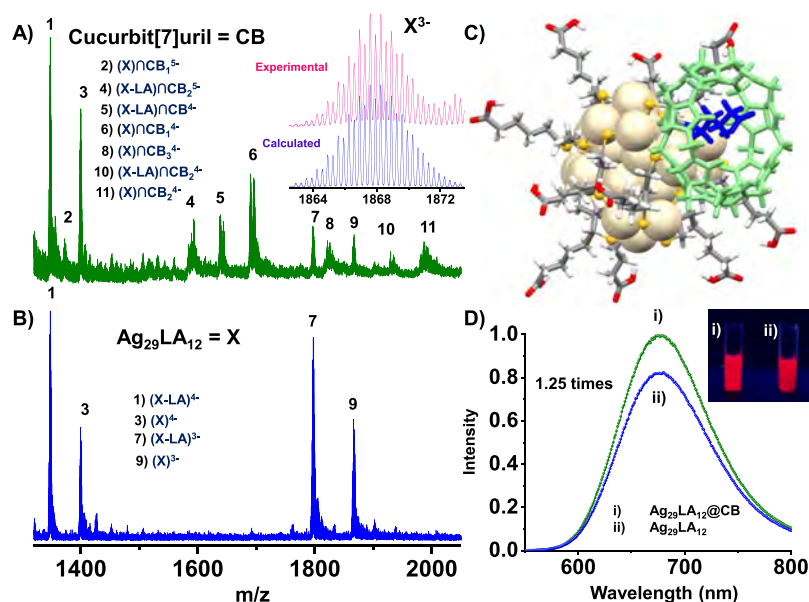


**Figure 1.** Full-range HRESI MS spectra of  $[\text{Ag}_{29}(\text{LA})_{12}\text{@CB}_n]$  complexes, where  $n = 1-3$  (A) and  $\text{Ag}_{29}(\text{LA})_{12}$  (B). Relative peak intensities of the isotopologues of  $\text{Ag}_{29}(\text{LA})_{12}^{3-}$  are presented in the inset of (A). Assignments of the peaks are provided in the inset of (A,B) with numbering, where  $X = \text{Ag}_{29}(\text{LA})_{12}$ . (C) Schematic representation of  $[\text{Ag}_{29}(\text{LA})_{12}\text{@CB}_n]$  for  $n = 1$ . Color codes: silver, light yellowish gray; sulfur, yellow; carbon, gray; oxygen, red. Encapsulated LA inside CB is in blue. CB is presented in light green color. (D) PL spectra of  $[\text{Ag}_{29}(\text{LA})_{12}\text{@CB}_n]$  complexes (i) and pure cluster (ii). Photographs of the solution of  $[\text{Ag}_{29}(\text{LA})_{12}\text{@CB}_n]$  complexes (i) and  $[\text{Ag}_{29}(\text{LA})_{12}]$  (ii) under UV light are shown in the inset of (D).

is a specific category of supramolecular adducts in which a molecule having a cavity hosts a guest molecule. We can simply term both of them as supramolecular complexes, as all inclusion complexes are supramolecular adducts, although all supramolecular adducts are not inclusion complexes.

Here, we report the supramolecular complexation of  $\text{Ag}_{29}\text{LA}_{12}$  (where LA is  $\alpha$ -lipoic acid) with CB and CDs in water. Such noncovalent interactions resulted in enhanced luminescence of about 1.5 and 1.25 times for  $\beta$ -CD and CB, respectively, compared to the parent cluster. We used mass spectrometry (MS) along with critical inputs from nuclear magnetic resonance (NMR) spectroscopy and computational studies to characterize  $\text{Ag}_{29}\text{LA}_{12}\text{@CD}_n$  and  $\text{Ag}_{29}\text{LA}_{12}\text{@CB}_n$  ( $n = 1-3$ ) complexes, which were stabilized mainly by vdWs and hydrogen-bonding interactions. Density functional theory (DFT) studies suggested that CB encapsulated one of the LA ligands, whereas CD interacted with a cavity on the cluster surface created by the ligands. Highly luminescent  $\text{Ag}_{29}\text{LA}_{12}\text{@}\beta\text{-CD}_n$  complexes were utilized to detect dopamine selectively in solution at very low concentrations (10 nM). Dopamine is one of the main neurotransmitters of both peripheral and central nervous systems, and a change of its concentration from the normal range has been connected with diseases such as Alzheimer's and Parkinson's diseases. Hence, the development of a simple method to detect dopamine is noteworthy. There have been a few methods introduced earlier to sense dopamine.<sup>29,30</sup>

## EXPERIMENTAL SECTION

**Chemicals and Materials.**  $\text{AgNO}_3$ ,  $\text{NaBH}_4$ ,  $(\pm)$ - $\alpha$ -lipoic acid, CDs ( $\alpha$ ,  $\beta$ , and  $\gamma$ ), CB,  $\text{D}_2\text{O}$ , phenylalanine, ascorbic acid, glucose, dopamine, and methanol were obtained from Sigma-Aldrich. Butanol and  $\text{H}_2\text{O}_2$  were obtained from Rankem. Milli-Q quality water was used throughout the experiment.

**Synthesis of  $[\text{Ag}_{29}(\text{LA})_{12}\text{@CD}_n]$  Complexes.** About 19 mg LA and 7 mg  $\text{NaBH}_4$  were mixed in 14 mL of water in a glass bottle. This mixture was stirred (using a magnetic pellet) until it became a clear solution. Next, about 700  $\mu\text{L}$  of 25 mM  $\text{AgNO}_3$  solution was added (the solution became turbid), followed by 10 mg  $\text{NaBH}_4$  in 2 mL of water. The bottle was covered with an aluminum foil to minimize the exposure of the clusters to light. After 4–5 h, the clusters were formed. About 10 mg of CD was added to the cluster solution, and the reaction was continued for about 2 h. The reaction was done at room temperature under continuous magnetic stirring. The samples were kept in a fridge after covering the bottle with an aluminum foil. The clusters were purified with BuOH by mixing 300  $\mu\text{L}$  of clusters, 400  $\mu\text{L}$  of BuOH, and 100  $\mu\text{L}$  of methanol in a 2 mL vial. The mixture was centrifuged to accelerate phase separation, and the upper colorless organic layer was removed. This was repeated until the clusters were sedimented. Typically, three to five extractions with BuOH were required. A gum-like material was obtained after purification.

**Synthesis of  $[\text{Ag}_{29}(\text{LA})_{12}\text{@CB}_n]$  Complexes.** About 2 mg of CB was dissolved in 2 mL of Milli-Q water. Next, about 100  $\mu\text{L}$  of this solution was added to the purified cluster solution at the required concentration.

**Instrumentation. Electrospray Ionization MS.** All MS measurements were performed using a Waters Synapt G2Si high-definition mass spectrometer equipped with electrospray ionization (ESI) and ion mobility separation. All measurements were carried out in the negative ion mode. The instrument was calibrated using NaI as the calibrant. The typical experimental parameters were: desolvation gas temperature, 150  $^\circ\text{C}$ ; source temperature, 100  $^\circ\text{C}$ ; desolvation gas flow, 400 L/h; capillary voltage, 3 kV; sample cone, 0 V; source offset, 0 V; trap collision energy, 2 V; and trap gas flow, 2 mL/min. The sample was infused at a flow rate of 30  $\mu\text{L}/\text{min}$ .

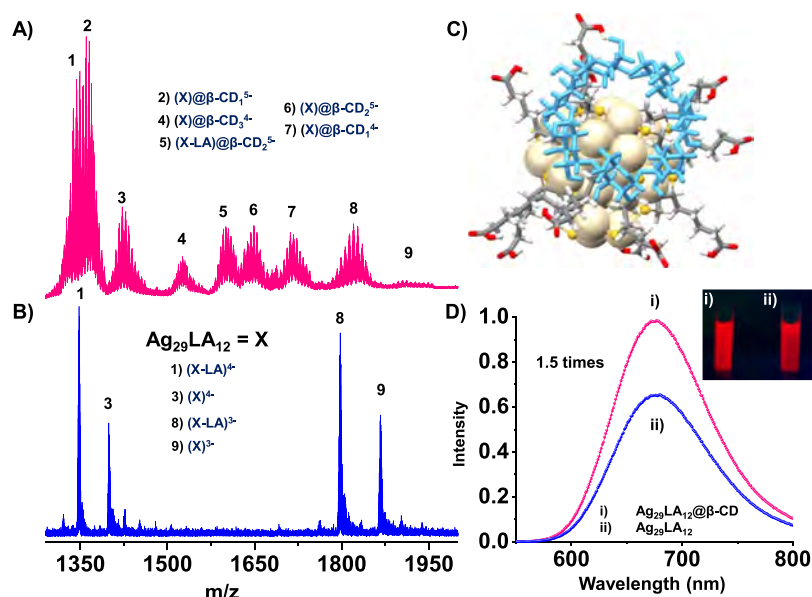


**Figure 2.** HRESI MS of  $[\text{Ag}_{29}(\text{LA})_{12}@\beta\text{-CD}_n]$  complexes, where  $n = 1-3$  (A) and  $\text{Ag}_{29}(\text{LA})_{12}$  (B). Assignments of the peaks are provided in the inset of (A,B) with numbering, where  $\text{X} = \text{Ag}_{29}(\text{LA})_{12}$ . Branching of peaks appeared because of the presence of Na adducts.  $[\text{X}@\text{CD}_3]^{4-}$  (peak 4) is lighter than  $[\text{X}@\text{CD}_1]^{4-}$  (peak 7) in (A) because of Na attachments. (C) Schematic representation of  $[\text{Ag}_{29}(\text{LA})_{12}@\beta\text{-CD}_n]$  for  $n = 1$ . Color codes: silver, light yellowish gray; sulfur, yellow; carbon, gray; oxygen, red. CD is presented in light blue color. (D) PL spectra of  $[\text{Ag}_{29}(\text{LA})_{12}@\beta\text{-CD}_n]$  complexes (i) and pure cluster (ii). Photographs of the solution of  $[\text{Ag}_{29}(\text{LA})_{12}@\beta\text{-CD}_n]$  complexes (i) and  $[\text{Ag}_{29}(\text{LA})_{12}]$  (ii) under UV light are shown in the inset of (D).

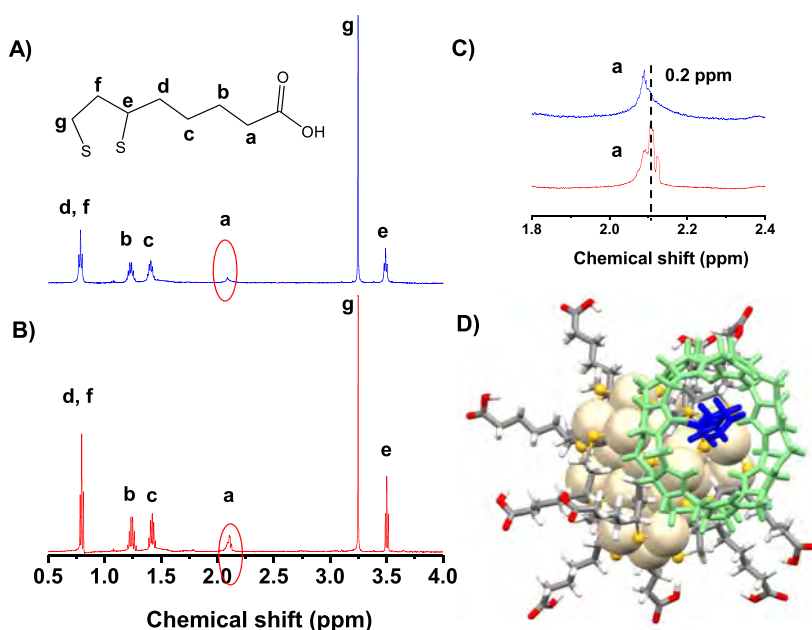


**Figure 3.**  $^1\text{H}$  NMR spectra of  $[\text{Ag}_{29}(\text{LA})_{12}@\text{CB}_n]$  (A) and  $\text{Ag}_{29}(\text{LA})_{12}$  (B). Assignments of the peaks are provided. (C) Zoomed-in view of the peak "a" from (A,B), which shows a significant change after the supramolecular complexation with  $\sim 0.2$  ppm chemical shift. (D) DFT-optimized structure of  $[\text{Ag}_{29}(\text{LA})_{12}@\text{CB}_1]$ . The color codes remain the same as in Figure 1. Encapsulated LA and CB are shown in blue and light green, respectively.

More details on instrumentation are presented in the [Supporting Information](#). Computational details are also presented in the [Supporting Information](#).

## RESULTS AND DISCUSSION

In the discussion presented below, supramolecular complexes are designated as  $\text{Ag}_{29}(\text{LA})_{12}@\text{CB}_n$  and  $\text{Ag}_{29}(\text{LA})_{12}@\text{CD}_n$ , although the exact nature of complexation will be confirmed only by a combination of studies.

**Characterization of  $[\text{Ag}_{29}(\text{LA})_{12}@\text{CB}_n]$  Complexes.** The supramolecular complexes of  $\text{Ag}_{29}(\text{LA})_{12}$  with CB were confirmed using high-resolution ESI MS (HRESI MS) (Figure 1A). ESI MS spectra of  $[\text{Ag}_{29}(\text{LA})_{12}@\text{CB}_n]$  and  $[\text{Ag}_{29}(\text{LA})_{12}]$  are shown in Figure 1A,B. The assignments of the peaks are given in the inset of Figure 1A with appropriate numbering. Peaks 2, 6, 8, and 11 correspond to  $(\text{X})@\text{CB}_1^{5-}$ ,  $(\text{X})@\text{CB}_1^{4-}$ ,  $(\text{X})@\text{CB}_3^{4-}$ , and  $(\text{X})@\text{CB}_2^{4-}$ , respectively, where  $\text{X} = \text{Ag}_{29}(\text{LA})_{12}$  (Figure 1B). Loss of ligands and CB was observed

in the case of  $[\text{Ag}_{29}(\text{LA})_{12}\cap\text{CB}_n]$  ( $n = 1-3$ ), which could be due to the voltages applied during ESI MS measurements. The loss of ligands was observed for the parent cluster also. Various charge states of the complexes were detected because of the presence of carboxylic acid groups on the cluster, which was also previously seen in the case of  $\text{Ag}_{29}\text{LA}_{12}$ <sup>31</sup> and  $\text{Ag}_{11}(\text{SG})_7$ .<sup>32</sup>  $[\text{X}\cap\text{CB}_3]^{4-}$  (peak 8) is lighter than  $[\text{X}\cap\text{CB}_2]^{4-}$  (peak 11) in Figure 1A. This is due to the number of  $\text{Na}^+$  attachments. Moreover, the supramolecular interactions of  $[\text{Ag}_{29}(\text{LA})_{12}\cap\text{CB}_n]$  complexes resulted in 1.25 times enhancement in luminescence, compared to the parent cluster (Figure 1D). However, the emission maximum of  $[\text{Ag}_{29}(\text{LA})_{12}\cap\text{CB}_n]$  complexes ( $\sim 680$  nm) was almost the same as that of  $\text{Ag}_{29}(\text{LA})_{12}$ . The emission spectra of the cluster and its supramolecular complexes with CB are provided in Figure 1D. Photographs of the solution of  $[\text{Ag}_{29}(\text{LA})_{12}\cap\text{CB}_n]$  complexes and  $[\text{Ag}_{29}(\text{LA})_{12}]$  under UV light are shown in the inset of Figure 1D. The optical absorption features showed similar nature to that of the cluster, with a slightly decreasing absorption, as shown in Figure S2.

**Characterization of  $[\text{Ag}_{29}(\text{LA})_{12}\cap\text{CD}_n]$  Complexes.** The as-synthesized  $[\text{Ag}_{29}(\text{LA})_{12}\cap\beta\text{-CD}_n]$  ( $n = 1-3$ ) complexes were characterized using HRESI MS. ESI MS spectra of  $[\text{Ag}_{29}(\text{LA})_{12}\cap\beta\text{-CD}_n]$  ( $n = 1-3$ ) complexes are provided in Figure 2A. The assignments of the peaks are mentioned in the inset of Figure 2A,B. Peaks 2, 4, 6, and 7 represent  $(\text{X})\cap\beta\text{-CD}_1^{5-}$ ,  $(\text{X})\cap\beta\text{-CD}_3^{4-}$ ,  $(\text{X})\cap\beta\text{-CD}_2^{5-}$ , and  $(\text{X})\cap\beta\text{-CD}_1^{4-}$ , respectively, where  $\text{X} = \text{Ag}_{29}(\text{LA})_{12}$ . The ESI MS spectrum of  $\text{Ag}_{29}(\text{LA})_{12}$  is provided in Figure 2B. The loss of ligands and CDs was similar in nature with the  $[\text{Ag}_{29}(\text{LA})_{12}\cap\text{CB}_n]$  ( $n = 1-3$ ) complexes. Moreover, various charge states of the complexes were observed in this case also. In the case of  $\alpha$  and  $\gamma$ -CD, similar types of adduct formation were confirmed using HRESI MS. The ESI MS spectra of  $[\text{Ag}_{29}(\text{LA})_{12}\cap\alpha\text{-CD}_n]$  and  $[\text{Ag}_{29}(\text{LA})_{12}\cap\gamma\text{-CD}_n]$  complexes are provided in Figures S3 and S4, respectively. After forming such supramolecular adducts,  $[\text{Ag}_{29}(\text{LA})_{12}\cap\beta\text{-CD}_n]$  complexes became more stable compared to only  $\text{Ag}_{29}(\text{LA})_{12}$ .  $[\text{Ag}_{29}(\text{LA})_{12}\cap\beta\text{-CD}_n]$  complexes were 1.5 times more luminescent compared to the parent cluster. The emission spectra of  $\text{Ag}_{29}(\text{LA})_{12}$  and its CD complexes are provided in Figure 2D. The UV-vis features of  $[\text{Ag}_{29}(\text{LA})_{12}\cap\beta\text{-CD}_n]$  and  $\text{Ag}_{29}(\text{LA})_{12}$  were almost similar, which indicated that the electronic structure of the cluster was unaltered by CD complexation (Figure S5). Photographs of the solution of  $[\text{Ag}_{29}(\text{LA})_{12}\cap\beta\text{-CD}_n]$  complexes and  $[\text{Ag}_{29}(\text{LA})_{12}]$  under UV light are provided in the inset of Figure 2D.

**NMR Study.** Solution-phase NMR studies were performed in order to understand the interactions between the cluster and CB. The  $^1\text{H}$  NMR spectra for  $[\text{Ag}_{29}(\text{LA})_{12}\cap\text{CB}_n]$  and  $\text{Ag}_{29}(\text{LA})_{12}$  cluster are shown in Figure 3A,B. Zoomed in views of peak “a” from Figure 3A,B are shown in Figure 3C, where a triplet peak was converted to a singlet peak along with  $\sim 0.2$  ppm upfield chemical shift because of the change in the environment of the proton of LA after supramolecular complexation. This supported the existence of supramolecular interactions in the solution phase. Similarly,  $^1\text{H}$  NMR for  $[\text{Ag}_{29}(\text{LA})_{12}\cap\beta\text{-CD}_n]$  complexes was also performed. The  $^1\text{H}$  NMR spectra for  $[\text{Ag}_{29}(\text{LA})_{12}\cap\beta\text{-CD}_n]$  and  $\text{Ag}_{29}(\text{LA})_{12}$  are shown in Figure S6A,B. Because of the strong interactions, almost all the peaks,  $\text{H}_1\text{--H}_6$ , showed an upfield shift.  $\text{H}_4$  of the  $\beta\text{-CD}$  peak overlapped with the “e” peak of LA. As a result, the overall intensity of the peak increased.

### Computational Study to Understand the Structures of $[\text{Ag}_{29}(\text{LA})_{12}\cap\text{CB}_n]$ and $[\text{Ag}_{29}(\text{LA})_{12}\cap\beta\text{-CD}_n]$ Complexes.

Lopez et al. reported that the core structure of  $\text{Ag}_{29}(\text{LA})_{12}$  is analogous to that of  $\text{Ag}_{29}(\text{BDT})_{12}$ .<sup>33</sup> Using this reported DFT method, we optimized the structure of  $\text{Ag}_{29}(\text{LA})_{12}^{3-}$ . We performed molecular docking, followed by DFT optimization, to understand the structures of  $[\text{Ag}_{29}(\text{LA})_{12}\cap\text{CB}_n]$  and  $[\text{Ag}_{29}(\text{LA})_{12}\cap\beta\text{-CD}_n]$  complexes. Molecular docking was carried out in order to get the lowest minimum geometry for  $[\text{Ag}_{29}(\text{LA})_{12}\cap\text{CB}_1]$  and  $[\text{Ag}_{29}(\text{LA})_{12}\cap\beta\text{-CD}_1]$ . We used  $\text{Ag}_{29}(\text{LA})_{12}$  as the “ligand” and supramolecular agents (CB and  $\beta\text{-CD}$ ) as the “receptor” molecules. DFT was carried out after obtaining the lowest energy structure from the docking study. The DFT-optimized structure of  $[\text{Ag}_{29}(\text{LA})_{12}\cap\text{CB}_1]$  is shown in Figures 3D and S7, where one CB molecule (light green) encapsulated one LA ligand (blue) of  $\text{Ag}_{29}(\text{LA})_{12}$ . The binding energy value was  $-12.58$  kcal/mol. The optimized structure of  $[\text{Ag}_{29}(\text{LA})_{12}\cap\text{CB}_1]$  revealed that vdWs and dipole–dipole interactions were responsible for such a type of complexation. Similarly, we optimized the structure of  $[\text{Ag}_{29}(\text{LA})_{12}\cap\beta\text{-CD}_1]$  using DFT. The optimized structure of this system is shown in Figure S8. Here, LA ligands anchored on the cluster surface formed a cavity, into which the CD molecule (light blue) could fit. The wider rim of CD interacted with the LA ligands of this cavity. The binding energy value was  $-70.01$  kcal/mol. vdW and hydrogen-bonding interactions were the primary reasons for such supramolecular complexation. We also obtained the structures of  $[\text{Ag}_{29}(\text{LA})_{12}\cap\text{CB}_2]$  and  $[\text{Ag}_{29}(\text{LA})_{12}\cap\beta\text{-CD}_2]$  complexes using molecular docking and DFT optimization. The structures and binding energies of  $[\text{Ag}_{29}(\text{LA})_{12}\cap\text{CB}_2]$  and  $[\text{Ag}_{29}(\text{LA})_{12}\cap\beta\text{-CD}_2]$  complexes are shown in Figures S9 and S10, respectively. Various possibilities of binding of CB and CD with the cluster were examined. From these calculations, it was confirmed that CB formed inclusion complexes with  $\text{Ag}_{29}(\text{LA})_{12}$ , whereas CD formed simple supramolecular adducts.

**Dopamine Sensing.** Dopamine has several important functions in brain and body. Previously, various methods such as electrochemical, calorimetric, fluorescence, and so forth were used for sensing this molecule, and a summary of such studies is provided in Table S1. As the cavity of the CD in the complexes is free to encapsulate other molecules, we used  $[\text{Ag}_{29}(\text{LA})_{12}\cap\beta\text{-CD}_n]$  to sense dopamine. The luminescence of  $[\text{Ag}_{29}(\text{LA})_{12}\cap\beta\text{-CD}_n]$  was quenched upon the addition of dopamine, at a concentration of 1 mM (Figure 4A).  $[\text{Ag}_{29}(\text{LA})_{12}\cap\beta\text{-CD}_n]$  did not respond to other related species like glucose,  $\text{H}_2\text{O}_2$ , phenylalanine, and ascorbic acid at a concentration of 1 mM (Figure 4A). These species tested are likely to exist in such situations. Photographs of the solutions of  $[\text{Ag}_{29}(\text{LA})_{12}\cap\beta\text{-CD}_n]$  before and after the addition of glucose,  $\text{H}_2\text{O}_2$ , phenylalanine, dopamine, and ascorbic acid are shown in Figure 4B. The vacant cavity of CD could encapsulate dopamine molecules, leading to such quenching. PL intensity decreased upon increasing the dopamine concentration in solution (Figure S11A). About 10 nM dopamine solution was detected by this method (Figure S11A). Comparison of our data with the literature is provided in Table S1. Previously, CD-based gold nanoparticles were used to sense dopamine.<sup>34</sup> Fluorescent gold nanoclusters were also used for the selective detection of dopamine.<sup>35</sup> Here, luminescent supramolecular complexes of atomically precise silver cluster were utilized to detect dopamine in water. This is the first example of dopamine sensing using supramolecular



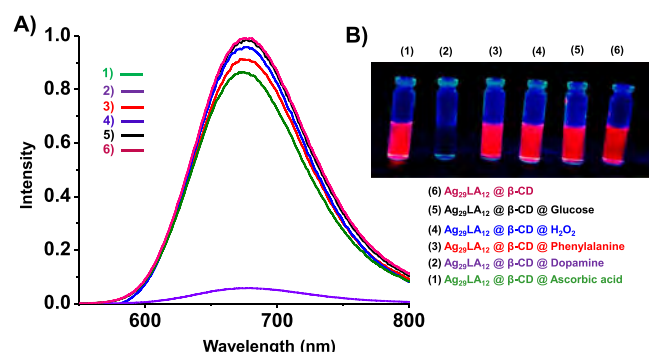


**Figure 4.** (A) PL spectra of  $[\text{Ag}_{29}(\text{LA})_{12}@\beta\text{-CD}_n]$  complexes before (6) and after the addition of glucose (5),  $\text{H}_2\text{O}_2$  (4), phenylalanine (3), dopamine (2), and ascorbic acid (1) and (B) their corresponding photographs. The final concentration of all above species was 1 mM. The color of the species in (A,B) is kept the same in the PL spectra.

complexes of atomically precise clusters. Quenching data at different concentrations of dopamine are provided in Figure S11A. The plot between PL quenching efficiency and dopamine concentration shows a linear relationship (Figure S11B).

Regarding other implications of these structures, we suggest that their isolation in the solid state can result in new classes of cluster-assembled solids. Such cluster-assembled solids are likely to be functional materials. The vacant cavity of  $\beta\text{-CD}$  in  $[\text{Ag}_{29}(\text{LA})_{12}@\beta\text{-CD}_n]$  complexes could be utilized for sensing organic pollutants in air, besides their use in drug delivery and bioimaging, as the cluster is likely to be biocompatible. Although these are only suggestions at the moment, we believe that such supramolecular complexes presented here may bring new aspects into the expanding science of NMCs.

## CONCLUSIONS

In summary, we showed the formation of supramolecular complexes of  $\text{Ag}_{29}(\text{LA})_{12}$  with CB and CDs. Noncovalent interactions enhanced the luminescence of the cluster. The formation of  $\text{Ag}_{29}\text{LA}_{12}@\text{CD}_n$  and  $\text{Ag}_{29}\text{LA}_{12}@\text{CB}_n$  ( $n = 1-3$ ) complexes was characterized using HRESI MS and NMR. Molecular docking and DFT calculations supported the experimental results. Supramolecular complexes of  $\text{Ag}_{29}\text{LA}_{12}@\beta\text{-CD}_n$  were used to detect dopamine in solution at a limit of 10 nM with high selectivity. Host–guest complexation could be observed for other clusters also depending on the symmetry, orientation, and geometry of the ligands surrounding the cluster.

## ASSOCIATED CONTENT

### Supporting Information

The Supporting Information is available free of charge at <https://pubs.acs.org/doi/10.1021/acs.jpcc.0c06770>.

Experimental and computational details; ESI MS and UV–vis spectra of  $[\text{Ag}_{29}(\text{LA})_{12}]$ ; UV–vis spectra of  $[\text{Ag}_{29}(\text{LA})_{12}@\text{CB}_n]$  and  $[\text{Ag}_{29}(\text{LA})_{12}]$ ; HRESI MS spectra of  $[\text{Ag}_{29}(\text{LA})_{12}@\alpha\text{-CD}_n]$  and  $[\text{Ag}_{29}(\text{LA})_{12}@\gamma\text{-CD}_n]$ ; UV–vis spectrum of  $[\text{Ag}_{29}(\text{LA})_{12}@\beta\text{-CD}_n]$ ;  $^1\text{H}$  NMR of  $[\text{Ag}_{29}(\text{LA})_{12}@\beta\text{-CD}_n]$  and  $\text{Ag}_{29}(\text{LA})_{12}$ ; DFT-optimized structures of  $[\text{Ag}_{29}(\text{LA})_{12}@\text{CB}_1]$ ,  $[\text{Ag}_{29}(\text{LA})_{12}@\beta\text{-CD}_1]$ ,  $[\text{Ag}_{29}(\text{LA})_{12}@\text{CB}_2]$ , and  $[\text{Ag}_{29}(\text{LA})_{12}@\beta\text{-CD}_2]$ ; PL spectra of  $[\text{Ag}_{29}(\text{LA})_{12}@\beta\text{-CD}_n]$ ; and coordinates of the structures (PDF)

## AUTHOR INFORMATION

### Corresponding Author

Thalappil Pradeep – DST Unit of Nanoscience and Thematic Unit of Excellence, Department of Chemistry, Indian Institute of Technology Madras, Chennai 600036, India; [orcid.org/0000-0003-3174-534X](https://orcid.org/0000-0003-3174-534X); Email: [pradeep@iitm.ac.in](mailto:pradeep@iitm.ac.in); Fax: +91-44 2257-0545

### Authors

Abhijit Nag – DST Unit of Nanoscience and Thematic Unit of Excellence, Department of Chemistry, Indian Institute of Technology Madras, Chennai 600036, India

Papri Chakraborty – DST Unit of Nanoscience and Thematic Unit of Excellence, Department of Chemistry, Indian Institute of Technology Madras, Chennai 600036, India

Athira Thacharon – DST Unit of Nanoscience and Thematic Unit of Excellence, Department of Chemistry, Indian Institute of Technology Madras, Chennai 600036, India

Ganesan Paramasivam – DST Unit of Nanoscience and Thematic Unit of Excellence, Department of Chemistry, Indian Institute of Technology Madras, Chennai 600036, India

Biswajit Mondal – DST Unit of Nanoscience and Thematic Unit of Excellence, Department of Chemistry, Indian Institute of Technology Madras, Chennai 600036, India

Mohammad Bodiuzzaman – DST Unit of Nanoscience and Thematic Unit of Excellence, Department of Chemistry, Indian Institute of Technology Madras, Chennai 600036, India

Complete contact information is available at:

<https://pubs.acs.org/doi/10.1021/acs.jpcc.0c06770>

### Author Contributions

A.N. designed and conducted all experiments. P.C., A.T., and A.N. synthesized the clusters and carried out the ESI MS measurements. G.P. carried out the DFT calculations. A.N. carried out the molecular docking simulations. The whole project was supervised by T.P. The manuscript was written through contributions of all authors. All authors have given approval to the final version of the manuscript.

### Notes

The authors declare no competing financial interest.

## ACKNOWLEDGMENTS

The authors thank the Department of Science and Technology, Government of India, for constantly supporting our research program on nanomaterials. A.N. and B.M. thank IIT Madras for doctoral fellowships. P.C. thanks the Council of Scientific and Industrial Research (CSIR) for her research fellowship. G.P. thanks IIT Madras for an Institute Postdoctoral fellowship. M.B. thanks University Grants Commission (UGC) for his research fellowship.

## ABBREVIATIONS

CB, cucurbit[7]uril; CDs, cyclodextrins; HRESI MS, high-resolution electrospray ionization mass spectrometry; NMR, nuclear magnetic resonance; DFT, density functional theory; NMCs, noble metal nanoclusters; vdWs, van der Waals; SBB, 4-(*t*-butyl)benzyl mercaptan

## REFERENCES

(1) Chakraborty, I.; Pradeep, T. Atomically Precise Clusters of Noble Metals: Emerging Link between Atoms and Nanoparticles. *Chem. Rev.* **2017**, *117*, 8208–8271.

- (2) Jin, R.; Zeng, C.; Zhou, M.; Chen, Y. Atomically Precise Colloidal Metal Nanoclusters and Nanoparticles: Fundamentals and Opportunities. *Chem. Rev.* **2016**, *116*, 10346–10413.
- (3) Chakraborty, P.; Pradeep, T. The Emerging Interface of Mass Spectrometry with Materials. *NPG Asia Mater.* **2019**, *11*, 48.
- (4) Song, X.-R.; Goswami, N.; Yang, H.-H.; Xie, J. Functionalization of Metal Nanoclusters for Biomedical Applications. *Analyst* **2016**, *141*, 3126–3140.
- (5) Yuan, X.; Luo, Z.; Yu, Y.; Yao, Q.; Xie, J. Luminescent Noble Metal Nanoclusters as an Emerging Optical Probe for Sensor Development. *Chem.—Asian J.* **2013**, *8*, 858–871.
- (6) Kurashige, W.; Niihori, Y.; Sharma, S.; Negishi, Y. Precise Synthesis, Functionalization and Application of Thiolate-Protected Gold Clusters. *Coord. Chem. Rev.* **2016**, *320–321*, 238–250.
- (7) Yamazoe, S.; Koyasu, K.; Tsukuda, T. Nonscalable Oxidation Catalysis of Gold Clusters. *Acc. Chem. Res.* **2014**, *47*, 816–824.
- (8) Mathew, A.; Pradeep, T. Noble Metal Clusters: Applications in Energy, Environment, and Biology. *Part. Part. Syst. Charact.* **2014**, *31*, 1017–1053.
- (9) Kang, X.; Zhu, M. Tailoring the Photoluminescence of Atomically Precise Nanoclusters. *Chem. Soc. Rev.* **2019**, *48*, 2422–2457.
- (10) Knoppe, S.; Bürgi, T. Chirality in Thiolate-Protected Gold Clusters. *Acc. Chem. Res.* **2014**, *47*, 1318–1326.
- (11) Joshi, C. P.; Bootharaju, M. S.; Alhilaly, M. J.; Bakr, O. M.  $[\text{Ag}_{25}(\text{SR})_{18}]^-$ : The “Golden” Silver Nanoparticle. *J. Am. Chem. Soc.* **2015**, *137*, 11578–11581.
- (12) Zhu, M.; Aikens, C. M.; Hollander, F. J.; Schatz, G. C.; Jin, R. Correlating the Crystal Structure of A Thiol-Protected  $\text{Au}_{25}$  Cluster and Optical Properties. *J. Am. Chem. Soc.* **2008**, *130*, 5883–5885.
- (13) Heaven, M. W.; Dass, A.; White, P. S.; Holt, K. M.; Murray, R. W. Crystal Structure of the Gold Nanoparticle  $[\text{N}(\text{C}_8\text{H}_{17})_4]^- [\text{Au}_{25}(\text{SCH}_2\text{CH}_2\text{Ph})_{18}]^-$ . *J. Am. Chem. Soc.* **2008**, *130*, 3754–3755.
- (14) AbdulHalim, L. G.; Bootharaju, M. S.; Tang, Q.; Del Gobbo, S.; AbdulHalim, R. G.; Eddaoudi, M.; Jiang, D.-e.; Bakr, O. M.  $\text{Ag}_{29}(\text{BDT})_{12}(\text{TPP})_4$ : A Tetravalent Nanocluster. *J. Am. Chem. Soc.* **2015**, *137*, 11970–11975.
- (15) Nag, A.; Chakraborty, P.; Bodiuzzaman, M.; Ahuja, T.; Antharjanam, S.; Pradeep, T. Polymorphism of  $\text{Ag}_{29}(\text{BDT})_{12}(\text{TPP})_4^{3-}$  Cluster: Interactions of Secondary Ligands and Their Effect on Solid State Luminescence. *Nanoscale* **2018**, *10*, 9851–9855.
- (16) Bodiuzzaman, M.; Ghosh, A.; Sugi, K. S.; Nag, A.; Khatun, E.; Varghese, B.; Paramasivam, G.; Antharjanam, S.; Natarajan, G.; Pradeep, T. Camouflaging Structural Diversity: Co-crystallization of Two Different Nanoparticles Having Different Cores But the Same Shell. *Angew. Chem., Int. Ed.* **2019**, *58*, 189–194.
- (17) Ghosh, A.; Bodiuzzaman, M.; Nag, A.; Jash, M.; Baksi, A.; Pradeep, T. Sequential Dihydrogen Desorption from Hydride-Protected Atomically Precise Silver Clusters and the Formation of Naked Clusters in the Gas Phase. *ACS Nano* **2017**, *11*, 11145–11151.
- (18) Tomihara, R.; Hirata, K.; Yamamoto, H.; Takano, S.; Koyasu, K.; Tsukuda, T. Collision-Induced Dissociation of Undecagold Clusters Protected by Mixed Ligands  $[\text{Au}_{11}(\text{PPh}_3)_8\text{X}_2]^+$  ( $\text{X} = \text{Cl}, \text{C}\equiv\text{CPh}$ ). *ACS Omega* **2018**, *3*, 6237–6242.
- (19) Maity, P.; Tsunoyama, H.; Yamauchi, M.; Xie, S.; Tsukuda, T. Organogold Clusters Protected by Phenylacetylene. *J. Am. Chem. Soc.* **2011**, *133*, 20123–20125.
- (20) Chakraborty, P.; Nag, A.; Chakraborty, A.; Pradeep, T. Approaching Materials with Atomic Precision Using Supramolecular Cluster Assemblies. *Acc. Chem. Res.* **2019**, *52*, 2–11.
- (21) Kang, X.; Zhu, M. Intra-cluster Growth Meets Inter-cluster Assembly: The Molecular and Supramolecular Chemistry of Atomically Precise Nanoclusters. *Coord. Chem. Rev.* **2019**, *394*, 1–38.
- (22) Nonappa; Haataja, J. S.; Timonen, J. V. I.; Malola, S.; Engelhardt, P.; Houbenov, N.; Lahtinen, M.; Häkkinen, H.; Ikkala, O. Reversible Supracolloidal Self-Assembly of Cobalt Nanoparticles to Hollow Capsids and Their Superstructures. *Angew. Chem.* **2017**, *129*, 6573–6577.
- (23) Crini, G. Review: A History of Cyclodextrins. *Chem. Rev.* **2014**, *114*, 10940–10975.
- (24) Mathew, A.; Natarajan, G.; Lehtovaara, L.; Häkkinen, H.; Kumar, R. M.; Subramanian, V.; Jaleel, A.; Pradeep, T. Supramolecular Functionalization and Concomitant Enhancement in Properties of  $\text{Au}_{25}$  Clusters. *ACS Nano* **2014**, *8*, 139–152.
- (25) Moussawi, M. A.; Leclerc-Laronze, N.; Floquet, S.; Abramov, P. A.; Sokolov, M. N.; Cordier, S.; Ponchel, A.; Monflier, E.; Bricout, H.; Landy, D.; et al. Polyoxometalate, Cationic Cluster, and  $\gamma$ -Cyclodextrin: From Primary Interactions to Supramolecular Hybrid Materials. *J. Am. Chem. Soc.* **2017**, *139*, 12793–12803.
- (26) Nag, A.; Chakraborty, P.; Paramasivam, G.; Bodiuzzaman, M.; Natarajan, G.; Pradeep, T. Isomerism in Supramolecular Adducts of Atomically Precise Nanoparticles. *J. Am. Chem. Soc.* **2018**, *140*, 13590–13593.
- (27) Chakraborty, P.; Nag, A.; Paramasivam, G.; Natarajan, G.; Pradeep, T. Fullerene-Functionalized Monolayer-Protected Silver Clusters:  $[\text{Ag}_{29}(\text{BDT})_{12}(\text{C}_{60})_n]^{3-}$  ( $n = 1–9$ ). *ACS Nano* **2018**, *12*, 2415–2425.
- (28) Chakraborty, P.; Nag, A.; Sugi, K. S.; Ahuja, T.; Varghese, B.; Pradeep, T. Crystallization of a Supramolecular Coassembly of an Atomically Precise Nanoparticle with a Crown Ether. *ACS Mater. Lett.* **2019**, *1*, 534–540.
- (29) Kim, D.-S.; Kang, E.-S.; Baek, S.; Choo, S.-S.; Chung, Y.-H.; Lee, D.; Min, J.; Kim, T.-H. Electrochemical Detection of Dopamine Using Periodic Cylindrical Gold Nanoelectrode Arrays. *Sci. Rep.* **2018**, *8*, 14049.
- (30) Su, H.; Sun, B.; Chen, L.; Xu, Z.; Ai, S. Colorimetric Sensing of Dopamine Based on the Aggregation of Gold Nanoparticles Induced by Copper Ions. *Anal. Methods* **2012**, *4*, 3981–3986.
- (31) van der Linden, M.; Barendregt, A.; van Bunningen, A. J.; Chin, P. T. K.; Thies-Weesie, D.; de Groot, F. M. F.; Meijerink, A. Characterisation, Degradation and Regeneration of Luminescent  $\text{Ag}_{29}$  Clusters in Solution. *Nanoscale* **2016**, *8*, 19901–19909.
- (32) Baksi, A.; Bootharaju, M. S.; Chen, X.; Häkkinen, H.; Pradeep, T.  $\text{Ag}_{11}(\text{SG})_7$ : A New Cluster Identified by Mass Spectrometry and Optical Spectroscopy. *J. Phys. Chem. C* **2014**, *118*, 21722–21729.
- (33) Lopez, P.; Lara, H. H.; Mullins, S. M.; Black, D. M.; Ramsower, H. M.; Alvarez, M. M.; Williams, T. L.; Lopez-Lozano, X.; Weissker, H.-C.; García, A. P.; et al. Tetrahedral (T) Closed-Shell Cluster of 29 Silver Atoms & 12 Lipoate Ligands,  $[\text{Ag}_{29}(\text{R}-\alpha\text{-LA})_{12}]^{(3-)}$ : Antibacterial and Antifungal Activity. *ACS Appl. Nano Mater.* **2018**, *1*, 1595–1602.
- (34) Wen, D.; Liu, W.; Herrmann, A.-K.; Haubold, D.; Holzschuh, M.; Simon, F.; Eychmüller, A. Simple and Sensitive Colorimetric Detection of Dopamine Based on Assembly of Cyclodextrin-Modified Au Nanoparticles. *Small* **2016**, *12*, 2439–2442.
- (35) Govindaraju, S.; Ankireddy, S. R.; Viswanath, B.; Kim, J.; Yun, K. Fluorescent Gold Nanoclusters for Selective Detection of Dopamine in Cerebrospinal Fluid. *Sci. Rep.* **2017**, *7*, 40298.



## Supporting Information for Publication

### Atomically Precise Noble Metal Cluster-Assembled Superstructures in Water: Luminescence Enhancement and Sensing

Abhijit Nag, Papri Chakraborty, Athira Thacharon, Ganesan Paramasivam, Biswajit Mondal, Mohammad Bodiuzzaman, and Thalappil Pradeep\*

DST Unit of Nanoscience and Thematic Unit of Excellence, Department of Chemistry  
Indian Institute of Technology Madras, Chennai-600036, India

Email: [pradeep@iitm.ac.in](mailto:pradeep@iitm.ac.in)

Contents		
Name	Descriptions	Page No.
	Experimental and computational details	S2
Figure S1	ESI MS and UV-vis spectra of $[\text{Ag}_{29}(\text{LA})_{12}]$	S4
Figure S2	UV-vis spectra of $[\text{Ag}_{29}(\text{LA})_{12} \cap \text{CB}_n]$ and $\text{Ag}_{29}(\text{LA})_{12}$	S5
Figure S3	HRESI MS of $[\text{Ag}_{29}(\text{LA})_{12} @ \alpha\text{-CD}_n]$	S6
Figure S4	HRESI MS of $[\text{Ag}_{29}(\text{LA})_{12} @ \gamma\text{-CD}_n]$	S7
Figure S5	UV-vis spectrum of $[\text{Ag}_{29}(\text{LA})_{12} @ \beta\text{-CD}_n]$	S8
Figure S6	$^1\text{H}$ NMR of $[\text{Ag}_{29}(\text{LA})_{12} @ \beta\text{-CD}_n]$ and $\text{Ag}_{29}(\text{LA})_{12}$	S9
Figure S7	DFT optimised structure of $[\text{Ag}_{29}(\text{LA})_{12} \cap \text{CB}_1]$	S10
Figure S8	DFT optimised structure of $[\text{Ag}_{29}(\text{LA})_{12} @ \beta\text{-CD}_1]$	S11

Figure S9	DFT optimised structure of $[\text{Ag}_{29}(\text{LA})_{12} \cap \text{CB}_2]$	S12
Figure S10	DFT optimised structure of $[\text{Ag}_{29}(\text{LA})_{12} @ \beta\text{-CD}_2]$	S13
Figure S11	PL spectra of $[\text{Ag}_{29}(\text{LA})_{12} @ \beta\text{-CD}_n]$ after addition of different concentration of dopamine	S14
Table S1	Different methods for dopamine detection available in the literature	S15
	Coordinates of the lowest energy geometry of $\text{Ag}_{29}\text{LA}_{12} \cap \text{CB}_1$	S16
	Coordinates of the lowest energy geometry of $\text{Ag}_{29}\text{LA}_{12} \cap \text{CD}_1$	S31

## Experimental Details

### Instrumentation

The UV-vis spectra were measured using a PerkinElmer Lambda 25 UV-vis spectrophotometer. PL spectra were collected using a HORIBA JOBIN YVON Nano Log instrument. The bandpass was set at 3 nm during the measurements. NMR measurements were performed using a Bruker 500 MHz NMR spectrometer. Transmission Electron Microscopy of the samples was performed using a JEOL 3010 instrument with a UHR polepiece.

### Computational Details

The interactions of  $\beta\text{-CD}$  and  $\text{CB}$  on the surface of a monolayer of  $\text{LA}$  protected  $\text{Ag}_{29}(\text{LA})_{12}^{3-}$  nanocluster was computationally studied by density functional theory (DFT) using GPAW (grid-based projector-augmented wave method) software package<sup>1-2</sup>. For this,  $\text{Ag}_{29}(\text{LA})_{12}^{3-}$  nanocluster was initially constructed from the crystal structure of  $\text{Ag}_{29}(\text{BDT})_{12}(\text{TPP})_4^{3-}$  nanocluster by replacing the BDT ligands by  $\text{LA}$ . The atomic PAW set-ups for each atoms are Ag ( $4d^{10} 5s^1$ ), S ( $3s^2 3p^4$ ), O ( $2s^2 2p^4$ ), C ( $2s^2 2p^2$ ) and H ( $1s^1$ ) which tells the valence electronic configuration and the inclusion of scalar-relativistic effects for Ag. First of all, the geometries of  $\text{Ag}_{29}(\text{LA})_{12}^{3-}$

nanocluster, cyclodextrin, and cucurbituril were separately optimized using the DZP basis set in LCAO mode along with the PBE (Perdew-Burke-Ernzerhof) exchange-correlation functional<sup>3</sup> with a grid spacing of 0.2 Å in LCAO mode. The convergence condition is that the forces acting on atoms were set to be 0.05 eV/Å, without imposing any symmetry constraints. Then the structures of the supramolecular complexes were obtained using molecular docking. The docked structures were re-optimized in DFT with the same level of theory.

Molecular docking studies have been carried out using AutoDock 4.2 and AutoDock Tools programs<sup>4</sup>. The DFT optimized structures of  $[\text{Ag}_{29}(\text{LA})_{12}]^5$  and  $\beta$ -CD were used for this study. We used  $[\text{Ag}_{29}(\text{LA})_{12}]$  as the ‘ligand’. The ‘receptor’ molecule was CD and this was the fixed and completely rigid central molecule. We assigned partial charges from DFT for all atoms of  $[\text{Ag}_{29}(\text{LA})_{12}]^{3-}$ . Receptor grids were generated using  $126 \times 126 \times 126$  grid points with a grid spacing of 0.375 Å and map types for all the ligand atoms were created using AutoGrid 4.6. The van der Waals radius  $\sigma$  (Å) and well depth  $\varepsilon$  (kcal/mol) for Ag of 2.63 Å and 4.560 kcal/mol, respectively, were taken from well-tested sources in literature<sup>6-7</sup> and these were added to the AutoDock parameter file which does not contain them by default. The grid parameter file (.gpf) was saved using MGL Tools-1.4.6.50. For docking, the docking parameter files (.dpf) were generated using MGLTools-1.4.6.50 and docking was performed using AutoDock4.2. The results of AutoDock generated an output file (.dlg), and the generated conformers were scored and ranked as per the interaction energy. Ten lowest energy conformers were obtained. The structure showing the lowest binding energy between the interacting molecules was used as an initial structure for DFT optimization. The free energies of binding were calculated subtracting the unbound energies from the sum of the intermolecular and internal energy terms in the adducts, which is a calculation that is performed within the AutoDock program. We obtained the structures of  $[\text{Ag}_{29}(\text{LA})_{12} \cap \text{CB}_n]$  complexes using similar process.

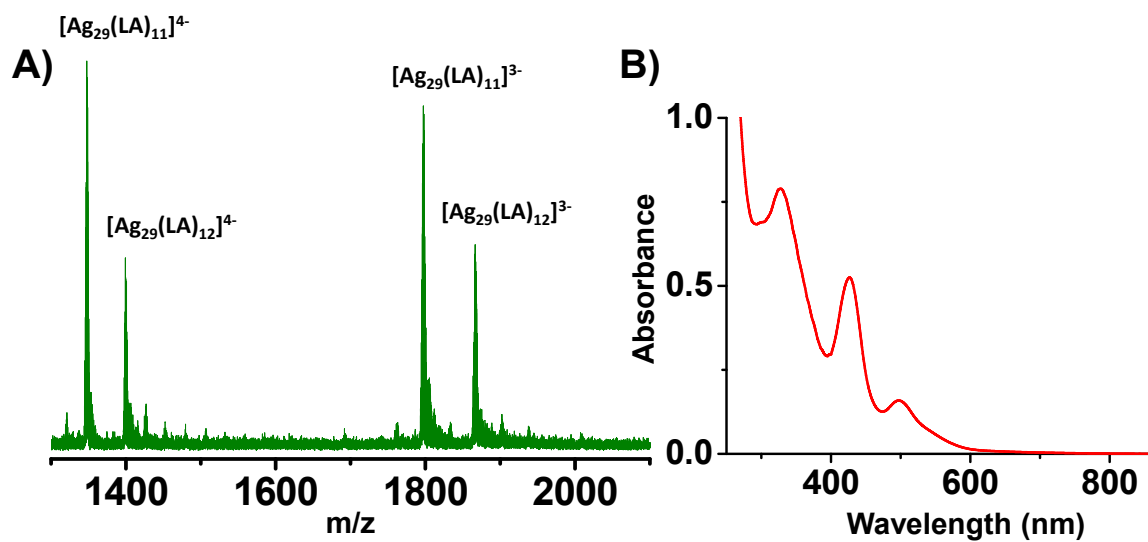


**Figure S1.** A) HRESI MS and B) UV-vis spectra of  $[Ag_{29}(LA)_{12}]$ . Different charge states of the cluster (3- and 4-) were observed in ESI MS. One loss of LA was noticed for both 3- and 4-charge states of the cluster.

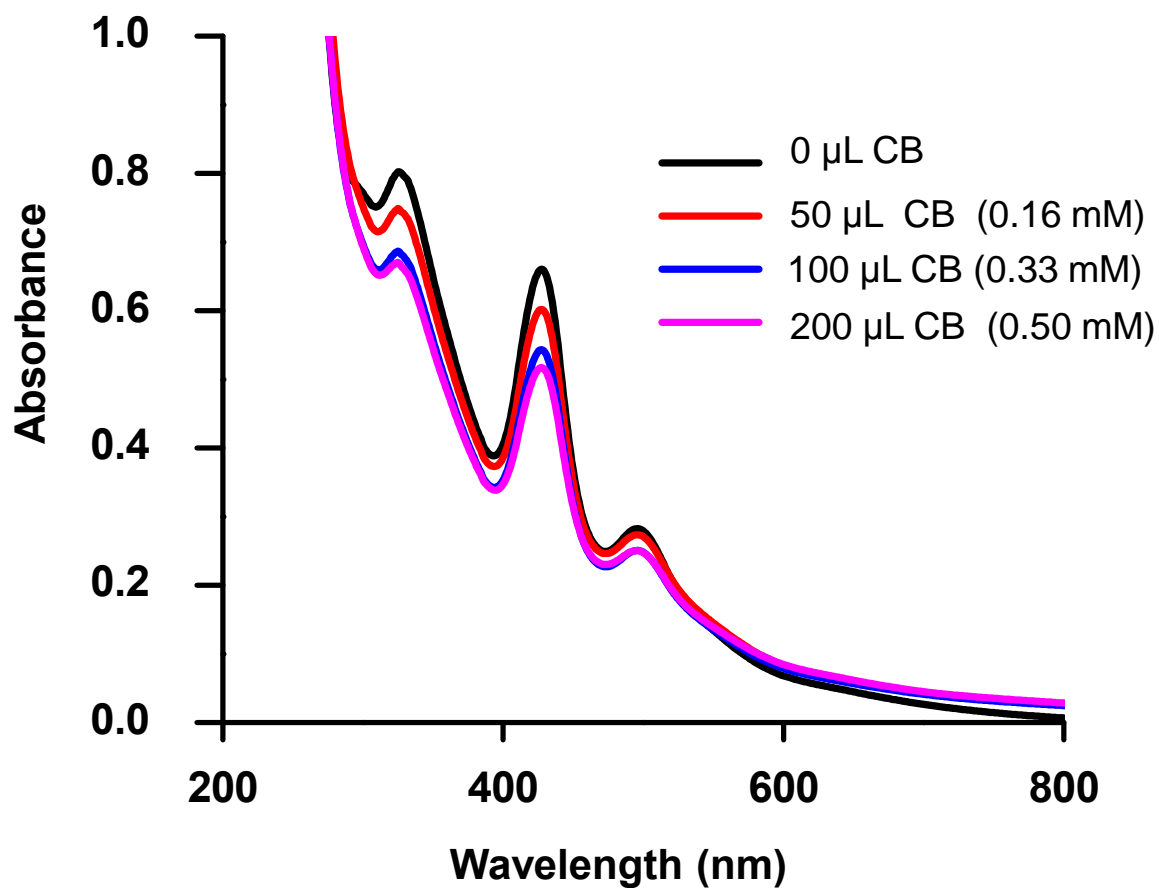


**Figure S2.** UV-vis spectra of  $\text{Ag}_{29}(\text{LA})_{12}$  and  $[\text{Ag}_{29}(\text{LA})_{12} \cap \text{CB}_n]$ . With increasing the concentration of cucurbituril in the solution, absorbance of the peaks was decreasing and a crossover point was detected at  $\sim 550$  nm.



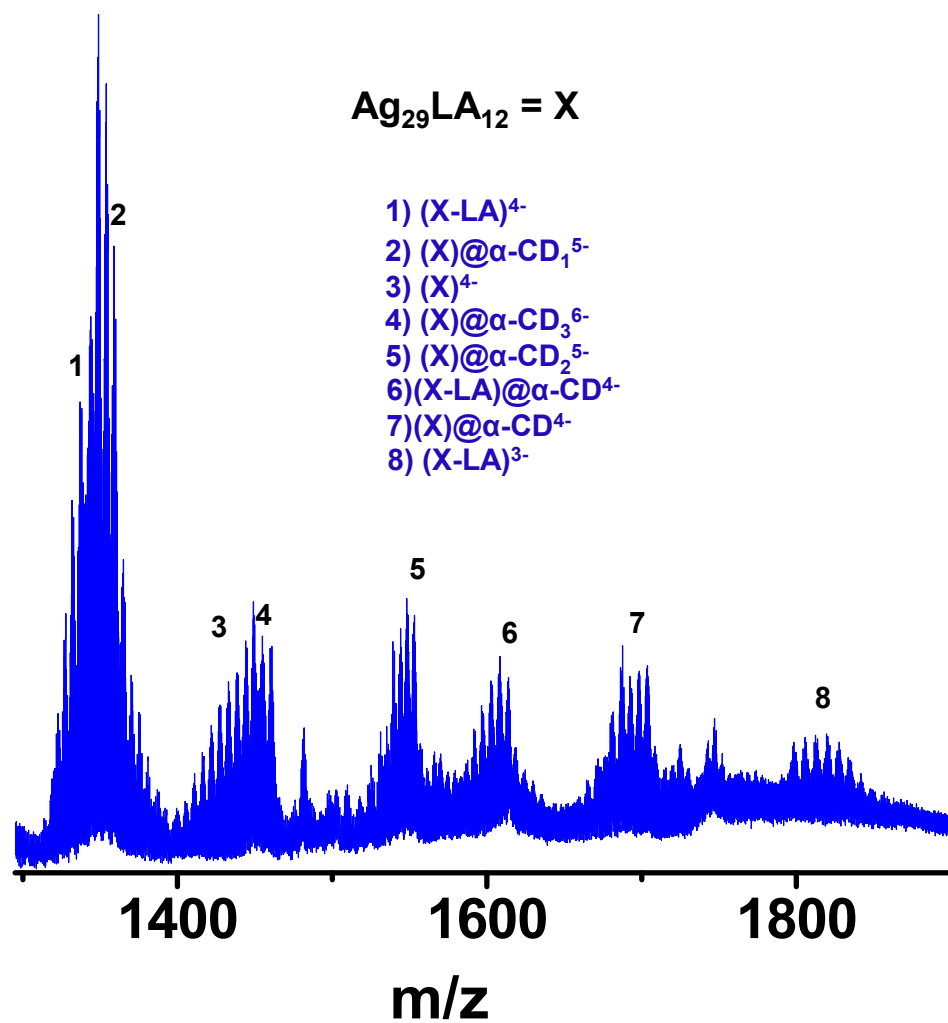


**Figure S3.** HRESI MS of  $[\text{Ag}_{29}(\text{LA})_{12}@\alpha\text{-CD}_n]$ , where  $n = 1\text{-}3$ . Assignments of the peaks are provided in the inset of Figure S3 with numbering, where  $\text{X} = \text{Ag}_{29}(\text{LA})_{12}$ . Branching of peaks was appearing because of Na adducts.

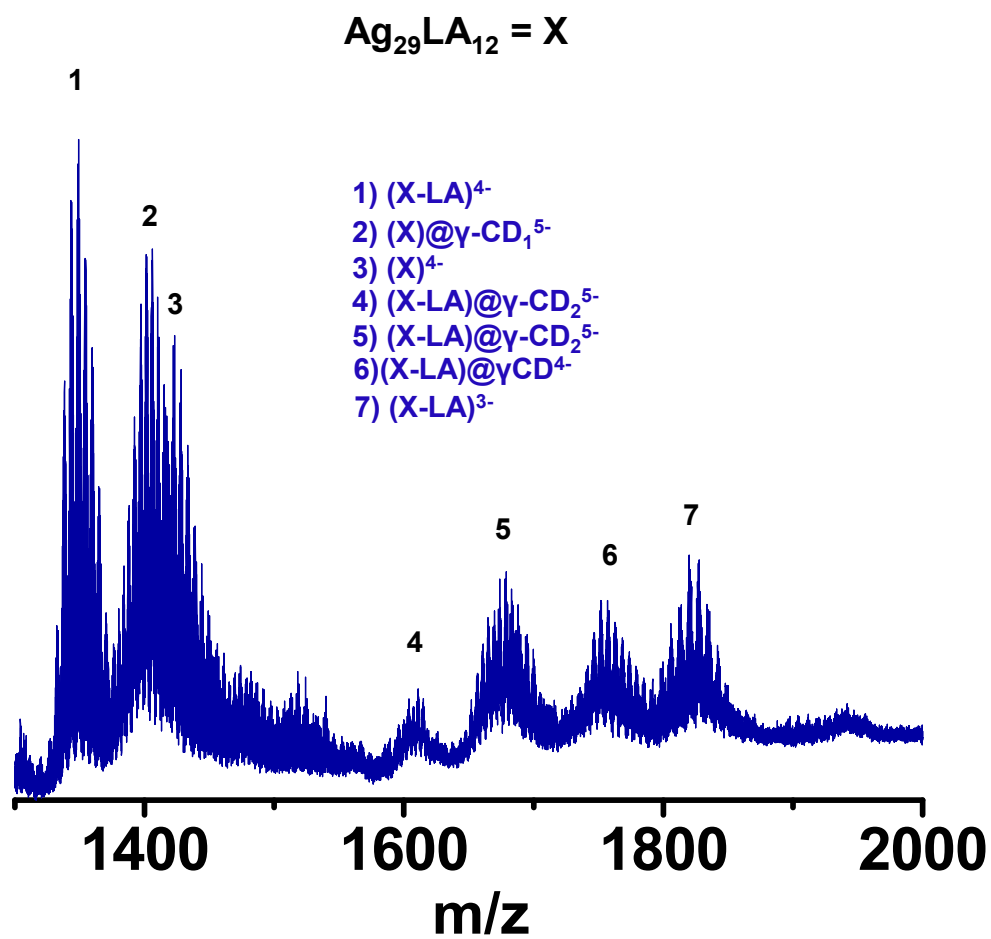


**Figure S4.** HRESI MS of  $[\text{Ag}_{29}(\text{LA})_{12}@\gamma\text{-CD}_n]$ , where  $n = 1-3$ . Assignments of the peaks are provided in the inset of Figure S4 with numbering, where  $\text{X} = \text{Ag}_{29}(\text{LA})_{12}$ . Branching of peaks was appearing because of Na adducts.

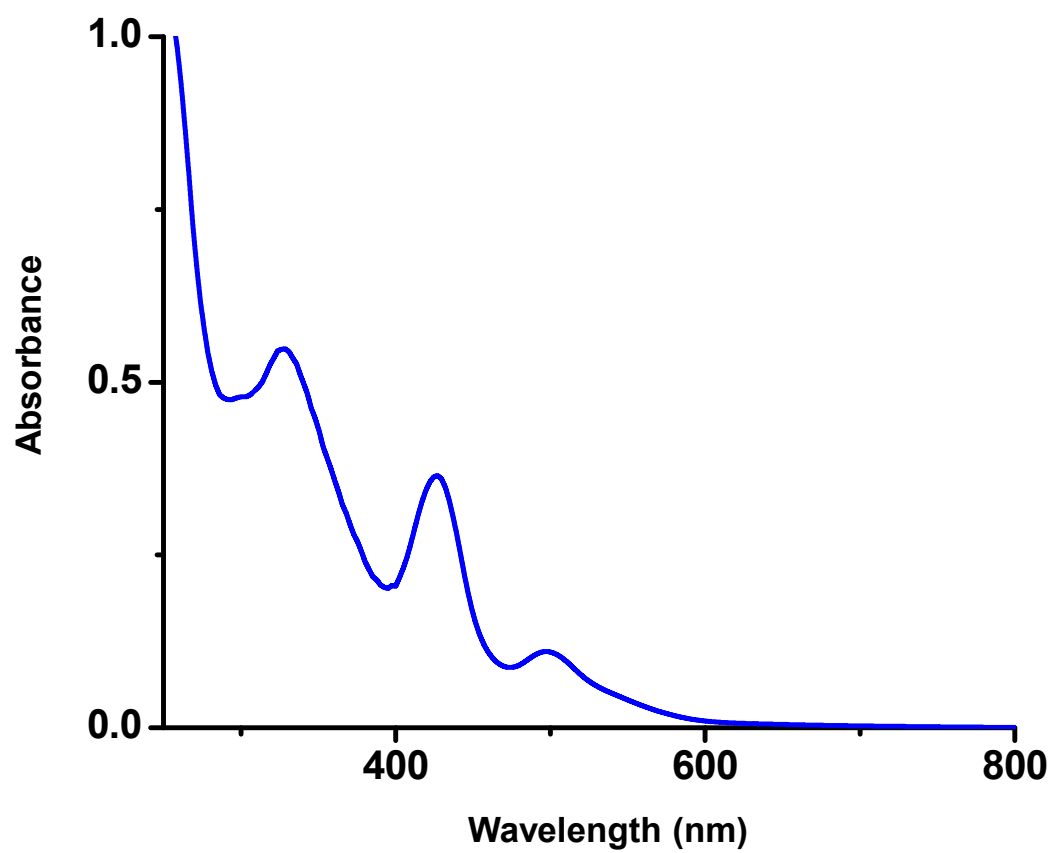


**Figure S5.** UV-vis spectrum of  $[Ag_{29}(LA)_{12}@β-CD_n]$  complexes. UV-vis features are similar to that of the parent cluster.

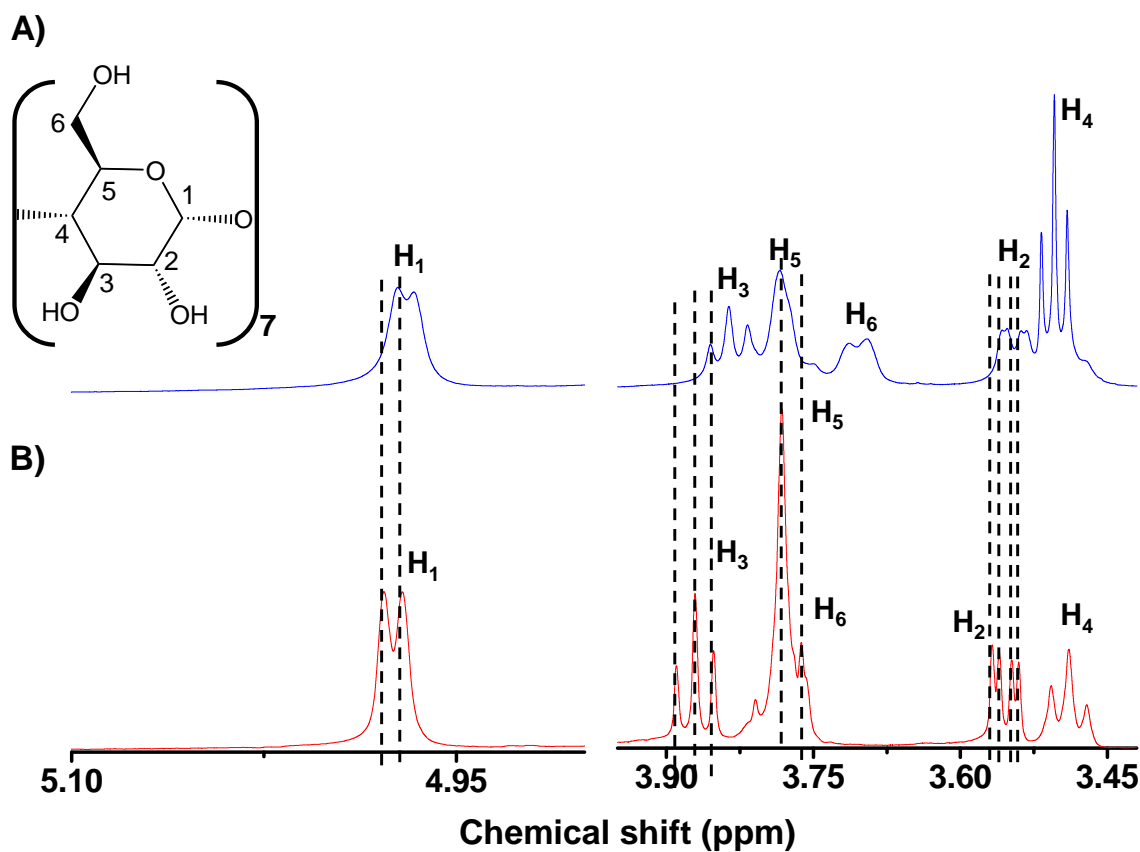


**Figure S6.**  $^1\text{H}$  NMR of  $[\text{Ag}_{29}(\text{LA})_{12}@\beta\text{-CD}_n]$  A) and  $\text{Ag}_{29}(\text{LA})_{12}$  B). Due to the strong interactions, almost all the peaks  $\text{H}_1$  to  $\text{H}_6$  got shifted in the upfield region.  $\text{H}_4$  of the CD peak is overlapped with the lipoic acid 'e' peak. As a result, the overall peak intensity increased.

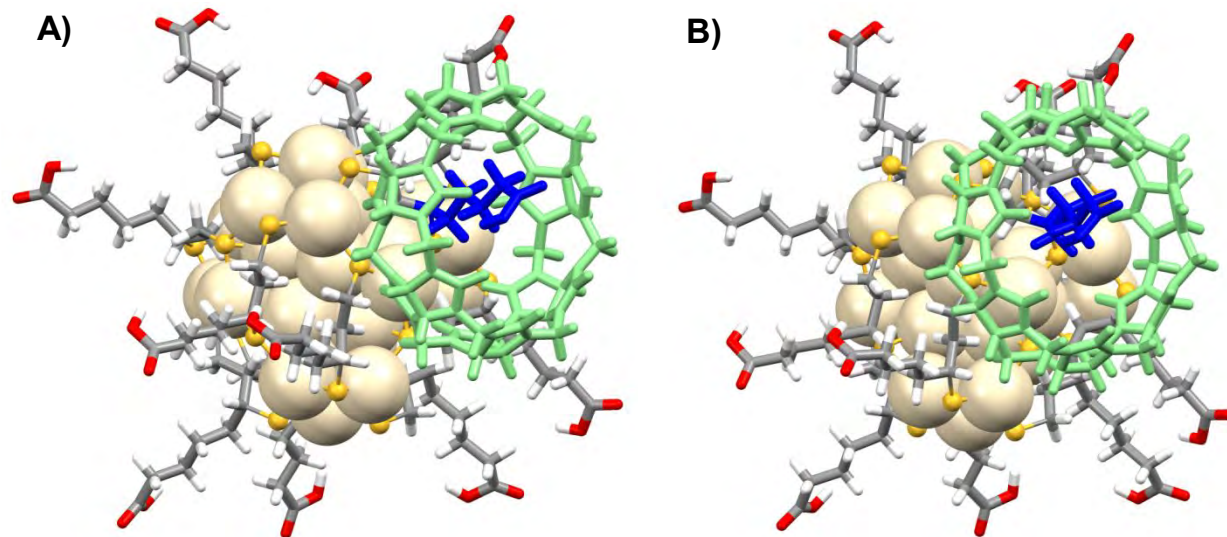


**Figure S7.** DFT optimised structure of  $[\text{Ag}_{29}(\text{LA})_{12} \cap \text{CB}_1]$  with different orientations, A) and B). Encapsulated LA and CB are shown in blue and light green, respectively.



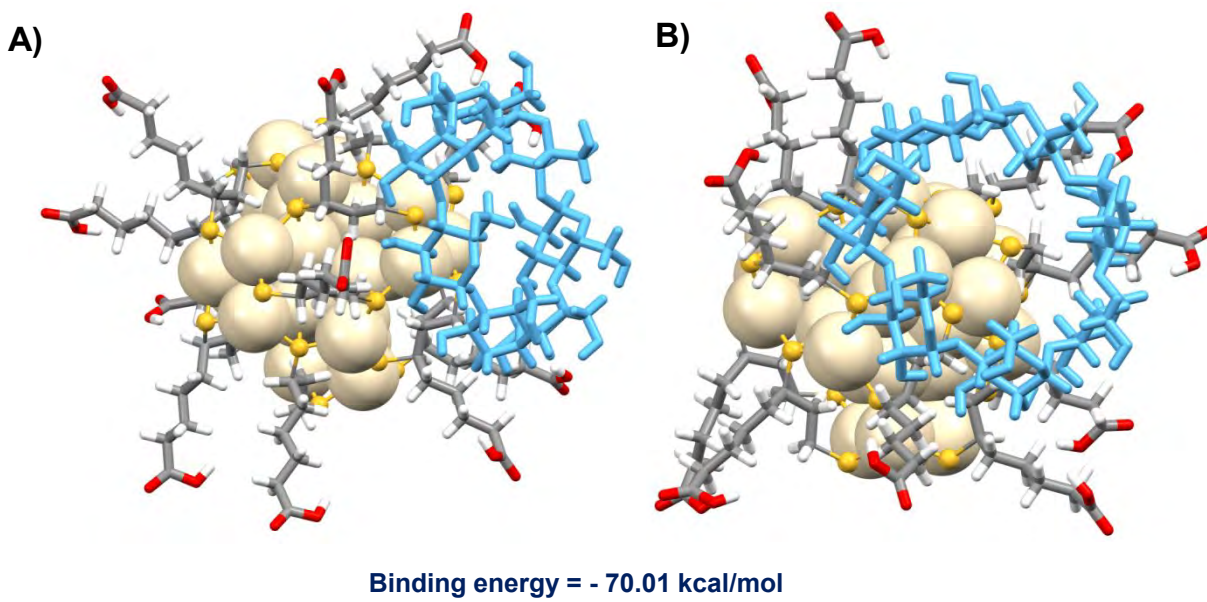
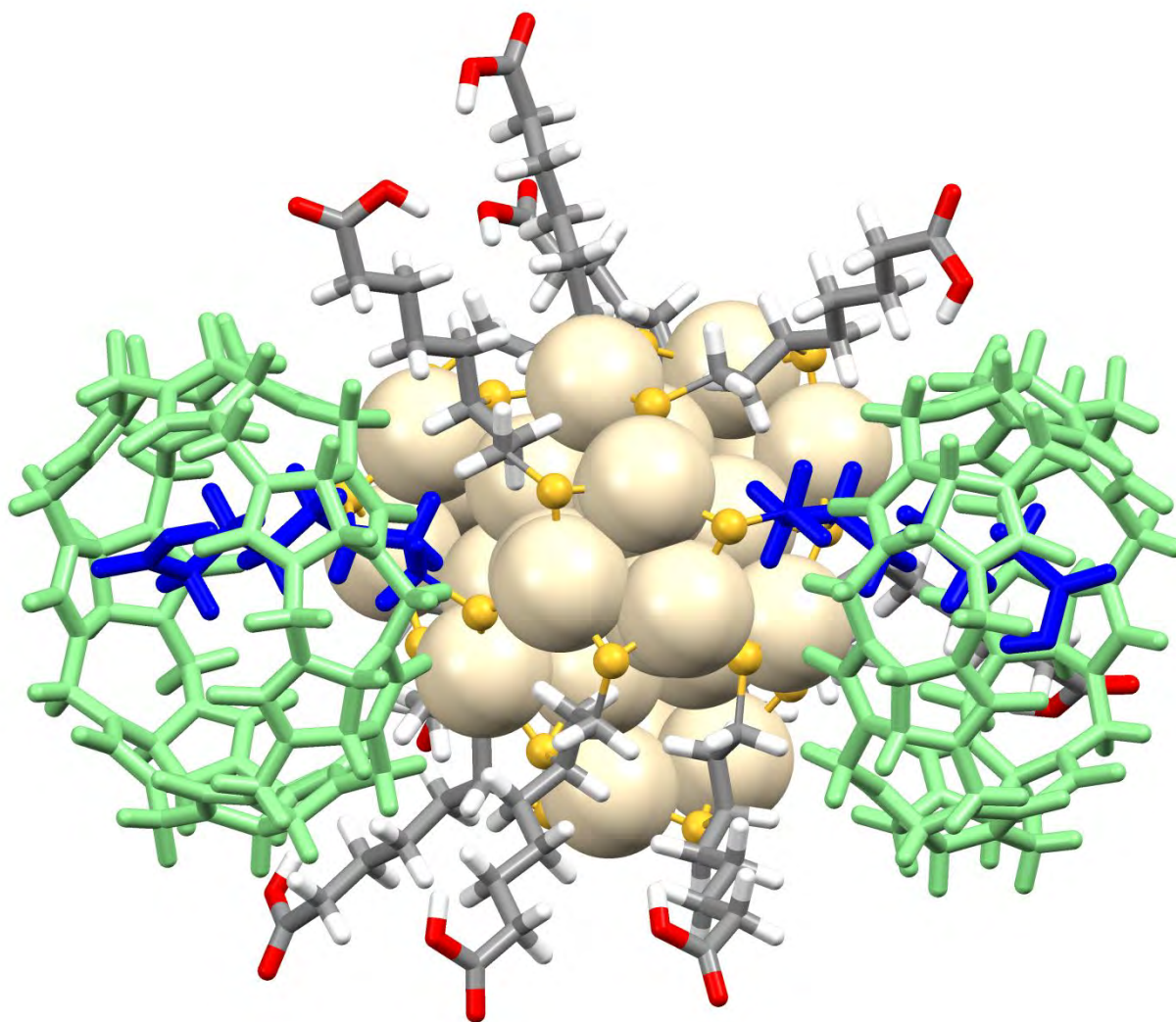
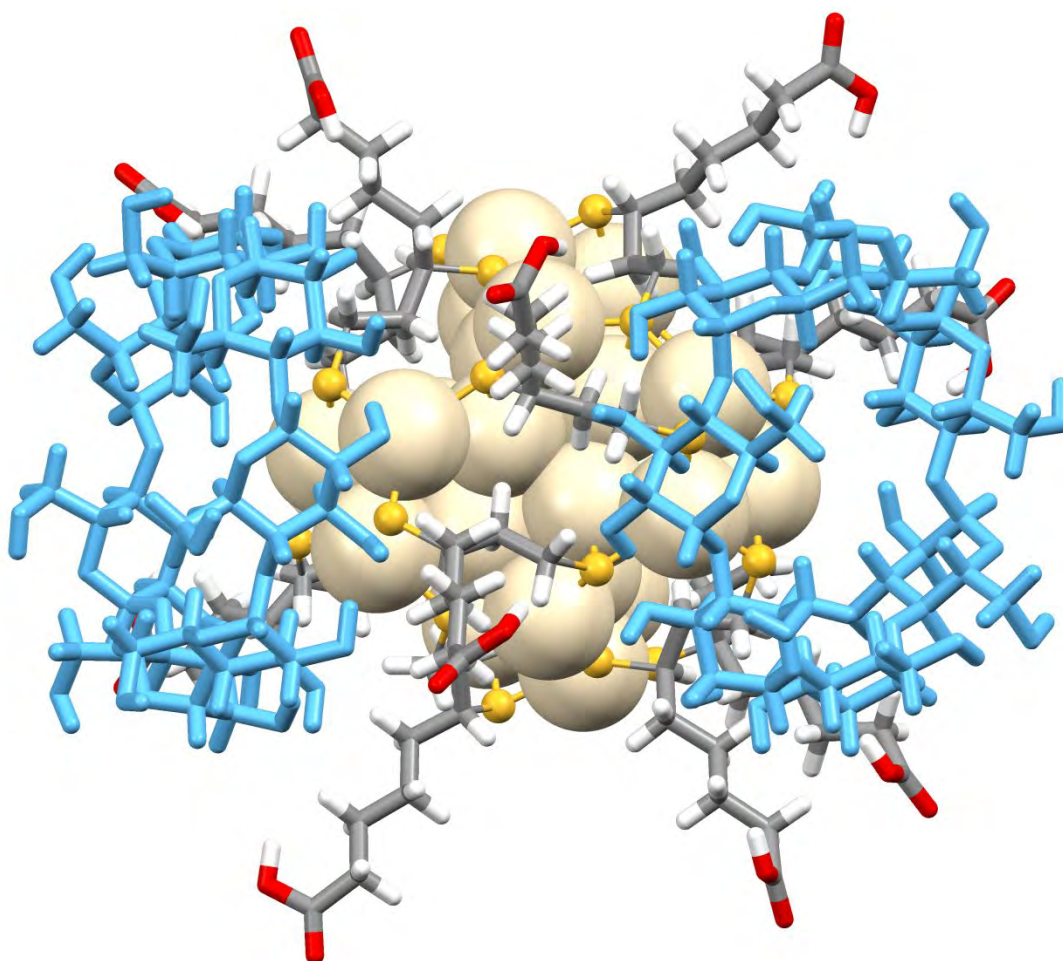


**Figure S8.** DFT optimised structure of  $[\text{Ag}_{29}(\text{LA})_{12}@\beta\text{-CD}_1]$  with different orientations, A) and B).  $\beta\text{-CD}$  is shown in light blue.



**Binding energy = - 10.05 kcal/mol**

**Figure S9.** DFT optimised structure of  $[\text{Ag}_{29}(\text{LA})_{12} \cap \text{CB}_2]$ . Encapsulated LA and CB are shown in blue and light green, respectively.



**Binding energy = - 64.93 kcal/mol**

**Figure S10.** DFT optimised structure of  $[\text{Ag}_{29}(\text{LA})_{12}@\beta\text{-CD}_2]$ .  $\beta$ -CDs are shown in light blue.

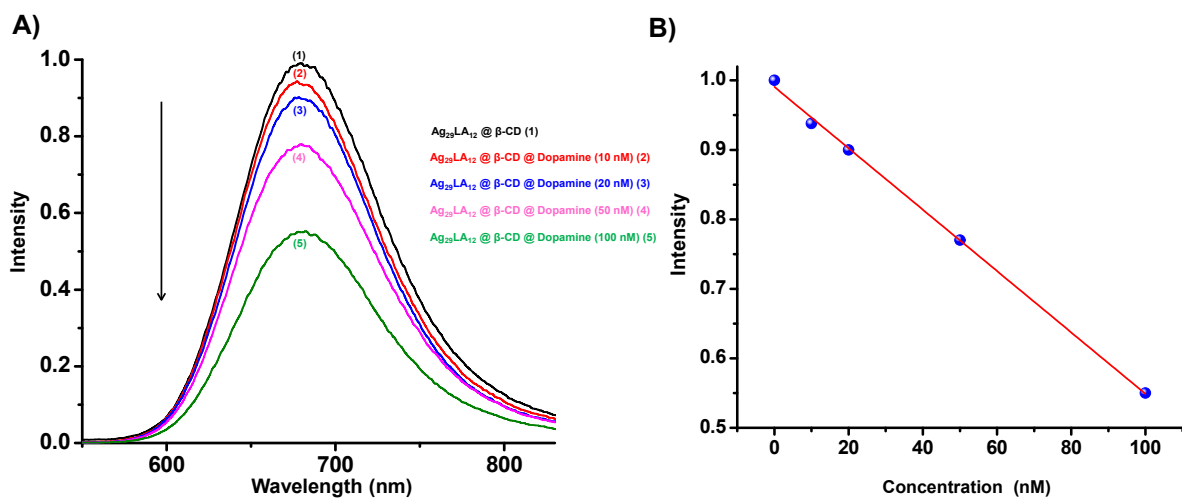


**Figure S11.** A) Dopamine concentration dependent quenching of a solution of  $[Ag_{29}(LA)_{12}@β-CD_n]$  complexes. With increase in the concentration of dopamine, PL intensity was decreased. B) Plot between PL quenching efficiency and dopamine concentration shows a linear relationship.

**Table S1.** Different methods for dopamine detection available in the literature.

Method used and references	Property used for detection	Detection limit
Periodic cylindrical gold nanoelectrode arrays <sup>8</sup>	Electrochemical	5.83 $\mu$ M
Colorimetric detection of dopamine using functionalized gold nanoparticles <sup>9</sup>	Plasmon absorption	0.5 nM
Colorimetric sensing of dopamine using hexagonal silver nanoparticles <sup>10</sup>	Plasmon absorption	0.031 $\mu$ M
Rotating droplet system <sup>11</sup>	Electrochemical	100 nM
Turn-on fluorescent sensing based on in situ formation of visible light emitting polydopamine nanoparticles <sup>12</sup>	Florescence of PDA nanoparticles	40 nM
Colorimetric Detection using cyclodextrin-modified Au nanoparticles <sup>13</sup>	Plasmon absorption	3 nM
Protein conjugated fluorescent gold nanoclusters <sup>14</sup>	Fluorescence of gold nanoclusters	10 nM
This work	Fluorescence of supramolecular complexes of atomically precise cluster	10 nM



**Coordinates of the lowest energy geometry of  $\text{Ag}_{29}\text{LA}_{12}\cap\text{CB}_1$**

O	21.222000	8.150000	5.720000
O	18.093000	12.492000	8.653000
O	24.161000	8.820000	7.958000
O	20.776000	13.095000	10.821000
O	24.856000	7.226000	11.180000
O	21.512000	11.435000	14.072000
O	22.973000	4.478000	12.958000
O	19.654000	8.750000	15.863000
O	19.886000	2.760000	11.993000
O	16.523000	6.986000	14.978000
O	17.846000	3.359000	8.901000
O	14.536000	7.549000	11.938000
O	18.471000	5.734000	6.239000
O	15.274000	9.991000	9.217000
N	19.297000	9.401000	5.574000
N	21.164000	10.414000	6.184000
N	18.050000	11.112000	6.807000
N	19.923000	12.192000	7.286000
N	23.036000	10.820000	7.680000
N	24.253000	10.517000	9.525000
N	21.757000	12.608000	8.799000
N	22.909000	12.212000	10.663000
N	24.770000	9.479000	11.639000
N	24.313000	8.039000	13.249000
N	23.386000	11.155000	12.760000
N	23.010000	9.739000	14.429000
N	23.113000	6.271000	14.423000
N	21.504000	4.793000	14.741000
N	21.796000	7.966000	15.558000

N	20.152000	6.489000	15.841000
N	19.450000	3.670000	14.050000
N	17.770000	3.294000	12.687000
N	18.133000	5.351000	15.221000
N	16.402000	4.939000	13.888000
N	16.411000	3.640000	10.694000
N	15.912000	4.627000	8.764000
N	15.075000	5.286000	11.895000
N	14.633000	6.323000	9.975000
N	16.355000	6.225000	6.982000
N	17.471000	7.794000	5.911000
N	15.098000	7.920000	8.203000
N	16.275000	9.490000	7.183000
C	20.638000	9.214000	5.839000
C	18.908000	10.798000	5.694000
C	20.231000	11.500000	6.061000
C	18.639000	11.973000	7.685000
C	22.592000	10.584000	6.342000
C	20.791000	13.176000	7.915000
C	23.853000	9.938000	8.367000
C	23.058000	12.157000	8.306000
C	23.844000	11.911000	9.603000
C	21.719000	12.670000	10.153000
C	25.272000	9.964000	10.364000
C	23.277000	12.400000	12.030000
C	24.657000	8.175000	11.927000
C	24.586000	10.333000	12.792000
C	24.302000	9.314000	13.917000
C	22.538000	10.828000	13.785000
C	24.399000	6.778000	13.957000
C	22.449000	9.247000	15.670000

C	22.558000	5.110000	13.928000
C	22.476000	6.711000	15.657000
C	21.359000	5.671000	15.843000
C	20.416000	7.836000	15.773000
C	20.779000	3.528000	14.586000
C	18.885000	6.025000	16.267000
C	19.108000	3.220000	12.833000
C	18.305000	3.969000	14.872000
C	17.123000	3.679000	13.938000
C	16.969000	5.872000	14.717000
C	17.032000	2.706000	11.594000
C	15.070000	5.070000	13.341000
C	16.818000	3.830000	9.403000
C	15.125000	4.204000	10.927000
C	14.787000	4.934000	9.608000
C	14.724000	6.501000	11.358000
C	15.991000	4.869000	7.335000
C	14.125000	7.357000	9.133000
C	17.555000	6.526000	6.363000
C	15.419000	7.337000	6.920000
C	16.213000	8.430000	6.200000
C	15.532000	9.218000	8.300000
C	18.462000	8.358000	5.017000
C	16.621000	10.854000	6.816000
H	18.396000	11.075000	4.796000
H	20.644000	12.214000	5.379000
H	22.894000	11.417000	5.742000
H	23.035000	9.657000	6.043000
H	20.182000	13.856000	8.473000
H	21.333000	13.662000	7.130000
H	23.426000	12.867000	7.596000

H	24.722000	12.501000	9.767000
H	26.003000	10.722000	10.554000
H	25.685000	9.123000	9.847000
H	22.535000	13.009000	12.503000
H	24.241000	12.865000	12.042000
H	25.428000	10.988000	12.878000
H	24.984000	9.249000	14.739000
H	25.036000	6.912000	14.806000
H	24.783000	6.059000	13.264000
H	21.732000	9.960000	16.020000
H	23.268000	9.116000	16.346000
H	23.214000	6.809000	16.425000
H	21.358000	5.066000	16.725000
H	20.705000	3.064000	15.547000
H	21.332000	2.941000	13.883000
H	18.314000	6.863000	16.608000
H	19.057000	5.309000	17.043000
H	18.398000	3.417000	15.784000
H	16.429000	2.912000	14.211000
H	16.264000	2.088000	12.010000
H	17.750000	2.168000	11.010000
H	14.587000	5.902000	13.810000
H	14.550000	4.154000	13.530000
H	14.495000	3.409000	11.267000
H	13.894000	4.659000	9.087000
H	15.035000	4.656000	6.905000
H	16.766000	4.235000	6.958000
H	13.764000	8.148000	9.757000
H	13.359000	6.910000	8.534000
H	14.508000	6.995000	6.474000
H	15.830000	8.837000	5.288000

H	19.102000	7.564000	4.694000
H	17.908000	8.822000	4.227000
H	16.237000	11.048000	5.836000
H	16.192000	11.495000	7.557000
Ag	15.738000	16.112000	16.160000
Ag	13.280000	15.986000	14.712000
Ag	15.730000	17.600000	13.699000
Ag	14.208000	18.524000	16.286000
Ag	18.207000	16.008000	17.594000
Ag	11.460000	14.296000	12.816000
Ag	12.989000	18.739000	13.521000
Ag	17.396000	19.398000	11.783000
Ag	12.483000	20.500000	17.993000
Ag	19.090000	20.407000	14.297000
Ag	18.491000	18.797000	18.716000
Ag	14.295000	13.621000	16.081000
Ag	13.320000	16.183000	17.690000
Ag	15.882000	14.662000	18.604000
Ag	17.191000	18.587000	16.000000
Ag	12.402000	11.709000	14.515000
Ag	13.122000	13.398000	18.890000
Ag	11.505000	17.805000	19.524000
Ag	17.588000	12.888000	20.516000
Ag	14.120000	19.606000	20.490000
Ag	15.609000	14.660000	13.707000
Ag	17.248000	13.683000	16.228000
Ag	18.133000	16.271000	14.600000
Ag	15.679000	17.630000	18.568000
Ag	14.003000	12.682000	11.887000
Ag	18.395000	13.500000	13.467000
Ag	19.123000	11.799000	17.884000



Ag	20.031000	17.817000	12.630000
Ag	20.198000	14.401000	19.411000
S	16.562000	13.376000	11.718000
S	14.746000	18.878000	11.703000
S	12.924000	20.510000	15.347000
S	20.246000	16.981000	18.788000
S	12.349000	13.929000	10.521000
S	19.055000	18.186000	10.388000
S	17.726000	21.705000	12.660000
S	21.373000	19.468000	13.894000
S	11.244000	16.912000	13.485000
S	11.346000	15.203000	18.992000
S	14.981000	13.358000	20.620000
S	18.516000	20.558000	16.902000
S	10.128000	12.681000	14.146000
S	10.201000	19.548000	18.319000
S	12.517000	18.249000	21.785000
S	13.770000	21.905000	19.553000
S	13.093000	11.615000	17.094000
S	18.548000	11.713000	15.259000
S	20.148000	15.286000	13.324000
S	16.707000	18.909000	20.509000
S	13.657000	10.390000	12.832000
S	17.933000	10.572000	19.656000
S	21.442000	12.686000	18.124000
S	19.328000	14.124000	21.754000
C	9.416000	13.473000	15.650000
H	8.813000	12.689000	16.131000
H	8.727000	14.260000	15.303000
C	10.449000	14.029000	16.620000
H	11.074000	14.764000	16.088000

H	11.123000	13.206000	16.903000
C	9.923000	14.663000	17.911000
H	9.371000	15.590000	17.690000
C	9.016000	13.742000	18.756000
H	9.301000	12.693000	18.573000
H	9.214000	13.934000	19.822000
C	7.514000	13.933000	18.512000
C	6.664000	13.077000	19.457000
C	5.157000	13.279000	19.255000
C	4.228000	12.523000	20.194000
O	4.620000	11.259000	20.550000
O	3.173000	12.955000	20.603000
H	7.254000	13.699000	17.467000
H	7.259000	14.995000	18.667000
H	6.941000	12.018000	19.298000
H	6.935000	13.315000	20.498000
H	4.879000	12.978000	18.230000
H	4.891000	14.341000	19.344000
H	5.499000	11.082000	20.164000
C	9.920000	17.494000	14.633000
H	9.167000	16.695000	14.683000
H	9.466000	18.344000	14.103000
C	10.394000	17.923000	16.024000
H	11.431000	18.281000	15.949000
H	10.426000	17.059000	16.702000
C	9.569000	19.048000	16.651000
H	9.727000	19.945000	16.031000
C	8.043000	18.770000	16.701000
H	7.835000	17.743000	16.358000
H	7.689000	18.835000	17.740000
C	7.267000	19.767000	15.836000

C	5.755000	19.536000	15.773000
C	5.070000	20.587000	14.884000
C	3.569000	20.457000	14.699000
O	3.105000	19.197000	14.422000
O	2.787000	21.380000	14.745000
H	7.667000	19.746000	14.808000
H	7.460000	20.784000	16.217000
H	5.574000	18.514000	15.388000
H	5.321000	19.563000	16.785000
H	5.521000	20.552000	13.876000
H	5.256000	21.596000	15.274000
H	3.848000	18.565000	14.479000
C	13.021000	15.491000	9.810000
H	12.186000	15.929000	9.243000
H	13.805000	15.211000	9.089000
C	13.549000	16.481000	10.842000
H	12.718000	16.739000	11.516000
H	14.303000	15.967000	11.462000
C	14.144000	17.787000	10.307000
H	15.054000	17.569000	9.728000
C	13.181000	18.614000	9.422000
H	12.146000	18.449000	9.764000
H	13.387000	19.684000	9.572000
C	13.298000	18.314000	7.921000
C	12.320000	19.123000	7.061000
C	12.517000	18.875000	5.556000
C	11.596000	19.645000	4.626000
O	10.258000	19.587000	4.925000
O	11.956000	20.265000	3.651000
H	13.140000	17.241000	7.728000
H	14.327000	18.540000	7.594000

H	11.290000	18.866000	7.371000
H	12.443000	20.196000	7.274000
H	12.374000	17.803000	5.333000
H	13.543000	19.121000	5.256000
H	10.135000	19.073000	5.745000
C	17.015000	14.476000	10.299000
H	16.111000	14.556000	9.682000
H	17.762000	13.901000	9.732000
C	17.568000	15.841000	10.701000
H	16.750000	16.478000	11.073000
H	18.241000	15.687000	11.557000
C	18.377000	16.620000	9.653000
H	19.271000	16.029000	9.391000
C	17.648000	17.006000	8.355000
H	16.661000	17.421000	8.618000
H	18.201000	17.838000	7.892000
C	17.489000	15.896000	7.308000
C	16.672000	16.359000	6.101000
C	16.529000	15.264000	5.028000
C	15.619000	15.656000	3.882000
O	14.289000	15.788000	4.205000
O	15.973000	15.865000	2.744000
H	16.998000	15.012000	7.741000
H	18.484000	15.561000	6.971000
H	15.674000	16.675000	6.449000
H	17.131000	17.253000	5.649000
H	16.137000	14.344000	5.495000
H	17.509000	15.024000	4.596000
H	14.164000	15.572000	5.147000
C	15.297000	22.575000	18.768000
H	15.842000	23.089000	19.575000

H	14.975000	23.339000	18.043000
C	16.179000	21.520000	18.115000
H	16.409000	20.760000	18.876000
H	15.600000	21.004000	17.333000
C	17.512000	22.001000	17.531000
H	17.342000	22.638000	16.648000
C	18.410000	22.754000	18.538000
H	18.176000	22.396000	19.554000
H	19.456000	22.469000	18.348000
C	18.334000	24.285000	18.483000
C	19.344000	24.924000	19.445000
C	19.464000	26.446000	19.308000
C	20.513000	27.141000	20.171000
O	21.009000	26.434000	21.232000
O	20.900000	28.272000	19.978000
H	17.319000	24.645000	18.718000
H	18.555000	24.622000	17.457000
H	19.048000	24.655000	20.477000
H	20.330000	24.462000	19.266000
H	18.503000	26.931000	19.548000
H	19.683000	26.729000	18.267000
H	20.614000	25.541000	21.233000
C	14.048000	21.851000	14.747000
H	14.088000	22.601000	15.550000
H	13.509000	22.298000	13.899000
C	15.441000	21.404000	14.307000
H	16.096000	21.265000	15.178000
H	15.358000	20.418000	13.830000
C	16.105000	22.343000	13.298000
H	15.465000	22.352000	12.400000
C	16.260000	23.803000	13.794000



H	15.868000	23.898000	14.821000
H	17.328000	24.064000	13.845000
C	15.532000	24.794000	12.884000
C	15.671000	26.257000	13.308000
C	14.865000	27.196000	12.402000
C	15.015000	28.687000	12.645000
O	15.220000	29.074000	13.943000
O	14.941000	29.529000	11.779000
H	14.461000	24.530000	12.846000
H	15.913000	24.681000	11.855000
H	15.326000	26.342000	14.357000
H	16.734000	26.545000	13.299000
H	13.789000	26.968000	12.498000
H	15.116000	27.031000	11.345000
H	15.293000	28.276000	14.502000
C	13.285000	16.741000	22.521000
H	12.477000	16.259000	23.091000
H	14.045000	17.082000	23.242000
C	13.875000	15.771000	21.504000
H	14.657000	16.291000	20.929000
H	13.081000	15.526000	20.782000
C	14.437000	14.448000	22.035000
H	15.355000	14.627000	22.617000
C	13.447000	13.632000	22.896000
H	12.422000	13.843000	22.546000
H	13.620000	12.561000	22.714000
C	13.555000	13.875000	24.407000
C	12.459000	13.147000	25.193000
C	12.588000	13.336000	26.711000
C	11.531000	12.674000	27.580000
O	10.236000	12.782000	27.147000

O	11.764000	12.106000	28.623000
H	13.507000	14.951000	24.637000
H	14.542000	13.528000	24.755000
H	11.482000	13.525000	24.834000
H	12.478000	12.073000	24.948000
H	12.554000	14.415000	26.946000
H	13.558000	12.966000	27.069000
H	10.230000	13.228000	26.279000
C	17.331000	17.853000	21.891000
H	16.526000	17.804000	22.639000
H	18.154000	18.444000	22.318000
C	17.815000	16.468000	21.473000
H	18.362000	16.569000	20.526000
H	16.952000	15.819000	21.253000
C	18.743000	15.741000	22.454000
H	19.667000	16.334000	22.560000
C	18.136000	15.531000	23.858000
H	17.045000	15.404000	23.757000
H	18.514000	14.590000	24.285000
C	18.440000	16.687000	24.823000
C	17.559000	16.711000	26.074000
C	17.849000	17.943000	26.949000
C	16.979000	18.086000	28.183000
O	15.627000	18.082000	27.966000
O	17.395000	18.211000	29.313000
H	18.320000	17.650000	24.304000
H	19.500000	16.638000	25.123000
H	16.502000	16.707000	25.751000
H	17.698000	15.792000	26.668000
H	17.718000	18.856000	26.342000
H	18.890000	17.933000	27.295000

H	15.453000	17.945000	27.016000
C	15.267000	9.724000	13.443000
H	15.765000	9.336000	12.543000
H	15.040000	8.864000	14.093000
C	16.152000	10.740000	14.156000
H	15.636000	11.092000	15.061000
H	16.244000	11.619000	13.500000
C	17.573000	10.292000	14.524000
H	17.546000	9.530000	15.320000
C	18.412000	9.769000	13.336000
H	18.096000	10.308000	12.427000
H	19.461000	10.056000	13.505000
C	18.389000	8.256000	13.084000
C	19.295000	7.891000	11.898000
C	19.442000	6.385000	11.658000
C	20.305000	5.950000	10.480000
O	20.371000	6.810000	9.419000
O	20.888000	4.890000	10.425000
H	17.366000	7.895000	12.892000
H	18.743000	7.728000	13.986000
H	18.873000	8.386000	11.002000
H	20.290000	8.337000	12.059000
H	18.450000	5.931000	11.491000
H	19.859000	5.884000	12.543000
H	19.882000	7.627000	9.640000
C	14.250000	10.269000	17.604000
H	14.341000	9.591000	16.743000
H	13.708000	9.735000	18.398000
C	15.607000	10.754000	18.106000
H	15.444000	11.678000	18.678000
H	16.251000	11.039000	17.258000

C	16.375000	9.797000	19.020000
H	15.767000	9.623000	19.924000
C	16.738000	8.434000	18.403000
H	17.023000	8.575000	17.346000
H	17.641000	8.060000	18.910000
C	15.648000	7.364000	18.522000
C	16.131000	5.985000	18.071000
C	15.061000	4.899000	18.259000
C	15.496000	3.493000	17.900000
O	16.070000	3.338000	16.664000
O	15.363000	2.523000	18.613000
H	14.750000	7.643000	17.948000
H	15.328000	7.297000	19.576000
H	16.446000	6.052000	17.012000
H	17.036000	5.711000	18.639000
H	14.172000	5.143000	17.650000
H	14.731000	4.866000	19.304000
H	16.148000	4.213000	16.239000
C	22.118000	18.733000	15.416000
H	22.665000	19.557000	15.898000
H	22.862000	17.992000	15.081000
C	21.111000	18.118000	16.381000
H	20.554000	17.327000	15.854000
H	20.371000	18.893000	16.630000
C	21.650000	17.560000	17.705000
H	22.261000	16.660000	17.527000
C	22.456000	18.568000	18.552000
H	22.041000	19.575000	18.378000
H	22.279000	18.344000	19.616000
C	23.972000	18.576000	18.328000
C	24.654000	19.654000	19.180000

C	26.181000	19.651000	19.048000
C	26.947000	20.676000	19.868000
O	26.360000	21.903000	20.020000
O	28.041000	20.480000	20.348000
H	24.221000	18.739000	17.269000
H	24.382000	17.587000	18.597000
H	24.239000	20.634000	18.876000
H	24.372000	19.515000	20.237000
H	26.462000	19.823000	17.994000
H	26.593000	18.671000	19.323000
H	25.472000	21.881000	19.613000
C	21.527000	14.703000	14.411000
H	22.268000	15.515000	14.446000
H	21.967000	13.869000	13.845000
C	21.112000	14.240000	15.805000
H	20.138000	13.738000	15.726000
H	20.951000	15.104000	16.468000
C	22.073000	13.254000	16.477000
H	22.081000	12.335000	15.868000
C	23.531000	13.753000	16.615000
H	23.555000	14.853000	16.540000
H	23.903000	13.504000	17.621000
C	24.473000	13.134000	15.576000
C	25.923000	13.609000	15.693000
C	26.846000	12.864000	14.722000
C	28.324000	13.201000	14.777000
O	28.641000	14.512000	15.015000
O	29.212000	12.398000	14.599000
H	24.109000	13.338000	14.556000
H	24.452000	12.037000	15.694000
H	25.947000	14.699000	15.502000

H	26.277000	13.465000	16.727000
H	26.523000	13.053000	13.684000
H	26.765000	11.778000	14.874000
H	27.817000	15.017000	15.159000

**Coordinates of the lowest energy geometry of  $\text{Ag}_{29}\text{LA}_{12}\cap\text{CD}_1$**

H	10.830000	17.282000	7.240000
O	13.263000	15.494000	6.489000
C	11.912000	15.131000	6.247000
O	11.021000	16.661000	7.989000
C	11.798000	13.667000	5.769000
O	10.452000	13.331000	5.426000
C	10.979000	15.322000	7.460000
C	9.546000	14.885000	7.097000
H	13.664000	14.777000	7.065000
O	12.677000	10.604000	3.938000
O	8.725000	17.559000	9.481000
H	15.647000	13.522000	7.028000
C	9.524000	13.448000	6.550000
C	8.177000	13.004000	5.980000
H	13.505000	10.067000	3.966000
C	7.564000	15.783000	8.249000
H	8.978000	11.669000	4.826000
C	7.601000	16.692000	9.494000
H	9.505000	17.039000	9.127000
O	12.291000	12.841000	6.835000
O	14.928000	13.467000	7.707000
O	8.232000	11.662000	5.477000
O	8.750000	14.976000	8.297000



O	6.383000	15.001000	8.177000
C	13.385000	11.958000	6.526000
C	12.001000	10.282000	5.163000
C	14.427000	12.112000	7.648000
C	12.880000	10.507000	6.396000
C	15.556000	11.075000	7.455000
O	14.007000	9.596000	6.238000
O	3.743000	14.262000	9.057000
C	7.493000	15.802000	10.751000
C	6.210000	14.114000	9.314000
H	6.810000	17.302000	11.827000
O	7.459000	16.568000	11.973000
C	4.877000	13.388000	9.085000
O	16.562000	11.117000	8.452000
H	3.553000	14.514000	9.998000
C	6.252000	14.903000	10.637000
C	14.930000	9.671000	7.327000
H	16.255000	10.561000	9.230000
O	14.294000	9.385000	8.577000
O	6.260000	14.002000	11.764000
H	6.659000	15.699000	13.425000
C	5.071000	13.935000	12.571000
O	13.812000	6.043000	7.210000
O	6.001000	15.554000	14.168000
C	14.583000	8.121000	9.213000
C	12.823000	6.810000	7.906000
O	16.327000	9.231000	10.551000
H	17.040000	8.676000	10.132000
O	4.417000	12.687000	12.446000
C	5.483000	14.242000	14.024000
C	13.309000	7.267000	9.280000

H	14.072000	5.341000	7.856000
C	15.141000	8.412000	10.615000
C	5.243000	11.564000	12.870000
C	6.433000	13.119000	14.501000
O	13.587000	6.032000	10.018000
C	4.387000	10.303000	12.686000
C	15.375000	7.085000	11.366000
C	5.747000	11.763000	14.310000
O	6.870000	13.303000	15.864000
O	3.208000	10.264000	13.492000
C	14.068000	6.260000	11.347000
O	15.869000	7.240000	12.689000
O	13.098000	6.977000	12.124000
O	6.721000	10.730000	14.650000
H	6.066000	13.525000	16.394000
H	15.105000	7.532000	13.269000
H	3.517000	10.145000	14.440000
C	10.953000	4.805000	11.850000
H	7.450000	11.758000	16.700000
C	12.501000	6.287000	13.238000
C	11.043000	5.925000	12.888000
C	6.350000	9.768000	15.639000
C	7.414000	7.949000	14.467000
C	12.605000	7.200000	14.474000
O	13.979000	7.495000	14.805000
O	6.202000	8.452000	15.087000
O	7.508000	11.043000	17.402000
O	9.796000	7.559000	14.838000
C	8.755000	9.275000	16.191000
C	7.047000	6.557000	13.947000
O	11.553000	3.594000	12.328000

C	7.410000	9.786000	16.756000
C	8.561000	7.918000	15.494000
H	14.361000	6.674000	15.207000
O	10.342000	5.400000	14.054000
O	9.772000	9.175000	17.215000
C	10.373000	6.294000	15.171000
H	11.191000	8.080000	16.750000
C	11.819000	6.567000	15.646000
H	11.132000	3.458000	13.213000
O	6.698000	5.654000	15.004000
O	11.843000	7.321000	16.845000
H	9.371000	8.654000	17.954000
H	5.988000	6.128000	15.505000
H	11.589000	15.804000	5.480000
H	12.373000	13.516000	4.879000
H	11.335000	14.693000	8.249000
H	9.154000	15.519000	6.330000
H	9.774000	12.841000	7.395000
H	7.904000	13.663000	5.182000
H	7.454000	13.036000	6.768000
H	7.544000	16.374000	7.358000
H	6.764000	17.358000	9.497000
H	13.834000	12.207000	5.587000
H	11.709000	9.253000	5.133000
H	11.154000	10.930000	5.246000
H	13.962000	11.919000	8.592000
H	12.315000	10.325000	7.286000
H	16.072000	11.328000	6.553000
H	8.374000	15.197000	10.799000
H	7.003000	13.400000	9.395000
H	4.930000	12.873000	8.149000

H	4.738000	12.722000	9.911000
H	5.376000	15.518000	10.641000
H	15.686000	8.944000	7.112000
H	4.355000	14.657000	12.238000
H	15.308000	7.568000	8.653000
H	11.947000	6.209000	8.033000
H	12.615000	7.683000	7.324000
H	4.626000	14.242000	14.665000
H	12.569000	7.885000	9.744000
H	14.422000	8.979000	11.168000
H	6.133000	11.476000	12.283000
H	7.320000	13.156000	13.904000
H	4.988000	9.452000	12.932000
H	4.059000	10.304000	11.667000
H	16.153000	6.563000	10.849000
H	4.886000	11.710000	14.943000
H	14.252000	5.291000	11.762000
H	9.923000	4.618000	11.629000
H	11.481000	5.117000	10.974000
H	13.008000	5.370000	13.455000
H	10.613000	6.833000	12.520000
H	5.393000	10.031000	16.038000
H	7.764000	8.567000	13.667000
H	12.159000	8.147000	14.255000
H	9.094000	9.993000	15.474000
H	7.885000	6.157000	13.416000
H	6.193000	6.661000	13.311000
H	7.103000	9.118000	17.534000
H	8.298000	7.192000	16.235000
H	9.813000	5.815000	15.947000
H	12.309000	5.652000	15.907000

Ag	15.738000	16.112000	16.160000
Ag	13.280000	15.986000	14.712000
Ag	15.730000	17.600000	13.699000
Ag	14.208000	18.524000	16.286000
Ag	18.207000	16.008000	17.594000
Ag	11.460000	14.296000	12.816000
Ag	12.989000	18.739000	13.521000
Ag	17.396000	19.398000	11.783000
Ag	12.483000	20.500000	17.993000
Ag	19.090000	20.407000	14.297000
Ag	18.491000	18.797000	18.716000
Ag	14.295000	13.621000	16.081000
Ag	13.320000	16.183000	17.690000
Ag	15.882000	14.662000	18.604000
Ag	17.191000	18.587000	16.000000
Ag	12.402000	11.709000	14.515000
Ag	13.122000	13.398000	18.890000
Ag	11.505000	17.805000	19.524000
Ag	17.588000	12.888000	20.516000
Ag	14.120000	19.606000	20.490000
Ag	15.609000	14.660000	13.707000
Ag	17.248000	13.683000	16.228000
Ag	18.133000	16.271000	14.600000
Ag	15.679000	17.630000	18.568000
Ag	14.003000	12.682000	11.887000
Ag	18.395000	13.500000	13.467000
Ag	19.123000	11.799000	17.884000
Ag	20.031000	17.817000	12.630000
Ag	20.198000	14.401000	19.411000
S	16.562000	13.376000	11.718000
S	14.746000	18.878000	11.703000

S	12.924000	20.510000	15.347000
S	20.246000	16.981000	18.788000
S	12.349000	13.929000	10.521000
S	19.055000	18.186000	10.388000
S	17.726000	21.705000	12.660000
S	21.373000	19.468000	13.894000
S	11.244000	16.912000	13.485000
S	11.346000	15.203000	18.992000
S	14.981000	13.358000	20.620000
S	18.516000	20.558000	16.902000
S	10.128000	12.681000	14.146000
S	10.201000	19.548000	18.319000
S	12.517000	18.249000	21.785000
S	13.770000	21.905000	19.553000
S	13.093000	11.615000	17.094000
S	18.548000	11.713000	15.259000
S	20.148000	15.286000	13.324000
S	16.707000	18.909000	20.509000
S	13.657000	10.390000	12.832000
S	17.933000	10.572000	19.656000
S	21.442000	12.686000	18.124000
S	19.328000	14.124000	21.754000
C	9.416000	13.473000	15.650000
H	8.813000	12.689000	16.131000
H	8.727000	14.260000	15.303000
C	10.449000	14.029000	16.620000
H	11.074000	14.764000	16.088000
H	11.123000	13.206000	16.903000
C	9.923000	14.663000	17.911000
H	9.371000	15.590000	17.690000
C	9.016000	13.742000	18.756000



H	9.301000	12.693000	18.573000
H	9.214000	13.934000	19.822000
C	7.514000	13.933000	18.512000
C	6.664000	13.077000	19.457000
C	5.157000	13.279000	19.255000
C	4.228000	12.523000	20.194000
O	4.620000	11.259000	20.550000
O	3.173000	12.955000	20.603000
H	7.254000	13.699000	17.467000
H	7.259000	14.995000	18.667000
H	6.941000	12.018000	19.298000
H	6.935000	13.315000	20.498000
H	4.879000	12.978000	18.230000
H	4.891000	14.341000	19.344000
H	5.499000	11.082000	20.164000
C	9.920000	17.494000	14.633000
H	9.167000	16.695000	14.683000
H	9.466000	18.344000	14.103000
C	10.394000	17.923000	16.024000
H	11.431000	18.281000	15.949000
H	10.426000	17.059000	16.702000
C	9.569000	19.048000	16.651000
H	9.727000	19.945000	16.031000
C	8.043000	18.770000	16.701000
H	7.835000	17.743000	16.358000
H	7.689000	18.835000	17.740000
C	7.267000	19.767000	15.836000
C	5.755000	19.536000	15.773000
C	5.070000	20.587000	14.884000
C	3.569000	20.457000	14.699000
O	3.105000	19.197000	14.422000

O	2.787000	21.380000	14.745000
H	7.667000	19.746000	14.808000
H	7.460000	20.784000	16.217000
H	5.574000	18.514000	15.388000
H	5.321000	19.563000	16.785000
H	5.521000	20.552000	13.876000
H	5.256000	21.596000	15.274000
H	3.848000	18.565000	14.479000
C	13.021000	15.491000	9.810000
H	12.186000	15.929000	9.243000
H	13.805000	15.211000	9.089000
C	13.549000	16.481000	10.842000
H	12.718000	16.739000	11.516000
H	14.303000	15.967000	11.462000
C	14.144000	17.787000	10.307000
H	15.054000	17.569000	9.728000
C	13.181000	18.614000	9.422000
H	12.146000	18.449000	9.764000
H	13.387000	19.684000	9.572000
C	13.298000	18.314000	7.921000
C	12.320000	19.123000	7.061000
C	12.517000	18.875000	5.556000
C	11.596000	19.645000	4.626000
O	10.258000	19.587000	4.925000
O	11.956000	20.265000	3.651000
H	13.140000	17.241000	7.728000
H	14.327000	18.540000	7.594000
H	11.290000	18.866000	7.371000
H	12.443000	20.196000	7.274000
H	12.374000	17.803000	5.333000
H	13.543000	19.121000	5.256000

H	10.135000	19.073000	5.745000
C	17.015000	14.476000	10.299000
H	16.111000	14.556000	9.682000
H	17.762000	13.901000	9.732000
C	17.568000	15.841000	10.701000
H	16.750000	16.478000	11.073000
H	18.241000	15.687000	11.557000
C	18.377000	16.620000	9.653000
H	19.271000	16.029000	9.391000
C	17.648000	17.006000	8.355000
H	16.661000	17.421000	8.618000
H	18.201000	17.838000	7.892000
C	17.489000	15.896000	7.308000
C	16.672000	16.359000	6.101000
C	16.529000	15.264000	5.028000
C	15.619000	15.656000	3.882000
O	14.289000	15.788000	4.205000
O	15.973000	15.865000	2.744000
H	16.998000	15.012000	7.741000
H	18.484000	15.561000	6.971000
H	15.674000	16.675000	6.449000
H	17.131000	17.253000	5.649000
H	16.137000	14.344000	5.495000
H	17.509000	15.024000	4.596000
H	14.164000	15.572000	5.147000
C	15.297000	22.575000	18.768000
H	15.842000	23.089000	19.575000
H	14.975000	23.339000	18.043000
C	16.179000	21.520000	18.115000
H	16.409000	20.760000	18.876000
H	15.600000	21.004000	17.333000

C	17.512000	22.001000	17.531000
H	17.342000	22.638000	16.648000
C	18.410000	22.754000	18.538000
H	18.176000	22.396000	19.554000
H	19.456000	22.469000	18.348000
C	18.334000	24.285000	18.483000
C	19.344000	24.924000	19.445000
C	19.464000	26.446000	19.308000
C	20.513000	27.141000	20.171000
O	21.009000	26.434000	21.232000
O	20.900000	28.272000	19.978000
H	17.319000	24.645000	18.718000
H	18.555000	24.622000	17.457000
H	19.048000	24.655000	20.477000
H	20.330000	24.462000	19.266000
H	18.503000	26.931000	19.548000
H	19.683000	26.729000	18.267000
H	20.614000	25.541000	21.233000
C	14.048000	21.851000	14.747000
H	14.088000	22.601000	15.550000
H	13.509000	22.298000	13.899000
C	15.441000	21.404000	14.307000
H	16.096000	21.265000	15.178000
H	15.358000	20.418000	13.830000
C	16.105000	22.343000	13.298000
H	15.465000	22.352000	12.400000
C	16.260000	23.803000	13.794000
H	15.868000	23.898000	14.821000
H	17.328000	24.064000	13.845000
C	15.532000	24.794000	12.884000
C	15.671000	26.257000	13.308000

C	14.865000	27.196000	12.402000
C	15.015000	28.687000	12.645000
O	15.220000	29.074000	13.943000
O	14.941000	29.529000	11.779000
H	14.461000	24.530000	12.846000
H	15.913000	24.681000	11.855000
H	15.326000	26.342000	14.357000
H	16.734000	26.545000	13.299000
H	13.789000	26.968000	12.498000
H	15.116000	27.031000	11.345000
H	15.293000	28.276000	14.502000
C	13.285000	16.741000	22.521000
H	12.477000	16.259000	23.091000
H	14.045000	17.082000	23.242000
C	13.875000	15.771000	21.504000
H	14.657000	16.291000	20.929000
H	13.081000	15.526000	20.782000
C	14.437000	14.448000	22.035000
H	15.355000	14.627000	22.617000
C	13.447000	13.632000	22.896000
H	12.422000	13.843000	22.546000
H	13.620000	12.561000	22.714000
C	13.555000	13.875000	24.407000
C	12.459000	13.147000	25.193000
C	12.588000	13.336000	26.711000
C	11.531000	12.674000	27.580000
O	10.236000	12.782000	27.147000
O	11.764000	12.106000	28.623000
H	13.507000	14.951000	24.637000
H	14.542000	13.528000	24.755000
H	11.482000	13.525000	24.834000

H	12.478000	12.073000	24.948000
H	12.554000	14.415000	26.946000
H	13.558000	12.966000	27.069000
H	10.230000	13.228000	26.279000
C	17.331000	17.853000	21.891000
H	16.526000	17.804000	22.639000
H	18.154000	18.444000	22.318000
C	17.815000	16.468000	21.473000
H	18.362000	16.569000	20.526000
H	16.952000	15.819000	21.253000
C	18.743000	15.741000	22.454000
H	19.667000	16.334000	22.560000
C	18.136000	15.531000	23.858000
H	17.045000	15.404000	23.757000
H	18.514000	14.590000	24.285000
C	18.440000	16.687000	24.823000
C	17.559000	16.711000	26.074000
C	17.849000	17.943000	26.949000
C	16.979000	18.086000	28.183000
O	15.627000	18.082000	27.966000
O	17.395000	18.211000	29.313000
H	18.320000	17.650000	24.304000
H	19.500000	16.638000	25.123000
H	16.502000	16.707000	25.751000
H	17.698000	15.792000	26.668000
H	17.718000	18.856000	26.342000
H	18.890000	17.933000	27.295000
H	15.453000	17.945000	27.016000
C	15.267000	9.724000	13.443000
H	15.765000	9.336000	12.543000
H	15.040000	8.864000	14.093000



C	16.152000	10.740000	14.156000
H	15.636000	11.092000	15.061000
H	16.244000	11.619000	13.500000
C	17.573000	10.292000	14.524000
H	17.546000	9.530000	15.320000
C	18.412000	9.769000	13.336000
H	18.096000	10.308000	12.427000
H	19.461000	10.056000	13.505000
C	18.389000	8.256000	13.084000
C	19.295000	7.891000	11.898000
C	19.442000	6.385000	11.658000
C	20.305000	5.950000	10.480000
O	20.371000	6.810000	9.419000
O	20.888000	4.890000	10.425000
H	17.366000	7.895000	12.892000
H	18.743000	7.728000	13.986000
H	18.873000	8.386000	11.002000
H	20.290000	8.337000	12.059000
H	18.450000	5.931000	11.491000
H	19.859000	5.884000	12.543000
H	19.882000	7.627000	9.640000
C	14.250000	10.269000	17.604000
H	14.341000	9.591000	16.743000
H	13.708000	9.735000	18.398000
C	15.607000	10.754000	18.106000
H	15.444000	11.678000	18.678000
H	16.251000	11.039000	17.258000
C	16.375000	9.797000	19.020000
H	15.767000	9.623000	19.924000
C	16.738000	8.434000	18.403000
H	17.023000	8.575000	17.346000

H	17.641000	8.060000	18.910000
C	15.648000	7.364000	18.522000
C	16.131000	5.985000	18.071000
C	15.061000	4.899000	18.259000
C	15.496000	3.493000	17.900000
O	16.070000	3.338000	16.664000
O	15.363000	2.523000	18.613000
H	14.750000	7.643000	17.948000
H	15.328000	7.297000	19.576000
H	16.446000	6.052000	17.012000
H	17.036000	5.711000	18.639000
H	14.172000	5.143000	17.650000
H	14.731000	4.866000	19.304000
H	16.148000	4.213000	16.239000
C	22.118000	18.733000	15.416000
H	22.665000	19.557000	15.898000
H	22.862000	17.992000	15.081000
C	21.111000	18.118000	16.381000
H	20.554000	17.327000	15.854000
H	20.371000	18.893000	16.630000
C	21.650000	17.560000	17.705000
H	22.261000	16.660000	17.527000
C	22.456000	18.568000	18.552000
H	22.041000	19.575000	18.378000
H	22.279000	18.344000	19.616000
C	23.972000	18.576000	18.328000
C	24.654000	19.654000	19.180000
C	26.181000	19.651000	19.048000
C	26.947000	20.676000	19.868000
O	26.360000	21.903000	20.020000
O	28.041000	20.480000	20.348000

H	24.221000	18.739000	17.269000
H	24.382000	17.587000	18.597000
H	24.239000	20.634000	18.876000
H	24.372000	19.515000	20.237000
H	26.462000	19.823000	17.994000
H	26.593000	18.671000	19.323000
H	25.472000	21.881000	19.613000
C	21.527000	14.703000	14.411000
H	22.268000	15.515000	14.446000
H	21.967000	13.869000	13.845000
C	21.112000	14.240000	15.805000
H	20.138000	13.738000	15.726000
H	20.951000	15.104000	16.468000
C	22.073000	13.254000	16.477000
H	22.081000	12.335000	15.868000
C	23.531000	13.753000	16.615000
H	23.555000	14.853000	16.540000
H	23.903000	13.504000	17.621000
C	24.473000	13.134000	15.576000
C	25.923000	13.609000	15.693000
C	26.846000	12.864000	14.722000
C	28.324000	13.201000	14.777000
O	28.641000	14.512000	15.015000
O	29.212000	12.398000	14.599000
H	24.109000	13.338000	14.556000
H	24.452000	12.037000	15.694000
H	25.947000	14.699000	15.502000
H	26.277000	13.465000	16.727000
H	26.523000	13.053000	13.684000
H	26.765000	11.778000	14.874000
H	27.817000	15.017000	15.159000

## References

1. Enkovaara, J.; Rostgaard, C.; Mortensen, J. J.; Chen, J.; Dulak, M.; Ferrighi, L.; Gavnholt, J.; Glinsvad, C.; Haikola, V.; Hansen, H. A.; Kristoffersen, H. H.; Kuisma, M.; Larsen, A. H.; Lehtovaara, L.; Ljungberg, M.; Lopez-Acevedo, O.; Moses, P. G.; Ojanen, J.; Olsen, T.; Petzold, V.; Romero, N. A.; Stausholm-Møller, J.; Strange, M.; Tritsarlis, G. A.; Vanin, M.; Walter, M.; Hammer, B.; Häkkinen, H.; Madsen, G. K. H.; Nieminen, R. M.; Nørskov, J. K.; Puska, M.; Rantala, T. T.; Schiøtz, J.; Thygesen, K. S.; Jacobsen, K. W., Electronic structure calculations with GPAW: a real-space implementation of the projector augmented-wave method. *J. Phys.: Condens. Matter* **2010**, *22*, 253202.
2. Mortensen, J. J.; Hansen, L. B.; Jacobsen, K. W., Real-space grid implementation of the projector augmented wave method. *Phys. Rev. B* **2005**, *71*, 035109.
3. Perdew, J. P.; Burke, K.; Ernzerhof, M., Generalized Gradient Approximation Made Simple. *Phys. Rev. Lett.* **1996**, *77*, 3865-3868.
4. M., M. G.; Ruth, H.; William, L.; F., S. M.; K., B. R.; S., G. D.; J., O. A., AutoDock4 and AutoDockTools4: Automated docking with selective receptor flexibility. *J. Comput. Chem.* **2009**, *30*, 2785-2791.
5. Lopez, P.; Lara, H. H.; M. Mullins, S.; M. Black, D.; M. Ramsower, H.; Alvarez, M. M.; Williams, T. L.; Lopez-Lozano, X.; Weissker, H.-C.; García, A. P.; Garzón, I. L.; Demeler, B.; Lopez-Ribot, J. L.; Yacamán, M. J.; Whetten, R. L., Tetrahedral (T) Closed-Shell Cluster of 29 Silver Atoms & 12 Lipoate Ligands,  $[\text{Ag}_{29}(\text{R-}\alpha\text{-LA})_{12}]^{(3-)}$ : Antibacterial and Antifungal Activity. *ACS Appl. Nano Mater.* **2018**, *1*, 1595-1602.
6. Pohjolainen, E.; Chen, X.; Malola, S.; Groenhof, G.; Häkkinen, H., A Unified AMBER-Compatible Molecular Mechanics Force Field for Thiolate-Protected Gold Nanoclusters. *J. Chem. Theory Comput.* **2016**, *12*, 1342-1350.
7. Heinz, H.; Vaia, R. A.; Farmer, B. L.; Naik, R. R., Accurate Simulation of Surfaces and Interfaces of Face-Centered Cubic Metals Using 12-6 and 9-6 Lennard-Jones Potentials. *J. Phys. Chem. C* **2008**, *112*, 17281-17290.
8. Kim, D.-S.; Kang, E.-S.; Baek, S.; Choo, S.-S.; Chung, Y.-H.; Lee, D.; Min, J.; Kim, T.-H., Electrochemical detection of dopamine using periodic cylindrical gold nanoelectrode arrays. *Scientific Reports* **2018**, *8*, 14049.

9. Kong, B.; Zhu, A.; Luo, Y.; Tian, Y.; Yu, Y.; Shi, G., Sensitive and Selective Colorimetric Visualization of Cerebral Dopamine Based on Double Molecular Recognition. *Angew. Chem. Int. Ed.* **2011**, *50*, 1837-1840.
10. Rostami, S.; Mehdinia, A.; Jabbari, A.; Kowsari, E.; Niroumand, R.; Booth, T. J., Colorimetric sensing of dopamine using hexagonal silver nanoparticles decorated by task-specific pyridinum based ionic liquid. *Sensor. Actuat. B: Chem.* **2018**, *271*, 64-72.
11. Kundys-Siedlecka, M.; Bączyńska, E.; Jönsson-Niedziółka, M., Electrochemical Detection of Dopamine and Serotonin in the Presence of Interferences in a Rotating Droplet System. *Anal. Chem.* **2019**, *91*, 10908-10913.
12. Yildirim, A.; Bayindir, M., Turn-on Fluorescent Dopamine Sensing Based on in Situ Formation of Visible Light Emitting Polydopamine Nanoparticles. *Anal. Chem.* **2014**, *86*, 5508-5512.
13. Wen, D.; Liu, W.; Herrmann, A.-K.; Haubold, D.; Holzschuh, M.; Simon, F.; Eychmüller, A., Simple and Sensitive Colorimetric Detection of Dopamine Based on Assembly of Cyclodextrin-Modified Au Nanoparticles. *Small* **2016**, *12*, 2439-2442.
14. Govindaraju, S.; Ankireddy, S. R.; Viswanath, B.; Kim, J.; Yun, K., Fluorescent Gold Nanoclusters for Selective Detection of Dopamine in Cerebrospinal fluid. *Sci. Rep.* **2017**, *7*, 40298-40298.

# Smartphone-based Fluoride-specific Sensor for Rapid and Affordable Colorimetric Detection and Precise Quantification at Sub-ppm Levels for Field Applications

Sritama Mukherjee, Manav Shah, Kamallesh Chaudhari, Arijit Jana, Chennu Sudhakar, Pillalamarri Srikrishnarka, Md Rabiul Islam, Ligy Philip, and Thalappil Pradeep\*



Cite This: *ACS Omega* 2020, 5, 25253–25263



Read Online

ACCESS |



Metrics & More

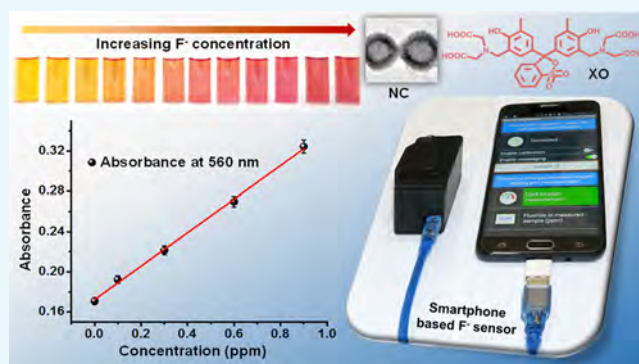


Article Recommendations



Supporting Information

**ABSTRACT:** Higher levels of fluoride ( $F^-$ ) in groundwater constitute a severe problem that affects more than 200 million people spread over 25 countries. It is essential not only to detect but also to accurately quantify aqueous  $F^-$  to ensure safety. The need of the hour is to develop smart water quality testing systems that would be effective in location-based real-time water quality data collection, devoid of professional expertise for handling. We report a cheap, handheld, portable mobile device for colorimetric detection and rapid estimation of  $F^-$  in water by the application of the synthesized core-shell nanoparticles (near-cubic ceria@zirconia nanocages) and a chemoresponsive dye (xylenol orange). The nanomaterial has been characterized thoroughly, and the mechanism of sensing has been studied in detail. The sensor system is highly selective toward  $F^-$  and shows unprecedented sensitivity in the range of 0.1–5 ppm of  $F^-$ , in field water samples, which is the transition regime, where remedial measures may be needed. It addresses multiple issues expressed by indicator-based metal complexes used to determine  $F^-$  previously. Consistency in the performance of the sensing material has been tested with synthetic  $F^-$  standards, water samples from  $F^-$  affected regions, and dental care products like toothpastes and mouthwash using a smartphone attachment and by the naked eye. The sensor performs better than what was reported by prior works on aqueous  $F^-$  sensing.



## 1. INTRODUCTION

Fluoride ( $F^-$ ), having the smallest anionic radius, highest charge density, and a hard Lewis base character, is a naturally occurring anion in groundwater worldwide.<sup>1</sup> It is a double-edged sword, as on the one hand, it is biologically and medically important for its essential roles in proper growth and maintenance of teeth, hair, nails, and bones and treatment of osteoporosis. While on the other hand, overexposure to  $F^-$  can cause dental fluorosis, skeletal fluorosis, kidney, and acute gastric problems.<sup>2</sup> This is because of its unique property of getting easily absorbed in the body, however excreted only slowly. The World Health Organization (WHO) and Environmental Protection Agency (USEPA) have set 1.0–1.5 mg/L (ppm) and 2–4 mg/L, respectively, as its preferred concentration in drinking water.<sup>3,4</sup> The major sources of exposure to fluoride are drinking water, food, dental products, and pesticides. While in USA, artificially fluoridated water (0.7–1.2 mg/L) is supplied to people keeping the necessary dietary intake in mind, on the contrary, population belonging to the contaminated geographical sites get exposed to 6–12 mg/L of  $F^-$ .<sup>4</sup> It is estimated that dental caries is the most prevalent of all conditions because of  $F^-$  poisoning, with 2.4

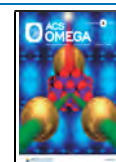
billion people globally suffering from caries of permanent teeth and 486 million children from that of primary teeth.<sup>5–7</sup> Hence, it is essential to develop superior analytical methods for  $F^-$  sensing and quantification for efficient water quality monitoring.

A number of  $F^-$  detection techniques, such as potentiometry,<sup>8</sup>  $^{19}F$  NMR analysis,<sup>8</sup> mass spectrometry,<sup>9</sup> ion chromatography,<sup>9</sup> electrochemical methods,<sup>10</sup> colorimetric methods,<sup>11</sup> and fluorescence-based sensing systems,<sup>11</sup> have been developed over the years.<sup>12</sup> Many of these techniques cannot be used for location-based real-time water quality data collection as they involve cumbersome measurements and are highly dependent on human intervention. Out of them, colorimetric sensing has the advantages of low cost, small size, simplicity,

Received: July 20, 2020

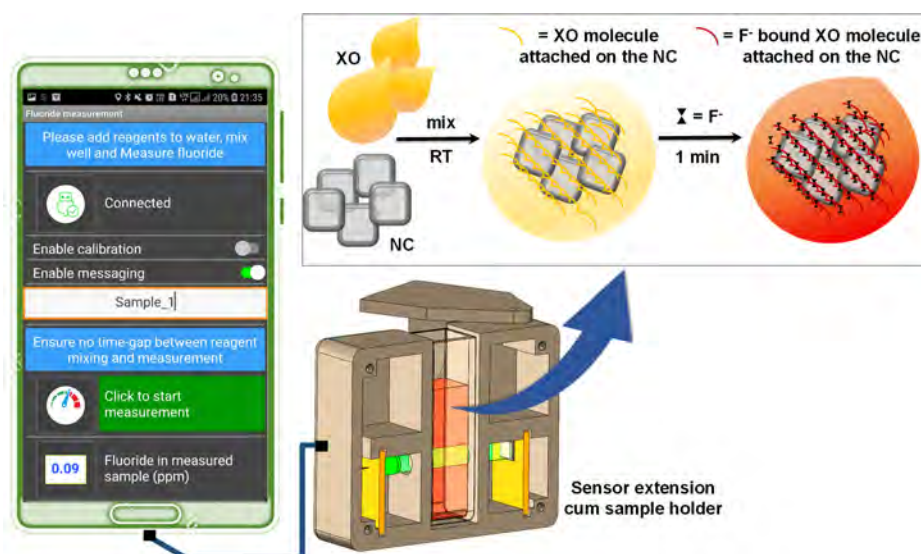
Accepted: September 7, 2020

Published: September 21, 2020





### Scheme 1. Schematic Representation of the Smartphone-Based $F^-$ Sensor and Its Sensing Mechanism Using Near-Cubic Ceria@Zirconia NCs and XO Dye



nondestructive in nature, high selectivity, quick response time, and wide applicability in field conditions.<sup>13</sup> Efficient colorimetric probes must have a receptor with a signaling unit which produces a noticeable physical change upon interaction with the analyte, which can be easily read out with the naked eye or an ultraviolet–visible (UV–vis) spectrophotometer.<sup>14</sup> The sensor molecules and  $F^-$  have been found to interact via different forces like hydrogen bonding, electrostatic interactions, Lewis acid coordination, chemical reaction, and so forth. Molecular detection based on a specific chemical reaction displays higher selectivity and stability than that based on noncovalent interactions.<sup>14</sup> Recently, many nanomaterials, including gold nanoparticles,<sup>15–18</sup>  $CeO_2$  nanoparticles ( $CeO_2$  NPs),<sup>19</sup> semiconductor quantum dots (QDs), carbon QDs,<sup>20</sup> metal–organic frameworks,<sup>21</sup> micellar nanoparticles,<sup>22</sup>  $SiO_2$  nanoparticles ( $SiO_2$  NPs),<sup>23</sup> graphene oxide (GO),<sup>24</sup> and so on, have been used for aqueous  $F^-$  removal and to design a variety of nanosensors because of their large surface areas and well-defined pores, improved solubility, ease of fabrication, low-cost, high sensitivity, and good biocompatibility. The success of a colorimetric method depends largely on the user's perception of colors which may lead to inconsistency in data collection. A few such test kits using lanthanum–alizarin complex, zirconyl-SPADNS reagent, and so on have been commercialized but they largely suffer from high chances of manual errors in interpreting feeble color variations and high cost.<sup>25</sup> Also, they involve serious interferences by anions like sulfate, chloride, and so forth, which compel the use of other chelating reagents, giving rise to expensive and complex multicomponent sensing systems.<sup>26,27</sup> In this direction, systems which are simple, stable, highly sensitive, and selective toward the analyte are of high preference. Moreover, the rapid development of smartphones with various embedded sensors or external sensors (e.g., circuit and probe) integrated with the smartphones for more sophisticated and accurate detection have enabled wide range of applications in environmental and health-related monitoring.<sup>28–30</sup>

We report a smartphone-integrated fluoride sensor platform based on colorimetric detection. The sensor is comprised of core–shell nanocages (NCs) and a chemoresponsive organic

dye for accurate, trace level detection of  $F^-$  in aqueous medium. Briefly, ethylene glycol-coated ceria@zirconia NCs ( $CeO_2@ZrO_2$  NC) with large surface area and high affinity toward  $F^-$  were used as a catalytic platform.<sup>31</sup> The NC system facilitates  $F^-$  interaction with xylenol orange (XO) for its specific recognition at sub-ppm levels. A simple smartphone attachment was developed for colorimetric readout using a combination of a light-emitting diode (LED) and a photodiode, which facilitates precise measurement of  $F^-$  in water samples as shown in Scheme 1. Using this device, we have demonstrated the quantification of  $F^-$  in various real water samples and dental care products within 1 min of reaction time. The device can be operated with an android application which provides instructions to the user as per requirements of the whole process and also provides data storage options such as short message service (SMS) and cloud storage. The consumable cost for  $F^-$  estimation using NC-based assay is ~1 cent/assay.

XO is a well-known indicator, and it has been used as a complexing agent with metals like zirconium/hafnium for determining  $F^-$ , but it gives inconsistent results in several cases. The zirconium–XO complex ( $Zr-XO$ ) shows pH-dependent absorbance values below pH 1.5, and above pH 4, it suffers from serious interference by ions like phosphate and sulfate, and the colored complex has bleaching tendency.<sup>32</sup> Such stability- and selectivity-related issues have been addressed in the following sections. There is a previous report of a mobile-based sensor using a commercial reagent having the  $Zr-XO$  complex.<sup>29</sup> In this, the color changes from pink to yellow when  $F^-$  ions break the metal ion–dye complex to form colorless zirconium fluoride. The sensor used the camera flash light of the smartphone as an optical source to capture and for RGB analysis of the photograph, making it highly dependent on the quality of the mobile device. There is another report on porous  $CeO_2-ZrO_2$  hollow nanosphere powder of ~100 nm diameter for  $F^-$  adsorption.<sup>33</sup> While ceria–zirconia mixed oxide NPs are widely known for their catalytic properties for various gas-phase reactions and oxygen storage capacity,<sup>34</sup> the present work is the first one on core–shell  $CeO_2@ZrO_2$  NC for colorimetric sensing. In our  $F^-$  sensing method, the small

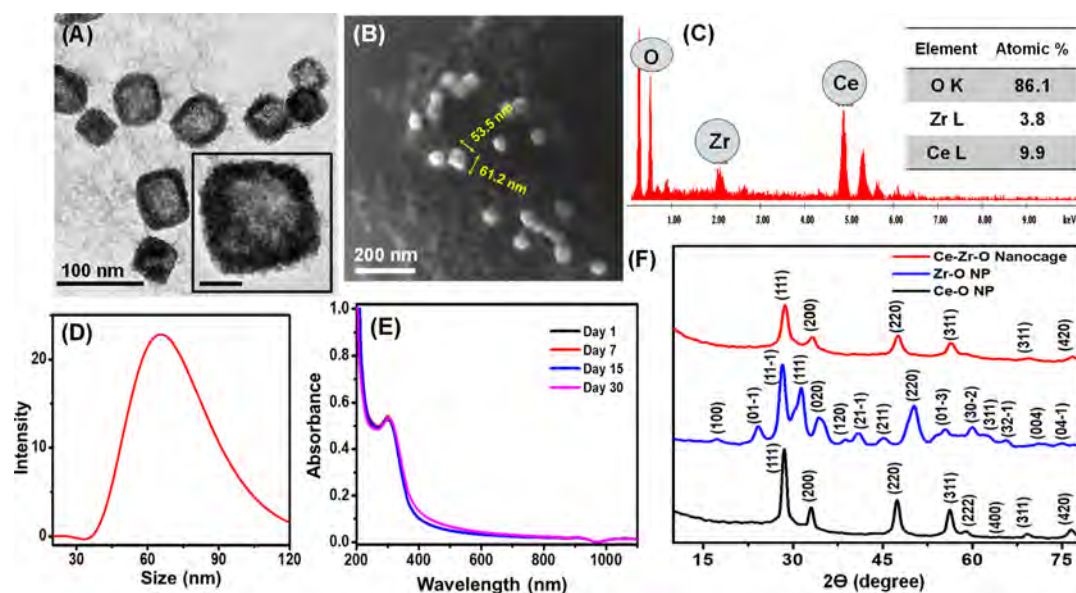


**Figure 1.** (A) TEM image showing the core–shell structure of  $\text{CeO}_2@\text{ZrO}_2$  NC with an HRTEM image in the inset, with a scale bar of 5 nm. (B) FESEM image showing a near cube-like structure. Edge length parameters are shown. (C) EDS showing the elemental composition of NCs. (D) DLS data showing the size range. (E) UV–vis data showing the stability of NCs from day 1–30. (F) XRD patterns of  $\text{CeO}_x$  and  $\text{ZrO}_2$  NPs individually and that of  $\text{CeO}_2@\text{ZrO}_2$  NC.

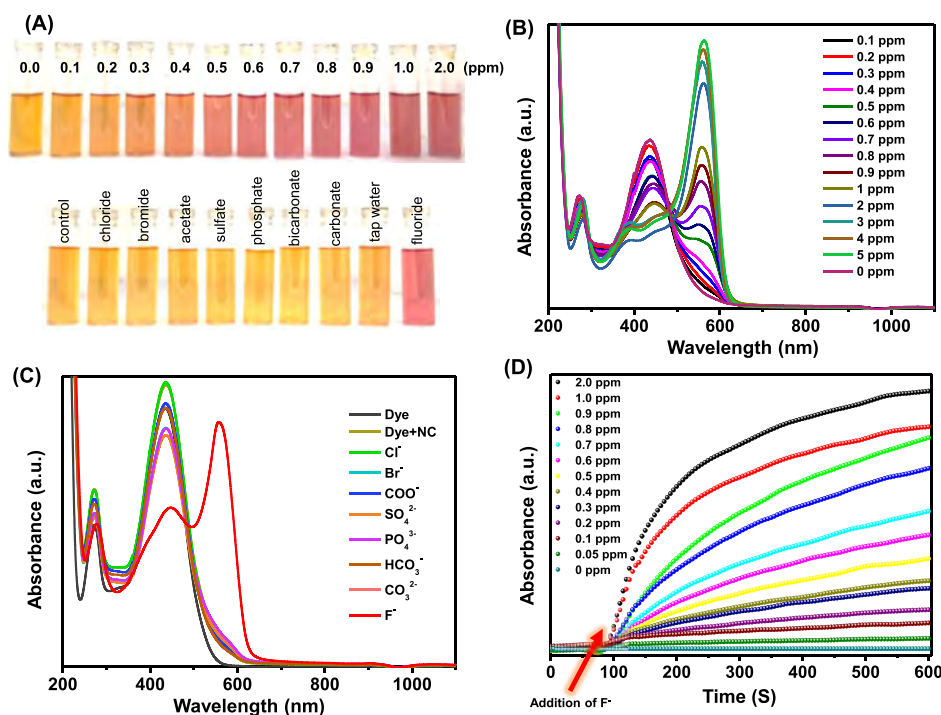


**Figure 2.** (A) Optical images of the colorimetric changes showing sensitivity of NC–XO system toward various  $\text{F}^-$  concentrations and its specificity toward  $\text{F}^-$  as compared to other anions. (B,C) Absorption spectra of the NC–XO system in the presence of various  $\text{F}^-$  concentrations and in the presence of various interfering anions, respectively. (D) Absorbance vs time plot showing kinetics of the interaction between the NC–XO system and various  $\text{F}^-$  concentrations responsible for color change.

smartphone extension plays the key role that can be attached to any mobile device irrespective of its quality as the latter is used only as a user interface for calibration and result display. While color is because of XO, the chemistry leading to the color change is mainly because of NC. Sensor optimization experiments revealed that its sensitivity was highly dependent upon the near-cubic shape of the NCs, and both the

components ( $\text{CeO}_2$  and  $\text{ZrO}_2$ ) were crucial for  $\text{F}^-$  sensing without directly taking part in the reaction with  $\text{F}^-$  ions.

## 2. RESULTS AND DISCUSSION

**2.1. Characterization of NCs.**  $\text{CeO}_2@\text{ZrO}_2$  core–shell nanoparticles were prepared by hydrothermal synthesis which resulted in the formation of near-cubic NC having an edge length of  $55 \pm 5$  nm, as shown in Figure 1B,D. Transmission

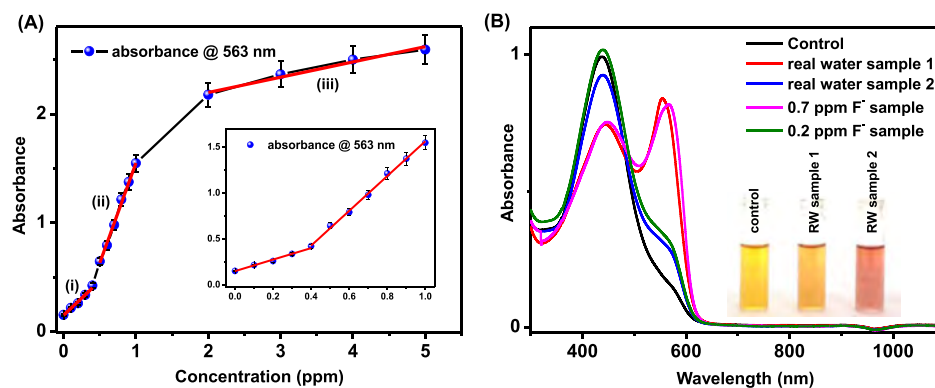


**Figure 3.** (A) Standard curve of absorbance vs concentration (ppm) for the NC–XO sensor response toward  $F^-$  solution (0–5 ppm). Two linear standard regimes in the 0–1 ppm concentration regime are shown in the inset. (B) Absorbance spectra for the sensor for real water samples compared with the response for  $F^-$  standards of the same concentration and an optical image of the colorimetric detection of  $F^-$  in real water samples (inset).

electron microscopy (TEM) images clearly show the core–shell nature of the NCs in Figure 1A. Large-area microscopic images are shown in Figures S1 and S2. Figure 1C shows the elemental composition of the NC showing that ceria, which is in the core, constitutes more than the amount of zirconia, in the shell. Figure 1E depicts the high stability of NCs over a period of one month when stored in ambient atmosphere, as there is no change in the absorption spectrum of the NCs. The powder X-ray diffraction (pXRD) pattern of NC, as shown in Figure 1F, has a cubic crystal system, which got a little broadened upon the formation of core–shell nanostructures with zirconia but mostly matches with that of the cubic phase of ceria, as it is the major constituent. It shows no similarity with the monoclinic system of zirconia which was synthesized as per the same procedure. A slight shift in the diffraction peak positions ( $2\theta = 28.4$ – $28.8^\circ$ ) could be noted for the NCs, which indicates that along with the particle growth, some compositional changes took place because of interphase mixing. Large-area field-emission scanning electron microscopy (FESEM) images of F-treated NC showed aggregation of particles upon interaction with high concentration of  $F^-$  ions (Figure S3).

**2.2. Testing of the NC–XO Sensor System.** Figure 2A shows colorimetric responses of the NC–XO sensor to different concentrations of  $F^-$  after mixing for 1 min at room temperature. The solution-phase NC–XO system turns from yellow to rose-red systematically in the presence of various concentrations of aqueous  $F^-$ , which is clearly observed with naked eyes because of the stark color difference. The red color intensifies as the concentration of  $F^-$  in the sample goes higher, but it gets saturated by 2 ppm  $F^-$  for naked eye detection because of the unavailability of active sites of the dye. Change in the color of the NC–XO system is because of change in the molecular structure of the dye. The absorbance peak of the NC–XO system (XO in acidic medium) is at 435 nm, and a broad peak at 560 nm is formed and eventually intensified after the addition of  $F^-$  to the system, in the 0.1–5 ppm concentration range. The absorption peaks at 280 and 435 nm of XO are because of the  $\Pi$ – $\Pi^*$  and intramolecular charge transfer (ICT) within the molecule, respectively.<sup>35</sup> While the origin of the new peak at 560 nm is because of nucleophilic addition of  $F^-$  to the cationic N-center of the dye leading to adduct formation, reduction in intensity of the 435 nm peak is because of the change in the ICT electronic transition.

Absorptivity coefficients were calculated at the absorbance maxima of 1 mM XO before and after analyte interaction, with 1 cm path length. While  $1.6 \times 10^3 \text{ M}^{-1} \text{ cm}^{-1}$  is the molar absorptivity for NC–XO at 435 nm before analyte interaction,  $0.7 \times 10^3 \text{ M}^{-1} \text{ cm}^{-1}$  (435 nm) and  $2.1 \times 10^3 \text{ M}^{-1} \text{ cm}^{-1}$  (560 nm) are the values for NC–XO after interaction with 2 ppm  $F^-$ . The sensor system has been tested with several common interfering anions present in groundwater in high concentrations like  $Cl^-$ ,  $Br^-$ ,  $COO^-$ ,  $SO_4^{2-}$ ,  $PO_4^{3-}$ ,  $HCO_3^-$ , and  $CO_3^{2-}$  (100 ppm tested), compared with 1 ppm of  $F^-$ , as shown in Figure 2C. None of these anions showed absorbance at 560 nm, which proves specificity of NC–XO toward  $F^-$ . Figure 2D shows the absorption kinetics of the sensor–analyte reaction. The reaction was monitored till 10 min after  $F^-$  solution of various concentrations (0.05–2 ppm) were added to the sensor starting from  $t = 100$  s of initiation. As it is clear from Figure 2D, the rate of change in absorbance is maximum during the first 60–100 s after  $F^-$  addition. After that, although the slope keeps increasing, the rate of change decreases and eventually proceeds toward saturation. In view of the observed kinetics, the operating time for the device was set as 60 s. Temperature-dependent kinetics for the same reaction was also studied for 10, 20, 30, and  $40^\circ\text{C}$  (Figure S4) which indicated that higher temperature would accelerate the rate of reaction, resulting in a spontaneous color change.

On the basis of the absorbance data (Figure 2B), a standard curve of absorbance versus concentration (ppm) was plotted which can be used for the quantification of  $F^-$  content in water as shown in Figure 3A. In the concentration regime of 0.1–1 ppm, we get two linear plots. Two real water samples were obtained from different  $F^-$  affected areas of India, namely, Hanumangarh (Rajasthan,  $29.58^\circ\text{N}$   $74.32^\circ\text{E}$ ) and Jayanagar (Bangalore,  $12.9308^\circ\text{N}$   $77.5838^\circ\text{E}$ ), which were tested with the NC–XO system, as shown in Figure 3B. Using the standard curve, the concentrations of those samples were determined and compared with the absorbance spectra of  $F^-$  standard solutions of the same concentration, which matched exactly. The colorimetric response NC–XO for real water samples can also be well perceived by naked eyes (inset Figure 3B). We note that the entire calibration curve shows three nearly linear regimes (i, ii, and iii). These regions are interpreted because of the mechanism of the sensing process, which will be discussed later.



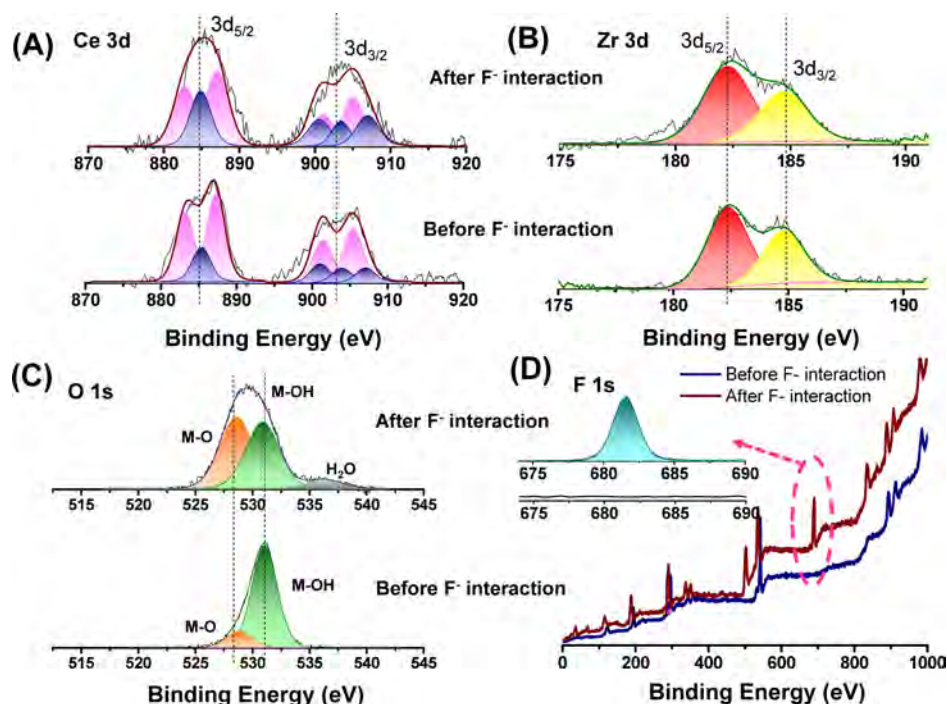


**Figure 4.** (A) Deconvoluted XPS spectra of (A) Ce 3d, (B) Zr 3d, (C) O 1s, and (D) survey spectra of NC–XO before and after interaction with  $F^-$ . The F 1s region is expanded in the inset of (D).

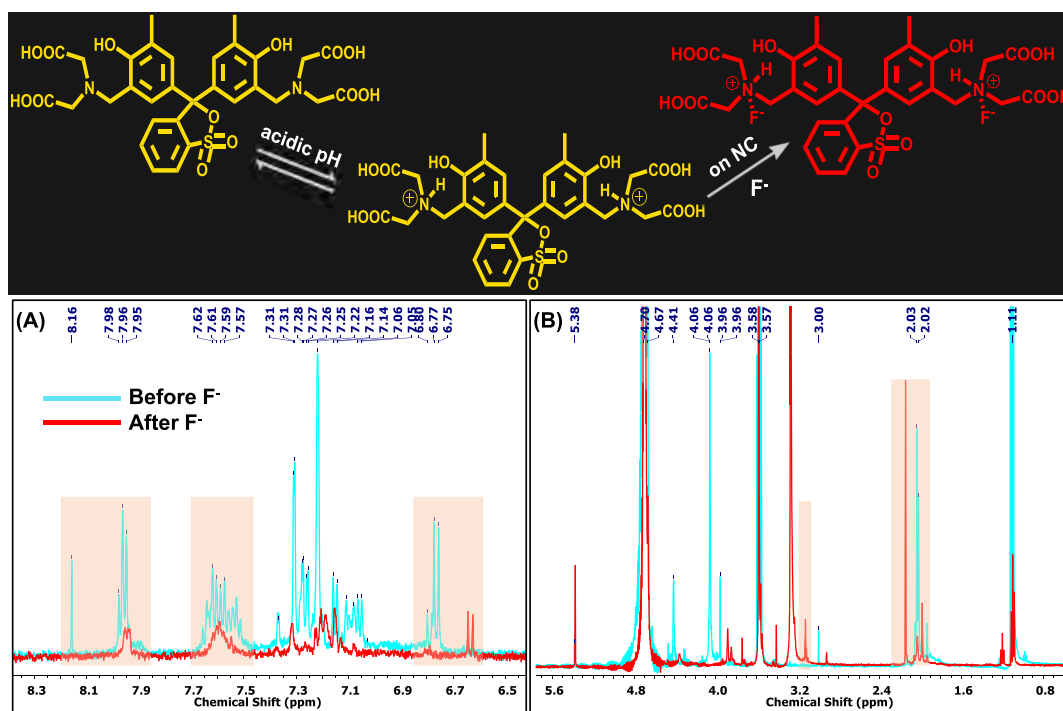


**Figure 5.** Plausible binding mechanism of  $F^-$  with the dye (top). (A,B) shows the zoomed-in regions of overlapping  $^1H$  NMR spectra (500 MHz,  $D_2O$ ) of (i) XO alone before  $F^-$  (in blue) and (ii) NC–XO–F after with  $F^-$  (in red) interaction. Specific regions of relevance are highlighted.

**2.3. Spectroscopic Studies on the Mechanism of Reaction.** X-ray photoelectron spectroscopy (XPS) investigation was carried out to study electronic interactions between the dye-bound NCs and  $F^-$  ions. The XPS samples were prepared by drop-casting (i) NC and (ii) NC–XO–F on specimen stubs, followed by air-drying. Deconvoluted XPS spectra in Figure 4A present a complicated Ce 3d profile of mixed  $Ce^{4+}$ – $Ce^{3+}$  states for partially reduced  $CeO_2$  specimen.

This gives rise to the possible final states,  $Ce\ 3d^9\ 4f^2\ O\ 2p^4$ ,  $Ce\ 3d^9\ 4f^1\ O\ 2p^5$ , and  $Ce\ 3d^9\ 4f^0\ O\ 2p^6$  belonging to  $CeO_2$ , mixed with  $Ce\ 3d^9\ 4f^2\ O\ 2p^4$  and  $Ce\ 3d^9\ 4f^1\ O\ 2p^5$  states belonging to  $Ce_2O_3$  because of overlapping of Ce 4f levels with O 2p in the valence band, during photoemission.<sup>36,37</sup> Two sets of spin-orbit multiplets, corresponding to  $3d_{5/2}$  and  $3d_{3/2}$  contributions show characteristic peaks around 885 and 903 eV, respectively. Set of peaks shaded with blue and pink colors

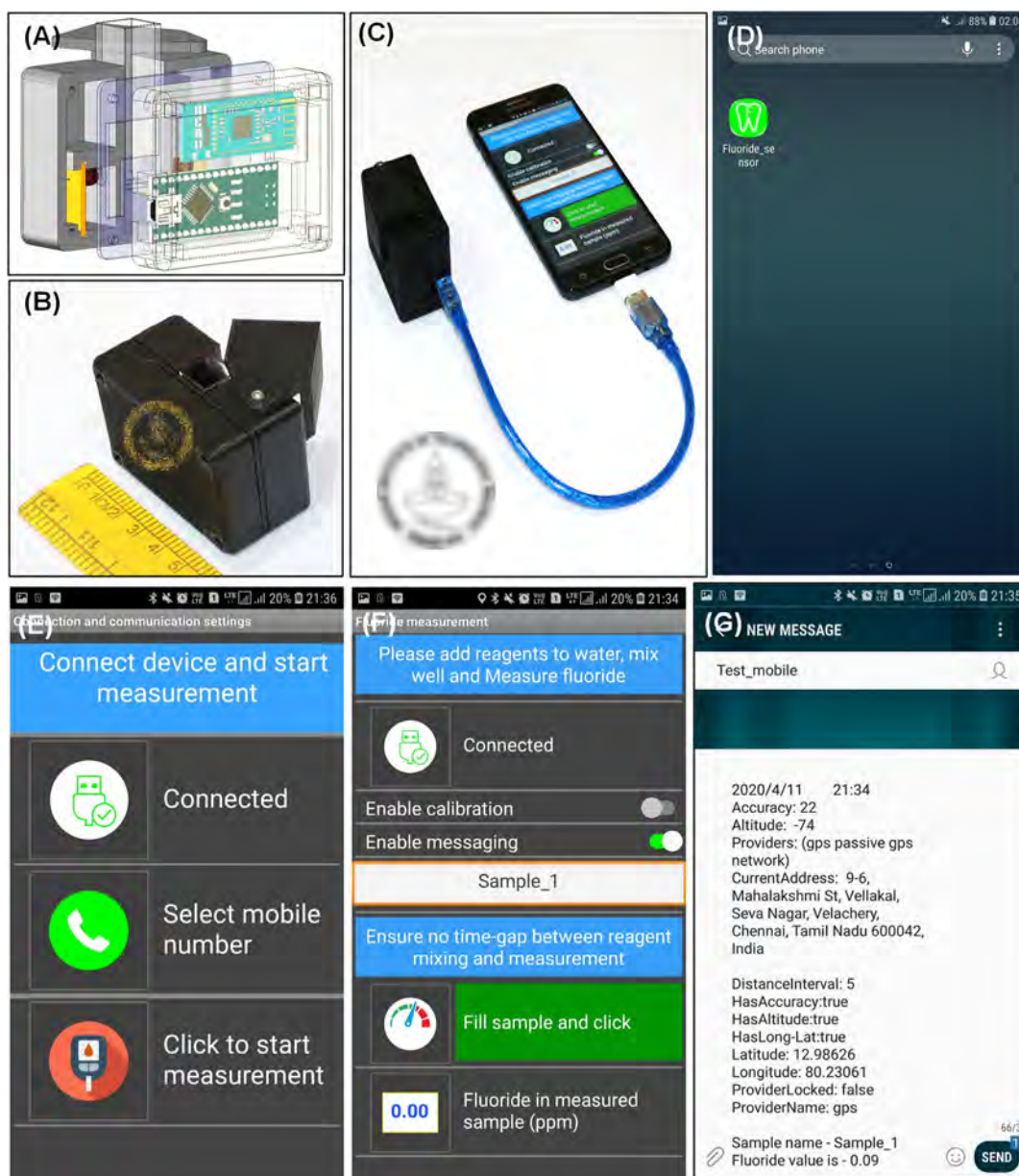


**Figure 6.** (A) Graphical representation of the extended sensor device cum sample holder. (B) Photograph of the sensor extension cum sample holder. (C) Photograph of the  $F^-$  sensor integrated with a smartphone. (D) Icon of the customized mobile application developed for the  $F^-$  sensor. (E,F) Screenshot images of the application of a precalibrated sensor for the detection process and for real-time data sharing and storage; and (G) final screen containing the result and the details related to the sample.

correspond to  $Ce^{4+}$  and  $Ce^{3+}$  oxidation states, respectively. It has been reported that  $F^-$  can modulate the surface charge and facilitate electron transfer of  $CeO_2$  NPs.<sup>19,38</sup> An increase in the blue peak area and decrease in the pink peak area upon interaction with electronegative  $F^-$  ion indicate oxidation of  $Ce^{3+}$  to  $Ce^{4+}$ . The electron binding energies located at 182.6 and 184.8 eV in Figure 4B can be attributed to Zr  $3d_{5/2}$  and  $3d_{3/2}$ , respectively, indicating that Zr is in the +4 valence state in the composite, which gets slightly broadened in the presence of  $F^-$ . Their comparable intensities and insignificant shift in the binding energy suggest that  $F^-$  is not having direct covalent bonding with any of these elements. However, O 1s spectra of NCs in Figure 4C show changes in peak intensities around 528.7 and 530.9 eV upon interaction with  $F^-$ . The decrease in intensity of M–OH is because of the attachment of dye with the –OH groups of the NCs and  $F^-$  ions interact directly with

the dye and not with the core–shell species, which is further proven by NMR analysis. However, addition of the dye to the parent NC increases the overall amount of O in the sample leading to the increase of M–O peak intensity. The XPS survey spectrum (top) in Figure 4D shows the emergence of the F 1s feature after the NCs got exposed to  $F^-$  in solution.

To further understand the  $F^-$  ion binding mechanism with the dye, we have studied  $^1H$  NMR for XO alone (i) and the NC–XO–F system (ii). Figure 5A,B shows the zoomed-in regions of overlapping  $^1H$  NMR spectra of XO before and after fluoride addition, for clarity. The decrease of signal intensity of (ii) in the aromatic region of the  $F^-$  attached XO is because of its interaction with  $CeO_2@ZrO_2$  NC having high electron density, which suggests binding of the dye with NC. The decrease of two COO–H proton integration peaks at the 7.9–8.3 ppm region of (ii) suggests that the dye gets attached to

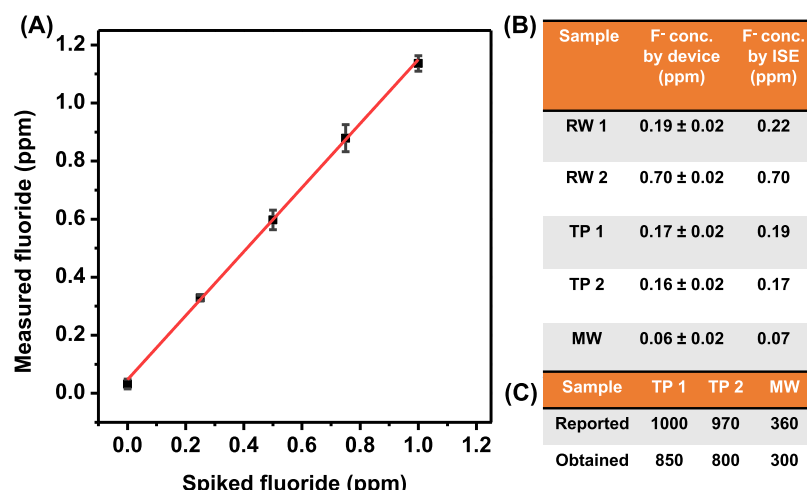


**Figure 7.** Response characteristics of the designed smartphone-based fluoride sensor device. (A) Device response curve for the lower level of spiked  $F^-$  concentrations in the range 0–1.2 ppm. (B) Device output for various real water samples and dental care product samples in the solution phase. TP1, TP2, and MW samples were diluted 5000 times for analysis. (C)  $F^-$  concentration in the as-received dental care products (all values are reported in ppm). See the text for the description of samples.

NC by a condensation reaction of  $-COOH$  (from dye) and  $-OH$  (from NC), by eliminating a water molecule. The alcoholic proton peaks at 6.75 ppm of the dye in (i) got shifted to 6.62 ppm (ii), indicating the shielding of these protons after subsequent binding to NC and  $F^-$ . As XO is acidified during the reagent preparation, addition of proton with each of its nitrogen centers leads to the formation of cationic centers, and this proton peak comes at 3.13 ppm as a singlet peak. Deshielding of the peak at 2.15 ppm in (ii) because of four  $CH_2$  protons is because of the close proximity of cationic nitrogen center and  $F^-$ . It was noted that  $F^-$  addition to the cationic nitrogen did not have any influence on the electron density of the aromatic part. Figure 5 also shows the mechanistic approach of  $F^-$  addition to XO. Approach by the small  $F^-$  ion to the sterically crowded tetravalent cationic N-center is the main reason of its selective sensing ability. The sensor is stable and works well with water samples of wide pH range, till pH 10.5 (Figure S7). However, beyond pH 11, the dye undergoes chemical transformation to give violet color, even in the absence of  $F^-$  in the medium. To confirm this,  $^1H$  NMR of the resultant violet sample was measured which did not match with that of NC–XO–F, as shown in Figure S9. The linear regimes in the standard curve, as shown in Figure 3A, are because of the change in reaction rates depending upon the availability of the amount of cationic N-centers to interact with  $F^-$  ions. Figure S8 shows full-length overlapping  $^1H$  NMR spectra of NC–XO before and after interaction with  $F^-$ .

The IR spectrum of the NC–XO system (Figure S5) shows slight shifts in the C–O and C=O stretching frequencies at 1078 and 1653  $cm^{-1}$  to higher wavenumbers upon interaction with  $F^-$ .

**2.4. Development and Testing of a Smartphone-Based Sensor Device.** Color changes in the NC–XO system is easy for readout with naked eyes. However, when it comes to distinguish color differences at lower concentrations, a precise and error free readout method is required. To enable this, a smartphone-enabled fluoride sensing device has been designed. Instead of laboratory measurements which are mainly electrode-based or focused on the UV–vis spectral scan, principle of the measurement using this device is based on monitoring the initial kinetics of the change in absorbance of

the NC–XO system. Unlike a spectral scan or single-point absorbance measurement, kinetics-based scan minimizes manual errors because of variation in time taken for sample preparation. This is possible because initial rate of change of absorbance is constant and almost linear for  $\sim 100$  s after  $F^-$  addition, as shown in Figure 2D. Because of this, rate of change measured within the initial  $\sim 60$  s time window remains constant for a specific  $F^-$  concentration.

The black-colored device was made by 3-D printing the polylactic acid polymer with 1.75 mm feed extruder using Dremmer Flashforge 3D printer. To lower the cost of the device, additional optics and use of sophisticated optical filters have been avoided. Instead of using a collimation lens, already collimated 565 nm LED (TLHG5800) with a typical luminous intensity of 700 mcd at 2.4 V has been used for illuminating the sample. For signal collection, a photodiode (TEMDS510FX01) with angle of half sensitivity  $\sim 65^\circ$  has been used so that signal from larger area can be collected without applying any focusing lens. The selected photodiode has spectral sensitivity in the region of 430–610 nm which is suitable for signal collection at 565 nm. LED and photodiode were interfaced with the smartphone using the Arduino-nano microcontroller and HC05 Bluetooth communication board (Figure 6A,B). However, to avoid battery usage, the device was powered through On-The-Go cable connected with the nanoboard (Figure 6C). A plastic cuvette was used for ease of handling and safety during field measurements. An android application “Fluoride\_sensor” was developed using the MIT app inventor 2 program to operate the device.<sup>39</sup> App is designed to work in a few simple steps based on the requirement of one time calibration before measurements. It is self-instructive as it informs user the next steps to be performed during the measurements. Typical workflow involves the following steps: click on app icon, connect with the device via bluetooth, enable calibration, select SMS options for data sharing, sample loading as per the instructions prompted by app, and finally, the recorded data (along with other relevant information) appears as SMS on the screen (Figure 6D–G, respectively). Screenshots of the workflow are provided in Figure S10. During measurements, mixture of 500  $\mu L$  of NC and 1 mM XO 1:1 (v/v) ratio was loaded into the



Table 1. Comparison of Performance Parameters between Various Studies for the F<sup>−</sup> Sensors

Sl no.	colorimetric probe	medium	detection range (ppm)	LOD (ppm)	reaction time (min)	refs
1	gold nanoparticles	DMF/phosphate buffer	2.3–28.4	2.3	15	42
2	gold nanoparticles	aqueous/EDTA	0.5–7	0.4	240	43
3	sensors based on benzohydrazide	DMSO	na	0.5	na	44
4	PAA–gold NPs/Al <sup>3+</sup>	Aqueous	0.1–2.8	0.04	10	45
5	boronic acid molecular sensor	Aqueous	0.1–1.5	0.1	na	46
6	ceria nanoparticles	aqueous/ABTS + acetate buffer	0–1.9	0.01	30	47
7	GO-SPS	aqueous/Tris-HCl buffer	0.1–1.9	0.01	30	48
8	Akvo Caddisfly	aqueous	0–2.0	0.1	1	29
9	Pocket Colorimeter II for fluoride (Hach) [zirconium-SPADNS]	aqueous	0.1–2.0	0.1	na	49
10	CeO <sub>2</sub> @ZrO <sub>2</sub> NC–XO	aqueous	0.1–5.0	0.06	1	this work

cuvette to which 2.5 mL of water sample need to be added. A simple three-point calibration can be done using 0, 0.5, and 1 ppm fluoride samples in deionized water. If no calibration is performed, the app uses fitting parameters from the previous calibration data.

The sensor device were repeatedly tested with various lab-prepared and field-collected fluoridated aqueous samples and dental products. Absorbance was also recorded for the response of NC–XO with the same samples, as shown in Figure S6. Two real water samples RW1 and RW2 were collected from the field in states located at two different parts of India, while dental care products included two toothpastes (TP1 and TP2) and a mouthwash, commercially available. Fluoridated toothpastes are used globally to ensure adequate fluoride bioavailability in the oral cavity during tooth brushing and their fluoride content must be chemically free and not bound with the abrasive used in the toothpaste formulation. So, the free fluoride content should be regularly checked in these products. For our analysis, the environmental water samples were having TDS values of 600–800 ppm that showed no interference with the F<sup>−</sup> measurement. However, water samples having higher turbidity and TDS > 2000 ppm can be pretreated by passing through a prefilter to get suitable sample for F<sup>−</sup> estimation. The dental care products were dissolved in water as per the reported procedure, and the resulting solutions were tested by the sensor device.<sup>40,41</sup> Before testing the samples, the device was calibrated and tested for various F<sup>−</sup> concentrations to check its accuracy which is shown in Figure 7A. Each of the samples were tested by keeping reaction time as 1 min. The F<sup>−</sup> content in each of them was also measured with the ion-selective electrode (ISE), which is applicable for only one specific target ion, for performance comparison, as shown in Figure 7B. The sensor parameters have also been compared to those of the reported materials and commercial sensors in Table 1. It clearly shows better performance in terms of limit of detection (LOD), concentration range of detection, and reaction time than most of the reported sensors.

To understand the importance of the choice of the sensing material in terms of its composition and shape, control experiments were performed with the zirconium–XO complex,<sup>29</sup> ZrO<sub>2</sub> NP–XO, CeO<sub>2</sub> NP–XO, and spherical CeO<sub>2</sub>@ZrO<sub>2</sub> core–shell–XO systems. Their colorimetric response toward 0, 0.1, 1, and 10 ppm F<sup>−</sup> were observed by the naked eye, as shown in Figure S11. While the zirconium–XO complex showed slight color change from pink to its lighter shade at 10 ppm, ZrO<sub>2</sub> or CeO<sub>2</sub> nanoparticles with XO systems did not show any significant color change even till 10

ppm. Instant and profound colorimetric response was observed in the case of the spherical CeO<sub>2</sub>@ZrO<sub>2</sub> core–shell–XO system, showing extremely high reactivity toward F<sup>−</sup> but regulating its rate of reaction was found difficult. Comparing these outcomes, it was concluded that not only the presence of both ceria and zirconia in the nanoscale regime was essential to detect lower F<sup>−</sup> concentrations, but the surface area of the nanomaterial is also an important factor for the selection of a suitable sensing material. Near-cubic CeO<sub>2</sub>@ZrO<sub>2</sub> NCs showed the optimum reaction kinetics and sensitivity; hence, they were chosen for the F<sup>−</sup> sensor. We believe that other nanoshell shapes such as spheres will also be effective in this context.

**2.5. Potential Nanoparticle Toxicity.** Two major considerations for NP toxicity are (1) size relative to their bulk counterparts and (2) mechanisms associated with capping agents leading to their uptake in biological systems. Generally, because of smaller sizes (and thus greater reactivities) of NPs, they are considered to lead to higher toxicity.<sup>50</sup> It is reported that handling dry powders (of nano cerium oxides), dry aggregates, and consolidated powders or granules have greater potential for dermal and inhalation exposure on workers than dispersions.<sup>51</sup> Also, the application of stabilizers prevents agglomeration-induced toxicity by increasing the stability of the suspension.<sup>52</sup> In our case, NCs of less than 75 nm size have been synthesized with the capping of ethylene glycol, resulting in stable and uniform ethanolic dispersion of NPs. In addition, they are used for sensing experiments in small quantities (125 μL of dispersion having about 80 μg of nanomaterials for each test), making their impact on environment less significant. However, the resultant mixture post individual tests can be stored in a leak-free container till it becomes some quantity. Then, the mixture containing CeO<sub>2</sub>@ZrO<sub>2</sub> nanoparticles and adsorbed XO dye can be treated with H<sub>2</sub>O<sub>2</sub> for dye degradation by chemical oxidation process, at room temperature. The degradation efficiency of peroxide is expected to be higher because of catalytic activity in the presence of the CeO<sub>2</sub>@ZrO<sub>2</sub> nanoparticles, as per literature.<sup>53</sup> On keeping the treated mixture as it is for a week, the adsorbed peroxide over the surface of the nanoparticles would diffuse into the aqueous bulk solvent giving a clean nanoparticle surface. However, the reusability of the nanoparticles for the purpose of sensing needs to be tested in the laboratory condition. The volume being handled, including other consumables used for sensing, is small, and therefore, potential environmental risk is minimized.

**2.6. Practical Aspects.** The cost of detection was estimated to be 7 cents/10 assay, and the smartphone attachment is estimated to cost US\$ 5 (excluding the phone), which taken together is orders of magnitude less expensive than commercial fluoride sensors. Major advantage of this nanoparticle-based sensor is that it minimizes the amount of reagents and sample consumption needed for each test, thereby reducing waste generation. Using the catalytic platform imparted by the nanoparticles, a LOD of 0.06 ppm was achieved. Metal-oxide nanoparticles are easy to handle, as they are stable entities and exhibit higher shelf-life. Further, the process does not involve the use of extra buffer media or corrosive acids, toxic chemicals like sodium arsenite to remove interference, and avoids mixed solvent systems to accelerate sensor performance. All of these make it simple and user-friendly compared to the commercially available  $F^-$  test kits. Moreover, this device does not involve purchase of any expensive display interface dedicated only to  $F^-$  measurement. The smartphone app and sensor extension are built in a way such that they can be modified easily for the detection of other contaminants, just by changing the active reagents.

### 3. CONCLUSIONS

In conclusion, we developed a cost-effective, field-deployable, and integrated sensing platform installed on a smartphone for fluoride detection and quantification with a high degree of sensitivity and specificity. The bicomponent sensing material was prepared using a mixture of near-cubic ceria–zirconia NC and XO dye, which rapidly changes color from yellow to red upon interaction with fluoride down to sub-ppm levels. The NCs have been thoroughly characterized for their properties and shelf life, and the sensing mechanism has been studied in detail by XPS and NMR spectroscopies. The sensing material has been tested against high concentrations of other common anions likely to be present in natural waters which gave negative results and proved its selectivity toward  $F^-$ . The smartphone reader was integrated to an external sensing attachment consisting of an LED and a photodiode-based optical setup for the estimation of the  $F^-$  content, having an LOD of 0.06 ppm. We demonstrated consistent performance of this portable sensor for simultaneous detection and quantification in environmental field water samples and various dental care products at a cost of less than 1 cent/assay. The aspects such as shape-dependent sensitivity and environmental impact of the nanomaterial used have been also explored.

### 4. EXPERIMENTAL SECTION

**4.1. Materials.** Zirconium oxychloride octahydrate ( $ZrOCl_2 \cdot 8H_2O$ ), cerium nitrate hexahydrate ( $Ce(NO_3)_6 \cdot 6H_2O$ ), XO sodium salt (XO), and ethylene glycol were purchased from Loba Chemie, SRL chemicals and Merck, respectively. Ethanol was procured from Changshu Chemicals, while hydrochloric acid and sodium fluoride were supplied by Hi-media. All synthesis and control experiments were done using distilled water.

**4.2. Methods.** **4.2.1. Preparation of NCs.** The  $CeO_2@ZrO_2$  core–shell NCs were synthesized by suitable modification of a reported procedure which involves the growth of  $ZrO_2$  on the colloidal seed of  $CeO_2$  nanoparticles.<sup>31</sup> 1 mL of 0.5 M cerium nitrate was mixed in 30 mL ethylene glycol and 3 mL water inside a hydrothermal bomb. The reaction mixture was heated at 180 °C for 12 h. After the temperature came

down to room temperature, 0.3 mL of 0.5 M zirconium oxychloride is added and again heated at 180 °C for 8 h. The resultant solution was centrifuged at 5000 rpm for 5 min, washed, and redispersed in ethanol. NCs were characterized by TEM, FESEM, energy-dispersive spectroscopy (EDS), XPS, dynamic light scattering (DLS), and XRD techniques.

**4.2.2. Preparation of XO Dye Solution.** 2 mL of 1 mM XO solution in water was taken to which 20  $\mu$ L of concentrated hydrochloric acid was added to obtain yellow color starting from violet. The acidified solution was kept undisturbed for 4 h and then diluted with water in 1:1 ratio.

**4.2.3. Procedure for Colorimetric Sensing.** Ethanolic dispersion of NCs and an acidic solution of the dye were mixed in 1:1 (v/v) ratio and added to 2.5 mL of  $F^-$ -contaminated water to observe the color change from yellow to red. Same steps are followed for absorbance and device-based experiments. The sensor responses were compared with ISE results for field samples and dental care products.

**4.3. Instrumentation.** Absorbance spectra were measured using a PerkinElmer Lambda 365 instrument in the range of 200–1100 nm. TEM and high-resolution TEM (HRTEM) were performed at an accelerating voltage of 200 kV on a JEOL 3010, 300 kV instrument equipped with a UHR polepiece. The accelerating voltage was kept low to ensure that beam-induced damage on the material was low. The samples for HRTEM were prepared as dispersions which were drop-casted on carbon-coated copper grids and allowed to dry under ambient conditions. FESEM (Tescan-Mira 3 LMH) imaging was done in high vacuum and low vacuum (up to 500 Pa) conditions with accelerating voltage from 50 V to 30 kV and 20 ns to 10 ms per pixel scanning speed. EDS was done by using FEI Quanta 200, typically at 20 kV acceleration voltage. XPS measurements were done using an ESCA Probe TPD spectrometer of Omicron Nanotechnology. Polychromatic Mg K $\alpha$  was used as the X-ray source ( $h\nu = 1253.6$  eV). Samples were spotted as drop-cast films on a sample stub. Constant analyzer energy of 20 eV was used for the measurements. Binding energy was calibrated with respect to C 1s at 284.8 eV. Residual fluoride concentration in water was measured (using TISAB) by a fluoride-ion selective electrode (ION 2700, Eutech Instruments). Device fabrication details are presented in the main text.

### ■ ASSOCIATED CONTENT

#### Supporting Information

The Supporting Information is available free of charge at <https://pubs.acs.org/doi/10.1021/acsomega.0c03465>.

Large-area TEM and FESEM of NC before and after  $F^-$  interaction, temperature-dependent kinetic plots for the interaction of NC–XO with  $F^-$ , IR spectra of NC–XO before and after interaction with  $F^-$ , absorbance plot of NC–XO response toward various fluoridated dental care products and the consequent standard curve, absorbance plot of NC–XO response toward  $F^-$  at different pH, full length overlapping  $^1H$  NMR spectra of NC–XO before and after interaction with  $F^-$ , full length  $^1H$  NMR spectrum of XO at high pH, workflow for using the  $F^-$  sensor app for sample measurement, and optical images of control experiments using with the zirconium–XO complex,  $ZrO_2$  NP–XO,  $CeO_2$  NP–XO, and spherical  $CeO_2@ZrO_2$  NC–XO systems for 0, 0.1, 1, and 10 ppm of  $F^-$  (PDF)

## ■ AUTHOR INFORMATION

## Corresponding Author

**Thalappil Pradeep** – DST Unit of Nanoscience (DST UNS) and Thematic Unit of Excellence (TUE), Department of Chemistry, Indian Institute of Technology Madras, Chennai 600036, India; [orcid.org/0000-0003-3174-534X](https://orcid.org/0000-0003-3174-534X); Phone: +91-44 2257 4208; Email: [pradeep@iitm.ac.in](mailto:pradeep@iitm.ac.in); Fax: +91-44 2257 0545/0509

## Authors

**Sritama Mukherjee** – DST Unit of Nanoscience (DST UNS) and Thematic Unit of Excellence (TUE), Department of Chemistry and EWRE Division, Department of Civil Engineering, Indian Institute of Technology Madras, Chennai 600036, India

**Manav Shah** – DST Unit of Nanoscience (DST UNS) and Thematic Unit of Excellence (TUE), Department of Chemistry, Indian Institute of Technology Madras, Chennai 600036, India

**Kamalesh Chaudhari** – DST Unit of Nanoscience (DST UNS) and Thematic Unit of Excellence (TUE), Department of Chemistry, Indian Institute of Technology Madras, Chennai 600036, India

**Arijit Jana** – DST Unit of Nanoscience (DST UNS) and Thematic Unit of Excellence (TUE), Department of Chemistry, Indian Institute of Technology Madras, Chennai 600036, India

**Chennu Sudhakar** – DST Unit of Nanoscience (DST UNS) and Thematic Unit of Excellence (TUE), Department of Chemistry, Indian Institute of Technology Madras, Chennai 600036, India

**Pillalamarri Srikrishnarka** – DST Unit of Nanoscience (DST UNS) and Thematic Unit of Excellence (TUE), Department of Chemistry, Indian Institute of Technology Madras, Chennai 600036, India; [orcid.org/0000-0001-5187-6879](https://orcid.org/0000-0001-5187-6879)

**Md Rabiul Islam** – DST Unit of Nanoscience (DST UNS) and Thematic Unit of Excellence (TUE), Department of Chemistry, Indian Institute of Technology Madras, Chennai 600036, India

**Ligy Philip** – EWRE Division, Department of Civil Engineering, Indian Institute of Technology Madras, Chennai 600036, India; [orcid.org/0000-0001-8838-2135](https://orcid.org/0000-0001-8838-2135)

Complete contact information is available at:

<https://pubs.acs.org/10.1021/acsomega.0c03465>

## Notes

The authors declare no competing financial interest.

## ■ ACKNOWLEDGMENTS

The authors thank Ramesh Kumar, IIT Madras, for helping to access 3-D printing facility; the Common facility, Department of Chemistry, IIT Madras, for pXRD and NMR measurements. The authors also thank the FESEM facility of CeNS, Bangalore, and Biswajit Mondal, IIT Madras, for TEM imaging. Authors thank the Department of Science and Technology, Government of India, for supporting our research program on nanotechnology for clean water.

## ■ REFERENCES

- (1) Jagtap, S.; Yenkie, M. K.; Labhsetwar, N.; Rayalu, S. Fluoride in Drinking Water and Defluoridation of Water. *Chem. Rev.* **2012**, *112*, 2454–2466.
- (2) Ayooob, S.; Gupta, A. K. Fluoride in Drinking Water: A Review on the Status and Stress Effects. *Crit. Rev. Environ. Sci. Technol.* **2006**, *36*, 433.

(3) *Fluoride in Drinking-Water Background Document for Development of WHO Guidelines for Drinking-Water Quality*; World Health Organization, 2004.

(4) National Research Council. *Fluoride in Drinking Water*; National Academies Press, 2006.

(5) Trieu, A.; Mohamed, A.; Lynch, E. Silver Diamine Fluoride versus Sodium Fluoride for Arresting Dentine Caries in Children: A Systematic Review and Meta-Analysis. *Sci. Rep.* **2019**, *9*, 1–9.

(6) Jia, B.; Zong, L.; Lee, J. Y.; Lei, J.; Zhu, Y.; Xie, H.; Clemens, J. L.; Feller, M. C.; Na, Q.; Dong, J.; et al. Maternal Supplementation of Low Dose Fluoride Alleviates Adverse Perinatal Outcomes Following Exposure to Intrauterine Inflammation. *Sci. Rep.* **2019**, *9*, 2575.

(7) Featherstone, J. D. B. Prevention and Reversal of Dental Caries: Role of Low Level Fluoride. *Community Dent. Oral Epidemiol.* **1999**, *27*, 31–40.

(8) Mao, S.; Chang, J.; Zhou, G.; Chen, J. Nanomaterial-Enabled Rapid Detection of Water Contaminants. *Small* **2015**, *11*, 5336–5359.

(9) Kim, H. N.; Guo, Z.; Zhu, W.; Yoon, J.; Tian, H. Recent Progress on Polymer-Based Fluorescent and Colorimetric Chemosensors. *Chem. Soc. Rev.* **2011**, *40*, 79–93.

(10) Bhandodkar, A. J.; Wang, J. Non-Invasive Wearable Electrochemical Sensors: A Review. *Trends Biotechnol.* **2014**, *32*, 363–371.

(11) Gilardi, G.; Zhou, L. Q.; Hibbert, L.; Cass, A. E. G. Engineering the Maltose Binding Protein for Reagentless Fluorescence Sensing. *Anal. Chem.* **1994**, *66*, 3840–3847.

(12) Ji, H.-F.; Thundat, T.; Dabestani, R.; Brown, G. M.; Britt, P. F.; Bonnesen, P. V. Ultrasensitive Detection of CrO4<sup>2-</sup> Using a Microcantilever Sensor. *Anal. Chem.* **2001**, *73*, 1572–1576.

(13) Guo, Y.; Li, J.; Chai, S.; Yao, J. Nanomaterials for the Optical Detection of Fluoride. *Nanoscale* **2017**, *9*, 17667–17680.

(14) Zhou, Y.; Zhang, J. F.; Yoon, J. Fluorescence and Colorimetric Chemosensors for Fluoride-Ion Detection. *Chem. Rev.* **2014**, *114*, 5511–5571.

(15) Du, J.; Jiang, L.; Shao, Q.; Liu, X.; Marks, R. S.; Ma, J.; Chen, X. Colorimetric Detection of Mercury Ions Based on Plasmonic Nanoparticles. *Small* **2013**, *9*, 1467–1481.

(16) Liu, Y.; Ai, K.; Cheng, X.; Huo, L.; Lu, L. Gold-Nanocluster-Based Fluorescent Sensors for Highly Sensitive and Selective Detection of Cyanide in Water. *Adv. Funct. Mater.* **2010**, *20*, 951–956.

(17) George, A.; Shibu, E. S.; Maliyekkal, S. M.; Bootharaju, M. S.; Pradeep, T. Luminescent, Freestanding Composite Films of Au 15 for Specific Metal Ion Sensing. *ACS Appl. Mater. Interfaces* **2012**, *4*, 639–644.

(18) Saha, K.; Agasti, S. S.; Kim, C.; Li, X.; Rotello, V. M. Gold Nanoparticles in Chemical and Biological Sensing. *Chem. Rev.* **2012**, *112*, 2739–2779.

(19) Liu, B.; Huang, Z.; Liu, J. Boosting the Oxidase Mimicking Activity of Nanoceria by Fluoride Capping: Rivaling Protein Enzymes and Ultrasensitive F<sup>-</sup> Detection. *Nanoscale* **2016**, *8*, 13562–13567.

(20) Guo, Y.; Zhang, L.; Zhang, S.; Yang, Y.; Chen, X.; Zhang, M. Fluorescent Carbon Nanoparticles for the Fluorescent Detection of Metal Ions. *Biosens. Bioelectron.* **2015**, *63*, 61–71.

(21) Ebrahim, F. M.; Nguyen, T. N.; Shyshkanov, S.; Gladysiak, A.; Favre, P.; Zacharia, A.; Itskos, G.; Dyson, P. J.; Stylianou, K. C. Selective, Fast-Response, and Regenerable Metal-Organic Framework for Sampling Excess Fluoride Levels in Drinking Water. *J. Am. Chem. Soc.* **2019**, *141*, 3052.

(22) Hu, J.; Dai, L.; Liu, S. Analyte-Reactive Amphiphilic Thermoresponsive Diblock Copolymer Micelles-Based Multifunctional Ratiometric Fluorescent Chemosensors. *Macromolecules* **2011**, *44*, 4699–4710.

(23) Xu, R.-X.; Yu, X.-Y.; Gao, C.; Jiang, Y.-J.; Han, D.-D.; Liu, J.-H.; Huang, X.-J. Non-Conductive Nanomaterial Enhanced Electrochemical Response in Stripping Voltammetry: The Use of Nanostructured Magnesium Silicate Hollow Spheres for Heavy Metal Ions Detection. *Anal. Chim. Acta* **2013**, *790*, 31–38.



- (24) Melaimi, M.; Gabbai, F. P. A Heteronuclear Bidentate Lewis Acid as a Phosphorescent Fluoride Sensor. *J. Am. Chem. Soc.* **2005**, *127*, 9680–9681.
- (25) Bellack, E.; Schouboe, P. J. Rapid Photometric Determination of Fluoride in Water: Use of Sodium 2-(p-Sulfophenylazo)-1,8-Dihydroxynaphthalene-3,6-Disulfonate-Zirconium Lake. *Anal. Chem.* **1958**, *30*, 2032–2034.
- (26) SPADNS Zirconium Lake method. <https://www.epa.gov/ttnemc01/qahandbook3/qaiiii1977/qavoliii-aug1977-sec3-10.pdf> (accessed March 26, 2020).
- (27) Fluoride Test Kit Method. <http://www.thermo.com.cn/Resources/201307/9131927687.pdf> (accessed March 26, 2020).
- (28) Hussain, I.; Ahamad, K. U.; Nath, P. Low-Cost, Robust, and Field Portable Smartphone Platform Photometric Sensor for Fluoride Level Detection in Drinking Water. *Anal. Chem.* **2017**, *89*, 767–775.
- (29) Levin, S.; Krishnan, S.; Rajkumar, S.; Halery, N.; Balkunde, P. Monitoring of Fluoride in Water Samples Using a Smartphone. *Sci. Total Environ.* **2016**, *551*–*552*, 101–107.
- (30) Balan Pillai, A.; Varghese, B.; Madhusoodanan, K. N. Design and Development of Novel Sensors for the Determination of Fluoride in Water. *Environ. Sci. Technol.* **2012**, *46*, 404–409.
- (31) Liang, X.; Wang, X.; Zhuang, Y.; Xu, B.; Kuang, S.; Li, Y. Formation of CeO<sub>2</sub>-ZrO<sub>2</sub> Solid Solution Nanocages with Controllable Structures via Kirkendall Effect. *J. Am. Chem. Soc.* **2008**, *130*, 2736–2737.
- (32) Yuchi, A.; Hokari, N.; Wada, H.; Nakagawa, G. Semi-xylene orange complex of zirconium(IV) as a photometric reagent system for fluoride based on mixed ligand complex formation. *Analyst* **1993**, *118*, 219–222.
- (33) Wang, J.; Xu, W.; Chen, L.; Jia, Y.; Wang, L.; Huang, X.-J.; Liu, J. Excellent Fluoride Removal Performance by CeO<sub>2</sub>-ZrO<sub>2</sub> Nanocages in Water Environment. *Chem. Eng. J.* **2013**, *231*, 198–205.
- (34) Devaiah, D.; Reddy, L. H.; Park, S.-E.; Reddy, B. M. Ceria–Zirconia Mixed Oxides: Synthetic Methods and Applications. *Catal. Rev.* **2018**, *60*, 177–277.
- (35) Belleza, O. J. V.; Villaraza, A. J. L. Ion Charge Density Governs Selectivity in the Formation of Metal-Xylene Orange (M-XO) Complexes. *Inorg. Chem. Commun.* **2014**, *47*, 87–92.
- (36) Handbook of Surface and Interface Analysis: Methods for Problem-Solving. <https://books.google.co.in/books?id=2F3QKUB-ZfAC&pg=PA169&lpg=PA169&dq=ce+4f+levels+overlaps+with+o+2p+orbitals&source=bl&ots=7jtEdF1XNs&sig=ACfU3U1ikqhQEIOFFEZwwFR-PGh9rlYQlQ&hl=en&sa=X&ved=2ahUKEw-jzdfR65ToAhVC4jgGHatiCL8Q6AEwA3oECAgQAQ#v=onepage&q=ce4flevelsoverlapswitho2porbitals&f=false> (accessed March 12, 2020).
- (37) Maslakov, K. I.; Teterin, Y. A.; Ryzhkov, M. V.; Popel, A. J.; Teterin, A. Y.; Ivanov, K. E.; Kalmykov, S. N.; Petrov, V. G.; Petrov, P. K.; Farnan, I. The Electronic Structure and the Nature of the Chemical Bond in CeO<sub>2</sub>. *Phys. Chem. Chem. Phys.* **2018**, *20*, 16167.
- (38) Shoko, E.; Smith, M. F.; McKenzie, R. H. Mixed Valency in Cerium Oxide Crystallographic Phases: Valence of Different Cerium Sites by the Bond Valence Method. *Phys. Rev. B: Condens. Matter Mater. Phys.* **2009**, *79*, 134108.
- (39) MIT App Inventor|Explore MIT App Inventor. <https://appinventor.mit.edu/> (accessed March 12, 2020).
- (40) Daines, T. L.; Morse, K. W. A Spectrophotometric Determination of Fluoride Adapted for the Freshman Laboratory. *J. Chem. Educ.* **1974**, *51*, 680–681.
- (41) Reshetnyak, V. Y.; Nesterova, O. V.; Admakin, O. I.; Dobrokhoto, D. A.; Avertseva, I. N.; Dostdar, S. A.; Khakimova, D. F. Evaluation of Free and Total Fluoride Concentration in Mouthwashes via Measurement with Ion-Selective Electrode. *BMC Oral Health* **2019**, *19*, 251.
- (42) Gu, J.-A.; Lin, Y.-J.; Chia, Y.-M.; Lin, H.-Y.; Huang, S.-T. Colorimetric and bare-eye determination of fluoride using gold nanoparticle agglomeration probes. *Microchim. Acta* **2013**, *180*, 801–806.
- (43) Sun, J.-F.; Liu, R.; Zhang, Z.-M.; Liu, J.-F. Incorporation of the fluoride induced SiO bond cleavage and functionalized gold nanoparticle aggregation into one colorimetric probe for highly specific and sensitive detection of fluoride. *Anal. Chim. Acta* **2014**, *820*, 139–145.
- (44) Madhuprasad; Nityananda Shetty, A.; Trivedi, D. R. Colorimetric receptors for naked eye detection of inorganic fluoride ion in aqueous media using ICT mechanism. *RSC Adv.* **2012**, *2*, 10499–10504.
- (45) Kumar, A.; Bhatt, M.; Vyas, G.; Bhatt, S.; Paul, P. Sunlight Induced Preparation of Functionalized Gold Nanoparticles as Recyclable Colorimetric Dual Sensor for Aluminum and Fluoride in Water. *ACS Appl. Mater. Interfaces* **2017**, *9*, 17359–17368.
- (46) Nishimura, T.; Xu, S.-Y.; Jiang, Y.-B.; Fossey, J. S.; Sakurai, K.; Bull, S. D.; James, T. D. A simple visual sensor with the potential for determining the concentration of fluoride in water at environmentally significant levels. *Chem. Commun.* **2013**, *49*, 478–480.
- (47) Liu, B.; Huang, Z.; Liu, J. Boosting the oxidase mimicking activity of nanoceria by fluoride capping: Rivaling protein enzymes and ultrasensitive F<sup>−</sup> detection. *Nanoscale* **2016**, *8*, 13562–13567.
- (48) Li, Y.; Duan, Y.; Zheng, J.; Li, J.; Zhao, W.; Yang, S.; Yang, R. Self-assembly of graphene oxide with a silyl-appended spiropyran dye for rapid and sensitive colorimetric detection of fluoride ions. *Anal. Chem.* **2013**, *85*, 11456–11463.
- (49) <http://www.hach.com/pocket-colorimeter-ii-fluoridespadns-ii-arsenic-free/product-details?id=7640445206> (accessed 2020-03-27).
- (50) Dahle, J.; Arai, Y. Environmental Geochemistry of Cerium: Applications and Toxicology of Cerium Oxide Nanoparticles. *Int. J. Environ. Res. Public Health* **2015**, *12*, 1253–1278.
- (51) Chemical Information Profile for Ceric Oxide Supporting Nomination for Toxicological Evaluation by the National Toxicology Program, 2006.
- (52) Nyoka, M.; Choonara, Y. E.; Kumar, P.; Kondiah, P. P. D.; Pillay, V. Synthesis of Cerium Oxide Nanoparticles Using Various Methods: Implications for Biomedical Applications. *Nanomaterials* **2020**, *10*, 242.
- (53) Issa Hamoud, H.; Azambre, B.; Finqueneisel, G. Reactivity of Ceria–Zirconia Catalysts for the Catalytic Wet Peroxidative Oxidation of Azo Dyes: Reactivity and Quantification of Surface Ce(IV)-Peroxo Species. *J. Chem. Technol. Biotechnol.* **2016**, *91*, 2462–2473.

## Supplementary Information

### Smartphone-based fluoride-specific sensor for rapid and affordable colorimetric detection and precise quantification at sub-ppm levels for field applications

*Sritama Mukherjee,<sup>†‡</sup> Manav Shah,<sup>†</sup> Kamalesh Chaudhari,<sup>†</sup> Arijit Jana,<sup>†</sup> Chennu Sudhakar,<sup>†</sup> Pillalamarri Srikrishnarka,<sup>†</sup> Md Rabiul Islam,<sup>†</sup> Ligy Philip<sup>‡</sup> and Thalappil Pradeep<sup>†\*</sup>*

<sup>†</sup> DST Unit of Nanoscience (DST UNS) and Thematic Unit of Excellence (TUE), Department of Chemistry, Indian Institute of Technology Madras, Chennai 600036, India.

<sup>‡</sup> EWRE Division, Department of Civil Engineering, Indian Institute of Technology Madras, Chennai 600036, India.

\*Corresponding author

E-mail: [pradeep@iitm.ac.in](mailto:pradeep@iitm.ac.in)

#### SUPPORTING INFORMATION CONTENT

Total number of pages: 13

Total number of figures: 11

#### TABLE OF CONTENTS

Supporting items	Title	Page no.
Figure S1	Large area TEM images showing the structure of ceria@zirconia nanocages.	S3

Figure S2	Large area FESEM images for ceria@zirconia nanocages showing their near cubic shapes.	S4
Figure S3	Large area FESEM images for aggregation of ceria@zirconia nanocages after their interaction with F- ions.	S5
Figure S4	Temperature dependent kinetics of NC-XO before and after interaction with F- ions.	S6
Figure S5	IR spectra showing NC-XO before and after interaction with F- ions.	S7
Figure S6	Absorbance spectra showing NC-XO interaction with standard F- solutions and various commercial dental products (left).	S8
Figure S7	Absorbance spectra of NC-XO before and after F- interaction, at various alkaline pH conditions.	S9
Figure S8	Overlapping full length $^1\text{H}$ NMR spectra of XO and NC-XO-F.	S10
Figure S9	Full length $^1\text{H}$ NMR spectra of XO at high pH.	S11
Figure S10	Steps for using the fluoride sensor app over an android supporting phone for connection, calibration and measurements.	S12
Figure S11	Optical images of control F- sensing experiments performed with zirconium-XO complex, $\text{ZrO}_2$ NP-XO, $\text{CeO}_2$ NP-XO and spherical $\text{CeO}_2@\text{ZrO}_2$ NC-XO systems for 0, 0.1, 1 and 10 ppm of F-.	S13



## Supplementary information 1

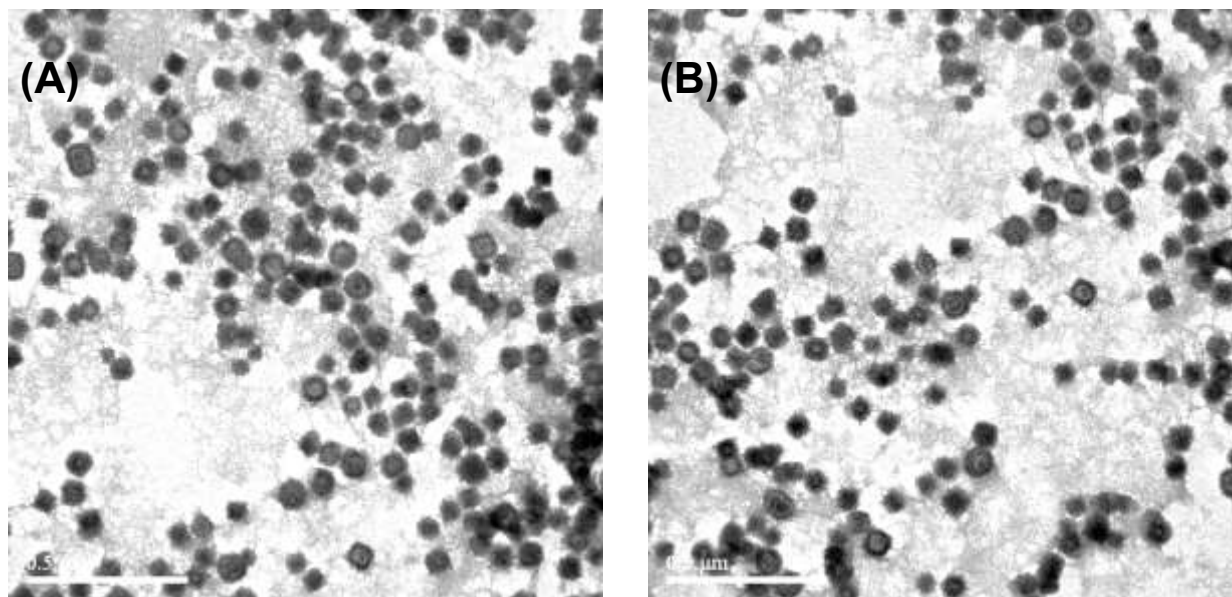


**Figure S1.** (A) and (B) show large area TEM images showing the structure of ceria@zirconia nanocages.

## Supplementary information 2

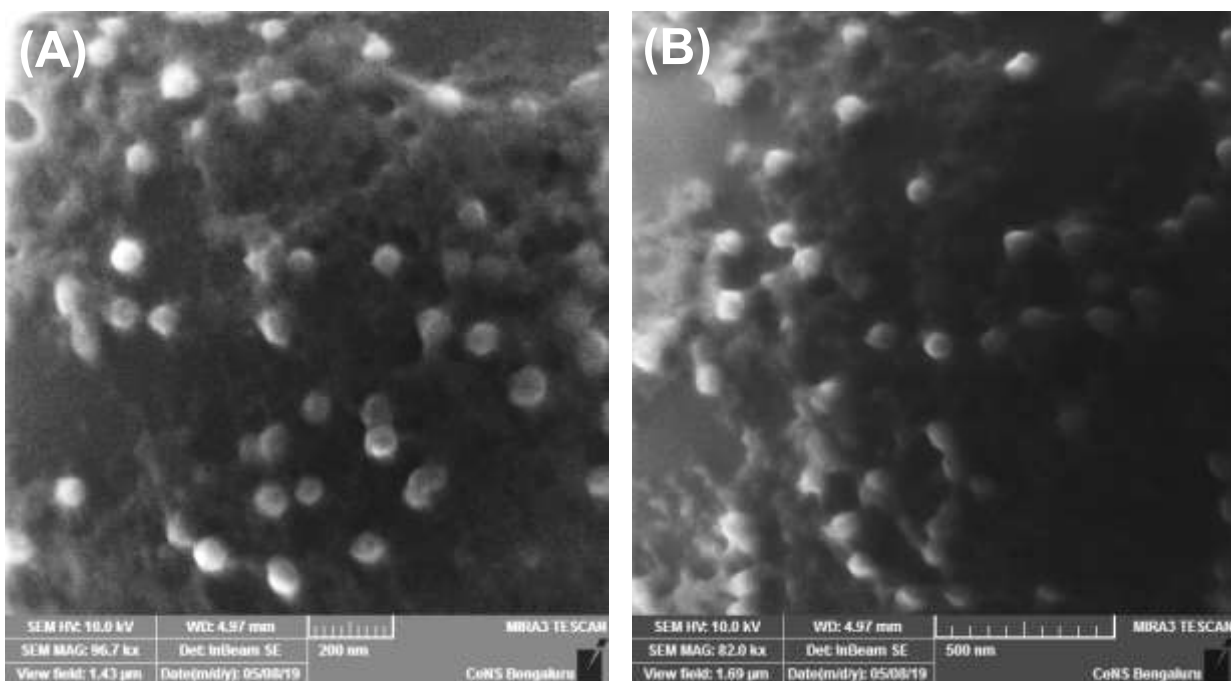


**Figure S2.** (A) and (B) show large area FESEM images for ceria@zirconia nanocages showing their near cubic shapes.

### Supplementary information 3

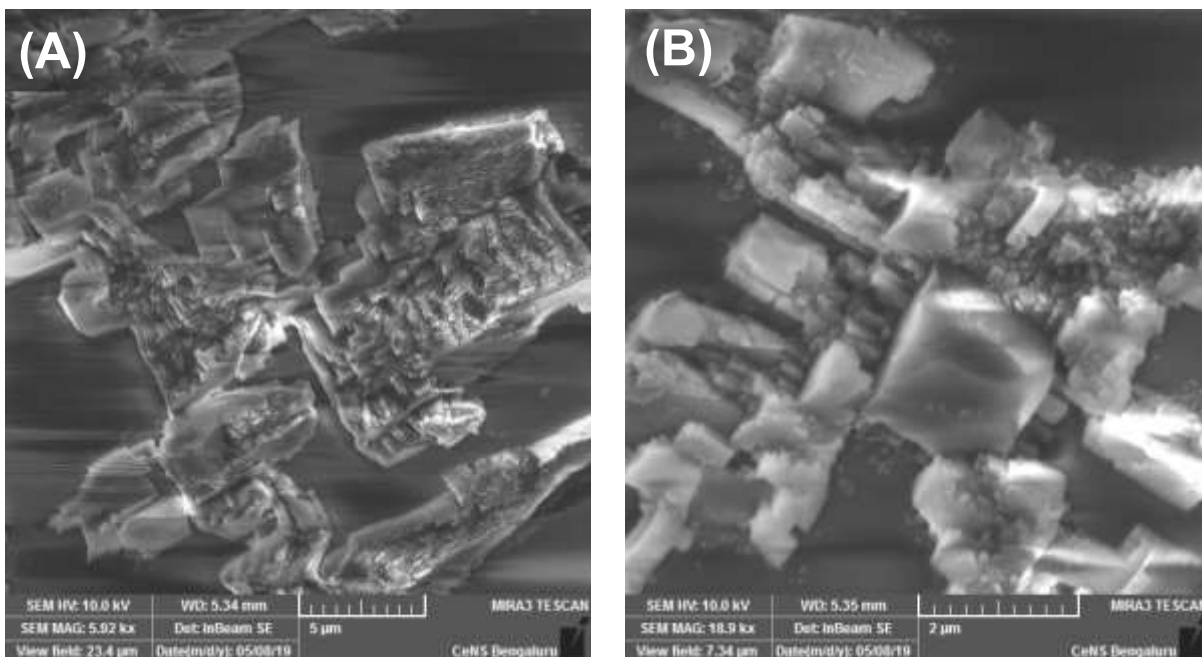


**Figure S3.** (A) and (B) show large area FESEM images of ceria@zirconia nanocages after their interaction with  $F^-$  ions.

The images show the aggregation of fluoride around the nanocages upon interacting with  $F^-$  in water.

#### Supplementary information 4

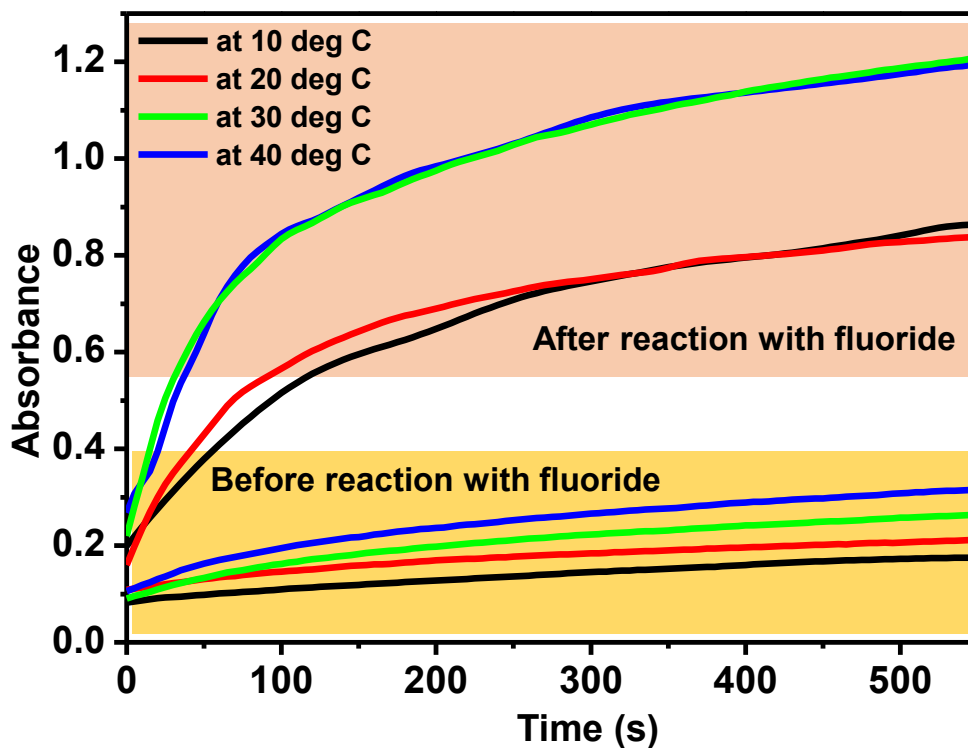


**Figure S4.** Temperature dependent kinetics of NC-XO before and after interaction with  $F^-$  ions.

The UV-vis spectra shows the NC-XO absorbance with and without  $F^-$  at 10, 20, 30 and 40°C. It is clear that higher temperature facilitates the reaction responsible for color change, thus rate of reaction increases. The kinetics of fluoridated samples show much higher increase than control samples.

## Supplementary information 5

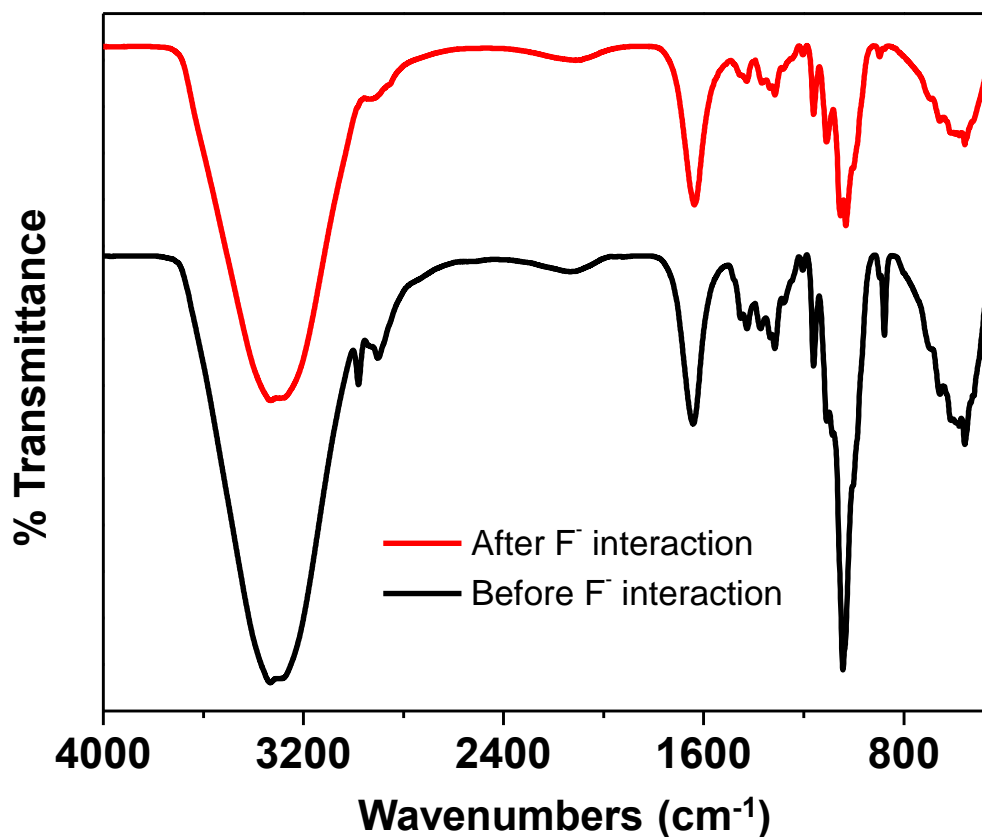


**Figure S5.** IR spectra showing NC-XO before and after interaction with F<sup>-</sup> ions.

The wide band at 3000–3600 cm<sup>-1</sup> is assigned to O–H vibrations. The sharp bands at ~2948 cm<sup>-1</sup> are assigned to the asymmetric and symmetric methylene stretching modes. The sharp bands at ~1078 cm<sup>-1</sup> are assigned to the C–O stretching vibration of alcohol. These characteristic bands can confirm the existence of glycol. The bands at ~1653 cm<sup>-1</sup> is assigned to the C=O vibrations, which implies that there is partly oxidation of glycol in the reaction process. Slight shifts in the C–O and C=O stretching frequencies to higher wavenumbers is observed upon interaction with F<sup>-</sup>.

## Supplementary information 6

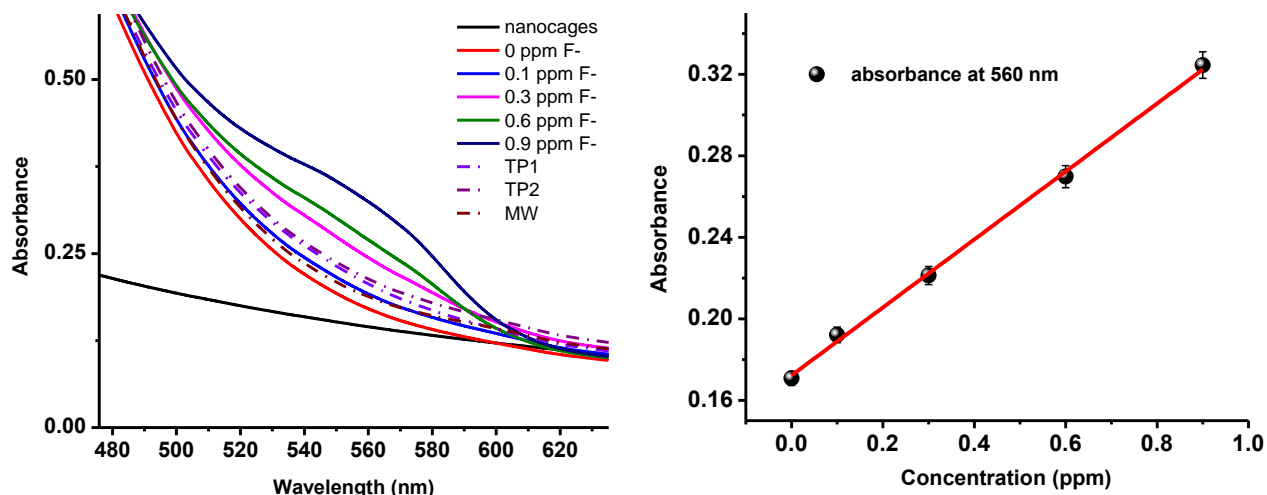


**Figure S6.** Absorbance spectra showing NC-XO interaction with standard F<sup>-</sup> solutions and various commercial dental products (left). Standard curve for F<sup>-</sup> content estimation in the dental products (right).

UV-vis spectra show the sensor response with 0, 0.1, 0.3, 0.6 and 0.9 ppm F<sup>-</sup> standards to make a standard curve, that helped to quantify the F<sup>-</sup> content in TP1, TP2 and MW samples by their respective absorbance values.



## Supplementary information 7

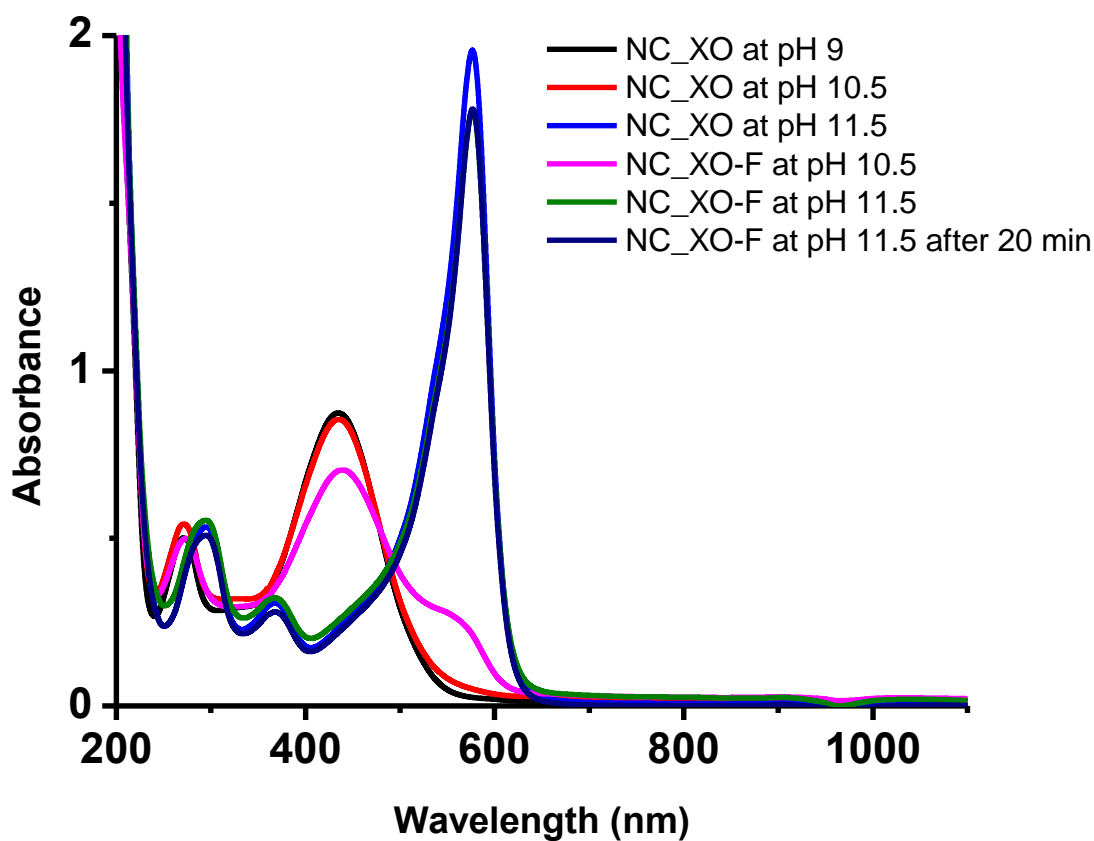


**Figure S7.** Absorbance spectra of NC-XO before and after F<sup>-</sup> interaction, at various alkaline pH conditions.

UV-vis spectra were taken to observe the pH dependent behavior of the sensor. Control studies showed that NC-XO gives consistent results till pH 10.5 in case of with and without F<sup>-</sup> samples. At pH 11.5 and beyond, NC-XO undergo color changes without any F<sup>-</sup> in the medium.

## Supplementary information 8

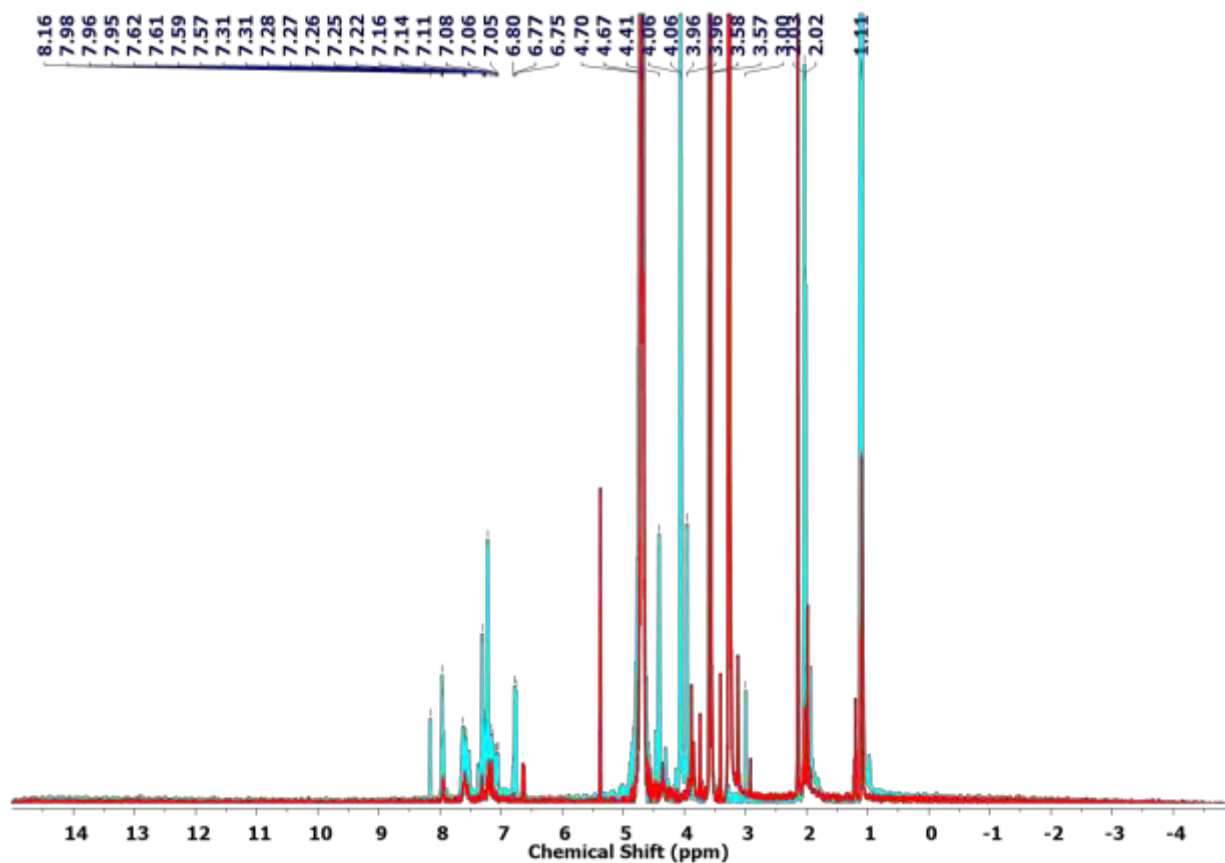


**Figure S8.** Overlapping full length  $^1\text{H}$  NMR spectra of XO and NC-XO-F.

XO:  $^1\text{H}$  NMR  $\{\text{D}_2\text{O}, 500 \text{ MHz}, \delta\} =$

2.02, 2.03 (two S, 6H,  $\text{CH}_3$ ), 3.96, 4.41 (two S, 12H,  $\text{CH}_2$ ), 6.77 (S, 2H, OH), 7.11 (m, 4H,  $\text{Ph-SO}_3^-$ ), 7.61 (m, 4H, Ph) 7.98 (m, 4H, COOH) 7.3 (m, 6H, benzene)

NC-XO-F:  $^1\text{H}$  NMR  $\{\text{D}_2\text{O}, 500 \text{ MHz}, \delta\} =$

2.03, 2.15 (m, 6H,  $\text{CH}_3$ ), 3.13 (S, 2H,  $\text{NH}^+$ ), 3.88, 4.35 (m, 12H,  $\text{CH}_2$ ), 6.62 (d, 1H, OH), 7.22 (m, 4H,  $\text{Ph-SO}_3^-$ ), 7.59 (m, 4H, Ph), 7.95 (d, 2H, COOH).

1H NMR spectrum of compound 10a in CDCl<sub>3</sub>. The x-axis is chemical shift (delta) from 14 to -4 ppm. The spectrum shows several peaks: aromatic protons between 6.4 and 8.4 ppm, a solvent peak at 7.26 ppm, a methoxy singlet at 3.96 ppm, a methine doublet at 3.18 ppm, a methyl doublet at 1.97 ppm, and a methyl singlet at 1.95 ppm. Integration values are shown below the peaks.

Chemical Shift (ppm)	Integration
8.38	0.72
8.19	2.69
8.16	2.89
8.14	6.12
7.06	0.97
6.55	
6.54	
6.50	
6.49	
6.47	
4.47	
3.96	3.96
3.18	3.18
1.97	5.51
1.95	6.00

The NMR peaks of XO at 11.5 and neutral pH (Figure S8) do not match, hence some chemical transformation in the dye structure at very high alkaline pH is evident.

## Supplementary information 10



**Figure S10.** (A) to (L) show steps for using the fluoride sensor app over an android supporting phone for connection, calibration and measurements (output values not to be considered).

### Supplementary information 11

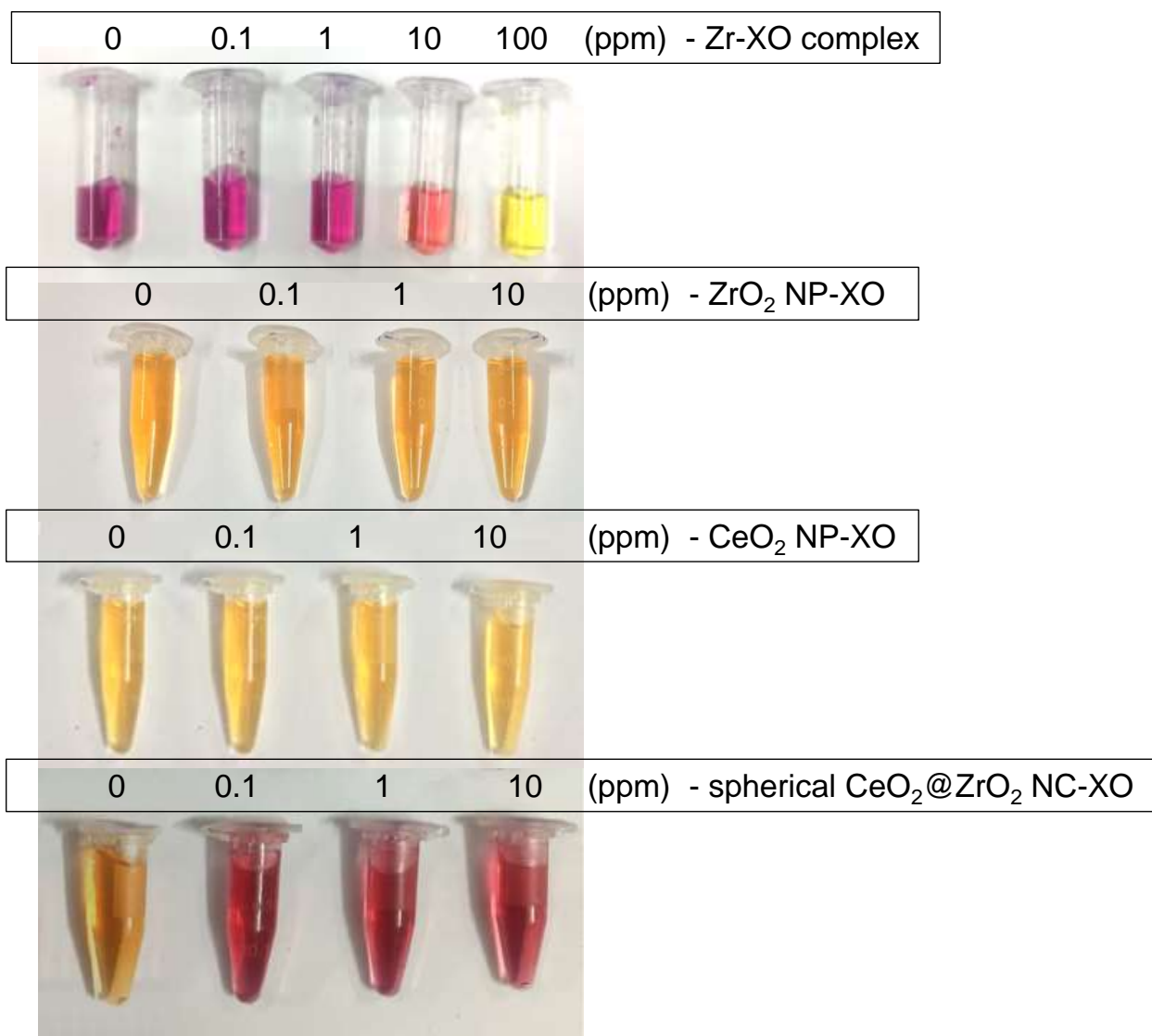


**Figure S11.** Optical images of control F<sup>-</sup> sensing experiments performed with zirconium-XO complex, ZrO<sub>2</sub> NP-XO, CeO<sub>2</sub> NP-XO and spherical CeO<sub>2</sub>@ZrO<sub>2</sub> NC-XO systems for 0, 0.1, 1 and 10 ppm of F<sup>-</sup>.



Cite this: *Chem. Commun.*, 2020, 56, 12550

Received 7th June 2020,  
Accepted 2nd September 2020

DOI: 10.1039/d0cc03983g

rsc.li/chemcomm

## Dual emitting Ag<sub>35</sub> nanocluster protected by 2-pyrene imine thiol†

Arijit Jana, <sup>ab</sup> Papri Chakraborty, <sup>a</sup> Wakeel Ahmed Dar,<sup>a</sup> Sourov Chandra, <sup>b</sup> Esma Khatun, <sup>a</sup> M. P. Kannan, <sup>a</sup> Robin H. A. Ras <sup>bc</sup> and Thalappil Pradeep <sup>\*a</sup>

**In this communication, we present the synthesis of 2-pyrene imine thiol (2-PIT)-protected Ag<sub>35</sub> nanoclusters using a ligand exchange-induced structural transformation reaction. The formation of the nanocluster and its composition were confirmed through several spectroscopic and electron microscopic studies. The UV-vis absorption spectrum showed a set of characteristic features of the nanocluster. This nanocluster showed blue emission under UV light due to pyrene to metal core charge-transfer, and NIR emission due to charge-transfer within the metal core. This is the first report on dual emitting pyrene protected atomically precise silver nanoclusters.**

Ligand protected metal nanoclusters (NCs) are an emerging class of quantum materials connecting the gap between atoms and bulk metallic materials.<sup>1,2</sup> Owing to their unique electrical, optical and other spectroscopic properties such as luminescence,<sup>3–5</sup> chirality,<sup>6</sup> *etc.*, they are important for applications such as catalysis,<sup>7</sup> CO<sub>2</sub> reduction,<sup>8</sup> bioimaging,<sup>9</sup> *etc.* The surface ligand environment not only stabilizes their fragile metal core but also determines their electronic properties.<sup>10,11</sup> The literature suggests that small organic thiol and phosphine co-protected silver nanoclusters such as Ag<sub>6</sub>,<sup>12</sup> Ag<sub>14</sub>,<sup>13</sup> Ag<sub>25</sub>,<sup>14</sup> Ag<sub>29</sub>,<sup>15</sup> Ag<sub>67</sub>,<sup>16</sup> *etc.*, are more promising compared to bulky DNA<sup>17,18</sup> and dendrimer<sup>19</sup> protected NCs in making structure–property correlations. Our group has reported silver NCs such as Ag<sub>16</sub>, Ag<sub>17</sub>,<sup>20</sup> Ag<sub>22</sub>,<sup>21</sup> Ag<sub>40</sub>, Ag<sub>46</sub>,<sup>22</sup> *etc.*, and their crystal structures as a step toward understanding their various functional properties. Generally, the light sensitivity and chemical instability of the Ag core limit their practical applications. In view of such

limitations, designing new multidentate ligands that can stabilize Ag NCs is important. In contrast to conventional organic thiols and phosphines used for protecting silver NCs, in this work we have used 2-pyrene imine thiol, a polycyclic aromatic hydrocarbon (PAH)-based ligand for Ag NC synthesis. Atomically precise silver NCs protected with electron dense pyrene ligands are a new class of functional hybrid nanomaterials, which show electronic, optical and other physical properties, due to a combination of both the ligand and the cluster core.

Pyrene is a good candidate among other PAHs, due to its multiple absorption and emission properties.<sup>23</sup> Due to their high emission quantum yield and excimer stability, pyrene functionalised nanoparticles (NPs) and dendrimers are widely used in optoelectronic,<sup>24,25</sup> molecular labelling,<sup>26</sup> and fluorescence sensing applications.<sup>27</sup> There are some reports on functionalised pyrene protected gold NPs, wherein the NPs show erratic emission of pyrene.<sup>28</sup> Due to the resonance energy transfer from the chromophore to the metallic core, the emission quenches significantly. The distance from the nanoparticle core to pyrene has a significant role in this energy transfer process.<sup>29</sup> Generally, increasing the distance from the metallic core to the pyrene center decreases quenching. In the case of a cluster, which has a molecular core, quenching is expected.

To obtain a highly stable silver NC, appended with PAHs, we have used 2-PIT and triphenylphosphine (TPP) as ligands. The synthesis of the 2-PIT ligand was through a high-temperature condensation reaction between pyrene aldehyde and 2 amino thio-phenol. Fig. 1a shows a schematic representation of the synthesis of the 2-PIT ligand. In brief, pyrene aldehyde was mixed with 2 amino thio-phenol in an argon atmosphere in a methanol-ethanol solvent mixture, under refluxed (60 °C) conditions. After 4 hour of reaction, a yellow colored ligand was filtered using a Whatman 42 filter paper and washed several times with the methanol-ethanol solvent mixture to remove excess starting materials. The as-prepared 2-PIT ligand was confirmed using <sup>1</sup>H and <sup>13</sup>C{<sup>1</sup>H} NMR (shown in Fig. S1 and S2 respectively, ESI†) and mass spectral studies.

The formation of the 2-PIT ligand was confirmed through single-crystal structure studies. Fig. 1b shows the crystal structure

<sup>a</sup> Department of Chemistry, DST Unit of Nanoscience (DST UNS) and Thematic Unit of Excellence (TUE), Indian Institute of Technology Madras, Chennai 600036, India. E-mail: pradeep@iitm.ac.in

<sup>b</sup> Department of Applied Physics, Aalto University, School of Science, Puumiehenkuja 2, 02150, Espoo, Finland

<sup>c</sup> Department of Bioproducts and Biosystems, Aalto University School of Chemical Engineering, 02150, Espoo, Finland

† Electronic supplementary information (ESI) available: Experimental details of synthesis and characterization. CCDC 2008467. For ESI and crystallographic data in CIF or other electronic format see DOI: 10.1039/d0cc03983g



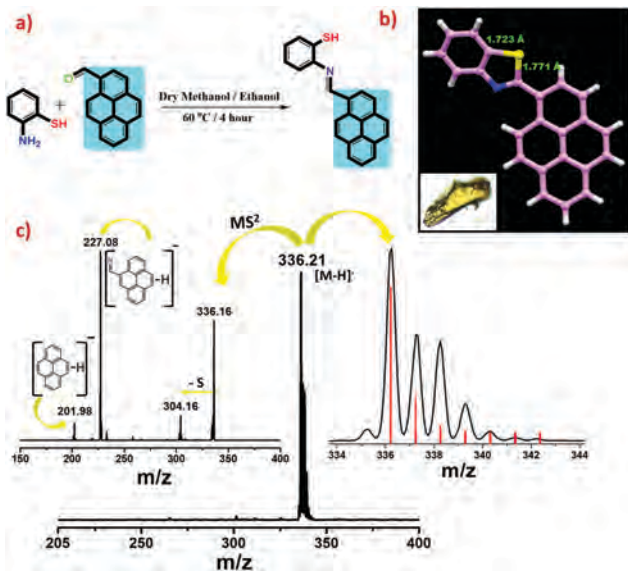


**Fig. 1** (a) Schematic representation of the synthesis of the 2-pyrene imine thiol ligand; (b) the crystal structure of the ligand (inset shows the optical image of the single crystal); (c) the mass spectrum and the MS/MS fragmentation data of the ligand (color codes of the atoms: violet = carbon; blue = nitrogen; yellow = sulphur; and gray = hydrogen).

of the ligand, which crystallized in the monoclinic  $P2_1/c$  crystal system. From the crystal structure, we observed that the C-H proton of the imine group and the S-H proton combined themselves and formed a five-membered ring. The distance of S and imine carbon is 1.77 Å compared to 1.72 Å distance of the C-S bond with the benzene ring, which indicates weak bonding with the imine carbon. Several C-H $\cdots$  $\pi$  intermolecular interactions in the intermolecular packing of the ligands are shown in Fig. S3 (ESI<sup>†</sup>); four molecules packed inside the unit cell in a lamellar fashion are visible. The negative mode electrospray ionisation mass spectrum (ESI-MS) in DCM showed a  $[M - H]^-$  ion peak at  $m/z$  336.21, which indicated the existence of the molecule in the thiol (SH) form in solution. The proton NMR spectrum shown in Fig. S1 (ESI<sup>†</sup>) with a single peak at 3.45 ppm confirmed the thiol form in solution. Furthermore, we confirmed the formation of the imine thiol form through MS/MS fragmentation studies, showing the loss of S, pyrene imine and pyrene moieties from the molecular ion peak, by varying the collision energy.

The  $Ag_{35}$  NC was prepared using a ligand exchange-induced structural transformation (LEIST) reaction from the  $Ag_{18}$  nanocluster. Fig. 2a shows a schematic representation of the synthetic procedure employed in the LEIST reaction. Product clusters were also formed by a controlled co-reduction reaction of metal thiolates in the presence of TPP. Detailed characterization of the  $Ag_{18}$  NCs through UV-vis absorption and MS studies is shown in Fig. S4 (ESI<sup>†</sup>). The conversion of  $Ag_{18}$  NC to  $Ag_{35}$  NC through several intermediates was reflected in the changing color of the reaction mixture. The changes in the UV-vis absorption features of these intermediates are shown in Fig. S5 (ESI<sup>†</sup>). A dark violet color appeared at the end of the reaction after 48 h. Fig. 2b shows the UV-vis absorption features of the purified NC. The nanocluster has well-defined sharp absorption features at

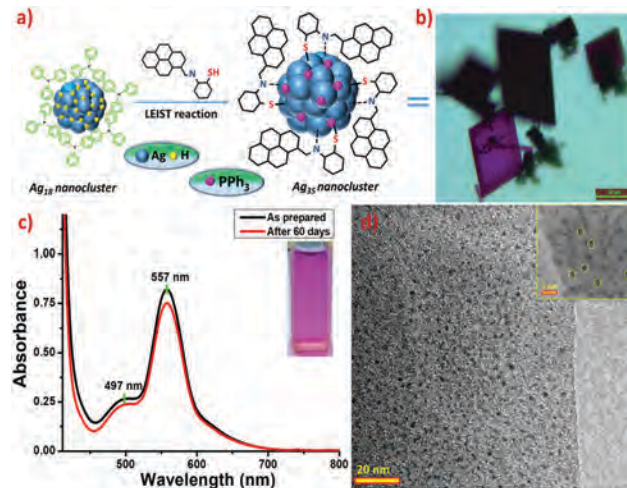


**Fig. 2** (a) Schematic representation of the synthesis of  $Ag_{35}$  NC by a LEIST reaction; (b) the optical microscopic image of the  $Ag_{35}$  NC crystals; (c) the UV-Visible absorption spectrum of  $Ag_{35}$  NC showing its stability (inset shows the photographic image of the NC solution in DCM); (d) the TEM image of the NC showing uniform particle distribution (inset shows the HRTEM image of the NCs, and some particles are encircled).

557 and 497 nm. The absorption features of the  $Ag_{35}$  NC remain unchanged after two months, indicating the good stability of the NC. The uniform particle size distribution of the NC was also confirmed using TEM imaging. The TEM images show small cluster particles < 2 nm in diameter (Fig. 2d).

The molecular composition of this NC was confirmed using the high resolution ESI-MS (HR ESI-MS) technique. During ESI-MS measurements, the ionization of the cluster was enhanced by adding a few drops of methanol. The instrumentation details are given in the ESI.<sup>†</sup> The full range mass spectrum shown in Fig. 3a indicates a sharp peak at  $m/z$  2659.7 in the 3+ charge state. This corresponds to a mass of 7971.1 for the molecular ion species. This peak was assigned as  $[Ag_{35}(2-PIT)_7(TPP)_7@H_2O]^{3+}$  by comparing its experimental isotopic distribution with the isotopic distribution of the simulated spectrum. The assignment was further verified using collision induced dissociation (CID) mass spectrometry measurements at different collision-energies (CEs), which are instrumental units of the Waters Synapt G2 Si mass spectrometer. The MS/MS fragmentation patterns are shown in Fig. 3b. From the MS/MS spectra, we observed that by varying the CE from 0 to 50, there were four sequential mass losses of 262 units, which indicates four TPP unit detachments from the cluster. Next, by increasing the CE from 50 to 150, further loss of TPP was not observed, which suggested that only 4 TPP molecules are weakly bonded to the outer shell of the cluster. At CE 150, a new peak appeared at 2755.5 with the 2+ charge state. The mass loss of 2468.18 indicated the loss of the  $[Ag_{13}(H_2O)(TPP)_4]$  fragment from the molecular ion peak. Next upon increasing the CE from 150 to 175, we observed further loss of three TPPs, which indicated that while four TPP molecules are loosely bound to the cluster surface, there were three other strongly bound TPP molecules. Upon further increasing the CE, five sequential mass losses of 124 units due to the loss of the aminothiophenol moieties

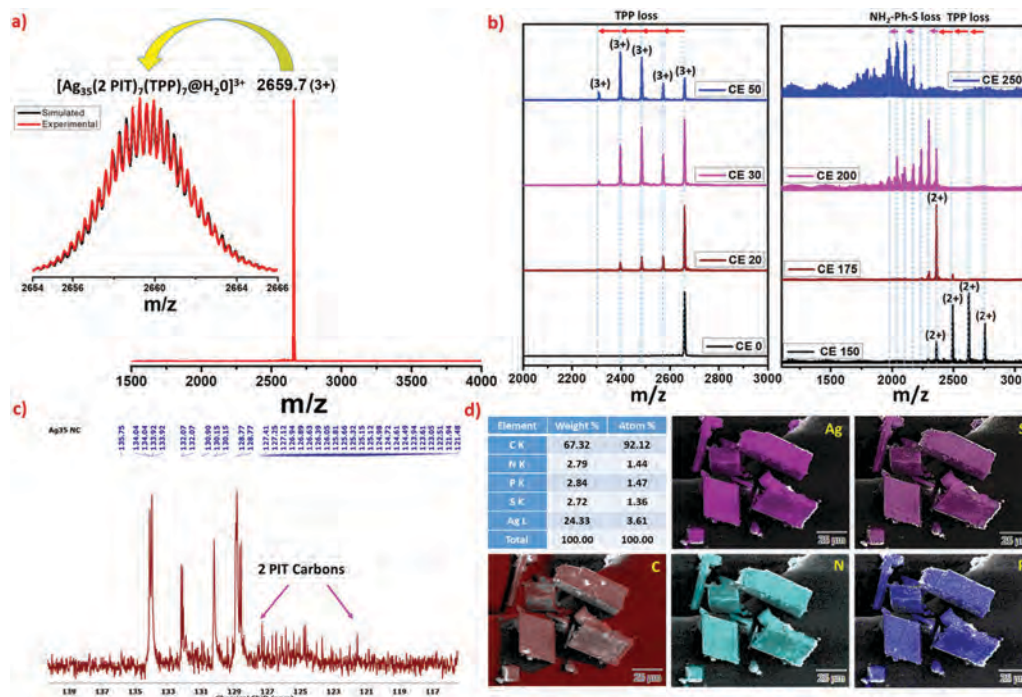


Fig. 3 (a) Positive mode ESI-MS spectrum of the  $\text{Ag}_{35}$  NC in DCM (inset shows the simulated and experimental isotopic distribution patterns of the 2659.7 peak); (b) MS/MS fragmentation pattern of the 2659.7 peak using different collision energies; (c)  $^{13}\text{C}\{^1\text{H}\}$  NMR spectrum of the  $\text{Ag}_{35}$  NC in  $\text{CDCl}_3$ ; (d) SEM EDS elemental mapping of NC crystals indicating their atomic composition.

from the NC, generated by the fragmentation of the 2-PIT ligand, were seen.

To further understand the binding of TPP and 2-PIT ligands, we studied the  $^{13}\text{C}$  and  $^{31}\text{P}$  NMR spectra of the NC. Fig. 3c shows the  $^{13}\text{C}$  NMR spectrum of the NCs, which exhibited 23 low intensity signature peaks of carbon in the 120–128 ppm window due to 2-PIT along with TPP signature peaks in the 128–135 ppm region. This clearly suggested the co-protection of the 2-PIT and TPP ligands. Multiplet peak splitting of the  $^{13}\text{C}$  spectrum for the TPP region is most probably due to the variation in the chemical environment of the TPP outside the NC surface. The broad  $^{31}\text{P}$  NMR signal at 9.32 ppm shown in Fig. S6 (ESI†) indicated TPP binding with the cluster. Although there are two sets of TPP molecules on the cluster surface, we were not able to distinguish between them through the  $^{31}\text{P}$  NMR spectrum. The XPS spectra are shown in Fig. S7 and S8 (Table S3) (ESI†) of the ligand and  $\text{Ag}_{35}$  NC, respectively. Among the four peaks of  $\text{Ag}_{35}$  NC, two peaks at 284.8 and 286.6 eV are comparable with the two peaks at 284.8 and 286.3 eV of the C 1s region of the 2-PIT ligand, which suggests the binding of the 2-PIT ligand. The two other peaks of the C 1s region at 288.2 and 289.4 eV are due to the two types of TPP ligands. The decrease in the binding energy of the N 1s and S 2p regions in the  $\text{Ag}_{35}$  NC, compared to the 2-PIT ligand, is probably due to the electron back donation from the metal core to the N and S end of the ligand. The higher electronegativity of N and S compared to Ag is also the reason behind it. The binding energy of 368.4 and 374.5 eV for the Ag 3d region suggests the metallic state of silver.

Although the as-grown cubical blackish-violet crystals of the NC showed optical polarisation, due to the lack of intense electron diffraction spots, we were not able to get the single-crystal structure of the NCs. Fig. 2b and Fig. S9 (ESI†) show the optical microscopic images of the single crystals grown after crystallization. The EDS elemental images of the single crystals are shown in Fig. 3d. The single crystal showed the existence of Ag, S, P, N and C in an atomic ratio of 3.61 : 1.36 : 1.47 : 1.44 : 92.12 in the crystal, which indicated the co-existence of 2-PIT and TPP ligands in the NC. The FTIR spectra of the 2-PIT ligand and  $\text{Ag}_{35}$  NC are shown in Fig. S10 (ESI†). The sharp feature at  $3049\text{ cm}^{-1}$  corresponded to the pyrene C–H stretching mode. Similar vibrational features are also observed there for the 2-PIT ligand. The broad O–H vibrational feature centered at  $3435\text{ cm}^{-1}$  indicated that  $\text{H}_2\text{O}$  is present in the NC.

Interestingly, the  $\text{Ag}_{35}$  nanocluster exhibits dual emission features in blue (449 nm) and NIR (896 nm) regions upon excitation at 417 and 530 nm, respectively (Fig. 4). Fig. 4a shows the excitation spectrum of the  $\text{Ag}_{35}$  NCs at 449 nm emission, demonstrating three major excitation peaks at 297, 365 and 417 nm. These low lying excitation maxima resembling the absorption maxima of the 2-PIT ligand are due to the charge transfer from pyrene to the metal core. The NIR emission peak at 896 nm corresponding to the excitation maxima at 530 and 558 nm is due to the metal shell to metal core charge transfer (MMCT) in the NC. Comparing the absorption maximum at 557 nm with the excitation maxima, we can conclude that the NIR emission is due to the charge transfer within the metal core.<sup>30</sup> A similar type of MMCT leading to NIR emission was

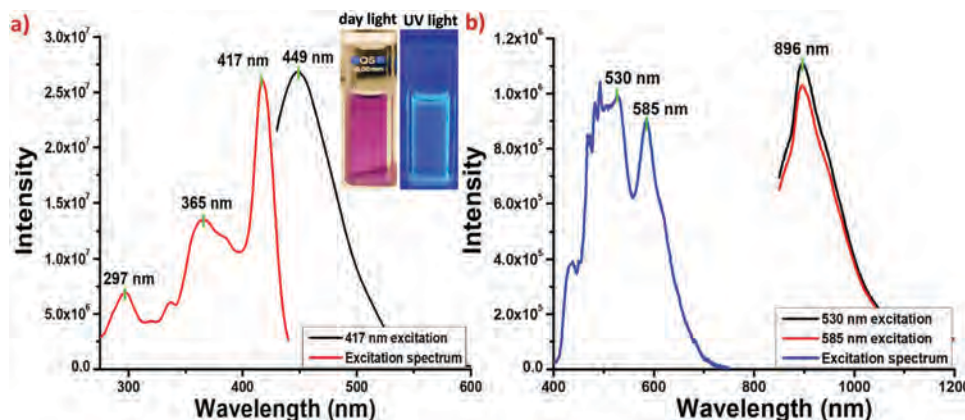


Fig. 4 (a) Photoluminescence excitation and emission spectra of the nanocluster (inset shows images of the cluster solution under day light and UV light) and (b) NIR emission and the corresponding excitation spectra of the nanocluster.

reported in the literature.<sup>31</sup> The Ag<sub>35</sub> nanocluster shows a dual emissive character of the ligand as well as the metal core and is the first example showing this behavior.

In conclusion, we have shown the synthesis of a 2-pyrene imine thiol protected Ag<sub>35</sub> nanocluster using a LEIST reaction. The formation of the NC was confirmed using UV-vis absorption spectroscopy, mass spectrometry, and multinuclear NMR, TEM, SEM, EDS, FTIR and XPS measurements. The cluster showed intense blue emission due to pyrene to metal core electron-transfer in the solution phase. There was also a comparable NIR emission observed due to metal-to-metal charge transfer. This work is a step toward making silver nanoclusters with a family of electron rich pyrene molecules having composite electronic features. Dual emission in such types of materials may be tuned for desired applications such as ion sensing and bio imaging.

This work was supported by the SPARC scheme, Govt. Of India through the grant, SPARC/2018-2019/P910/SL. The authors would like to thank the Sophisticated Analytical Instrument Facility, IIT Madras (SAIF, IITM), for single crystal XRD measurement. AJ acknowledges financial support from IIT Madras.

## Conflicts of interest

There are no conflicts to declare.

## Notes and references

- 1 R. Jin, C. Zeng, M. Zhou and Y. Chen, *Chem. Rev.*, 2016, **116**, 10346–10413.
- 2 I. Chakraborty and T. Pradeep, *Chem. Rev.*, 2017, **117**, 8208–8271.
- 3 X. Kang and M. Zhu, *Chem. Soc. Rev.*, 2019, 2422–2457.
- 4 Z. Wang, J. W. Liu, H. F. Su, Q. Q. Zhao, M. Kurmoo, X. P. Wang, C. H. Tung, D. Sun and L. S. Zheng, *J. Am. Chem. Soc.*, 2019, **141**, 17884–17890.
- 5 Z. Wang, H. Su, Y. Tan, S. Schein, S. Lin, W. Liu, S. Wang, W. Wang, C. Tung, D. Sun and L. Zheng, *Proc. Natl. Acad. Sci. U. S. A.*, 2017, **114**, 12132–12137.
- 6 Y. Chen, C. Liu, Q. Tang, C. Zeng, T. Higaki, A. Das, D. Jiang, R. N. Rosi and J. Rongchao, *J. Am. Chem. Soc.*, 2016, **138**, 1482–1485.
- 7 Y. Wu, D. Wang and Y. Li, *Chem. Soc. Rev.*, 2014, **43**, 2112–2124.
- 8 Y. Liu, X. Chai, X. Cai, M. Chen, R. Jin, W. Ding and Y. Zhu, *Angew. Chem., Int. Ed.*, 2018, **130**, 1–6.
- 9 Z. Luo, K. Zheng and J. Xie, *Chem. Commun.*, 2014, **50**, 5143–5155.
- 10 J. Liu, Z. Wang, Y. Chai, M. Kurmoo, Q. Zhao, X. Wang, C. Tung and D. Sun, *Angew. Chem., Int. Ed.*, 2019, **58**, 6276–6279.
- 11 Z. Wang, H. Su, C. Tung and D. Sun, *Nat. Commun.*, 2018, **9**, 4407.
- 12 Z. Han, X. Dong, P. Luo, S. Li, Z. Wang, S. Zang and T. C. W. Mak, *Sci. Adv.*, 2020, **6**, 1–9.
- 13 Z. Wang, M. Wang, Y. Li, P. Luo, T. Jia, R. Huang, S. Zang and T. C. W. Mak, *J. Am. Chem. Soc.*, 2018, **140**, 1069–1076.
- 14 C. P. Joshi, M. S. Bootharaju, M. J. Alhilaly and O. M. Bakr, *J. Am. Chem. Soc.*, 2015, **137**, 11578–11581.
- 15 L. G. Abdulhalim, M. S. Bootharaju, Q. Tang, S. Del Gobbo, R. G. Abdulhalim, M. Eddaoudi, D. Jiang and O. M. Bakr, *J. Am. Chem. Soc.*, 2015, **137**, 11970–11975.
- 16 M. J. Alhilaly, M. S. Bootharaju, C. P. Joshi, T. M. Besong, A. Emwas, R. Juarez-mosqueda, S. Kaappa, S. Malola and K. Adil, *J. Am. Chem. Soc.*, 2016, **138**, 14727–14732.
- 17 S. Y. New, S. T. Lee and X. D. Su, *Nanoscale*, 2016, **8**, 17729–17746.
- 18 Z. Yuan, Y. Chen, H. Li, H. Chang and Y. Chen, *Chem. Commun.*, 2014, **50**, 9800–9815.
- 19 W. Lesniak, A. U. Bielinska, K. Sun, K. W. Janczak, X. Shi, J. R. Baker Jr and L. P. Balogh, *Nano Lett.*, 2005, **5**, 2123–2130.
- 20 W. A. Dar, M. Bodiuzzaman, D. Ghosh, G. Paramasivam, E. Khatun, K. S. Sugi and T. Pradeep, *ACS Nano*, 2019, **13**, 13365–13373.
- 21 E. Khatun, M. Bodiuzzaman, K. S. Sugi, P. Chakraborty and T. Pradeep, *ACS Nano*, 2019, **13**, 5753–5759.
- 22 M. Bodiuzzaman, A. Ghosh, K. S. Sugi, A. Nag, E. Khatun, B. Varghese, G. Paramasivam and T. Pradeep, *Angew. Chem., Int. Ed.*, 2018, **57**, 1–7.
- 23 F. M. Winnik, *Chem. Rev.*, 1993, **93**, 587–614.
- 24 T. M. Figueira-duarte and M. Klaus, *Chem. Rev.*, 2011, **111**, 7260–7314.
- 25 F. Zinna, S. Voci, L. Arrico, E. Brun, A. Homberg, L. Bouffier, T. Funaioli, J. Lacour, N. Sojic and L. Di Bari, *Angew. Chem., Int. Ed.*, 2019, **58**, 6952–6956.
- 26 U. Drechsler, B. Erdogan and V. M. Rotello, *Chem. – Eur. J.*, 2004, **10**, 5570–5579.
- 27 A. Senthamizhan, A. Celebioglu, S. Bayir, M. Gorur, E. Doganci, F. Yilmaz and T. Uyar, *ACS Appl. Mater. Interfaces*, 2015, **7**, 21038–21046.
- 28 G. Battistini, P. G. Cozzi, J. Jalkanen, M. Montalti, L. Prodi, N. Zaccaroni and F. Zerbetto, *ACS Nano*, 2008, **2**, 77–84.
- 29 K. G. Thomas and P. V. Kamat, *Acc. Chem. Res.*, 2003, **36**, 888–898.
- 30 Z. Guan, J. Zeng, Z. Nan, X. Wan, Y. Lin and Q. Wang, *Sci. Adv.*, 2016, **1**, 1–8.
- 31 F. Tian and R. Chen, *J. Am. Chem. Soc.*, 2019, **141**, 7107–7114.



## Electronic Supplementary Information

### **Dual Emitting Ag<sub>35</sub> Nanocluster Protected by 2-Pyrene Imine Thiol**

Arijit Jana<sup>a,b</sup>, Papri Chakraborty<sup>a</sup>, Wakeel Ahmed Dar<sup>a</sup>, Sourov Chandra<sup>b</sup>, Esma Khatun<sup>a</sup>, M. P. Kannan<sup>a</sup>, Robin H. A. Ras<sup>b,c</sup>, Thalappil Pradeep<sup>a,\*</sup>.

<sup>a</sup>DST Unit of Nanoscience (DST UNS) and Thematic Unit of Excellence (TUE), Department of Chemistry, Indian Institute of Technology, Madras, Chennai – 600036, India.

<sup>b</sup>Department of Applied Physics, Aalto University School of Science, Puumiehenkuja 2, 02150 Espoo, Finland.

<sup>c</sup>Department of Bioproducts and Biosystems, Aalto University School of Chemical Engineering, 02150, Espoo, Finland.

\*Email: [pradeep@iitm.ac.in](mailto:pradeep@iitm.ac.in)

<b>Items</b>	<b>Descriptions</b>	<b>Page No.</b>
1)	Experimental section	2
2)	Instrumentation	3-6
Fig. S1	<sup>1</sup> H NMR spectrum of the 2-PIT ligand in CDCl <sub>3</sub> solvent	7
Fig. S2	<sup>13</sup> C { <sup>1</sup> H} NMR spectrum of 2-PIT ligand	8
Fig. S3	Unit cell packing of 2-PIT ligand showing different intermolecular interactions	9
Fig. S4	UV-Visible absorption spectrum and ESI-MS spectrum of Ag <sub>18</sub> NCs	10
Fig. S5	Optical images of the vial during the reaction including UV-Visible spectra of the different intermediates	11
Fig. S6	<sup>31</sup> P { <sup>1</sup> H} NMR spectrum of Ag <sub>35</sub> NC	12
Fig. S7	XPS spectra of the 2-PIT ligand having each component peak fitting	13
Fig. S8	XPS spectra of Ag <sub>35</sub> NCs having each component peak fitting	14
Fig. S9	Optical microscopic images of the NC crystals and its weak diffraction spots	15
Fig S10	IR spectra of 2-PIT ligand and Ag <sub>35</sub> nanocluster	16

## **Experimental Section:**

### **1) Chemicals used:**

Pyrenecarboxaldehyde and 2-aminothiophenol were purchased from Sigma-Aldrich and Avra, India chemicals, respectively. Silver nitrate ( $\text{AgNO}_3$ ) was purchased from Rankem chemicals. Sodium borohydride ( $\text{NaBH}_4$ , 98%) and triphenylphosphine (TPP) were purchased from Aldrich chemicals. All the chemicals were commercially available and used as such without any further purification. Solvent grade dichloromethane (DCM), chloroform ( $\text{CHCl}_3$ ), n-hexane, and methanol (99.5%) were purchased from Rankem chemicals and Finar, India respectively. Milli-Q water was used as the source of water for  $\text{Ag}_{18}$  nanocluster synthesis. Deuterated solvent ( $\text{CDCl}_3$ ) was purchased from Aldrich chemical.

### **2) Synthesis of $[\text{Ag}_{18}(\text{PPh}_3)_{10}\text{H}_{16}]^{+2}\text{NCs}$ :**

$\text{Ag}_{18}$  NCs were synthesized by following the previous literature.<sup>[S1]</sup> In Brief, at room temperature, 20 mg silver nitrate ( $\text{AgNO}_3$ ) was dissolved in 5 mL methanol and 8 mL  $\text{CHCl}_3$  under ultrasonic condition. After that, 70 mg triphenylphosphene (TPP) was dissolved in 2 ml methanol and added to it under stirring condition. After 20 min of reaction, 6.5 mg  $\text{NaBH}_4$ , dissolved in 0.75 mL milli-Q water, was added to it quickly. After addition of  $\text{NaBH}_4$ , reaction mixture became clean yellow solution which gradually converted to dark brownish solution and finally became dark green solution which indicated the formation of  $\text{Ag}_{18}$  NC. After 3.5 hour reaction, mixed solvent were removed at reduced pressure. Dark greenish nanocluster was dissolved in cold water to remove excess  $\text{NaBH}_4$  and  $\text{AgNO}_3$ . Finally, dark greenish  $\text{Ag}_{18}$  nanocluster was extracted using methanol. Formation of the NC was confirmed using UV-Vis spectroscopy and mass spectrometry, as shown in Fig. S4. The yield of the reaction was 25 % in terms of silver.

### **3) Synthesis of 2 pyrene imine thiol ligand:**

1000 mg (4.35 mM) of pyrene aldehyde was mixed with 762 mg (6.09 mM, 1.4 eq) of 2 amino thiophenol in an argon atmosphere. After 20 min of solid state mixing, 20 ml methanol and 10 ml ethanol was mixed with them and put for 4 hour refluxion at 60 °C. After the reaction, yellow color ligand was filtered using Whatman 42 filter paper and washed several times with excess ethanol and methanol to remove the excess starting materials. (Yield of the product: 1.58 gm, 90 %, yellow color). 2-PIT ligands were non emissive in both solid state as well as in solution.

**$^1\text{H}$  NMR ( $\text{CDCl}_3$ , 500 MHz)  $\delta$  =** 3.45 (s, 1H, S-H); 6.62 (m, 2H, Ar-H); 7.15 (m, 2H, Ar-H); 7.54 (dt, 1H, Pyr-H); 8.1 (m, 4H, Pyr-H); 8.27 (m, 4H, Pyr-H); 8.47 (t, 1H NC-H).

**$^{13}\text{C}$   $\{^1\text{H}\}$  NMR ( $\text{CDCl}_3$ , 125 MHz)  $\delta$  =** 168.16, 136.62, 132.99, 131.29, 130.65, 129.17, 128.97, 128.55, 127.19, 127.05, 126.79, 126.59, 126.42, 126.33, 126.03, 125.74, 125.28, 124.70, 123.47, 122.95, 121.43, 118.14, 115.21 ppm.

#### **4) Synthesis of Ag<sub>35</sub> nanocluster:**

Ag<sub>35</sub> nanocluster was prepared using modified ligand exchange reaction. About 15 mg purified Ag<sub>18</sub> nanocluster in 20 ml methanol was mixed with 4.5-5 mg 2-PIT ligand dissolved in 2-3 ml DCM solvent in dark condition. After 1 hour reaction at room temperature, greenish color Ag<sub>18</sub> nanocluster converted to a dark reddish color solution. After 24 hour reaction solution became wine red. Based on the UV-Vis absorption spectrum of these intermediates shown in Fig.S5b, which infers that these are mixed Ag-thiolate and Ag-phosphine complexes. The reaction was continued upto 48 hour which lead to the formation of dark violet colored Ag<sub>35</sub> nanocluster. After that, the solvents were evaporated in rotary evaporator and the cluster was washed several times with ethanol and water to remove excess ligands and silver precursors. Purified Ag<sub>35</sub> nanocluster, soluble in dichloromethane and chloroform, was used for further studies.

#### **5) Crystallization of Ag<sub>35</sub> nanocluster:**

30 mg purified Ag<sub>35</sub> nanocluster in 2.5 ml DCM solvent, layered with 0.75-1 ml hexane, led to the formation of cubical nanocluster crystals.

### **Instrumentation:**

#### **1) UV Visible spectroscopic measurements:**

Perkin Elmer Lambda 365 UV Visible spectrophotometer was used to study the optical absorption spectra for the clusters in the wavelength region of 200 to 1100 nm.

#### **2) ESI MS spectra:**

Mass spectrum of 2-pyrene imine thiol (2-PIT) was recorded using an ion trap Thermo Scientific LTQ XL mass spectrometer. Mass spectrum of Ag<sub>18</sub> and Ag<sub>35</sub> NCs were collected using Waters Synapt G2Si HDMS instrument. Both Ag<sub>18</sub> and Ag<sub>35</sub> NCs were measured in the positive ion mode. All the fragmentation experiments were recorded by varying the collision energy in the trap and transfer chambers of the same instrument. An optimized condition of capillary voltage 3 kV, spray current 100 nA, cone voltage 1 kV were used to record the mass spectrum of the cluster.

#### **3) Microscopic characterizations:**

##### **a) Optical imaging:**

All the optical microscopic images of the crystal were collected in 10X magnification using LEICA optical microscope equipped with LAS V4.8 software.

##### **b) TEM imaging:**

Size distribution of the NCs were recorded using Transmission electron microscopy, which was recorded at -40°C by using a JEOL 3010 high resolution transmission electron microscope operated at 200 kV. A Gatan multistage CCD camera was used to record the image.



**c) SEM EDS study:**

SEM EDS measurements were performed using Verios G4 UC, Thermo Scientific HRSEM instrument.

**4) Photoluminescence spectra:**

Photoluminescence spectra were measured using Jobin Yvon Nanolog spectrofluorometer equipped with Fluorescence V3 software.

**5) XPS study:**

X ray photoelectron spectroscopy were recorded using ESCA probe TPD equipped with polychromatic Mg K $\alpha$  X ray source ( $h\nu = 1253.6$  eV). DCM soluble cluster solution were spotted onto the XPS grid for the measurements.

**6) FTIR spectroscopic measurements:**

IR spectra of the 2-PIT ligand and Ag<sub>35</sub> NCs were recorded using Perkin Elmer FT-IR spectrometer.

**7) Single crystal XRD measurements:**

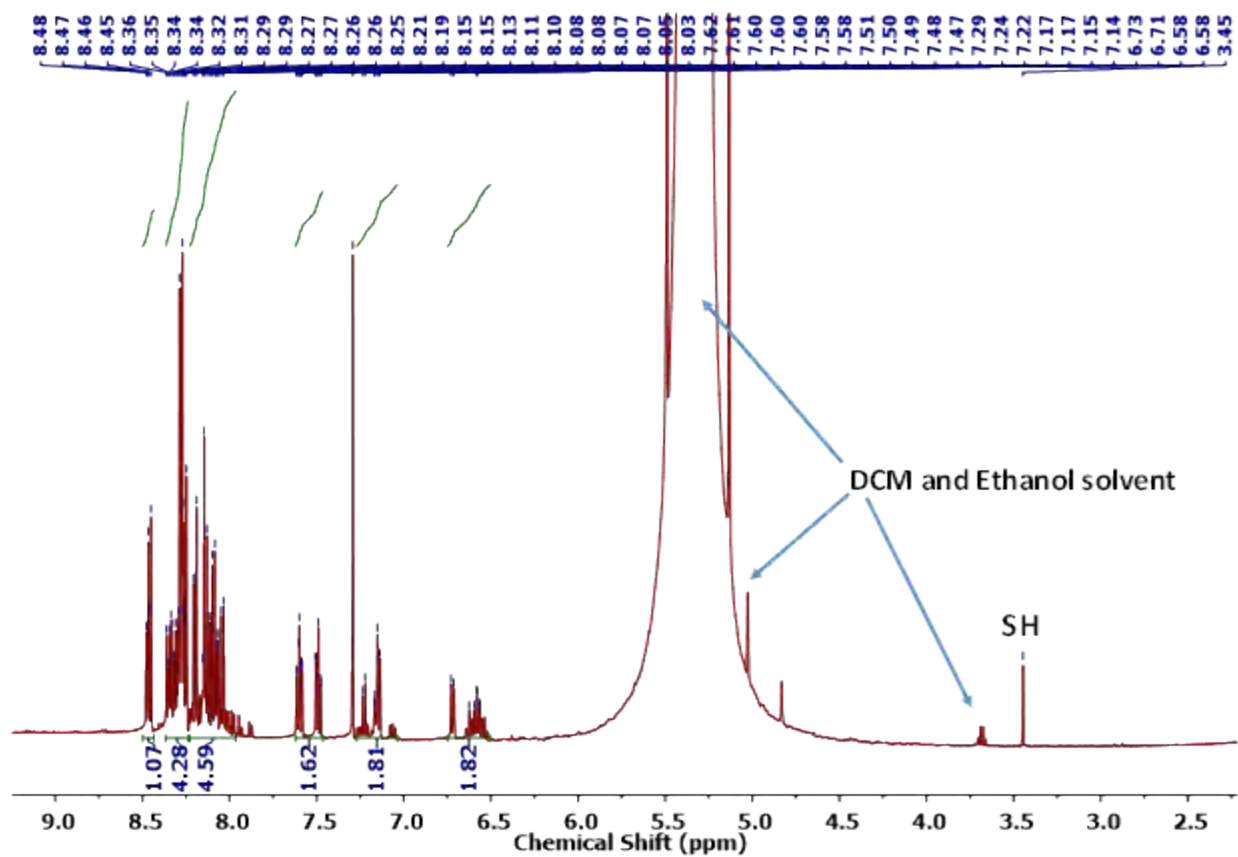
Single crystal X-ray diffraction data was collected using Bruker D8 VENTURE SC-XRD diffractometer, equipped with monochromatic Mo(K $\alpha$ ) (  $\lambda = 0.71073$  ) radiation at 296K. The structure was solved using SHELXL-2018 (Sheldrick, 2018) and refined using full matrix least squares techniques. The program APEX3-SAINT V8.37A (Bruker-2016) was used for integrating the frames. Hydrogen, carbon atoms were fixed at calculated positions and refined model. All the molecular structures, interaction and molecular packing were obtained using the Mercury software (Version 3.9).

Table S1. Crystal data and structure refinement for 2-pyrene imine thiol.

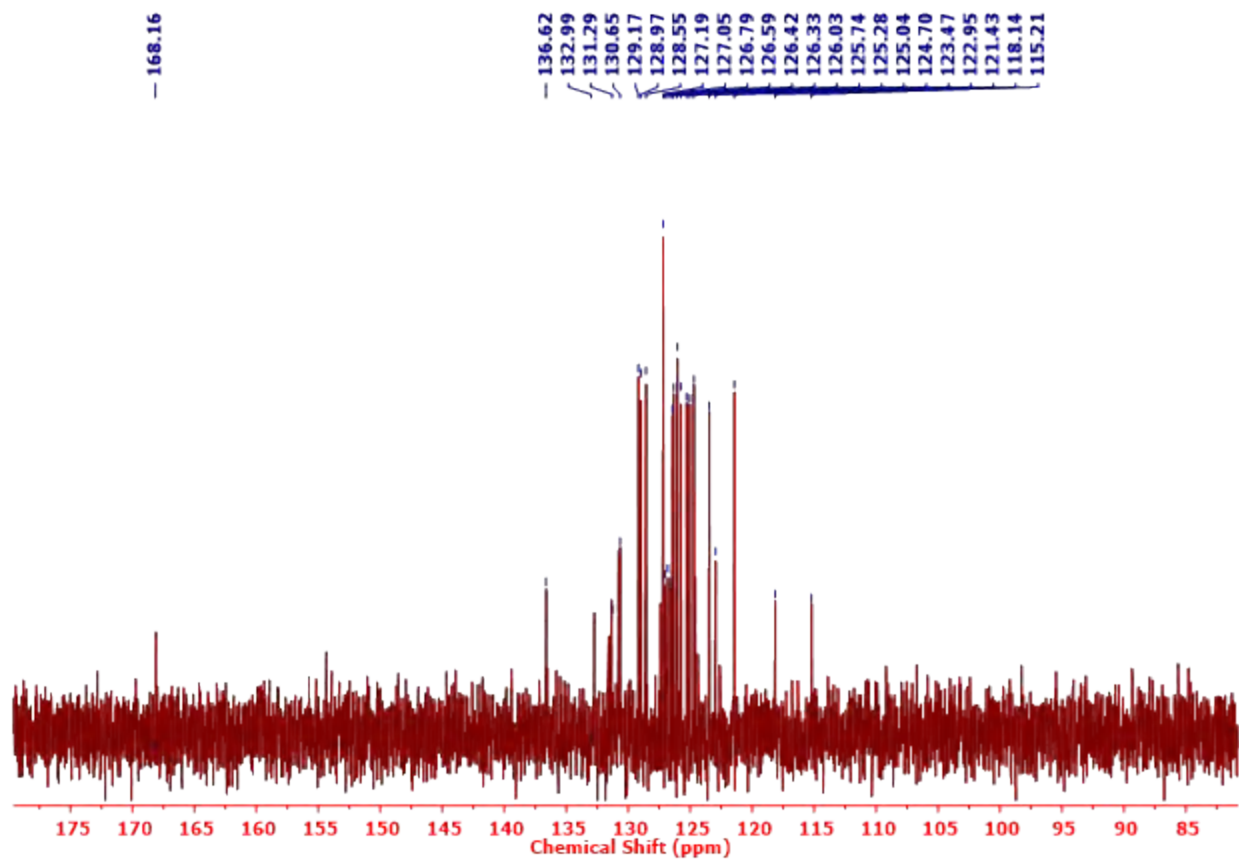
Identification code	AJ/2-PIT	
Empirical formula	C <sub>23</sub> H <sub>13</sub> N S	
Formula weight	335.40	
Temperature	296(2) K	
Wavelength	0.71073 Å	
Crystal system	Monoclinic	
Space group	P2 <sub>1</sub> /c	
Unit cell dimensions	a = 21.4278(11) Å	α = 90°.
	b = 4.9469(2) Å	β = 107.158(2)°.
	c = 15.5164(8) Å	γ = 90°.
Volume	1571.56(13) Å <sup>3</sup>	
Z	4	
Density (calculated)	1.418 Mg/m <sup>3</sup>	
Absorption coefficient	0.210 mm <sup>-1</sup>	
F(000)	696	
Crystal size	0.150 x 0.150 x 0.100 mm <sup>3</sup>	
Theta range for data collection	3.409 to 24.993°.	
Index ranges	-25 ≤ h ≤ 25, -5 ≤ k ≤ 5, -18 ≤ l ≤ 18	
Reflections collected	31947	
Independent reflections	2751 [R(int) = 0.0901]	
Completeness to theta = 24.993°	99.7 %	
Absorption correction	Semi-empirical from equivalents	
Max. and min. transmission	0.7445 and 0.6331	
Refinement method	Full-matrix least-squares on F <sup>2</sup>	
Data / restraints / parameters	2751 / 0 / 226	
Goodness-of-fit on F <sup>2</sup>	1.150	
Final R indices [I > 2σ(I)]	R1 = 0.0679, wR2 = 0.1488	
R indices (all data)	R1 = 0.0888, wR2 = 0.1600	
Extinction coefficient	n/a	
Largest diff. peak and hole	0.407 and -0.319 e.Å <sup>-3</sup>	

Table S2. Atomic coordinates ( $\times 10^4$ ) and equivalent isotropic displacement parameters ( $\text{\AA}^2 \times 10^3$ ) for 1.  $U(\text{eq})$  is defined as one third of the trace of the orthogonalized  $U^{ij}$  tensor.

	x	y	z	$U(\text{eq})$
C(1)	5785(2)	8045(7)	4465(2)	39(1)
C(2)	5228(2)	9511(7)	4019(2)	44(1)
C(3)	5266(2)	11345(7)	3382(2)	46(1)
C(4)	5852(2)	11734(7)	3165(2)	49(1)
C(5)	6398(2)	10249(7)	3592(2)	48(1)
C(6)	6370(2)	8388(6)	4239(2)	38(1)
C(7)	6721(2)	5275(6)	5304(2)	37(1)
C(8)	7134(2)	3299(7)	5916(2)	37(1)
C(9)	6941(2)	2449(7)	6661(2)	46(1)
C(10)	7285(2)	572(8)	7258(2)	49(1)
C(11)	7844(2)	-614(7)	7152(2)	42(1)
C(12)	8210(2)	-2596(8)	7763(2)	54(1)
C(13)	8734(2)	-3793(8)	7625(2)	55(1)
C(14)	8952(2)	-3137(7)	6867(2)	47(1)
C(15)	9491(2)	-4386(8)	6709(3)	56(1)
C(16)	9691(2)	-3689(8)	5976(3)	60(1)
C(17)	9361(2)	-1767(8)	5376(3)	53(1)
C(18)	8819(2)	-433(7)	5502(2)	41(1)
C(19)	8610(2)	-1135(6)	6258(2)	38(1)
C(20)	8050(2)	154(6)	6395(2)	36(1)
C(21)	7702(2)	2142(6)	5779(2)	34(1)
C(22)	7941(2)	2818(7)	5032(2)	40(1)
C(23)	8469(2)	1587(7)	4909(2)	44(1)
N(1)	6883(1)	6787(6)	4721(2)	42(1)
S(1)	5902(1)	5684(2)	5314(1)	46(1)



**Fig. S1:**  $^1\text{H}$  NMR spectrum of 2-pyrene imine thiol ligand in  $\text{CDCl}_3$  solvent. (DCM, ethanol peaks are due to impurity).



**Fig. S2:**  $^{13}\text{C}$   $\{^1\text{H}\}$  NMR spectrum of 2-pyrene imine thiol ligand in  $\text{CDCl}_3$  solvent.

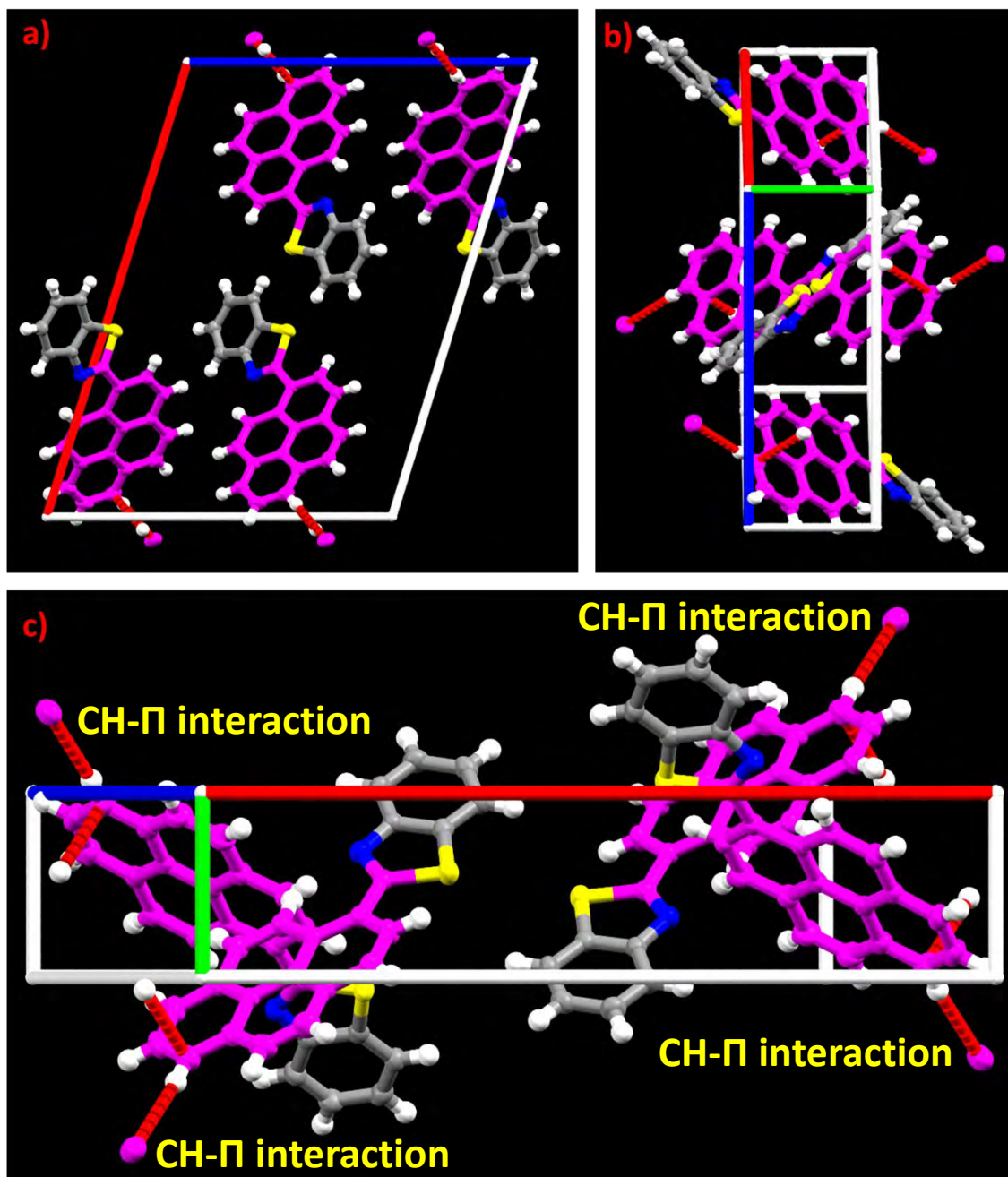


**Fig. S3:** a, b, c) Single crystal unit cell packing of 2-PIT molecule in three different orientations. Several C-H - $\pi$  intermolecular interactions leading to the crystallization are shown here.



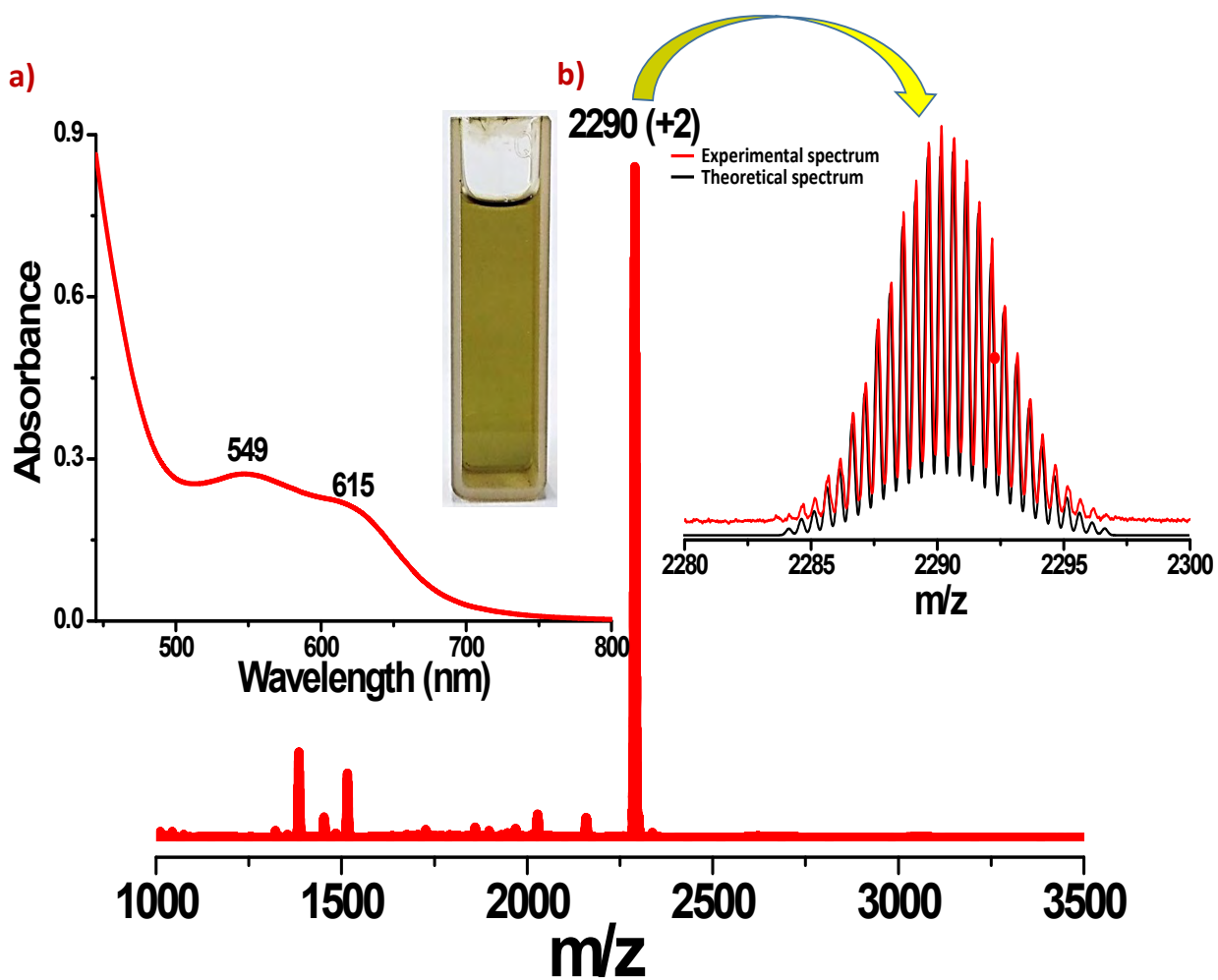


**Fig. S4:** a) UV-Visible absorption spectrum of  $\text{Ag}_{18}$  NC in methanol (inset digital image of the nanocluster); b) positive mode ESI-MS spectrum of the NC (inset shows experimental and theoretical spectrum).

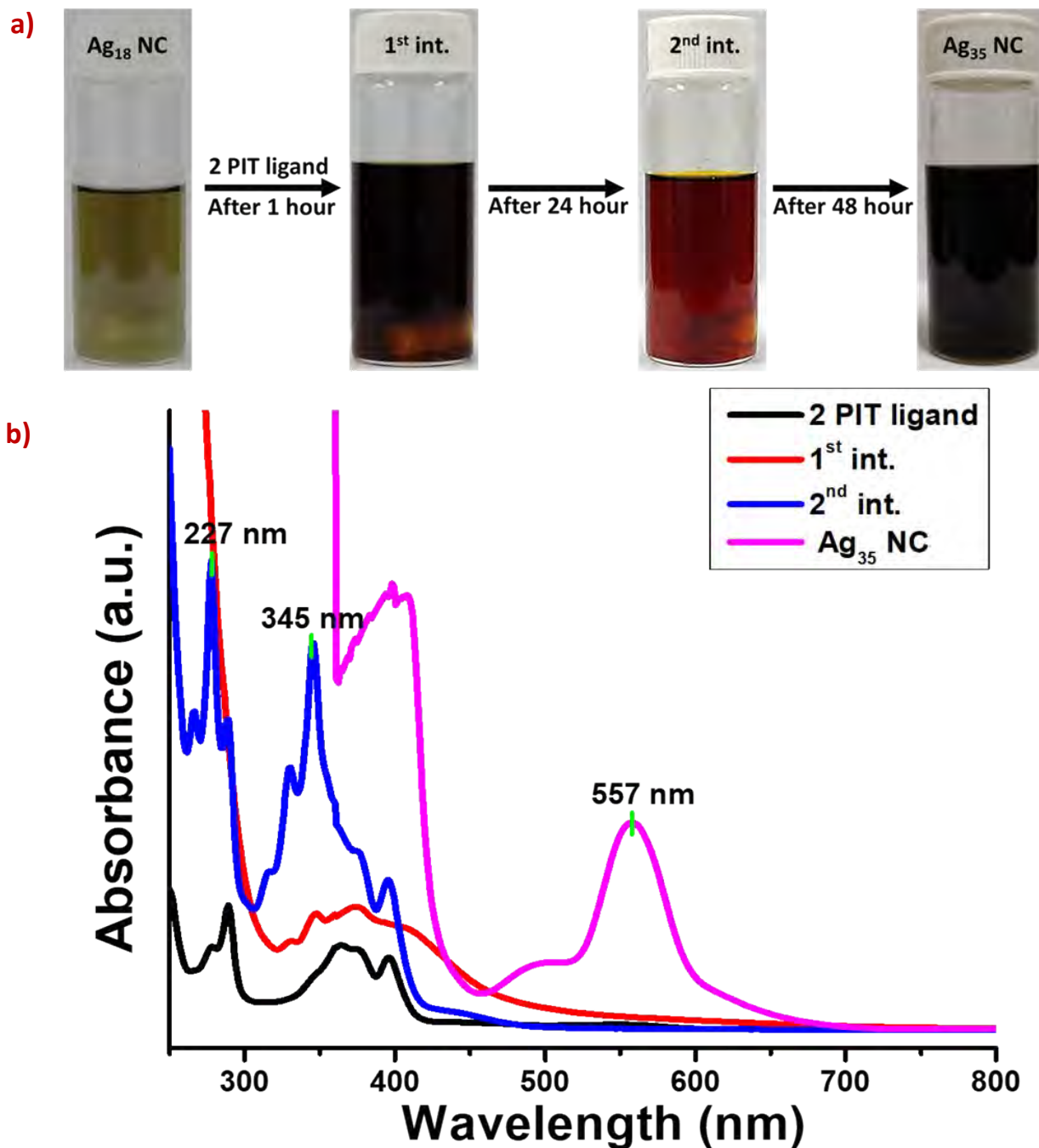


**Fig. S5:** a) Photographs of the reaction mixtures during the course of the reaction; b) UV-Vis absorption spectrum of the ligand, intermediates and Ag<sub>35</sub> NC. (emergence of the characteristic peak at 557 nm indicated the formation of Ag<sub>35</sub> NC).

Ag<sub>35</sub> NC

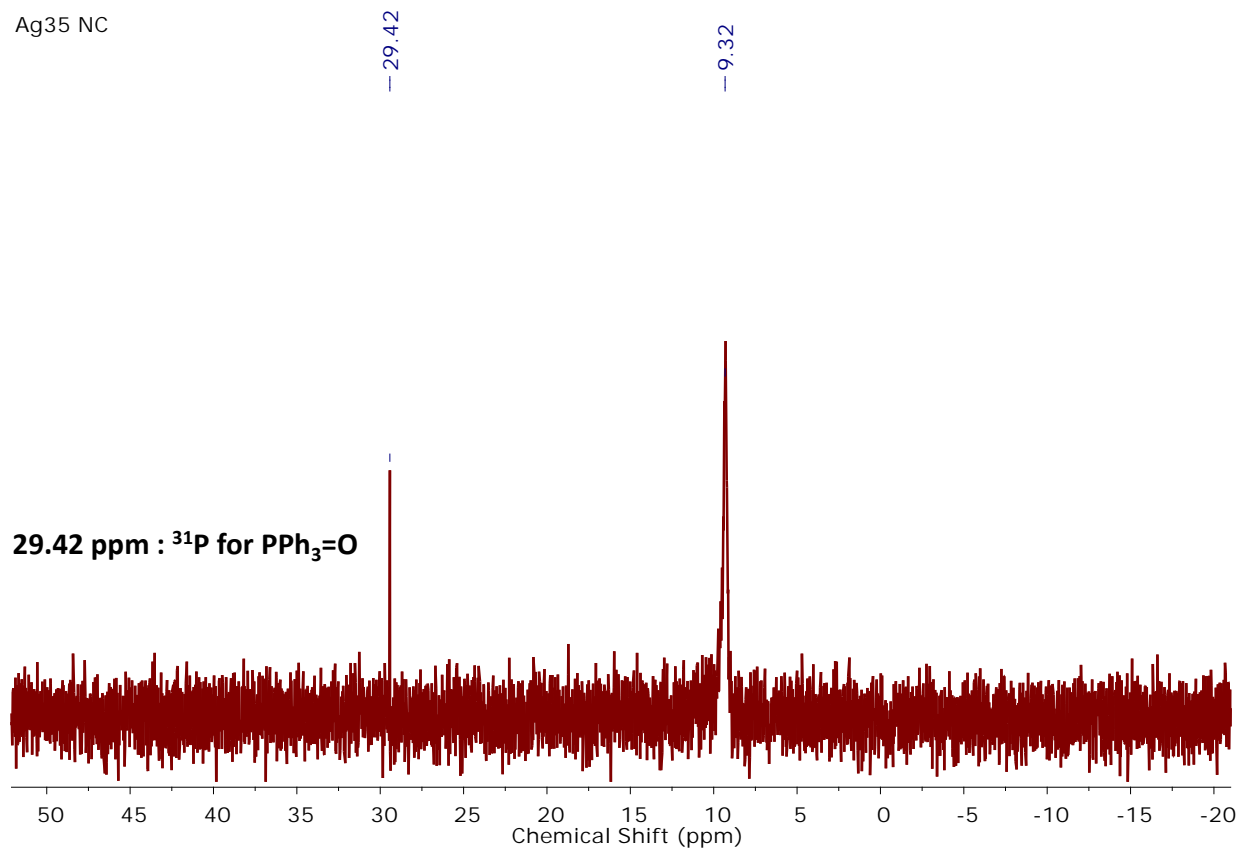


**Fig. S6:** <sup>31</sup>P {<sup>1</sup>H} NMR spectrum of Ag<sub>35</sub> nanocluster in CDCl<sub>3</sub> solvent (broad NMR peak at 9.32 ppm indicating phosphorous of PPh<sub>3</sub> binding with cluster).

### XPS analysis:

The XPS spectra are shown in Fig. S7 and S8 (Table S3) of the ligand and Ag<sub>35</sub> NC, respectively. Among the four peaks of Ag<sub>35</sub> NC, two peaks at 284.8 and 286.6 eV are comparable with the two peaks at 284.8 and 286.3 eV of the C 1s region of the 2-PIT ligand, which suggests the binding of the 2-PIT ligand. The two other peaks of the C 1s region at 288.2 and 289.4 eV are due to the two types of TPP ligands. The decrease in the binding energy of the N 1s and S 2p regions in the Ag<sub>35</sub> NC, compared to the 2-PIT ligand, is probably due to the electron back donation from the metal core to the N and S end of the ligand. The higher electronegativity of N and S compared to Ag is also the reason behind it. The binding energy of 368.4 and 374.5 eV for the Ag 3d region suggests the metallic state of silver.

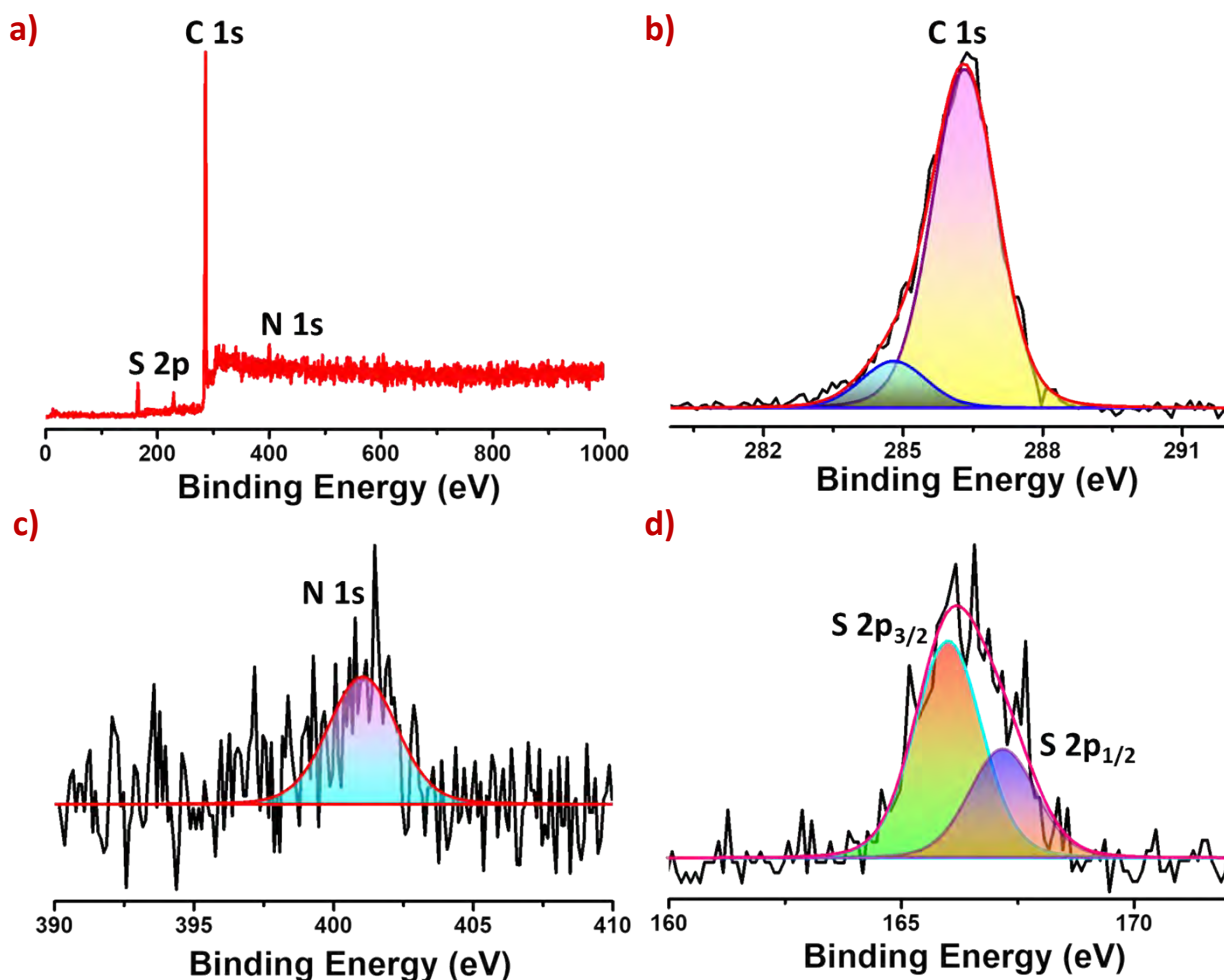


**Fig. S7:** XPS spectra of 2-PIT ligand a) survey spectrum indicating C, N and S characteristic peak; peak fitting of b) C 1s showing two fitted peaks; c) N 1s and, d) S 2p regions.

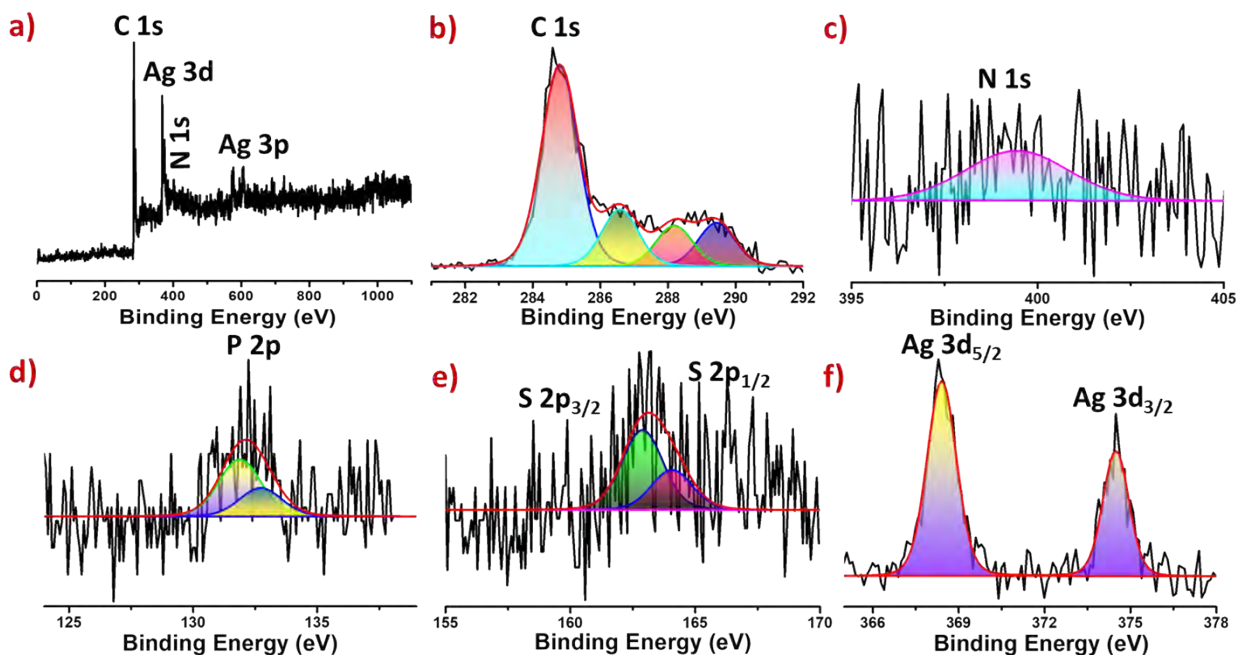


**Fig. S8:** XPS spectra of the Ag<sub>35</sub> NCs; a) survey spectrum of the NCs indicating different regions; peak fitting of the b) C 1s indicating four fitted peaks; c) N 1s; d) P 2p; e) S 2p; f) Ag 3d regions.

**Table S3:** Comparative binding energy of Ag<sub>35</sub> NC and 2-PIT ligand in different spectral region.

Spectral regions	Binding energy (Ag <sub>35</sub> NC)	Binding energy (2-PIT ligand)
C 1s	284.8 eV 286.6 eV 288.2 eV 289.4 eV	284.8 eV 286.3 eV
N 1s	399.4 eV	401 eV
S 2p	162.8 eV (S 2p <sub>3/2</sub> ) 164 eV (S 2p <sub>1/2</sub> )	166 eV (S 2p <sub>3/2</sub> ) 167.1 eV (S 2p <sub>1/2</sub> )
P 2p	131.8 eV 132.7 eV	
Ag 3d	368.4 eV (Ag 3d <sub>5/2</sub> ) 374.5 eV (Ag 3d <sub>3/2</sub> )	

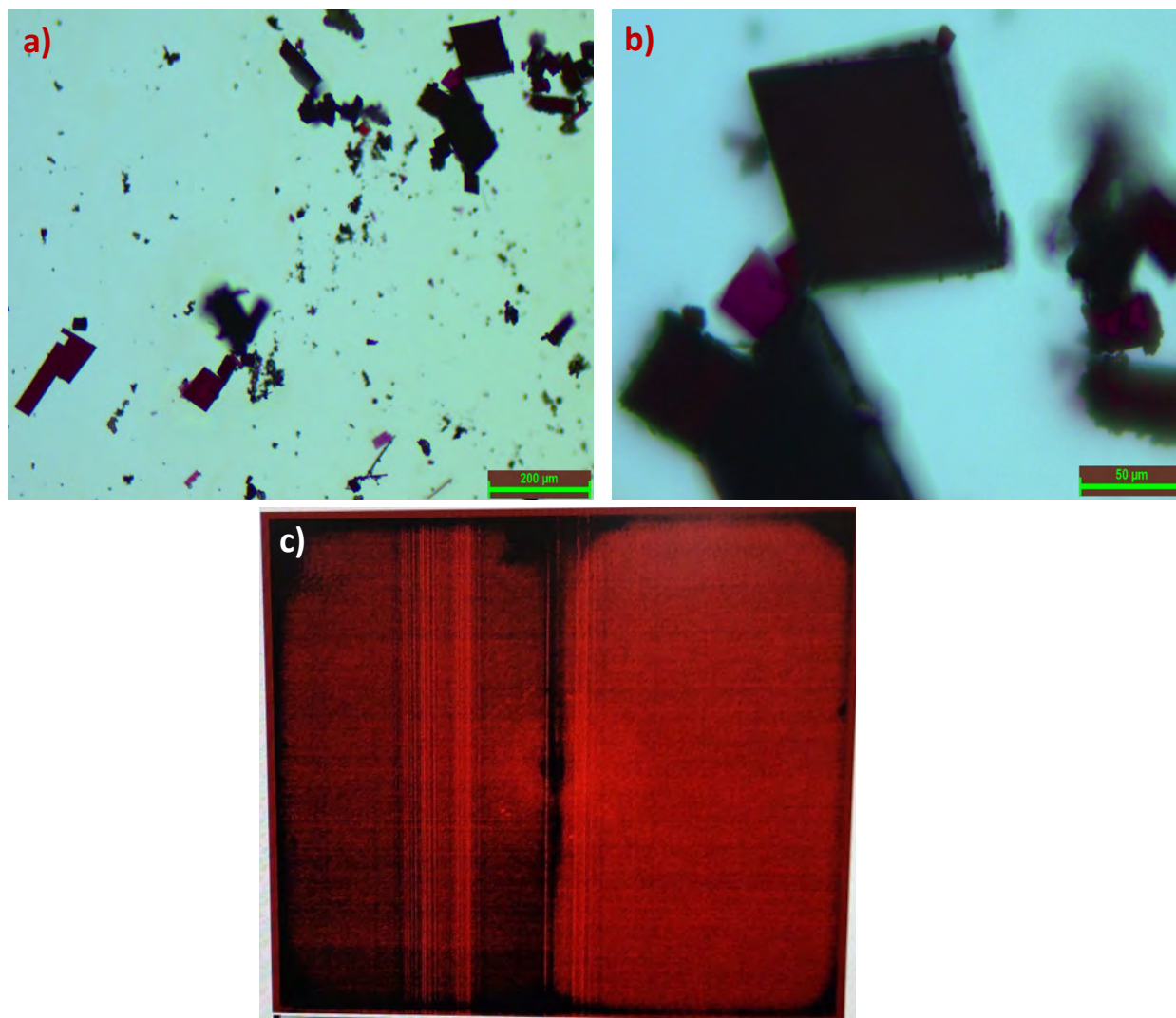


**Fig. S9:** a) Large area optical microscopic images of the nanocluster crystals; b) magnified image under bright field; c) photographs of weak single-crystal X-ray diffraction spots.



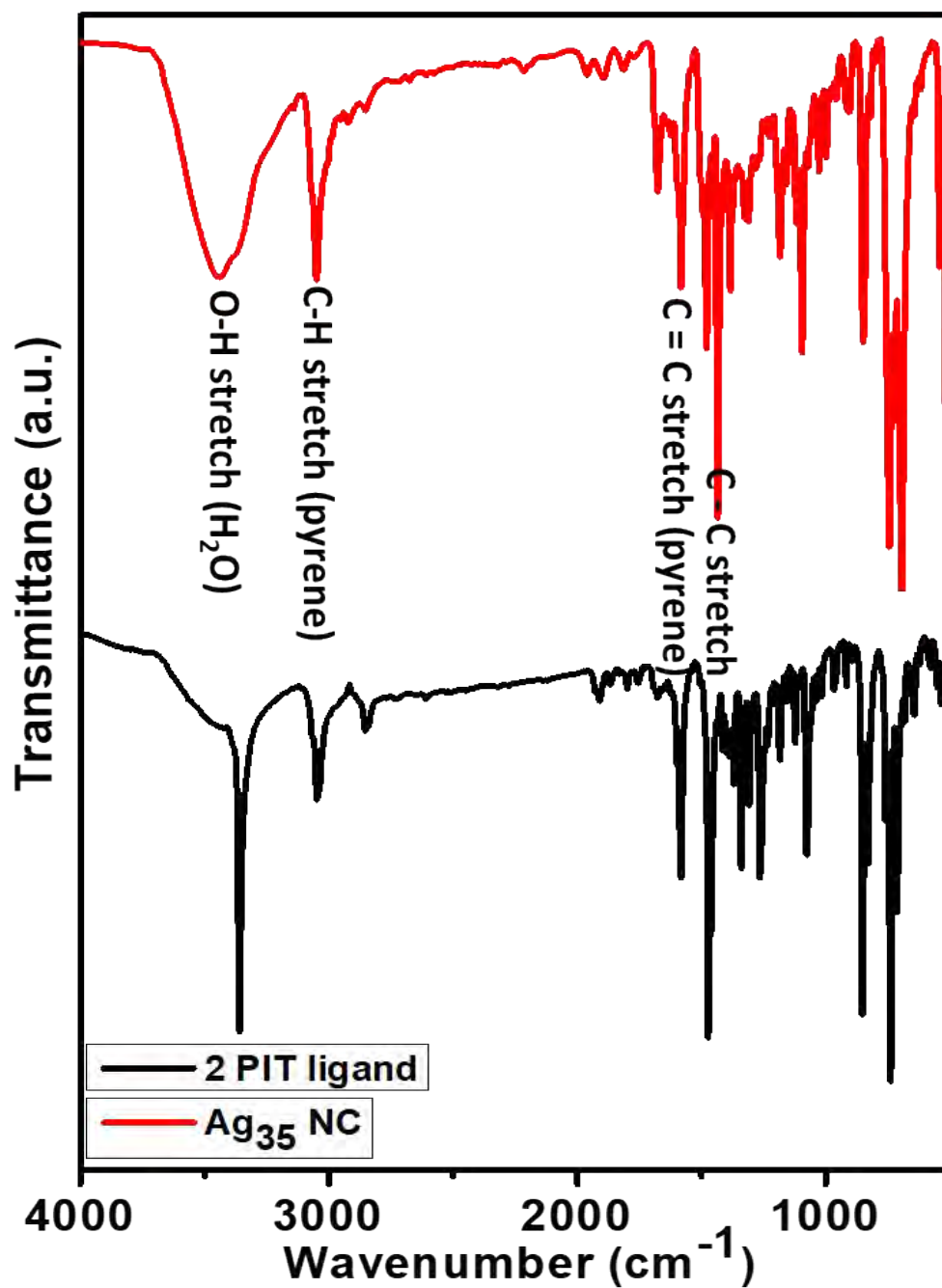


**Fig. S10:** The IR spectra of 2-PIT ligand and  $\text{Ag}_{35}$  NC (pyrene C-H, C=C and  $\text{H}_2\text{O}$  stretching peaks are marked here).

**References:**

- S1 O. M. Bakr, Megalamane S. Bootharaju, Raju Dey, Lieven E. Gevers, Mohamed N. Hedhili, Jean-Marie Basset, *J. Am. Chem. Soc.*, 2016, **138**, 13770–13773.

# Cocrystals of Atomically Precise Noble Metal Nanoclusters

Mohammad Bodiuzzaman, Wakeel Ahmed Dar, and Thalappil Pradeep\*

Cocrystallization is a phenomenon involving the assembly of two or more different chemical entities in a lattice, occurring typically through supramolecular interactions. In this concept, recent advancements in the cocrystallization of atomically precise noble metal clusters and their potential future directions are presented. Different strategies to create coassemblies of thiolate-protected noble metal nanoclusters are presented first. An approach is the simultaneous synthesis, and cocrystallization of two clusters having similar structures. A unique pair of clusters found recently, namely Ag<sub>40</sub> and Ag<sub>46</sub> with same core but different shell are taken to illustrate this. In another category, the case of the same core is presented, namely Ag<sub>116</sub> with different shells, as in a mixture of Ag<sub>210</sub> and Ag<sub>211</sub>. Next, an intercluster reaction is presented to create cocrystals through selective crystallization of the reaction products. The coexistence of competing effects, magic sizes, and magic electron shells in a coassembly of alloy nanoclusters is discussed next. Finally, an assembly strategy for nanoclusters using electrostatic interactions is described. This concept is concluded with a future perspective on the emerging possibilities of such solids. Advancements in this field will certainly help the development of novel materials with exciting properties.

bridging link between atoms and bulk state of materials. NCs have precise molecular formulae and possess many properties that are similar to those of molecules (e.g., quantized energy levels, optical absorption, and emission, nonlinear optical properties, electrochemical properties, chirality, and magnetism).<sup>[4,8,9]</sup> The properties of NCs depend heavily on their size, geometry, and composition, due to the quantum confinement effects.<sup>[10]</sup> They also vary drastically with the number of constituting atoms. This has greatly strengthened the importance of cluster chemistry.<sup>[11]</sup>

Among the NCs, the most important family of stable clusters belong to those of noble metals, typically protected with thiolates. Considering the affinity of thiols toward gold or silver, Brust et al.<sup>[12,13]</sup> have introduced thiols as ligands, and the era of monolayer protected clusters was born with thiol protection. Till date many clusters have been synthesized following the

modified Brust synthesis method.


Single crystal X-ray structures are considered as the holy grail of cluster science. More than 500 clusters (as on June 2020) have single crystal structures.<sup>[3,5,15,16]</sup> Exploring the total structures of metal NCs is of great significance for explaining their stability, metal sulfur interface, and different properties. Nanoclusters are generally represented as M<sub>x</sub>(SR)<sub>y</sub> (where *x* and *y* represent the number of metal atoms and protecting ligands, respectively, and the latter are typically thiols, and they bind to the metal surface as thiolate, -SR). Nanoclusters can also be stabilized by thiol-phosphine mixtures. Thiol is used to provide primary protection to the cluster, and phosphine acts as a secondary ligand. In presence of multiple ligands, stability and properties of NCs were enhanced than those composed of single ligands.<sup>[6]</sup> Particularly, secondary ligands help in crystallizing molecules as well as enhancing their optical properties.<sup>[17,18]</sup> After synthesis, the most important effort is to understand the cluster with molecular tools, such as mass spectrometry to assign the precise composition. Subsequently, the purified and often size separated cluster is assembled leading to a well-ordered crystal. A number of techniques can be used to understand the composition and structure. This approach is depicted in **Scheme 1**. Atomic-level doping of foreign metals in the parent cluster is known to create doped or alloy clusters, which exhibit enhanced stability and improved optical and catalytic properties.<sup>[19]</sup> Precise molecular structure, electronic energy levels, optical absorption and emission,<sup>[10]</sup> reactivity,<sup>[20,21]</sup> electroreduction,<sup>[22]</sup> water oxidation,<sup>[23]</sup> sensing,<sup>[24,25]</sup> bioimaging,<sup>[26]</sup> catalysis,<sup>[22,27]</sup> and an expanding

## 1. Introduction

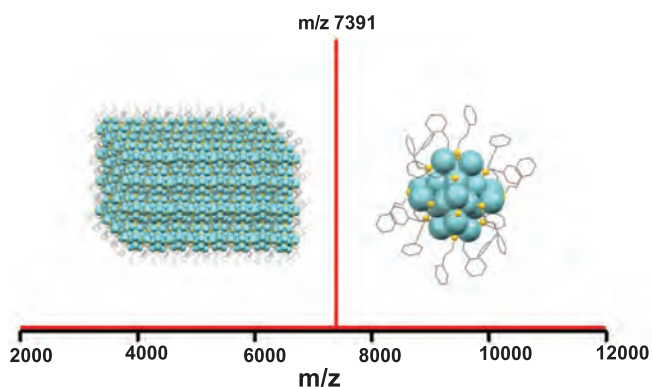
### 1.1. Monolayer Protected Clusters

Atomically precise nanoclusters (NCs) may be defined as nanomaterials composed of a specific number of constituent atoms, typically metals, held together by metal-metal bonds as in Au<sub>25</sub>, Au<sub>38</sub>, Au<sub>102</sub>, Au<sub>144</sub>, Ag<sub>25</sub>, Ag<sub>29</sub>, Ag<sub>44</sub>, and PdAu<sub>24</sub> with fixed number of ligands and precise charges, so that the overall entity has a well-defined composition, structure, and associated properties.<sup>[1–7]</sup> Nuclearity of the cluster is the number of metal atoms in this core which has a diameter in the range of 1–3 nm. NCs behave like molecules and are not generally plasmonic in nature and exhibit optical properties distinctly different from those of traditional nanoparticles. Bonding between the atoms in NCs is different from those in bulk metals or in nanoparticles. Their sizes (<3 nm) fall between atoms and nanoparticles, and therefore, this regime of matter is considered as the

Dr. M. Bodiuzzaman, Dr. W. A. Dar, Prof. T. Pradeep  
Department of Chemistry  
DST Unit of Nanoscience and Thematic Unit of Excellence  
Indian Institute of Technology Madras  
Chennai 600036, India  
E-mail: pradeep@iitm.ac.in

 The ORCID identification number(s) for the author(s) of this article can be found under <https://doi.org/10.1002/sml.202003981>.

DOI: 10.1002/sml.202003981



**Scheme 1.** An atomically precise cluster characterized by molecular tools, such as mass spectrometry, is assembled to give a cluster crystal. For illustration, the cluster used here is  $\text{Au}_{25}(\text{SCH}_2\text{CH}_2\text{C}_6\text{H}_5)_{18}^-$ . The ligand employed here,  $\text{C}_6\text{H}_5\text{CH}_2\text{CH}_2\text{SH}$  or phenylethanethiol, binds to the cluster core as phenylethanethiolate,  $\text{C}_6\text{H}_5\text{CH}_2\text{CH}_2\text{S}^-$ , referred to as PET). Mass spectrum. Reproduced with permission.<sup>[14]</sup> Copyright 2017, American Chemical Society.

body of emerging properties, increasingly reaffirm the molecular nature of such systems. For specific aspects of cluster synthesis, characterization, and crystallization, please consult other articles in this special issue on clusters.

## 1.2. Cluster Crystals

Assembling such clusters with similar molecular entities has been explored from the very early period of cluster science, and the very first example of gold clusters protected with phosphine was cocrystallized with a Keggin anion,  $\alpha\text{-}[\text{PW}_{12}\text{O}_{40}]^{3-}$  in 2006.<sup>[28]</sup> Coassemblies composed of fullerenes and clusters of cobalt and iron have been reported subsequently.<sup>[29,30]</sup> Recently, Roy group reported superconductivity in cluster assembled solids of  $\text{Re}_6\text{Se}_8\text{Cl}_2$ .<sup>[31]</sup> The emergence of thiolated gold clusters with chemical and physical stability, exhibiting new properties, such as distinct optical absorption and visible to near-infrared emission present new possibilities for their assembled solids. Existence of well-defined cluster shapes derived from polyhedra belonging to different categories and the presence of covalently anchored ligands on metal cores, capable of making specific noncovalent interactions between protected clusters and possibilities of inclusion complexes with ligands, together expand the possibility of assembly of thiolated noble metal clusters.<sup>[32,33]</sup>

Cocrystallization is a well-known approach used for the design of diverse new multicomponent solids. Current attraction of cocrystals is mainly due to their applications in pharmaceuticals in terms of modifying the physicochemical properties of drugs.<sup>[35]</sup> A few examples of cocrystals of small molecules are presented in **Table 1**. They have multiple advantages as follows: a) Novelty: Cocrystallization leads to unique solids in terms of their structures and properties. b) Utility: Cocrystals show different physicochemical properties which have been exploited for specific and wide-ranging applications as in electronics, solar cells, energy storage, and luminescent materials. c) Multiplicity: A large number of products are possible as thousands of organic compounds can make cocrystals. d) Greenness: The accessibility of hundreds of

precursors for cocrystallization and comparatively easy synthetic methods lead to the saving of energy, effort, and time.

In the recent past, we find that research on cocrystallization is expanding from pharmaceuticals to materials. Cocrystallization of different NCs could lead to potential new physicochemical properties differing from those of their simple physical mixtures. In such a physical mixture, the periodicity of building blocks and associated ordered supramolecular interactions will be absent which can bring modification in mechanical properties, optical and electrical transport properties as physical properties, such as melting point. Cocrystals of clusters reported are listed in **Table 1**. The concept of cocrystallization is very new in thiolate-protected atomically precise nanoclusters. Emerging examples for such systems are beginning to be available, and a rich diversity in this category of materials is definite to make a lasting impact in chemical science. In this Concept, we explore the new directions of this emerging science, manifested in noble metal cluster cocrystals. These are as follows:

- Simultaneous encapsulation of externally similar structures in a single crystal.
- Selective crystallization from a reaction mixture as a result of interparticle reaction.
- Coexistence of competing effects (magic sizes vs magic electron shells) in alloy nanoparticles to form cocrystals.
- Cocrystals composed of +ve and -ve clusters making an ionic cluster solid.

These aspects are summarized in **Scheme 2**. In the sections below, we discuss each of these specific categories.

## 2. Simultaneous Encapsulation of Similar Structures in a Single Crystal

A large number of atomically precise metal nanoclusters are crystallized in the recent past.<sup>[3,6,56–64]</sup> They can be understood by the divide and protect rule<sup>[65]</sup> in which metallic cores are surrounded by a polymeric shell, usually made by staple motifs. In general, clusters are formed starting with well-known icosahedral cores with appropriate capping and protecting linkages, often arranged as monomeric (-SR-M-SR-) or dimeric (-SR-M-SR-M-SR-), etc., staples. The staple linkage around the core is called a shell. Among gold clusters,  $\text{Au}_{25}(\text{SR})_{18}$  is an intensely studied one because of its versatility toward ligands. It consists of an  $\text{Au}_{13}$  icosahedral core, protected by 6  $\text{Au}_2(\text{SR})_3$  staples making a  $\text{Au}_{12}\text{SR}_{18}$  shell (**Figure 1A**).<sup>[4]</sup> Similar core and shell structure was observed in  $\text{Ag}_{25}(\text{SR})_{18}$  by the Bakr group.<sup>[62]</sup>  $\text{Ag}_{29}(\text{S}_2\text{R})_{12}(\text{PPh}_3)_4$ , another intensely studied cluster system consists of the  $\text{Ag}_{13}$  icosahedral core and  $\text{Ag}_{16}\text{S}_{24}\text{P}_4$  shell. These core and shell structures are summarized in **Figure 1**. Other core structures, namely, face-centered cube, simple cube, biicosahedra, body centered cube, and multiple metallic layer core structures have also been observed.<sup>[58,61,66–69]</sup> Combined unit of the core and shell structures create 3D atomic structures of clusters. This molecular framework with structural rigidity is also associated with magic electronic structure, to ensure that such systems are stable.<sup>[70]</sup> Understanding of such structures

**Table 1.** Some examples of cocrystals of small molecules, clusters, and their importance. In the category of small molecules, only illustrative examples are given.

Type	Cocrystals	Importance	Ref.
Small molecules	Cis-itraconazole and 1,4-dicarboxylic acids, Vitamins D <sub>2</sub> (VD <sub>2</sub> ) and D <sub>3</sub> (VD <sub>3</sub> ), hexamethylenebisacetamide and aliphatic even-numbered dicarboxylic acids, aspirin and 4,4'-bipyridine, fluoxetine hydrochloride and benzoic acid, fluoxetine hydrochloride and fumaric acid, acetaminophen with theophylline, acetaminophen and its hydrochloride salt	Pharmaceutical applications	[34–40]
	1,2-bis(2-methyl-5-(1-naphthyl)-3-thienyl)perfluorocyclopentene and perfluoronaphthalene	Converts light into mechanical work	[41]
	2,4,6,8,10,12-hexanitro-2,4,6,8,10,12-hexaazaiso-wurtzitane and 2,4,6-trinitrotoluene (TNT)	Smart materials	[42]
	Anthracene and tetracene	Novel fluorophores for solar concentrators	[43]
	Gallic acid and isoniazid	Structural insights into proton conduction	[44]
	2,7-di-tert-butyl-10,14-di(thiophen-2-yl)phenanthro[4,5-abc][1,2,5]thiadiazolo[3,4-i]phenazine and tetracyanoquinodimethane (TCNQ)	Switching of p-type semiconductor to n-type semiconductor	[45]
	Caffeine, 4-chloro-3-nitrobenzoic acid and methanol, p-phenylenediamine and N-phenyl-p-phenylenediamine	New organic functional materials	[46,47]
Cocrystals of clusters	[Au <sub>9</sub> (PPh <sub>3</sub> ) <sub>8</sub> ] <sub>2</sub> [V <sub>10</sub> O <sub>28</sub> H <sub>3</sub> ] <sub>2</sub>	Crystal structure	[48]
	[(In <sub>3</sub> GeS <sub>7</sub> )(Cu <sub>5</sub> In <sub>30</sub> S <sub>56</sub> )] <sup>18-</sup> [(H <sub>2</sub> TMDP) <sup>2+</sup> ] <sub>9</sub> (TMDP = 4,4'-trimethylenedipiperidine)	Crystal structure	[49]
	[Co <sub>6</sub> Te <sub>8</sub> (PEt <sub>3</sub> ) <sub>6</sub> ][Fe <sub>8</sub> O <sub>4</sub> pz <sub>12</sub> Cl <sub>4</sub> ] (pz = pyrazolate)	Crystal structure	[50]
	[Co <sub>6</sub> Te <sub>8</sub> (PnPr <sub>3</sub> ) <sub>6</sub> ][C <sub>60</sub> ] <sub>3</sub> and [Co <sub>6</sub> Se <sub>8</sub> (PEt <sub>3</sub> ) <sub>6</sub> ][C <sub>60</sub> ] <sub>3</sub>	Electronic transport properties	[30]
Recent trends in cocrystallization of thiolate-protected noble metal nanoclusters	(Ag <sub>210</sub> (iPr <sub>3</sub> PhS) <sub>71</sub> (Ph <sub>3</sub> P) <sub>5</sub> Cl and Ag <sub>211</sub> (iPr <sub>3</sub> PhS) <sub>71</sub> (Ph <sub>3</sub> P) <sub>6</sub> Cl	Crystal structure	[51]
	[Ag <sub>46</sub> (SPhMe <sub>2</sub> ) <sub>24</sub> (PPh <sub>3</sub> ) <sub>8</sub> ] <sup>2+</sup> and [Ag <sub>40</sub> (SPhMe <sub>2</sub> ) <sub>24</sub> (PPh <sub>3</sub> ) <sub>8</sub> ] <sup>2+</sup>	Crystal structure	[52]
	[(AuAg) <sub>267</sub> (SR) <sub>80</sub> ] and [(AuAg) <sub>45</sub> (SR) <sub>27</sub> (PPh <sub>3</sub> ) <sub>6</sub> ]	Crystal structure	[53]
	[Ag <sub>16</sub> (S <sup>t</sup> Bu) <sub>8</sub> (CF <sub>3</sub> COO) <sub>7</sub> (ACN) <sub>3</sub> Cl] <sup>+</sup> [Ag <sub>17</sub> (S <sup>t</sup> Bu) <sub>8</sub> (CF <sub>3</sub> COO) <sub>7</sub> (ACN) <sub>3</sub> Cl] <sup>+</sup>	Reaction and cocrystallization	[54]
	[Ag <sub>26</sub> Au(2-EBT) <sub>18</sub> (PPh <sub>3</sub> ) <sub>6</sub> ] <sup>+</sup> and [Ag <sub>24</sub> Au(2-EBT) <sub>18</sub> ] <sup>-</sup>	Ionic cocrystal	[55]

obviously shows the appearance of common outer shell having varied inner cores and vice versa.

## 2.1. Same Shell but Different Core

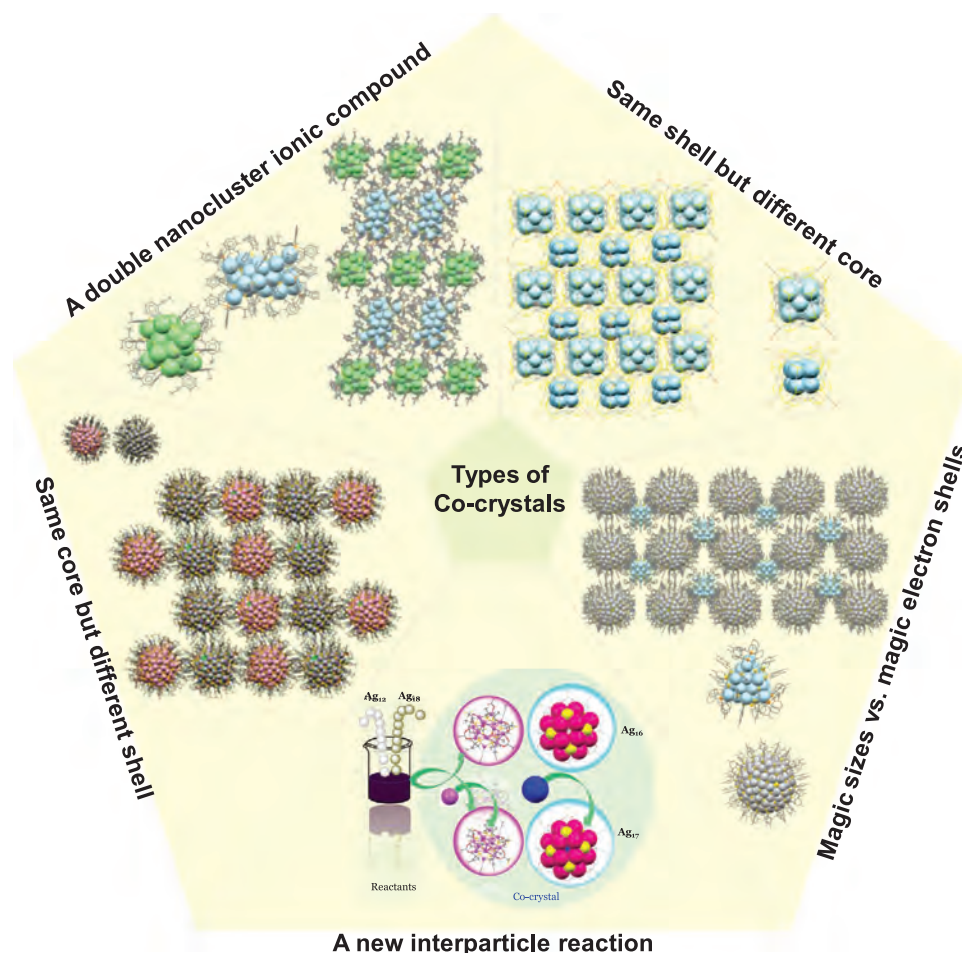
Mixed ligand protected molecular pieces of silver, namely, [Ag<sub>46</sub>(DMBT)<sub>24</sub>(TPP)<sub>8</sub>](NO<sub>3</sub>)<sub>2</sub> and [Ag<sub>40</sub>(DMBT)<sub>24</sub>(TPP)<sub>8</sub>](NO<sub>3</sub>)<sub>2</sub> (shortened as Ag<sub>46</sub> and Ag<sub>40</sub>, respectively) with the same shell but different inner cores were synthesized simultaneously.<sup>[52]</sup> A mixture of purified clusters was crystallized in a monoclinic crystal system with space group, C2/m.

Structural refinement unambiguously confirmed that there are two types of clusters in the crystal. These clusters exhibited almost the same structures but differed by six metals in them and can exchange their positions. Total structures of both the clusters revealed that six atomic locations of the core of [Ag<sub>46</sub>(DMBT)<sub>24</sub>(TPP)<sub>8</sub>] are empty in [Ag<sub>40</sub>(DMBT)<sub>24</sub>(TPP)<sub>8</sub>]. Due to identical structures of the outer shell, clusters were not able to differentiate themselves and got cocrystallized. Therefore, the difference in the inner core does not affect the

growth process of the crystals, and both the clusters got nucleated in equal proportions in a single crystal. An examination of the clusters [Ag<sub>40</sub>(DMBT)<sub>24</sub>(TPP)<sub>8</sub>] and [Ag<sub>46</sub>(DMBT)<sub>24</sub>(TPP)<sub>8</sub>] revealed simple cubic (Ag<sub>8</sub>) and face-centered cubic (Ag<sub>14</sub>) structures, respectively, as the inner cores. These inner cores are protected by a common outer shell, [Ag<sub>32</sub>(DMBT)<sub>24</sub>(TPP)<sub>8</sub>] to form the molecular architecture. The structures of the inner core and outer shell are presented in **Figure 2A–D**. Both the clusters were assembled in exactly the same fashion to form the solid (**Figure 2G,H**). In a unit cell, there are two molecules which are connected through supramolecular interactions. In two dimensional lattices, both the clusters were assembled in the same way. Ag<sub>40</sub> was packed into centered rectangular and rectangular 2D lattices along the z and x directions, respectively. The same packing was seen for Ag<sub>46</sub> also.

Encapsulation of those clusters in a single crystal was further proved by high resolution mass spectrometry (HR ESI MS). ESI MS of a crystal dissolved in methanol showed multiple peaks which were assigned as Ag<sub>40</sub><sup>2+</sup>, Ag<sub>40</sub><sup>3+</sup>, and Ag<sub>46</sub><sup>2+</sup> (with the ligand structure intact). Collision induced dissociation studies were performed to confirm the compositions.





**Scheme 2.** Schematic representation of the concepts of emerging science manifested in noble metal cluster cocrystals. The image of interparticle reaction is reproduced with permission.<sup>[91]</sup> Copyright 2019, American Chemical Society.

## 2.2. Same Core, Different Shell

Another category of encapsulation of similar structures is one with the same metallic core with a different shell. In this concept, a ligand control methodology was developed to synthesize two silver nanoparticles, namely  $\text{Ag}_{210}$  and  $\text{Ag}_{211}$ , which were crystallized in one crystal. They contain the same pseudofivefold symmetric  $\text{Ag}_{116}$  core, which is made of three shells like  $\text{Ag}_{19}@\text{Ag}_{52}@\text{Ag}_{45}$  (Figure 3A–C).  $\text{Ag}_{19}$  consists of three shared pentagonal bipyramidal structures (Figure 3A).  $\text{Ag}_{52}$  is made of six layers of silver atoms, top and bottom layers contain pentagonal pyramids, and in-between, it has four  $\text{Ag}_{10}$  layers (Figure 3C). Three chain-like layers of  $\text{Ag}_{15}$  construct  $\text{Ag}_{45}$  (Figure 3C).  $\text{Ag}_{116}$  core is covered by shells of  $\text{Ag}_{89}(\text{SR})_{71}\text{Cl}[\text{Ag}(\text{Ph}_3\text{P})]_5$  and  $\text{Ag}_{89}(\text{SR})_{71}\text{Cl}[\text{Ag}(\text{Ph}_3\text{P})]_6$  to create  $\text{Ag}_{210}$  and  $\text{Ag}_{211}$ , respectively (Figure 3). These shells are formed by combining different irregular geometrical structures which make them distorted.

Single crystal X-ray diffraction (SCXRD) analysis clearly showed that both the particles have exactly the same core of  $\text{Ag}_{116}$  but differ in shell structure by a unit of silver phosphine complex. This slight change in the secondary ligands resulted in the formation of two distinct particles. In  $\text{Ag}_{211}$ , five  $[\text{Ag}(\text{Ph}_3\text{P})]$  units are bonded to the core at corners of the

pentagon, also called as equatorial positions, perpendicular to the fivefold axis (Figure 3F). The sixth  $\text{AgPPh}_3$  is bonded at the middle of the pentagon and parallel to the fivefold axis, called a polar site (Figure 3F). The pentagon is shown with a green dotted line in Figure 3F. In  $\text{Ag}_{210}$ , one corner of the pentagon is missing; other sites of shell are the same as that of  $\text{Ag}_{211}$  (Figure 3G). However, this one unit change of  $\text{AgPPh}_3$  complex in the shell structure did not affect the growth process during crystallization of  $\text{Ag}_{210}$  and  $\text{Ag}_{211}$ . Seemingly, a large core in both particles enables the cocrystal formation. Another example of this type is made of  $\text{Pt}_1\text{Ag}_{28}(\text{S-Adm})_{20}$  and  $\text{Pt}_1\text{Ag}_{28}(\text{S-Adm})_{18}(\text{HOS-Adm})_2$  (S-Adm is denoted as adamantanethiolate). Hydroxyl group on the surface creates such type of structural diversity.<sup>[71]</sup>

## 3. Selective Crystallization from a Reaction Mixture Leading to Cocystals by a New Type of Interparticle Reaction

Chemical reaction of clusters or interparticle reactions is a new class of reactions first observed by our group, which explains the interchange of metals and protecting ligands between

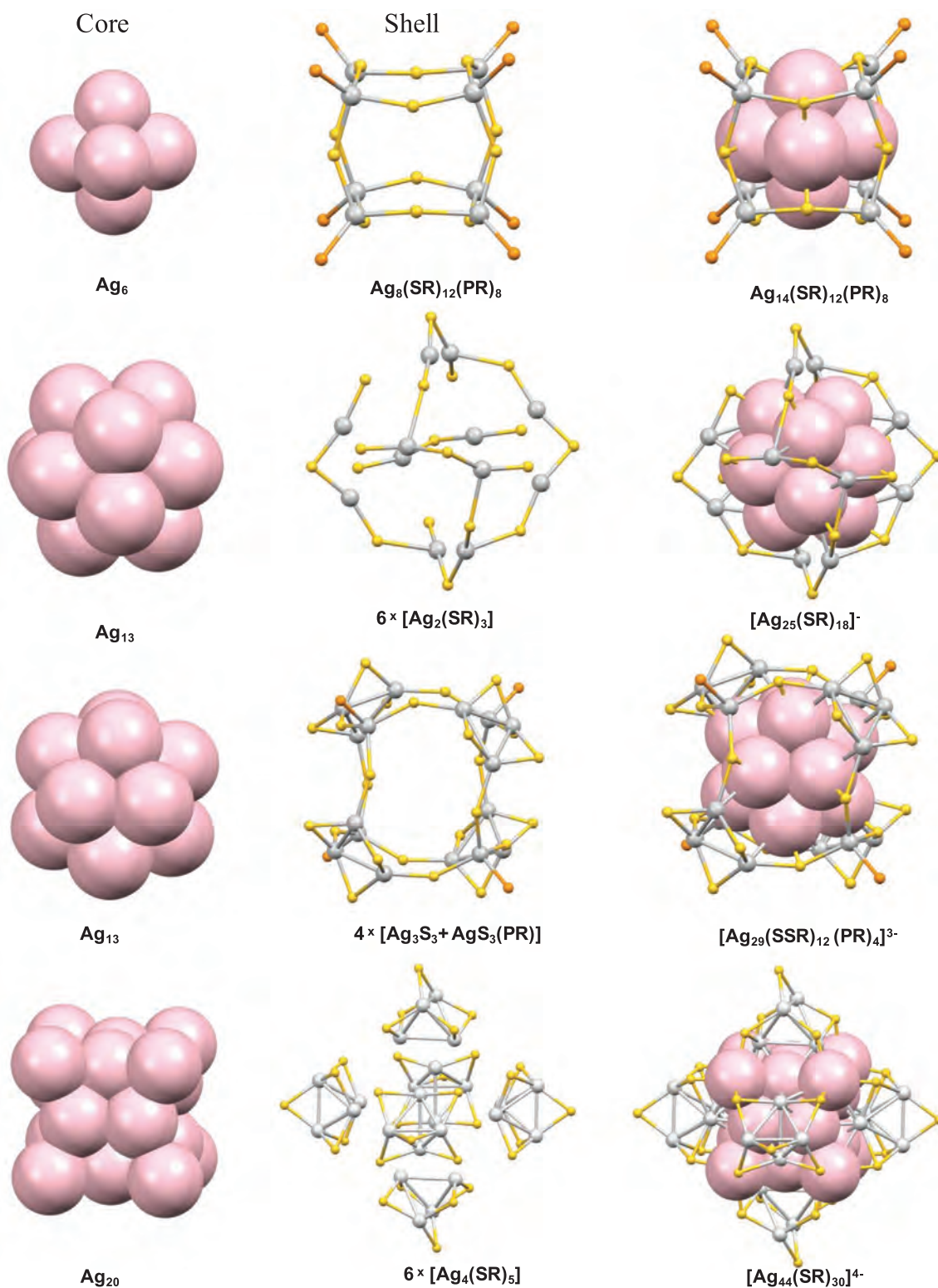


**Figure 1.** Crystal structures of three well-known clusters to understand core and shell structure. Colors and diameters of core and staple atoms of shown differently to understand the structural motifs clearly.

different atomically precise clusters, resulting in the formation of new clusters.<sup>[20,72]</sup> Such types of reactions were carried out by reacting ligand protected clusters made of different metal

atoms, for example, Ag and Au NCs. Reaction between Au<sub>25</sub> and Ag<sub>44</sub> was the first to be reported, followed by the reaction of Ag<sub>25</sub> and Au<sub>25</sub>.<sup>[72]</sup> In such reactions, a series of alloy clusters



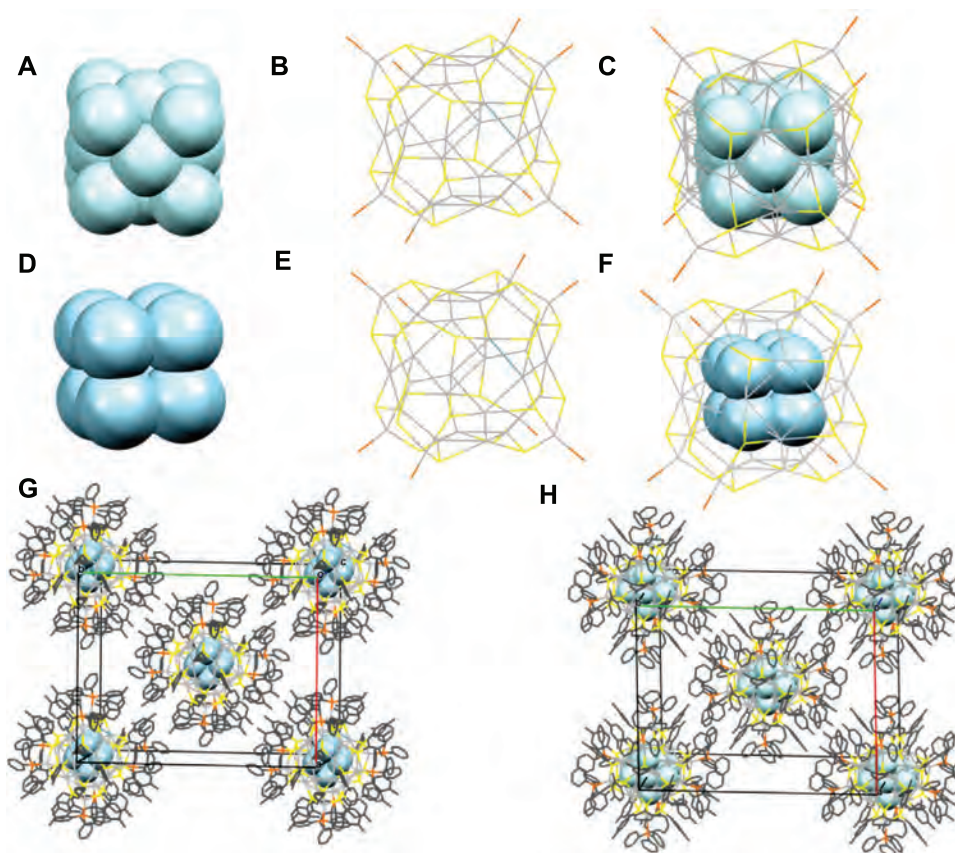


**Figure 2.** Structural anatomy of  $[\text{Ag}_{40}(\text{SPhMe}_2)_{24}(\text{PPh}_3)_8]$  and  $[\text{Ag}_{46}(\text{SPhMe}_2)_{24}(\text{PPh}_3)_8]$  clusters. A,D)  $\text{Ag}_8$  and  $\text{Ag}_{14}$  inner core structures (the metal structure that is not connected to ligands) of  $[\text{Ag}_{40}(\text{SPhMe}_2)_{24}(\text{PPh}_3)_8]$  and  $[\text{Ag}_{46}(\text{SPhMe}_2)_{24}(\text{PPh}_3)_8]$ , respectively.  $\text{Ag}_8$  and  $\text{Ag}_{14}$  correspond to simple cubic and face-centered cubic structures, respectively. B,E) Common shell,  $\text{Ag}_{32}\text{S}_{24}\text{P}_8$ , structures of the clusters without inner cores. C,F) The structures of  $[\text{Ag}_{40}\text{S}_{24}\text{P}_8]$  and  $[\text{Ag}_{46}\text{S}_{24}\text{P}_8]$ , respectively. G,H) Organization of  $\text{Ag}_{40}$  and  $\text{Ag}_{46}$ , respectively, in a unit cell.

were formed. In this context, it is important to mention another methodology to create alloy NCs is antigalvanic reaction. In this process, more noble metal ions are reduced by less noble metal.<sup>[73]</sup> In intercluster reaction, both galvanic and antigalvanic reactions occur simultaneously. Many interparticle reactions using different clusters have been explored.<sup>[74–79]</sup> In view of this, our group was interested in creating new mixed-solids by extending our previous work. A homometallic interparticle reaction methodology was developed to synthesize new NCs.

Interparticle reaction was studied between nanoclusters containing similar metal atoms such as  $[\text{Ag}_{12}(\text{S}^t\text{Bu})_8(\text{CF}_3\text{COO})_5(\text{ACN})]^{+}$  denoted as  $\text{Ag}_{12}$ , ( $\text{S}^t\text{Bu}$  = tert-butylthiolate,  $\text{CF}_3\text{COO}$  = trifluoroacetate) and  $[\text{Ag}_{18}(\text{TPP})_{10}\text{H}_{16}]^{2+}$  denoted as  $\text{Ag}_{18}$ , (TPP = triphenylphosphine) resulting in the formation of two product nanoclusters viz.,  $[\text{Ag}_{16}(\text{S}^t\text{Bu})_8(\text{CF}_3\text{COO})_7(\text{ACN})_3\text{Cl}]^{+}$  and  $[\text{Ag}_{17}(\text{S}^t\text{Bu})_8(\text{CF}_3\text{COO})_7(\text{ACN})_3\text{Cl}]^{+}$  denoted as  $\text{Ag}_{16}$  and  $\text{Ag}_{17}$ , respectively. Interestingly, in a single crystal, the populations of  $\text{Ag}_{16}$  and  $\text{Ag}_{17}$  were in the ratio of 2:1 and in the product mixture, however, equal population (1:1) was observed. These results have been confirmed by SCXRD and HR ESI MS. Therefore, this type of reaction suggests the formation of a cocrystal, involving selective crystallization. Seemingly, selective crystallization happened because of the enhanced stability

of solids at a particular ratio. The ratio of nanoclusters in the solid is determined by their potential energy minimum. We tried to prove the existence of equal concentrations of  $\text{Ag}_{16}$  and  $\text{Ag}_{17}$  NCs in the solution by nuclear magnetic resonance spectroscopy but due to their same shell structures, useful information could not be obtained. We attempted to separate the component clusters by high performance liquid chromatography (HPLC) and thin layer chromatography (TLC) but it was also unsuccessful. In HPLC and TLC procedures, clusters were degraded on the column and TLC plate, respectively. This inability did not surprise us as while HPLC and TLC are well known for gold clusters, very few reports exist for silver clusters.

ESI MS of the product solution in positive ion mode shows the formation of NCs in the solution with  $m/z$  at 3055, 3277, and 3499, corresponding to  $[\text{Ag}_{17}(\text{S}^t\text{Bu})_8(\text{CF}_3\text{COO})_7(\text{ACN})_3\text{Cl}]^{+}$ ,  $[\text{Ag}_{16}(\text{S}^t\text{Bu})_8(\text{CF}_3\text{COO})_6(\text{ACN})_3\text{Cl}]^{+}$ , and  $[\text{Ag}_{15}(\text{S}^t\text{Bu})_8(\text{CF}_3\text{COO})_5(\text{ACN})_3\text{Cl}]^{+}$ , respectively (Figure 4A). The peak separation is  $m/z$  1.00, for each of the clusters indicating +1 charge state of the NCs. The formation of NCs was verified by matching their isotopic distributions as shown at the inset of Figure 4A. The stability of peaks was further analyzed using collision-induced dissociation (CID) experiments on the peaks with  $m/z$  3277 and 3499. Analysis of CID studies showed

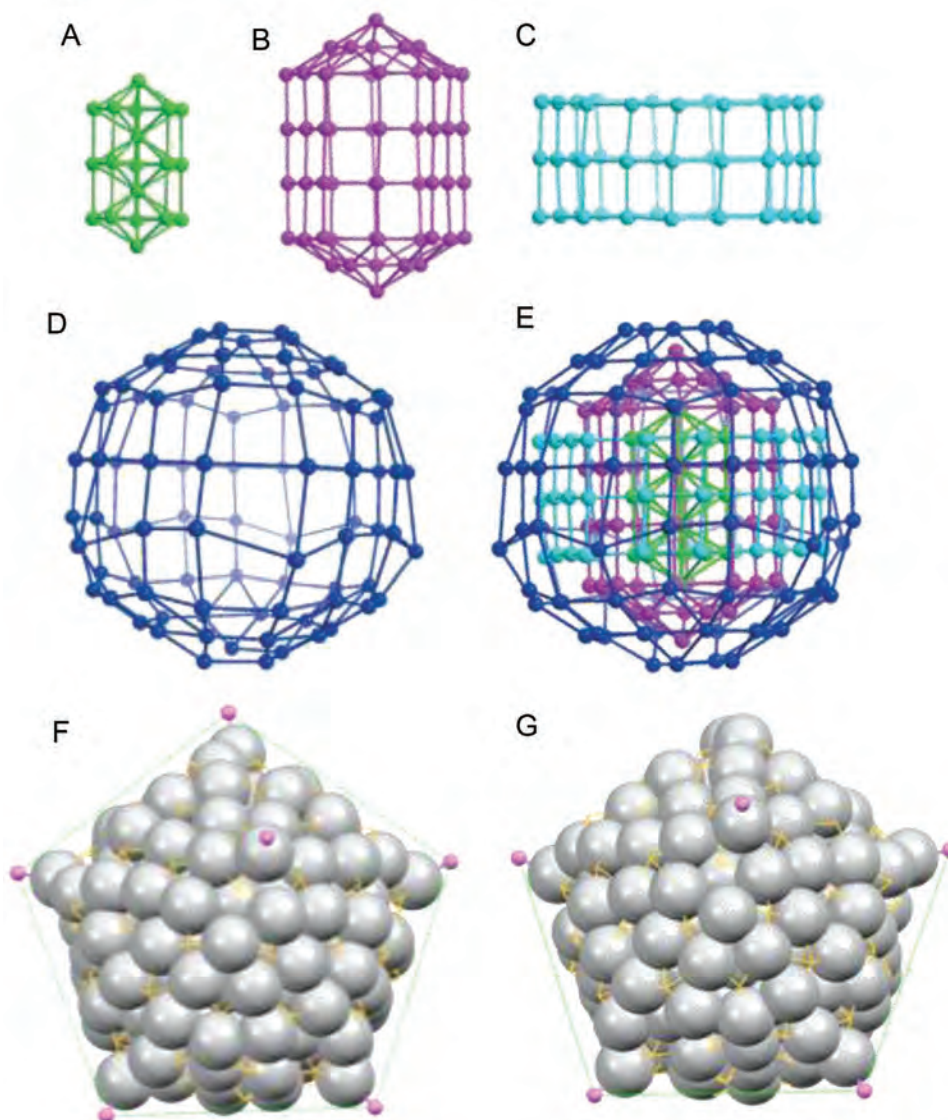


**Figure 3.** Common core structures present in  $\text{Ag}_{210}$  and  $\text{Ag}_{211}$ . A)  $\text{Ag}_{19}$ , B)  $\text{Ag}_{52}$ , C)  $\text{Ag}_{45}$  pentagonal cylinder, D) Outermost  $\text{Ag}_{89}$  shell, and E) Full shell structure  $\text{Ag}_{15}@\text{Ag}_{52}@\text{Ag}_{45}@\text{Ag}_{89}$ . F, G) Structures of  $\text{Ag}_{211}$  and  $\text{Ag}_{210}$ , respectively. Reproduced with permission.<sup>[51]</sup> Copyright 2019, Wiley-VCH.

that  $\text{Ag}_{15}$  was the fragmented peak of  $\text{Ag}_{16}$  due to the loss of  $\text{CF}_3\text{COOAg}$ . However, CID measurements of  $m/z$  3499 ( $\text{Ag}_{17}$ ) showed the removal of ligands alone with increasing collision energy, indicating that  $\text{Ag}_{16}$  was a discrete entity. Therefore, CID studies showed that the solution had two types of NCs ( $\text{Ag}_{16}$  and  $\text{Ag}_{17}$ ). The populations of peaks corresponding to  $\text{Ag}_{16}$  and  $\text{Ag}_{17}$  in product solution and crystals dissolved in acetonitrile are in 1:1 and 2:1, respectively. ESI MS of the supernatant after crystallization showed peaks at the same  $m/z$ , similar to those obtained from crystal and product solutions, although with unequal populations. These results suggested that a single crystal showed selective crystallization of 2:1 of  $\text{Ag}_{16}$  and  $\text{Ag}_{17}$  NCs, respectively, even though the NCs were of equal concentrations in the product solution. An attempt to isolate these NCs was made using different synthetic protocols, but we were unable to succeed in this case. This reaction is the first

reaction where interparticle reaction between silver NCs resulted in product cocrystals by selective crystallization. A balanced chemical equation was written based on the findings from ESI MS and SCXRD data (considering the contribution of silver and sulfur atoms alone) (**Scheme 3**).

ESI MS intensities of the product solution and the supernatant obtained after crystallization provide evidence for a balanced chemical reaction. From ESI MS, equal populations of NCs in the product solution got changed into 2:1 in the crystal ( $\text{Ag}_{16}:\text{Ag}_{17}$ ). ESI MS of the supernatant, after crystal formation, showed increased intensity of  $\text{Ag}_{17}$ , even though the ratio was not 1:2, which was attributed to the preferential incorporation of the clusters in the crystals. The formation of cocrystal nanoclusters arising from interparticle reactions was studied using time-dependent ESI MS and UV-vis spectroscopy. Studies were carried out at different time intervals,  $t = 2, 5, 15, 30$ , and

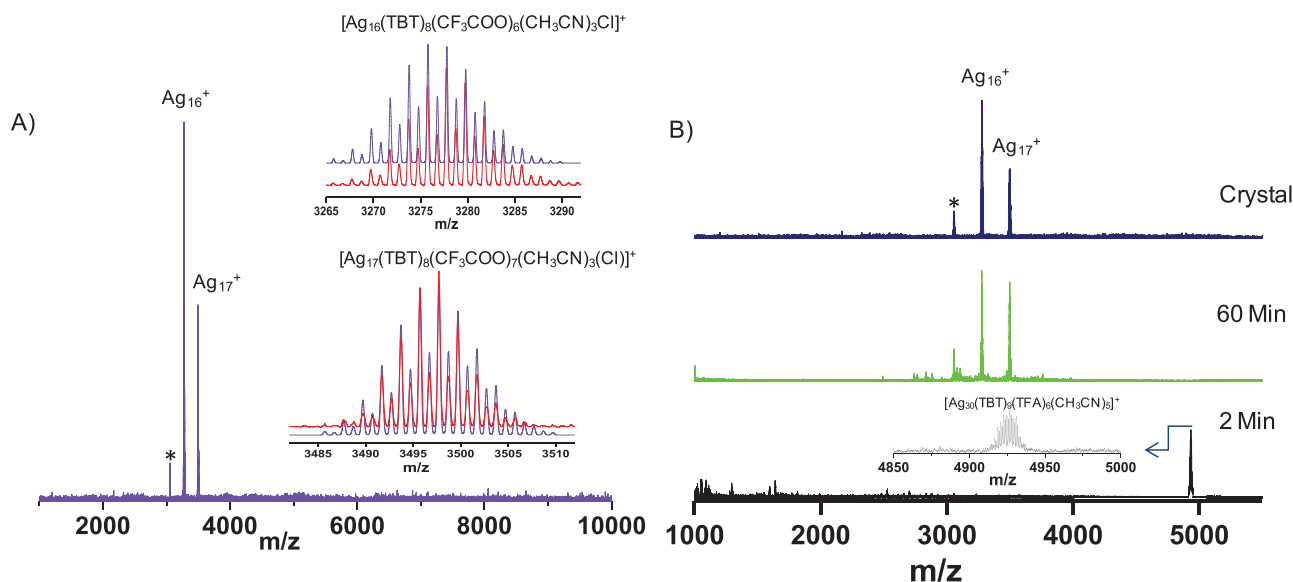


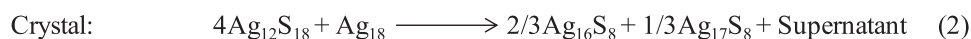
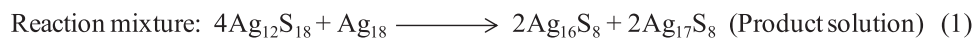
**Figure 4.** A) ESI MS of crystals of a mixture of  $\text{Ag}_{16}$  and  $\text{Ag}_{17}$  dissolved in acetonitrile. Major peaks are assigned as  $[\text{Ag}_{17}(\text{S}'\text{Bu})_8(\text{CF}_3\text{COO})_7(\text{ACN})_3(\text{Cl})]^+$  and  $[\text{Ag}_{16}(\text{S}'\text{Bu})_8(\text{CF}_3\text{COO})_6(\text{ACN})_3(\text{Cl})]^+$ . Isotopic distributions of the experimental spectra (violet trace) are compared with the simulated spectra (red trace) in the inset. B) ESI MS spectra as a function of time of the reaction mixture during the synthesis of  $\text{Ag}_{16}^+$  and  $\text{Ag}_{17}^+$ . Peak marked as \* corresponds to the loss of  $\text{CF}_3\text{COOAg}$ . Reproduced with permission.<sup>[54]</sup> Copyright 2019, American Chemical Society.

60 min, and 7 days after the reaction. ESI MS measurements in the positive ion mode showed that individual peaks corresponding to  $\text{Ag}_{12}$  and  $\text{Ag}_{18}$  did not appear. ESI MS recorded after 2 min of the reaction showed that a distinctive peak at  $m/z$  4928 emerged whose molecular mass was equal to that of  $[\text{Ag}_{30}(\text{S}'\text{Bu})_9(\text{CF}_3\text{COO})_6(\text{ACN})_5]^+$ , abbreviated as  $\text{Ag}_{30}$ , indicating that an addition reaction had taken place between the reactant nanoclusters (Figure 4B). During the reaction, low molecular weight species having  $m/z < 1000$  appeared, which could be due to the formation of thiolates and phosphines. After 5 min of the reaction, ESI MS showed the appearance of many new peaks in the region between  $m/z$  1000–3000, corresponding to short lived intermediate species formed during the reaction, and the peak at  $m/z$  4928 disappeared suggesting its conversion to lower molecular mass intermediates. This may be interpreted as a top-down approach in synthesis. From the time,  $t = 15$ –30 min, ESI MS shows a dynamic change during the reaction and a color change was visible. After 30 min of the reaction, three characteristic peaks emerged whose  $m/z$  values at 3499, 3277, and 3055 corresponded to  $[\text{Ag}_{17}(\text{S}'\text{Bu})_8(\text{CF}_3\text{COO})_7(\text{ACN})_3\text{Cl}]^+$ ,  $[\text{Ag}_{16}(\text{S}'\text{Bu})_8(\text{CF}_3\text{COO})_6(\text{ACN})_3\text{Cl}]^+$ , and  $[\text{Ag}_{15}(\text{S}'\text{Bu})_8(\text{CF}_3\text{COO})_5(\text{ACN})_3\text{Cl}]^+$ , respectively. The reaction appeared to be completed in 1 h, as evident from the disappearance of the reaction intermediate. Intensities of the peaks corresponding to  $\text{Ag}_{16}$

and  $\text{Ag}_{17}$  increased significantly. ESI MS of a few crystals dissolved in acetonitrile were similar ( $m/z$  3055, 3277, and 3499) to the MS obtained after 1 h of the reaction but with varying intensities. It therefore, suggested that the nanoclusters got formed after 1 h. During the course of the reaction, as many as 21 heteroleptic reaction intermediates denoted by a general formula,  $[\text{Ag}_a(\text{STBU})_b(\text{CF}_3\text{COO})_c(\text{ACN})_d\text{Cl}_e]^+$  where  $a = 6$ –15 and 30,  $b = 2$ –9,  $c = 1$ –6,  $d = 0$ –5, and  $e = 0$ –1 were identified, which underwent various rearrangements via a growth mechanism forming the product nanoclusters,  $\text{Ag}_{16}$  and  $\text{Ag}_{17}$ . These intermediates size focus leading to stable product nanoclusters  $[\text{Ag}_{16}(\text{S}'\text{Bu})_8(\text{CF}_3\text{COO})_6(\text{ACN})_3\text{Cl}]^+$  and  $[\text{Ag}_{17}(\text{S}'\text{Bu})_8(\text{CF}_3\text{COO})_7(\text{ACN})_3\text{Cl}]^+$ .

#### 4. Cocrystals Due to Magic Sizes and Magic Electron Shells

Ligand protected nanoclusters of noble metals are synthesized by reducing the complexes formed by metal salts with protecting ligands. A reasonable control over their size and atomic structure is obtained via a complex process which is influenced by various parameters during syntheses, such as the ratio of metal to ligand, temperature, the kinetics of reduction,



**Scheme 3.** Chemical equations of the intercluster reaction.



subsequent steps, in particular size focusing, and cleaning. A common view is that the creation of protected clusters can be arrested during their nucleation or etching when a magic size and composition is formed.<sup>[80]</sup> The factors which can control the production of magic cluster are the following

- i) Suitable surface structures which can protect the metallic core;
- ii) Appropriate atomic packing often observed as spherical structures of concentric shells of polyhedra and
- iii) Closed-shell electronic structure stabilizing smaller nano-clusters by a large highest occupied molecular orbital (HOMO)-lowest unoccupied molecular orbital (LUMO) gap.

The synthetic method chosen can offer some strategies for the creation of magic cores and consequent electronic structures. A mixture of  $(\text{AuAg})_{267}$  and  $(\text{AuAg})_{45}$  was synthesized by reducing a complex of metal precursors and ligands by sodium borohydride at 0 °C. Transmission electron microscopic (TEM)

data revealed that the final product contained two monodisperse particles with significant variation in sizes. Larger particle was around 2.5 nm, and the other one was of 1.1 nm. It was difficult to conclude from the TEM data that it formed a cocrystal or a simple mixture of two different particles. Fortunately, authors were able to get single crystals from the reaction mixture, and TEM data were validated by SCXRD. Single crystal X-ray analysis showed that there were two kinds of molecules,  $(\text{AuAg})_{267}(\text{SR})_{80}$  and  $(\text{AuAg})_{45}(\text{SR})_{27}(\text{PPh}_3)_6$  in the lattice, as shown in **Figure 5A**. Smaller cluster was anisotropic in shape but the larger one was spherical. In order to understand the core structure of  $(\text{AuAg})_{267}(\text{SR})_{80}$ , an analysis was performed by removing the protecting ligands. Geometrical anatomy can be presented by four layers,  $k_0(1)@k_1(12)@k_2(42)@k_3(92)@k_4(120)$ .

Here, it is appropriate to mention the previous work of Mackay, who reported in 1962 a sequence in the close packed assembly of spheres.<sup>[81]</sup> He proposed that an assembly of spheres can form concentric layers of icosahedra; packed on the first layer, composed of a 13 sphere icosahedron. In general,  $n$ th

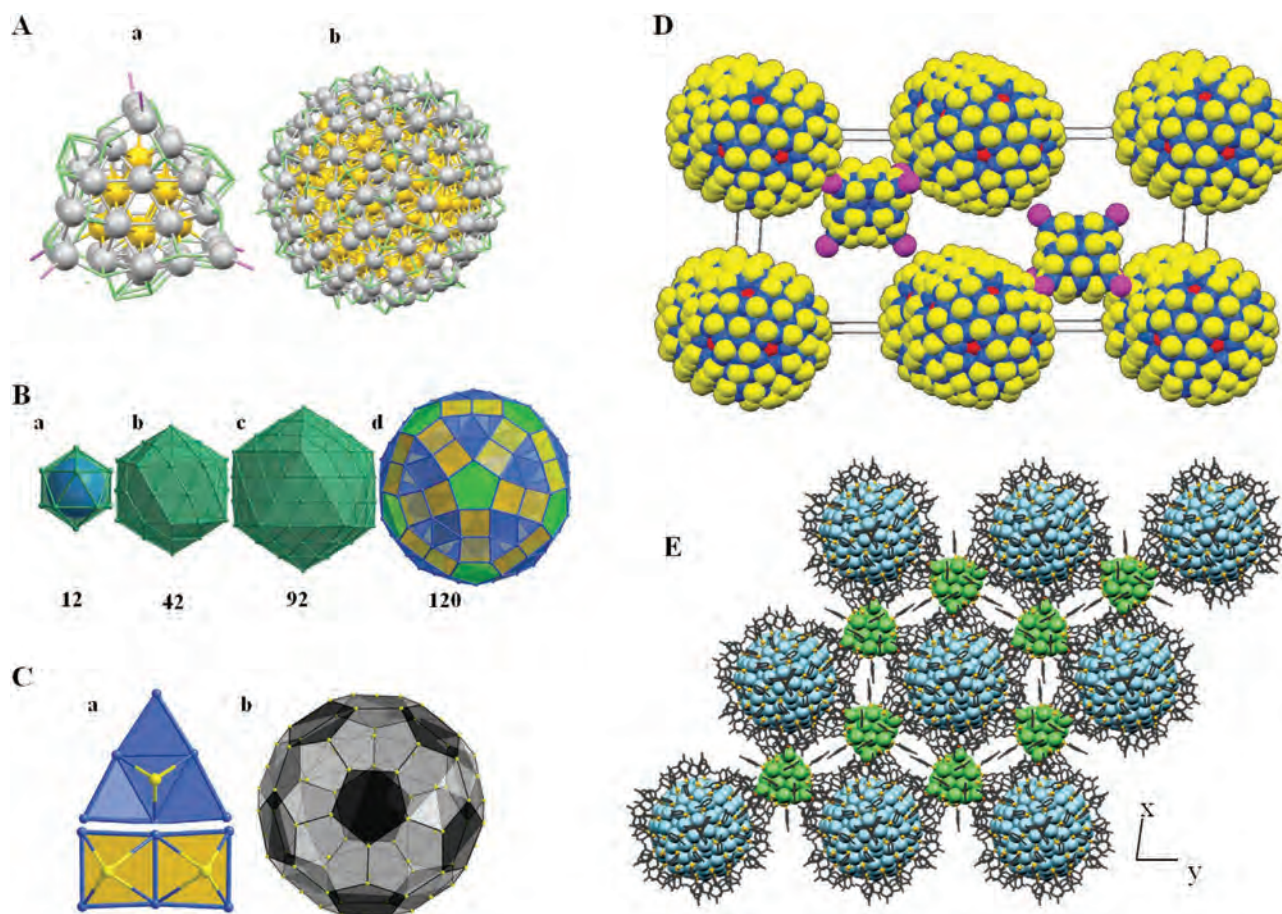


**Figure 5.** A) Crystal structures of component clusters,  $(\text{AuAg})_{45}$  and  $(\text{AuAg})_{267}$ . a) Structures of trigonal prismatic  $(\text{AuAg})_{45}$  and spherical  $(\text{AuAg})_{267}$  nanoparticles. B) Dissection of the metal framework of  $(\text{AuAg})_{267}$  to understand the core structures. Four layers of metal atoms, a–d). a) First Mackay icosahedral core of 12 metal atoms, b) second Mackay layer of 42 metal atoms, c) third Mackay layer of 92 metal atoms, d) fourth anti-Mackay layer of 120 metal atoms. Number of metal atoms is mentioned at the bottom of the structures. Reproduced with permission.<sup>[53]</sup> Copyright 2018, Springer Nature. C) Capping of metal framework by thiolates. a) Triangle and square-like metal structures are capped by sulfur atoms. b) 80 sulfur atoms form buckyball-type structures. Reproduced with permission.<sup>[53]</sup> Copyright 2018, Springer Nature. D) Unit cell representation of  $(\text{AuAg})_{267}$  and  $(\text{AuAg})_{45}$ . There are two units of each particle in the unit cell. Larger components are placed at the corners and edges, while smaller ones are at the inside of the hexagonal unit cell. Reproduced with permission.<sup>[53]</sup> Copyright 2018, Springer Nature. E) Self-assembled packing structure of  $(\text{AuAg})_{45}$  and  $(\text{AuAg})_{267}$ , along  $z$  direction.

icosahedral layer is made of  $10n^2 + 2$  spheres (for the 13 sphere icosahedron,  $n = 1$ ). At that time, no crystallographic packing of such types of assemblies was known, and later on  $M_{55}$  clusters were observed in multiple reports which were characterized by mass spectrometry and theoretical studies. It was predicted that  $M_{55}$  contained a  $M_{13}$  (central icosahedron) and a  $M_{42}$  ( $10 \cdot 2^2 + 2$ ) icosahedral shell, which means it contained two layers of Mackay icosahedra. It was often called as magic cluster system as it had two complete Mackay icosahedra. Over the last decades, the two layer  $M_{55}$  Mackay icosahedron was revealed in various noble metal nanomaterials by SCXRD, namely,  $Pd_{145}$ ,<sup>[82]</sup>  $Pd_{164-x}Pt_x$ ,<sup>[83]</sup>  $Au_{133}$ ,<sup>[60,84]</sup> and  $Pd_{55}$ .<sup>[85]</sup> However, 3rd layer Mackay icosahedron was not observed in these clusters, and it was called an anti-Mackay layer. The major difference between Mackay and anti-Mackay packing structure is in stacking of atoms in the atomic structure. In Mackay, atoms are stacked in face-centered cubic (ABCA...) fashion, and in anti-Mackay, the stacking is hexagonal cubic (ABAB...). It was observed that after successive stacking of Mackay icosahedra (ABCA...), there was stacking faults, i.e., ABA... kind of arrangements.<sup>[86]</sup> This stacking does not follow Mackay's rule, and it is called as anti-Mackay icosahedra. In  $(AuAg)_{267}$ , the next Mackay layer on  $M_{55}$  was observed giving three complete Mackay or magic layers of  $k_0(1)@k_1(12)$  ( $10 \cdot 1^2 + 2$ )  $@k_2(42)$  ( $10 \cdot 2^2 + 2$ )  $@k_3(92)$  ( $10 \cdot 3^2 + 2$ ) to form  $M_{147}$ . The fourth layer,  $k_4(120)$  is not composed of 162 atoms ( $10 \cdot 4^2 + 2$ ) and therefore not following Mackay's proposed formula and is called as anti-Mackay layer. The three layers are presented as M as it can be Au or Ag. SCXRD refinement revealed that there are positional disorders in their atomic positions. Average occupancies of three layers are not 100% with respect to silver or gold. However, the atoms of fourth layer have 100% average occupancies of Ag. The 120 silver atoms of the fourth layer are bonded to each other to construct a semiregular polyhedron which is made of 20 triangles, 60 squares, and 12 pentagons. The center of every triangle and square face of the fourth layer are connected by thiolates as shown in Figure 5C(a,b). This connectivity occurred in such a way that eighty sulfur atoms form a fullerene-like structure (Figure 5C(b)). The other component of the cocrystal,  $(AuAg)_{45}$  exhibits a shape of trigonal prism, while the larger counterpart is spherical.  $(AuAg)_{45}$  contains  $Au_9$  core inside a trigonal prism of 36 silver atoms to form  $Au_9Ag_{36}$ . There are no Mackay icosahedral cores inside it. Surface silver atoms are protected by  $AgS_3P$  and  $AgS_3$  units. This structure is similar to the previously reported structure of  $Au_9Ag_{36}(SPhCl_2)_{27}(PPh_3)_6$ .<sup>[87]</sup>

It is interesting to see the diversity in terms of the size and shape of the component clusters of the cocrystals. Stabilizing factors are also different as  $(AuAg)_{267}$  is stabilized by magic Mackay icosahedral cores, while geometry of  $(AuAg)_{45}$  does not provide stability. Stability of  $(AuAg)_{45}$  must originate from its electronic structure, which will be discussed later. These diverse  $(AuAg)_{267}$  and  $(AuAg)_{45}$  components serve as the building blocks and were assembled into a 3D structures. The cocrystal forms a hexagonal unit cell and  $(AuAg)_{267}$  molecules form the hexagonal layer (Figure 5D). All the octahedral sites in this structure are filled by  $(AuAg)_{45}$ . SCXRD resolved that in the lattice,  $(AuAg)_{267}$  is neighbored by six  $(AuAg)_{45}$  nanoclusters and vice versa. The main driving force for adopting this kind of packing is strong supramolecular forces between the ligands

of both the particles. Orientations of thiolates of  $(AuAg)_{267}$  and phosphines of  $(AuAg)_{45}$  are perfectly matched to form strong C–H... $\pi$  interactions (at a distance of  $\approx 2.6$  Å).

The electronic structures of both nanoclusters were analyzed by density functional theory which shows the expected HOMO–LUMO gap (0.71 eV) for 18 electrons  $(AuAg)_{45}$  nanocluster. As expected, the closing of the  $1D^{10}$  shell at 18 electrons is indicated by the projection to angular momentum components and after the closing of the  $2S^2$  shell, the energy gap at 20 electrons becomes 0.65 eV. Therefore, the closure of an electron shell at 18 electrons, i.e., at a magic electron number, clearly stabilizes this cluster energetically. By contrast  $(AuAg)_{267}$  displays 187 free electrons assuming the cluster is neutral. Because this particle is almost spherical, the electronic structure of the metal core is understood by the simplified jellium model. Projected local density of states of the  $(AuAg)_{267}$  cluster models do not display an energy gap of 187 electrons. The electronic structure does not have any primary mechanism to stabilize the atomic structure of  $(AuAg)_{267}$  due to the lack of measurable HOMO–LUMO energy gap. Therefore, the stability must derive from the special geometric arrangement of the metal atoms which lead to the magic Mackay/anti-Mackay icosahedral shells and the protective ligand shell structure, as discussed above. The lack of a certain HOMO–LUMO gap was also evidenced from differential pulse voltammetry (DPV). DPV of a solution of cocrystals exhibited 14 peaks which were evenly spaced, and no detectable HOMO–LUMO gap was seen from the reduction and oxidation peaks (Figure 6B(b)).

UV–vis optical absorption spectra of a mixture of  $(AuAg)_{267}$  and  $(AuAg)_{45}$ , as well as the two separate entities is shown in Figure 6B. Solutions of cocrystals showed a plasmon band at 460 nm, while  $(AuAg)_{45}$  displayed molecule-like features. The contribution of larger nanoparticle is high in the optical spectrum due to its large extinction coefficient.

## 5. Cocrystals Consisted of +ve and –ve Clusters Making a Double Nuclear Ionic Compound

Nanoclusters can bear positive or negative charges; therefore, an obvious question is whether the charged nanoclusters can pack together in crystals by electrostatic forces.<sup>[7,88]</sup> The first attempt was made to answer this question by mixing anionic and cationic  $Au_{25}$  nanoclusters, which had not been successful till now.<sup>[55]</sup> This is likely due to the instability of the positively charged  $Au_{25}$ .<sup>[89]</sup>

He et al., reported the synchronous synthesis of cationic and anionic nanoclusters and the in situ formation of the expected compound via a one-pot reaction.<sup>[55]</sup> Initially, polydisperse particles were synthesized by reducing a complex of silver and ligands, then they were size focused in presence of gold precursor and excess phosphines. The supernatant solution was subjected to the diffusion of hexane to produce black crystals. SCXRD data suggested that the as-obtained product may be written as  $[Ag_{26}Au(2\text{-EBT})_{18}(PPh_3)_6]^+ [Ag_{24}Au(2\text{-EBT})_{18}]^-$ , a double nanocluster ionic compound (DNIC). Such a material is very interesting as it can be regarded as an ionic compound; however, it is different from normal ionic compounds as both the oppositely charged species are nanoclusters.<sup>[90]</sup> It is important to note that such a type of compound has not been

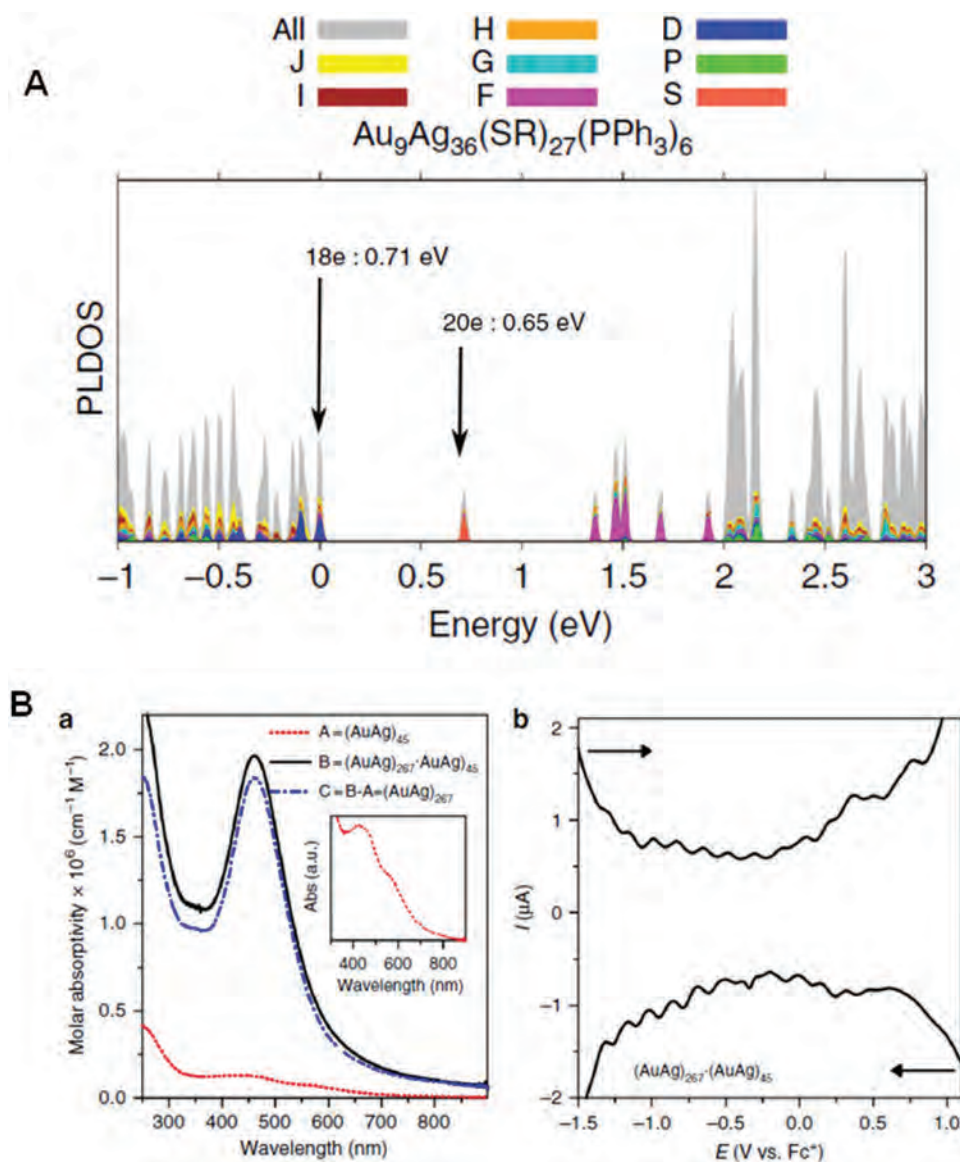


**Figure 6.** A) Predicted electronic structures of  $(\text{AuAg})_{267}$  and  $(\text{AuAg})_{45}$ . The molecules were optimized by density functional theory using coordinates of crystal structure. Energy of the highest occupied molecular orbital (HOMO) was kept at zero. Detectable energy gaps near the HOMO are shown. B,a) Optical absorption spectra of co-crystals and isolated  $(\text{AuAg})_{45}$  in dichloromethane. b) Differential pulse voltammetry of a solution obtained from cocrystals. Reproduced with permission.<sup>[53]</sup> Copyright 2018, Springer Nature.

observed before in a noble metal nanocluster system. Both the clusters,  $\text{Ag}_{26}\text{Au}$  and  $\text{Ag}_{24}\text{Au}$ , do not assemble in an as ion-pair mode but in a layer-by-layer fashion (Figure 7A). Each layer consists of  $\text{Ag}_{26}\text{Au}$  or  $\text{Ag}_{24}\text{Au}$  nanoclusters with a honeycomb-like structure, along the (001) plane (Figure 7B).

Multilayer stacking structure of the cocrystal,  $\text{Ag}_{50}\text{Au}_2$  nanoclusters revealed that besides electrostatic interactions, both the components,  $\text{Ag}_{26}\text{Au}$  and  $\text{Ag}_{24}\text{Au}$  nanoclusters are held together via different supramolecular interactions. These include  $\text{C}-\text{H} \cdots \pi$ , T-shaped  $\pi \cdots \pi$ , and  $\text{H} \cdots \text{H}$  interactions, with distances of 2.8–3.2, 4.8–5.8, and 2.3–2.8 Å, respectively.  $\text{Ag}_{24}\text{Au}(\text{SR})_{18}$  was crystallized separately and the arrangement of the atoms in the single-component nanocluster compound  $[\text{PPh}_4]^+[\text{Ag}_{24}\text{Au}(\text{SR})_{18}]^-$  is similar to that in the cocrystal of

$\text{Ag}_{24}\text{Au}$  of  $\text{Ag}_{50}\text{Au}_2$ , although the supramolecular interactions and packing of  $\text{Ag}_{24}\text{Au}(\text{SR})_{18}$  in the crystals are not the same from the packing of  $\text{Ag}_{24}\text{Au}$  in the crystals. The four benzene rings of each  $\text{PPh}_4$  are bonded with four  $[\text{Ag}_{24}\text{Au}(\text{SR})_{18}]$  from the top, and bottom layers by  $\text{C}-\text{H} \cdots \pi$  interactions and the distances are in the range of 2.8–3.1 Å. Thus, it is clear that supramolecular interactions drive the formation of the cocrystal of DNIC, although ionic interactions hold the ion pairs together.

## 6. Conclusions and Perspective

In conclusion, the concept of cocrystallization of structurally similar atomically precise nanoclusters, leading to new solids



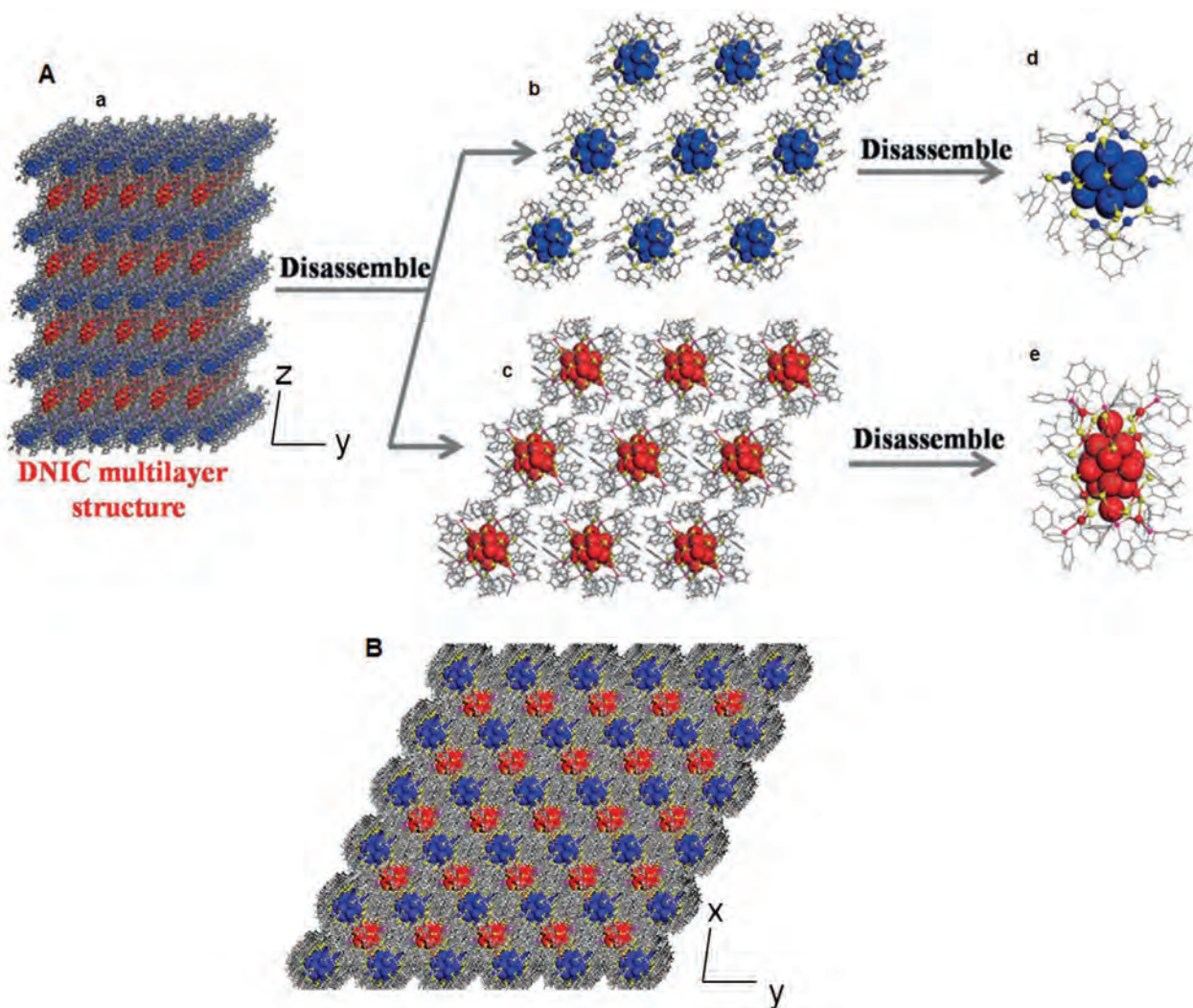


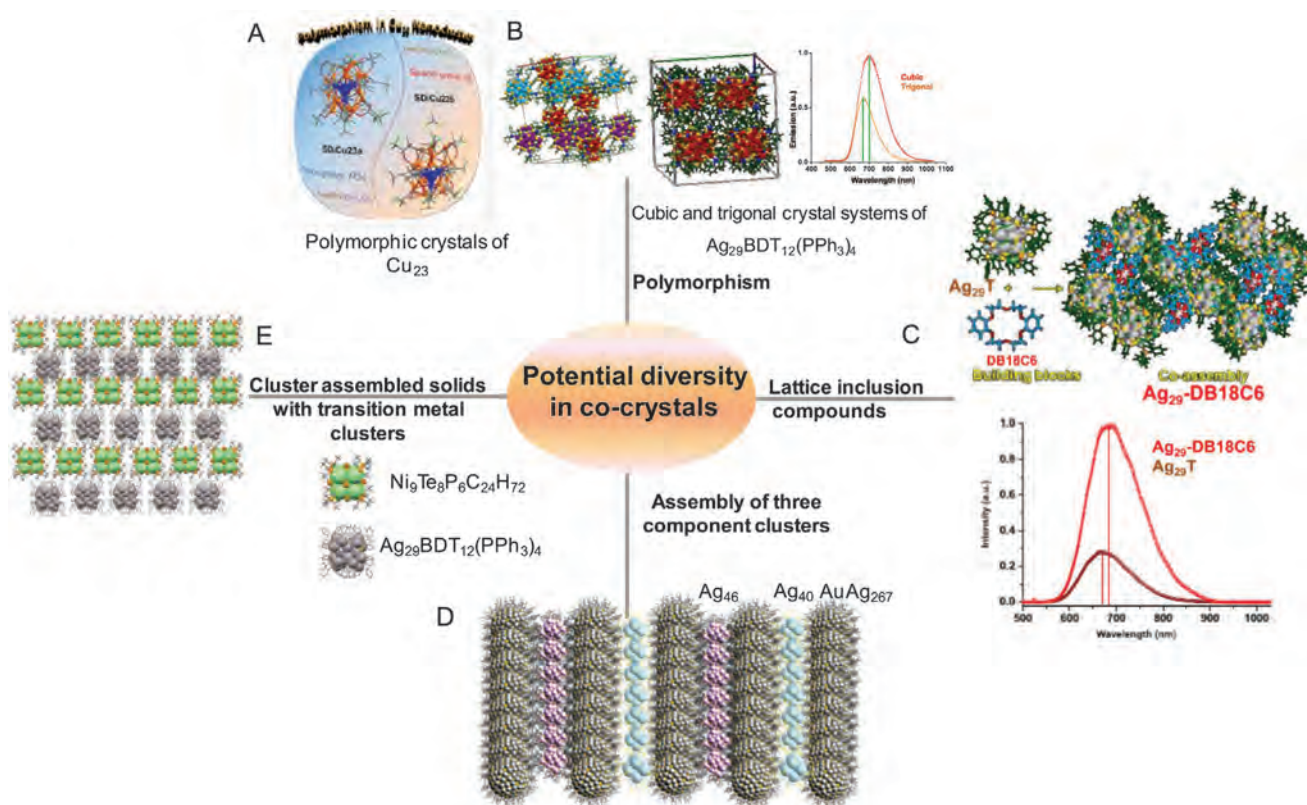
**Figure 7.** A) Demonstration of the coassembly of  $[\text{Ag}_{26}\text{Au}(\text{2-EBT})_{18}(\text{TPP})_6]^+$  and  $[\text{Ag}_{24}\text{Au}(\text{2-EBT})_{18}]^-$ . a) Double ionic cluster ionic compound; Layers of b)  $\text{Ag}_{24}\text{Au}$  and c)  $\text{Au}_{26}\text{Ag}$ ; d) individual  $\text{Ag}_{24}\text{Au}$ , and e)  $\text{Ag}_{26}\text{Au}$  nanoclusters. B) Multilayer stacking structure of the DNIC  $\text{Ag}_{50}\text{Au}_2$  nanoclusters (viewed from Z direction). Color code: blue and red, Ag; yellow, S; magenta, P; gray, C; white, H. Reproduced with permission.<sup>[39]</sup> Copyright 2019, Wiley-VCH.

by different approaches is presented. Five distinct categories of assemblies were presented. 1) Crystals composed of different cores with the same shell. A unique pair of  $\text{Ag}_{40}$  and  $\text{Ag}_{46}$  was cocrystallized with this strategy. 2) Clusters of the same number of metal atoms in the core. An example known is the large metallic shell-like Russian-doll,  $\text{Ag}_{19}@\text{Ag}_{52}@\text{Ag}_{45}@\text{Ag}_{89}$  (in total,  $\text{Ag}_{205}$ ) containing clusters, covered by the same number of thiolates and chloride ligands but different number of silver-phosphine complex units, crystallized together. 3) Another class is an interparticle reaction of two ligand protected atomically precise NCs,  $\text{Ag}_{12}$  and  $\text{Ag}_{18}$  forming products,  $\text{Ag}_{16}$  and  $\text{Ag}_{17}$ , which crystallized together. Detailed analysis revealed that the population of  $\text{Ag}_{16}$  and  $\text{Ag}_{17}$  formed initially in the solution was almost equal, but selective encapsulation happened in the solid state. 4) Coassembly of large and small clusters, example being large  $(\text{AuAg})_{267}$  and tiny  $(\text{AuAg})_{45}$  clusters, assembled into a two-component hierarchical structure. It exemplified a unique particle growth from solution, driven by magic sizes and stable electronically closed-shells. Particularly,  $(\text{AuAg})_{267}$  acquired a magic size close packing, while  $(\text{AuAg})_{45}$  had a 18

electron superatom structure. 5) The idea of a double ionic cluster assembly was introduced by the system,  $[\text{Ag}_{26}\text{Au}(\text{2-EBT})_{18}(\text{PPh}_3)_6]^+ [\text{Ag}_{24}\text{Au}(\text{2-EBT})_{18}]^-$  through an in situ cluster growth approach.

These examples suggest the possibility of the coexistence of diverse clusters and their cocrystallisation in varying ways. Such nanomaterials, like superlattices might be a step forward to understand cluster assembled materials with exciting properties. Interesting cluster solids may be made with combinations of luminescent and nonluminescent clusters, magnetic and nonmagnetic clusters as well as plasmonic and luminescent clusters. Cocrystals of anisotropic and isotropic clusters may also be possible. These new solids may help us understand the synergistic effects of individual clusters.

The diversity of atomically precise clusters is quite large, and it presents potential directions for the future to create new solids. Polymorphic crystals of nanoclusters were introduced by our group.<sup>[63]</sup> It is highly possible to create polymorphism in cocrystals of nanoclusters which may exhibit new electronic properties. So far most of the studies were of binary systems.



**Scheme 4.** A schematic representation of potential diversity in cocrystals of atomically precise clusters. A) Reproduced with permission.<sup>[93]</sup> Copyright 2020, American Chemical Society. B) Reproduced with permission.<sup>[63]</sup> Copyright 2018, The Royal Society of Chemistry. C) Reproduced with permission.<sup>[92]</sup> Copyright 2019, American Chemical Society.

It will be interesting if we can realize multicomponent cluster cocrystals. Recently, three superatom alloy and pure clusters were crystallized together.<sup>[91]</sup> Multicomponent solids may have exciting physicochemical, electrical, and mechanical properties, which will help the growth of this very new field. Our group reported a supramolecular assembly of  $\text{Ag}_{29}$  clusters and crown ether<sup>[92]</sup> which suggests possibilities of cocrystallizing different clusters by suitable supramolecular building blocks. Another exciting possibility is to combine noble metal nanoclusters with clusters of transition metals. Let us take an interesting example of a cocrystal of magnetic  $\text{Ni}_9$  clusters<sup>[50]</sup> with luminescent  $\text{Ag}_{29}$  clusters.<sup>[6]</sup> This kind of materials may give completely new properties and can amplify their existing properties. Several of these possibilities are summarized in **Scheme 4**.

In our opinion, the major challenge to create such solids is to create generalized approaches for diverse building blocks. A critically limiting factor in assembling clusters is the fast interparticle reactivity and diffusion of atoms, which are significant at this length scale.<sup>[20,94]</sup> We believe that different research groups across the world will take initiatives to take this newly growing field to greater heights. The prime motive to create such assemblies will be the potentially interesting properties of such materials, such as a combination of luminescence and magnetism, luminescence and chirality, etc. It is important to recall that molecular clusters, such as  $\text{C}_{60}$  completely new properties, such as superconductivity and magnetism by forming charge-transfer complexes.

The driving force for cocrystallization might be the stability of multicomponent systems. Mechanism of cocrystal

formation is not clear yet. Possibly, it largely depends on the geometric and electronic structures of the component clusters. Detailed mechanism of such cluster growth and their encapsulation in a single crystal would need additional studies. New directions of these materials will also depend on the power of experimental and computational methods that can be developed in the coming years to understand emergent phenomena.

## Acknowledgements

The authors thank the Department of Science and Technology (DST) for supporting the research program. M.B. thanks U.G.C. for his research fellowship. W.A.D. thanks SERB-DST for the award of a National Postdoctoral Fellowship (NPDF).

## Conflict of Interest

The authors declare no conflict of interest.

## Keywords

cluster crystals, cocrystals, crystallization, nanoclusters

Received: July 1, 2020

Revised: August 21, 2020

Published online:



- [1] I. Chakraborty, T. Pradeep, *Chem. Rev.* **2017**, *117*, 8208.
- [2] R. Jin, C. Zeng, M. Zhou, Y. Chen, *Chem. Rev.* **2016**, *116*, 10346.
- [3] P. D. Jadzinsky, G. Calero, C. J. Ackerson, D. A. Bushnell, R. D. Kornberg, *Science* **2007**, *318*, 430.
- [4] M. Zhu, C. M. Aikens, F. J. Hollander, G. C. Schatz, R. Jin, *J. Am. Chem. Soc.* **2008**, *130*, 5883.
- [5] N. Yan, N. Xia, L. Liao, M. Zhu, F. Jin, R. Jin, Z. Wu, *Sci. Adv.* **2018**, *4*, eaat7259.
- [6] L. G. AbdulHalim, M. S. Bootharaju, Q. Tang, S. Del Gobbo, R. G. AbdulHalim, M. Eddaoudi, D.-e. Jiang, O. M. Bakr, *J. Am. Chem. Soc.* **2015**, *137*, 11970.
- [7] A. Desireddy, B. E. Conn, J. Guo, B. Yoon, R. N. Barnett, B. M. Monahan, K. Kirschbaum, W. P. Griffith, R. L. Whetten, U. Landman, T. P. Bigioni, *Nature* **2013**, *501*, 399.
- [8] T.-Q. Yang, B. Peng, B.-Q. Shan, Y.-X. Zong, J.-G. Jiang, P. Wu, K. Zhang, *J. Nanomater.* **2020**, *10*, 261.
- [9] A. Mathew, E. Varghese, S. Choudhury, S. K. Pal, T. Pradeep, *Nanoscale* **2015**, *7*, 14305.
- [10] I. Diez, R. H. A. Ras, *Nanoscale* **2011**, *3*, 1963.
- [11] A. Mathew, T. Pradeep, *Part. Part. Syst. Charact.* **2014**, *31*, 1017.
- [12] M. Brust, J. Fink, D. Bethell, D. J. Schiffrin, C. Kiely, *J. Chem. Soc., Chem. Commun.* **1995**, 1655.
- [13] M. Brust, M. Walker, D. Bethell, D. J. Schiffrin, R. Whyman, *Chem. Soc., Chem. Commun.* **1994**, 0, 801.
- [14] K. R. Krishnadas, D. Ghosh, A. Ghosh, G. Natarajan, T. Pradeep, *J. Phys. Chem. C* **2017**, *121*, 23224.
- [15] Z.-J. Guan, J.-L. Zeng, Z.-A. Nan, X.-K. Wan, Y.-M. Lin, Q.-M. Wang, *Sci. Adv.* **2016**, *2*, e1600323.
- [16] E. Khatun, M. Bodiuzzaman, K. S. Sugi, P. Chakraborty, G. Paramasivam, W. A. Dar, T. Ahuja, S. Antharjanam, T. Pradeep, *ACS Nano* **2019**, *13*, 5753.
- [17] X. Kang, S. Wang, M. Zhu, *Chem. Sci.* **2018**, *9*, 3062.
- [18] E. Khatun, A. Ghosh, P. Chakraborty, P. Singh, M. Bodiuzzaman, P. Ganesan, G. Natarajan, J. Ghosh, S. K. Pal, T. Pradeep, *Nanoscale* **2018**, *10*, 20033.
- [19] A. Ghosh, O. F. Mohammed, O. M. Bakr, *Acc. Chem. Res.* **2018**, *51*, 3094.
- [20] K. R. Krishnadas, A. Baksi, A. Ghosh, G. Natarajan, A. Som, T. Pradeep, *Acc. Chem. Res.* **2017**, *50*, 1988.
- [21] Q. Yao, Y. Feng, V. Fung, Y. Yu, D.-e. Jiang, J. Yang, J. Xie, *Nat. Commun.* **2017**, *8*, 1555.
- [22] Y. Du, H. Sheng, D. Astruc, M. Zhu, *Chem. Rev.* **2020**, *120*, 526.
- [23] S. Zhao, R. Jin, H. Abroshan, C. Zeng, H. Zhang, S. D. House, E. Gottlieb, H. J. Kim, J. C. Yang, R. Jin, *J. Am. Chem. Soc.* **2017**, *139*, 1077.
- [24] L. Zhang, E. Wang, *Nano Today* **2014**, *9*, 132.
- [25] A. Mathew, P. R. Sajanlal, T. Pradeep, *Angew. Chem., Int. Ed.* **2012**, *51*, 9596.
- [26] L.-Y. Chen, C.-W. Wang, Z. Yuan, H.-T. Chang, *Anal. Chem.* **2015**, *87*, 216.
- [27] J. Fang, B. Zhang, Q. Yao, Y. Yang, J. Xie, N. Yan, *Coord. Chem. Rev.* **2016**, *322*, 1.
- [28] M. Schulz-Dobrick, M. Jansen, *Eur. J. Inorg. Chem.* **2006**, *2006*, 4498.
- [29] S. A. Claridge, A. W. Castleman, S. N. Khanna, C. B. Murray, A. Sen, P. S. Weiss, *ACS Nano* **2009**, *3*, 244.
- [30] X. Roy, C.-H. Lee, A. C. Crowther, C. L. Schenck, T. Besara, R. A. Lalancette, T. Siegrist, P. W. Stephens, L. E. Brus, P. Kim, M. L. Steigerwald, C. Nuckolls, *Science* **2013**, *341*, 157.
- [31] E. J. Telford, J. C. Russell, J. R. Swann, B. Fowler, X. Wang, K. Lee, A. Zangiabadi, K. Watanabe, T. Taniguchi, C. Nuckolls, P. Batail, X. Zhu, J. A. Malen, C. R. Dean, X. Roy, *Nano Lett.* **2020**, *20*, 1718.
- [32] A. Nag, P. Chakraborty, G. Paramasivam, M. Bodiuzzaman, G. Natarajan, T. Pradeep, *J. Am. Chem. Soc.* **2018**, *140*, 13590.
- [33] A. Mathew, G. Natarajan, L. Lehtovaara, H. Häkkinen, R. M. Kumar, V. Subramanian, A. Jaleel, T. Pradeep, *ACS Nano* **2014**, *8*, 139.
- [34] J.-R. Wang, Q. Yu, W. Dai, X. Mei, *Chem. Commun.* **2016**, *52*, 3572.
- [35] J. F. Remenar, S. L. Morissette, M. L. Peterson, B. Moulton, J. M. MacPhee, H. R. Guzmán, Ö. Almarsson, *J. Am. Chem. Soc.* **2003**, *125*, 8456.
- [36] C. B. Aakeröy, S. Forbes, J. Desper, *J. Am. Chem. Soc.* **2009**, *131*, 17048.
- [37] R. D. B. Walsh, M. W. Bradner, S. Fleischman, L. A. Morales, B. Moulton, N. Rodríguez-Hornedo, M. J. Zaworotko, *Chem. Commun.* **2003**, 186.
- [38] S. L. Childs, L. J. Chyall, J. T. Dunlap, V. N. Smolenskaya, B. C. Stahly, G. P. Stahly, *J. Am. Chem. Soc.* **2004**, *126*, 13335.
- [39] S. Karki, T. Friščić, L. Fábrián, P. R. Laity, G. M. Day, W. Jones, *Adv. Mater.* **2009**, *21*, 3905.
- [40] S. R. Perumalla, L. Shi, C. C. Sun, *CrystEngComm* **2012**, *14*, 2389.
- [41] M. Morimoto, M. Irie, *J. Am. Chem. Soc.* **2010**, *132*, 14172.
- [42] O. Bolton, A. J. Matzger, *Angew. Chem., Int. Ed.* **2011**, *50*, 8960.
- [43] G. Griffini, L. Brambilla, M. Levi, C. Castiglioni, M. Del Zoppo, S. Turri, *RSC Adv.* **2014**, *4*, 9893.
- [44] R. Kaur, S. S. R. R. Perumal, A. J. Bhattacharyya, S. Yashonath, T. N. Guru Row, *Cryst. Growth Des.* **2014**, *14*, 423.
- [45] J. Zhang, P. Gu, G. Long, R. Ganguly, Y. Li, N. Aratani, H. Yamada, Q. Zhang, *Chem. Sci.* **2016**, *7*, 3851.
- [46] S. Ghosh, C. M. Reddy, *Angew. Chem., Int. Ed.* **2012**, *51*, 10319.
- [47] G. Delori, A. J. Urquhart, I. D. H. Oswald, *CrystEngComm* **2016**, *18*, 5360.
- [48] M. Schulz-Dobrick, M. Jansen, *Inorg. Chem.* **2007**, *46*, 4380.
- [49] L. Wang, T. Wu, X. Bu, X. Zhao, F. Zuo, P. Feng, *Inorg. Chem.* **2013**, *52*, 2259.
- [50] A. Turkiewicz, D. W. Paley, T. Besara, G. Elbaz, A. Pinkard, T. Siegrist, X. Roy, *J. Am. Chem. Soc.* **2014**, *136*, 15873.
- [51] J.-Y. Liu, F. Alkan, Z. Wang, Z.-Y. Zhang, M. Kurmoo, Z. Yan, Q.-Q. Zhao, C. M. Aikens, C.-H. Tung, D. Sun, *Angew. Chem., Int. Ed.* **2019**, *58*, 195.
- [52] M. Bodiuzzaman, A. Ghosh, K. S. Sugi, A. Nag, E. Khatun, B. Varghese, G. Paramasivam, S. Antharjanam, G. Natarajan, T. Pradeep, *Angew. Chem., Int. Ed.* **2019**, *58*, 189.
- [53] J. Yan, S. Malola, C. Hu, J. Peng, B. Dittich, B. K. Teo, H. Häkkinen, L. Zheng, N. Zheng, *Nat. Commun.* **2018**, *9*, 3357.
- [54] W. A. Dar, M. Bodiuzzaman, D. Ghosh, G. Paramasivam, E. Khatun, K. S. Sugi, T. Pradeep, *ACS Nano* **2019**, *13*, 13365.
- [55] L. He, Z. Gan, N. Xia, L. Liao, Z. Wu, *Angew. Chem., Int. Ed.* **2019**, *58*, 9897.
- [56] C. Zeng, H. Qian, T. Li, G. Li, N. L. Rosi, B. Yoon, R. N. Barnett, R. L. Whetten, U. Landman, R. Jin, *Angew. Chem., Int. Ed.* **2012**, *51*, 13114.
- [57] H. Yang, J. Yan, Y. Wang, H. Su, L. Gell, X. Zhao, C. Xu, B. K. Teo, H. Häkkinen, N. Zheng, *J. Am. Chem. Soc.* **2017**, *139*, 31.
- [58] C. Liu, T. Li, H. Abroshan, Z. Li, C. Zhang, H. J. Kim, G. Li, R. Jin, *Nat. Commun.* **2018**, *9*, 744.
- [59] W. Du, S. Jin, L. Xiong, M. Chen, J. Zhang, X. Zou, Y. Pei, S. Wang, M. Zhu, *J. Am. Chem. Soc.* **2017**, *139*, 1618.
- [60] A. Dass, S. Theivendran, P. R. Nimmala, C. Kumara, V. R. Jupally, A. Fortunelli, L. Sementa, G. Barcaro, X. Zuo, B. C. Noll, *J. Am. Chem. Soc.* **2015**, *137*, 4610.
- [61] J. Chai, S. Yang, Y. Lv, T. Chen, S. Wang, H. Yu, M. Zhu, *J. Am. Chem. Soc.* **2018**, *140*, 15582.
- [62] C. P. Joshi, M. S. Bootharaju, M. J. Alhilaly, O. M. Bakr, *J. Am. Chem. Soc.* **2015**, *137*, 11578.
- [63] A. Nag, P. Chakraborty, M. Bodiuzzaman, T. Ahuja, S. Antharjanam, T. Pradeep, *Nanoscale* **2018**, *10*, 9851.
- [64] Y. Shichibu, Y. Negishi, T. Watanabe, N. K. Chaki, H. Kawaguchi, T. Tsukuda, *J. Phys. Chem. C* **2007**, *111*, 7845.
- [65] H. Häkkinen, M. Walter, H. Grönbeck, *J. Phys. Chem. B* **2006**, *110*, 9927.
- [66] M. J. Alhilaly, M. S. Bootharaju, C. P. Joshi, T. M. Besong, A.-H. Emwas, R. Juárez-Mosqueda, S. Kaappa, S. Malola, K. Adil,

- A. Shkurenko, H. Häkkinen, M. Eddaoudi, O. M. Bakr, *J. Am. Chem. Soc.* **2016**, 138, 14727.
- [67] E. G. Mednikov, L. F. Dahl, *Small* **2008**, 4, 534.
- [68] R. Jin, Y. Zhu, H. Qian, *Chem. – Eur. J.* **2011**, 17, 6584.
- [69] C. Liu, T. Li, G. Li, K. Nobusada, C. Zeng, G. Pang, N. L. Rosi, R. Jin, *Angew. Chem., Int. Ed.* **2015**, 54, 9826.
- [70] M. Walter, J. Akola, O. Lopez-Acevedo, P. D. Jadzinsky, G. Calero, C. J. Ackerson, R. L. Whetten, H. Grönbeck, H. Häkkinen, *Proc. Natl. Acad. Sci. USA* **2008**, 105, 9157.
- [71] X. Kang, F. Xu, X. Wei, S. Wang, M. Zhu, *Sci. Adv.* **2019**, 5, eaax7863.
- [72] K. R. Krishnadas, A. Ghosh, A. Baksi, I. Chakraborty, G. Natarajan, T. Pradeep, *J. Am. Chem. Soc.* **2016**, 138, 140.
- [73] Z. Gan, N. Xia, Z. Wu, *Acc. Chem. Res.* **2018**, 51, 2774.
- [74] K. R. Krishnadas, A. Baksi, A. Ghosh, G. Natarajan, T. Pradeep, *Nat. Commun.* **2016**, 7, 13447.
- [75] K. R. Krishnadas, A. Baksi, A. Ghosh, G. Natarajan, T. Pradeep, *ACS Nano* **2017**, 11, 6015.
- [76] A. Ghosh, D. Ghosh, E. Khatun, P. Chakraborty, T. Pradeep, *Nanoscale* **2017**, 9, 1068.
- [77] B. Zhang, O. V. Safonova, S. Pollitt, G. Salassa, A. Sels, R. Kazan, Y. Wang, G. Rupprechter, N. Barrabés, T. Bürgi, *Phys. Chem. Chem. Phys.* **2018**, 20, 5312.
- [78] M. Suyama, S. Takano, T. Nakamura, T. Tsukuda, *J. Am. Chem. Soc.* **2019**, 141, 14048.
- [79] B. Zhang, G. Salassa, T. Bürgi, *Chem. Commun.* **2016**, 52, 9205.
- [80] *Protected Metal Clusters: From Fundamentals to Applications*, (Eds: T. Tsukuda, H. Hakkinen) Elsevier Ltd., Oxford **2015**, 9, 357.
- [81] A. L. Mackay, *Acta Crystallogr.* **1962**, 15, 916.
- [82] N. T. Tran, D. R. Powell, L. F. Dahl, *Angew. Chem., Int. Ed.* **2000**, 39, 4121.
- [83] E. G. Mednikov, M. C. Jewell, L. F. Dahl, *J. Am. Chem. Soc.* **2007**, 129, 11619.
- [84] C. Zeng, Y. Chen, K. Kirschbaum, K. Appavoo, M. Y. Sfeir, R. Jin, *Sci. Adv.* **2015**, 1, e1500045.
- [85] J. D. Erickson, E. G. Mednikov, S. A. Ivanov, L. F. Dahl, *J. Am. Chem. Soc.* **2016**, 138, 1502.
- [86] K. H. Kuo, *J. Struct. Chem.* **2002**, 13, 221.
- [87] L. Liao, S. Zhuang, P. Wang, Y. Xu, N. Yan, H. Dong, C. Wang, Y. Zhao, N. Xia, J. Li, H. Deng, Y. Pei, S.-K. Tian, Z. Wu, *Angew. Chem., Int. Ed.* **2017**, 56, 12644.
- [88] C. M. Aikens, *J. Phys. Chem. C* **2008**, 112, 19797.
- [89] Z. Wu, R. Jin, *Nano Lett.* **2010**, 10, 2568.
- [90] Z. Wu, R. Jin, *Chem. – Eur. J.* **2011**, 17, 13966.
- [91] J.-H. Liao, S. Kahlal, Y.-C. Liu, M.-H. Chiang, J.-Y. Saillard, C. W. Liu, *J. Cluster Sci.* **2018**, 29, 827.
- [92] P. Chakraborty, A. Nag, K. S. Sugi, T. Ahuja, B. Varghese, T. Pradeep, *ACS Mater. Lett.* **2019**, 1, 534.
- [93] B.-L. Han, Z. Liu, L. Feng, Z. Wang, R. K. Gupta, C. M. Aikens, C.-H. Tung, D. Sun, *J. Am. Chem. Soc.* **2020**, 142, 5834.
- [94] K. R. Krishnadas, G. Natarajan, A. Baksi, A. Ghosh, E. Khatun, T. Pradeep, *Langmuir* **2019**, 35, 11243.

# [Ag<sub>15</sub>H<sub>13</sub>(DPPH)<sub>5</sub>]<sup>2+</sup> and [Ag<sub>27</sub>H<sub>22</sub>(DPPB)<sub>7</sub>]<sup>3+</sup>: Two New Hydride and Phosphine Co-Protected Clusters and Their Fragmentation Leading to Naked Clusters, Ag<sub>13</sub><sup>+</sup> and Ag<sub>25</sub><sup>+</sup>

Madhuri Jash, Esma Khatun, Papri Chakraborty, Chennu Sudhakar, and Thalappil Pradeep\*

Cite This: *J. Phys. Chem. C* 2020, 124, 20569–20577

Read Online

ACCESS |



Metrics &amp; More

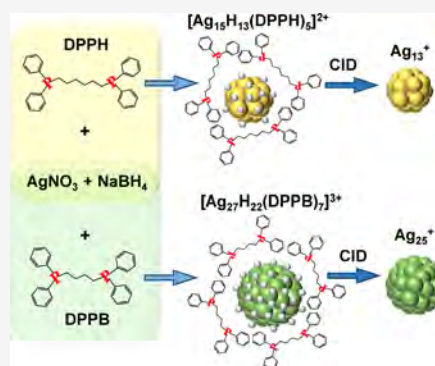


Article Recommendations



Supporting Information

**ABSTRACT:** Here, we report the synthesis of two new hydride and phosphine coprotected clusters [Ag<sub>15</sub>H<sub>13</sub>(DPPH)<sub>5</sub>]<sup>2+</sup> (DPPH = 1,6-bis(diphenylphosphino)-hexane) and [Ag<sub>27</sub>H<sub>22</sub>(DPPB)<sub>7</sub>]<sup>3+</sup> (DPPB = 1,4-bis(diphenylphosphino)butane). The cluster composition was confirmed by high-resolution electrospray ionization mass spectrometric (HRESI MS) studies and also by other supporting data. To the best of our knowledge, the newly synthesized [Ag<sub>15</sub>H<sub>13</sub>(DPPH)<sub>5</sub>]<sup>2+</sup> and [Ag<sub>27</sub>H<sub>22</sub>(DPPB)<sub>7</sub>]<sup>3+</sup> clusters are the smallest and the largest known hydride and phosphine coprotected silver clusters, respectively, synthesized in the solution phase. Collision-induced dissociation (CID) was used to probe their fragmentation pattern in the gas phase, which also supported their compositions. During the CID experiment, naked clusters Ag<sub>13</sub><sup>+</sup> and Ag<sub>25</sub><sup>+</sup> got formed starting from the ligated Ag<sub>15</sub> and Ag<sub>27</sub> clusters, respectively, where the number of metal atoms remained nearly the same as in the parent clusters. Collision energy-dependent fragmentation pathways of the formation of naked clusters have been explored in detail. We suggest that silver clusters protected by hydride and phosphine ligands may become useful precursors to make new naked clusters in the gas phase.



## INTRODUCTION

New methods for the synthesis of atomically precise noble metal nanoclusters have been explored extensively in the past few decades due to the potential applications of these materials in catalysis, energy storage, sensing, drug delivery, optics, etc.<sup>1–7</sup> Their photophysical properties have also gained much attention.<sup>8,9</sup> An atomically precise cluster is composed of a core (or arrangement of metal atoms) and its shell (arrangement of ligands and bonding between them and the metal core). Staple units are formed by the interaction of sulfur of the thiol commonly used as the ligand and the surface metal atoms, but this is not a general case and examples include phosphine-protected systems.<sup>10,11</sup> The properties of nanoclusters can be manipulated either by changing the core or the ligand surface, which will in turn alter their total structure.<sup>12,13</sup> Therefore, the introduction of new ligand results in a new cluster system, which can be a promising synthetic approach for a new class of materials. Liquid phase synthesis of noble metal nanoclusters has been investigated widely with classic ligands, namely thiols,<sup>14,15</sup> phosphines,<sup>16,17</sup> alkynyls<sup>18</sup> and/or their combinations.<sup>19</sup> The use of these organic ligands results in a wide range of nuclearities in nanoclusters which have been characterized as Au<sub>102</sub>,<sup>20</sup> Au<sub>25</sub>,<sup>21</sup> Au<sub>18</sub>,<sup>22</sup> Ag<sub>44</sub>,<sup>23</sup> Ag<sub>25</sub>,<sup>24</sup> Ag<sub>29</sub>,<sup>25</sup> etc., by varying ligands and synthetic methods.

In the context of increasing the global energy demand, metal hydrides,<sup>26</sup> complex hydrides,<sup>27</sup> and metal–organic frameworks (MOFs)<sup>28</sup> have been explored to discover new

hydrogen storage materials. For the last three decades, group 11 metal (copper, silver, gold) hydrides have become an emerging category of research in terms of their new molecular structures, interesting properties, and hydrogen related applications.<sup>29</sup> A series of copper hydride clusters have been explored by different research groups in view of their various applications, like energy storage and conversion.<sup>30,31</sup> In contrast, inorganic ligands (H<sup>−</sup> and OH<sup>−</sup>) have rarely been used for the synthesis of Au and Ag nanoclusters. Their use could have given us the opportunity to find different core sizes and enhanced properties. So far, reports of Ag clusters by using hydride as inorganic ligand are much fewer and should be further explored. Mass spectrometry-based investigations have identified low-nuclearity clusters with very few hydride ligands.<sup>32</sup> For hydride protected clusters, the presence of coligands is necessary to give them adequate stability. In 2016, Bakr group reported a new class of silver clusters where hydrides are majority ligands in the presence of phosphines, the latter acted as coligands. They have synthesized hydride rich [Ag<sub>18</sub>H<sub>16</sub>(TPP)<sub>10</sub>]<sup>2+</sup>, [Ag<sub>25</sub>H<sub>22</sub>(DPPE)<sub>8</sub>]<sup>3+</sup>, and

Received: June 27, 2020

Revised: August 26, 2020

Published: August 26, 2020



$[\text{Ag}_{26}\text{H}_{22}(\text{TFPP})_{13}]^{2+}$  clusters using TPP (triphenylphosphine), DPPE (1,2-bis(diphenylphosphino)ethane), and TFPP (tris(4-fluorophenyl)phosphine) coligands, respectively.<sup>33</sup> High resolution ESI mass spectra with distinct isotopic patterns helped them to identify the compositions of these hydride-protected clusters. In 2017, a report from our group showed that these clusters can be the starting materials to create naked silver clusters in the gas phase by collision-induced dissociation (CID).<sup>34</sup> We have also demonstrated that naked clusters can be formed outside the mass spectrometer by thermal desorption of hydrogen and phosphine ligands.<sup>35</sup> The formation of naked clusters with specific nuclearity was investigated further to understand their structures, fragmentation pathways, and reactivity in the gas phase.<sup>36</sup>

To explore the diversity of hydride and phosphine coprotected silver clusters, we have synthesized two new silver nanoclusters by varying the synthetic parameters like the phosphine ligand used, reaction time and rate of mixing. We find that by changing the phosphine from DPPH (1,6-bis(diphenylphosphino)hexane) to DPPB (1,4-bis(diphenylphosphino)butane), we get two different clusters,  $[\text{Ag}_{15}\text{H}_{13}(\text{DPPH})_5]^{2+}$  and  $[\text{Ag}_{27}\text{H}_{22}(\text{DPPB})_7]^{3+}$ . These clusters are thoroughly characterized by high-resolution electrospray ionization mass spectrometry (HRESI MS), optical spectroscopy, nuclear magnetic resonance (NMR) spectroscopy, X-ray photoelectron spectroscopy (XPS), scanning electron microscopy energy-dispersive X-ray spectroscopy (SEM EDS) and transmission electron microscopy (TEM). The in situ gas phase fragmentation or CID of these newly synthesized clusters have also been studied in detail. Fragmentation study confirms the number of hydrogen and phosphine ligands and also results in naked clusters,  $\text{Ag}_{13}^+$  and  $\text{Ag}_{25}^+$  starting from  $\text{Ag}_{15}$  and  $\text{Ag}_{27}$  clusters, respectively. Further confirmation of hydride protection comes from deuterium labeling experiments.

## ■ EXPERIMENTAL SECTION

**Reagents and Materials.** Silver nitrate ( $\text{AgNO}_3$ , 99.9%) was purchased from Rankem India. 1,4-Bis(diphenylphosphino)butane (DPPB) and 1,6-bis(diphenylphosphino)hexane (DPPH) were purchased from Spectrochem. Sodium borohydride ( $\text{NaBH}_4$ , 98%) and sodium borodeuteride ( $\text{NaBD}_4$ , 98 atom % D) were purchased from Sigma-Aldrich. All solvents such as dichloromethane (DCM) and methanol (MeOH) were purchased from Rankem and were of analytical grade.  $\text{CDCl}_3$  (99.8 atom % D) was purchased from Sigma-Aldrich for NMR measurements. All of the chemicals were used without further purification.

**Synthesis of  $[\text{Ag}_{15}\text{H}_{13}(\text{DPPH})_5]^{2+}$  (I).** To synthesize cluster I, a reported method was used with some modifications.<sup>33</sup> In a typical synthesis method, 20 mg of  $\text{AgNO}_3$  was dissolved in 5 mL of MeOH, followed by the addition of 75 mg of DPPH dissolved in 9 mL of DCM under constant stirring. After 20 min of stirring, 35 mg of  $\text{NaBH}_4$  in 1 mL of ice-cold water was added. The addition of  $\text{NaBH}_4$  immediately changed the color of the reaction mixture from colorless to light yellow. The reaction was vigorously stirred ( $\sim 1000$  rpm) under dark at room temperature. After 20 min of stirring, the color of the solution changed to green from light yellow. Then at 2 h of reaction, the green color changed to dark yellow, which indicated the formation of the cluster,  $[\text{Ag}_{15}\text{H}_{13}(\text{DPPH})_5]^{2+}$ . The yellow solution was evaporated under vacuum and washed with cold deionized (DI) water.

Then the solid yellow material was dissolved in methanol and the solution was centrifuged for 5 min at 8000 rpm for 2 times to remove the excess phosphine ligands. The yellow supernatant containing cluster was vacuum evaporated and dissolved in 2 mL of methanol for further characterization. For mass spectrometric experiments, 100  $\mu\text{L}$  of the cluster solution was diluted to 1 mL by methanol. To synthesize the deuterated  $\text{Ag}_{15}$  analogue, a similar method was followed by replacing  $\text{NaBH}_4$  with  $\text{NaBD}_4$ .

**Synthesis of  $[\text{Ag}_{27}\text{H}_{22}(\text{DPPB})_7]^{3+}$  (II).** For synthesis of cluster II, the above-mentioned procedure was followed only by exchanging DPPH with DPPB and keeping all other chemicals the same. After adding the  $\text{NaBH}_4$  solution, the reaction mixture became light yellow immediately. Then the reaction was kept for vigorous stirring ( $\sim 1000$  rpm) at room temperature under dark condition. Over 3 h of continuous stirring, the color of the solution changed to blackish green which indicated the formation of the cluster,  $[\text{Ag}_{27}\text{H}_{22}(\text{DPPB})_7]^{3+}$ . To synthesize the deuterated  $\text{Ag}_{27}$  analogue, a similar method was followed by replacing  $\text{NaBH}_4$  with  $\text{NaBD}_4$ .

**Instrumentation. UV–vis Absorption Spectroscopy.** UV–vis spectra of nanoclusters were recorded using a PerkinElmer Lambda 25 UV–vis spectrometer. Absorption spectra were typically measured in the range of 200–1100 nm with a band-pass filter of 1 nm.

**ESI MS.** The electrospray ionization mass spectra (ESI MS) were measured using a Waters Synapt G2Si High Definition Mass Spectrometer. This mass spectrometer consists of an electrospray source, quadrupole ion guide/trap, ion mobility cell and TOF analyzer. Nitrogen gas was used as the nebulizer gas, and all of the mass spectra were collected in positive ion mode. Mass spectrometric measurements were made using the following conditions:

**For Detecting the Hydride and Phosphine Coprotected Silver Nanoclusters (I and II).** Flow rate, 30  $\mu\text{L}/\text{min}$ ; capillary voltage, 3 kV; cone voltage, 20 V; source offset, 20 V; source temperature, 100  $^\circ\text{C}$ ; desolvation temp, 150  $^\circ\text{C}$ ; desolvation gas flow, 400 L/h; trap gas flow, 5 L/h.

**For MS/MS Studies of I and II.** For MS/MS or collision-induced dissociation (CID) studies, the molecular ion peaks were at first selected in the quadrupole and then were fragmented inside the trap by changing the collision energy (CE).

Flow rate, 30  $\mu\text{L}/\text{min}$ ; capillary voltage, 3 kV; cone voltage, 20 V; source offset, 20 V; trap collision energy, 2–110 (variable); source temperature, 100  $^\circ\text{C}$ ; desolvation temperature, 150  $^\circ\text{C}$ ; desolvation gas flow, 400 L/h; trap gas flow, 5 L/h.

**NMR Spectroscopy.** Nuclear magnetic resonance (NMR) spectroscopy measurements were done at room temperature by using a Bruker 500 MHz NMR spectrometer. Pure ligands (DPPH and DPPB) and the clusters I and II were dissolved in  $\text{CDCl}_3$  to collect  $^1\text{H}$  and  $^{31}\text{P}$  NMR spectra.

**XPS.** X-ray photoelectron spectroscopy (XPS) of nanoclusters was performed by using an ESCA Probe TPD spectrometer of Omicron Nanotechnology. A monochromatic  $\text{Al K}\alpha$  (1486.69 eV) X-ray source was used. Samples were drop casted on a sample stub and measurements were carried out with a constant analyzer energy of 50 eV for the survey scans and 20 eV for the specific regions. Binding energies in the spectra were calibrated with respect to the C 1s peak at 284.8 eV.



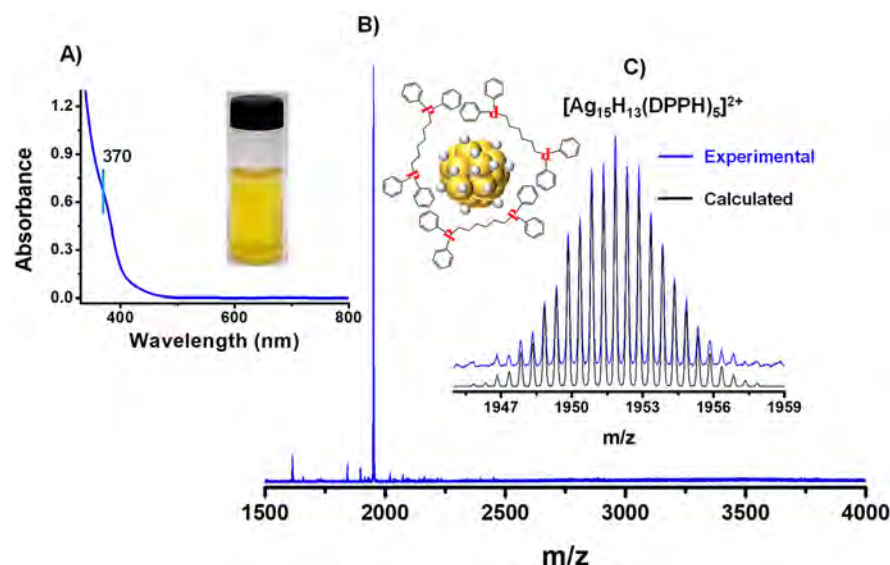


**Figure 1.** (A) UV–vis absorption spectrum of I. Inset: Photograph of the cluster in methanol. (B) HRESI MS of I in positive mode which shows an intense peak at  $m/z$  1951.8, corresponding to  $[\text{Ag}_{15}\text{H}_{13}(\text{DPPH})_5]^{2+}$ . Inset: schematic of the  $[\text{Ag}_{15}\text{H}_{13}(\text{DPPH})_5]^{2+}$  cluster. (C) Comparison of the experimental and calculated isotopic distributions of I.

**SEM EDS.** Scanning electron microscopy energy-dispersive X-ray spectroscopy (SEM EDS) analysis were performed using a FEI QUANTA-200 SEM. Samples were prepared by drop-casting methanolic solutions of nanoclusters on an ITO plate, which were dried under room temperature.

**TEM.** Transmission electron microscopy (TEM) was performed using a JEOL 3010, 300 kV instrument at an accelerating voltage of 200 kV. The accelerating voltage was kept low to reduce beam-induced damage. Samples were prepared by drop casting the methanol solution of the clusters on carbon-coated copper grids and dried under ambient conditions.

## RESULTS AND DISCUSSION

Both the clusters,  $[\text{Ag}_{15}\text{H}_{13}(\text{DPPH})_5]^{2+}$  (I) and  $[\text{Ag}_{27}\text{H}_{22}(\text{DPPB})_7]^{3+}$  (II), were synthesized by reducing the silver-phosphine complexes in the presence of  $\text{NaBH}_4$ , which act as a reducing agent as well as the source of hydride ligands (a detailed synthetic procedure is given in the [Experimental Section](#)). For the synthesis of cluster I, at first Ag-DPPH complex was made in MeOH/DCM solvent and then it was reduced by ice-cold  $\text{NaBH}_4$  solution under vigorous stirring at  $\sim 1000$  rpm. After 2 h of reaction, the solution became dark yellow in color (inset of [Figure 1A](#)), which shows a small peak at 370 nm in the optical absorption spectrum, as presented in [Figure 1A](#). To probe the molecular composition, high-resolution electrospray ionization mass spectrometry (HRESI MS) has been performed using the yellow methanolic solution. The positive mode HRESI MS data ([Figure 1B](#)) show a sharp peak at  $m/z$  1951.8, which suggests the formation of a monodispersed cluster, and there was no other cluster peak up to  $m/z$  10 000. The expanded spectrum shows the difference between two successive peaks in the isotopic distribution of cluster as  $m/z$  0.5, which implies that the cluster is in +2 charge state. The peak was assigned as  $[\text{Ag}_{15}\text{H}_{13}(\text{DPPH})_5]^{2+}$  where the isotopic pattern, which is made by the different isotopic abundances of the constituent elements, was used to assign the accurate composition. [Figure 1C](#) presents a comparison between the experimental spectrum (blue trace)

and the calculated spectrum (black trace), which matched perfectly. The presence and number of hydrogens in the cluster were further confirmed by synthesizing cluster I with  $\text{NaBD}_4$  instead of  $\text{NaBH}_4$  and keeping all other conditions the same. The deuterated analogue shows an ESI MS peak at  $m/z$  1958.3, due to  $[\text{Ag}_{15}\text{D}_{13}(\text{DPPH})_5]^{2+}$ . An exact match of experimental (pink trace) and calculated (black trace) isotopic pattern is shown in [Figure S1A](#), which validates the composition of the cluster as  $[\text{Ag}_{15}\text{D}_{13}(\text{DPPH})_5]^{2+}$ . Hence, 13 hydrogen ligands were confirmed by the mass shift of  $\Delta m/z = 6.5$  in between  $[\text{Ag}_{15}\text{H}_{13}(\text{DPPH})_5]^{2+}$  and  $[\text{Ag}_{15}\text{D}_{13}(\text{DPPH})_5]^{2+}$  clusters ( $\Delta m = 13$ ,  $z = 2$ ), shown in [Figure S1B](#).

It is noteworthy that during the synthesis of cluster I, within 20 min of addition of  $\text{NaBH}_4$ , the color of the solution changed to green from light yellow. Then the green solution became dark yellow upon 2 h of continuous stirring resulting the final product  $[\text{Ag}_{15}\text{H}_{13}(\text{DPPH})_5]^{2+}$  (I). Hence, to know the actual composition of the intermediate green solution, we studied the UV–vis and ESI MS. To collect the green solution, the stirring was stopped after 1 h when the solution was green in color. However, as soon as the stirring was stopped, the green color changed to yellowish green within 5 min, and after 15 min, it became fully dark yellow. [Figure S2](#) shows the time-dependent UV–vis spectrum of these three differently colored solutions with their corresponding photographs, which show a visible change in their optical spectrum. We have also checked the time-dependent ESI MS, which is shown in [Figure S3](#). The mass spectrum of the pure green solution exhibits the presence of  $[\text{Ag}_{22}\text{H}_{21}(\text{DPPH})_6]^{2+}$  cluster, whereas the yellowish green solution shows higher abundance of  $[\text{Ag}_{15}\text{H}_{13}(\text{DPPH})_5]^{2+}$  compared to  $[\text{Ag}_{22}\text{H}_{21}(\text{DPPH})_6]^{2+}$ . After 15 min of stopping stirring, the green solution becomes dark yellow and the entire composition becomes  $[\text{Ag}_{15}\text{H}_{13}(\text{DPPH})_5]^{2+}$  (I), which is shown in [Figure 1](#). From these results, we can conclude that the synthesis of  $[\text{Ag}_{15}\text{H}_{13}(\text{DPPH})_5]^{2+}$  (yellow) involves the formation of an intermediate cluster,  $[\text{Ag}_{22}\text{H}_{21}(\text{DPPH})_6]^{2+}$  (green). This observation suggests the formation of a stable cluster through an etching process, where the rate of this step

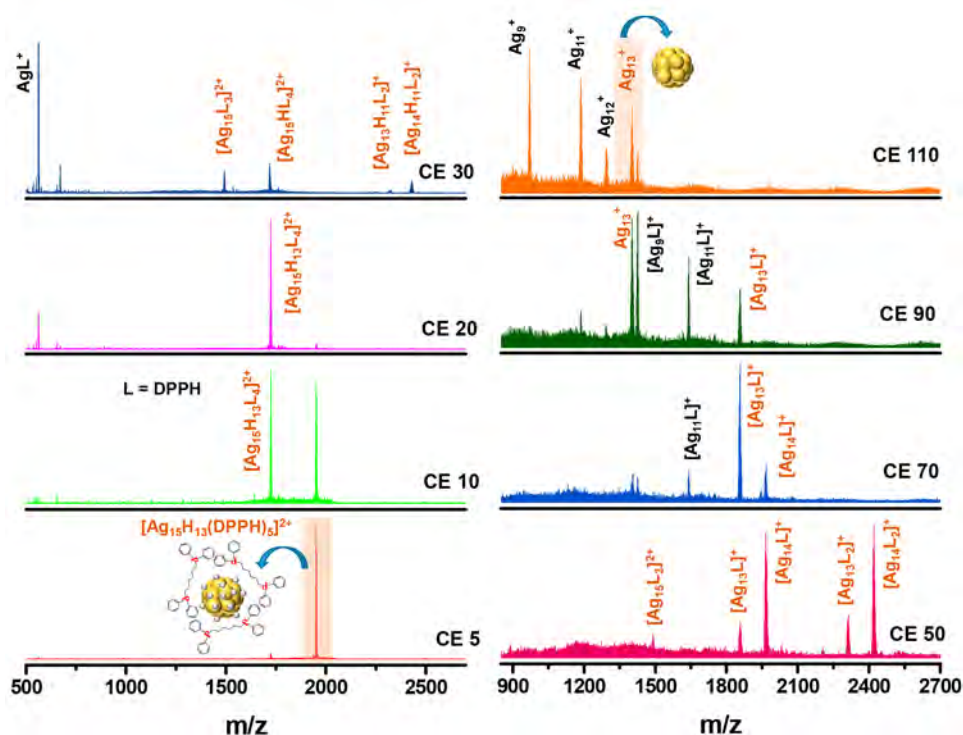


**Figure 2.** MS/MS spectra of  $[\text{Ag}_{15}\text{H}_{13}(\text{DPPH})_5]^{2+}$  (**1**) with increasing CE from 5 to 110 (in instrumental units). Ligand DPPH is represented by “L”. Due to the increase in CE, detachment of hydrogens, DPPH and  $[\text{AgDPPH}]^+$  happened from the parent nanoclusters which resulted in formation of the naked cluster,  $\text{Ag}_{13}^+$ . The ions written in brown are involved in the formation of naked cluster  $\text{Ag}_{13}^+$ . Schematic illustrations of the protected parent cluster and the naked cluster are shown in the inset.

is also dependent on the stirring speed.<sup>37</sup> Due to the instability of the intermediate green cluster, it was not possible to characterize it further.

Both the clusters  $[\text{Ag}_{15}\text{H}_{13}(\text{DPPH})_5]^{2+}$  and  $[\text{Ag}_{27}\text{H}_{22}(\text{DPPB})_7]^{3+}$  were stable for about 1 month if stored at  $\sim 4^\circ\text{C}$ . However, they tend to degrade or become unstable after complete removal of excess phosphines from the solution by centrifugation. Crystallization demands removal of excess ligands and byproducts. As a result, obtaining crystals of  $[\text{Ag}_{15}\text{H}_{13}(\text{DPPH})_5]^{2+}$  and  $[\text{Ag}_{27}\text{H}_{22}(\text{DPPB})_7]^{3+}$  has been challenging due to their instability after cleaning. We have tried to remove excess phosphines by precipitating them at lower temperature during crystallization, but the effort was not successful until now.

For the characterization of cluster I,  $^1\text{H}$  and  $^{31}\text{P}$  NMR spectroscopy has been done and the data are compared with those of the ligand DPPH (Figures S4 and S5). In Figure S6A, the XPS survey spectrum confirms the presence of C, O, P, and Ag. The specific regions of Ag and P are deconvoluted in Figure S6B,C, respectively. The XPS peak corresponding to Ag  $3d_{5/2}$  appears at 368.0 eV, which confirms Ag in zero oxidation state. SEM EDS analysis also confirms the presence of Ag and P in cluster I. The atomic ratio of Ag and P obtained from this analysis is close to the atomic ratio of Ag and P in cluster I (Figure S7). TEM image of cluster I reveals that the average particle size is  $1.46 \pm 0.13$  nm (Figure S8).

As these hydride and phosphine coprotected silver nano-clusters can create naked silver clusters in the gas phase, the process of dissociation was investigated in detail. The newly synthesized cluster  $[\text{Ag}_{15}\text{H}_{13}(\text{DPPH})_5]^{2+}$  (**I**) was selected by a quadrupole mass filter in the G2Si mass spectrometer and was subjected to collision induced dissociation (CID) with Ar gas

inside the trap. Figure 2 presents a detailed study of CID of cluster I, which helps in understanding the fragmentation pathway as well as naked cluster formation. At first, the parent ion peak at  $m/z$  1951.8 was mass selected, and then with increase in collision energy (CE), fragmentation of the parent ion started to appear. The major peak of the parent ion was seen up to CE 5, whereas, at CE 10 onward, the extent of fragmentation increased with continuous decrease in parent ion intensity. Up to a CE of 30, the parent ion  $[\text{Ag}_{15}\text{H}_{13}(\text{DPPH})_5]^{2+}$  ( $m/z$  1951.8) underwent a loss of two DPPH and 13 hydrogens to produce  $[\text{Ag}_{15}(\text{DPPH})_3]^{2+}$  ( $m/z$  1490.9). After that at CE 50, doubly charged  $[\text{Ag}_{15}(\text{DPPH})_3]^{2+}$  becomes singly charged  $[\text{Ag}_{14}(\text{DPPH})_2]^+$  ( $m/z$  2418.8) by losing one  $[\text{AgDPPH}]^+$ . Then there were losses of one Ag and one DPPH from  $[\text{Ag}_{14}(\text{DPPH})_2]^+$ , creating  $[\text{Ag}_{13}(\text{DPPH})_2]^+$  ( $m/z$  2310.2) and  $[\text{Ag}_{14}(\text{DPPH})]^+$  ( $m/z$  1963.9), respectively. Next, by increasing the CE to 70,  $[\text{Ag}_{14}(\text{DPPH})_2]^+$ ,  $[\text{Ag}_{13}(\text{DPPH})_2]^+$ , and  $[\text{Ag}_{14}(\text{DPPH})]^+$  got further dissociated to  $[\text{Ag}_{13}(\text{DPPH})]^+$  ( $m/z$  1855.9) by consecutive steps. At CE 90,  $[\text{Ag}_{13}(\text{DPPH})]^+$  started losing the remaining DPPH ligand and formed the naked cluster,  $\text{Ag}_{13}^+$  ( $m/z$  1401.7). All of the ligands were completely desorbed from the parent cluster,  $[\text{Ag}_{15}\text{H}_{13}(\text{DPPH})_5]^{2+}$  at CE 110 and resulted in  $\text{Ag}_{13}^+$  with other possible smaller naked clusters due to the application of higher CE. There is a second possible fragmentation pathway of parent ion for the formation of  $\text{Ag}_{13}^+$ . In this second pathway, at first, parent ion  $[\text{Ag}_{15}\text{H}_{13}(\text{DPPH})_5]^{2+}$  ( $m/z$  1951.8) lost one DPPH and generated  $[\text{Ag}_{15}\text{H}_{13}(\text{DPPH})_4]^{2+}$  ( $m/z$  1724.3) at CE 20. Then at CE 30, it underwent an  $[\text{AgH}_2(\text{DPPH})_2]^+$  loss to produce singly charged  $[\text{Ag}_{14}\text{H}_{11}(\text{DPPH})_2]^+$  ( $m/z$  2430.1). Next,  $[\text{Ag}_{14}\text{H}_{11}(\text{DPPH})_2]^+$

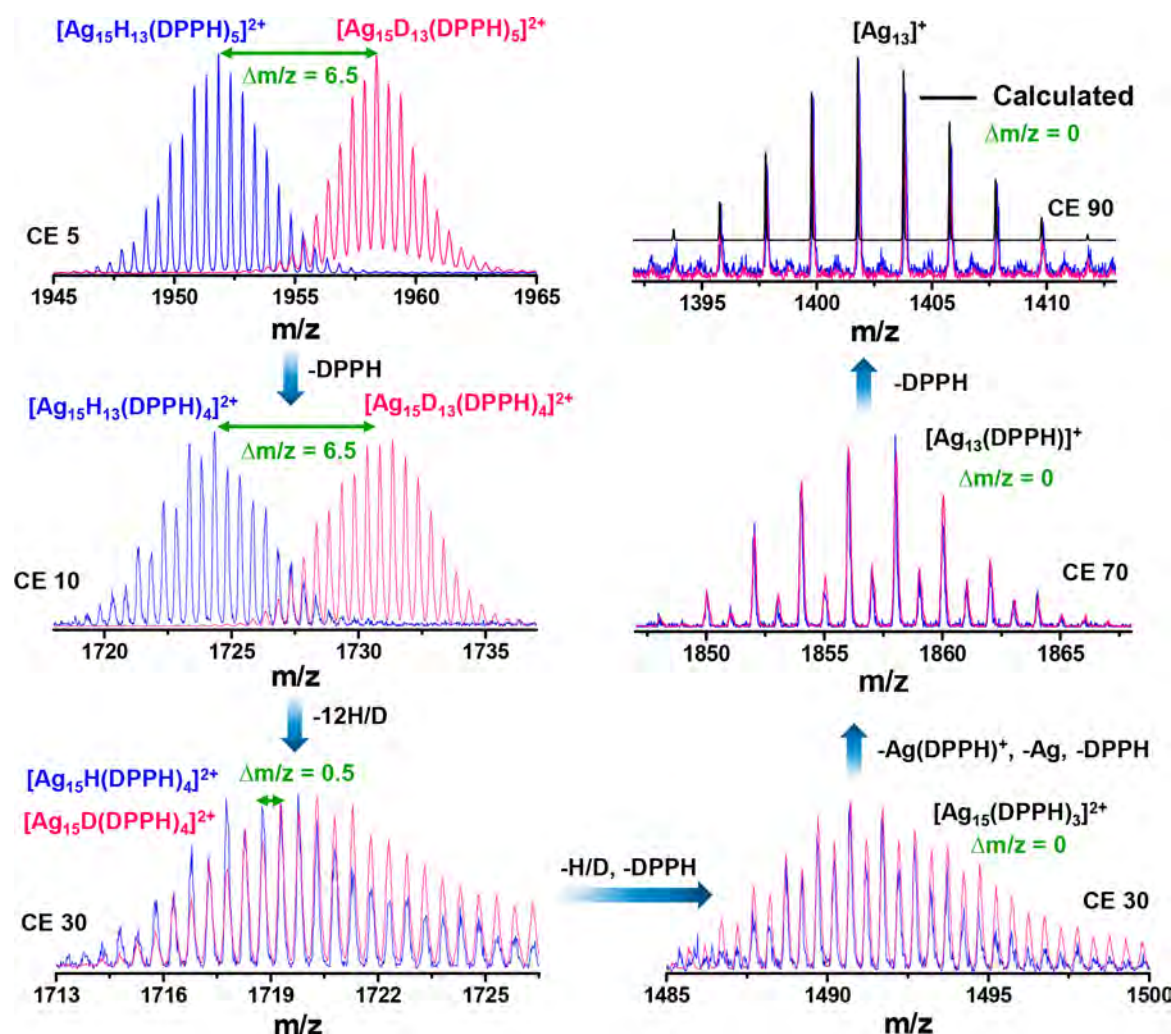


**Figure 3.** Expanded ESI MS of  $[\text{Ag}_{15}\text{H}_{13}(\text{DPPH})_5]^{2+}$  (blue trace) and  $[\text{Ag}_{15}\text{D}_{13}(\text{DPPH})_5]^{2+}$  (pink trace) at different CE during the formation of naked cluster  $\text{Ag}_{13}^+$ . The mass shift ( $\Delta m/z$ ) in between the blue and pink trace confirms the presence of hydrogen in the fragmented ions. The isotopic distribution of  $\text{Ag}_{13}^+$  confirms the absence of hydrogen atoms, which also matches with the calculated pattern (black trace).

was fragmented again to give  $[\text{Ag}_{13}(\text{DPPH})]^{+}$  ( $m/z$  1855.9) and ultimately it produced naked cluster  $\text{Ag}_{13}^+$  ( $m/z$  1401.7).

To confirm the complete removal of hydrogens from the parent cluster  $[\text{Ag}_{15}\text{H}_{13}(\text{DPPH})_5]^{2+}$ , the fragmentation pathway was compared with its deuterated analogue,  $[\text{Ag}_{15}\text{D}_{13}(\text{DPPH})_5]^{2+}$  (Figure 3). In Figure 3, we have compared the first fragmentation pathway of the parent ion which is described in Figure 2. The second fragmentation method is compared in Figure S9. In Figure 3, the expanded ESI MS of blue and pink traces correspond to the parent or fragmented ions generated from  $[\text{Ag}_{15}\text{H}_{13}(\text{DPPH})_5]^{2+}$  and  $[\text{Ag}_{15}\text{D}_{13}(\text{DPPH})_5]^{2+}$  clusters, respectively. The mass shift ( $\Delta m/z$ ) in between the blue and pink traces happened due to the replacement of hydrogen atoms with the deuterium atoms in the deuterated analogue. At CE 5, the mass shift is  $m/z = 6.5$  in-between  $[\text{Ag}_{15}\text{H}_{13}(\text{DPPH})_5]^{2+}$  ( $m/z$  1951.8) and  $[\text{Ag}_{15}\text{D}_{13}(\text{DPPH})_5]^{2+}$  ( $m/z$  1958.3) clusters, which refers to the presence of 13 hydrogen atoms ( $\Delta m = 13$ , charge state  $z = 2$ ) in the parent cluster. At CE 10, due to one DPPH loss, the fragmented ions were generated at  $m/z$  1724.3 (blue trace) and  $m/z$  1730.8 (pink trace). These generated ions show the same mass shift of  $\Delta m/z = 6.5$  ( $\Delta m = 13$ ,  $z = 2$ ), which confirms that there was no hydrogen losses in this step. In the

next step at CE 30, the mass shift in between  $m/z$  1718.8 (blue trace) and  $m/z$  1719.3 (pink trace) is  $\Delta m/z = 0.5$  ( $\Delta m = 1$ ,  $z = 2$ ), which tells about the existence of one hydrogen in the daughter ion, after the desorption of 12 hydrogens and the formation of  $[\text{Ag}_{15}\text{H}(\text{DPPH})_4]^{2+}$ . At the same CE 30,  $[\text{Ag}_{15}\text{H}(\text{DPPH})_4]^{2+}$  further underwent fragmentation and generated a peak at  $m/z$  1490.9 (blue trace), which shows a mass shift of  $\Delta m/z = 0$  ( $\Delta m = 0$ ,  $z = 2$ ) with its deuterated counterpart (pink trace). This step confirms the complete removal of hydrogens from the parent cluster and the generation of  $[\text{Ag}_{15}(\text{DPPH})_3]^{2+}$ . Next,  $[\text{Ag}_{15}(\text{DPPH})_3]^{2+}$  was fragmented by  $[\text{AgDPPH}]^{+}$ , Ag, and DPPH consecutively to produce singly charged  $[\text{Ag}_{13}(\text{DPPH})]^{+}$  ( $m/z$  1855.9) with no mass shift, and finally at CE 90, the naked cluster  $\text{Ag}_{13}^+$  was generated after losing the last DPPH. Expanded peak shapes of  $\text{Ag}_{13}^+$  ( $m/z$  1401.7), generated from  $[\text{Ag}_{15}\text{H}_{13}(\text{DPPH})_5]^{2+}$  (blue trace) and  $[\text{Ag}_{15}\text{D}_{13}(\text{DPPH})_5]^{2+}$  (pink trace), merged with each other ( $\Delta m/z = 0$ ) and also their isotopic distributions match with the calculated one (black trace). These observations confirm the formation of the naked cluster,  $\text{Ag}_{13}^+$ . By the same way, complete hydrogen desorption from cluster I has been confirmed for the second fragmentation pathway, which is shown in Figure S9. Here at CE 5 and 10,



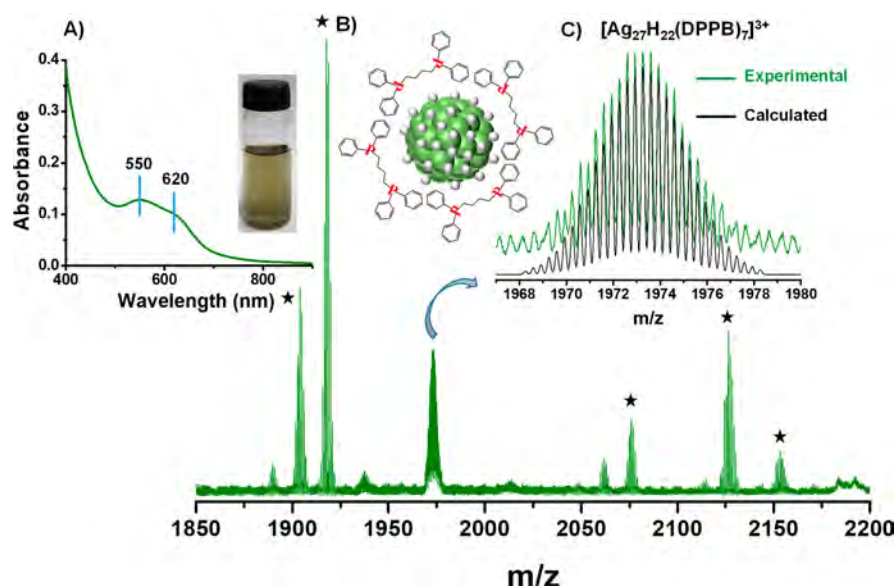


**Figure 4.** (A) UV-vis absorption spectrum of **II**. Inset: Photograph of the cluster in methanol. (B) HRESI MS of **II** in positive mode which shows an intense peak at  $m/z$  1973.2 corresponding to  $[\text{Ag}_{27}\text{H}_{22}(\text{DPPB})_7]^{3+}$ . Inset: Schematic of the  $[\text{Ag}_{27}\text{H}_{22}(\text{DPPB})_7]^{3+}$  cluster. (C) Comparison of the experimental and calculated isotopic distribution of **II**. The \* peaks refer to unidentified species.

the same kind of fragmentation and mass shift happened, which was observed in Figure 3. At CE 30, the fragmented peaks were generated at  $m/z$  2430.1 (blue trace) and  $m/z$  2441.2 (pink trace) showing a mass shift of  $\Delta m/z = 11$  ( $\Delta m = 11, z = 1$ ), which confirms the presence of 11 hydrogens in the  $[\text{Ag}_{14}\text{H}_{11}(\text{DPPH})_2]^+$  ion. At the same CE 30,  $[\text{Ag}_{14}\text{H}_{11}(\text{DPPH})_2]^+$  further created a fragmented peak at  $m/z$  2322.2 (blue trace), which shows the same mass shift of  $\Delta m/z = 11$  ( $\Delta m = 11, z = 1$ ) with its deuterated counterpart (pink trace,  $m/z$  2333.3). This step confirms that there was only one Ag loss and no hydrogen loss. The newly generated  $[\text{Ag}_{13}\text{H}_{11}(\text{DPPH})_2]^+$  ion again lost 11 hydrogens and one DPPH to create  $[\text{Ag}_{13}(\text{DPPH})]^+$  ( $m/z$  1855.9) and it did not show any mass shift with its deuterated counterpart. Finally at CE 90, naked cluster  $\text{Ag}_{13}^+$  ( $m/z$  1401.7) was formed with no mass shift ( $\Delta m/z = 0$ ) in between the blue and pink traces and confirms the removal of all hydrogens from the parent cluster **I**. The CE dependent full range MS/MS spectra of  $[\text{Ag}_{15}\text{D}_{13}(\text{DPPH})_5]^{2+}$  cluster are given in Figure S10. The fragmentation pathway of cluster **I**, confirmed by the MS/MS experiments of  $[\text{Ag}_{15}\text{H}_{13}(\text{DPPH})_5]^{2+}$  and  $[\text{Ag}_{15}\text{D}_{13}(\text{DPPH})_5]^{2+}$ , has been represented as a flowchart in Figure S11.

As the size of nanoclusters is very much dependent on phosphine's structure in the ligand shell, here we have used another diphosphine with shorter chain length, DPPB. The cluster synthesis is similar to the previous  $\text{Ag}_{15}$  method, where only DPPH is replaced by DPPB ligand (details are in the Experimental Section). In this synthesis, we get a blackish green solution (inset of Figure 4A) after 3 h of continuous stirring at  $\sim 1000$  rpm. It is important to mention that for the synthesis of both the clusters (DPPH and DPPB protected) stirring at higher rpm ( $\sim 1000$ ) is very much necessary and complexes are formed otherwise, instead of nanoclusters. The reason can be that faster reduction kinetics is required to facilitate the formation of higher mass clusters compared to lower mass complexes.

The DPPB protected silver cluster **II** exhibits similar kinds of optical features like  $\text{Ag}_{18}$  cluster, and the latter was reported

before.<sup>33</sup> However, here both the optical peaks are red-shifted compared to  $\text{Ag}_{18}$  and appeared at 550 and 620 nm, which can be due to the formation of differently sized cluster core (Figure 4A). The positive mode HRESI MS data (Figure 4B) of the methanolic blackish green solution (cluster **II**) shows a peak at  $m/z$  1973.2 with peak separation of  $m/z$  0.33, which confirms the charge state of +3. Along with this +3 charge state cluster, there were some +1 charge state peaks, which are unidentified and can be due to the byproduct of the reaction. The  $m/z$  1973.2 peak was assigned as  $[\text{Ag}_{27}\text{H}_{22}(\text{DPPB})_7]^{3+}$ , where the isotopic pattern of the experimental spectrum (olive trace) matches exactly with the calculated one (black trace), shown in Figure 4C. The number of hydrogens in cluster **II** was confirmed by synthesizing the cluster with  $\text{NaBD}_4$  instead of  $\text{NaBH}_4$ .

The deuterated analogue shows an ESI MS peak at  $m/z$  1980.6 due to  $[\text{Ag}_{27}\text{D}_{22}(\text{DPPB})_7]^{3+}$ . The exact match of experimental (red trace) and calculated (black trace) isotopic pattern is shown in Figure S12A, which validates the composition of  $[\text{Ag}_{27}\text{D}_{22}(\text{DPPB})_7]^{3+}$ . The mass shift in between the  $[\text{Ag}_{27}\text{H}_{22}(\text{DPPB})_7]^{3+}$  and  $[\text{Ag}_{27}\text{D}_{22}(\text{DPPB})_7]^{3+}$  clusters was  $\Delta m/z = 7.3$  ( $\Delta m = 22, z = 3$ ) which confirms the presence of 22 hydrogens in cluster **II**, shown in Figure S12B.  $[\text{Ag}_{27}\text{H}_{22}(\text{DPPB})_7]^{3+}$  was further characterized with  $^1\text{H}$  and  $^{31}\text{P}$  NMR by comparing with ligand DPPB (Figures S13 and S14). The XPS survey spectrum (Figure S15A) confirms the presence of C, O, P, and Ag elements in the cluster and the deconvoluted spectra of Ag 3d and P 2p regions are shown in Figure S15B,C, respectively. The XPS peak due to Ag 3d<sub>5/2</sub> appears at 368.2 eV, which confirms that Ag is in zero oxidation state. The presence of Ag and P were also confirmed by SEM EDS and their ratio (Ag:P) obtained from EDS analysis was close to the atomic ratio of Ag and P in cluster **II** (Figure S16). The average particle size of cluster **II** is  $1.72 \pm 0.14$  nm, which is obtained from the TEM image of the cluster (Figure S17).

Formation of naked cluster was also investigated from  $[\text{Ag}_{27}\text{H}_{22}(\text{DPPB})_7]^{3+}$  (**II**) by doing CID of the parent cluster, inside the trap of the G2Si mass spectrometer. Figure 5

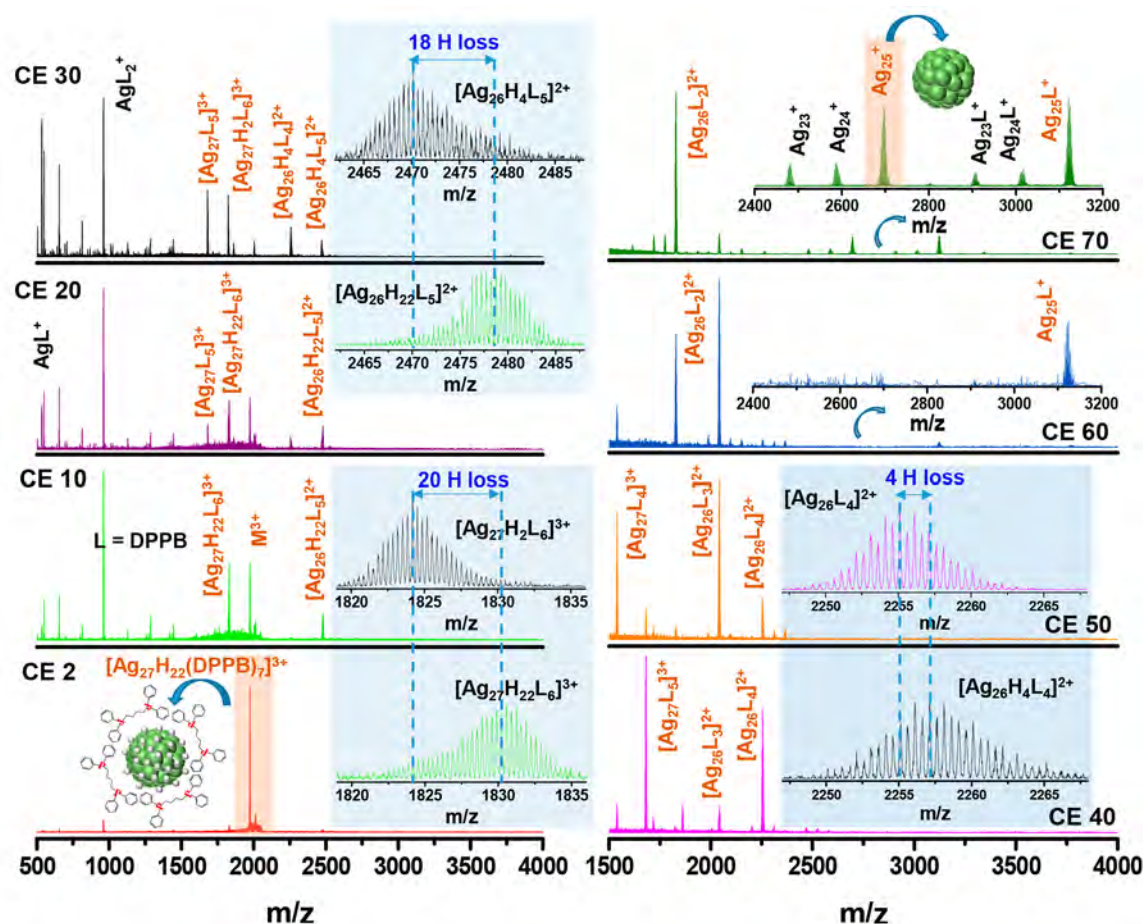


**Figure 5.** MS/MS spectra of  $[\text{Ag}_{27}\text{H}_{22}(\text{DPPB})_7]^{3+}$  (II) with increasing CE from 2 to 70 (in instrumental units). Ligand DPPB is represented by “L”. Due to the increase in CE, detachments of hydrogens, DPPB, and  $[\text{AgDPPB}]^+$  happened from the parent nanoclusters forming the naked cluster,  $\text{Ag}_{25}^+$ . The ions labeled in brown are involved in the formation of naked cluster  $\text{Ag}_{25}^+$ . Schematic illustrations of the protected parent cluster and naked cluster are shown in the insets.

represents a detailed study of the CID of cluster II, which helps us to understand the CE-dependent fragmentation pathway and formation of naked cluster. For that, the parent ion  $[\text{Ag}_{27}\text{H}_{22}(\text{DPPB})_7]^{3+}$  ( $m/z$  1973.2) was mass selected and then CE was increased slowly to get the fragmented ions. At CE 2, there was a major peak of the parent ion. Here also we observed two fragmentation pathways for the formation of the naked cluster. In the first way, at CE 10, the parent ion ( $m/z$  1973.2) undergoes one DPPB ligand loss and forms  $[\text{Ag}_{27}\text{H}_{22}(\text{DPPB})_6]^{3+}$  ( $m/z$  1830.8). Next,  $[\text{Ag}_{27}\text{H}_{22}(\text{DPPB})_6]^{3+}$  undergoes the loss of 20 hydrogens and forms  $[\text{Ag}_{27}\text{H}_2(\text{DPPB})_6]^{3+}$  ( $m/z$  1824.1) at CE 30. The expanded ESI MS of these 20 hydrogen losses is shown in Figure 5 inset (left column, down). At the same CE, some of the  $[\text{Ag}_{27}\text{H}_2(\text{DPPB})_6]^{3+}$  got fragmented to  $[\text{Ag}_{27}(\text{DPPB})_5]^{3+}$  ( $m/z$  1681.4) after one DPPB and two hydrogen losses. This  $[\text{Ag}_{27}(\text{DPPB})_5]^{3+}$  ion also can be formed from  $[\text{Ag}_{27}\text{H}_{22}(\text{DPPB})_6]^{3+}$  by one DPPB and 22 hydrogen losses. At CE 40,  $[\text{Ag}_{27}\text{H}_{22}(\text{DPPB})_6]^{3+}$  and  $[\text{Ag}_{27}\text{H}_2(\text{DPPB})_6]^{3+}$  were fully converted to  $[\text{Ag}_{27}(\text{DPPB})_5]^{3+}$ , and it further undergoes one DPPB loss at CE 40 to form  $[\text{Ag}_{27}(\text{DPPB})_4]^{3+}$  ( $m/z$  1539.4). At CE 50, by losing one  $[\text{AgDPPB}]^+$ , triply charged  $[\text{Ag}_{27}(\text{DPPB})_4]^{3+}$  got converted to doubly charged  $[\text{Ag}_{26}(\text{DPPB})_3]^{2+}$  ( $m/z$  2041.9). Next, at CE 60, there was one DPPB and one  $[\text{AgDPPB}]^+$  loss and formation of singly charged  $[\text{Ag}_{25}(\text{DPPB})]^{2+}$  ion ( $m/z$  3122.7). Finally, at CE 70, the

naked cluster  $\text{Ag}_{25}^+$  ( $m/z$  2696.6) was formed from  $[\text{Ag}_{25}(\text{DPPB})]^{2+}$  with other smaller size naked clusters,  $\text{Ag}_{24}^+$  and  $\text{Ag}_{23}^+$  due to the application of higher CE. In the second fragmentation method, at first the parent ion  $[\text{Ag}_{27}\text{H}_{22}(\text{DPPB})_7]^{3+}$  ( $m/z$  1973.2) loses one  $[\text{Ag}(\text{DPPB})_2]^+$  unit and gets converted to doubly charged  $[\text{Ag}_{26}\text{H}_{22}(\text{DPPB})_5]^{2+}$  ( $m/z$  2479.2) at CE 10. Then at CE 30, it loses 18 hydrogens and forms  $[\text{Ag}_{26}\text{H}_4(\text{DPPB})_5]^{2+}$  ( $m/z$  2470.2), followed by the formation of  $[\text{Ag}_{26}\text{H}_4(\text{DPPB})_4]^{2+}$  ( $m/z$  2257.1) after one DPPB loss. Expanded view of the loss of 18 hydrogens is shown in Figure 5 inset (left column, up). Next,  $[\text{Ag}_{26}\text{H}_4(\text{DPPB})_4]^{2+}$  again loses four hydrogens and forms  $[\text{Ag}_{26}(\text{DPPB})_4]^{2+}$  ( $m/z$  2255.0) at CE 40. Expanded views of the mass shift due to the loss of four hydrogens is shown in Figure 5 inset (right column, down). After all of the hydrogens are lost, there was two consecutive losses of DPPB from  $[\text{Ag}_{26}(\text{DPPB})_4]^{2+}$  making  $[\text{Ag}_{26}(\text{DPPB})_2]^{2+}$  ( $m/z$  1828.9). Next, after one  $[\text{AgDPPB}]^+$  loss singly charged  $[\text{Ag}_{25}(\text{DPPB})]^{2+}$  ( $m/z$  3122.7) was formed, which was further fragmented to the naked cluster  $\text{Ag}_{25}^+$  ( $m/z$  2696.6) at CE 70. To confirm the removal of all DPPB and hydrogen ligands, we have compared the experimentally obtained isotopic patterns (olive trace) of  $\text{Ag}_{25}^+$  with the calculated one (black trace), which shows the exact match between them (Figure S18). Due to the lower intensity of the ESI MS peak of  $[\text{Ag}_{27}\text{D}_{22}(\text{DPPB})_7]^{3+}$ , we were not able to fragment that ion



to compare the hydrogen atom loss with the deuterium atoms. We hope that the detailed study of all of the ligand losses in Figure 5 will be sufficient to understand and prove the formation of naked cluster  $\text{Ag}_{25}^+$ . The full fragmentation pathway of cluster II, confirmed by the MS/MS experiments, is presented in a flowchart and shown in Figure S19.

According to the electron counting rule,  $[\text{Ag}_{15}\text{H}_{13}(\text{DPPH})_5]^{2+}$  possesses zero free electron (geometric stability) and  $[\text{Ag}_{27}\text{H}_{22}(\text{DPPB})_7]^{3+}$  possesses two free electrons (electronic stability). The silver naked clusters generated from the reported hydride and phosphine coprotected silver clusters were  $\text{Ag}_{17}^+$ ,  $\text{Ag}_{21}^+$ , and  $\text{Ag}_{19}^+$ . Here, we are reporting the formation of  $\text{Ag}_{13}^+$  and  $\text{Ag}_{25}^+$  from  $[\text{Ag}_{15}\text{H}_{13}(\text{DPPH})_5]^{2+}$  and  $[\text{Ag}_{27}\text{H}_{22}(\text{DPPB})_7]^{3+}$ , respectively. As diphosphines are more strongly bonded to the metal core compared to monophosphines, here CE-dependent fragmentation has been performed instead of cone voltage-dependent fragmentation to make naked clusters. As of now,  $\text{Ag}_{13}^+$  is the smallest and  $\text{Ag}_{25}^+$  is the largest known naked clusters of silver which could be created from monolayer protected silver nanoclusters.

## CONCLUSIONS

In conclusion, we have reported two new hydride and diphosphine coprotected silver nanoclusters,  $[\text{Ag}_{15}\text{H}_{13}(\text{DPPH})_5]^{2+}$  and  $[\text{Ag}_{27}\text{H}_{22}(\text{DPPB})_7]^{3+}$ . These weakly ligated silver clusters can be used as the source of hydrogen and as a reagent for chemical transformations. The naked clusters  $\text{Ag}_{13}^+$  (12 valence electrons) and  $\text{Ag}_{25}^+$  (24 valence electrons) were created from parent hydride and phosphine coprotected clusters,  $\text{Ag}_{15}$  and  $\text{Ag}_{27}$ , respectively, in their cationic form by CID experiments. The favored formation and stability of these odd numbered cationic silver naked clusters can be correlated to the odd–even effect which refers the higher stability of the closed electronic shells. A detailed study of the fragmentation steps during the formation of naked clusters can help to elucidate the cluster structures, though the determination of crystal structure is very much needed to understand the process in detail. Here we have demonstrated that tuning the size of monolayer protected clusters gives us the opportunity to explore the various sizes of silver naked clusters in the gas phase. We hope that our results will provide new insights into ion–molecule reactions, gas phase unimolecular chemistry and soft landing of metal clusters. We note that  $\text{M}_{25}\text{L}_{18}^-$  ( $\text{M} = \text{Au}, \text{Ag}$ ;  $\text{L} = \text{SR}$ ) clusters are the most thoroughly investigated clusters in the family of atomically precise noble metal clusters and  $\text{Au}_{25}$  naked cluster has been seen only in the dissociation of protein protected clusters.<sup>38</sup>

## ASSOCIATED CONTENT

### Supporting Information

The Supporting Information is available free of charge at <https://pubs.acs.org/doi/10.1021/acs.jpcc.0c05867>.

Characterization of clusters by UV–vis, ESI MS, NMR, XPS, SEM EDS and TEM; complete fragmentation pathway of clusters (PDF)

## AUTHOR INFORMATION

### Corresponding Author

Thalappil Pradeep – DST Unit of Nanoscience (DST UNS) and Thematic Unit of Excellence (TUE), Department of

Chemistry, Indian Institute of Technology Madras, Chennai 600 036, India; [orcid.org/0000-0003-3174-534X](https://orcid.org/0000-0003-3174-534X); Email: [pradeep@iitm.ac.in](mailto:pradeep@iitm.ac.in)

## Authors

**Madhuri Jash** – DST Unit of Nanoscience (DST UNS) and Thematic Unit of Excellence (TUE), Department of Chemistry, Indian Institute of Technology Madras, Chennai 600 036, India

**Esma Khatun** – DST Unit of Nanoscience (DST UNS) and Thematic Unit of Excellence (TUE), Department of Chemistry, Indian Institute of Technology Madras, Chennai 600 036, India

**Papri Chakraborty** – DST Unit of Nanoscience (DST UNS) and Thematic Unit of Excellence (TUE), Department of Chemistry, Indian Institute of Technology Madras, Chennai 600 036, India

**Chennu Sudhakar** – DST Unit of Nanoscience (DST UNS) and Thematic Unit of Excellence (TUE), Department of Chemistry, Indian Institute of Technology Madras, Chennai 600 036, India

Complete contact information is available at:

<https://pubs.acs.org/doi/10.1021/acs.jpcc.0c05867>

## Notes

The authors declare no competing financial interest.

## ACKNOWLEDGMENTS

We thank the Department of Science and Technology, Government of India for constantly supporting our research program. M.J. thanks UGC for her senior research fellowship. E.K. and C.S. thank IIT Madras for their research fellowships. P.C. thanks IIT Madras for institute postdoctoral fellowship.

## REFERENCES

- (1) Chakraborty, I.; Pradeep, T. Atomically Precise Clusters of Noble Metals: Emerging Link between Atoms and Nanoparticles. *Chem. Rev.* **2017**, *117*, 8208–8271.
- (2) Tyo, E. C.; Vajda, S. Catalysis by Clusters with Precise Numbers of Atoms. *Nat. Nanotechnol.* **2015**, *10*, 577–588.
- (3) Abbas, M. A.; Kim, T.-Y.; Lee, S. U.; Kang, Y. S.; Bang, J. H. Exploring Interfacial Events in Gold-Nanocluster-Sensitized Solar Cells: Insights into the Effects of the Cluster Size and Electrolyte on Solar Cell Performance. *J. Am. Chem. Soc.* **2016**, *138*, 390–401.
- (4) Xie, J.; Zheng, Y.; Ying, J. Y. Highly Selective and Ultrasensitive Detection of  $\text{Hg}_2^{2+}$  Based on Fluorescence Quenching of Au Nanoclusters by  $\text{Hg}_2^{2+}$ – $\text{Au}^+$  Interactions. *Chem. Commun.* **2010**, *46*, 961–963.
- (5) Lin, C.-A. J.; Yang, T.-Y.; Lee, C.-H.; Huang, S. H.; Sperling, R. A.; Zanella, M.; Li, J. K.; Shen, J.-L.; Wang, H.-H.; Yeh, H.-I.; et al. Synthesis, Characterization, and Bioconjugation of Fluorescent Gold Nanoclusters toward Biological Labeling Applications. *ACS Nano* **2009**, *3*, 395–401.
- (6) Duan, G.-X.; Tian, L.; Wen, J.-B.; Li, L.-Y.; Xie, Y.-P.; Lu, X. An Atomically Precise all-tert-butylethynide-protected  $\text{Ag}_{51}$  Superatom Nanocluster with Color Tunability. *Nanoscale* **2018**, *10*, 18915–18919.
- (7) Chai, O. J. H.; Liu, Z.; Chen, T.; Xie, J. Engineering Ultrasmall Metal Nanoclusters for Photocatalytic and Electrocatalytic Applications. *Nanoscale* **2019**, *11*, 20437–20448.
- (8) Veenstra, A. P.; Monzel, L.; Baksi, A.; Czekner, J.; Lebedkin, S.; Schneider, E. K.; Pradeep, T.; Unterreiner, A.-N.; Kappes, M. M. Ultrafast Intersystem Crossing in Isolated  $\text{Ag}_{29}(\text{BDT})_{12}^{3-}$  Probed by Time-Resolved Pump–Probe Photoelectron Spectroscopy. *J. Phys. Chem. Lett.* **2020**, *11*, 2675–2681.



- (9) Hirata, K.; Kim, K.; Nakamura, K.; Kitazawa, H.; Hayashi, S.; Koyasu, K.; Tsukuda, T. Photoinduced Thermionic Emission from  $[M_{25}(SR)_{18}]^-$  ( $M = Au, Ag$ ) Revealed by Anion Photoelectron Spectroscopy. *J. Phys. Chem. C* **2019**, *123*, 13174–13179.
- (10) Jin, R.; Zeng, C.; Zhou, M.; Chen, Y. Atomically Precise Colloidal Metal Nanoclusters and Nanoparticles: Fundamentals and Opportunities. *Chem. Rev.* **2016**, *116*, 10346–10413.
- (11) Konishi, K.; Iwasaki, M.; Shichibu, Y. Phosphine-Ligated Gold Clusters with Core+exo Geometries: Unique Properties and Interactions at the Ligand–Cluster Interface. *Acc. Chem. Res.* **2018**, *51*, 3125–3133.
- (12) Joshi, C. P.; Bootharaju, M. S.; Bakr, O. M. Tuning Properties in Silver Clusters. *J. Phys. Chem. Lett.* **2015**, *6*, 3023–3035.
- (13) Tian, S.; Li, Y.-Z.; Li, M.-B.; Yuan, J.; Yang, J.; Wu, Z.; Jin, R. Structural Isomerism in Gold Nanoparticles Revealed by X-ray Crystallography. *Nat. Commun.* **2015**, *6*, 8667.
- (14) Negishi, Y.; Arai, R.; Niihori, Y.; Tsukuda, T. Isolation and Structural Characterization of Magic Silver Clusters Protected by 4-(tert-butyl)benzyl mercaptan. *Chem. Commun.* **2011**, *47*, 5693–5695.
- (15) Dhayal, R. S.; Liao, J.-H.; Liu, Y.-C.; Chiang, M.-H.; Kahlal, S.; Saillard, J.-Y.; Liu, C. W.  $[Ag_{21}\{S_2P(OiPr)_2\}_{12}]^+$ : An Eight-Electron Superatom. *Angew. Chem., Int. Ed.* **2015**, *54*, 3702–3706.
- (16) Zhang, Q.-F.; Williard, P. G.; Wang, L.-S. Polymorphism of Phosphine-Protected Gold Nanoclusters: Synthesis and Characterization of a New 22-Gold-Atom Cluster. *Small* **2016**, *12*, 2518–2525.
- (17) McKenzie, L. C.; Zaikova, T. O.; Hutchison, J. E. Structurally Similar Triphenylphosphine-Stabilized Undecagolds,  $Au_{11}(PPh_3)_7Cl_3$  and  $[Au_{11}(PPh_3)_8Cl_2]Cl$ , Exhibit Distinct Ligand Exchange Pathways with Glutathione. *J. Am. Chem. Soc.* **2014**, *136*, 13426–13435.
- (18) Lei, Z.; Wan, X.-K.; Yuan, S.-F.; Guan, Z.-J.; Wang, Q.-M. Alkynyl Approach toward the Protection of Metal Nanoclusters. *Acc. Chem. Res.* **2018**, *51*, 2465–2474.
- (19) Du, W.; Jin, S.; Xiong, L.; Chen, M.; Zhang, J.; Zou, X.; Pei, Y.; Wang, S.; Zhu, M.  $Ag_{50}(Dppm)_6(SR)_{30}$  and Its Homologue  $Au_xAg_{50-x}(Dppm)_6(SR)_{30}$  Alloy Nanocluster: Seeded Growth, Structure Determination, and Differences in Properties. *J. Am. Chem. Soc.* **2017**, *139*, 1618–1624.
- (20) Jadzinsky, P. D.; Calero, G.; Ackerson, C. J.; Bushnell, D. A.; Kornberg, R. D. Structure of a Thiol Monolayer-Protected Gold Nanoparticle at 1.1 Å Resolution. *Science* **2007**, *318*, 430–433.
- (21) Zhu, M.; Aikens, C. M.; Hollander, F. J.; Schatz, G. C.; Jin, R. Correlating the Crystal Structure of a Thiol-Protected  $Au_{25}$  Cluster and Optical Properties. *J. Am. Chem. Soc.* **2008**, *130*, 5883–5885.
- (22) Chen, S.; Wang, S.; Zhong, J.; Song, Y.; Zhang, J.; Sheng, H.; Pei, Y.; Zhu, M. The Structure and Optical Properties of the  $[Au_{18}(SR)_{14}]$  Nanocluster. *Angew. Chem., Int. Ed.* **2015**, *54*, 3145–3149.
- (23) Desiredy, A.; Conn, B. E.; Guo, J.; Yoon, B.; Barnett, R. N.; Monahan, B. M.; Kirschbaum, K.; Griffith, W. P.; Whetten, R. L.; Landman, U.; et al. Ultrastable Silver Nanoparticles. *Nature* **2013**, *501*, 399–402.
- (24) Joshi, C. P.; Bootharaju, M. S.; Alhilaly, M. J.; Bakr, O. M.  $[Ag_{25}(SR)_{18}]^-$ : The “Golden” Silver Nanoparticle. *J. Am. Chem. Soc.* **2015**, *137*, 11578–11581.
- (25) AbdulHalim, L. G.; Bootharaju, M. S.; Tang, Q.; Del Gobbo, S.; AbdulHalim, R. G.; Eddaoudi, M.; Jiang, D.-e.; Bakr, O. M.  $Ag_{29}(BDT)_{12}(TPP)_4$ : A Tetravalent Nanocluster. *J. Am. Chem. Soc.* **2015**, *137*, 11970–11975.
- (26) Sakintuna, B.; Lamari-Darkrim, F.; Hirscher, M. Metal Hydride Materials for Solid Hydrogen Storage: A Review. *Int. J. Hydrogen Energy* **2007**, *32*, 1121–1140.
- (27) Grochala, W.; Edwards, P. P. Thermal Decomposition of the Non-Interstitial Hydrides for the Storage and Production of Hydrogen. *Chem. Rev.* **2004**, *104*, 1283–1315.
- (28) Suh, M. P.; Park, H. J.; Prasad, T. K.; Lim, D.-W. Hydrogen Storage in Metal-Organic Frameworks. *Chem. Rev.* **2012**, *112*, 782–835.
- (29) Jordan, A. J.; Lalic, G.; Sadighi, J. P. Coinage Metal Hydrides: Synthesis, Characterization, and Reactivity. *Chem. Rev.* **2016**, *116*, 8318–8372.
- (30) Dhayal, R. S.; van Zyl, W. E.; Liu, C. W. Polyhydrido Copper Clusters: Synthetic Advances, Structural Diversity, and Nanocluster-to-Nanoparticle Conversion. *Acc. Chem. Res.* **2016**, *49*, 86–95.
- (31) Dhayal, R. S.; van Zyl, W. E.; Liu, C. W. Copper Hydride Clusters in Energy Storage and Conversion. *Dalton Trans.* **2019**, *48*, 3531–3538.
- (32) Zavras, A.; Khairallah, G. N.; Connell, T. U.; White, J. M.; Edwards, A. J.; Donnelly, P. S.; O’Hair, R. A. J. Synthesis, Structure and Gas-Phase Reactivity of a Silver Hydride Complex  $[Ag_3\{(PPh_2)_2CH_2\}_3(\mu_3-H)(\mu_3-Cl)]BF_4$ . *Angew. Chem., Int. Ed.* **2013**, *52*, 8391–8394.
- (33) Bootharaju, M. S.; Dey, R.; Gevers, L. E.; Hedhili, M. N.; Basset, J.-M.; Bakr, O. M. A New Class of Atomically Precise, Hydride-Rich Silver Nanoclusters co-protected by Phosphines. *J. Am. Chem. Soc.* **2016**, *138*, 13770–13773.
- (34) Ghosh, A.; Bodiuzzaman, M.; Nag, A.; Jash, M.; Baksi, A.; Pradeep, T. Sequential Dihydrogen Desorption from Hydride-Protected Atomically Precise Silver Clusters and Formation of Naked Clusters in Gas Phase. *ACS Nano* **2017**, *11*, 11145–11151.
- (35) Jash, M.; Reber, A. C.; Ghosh, A.; Sarkar, D.; Bodiuzzaman, M.; Basuri, P.; Baksi, A.; Khanna, S. N.; Pradeep, T. Preparation of Gas Phase Naked Silver Cluster Cations Outside a Mass Spectrometer from Ligand Protected Clusters in Solution. *Nanoscale* **2018**, *10*, 15714–15722.
- (36) Baksi, A.; Jash, M.; Bag, S.; Mudedla, S. K.; Bodiuzzaman, M.; Ghosh, D.; Paramasivam, G.; Subramanian, V.; Pradeep, T. Mechanistic Elucidation of the Structure and Reactivity of Bare and Hydride-Protected  $Ag_{17}^+$  Clusters. *J. Phys. Chem. C* **2019**, *123*, 28494–28501.
- (37) Hudgens, J. W.; Pettibone, J. M.; Senftle, T. P.; Bratton, R. N. Reaction Mechanism Governing Formation of 1,3-Bis-(diphenylphosphino)propane-Protected Gold Nanoclusters. *Inorg. Chem.* **2011**, *50*, 10178–10189.
- (38) Baksi, A.; Pradeep, T.; Yoon, B.; Yannouleas, C.; Landman, U. Bare Clusters Derived from Protein Templates:  $Au_{25}^+$ ,  $Au_{38}^+$  and  $Au_{102}^+$ . *ChemPhysChem* **2013**, *14*, 1272–1282.

## Supporting Information

### **[Ag<sub>15</sub>H<sub>13</sub>(DPPH)<sub>5</sub>]<sup>2+</sup> and [Ag<sub>27</sub>H<sub>22</sub>(DPPB)<sub>7</sub>]<sup>3+</sup>: Two New Hydride and Phosphine Co-Protected Clusters and Their Fragmentation Leading to Naked Clusters, Ag<sub>13</sub><sup>+</sup> and Ag<sub>25</sub><sup>+</sup>**

Madhuri Jash, Esma Khatun, Papri Chakraborty, Chennu Sudhakar and Thalappil Pradeep\*

DST Unit of Nanoscience (DST UNS) and Thematic Unit of Excellence (TUE), Department of Chemistry, Indian Institute of Technology Madras, Chennai 600 036, India

\*To whom correspondence should be addressed. E-mail: [pradeep@iitm.ac.in](mailto:pradeep@iitm.ac.in)

## Table of Contents

Name	Description	Page No.
S1	Characterization of [Ag <sub>15</sub> D <sub>13</sub> (DPPH) <sub>5</sub> ] <sup>2+</sup> cluster	S3
S2	Time dependent UV-vis spectra of sample I during synthesis	S4
S3	Time dependent ESI MS of sample I during synthesis	S5
S4	<sup>1</sup> H NMR spectra of DPPH and [Ag <sub>15</sub> H <sub>13</sub> (DPPH) <sub>5</sub> ] <sup>2+</sup> cluster	S6
S5	<sup>31</sup> P NMR spectra of DPPH and [Ag <sub>15</sub> H <sub>13</sub> (DPPH) <sub>5</sub> ] <sup>2+</sup> cluster	S7
S6	XPS spectra of [Ag <sub>15</sub> H <sub>13</sub> (DPPH) <sub>5</sub> ] <sup>2+</sup> cluster	S8
S7	SEM EDS of [Ag <sub>15</sub> H <sub>13</sub> (DPPH) <sub>5</sub> ] <sup>2+</sup> cluster	S9
S8	TEM analysis of [Ag <sub>15</sub> H <sub>13</sub> (DPPH) <sub>5</sub> ] <sup>2+</sup> cluster	S10
S9	Comparison of the fragmentation pathway of [Ag <sub>15</sub> H <sub>13</sub> (DPPH) <sub>5</sub> ] <sup>2+</sup> and [Ag <sub>15</sub> D <sub>13</sub> (DPPH) <sub>5</sub> ] <sup>2+</sup> clusters	S11
S10	MS/MS of [Ag <sub>15</sub> D <sub>13</sub> (DPPH) <sub>5</sub> ] <sup>2+</sup> cluster	S12
S11	Fragmentation pathway of [Ag <sub>15</sub> H <sub>13</sub> (DPPH) <sub>5</sub> ] <sup>2+</sup> cluster	S13
S12	Characterization of [Ag <sub>27</sub> D <sub>22</sub> (DPPB) <sub>7</sub> ] <sup>3+</sup> cluster	S14
S13	<sup>1</sup> H NMR spectra of DPPB and [Ag <sub>27</sub> H <sub>22</sub> (DPPB) <sub>7</sub> ] <sup>3+</sup> cluster	S15
S14	<sup>31</sup> P NMR spectra of DPPB and [Ag <sub>27</sub> H <sub>22</sub> (DPPB) <sub>7</sub> ] <sup>3+</sup> cluster	S16
S15	XPS spectra of [Ag <sub>27</sub> H <sub>22</sub> (DPPB) <sub>7</sub> ] <sup>3+</sup> cluster	S17
S16	SEM EDS of [Ag <sub>27</sub> H <sub>22</sub> (DPPB) <sub>7</sub> ] <sup>3+</sup> cluster	S18
S17	TEM analysis of [Ag <sub>27</sub> H <sub>22</sub> (DPPB) <sub>7</sub> ] <sup>3+</sup> cluster	S19

S18	Comparison between the experimental and calculated spectra of $\text{Ag}_{25}^+$	S20
S19	Fragmentation pathway of $[\text{Ag}_{27}\text{H}_{22}(\text{DPPB})_7]^{3+}$ cluster	S21

## Supporting information 1

### Characterization of $[\text{Ag}_{15}\text{D}_{13}(\text{DPPH})_5]^{2+}$ cluster:

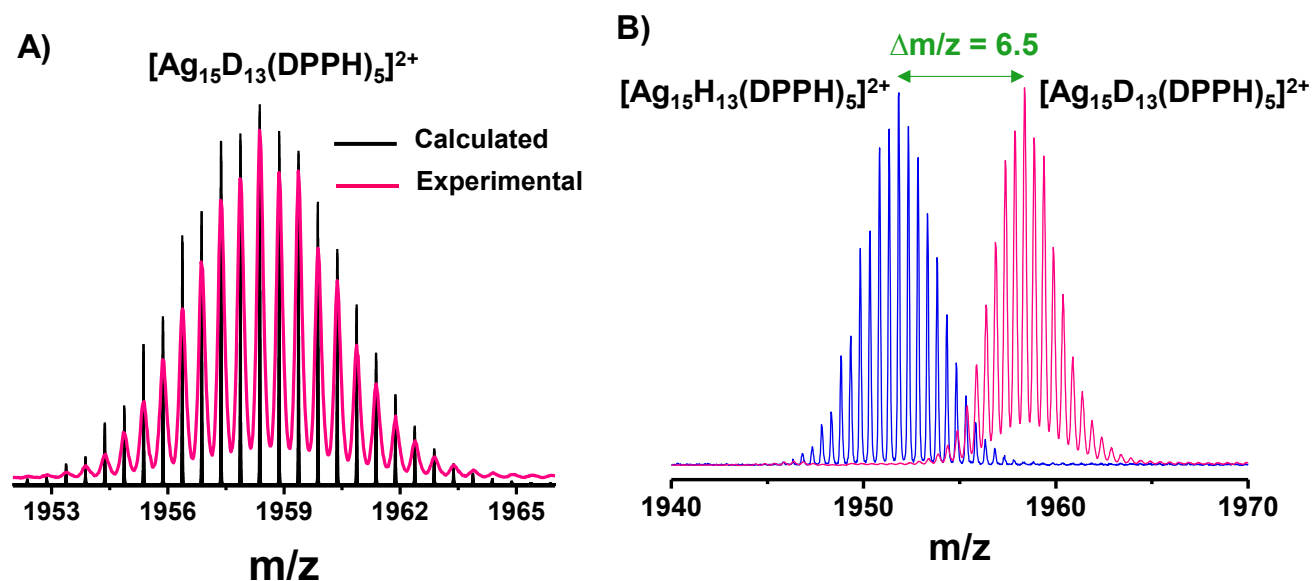


**Figure S1.** (A) Experimental mass spectrum (pink trace) of  $[\text{Ag}_{15}\text{D}_{13}(\text{DPPH})_5]^{2+}$  cluster match well with its calculated (black trace) isotopic pattern. (B) The ESI MS of  $[\text{Ag}_{15}\text{H}_{13}(\text{DPPH})_5]^{2+}$  and  $[\text{Ag}_{15}\text{D}_{13}(\text{DPPH})_5]^{2+}$  showing the mass shift due to the exchange of hydrogen atoms with deuterium atoms.

## Supporting information 2

### Time dependent UV-vis spectra of sample I during synthesis:

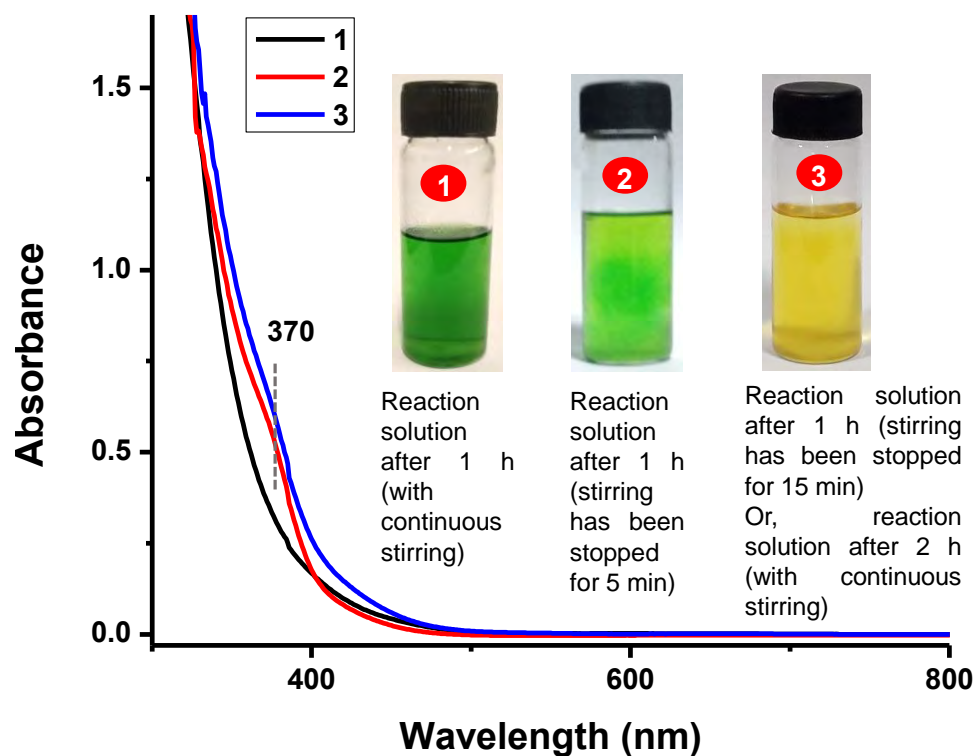


**Figure S2.** Time dependent UV-vis spectra during the synthesis of sample I with their corresponding photographs in inset. The photographs show that during 1 h of synthesis with continuous stirring, the color of the solution remains green (1). Whereas, by stopping the stirring after 1 h, the color changed immediately from green to yellowish green within 5 min (2). After 15 min of stopping stirring, the color became fully dark yellow (3). The bottle labeled 3 also represents the same solution when the reaction was continuously stirred for 2 h.

## Supporting information 3

### Time dependent ESI MS of sample I during synthesis:

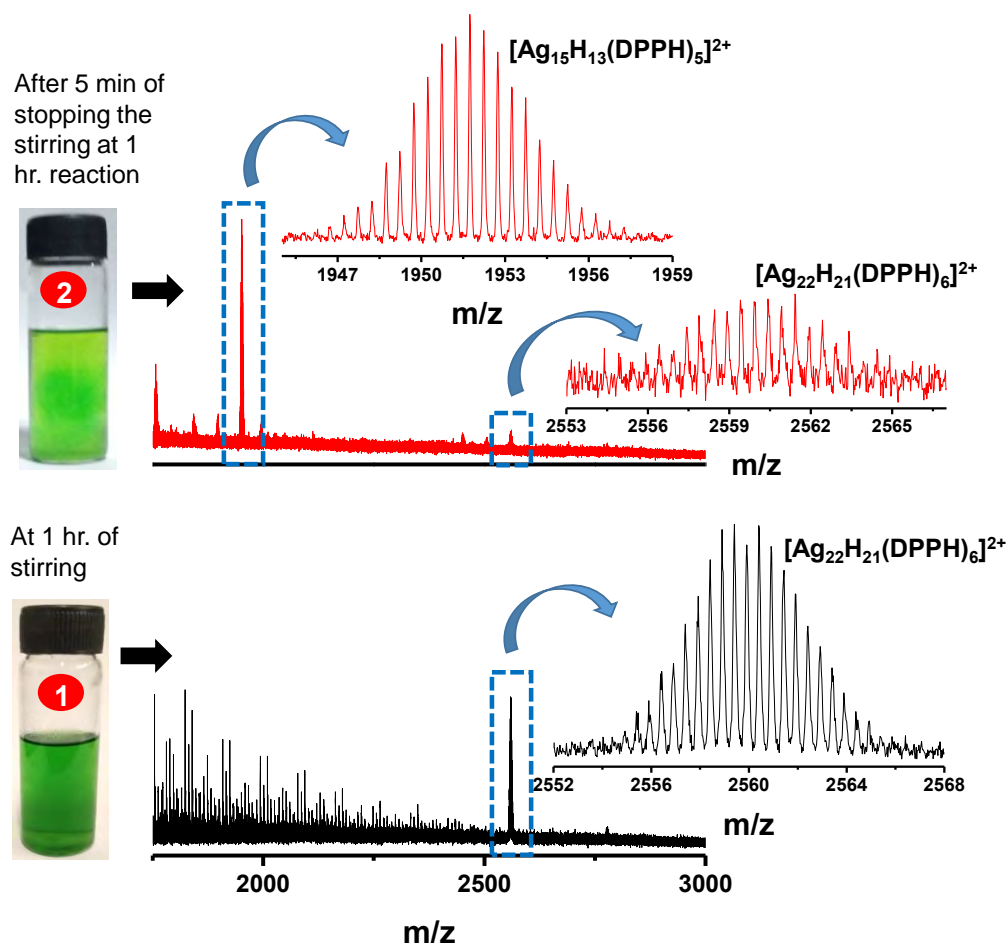


**Figure S3.** Time dependent ESI MS during the synthesis of sample **I** with their corresponding photographs (on the left). The ESI MS of green solution (1) shows the presence of  $[Ag_{22}H_{21}(DPPH)_6]^{2+}$  cluster during 1 h stirring. Whereas, after 5 min of stopping the stirring the green color was converted to yellowish green (2) and the intensity of  $[Ag_{22}H_{21}(DPPH)_6]^{2+}$  decreased significantly in the ESI MS along with increased intensity of  $[Ag_{15}H_{13}(DPPH)_5]^{2+}$  (sample **I**).



## Supporting information 4

### $^1\text{H}$ NMR spectra of DPPH and $[\text{Ag}_{15}\text{H}_{13}(\text{DPPH})_5]^{2+}$ cluster:

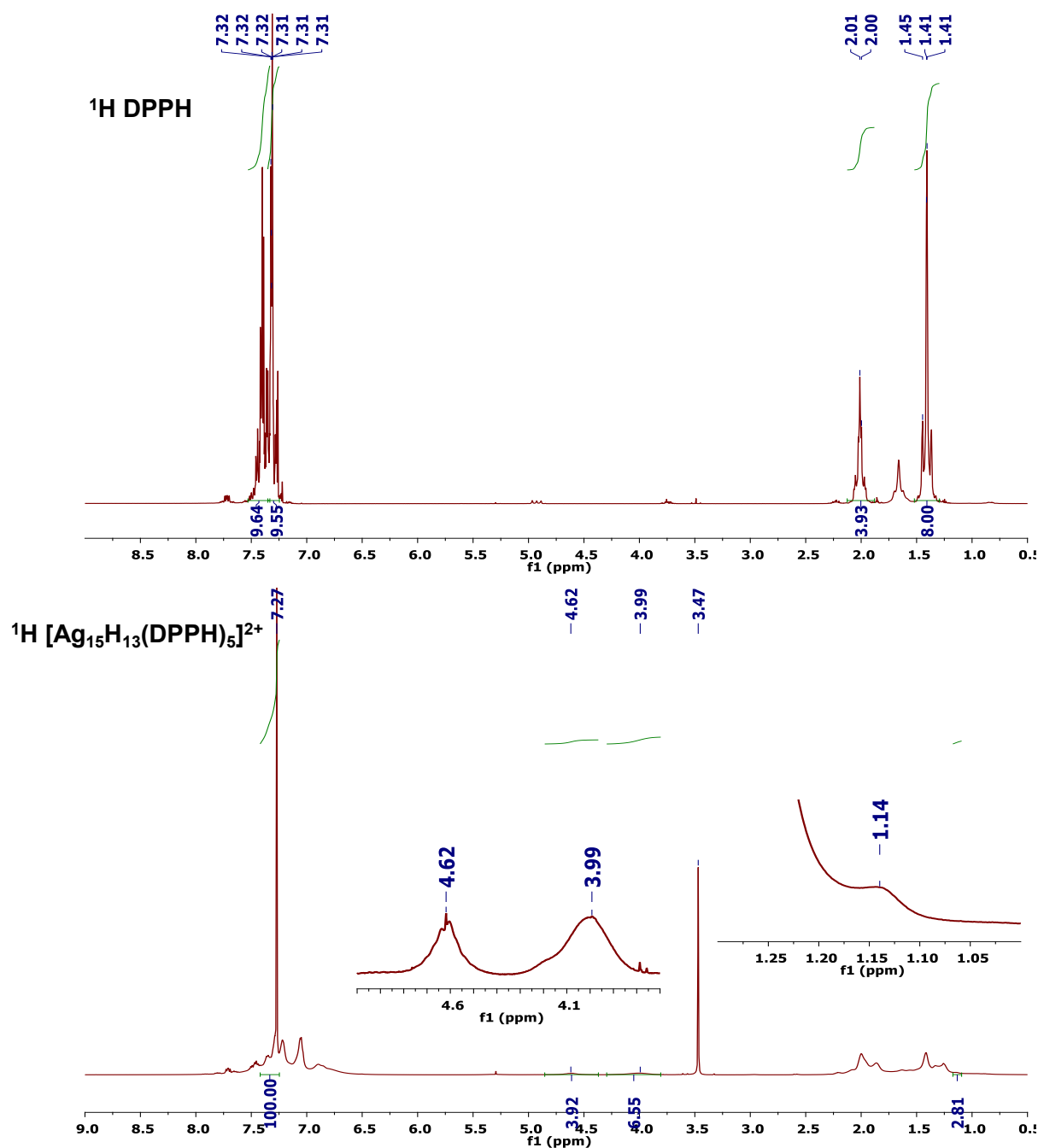


**Figure S4.**  $^1\text{H}$  NMR spectra of DPPH and  $[\text{Ag}_{15}\text{H}_{13}(\text{DPPH})_5]^{2+}$  clusters. Broad peaks of  $[\text{Ag}_{15}\text{H}_{13}(\text{DPPH})_5]^{2+}$  at 1.14, 3.99 and 4.62 ppm confirm the presence of hydride protected clusters.

## Supporting information 5

$^{31}\text{P}$  NMR spectra of DPPH and  $[\text{Ag}_{15}\text{H}_{13}(\text{DPPH})_5]^{2+}$  cluster:

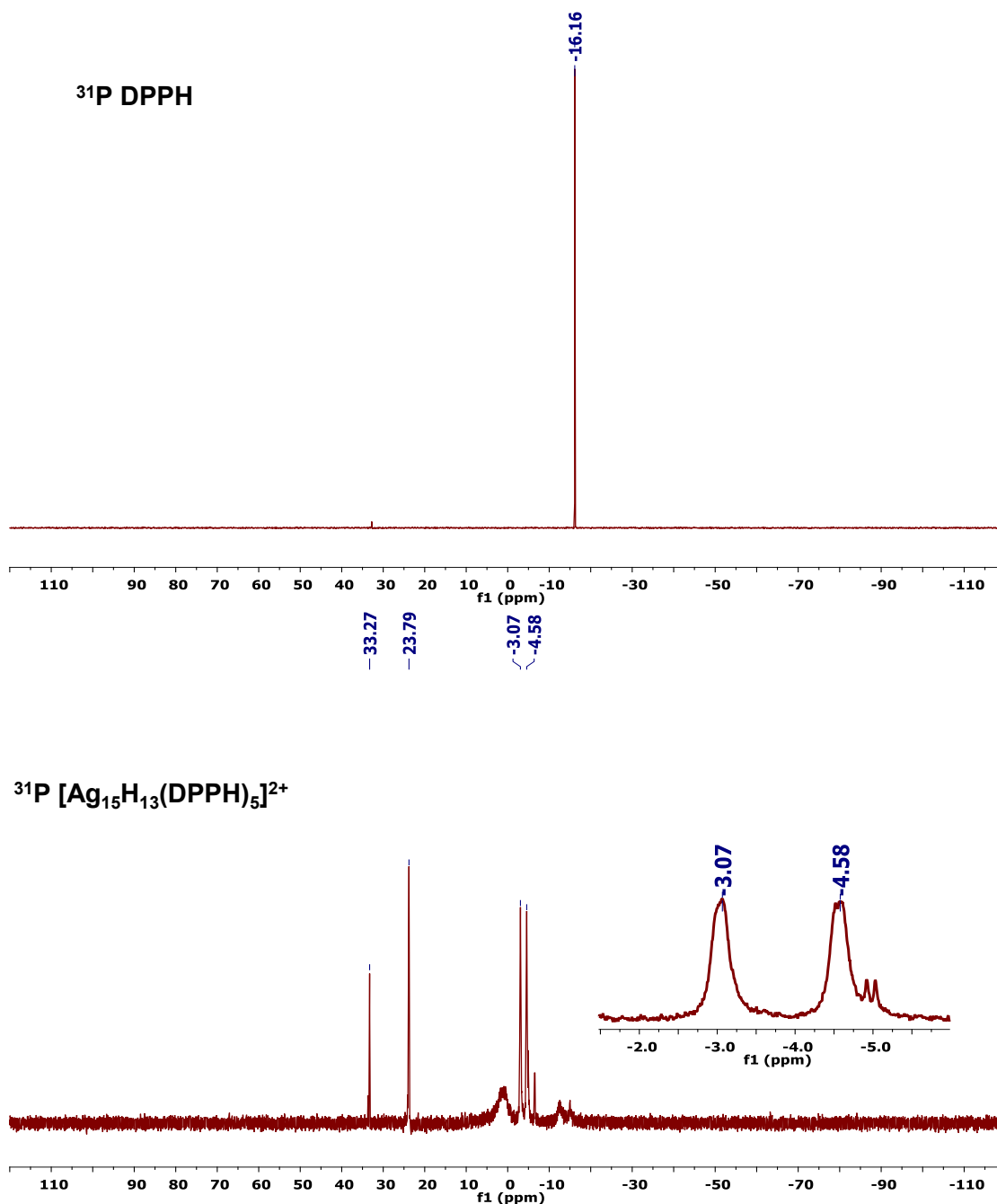


**Figure S5.**  $^{31}\text{P}$  NMR spectra of DPPH and  $[\text{Ag}_{15}\text{H}_{13}(\text{DPPH})_5]^{2+}$  clusters. The  $^{31}\text{P}$  signal at -16.16 ppm for DPPH ligand disappears in the  $[\text{Ag}_{15}\text{H}_{13}(\text{DPPH})_5]^{2+}$  cluster due to the binding of ligands with metal core, which is also confirmed by the appearance of new broad peaks at -4.58 and -3.07 ppm in the nanoclusters. Peaks at 23.79 and 33.27 ppm are due to phosphine oxides.

## Supporting information 6

### XPS spectra of $[\text{Ag}_{15}\text{H}_{13}(\text{DPPH})_5]^{2+}$ cluster:

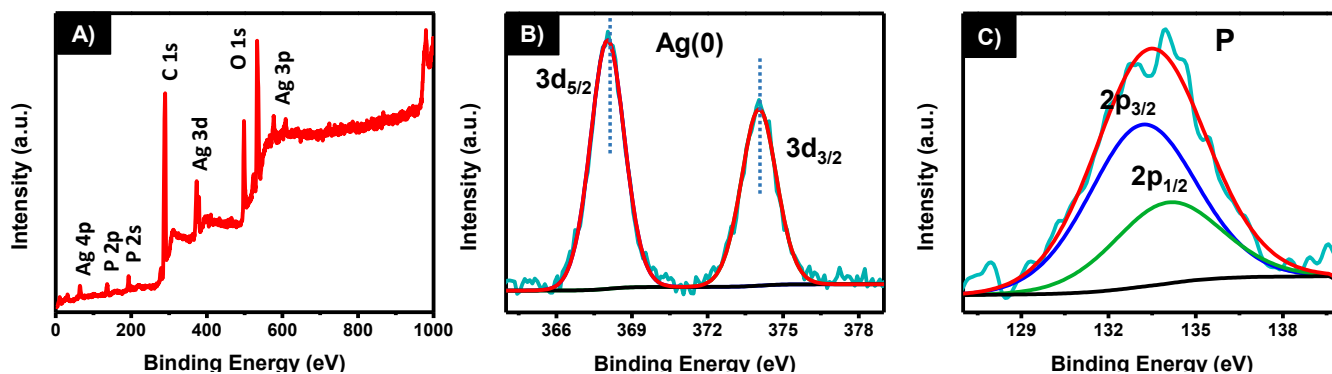


**Figure S6.** (A) XPS survey spectrum of  $[\text{Ag}_{15}\text{H}_{13}(\text{DPPH})_5]^{2+}$  showing all the expected elements (Ag, P and C). (B) The Ag 3d region. Ag 3d<sub>5/2</sub> at 368.04 eV indicates the presence of Ag(0) state. (C) P 2p region of the nanocluster. P 2p<sub>3/2</sub> appears at 133.24 eV.

## Supporting information 7

### SEM EDS of $[\text{Ag}_{15}\text{H}_{13}(\text{DPPH})_5]^{2+}$ cluster:

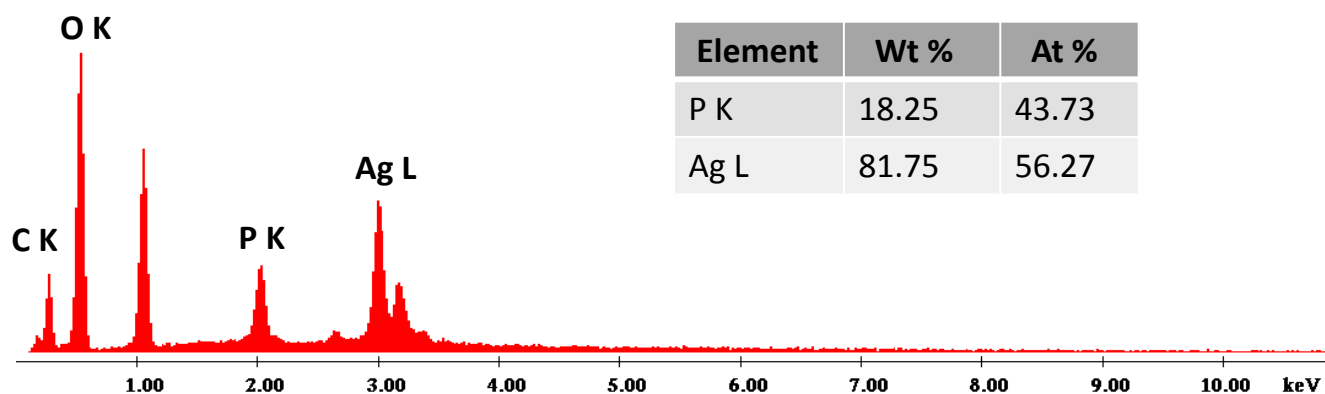


**Figure S7.** SEM EDS of  $[\text{Ag}_{15}\text{H}_{13}(\text{DPPH})_5]^{2+}$  cluster with quantification of elements. Ag:P atomic ratio matches well with the Ag:P ratio obtained from the molecular formula of the cluster.

## Supporting information 8

### TEM analysis of $[\text{Ag}_{15}\text{H}_{13}(\text{DPPH})_5]^{2+}$ cluster:

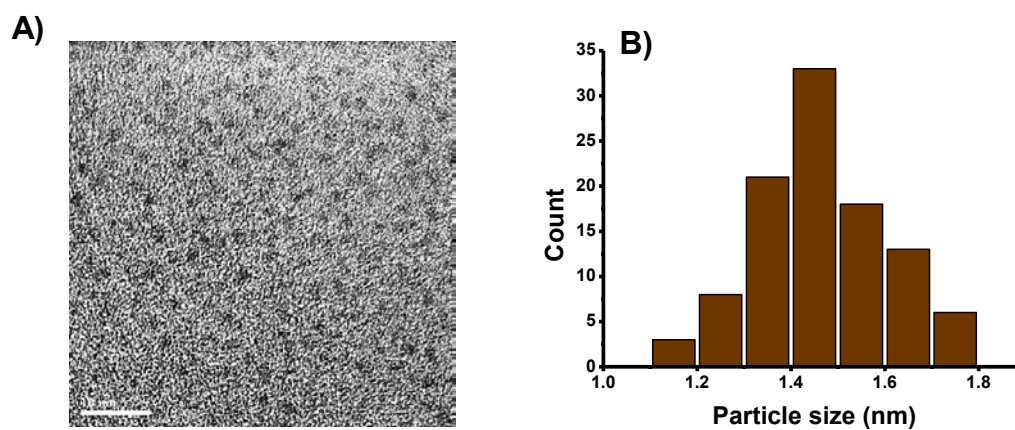


**Figure S8.** (A) TEM image of the  $[\text{Ag}_{15}\text{H}_{13}(\text{DPPH})_5]^{2+}$  cluster. Scale bar is 10 nm. (B) Particle distribution shows an average size of  $1.46 \pm 0.13$  nm for this nanocluster.

## Supporting information 9

### Comparison of the fragmentation pathway of $[\text{Ag}_{15}\text{H}_{13}(\text{DPPH})_5]^{2+}$ and $[\text{Ag}_{15}\text{D}_{13}(\text{DPPH})_5]^{2+}$ clusters:

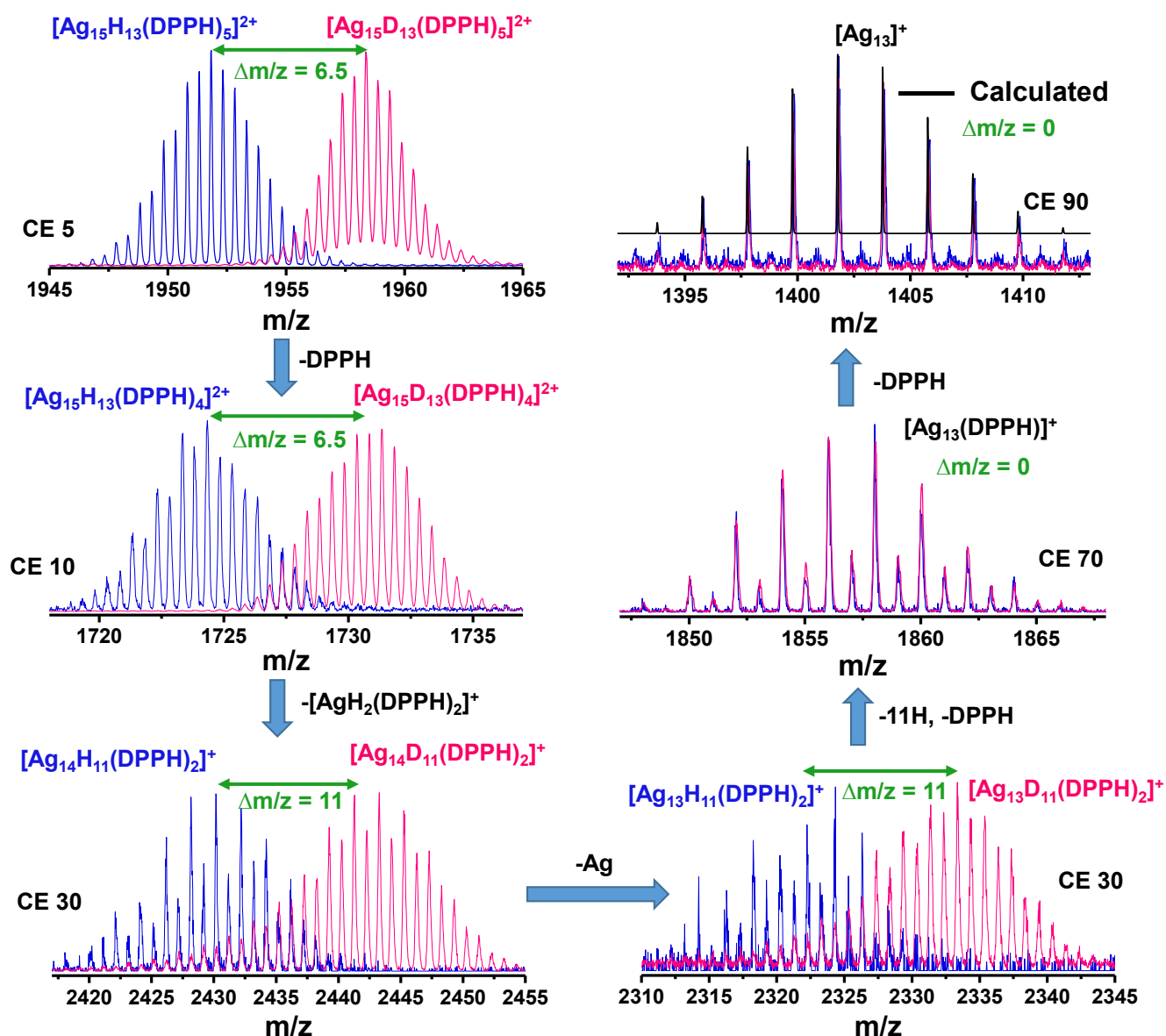


**Figure S9.** Expanded ESI MS of  $[\text{Ag}_{15}\text{H}_{13}(\text{DPPH})_5]^{2+}$  (blue trace) and  $[\text{Ag}_{15}\text{D}_{13}(\text{DPPH})_5]^{2+}$  (pink trace) at different collision energies during the formation of naked cluster,  $\text{Ag}_{13}^{+}$  by another possible pathway. The mass shift ( $\Delta m/z$ ) in between the blue and pink traces confirms the presence of hydrogen in the particular fragmented ions. The isotopic distribution of  $\text{Ag}_{13}^{+}$  confirms the absence of hydrogen atoms, which also matches with the calculated pattern (black trace).



## Supporting information 10

### MS/MS of $[\text{Ag}_{15}\text{D}_{13}(\text{DPPH})_5]^{2+}$ cluster:

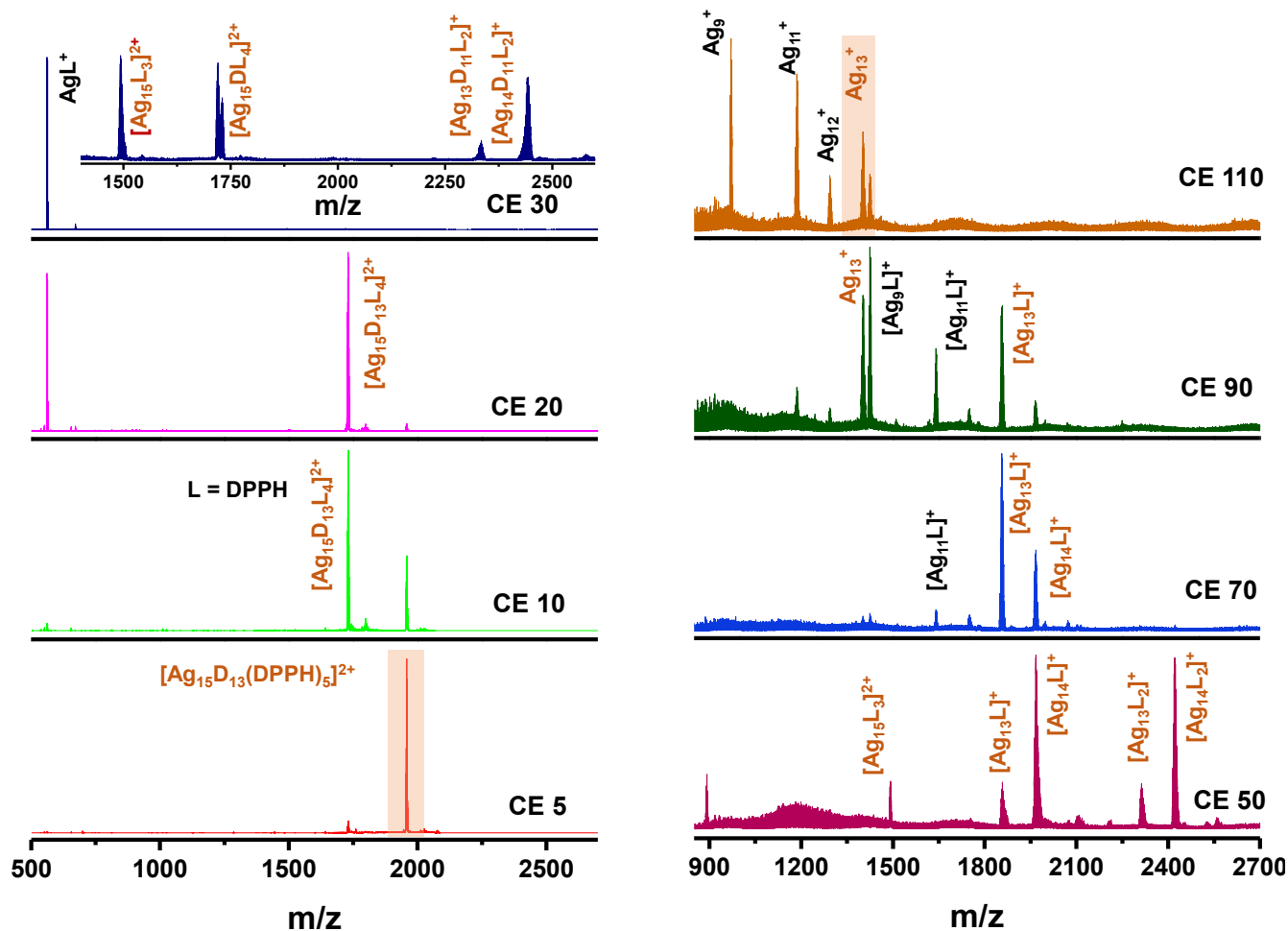


**Figure S10.** Collision energy dependent MS/MS spectra of the  $[\text{Ag}_{15}\text{D}_{13}(\text{DPPH})_5]^{2+}$  cluster. Increase in collision energy from 5 to 110 (in instrumental units) results in the detachment of deuterium, DPPH and  $[\text{AgDPPH}]^+$  from  $[\text{Ag}_{15}\text{D}_{13}(\text{DPPH})_5]^{2+}$  resulting in  $\text{Ag}_{13}^+$ . Fragments labeled in brown lead to the formation of naked cluster,  $\text{Ag}_{13}^+$ .

## Supporting information 11

### Fragmentation pathway of $[\text{Ag}_{15}\text{H}_{13}(\text{DPPH})_5]^{2+}$ cluster:

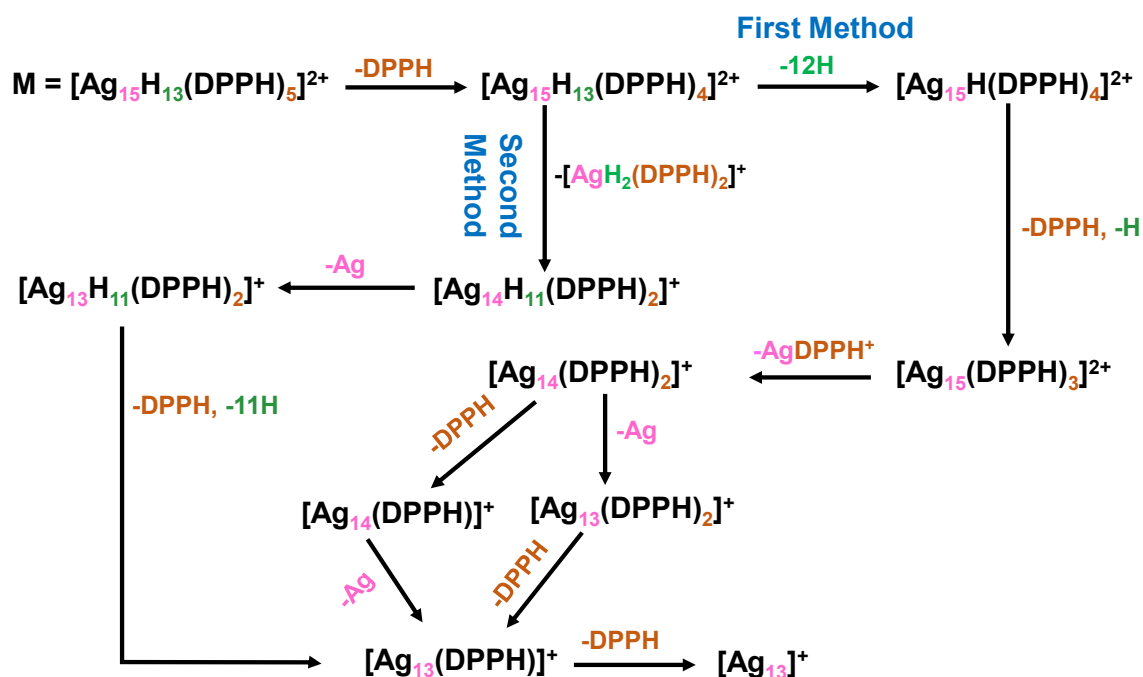


**Figure S11.** Collision energy dependent fragmentation pathway of  $[\text{Ag}_{15}\text{H}_{13}(\text{DPPH})_5]^{2+}$  cluster towards the formation of naked cluster,  $\text{Ag}_{13}^+$ . Hydrogen and DPPH loss do not involve any alternation of charge state of the resulting cluster. Whereas,  $[\text{AgDPPH}]^+$  loss results in the reduction of charge state from +2 to +1.

## Supporting information 12

### Characterization of $[\text{Ag}_{27}\text{D}_{22}(\text{DPPB})_7]^{3+}$ cluster:

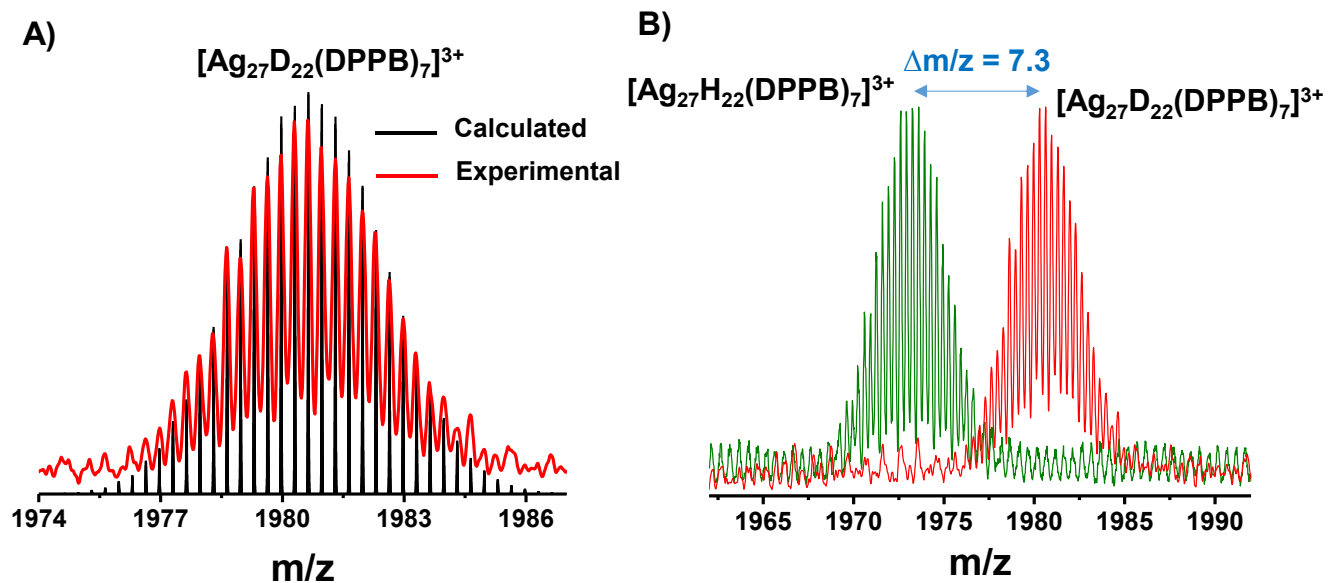


**Figure S12.** (A) Experimental mass spectrum (red trace) of  $[\text{Ag}_{27}\text{D}_{22}(\text{DPPB})_7]^{3+}$  cluster and it matches well with its calculated (black trace) isotopic pattern. (B) The ESI MS of  $[\text{Ag}_{27}\text{H}_{22}(\text{DPPB})_7]^{3+}$  and  $[\text{Ag}_{27}\text{D}_{22}(\text{DPPB})_7]^{3+}$  showing a mass shift due to the exchange of hydrogen atoms with deuterium atoms.

## Supporting information 13

$^1\text{H}$  NMR spectra of DPPB and  $[\text{Ag}_{27}\text{H}_{22}(\text{DPPB})_7]^{3+}$  cluster:

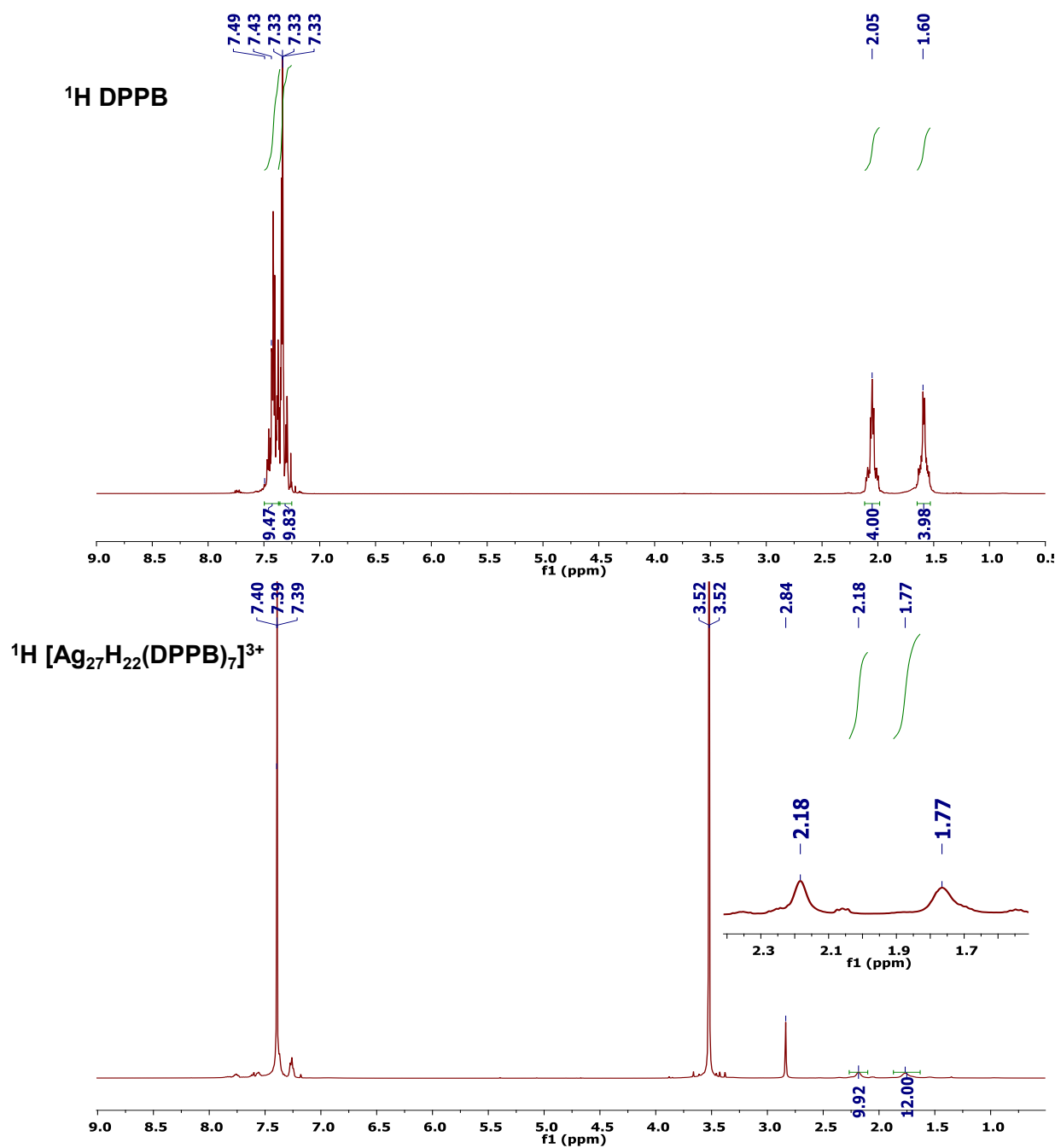


**Figure S13.**  $^1\text{H}$  NMR spectra of DPPB and  $[\text{Ag}_{27}\text{H}_{22}(\text{DPPB})_7]^{3+}$  clusters. Broad peaks of  $[\text{Ag}_{27}\text{H}_{22}(\text{DPPB})_7]^{3+}$  at 1.77 and 2.18 ppm confirm the presence of hydride protected nanoclusters.

## Supporting information 14

$^{31}\text{P}$  NMR spectra of DPPB and  $[\text{Ag}_{27}\text{H}_{22}(\text{DPPB})_7]^{3+}$  cluster:

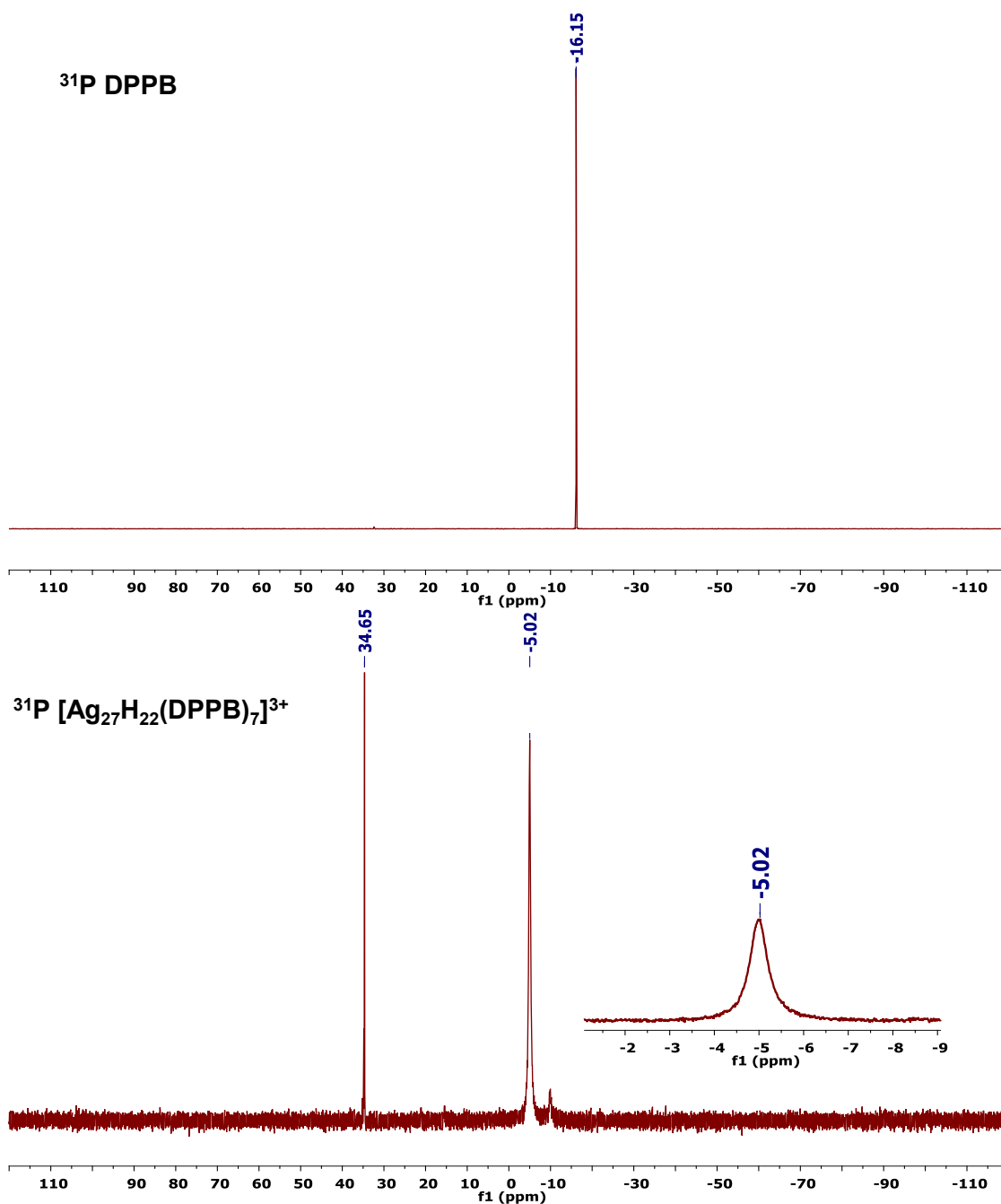


**Figure S14.**  $^{31}\text{P}$  NMR spectra of DPPB and  $[\text{Ag}_{27}\text{H}_{22}(\text{DPPB})_7]^{3+}$  clusters. The  $^{31}\text{P}$  signal at -16.15 ppm for DPPB ligand disappears in the  $[\text{Ag}_{27}\text{H}_{22}(\text{DPPB})_7]^{3+}$  cluster due to the binding of ligands with the metal core, which is also confirmed by the appearance of new broad peaks at -5.02 ppm in the nanoclusters. Peak at 34.65 ppm is due to phosphine oxides.

## Supporting information 15

### XPS spectra of $[\text{Ag}_{27}\text{H}_{22}(\text{DPPB})_7]^{3+}$ cluster:

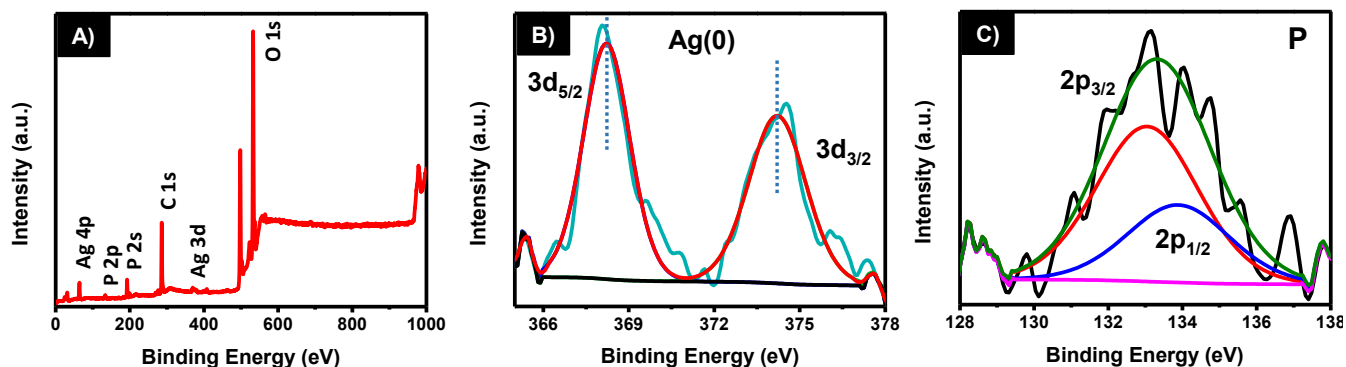


**Figure S15.** (A) XPS survey spectrum of  $[\text{Ag}_{27}\text{H}_{22}(\text{DPPB})_7]^{3+}$  showing all the expected elements (Ag, P and C). (B) Ag 3d spectrum of the nanocluster. Ag  $3d_{5/2}$  appears at 368.22 eV indicating the presence of Ag(0) state. (C) P 2p spectrum of the nanocluster. P  $2p_{3/2}$  appears at 133.03 eV.



## Supporting information 16

### SEM EDS of $[\text{Ag}_{27}\text{H}_{22}(\text{DPPB})_7]^{3+}$ cluster:

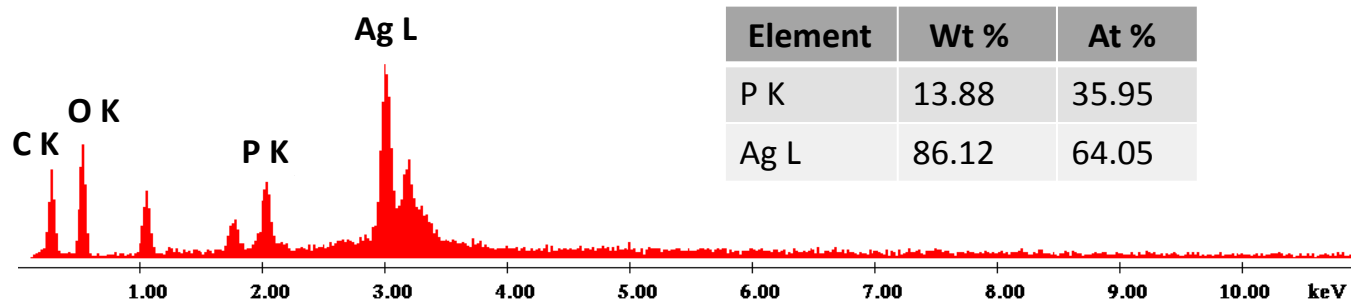


**Figure S16.** SEM EDS of  $[\text{Ag}_{27}\text{H}_{22}(\text{DPPB})_7]^{3+}$  cluster with quantification of elements. Ag:P atomic ratio matches well with the Ag:P ratio obtained from the molecular formula of the cluster.

## Supporting information 17

### TEM analysis of $[\text{Ag}_{27}\text{H}_{22}(\text{DPPB})_7]^{3+}$ cluster:

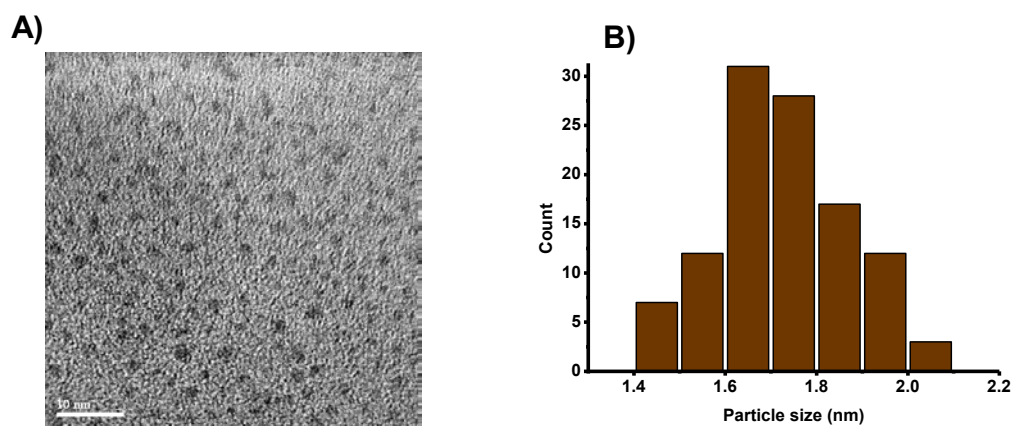


**Figure S17.** (A) TEM image of the  $[\text{Ag}_{27}\text{H}_{22}(\text{DPPB})_7]^{3+}$  cluster. Scale bar is 10 nm. (B) Particle distribution shows an average size of  $1.72 \pm 0.14$  nm for this nanocluster.

## Supporting information 18

Comparison between the experimental and the calculated spectra of  $\text{Ag}_{25}^+$ :

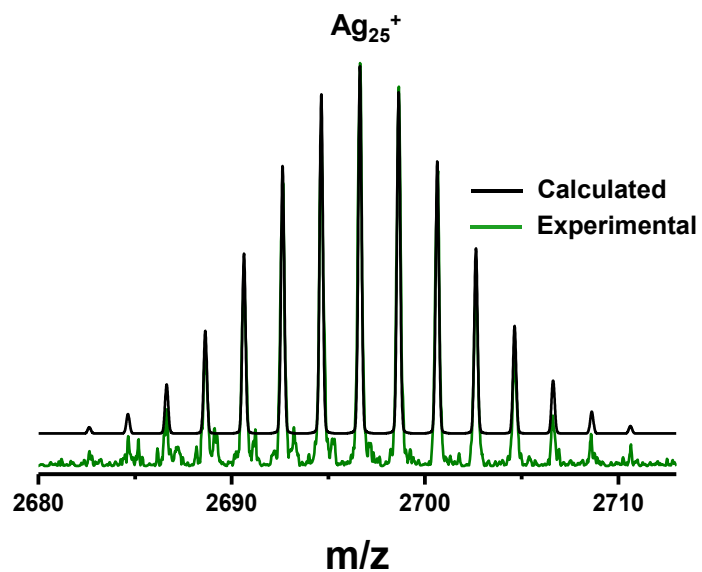
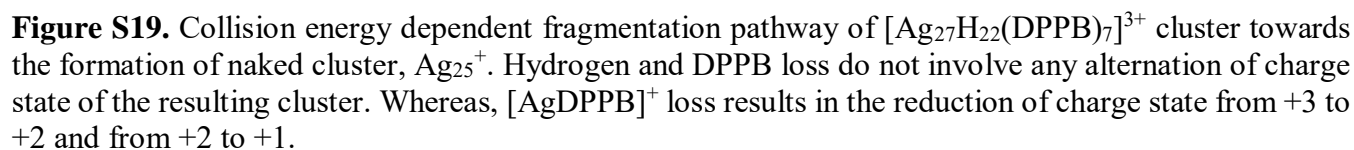


**Figure S18.** Experimental mass spectrum (green trace) of  $\text{Ag}_{25}^+$  matches well with the calculated (black trace) isotopic pattern.

### Fragmentation pathway of $[\text{Ag}_{27}\text{H}_{22}(\text{DPPB})_7]^{3+}$ cluster:



# Manifestation of Structural Differences of Atomically Precise Cluster-Assembled Solids in Their Mechanical Properties

Korath Shivan Sugi, Payel Bandyopadhyay, Mohammad Bodiuzzaman, Abhijit Nag, Manjapoyil Hridya, Wakeel Ahmed Dar, Pijush Ghosh,\* and Thalappil Pradeep\*



Cite This: *Chem. Mater.* 2020, 32, 7973–7984



Read Online

ACCESS |



Metrics & More

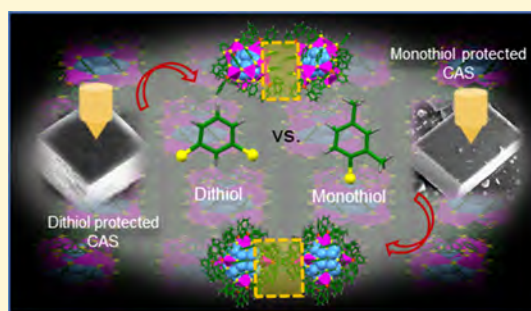


Article Recommendations



Supporting Information

**ABSTRACT:** Cluster-assembled solids (CASs) formed by the self-assembly of monodispersed atomically precise monolayer-protected noble metal clusters are attractive due to their collective properties. The physical stability and mechanical response of these materials remain largely unexplored. We have investigated the mechanical response of single crystals of atomically precise dithiol-protected  $\text{Ag}_{29}$  polymorphs, monothiol-protected  $\text{Ag}_{46}$ , and a cocrystal of the latter with  $\text{Ag}_{40}$  (formulas of the clusters have been simplified merely with the number of metal atoms). The  $\text{Ag}_{29}$  polymorphs crystallize in cubic and trigonal lattices ( $\text{Ag}_{29}$  C and  $\text{Ag}_{29}$  T, respectively), and  $\text{Ag}_{46}$  and its cocrystal with  $\text{Ag}_{40}$  crystallize in trigonal and monoclinic lattices ( $\text{Ag}_{46}$  T and  $\text{Ag}_{40/46}$  M, respectively). The time and loading-rate-dependent mechanical properties of the CASs are elucidated by measuring nanoindentation creep and stress relaxation. The obtained Young's modulus ( $E_r$ ) values of the CASs were similar to those of zeolitic imidazolate frameworks (ZIFs) and show the trend  $\text{Ag}_{29}$  T >  $\text{Ag}_{29}$  C >  $\text{Ag}_{40/46}$  M >  $\text{Ag}_{46}$  T. We have also studied the viscoelastic properties of all of the four CASs and found that the value of  $\tan \delta$ /damping factor of monothiol-protected  $\text{Ag}_{46}$  T was higher than that of other CASs. The unusual mechanical response of CASs was attributed to the supramolecular interactions at the surface of nanoclusters. This observation implies that the stiffness and damping characteristics of the materials can be modulated by ligand and surface engineering. These studies suggest the possibility of distinguishing between the crystal structures using mechanical properties. This work provides an understanding that is critical for designing nanocluster devices capable of withstanding mechanical deformations.



## INTRODUCTION

Monolayer-protected atomically precise clusters<sup>1,2</sup> of noble metals are some of the most intensely studied materials of recent times. Molecular properties of these systems, such as distinct photoabsorption,<sup>3–5</sup> molecular chirality,<sup>6,7</sup> photoluminescence,<sup>8</sup> and nonlinear optical properties,<sup>9</sup> have been of interest from diverse perspectives such as sensing,<sup>10</sup> catalysis,<sup>11</sup> and biolabeling.<sup>12</sup> Such molecular clusters can act as building blocks in creating self-assembled cluster materials, which are atomically precise, varied in composition, and diverse in structure. Their self-assembly can be tailored by tuning the underlying molecular or nanoscale interactions such as dipolar, van der Waals, electrostatic, and hydrogen-bonding.<sup>13</sup> The archives of molecular clusters are rich with exciting properties, and therefore, the resulting cluster-assembled solids (CASs) hold the promise of high tunability in a range of material properties. The combination of atomic precision and intercluster interactions in CASs can result in novel collective properties, including tunable electrical transport,<sup>14</sup> mechanical properties,<sup>15,16</sup> magnetism,<sup>17,18</sup> and luminescence,<sup>19,20</sup> which have been explored only to a limited extent.

Metals, alloys, and ceramics are typically stiff and hard due to their underlying strong metallic, covalent, and ionic bonds, while the molecular crystals with weaker noncovalent interactions are softer.<sup>16,21–23</sup> Such soft molecular crystals show ferroelectric<sup>24,25</sup> and piezoelectric<sup>26</sup> properties that find applications in fields such as flexible electronics. The physical, chemical, and mechanical properties of materials depend on their crystal structures as well as the structural arrangements and intermolecular interactions. The mechanical properties of molecular crystals can be modulated through crystal engineering.<sup>21</sup> It is known that depth-sensing techniques, such as nanoindentation (NI), can be used to study the mechanical properties of single crystals with high precision. The mechanical properties of different types of molecular materials such as active pharmaceutical ingredients (APIs),<sup>27–29</sup> metal-organic frameworks (MOFs),<sup>30–32</sup> hybrid organic–inorganic

Received: July 13, 2020

Revised: August 20, 2020

Published: August 21, 2020



perovskites (HOIPs),<sup>33–35</sup> and bio-organic peptide-based materials<sup>36</sup> have been investigated in detail using nano-indentation. These lend insights into the crystal structure–mechanical property correlations in them. Recent investigations on the three single crystals of naphthalene diimide derivatives having similar molecular structures showed different mechanical responses,<sup>37</sup> which were correlated to the weak interactions in crystal packing. The studies of Dey et al., on elastically bendable organic cocrystals of caffeine (CAF) and 4-chloro-3-nitrobenzoic acid (CNB), suggested that the exceptional mechanical stiffness and high hardness are due to the mechanically interlocked weak hydrogen-bonding networks and supramolecular interactions.<sup>38</sup> The exceptional elasticity of 2-hydroxy-5-methyl benzylidene amino phenyl-3-phenylacrylonitrile crystals in liquid nitrogen was attributed to the supramolecular interactions in the crystal.<sup>39</sup> In addition, acicular crystals of bis(acetylacetonato)copper(II) ([Cu(acac)<sub>2</sub>]), a classic coordination compound, also displayed significant elastic flexibility without losing crystallinity.<sup>40</sup> Through synchrotron X-ray measurements, it was observed that under strain, the molecules in the [Cu(acac)<sub>2</sub>] crystal rotate reversibly and thus reorganize to allow the mechanical compression and expansion required for elasticity and still maintain the integrity of the crystal structure. Theoretical studies of atomically precise Ag<sub>44</sub> CASs suggest the existence of similar ligand-flexure-induced softness.<sup>16</sup> The mechanical response of Ag<sub>29</sub> CAS had been probed by nanoindentation, and the softness of the material was attributed to the protecting ligands.<sup>15</sup> This implies that a correlation between mechanical properties and structures could exist in CASs as well. An investigation of these becomes possible today as several cluster systems with varying structures are now available. Miniaturization of various devices requires such materials that can be controlled and self-assembled into the form desirable. To successfully incorporate these materials into flexible electronic devices, knowledge of their mechanical deformation is necessary. The design principles to modulate the response of CASs to mechanical stress need further inputs.

In this paper, we report distinct differences in the mechanical properties of diverse mixed-ligand-protected clusters, mainly the two polymorphic Ag<sub>29</sub><sup>41</sup> clusters. The already known cubic (Ag<sub>29</sub> C)<sup>41</sup> and the newly discovered trigonal (Ag<sub>29</sub> T)<sup>42</sup> systems have been studied. Variations in the properties are directly related to the structural differences and intermolecular interactions in their crystal packing. Similar studies have been extended to Ag<sub>46</sub><sup>43</sup> (Ag<sub>46</sub> T) and its cocrystal with Ag<sub>40</sub> (Ag<sub>40/46</sub> M) to reaffirm the importance of the structure and supramolecular interactions in determining mechanical properties. Hence, the study has broad implications in crystal engineering of various flexible, ordered molecular materials.

## ■ EXPERIMENTAL METHODS

**Chemicals.** All chemicals, including sodium borohydride (NaBH<sub>4</sub>, 99.99% metal basis), triphenylphosphine (TPP), benzene-1,3-dithiol (BDT), 2,4-dimethylbenzenethiol (2,4-DMBT), and 2,5-dimethylbenzenethiol (2,5-DMBT) were purchased from Sigma-Aldrich. Silver nitrate (AgNO<sub>3</sub>, 99%) was purchased from Rankem. Solvents including methanol, dichloromethane (DCM), and dimethylformamide (DMF) were of high-performance liquid chromatography (HPLC) grade.

**Synthesis of Ag<sub>29</sub> Nanoclusters (NCs).** Synthesis of Ag<sub>29</sub> nanoclusters (NCs) was performed by following a previously reported procedure.<sup>41</sup> Briefly, Ag<sub>29</sub>(BDT)<sub>12</sub> NCs were prepared by dissolving

25 mg of silver nitrate in 5 mL of methanol. To this, 10 mL of DCM and 15  $\mu$ L of BDT were added. The color of the solution changed to turbid yellow after the addition of BDT. It became colorless by the addition of 200 mg of TPP (in 1 mL of DCM). After 15 min, 10.5 mg of NaBH<sub>4</sub> in 500  $\mu$ L of cold deionized (DI) water was added. The reaction was stopped after 3 h continuous stirring. The resulting orange solution was centrifuged, and the supernatant was discarded. The residue was washed several times with methanol to remove excess thiols and thiolates, and it was dispersed in DMF.

**Synthesis of Ag<sub>46</sub> Nanoclusters.** The synthesis and purification procedures were almost the same as those described for the mixture (see below). Here, 2,5-dimethylbenzenethiol was used in place of 2,4-dimethylbenzenethiol.

**Synthesis of a Mixture of Ag<sub>40</sub> and Ag<sub>46</sub> Nanoclusters.** It was synthesized by a ligand exchange-induced structure transformation (LEIST) process. [Ag<sub>18</sub>(TPP)<sub>10</sub>H<sub>16</sub>]<sup>2+</sup> was taken as the precursor in this reported procedure.<sup>43</sup> About 5 mg of the clean Ag<sub>18</sub> cluster was taken in MeOH. To this, 0.75  $\mu$ L of 2,4-dimethylbenzenethiol (DMBT) was added under stirring conditions. The reaction was allowed to continue for 12 h. After 12 h, the initial greenish reaction mixture changed to reddish-brown, which indicated the formation of the product. Then, the reaction mixture was centrifuged at 5000 rpm for 5 min to remove all of the insoluble precipitates, and the solvent was removed under reduced pressure. Around 1 mL of MeOH was added to precipitate the material, and it was centrifuged. The precipitate was dried and washed several times with hexane to remove excess TPP. This cleaned material was dried and dissolved in DCM, which was used for characterization.

**Crystallization of Ag<sub>29</sub>C Nanoclusters.** The purified clusters (15 mg) were dispersed in DMF and filtered using a syringe filter. The concentrated cluster solution was drop-casted on a microscope slide and kept undisturbed at room temperature. After 3–4 days, luminescent red crystals were observed.

**Crystallization of Ag<sub>29</sub>T Nanoclusters.** The purified clusters (20 mg) were dispersed in DMF and filtered using a syringe filter. The concentrated cluster solution was kept for vapor diffusion with methanol. After 10 days, luminescent red crystals were observed. The vapor diffusion method resulted in trigonal Ag<sub>29</sub> crystals alone. This observation was further confirmed by monitoring the birefringence of obtained trigonal crystals using a polarization microscope. We have not observed any Ag<sub>29</sub> C crystals by the vapor diffusion method.

**Crystallization Ag<sub>46</sub>T Nanoclusters.** Around 40 mg of the purified cluster was dissolved in 1.5 mL of distilled DCM and 0.5 mL of MeOH, filtered by a syringe filter of pore size 0.22  $\mu$ m, layered by distilled hexane at 1:1 (by volume) ratio, and kept at 4 °C. After approximately 1 week, black hexagonal crystals were observed.

**Crystallization of Ag<sub>40/46</sub> M Nanoclusters.** A 40 mg of the solid cluster mixture was dissolved in 2 mL of distilled DCM, filtered by a syringe filter of pore size 0.22  $\mu$ m, layered by distilled hexane at 1:1 (by volume) ratio, and kept at 4 °C. After approximately 1 week, black crystals were observed. Several batches of crystallization were carried out to obtain crystals in quantity as well as quality.

**Characterization. UV–Vis Spectroscopy.** Optical absorption spectra of samples were obtained using a PerkinElmer Lambda 25 spectrometer.

**Electrospray Ionization Mass Spectrometry (ESI MS).** The mass spectra of samples were measured using a Waters Synapt G2-Si high-resolution mass spectrometer.

**Scanning Electron Microscopy (SEM) and Energy-Dispersive X-ray (EDAX) Measurements.** Scanning electron microscopy (SEM) and energy-dispersive X-ray (EDAX) analyses were done using an FEI Quanta-200 SEM.

**Single-Crystal X-ray Diffraction (SCXRD).** Face indexing was measured using a Bruker Kappa APEX III CMOS diffractometer using Cu K $\alpha$  ( $\lambda$  = 1.54178 Å) radiation.

**Nanoindentation Measurements.** Nanoindentation (NI) experiments were conducted using a Hysitron TI Premier nanomechanical testing instrument. We have used a Berkovich indenter of 150 nm radius in our experiments. The indentation loads of 200, 500, and 10 000  $\mu$ N were used with a trapezoidal load function. In situ



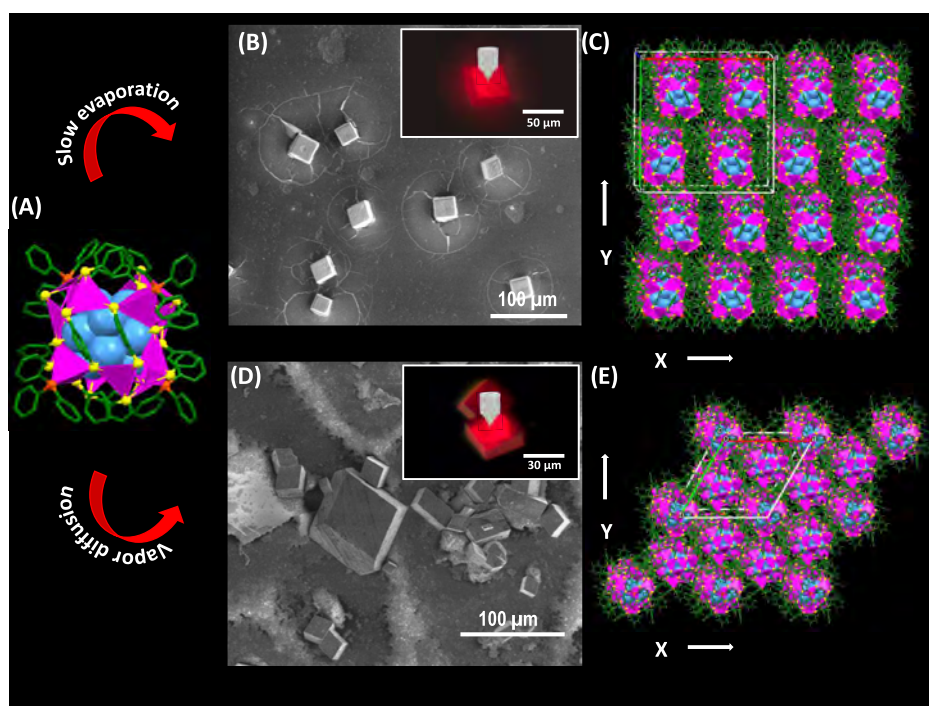


**Figure 1.** (A) View of the crystal structure of the  $\text{Ag}_{29}$  cluster. Images (B) and (D) are the SEM images of the three-dimensional (3D) crystals of  $\text{Ag}_{29}$  C and  $\text{Ag}_{29}$  T. Insets of (B) and (D) show a schematic representation of the nanoindentation experiments. Images (C) and (E) are the  $2 \times 2$  unit cells of  $\text{Ag}_{29}$  C and  $\text{Ag}_{29}$  T CASs viewed along their Z axes. Color codes: cerulean/magenta, Ag; yellow, S; orange, P; and green, C.

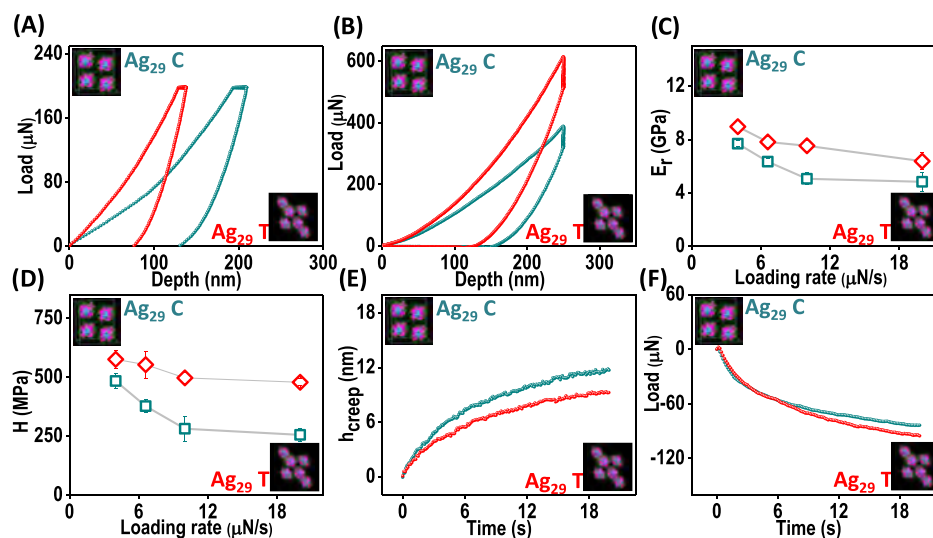


**Figure 2.** (A, B) Representative load- and displacement-controlled load–displacement plots of  $\text{Ag}_{29}$  C (cyan trace) and  $\text{Ag}_{29}$  T (red trace) with 200  $\mu\text{N}$  load and a loading/unloading time of 20 s. (C, D) Loading-rate-dependent variation of  $E_r$  and  $H$  values of  $\text{Ag}_{29}$  C and  $\text{Ag}_{29}$  T crystal systems. (E, F) Creep and stress relaxation of  $\text{Ag}_{29}$  C and  $\text{Ag}_{29}$  T cluster crystals. Color codes: cerulean/magenta, Ag; yellow, S; orange, P; and green, C.

scanning probe microscopy (SPM) was used to examine the surface topographies prior to and after indentation. The  $E_r$  and  $H$  were calculated by applying the Oliver and Pharr method,<sup>44</sup> which used the initial part of the unloading segment of the load–displacement curve. Nanoindentation experiments were performed on 10 different crystals of each silver CASs. On each single-cluster crystal, three repetitive experiments were performed. The CASs of all of the four silver NCs used had a length in the range of 20–60  $\mu\text{m}$  with a thickness of 10–20  $\mu\text{m}$ . To reduce the possible solvent effects, the nanoindentation studies were performed on evacuated/aged crystals.

**Nano Dynamic Mechanical Analysis (Nano DMA) Measurements.** DMA was performed using load-controlled frequency sweep mode. In this mode, the oscillating dynamic load of 10  $\mu\text{N}$  was

superimposed on a static load of 200  $\mu\text{N}$  over a frequency range of 10–200 Hz. By applying a sinusoidal force signal and capturing the displacement response, the magnitudes of storage modulus, loss modulus, and damping factors were calculated.

## RESULTS AND DISCUSSION

**$\text{Ag}_{29}$  CASs and Their Crystal Structures.** The CASs of atomically precise mixed-ligand-protected  $\text{Ag}_{29}$  and  $\text{Ag}_{46}$  nanoclusters (NCs) with different crystal packings and densities were used in this work (Table S1). As these cluster systems are known already, we present only essential information here. Both cluster systems are co-protected by

primary thiol ligands and secondary phosphine ligands. The well-established polymorphs of bidentate ligand-protected  $[\text{Ag}_{29}(\text{BDT})_{12}(\text{TPP})_4]$  NCs (1,3 benzenedithiol, BDT; triphenylphosphine, TPP), labeled as  $\text{Ag}_{29}$  C and  $\text{Ag}_{29}$  T, were obtained by varying the crystallization strategy (Figure 1A).<sup>41,42</sup> In our study, the  $[\text{Ag}_{29}(\text{BDT})_{12}(\text{TPP})_4]$  cluster was synthesized following a reported protocol<sup>41</sup> as described in the experimental section and characterized using optical absorption and electrospray ionization mass spectrometry (ESI MS) (Figures S1 and S2). We have followed the same reported procedure<sup>41,42</sup> to obtain crystals of acceptable quality and dimensions (Figure 1B,D). The total structure of individual clusters was determined by single-crystal X-ray crystallography. The structural anatomy of the  $\text{Ag}_{29}$  cluster reveals the existence of the  $\text{Ag}_{13}$  icosahedral core in it (Figure S3A), which is further capped by  $\text{Ag}_{16}\text{S}_{24}\text{P}_4$  motifs (Figure S3B) to form the  $\text{Ag}_{29}(\text{BDT})_{12}\text{TPP}_4$  architecture (Figure S3E). The supra-molecular arrangements in cubic and trigonal systems are quite different (Figure S3F,G).

**Mechanical Response of  $\text{Ag}_{29}$  C and  $\text{Ag}_{29}$  T.** The difference in the crystal packing (Figure 1C,E) and density (Table S1) of  $\text{Ag}_{29}$  polymorphs can result in distinct changes in mechanical properties. This prompted us to probe the mechanical response of CASs using the nanoindentation technique. The indented plane is  $(\bar{1}01)$  in the case of  $\text{Ag}_{29}$  T (Figure S4), whereas the indentation tests were performed on the major face, preferentially oriented in the direction normal to the loading direction in the case of other systems. The load-controlled and displacement-controlled modes were used to study creep and stress relaxation. To study the creep behavior, a fixed load was held for some time and the displacement in the sample was recorded. Similarly, in the stress relaxation study, a fixed displacement was maintained and the reduction in the stress value was monitored. These experiments revealed new insights into the time-dependent mechanical behavior of cluster materials. The load–displacement plots of load-controlled and displacement-controlled nanoindentation tests on  $\text{Ag}_{29}$  C and  $\text{Ag}_{29}$  T are shown in Figure 2A,B, respectively. The corresponding piezo images of residual indentation imprints on both  $\text{Ag}_{29}$  CASs are shown in Figure S5. The absence of pop-ins on the load–displacement curves of both  $\text{Ag}_{29}$  CASs during loading is an indication of smooth penetration of the indenter and no local plasticity or phase change in response to the applied mechanical stress, unlike in most anisotropic molecular crystals with low symmetry.<sup>28,45</sup> The load-controlled load–displacement plot shows a significant residual displacement in crystals of  $\text{Ag}_{29}$  C compared to  $\text{Ag}_{29}$  T, suggesting it to be less hard. The hardness ( $H$ ) values of  $\text{Ag}_{29}$  C and T crystals are  $282.19 \pm 53.33$  and  $498.15 \pm 23.61$  MPa, respectively, which corroborated well with this observation. The observed reduced Young's modulus ( $E_r$ ) values of  $\text{Ag}_{29}$  C and T systems are  $5.66 \pm 0.44$  and  $7.53 \pm 0.41$  GPa, respectively, indicating that density is not the dominant factor in controlling the modulus of the crystals (Table 1). The measurement of  $\nu$  is complicated (due to the

sample size and other factors) for such cluster-assembled solids. In view of this, the experimentally determined Young's Modulus ( $E_r$ ) is reported here rather than the bulk modulus. Both the crystals show creep during holding time, which implies a significant viscoelastic deformation in the crystals. For viscous materials, the stress is proportional to the strain rate, unlike purely elastic materials. To investigate the rate-dependent deformation behavior, we have performed indentation experiments at different loading rates (Figures S6 and S7). The values of  $E_r$  and  $H$  for both the crystals at different loading rates are plotted in Figure 2C,D, respectively. It is evident from the plot that the magnitudes of  $E_r$  and  $H$  reduce significantly with an increase in the loading rate until  $10 \mu\text{N/s}$ . Figure 2E shows the result of the creep study performed on both C and T  $\text{Ag}_{29}$  crystals applying quasi-static nano-indentation. The constant load was maintained at approximately  $200 \mu\text{N}$ . Instead of creep strain, the absolute value of the displacement of the indenter is reported here. The creep plots of both the  $\text{Ag}_{29}$  crystals indicate a two-stage creep response: primary and secondary. Creep plots at higher loads such as  $500$  and  $10\,000 \mu\text{N}$  (Figure S8) reveal that unlike some metals and polymers, the tertiary creep region is not observed in the case of  $\text{Ag}_{29}$  CASs, which usually originates due to the rapid growth and coalescence of voids in the crystals. Here, we have observed only the secondary stage of creep for both the CASs. The upward slope (not totally flat) in the creep plots suggests the possibility of reduced coalescence of voids at this stage. In such CASs, the observed displacement/strain at the primary stage of creep (Figure 2E) could typically originate from the ligand-flexure- or stress-induced buckling of the ligands. The relatively steady secondary stage indicates the nucleation of voids under the sustained load. Strain hardening is the increased resistance to plastic deformation, and such effects dominate during the transient period of the initial creep test.<sup>46</sup> We have performed four consecutive creep experiments on the same area of  $\text{Ag}_{29}$  C and T crystals to probe the strain hardening effects (Figure S9). A comparison of first and fourth creep plots shows a significant reduction of displacement. The reduced displacement offers a shred of evidence for higher resistance to plastic deformation, quantified by an increase in hardness. This observation implies the existence of strain hardening in the  $\text{Ag}_{29}$  polymorphs. This is a crucial information when these crystals are used at a load range beyond the elastic limit in real-life applications. They also undergo stress relaxation, when held at certain displacement, as indicated in Figure 2F. This further validates the time-dependent behavior of these cluster crystals and complements the observed creep response. Both the crystals show a pronounced increase in creep and stress relaxation as a function of loading rate (Figure S10). To depict the viscoelastic properties of the tested materials, the stress relaxation curves were fitted to an analytical expression extracted from a rheological model composed of springs and dashpots<sup>47,48</sup> (Figures S11 and S12). The fit of our model captures the behavior of both  $\text{Ag}_{29}$  crystals tested in stress relaxation experiments, allowing us to extract relaxation modulus ( $G^\circ(t)$ ) values in addition to relaxation times ( $\tau$ ) (Table S2), which substantiate well with the observed  $E_r$  values.

**Structural Basis for Exceptional Mechanical Response of  $\text{Ag}_{29}$  Polymorphs.** In our studies of  $\text{Ag}_{29}$  polymorphs, we have observed that apart from density, there are other factors that control the mechanical response of CASs.

**Table 1. Measured Young's Modulus ( $E_r$ ) and Hardness ( $H$ ) Values of the  $\text{Ag}_{29}$  CASs, Compared with Their Density ( $\rho$ )**

CASs	$\rho$ ( $\text{g/cm}^3$ )	$E_r$ (GPa)	$H$ (MPa)
$\text{Ag}_{29}$ C	2.11	$5.66 \pm 0.44$	$282.19 \pm 53.33$
$\text{Ag}_{29}$ T	2.04	$7.53 \pm 0.41$	$498.15 \pm 23.61$

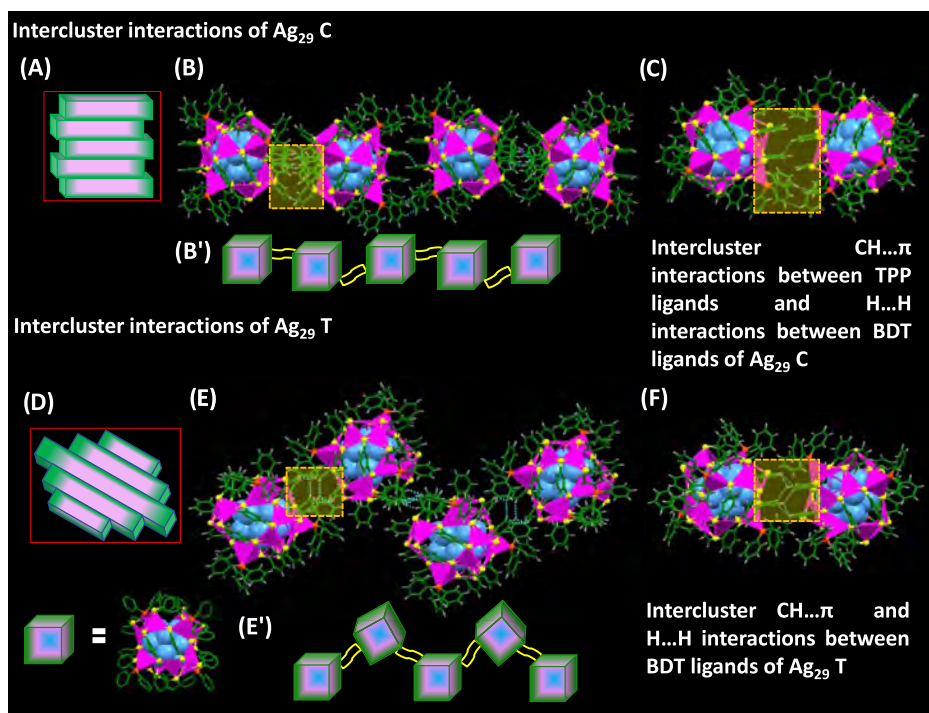


**Figure 3.** Anatomy of intercluster interactions of  $\text{Ag}_{29}$  C and  $\text{Ag}_{29}$  T. (A, D) Schematic representations of packing in  $\text{Ag}_{29}$  C and T crystals. (B, E) Illustrations of intercluster interactions in one-dimensional (1D) assembly of  $\text{Ag}_{29}$  C and T clusters. (B', E') Schematic representations of intercluster interactions in 1D assembly of  $\text{Ag}_{29}$  C and T systems. (C, F) Illustration of intercluster interactions between two  $\text{Ag}_{29}$  C and  $\text{Ag}_{29}$  T clusters. Color codes: cerulean/magenta, Ag; yellow, S; orange, P; green, C; and gray, H.

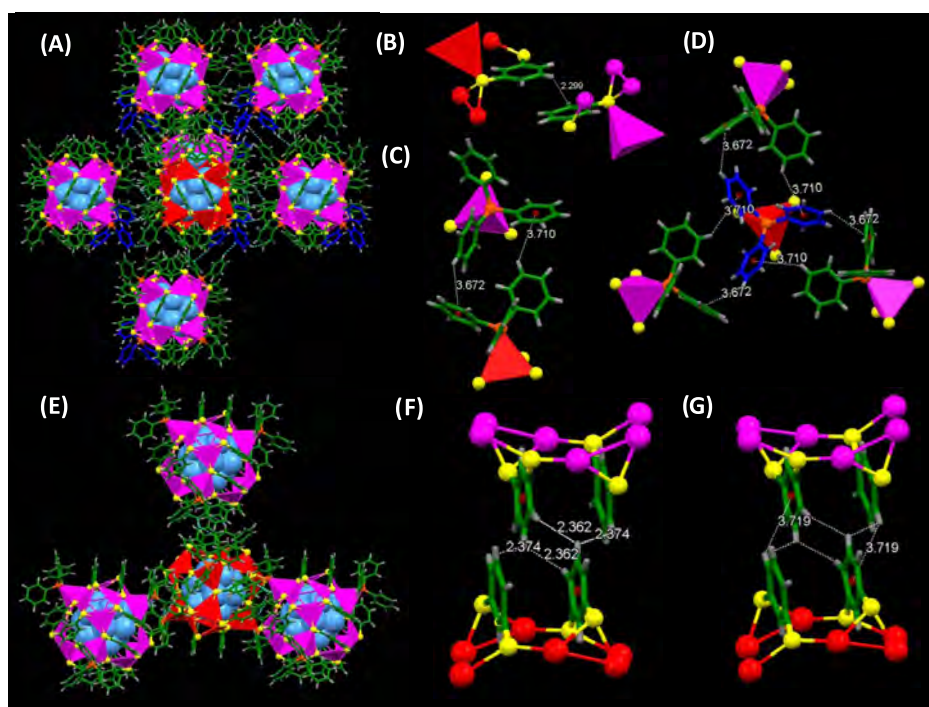


**Figure 4.** Supramolecular interactions in  $\text{Ag}_{29}$  C and T systems. (A, E) Interaction of the  $\text{Ag}_{29}$  cluster with neighboring clusters in cubic and trigonal lattices. Specific intercluster interactions are shown in (B)–(G). (B)  $\text{H}\cdots\text{H}$  interaction between BDT ligands in the  $\text{Ag}_{29}$  C lattice. (C, D)  $\text{CH}\cdots\pi$  interactions between TPP ligands in the  $\text{Ag}_{29}$  C lattice. (F, G)  $\text{H}\cdots\text{H}$  and  $\text{CH}\cdots\pi$  interactions between BDT ligands of  $\text{Ag}_{29}$  T. Color codes: cerulean/magenta/red, Ag; yellow, S; orange, P; green/blue, C; and gray, H.

Here, we are considering only the intercluster ligand interactions that are preserved well in the solid state.<sup>49</sup> Interestingly, taking a closer look at the arrangement of NCs, one can find that both the  $\text{Ag}_{29}$  polymorphs assemble linearly

to form 3D crystals (Figure S13). A schematic of such a linear assembly of  $\text{Ag}_{29}$  polymorphs is shown in Figure 3A,D. The neighboring NCs interact through specific intercluster interactions induced by BDT and TPP ligands (Figure



3B,E), which control the crystal packing of the cluster molecules (Figure 3B',E'). The surface structures of both the crystals in the solid state are mainly stabilized by intermolecular CH $\cdots\pi$  interactions, in which the C–H bonds interact with the  $\pi$  electrons of phenyl rings (Figure 3C,F). Such surface structures of NCs are reminiscent of biomolecules such as proteins.<sup>50,51</sup> The strength of the CH $\cdots\pi$  interactions is ca. 1.5–2.5 kcal/mol.<sup>51</sup> Apart from this, several other van der Waals interactions such as H $\cdots$ H and  $\pi\cdots\pi$  stacking were also observed. In the case of Ag<sub>29</sub> C, we have found that the TPP ligands bundle in two ways: double bundles (L<sub>1</sub>, having a pair of CH $\cdots\pi$  interactions) and triple bundles (L<sub>3</sub>, having three pairs of CH $\cdots\pi$  interactions) (Figure S14). The high connectivity in such molecular networks enables direct interactions with six nearest neighboring clusters via H $\cdots$ H,  $\pi\cdots\pi$ , and CH $\cdots\pi$  interactions (Figure 4A). The relevant intercluster interactions of both Ag<sub>29</sub> polymorphs are assessed and listed in Table 2. There are six H $\cdots$ H and parallel-

**Table 2.** Intercluster Intermolecular Interactions of Ag<sub>29</sub> C and T Crystals<sup>a</sup>

crystal system	H $\cdots$ H interactions	$\pi\cdots\pi$ interactions	CH $\cdots\pi$ interactions	
	between BDT ligands	between BDT ligands	between TPP ligands	between BDT ligands
Ag <sub>29</sub> C	6 (6 $\times$ 1)	6 (6 $\times$ 1)	12 (6 $\times$ 2)	
Ag <sub>29</sub> T	12 (3 $\times$ 4)	6 (3 $\times$ 2)		6 (3 $\times$ 2)

<sup>a</sup>Total no. of interactions = no. of clusters having direct interactions  $\times$  no. of interactions by each cluster.

displaced  $\pi\cdots\pi$  contacts between the BDT ligands of an Ag<sub>29</sub> cluster and its six neighboring clusters in the cubic lattice. The bond distances of the H $\cdots$ H and  $\pi\cdots\pi$  contacts are 2.29 Å

(Figure 4B) and 5.87 Å (Figure S15A), respectively. Twelve CH $\cdots\pi$  interactions were also observed between the four secondary TPP ligands of the Ag<sub>29</sub> cluster and its six neighboring clusters. Among the four TPP ligands, three will have a pair of edge-to-face or T-shaped CH $\cdots\pi$  interactions (L<sub>1</sub>) with the TPP ligands of the adjacent three clusters (Figure S15B). The remaining one TPP (highlighted in blue in Figure S14) will act as a soft base  $\pi$ -system leading to the formation of three pairs of T-shaped CH $\cdots\pi$  interactions (L<sub>3</sub>) with three neighboring clusters (Figure S15C,D). The L<sub>1</sub> and L<sub>3</sub> bundles together constitute a total of 12 CH $\cdots\pi$  contacts between TPP ligands of adjacent clusters. The bond lengths and bond angles of such CH $\cdots\pi$  contacts range from 3.67 to 3.71 Å (Figure 4C,D) and 118–140° (Figure S16A,B), respectively. The observed CH $\cdots\pi$  bond lengths of Ag<sub>29</sub> polymorphs were similar to those of meso-tetrakis[4-(benzyloxy)phenyl] porphyrins.<sup>52</sup>

The interactions that direct the 3D crystal assembly are quite different in Ag<sub>29</sub> T in comparison to Ag<sub>29</sub> C (Figure 4E). These nanoscale building blocks were found to hold together by two pairs of H $\cdots$ H (Figure 4F) and  $\pi\cdots\pi$  (Figure S17A), and a pair of parallelly displaced CH $\cdots\pi$  (Figure 4G) interactions that act as structure-directing units promoting crystallization. The intercluster interactions between the TPP ligands are not observed in the case of the Ag<sub>29</sub> T system. The interactions between BDT ligands of adjacent clusters (Figure S15B) were reminiscent of the chair conformer of cyclohexane. The three pairs of BDT ligands of each cluster will interact with BDT ligands of three adjacent clusters via 12 H $\cdots$ H (Figure 4F), 6  $\pi\cdots\pi$  (Figure S15A), and 6 parallelly displaced CH $\cdots\pi$  (Figure 4G) interactions (Table 2). The bond length of intermolecular weak H $\cdots$ H interactions was 2.36 Å, which is slightly higher than in Ag<sub>29</sub> C crystals (2.29 Å). The average

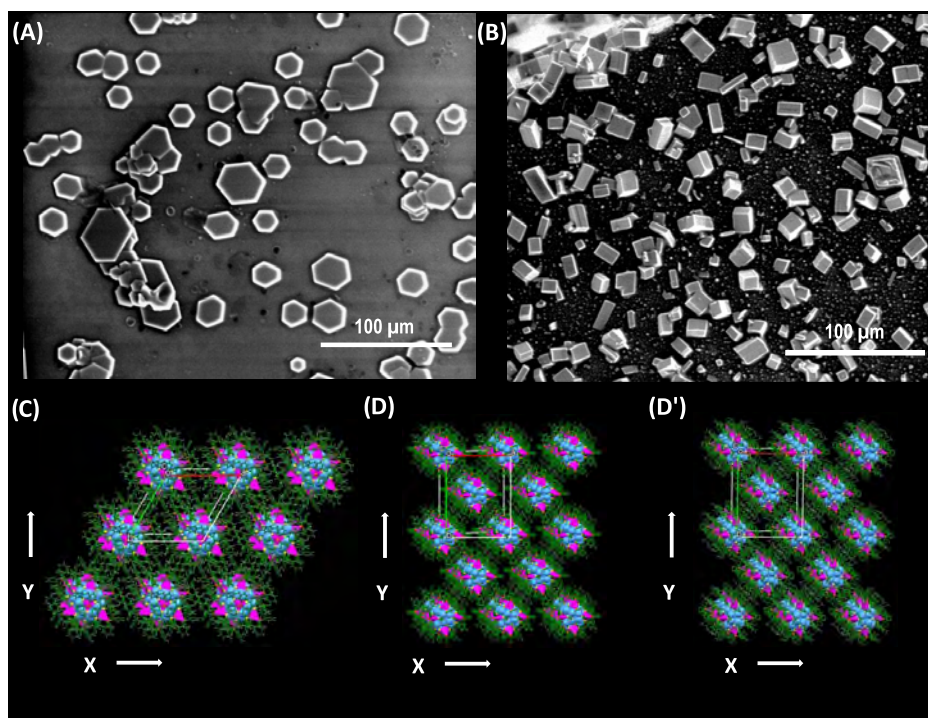


**Figure 5.** (A, B) SEM images of the 3D crystals of Ag<sub>46</sub> T and Ag<sub>40/46</sub> M. (C, D, D') The 2  $\times$  2  $\times$  2 unit cells of Ag<sub>46</sub> T, Ag<sub>40</sub> M, and Ag<sub>46</sub> M clusters viewed along the Z axis. (D) and (D') refer to the structures of Ag<sub>40</sub> and Ag<sub>46</sub>, respectively, in the Ag<sub>40/46</sub> M cocrystal. Color codes: cerulean/magenta, Ag; yellow, S; orange, P; and green, C.

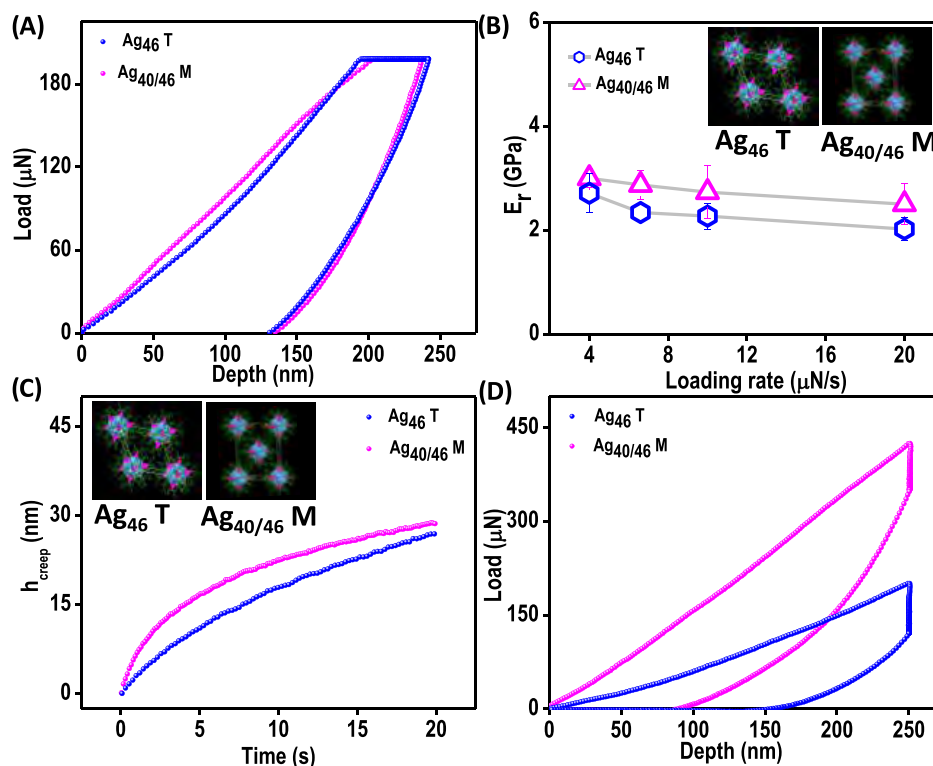


**Figure 6.** (A) Representative load-controlled load–displacement plots of  $\text{Ag}_{46}$  T (blue trace) and  $\text{Ag}_{40/46}$  M (pink trace) with 200  $\mu\text{N}$  load with a loading/unloading time of 20 s. (B) Variation of  $E_r$  values with the loading rate. (C) Creep response of  $\text{Ag}_{46}$  T (blue trace) and  $\text{Ag}_{40/46}$  M (pink trace) crystal systems. Inset images are the unit cells of  $\text{Ag}_{46}$  T and  $\text{Ag}_{40/46}$  M crystals. (D) Representative displacement-controlled load–displacement plots of  $\text{Ag}_{46}$  T (blue trace) and  $\text{Ag}_{40/46}$  M (pink trace) with 250 nm displacement. Color codes: cerulean/magenta, Ag; yellow, S; orange, P; and green, C.

bond length of the  $\text{CH}\cdots\pi$  interaction is  $3.71 \pm 0.2 \text{ \AA}$ , with a bond angle of  $144^\circ$  (Figure S17C). The strength of  $\text{CH}\cdots\pi$  interactions depends on the bond distances between the hydrogen atom (in C–H) and the plane of the aromatic ring [less than  $2.9 \text{ \AA}$ ] as well as  $\text{CH}\cdots\pi$  access angles (varied from  $140$  to  $180^\circ$ ).<sup>53</sup> Here, both cubic and trigonal systems are having slightly larger intercluster  $\text{CH}\cdots\pi$  bond distances and thus they are weaker in nature. The  $\text{CH}\cdots\pi$  contacts of  $\text{Ag}_{29}$  C crystals involve the secondary TPP ligands, whereas, these are between primary BDT ligands in  $\text{Ag}_{29}$  T. Also, a study of the molecular arrangement of benzene at 0.15 and 0.91 GPa reveals a significant shift in the  $\text{CH}\cdots\pi$ -bonded networks and substantial collapse of the voids between the molecules.<sup>54</sup> The observed higher  $E_r$  and  $H$  in the  $\text{Ag}_{29}$  T crystal compared to  $\text{Ag}_{29}$  C might be due to the following factors: (i) The intercluster interactions are between the primary BDT ligands rather than the secondary TPP ligands. (ii) The presence of two pairs of  $\text{H}\cdots\text{H}$  interactions between BDT ligands that extend as a zig-zag chain connecting adjacent molecules, as well as a pair of  $\text{CH}\cdots\pi$  interactions between the BDT ligands. The disruption of internal molecular rotations can influence the mechanical deformation of the crystals.<sup>55</sup> Such restrictions in the flexibility might not be there in the case of  $\text{Ag}_{29}$  C as the  $\text{CH}\cdots\pi$  interactions are mainly between the TPP ligands. The absence of clear slip planes in the above crystal systems is due to their interconnected network-like structures.<sup>56</sup>

#### Crystal Structures of $\text{Ag}_{46}$ and Its Cocrystal with $\text{Ag}_{40}$ .

In the preceding sections, we understood that the structures could be distinguished by their distinctive mechanical properties. The surface and core structures of  $\text{Ag}_{46}$  systems are completely different from those of  $\text{Ag}_{29}$  polymorphs. Also,

the structural differences in  $\text{Ag}_{46}$  and its cocrystal can reveal new insights into the mechanical response of CASs. This prompted us to perform nanoindentation studies on monothiol-protected  $[\text{Ag}_{46}(2,5\text{-DMBT})_{24}(\text{TPP})_8]$  NCs (2,5-dimethylbenzenethiol, 2,5-DMBT; triphenylphosphine, TPP) crystallized in a trigonal lattice ( $\text{Ag}_{46}$  T) and a cocrystal of  $\text{Ag}_{46}$  and  $\text{Ag}_{40}$  in a monoclinic lattice ( $\text{Ag}_{40/46}$  M). Ligands for both the clusters in  $\text{Ag}_{40/46}$  are 2,4-dimethylbenzenethiol (2,4-DMBT) along with TPP. The clusters were synthesized following the protocol<sup>43</sup> as described in the **Experimental Methods** and characterized using optical absorption and ESI MS studies (Figures S18 and S19). Figure 5A,B shows the SEM images of  $\text{Ag}_{46}$  T and  $\text{Ag}_{40/46}$  M single crystals. Figure 5C, D, D' represents the packing of  $\text{Ag}_{46}$  clusters and  $\text{Ag}_{40/46}$  cocrystals in a trigonal lattice with the space group P-3 and monoclinic lattice with the space group  $C2/m$ , respectively. Successive jobs of least-squares refinement followed by the Fourier difference map could finally yield the structure of  $\text{Ag}_{40}$  and  $\text{Ag}_{46}$  from the cocrystal. The occupancy of each cluster was 50% in the  $\text{Ag}_{40/46}$  M crystal system.<sup>43</sup> The structure of  $\text{Ag}_{46}$  is similar in  $\text{Ag}_{46}$  T (Figure S20) and  $\text{Ag}_{40/46}$  M (Figure S21). The  $\text{Ag}_{46}$  cluster consists of a  $\text{Ag}_{14}$  inner core (Figures S20A and S21A) protected by a  $\text{Ag}_{24}$  outer core (Figures S20B and S21B). This  $\text{Ag}_{38}$  motif is further protected by eight  $\text{Ag}_3\text{P}$  units (Figures S20C,D and S21C,D), resulting in a  $\text{Ag}_{46}\text{S}_{24}\text{P}_8$  architecture. The  $\text{Ag}_{40}$  cluster in the cocrystal consists of a  $\text{Ag}_8$  inner core (Figure S21F) with the rest of the structure the same as that of  $\text{Ag}_{46}$  (Figure S21G–I).

**Mechanical Response of  $\text{Ag}_{46}$  and Its Cocrystal with  $\text{Ag}_{40}$ .** The nanoindentation studies were performed by keeping all conditions the same except that in the case of  $\text{Ag}_{46}$  T, the

holding time of 50 s was used for the dissipation of creep. The load-controlled load–displacement plots are depicted in Figure 6A. The residual indentation imprint on the Ag<sub>46</sub> T system is represented in Figure S22. We could not observe such an indentation imprint in the case of Ag<sub>40/46</sub> M crystal with 200  $\mu$ N load. The obtained  $E_r$  values from the load-controlled load–displacement plots reveal the compliant nature of the Ag<sub>46</sub> T system compared to Ag<sub>40/46</sub> M (Table S3). The loading-rate-dependent experiments were performed on Ag<sub>46</sub> T and Ag<sub>40/46</sub> M systems (Figures S23 and S24). An increase in the values of  $E_r$  (Figure 6B) and  $H$  (Figure S25) was observed as a function of the loading rate of both the crystal systems. The Ag<sub>40/46</sub> M system showed larger creep behavior (Figure 6C) compared to the Ag<sub>46</sub> T system. Similar to Ag<sub>29</sub> systems, the creep behavior of Ag<sub>46</sub> T and Ag<sub>40/46</sub> M systems consists of primary and secondary stages. The tertiary creep region was not observed even at loads of 500 and 10 000  $\mu$ N (Figure S26A,B). The strain hardening behavior of Ag<sub>46</sub> systems is shown in Figure S27. We have also performed displacement-controlled experiments (Figure 6D) and evaluated the stress relaxation behavior of Ag<sub>46</sub> systems (Figure S28). The Ag<sub>46</sub> systems also show a pronounced increase in creep (Figure S29A,B) and stress relaxation (Figure S29C,D) as a function of loading rate, similar to the Ag<sub>29</sub> polymorphs. The experimental stress–relaxation curves were fitted to an analytical expression extracted from a rheological model used previously (Figure S30A,B), and the  $G^0(t)$  and  $\tau$  were extracted (Table S4). The extracted relaxation modulus values corroborated well with the  $E_r$  values of the Ag<sub>46</sub> systems.

**Structural Basis for the Mechanical Response of Ag<sub>46</sub> and Its Cocrystal with Ag<sub>40</sub>.** The structural basis for the differences in mechanical responses of Ag<sub>46</sub> systems was analyzed through the examination of crystal packing (Figure S31A,B). The intercluster supramolecular interactions of Ag<sub>46</sub> T and Ag<sub>40/46</sub> M crystal systems are summarized in Table 3,

**Table 3. Intercluster Intermolecular Interactions of Ag<sub>46</sub> T and Ag<sub>40/46</sub> M Crystals<sup>a</sup>**

crystal system	H...H interactions		CH... $\pi$ interactions	
	between TPP and 2,5-DMBT ligands	between TPP ligands	between TPP and 2,5-DMBT ligands	between 2,5-DMBT ligands
Ag <sub>46</sub> T	12 (6 $\times$ 2)	12 (2 $\times$ 6)		
crystal system	H...H interactions		CH... $\pi$ interactions	
	between 2,4-DMBT ligands	between TPP ligands	between TPP and 2,4-DMBT ligands	between 2,4-DMBT ligands
Ag <sub>40/46</sub> M	6 (2 $\times$ 3)		8 (4 $\times$ 2)	4 (2 $\times$ 2)

<sup>a</sup>Total no. of interactions = no. of clusters having direct interactions  $\times$  no. of interactions by each cluster.

which reveal the complex interactions of the Ag<sub>46</sub> CASs. Each cluster in the molecular network of the Ag<sub>46</sub> T system has direct interactions with eight neighboring clusters via H...H and CH... $\pi$  interactions (Figure S32A,B). The TPP and 2,5-DMBT ligands of six adjacent clusters will interact via a pair of H...H interactions, leading to hexagonal close packing of Ag<sub>46</sub> clusters (Figure S33A,B). The average bond length of such a H...H interaction is 2.36 Å (Figure 7A). Apart from this, the two pole site TPP ligands of the Ag<sub>46</sub> clusters interact with the pole site TPP ligands of other two neighboring clusters via six CH... $\pi$  interactions (Figure S34A,B). The bond length and

bond angle of the CH... $\pi$  interactions are 3.21 Å (Figure 7B) and 120°, respectively (Figure S34C). Such weak supramolecular interactions would allow the clusters to undergo intercluster rotations, leading to compliant behavior. In the Ag<sub>40/46</sub> M cocrystal system, each cluster interacts with six neighboring clusters via CH... $\pi$  and H...H interactions (Figure S35A,B). There are two types of CH... $\pi$  interactions that direct the packing of Ag<sub>40/46</sub> clusters in the monoclinic lattice. Type I interaction (CH... $\pi$  (I)) is between TPP and 2,4-DMBT (Figures 7C and S36A), whereas type II interaction (CH... $\pi$  (II)) is between the 2,4-DMBT ligands (Figure 7D). Among the six neighboring clusters, four of them are connected by type I, CH... $\pi$  contacts having bond length and bond angle of 3.11 Å (Figure 7C) and 131° (Figure S36B), respectively. The remaining two clusters are connected by a pair of type II, CH... $\pi$  contacts formed between the primary 2,4-DMBT ligands, having a bond length and a bond angle of 3.74 Å (Figure 7D) and 155° (Figure S36C), respectively. The types I and II together constitute twelve CH... $\pi$  interactions. Besides that, three H...H interactions with a bond length of 2.06  $\pm$  1 Å were observed between the 2,4-DMBT ligands (Figure 7E). Unlike the Ag<sub>46</sub> T system, the Ag<sub>40/46</sub> M system contains supramolecular interactions between the primary 2,4-DMBT ligands, similar to Ag<sub>29</sub> T systems. Such interlocked and corrugated molecular packing of clusters imparts rigidity to the molecular crystal, which in turn manifests the  $E_r$  and  $H$  values.

**Dynamic Mechanical Analysis (DMA) of CASs.** To have a deeper understanding of the material properties, we have performed dynamical mechanical analysis (DMA) to understand the frequency sensitivity of different viscoelastic properties. Generally, such measurements are not performed in the case of molecular crystals; nevertheless, the creep behavior of the CASs prompted us to investigate the viscoelastic properties. The storage modulus depicts the energy stored in a system. The storage modulus values of all of the four crystal systems do not show significant frequency sensitivity (Figure 8A). The observed loss modulus value was higher for Ag<sub>46</sub> T compared to the other three crystal systems (Figure S37). The loss modulus of Ag<sub>29</sub> polymorphs shows significant frequency sensitivity compared to that of the Ag<sub>46</sub> crystal systems. Interestingly, we have observed that the damping or loss factor of Ag<sub>46</sub> T is higher than that of other cluster systems (Figure 8B) and is similar to that of natural rubber<sup>57</sup> irrespective of low storage modulus values. This observation points out a new possibility of using CASs as dampening materials. Studies of acoustic vibrations in nanometer-scale particles can provide fundamental insights into the mechanical properties of materials.<sup>58</sup> The stimulus-induced flexible metal-organic frameworks (MOFs) are highly attractive to absorb/store energy with promising prospects as nanodampers or nanosprings.<sup>59,60</sup> The two factors that vary the breathing modes of a structure are the deformation of the bond angle and the distance between ligands.<sup>61</sup> The energy of the crystal increases when bonds are deformed and decreases when the distance between the aromatic rings decreases. In the case of atomically precise clusters, the intrinsic damping has contributions due to the ligand-flexure-induced changes occurring in the metal cores and the surface layer of ligands. Recently, Maioli et al. studied the elastic properties of ligand-protected clusters, experimentally and theoretically, and two periods, corresponding to fundamental breathing and quadrupolar-like acoustic modes, were detected.<sup>62</sup> They have observed a stagnation in acoustic response and attributed it



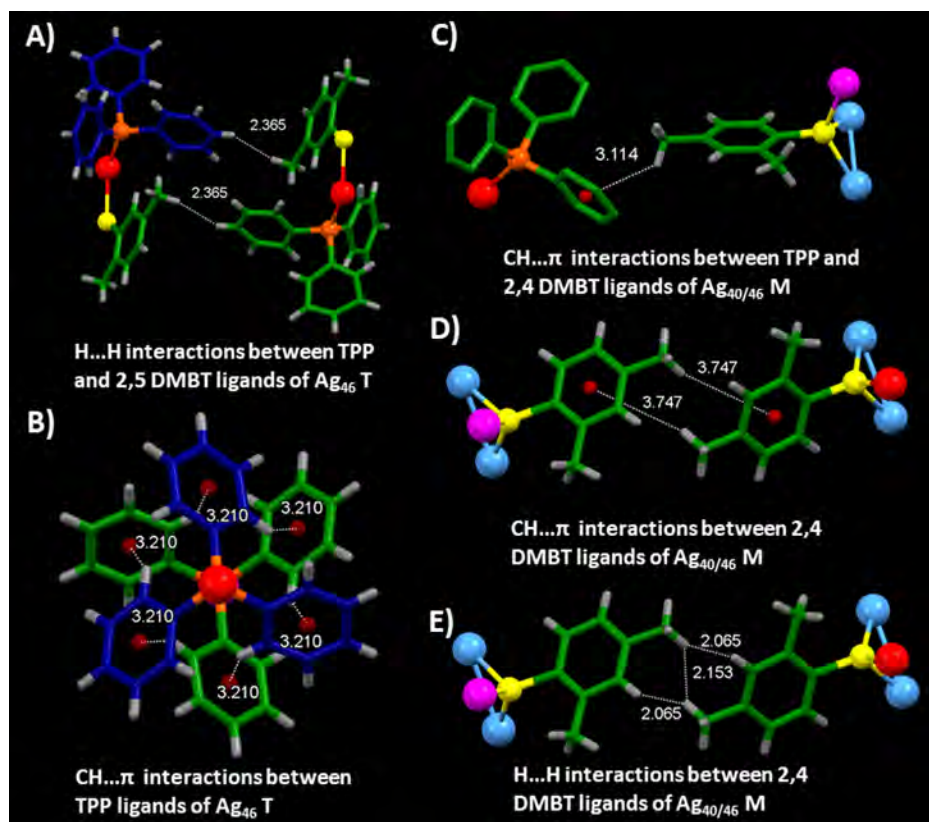


**Figure 7.** Supramolecular interactions in  $\text{Ag}_{46}$  T and  $\text{Ag}_{40/46}$  M systems. (A) Intercluster H...H interactions between TPP and 2,5-DMBT ligands of  $\text{Ag}_{46}$  clusters in a trigonal lattice. Specific intercluster interactions are shown in (B)–(E). (B) CH... $\pi$  interactions between TPP ligands in the  $\text{Ag}_{46}$  trigonal lattice. (C) CH... $\pi$  interactions between TPP and 2,4-DMBT ligands in the  $\text{Ag}_{40/46}$  monoclinic lattice. (D, E) CH... $\pi$  and H...H interactions between 2,4-DMBT ligands in the  $\text{Ag}_{40/46}$  monoclinic lattice. Color codes: cerulean/magenta/red, Ag; yellow, S; orange, P; green/blue, C; and gray, H.

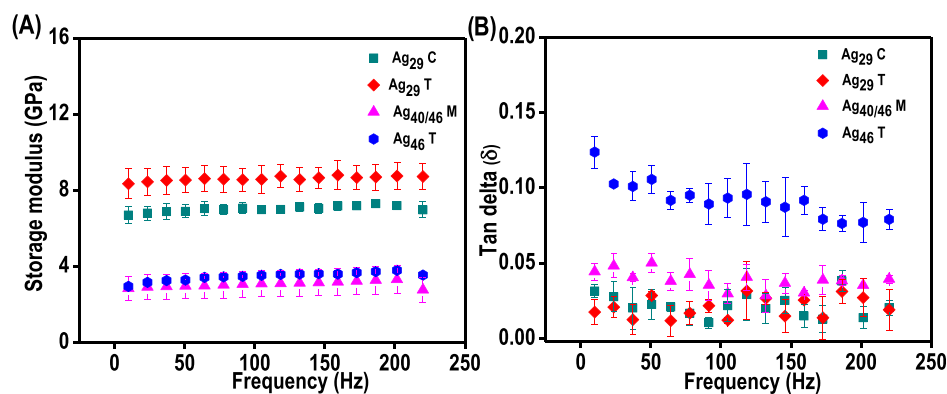


**Figure 8.** (A, B) Variation of storage modulus and  $\tan \delta$  as a function of frequency of  $\text{Ag}_{29}$  C (cyan trace),  $\text{Ag}_{29}$  T (red trace),  $\text{Ag}_{46}$  T (blue trace), and  $\text{Ag}_{40/46}$  M (pink trace).

to the mechanical mass loading effects of protecting ligands. The observed damping behavior of  $\text{Ag}_{46}$  T crystals opens up the prospects that by tailoring the nature of the metal cores and protecting ligands, different materials such as dampers and molecular springs can be obtained.

Investigation of the mechanical response of  $\text{Ag}_{29}$  polymorphs and  $\text{Ag}_{46}$  systems having different surface and core structures revealed a few fascinating insights. The compliant nature of the interconnected molecular cluster frameworks is largely driven by the protecting ligands. The cluster surface structures with dithiol ligands show higher  $E_r$  and  $H$  values than monothiol-protected clusters due to the structural rigidity<sup>63</sup> offered by

dithiol ligands. Also, the interrogation of crystal packing reveals that the cluster crystals stabilized by CH... $\pi$  contacts involving the primary thiol ligands show higher  $E_r$  and  $H$  values ( $\text{Ag}_{29}$  T and  $\text{Ag}_{40/46}$  M) than those directed by secondary phosphine ligands. In CASs, the cluster molecules are assembled in such a way that sufficient reorientation (rotation) of the molecules is possible without breaking the overall continuity of crystal packing. The cluster crystals assembled with weak supramolecular interactions may allow some elastic flexibility. Interlocked packing of the cluster molecules facilitates the elastic deformation. However, the absence of mechanical resistance to slip may eventually assist plastic deformation

(irreversible);<sup>40</sup> hence, only limited elasticity is expected. The flexure of NCs in the crystals could allow this material to serve as an energy-absorbing structure, which can convert stress to mechanical motion and can be used as molecular-scale sensors and switches. In view of our study, we postulate that it is possible to control the mechanical properties of CAs by tuning the strength and type of supramolecular interactions present between clusters. The stiffness of the CAs is enormously dependent on the rigidity and intermolecular interactions of the primary thiol ligands. We believe that there will be anisotropy in such cluster-assembled solids. Attempts to probe different faces of the crystal were not successful.

## CONCLUSIONS

In summary, we demonstrated the mechanical response of CAs protected by monolayers. The atomically precise CAs of silver show large creep deformation, stress relaxation, and a pronounced rate-dependent mechanical behavior. This unusual behavior is attributed to the weak supramolecular interactions of the protecting ligands on the surface of the nanoclusters. The CAs protected by dithiols show superior  $E_r$  and  $H$  compared to the monothiol-protected CAs. CAs having supramolecular interactions between the primary ligands are stiffer than their counterparts. We have also observed that the  $\tan \delta$  value of the  $\text{Ag}_{46}$  T system is comparable to that of natural rubber. By modeling the creep and relaxation behavior using rheological components, we determined both the elastic and viscous characteristics of the CAs. The present study has implications in creating flexible materials from atomically precise clusters. The results obtained will help in the effective design of flexible nanocluster devices since the low hardness and the viscoelastic properties demonstrated are not conducive to flexible applications. It is also essential to look into other CAs having supramolecular interactions or mechanically interlocked structures, which can be used as solids in materials engineering. With growing interest in engineering of materials with desired functions responding to external stimuli, the insights gained in this work will help future investigations.

## ASSOCIATED CONTENT

### Supporting Information

The Supporting Information is available free of charge at <https://pubs.acs.org/doi/10.1021/acs.chemmater.0c02905>.

ESI MS data, optical images, structural anatomy of crystal structures, face index analysis, piezo images, load–displacement plots, and Maxwell–Weichert model (PDF)

## AUTHOR INFORMATION

### Corresponding Authors

**Pijush Ghosh** – Department of Applied Mechanics, Indian Institute of Technology Madras, Chennai 600036, India; [orcid.org/0000-0002-6077-6498](https://orcid.org/0000-0002-6077-6498); Email: [pijush@iitm.ac.in](mailto:pijush@iitm.ac.in)

**Thalappil Pradeep** – DST Unit of Nanoscience (DST UNS) and Thematic Unit of Excellence (TUE), Department of Chemistry, Indian Institute of Technology Madras, Chennai 600036, India; [orcid.org/0000-0003-3174-534X](https://orcid.org/0000-0003-3174-534X); Email: [pradeep@iitm.ac.in](mailto:pradeep@iitm.ac.in)

## Authors

**Korath Shivan Sugi** – DST Unit of Nanoscience (DST UNS) and Thematic Unit of Excellence (TUE), Department of Chemistry, Indian Institute of Technology Madras, Chennai 600036, India

**Payel Bandyopadhyay** – Department of Applied Mechanics, Indian Institute of Technology Madras, Chennai 600036, India

**Mohammad Bodiuzzaman** – DST Unit of Nanoscience (DST UNS) and Thematic Unit of Excellence (TUE), Department of Chemistry, Indian Institute of Technology Madras, Chennai 600036, India

**Abhijit Nag** – DST Unit of Nanoscience (DST UNS) and Thematic Unit of Excellence (TUE), Department of Chemistry, Indian Institute of Technology Madras, Chennai 600036, India

**Manjapoyil Hridya** – DST Unit of Nanoscience (DST UNS) and Thematic Unit of Excellence (TUE), Department of Chemistry, Indian Institute of Technology Madras, Chennai 600036, India

**Wakeel Ahmed Dar** – DST Unit of Nanoscience (DST UNS) and Thematic Unit of Excellence (TUE), Department of Chemistry, Indian Institute of Technology Madras, Chennai 600036, India

Complete contact information is available at: <https://pubs.acs.org/doi/10.1021/acs.chemmater.0c02905>

## Author Contributions

The problem was suggested by T.P. K.S.S. prepared the CAs and conducted most of the studies. P.B., K.S.S., and P.G. performed and analyzed the mechanical measurements. M.B., A.N., M.H., and W.A.D. helped in the characterization of clusters. The manuscript was written through contributions of all authors. All authors have given approval to the final version of the manuscript.

## Notes

The authors declare no competing financial interest.

## ACKNOWLEDGMENTS

We thank the Department of Science and Technology, Government of India, for constantly supporting our research program on nanomaterials. We thank the Sophisticated Analytical Instruments Facility, Indian Institute of Technology Madras, for face index analysis. We thank Sudhadevi Antharjanam for her help and suggestions in this work. KSS and MB thank the University Grants Commission (UGC), Govt. of India, for a research fellowship. PB thanks IIT Madras for an Institute Postdoctoral Fellowship. AN thanks IIT Madras for an Institute Doctoral Fellowship. WAD thanks SERB-DST for the award of a National Postdoctoral Fellowship (NPDF).

## REFERENCES

- (1) Jin, R.; Zeng, C.; Zhou, M.; Chen, Y. Atomically Precise Colloidal Metal Nanoclusters and Nanoparticles: Fundamentals and Opportunities. *Chem. Rev.* **2016**, *116*, 10346–10413.
- (2) Chakraborty, I.; Pradeep, T. Atomically Precise Clusters of Noble Metals: Emerging Link between Atoms and Nanoparticles. *Chem. Rev.* **2017**, *117*, 8208–8271.
- (3) Jin, R. Atomically precise metal nanoclusters: stable sizes and optical properties. *Nanoscale* **2015**, *7*, 1549–1565.
- (4) Jin, R.; Zhao, S.; Xing, Y.; Jin, R. All-thiolate-protected silver and silver-rich alloy nanoclusters with atomic precision: stable sizes, structural characterization and optical properties. *CrystEngComm* **2016**, *18*, 3996–4005.

- (5) Jin, R.; Zhu, Y.; Qian, H. Quantum-Sized Gold Nanoclusters: Bridging the Gap between Organometallics and Nanocrystals. *Chem. – Eur. J.* **2011**, *17*, 6584–6593.
- (6) Jadzinsky, P. D.; Calero, G.; Ackerson, C. J.; Bushnell, D. A.; Kornberg, R. D. Structure of a Thiol Monolayer-Protected Gold Nanoparticle at 1.1 Å Resolution. *Science* **2007**, *318*, 430.
- (7) Zeng, C.; Chen, Y.; Kirschbaum, K.; Appavoo, K.; Sfeir, M. Y.; Jin, R. Structural patterns at all scales in a nonmetallic chiral Au133(SR)52 nanoparticle. *Sci. Adv.* **2015**, *1*, No. e1500045.
- (8) Kang, X.; Zhu, M. Tailoring the photoluminescence of atomically precise nanoclusters. *Chem. Soc. Rev.* **2019**, *48*, 2422–2457.
- (9) Russier-Antoine, I.; Bertorelle, F.; Vojkovic, M.; Rayane, D.; Salmon, E.; Jonin, C.; Dugourd, P.; Antoine, R.; Brevet, P.-F. Non-linear optical properties of gold quantum clusters. The smaller the better. *Nanoscale* **2014**, *6*, 13572–13578.
- (10) Mathew, A.; Sajanlal, P. R.; Pradeep, T. Selective Visual Detection of TNT at the Sub-zeptomole Level. *Angew. Chem., Int. Ed.* **2012**, *51*, 9596–9600.
- (11) Li, G.; Jin, R. Atomically Precise Gold Nanoclusters as New Model Catalysts. *Acc. Chem. Res.* **2013**, *46*, 1749–1758.
- (12) Yu, J.; Choi, S.; Dickson, R. M. Shuttle-Based Fluorogenic Silver-Cluster Biolabels. *Angew. Chem., Int. Ed.* **2009**, *48*, 318–320.
- (13) Wu, Z.; Yao, Q.; Zang, S.; Xie, J. Directed Self-Assembly of Ultrasmall Metal Nanoclusters. *ACS Mater. Lett.* **2019**, *1*, 237–248.
- (14) Li, Q.; Russell, J. C.; Luo, T.-Y.; Roy, X.; Rosi, N. L.; Zhu, Y.; Jin, R. Modulating the hierarchical fibrous assembly of Au nanoparticles with atomic precision. *Nat. Commun.* **2018**, *9*, No. 3871.
- (15) Sugi, K. S.; Mallikarjunachari, G.; Som, A.; Ghosh, P.; Pradeep, T. Probing the Mechanical Response of Luminescent Dithiol-Protected Ag29(BDT)12(TPP)4 Cluster Crystals. *ChemNanoMat* **2018**, *4*, 401–408.
- (16) Yoon, B.; Luedtke, W. D.; Barnett, R. N.; Gao, J.; Desiredy, A.; Conn, B. E.; Bigioni, T.; Landman, U. Hydrogen-bonded structure and mechanical chiral response of a silver nanoparticle superlattice. *Nat. Mater.* **2014**, *13*, 807–811.
- (17) De Nardi, M.; Antonello, S.; Jiang, D.-e.; Pan, F.; Rissanen, K.; Ruzzi, M.; Venzo, A.; Zoleo, A.; Maran, F. Gold Nanowired: A Linear (Au25)<sub>n</sub> Polymer from Au25 Molecular Clusters. *ACS Nano* **2014**, *8*, 8505–8512.
- (18) Agrachev, M.; Antonello, S.; Dainese, T.; Ruzzi, M.; Zoleo, A.; Aprà, E.; Govind, N.; Fortunelli, A.; Sementa, L.; Maran, F. Magnetic Ordering in Gold Nanoclusters. *ACS Omega* **2017**, *2*, 2607–2617.
- (19) Khatun, E.; Bodiuzzaman, M.; Sugi, K. S.; Chakraborty, P.; Paramasivam, G.; Dar, W. A.; Ahuja, T.; Antharjanam, S.; Pradeep, T. Confining an Ag10 Core in an Ag12 Shell: A Four-Electron Superatom with Enhanced Photoluminescence upon Crystallization. *ACS Nano* **2019**, *13*, 5753–5759.
- (20) Huang, R.-W.; Dong, X.-Y.; Yan, B.-J.; Du, X.-S.; Wei, D.-H.; Zang, S.-Q.; Mak, T. C. W. Tandem Silver Cluster Isomerism and Mixed Linkers to Modulate the Photoluminescence of Cluster-Assembled Materials. *Angew. Chem., Int. Ed.* **2018**, *57*, 8560–8566.
- (21) Saha, S.; Mishra, M. K.; Reddy, C. M.; Desiraju, G. R. From Molecules to Interactions to Crystal Engineering: Mechanical Properties of Organic Solids. *Acc. Chem. Res.* **2018**, *51*, 2957–2967.
- (22) Naumov, P.; Chizhik, S.; Panda, M. K.; Nath, N. K.; Boldyreva, E. Mechanically Responsive Molecular Crystals. *Chem. Rev.* **2015**, *115*, 12440–12490.
- (23) Liu, F.; Hooks, D. E.; Li, N.; Robinson, J. F.; Wacker, J. N.; Swift, J. A. Molecular Crystal Mechanical Properties Altered via Dopant Inclusion. *Chem. Mater.* **2020**, *32*, 3952–3959.
- (24) Harada, J.; Shimojo, T.; Oyamaguchi, H.; Hasegawa, H.; Takahashi, Y.; Satomi, K.; Suzuki, Y.; Kawamata, J.; Inabe, T. Directionally tunable and mechanically deformable ferroelectric crystals from rotating polar globular ionic molecules. *Nat. Chem.* **2016**, *8*, 946–952.
- (25) Owczarek, M.; Hujsak, K. A.; Ferris, D. P.; Prokofjevs, A.; Majerz, I.; Szklarz, P.; Zhang, H.; Sarjeant, A. A.; Stern, C. L.; Jakubas, R.; Hong, S.; Dravid, V. P.; Stoddart, J. F. Flexible ferroelectric organic crystals. *Nat. Commun.* **2016**, *7*, No. 13108.
- (26) Guerin, S.; Stapleton, A.; Chovan, D.; Mouras, R.; Gleeson, M.; McKeown, C.; Noor, M. R.; Silien, C.; Rhen, F. M. F.; Kholkin, A. L.; Liu, N.; Soulimane, T.; Tofail, S. A. M.; Thompson, D. Control of piezoelectricity in amino acids by supramolecular packing. *Nat. Mater.* **2018**, *17*, 180–186.
- (27) Mishra, M. K.; Varughese, S.; Ramamurty, U.; Desiraju, G. R. Odd–Even Effect in the Elastic Moduli of  $\alpha,\omega$ -Alkanedicarboxylic Acids. *J. Am. Chem. Soc.* **2013**, *135*, 8121–8124.
- (28) Varughese, S.; Kiran, M. S. R. N.; Ramamurty, U.; Desiraju, G. R. Nanoindentation in Crystal Engineering: Quantifying Mechanical Properties of Molecular Crystals. *Angew. Chem., Int. Ed.* **2013**, *52*, 2701–2712.
- (29) Hu, S.; Mishra, M. K.; Sun, C. C. Twistable Pharmaceutical Crystal Exhibiting Exceptional Plasticity and Tabletability. *Chem. Mater.* **2019**, *31*, 3818–3822.
- (30) Tan, J. C.; Bennett, T. D.; Cheetham, A. K. Chemical structure, network topology, and porosity effects on the mechanical properties of Zeolitic Imidazolate Frameworks. *Proc. Natl. Acad. Sci. U.S.A.* **2010**, *107*, 9938–9943.
- (31) Spencer, E. C.; Kiran, M. S. R. N.; Li, W.; Ramamurty, U.; Ross, N. L.; Cheetham, A. K. Pressure-Induced Bond Rearrangement and Reversible Phase Transformation in a Metal–Organic Framework. *Angew. Chem., Int. Ed.* **2014**, *53*, 5583–5586.
- (32) Tan, J. C.; Cheetham, A. K. Mechanical properties of hybrid inorganic–organic framework materials: establishing fundamental structure–property relationships. *Chem. Soc. Rev.* **2011**, *40*, 1059–1080.
- (33) Rakita, Y.; Cohen, S. R.; Kedem, N. K.; Hodes, G.; Cahen, D. Mechanical properties of APbX<sub>3</sub> (A = Cs or CH<sub>3</sub>NH<sub>3</sub>; X = I or Br) perovskite single crystals. *MRS Commun.* **2015**, *5*, 623–629.
- (34) Sun, S.; Fang, Y.; Kieslich, G.; White, T. J.; Cheetham, A. K. Mechanical properties of organic–inorganic halide perovskites, CH<sub>3</sub>NH<sub>3</sub>PbX<sub>3</sub> (X = I, Br and Cl), by nanoindentation. *J. Mater. Chem. A* **2015**, *3*, 18450–18455.
- (35) Reyes-Martinez, M. A.; Abdelhady, A. L.; Saidaminov, M. I.; Chung, D. Y.; Bakr, O. M.; Kanatzidis, M. G.; Soboyejo, W. O.; Loo, Y.-L. Time-Dependent Mechanical Response of APbX<sub>3</sub> (A = Cs, CH<sub>3</sub>NH<sub>3</sub>; X = I, Br) Single Crystals. *Adv. Mater.* **2017**, *29*, No. 1606556.
- (36) Avinash, M. B.; Raut, D.; Mishra, M. K.; Ramamurty, U.; Govindaraju, T. Bioinspired Reductionistic Peptide Engineering for Exceptional Mechanical Properties. *Sci. Rep.* **2015**, *5*, No. 16070.
- (37) Devarapalli, R.; Kadambi, S. B.; Chen, C.-T.; Krishna, G. R.; Kammari, B. R.; Buehler, M. J.; Ramamurty, U.; Reddy, C. M. Remarkably Distinct Mechanical Flexibility in Three Structurally Similar Semiconducting Organic Crystals Studied by Nanoindentation and Molecular Dynamics. *Chem. Mater.* **2019**, *31*, 1391–1402.
- (38) Dey, S.; Das, S.; Bhunia, S.; Chowdhury, R.; Mondal, A.; Bhattacharya, B.; Devarapalli, R.; Yasuda, N.; Moriwaki, T.; Mandal, K.; Mukherjee, G. D.; Reddy, C. M. Mechanically interlocked architecture aids an ultra-stiff and ultra-hard elastically bendable cocrystal. *Nat. Commun.* **2019**, *10*, No. 3711.
- (39) Liu, H.; Ye, K.; Zhang, Z.; Zhang, H. An Organic Crystal with High Elasticity at an Ultra-Low Temperature (77 K) and Shapeability at High Temperatures. *Angew. Chem., Int. Ed.* **2019**, *58*, 19081–19086.
- (40) Worthy, A.; Grosjean, A.; Pfrunder, M. C.; Xu, Y.; Yan, C.; Edwards, G.; Clegg, J. K.; McMurtrie, J. C. Atomic resolution of structural changes in elastic crystals of copper(II) acetylacetonate. *Nat. Chem.* **2018**, *10*, 65–69.
- (41) AbdulHalim, L. G.; Bootharaju, M. S.; Tang, Q.; Del Gobbo, S.; AbdulHalim, R. G.; Eddaoudi, M.; Jiang, D.-e.; Bakr, O. M. Ag29(BDT)12(TPP)4: A Tetraivalent Nanocluster. *J. Am. Chem. Soc.* **2015**, *137*, 11970–11975.
- (42) Nag, A.; Chakraborty, P.; Bodiuzzaman, M.; Ahuja, T.; Antharjanam, S.; Pradeep, T. Polymorphism of Ag29(BDT)12(TPP)-43– cluster: interactions of secondary ligands and their effect on solid state luminescence. *Nanoscale* **2018**, *10*, 9851–9855.



- (43) Bodiuzzaman, M.; Ghosh, A.; Sugi, K. S.; Nag, A.; Khatun, E.; Varghese, B.; Paramasivam, G.; Antharjanam, S.; Natarajan, G.; Pradeep, T. Camouflaging Structural Diversity: Co-crystallization of Two Different Nanoparticles Having Different Cores But the Same Shell. *Angew. Chem., Int. Ed.* **2019**, *58*, 189–194.
- (44) Oliver, W. C.; Pharr, G. M. An improved technique for determining hardness and elastic modulus using load and displacement sensing indentation experiments. *J. Mater. Res.* **1992**, *7*, 1564–1583.
- (45) Oliver, W. C.; Pharr, G. M. Measurement of hardness and elastic modulus by instrumented indentation: Advances in understanding and refinements to methodology. *J. Mater. Res.* **2004**, *19*, 3–20.
- (46) Wang, Z.; Guo, S.; Wang, Q.; Liu, Z.; Wang, J.; Yang, Y.; Liu, C. T. Nanoindentation characterized initial creep behavior of a high-entropy-based alloy CoFeNi. *Intermetallics* **2014**, *53*, 183–186.
- (47) Kaufman, J. D.; Miller, G. J.; Morgan, E. F.; Klapperich, C. M. Time-dependent mechanical characterization of poly(2-hydroxyethyl methacrylate) hydrogels using nanoindentation and unconfined compression. *J. Mater. Res.* **2008**, *23*, 1472–1481.
- (48) Roylance, D.; Cohen, K. C.; Jenkins, C. H.; Khanna, S. K. Mechanics of materials: A materials science perspective. *Proc. Inst. Mech. Eng., Part L* **2001**, *215*, 141–145.
- (49) Higaki, T.; Liu, C.; Zhou, M.; Luo, T.-Y.; Rosi, N. L.; Jin, R. Tailoring the Structure of 58-Electron Gold Nanoclusters: Au<sub>103</sub>S<sub>2</sub>-(S-Nap)<sub>41</sub> and Its Implications. *J. Am. Chem. Soc.* **2017**, *139*, 9994–10001.
- (50) Plevin, M. J.; Bryce, D. L.; Boisbouvier, J. Direct detection of CH/ $\pi$  interactions in proteins. *Nat. Chem.* **2010**, *2*, 466–471.
- (51) Nishio, M. The CH/ $\pi$  hydrogen bond in chemistry. Conformation, supramolecules, optical resolution and interactions involving carbohydrates. *Phys. Chem. Chem. Phys.* **2011**, *13*, 13873–13900.
- (52) Kuś, P.; Kusz, J.; Książek, M. Aromatic C–H $\cdots\pi$ , C–H $\cdots$ O and parallel aromatic–aromatic interactions in the crystal structure of meso-tetrakis[4-(benzyloxy)phenyl]porphyrin. *J. Chem. Crystallogr.* **2020**, *50*, 21–27.
- (53) Osamu, T.; Yuji, K.; Sachiyo, I.; Ko, S.; Michio, I.; Shuji, T.; Yoji, U.; Sei, T.; Motohiro, N. Hydrogen-Bond-Like Nature of the CH/ $\pi$  Interaction as Evidenced by Crystallographic Database Analyses and Ab Initio Molecular Orbital Calculations. *Bull. Chem. Soc. Jpn.* **2001**, *74*, 2421–2430.
- (54) Katrusiak, A.; Podsiadło, M.; Budzianowski, A. Association CH $\cdots\pi$  and No van der Waals Contacts at the Lowest Limits of Crystalline Benzene I and II Stability Regions. *Cryst. Growth Des.* **2010**, *10*, 3461–3465.
- (55) Mondal, A.; Bhattacharya, B.; Das, S.; Bhunia, S.; Chowdhury, R.; Dey, S.; Reddy, C. M. Metal-like Ductility in Organic Plastic Crystals: Role of Molecular Shape and Dihydrogen Bonding Interactions in Aminoboranes. *Angew. Chem., Int. Ed.* **2020**, *59*, 10971–10980.
- (56) Avinash, M. B.; Raut, D.; Mishra, M. K.; Ramamurty, U.; Govindaraju, T. Bioinspired Reductionistic Peptide Engineering for Exceptional Mechanical Properties. *Sci. Rep.* **2015**, *5*, No. 16070.
- (57) Wang, W.; Zhao, D.; Yang, J.; Nishi, T.; Ito, K.; Zhao, X.; Zhang, L. Novel Slide-Ring Material/Natural Rubber Composites with High Damping Property. *Sci. Rep.* **2016**, *6*, No. 22810.
- (58) Pelton, M.; Sader, J. E.; Burgin, J.; Liu, M.; Guyot-Sionnest, P.; Gosztola, D. Damping of acoustic vibrations in gold nanoparticles. *Nat. Nanotechnol.* **2009**, *4*, 492–495.
- (59) Eroshenko, V.; Regis, R.-C.; Soulard, M.; Patarin, J. Energetics: A New Field of Applications for Hydrophobic Zeolites. *J. Am. Chem. Soc.* **2001**, *123*, 8129–8130.
- (60) Yot, P. G.; Wahiduzzaman, M.; Elkaim, E.; Fertey, P.; Fabry, P.; Serre, C.; Maurin, G. Modulation of the mechanical energy storage performance of the MIL-47(VIV) metal organic framework by ligand functionalization. *Dalton Trans.* **2019**, *48*, 1656–1661.
- (61) Beurroies, I.; Boulhout, M.; Llewellyn, P. L.; Kuchta, B.; Férey, G.; Serre, C.; Denoyel, R. Using Pressure to Provoke the Structural Transition of Metal–Organic Frameworks. *Angew. Chem., Int. Ed.* **2010**, *49*, 7526–7529.
- (62) Maioli, P.; Stoll, T.; Saucedo, H. E.; Valencia, I.; Demessence, A.; Bertorelle, F.; Crut, A.; Vallée, F.; Garzón, I. L.; Cerullo, G.; Del Fatti, N. Mechanical Vibrations of Atomically Defined Metal Clusters: From Nano- to Molecular-Size Oscillators. *Nano Lett.* **2018**, *18*, 6842–6849.
- (63) Kang, X.; Wang, S.; Zhu, M. Observation of a new type of aggregation-induced emission in nanoclusters. *Chem. Sci.* **2018**, *9*, 3062–3068.

## Supporting Information

### Manifestation of Structural Differences of Atomically Precise Cluster Assembled Solids in Their Mechanical Properties

Korath Shivan Sugi,<sup>a</sup> Payel Bandyopadhyay,<sup>b</sup> Mohammad Bodiuzzaman,<sup>a</sup> Abhijit Nag,<sup>a</sup> Manjapoyil Hridya,<sup>a</sup> Wakeel Ahmed Dar,<sup>a</sup> Pijush Ghosh,<sup>\*b</sup> and Thalappil Pradeep<sup>\*a</sup>

<sup>a</sup> *DST Unit of Nanoscience (DST UNS) and Thematic Unit of Excellence (TUE), Department of Chemistry, Indian Institute of Technology Madras, Chennai 600 036, India*

<sup>b</sup> *Department of Applied Mechanics, Indian Institute of Technology Madras, Chennai 600036, India.*

*\*E-mail:* [pijush@iitm.ac.in](mailto:pijush@iitm.ac.in) and [pradeep@iitm.ac.in](mailto:pradeep@iitm.ac.in)

### Table of contents

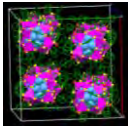
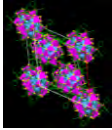
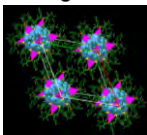
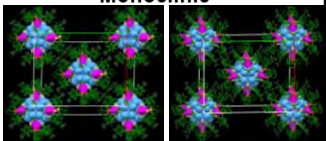
SL. No.	Description	Page No.
Table S1	Structural parameters of the cluster single crystals tested	4
Figure S1	Characterization of Ag <sub>29</sub> C clusters	4
Figure S2	Characterization of Ag <sub>29</sub> T clusters	5
Figure S3	Structural anatomy of Ag <sub>29</sub> C and Ag <sub>29</sub> T cluster crystals	6
Figure S4	Face index analysis of Ag <sub>29</sub> T	6
Figure S5	Piezo images of residual indentation imprint on Ag <sub>29</sub> C and Ag <sub>29</sub> T crystals	7
Figure S6	Loading rate-dependent load-displacement plots of Ag <sub>29</sub> C crystals	7
Figure S7	Loading rate-dependent load-displacement plots of Ag <sub>29</sub> T crystals	8
Figure S8	Experimental creep of Ag <sub>29</sub> C and Ag <sub>29</sub> T cluster crystals with 500 $\mu$ N and 10,000 $\mu$ N load	8
Figure S9	Strain hardening of Ag <sub>29</sub> C and Ag <sub>29</sub> T cluster crystals	9
Figure S10	Variation of experimental creep and stress relaxation of Ag <sub>29</sub> C and Ag <sub>29</sub> T cluster crystals with loading rate	10

Figure S11	Maxwell-Weichert model	11
Figure S12	Fitted stress relaxation curves of Ag <sub>29</sub> C and Ag <sub>29</sub> T systems	12
Table S2	G <sub>0</sub> , G <sub>1</sub> , $\tau_1$ , and $\tau_2$ values of Ag <sub>29</sub> C and Ag <sub>29</sub> T systems	12
Figure S13	Crystal packing of Ag <sub>29</sub> C and Ag <sub>29</sub> T systems	12
Figure S14	Ag <sub>29</sub> cluster in cubic lattice having two TPP bundles	13
Figure S15	Intercluster interactions of Ag <sub>29</sub> clusters in cubic lattice	14
Figure S16	Bond angle of the CH... $\pi$ interactions in Ag <sub>29</sub> C crystal	14
Figure S17	Intercluster interactions of Ag <sub>29</sub> clusters in trigonal lattice	15
Figure S18	Characterization of Ag <sub>46</sub> T clusters	16
Figure S19	Characterization of Ag <sub>40/46</sub> M clusters	17
Figure S20	Structural anatomy of Ag <sub>46</sub> T cluster crystals	17
Figure S21	Structural anatomy of Ag <sub>40/46</sub> M cluster crystals	18
Figure S22	Piezo image of residual indentation imprint on Ag <sub>46</sub> T crystal	19
Table S3	E <sub>r</sub> and H values of Ag <sub>46</sub> T and Ag <sub>40/46</sub> M crystal systems	19
Figure S23	Loading rate-dependent load-displacement plots of Ag <sub>46</sub> T crystals	20
Figure S24	Loading rate-dependent load-displacement plots of Ag <sub>40/46</sub> M crystals	21
Figure S25	Variation of H with loading rate of Ag <sub>46</sub> T and Ag <sub>40/46</sub> M	21
Figure S26	Experimental creep of Ag <sub>46</sub> T and Ag <sub>40/46</sub> M cluster crystals at 500 $\mu$ N and 10,000 $\mu$ N load	22
Figure S27	Strain hardening of Ag <sub>46</sub> T and Ag <sub>40/46</sub> M cluster crystals	22
Figure S28	Stress relaxation plots of Ag <sub>46</sub> T and Ag <sub>40/46</sub> M cluster	23



	crystals	
Figure S29	Variation of experimental creep and stress relaxation of Ag <sub>46</sub> T and Ag <sub>40/46</sub> M cluster crystals with loading rate	24
Figure S30	Fitted stress relaxation curves of Ag <sub>46</sub> T and Ag <sub>40/46</sub> M crystal systems	24
Table S4	G <sub>α</sub> , G <sub>0</sub> , τ <sub>1</sub> , and τ <sub>2</sub> values of Ag <sub>46</sub> T and Ag <sub>40/46</sub> M crystal systems	25
Figure S31	Intercluster interactions of Ag <sub>46</sub> T and Ag <sub>40/46</sub> M crystals	25
Figure S32	Supramolecular interactions of Ag <sub>46</sub> cluster in trigonal lattice	25
Figure S33	H...H interactions of Ag <sub>46</sub> clusters in trigonal lattice	26
Figure S34	CH...π interactions between TPP ligands of Ag <sub>46</sub> clusters in trigonal lattice	27
Figure S35	Intercluster interactions of Ag <sub>40/46</sub> clusters in monoclinic lattice	27
Figure S36	CH...π interactions directing the assembly of Ag <sub>40/46</sub> clusters in monoclinic lattice	28
Figure S37	Variation of loss modulus with frequency of all the four crystal systems	29

**Table S1.** Structural parameters of the cluster single crystals tested.

Cluster	Ligand	Crystal system	Density	Z
$\text{Ag}_{29}(\text{BDT})_{12}(\text{TPP})_4$	1,3 Benzene dithiol	Cubic 	$2.116 \text{ g/cm}^{-3}$	8
$\text{Ag}_{29}(\text{BDT})_{12}(\text{TPP})_4$	1,3 Benzene dithiol	Trigonal 	$2.041 \text{ g/cm}^{-3}$	6
$\text{Ag}_{46}(\text{DMBT})_{24}(\text{TPP})_8$	2,5 Dimethyl benzene thiol	Trigonal 	$1.322 \text{ g/cm}^{-3}$	1
$\text{Ag}_{40}(\text{DMBT})_{24}(\text{TPP})_8 + \text{Ag}_{46}(\text{DMBT})_{24}(\text{TPP})_8$	2,4 Dimethyl benzene thiol	Monoclinic 	$1.497 \text{ g/cm}^{-3}$	2

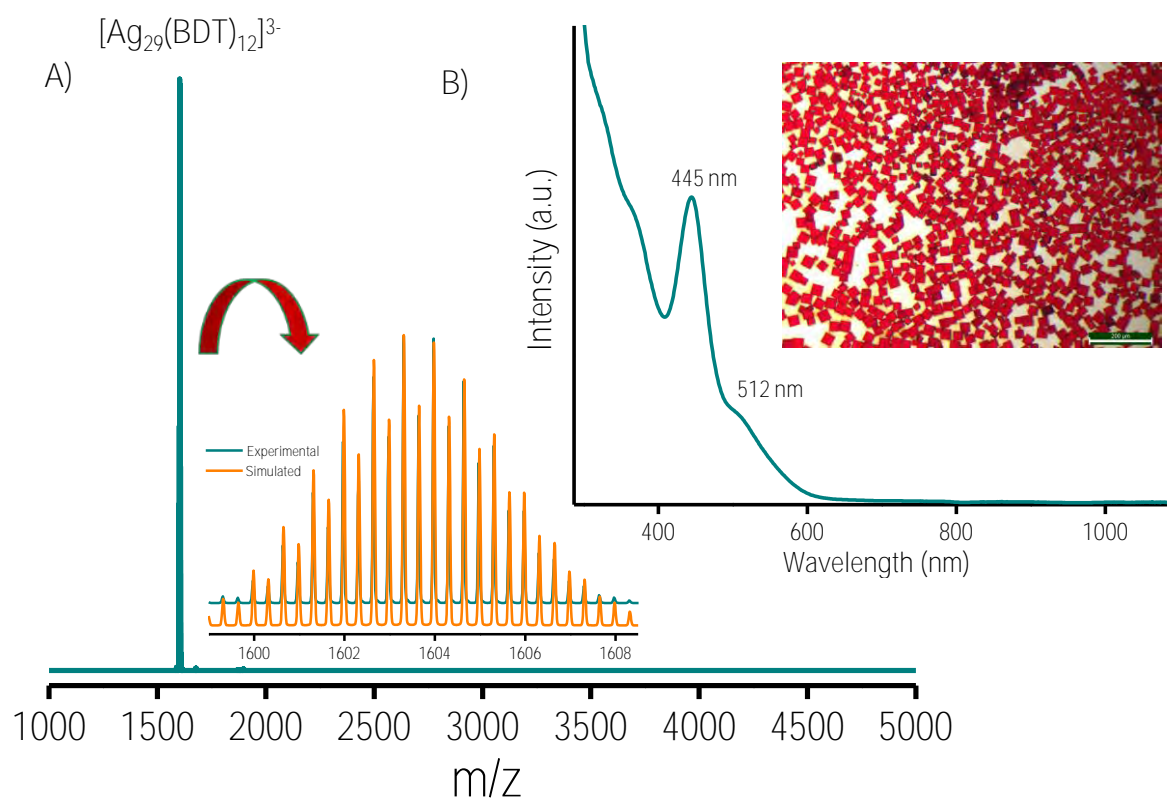


**Figure S1.** Characterization of  $\text{Ag}_{29}$  C clusters. A) Full range ESI MS of  $\text{Ag}_{29}(\text{BDT})_{12}(\text{TPP})_4$  clusters in negative mode. Inset shows the comparison of experimental (cyan trace) and

simulated (orange trace) isotopic distributions of the cluster. B) UV-vis absorption spectrum of the  $\text{Ag}_{29}(\text{BDT})_{12}(\text{TPP})_4$  cluster in dimethylformamide (DMF). Inset of the B shows the optical images of  $\text{Ag}_{29}$  C crystals collected in the transmission mode.

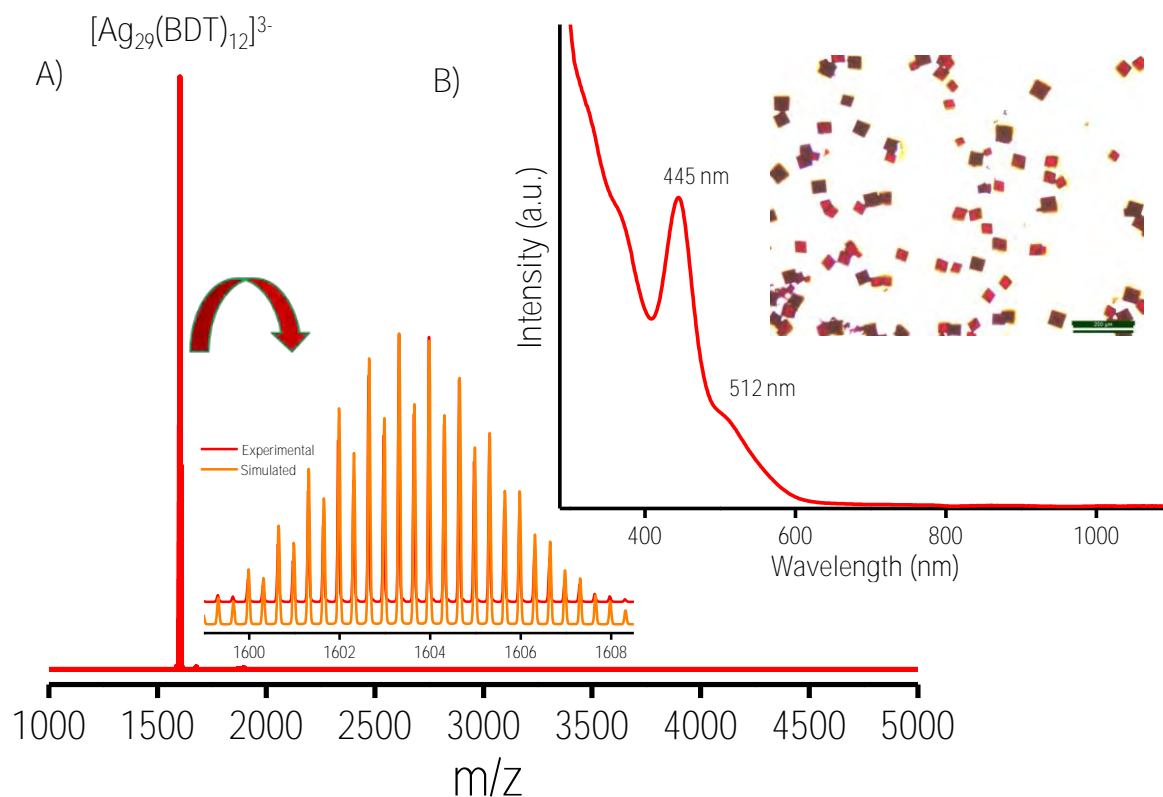


**Figure S2.** Characterization of  $\text{Ag}_{29}$  T clusters. A) Full range ESI MS of  $\text{Ag}_{29}(\text{BDT})_{12}(\text{TPP})_4$  clusters in negative mode. Inset shows the comparison of experimental (red trace) and simulated (orange trace) isotopic distributions of the cluster. B) UV-vis absorption spectrum of the  $\text{Ag}_{29}(\text{BDT})_{12}(\text{TPP})_4$  cluster in DMF. Inset of the B shows the optical images of  $\text{Ag}_{29}$  T crystals collected in transmission mode.

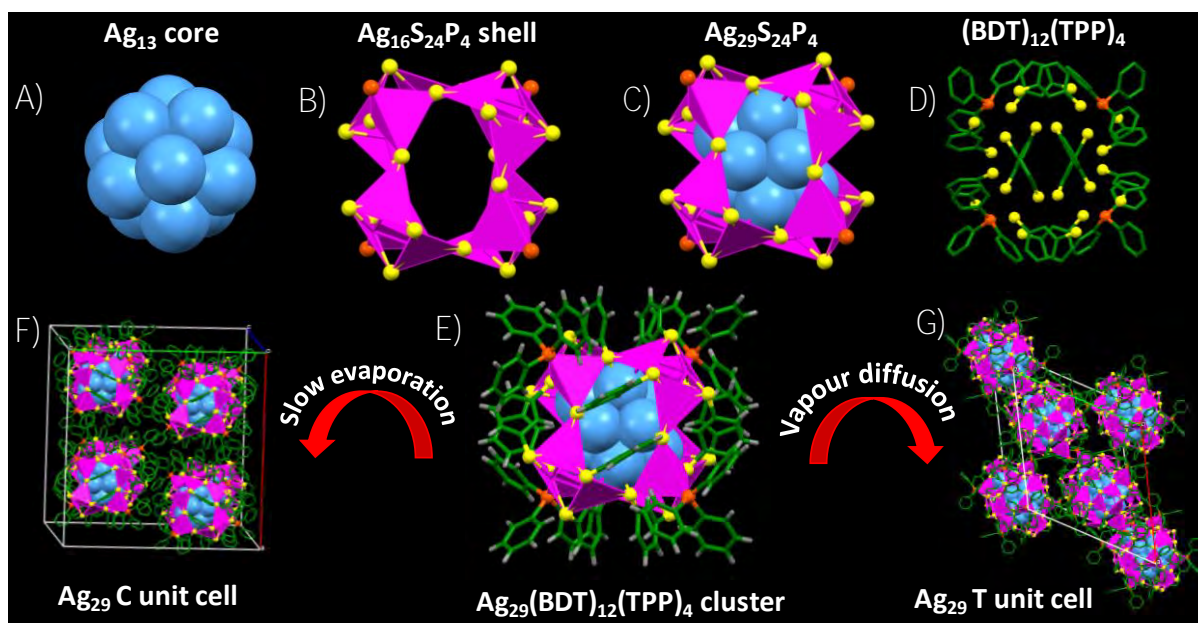


**Figure S3.** Structural anatomy of  $\text{Ag}_{29}$  C and T clusters. A)  $\text{Ag}_{13}$  centred icosahedral core; B)  $\text{Ag}_{16}\text{S}_{24}\text{P}_4$  shell; C)  $\text{Ag}_{29}\text{S}_{24}\text{P}_4$  motifs where the ligands are omitted for clarity. D) The packing of BDT and TPP ligands in an  $\text{Ag}_{29}$  cluster. E) Total structure of  $\text{Ag}_{29}(\text{BDT})_{12}(\text{TPP})_4$  cluster. F) and G) are the unit cell packing of  $\text{Ag}_{29}$  C and  $\text{Ag}_{29}$  T. Color codes: cerulean/magenta, Ag; yellow, S; orange, P; green, C; grey, H.

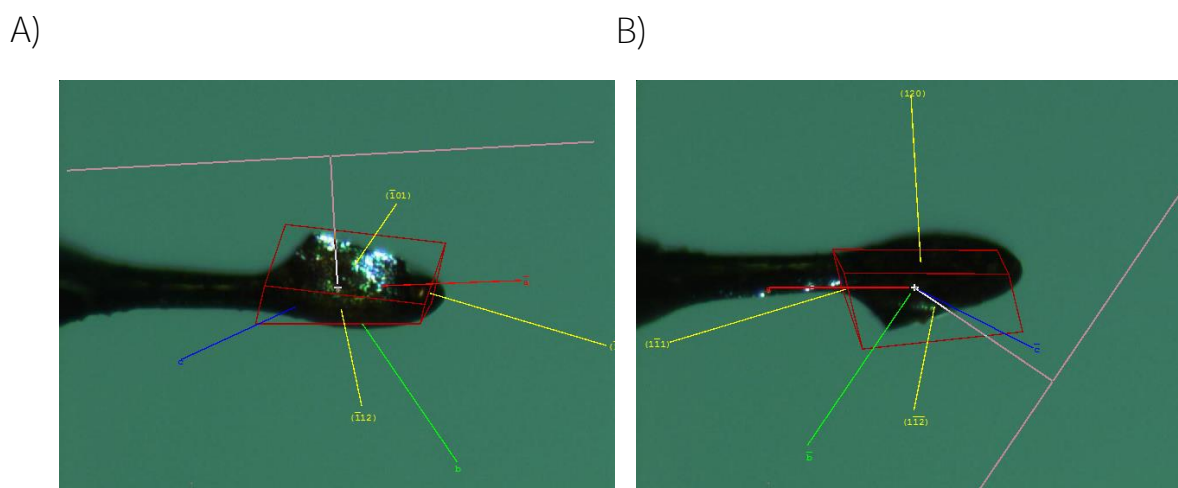


**Figure S4.** Face index analysis of  $\text{Ag}_{29}$  T based on single crystal X-ray crystallography. The crystal is mounted on MiTeGen loop.

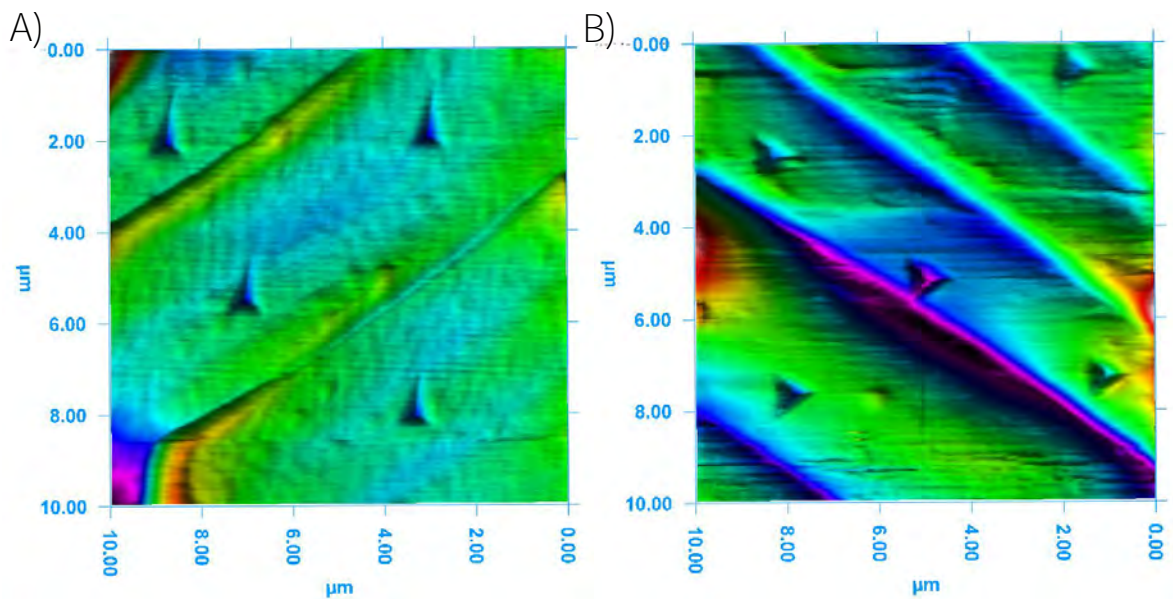


**Figure S5.** Piezo images showing residual indentation imprint on A) Ag<sub>29</sub> C and B) Ag<sub>29</sub> T crystals.

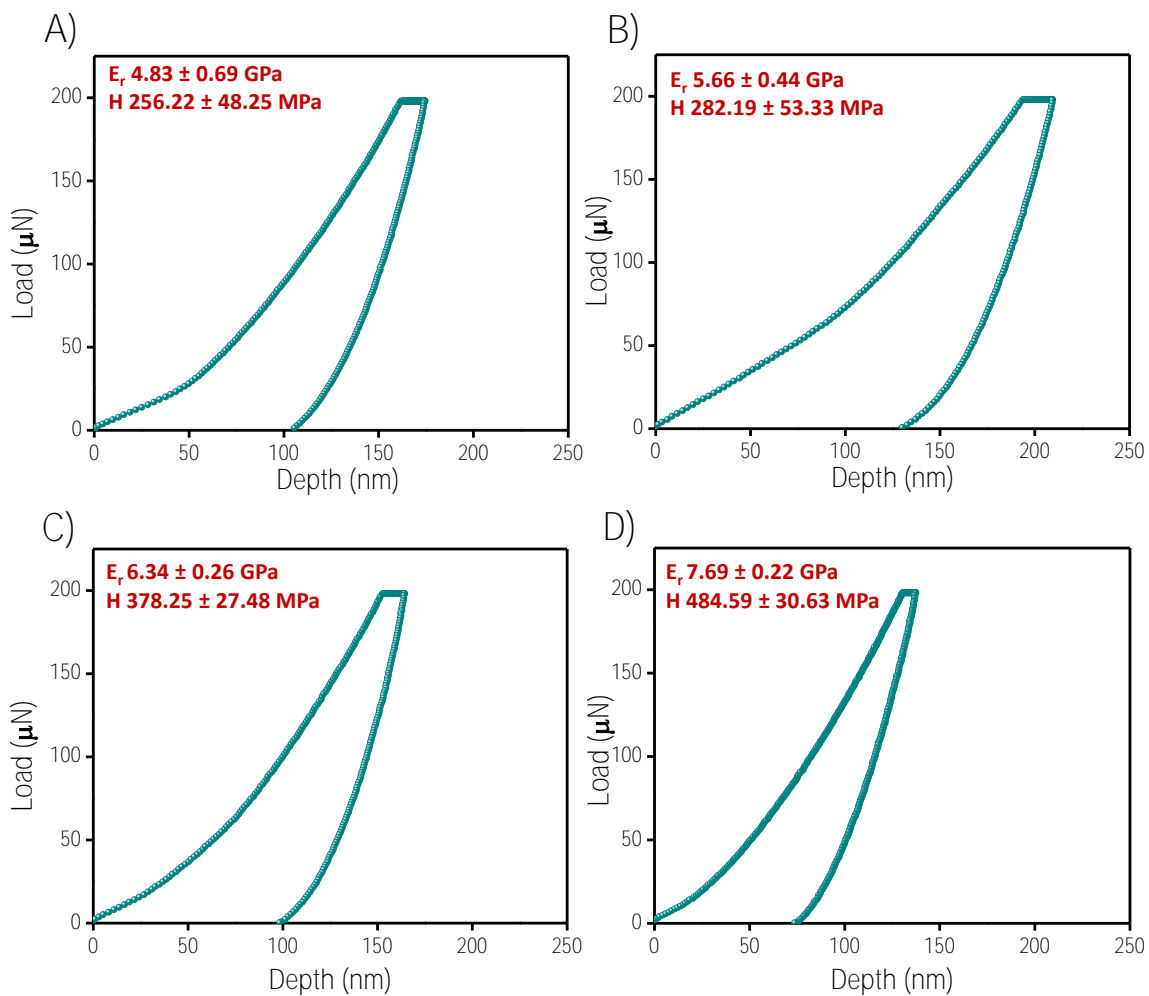


**Figure S6.** Load-displacement curves of Ag<sub>29</sub> C crystals with loading rates of A) 20, B) 10, C) 6.6, and D) 4  $\mu\text{N/s}$ , respectively.

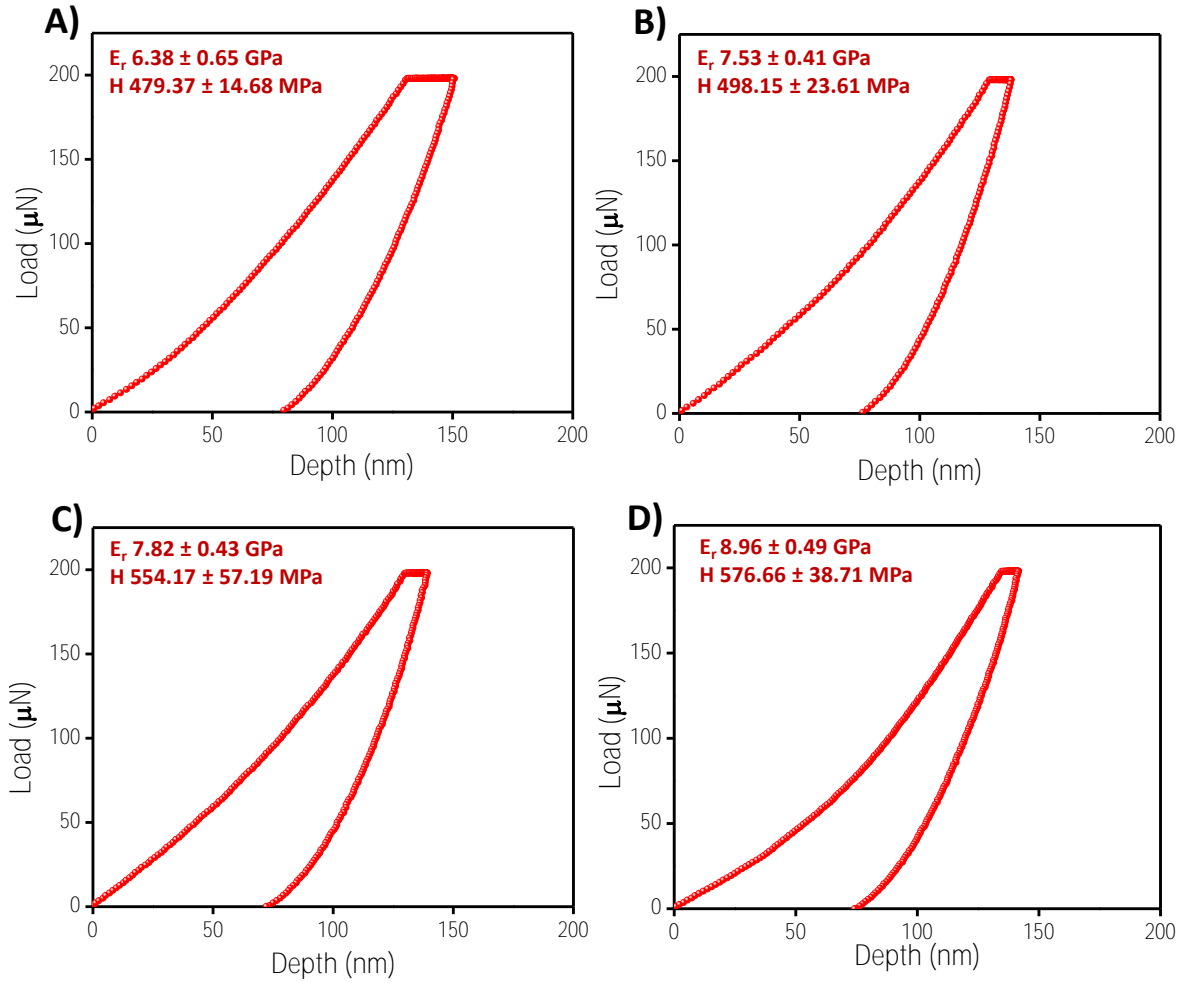


**Figure S7.** Load-displacement curves of Ag<sub>29</sub> T crystals with loading rates of A) 20, B) 10, C) 6.6, and D) 4  $\mu\text{N/s}$ , respectively.

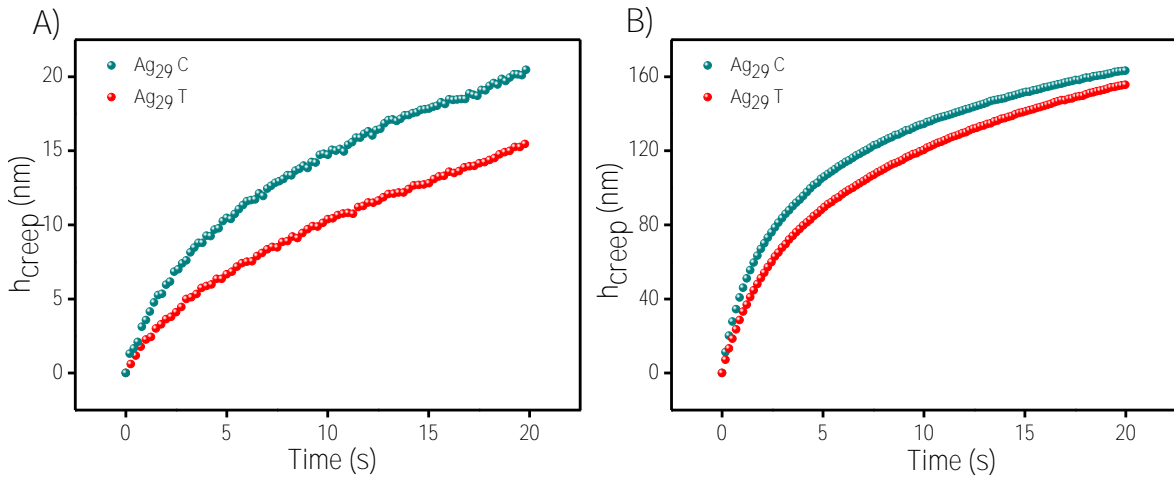


**Figure S8.** Experimental creep curves corresponding to Ag<sub>29</sub> C (cyan trace) and Ag<sub>29</sub> T (red trace) crystal system at a load of A) 500  $\mu\text{N}$  and B) 10,000  $\mu\text{N}$ , respectively.



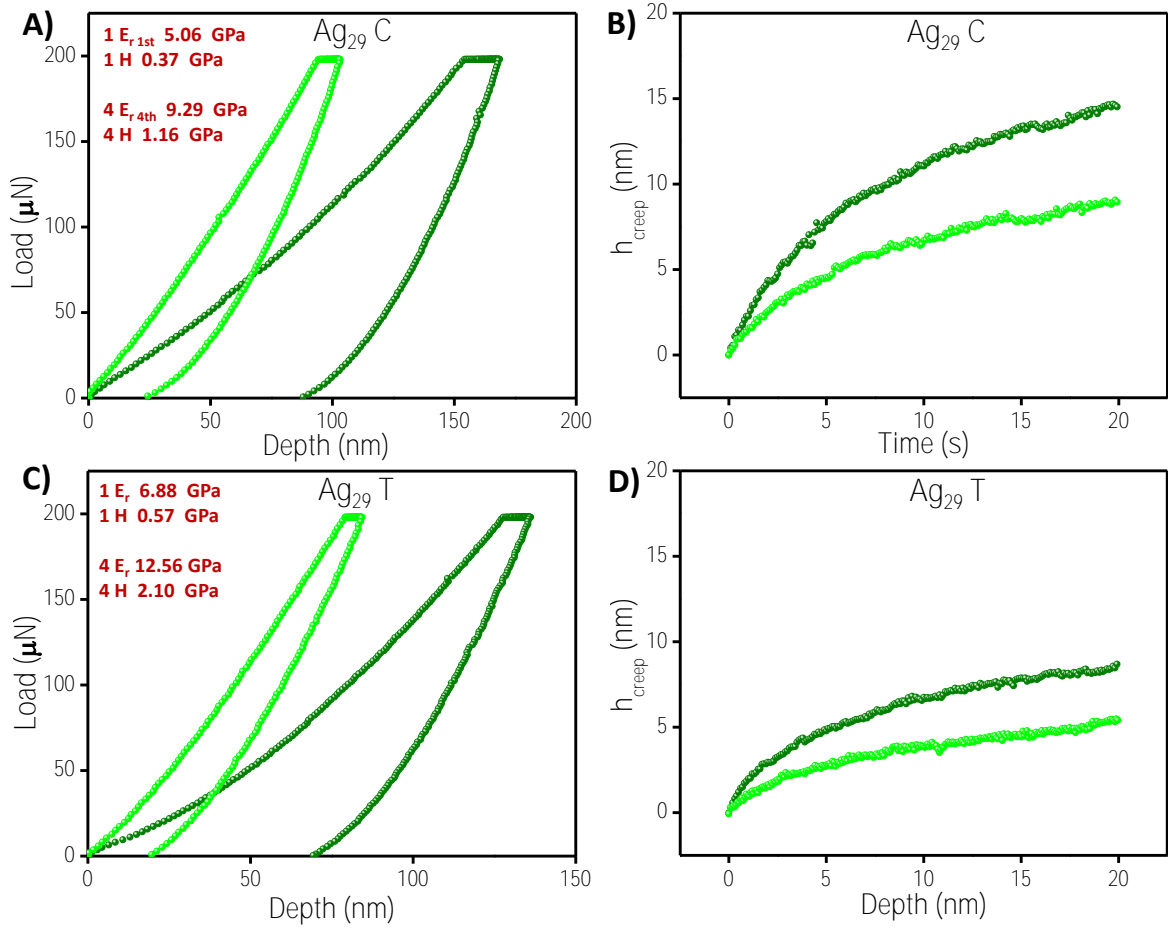


**Figure S9.** All single-crystal samples underwent the same experiment four times on the same indentation area. A) and C) are the load-displacement plots of  $\text{Ag}_{29}$  C and  $\text{Ag}_{29}$  T crystals (first cycle olive and fourth cycle green). B) and D) are the creep displacement plots of  $\text{Ag}_{29}$  C and  $\text{Ag}_{29}$  T (first cycle olive and fourth green). Corresponding  $E_r$  and  $H$  values are indicated. A significant reduction in creep displacement is observed for the fourth measurement indicating an increased resistance to plastic deformation. This observation is consistent with strain hardening.

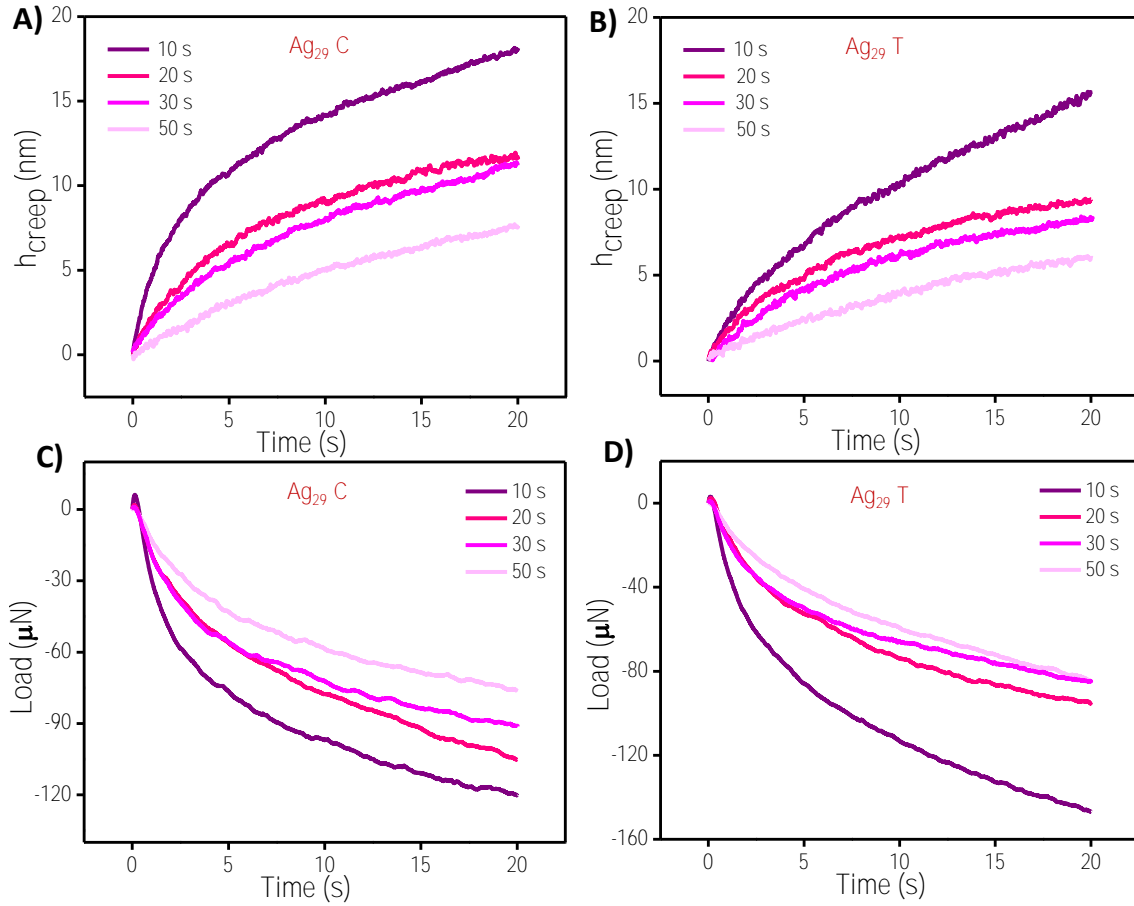


**Figure S10.** Experimental creep curves with loading rates of 20, 10, 6.6, and 4  $\mu\text{N/s}$  (top A and B) and stress relaxation curves with displacement rates of 25, 12.5, 8.33, and 5 nm/s. (bottom C and D) corresponding to  $\text{Ag}_{29}\text{C}$  and  $\text{Ag}_{29}\text{T}$  crystal systems.

### Modelling of stress-relaxation

The relaxation of the maximum load during holding to a certain depth is related to the time dependent, i.e., viscoelastic behaviour of the material. The instantaneous, i.e., elastic behaviour can be captured by a spring and the viscous behaviour can be depicted by a dashpot. A spring connected with a dashpot is called as a Maxwell element. One or more Maxwell element in parallel are used to model the stress relaxation of a material.

For a spherical indenter tip, the load–displacement relationship for a Hertzian elastic solid<sup>1</sup> is showed in equation [1]

$$P = 8G \frac{\sqrt{Rh^3(t)}}{3(1-\nu)} \quad [1]$$

where  $G$  is the shear modulus,  $R$  is the indenter radius,  $\nu$  is the Poisson's ratio, and  $h(t)$  is the displacement as a function of time. For the generalized Maxwell–Wiechert viscoelastic model,<sup>2, 3</sup> this equation can be rewritten in terms of a time-dependent relaxation modulus function,  $G_{\text{rel}}(t)$ , for the stress-relaxation response to an instantaneous ramp displacement,  $h_0$ .

$$P = 4G_{rel}(t) \frac{\sqrt{Rh_0^3}}{3} \quad [2]$$

The stress relaxation data of the four CAS systems are fitted with two parameter Maxwell-Weichert model i.e., Figure S11. The total stress in the network will be the summation of the stress in individual arm. So, total stress  $\sigma$

$$\sigma = \sigma_e + \sum_j \sigma_j \quad [3]$$

So, the relaxation modulus  $G_{rel}(t)$  is given by

$$G_{rel}(t) = \frac{\sigma}{\epsilon_0} = G_e + \sum_j G_j \exp\left(-\frac{t}{\tau_j}\right) \quad [4]$$

The experimental data of four crystals have been plotted and fitted in two parameter Maxwell-Weichert model which is described in Figure S11.  $G_\infty$  is the relaxation modulus at  $t$  tends to infinity which is equal to  $G_e$ .  $G_0$  is the value of instantaneous relaxation modulus, i.e., relaxation modulus at  $t=0$  and which is  $G_\infty + \sum_j G_j$ . The  $\tau_1$  and  $\tau_2$  are the primary and secondary relaxation times, i.e., the relaxation times of the first and second arm respectively.

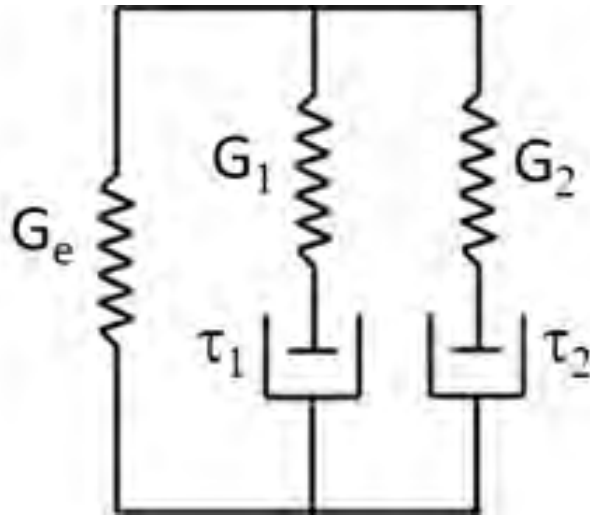


**Figure. S11.** Maxwell-Weichert model.

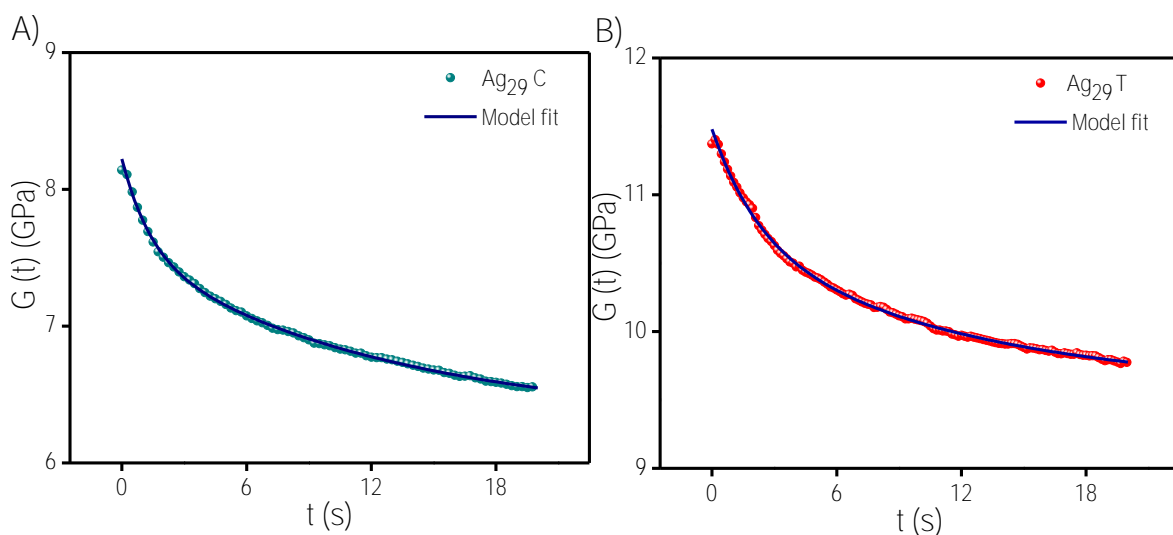


**Figure S12.** Experimental stress relaxation curves of A) Ag<sub>29</sub> C and B) Ag<sub>29</sub> T crystals fitted with the model (blue solid line) which captures the stress relaxation behaviour.

**Table S2.**  $G_0$ ,  $G_\alpha$ ,  $\tau_1$  and  $\tau_2$  values of Ag<sub>29</sub> C and T systems.

CAS	$G_0$ (GPa)	$G_\alpha$ (GPa)	$\tau_1$ (s)	$\tau_2$ (s)	$R^2$
Ag <sub>29</sub> C	8.21	6.28	1.37	12.81	0.99
Ag <sub>29</sub> T	11.50	9.58	12.16	2.22	0.99

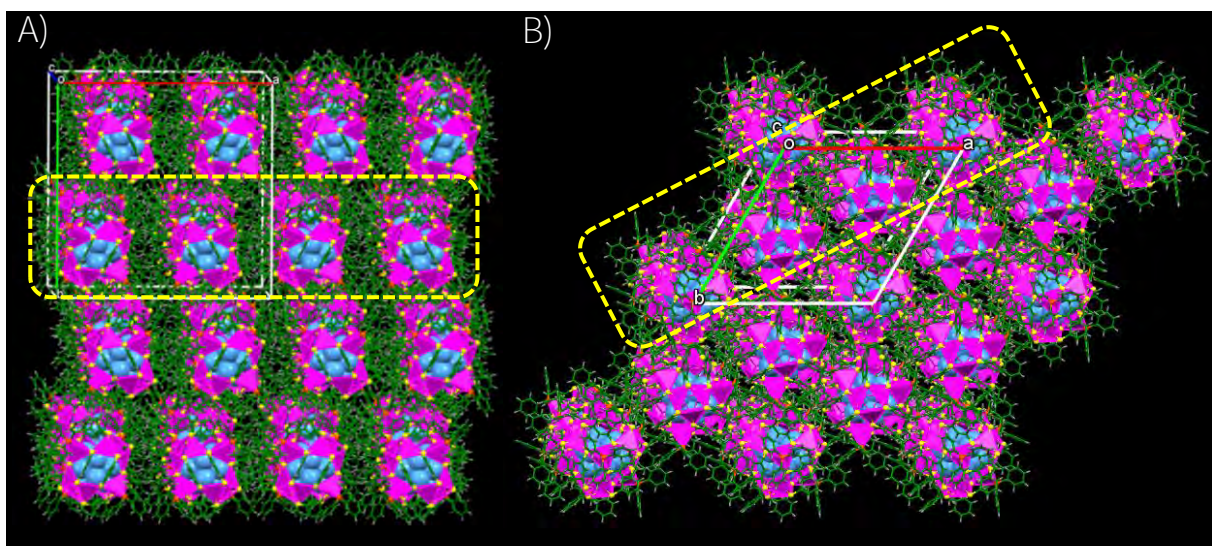


**Figure S13.** The 2x2x2 packing of A) Ag<sub>29</sub> C and B) Ag<sub>29</sub> T crystals showing linear arrangements of clusters (dotted yellow line). Color codes: cerulean/magenta, Ag; yellow, S; orange, P; green, C; grey, H.

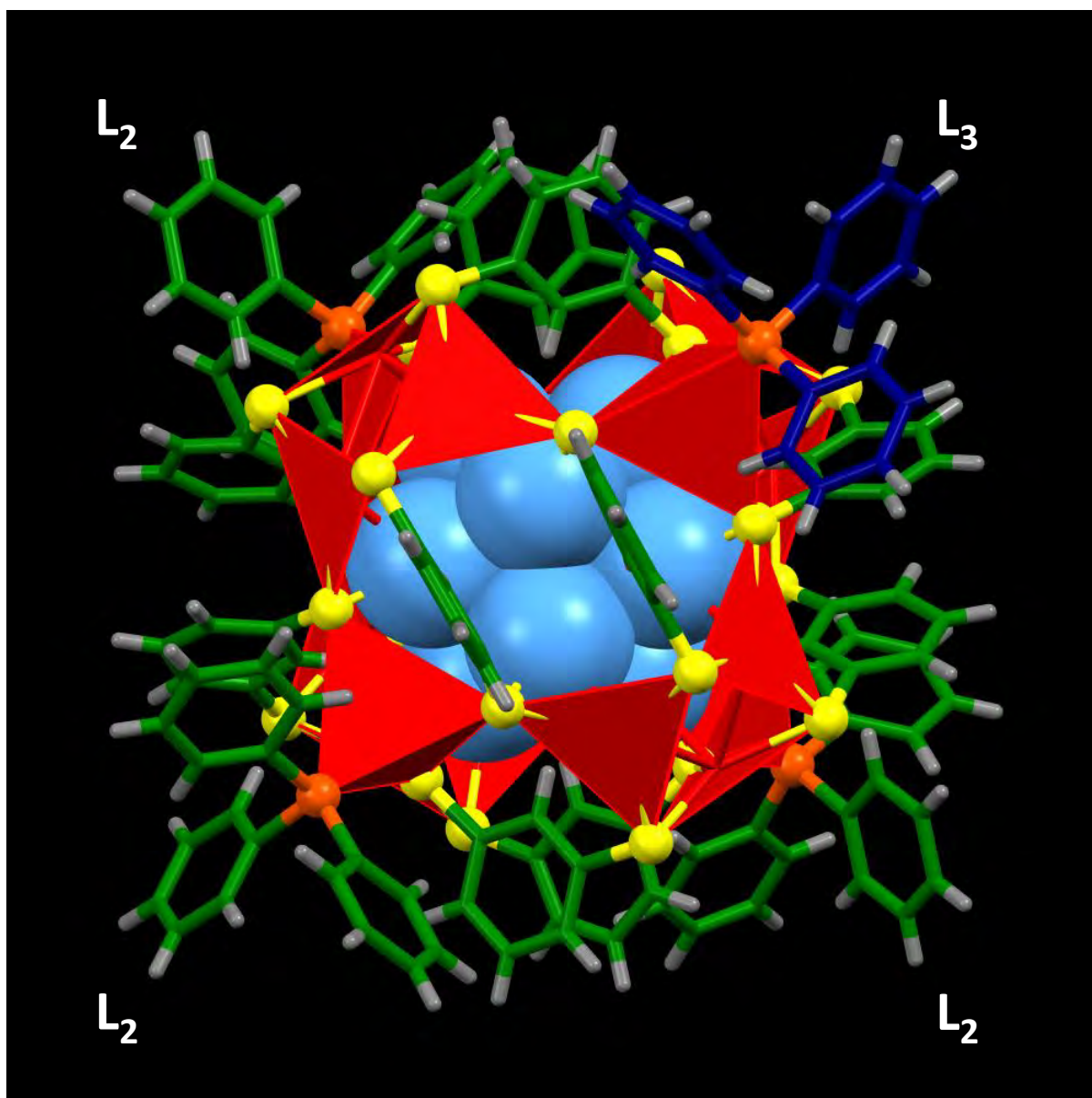


**Figure S14.** Total structure of Ag<sub>29</sub> C with TPP ligand bundles in two ways: double-bundles (L<sub>2</sub>) and triple bundles (L<sub>3</sub>- blue trace) of CH... $\pi$  interactions. Color codes: cerulean/red, Ag; yellow, S; orange, P; green/blue, C; grey, H.

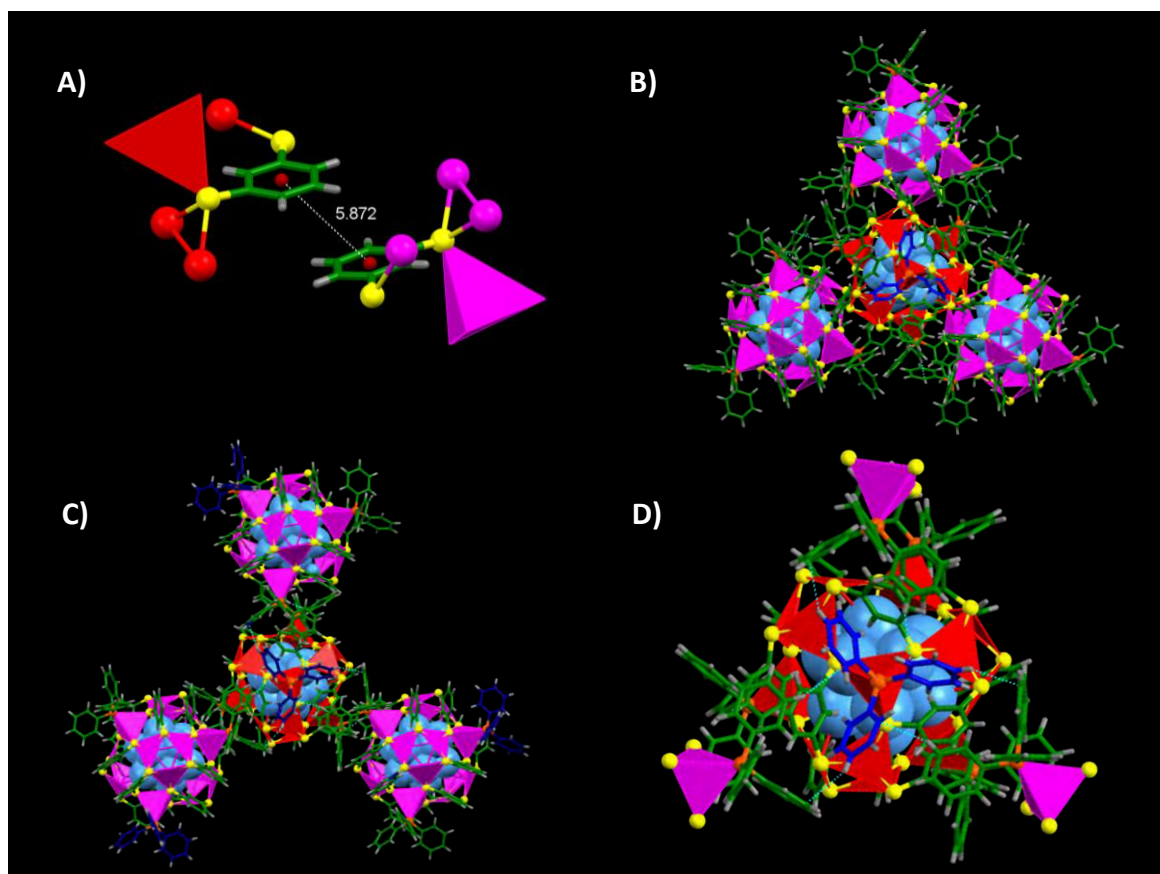


**Figure S15.** The intercluster interactions in  $\text{Ag}_{29}$  clusters in cubic lattice. A) The parallelly displaced  $\pi\cdots\pi$  interactions between the BDT ligands of  $\text{Ag}_{29}$  clusters in cubic lattice. B) Intercluster  $\text{CH}\cdots\pi$  interactions between the remaining three TPP ligands with other three clusters. C) and D) Intercluster  $\text{CH}\cdots\pi$  interactions of one TPP ligand (highlighted in blue) with TPP ligands of three neighbouring clusters in cubic lattice. Color codes: cerulean/magenta/red, Ag; yellow, S; orange, P; green/blue, C; grey, H.

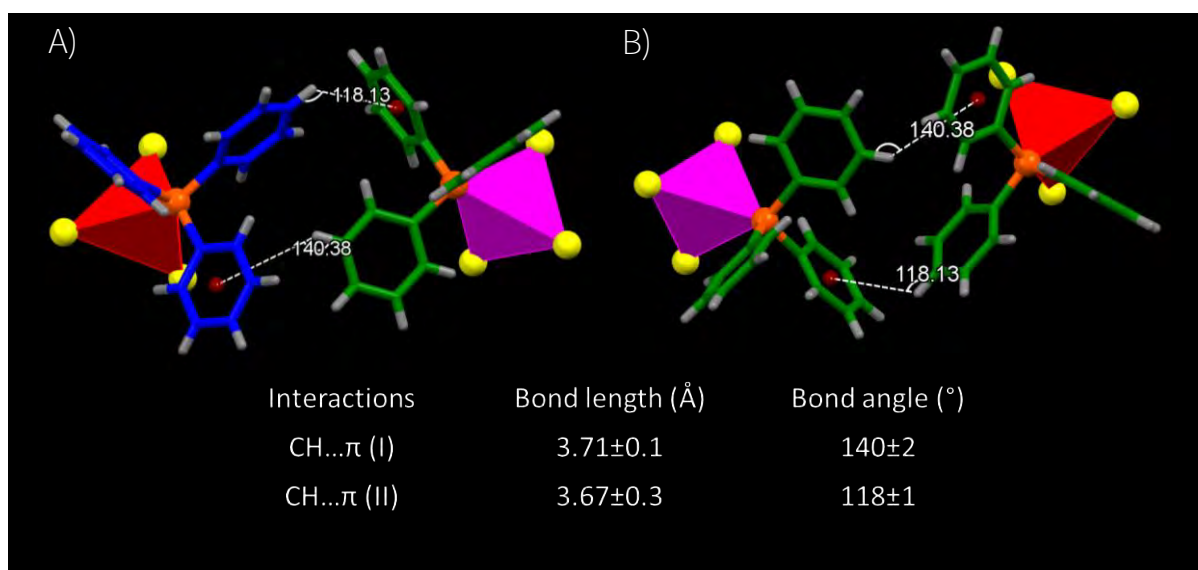




**Figure S16.** A) and B) shows the bond angle of the CH... $\pi$  interactions in Ag<sub>29</sub> cubic lattice. Color codes: magenta/red, Ag; yellow, S; orange, P; green/blue, C; grey, H.

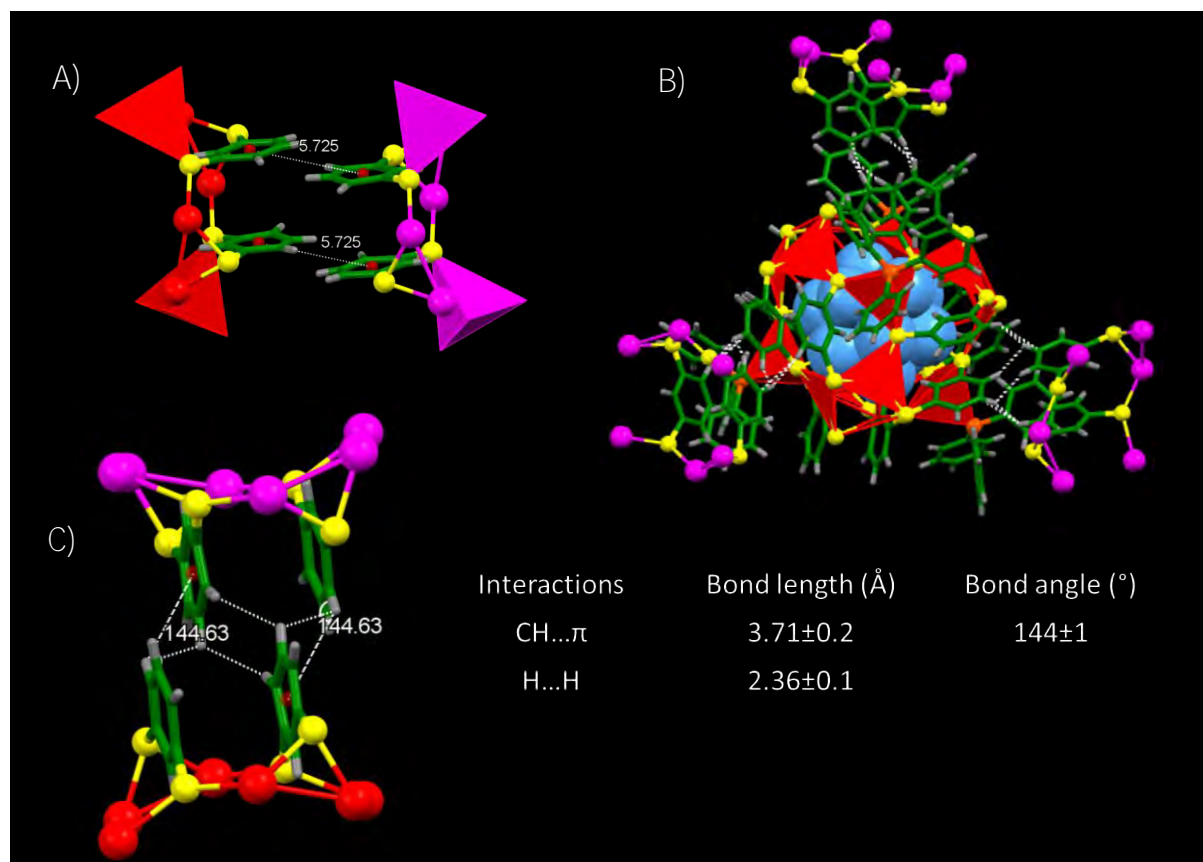


**Figure S17.** Supramolecular interactions of Ag<sub>29</sub> clusters in trigonal lattice. A) The parallelly displaced  $\pi$ ... $\pi$  interactions between the BDT ligands of Ag<sub>29</sub> clusters in trigonal lattice. B) The CH... $\pi$  and H...H interactions in Ag<sub>29</sub> T crystals. C) The bond angle of CH... $\pi$  interactions between BDT ligands. Color codes: cerulean/magenta/red, Ag; yellow, S; orange, P; green, C; grey, H.

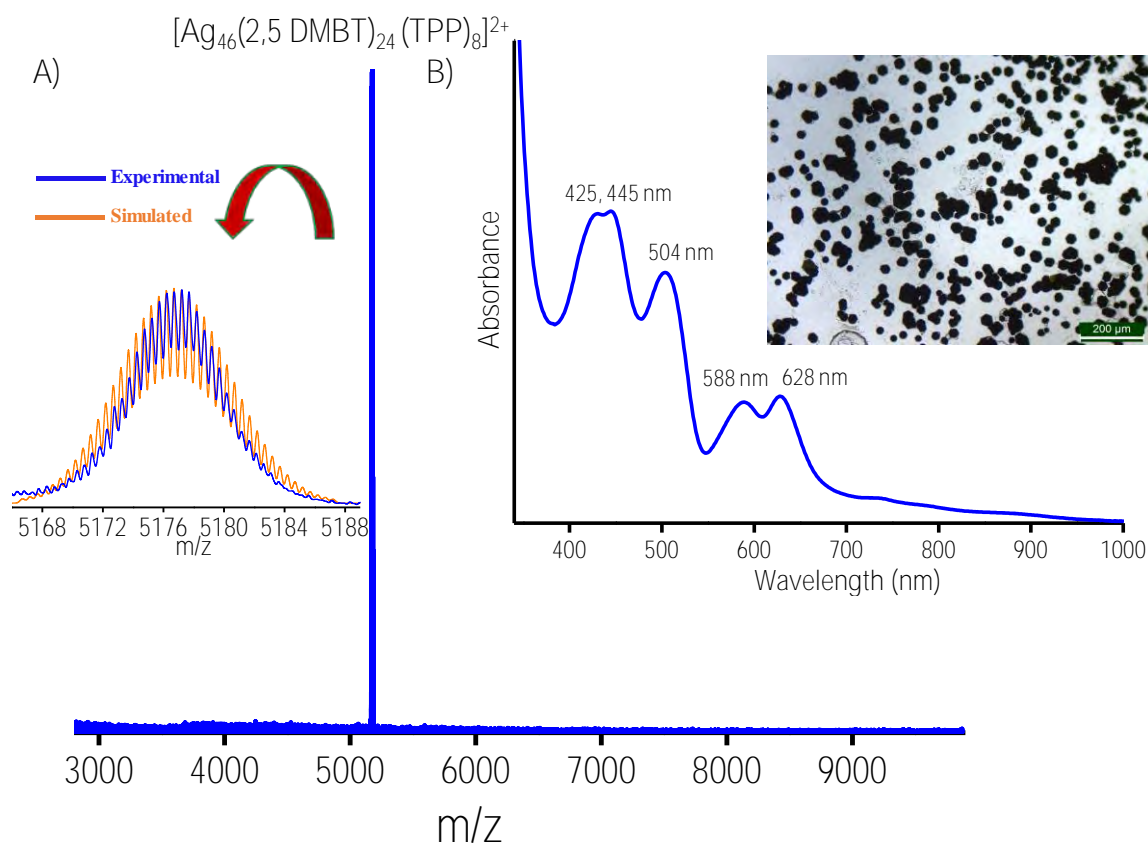


**Figure S18.** A) Full range ESI MS of clusters in positive ion mode. The peak is due to  $[Ag_{46}(2,5 \text{ DMBT})_{24}(PPh_3)_8]^{2+}$ . Inset of A show the comparison of experimental (blue trace) and simulated (orange trace) isotopic distributions of the cluster. B) UV-vis absorption spectrum of the cluster in dichloromethane. Inset is the optical image of  $Ag_{46}$  T crystals in transmission mode.

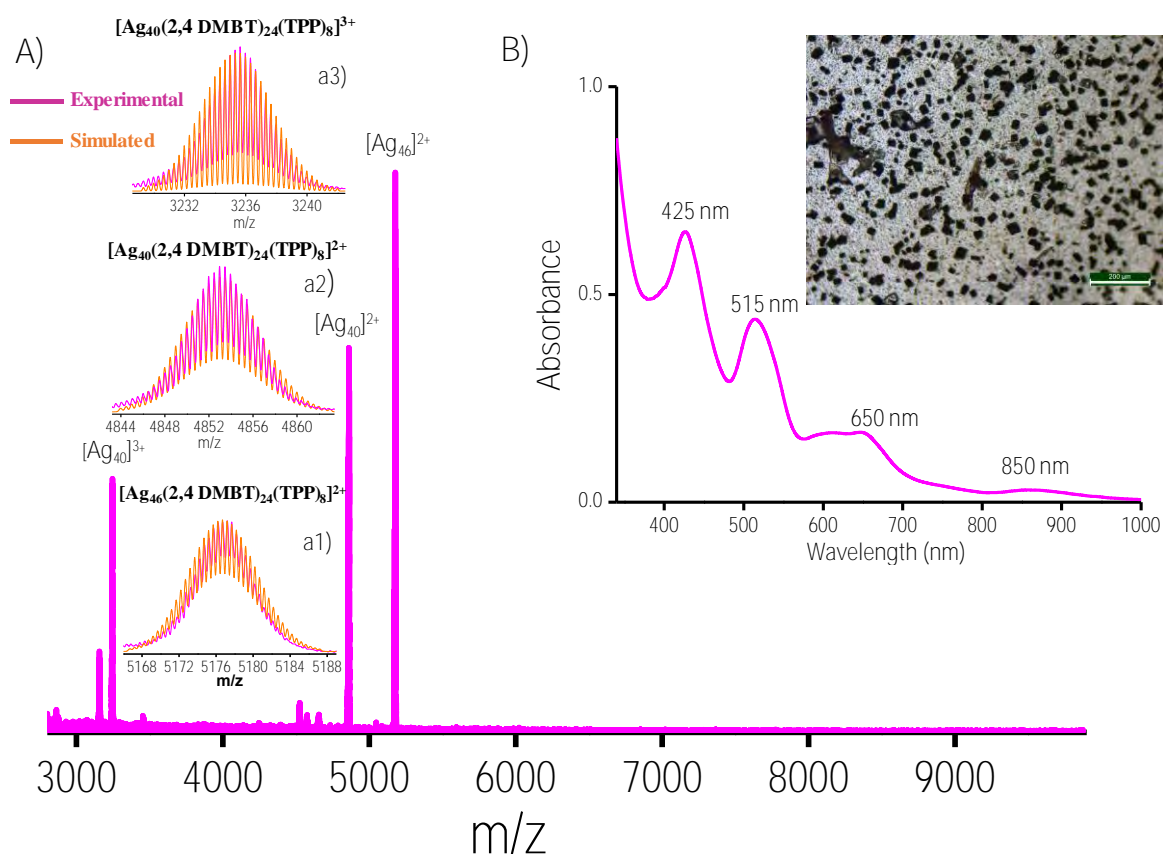


**Figure S19.** A) Full-range ESI MS of clusters in positive ion mode. The major peaks are due to  $\text{Ag}_{40}^{3+}$ ,  $\text{Ag}_{40}^{2+}$ , and  $\text{Ag}_{46}^{2+}$ . The a1, a2 and a3 are the comparison of experimental (pink trace) and simulated (orange trace) isotopic distributions of  $\text{Ag}_{46}^{2+}$ ,  $\text{Ag}_{40}^{2+}$ , and  $\text{Ag}_{40}^{3+}$ . B) UV-Vis absorption spectrum of the clusters in dichloromethane. Inset is the optical image of  $\text{Ag}_{40/46}$  M crystals in transmission mode.

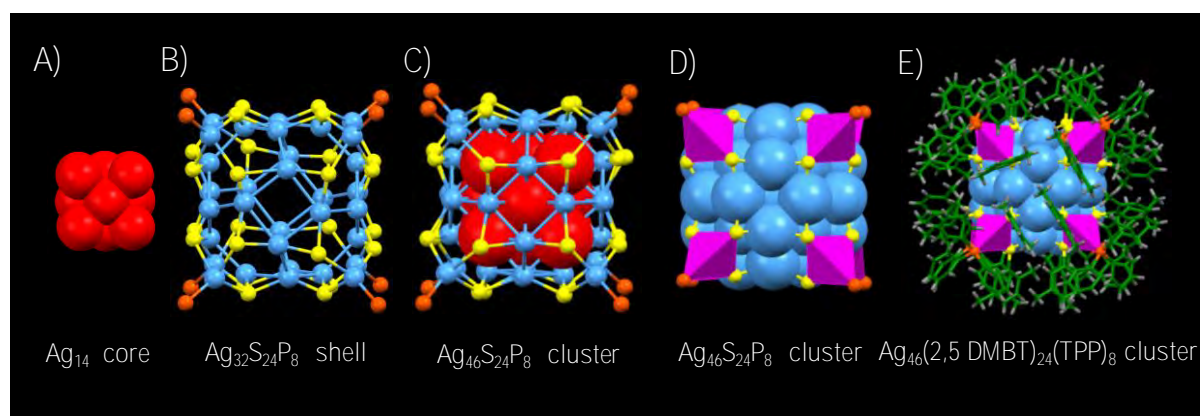


**Figure S20.** Structural anatomy of  $\text{Ag}_{46}$  T clusters. A) The  $\text{Ag}_{14}$  core; B) The  $\text{Ag}_{32}\text{S}_{24}\text{P}_8$  motifs; C) and D)  $\text{Ag}_{46}\text{S}_{24}\text{P}_8$  cluster in ball and stick and polyhedral model where the carbon tail of the ligands is omitted for clarity. E) The total structure of  $\text{Ag}_{46}(2,5 \text{ DMBT})_{24}(\text{TPP})_8$  clusters. Color codes: cerulean/magenta/red, Ag; yellow, S; orange, P; green, C; grey, H.

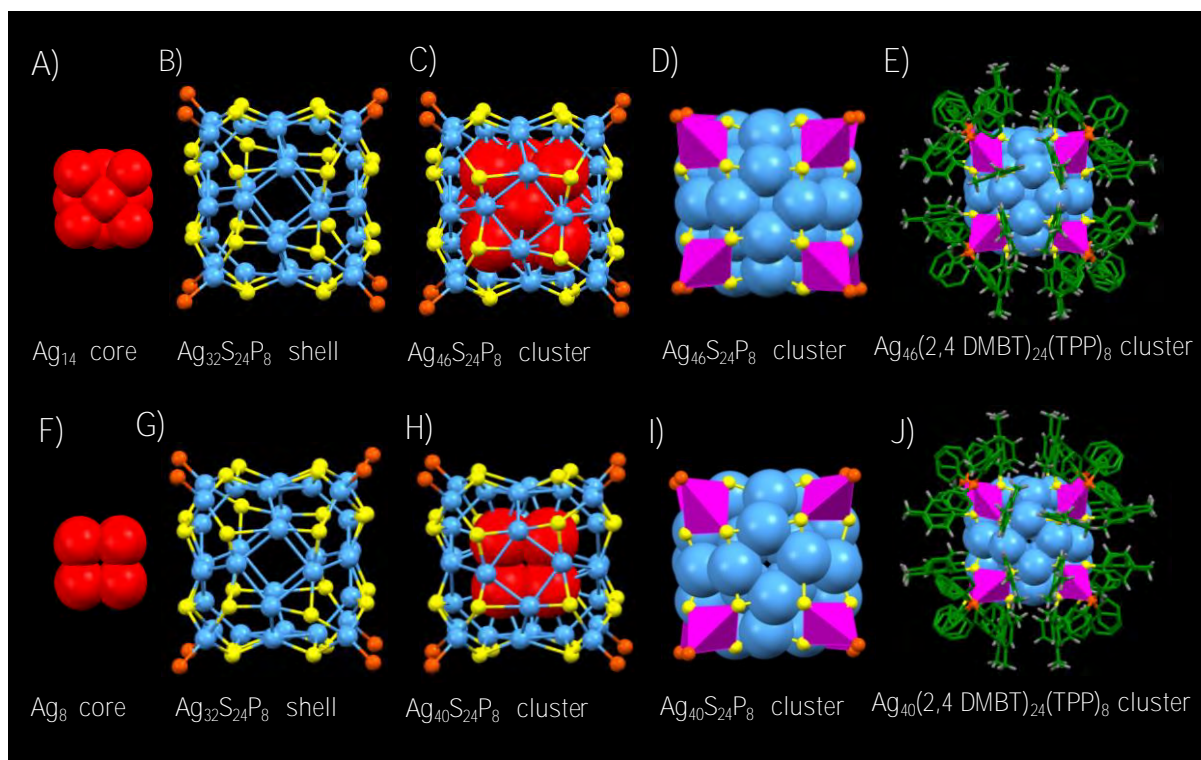


**Figure S21.** Structural anatomy of  $\text{Ag}_{46}$  and  $\text{Ag}_{40}$  clusters. A) and F) are the  $\text{Ag}_{14}$  and  $\text{Ag}_8$  inner core of  $\text{Ag}_{46}$  and  $\text{Ag}_{40}$  clusters; B) and G) are the  $\text{Ag}_{32}\text{S}_{24}\text{P}_8$  shell that protects the inner cores of both  $\text{Ag}_{46}$  and  $\text{Ag}_{40}$  clusters; C) and H) are the  $\text{Ag}_{46}\text{S}_{24}\text{P}_8$  and  $\text{Ag}_{40}\text{S}_{24}\text{P}_8$  clusters in ball and stick model where the carbon tail of the ligands are omitted for clarity. D) and I) are the  $\text{Ag}_{46}\text{S}_{24}\text{P}_8$  and  $\text{Ag}_{40}\text{S}_{24}\text{P}_8$  clusters in polyhedral model. E) and J) are the total structure of  $\text{Ag}_{46}(2,4 \text{ DMBT})_{24}(\text{TPP})_8$  and  $\text{Ag}_{40}(2,4 \text{ DMBT})_{24}(\text{TPP})_8$  clusters. Color codes: cerulean/magenta/red, Ag; yellow, S; orange, P; green, C; grey, H.

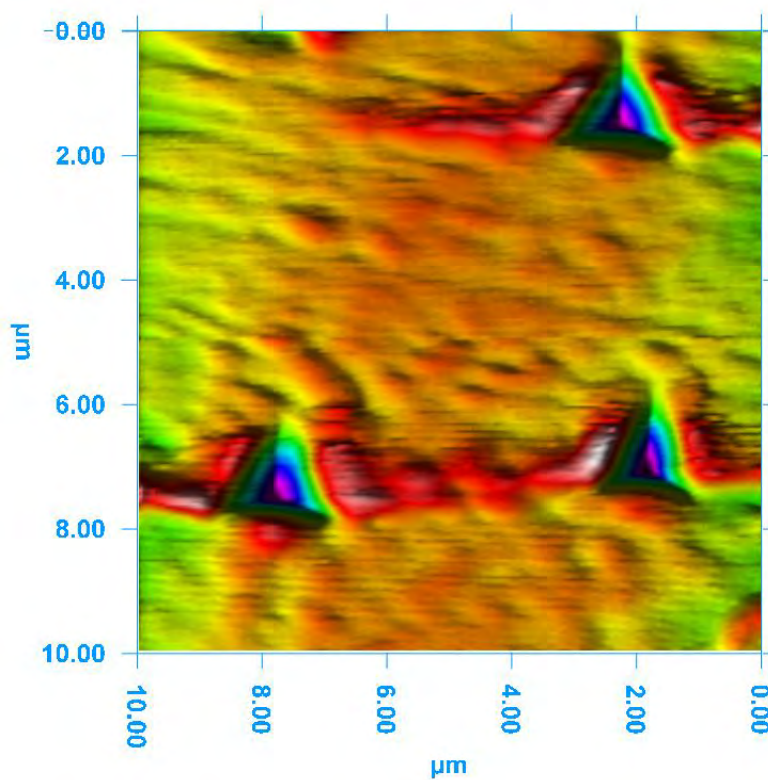


**Figure S22.** Piezo image showing residual indentation imprint on Ag<sub>46</sub> T system.

**Table S3** Measured  $E_r$  and  $H$  of Ag<sub>46</sub> T and Ag<sub>40/46</sub> M compared with their  $\rho$ .

CASs	$\rho$ (g/cm <sup>-3</sup> )	$E_r$ (GPa)	$H$ (MPa)
Ag <sub>46</sub> T	1.322	2.27±0.25	168.10±25.52
Ag <sub>40/46</sub> M	1.497	2.73±0.51	166.70±28.02

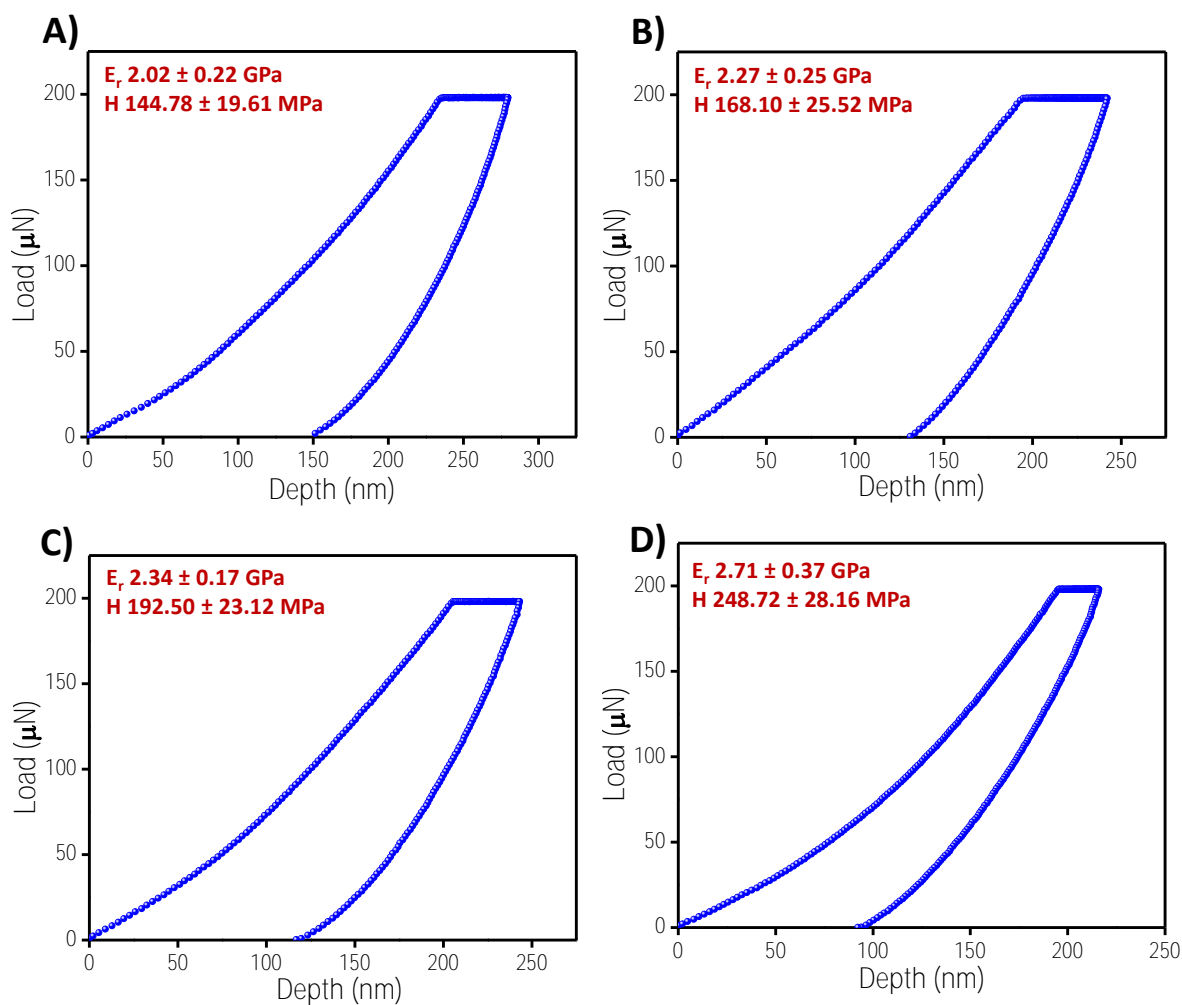


**Figure S23.** Load-displacement curves of  $\text{Ag}_{46}\text{T}$  crystals with loading rates of A) 20, B) 10, C) 6.6, and D) 4  $\mu\text{N/s}$ , respectively. The creep time of 50 s was used in this case to dissipate creep.



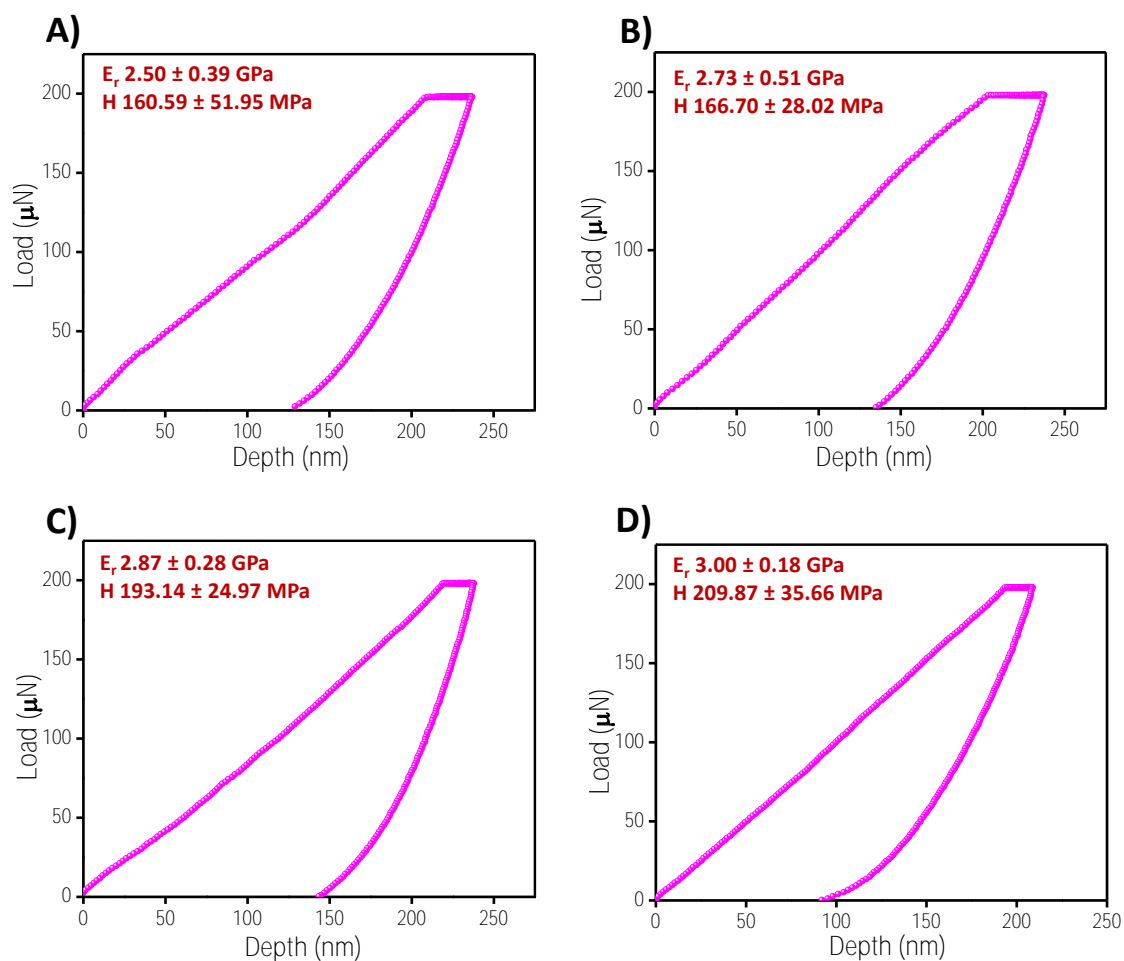


**Figure S24.** Load-displacement curves of Ag<sub>40/46</sub> M crystals with loading rates of A) 20, B) 10, C) 6.6, and D) 4  $\mu\text{N/s}$ , respectively.

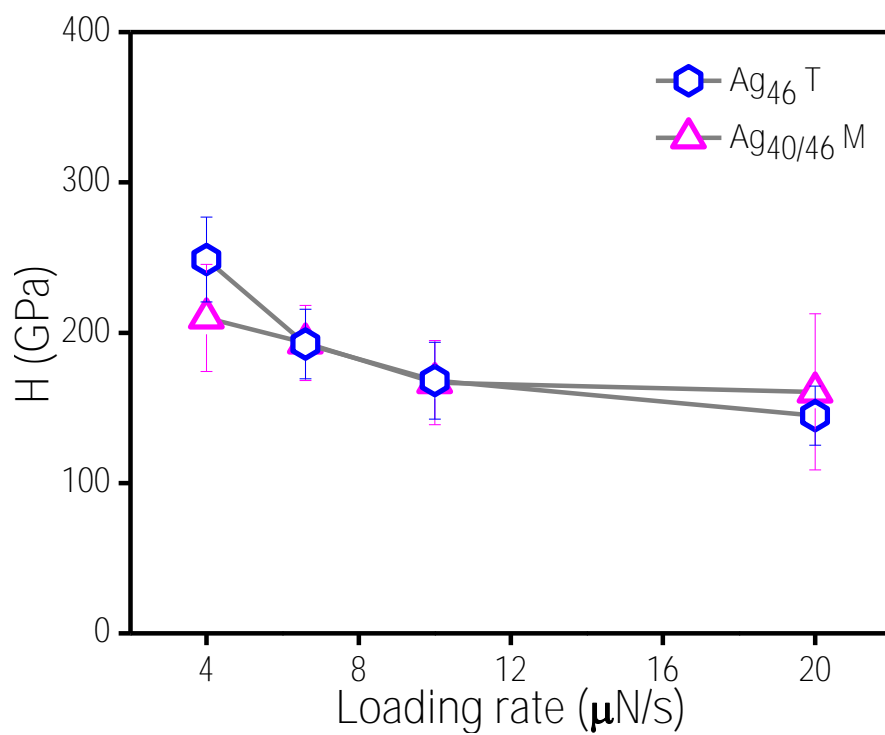


**Figure S25.** Variation of  $H$  with the loading rate of  $\text{Ag}_{46}\text{T}$  (blue trace) and  $\text{Ag}_{40/46}\text{M}$  (pink trace) crystal systems

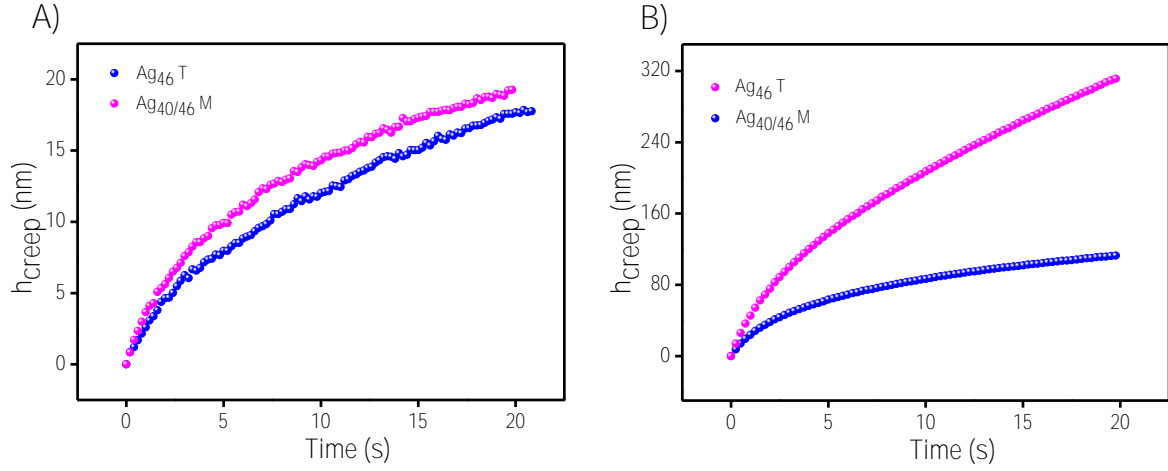


**Figure S26.** Experimental creep curves corresponding to  $\text{Ag}_{46}\text{T}$  (blue trace) and  $\text{Ag}_{40/46}\text{M}$  (pink trace) crystal systems at a load of A) 500  $\mu\text{N}$  and B) 10,000  $\mu\text{N}$ , respectively.

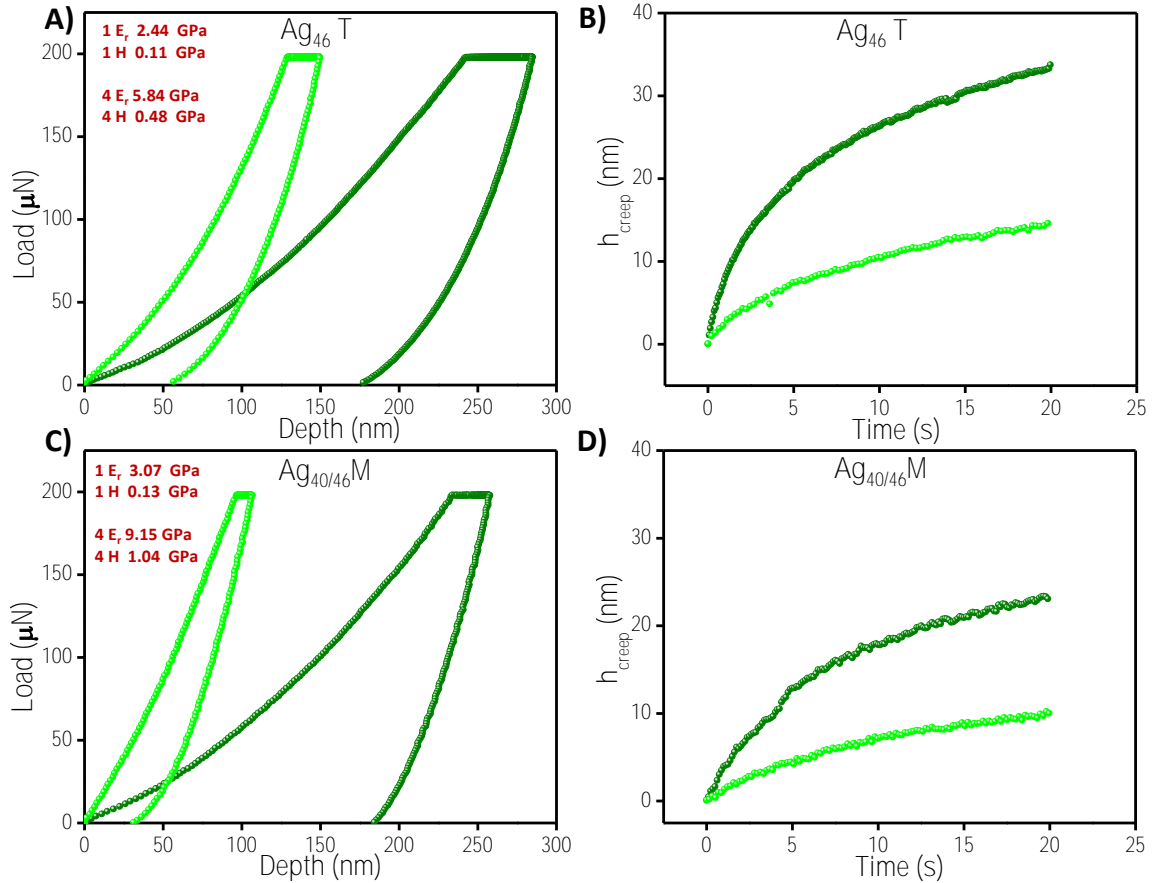


**Figure S27.** All single-crystal samples underwent the same experiment four times on the same indentation area. A) and C) are the load-displacement plots of  $\text{Ag}_{46}\text{T}$  and  $\text{Ag}_{40/46}\text{M}$  crystals (first cycle olive and fourth cycle green). B) and D) are the creep displacement plots

of Ag<sub>40/46</sub> M and Ag<sub>46</sub> T (first cycle olive and fourth green). Corresponding E<sub>r</sub> and H values are indicated.

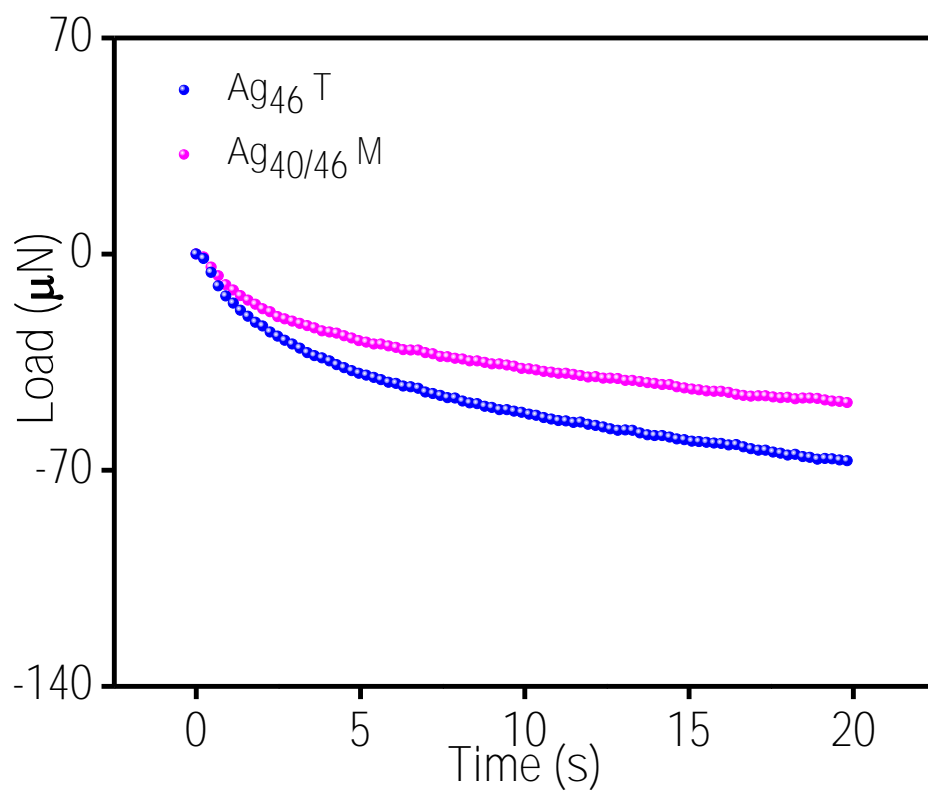


**Figure S28.** Stress relaxation plot of Ag<sub>46</sub> T (blue trace) and Ag<sub>40/46</sub> M (pink trace) cluster crystals.

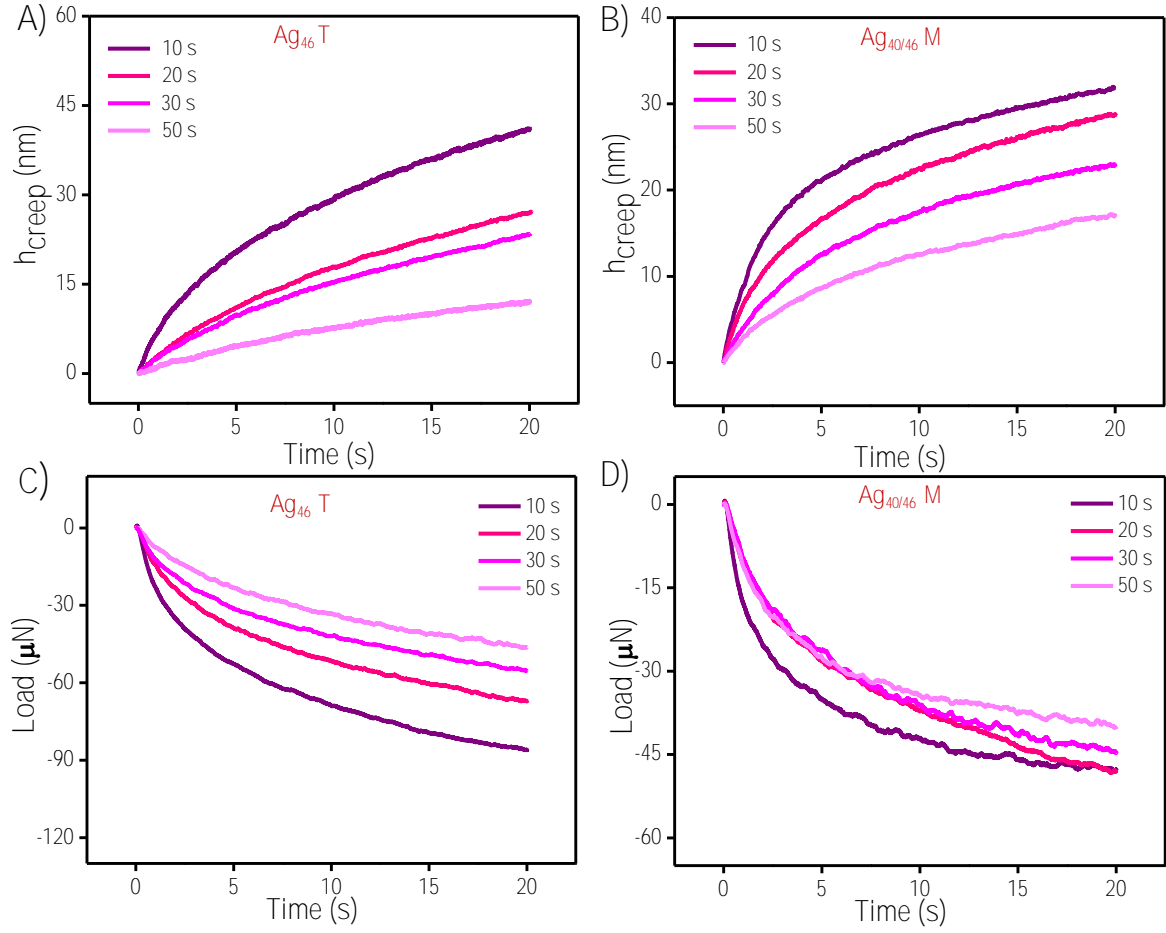


**Figure S29.** Experimental creep curves with loading rates of 20, 10, 6.6, and 4  $\mu\text{N/s}$  (top A and B) and stress relaxation curves with displacement rates of 25, 12.5, 8.33, and 5  $\text{nm/s}$  (bottom C and D) corresponding to  $\text{Ag}_{46}\text{T}$  and  $\text{Ag}_{40/46}\text{M}$  crystal systems.

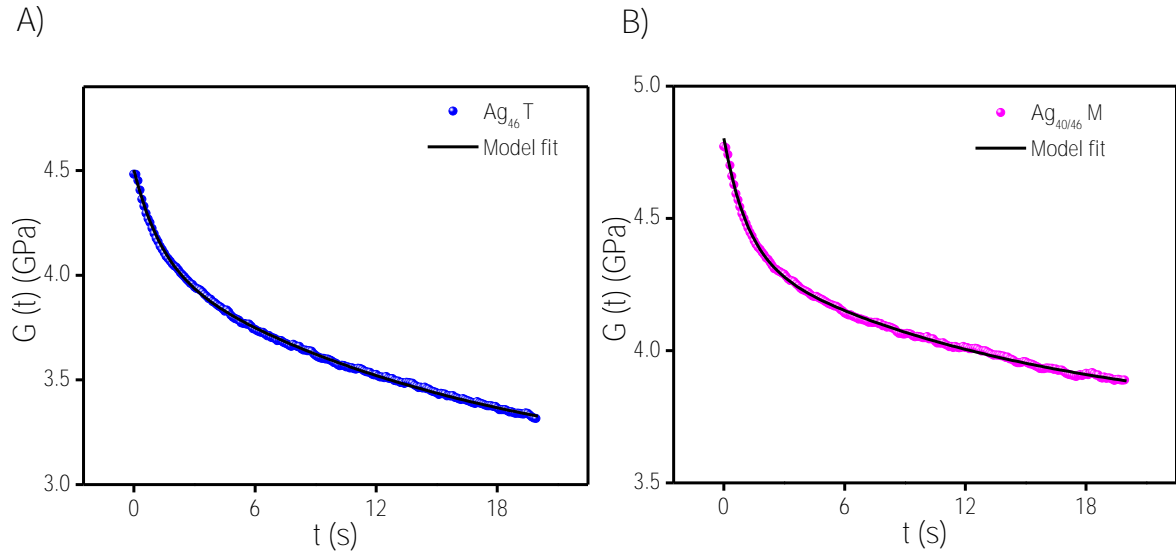


**Figure S30.** Experimental stress relaxation curves of A)  $\text{Ag}_{46}\text{T}$  and B)  $\text{Ag}_{40/46}\text{M}$  crystals fitted with the model (black solid line) which captures the stress relaxation behaviour.

**Table S4.**  $G_0$ ,  $G_\alpha$ ,  $\tau_1$ , and  $\tau_2$  values of  $\text{Ag}_{46}$  T and  $\text{Ag}_{40/46}$  M systems.

CASs	$G_0$ (GPa)	$G_\alpha$ (GPa)	$\tau_1$ (s)	$\tau_2$ (s)	$R^2$
$\text{Ag}_{46}$ T	4.49	3.02	1.33	16.25	0.99
$\text{Ag}_{40/46}$ M	4.79	3.72	14.48	1.14	0.99

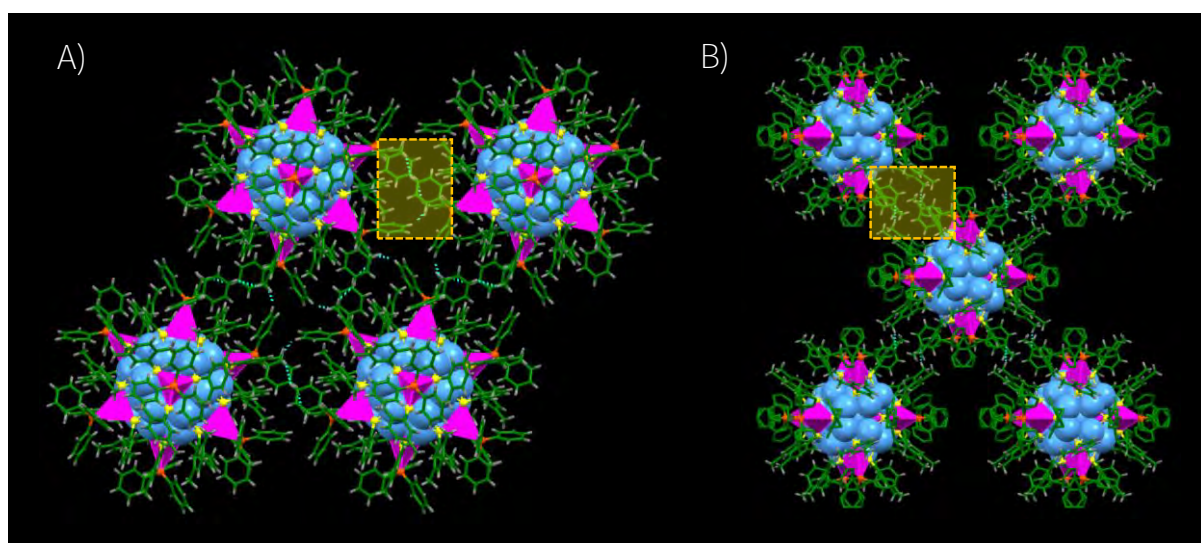


**Figure S31.** A) and B) Intercluster interactions of  $\text{Ag}_{46}$  T and  $\text{Ag}_{40/46}$  M. Color codes: cerulean/magenta, Ag; yellow, S; orange, P; green, C; grey, H.

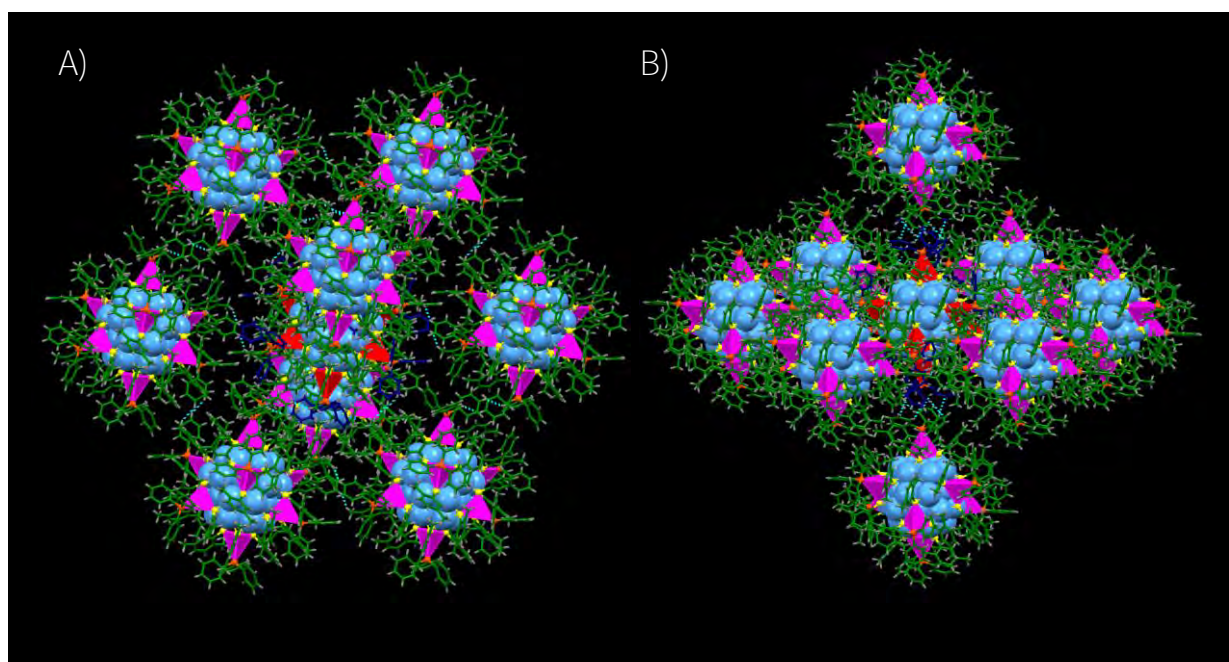


**Figure S32.** The supramolecular interactions in  $\text{Ag}_{46}$  T crystal. A) and B) shows different view of the interactions of each  $\text{Ag}_{46}$  cluster with eight neighbouring clusters in trigonal lattice. Color codes: cerulean/magenta/red, Ag; yellow, S; orange, P; green/blue, C; grey, H.

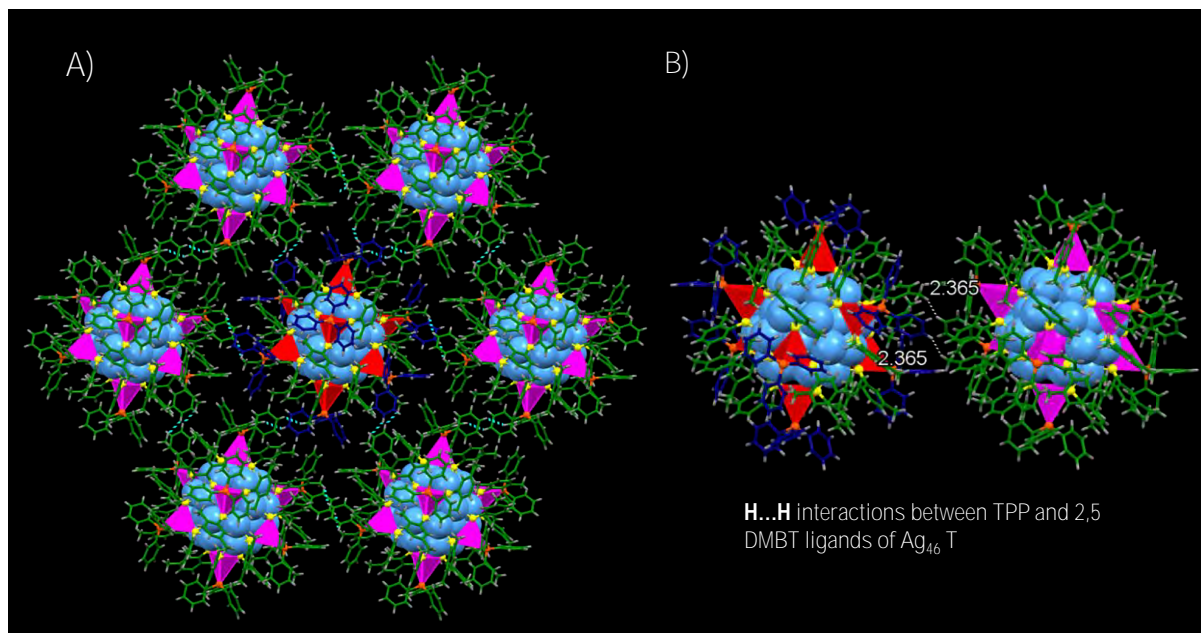


**Figure S33.** H...H interactions between TPP and 2,5 DMBT ligands in  $\text{Ag}_{46}$  T crystal. A) The view of H...H interactions between TPP and 2,5 DMBT ligands of  $\text{Ag}_{46}$  clusters with neighbouring six clusters. B) Shows the bond length of the H...H interactions. Color codes: cerulean/magenta/red, Ag; yellow, S; orange, P; green/blue, C; grey, H.



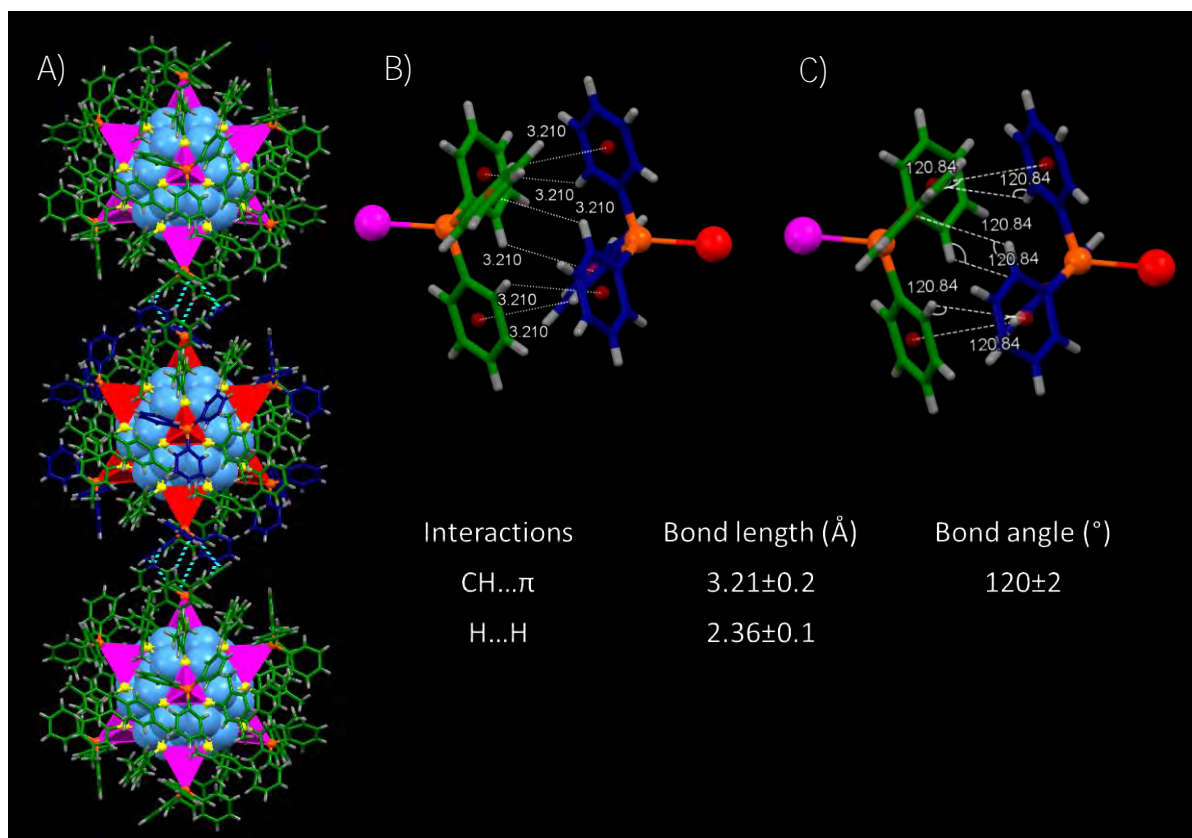


**Figure S34.** A) The six pair of CH... $\pi$  interactions between the pole site TPP ligands in Ag<sub>46</sub> T crystal. B) and C) shows the bond length and bond angle of six pair of CH... $\pi$  interactions. Color codes: cerulean/magenta/red, Ag; yellow, S; orange, P; green/blue, C; grey, H.

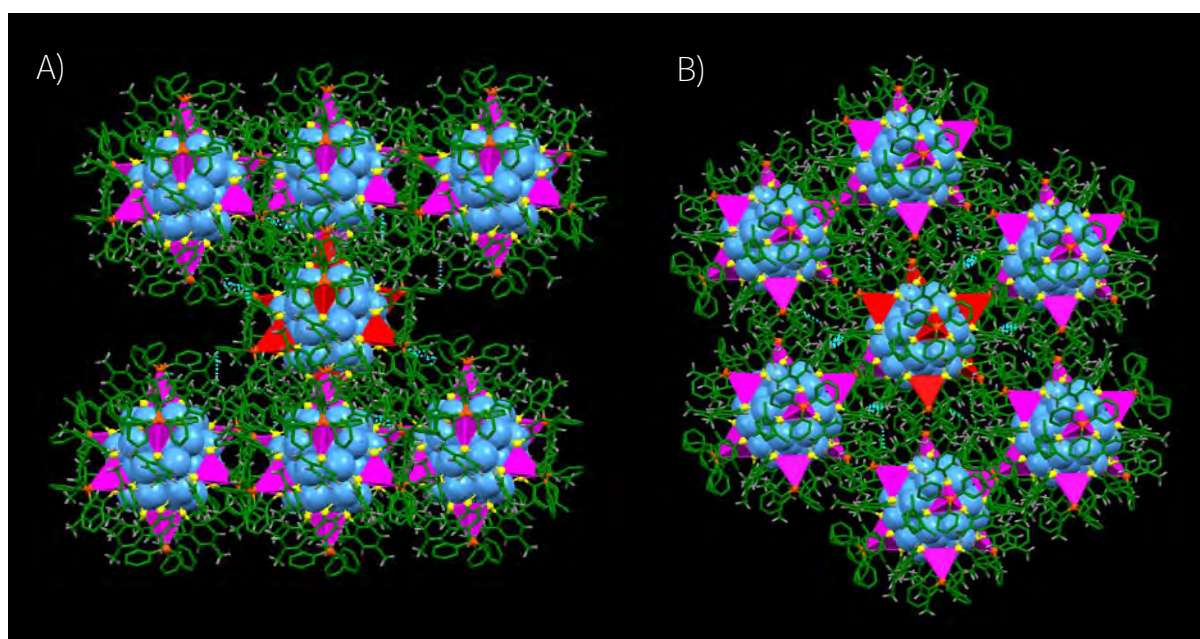


**Figure S35.** A) and B) shows the different view of the interaction of Ag<sub>40/46</sub> cluster with its neighbouring clusters in a monoclinic lattice. Color codes: cerulean/magenta/red, Ag; yellow, S; orange, P; green, C; grey, H.

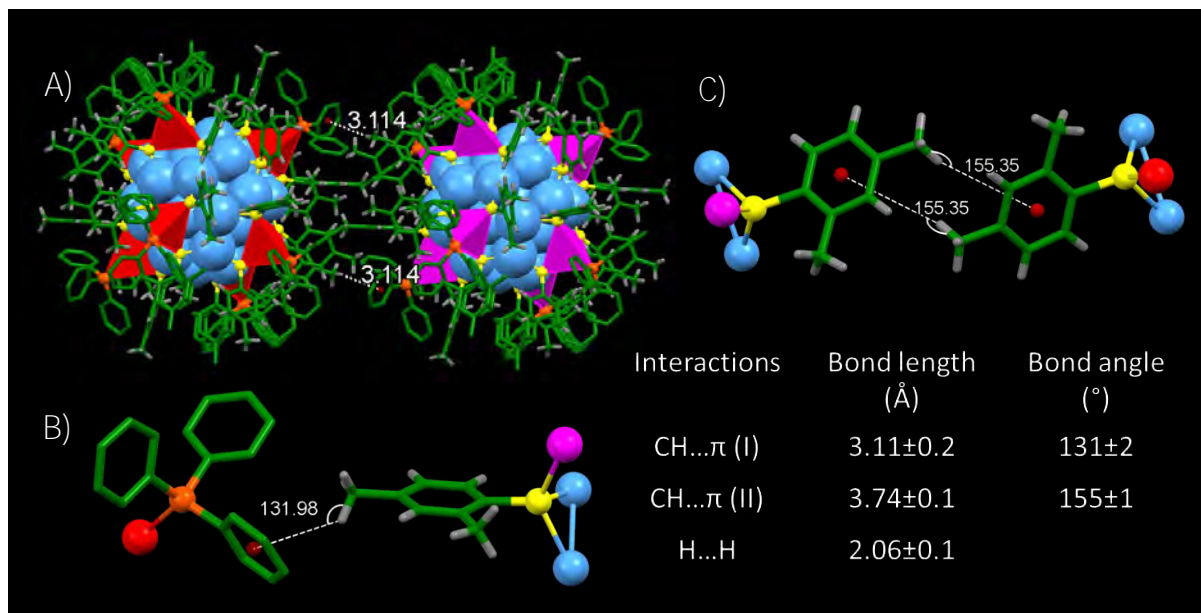


**Figure S36.** A) CH...π interactions between TPP and 2,4 DMBT ligands. B) The bond angle of CH...π interactions between the TPP and 2,4 DMBT ligands in the monoclinic lattice. C) The bond angle of the CH...π interactions between two 2,4 DMBT ligands in the monoclinic lattice. Color codes: cerulean/magenta/red, Ag; yellow, S; orange, P; green, C; grey, H.

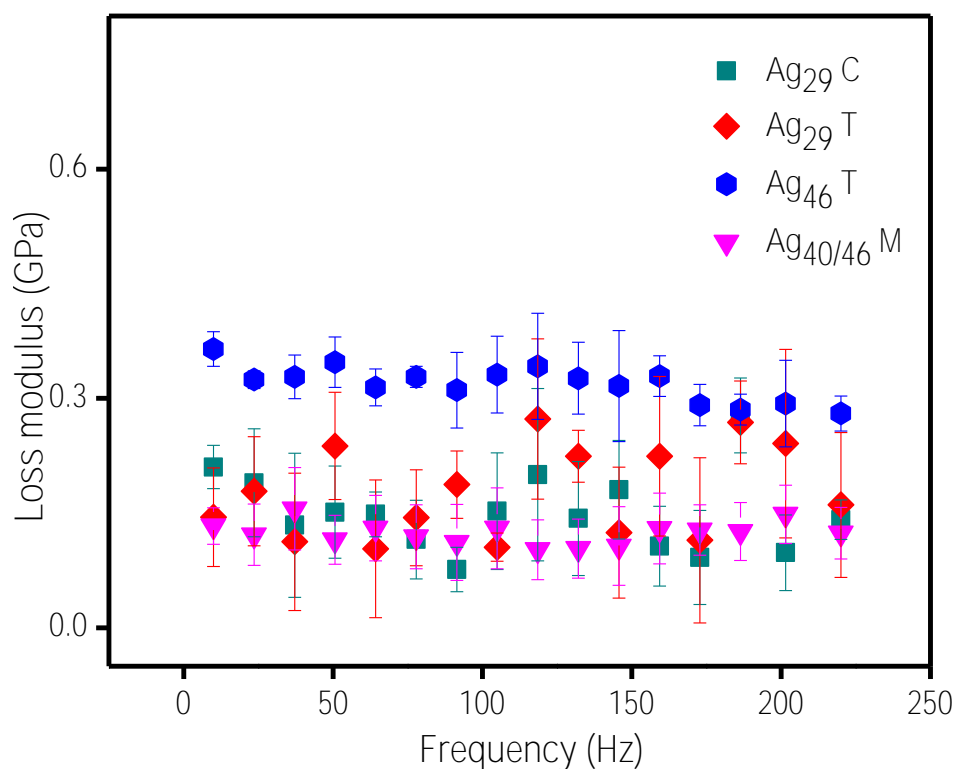


**Figure S37.** Variation of loss modulus with frequency of Ag<sub>29</sub> C (cyan trace), Ag<sub>29</sub> T (red trace), Ag<sub>46</sub> T (blue trace), and Ag<sub>40/46</sub> M (pink trace).

## References

1. Cheng, L.; Xia, X.; Scriven, L. E.; Gerberich, W. W., Spherical-tip indentation of viscoelastic material. *Mechanics of Materials* **2005**, 37, (1), 213-226.
2. Kaufman, J. D.; Miller, G. J.; Morgan, E. F.; Klapperich, C. M., Time-dependent mechanical characterization of poly(2-hydroxyethyl methacrylate) hydrogels using nanoindentation and unconfined compression. *Journal of Materials Research* **2011**, 23, (5), 1472-1481.
3. Roylance, D.; Cohen, K. C.; Jenkins, C. H.; Khanna, S. K., Mechanics of materials: A materials science perspective. *Proceedings of the Institution of Mechanical Engineers, Part L: Journal of Materials: Design and Applications* **2001**, 215, (3), 141-145.

# Nonstoichiometric Copper Sulfide Nanostructures at the Brass–Rubber Interface: Implications for Rubber Vulcanization Temperature in the Tire Industry

M. P. Kannan, Anirban Som, Tripti Ahuja, Vidhya Subramanian, A. Sreekumaran Nair,\* and Thalappil Pradeep\*



Cite This: *ACS Appl. Nano Mater.* 2020, 3, 7685–7694



Read Online

ACCESS |



Metrics & More



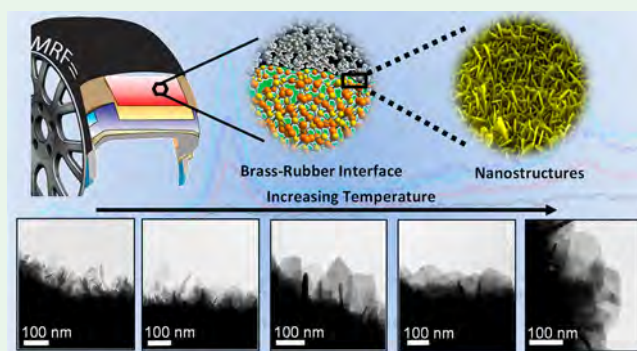
Article Recommendations



Supporting Information

**ABSTRACT:** Brass (which is an alloy of copper and zinc)-coated steel cords (BCSCs) in the form of belts are embedded in a rubber compound in radial tires (beneath the tread) to give stability and strength to the tread region of the tires. The life of the tires also depends on the strength and durability of the bond between the BCSCs and rubber. During the vulcanization process with sulfur, a series of sulfide and oxide nanostructures of copper and zinc are formed at the brass–rubber interface. These nanostructures have a dendritic morphology that can reinforce rubber primarily through mechanical interlocking created through the flow of rubber chains into the dendritic cavities followed by formation of cross-links between rubber chains during vulcanization. The strength and durability of the bonding depend on a number of parameters such as rubber compound formulation, vulcanization temperature (VT) and time, nanostructure thickness (height), and chemical composition of the nanostructures (the so-called adhesion interface). A few methods have been stated in the literature for assessing the chemical composition and thickness of the adhesion interface. However, simple, reliable, and newer methodologies are needed for a better understanding of the same. This paper details a new approach called the “brass mesh experiment” to assess the thickness of the adhesion interface formed under particular vulcanization conditions using microscopy. Raman imaging and spectroscopy were employed to determine the chemical composition of the interface with complementary data from X-ray photoelectron spectroscopy and X-ray diffraction. Using the methodologies, VT optimization was done for a tire compound formulation, and this was verified by the generally accepted pull-out force method. We believe that the methodologies outlined in this paper can trigger further research for a better understanding of the adhesion interface in radial tires.

**KEYWORDS:** brass–rubber interface, nonstoichiometric copper sulfide, Raman imaging, adhesion, vulcanization, interfacial nanostructures



## INTRODUCTION

Radial design, a game changer in tire technology, revolutionized the world of tires for its excellent combination of low fuel consumption, softer ride, and long service life.<sup>1,2</sup> On road, the ply region of the radial tire (RT) experiences maximum stress and is prone to deformation upon prolonged usage.<sup>3</sup> This fundamental problem necessitates the requirement of extensive use of brass-coated steel cords (BCSCs) as reinforcing materials embedded in the ply region perpendicular to the direction of its movement on the road, thereby enhancing the durability of tires.<sup>2,4</sup> The brass layer is deposited on steel wires through electrolysis in a cyanide solution. Treatment processes like current density, pH, copper (Cu) to zinc (Zn) ratio, and temperature play an important role in adjusting the composition of the brass. Finally, a heat treatment (650 °F) is done to improve coating continuity

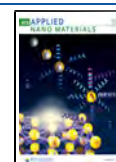
and surface composition. The surface composition of BCSC in contact with rubber (before vulcanization) is depicted in Figure 1.

Under normal conditions, the ply rubber compound (a terminology used in the tire literature, referring to a mixture of natural rubber, carbon black, and sulfur) and BCSC do not adhere to each other. This is when the vulcanization method comes into play. In general, various vulcanization methods are followed to prepare a metal–rubber composite like compres-

Received: May 12, 2020

Accepted: July 20, 2020

Published: July 20, 2020





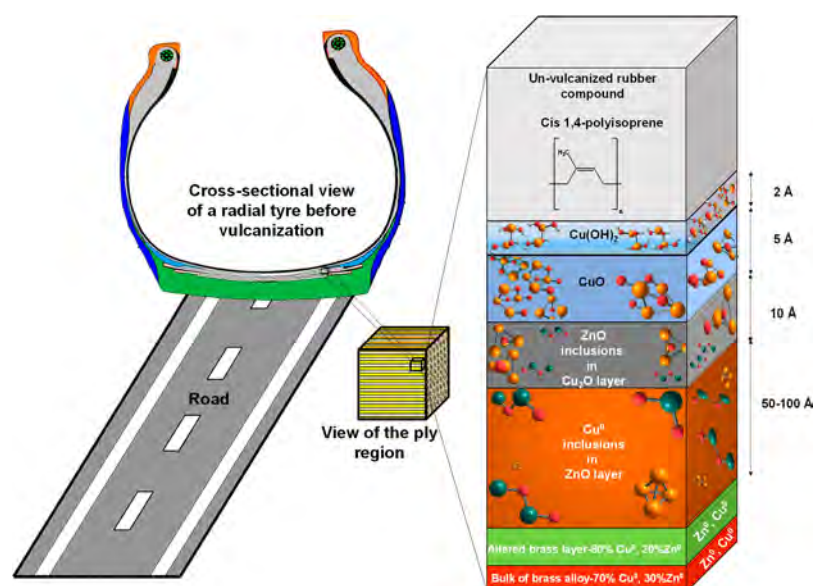


**Figure 1.** Schematic representation of the brass–rubber interface before vulcanization. The species and thickness mentioned are not to scale.

sion and injection molding.<sup>5,6</sup> The most predominant happens to be the compression molding technique that uses sliced pieces of rubber compound matching the size of a metal mold cavity.<sup>7</sup> This assembly is layered with cut BCSC and another rubber compound creating a sandwich-like structure. The mold is preheated at different temperatures based on the requirement. Later, the vulcanization of the sandwiched BCSC structure is performed in the mold with pressures higher than 3.5 MPa and is maintained constant throughout the molding cycle. During vulcanization, both the systems adhere by the formation of an interface with a dendritic morphology composed of copper(II) sulfide ( $\text{CuS}$ ), copper(I) sulfide ( $\text{Cu}_2\text{S}$ ), nonstoichiometric copper sulfides ( $\text{Cu}_{2-x}\text{S}$ ),  $\text{ZnO}$ , and zinc(II) sulfide ( $\text{ZnS}$ ). At the early stages of vulcanization, the degree of S–rubber cross-linking is small, and hence the rubber will be in a viscous state. As vulcanization proceeds, the rubber starts to flow into the dendrites having a mixture of  $\text{CuS}$ ,  $\text{Cu}_2\text{S}$ ,  $\text{Cu}_{2-x}\text{S}$ ,  $\text{ZnO}$ , and  $\text{ZnS}$  (wetting process) and interlocks rigidly, leading to robust interfacial adhesion.<sup>8–10</sup> The strength of the interface formed in the ply region is the lifeline of RTs, and it is a skill to engineer the interface to achieve maximum interfacial strength which is determined by the optimum growth of the interfacial nanostructures.<sup>11–14</sup>

From several microscopic and spectroscopic studies such as scanning electron microscopy (SEM), cross-sectional transmission electron microscopy (TEM), X-ray photoelectron spectroscopy (XPS) depth profiling, Raman spectroscopy, time-of-flight secondary ion mass spectrometry (TOF-SIMS), and X-ray diffraction (XRD), it has been inferred that various factors such as interface thickness, morphology, crystal phase, and chemical composition at the interface play a significant role in enhancing adhesion between brass and rubber.<sup>15–28</sup> However, these techniques have their own limitations and inadequacies.<sup>13,16,19,20,26,27,29,30</sup> Some limitations include a cumbersome preparation process (sectioning and ion polishing) for TEM and damage of the sample due to the use of argon ion ( $\text{Ar}^+$ ) sputtering (for XPS), and therefore a new methodology for the measurement of interfacial characteristics is necessary.<sup>12,13</sup>

Several issues apparent in the literature are presented below. SEM suggested that copper sulfide nanostructures were formed only in some regions of the vulcanized BCSCs, which made information about interfacial bonding inconclusive.<sup>30</sup> Until 1977, tire chemists have dealt with the identification of only  $\text{CuS}$  and  $\text{Cu}_2\text{S}$  crystalline phases in the adhesion interface. Subsequent investigations using grazing incidence XRD (GIXRD) have shown that  $\text{Cu}_{1.8}\text{S}$  is also formed along with  $\text{CuS}$  and  $\text{Cu}_2\text{S}$ .<sup>31</sup> XPS studies, since 1980, helped in understanding the interfacial chemical composition. Researchers have established the relative atomic percentages of elements at the interface during vulcanization. However, a fundamental knowledge gap still exists on the chemical states of elements at different VTs.<sup>26</sup> Raman spectroscopy and imaging tools were relatively unexplored in finding the composition of the interface, except for a report on a model system involving ionic liquid and S.<sup>32</sup> Previous work in understanding the role of VT on the brass–rubber interface is insufficient.<sup>15</sup> There is still considerable uncertainty concerning the morphology and interface thickness as a function of VT.

Despite the vast amount of literature on the subject, a reliable methodology to assess the interfacial thickness and its chemical composition is still nonexistent. Here, we present a novel method for measuring the interface thickness by a “brass mesh experiment” using transmission electron microscopy. The methodology helped us to understand the evolution of morphology of the copper sulfide nanostructures at the interface with an increase in VT and find the different crystalline phases formed at the interface. The study also presents, for the first time, the usefulness of Raman imaging to see the spatial distribution of chemical species at the interface, specifically the distribution of sulfides and oxides of copper and zinc. This paper also features a comprehensive investigation using complementary techniques such as FESEM, XRD, and XPS. Because the vulcanization of the rubber compound along with BCSC/mesh was performed at the pressure and time used in actual RTs, the results reported here are closer to reality, providing new insights for rubber technologists.

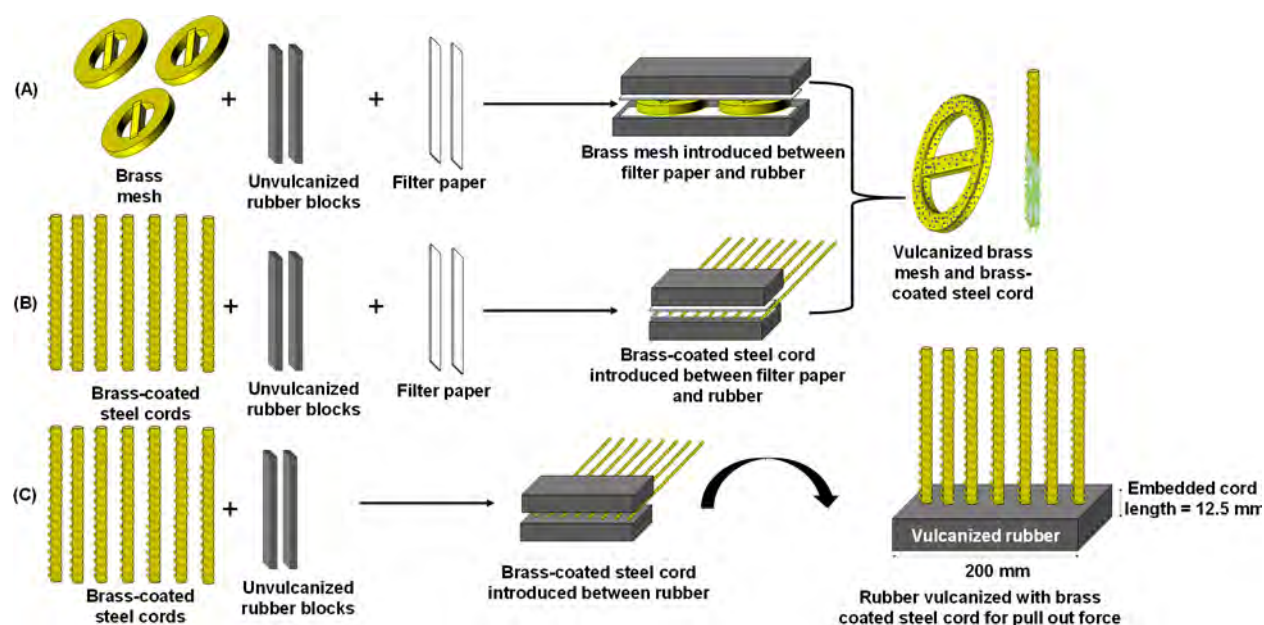


**Figure 2.** Schematic showing vulcanization procedure used for sample preparation. (A, B) Vulcanization of brass mesh and BCSC using the filter paper method. (C) Vulcanization of rubber block with BCSC for performing the POF.

## MATERIALS AND METHODS

**Rubber Compound Preparation.** The preparation of the rubber compound proceeds in two stages. Raw materials such as natural rubber, fillers, plasticizers, activators, adhesion promoters, S (in the form of  $S_8$ ), *N*-dicyclohexylbenzothiazole-2-sulfenamide (DCBS), and methylene donor and acceptor were mixed in a Kobelco lab Banbury (1.8 L capacity) in stage 1. Subsequently, S and DCBS were added into the rubber mixer in stage 2. The prepared rubber compound was then vulcanized along with BCSC by using the filter paper method.<sup>29</sup> The raw materials were procured from bulk manufacturers.

**Interfacial Thickness Measurement Using Brass Mesh Experiment.** A brass foil having 0.3 mm thickness with an equivalent composition to that of industrial BCSC was purchased from Krishna Copper Private Limited (Gujarat, India). The foil was then cut to a 3.05 mm diameter with a YAG laser (Nd:YAG Laser Tech., India), operating at a power of 800 W. Figure S1 shows a schematic of the prepared brass mesh which was then used in the filter paper method.

**Sample Preparation.** BCSCs having a brass composition of 70% Cu and 30% Zn were used in the present investigation. The filter paper method was used to understand the growth of nanostructures on brass surfaces during the process of vulcanization. It creates a clean modified metal surface without the rubber covering it and is therefore useful for spectroscopic and microscopic investigations. Whatman grade 42 filter paper of 12.5 cm diameter and pore size of 2.5  $\mu\text{m}$  manufactured by GE Healthcare Life Sciences was procured from Modern Scientific, India. The rubber compound was kept on either side of the two filter papers, as shown in Figure 2A,B, and the regions between the filter papers were sandwiched with the brass mesh (for TEM) and steel cord (for SEM, XPS, XRD, and Raman). Filter papers prevent the polymer and carbon black from interacting directly with the brass surfaces; however, they will allow S, accelerator, and metal ions from the vulcanizing mix to pass through and react with the brass surfaces.<sup>29</sup> This sandwiched assembly was then vulcanized at different temperatures. Post-vulcanization, the rubber was cut open to remove the reacted BCSC and the brass mesh. The samples were hermetically sealed in a  $N_2$  atmosphere before analyses.

**Characterization.** The nanostructures grown on the BCSC and the brass mesh were analyzed by using different characterization techniques. The morphology of the nanostructures was observed with a NanoSEM 600 field-emission scanning electron microscope (FESEM) at 10 kV. The crystallinity of the nanostructures was studied by using XRD with a Bruker D8 discovery diffractometer

using Cu  $K\alpha$  radiation (wavelength = 1.54 Å) between  $10^\circ$  and  $80^\circ$  ( $2\theta$ ) with a step size of  $0.1^\circ$ . XRD results were analyzed by using X'Pert HighScore software. JEOL TEM was used at an electron accelerating voltage of 200 kV to image the brass mesh. ImageJ software was used to calculate the thickness of interface formed on the brass mesh. Data from 20 such TEM measurements were taken for the calculation of the average interface thickness. To understand the chemical state of the species formed at the interface, XPS was performed by using an ESCA probe TPD spectrometer of Omicron Nanotechnology with a polychromatic Al  $K\alpha$  ( $h\nu = 1486.6$  eV) X-ray source. The binding energy of all the elements was calibrated with respect to C 1s at 284.8 eV. Finally, in an attempt to understand the distribution of sulfides and oxides of Cu and Zn along vulcanized BCSC, a CRM Alpha 300 S AFM-Raman spectrometer of WiTec GmbH (Germany, 633 nm laser excitation) was used to perform Raman spectroscopy and Raman imaging.

**Preparation of Metal–Rubber Composite.** The compression molding technique was used to prepare a metal–rubber composite having dimensions of 200 mm  $\times$  12.5 mm (Figure 2C).<sup>5,6</sup> This procedure starts with making a thin sheet of the rubber compound and cutting it into pieces that fit into a metal mold cavity.<sup>7</sup> BCSCs were cut carefully and placed over the rubber compound in the mold as shown in Figure 2C. To this rubber compound, one more layer of the rubber block was assembled. The mold was then preheated to different temperatures (130–170  $^\circ\text{C}$ ) based on the requirement. Later the top mold was placed over the bottom half and then clamped by a steel bar to stop the BCSC from moving during molding. Vulcanization of BCSCs assembled between the rubber compounds was performed in the mold at different temperatures with a pressure of more than 3.5 MPa on the mold surface. The pressure helped the rubber to be in contact with the whole of the mold area. Temperature and pressure were maintained constant throughout the molding cycle. Post-vulcanization, the compression molding process produces rubber flashes that were removed. After vulcanization, the blocks were preserved at room temperature for 16 h before testing.

**Pull-Out Force (POF) Experiment.** The POF test method measures the force necessary to pull out the vulcanized BCSCs out of rubber.<sup>33</sup> A POF experiment begins with preparation of the sample specimen. The steel cords along with the rubber were vulcanized according to ASTM D2229. The POF measurement was performed at  $24 \pm 2$   $^\circ\text{C}$  by using the Instron 3300 series universal testing system. Figure S2 shows a schematic of the POF measurement system. The equipment consists of a lower fixture to place the vulcanized rubber



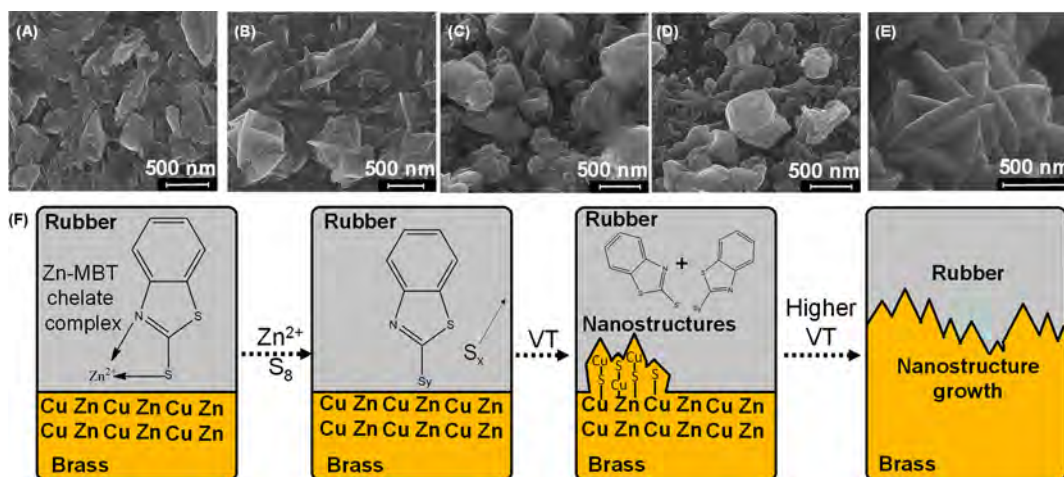


**Figure 3.** Field-emission scanning electron micrographs of the nanostructures formed at various VTs: (A) 130, (B) 140, (C) 150, (D) 160, and (E) 170 °C. (F) Schematic showing the mechanism of growth of nanostructures at the interface.  $S_x$  and  $S_y$  in the mechanism represent  $S_1$  to  $S_8$ .

block and a clamp to hold BCSCs (Figure S2A). The vulcanized rubber block was pushed to the lower fixture of the equipment and made sure that the sample could be moved inside the fixture without damaging the specimen (Figure S2B). The steel wire was then clamped to the bracket and pulled (Figure S2C,D). The steel cords pulled out of the rubber block were preserved to examine the amount of rubber coverage on the steel cords.

## RESULTS AND DISCUSSION

**Morphology of Nanostructures Formed on the BCSC Using FESEM and EDS.** Figure 3A–E presents the formation of nanostructures as a function of VT (from 130 to 170 °C). The nanostructures formed at the interface mechanically interlocks with the rubber, and this results in adhesion. It is quite apparent from the SEM images that there is a change in the interfacial morphology and surface roughness as a function of VT. The formation of flaky nanostructures on the surface was noticeable at 130 °C. A further increase in temperature to 140 °C showed the growth of the flaky nanostructures. The morphology of the nanostructures was changed from flaky to nanopillar-like structures with increase in VT (from 130 to 140 °C). At VTs higher than 150 °C (i.e., at 160 and 170 °C, respectively), further growth of the nanostructures was observed. Overall, these observations indicated that the morphology of the nanostructures in the brass–rubber interface can be controlled with VT. During vulcanization, continuous diffusion of active sulfurating species (from rubber) to brass surface results in interfacial growth. At higher VTs, the concentration of active sulfurating species at the interface is high, and this leads to the growth of larger and thicker nanostructures.<sup>15</sup> Additionally, we have obtained optical microscopic images (Figure S3) of the BCSC at different VTs to verify the consistency of the vulcanization.

Energy-dispersive X-ray spectroscopy (EDS) was used to get the concentration (wt %) of different elements at the interface. Figure S4 shows the EDS spectra of the vulcanized steel cords at temperatures between 130 and 170 °C. Raster scanning at more than three places of the vulcanized steel cord revealed the presence of significant amounts of Cu, Zn, Fe, S, and O. There were significant differences in the concentrations of Cu and Zn (could have originated from CuS, Cu<sub>2-x</sub>S, Cu<sub>2</sub>S, ZnS, and ZnO) with increase in VT. However, a clear trend of increase in concentrations of Fe and O was noticeable between 130 and 170 °C. At higher VTs, increase in intensities of S (Figure S4)

indicated the increased formation of the sulfides of Cu and Zn. The most surprising aspect of the EDS result is the absence of cobalt (Co) precursor that was added to the rubber compound for enhancing interfacial adhesion, suggesting that the concentration of Co could be below the detection limit of EDS. As per Table S1, higher VT also promotes a higher rubber–rubber cross-link (cross-link density) through S.<sup>34</sup> Additionally, VT affects the physical properties such as modulus, tensile strength, and elongation at break (EB) of the rubber. The 10%, 100%, and 300% modulus signify the tensile strength of the rubber at 10%, 100%, and 300% elongation of rubber compound at different VTs.<sup>35</sup> From Figure S5, it is seen that 10%, 100%, and 300% modulus of rubber decrease with increased VT, implying that the rubber has become harder and breaks at high VT.<sup>15</sup> The EB of the rubber compound decreases with an increase in VT, implying that the rubber vulcanized at higher VTs fractures easily.

**Mechanism of Nanostructure Growth.** Figure 3F depicts the growth of metal sulfide nanostructures at the interface that could be explained through a series of steps highlighting the formation of a rubber accelerator intermediate (2-mercaptobenzothiazole (MBT), 2,2'-dithiobenzothiazole (MBTS), zinc–MBTS (ZMBTS), and active sulfurating complex). The characterization of these chemical structures has been done by using TOF-SIMS.<sup>8</sup> The nanostructure growth begins with the partial dissolution of ZnO on the surface of BCSC by a vulcanization promoter, stearic acid, present in the rubber compound ( $\text{ZnO} + 2\text{C}_{17}\text{H}_{35}\text{COOH} \rightarrow \text{Zn}(\text{OOC}_{17}\text{H}_{35})_2 + \text{H}_2\text{O}$ ).<sup>12</sup> This reaction exposes pure brass, thereby increasing its surface activity. At the same time, the vulcanization accelerator, DCBS, present in the rubber compound dissociates into MBT and MBTS.<sup>36</sup> In the next stage,  $\text{Zn}^{2+}$  forms a chelate with MBT and attaches it to the N and S sites to form ZMBTS. Simultaneously, the  $\text{S}_7-\text{S}^-$  ( $\text{S}^-$  ion) is formed from  $\text{S}_8$ , which then reacts with ZMBTS to form dibenzothiazole polysulfide (DBTP or active sulfurating complex). In addition, DBTP reacts with the surface of brass, forming a metal–S–accelerator bond ( $\text{Cu/Zn-S-Acc}$ ). At elevated vulcanization temperatures, Cu/Zn–S–Acc bonds dissociate to form Cu/Zn sulfides and a polysulfide accelerator intermediate ( $\text{S}_{x-1}-\text{Acc}$  where  $x = 8$ ). The sulfidation reaction happening during vulcanization is a diffusion-driven process, where constant diffusion of Cu to the surface of brass occurs,

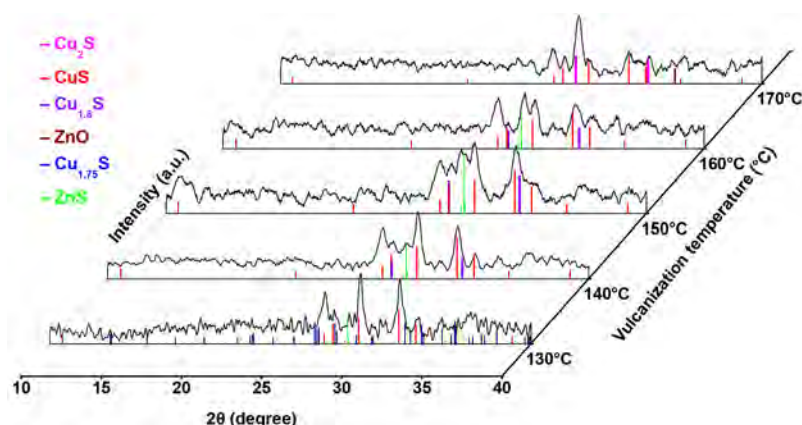


Figure 4. XRD patterns of the vulcanized BCSC at different VTs.

thus thickening the interface. Diffused Cu further reacts with accelerator moieties to form  $\text{Cu}_{2-x}\text{S}$ .<sup>13</sup> Consequently, the growth of nanostructures continues to happen due to the buildup of the active sulfurating complex near the brass surface.  $\text{Cu}_{2-x}\text{S}$  consists of cationic vacancies through which  $\text{Cu}^+$  ions diffuse to the surface.<sup>12</sup> At higher VTs, it is expected to have more active sulfurating complex on the brass surface, leading to the growth of thicker and larger nanostructures.<sup>15</sup>

**Crystallinity of the Adhesion Interface Using XRD.** A crystalline interface does not provide enough adhesion with rubber, and it fails quickly. It is also well known that higher VTs contribute to the conversion of an amorphous interface to a crystalline interface, leading to a brittle adhesion layer between BCSC and rubber. Hence, we performed XRD studies to identify different crystalline phases formed at the interface at different VTs. Figure S6 portrays the XRD pattern of unvulcanized BCSC. Before vulcanization, the most prominent peaks correspond to those of brass. Figure 4 illustrates the XRD patterns of the vulcanized steel cords as a function of temperature. It has been reported in the literature that recognition of  $\text{Cu}_{2-x}\text{S}$  crystallographic phases is difficult as it exists in diverse crystal structures and compositions.<sup>37–39</sup> However, the coexistence of multiple phases of  $\text{Cu}_{2-x}\text{S}$  ( $\text{CuS}$ , anilite ( $\text{Cu}_{1.75}\text{S}$ ), digenite ( $\text{Cu}_{1.8}\text{S}$ ), and chalcocite ( $\text{Cu}_2\text{S}$ )) has been observed in our present work along with other chemical species like  $\text{ZnS}$  and  $\text{ZnO}$ . The proportions in which these chemical species ( $\text{Cu}_{2-x}\text{S}$ ,  $\text{Cu}_2\text{S}$ ,  $\text{CuS}$ ,  $\text{ZnS}$ , and  $\text{ZnO}$ ) get formed during vulcanization is important in interfacial adhesion.<sup>40,41</sup> At 130 °C, the diffraction patterns of the steel cords matched with those of  $\text{Cu}_{1.75}\text{S}$  (ICSD no. 16011),  $\text{CuS}$  (ICSD no. 26968), and  $\text{ZnS}$  (ICSD no. 107176). Formations of  $\text{CuS}$  and  $\text{Cu}_{1.8}\text{S}$  (ICSD no. 57213) along with  $\text{ZnS}$  were noted at 140 °C. The composition remained almost the same until 160 °C while  $\text{CuS}$ ,  $\text{Cu}_2\text{S}$  (ICSD no. 159435), and  $\text{ZnO}$  (ICSD no. 163382) were present at 170 °C. Vulcanization at a lower temperature leads to the formation of  $\text{CuS}$ ,  $\text{Cu}_{1.75}\text{S}$ ,  $\text{Cu}_{1.8}\text{S}$ , and  $\text{ZnS}$  at the brass–rubber interface. However, this was overtaken by the formation of  $\text{CuS}$ ,  $\text{Cu}_2\text{S}$ , and  $\text{ZnO}$  at 170 °C (Table 1). An interface comprising the right ratios of  $\text{CuS}$ ,  $\text{Cu}_{1.8}\text{S}$ , and  $\text{ZnS}$  formed at a VT of 140 °C must be the probable reason for increased POF. These findings help us to understand that 140 °C serves as the optimum VT for the formation of the right adhesion interface with the present rubber formulation.

**Measurement of Interfacial Thickness and Understanding the Formation of the Multiphase Junction by**

Table 1. Crystalline Composition of the Brass–Rubber Interface at Different VTs

S. no.	vulcanization temp (°C)	crystalline composition at the brass–rubber interface
1	130	$\text{CuS}$ , $\text{Cu}_{1.75}\text{S}$ , and $\text{ZnS}$
2	140–160	$\text{CuS}$ , $\text{Cu}_{1.8}\text{S}$ , and $\text{ZnS}$
3	170	$\text{CuS}$ , $\text{Cu}_2\text{S}$ , and $\text{ZnO}$

**TEM.** In this section, we demonstrate a new methodology of estimating the thickness of the brass–rubber interface through the brass-mesh experiment. The SEM images showed that temperature is a crucial parameter for the growth of the nanostructures at the interface. A new approach was therefore adopted in the present work which helps us to quantify the interfacial thickness at various VTs. This involved the *in situ* growth of the interface on the brass mesh as explained before. Upon varying the VT, the average interfacial thickness was tuned between 50 and 190 nm, as illustrated in Figures 5A–E and 5F. The average interfacial thickness was around 100 nm at 140 °C and increased to 120 nm at 150 °C. A further increase in temperature to 160 and 170 °C resulted in the formation of heightened hexagon-shaped structures with an average thickness of 168 and 189 nm, respectively. It is encouraging to compare the interfacial thickness to the values of POF (a generally accepted means to test the interfacial strength). Comparing Figure 5A–E with Figure 5F–H, we interpret that the adhesion is determined by the interface thickness.

The interfacial structures grow in size from ~92 to ~189 nm as the VT is increased from 130 to 170 °C. However, the POF displayed a different trend, first increasing with an increase of VT from 130 to 140 °C and subsequently reducing with a further increase of VT from 150 to 170 °C. This is because the growth of the interfacial nanostructures reaches an optimum in terms of thickness and chemical composition (for bonding with rubber) at 140 °C, and a further increase in VT results in thicker and larger crystalline nanostructures, resulting in a weak interfacial strength with rubber.<sup>12,13</sup> It can therefore be concluded that 140 °C serves as the optimum VT in the present case as the interfacial thickness and its composition were proper for better bonding with rubber.

Figures 5A1 to 5E1 represent high-resolution TEM images of the hexagonal nanostructures formed at the interface. It is quite evident from Figures 5A1 to 5E1 that a heterojunction having different compositions (i.e., multiphase system) was



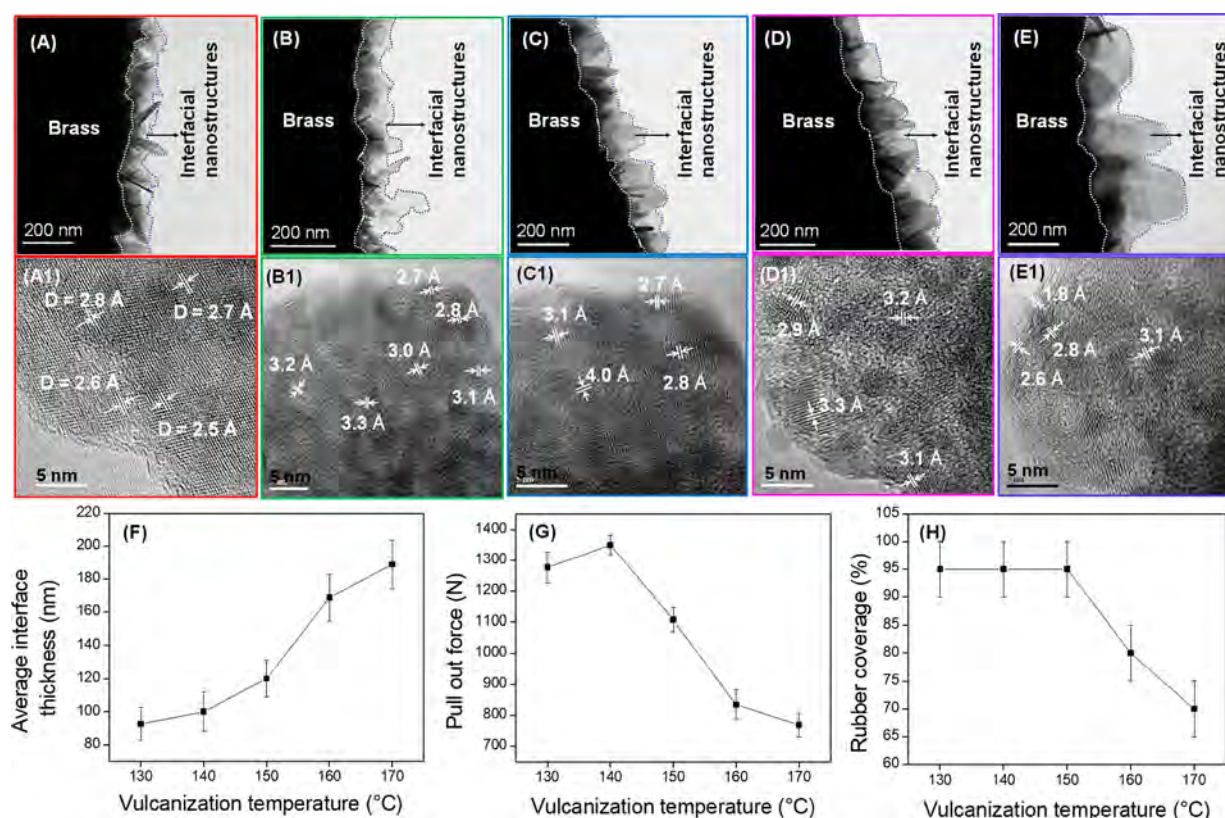


**Figure 5.** Bright-field TEM images of the hexagonal nanoplates grown over brass mesh vulcanized at (A) 130, (B) 140, (C) 150, (D) 160, and (E) 170 °C. Corresponding HRTEM images are in (A1)–(E1). Scale bar: 5 nm. Various lattice dimensions seen are marked. Graphical representation of (F) the average interface thickness, (G) variation in POF, and (H) rubber coverage as a function of vulcanization temperature.

formed. After vulcanization, rubber is in immediate contact with these phases, and the presence of each phase marks its importance at the interface. The lattice spacings at 130 °C corresponded to the presence of (103) planes of CuS, (018) planes of ZnS, and (301) and (221) planes of  $\text{Cu}_{1.75}\text{S}$ , which are in line with the XRD patterns (Figure 4).<sup>42,43</sup> The topmost layer of nanostructures that are in contact with rubber was composed of a triphase composition (having four lattice fringes) of CuS,  $\text{Cu}_{1.75}\text{S}$ , and ZnS. At 140 °C, the lattice structure is comprised of the (013) plane of CuS, the (111) plane of  $\text{Cu}_{1.8}\text{S}$ , and the (014) and (015) planes of ZnS, which was more or less the same until 160 °C.<sup>44</sup> The lattice spacing at 170 °C corresponded to the presence of the (013) plane of CuS, the (111) plane of  $\text{Cu}_2\text{S}$ , and the (011) plane of ZnO.<sup>45</sup>

Through the TEM experiments using the brass mesh, we have presented a simple technique to measure the thickness of the brass–rubber interface and its chemical composition and have correlated the interface thickness with POF measurements.

**3.4. Understanding the Chemical State at the Brass–Rubber Interface.** XPS analysis was performed on the vulcanized steel cords to find the chemical composition and oxidation states of the elements formed at the interface. Generally, in copper chalcogenides, the valence band is formed from the p orbital while the conduction band is constructed from 4s and 4p orbitals of Cu.<sup>46</sup> In the case of stoichiometric  $\text{Cu}_2\text{S}$ , the valence band is filled up. On the contrary, the structure of CuS is distinct from that of  $\text{Cu}_2\text{S}$ . CuS has a repeating layer of  $\text{CuS}_3$  that is sandwiched between  $\text{CuS}_4$  tetrahedra, and this triple layer is connected to other triple layers through disulfide bonds. The valency of Cu in CuS is

found to be between 1 and 1.5, and recent calculations suggest the valency of Cu to be 1.33.<sup>47,48</sup> When nonstoichiometry occurs during vulcanization, Cu vacancies are created in the lattice which affects the valency of the cation. In addition to CuS and  $\text{Cu}_2\text{S}$ , other types of  $\text{Cu}_{2-x}\text{S}$  are also formed in the adhesion interface, but distinguishing them by using XPS is challenging. To cite an example, the difference in binding energy (BE) between  $\text{Cu}_2\text{S}$  and  $\text{Cu}_{1.75}\text{S}$  is just 0.2 eV.

The different chemical species formed at the interface are reflected from the change in peak binding energy values of XPS. Figure S7 indicates that the unvulcanized brass surface had a higher peak intensity of Zn than of Cu, proving that ZnO was present on the surface before vulcanization. The C 1s peaks originated from either the tiny amount of filter paper sticking on the surface or as a result of adventitious C, while O 1s was identified to be from the metal oxides. Figure 6 shows the peak fitting analysis of S 2p, Cu 2p<sub>3/2</sub> and 2p<sub>1/2</sub>, Zn 2p<sub>3/2</sub> regions. Cu- and S-related peaks started to increase during vulcanization as a result of the formation of copper sulfides. Vulcanization of the BCSC from 130 to 160 °C gave rise to CuS (BE = 932.2 eV) and ZnS (BE = 1021.8 eV) at the interface. Even though  $\text{Cu}_{1.75}\text{S}$  and  $\text{Cu}_{1.8}\text{S}$  were formed between 130 and 160 °C (as found by XRD and TEM), no separate peaks for them were observed in XPS. We note that the difference in binding energy between CuS and  $\text{Cu}_{2-x}\text{S}$  is very narrow. At 170 °C, the interface mostly consists of  $\text{Cu}_2\text{S}$  (BE = 932.8 eV) and ZnO (BE = 1022.5 eV).<sup>32</sup> More information about the chemical state of the interface was obtained from the S 2p core-level XPS data. The 2p<sub>3/2</sub>/2p<sub>1/2</sub> doublet of S was fitted with a  $\Delta J$  of 1.18 eV. Vulcanization at 130–160 °C resulted in S 2p<sub>3/2</sub> at 161.2 eV, confirming the

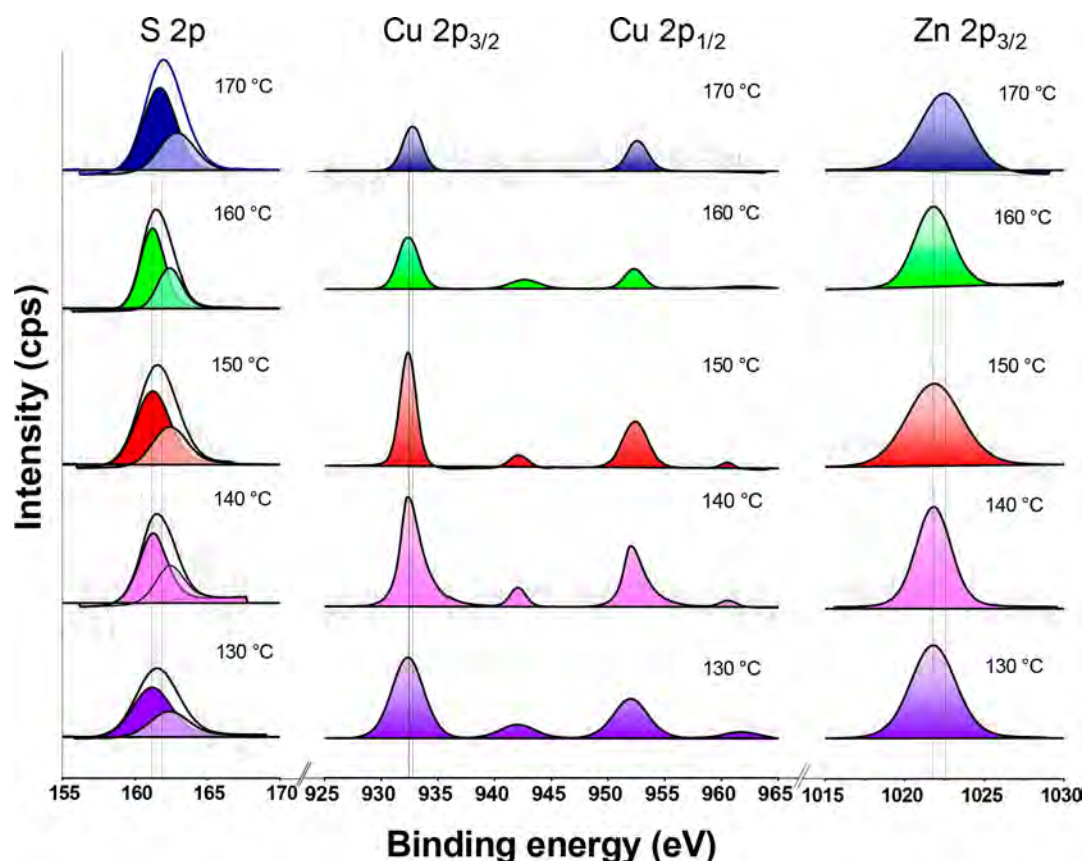


**Figure 6.** High-resolution XPS spectra of S 2p, Cu 2p<sub>3/2</sub>, Cu 2p<sub>1/2</sub>, and Zn 2p<sub>3/2</sub> formed during vulcanization of BCSC from 130 to 170 °C. The dark lines in the spectra depict peak fitting.

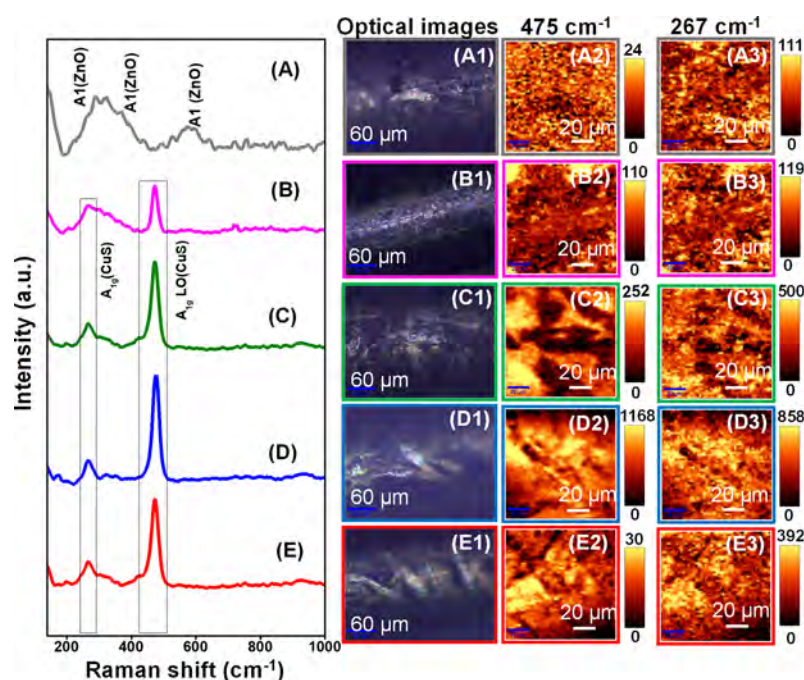


**Figure 7.** Raman spectra of BCSC at (A) 170, (B) 160, (C) 150, (D) 140, and (E) 130 °C. Images (A1) to (E1) represent Raman optical images (scale: 60  $\mu\text{m}$ ), images (A2) to (E2) correspond to confocal Raman maps of CuS at 475  $\text{cm}^{-1}$  (scale: 20  $\mu\text{m}$ ), and images (A3) to (E3) correspond to confocal Raman maps of CuS at 267  $\text{cm}^{-1}$  (scale: 20  $\mu\text{m}$ ). The color bars on the extreme right indicate the CCD counts.

presence of CuS. At 170 °C, the emergence of S 2p<sub>3/2</sub> at 161.7 eV was seen due to Cu<sub>2</sub>S.

The amount of Cu, Zn, O, and S present at the interface during vulcanization is a measure of interfacial adhesion. The atomic percent (at. %) found by XPS showed that Cu and S



kept increasing from 130 to 170 °C in vulcanized BCSC (Figure S8). This indicates an increase in copper sulfide formation with increase in VT. Increase of Cu at. % correlated directly to a reduction in POF at higher VTs. The at. % of Zn and O increases up to 170 °C VT, indicating the formation of ZnO. Higher Cu at. % indicated that the interface thickness increased with VT, and a thicker interface is prone to break easily under the application of stress.

**Understanding CuS Concentration Distribution throughout the Brass–Rubber Interface Using Confocal Raman Spectroscopy and Microscopy.** Raman spectroscopy coupled with imaging is a powerful technique that provides detailed chemical information about the interface. Figures S9A and S9B represent the optical image and Raman spectra of the unreacted BCSC. Raman spectra of unreacted BCSC suggested the presence of CuO along with ZnO on the surface of brass. Raman spectra of the BCSC after vulcanization are shown in Figures 7A–E, representing a change in the chemical nature of brass, post-vulcanization (130–170 °C). The interface was investigated pixel by pixel through the Raman map to generate false-color images (Raman mapping) based on the interfacial chemical composition. Figures 7A1 to 7E1 depict the optical images, and Figures 7A2 to 7E2 show the confocal Raman maps at 475 cm<sup>-1</sup>; Figures 7A3 to 7E3 are due to the feature at 267 cm<sup>-1</sup>.

Sharp peaks were observed at 475 and 267 cm<sup>-1</sup> between 130 and 160 °C. The former peak corresponded to A<sub>1g</sub> LO of CuS while the latter corresponded to A<sub>1g</sub> peak of CuS.<sup>32,42</sup> It can be noted that the peak intensities were stronger at 130, 140, and 150 °C and have comparatively reduced in intensity at 160 °C. Distinguishing a mixture of Cu<sub>1.75</sub>S and Cu<sub>1.8</sub>S in CuS from the Raman spectrum is challenging, as both Cu<sub>1.75</sub>S and Cu<sub>1.8</sub>S show a prominent peak at 469 cm<sup>-1</sup>. However, Raman peaks corresponding to ZnS get submerged as the intensities of CuS (475 and 274 cm<sup>-1</sup>) were multifold more than ZnS. Characteristic peaks at 574, 437, 407, and 380 cm<sup>-1</sup> corresponded to the presence of ZnO at 170 °C. XRD and XPS results support the formation of Cu<sub>1.95</sub>S and Cu<sub>2</sub>S along with ZnO at 170 °C, but no peak for Cu<sub>2</sub>S is seen in Figures 7A–E, as it is a Raman-inactive molecule.

Raman mapping using the peaks at 475 and 267 cm<sup>-1</sup> showed that CuS is more prominent in the adhesion interface. Bright regions were observed in the generated heat maps shown in Figures 7A2 to 7E3. The gradual increase in the black regions from 130 to 170 °C indicates regions in the steel cord that are having lesser concentration of CuS. From these data, we believe that Raman mapping can be used as a tool to understand the concentration distribution of CuS at the brass–rubber interface as a function of VT.

## CONCLUSION

We developed a methodology, the “brass-mesh experiment”, for measuring the growth of nanostructures formed at the interface between rubber and brass as a function of vulcanization temperature (VT, 130–170 °C). The interfacial nanostructures grow in size (thickness) from ~90 to ~190 nm as the VT was increased from 130 to 170 °C. Scanning electron microscopy (SEM) shows that the morphology of the nanostructures varies from flaky type to nanopillar-like with increase in VT. The brass-mesh TEM study shows that the nanostructures grow in size, and the lattice-resolved TEM images indicated the formation of CuS, Cu<sub>1.75</sub>S, Cu<sub>1.8</sub>S, ZnS, and ZnO under the vulcanization conditions. This was

additionally confirmed by X-ray diffraction (XRD) and X-ray photoelectron spectroscopy (XPS) investigations. Raman spectroscopy and imaging are used for the first time in the literature to map the spatial distribution of the sulfides and oxides formed. Using the above methodology, we could optimize the vulcanization temperature to 140 °C for the mentioned rubber composition. We believe that the results presented in this paper will be immensely useful to the tire and allied rubber industries and will trigger further research in this area as the interfacial adhesion is crucial to the durability of radial tires and safety of passengers.

## ASSOCIATED CONTENT

### Supporting Information

The Supporting Information is available free of charge at <https://pubs.acs.org/doi/10.1021/acsanm.0c01298>.

Schematic image of laser cut mesh from brass foil that is used for interfacial thickness experiment; schematic showing pull-out force measurement procedure; microscopic images of reacted brass-coated steel cords with change in vulcanization temperature; SEM-EDS data of vulcanized cords; physical properties of rubber compound with increasing vulcanization temperature; XRD pattern of unvulcanized brass-coated steel cord; XPS survey spectra of unreacted brass-coated steel cord under ambient conditions; relative at. % obtained from XPS; Raman spectra and LED white light image of unreacted BCSC; total cross-link density of rubber compound at different vulcanization temperatures (PDF)

## AUTHOR INFORMATION

### Corresponding Authors

A. Sreekumaran Nair – R&D Centre, MRF Limited, Chennai 600019, India; [orcid.org/0000-0001-9258-8566](https://orcid.org/0000-0001-9258-8566);

Email: [sreekumaran.nair@mrfmail.com](mailto:sreekumaran.nair@mrfmail.com)

Thalappil Pradeep – DST Unit of Nanoscience (DST UNS) and Thematic Unit of Excellence (TUE), Department of Chemistry, Indian Institute of Technology Madras, Chennai 600036, India; [orcid.org/0000-0003-3174-534X](https://orcid.org/0000-0003-3174-534X);

Email: [pradeep@iitm.ac.in](mailto:pradeep@iitm.ac.in)

### Authors

M. P. Kannan – DST Unit of Nanoscience (DST UNS) and Thematic Unit of Excellence (TUE), Department of Chemistry, Indian Institute of Technology Madras, Chennai 600036, India; R&D Centre, MRF Limited, Chennai 600019, India; [orcid.org/0000-0001-5526-2620](https://orcid.org/0000-0001-5526-2620)

Anirban Som – DST Unit of Nanoscience (DST UNS) and Thematic Unit of Excellence (TUE), Department of Chemistry, Indian Institute of Technology Madras, Chennai 600036, India; [orcid.org/0000-0002-6646-679X](https://orcid.org/0000-0002-6646-679X)

Tripti Ahuja – DST Unit of Nanoscience (DST UNS) and Thematic Unit of Excellence (TUE), Department of Chemistry, Indian Institute of Technology Madras, Chennai 600036, India; [orcid.org/0000-0002-9256-2689](https://orcid.org/0000-0002-9256-2689)

Vidhya Subramanian – DST Unit of Nanoscience (DST UNS) and Thematic Unit of Excellence (TUE), Department of Chemistry, Indian Institute of Technology Madras, Chennai 600036, India; [orcid.org/0000-0002-6076-3515](https://orcid.org/0000-0002-6076-3515)

Complete contact information is available at:

<https://pubs.acs.org/doi/10.1021/acsanm.0c01298>

## Funding

This work was financially supported by MRF Ltd. through a research grant. Equipment used in this work was supported by the Department of Science and Technology.

## Notes

The authors declare no competing financial interest.

## ACKNOWLEDGMENTS

The authors thank Prof. G. U. Kulkarni, Jawaharlal Nehru Centre for Advanced Scientific Research (JNCASR), for FESEM measurements. T.P. thanks MRF Ltd. for a research grant. The authors thank the Department of Science and Technology, Government of India, for equipment support through the Nano Mission.

## REFERENCES

- (1) Kane, K.; Jumel, J.; Lallet, F.; Mbiakop Ngassa, A.; Vacherand, J. M.; Shanahan, M. E. R. A novel inflation adhesion test for elastomeric matrix/steel cord. *Int. J. Solids Struct.* **2019**, *160*, 40–50.
- (2) Ogawa, H.; Furuya, S.; Koseki, H.; Iida, H.; Sato, K.; Yamagishi, K. A Study on the Contour of the Truck and Bus Radial Tire. *Tire Sci. Technol.* **1990**, *18* (4), 236–261.
- (3) Dhanalakshmi, J.; Vijayakumar, C. T. Thermal studies on dry bonding adhesive system for potential rubber article applications. *J. Adhes. Sci. Technol.* **2020**, *34* (3), 233–245.
- (4) Han, Y. H.; Becker, E. B.; Fahrendthold, E. P.; Kim, D. M. Fatigue Life Prediction for Cord-Rubber Composite Tires Using a Global-Local Finite Element Method. *Tire Sci. Technol.* **2004**, *32* (1), 23–40.
- (5) Park, C. H.; Lee, W. I.; Yoo, Y. E.; Kim, E. G. A study on fiber orientation in the compression molding of fiber reinforced polymer composite material. *J. Mater. Process. Technol.* **2001**, *111* (1), 233–239.
- (6) Hamed, G. R.; Huang, J. Combining Cobalt and Resorcinolic Bonding Agents in Brass-Rubber Adhesion. *Rubber Chem. Technol.* **1991**, *64* (2), 285–295.
- (7) Maghsoudi, K.; Momen, G.; Jafari, R.; Farzaneh, M. Direct replication of micro-nanostructures in the fabrication of super-hydrophobic silicone rubber surfaces by compression molding. *Appl. Surf. Sci.* **2018**, *458*, 619–628.
- (8) Van Ooij, W. J. Mechanism and Theories of Rubber Adhesion to Steel Tire Cords—An Overview. *Rubber Chem. Technol.* **1984**, *57* (3), 421–456.
- (9) Buytaert, G.; Coornaert, F.; Dekeyser, W. Characterization of the Steel Tire Cord - Rubber Interface. *Rubber Chem. Technol.* **2009**, *82* (4), 430–441.
- (10) Pekachaki, H. M.; Taghvaei-Ganjali, S.; Motiee, F.; Saber-Tehrani, M. Application of Calixarene Derivatives as Tackifier Resin in Rubber Compounds for Tire Applications. *Rubber Chem. Technol.* **2019**, *92* (3), 467–480.
- (11) Vandenabeele, C.; Bulou, S.; Maurau, R.; Siffer, F.; Belmonte, T.; Choquet, P. Organo-Chlorinated Thin Films Deposited by Atmospheric Pressure Plasma-Enhanced Chemical Vapor Deposition for Adhesion Enhancement between Rubber and Zinc-Plated Steel Monofilaments. *ACS Appl. Mater. Interfaces* **2015**, *7* (26), 14317–14327.
- (12) Van Ooij, W. J.; Harakuni, P. B.; Buytaert, G. Adhesion of Steel Tire Cord to Rubber. *Rubber Chem. Technol.* **2009**, *82* (3), 315–339.
- (13) Fulton, W. S. Steel Tire Cord-Rubber Adhesion, Including the Contribution of Cobalt. *Rubber Chem. Technol.* **2005**, *78* (3), 426–457.
- (14) Sarlin, E.; Rosling, A.; Honkanen, M.; Lindgren, M.; Juutilainen, M.; Poikelispää, M.; Laiho, P.; Vippola, M.; Vuorinen, J. Effect of Environment on Bromobutyl Rubber-Steel Adhesion. *Rubber Chem. Technol.* **2020**, *93*, 429–444.
- (15) Jeon, G. S.; Seo, G. Influence of Cure Conditions on the Adhesion of Rubber Compound to Brass-plated Steel Cord. Part I. Cure Temperature. *J. Adhes.* **2001**, *76* (3), 201–221.
- (16) Ozawa, K.; Kakubo, T.; Amino, N.; Mase, K.; Ikenaga, E.; Nakamura, T. Angle-Resolved HAXPES Investigation on the Chemical Origin of Adhesion between Natural Rubber and Brass. *Langmuir* **2017**, *33* (38), 9582–9589.
- (17) Ling, C. Y.; Hirvi, J. T.; Suvanto, M.; Bazhenov, A. S.; Markkula, K.; Hillman, L.; Pakkanen, T. A. Effect of cobalt additives and mixed metal sulfides at rubber-brass interface on rubber adhesion: a computational study. *Theor. Chem. Acc.* **2017**, *136* (2), 24.
- (18) Chen, Y.; Schlarb, J. L. Steel Cord-Rubber Adhesion with SEM/EDX. *Tire Sci. Technol.* **2018**, *46* (1), 27–37.
- (19) Ozawa, K.; Kakubo, T.; Shimizu, K.; Amino, N.; Mase, K.; Komatsu, T. High-resolution photoelectron spectroscopy analysis of sulfidation of brass at the rubber/brass interface. *Appl. Surf. Sci.* **2013**, *264*, 297–304.
- (20) Fulton, W. S.; Sykes, D. E.; Smith, G. C. SIMS depth profiling of rubber-tyre cord bonding layers prepared using 64Zn depleted ZnO. *Appl. Surf. Sci.* **2006**, *252* (19), 7074–7077.
- (21) Patil, P. Y.; Van Ooij, W. J. Mechanism of Improved Aged Rubber-to-Brass Adhesion Using One-Component Resins. *Rubber Chem. Technol.* **2005**, *78* (1), 155–173.
- (22) Kim, J. M.; van Ooij, W. J. Study of the effects of compounding ingredients on the adhesion layer between squalene model compound and brass by GPC and TOF-SIMS. *J. Adhes. Sci. Technol.* **2003**, *17* (2), 165–178.
- (23) Shimizu, K.; Miyata, T.; Nagao, T.; Kumagai, A.; Jinnai, H. Visualization of the tensile fracture behaviors at adhesive interfaces between brass and sulfur-containing rubber studied by transmission electron microscopy. *Polymer* **2019**, *181*, 121789.
- (24) Kakubo, T.; Shimizu, K.; Kumagai, A.; Matsumoto, H.; Tsuchiya, M.; Amino, N.; Jinnai, H. Degradation of a Metal-Polymer Interface Observed by Element-Specific Focused Ion Beam-Scanning Electron Microscopy. *Langmuir* **2020**, *36* (11), 2816–2822.
- (25) Jeon, G. S. On characterizing microscopically the adhesion interphase for the adhesion between metal and rubber compound Part III. Effect of brass-plating amount for brass-plated steel cord. *J. Adhes. Sci. Technol.* **2017**, *31* (24), 2667–2681.
- (26) Ozawa, K.; Mase, K. Evidence for chemical bond formation at rubber-brass interface: Photoelectron spectroscopy study of bonding interaction between copper sulfide and model molecules of natural rubber. *Surf. Sci.* **2016**, *654*, 14–19.
- (27) Ozawa, K.; Kakubo, T.; Shimizu, K.; Amino, N.; Mase, K.; Ikenaga, E.; Nakamura, T.; Kinoshita, T.; Oji, H. In situ chemical state analysis of buried polymer/metal adhesive interface by hard X-ray photoelectron spectroscopy. *Appl. Surf. Sci.* **2014**, *320*, 177–182.
- (28) Jeon, G. S.; Seo, G. Influence of Cure Conditions on the Adhesion of Rubber Compound to Brass-plated Steel Cord. Part II. Cure Time. *J. Adhes.* **2001**, *76* (3), 223–244.
- (29) Hotaka, T.; Ishikawa, Y.; Mori, K. Characterization of Adhesion Interlayer Between Rubber and Brass by a Novel Method of Sample Preparation. *Rubber Chem. Technol.* **2007**, *80* (1), 61–82.
- (30) Ziegler, E.; Macher, J.; Gruber, D.; Pöhl, P.; Kern, W.; Lummerstorfer, T.; Feldgitscher, C.; Holzner, A.; Trimmel, G. Investigation of the Influence of Stearic Acid on Rubber-Brass Adhesion. *Rubber Chem. Technol.* **2012**, *85* (2), 264–276.
- (31) Van Ooij, W. J. The Role of XPS in the Study and Understanding of Rubber-to-Metal Bonding. *Surf. Sci.* **1977**, *68*, 1–9.
- (32) Baert, K.; Breugelmans, T.; Buytaert, G.; Brabant, J. V.; Hubin, A. The combination of surface enhanced Raman spectroscopy and an ionic liquid as a model system to study the adhesion interface between sulfur and brass. *J. Raman Spectrosc.* **2013**, *44* (3), 377–381.
- (33) Seo, G. Stabilizing the adhesion interphase between rubber compounds and brass film by the addition of resorcinol formaldehyde resin to the rubber. *J. Adhes. Sci. Technol.* **1997**, *11* (11), 1433–1445.
- (34) Mukhopadhyay, R.; Sadhan, K. D.; Chakraborty, S. N. Effect of Vulcanization Temperature and Vulcanization Systems on The Structure and Properties of Natural Rubber Vulcanizates. *Polymer* **1977**, *18* (12), 1243–1249.



- (35) Debasish, D.; Debapriya, D.; Adhikari, B. The effect of grass fiber filler on curing characteristics and mechanical properties of natural rubber. *Polym. Adv. Technol.* **2004**, *15* (12), 708–715.
- (36) Ghosh, P.; Katore, S.; Patkar, P.; Caruthers, J. M.; Venkatasubramanian, V.; Walker, K. A. Sulfur Vulcanization of Natural Rubber for Benzothiazole Accelerated Formulations: From Reaction Mechanisms to a Rational Kinetic Model. *Rubber Chem. Technol.* **2003**, *76* (3), 592–693.
- (37) Luther, J. M.; Jain, P. K.; Ewers, T.; Alivisatos, A. P. Localized surface plasmon resonances arising from free carriers in doped quantum dots. *Nat. Mater.* **2011**, *10* (5), 361–366.
- (38) Li, W.; Zamani, R.; Rivera Gil, P.; Pelaz, B.; Ibanez, M.; Cadavid, D.; Shavel, A.; Alvarez-Puebla, R. A.; Parak, W. J.; Arbiol, J.; Cabot, A. CuTe Nanocrystals: Shape and Size Control, Plasmonic Properties, and Use as SERS Probes and Photothermal Agents. *J. Am. Chem. Soc.* **2013**, *135* (19), 7098–7101.
- (39) Li, W.; Zamani, R.; Ibanez, M.; Cadavid, D.; Shavel, A.; Morante, J. R.; Arbiol, J.; Cabot, A. Metal Ions To Control the Morphology of Semiconductor Nanoparticles: Copper Selenide Nanocubes. *J. Am. Chem. Soc.* **2013**, *135* (12), 4664–4667.
- (40) Hotaka, T.; Ishikawa, Y.; Mori, K. Effect of Compound Ingredients on Adhesion between Rubber and Brass-Plated Steel Cord. *Rubber Chem. Technol.* **2005**, *78* (2), 175–187.
- (41) Chandra, A. K.; Mukhopadhyay, R.; Konar, J.; Ghosh, T. B.; Bhowmick, A. K. X-ray photoelectron spectroscopy and Auger electron spectroscopy of the influence of cations and anions of organometallic adhesion promoters on the interface between steel cord and rubber skim compounds. *J. Mater. Sci.* **1996**, *31* (10), 2667–2676.
- (42) Shawky, A.; El-Sheikh, S. M.; Gaber, A.; El-Hout, S. I.; El-Sherbiny, I. M.; Ahmed, A. I. Urchin-like CuS nanostructures: simple synthesis and structural optimization with enhanced photocatalytic activity under direct sunlight. *Appl. Nanosci.* **2020**, *10*, 2153–2164.
- (43) Patrick, R. A. D.; Mosselmans, J. F. W.; Charnock, J. M.; England, K. E. R.; Helz, G. R.; Garner, C. D.; Vaughan, D. J. The structure of amorphous copper sulfide precipitates: An X-ray absorption study. *Geochim. Cosmochim. Acta* **1997**, *61* (10), 2023–2036.
- (44) Park, H.; Kwon, J.; Kim, J.; Park, K.; Song, T.; Paik, U. Facile Growth of Metal-Rich Cu<sub>1.75</sub>S and Cu<sub>1.8</sub>S Microspheres Assembled with Mesoporous Nanosheets and Their Application in Na-Ion Batteries. *Cryst. Growth Des.* **2020**, *20*, 3325–3333.
- (45) Peng, M.; Ma, L.-L.; Zhang, Y.-G.; Tan, M.; Wang, J.-B.; Yu, Y. Controllable synthesis of self-assembled Cu<sub>2</sub>S nanostructures through a template-free polyol process for the degradation of organic pollutant under visible light. *Mater. Res. Bull.* **2009**, *44* (9), 1834–1841.
- (46) Garba, E. J. D.; Jacobs, R. L. The electronic structure of Cu<sub>2-x</sub>Se. *Physica B+C* **1986**, *138* (3), 253–260.
- (47) Liang, W.; Whangbo, M. H. Conductivity anisotropy and structural phase transition in Covellite CuS. *Solid State Commun.* **1993**, *85* (5), 405–408.
- (48) Mazin, I. I. Structural and electronic properties of the two-dimensional superconductor CuS with 1 1/3-valent copper. *Phys. Rev. B: Condens. Matter Mater. Phys.* **2012**, *85* (11), 115–133.

## Supporting information

### Non-Stoichiometric Copper Sulfide Nanostructures at the Brass-Rubber Interface: Implications for Rubber Vulcanization Temperature in the Tire Industry

*M. P. Kannan,<sup>††</sup> Anirban Som,<sup>‡</sup> Tripti Ahuja,<sup>‡</sup> Vidhya Subramanian<sup>‡</sup> A. Sreekumaran Nair,<sup>\*†</sup> and Thalappil Pradeep<sup>\*‡</sup>*

<sup>‡</sup>DST Unit of Nanoscience (DST UNS) and Thematic Unit of Excellence (TUE), Department of Chemistry, Indian Institute of Technology Madras, Chennai 600036, India.

<sup>†</sup>MRF Limited, R&D Centre, Tiruvottiyur, Chennai 600019, India.

\*For correspondence, E-mail: sreekumaran.nair@mrfmail.com, pradeep@iitm.ac.in

#### Table of contents

Figures	Title	Page no.
Figure S1	Schematic of laser cut mesh from brass foil	S-3
Figure S2	Schematic showing pull-out force measurement procedure.	S-3
Figure S3	Microscopic images of reacted brass coated steel cords with change in vulcanization temperature	S-4
Figure S4	SEM-EDS data of vulcanized cords	S-5
Figure S5	Physical properties of rubber compound with increasing vulcanization temperature	S-6
Figure S6	XRD pattern of un-vulcanized brass-coated steel cord	S-7
Figure S7	XPS survey spectra of unreacted brass-coated steel cord under ambient conditions and high resolution XPS spectra of O 1s, Cu 2p <sub>3/2</sub> and Zn 2p <sub>3/2</sub>	S-8

Figure S8	Relative atomic % obtained from XPS	S-9
Figure S9	LED white light image of unreacted brass-coated steel cord and Raman spectra of unreacted brass-coated steel cord	S-10
Table S1	Total crosslink density of rubber compound at different vulcanization temperatures	S-11



**Figure S1.** Schematic image of laser cut mesh from brass foil that is used for interfacial thickness experiment.

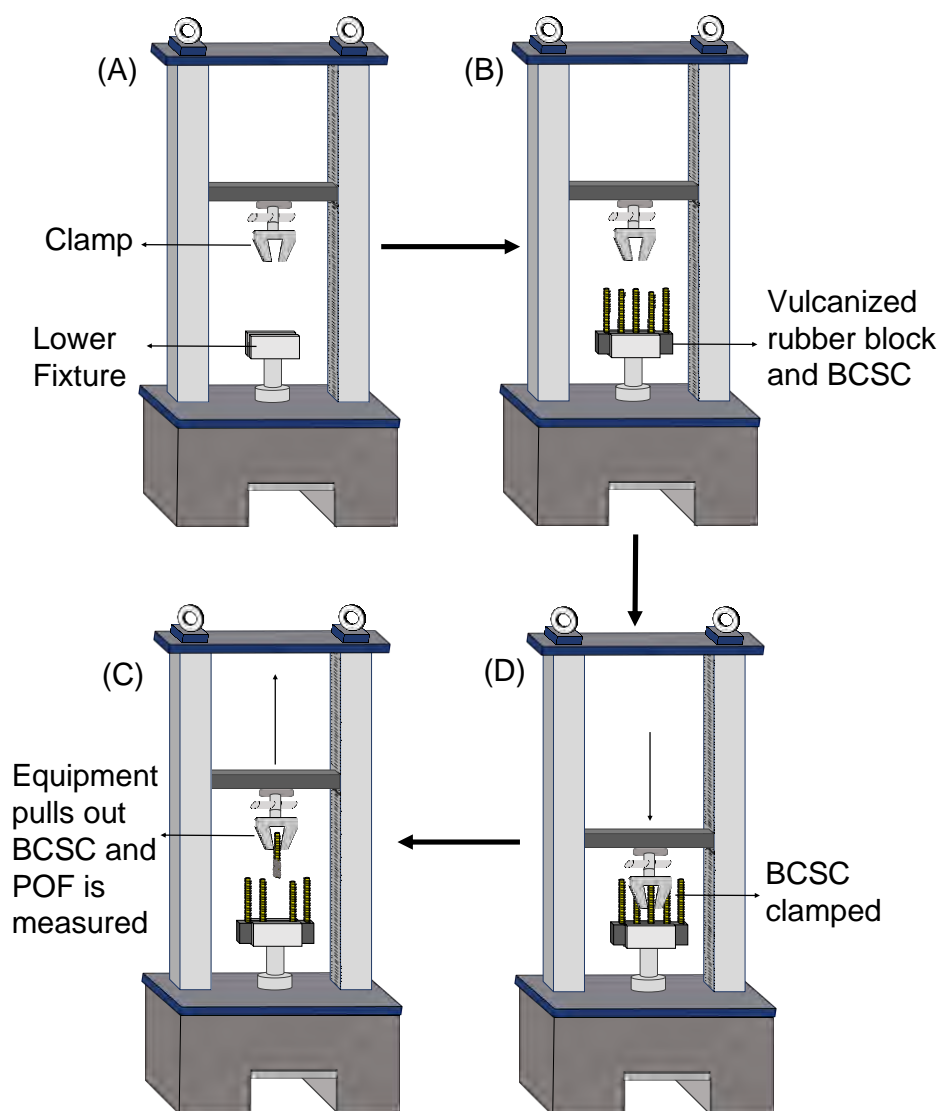
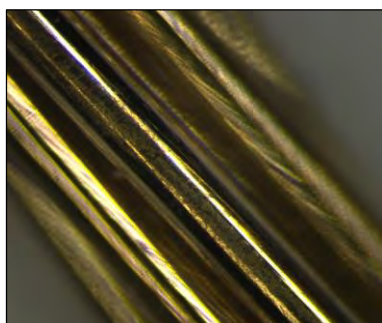


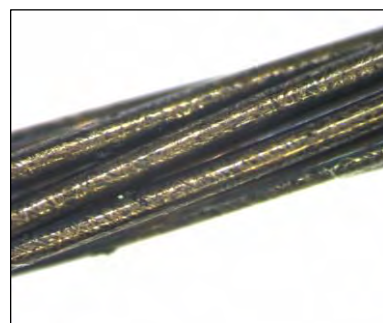
**Figure S2.** Schematic showing pull-out force measurement procedure.



Unreacted brass



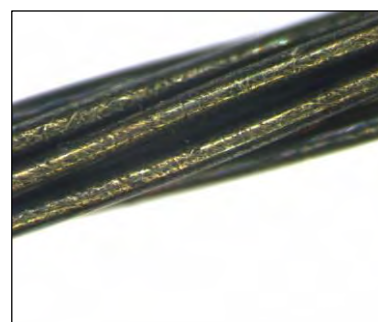
Vulcanized at 130 °C



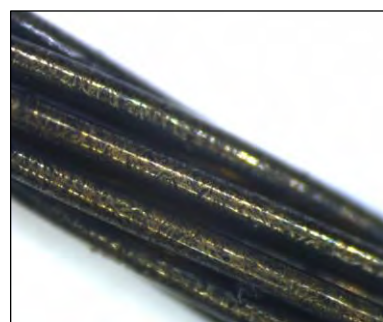
Vulcanized at 140 °C



Vulcanized at 150 °C



Vulcanized at 160 °C



Vulcanized at 170 °C

**Figure S3.** Microscopic images of reacted brass-coated steel cords with change in vulcanization temperature. Scale: 50x.

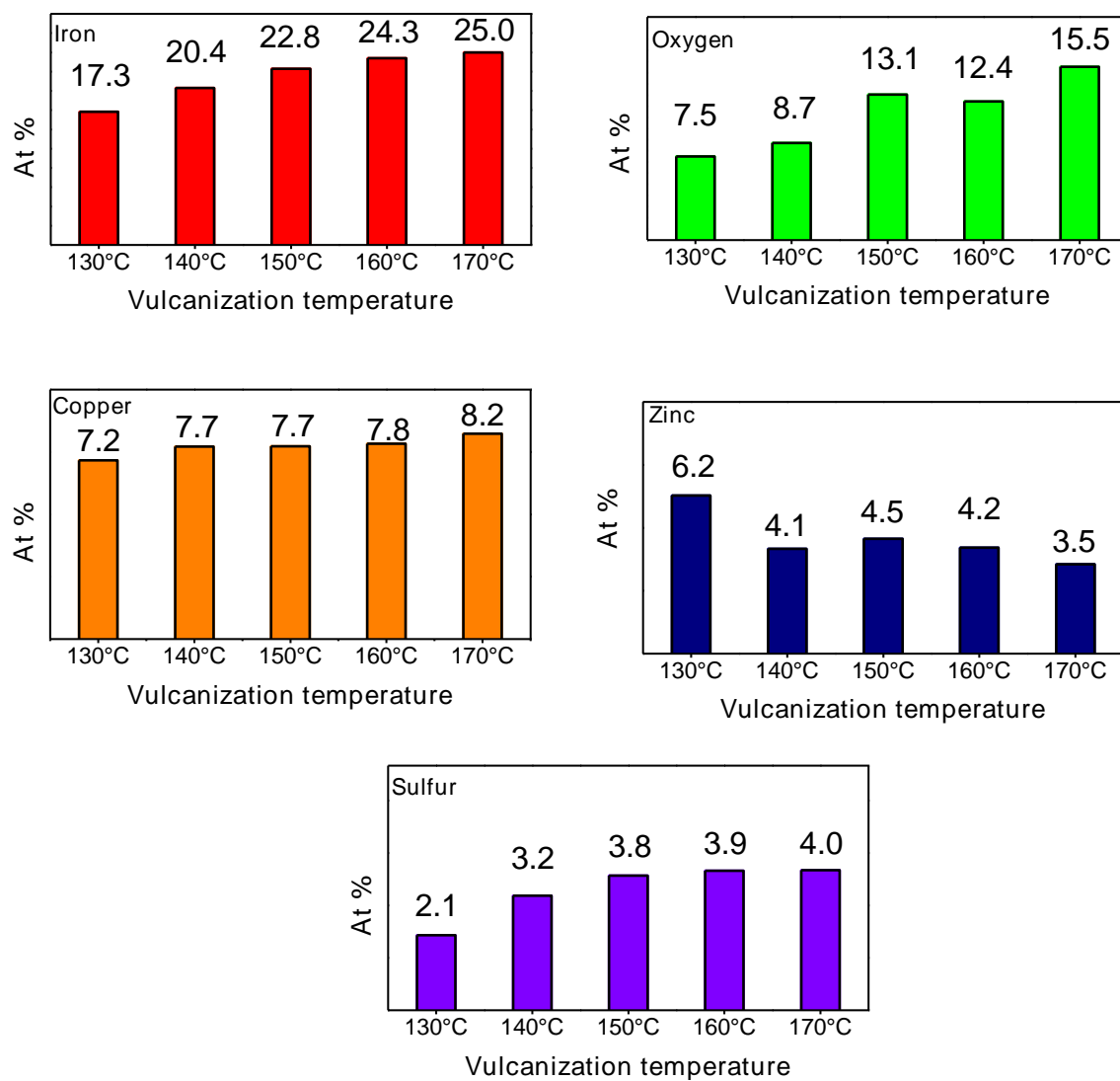


**Figure S4.** SEM-EDS data of vulcanized cords.



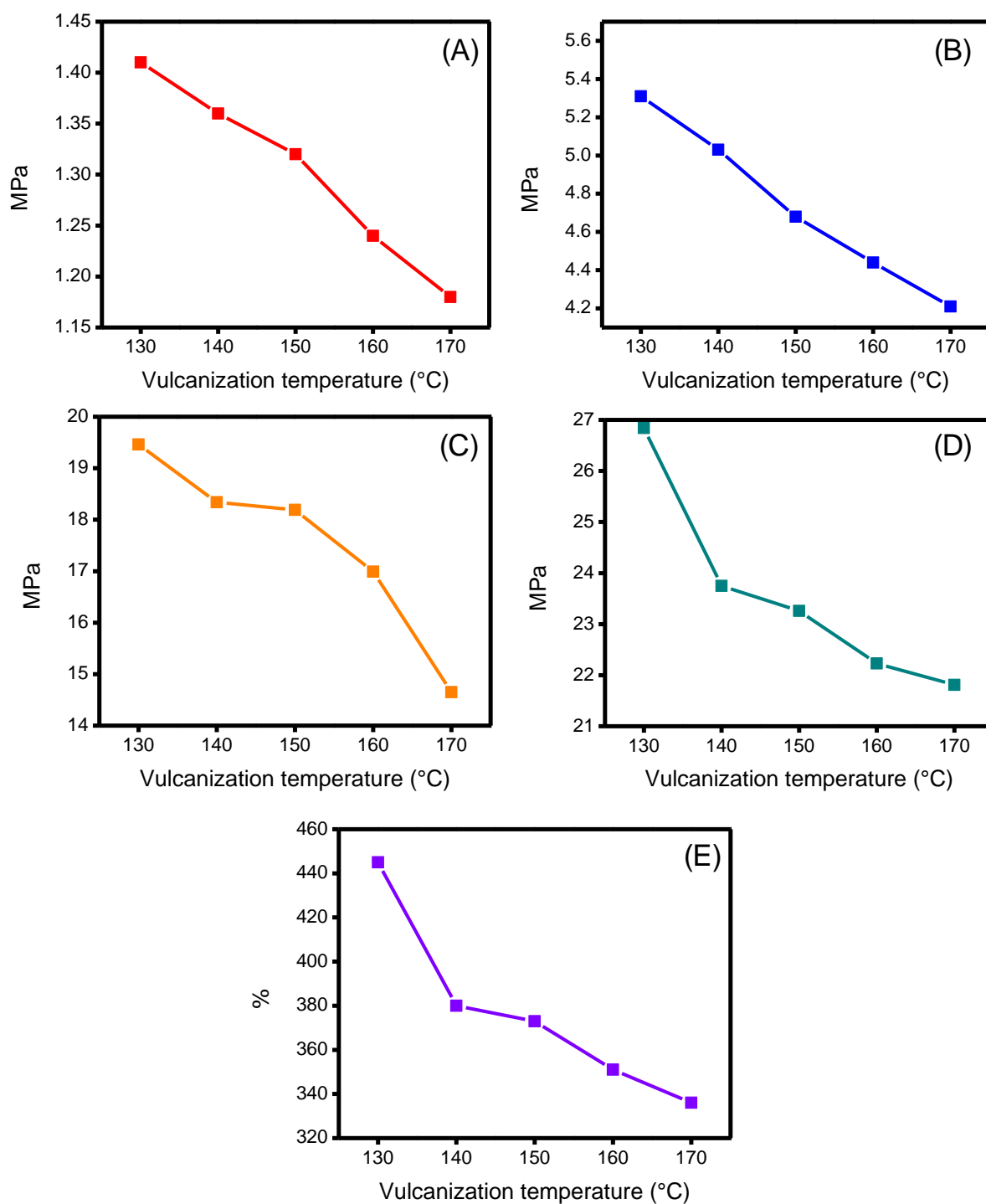


**Figure S5.** Physical properties of rubber compound with increasing vulcanization temperature : (A) 10 % modulus, (B) 100 % modulus, (C) 300 % modulus, (D) Tensile strength and (E) EB.

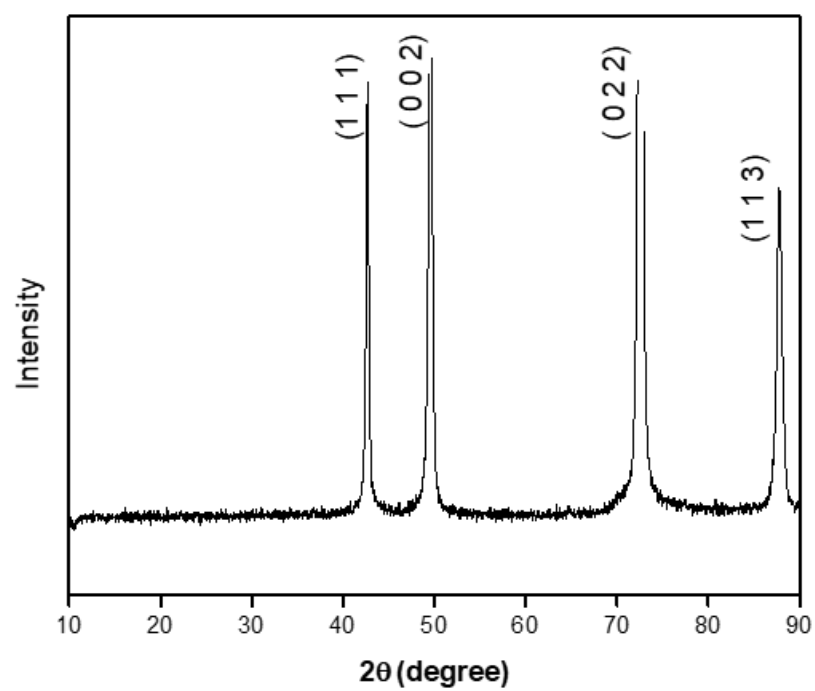


**Figure S6.** XRD pattern of un-vulcanized brass-coated steel cord.

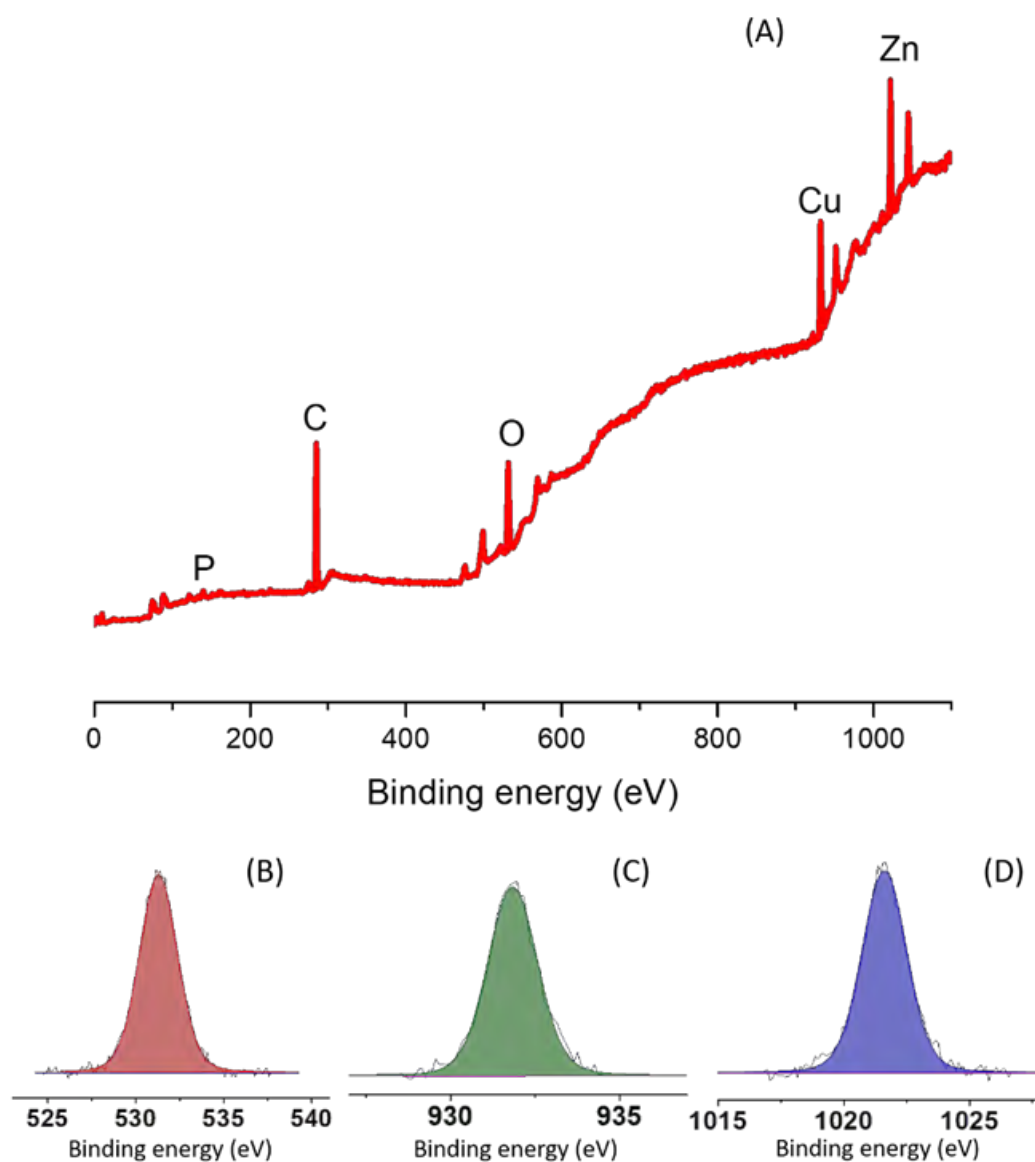


**Figure S7.** (A) XPS survey spectra of unreacted brass-coated steel cord under ambient conditions. (B), (C) and (D) High resolution XPS spectra of O 1s, Cu 2p<sub>3/2</sub> and Zn 2p<sub>3/2</sub>.

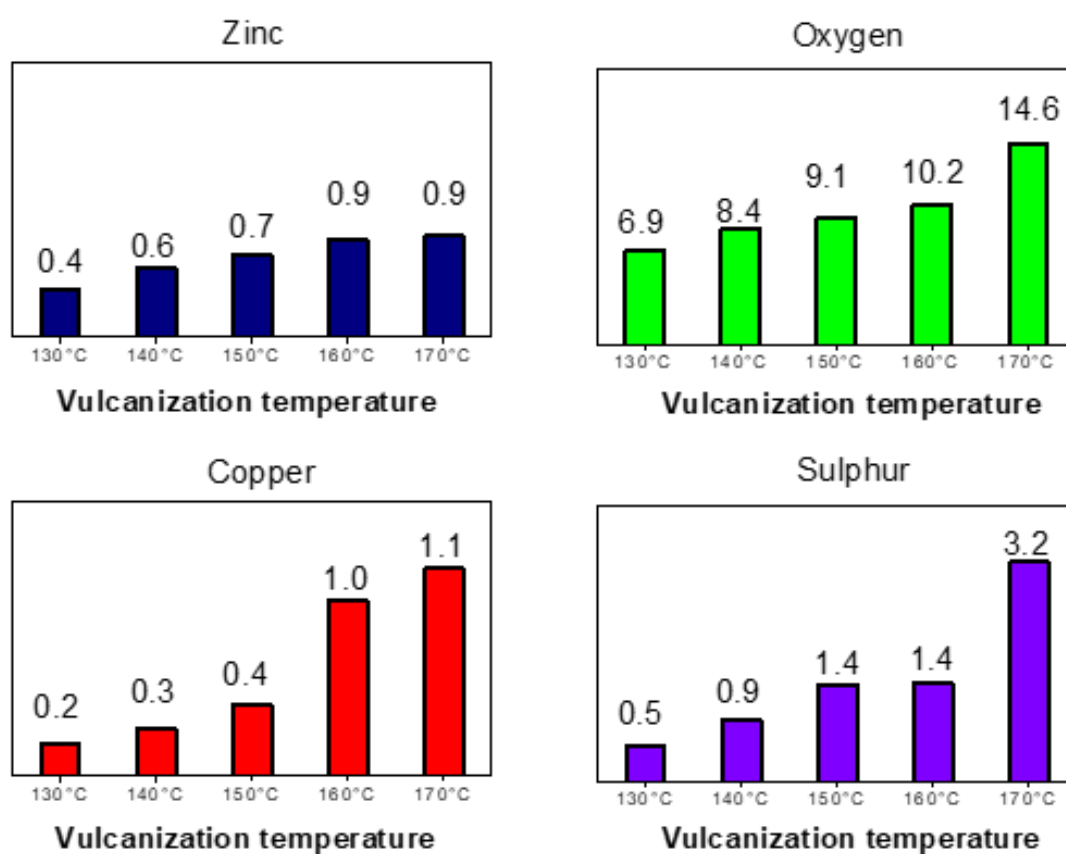


**Figure S8.** Relative atomic % obtained from XPS.

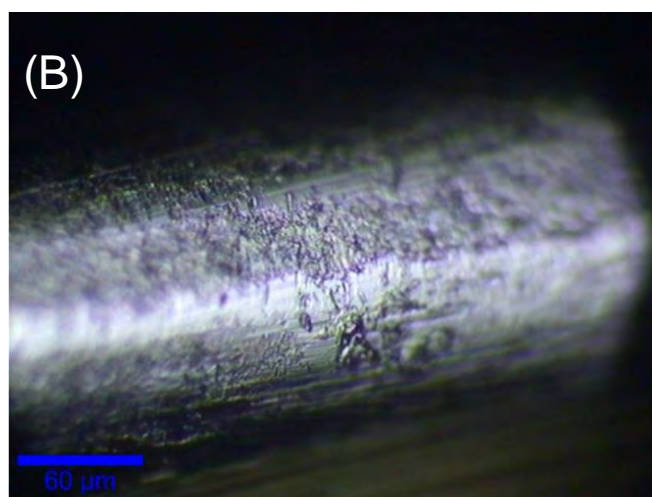
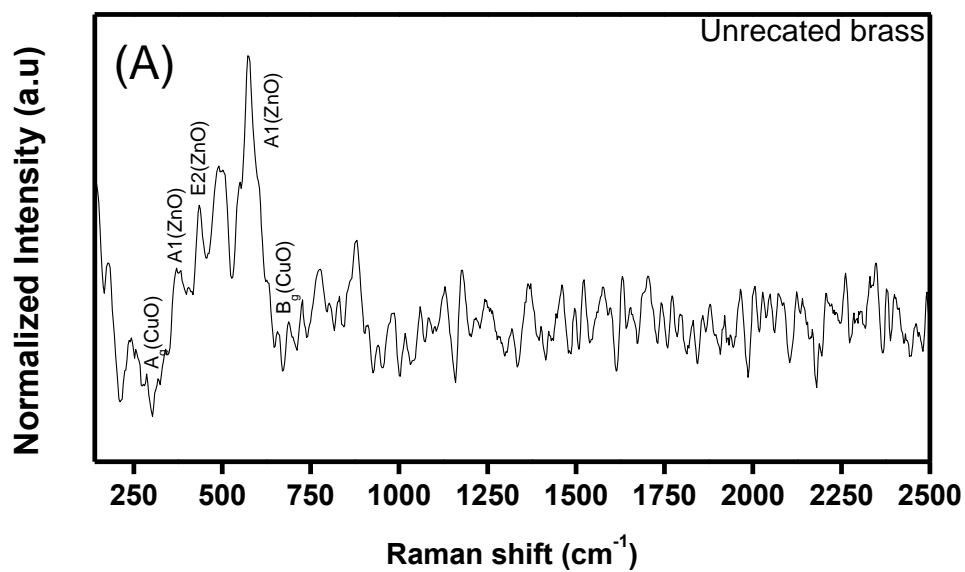


**Figure S9.** (A) Raman spectra of unreacted brass-coated steel cord and (B) LED white light image of unreacted brass-coated steel cord.

**Table S1.** Total crosslink density of rubber compound at different vulcanization temperature.

<b>Vulcanization temperature (°C)</b>	<b>Total crosslink density (mol/cc)</b>
130	9.42 E-05
140	1.30 E-04
150	1.56 E-04
160	1.93 E-04
170	2.42 E-04





Cite this: DOI: 10.1039/d0sc02467h

All publication charges for this article have been paid for by the Royal Society of Chemistry

# Accelerated microdroplet synthesis of benzimidazoles by nucleophilic addition to protonated carboxylic acids†

Pallab Basuri,<sup>a</sup> L. Edwin Gonzalez,<sup>b</sup> Nicolás M. Morato,<sup>b</sup> Thalappil Pradeep<sup>b</sup> and R. Graham Cooks<sup>b</sup>

We report a metal-free novel route for the accelerated synthesis of benzimidazole and its derivatives in the ambient atmosphere. The synthetic procedure involves 1,2-aromatic diamines and alkyl or aryl carboxylic acids reacting in electrostatically charged microdroplets generated using a nano-electrospray (nESI) ion source. The reactions are accelerated by orders of magnitude in comparison to the bulk. No other acid, base or catalyst is used. Online analysis of the microdroplet accelerated reaction products is performed by mass spectrometry. We provide evidence for an acid catalyzed reaction mechanism based on identification of the intermediate arylamides. Their dehydration to give benzimidazoles occurs in a subsequent thermally enhanced step. It is suggested that the extraordinary acidity at the droplet surface allows the carboxylic acid to function as a C-centered electrophile. Comparisons of this methodology with data from thin film and bulk synthesis lead to the proposal of three key steps in the reaction: (i) formation of an unusual reagent (protonated carboxylic acid) because of the extraordinary conditions at the droplet interface, (ii) accelerated bimolecular reaction because of limited solvation at the interface and (iii) thermally assisted elimination of water. Eleven examples are shown as evidence of the scope of this chemistry. The accelerated synthesis has been scaled-up to establish the substituent-dependence and to isolate products for NMR characterization.

Received 30th April 2020  
Accepted 13th July 2020

DOI: 10.1039/d0sc02467h

rsc.li/chemical-science

## Introduction

Carbon–nitrogen (C–N) coupling chemistry<sup>1</sup> is of comparable or even greater importance than is carbon–carbon coupling<sup>2</sup> especially in the context of pharmaceutically active small molecules.<sup>3</sup> These reactions involve *in situ* conversion of pre-catalysts (often ligated Pd) to the active catalyst and activation of the amine by base – typically an organic base, so permitting reaction in a homogeneous liquid phase.<sup>4</sup> An enormous number of catalysts has been explored and C–N bond formation is currently possible under relatively mild conditions using Pd, Cu and other organometallic catalysts. Conceptually, an alternative to nucleophilic substitution at an aryl or alkyl (pseudo) halide is the acid catalyzed nucleophilic substitution at a carbonyl carbon, effectively amine addition to an acylium ion. Examples of accelerated droplet chemistry involving somewhat related mechanisms are known, in particular the acid catalyzed

reaction of ketones with amines to form imines.<sup>5–13</sup> It seems likely that the extraordinarily high acidity at the surface of aqueous droplets drives these rapid reactions, even in cases like this study where the solvent is nominally non-aqueous. We explore C–N coupling of amines using protonated carboxylic acids as reagents (clearly counter-intuitive entities, given that neutral carboxylic acids are normally proton donors not acceptors). The addition/water elimination product, the substituted amide, is not our primary focus here; rather we are most interested in systems in which the presence of an *ortho* amino group allows further reaction to give a cyclic benzimidazole.

Benzimidazoles are an important class of heterocyclic compounds due to their wide application as active pharmaceutical moieties. Albendazole, mebendazole, triclabendazole, droperidol and pimozide are examples of drugs containing a benzimidazole scaffold.<sup>14</sup> These drugs are used to treat cancers<sup>15</sup> and ulcers,<sup>16</sup> as well as fungal,<sup>17</sup> viral<sup>18</sup> and parasitic infections.<sup>19</sup> The parent compound also serves as a precursor for the synthesis of vitamin B12.<sup>20</sup> Derivatives of benzimidazoles are used industrially as ultraviolet filters and pigments.<sup>21,22</sup> Conventionally, benzimidazole synthesis requires heating 1,2-phenylenediamine (PDA) with concentrated carboxylic acid for hours at high temperature, followed by the addition of a strong Lewis base to obtain the product.<sup>23,24</sup> Recently, aldehydes and

<sup>a</sup>DST Unit of Nanoscience (DST UNS), Thematic Unit of Excellence (TUE), Department of Chemistry, Indian Institute of Technology Madras, Chennai 600036, India

<sup>b</sup>Department of Chemistry, Purdue University, West Lafayette, Indiana 47907, USA. E-mail: cooks@purdue.edu

† Electronic supplementary information (ESI) available: MS, MS/MS, <sup>1</sup>H NMR and UV-vis spectra; kinetic plots; experimental diagrams. See DOI: 10.1039/d0sc02467h



alcohols have been used as additives to facilitate the bulk reaction.<sup>25,26</sup> Moreover, the reaction can be performed at a milder temperature by adding catalysts such as cobalt,<sup>27</sup> palladium,<sup>28</sup> copper<sup>29</sup> and even boranes.<sup>30</sup> Despite the use of a metal catalyst, the reaction generally takes 6 to 12 hours to accomplish. Reactions involving radical pathways under UV-radiation are faster but require a radical generator such as rose bengal.<sup>31</sup> Other strategies have included the use of microwave irradiation in presence of triphenyl phosphite.<sup>32</sup> Nevertheless, in terms of sustainable synthesis, reactions that occur rapidly under mild conditions remain highly desirable.

In this study, we demonstrate a metal-free synthetic strategy in which the rate of the benzimidazole synthesis is accelerated and occurs under ambient conditions inside charged microdroplets during their brief time of flight in the open air either into a mass spectrometer or, in scaled-up experiments (see below), onto a droplet collector. These electrosprayed microdroplets behave like micro/nano-reactors which undergo rapid desolvation and coulombic fission while finally releasing unsolvated product ions into the vacuum of the mass spectrometer.

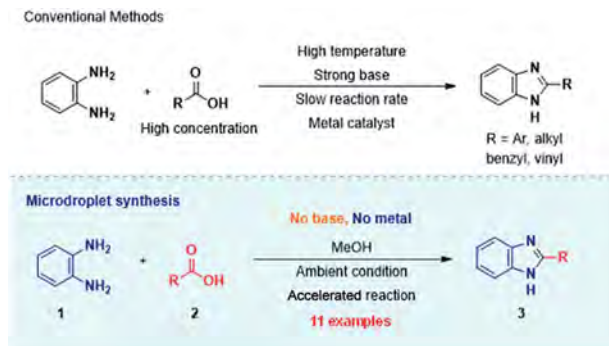
Examples of reactions known to be accelerated in the microdroplet environment include Suzuki coupling,<sup>33</sup> Fisher indole synthesis,<sup>10</sup> Katritzky transamination,<sup>34</sup> Claisen–Schmidt condensation,<sup>35</sup> Eschenmoser coupling,<sup>35</sup> Dakin reaction,<sup>36</sup> Baeyer–Villiger oxidation,<sup>36</sup> *N*-alkylation of indoles,<sup>37</sup> Combes reaction,<sup>12</sup> Pomeranz–Fritsch synthesis,<sup>12</sup> and cycloaddition reactions.<sup>38</sup> These microdroplet accelerated reactions can be performed under ambient conditions using nESI<sup>10</sup> or, in larger volumes, using electrosonic spray ionization (ESSI).<sup>12</sup> Levitated Leidenfrost droplets<sup>13</sup> allow milligram quantities of compounds to be synthesized in times on the order of minutes. Here, we use both nESI and ESSI, as well as mass spectral fragmentation patterns (MS/MS experiments) to generate and identify reaction intermediates and products, supplemented by isotope labeling and pH dependence experiments.

In addition to being the focus for accelerated organic reactions as discussed here, sprays have also seen use in materials preparation, sometimes on a commercial scale as in the case of electrospinning.<sup>39</sup> Other examples include fabrication of silver nanobrushes,<sup>40</sup> metallic palladium nanosheets,<sup>41</sup> high entropy alloys,<sup>42</sup> dandelion-like CuO–Ag hybrid hierarchical nanostructures,<sup>43</sup> hybrid perovskite quantum nanostructures,<sup>44</sup> and multi-metal 3D printed microstructures.<sup>45</sup>

## Results and discussion

### Droplet reactions and MS analysis

Scheme 1 displays the reaction conditions used in conventional<sup>23,24</sup> and microdroplet benzimidazole synthesis. The droplet reaction was performed by electrospraying a 1 : 1 molar ratio of *o*-aryl diamine and carboxylic acid at 2–2.5 kV applied potential using nESI emitters of 5  $\mu$ m tip diameter. The solvent was methanol and the concentration of each reactant was 8 mM. Collision-induced dissociation (CID) with He as collision gas was used to record MS/MS spectra for the characterization of products and intermediates. The scope of the microdroplet synthesis was



Scheme 1 Synthesis of benzimidazole and its derivatives by conventional methods<sup>22,23</sup> (above) and microdroplet synthesis (below).

assessed using seven diamines (1,2-phenylenediamine (PDA), 4-methyl-1,2-phenylenediamine, 4,5-dimethyl-1,2-phenylenediamine, 4-nitro-1,2-phenylenediamine, 4-chloro-1,2-phenylenediamine, 4-methoxy-1,2-phenylenediamine and 1,2-diaminonaphthalene) and five carboxylic acids (formic acid (FA), acetic acid (AA), trifluoroacetic acid (TFAA), propanoic acid (PA) and benzoic acid (BA)).

Fig. 1 compares the mass spectrum of PDA recorded with and without addition of formic acid. There is no benzimidazole product without the acid, the only signal being that at  $m/z$  109 corresponding to protonated PDA. The inset of Fig. 1A schematically illustrates the procedure used for microdroplet synthesis. The MS/MS spectrum of the ion at  $m/z$  109 shows a characteristic neutral loss of ammonia (ESI, Fig. S1A†) confirming that the peak corresponds to protonated PDA. The ion at  $m/z$  119 observed when the reaction mixture was electrosprayed, fragmented by loss of a HCN molecule during CID (Fig. S1B†). This strongly suggests that the ion corresponds to protonated benzimidazole formed as a result of the reaction

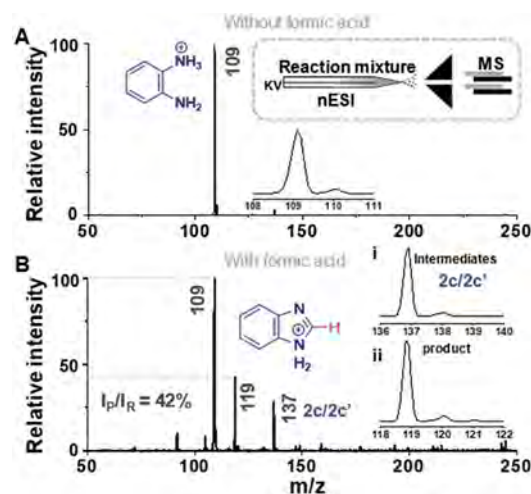


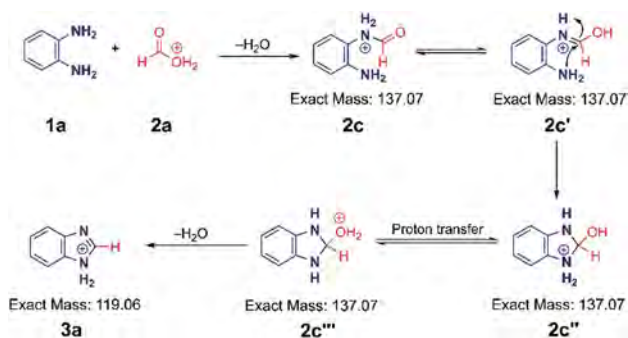
Fig. 1 Microdroplet synthesis of benzimidazole. (A) Mass spectrum of PDA in methanol without addition of formic acid. Insets show the isotopic distribution of the peak at  $m/z$  109 and a schematic illustration of the setup. (B) Mass spectrum of PDA with FA at 1 : 1 molar ratio in methanol. Insets show the isotopic distributions of the peaks at (i)  $m/z$  137 and (ii)  $m/z$  119.  $I_P$  and  $I_R$  refer to the intensity of signals for product and reactant, respectively.



between PDA and FA. We verified this assignment by comparison with the MS/MS spectrum of the authentic compound (Fig. S2B†). In addition to the product,  $m/z$  119, the mass spectrum of the reaction mixture shows a peak at  $m/z$  137, which corresponds to a hydrated intermediate. This ion might be the formamide (*i.e.* **2c** in Scheme 2) in acyclic or cyclized form, each including two tautomers. This mass-selected ion dissociates under CID to give a major peak at  $m/z$  109 and a minor peak at  $m/z$  119 (Fig. S1C†) consistent with both the acyclic formamide (which fragments back to starting material) and with the cyclic product (which undergoes dehydration to the benzimidazole).

A similar electrospray reaction was conducted between PDA and AA. This reaction produces 2-methylbenzimidazole, seen as the protonated form at  $m/z$  133 in the full mass spectrum (Fig. S3A†), and confirmed by comparison of its MS/MS spectrum (Fig. S3B†) with that of the authentic compound (Fig. S4B†). The peak at  $m/z$  151 in the full mass spectrum is assigned to the formation of the intermediate amide. Fragmentation of this ion shows a major peak at  $m/z$  109, which corresponds to the starting reagent and, most significantly, it shows neutral loss of a water molecule to form the protonated reaction product at  $m/z$  133 (Fig. S3C†).

To confirm that these reactions do not occur upon immediate mixing of the reagents in methanol, UV-vis and  $^1\text{H}$  NMR spectra of the authentic products and the reaction mixtures of the benzimidazole and 2-methylbenzimidazole synthesis were obtained.  $^1\text{H}$  NMR experiments were performed in deuterated chloroform for benzimidazole and the reaction mixture used to generate it, while deuterated methanol was used for 2-methylbenzimidazole and its reaction mixture. The mixtures of reagents were kept for 10 minutes at room temperature before recording the spectra. The UV-vis spectrum of the PDA/FA mixture (Fig. S5†) shows an expected small shift compared to the PDA spectrum upon addition of formic acid, which protonates the amine. However, the spectral signatures corresponding to the product were not observed in the UV-vis spectrum of the reaction mixture or in the  $^1\text{H}$  NMR spectra of these solutions (Fig. S6–S9†). Analogous results were obtained for the reaction between PDA and AA (Fig. S10–S14†). These results confirm that the reagents do not react in bulk.



**Scheme 2** Proposed mechanism for the acid-catalysed benzimidazole synthesis in charged microdroplets. A similar mechanism can be written starting from the more stable carbonyl protonated form of the acid.

Rough estimates of the yields of the microdroplet synthesis reactions were obtained by measuring the conversion ratio (CR): the ratio of the intensity between the product (P) and the sum of the intensities of the starting material (SM), intermediate (I), and product, *viz.*,  $[P]/([SM] + [P] + [I])$ .<sup>41</sup> Note that this estimate does not correct for differences in ionization energy so more accurate yields were obtained by collecting and purifying product (see below). The conversion ratios for the benzimidazole and 2-methylbenzimidazole syntheses were 27% and 3%, respectively (measured with MS inlet capillary temperature at 50 °C). This difference in the conversion ratio is surprisingly large but consistent with the expected lower electrophilicity of the methyl substituted carbon in AA *vs.* the unsubstituted carbon of FA. We noticed a change in the conversion ratios as a function of the mass spectrometer inlet capillary temperature as is now discussed.

### Temperature effects

Studies of the Pomeranz–Fritsch and the Combes reactions showed that the temperature of the MS inlet can play an important role, with increasing inlet temperatures having opposite effects on the rate of these two reactions.<sup>46</sup> In the benzimidazole synthesis, a significant increase in the product yield was observed upon increasing the inlet temperature. Both the FA and the AA reactions showed maximum conversion ratios at higher, albeit different, temperatures (Fig. 2A and B). In the case of PDA/FA a maximum was observed at 300 °C while for PDA/AA the maximum was reached at 350 °C. It was also noted in both cases, that the intensity of the intermediate peak decreases and almost disappears as the temperature is raised above 200 °C. Mass spectra of the reaction mixtures for the

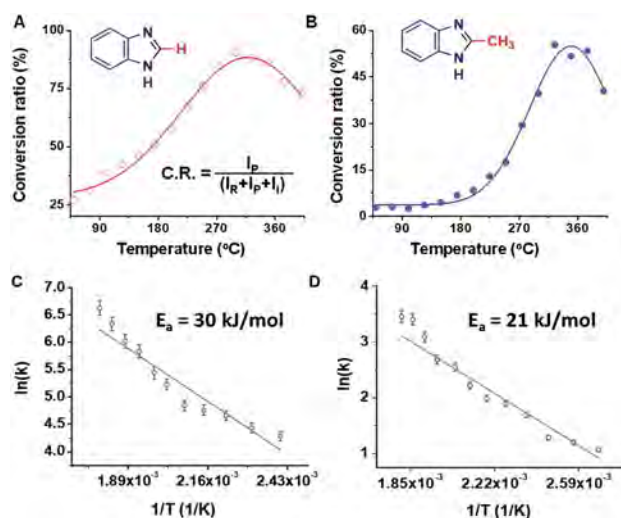


**Fig. 2** Effect of inlet temperature of the mass spectrometer on ion intensity, showing conversion ratio (CR) *vs.* temperature plot for synthesis of (A) benzimidazole and (B) 2-methylbenzimidazole. The equation inset in (A) is used to calculate conversion ratio, where R, P, and I refer to reagent, product and intermediate, respectively. Plots (C) and (D) display temperature-dependent rates plotted against  $1/T$  and give activation energies for the reactions leading to benzimidazole and 2-methylbenzimidazole, respectively.





benzimidazole and 2-methylbenzimidazole syntheses at eight different temperatures ranging from 50 to 400 °C are shown in Fig. S15.† Based on the temperature dependence for PDA/FA (Fig. S15A†) the relative abundance of the product peak at  $m/z$  119 increases from 50 to 180 °C and it becomes the base peak at 200 °C, decreasing beyond this point. The intermediate peak at  $m/z$  137 also decreases sharply in this temperature range (Fig. S16†). The PDA/AA reaction shows a similar trend but over a higher temperature range (270 to 400 °C) and with a sharper increase in product signal,  $m/z$  133 (Fig. S15B†). These observations also show that ionization efficiency decreases with increasing temperature so, in spite of the increase in product ions through conversion to reagents to products, there is a net decrease at high temperature.

The temperature data are ascribed to removal of water shifting the dehydration/rehydration equilibrium to favor product formation. Although the effect of temperature is expected to be different for the different reactions because of their different energy requirements, the large difference between the product peak maxima (180 °C for benzimidazole but 350 °C for 2-methyl benzimidazole) is noteworthy. A plot of the inverse temperature dependence of these two reactions allows an estimation of activation energies. This is done in Fig. 2C and D, from which the values are 30 kJ mol<sup>-1</sup> vs. 21 kJ mol<sup>-1</sup>.

### Mechanism (Scheme 2)

Based on the above data, we speculate that the reaction must go through an acid catalyzed pathway, but not one driven by protonation of the amine. It is known that the proton concentration at the surface of positively charged electro-sprayed aqueous droplets is much higher than in the bulk.<sup>47–49</sup> So we propose that a very high proton concentration at the surface of a droplet containing water will protonate neutral formic acid to create the electrophilic carbon (2a) which is subject to nucleophilic attack by the lone electron pair of the amine. (We observed protonated formic and trifluoroacetic acid in the mass spectra (Fig. S17A and B†). This was confirmed by an MS/MS experiment (Fig. S17C†) on protonated TFAA). Subsequent loss of water results in the formation of a formamide intermediate (2c). Intramolecular nucleophilic attack at the carbon in the enol form of the intermediate (2c') by the lone pair of the adjacent nitrogen forms the five-membered cyclic intermediate (2c''). Finally, dehydration of its tautomer (2c''') leads to protonated benzimidazole (3a) as the final product. The intermediates 2c, 2c', 2c'' and 2c''' are indistinguishable by mass/charge ratio, all occurring at  $m/z$  137 (Fig. 1B). The MS/MS spectrum of  $m/z$  137 (Fig. S1C†) shows that this ion can either fragment back to protonated PDA ( $m/z$  109) by loss of CO or lose water to form the benzimidazole product ( $m/z$  119). These two processes give us confidence in the fact that the ion  $m/z$  137 encompasses several isomers, as illustrated in Scheme 2. An analogous intermediate,  $m/z$  151, is noted for the PDA/AA reaction and its fragmentation pattern (Fig. S3B†) confirms this.

The mechanism illustrated in Scheme 2 was also tested using formic-d acid (DCOOH). We expected isotopically labeled

intermediates and product according to the proposed reaction pathway and observed the deuterated benzimidazole at  $m/z$  120 and the deuterated intermediate at  $m/z$  138 (Fig. S18A†). Fragmentation of the  $m/z$  138 peak gives the protonated reagent ( $m/z$  109) as well as the deuterated product ( $m/z$  120). Analogously, isotopically labeled 2-methylbenzimidazole at  $m/z$  136 and the intermediate at  $m/z$  154 were observed with CD<sub>3</sub>COOH (Fig. S18B†). These results agree with expectations and support the suggestion that reaction occurs through a protonated carboxylic acid pathway.

The fact that acids catalyze the formation of benzimidazole is well known.<sup>50</sup> We suggest that the extraordinary acidity of microdroplets catalyzes the reaction on the milli- or micro-second time scale. Only in a formal sense (acid is not added to the reaction mixture) could one say that the droplet reaction is not acid catalyzed. More evidence for acid catalysis is shown below in connection with changes in solvent to increase the proportion of water.

### Thin film reactions

Our view of the reaction mechanism is that as the droplets evaporate, the increasingly high acidity of the droplet surface allows protonation of the carboxylic acid followed by nucleophilic attack by an amino group and dehydration, before cyclization and then a second dehydration event. It seems likely that the dehydration of the intermediate is the slow step in the reaction, hence the effect of the inlet temperature. If these arguments are correct, then it should be possible to observe the accelerated reaction entirely at ambient temperature (keeping the MS inlet at the lowest possible temperature of 50 °C). To test this claim, a thin film of reaction mixture in methanol was held at ambient temperature in the open lab. The mixture contained a trace (2.5 ppm) of a non-volatile acid, *p*-toluenesulfonic acid. This was added as a result of earlier ambient temperature accelerated thin film reactions<sup>11</sup> in which traces of nonvolatile additives allowed continuous long-term reaction involving elimination of water or other small molecules.<sup>51</sup> The nonvolatile acid helps to create and maintain a micro/nano-thin film. Kinetic data were recorded by MS (Fig. S19†) to follow benzimidazole and 2-methylbenzimidazole formation in this thin film experiment. In parallel with earlier studies on the base-catalyzed Katritzky transamination, we see that the reaction does not occur during an initial period of some minutes (while most of the methanol is evaporating) but it then increases in rate before plateauing after 6 hours, with 120% and 16% product-to-reagent peak intensity ratios for benzimidazole and 2-methylbenzimidazole, respectively. Clearly, the reactions are accelerated in the thin film compared to bulk, and increasingly so as the film becomes thinner with continued methanol evaporation. However, the reaction rate is moderate in comparison to the ambient droplet phase synthesis (using ESSI as discussed below) and small in comparison to the elevated temperature nESI microdroplet synthesis already discussed. The large differences in rate associated with simple methyl substitution are also replicated. These data support the conclusions on the reaction mechanism already outlined.



## Solvent effects

The mechanistic arguments also need to include consideration of the solvent system, especially because we invoke a highly acidic environment at the droplet surface. Experiments done by varying the percentage of water in methanol over the range 1–50% showed that a low percentage of water (1–10%) favors the reaction (Fig. S20†). The relative product plus intermediate ion intensity increases from 62 to 95% over this range. However, at higher water concentrations the relative intensity of the product plus intermediate peaks decreases significantly to 52–54% and when the reaction is performed in dry ACN we observe no product at all (Fig. S21†). These results are consistent with a balance between reagent solubility, methanol evaporation and formation of a superacid surface layer of water in the almost fully evaporated microdroplets. This clearly aligns with literature data<sup>47–49</sup> on the high acidity of the surfaces of aqueous droplets while extending the concept of superacid formation in microdroplets to organic/aqueous mixed solvents. We imagine that water, being a stronger base than methanol, takes the charge and occupies the surface of a small methanol droplet thereby protonating neutral formic acid and initiating the benzimidazole synthesis. The final (dehydration) step, however, is impeded in aqueous solutions.

## pH dependence

We assessed the effect of decreasing the pH of the reaction mixture by adding equimolar concentrations of a strong inorganic acid, HCl. In the case of the microdroplet reaction of PDA/FA, addition of HCl does not cause significant changes in the mass spectrum of the reaction mixture (Fig. S22†). This lack of observable effect of pH reduction is consistent with the suggestion that the superacid at the surface of positively-charged water-containing droplets is responsible for protonating the carboxylic acid. The addition of HCl will reduce the pH in the core of the droplet, without changing the protonation of the carboxylic acid at the surface.

## Acceleration factors

The apparent acceleration factor (AAF) of a reaction can be calculated by comparing the product to starting material intensity ratio in the microdroplet reaction to the value in the bulk reaction carried out for the same period of time, *viz.*  $([P]/[SM])_{\text{droplet}}/([P]/[SM])_{\text{bulk}}$ .<sup>33</sup> Alternatively, it can be measured by recording the ratio of the time required to reach the same conversion ratio for both the conditions. To measure the AAF we performed a bulk reaction using an equimolar ratio of PDA and AA in methanol at ambient temperature. The AAF was calculated from the kinetic data as plotted in Fig. S23.† This simple method of approximating the apparent acceleration factor (not the true acceleration factor which is the ratio of rate constants) shows that the microdroplet reaction is accelerated by a very large factor (almost  $10^9$ ). This is not intended as a quantitative measure because the role of the inlet temperature in driving the reaction has not been considered.

We compared high temperature microdroplet data with bulk reaction data obtained by refluxing the reaction mixture in

methanol for 24 hours. Comparison was made between product formation in this bulk reaction (analysed using inlet temperature of 50 °C to minimize droplet reactions during analysis), with that in microdroplet reactions using 200 °C inlet temperature (Fig. S24A†). The data show that the relative intensity of the product peak at *m/z* 133 is significantly lower (*ca.*  $\times 5$ ) in the bulk than in the microdroplet experiment in spite of the difference of many orders of magnitude in reaction time. This difference becomes even more significant with higher inlet temperatures, which provide exponentially larger reaction acceleration factors (Fig. S24B†). The apparent acceleration factor at 50 °C inlet temperature was  $1.1 \times 10^8$  and it increased to  $6.6 \times 10^8$  at 350 °C. This is just one example of a very high AAF, others are shown later in the article. Factors of similar magnitude have been reported for the Biginelli reaction where similar temperature effects are associated with the last step of a reaction.<sup>52</sup>

## Scope of ambient droplet reaction

The results of a systematic study of the scope of the microdroplet synthesis of benzimidazoles was undertaken, now using ambient temperatures accessed by ESSI. This procedure not only allows the entire reaction to occur at ambient temperature but it also allows ready scale up to several hundred mg. MS and NMR were used to characterize and quantify the reaction products which were collected on a surface rather than being directly transferred into the MS. The results are summarized in Table 1, which gives the experimental conversion ratio (CR), the apparent acceleration factor (AAF) and the experimentally determined yield, as measured after product isolation by flash chromatography.

The mass spectra of the isolated products typically show a single peak due to the protonated product with no trace of reagents or intermediates, as typified by benzimidazole (Fig. S25†). The <sup>1</sup>H NMR of this isolated product shown in Fig. S26† also demonstrates moderately high purity. We found the actual yield of the product of benzimidazole synthesis to be 72% (entry 1, Table 1). However, the yield was reduced to 16% in the case of 2-methylbenzimidazole (entry 2, Table 1) presumably due to the inductive effect of the methyl group in the carboxylic acid, which weakens the electrophilic center of the acid. MS and NMR spectra are presented in Fig. S27 and S28.† Product isolation using flash chromatography was not always effective in separating all the products as reflected in these mass and NMR spectra. Other 2-substituted benzimidazoles were synthesized by varying the structures of the carboxylic acids. An electron withdrawing group such as CF<sub>3</sub> in the carboxylic acid increases the yield to 22% (entry 3, Table 1). The ethyl substituted benzimidazole (entry 4, Table 1) has a 10% yield, similar to the methyl substituted case. Correspondingly, the phenyl substituent on the carboxylic acid provides a lower yield (5%) due to resonance electron donation.

The reaction scope was further extended by performing reactions between formic acid and several substituted *o*-aryl diamines, specifically: 4-methyl-1,2-phenylenediamine, 4,5-dimethyl-1,2-phenylenediamine, 4-nitro-1,2-phenylenediamine, 4-chloro-1,2-



Table 1 Scope of microdroplet synthesis of benzimidazoles from substituted *o*-aromatic diamines and aromatic/aliphatic carboxylic acids<sup>a</sup>

Entry	Diamine 1	Acid 2	Product 3	AAF × 10 <sup>9</sup>	C.R.	Yield%
1				0.83	27	72
2				0.74	3	16
3				0.11	18	22
4				25	1	10
5				0.02	5	5
6				0.25	37	93
7				4.2	3	38
8				No reaction	No reaction	No reaction
9				0.59	14	60
10				0.04	36	67
11				200	6	29

<sup>a</sup> The reactions were performed using a home built ESSI source. Each diamine (200 mg) was used in a 1 : 1 molar ratio with the acid in methanol. The flow rate and the gas pressure used for droplet deposition were 10  $\mu\text{L min}^{-1}$  and 30 psi. The ESSI experiment was done under ambient conditions (in contrast to the nESI data reported above, which used an inlet temperature of 50 °C unless otherwise indicated). In a few cases the CR and the yield trends differ, likely due to poor product separation by flash chromatography.

phenylenediamine, 4-methoxy-1,2-phenylenediamine and 1,2-diaminonaphthalene, to synthesize 4-methylbenzimidazole (5f), 4,5-dimethylbenzimidazole (5g), 4-nitrobenzimidazole (5h), 4-chlorobenzimidazole (5i), 4-methoxybenzimidazole (5j), and naphth[1,2]imidazole (5k), respectively (entries 6–11 in Table 1). It is observed that for the first two cases the inductive effect facilitates product formation leading to 93 and 38% product yields, respectively. We suspect that a steric effect reduces the product yield in the case of the dimethyl substituted amine. However, the conjugated strong electron withdrawing group (nitro-) results in no product formation (entry 8, Table 1), while the chloro- and the methoxy-substituted products (entry 9 and 10, Table 1) have yields of 60% and 67%, respectively. We also extended the method to the synthesis

naphth[1,2]imidazole (entry 11, Table 1) and observed product in 29% of yield, with a very high AAF of the order of  $2 \times 10^{11}$ . <sup>1</sup>H NMR and mass spectra of the isolated products are available in the ESI.†

There is a rough correlation between the experimentally observed isolated yields and the experimentally estimated acceleration factors (as seen in Table 1). There is also rough agreement with the electron donating/withdrawing character of the diamine and the carboxylic acid (with some exceptions potentially due to steric effects). The AAF for the benzimidazole synthesis ( $0.83 \times 10^9$ ) is on the same order of other reactions with substituted amines and carboxylic acids. However, the increase of AAF in case of the reactions of PDA/PA ( $2.5 \times 10^{10}$ ), 4,5-dimethyl PDA/FA ( $4.2 \times 10^9$ ) and naphthalene-1,2-diamine/





FA ( $2 \times 10^{11}$ ) may be due to their low reactivity in bulk because of steric effects. The high yield (and conversion ratio) for the methoxyphenylenediamine (entry 10, Table 1) is consistent with the expected high reactivity of the amine due to the electron donation by the oxygen of the methoxyl group. These relationships provide strong evidence for the nucleophilic attack at the carboxylic acid carbon which must be ascribed to the extraordinary acidity at the droplet (and thin film) interfaces.

## Experimental

### Online reaction monitoring

Online monitoring was carried out using a nESI source in which the reagents were mixed prior to being sprayed. The nESI tip (5  $\mu\text{m}$  diameter) was held 1 cm away from the inlet of the mass spectrometer. The applied potential for spray generation was kept at 2–2.5 kV. The capillary and tube lens voltages were set to 50 and 100 V, respectively. For the temperature dependence study, the capillary temperature was initially set to 50 °C but later increased to a final temperature of 400 °C. Unless otherwise noted, the mass spectrometric studies were performed at 50 °C inlet temperature. All mass spectra were recorded by averaging 4 microscans of 100 ms scan times. A linear ion trap was used for all MS studies, and CID with He as collision gas was used for MS/MS analysis.

### Thin film synthesis

Thin film reactions were performed by applying a thin film of the reactants onto the surface of parafilm. The parafilm was wrapped around a glass slide to prevent catalysis by the glass. The thin film of reaction mixture was produced by drop-casting 5  $\mu\text{L}$  of mixture containing 2.5 ppm of *p*-toluenesulfonic acid onto the parafilm surface. The film was allowed to dry slowly in ambient air. Sampling was done by transferring the crude product into 10  $\mu\text{L}$  of methanol and then quenching by diluting the sample  $\times 10$  in methanol before measuring by nESI. Measurements at different times were done using different thin films. All thin film reactions were performed in triplicate to verify reproducibility.

### Scaled-up reactions and product isolation

Scaling-up and product deposition used ambient ESSI. Scale-up was achieved by increasing the flux of droplets using a high flow rate of the solution in a fused silica capillary (150  $\mu\text{m}$  of ID and 300  $\mu\text{m}$  of OD). A flow rate of 10  $\mu\text{L min}^{-1}$  was used with +3 kV applied potential and 30 psi nebulization  $\text{N}_2$  gas pressure. HPLC grade methanol was used for the preparation of all the reaction mixtures. The amount of starting material used for the deposition experiment was 200 mg in each case. The collected crude product mixture was dissolved in methanol to perform thin layer chromatography to allow optimization of the solvent system for better separation of product from the crude. With this information the crude reaction mixture was separated using normal-phase silica flash column chromatography in a Biotage automated flash chromatography column. A methanol and DCM solvent gradient was selected for column

chromatography based on the  $R_f$  value of the reagent and the product. The fractionated solutions were characterized using nESI MS and  $^1\text{H}$  NMR. The fractions which contained the product were mixed and solvent was removed at reduced pressure to obtain isolated solid product. Yields of the microdroplet reactions were calculated using the mass of the recovered solid.

### Bulk synthesis

The bulk synthesis of 2-methylbenzimidazole was performed by mixing equimolar methanolic solutions of PDA and AA in a 500 mL two-neck round bottom flask fitted with a condenser. The final concentrations of each reagent in the mixture was 8 mM. The reaction mixture was then stirred and refluxed using a sand bath for continuous heating for 24 hours. The time dependent studies were carried out by removing 15  $\mu\text{L}$  aliquots of sample at fixed time intervals. Bulk reactions were also carried out under ambient conditions and characterized in a similar way.

Monitoring of time dependent mass spectra of the bulk reaction mixture was performed after dilution. The dilution was done to quench the reaction as well as to avoid microdroplet synthesis. Inlet temperature was also set to 50 °C and the tip of the nESI emitter was kept as close as possible to the inlet of the mass spectrometer to prevent reaction during bulk product analysis. The applied potential to generate the electrospray plume was 1 kV.  $([P]/[SM])_{\text{bulk}}$  data of the 24 hour sample was used to calculate the apparent acceleration factor.

## Conclusions

It is commonplace knowledge that amines and carboxylic acids react in Brønsted fashion to produce a salt, while amines react with carboxylic acid halides by nucleophilic substitution to give amides. The corresponding nucleophilic substitution with an acid would require the carboxylic acid to be protonated to give the conjugate base which could then eliminate water. This situation would call for extraordinary conditions in which a very strong acid is present so that not only is the ionization of the acid to its conjugated base suppressed by the common ion effect, but the neutral acid itself is protonated so it can react as a carbon-centered Lewis acid. These conditions are satisfied in the benzimidazole chemistry examined in this study.

Accelerated microdroplet synthesis of benzimidazole and its derivatives have been demonstrated under ambient conditions. The reaction involves aromatic-1,2-diamines and carboxylic acids in a metal free environment with no requirement of addition of base to complete the product formation. Online mass spectrometric monitoring enables detection of reaction intermediates and provides an understanding of the reaction mechanism. Ten examples are shown to illustrate the scope of the microdroplet synthesis.

The described mechanism of benzimidazole synthesis has three elements: (i) the formation of a highly reactive reagent because of the extraordinary conditions in at the interface (protonated of the carboxylic acid), (ii) the accelerated bimolecular reaction because of limited solvation at the interface and



(iii) the thermally assisted elimination of water. Point (i) is supported by the effect of adding water to the methanol solvent. Point (ii) is suggested by analogy to other organic solvent droplet reactions where this mechanism is supported by experimental and recent computations.<sup>53</sup> Point (iii) is shown directly by the experiments. Note that bimolecular reaction acceleration is seen in formation of the intermediate amide and that the thermal elimination of water is a subsequent and secondary factor. We think that many other droplet-accelerated reactions will contain some elements in common with this case.

## Conflicts of interest

There are no conflicts to declare.

## Acknowledgements

PB thanks IIT Madras and acknowledges a visiting doctoral fellowship from the Science and Engineering Board of India. RGC acknowledges support of the US National Science Foundation (1908057).

## References

- P. Ruiz-Castillo and S. L. Buchwald, *Chem. Rev.*, 2016, **116**, 12564–12649.
- E. Negishi, *Pure Appl. Chem.*, 1981, **53**, 2333–2356.
- T. Cernak, K. D. Dykstra, S. Tyagarajan, P. Vachal and S. W. Krska, *Chem. Soc. Rev.*, 2016, **45**, 546–576.
- L. M. Baumgartner, J. M. Dennis, N. A. White, S. L. Buchwald and K. F. Jensen, *Org. Process Res. Dev.*, 2019, **23**, 1594–1601.
- X. Yan, R. M. Bain and R. G. Cooks, *Angew. Chem., Int. Ed.*, 2016, **55**, 12960–12972.
- S. T. Ayrton, R. G. Cooks and M. Pugia, *Analyst*, 2016, **141**, 5389–5403.
- R. D. Espy, M. Wlekinski, X. Yan and R. G. Cooks, *TrAC, Trends Anal. Chem.*, 2014, **57**, 135–146.
- A. K. Badu-Tawiah, D. I. Campbell and R. G. Cooks, *J. Am. Soc. Mass Spectrom.*, 2012, **23**, 1077–1084.
- A. Saidykhan, Y. Nazir, W. H. C. Martin, R. T. Gallager and R. D. Bowen, *Eur. J. Mass Spectrom.*, 2017, **24**, 3–11.
- R. M. Bain, S. T. Ayrton and R. G. Cooks, *J. Am. Soc. Mass Spectrom.*, 2017, **28**, 1359–1364.
- Z. Wei, X. Zhang, J. Wang, S. Zhang, X. Zhang and R. G. Cooks, *Chem. Sci.*, 2018, **9**, 7779–7786.
- S. Banerjee and R. N. Zare, *Angew. Chem., Int. Ed.*, 2015, **54**, 14795–14799.
- R. M. Bain, C. J. Pulliam, F. Thery and R. G. Cooks, *Angew. Chem., Int. Ed.*, 2016, **55**, 10478–10482.
- K. Anand and S. Wakode, *Int. J. Chem. Stud.*, 2017, **5**, 350–362.
- B. Chu, F. Liu, L. Li, C. Ding, K. Chen, Q. Sun, Z. Shen, Y. Tan, C. Tan and Y. Jiang, *Cell Death Dis.*, 2015, **6**, e1686.
- A. Bettarello, *Dig. Dis. Sci.*, 1985, **30**, 36S–42S.
- Y.-B. Bai, A.-L. Zhang, J.-J. Tang and J.-M. Gao, *J. Agric. Food Chem.*, 2013, **61**, 2789–2795.
- M. Tonelli, M. Simone, B. Tasso, F. Novelli, V. Boido, F. Sparatore, G. Paglietti, S. Pricl, G. Giliberti, S. Blois, C. Ibba, G. Sanna, R. Loddo and P. La Colla, *Bioorg. Med. Chem.*, 2010, **18**, 2937–2953.
- L. H. Jaeger and F. A. Carvalho-Costa, *BMC Vet. Res.*, 2017, **13**, 358.
- M. J. Warren, *Proc. Natl. Acad. Sci. U. S. A.*, 2006, **103**, 4799.
- A. Bino, A. Baldisserotto, E. Scalambra, V. Dissette, D. E. Vedaldi, A. Salvador, E. Durini, S. Manfredini and S. Vertuani, *J. Enzyme Inhib. Med. Chem.*, 2017, **32**, 527–537.
- D. V. Dikshit, S. D. Deval and K. D. Deodhar, *Dyes Pigm.*, 1985, **6**, 39–46.
- E. C. Wagner and W. H. Millett, *Org. Synth.*, 1939, **19**, 12–14.
- P. N. Preston, *Chem. Rev.*, 1974, **74**, 279–314.
- D. Mahesh, P. Sadhu and T. Punniyamurthy, *J. Org. Chem.*, 2015, **80**, 1644–1650.
- K. Das, A. Mondal and D. Srimani, *J. Org. Chem.*, 2018, **83**, 9553–9560.
- P. Daw, Y. Ben-David and D. Milstein, *ACS Catal.*, 2017, **7**, 7456–7460.
- J. E. R. Sadig, R. Foster, F. Wakenhut and M. C. Willis, *J. Org. Chem.*, 2012, **77**, 9473–9486.
- Y. Kim, M. R. Kumar, N. Park, Y. Heo and S. Lee, *J. Org. Chem.*, 2011, **76**, 9577–9583.
- W. Cui, R. B. Kargbo, Z. Sajjadi-Hashemi, F. Ahmed and J. F. Gauuan, *Synlett*, 2012, **23**, 247–250.
- J. Kovvuri, B. Nagaraju, A. Kamal and A. K. Srivastava, *ACS Comb. Sci.*, 2016, **18**, 644–650.
- S. Lin, Y. Isome, E. Stewart, J. Liu, D. Yohannes and L. Yu, *Tetrahedron Lett.*, 2006, **47**, 2883–2886.
- P. W. Fedick, K. Iyer, Z. Wei, L. Avramova, G. O. Capek and R. G. Cooks, *J. Am. Soc. Mass Spectrom.*, 2019, **30**, 2144–2151.
- R. L. Schrader, P. W. Fedick, T. F. Mehari and R. G. Cooks, *J. Chem. Educ.*, 2019, **96**, 360–365.
- C. Liu, J. Li, H. Chen and R. N. Zare, *Chem. Sci.*, 2019, **10**, 9367–9373.
- D. Gao, F. Jin, J. K. Lee and R. N. Zare, *Chem. Sci.*, 2019, **10**, 10974–10978.
- E. Gnanamani, X. Yan and R. N. Zare, *Angew. Chem., Int. Ed.*, 2020, **59**, 3069–3072.
- R. M. Bain, S. Sathyamoorthi and R. N. Zare, *Angew. Chem., Int. Ed.*, 2017, **56**, 15083–15087.
- C.-L. Zhang and S.-H. Yu, *Chem. Soc. Rev.*, 2014, **43**, 4423–4448.
- D. Sarkar, M. K. Mahitha, A. Som, A. Li, M. Wlekinski, R. G. Cooks and T. Pradeep, *Adv. Mater.*, 2016, **28**, 2223–2228.
- D. Sarkar, R. Singh, A. Som, C. K. Manju, M. A. Ganayee, R. Adhikari and T. Pradeep, *J. Phys. Chem. C*, 2018, **122**, 17777–17783.
- Y. Yang, B. Song, X. Ke, F. Xu, K. N. Bozhilov, L. Hu, R. Shahbazian-Yassar and M. R. Zachariah, *Langmuir*, 2020, **36**, 1985–1992.
- H. Fang, D. Wang, L. Yuan, X. Wu, H. Guo, H. Chen, K. Huang and S. Feng, *New J. Chem.*, 2017, **41**, 2878–2882.
- R. Naphade, S. Nagane, G. S. Shanker, R. Fernandes, D. Kothari, Y. Zhou, N. P. Padture and S. Ogale, *ACS Appl. Mater. Interfaces*, 2016, **8**, 854–861.



- 45 A. Reiser, M. Lindén, P. Rohner, A. Marchand, H. Galinski, A. S. Sologubenko, J. M. Wheeler, R. Zenobi, D. Poulikakos and R. Spolenak, *Nat. Commun.*, 2019, **10**, 1853.
- 46 S. Banerjee and R. N. Zare, *J. Phys. Chem. A*, 2019, **123**, 7704–7709.
- 47 H. Wei, E. P. Vejerano, W. Leng, Q. Huang, M. R. Willner, L. C. Marr and P. J. Vikesland, *Proc. Natl. Acad. Sci. U. S. A.*, 2018, **115**, 7272–7277.
- 48 J. L. Lee, D. Samanta, H. G. Nam and R. N. Zare, *J. Am. Chem. Soc.*, 2019, **141**, 10585–10589.
- 49 K. Luo, J. Li, Y. Cao, C. Liu, J. Ge, H. Chen and R. N. Zare, *Chem. Sci.*, 2020, **11**, 2558–2565.
- 50 I. Mohammadpoor-Baltork, M. Moghadam, S. Tangestaninejad, V. Mirkhani, M. A. Zolfigol and S. F. Hojati, *J. Iran. Chem. Soc.*, 2008, **5**, S65–S70.
- 51 Z. Wei, M. Wlekinski, C. Ferreira and R. G. Cooks, *Angew. Chem., Int. Ed.*, 2017, **56**, 9386–9390.
- 52 N. Sahota, D. I. AbuSalim, M. L. Wang, C. J. Brown, Z. Zhang, T. J. El-Baba, S. Cook and D. E. Clemmer, *Chem. Sci.*, 2019, **10**, 4822–4827.
- 53 N. Narendra, X. Chen, J. Wang, J. Charles, R. G. Cooks and T. Kubis, *J. Phys. Chem. A*, 2020, **124**, 4984–4989.



## Supporting Information

### Accelerated Microdroplet Synthesis of Benzimidazoles by Nucleophilic Addition to Protonated Carboxylic Acids

*Pallab Basuri,<sup>a</sup> L. Edwin Gonzalez,<sup>b</sup> Nicolás M. Morato,<sup>b</sup> Thalappil Pradeep<sup>\*a</sup> and R. Graham Cooks<sup>\*b</sup>*

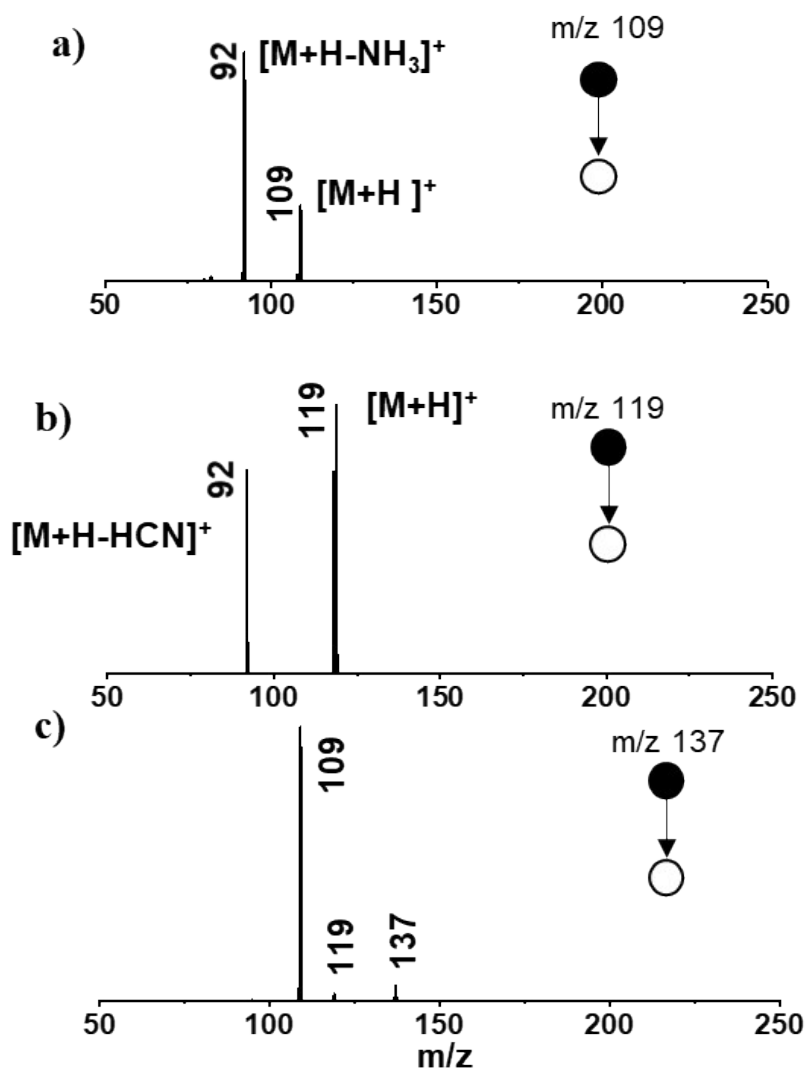
<sup>a</sup> DST Unit of Nanoscience (DST UNS), Thematic Unit of Excellence (TUE), Department of Chemistry, Indian Institute of Technology Madras, Chennai 600036, India.

<sup>b</sup> Aston Labs, Department of Chemistry, Purdue University, 560 Oval Drive, West Lafayette, IN 47907, USA

\*Corresponding authors

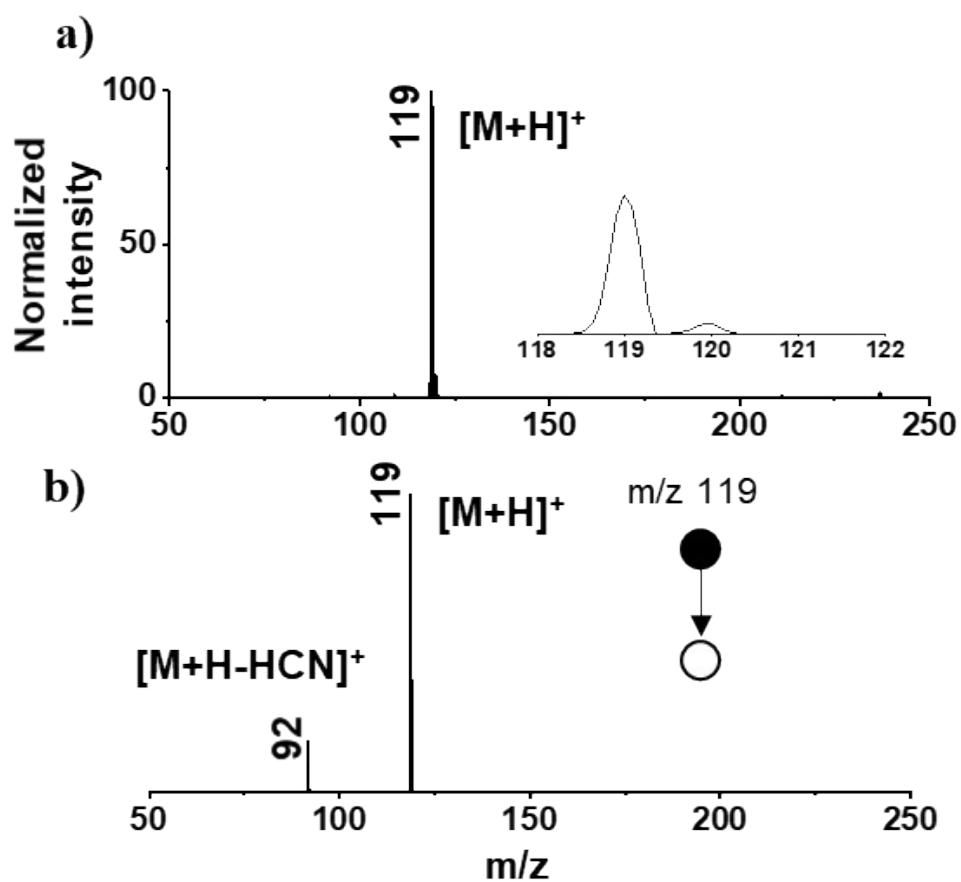
# Table of Contents

Figure S1 .....	03
Figure S2 .....	04
Figure S3 .....	05
Figure S4 .....	06
Figure S5 .....	07
Figure S6 .....	08
Figure S7 .....	09
Figure S8 .....	10
Figure S9 .....	11
Figure S10 .....	12
Figure S11 .....	13
Figure S12 .....	14
Figure S13 .....	15
Figure S14 .....	16
Figure S15 .....	17
Figure S16.....	18
Figure S17.....	19
Figure S18 .....	20
Figure S19 .....	21
Figure S20 .....	22
Figure S21 .....	23
Figure S22 .....	24
Figure S23 .....	25
Figure S24 .....	26
Figure S25 .....	27
Figure S26 .....	28
Figure S27 .....	29
Figure S28 .....	30
Figure S29 .....	31
Figure S30 .....	32
Figure S31 .....	33
Figure S32 .....	34
Figure S33 .....	35
Figure S34 .....	36
Figure S35 .....	37
Figure S36 .....	38
Figure S37 .....	39
Figure S38 .....	40
Figure S39 .....	41
Figure S40 .....	42
Figure S41 .....	43
Figure S42 .....	44
Figure S43 .....	45
Figure S44 .....	46
Figure S45 .....	47
Figure S46 .....	48



**Figure S1.** MS/MS spectra of (a) reagent peak at  $m/z$  109, (b) product peak at  $m/z$  119, and (c) intermediate peak at  $m/z$  137 for nESI microdroplet synthesis in methanol.





**Figure S2.** Mass spectra of benzimidazole standard. (a) Mass spectrum of 1 mM solution of benzimidazole in methanol. Inset shows the isotopic distribution of the peak. (b) MS/MS spectrum of protonated benzimidazole at  $m/z$  119.

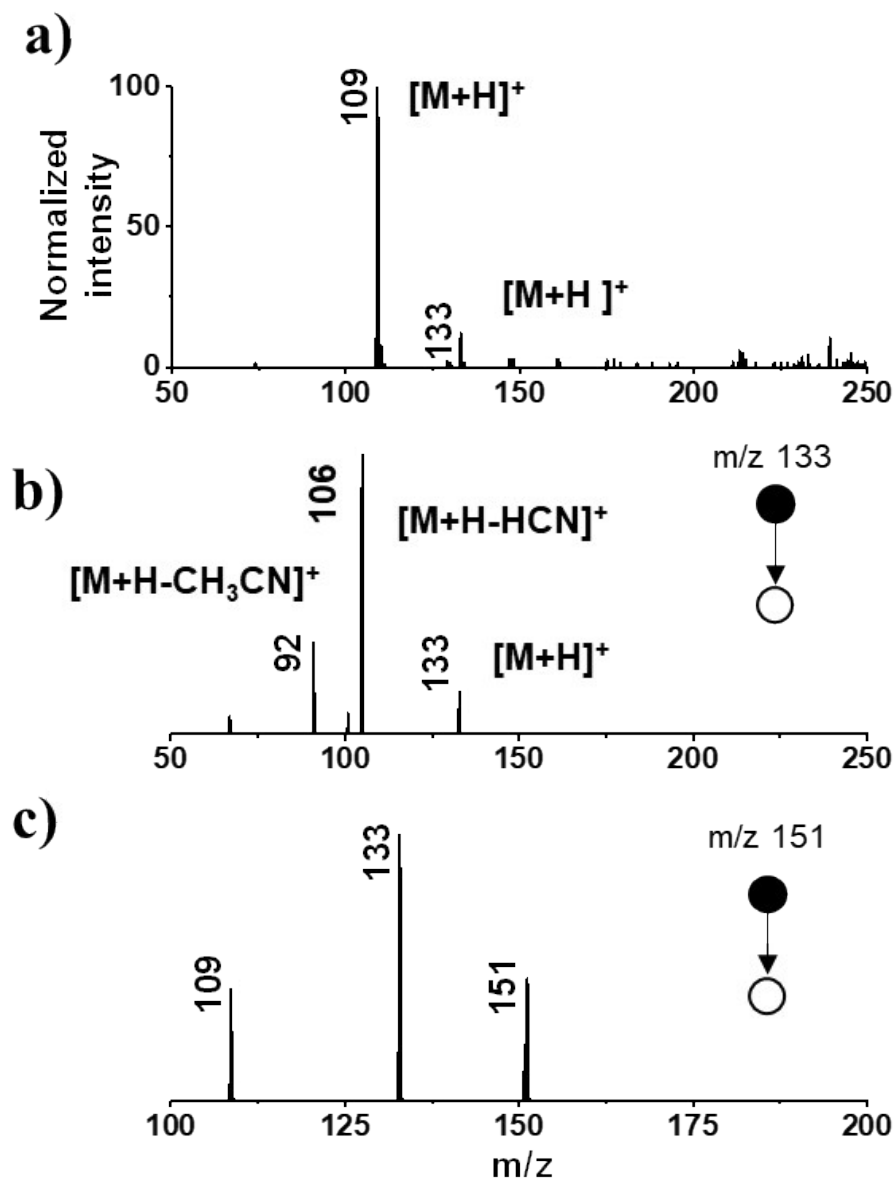


**Figure S3.** Microdroplet synthesis of 2-methylbenzimidazole. (a) Mass spectrum of the reaction mixture containing phenylenediamine (PDA) and acetic acid in methanol. The final concentration of the individual reagents is 8 mM. (b) MS/MS spectrum of the product at  $m/z$  133 (c) MS/MS spectrum of intermediate at  $m/z$  151.

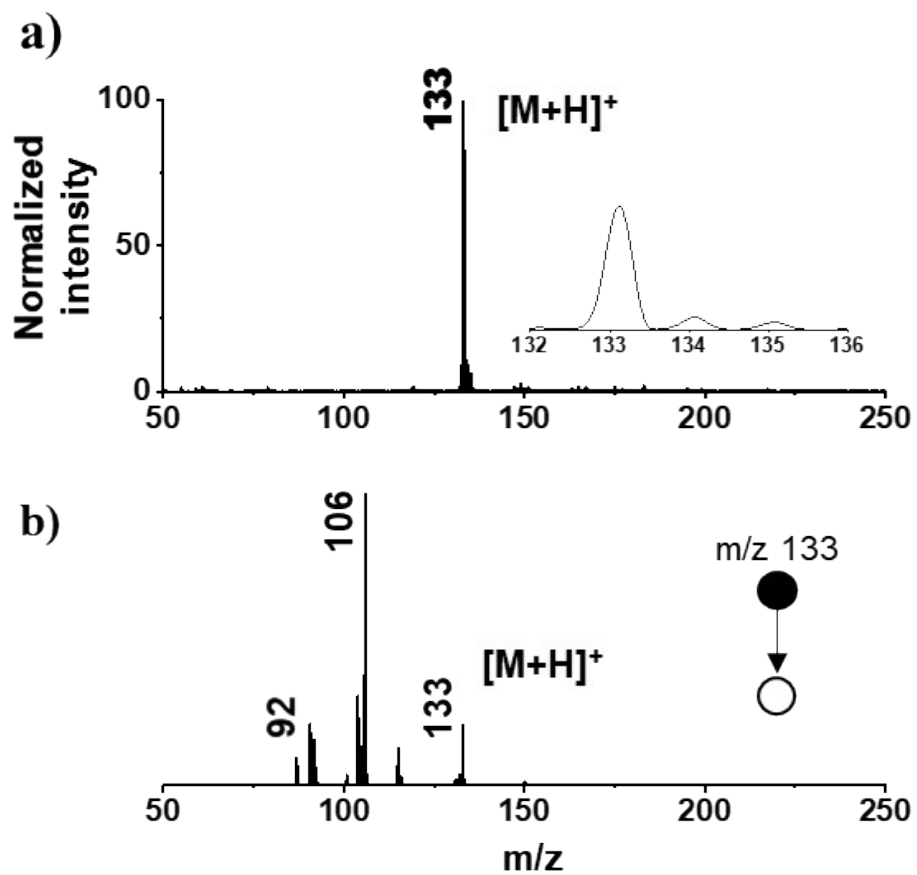


**Figure S4.** Mass spectra of 2-methylbenzimidazole standard. (a) Mass spectrum of 1 mM solution of 2-methylbenzimidazole in methanol. Inset shows the isotopic distribution. (b) MS/MS spectrum of protonated 2-methylbenzimidazole at  $m/z$  133.

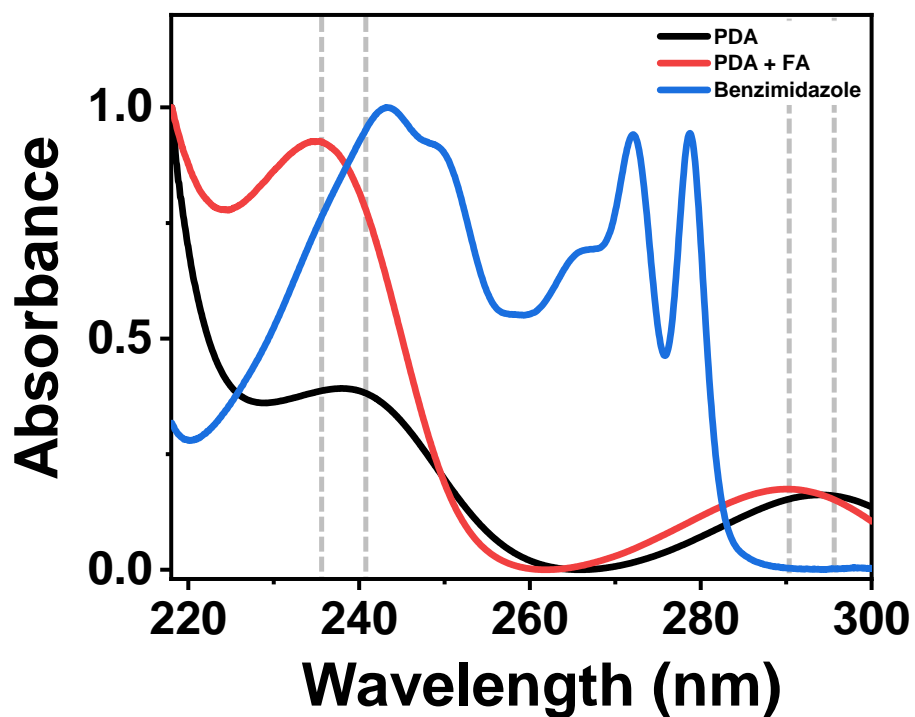


**Figure S5.** UV-vis spectra of *o*-phenylenediamine (black), reaction mixture for the synthesis of benzimidazole (red) and standard product (blue), all in methanol. The shift in the UV-vis spectra, as indicated by dotted lines, is due to the addition of formic acid and corresponds to Brønsted acid formation in solution by addition of a proton.

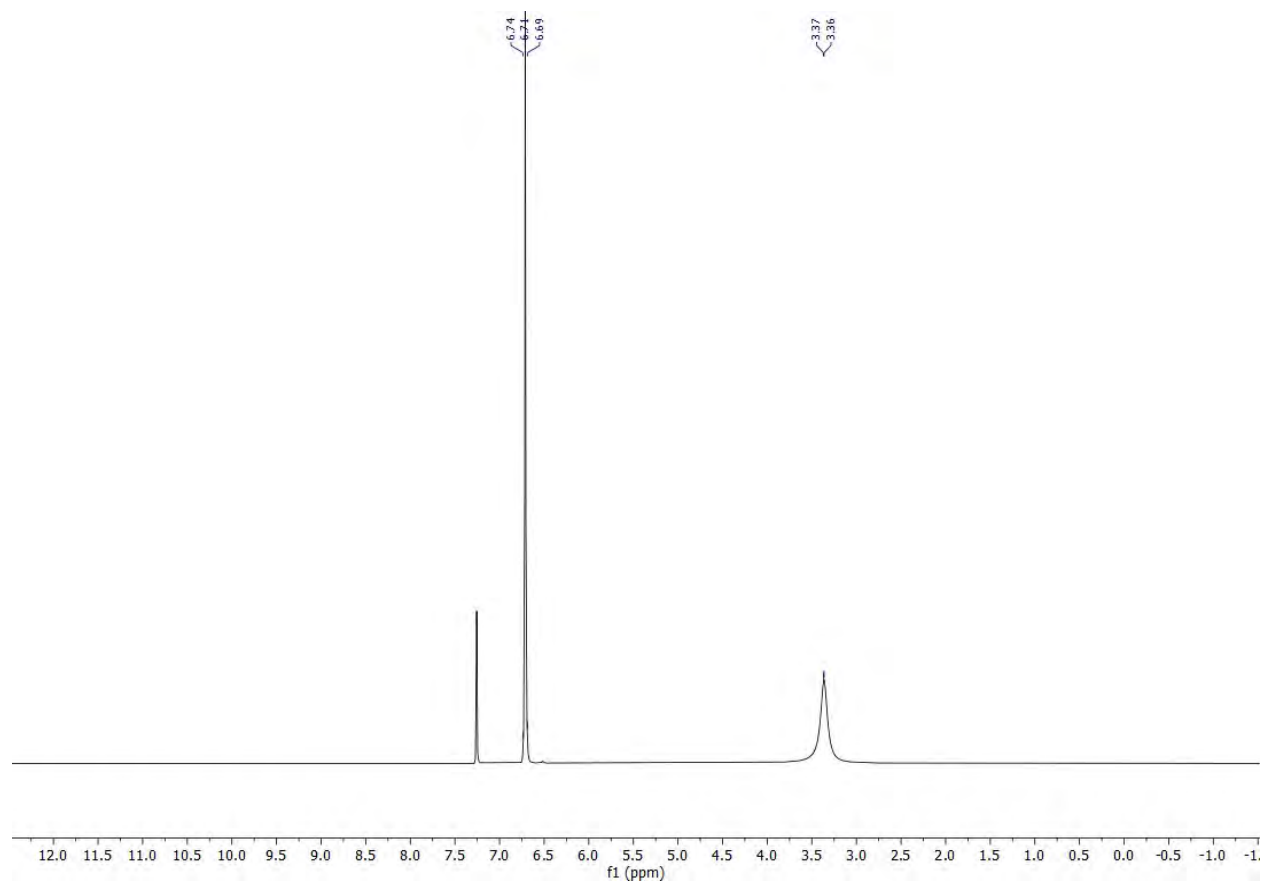


**Figure S6.** <sup>1</sup>H NMR data (400 MHz, CDCl<sub>3</sub>) for *o*-phenylenediamine in CDCl<sub>3</sub>. (δ 6.71 (s, 1H), 3.49 – 3.23 (m, 1H). Solvent peak is observed at 7.26 ppm).

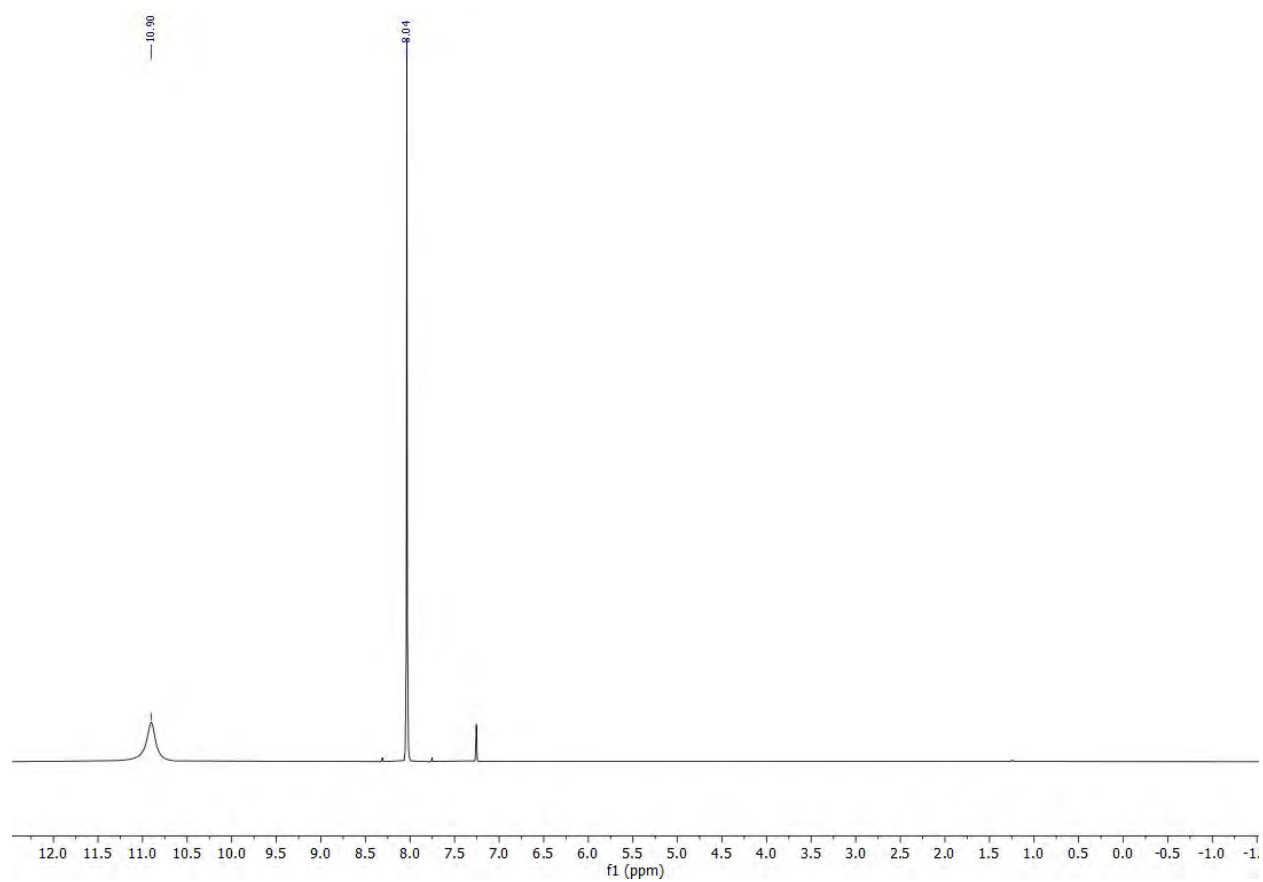


**Figure S7.**  $^1\text{H}$  NMR data (400 MHz,  $\text{CDCl}_3$ ) for formic acid.  $\delta$  10.90 (s, 1H), 8.04 (s, 1H). Solvent peak is observed at 7.26 ppm.



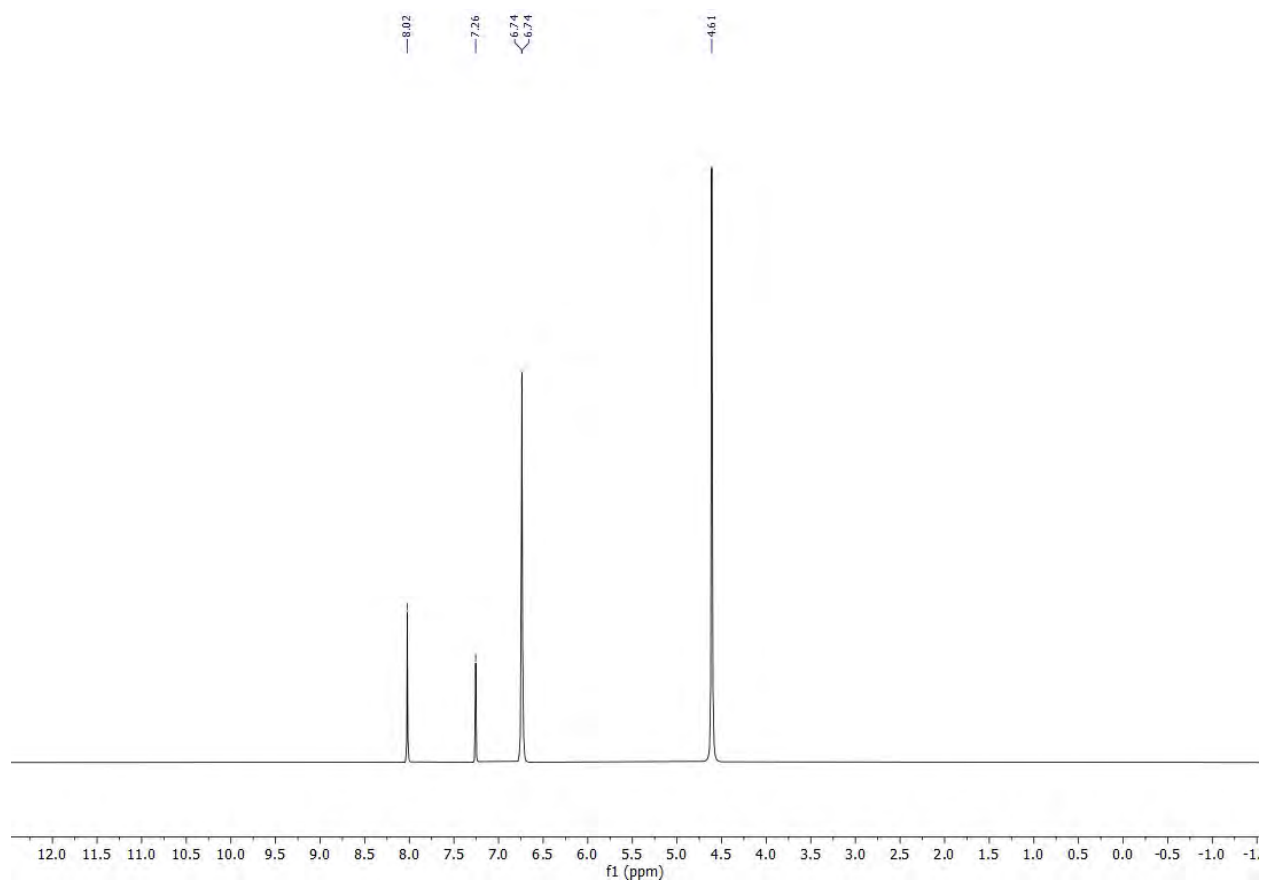


**Figure S8.** <sup>1</sup>H NMR data (400 MHz, CDCl<sub>3</sub>) for a mixture of *o*-phenylenediamine and formic acid.  $\delta$  8.02 (s, 1H), 6.79 – 6.69 (m, 5H), 4.61 (s, 7H). Solvent peak is observed at 7.26 ppm.

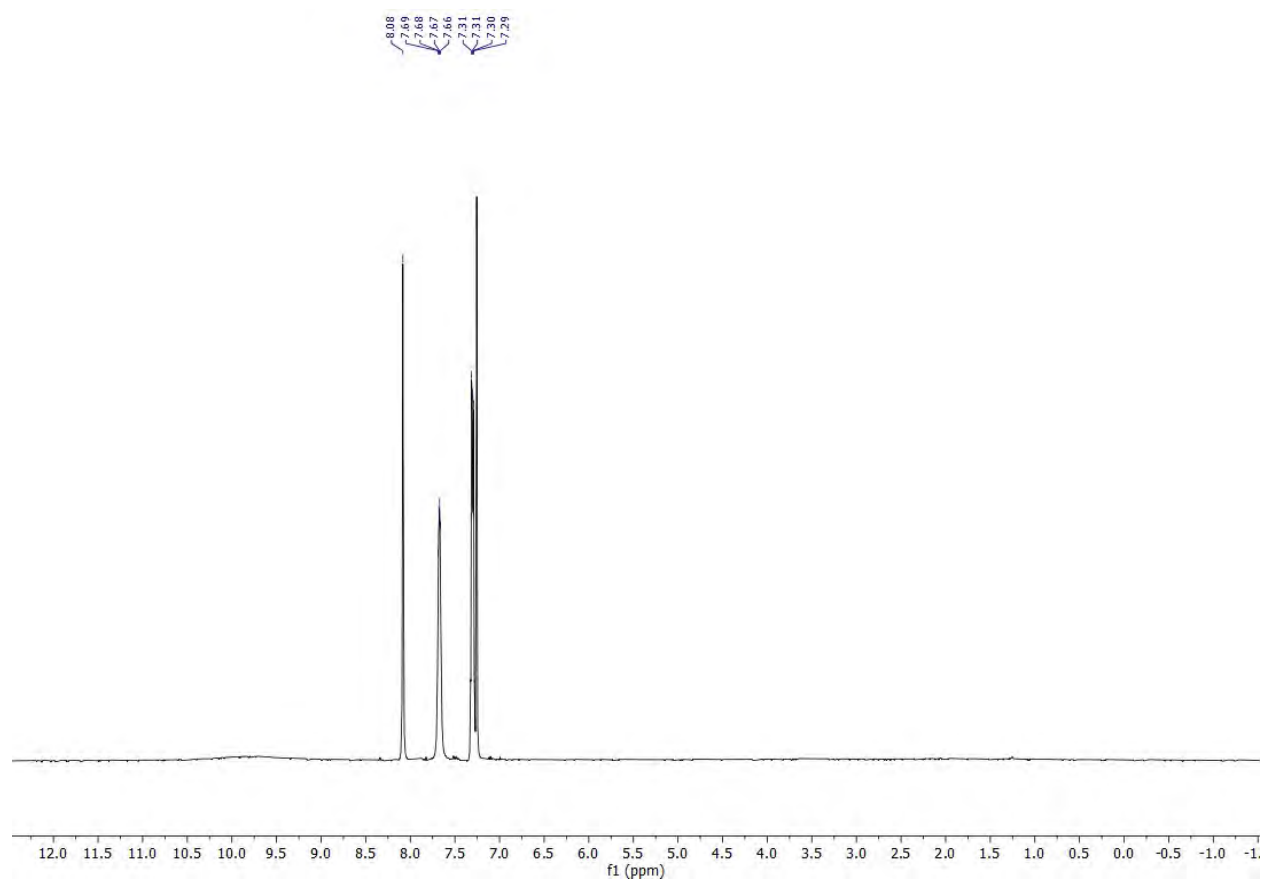


**Figure S9.** <sup>1</sup>H NMR data (400 MHz, CDCl<sub>3</sub>) for benzimidazole standard.  $\delta$  8.08 (s, 1H), 7.71 – 7.64 (m, 2H), 7.31 (dt,  $J$  = 6.1, 3.6 Hz, 2H). Solvent peak is observed at 7.26 ppm.

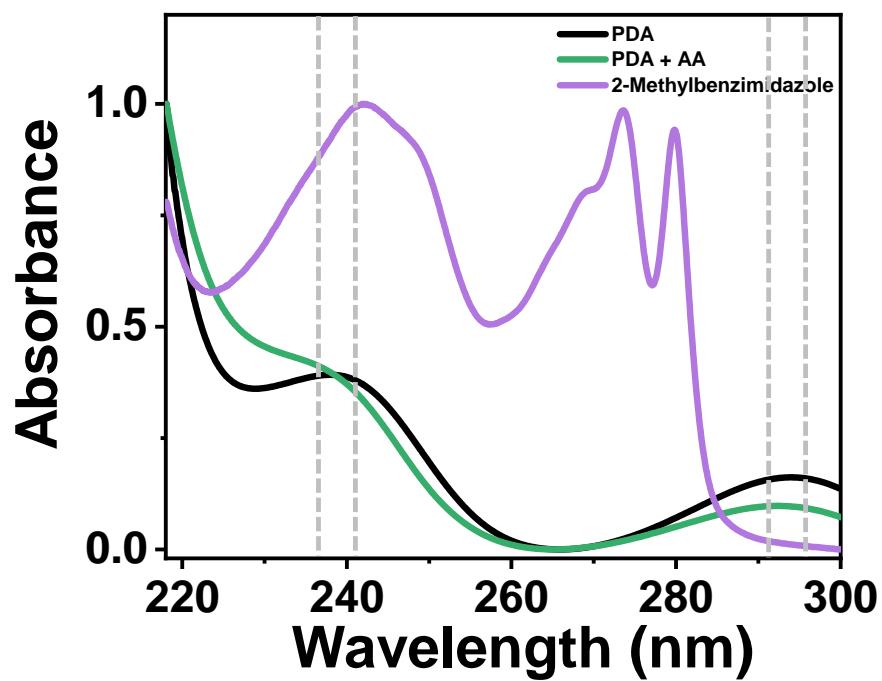


**Figure S10.** UV-vis spectra of *o*-phenylenediamine (black), its mixture with acetic acid (green) and standard 2-methylbenzimidazole (violet) in methanol.

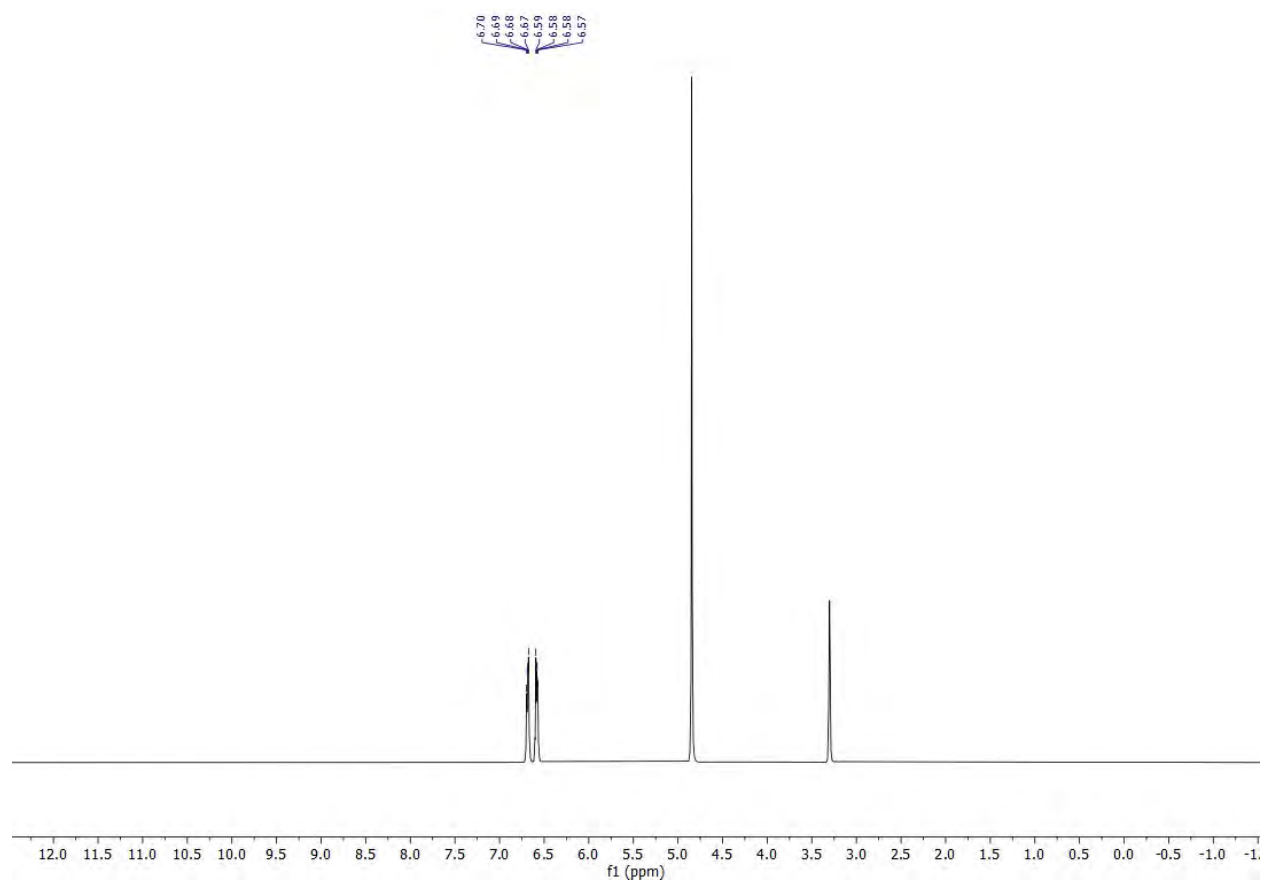


**Figure S11.**  $^1\text{H}$  NMR data (400 MHz,  $\text{CDCl}_3$ ) for *o*-phenylenediamine standard.  $\delta$  6.69 (dd,  $J = 5.7, 3.5$  Hz, 1H), 6.58 (dd,  $J = 5.8, 3.4$  Hz, 1H).

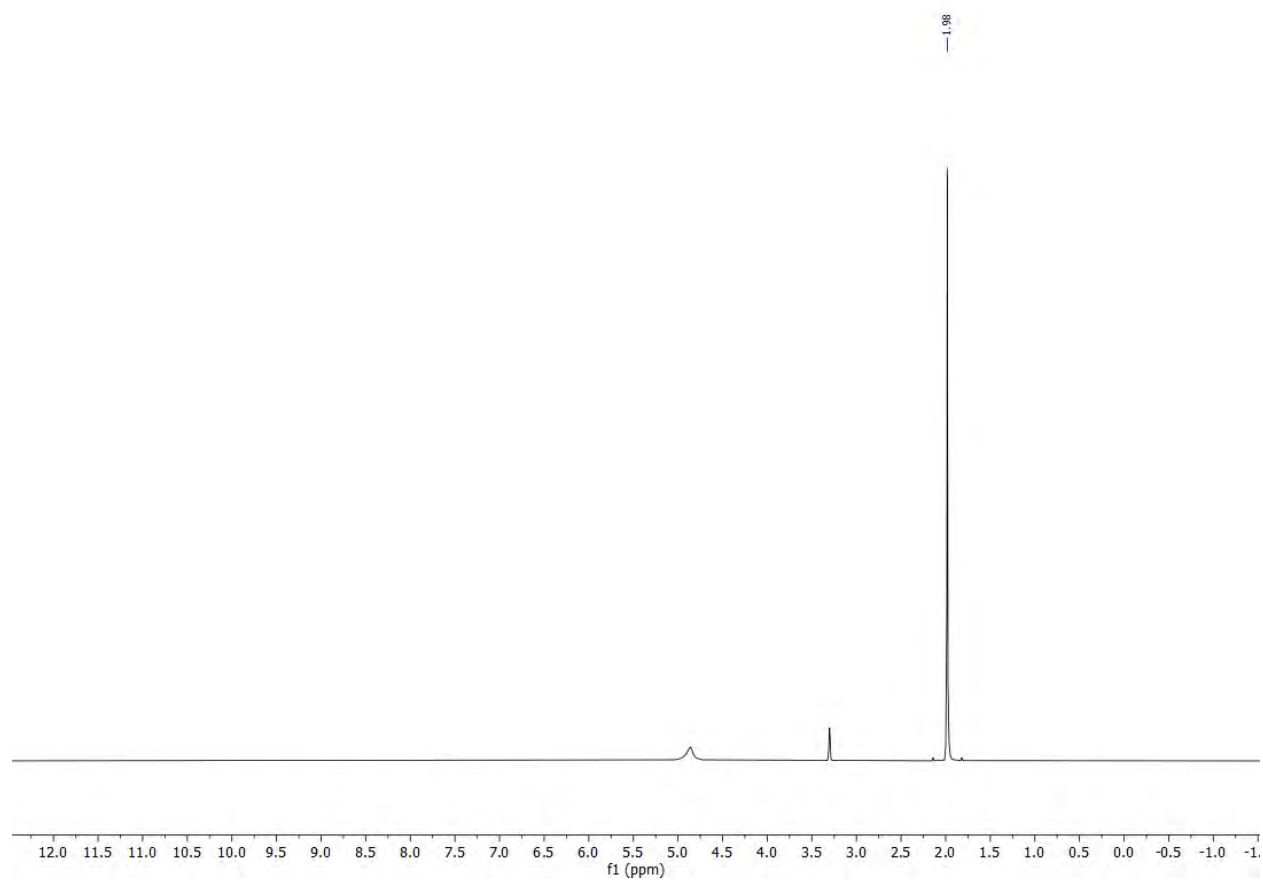


**Figure S12.**  $^1\text{H}$  NMR data for acetic acid(400 MHz, MeOD)  $\delta$  1.98 (s, 1H). Peaks at 4.85 ppm and 3.30 ppm are solvent peaks.

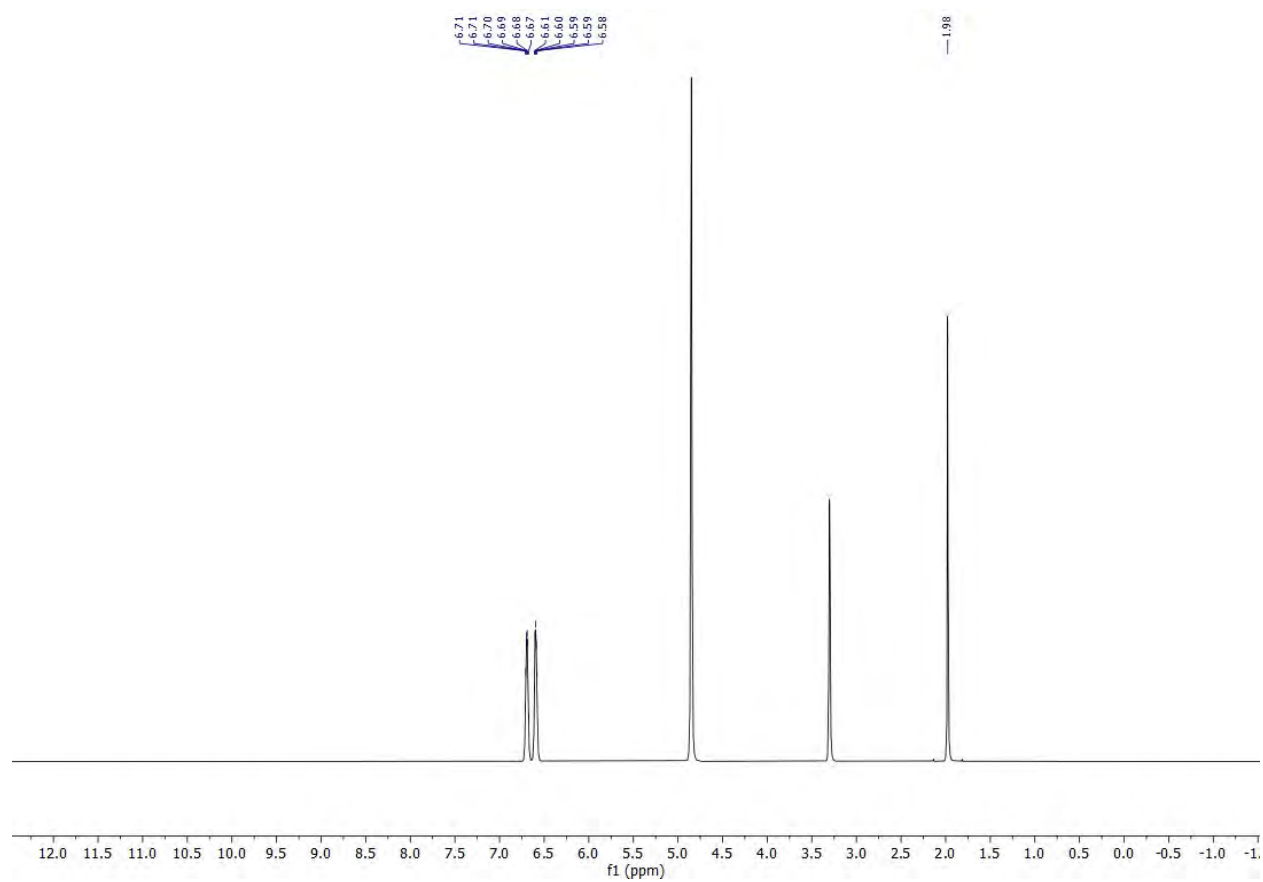


**Figure S13.**  $^1\text{H}$  NMR data for mixture of *o*-phenylenediamine and acetic acid (400 MHz, MeOD)  $\delta$  6.69 (dq,  $J = 6.4, 3.6, 3.0$  Hz, 1H), 6.59 (dt,  $J = 5.8, 2.8$  Hz, 1H), 1.98 (s, 1H). Peaks at 4.85 ppm and 3.30 ppm are due to solvent.



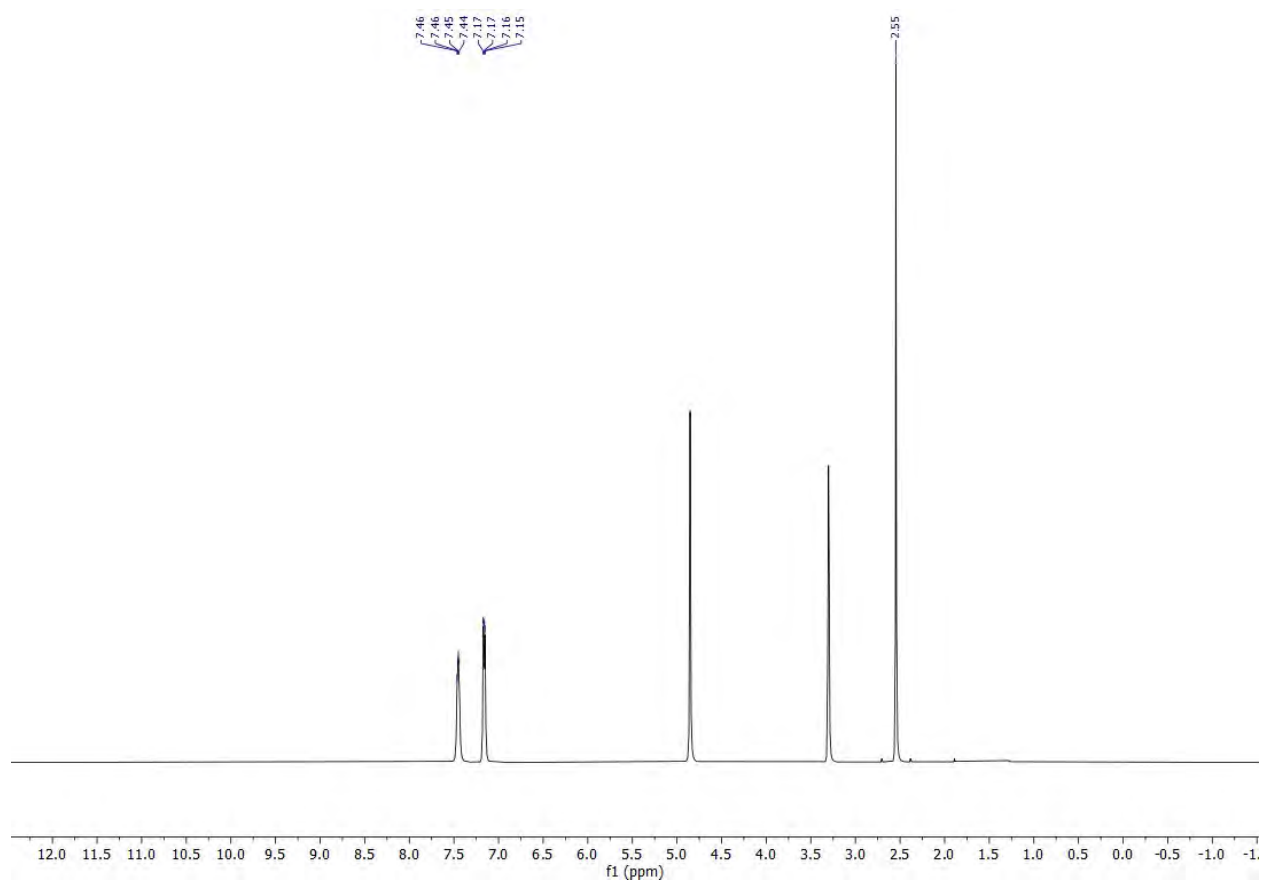


**Figure S14.**  $^1\text{H}$  NMR data (400 MHz,  $\text{MeOD}$ ) for 2-methylbenzimidazole standard.  $\delta$  7.51 – 7.37 (m, 1H), 7.16 (dd,  $J = 6.0, 3.2$  Hz, 1H), 2.55 (s, 2H). Peaks at 4.85 ppm and 3.30 ppm are due to solvent.

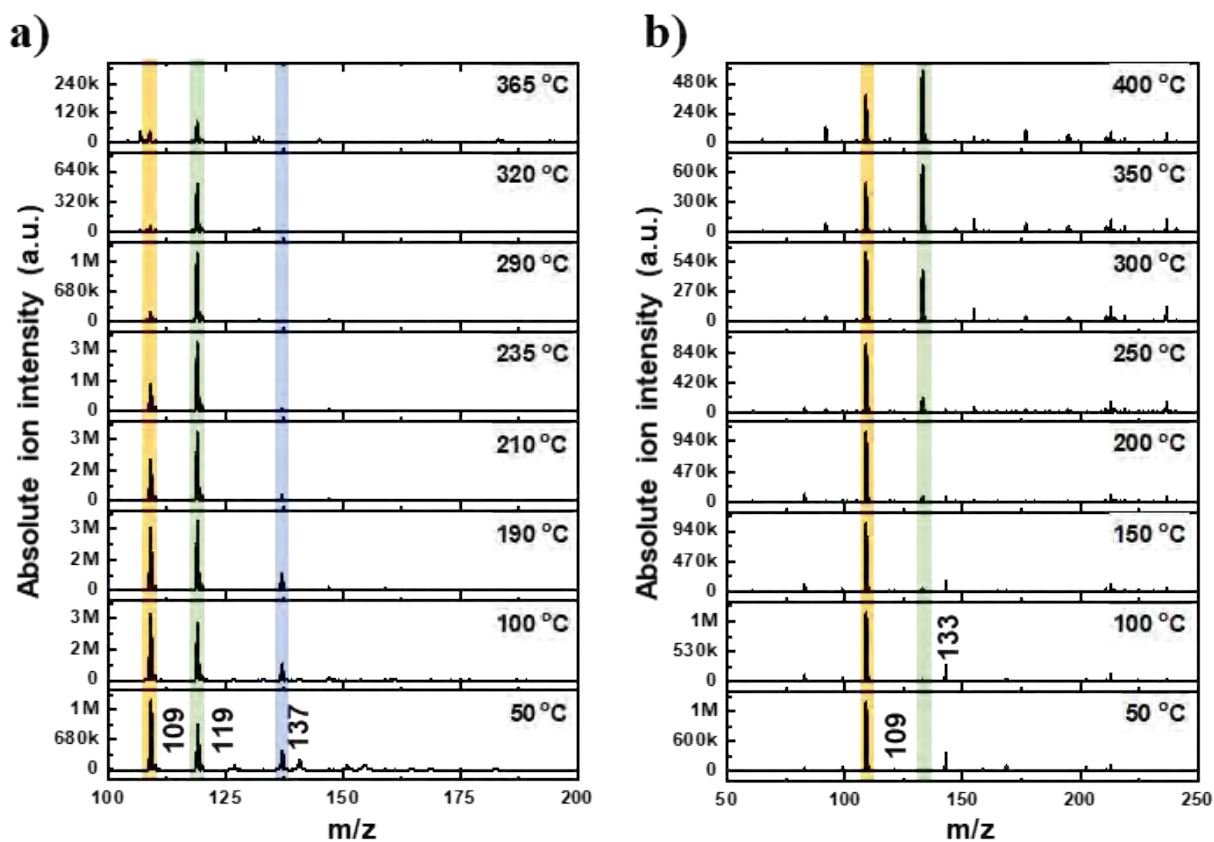


**Figure S15.** Temperature dependent mass spectra for microdroplet synthesis in methanol of a) benzimidazole and b) 2-methylbenzimidazole. The reagent peak at  $m/z$  109, as indicated by yellow shading, decreases with increasing temperature, whereas, the product peaks at  $m/z$  119 and  $m/z$  133, as indicated by green shading, increase with increasing temperature.

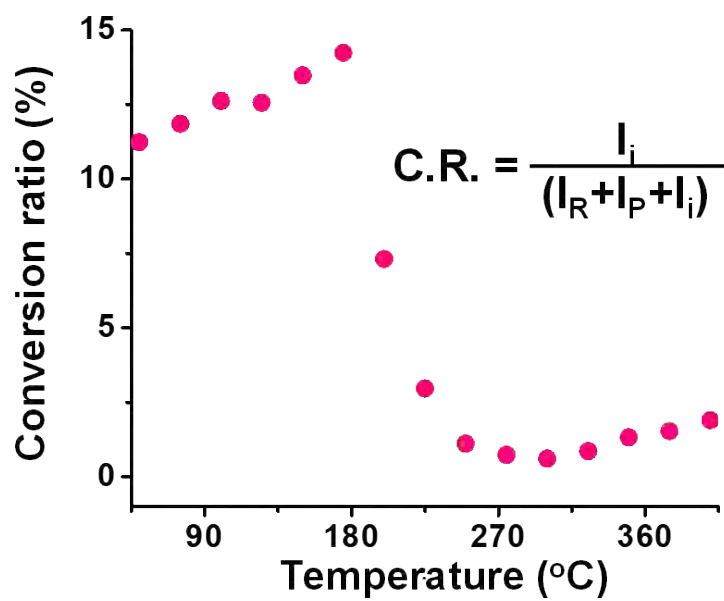


**Figure S16.** Conversion ratio versus temperature plot for the intermediate ( $m/z$  137) in benzimidazole synthesis in methanol microdroplets. Inset shows the equation for conversion ratio.

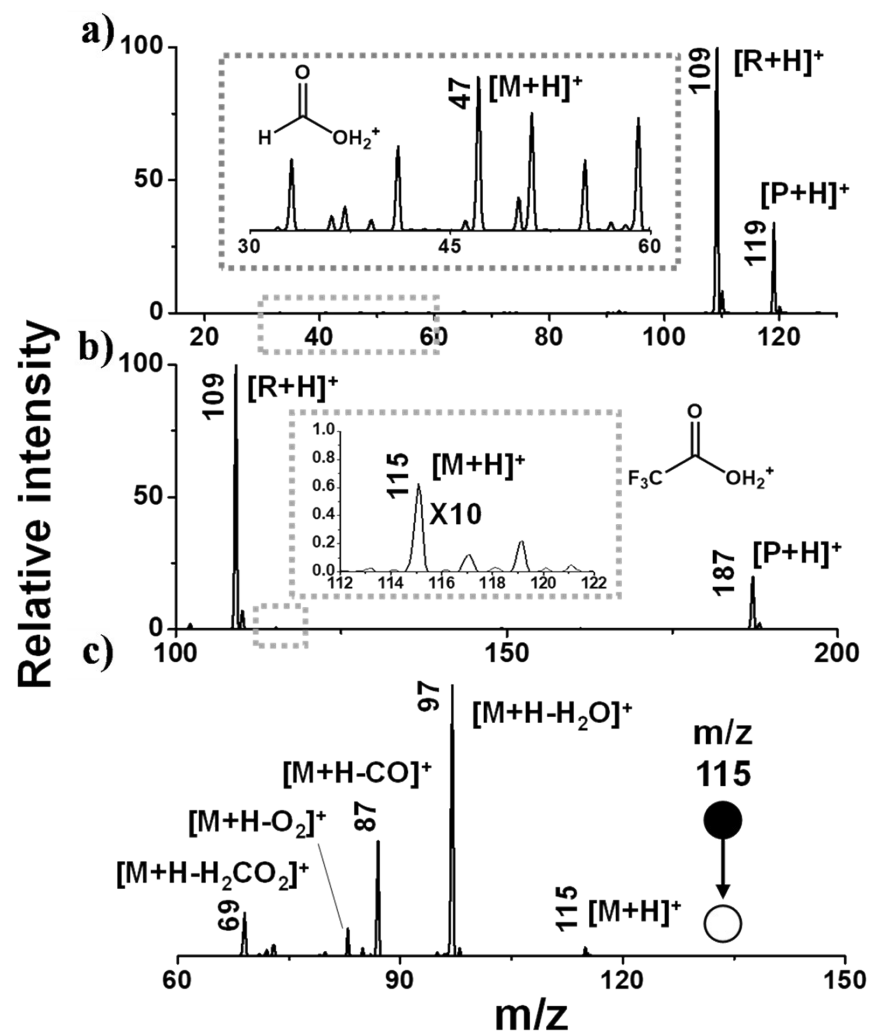


**Figure S17.** Mass spectra of reaction mixtures containing (a) o-phenylenediamine and formic acid (b) trifluoroacetic acid and (c) MS/MS spectrum of protonated trifluoroacetic acid. Zoom-in view of selected mass ranges in (a) and (b) showing peaks corresponding to protonated formic acid and trifluoroacetic acid. The solutions were prepared in HPLC grade methanol at 8 mM concentration.

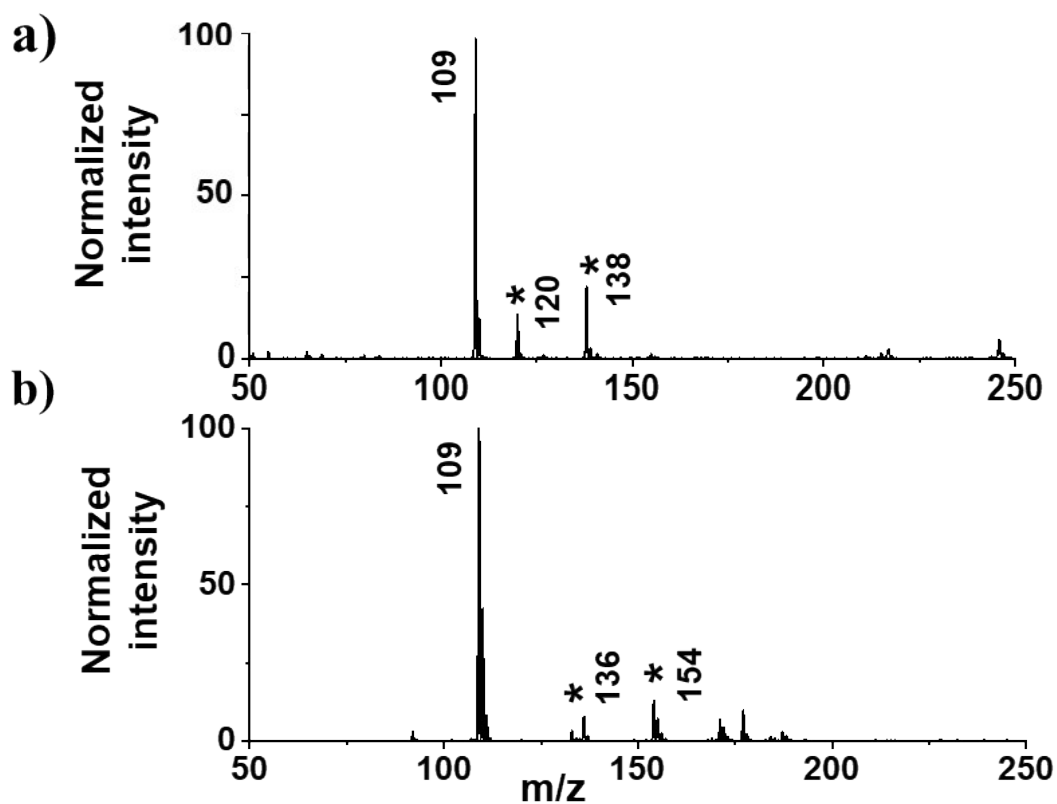


**Figure S18.** Isotope labeling experiments. Mass spectra showing reaction mixture for microdroplet reaction of phenylenediamine with (a) deuterated formic acid ( $\text{DCOOH}$ ) and (b) acetic acid ( $\text{CD}_3\text{COOH}$ ). The isotopically labeled product peaks are indicated with stars. The solvent used for the reaction is deuterated methanol. The temperature of the inlet was set to 50 °C for these experiments.

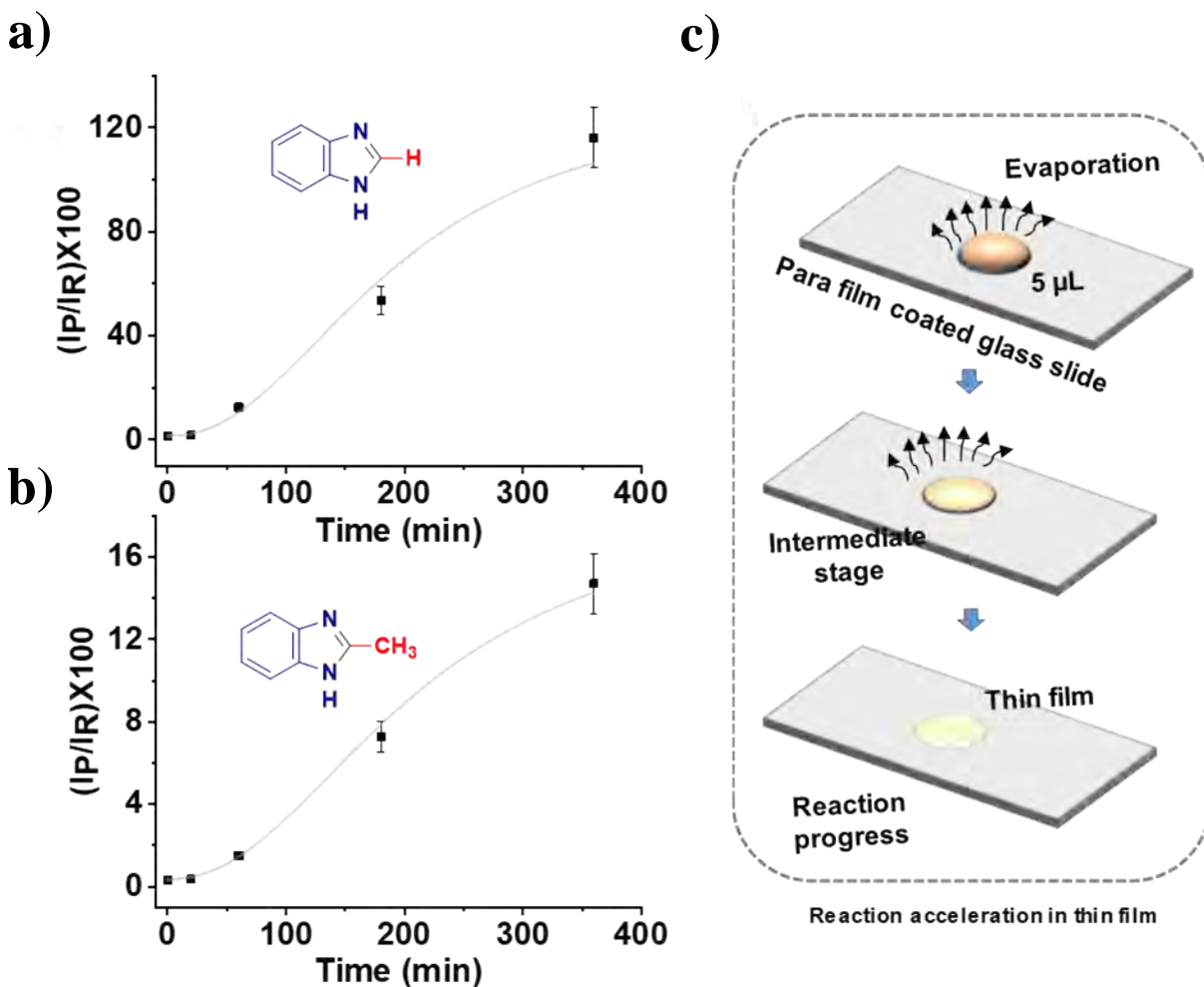


**Figure S19.** Ratio of product ion to reagent ion intensity for ambient thin film synthesis in methanol containing traces of *p*-toluenesulfonic acid to increase the lifetime of the fluid state for (a) benzimidazole and (b) 2-methylbenzimidazole. c) Schematic illustration of the thin film experiments from Z. Wei, M. Wlekinski, C. Ferreira and R. G. Cooks, *Angewandte Chemie International Edition*, 2017, **56**, 9386-9390. Note the induction period of some minutes while the methanol evaporates.



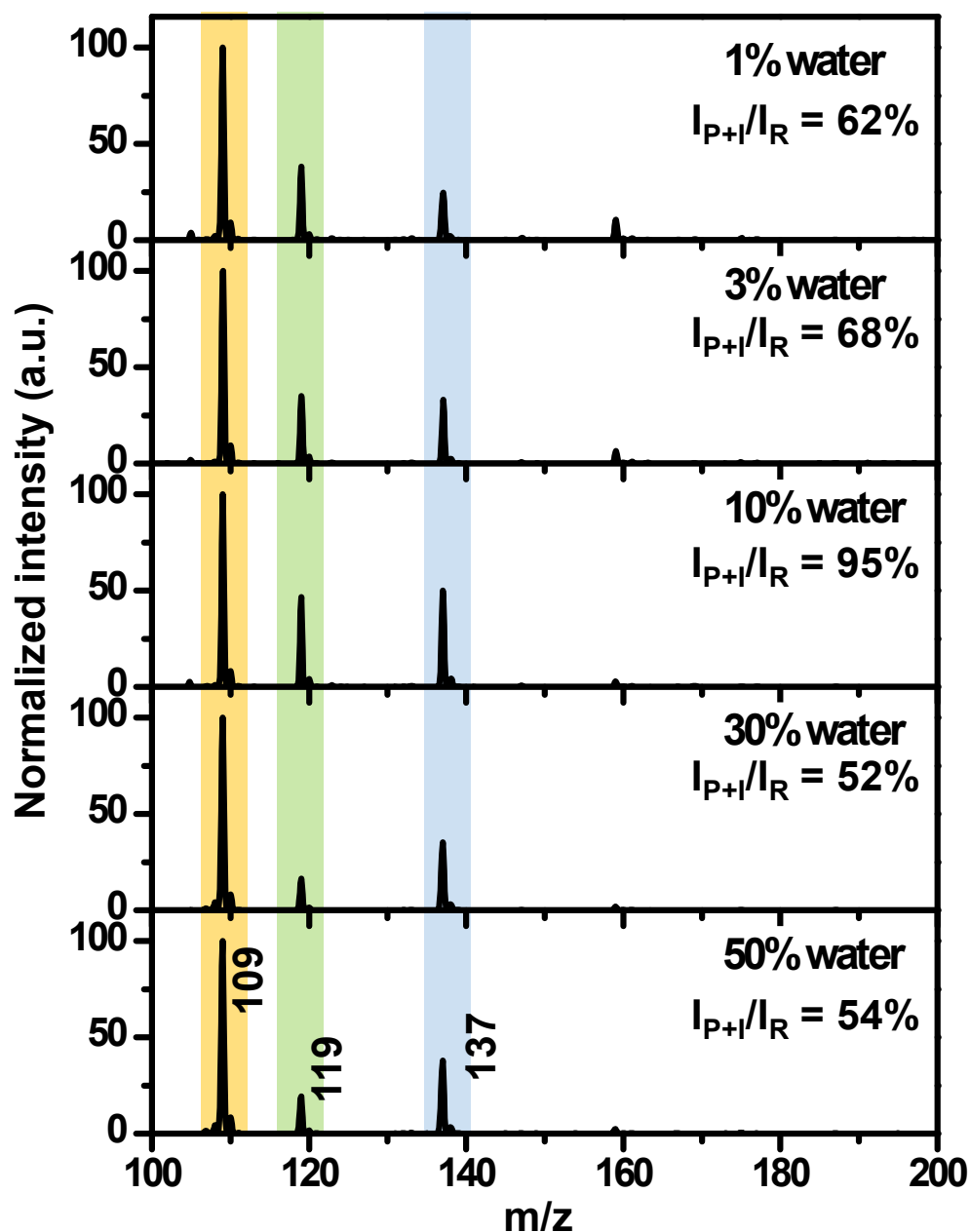


**Figure S20.** Benzimidazole reaction in presence of macroscopic amounts of water in methanol monitored by relative intensity of the product ion  $m/z$  117 plus the intermediate ion  $m/z$  137 vs. that of the reagent ion  $m/z$  109. As the water concentration is increased up to 10%, we see increased product and intermediate formation. Above this concentration the relative product and intermediate intensities fall.

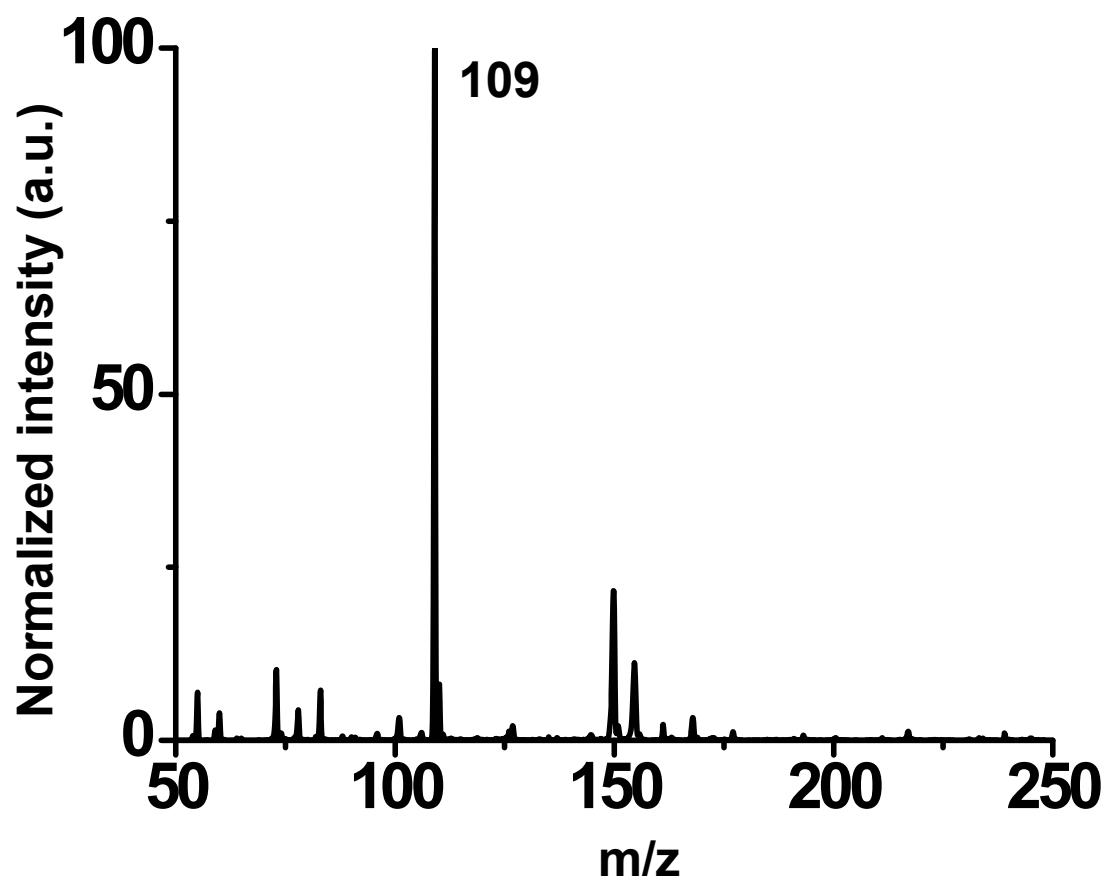


**Figure S21.** Benzimidazole reaction in dry ACN. Note the low signal (noise) and the absence of both product and intermediate ion signals. Other than the reagent signal, the peaks seen in the mass spectrum are from background.

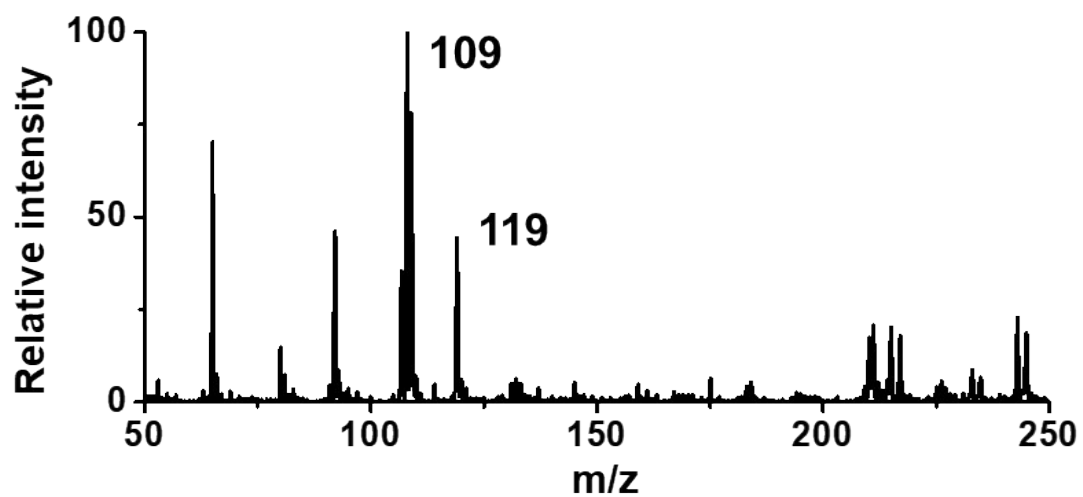


**Figure S22.** Mass spectrum of o-phenylenediamine/formic acid mixture in methanol in the presence of HCl. Concentrations of reactants and of HCl were 8 mM. Similar CRs were observed with and without HCl.

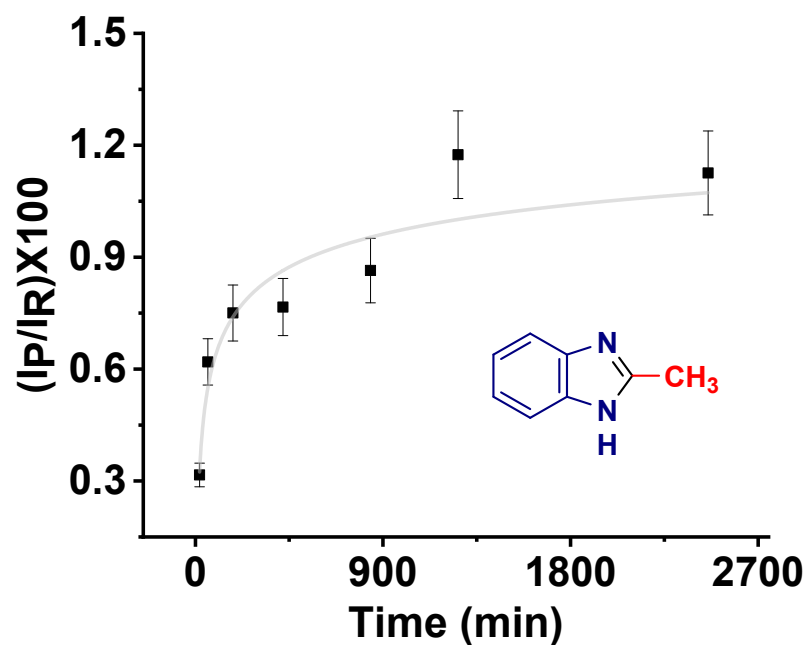


**Figure S23.** Product to reagent ion intensity ratio for the bulk reaction in methanol under ambient conditions for 2-methylbenzimidazole synthesis. Inset shows the molecular structure of the product. The starting concentration of each reagent in methanol was  $\approx 8$  mM. The reaction was performed in a closed 500 mL round bottom flask and MS analysis was done using 50 °C inlet temperature to avoid reaction acceleration during bulk product analysis.

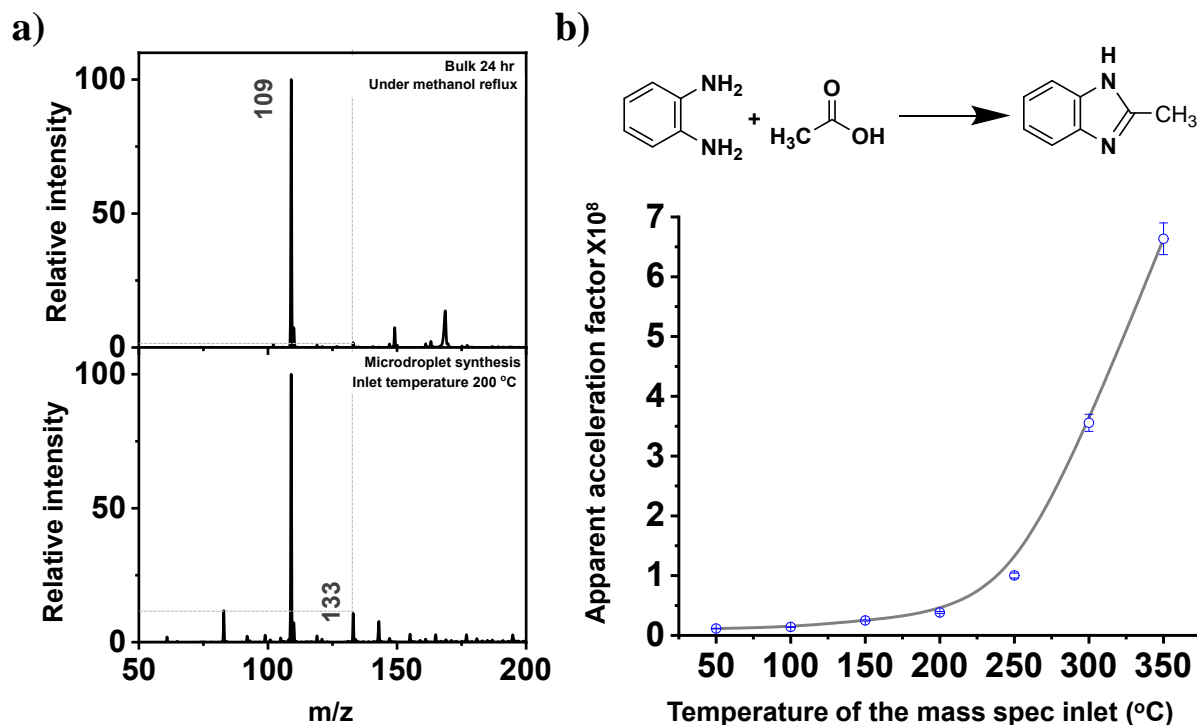


**Figure S24.** Effect of inlet temperature on accelerated formation of 2-methylbenzimidazole ( $m/z$  133) from phenylenediamine ( $m/z$  109). (a) Comparison of mass spectrum of bulk reaction mixture after 24 h under methanol reflux with that for microdroplet synthesis at 200 °C inlet temperature. (b) Temperature of MS inlet vs. apparent reaction rate acceleration factor. Inset shows the reaction scheme. Apparent acceleration factor considered the difference in reaction time of the droplet and bulk reactions. Note that the bulk reaction analysis was performed at constant 50 °C inlet temperature to avoid reaction acceleration during the analysis.

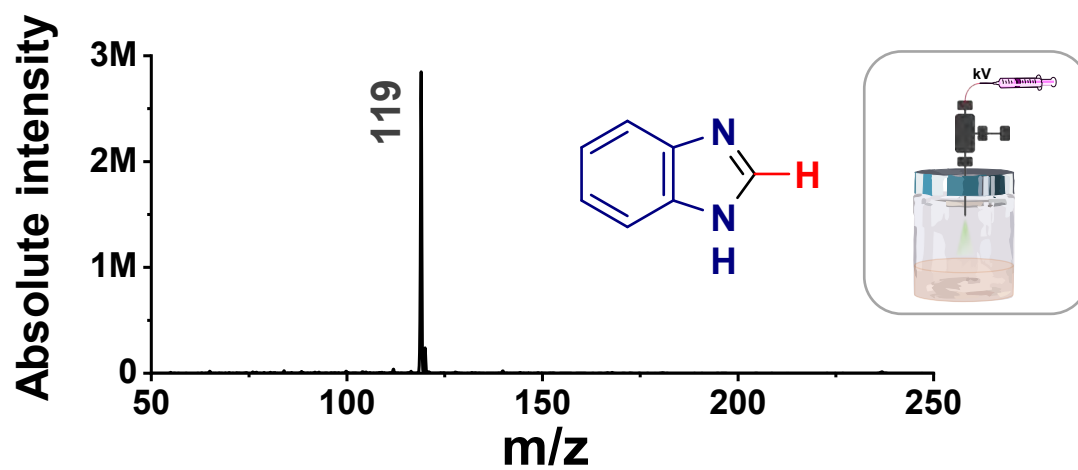


**Figure S25.** Mass spectrum of the isolated product after benzimidazole synthesis in methanol by spray deposition with a diagram that depicts the spray deposition reaction setup. The crude mixture was separated using flash column chromatography. Yield was determined to be about 72%.



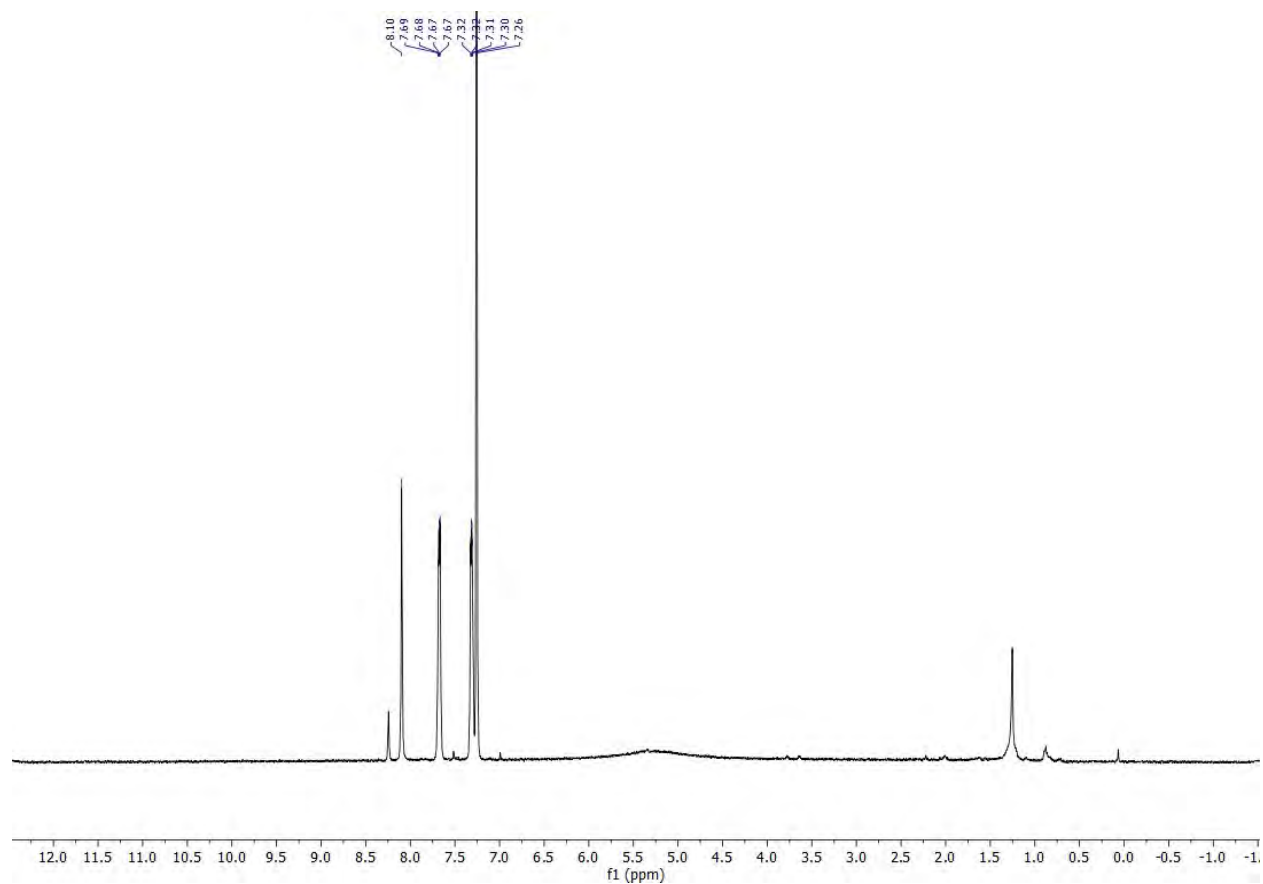


**Figure S26.** <sup>1</sup>H NMR (400 MHz, CDCl<sub>3</sub>) of the isolated product from the deposited sample in benzimidazole spray deposition synthesis.  $\delta$  8.24 (s, 1H), 8.10 (s, 6H), 7.68 (dd,  $J$  = 6.1, 3.2 Hz, 11H), 7.31 (dd,  $J$  = 6.1, 3.2 Hz, 11H), 7.26 (s, 18H), 1.25 (s, 5H). Peak at 7.26ppm is the solvent peak and 8.24ppm peak is an impurity.

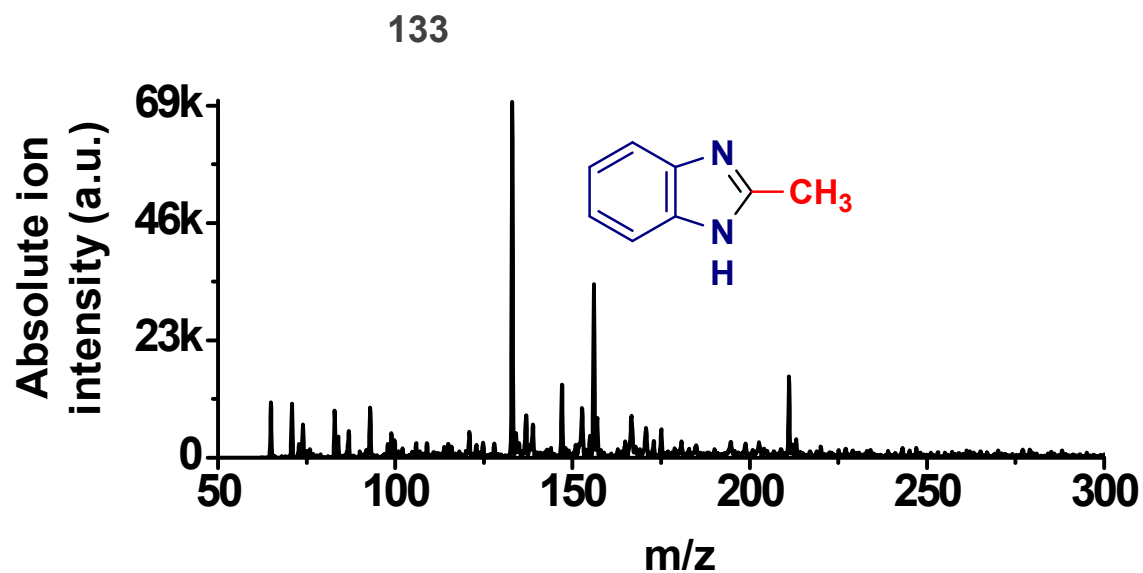


**Figure S27.** Mass spectrum of the isolated product of the deposited sample for the 2-benzimidazole spray synthesis. Low isolated yield resulted in noise in the mass spectrum.

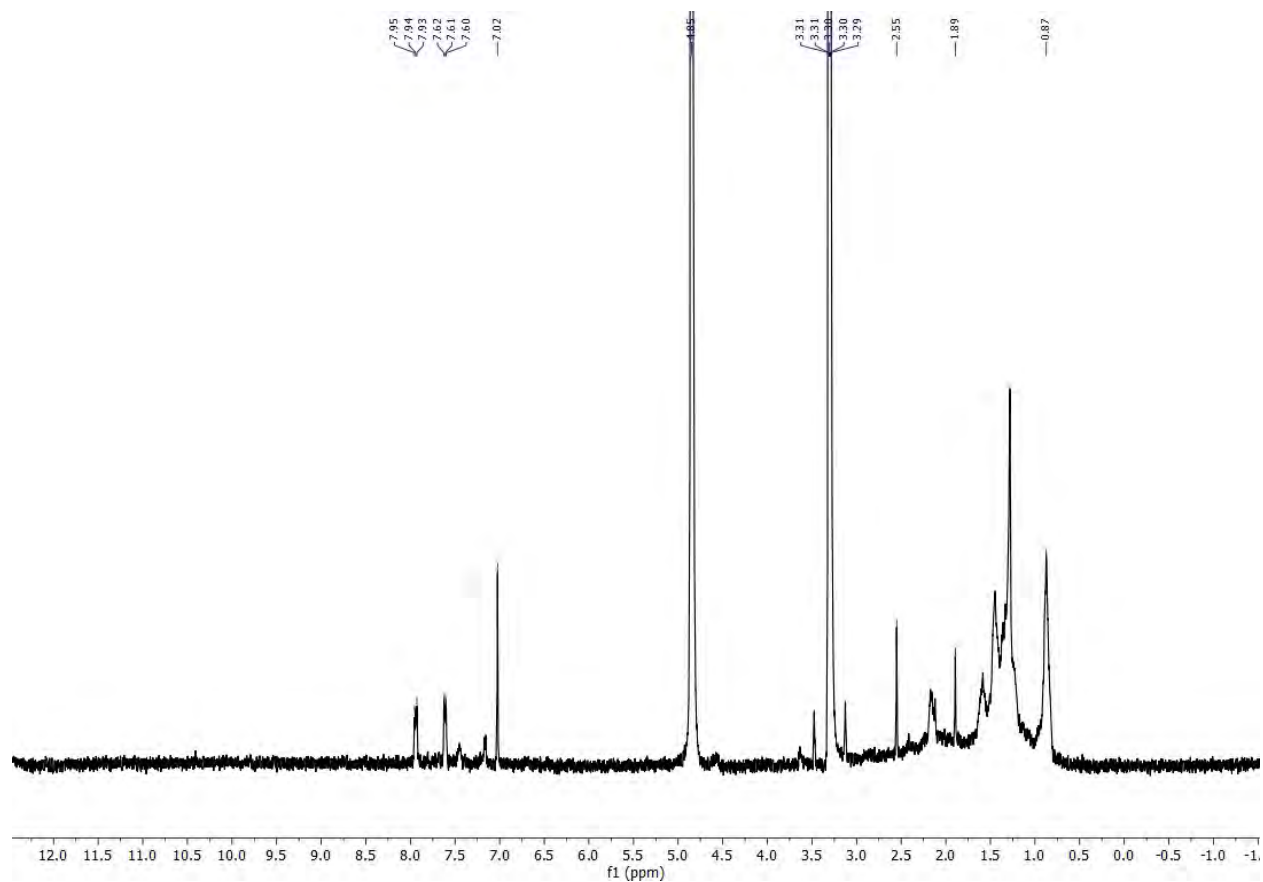


**Figure S28.** <sup>1</sup>H NMR (400 MHz, MeOD) for the isolated product of the deposited sample from the 2-methylbenzimidazole spray synthesis.  $\delta$  7.96 – 7.91 (m, 2H), 7.65 – 7.58 (m, 1H), 7.02 (s, 2H), 2.55 (s, 1H). Peaks at 4.85 and 3.29-3.31 ppm are solvent peaks while other minor peaks are from impurities.

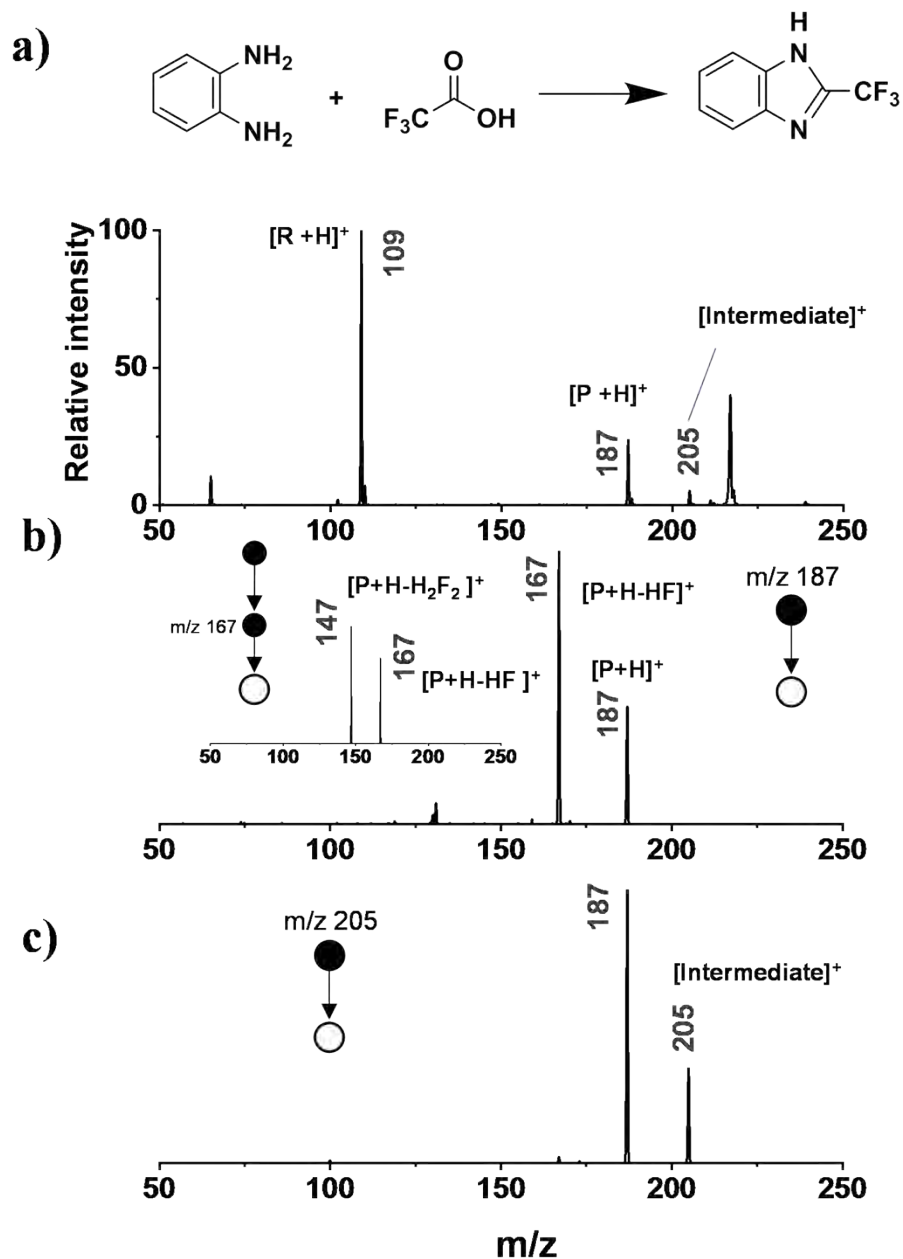


**Figure S29.** (a) Online mass spectrum of microdroplet reaction between *o*-phenylenediamine and trifluoroacetic acid in methanol at 50 °C inlet temperature. The MS/MS spectrum of the (b) product and (c) intermediate are shown. The reagent and the product are denoted as R and P.

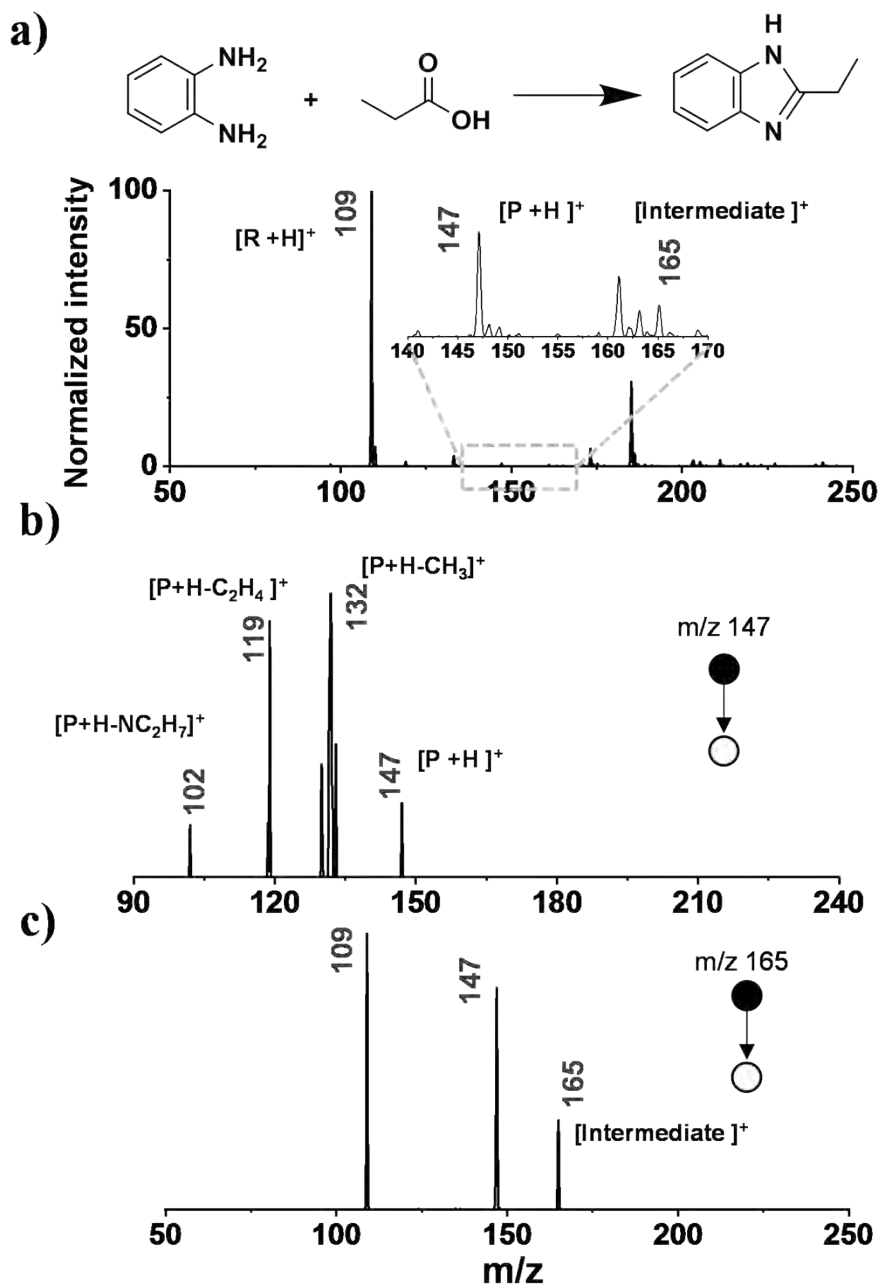


**Figure S30.** a) Online MS of microdroplet reaction between *o*-phenylenediamine and propanoic acid in methanol at 50 °C inlet temperature. The MS/MS spectrum of the (b) product and (c) intermediate are shown. The reagent and the product are denoted as R and P.

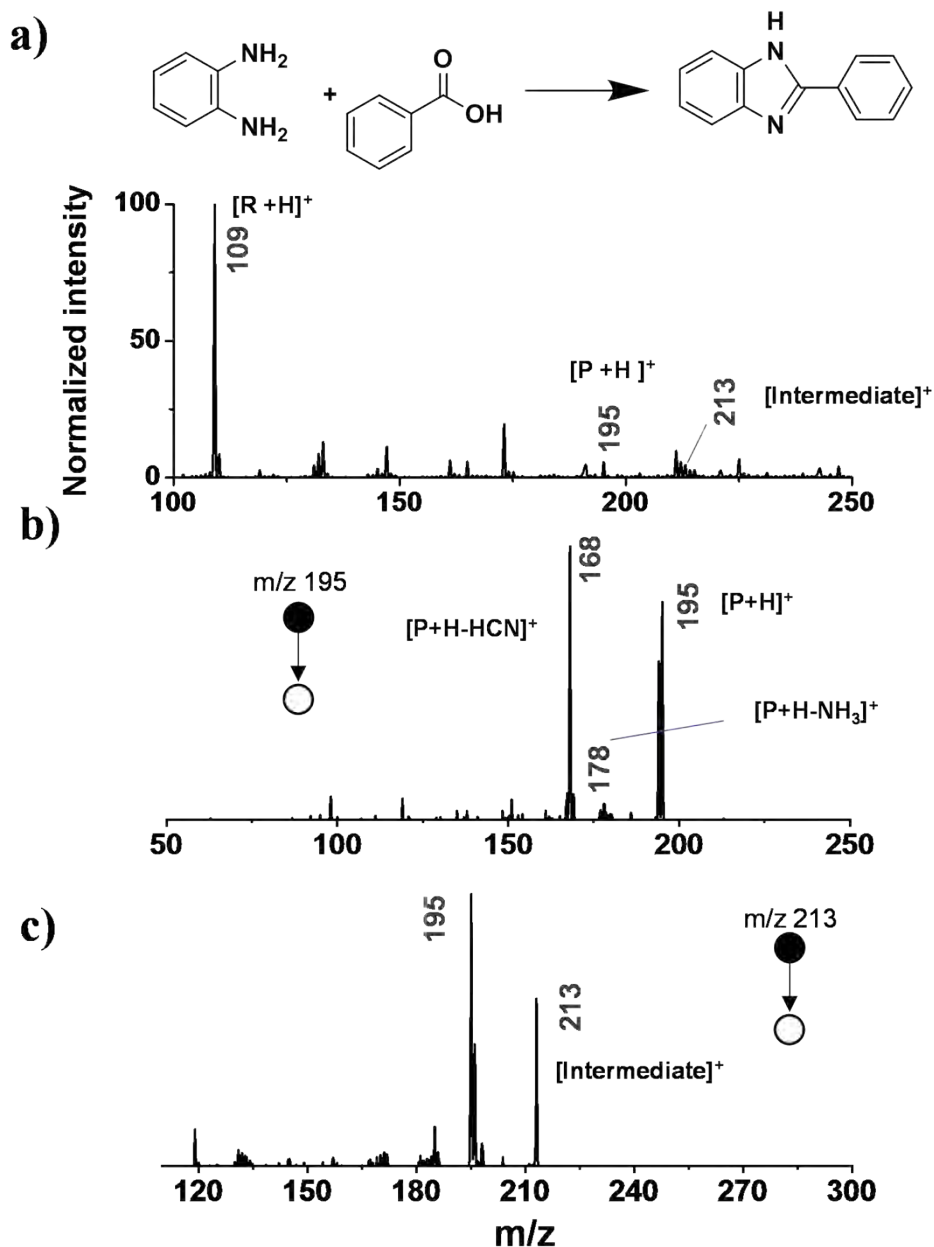


**Figure S31.** (a) Online MS of microdroplet reaction between *o*-phenylenediamine and benzoic acid in methanol at 50 °C inlet temperature. The MS/MS spectrum of (b) product and (c) intermediate are shown. The reagent and the product are denoted as R and P.



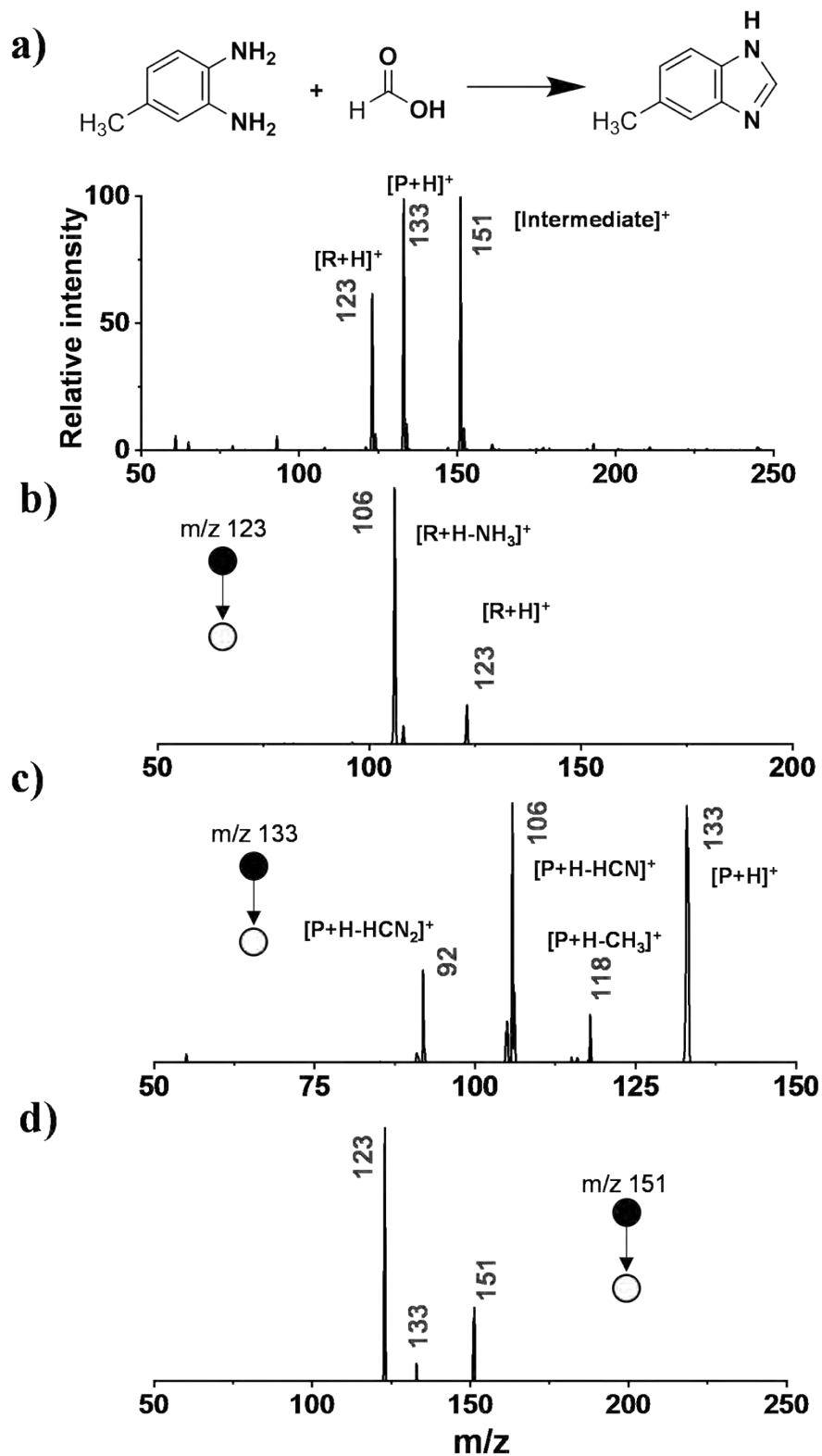


**Figure S32.** (a) Online MS of microdroplet reaction between 4-methyl-1,2-phenylenediamine and formic acid in methanol at 50 °C inlet temperature. MS/MS spectrum of the (b) reagent, (c) product, and (d) intermediate. The reagent and the product are denoted as R and P.

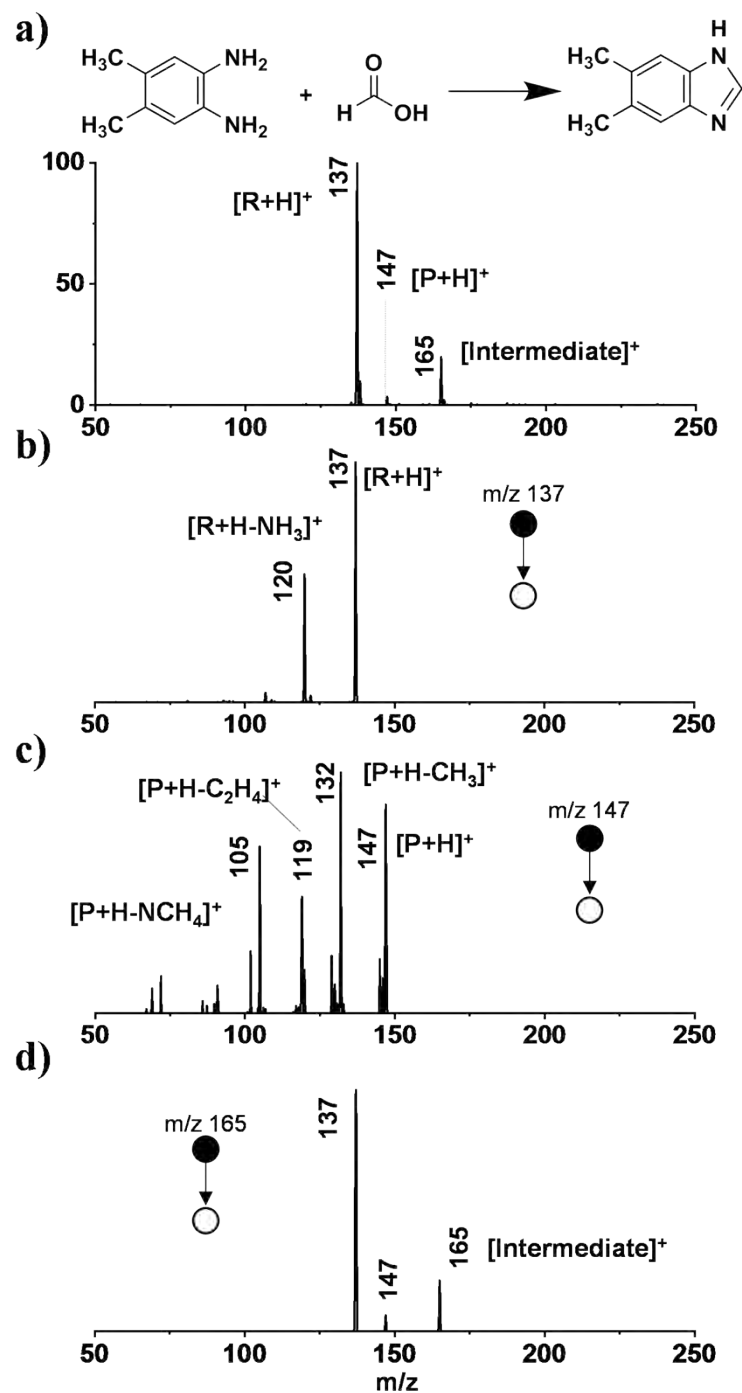


**Figure S33.** (a) Online MS of microdroplet reaction between 4,5-dimethylo-phenylenediamine and formic acid in methanol at 50 °C inlet temperature. MS/MS spectra of the (b) reagent (c) product and (d) intermediate. The reagent and the product are denoted as R and P.

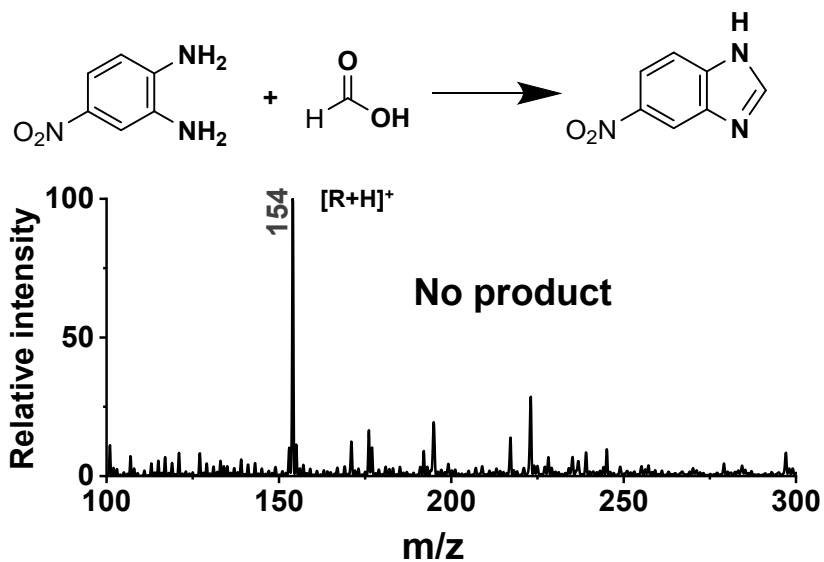


**Figure S34.** Online MS of microdroplet reaction between 4-nitro-1,2-phenylenediamine and formic acid in methanol at 50 °C inlet temperature. No product formation observed. The reagent is denoted as R.

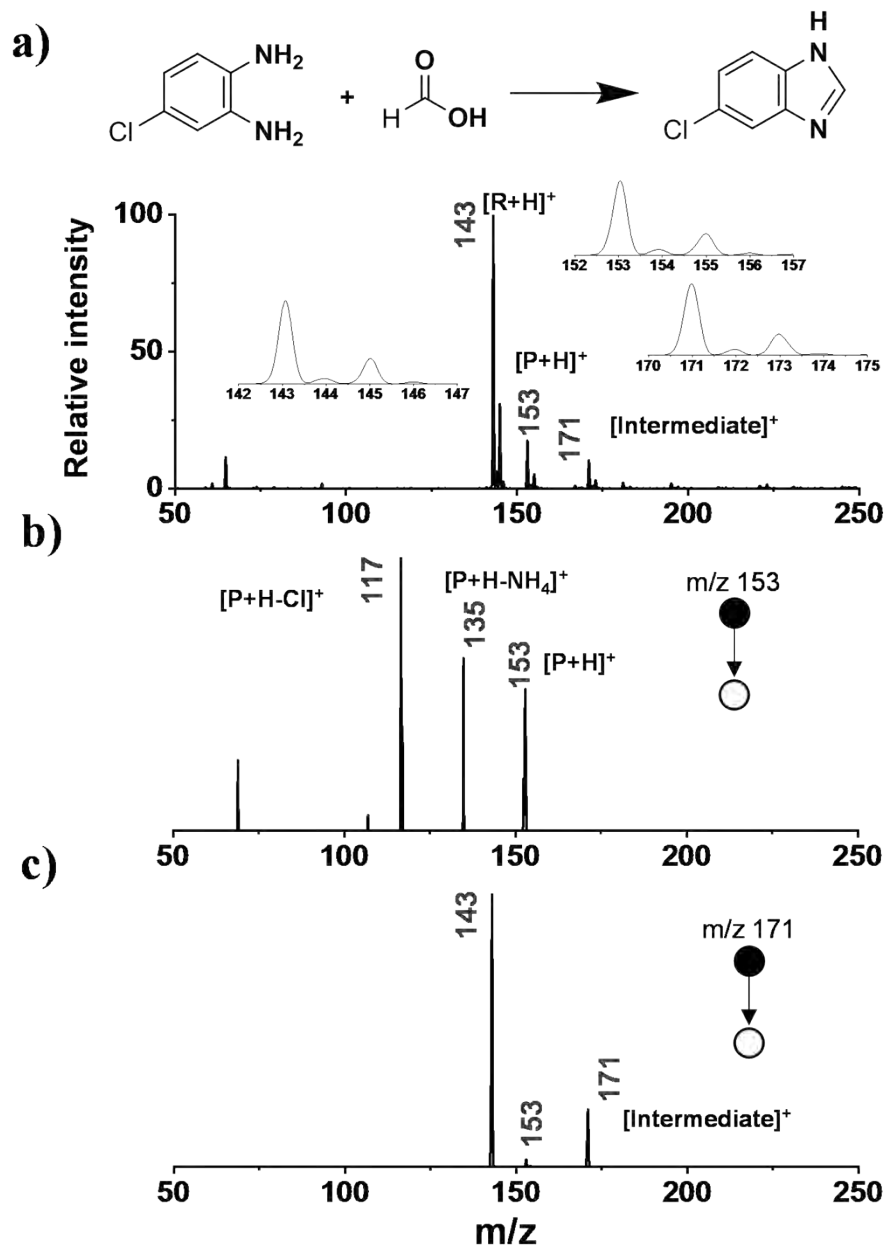


**Figure S35.** (a) Online MS of microdroplet reaction between 4-chloro-1,2-phenylenediamine and formic acid in methanol at 50 °C inlet temperature. MS/MS spectrum of (b) product and (c) intermediate. The reagent and the product are denoted as R and P.

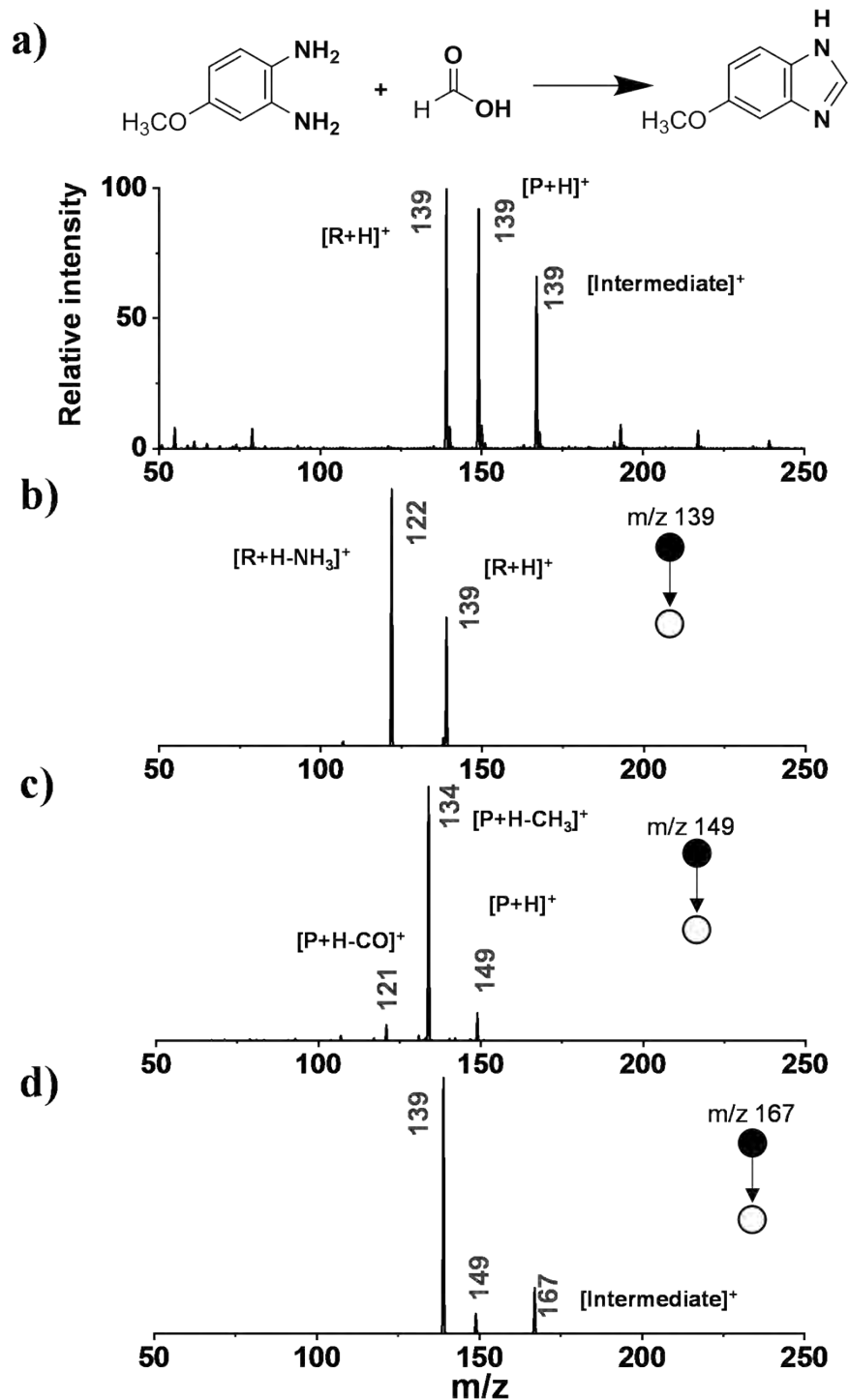


**Figure S36.** (a) Online MS of microdroplet reaction between 4-methoxy-1,2-phenylenediamine and formic acid in methanol at 50 °C inlet temperature. The fragmentation pattern of (b) reagent (c) product and (d) intermediate. The reagent and the product are denoted as R and P.

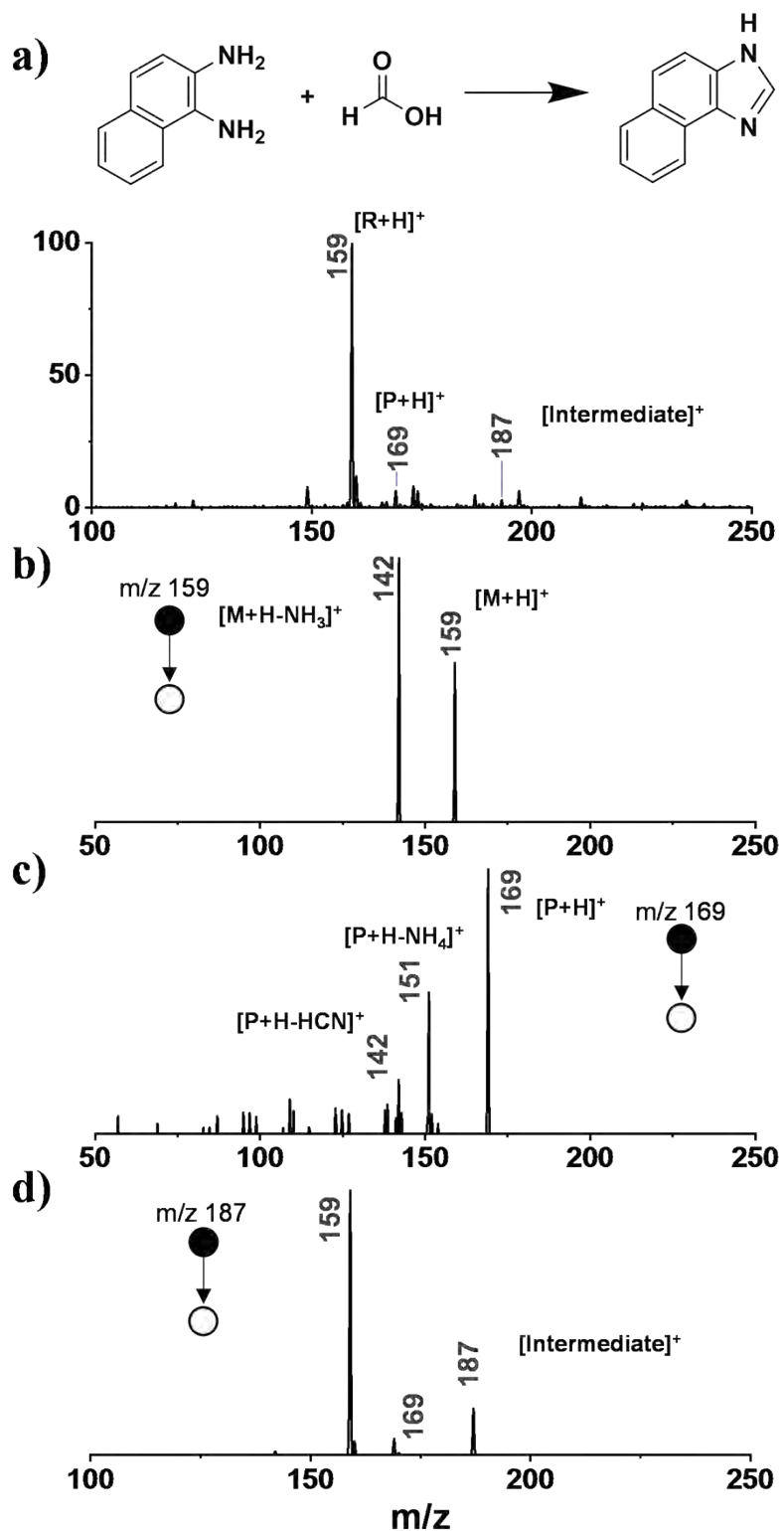


**Figure S37.** (a) Online MS of microdroplet reaction between 1,2-diaminonaphthalene and formic acid in methanol at 50 °C inlet temperature. The MS/MS spectra of (b) reagent (c) product and (d) intermediate. The reagent and the product are denoted as R and P.



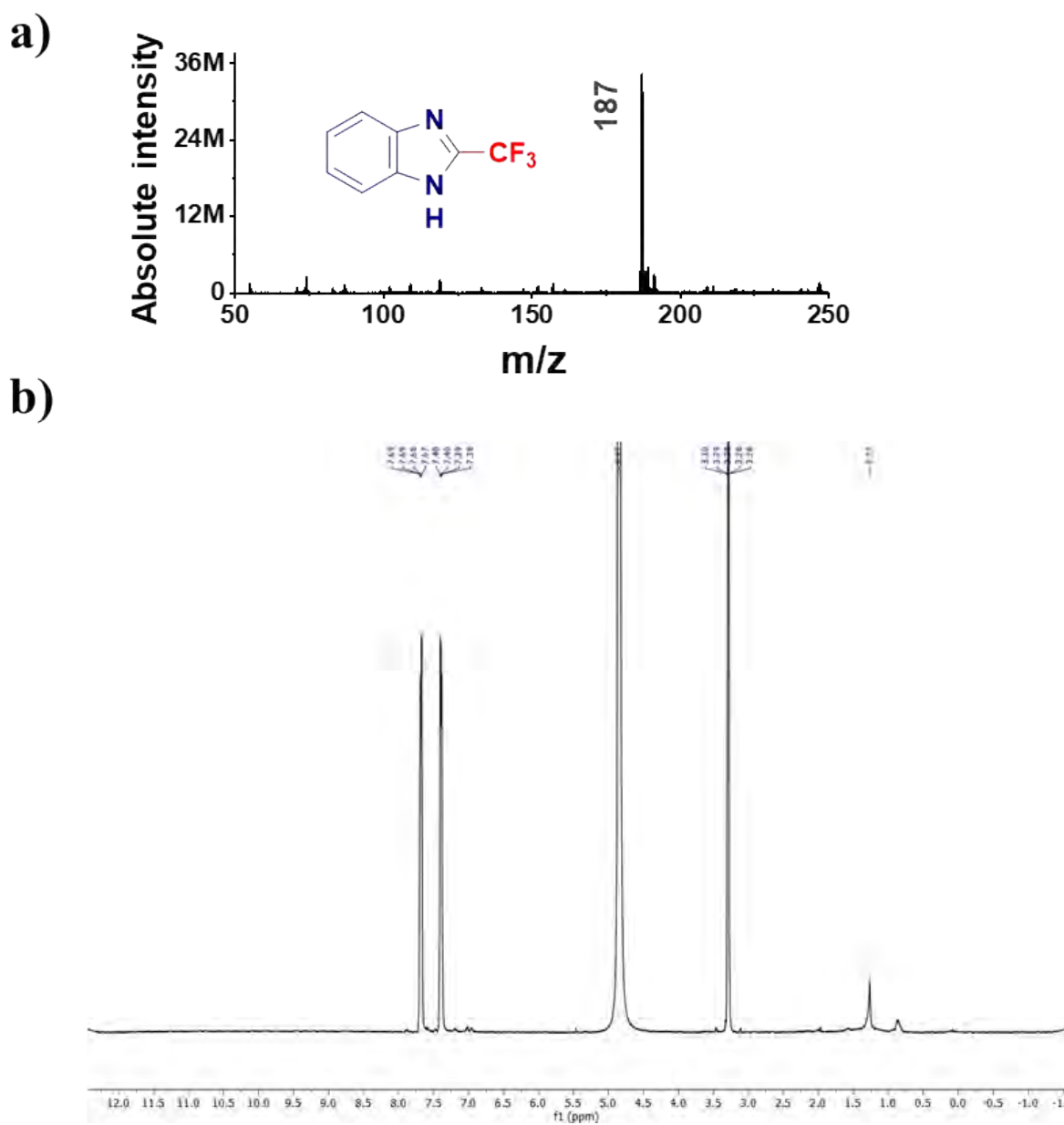


**Figure S38.** Characterization of isolated product of spray deposition reaction between trifluoroacetic acid and *o*-phenylenediamine. (a) Mass spectrum and (b)  $^1\text{H}$  NMR (400 MHz, MeOD) of the product.  $\delta$  7.69 (dd,  $J$  = 6.2, 3.2 Hz, 1H), 7.40 (dd,  $J$  = 6.3, 3.2 Hz, 1H). Peaks 4.85ppm and 3.28-3.30ppm are solvent peaks.

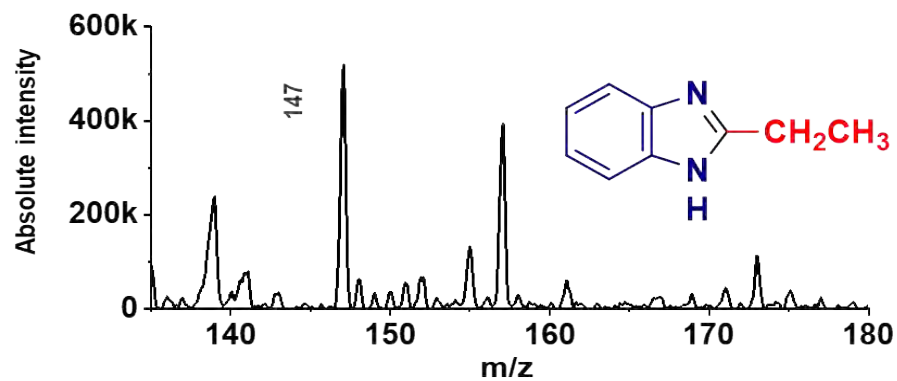


**Figure S39.** Characterization of isolated product of the spray deposition reaction between propanoic acid and *o*-phenylenediamine in methanol. Due to poor separation, an NMR of the isolated product was not obtained.

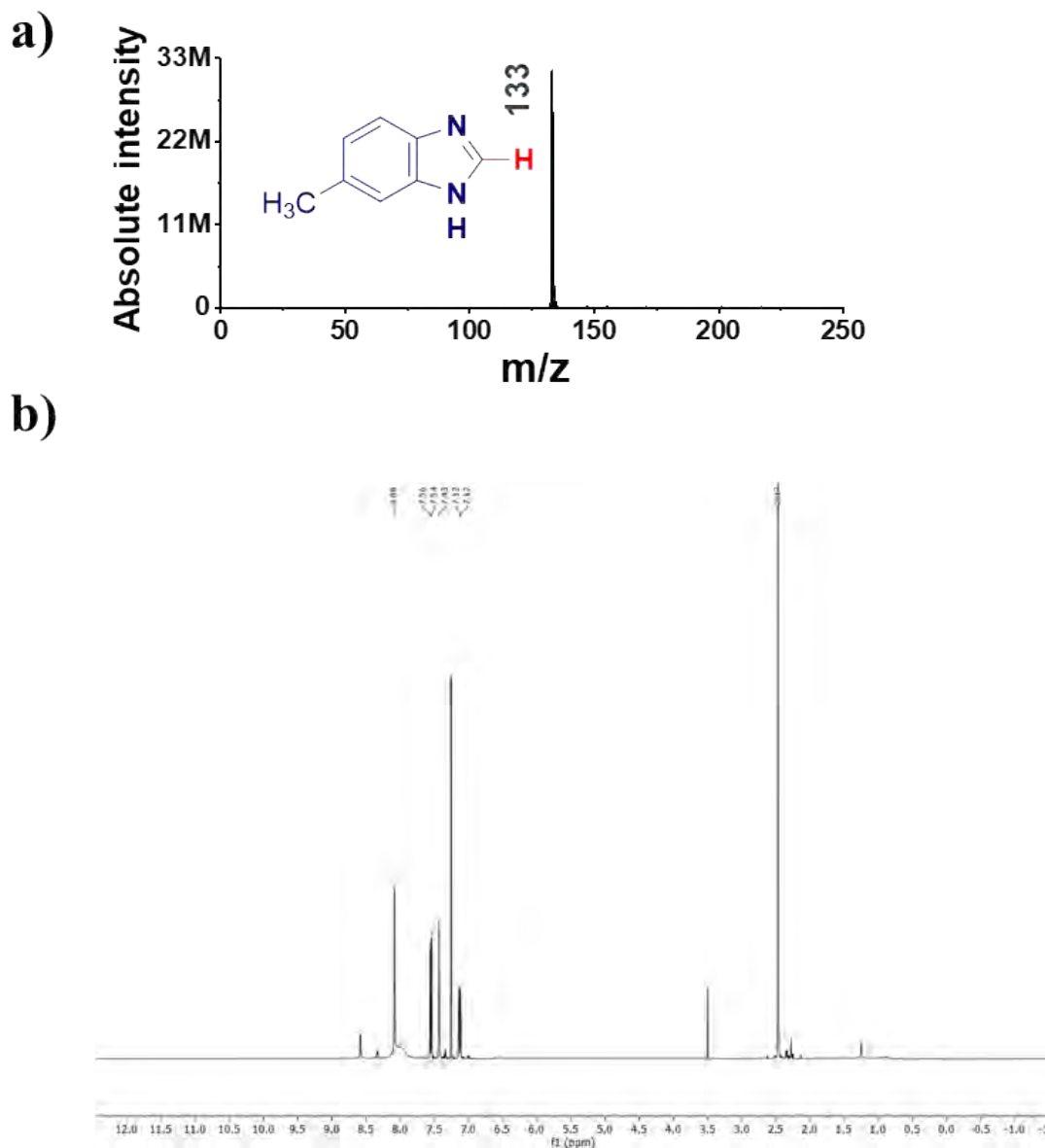


**Figure S40.** Characterization of isolated product of spray deposition reaction between formic acid and 4-methy-1,2-phenylenediamine. (a) Mass spectrum and (b) <sup>1</sup>H NMR (400 MHz, CDCl<sub>3</sub>) spectrum of the product.  $\delta$  8.08 (s, 1H), 7.55 (d,  $J$  = 8.3 Hz, 1H), 2.47 (s, 3H). Peak in 7.26ppm region is the solvent peak. Other peaks are due to artifacts or by-products.

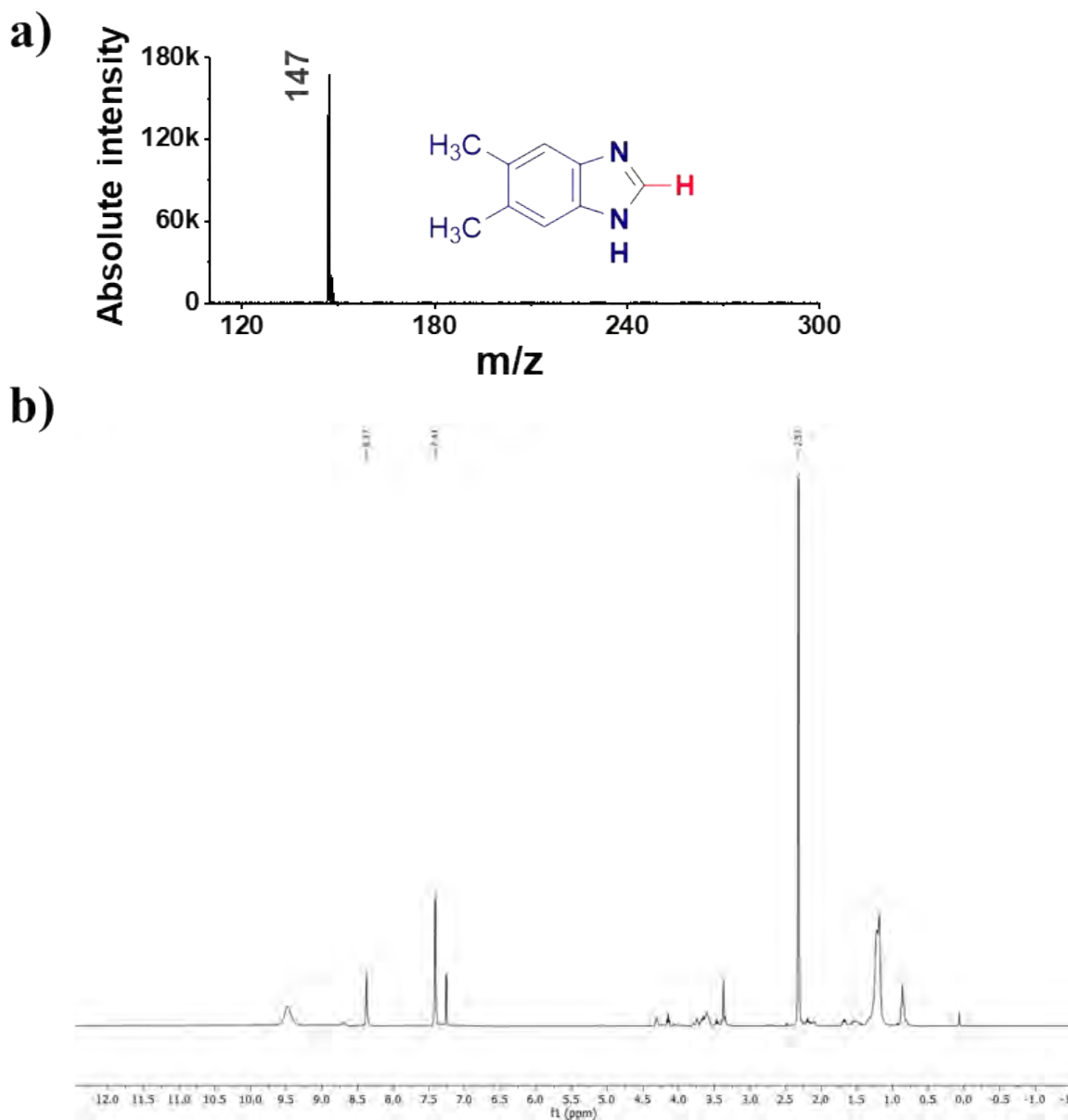


**Figure S41.** Characterization of the isolated product of spray deposition reaction between formic acid and 4,5-dimethyl-1,2-phenylenediamine in methanol. a) Mass spectrum and b)  $^1\text{H}$  NMR (400 MHz,  $\text{CDCl}_3$ )  $\delta$  8.37 (s, 1H), 7.41 (s, 2H), 2.32 (s, 6H). Peak in 7.26 ppm region is the solvent peak. Unlabeled peaks represent minor reaction products.

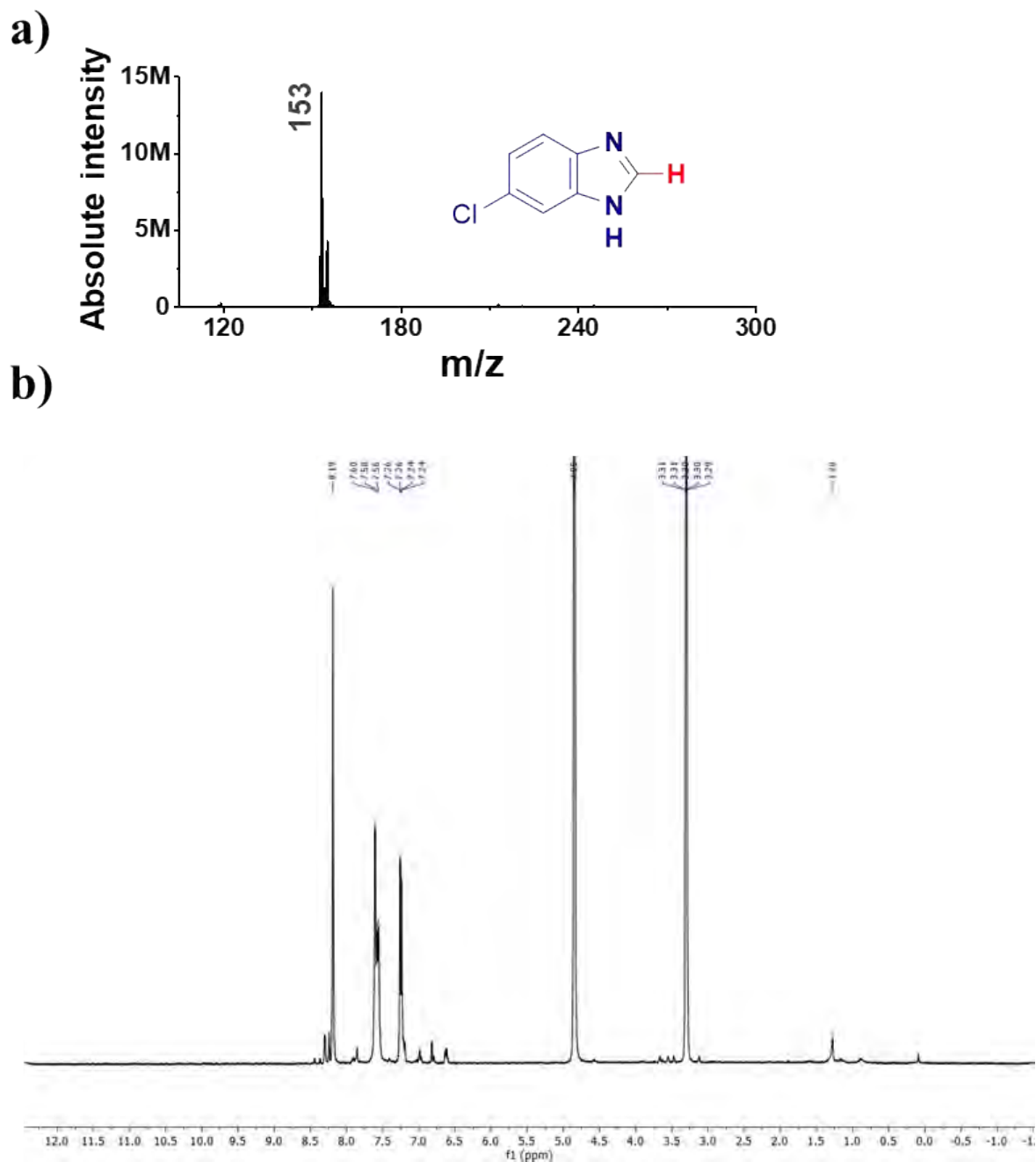


**Figure S42.** Characterization of isolated product of spray deposition reaction between formic acid and 4-chloro-1,2-phenylenediamine in methanol. (a) Mass spectrum and (b)  $^1\text{H}$  NMR (400 MHz, MeOD).  $\delta$  8.19 (s, 1H), 7.60 (s, 1H), 7.57 (d,  $J = 8.7$  Hz, 1H), 7.25 (dd,  $J = 8.5, 2.0$  Hz, 1H). Peaks 4.85ppm and 3.29-3.31ppm are solvent peaks.

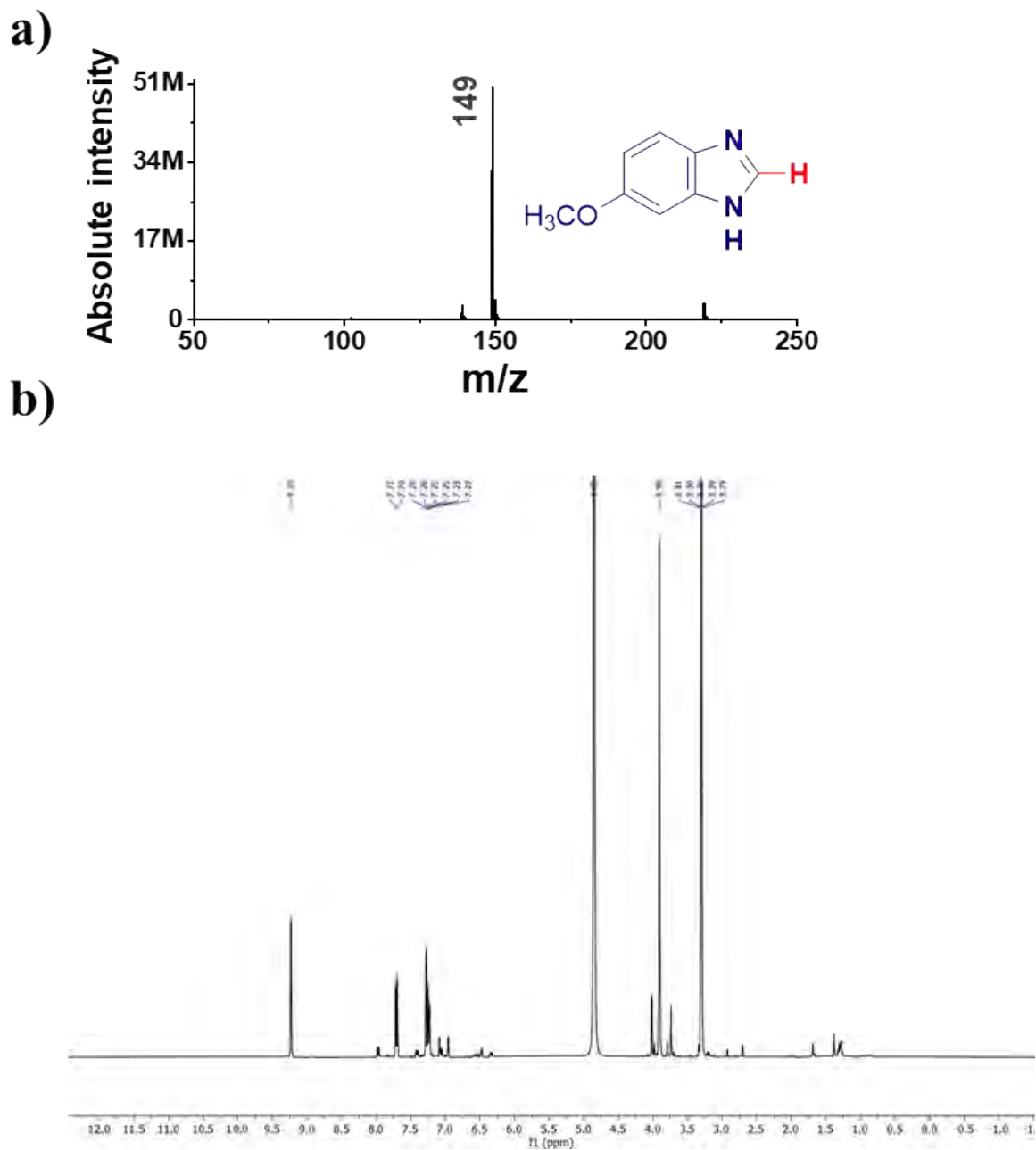


**Figure S43.** Characterization of isolated product of spray deposition reaction between formic acid and 4-methoxy-1,2-phenylenediamine in methanol. a) Mass spectrum and b)  $^1\text{H}$  NMR (400 MHz, MeOD).  $\delta$  9.24 (s, 1H), 7.71 (d,  $J = 9.0$  Hz, 1H), 7.31 – 7.17 (m, 2H), 3.91 (s, 3H). Peaks 4.85ppm and 3.29-3.31ppm are solvent peaks.



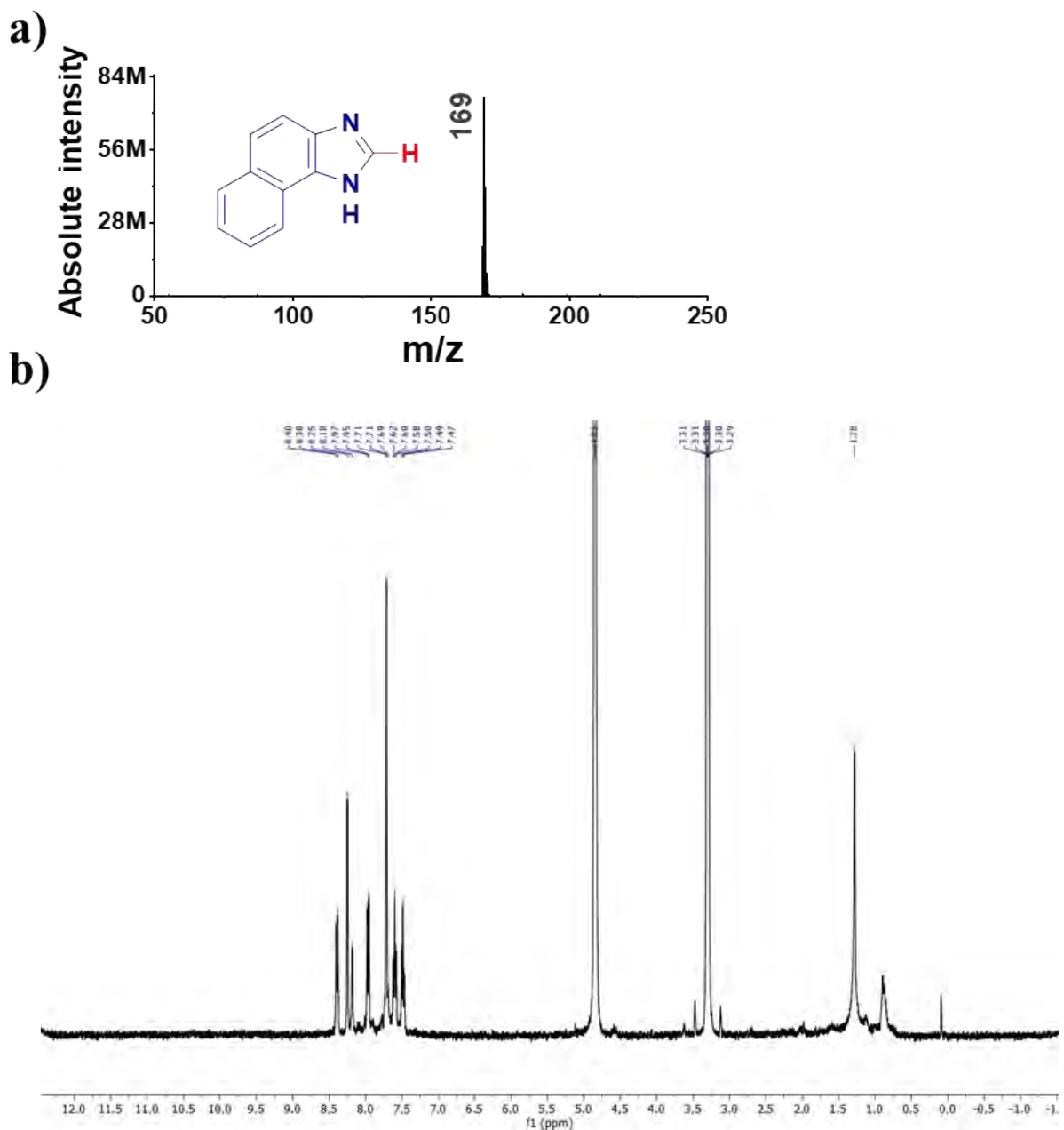


**Figure S44.** Characterization of isolated product of spray deposition reaction between formic acid and 1,2-diaminonaphthalene in methanol. (a) Mass spectrum and (b)  $^1\text{H}$  NMR (400 MHz, MeOD).  $\delta$  8.39 (d,  $J = 8.2$  Hz, 1H), 8.25 (s, 1H), 8.18 (s, 1H), 7.96 (d,  $J = 8.2$  Hz, 1H), 7.71 (d,  $J = 1.5$  Hz, 2H), 7.60 (t,  $J = 7.7$  Hz, 1H), 7.49 (t,  $J = 7.6$  Hz, 1H). Peaks 4.85ppm and 3.29-3.31ppm are solvent peaks.

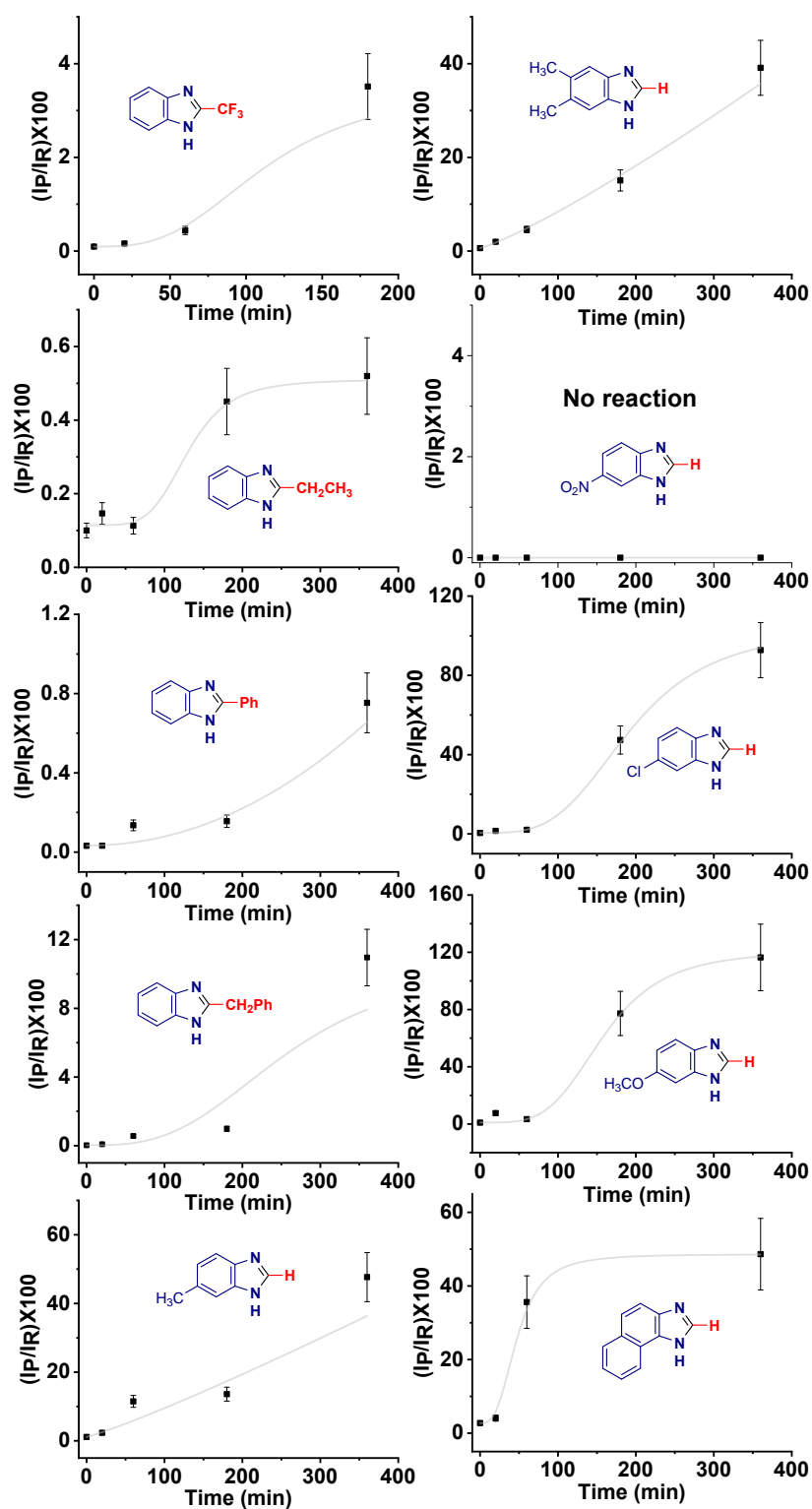


**Figure S45.** Kinetics data for thin film reactions. Reactions were done for 6 h in methanol under ambient conditions. Lines are drawn only as guides.

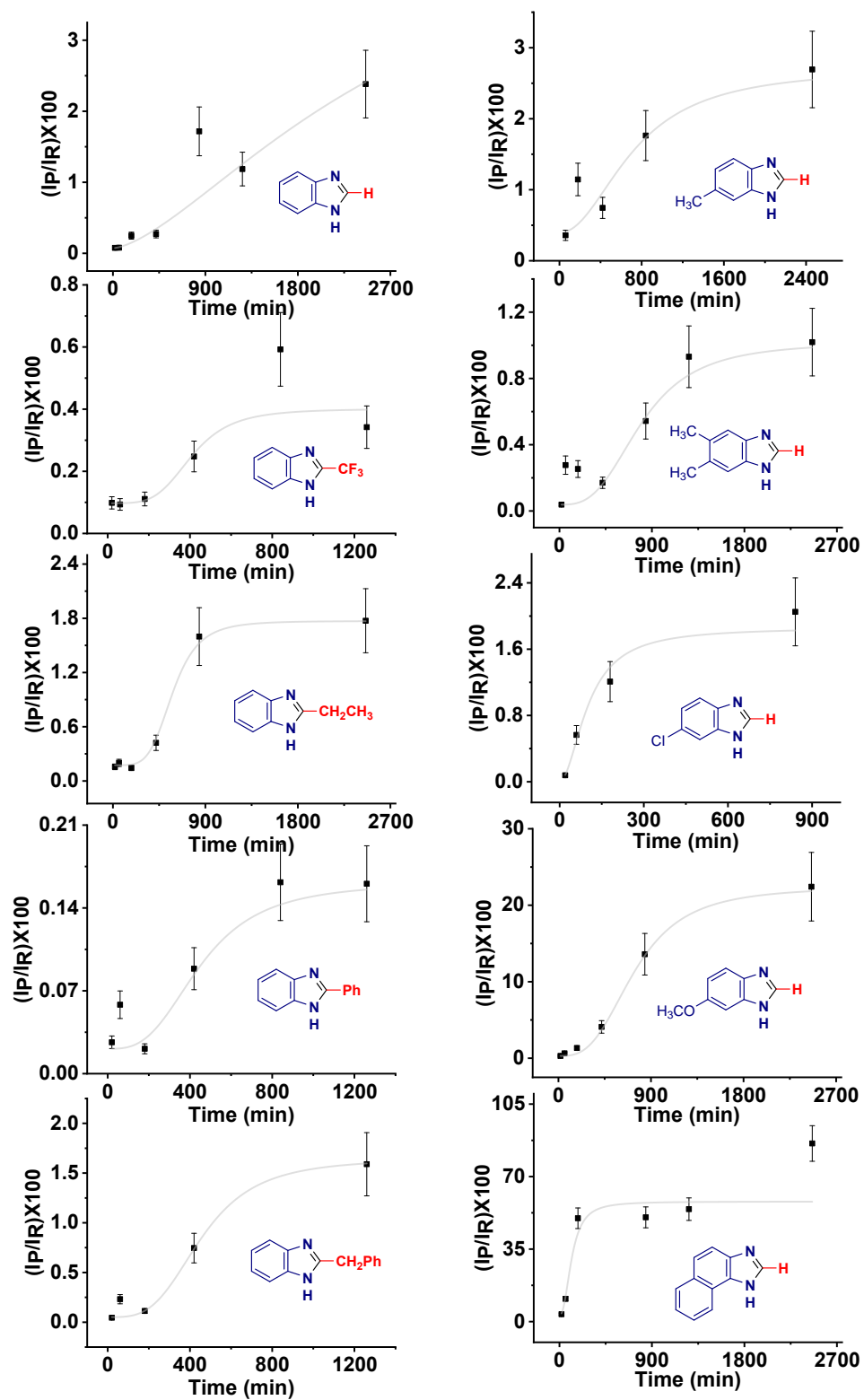


**Figure S46.** Kinetics data for bulk reactions. Reactions were done for 41 h in methanol under ambient conditions. Lines are drawn only as guides.

## Probing Subtle Changes in Molecular Orientations Using Ambient Electro spray Deposition Raman Spectroscopy (AESD RS)

Atanu Ghosh, Tripti Ahuja, Kamallesh Chaudhari, and Thalappil Pradeep\*

Cite This: *J. Phys. Chem. C* 2020, 124, 16644–16651

Read Online

ACCESS |



Metrics &amp; More

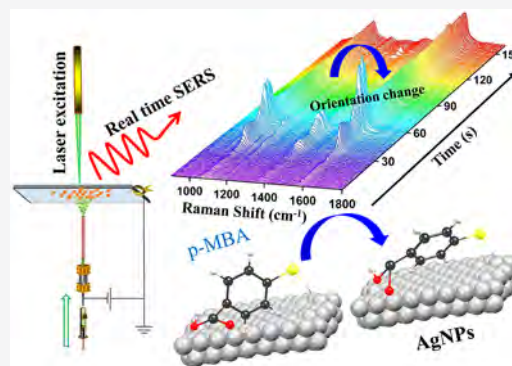


Article Recommendations



Supporting Information

**ABSTRACT:** Herein, subtle changes in the molecular orientations of different thiols upon interaction with soft-landed silver nanoparticles (AgNPs) have been probed using the technique called ambient electro spray deposition Raman spectroscopy (AESD RS). The method collects real-time surface-enhanced Raman scattering (SERS) spectra of analytes as Raman-active AgNPs were electrodeposited on a substrate. We have used *p*-mercaptobenzoic acid (*p*-MBA), benzenethiol (BT), and cyclohexanethiol (CHT) as proof-of-concept ligands for understanding variations in molecular orientations as a function of time, immediately after 30–40 s of electro spray of AgNPs. During time-dependent SERS measurements, we observed that the carboxylate ( $\text{COO}^-$ ) group of *p*-MBA preferred a flat orientation on the NP surface upon interaction with the electro sprayed AgNPs, which later transformed into a tilted two-legged standing-up orientation. We also observed a concomitant change in the orientation of the phenyl ring, which transformed from tilted to a flat orientation with respect to the NP surface. We have found that the time of tilting depends on the concentration of the analyte used for analysis. Additional information on the orientation flipping of thiols was achieved by performing real-time SERS experiments on other thiol derivatives such as CHT and BT. In the case of BT, SERS intensity variations were similar to *p*-MBA, which were attributed to the changes in orientation. However, in the case of CHT, such SERS intensity variations were absent. Time-dependent SERS spectra of *p*-MBA, BT, and CHT suggested that the interaction between the  $\pi$ -cloud of the phenyl ring and AgNPs could be one of the triggering factors for such orientation flipping of thiols on NP surfaces.



## INTRODUCTION

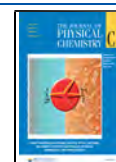
Thiolated molecules have been widely explored using surface-enhanced Raman spectroscopy (SERS) due to their strong binding affinity toward noble metal nanoparticles (NPs).<sup>1,2</sup> They form stable M–S (M = Ag, Au, Cu) bonds by chemisorption.<sup>3,4</sup> Orientations of analytes on NP surfaces provide crucial information about NP stabilization,<sup>5,6</sup> metal-adsorbate binding, and reactivity of the adsorbed species.<sup>7,8</sup> Optical methods such as second harmonic generation (SHG), infrared reflectance (IR), ellipsometry, fluorescence, and SERS are the known techniques to understand and determine the orientations of analytes precisely.<sup>9–14</sup> Among all, SERS has been used extensively over the last 2 decades for studies of surface chemistry. High enhancement factor in terms of signal intensity and unique information about molecular vibrations have been derived with this technique.<sup>10,15–18</sup> Weak Raman signals of molecules can be enhanced to  $\sim 10^6$ – $10^{14}$  times in SERS,<sup>19</sup> which enables this technique to be used even for single molecule detection.<sup>20–22</sup> In SERS, understanding of orientation of molecules is achieved with the comprehensive analysis of the relative intensity variations of specific vibrational modes of the analytes.<sup>23–25</sup> Creighton first introduced a procedure for qualitative analysis of the orientation of ligands on spherical NPs,<sup>26,27</sup> which was later expanded to both

smooth and roughened surfaces of AgNPs.<sup>28</sup> While performing SERS of benzenethiol (BT) in media of varying refractive indices, Carron and Hurley introduced a precise method for the determination of orientation of BT on the NP surface, with the help of axial and azimuthal angles.<sup>7</sup> The axial angle ( $\theta$ ) is defined as the angle between the  $\text{C}_2$  axis of BT and the metal surface, and the azimuthal angle ( $\phi$ ) is the angle of rotation of the phenyl plane about the  $\text{C}_2$  axis. They found that the values of  $\theta$  were 85 and 76° for BT on silver (Ag) and gold (Au) surfaces, respectively. The  $\phi$  was found to vary from 32 to 0° for Ag to Au.<sup>7</sup> For aromatic carboxylic acid derivatives, three distinct geometries of the carboxylate ( $\text{COO}^-$ ) group were proposed on the Ag surface based on the intensity variations of the  $\text{COO}^-$  vibrational bands.<sup>29</sup> When the intensity of symmetric stretching vibration  $\nu_s(\text{COO}^-)$  was stronger than that of bending vibration  $\delta(\text{COO}^-)$ , the  $\text{COO}^-$  group interacts

Received: May 8, 2020

Revised: June 16, 2020

Published: July 2, 2020



with the NP surface through its  $\pi$ -electrons and attains a flat orientation. On the other hand, when  $\text{COO}^-$  becomes two-legged, having a standing-up geometry, the intensity of  $\delta(\text{COO}^-)$  band increases with respect to  $\nu_s(\text{COO}^-)$ . The increase in the relative intensity of  $\delta(\text{COO}^-)$  with respect to  $\nu_s(\text{COO}^-)$  dictates the tilting of the carboxylate group on the surface. Schematic representations of these two orientations of the  $\text{COO}^-$  group are shown in Figure 1a,b.

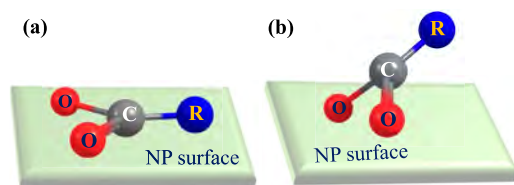


**Figure 1.** Schematic representations of orientations of  $\text{COO}^-$  on the NP surface. (a) Flat orientation and (b) two-legged standing-up orientation of  $\text{COO}^-$  ( $-\text{R}$  represents an aromatic ring).

In a similar way, Joo et al. had investigated the conformational changes of cyclohexanethiol (CHT) on AuNPs and Au plates using SERS.<sup>30</sup> The equatorial chair conformers appeared to be dominant at higher concentrations, whereas both the equatorial and axial chair conformers of CHT exist at lower concentrations, corresponding to a near-monolayer coverage limit.<sup>30</sup> *Para*-mercaptobenzoic acid (*p*-MBA) is one such aromatic thiol that has been used as a good Raman tag in various applications such as imaging, sensing, etc.,<sup>31</sup> owing to its large scattering cross section. Different orientations of *p*-MBA on NP surfaces have been revealed by theoretical and experimental SERS studies.<sup>3,29,32</sup> Like these, there are several other reports that have discussed molecular orientations of

analytes on NP surfaces,<sup>7,13,14,23,25,29,30,33</sup> but in all such studies, the orientations were determined once analytes got adsorbed and pinned at the NP surface. In such cases, we lack information about the orientations of the analyte during the time of adsorption and consequently their interactions with the NP surface.

In this paper, we have used our recently developed technique named ambient electrospray deposition Raman spectroscopy (AESD RS)<sup>34</sup> to probe orientations of different thiols in real time, starting from the time of analyte adsorption on the NP surface. The AESD method was integrated with a miniaturized Raman spectrometer to monitor early events at the time of molecule–NP interaction, which was completely ignored in the cases of conventional drop-casted and spin-coated SERS samples. We collected time-dependent SERS spectra of analytes while electrospray of preformed AgNPs was happening, which revealed several new insights on the molecular behavior of analytes pinned on NP surfaces. We report orientation changes of *p*-MBA upon its interaction with soft-landed AgNPs at neutral pH and have probed the fluttering nature of phenyl thiols on the NP surface. We observed that the  $\text{COO}^-$  functionality of *p*-MBA acquired a two-legged standing-up orientation from a flat orientation, gradually with time. The phenyl ring was also transformed from a tilted position to a flat orientation with respect to the NP surface. The tilting depends on several factors such as analyte concentration, pH, morphologies of the NP surface, local temperature at the analyte–NP junction, laser power, etc.<sup>29,30,35–37</sup> It is evident that the concentration and functional groups of analytes play an important role in tuning the molecular orientations upon interaction with AgNPs that have been explored in detail here. Keeping functionality of molecules as the triggering factor, other thiols such as BT and

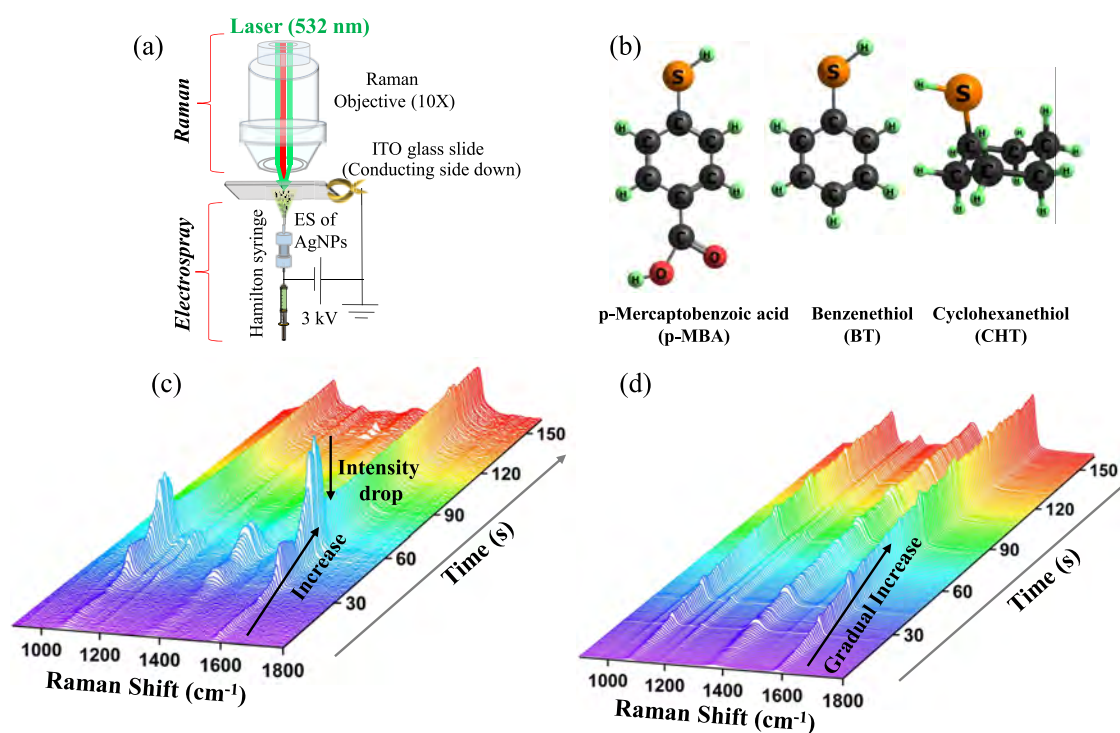


**Figure 2.** (a) Schematic of the AESD RS setup, (b) ball-and-stick molecular structures of the analytes possessing different functionalities used for this study, (c) intensity variation of 160 SERS spectra of  $1\ \mu\text{M}$  *p*-MBA collected using AESD RS and (d) intensity variation for a mixture of *p*-MBA ( $1\ \mu\text{M}$ ) and AgNPs (1:5 volume ratio) drop-casted on an ITO glass slide.



CHT were also investigated to understand their molecular behavior at the time of analyte–NP interaction. SERS analyses in real time using AESD RS have unveiled that when a molecule possesses a phenyl ring, it changes from tilted to the flat orientation, whereas in the case of a cyclohexane ring, such a change was absent. We believe that such real-time SERS studies will help in understanding the molecular events that can be useful for enhancing sensitivity in applications like sensing and catalysis.

## MATERIALS AND METHODS

Silver nitrate (99.9%) was purchased from Rankem. Trisodium citrate (>99%) was received from Merck Life Science Private Limited. Molecules such as *p*-MBA, CHT, and BT were purchased from Sigma-Aldrich. Indium tin oxide (ITO)-coated glass slides were purchased from Zhuhai Kaivo Electronic Components Co. Ltd. Fused silica capillary was received from Fisher Scientific. Other reagents including the solvents were of analytical grade and were used without further purification. Deionized water (DI) ( $\sim 18.2 \text{ M}\Omega\cdot\text{cm}$ ), obtained from Milli-Q, was used throughout the experiments.

**Synthesis of Silver Nanoparticles.** Citrate-capped silver sols were prepared using the modified Turkevich<sup>38</sup> method where 17 mg of  $\text{AgNO}_3$  was dissolved in 100 mL  $\text{H}_2\text{O}$  and the solution was heated to 100 °C. A solution of 1% sodium citrate (4 mL) was added dropwise to the boiling solution with constant stirring. The solution was kept boiling for 10–15 min till it became pale yellow. The colored solution was allowed to cool to room temperature and was finally stored in the dark at 4 °C. For electrospray deposition experiments, diluted AgNPs in DI water (1:1) were used.

**Preparation of SERS Substrates.** Ethanolic solutions (40  $\mu\text{L}$ ) of *p*-MBA, BT, and CHT (concentrations 10 and 1  $\mu\text{M}$ ) were drop-casted on the conducting surface of an ITO glass slide and allowed to dry under ambient conditions in the dark. Note that no Raman signals were obtained from these analytes in the absence of electrospray of AgNPs.

**SERS Measurements.** SERS signals were collected after electrospraying preformed AgNPs for 30–40 s. Signals were collected from the opposite side of the ITO where the analyte was drop-casted (see Figure 2a for details). For real-time analysis, multiple spectra were collected at an interval of 1 s with an accumulation time of 0.3 s. Experimental details on SERS spectral collection are discussed in the Supporting Information.

**Instrumentation.** UV–visible spectroscopic measurements were performed using a PerkinElmer Lambda 25 spectrophotometer in the range of 200–1100 nm. Transmission electron microscopy (TEM) measurements were performed using a JEOL 3010, 300 kV instrument. As-synthesized AgNPs were spotted on a carbon-coated copper (Cu) grid followed by air-drying. For an electrosprayed sample, the Cu grid was placed near to the tip of the silica capillary and preformed AgNPs were sprayed for 30 s on the grid followed by air-drying. A frequency-doubled Nd:YAG laser (532 nm) with a maximum output power of 20 mW was used for excitation of the sample. Dark-field imaging of NPs was performed using the Cytoviva setup equipped with a high-resolution dark-field condenser and a 100 $\times$  (oil) objective. Also, plasmonic scattering spectra were measured using the Specim V10E spectrometer (400–1000 nm) at a spectral resolution of  $\pm 1.3 \text{ nm}$ .

**AESD RS Setup.** A custom-built AESD RS setup (schematic in Figure 2a) incorporates a nanoESI emitter with a high-voltage DC power supply of  $\sim 2.5$ –3 kV and a Raman spectrometer (Research India Co.) with a 532 nm excitation laser, which puts 20 mW power on the sample. A grating of 1800 grooves/mm and an accumulation time of 0.3 s were used. The home-made electrospray source was made by continuously infusing a dilute solution of preformed AgNPs through a fused silica capillary using a 500  $\mu\text{L}$  Hamilton syringe and a syringe pump. The inner and outer diameters of the fused capillary were 150 and 300  $\mu\text{m}$ , respectively. The flow rate was set to 0.5  $\mu\text{L}/\text{min}$  that generated a gentle electrospray plume. The positive polarity of a high-voltage DC power supply was connected to the needle of the syringe to apply the required potential. A fused silica capillary was connected to the syringe through a finger-tight union connector. The tip of the capillary was placed in such a way that the nanoparticle soft-landing can be done over one side of the ITO plate containing the analyte of interest. The ITO plate was then connected to the ground to dissipate the charge of the soft-landed AgNPs.

## RESULTS AND DISCUSSION

**Real-Time SERS Monitoring of Analytes Using AESD RS.** In our recent work, we had reported rapid and sensitive detection of various analytes (*p*-MBA, 2,4-dinitro toluene, and *Escherichia coli*) using the AESD RS method.<sup>34</sup> In the current work, we have used the same technique to collect real-time SERS spectra of different thiols and to investigate the subtle changes in the orientations of the molecules in the early stages of their interaction with soft-landed AgNPs. The technique uses a silica capillary for AESD coupled with a miniature Raman spectrometer to monitor time-dependent SERS of adsorbed thiol molecules. A schematic of the setup is presented in Figure 2a. Here, preformed AgNPs were soft-landed using AESD on various thiol-based analytes, drop-casted on ITO glass slides. Characterization studies of the as-synthesized and electrosprayed AgNPs were performed using UV–vis absorption spectroscopy, transmission electron microscopy (TEM), dark-field microscopy (DFM), and plasmonic scattering spectroscopy (Figure S1). TEM images suggest some morphological changes of AgNPs after ES. Plasmonic scattering spectra from isolated NPs (before and after ES) also suggest some changes in plasmonic properties of these AgNPs after ES due to aggregation and morphological changes (see Figure S1). Three thiol molecules (*p*-MBA, BT, and CHT), containing different functional groups and rings, were chosen for this study (Figure 2b). *p*-MBA has an auxiliary group (carboxylic acid) along with the BT backbone, whereas CHT lacks the electron-rich phenyl ring. Using a flow rate of 0.5  $\mu\text{L}/\text{min}$ , AgNPs were electrosprayed for 30–40 s continuously until SERS signals started to appear. To understand such real-time changes in molecules, time-dependent SERS spectra were collected immediately after the electrospray of AgNPs. For real-time SERS measurements, every spectrum was collected with an accumulation time of 0.3 s, with a time-gap of 1 s. Spectral collection was started from the time of electrospray, but during the initial period (30–40 s), no SERS signals were observed. More details on spectral collection using AESD RS are provided in the Supporting Information (in the section Experimental Details on SERS Spectral Collection Using AESD RS). During data processing, spectrum at zero time was designated as the first spectrum, at



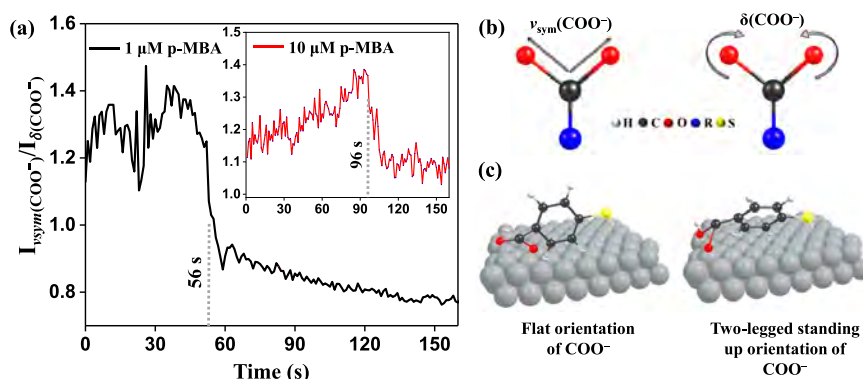


**Figure 3.** (a) Relative intensity plot of  $\nu_{\text{sym}}(\text{COO}^-)$  and  $\delta(\text{COO}^-)$  as a function of time for 1  $\mu\text{M}$  *p*-MBA (flipping time is 56 s); the inset shows a similar plot for 10  $\mu\text{M}$  *p*-MBA (flipping time is 96 s); (b) schematic representations of  $\nu_{\text{sym}}(\text{COO}^-)$  and  $\delta(\text{COO}^-)$  modes; (c) two different orientations of  $\text{COO}^-$  of *p*-MBA: flat orientation (left) and two-legged standing-up orientation (right).

which time SERS signals from the analyte were observed (Figure 2c).

Variations in the intensity of the time-dependent SERS spectra of *p*-MBA (1  $\mu\text{M}$ ) are presented as a waterfall plot in Figure 2c. SERS signals increase gradually with time followed by a sudden decrease. A similar trend of intensity was also observed for 10  $\mu\text{M}$  *p*-MBA. Time-dependent spectra of 10  $\mu\text{M}$  *p*-MBA are shown in Figure S2. Two dominating features at 1080 and 1586  $\text{cm}^{-1}$  were observed in all of the spectra of *p*-MBA, which were assigned to the  $\nu_{8a}$  and  $\nu_{12}$  aromatic ring vibrations, respectively. The peak at 1378  $\text{cm}^{-1}$  is due to the symmetric stretching of the carboxylate group ( $\nu_{\text{sym}}(\text{COO}^-)$ ). The bending mode of carboxylate  $\delta(\text{COO}^-)$  appears at 844  $\text{cm}^{-1}$ . In all of the measurements, 910 and 2580  $\text{cm}^{-1}$  peaks were absent, which correspond to  $\delta(\text{CSH})$  and  $\nu(\text{SH})$ , respectively, suggesting the formation of an Ag–S bond. Complete vibrational band assignments of *p*-MBA are given in Table S1. As a control measurement, 100  $\mu\text{L}$  of *p*-MBA (1  $\mu\text{M}$  in EtOH) and 500  $\mu\text{L}$  of diluted AgNPs were mixed well and kept in the dark for 2 h for equilibrium adsorption. About 40  $\mu\text{L}$  of the mixture was drop-casted on ITO to collect time-dependent SERS spectra. In the drop-casted time-dependent SERS, there was no delay of 30–40 s, which was present in AESD. As soon as the drop-casted sample was irradiated with laser, SERS signals were obtained and collected. Thus, the spectrum at time zero is the first accumulated spectrum. A waterfall plot of the spectra obtained in the above-mentioned (conventional SERS) method is presented in Figure 2d. However, in both the ES and conventional SERS, peak positions of vibrational modes match very well with the literature, but, interestingly, no sudden jump in intensity or decrease after a gradual increase in SERS intensity was observed in the case of conventional (drop-casted) SERS (Figure 2d). Similar results were observed in the case of 10  $\mu\text{M}$  *p*-MBA (Figures S2 and S3). A gradual increase in the SERS intensity with time was observed in both the cases which could be because of the creation of new hotspots due to molecular diffusion or the reshaping of NPs triggered by local heating in the presence of laser.<sup>39,40</sup> Also, the absence of a sudden decrease of intensity in the conventional SERS method provides an indication of some early events that are happening at the time of analyte adsorption on NP surface. Such fall in intensity after the gradual rise is attributed to changes in the orientations of the analyte upon interaction with soft-landed AgNPs (see below), which was absent in the drop-casted sample. In the case of ambient electrospray deposition, charged

nanodroplets play an important role for SERS enhancement. As in our previous work,<sup>34</sup> distance-dependent (distance between the capillary tip to the ITO collector surface) experiments were performed to understand the role of soft-landed charged AgNPs. We observed that with the increase in distance between the tip and the collector, SERS intensity decreases. These observations indicated the qualitative contribution of charged droplets to SERS intensity. However, these contributions are limited to SERS intensities and not to molecular reorientations or discrete transitions during AESD RS.

**Varying Concentration of Analytes: A Key Factor for Flipping and Orientation Changes.** To understand the reason for the sudden decrease of SERS intensity in the time-dependent spectra, a plot of the intensity ratio of  $\nu_{\text{sym}}(\text{COO}^-)$  and  $\delta(\text{COO}^-)$  of *p*-MBA was plotted as a function of time. The plots of relative intensity vs time for 1 and 10  $\mu\text{M}$  are shown in Figure 3a.

As reported previously,<sup>29</sup> when the relative intensity of  $\nu_{\text{sym}}(\text{COO}^-)$  is higher than that of  $\delta(\text{COO}^-)$ , i.e.,  $I_{\nu_{\text{sym}}(\text{COO}^-)}/I_{\delta(\text{COO}^-)}$  is greater than 1,  $\text{COO}^-$  adopts a flat orientation with respect to the surface. On the other hand, it takes a tilted two-legged standing-up orientation, when  $I_{\nu_{\text{sym}}(\text{COO}^-)}/I_{\delta(\text{COO}^-)}$  decreases. Schematic representations of the vibrational modes of  $\nu_{\text{sym}}(\text{COO}^-)$  and  $\delta(\text{COO}^-)$  are shown in Figure 3b, and schematic representations of the flat and two-legged standing-up orientations of the  $\text{COO}^-$  group are shown in Figure 3c. From the plots of relative intensities (1 and 10  $\mu\text{M}$ ), it is evident that the intensity ratio changes with time, which suggested the changes in the molecular orientation occurring on the NP surface. A point of transformation of the flat orientation to the tilted two-legged standing-up orientation of  $\text{COO}^-$  is shown with gray dotted lines in Figure 3a. The inset in Figure 3a shows a similar type of relative intensity drop at longer times for higher concentration (10  $\mu\text{M}$ ), which indicates that the time required for such orientation tilting and the extent of tilting depend on the analyte concentration. For 1  $\mu\text{M}$ , the time required for flipping was  $\sim 56$  s, which increased to  $\sim 96$  s for 10  $\mu\text{M}$ . The requirement of more time for flipping at higher concentrations of analytes is anticipated from the space-filling model of molecules over the NP surfaces. This model suggests that the monolayers get more tightly packed on the surface at higher concentrations of the thiol, which make their reorientation difficult, explaining the delay and lesser extent of flipping. The oscillatory behavior observed in the plots (Figure 3a) is not

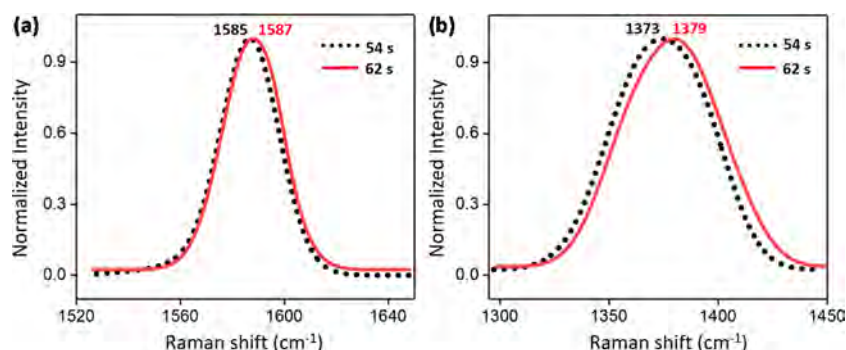


**Figure 4.** Fitted peak (cumulative Gaussian fit) of  $\nu_{8a}$  (ring) stretching (a) and bending  $\delta(\text{COO}^-)$  (b) mode for  $1\ \mu\text{M}$  *p*-MBA at two different time points (54 s, before flipping and 62 s, after flipping).

fully understood yet; however, we believe that such a behavior originates from the periodic molecular fluttering of self-assembled thiols over the NP surface. Citrate also contributes to SERS intensity of colloidal silver.<sup>41</sup> To check the contribution of citrate in our real-time SERS measurements, we did a control experiment where we used citrate-capped AgNPs alone for ES purpose and obtained the signal. The SERS spectra of only such AgNPs are compared to the SERS spectra of *p*-MBA interacted with soft-landed AgNPs, and the corresponding data are shown in Figure S4. The SERS signals of citrate are very weak in nature compared to *p*-MBA, and the peak positions for  $\text{COO}^-$  are entirely different for citrate and *p*-MBA. Therefore, we rule out the contribution of citrate in the observed change in molecular orientations. In solution chemistry, solvents also play a very important role in molecular adsorption and orientations over surfaces.<sup>42,43</sup> However, the observed effect is absent in the drop-casted and the spin-coated samples. While performing real-time SERS measurements using AESD RS, we took ethanolic solutions of analytes (*p*-MBA, BT, and CHT), which were drop-casted on cleaned ITO glass slides. The drop-casted analytes were dried before performing the ES experiments. Hence, the solvent of analytes will not play a role in change in molecular orientations. The presence of water used as a solvent of AgNPs is another possibility to cause changes in molecules when NPs were soft-landed on drop-casted analytes. However, while ES, due to Coulombic repulsion, the solvent gets evaporated and mostly NPs interact with analytes. Even if micrometer droplets were deposited, they would be evaporated quickly. We observed that changes in the orientation were seen even when the Raman experiment was performed 30–40 s after ES deposition, during which time any droplet would have evaporated. Thus, overall, solvents have minimal or no role in the molecular flipping while performing real-time SERS experiments via AESD RS.

**Additional Investigations on Flipping and Orientation Changes.** In SERS, the peak position and peak width are two significant parameters that also provide information about the molecular orientation. Gao and Weaver have reported that in the case of benzene adsorption on the Au surface, the broadening of phenyl vibrations gave the orientation of the benzene over the NP surface.<sup>8</sup> Here, we analyzed the changes in SERS peak positions and broadness with time for different thiols to confirm the real-time changes occurring in the molecular orientation. Gaussian peak fitting was performed on the peak at  $1586\ \text{cm}^{-1}$  ( $\nu_{8a}$  ring vibration) (Figure S5a,b) at two different times (54 and 62 s), which were the point of transformation for the molecular orientation (Figure 3a) of the

phenyl ring in the case of  $1\ \mu\text{M}$  *p*-MBA. The SERS peaks were fitted using multiple Gaussians to achieve the best fitting. The final fitted peak after multiple Gaussians is called as a cumulative fitted peak. Cumulative fitted peaks at two different times are shown in Figure 4a, which showed a blue shift of  $2\ \text{cm}^{-1}$  for the phenyl vibration along with an increase in full width at half-maximum (FWHM), which gave the unequivocal information about the interactions of the phenyl ring with the AgNPs. The increase in FWHM suggests that the phenyl ring of *p*-MBA interacts more closely with the surface by attaining a flat geometry. Similarly, we analyzed the peak at  $1380\ \text{cm}^{-1}$  corresponding to  $\nu_{\text{sym}}(\text{COO}^-)$  (Figure 4b), which also showed a  $6\ \text{cm}^{-1}$  blue shift with a negligible change in FWHM, corroborating the proposed change in orientation of  $\text{COO}^-$  from the flat to the tilted two-legged standing-up orientation. Figure 3c represents the two different orientations of  $\text{COO}^-$  and the phenyl ring of *p*-MBA on the AgNP surface. Initially,  $\text{COO}^-$  preferred flat geometry, while the phenyl ring stayed tilted with respect to the surface, but after a certain time, the  $\text{COO}^-$  changed its orientation to the two-legged standing-up geometry, while the phenyl ring became flat on the surface interacting with its  $\pi$ -electrons.

To further explore the fundamental reason of flipping in thiolated molecules, we extended the real-time SERS analysis to other functionalized thiols having different rings and auxiliary functional groups. We chose two other thiol-based derivatives: BT, which contains the aromatic ring without any auxiliary group, and the other CHT that possess neither aromatic ring nor any auxiliary group but contains a cyclohexyl ring (see Figure 2b). Similar time-dependent SERS measurements were performed for  $1\ \mu\text{M}$  solutions of BT and CHT, separately. The temporal SERS intensity maps for BT and CHT are shown in Figure 5a,b, respectively. Vibrational band assignments of BT and CHT are given in Tables S2 and S3, respectively.<sup>7,30,35</sup> As in the case of *p*-MBA, we found similar SERS intensity variations in BT, suggesting the orientation change of the phenyl ring on the AgNP surface. On the other hand, we did not notice any such decrease in SERS intensity in the case of CHT (Figure 5b), which suggested that flipping did not happen in CHT upon interaction with soft-landed AgNPs. While in the case of *p*-MBA, the FWHM analysis of SERS peaks suggested the changes in orientations, in contrast, CHT, lacking the phenyl ring and the additional functional groups, did not show prominent changes in peak broadness and peak position ( $991\ \text{cm}^{-1}$ ) with time (see Figure S6), which suggested no change in the orientation of CHT with time, supporting the results of real-time SERS spectra. Moreover, the

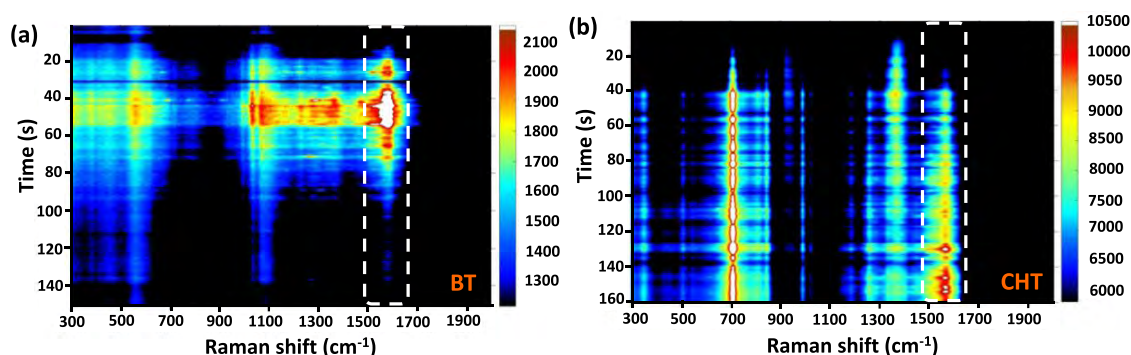


Figure 5. Temporal SERS intensity map of 1  $\mu\text{M}$  (a) BT and (b) CHT.

spectral assignments revealed that the axial conformation of CHT was favored in our experiments. The above results suggested favorable interaction of the aromatic  $\pi$ -cloud and AgNP surface in *p*-MBA and BT as a triggering factor for molecular flipping, which was absent in CHT. The above-mentioned time-dependent SERS performed on *p*-MBA, BT, and CHT also suggested that the distinct change in the molecular orientations is due to collective transition in adsorbates and not due to a discrete transition in the surface states.

## CONCLUSIONS

In conclusion, we have studied real-time SERS of thiolated molecules (*p*-MBA, BT, and CHT) using the AESD RS technique to understand the early events happening in such molecules upon interaction with soft-landed AgNPs. Time-dependent SERS analysis revealed that  $\text{COO}^-$  of *p*-MBA transformed its orientation from a flat to a two-legged standing-up geometry with time along with a tilting in the phenyl ring orientation. The time required for such flipping and extent of orientation change depended on the concentration of analytes. It was found that the time of flipping was  $\sim 56$  s for 1  $\mu\text{M}$  and  $\sim 96$  s for 10  $\mu\text{M}$ . To better understand the principal reason behind this phenomenon, we extended our analysis to BT and CHT, possessing different functionalities. SERS intensity maps of these two thiols suggested that  $\pi$ -electrons of the phenyl ring and their interactions with the NP surface play crucial roles in the flipping of orientation, which was further confirmed from the analysis of FWHM of SERS peaks. This work shows a promising direction toward the determination of orientation of analytes at their early stages of adsorption over NP surfaces, which will be widely useful in applications like catalysis and sensing.

## ASSOCIATED CONTENT

### Supporting Information

The Supporting Information is available free of charge at <https://pubs.acs.org/doi/10.1021/acs.jpcc.0c04116>.

Characterization of the as-synthesized and electro-sprayed AgNPs using UV-vis absorption spectroscopy, TEM, and DFM; real-time SERS spectra of 10  $\mu\text{M}$  *p*-MBA at the time of electrospray of AgNPs and SERS spectra of a 10  $\mu\text{M}$  *p*-MBA and AgNP mixture (1:5) drop-casted on ITO; Gaussian peak fitting of *p*-MBA and CHT at different time intervals; vibrational band assignments of *p*-MBA, BT, and CHT (PDF)

## AUTHOR INFORMATION

### Corresponding Author

Thalappil Pradeep – DST Unit on NanoScience (DST UNS) and Thematic Unit of Excellence (TUE), Department of Chemistry, Indian Institute of Technology Madras, Chennai 600036, India; [orcid.org/0000-0003-3174-534X](https://orcid.org/0000-0003-3174-534X); Phone: +91044-2257-4208; Email: [pradeep@iitmadras.ac.in](mailto:pradeep@iitmadras.ac.in)

### Authors

Atanu Ghosh – DST Unit on NanoScience (DST UNS) and Thematic Unit of Excellence (TUE), Department of Chemistry, Indian Institute of Technology Madras, Chennai 600036, India

Tripti Ahuja – DST Unit on NanoScience (DST UNS) and Thematic Unit of Excellence (TUE), Department of Chemistry, Indian Institute of Technology Madras, Chennai 600036, India

Kamalesh Chaudhari – DST Unit on NanoScience (DST UNS) and Thematic Unit of Excellence (TUE), Department of Chemistry, Indian Institute of Technology Madras, Chennai 600036, India

Complete contact information is available at: <https://pubs.acs.org/doi/10.1021/acs.jpcc.0c04116>

### Author Contributions

A.G. and T.A. contributed equally. A.G., T.A., and T.P. conceived the experiments. A.G. performed SERS measurements using AESD RS. K.C. helped in image processing and figures. The manuscript was written jointly by all of the authors.

### Notes

The authors declare no competing financial interest.

## ACKNOWLEDGMENTS

The authors thank the Department of Science and Technology, Government of India, with project number SR/NM/TP-92/2016(G) for constantly supporting our research program. A.G. acknowledges the Department of Chemistry, IIT Madras. T.A. acknowledges the institute graduate fellowship. The authors also acknowledge Dr. Ganesan Paramasivam for helpful discussions.

## ABBREVIATIONS

AESDambient electrospray deposition; AESD RSambient electrospray deposition Raman spectroscopy; AgNPsilver nanoparticles; *p*-MBA

-mercaptobenzoic acid; BTbenzenethiol; CHTcyclohexane thiol; TEMtransmission electron microscopy; DFMdark-field microscopy; ITOindium tin oxide



## REFERENCES

- (1) Sandström, P.; Boncheva, M.; Åkerman, B. Nonspecific and Thiol-Specific Binding of DNA to Gold Nanoparticles. *Langmuir* **2003**, *19*, 7537–7543.
- (2) Sellers, H.; Ulman, A.; Shnidman, Y.; Eilers, J. E. Structure and Binding of Alkanethiolates on Gold and Silver Surfaces: Implications for Self-Assembled Monolayers. *J. Am. Chem. Soc.* **1993**, *115*, 9389–9401.
- (3) Ho, C. H.; Lee, S. SERS and DFT Investigation of the Adsorption Behavior of 4-Mercaptobenzoic Acid on Silver Colloids. *Colloids Surf., A* **2015**, *474*, 29–35.
- (4) Maiti, N.; Chadha, R.; Das, A.; Kapoor, S. Surface Selective Binding of 2,5-Dimercapto-1,3,4-Thiadiazole (DMTD) on Silver and Gold Nanoparticles: A Raman and DFT Study. *RSC Adv.* **2016**, *6*, 62529–62539.
- (5) Park, J. W.; Shumaker-Parry, J. S. Structural Study of Citrate Layers on Gold Nanoparticles: Role of Intermolecular Interactions in Stabilizing Nanoparticles. *J. Am. Chem. Soc.* **2014**, *136*, 1907–1921.
- (6) Al-Johani, H.; Abou-Hamad, E.; Jedidi, A.; Widdifield, C. M.; Viger-Gravel, J.; Sangaru, S. S.; Gajan, D.; Anjum, D. H.; Ould-Chikh, S.; Hedhili, M. N.; et al. The Structure and Binding Mode of Citrate in the Stabilization of Gold Nanoparticles. *Nat. Chem.* **2017**, *9*, 890–895.
- (7) Carron, K. T.; Hurley, L. G. Axial and Azimuthal Angle Determination with Surface-Enhanced Raman Spectroscopy: Thiophenol on Copper, Silver, and Gold Metal Surfaces. *J. Phys. Chem. A* **1991**, *95*, 9979–9984.
- (8) Gao, P.; Weaver, M. J. Surface-Enhanced Raman Spectroscopy as a Probe of Adsorbate-Surface Bonding: Benzene and Monosubstituted Benzenes Adsorbed at Gold Electrodes. *J. Phys. Chem. B* **1985**, *89*, 5040–5046.
- (9) Shannon, V. L.; Koos, D. A.; Kellar, S. A.; Huifang, P.; Richmond, G. L. Rotational Anisotropy in the Second Harmonic Response from Cu(111) in Aqueous Solutions. *J. Phys. Chem. C* **1989**, *93*, 6434–6440.
- (10) Haddad, A.; Comanescu, M. A.; Green, O.; Kubic, T. A.; Lombardi, J. R. Detection and Quantitation of Trace Fentanyl in Heroin by Surface-Enhanced Raman Spectroscopy. *Anal. Chem.* **2018**, *90*, 12678–12685.
- (11) Chamberlain, J. Reflection Spectroscopy. *Phys. Bull.* **1971**, *22*, 333–336.
- (12) Seballos, L.; Olson, T. Y.; Zhang, J. Z. Effects of Chromophore Orientation and Molecule Conformation on Surface-Enhanced Raman Scattering Studied with Alkanic Acids and Colloidal Silver Nanoparticles. *J. Chem. Phys.* **2006**, *125*, No. 234706.
- (13) Brolo, A. G.; Jiang, Z.; Irish, D. E. The Orientation of 2,2'-Bipyridine Adsorbed at a SERS-Active Au(1 1 1) Electrode Surface. *J. Electroanal. Chem.* **2003**, *547*, 163–172.
- (14) Lee, C. J.; Lee, S. Y.; Karim, M. R.; Lee, M. S. Comparison of the Adsorption Orientation for 2-Mercaptobenzothiazole and 2-Mercaptobenzoxazole by SERS Spectroscopy. *Spectrochim. Acta, Part A* **2007**, *68*, 1313–1319.
- (15) Dick, S.; Konrad, M. P.; Lee, W. W. Y.; McCabe, H.; McCracken, J. N.; Rahman, T. M. D.; Stewart, A.; Xu, Y.; Bell, S. E. J. Surface-Enhanced Raman Spectroscopy as a Probe of the Surface Chemistry of Nanostructured Materials. *Adv. Mater.* **2016**, *28*, 5705–5711.
- (16) Bell, S. E. J.; Mackle, J. N.; Sirimuthu, N. M. S. Quantitative Surface-Enhanced Raman Spectroscopy of Dipicolinic Acid - Towards Rapid Anthrax Endospore Detection. *Analyst* **2005**, *130*, 545–549.
- (17) Kneipp, K.; Kneipp, H.; Itzkan, I.; Dasari, R. R.; Feld, M. S. Ultrasensitive Chemical Analysis by Raman Spectroscopy. *Chem. Rev.* **1999**, *99*, 2957–2976.
- (18) Tian, Z. Q. Surface-Enhanced Raman Spectroscopy: Advancements and Applications. *J. Raman Spectrosc.* **2005**, *36*, 466–470.
- (19) Langer, J.; De Aberasturi, D. J.; Aizpurua, J.; Alvarez-Puebla, R. A.; Auguie, B.; Baumberg, J. J.; Bazan, G. C.; Bell, S. E. J.; Boisen, A.; Brolo, A. G.; et al. Present and Future of Surface-Enhanced Raman Scattering. *ACS Nano* **2020**, *14*, 28–117.
- (20) Etchegoin, P. G.; Le Ru, E. C. Resolving Single Molecules in Surface-Enhanced Raman Scattering within the Inhomogeneous Broadening of Raman Peaks. *Anal. Chem.* **2010**, *82*, 2888–2892.
- (21) Chen, H. Y.; Lin, M. H.; Wang, C. Y.; Chang, Y. M.; Gwo, S. Large-Scale Hot Spot Engineering for Quantitative SERS at the Single-Molecule Scale. *J. Am. Chem. Soc.* **2015**, *137*, 13698–13705.
- (22) Liu, K.; Bai, Y.; Zhang, L.; Yang, Z.; Fan, Q.; Zheng, H.; Yin, Y.; Gao, C. Porous Au-Ag Nanospheres with High-Density and Highly Accessible Hotspots for SERS Analysis. *Nano Lett.* **2016**, *16*, 3675–3681.
- (23) Loo, B. H. Molecular Orientation of Thiourea Chemisorbed on Copper and Silver Surfaces. *Chem. Phys. Lett.* **1982**, *89*, 346–350.
- (24) Arenas, J. F.; Castro, J. L.; Otero, J. C.; Marcos, J. I. SERS of Dicarboxylic Acids on Silver Sols. *J. Raman Spectrosc.* **1995**, *26*, 637–641.
- (25) Fleger, Y.; Mastai, Y.; Rosenbluh, M.; Dressler, D. H. SERS as a Probe for Adsorbate Orientation on Silver Nanoclusters. *J. Raman Spectrosc.* **2009**, *40*, 1572–1577.
- (26) Creighton, J. A. Surface Raman Electromagnetic Enhancement Factors for Molecules at the Surface of Small Isolated Metal Spheres: The Determination of Adsorbate Orientation from Sers Relative Intensities. *Surf. Sci.* **1983**, *124*, 209–219.
- (27) Creighton, J. A. The Effective Raman Tensor for SER Scattering by Molecules Adsorbed at the Surface of a Spherical Particle. *Surf. Sci.* **1985**, *158*, 211–221.
- (28) Moskovits, M.; Suh, J. S. Surface Selection Rules for Surface-Enhanced Raman Spectroscopy: Calculations and Application to the Surface-Enhanced Raman Spectrum of Phthalazine on Silver. *J. Phys. Chem. D* **1984**, *88*, 5526–5530.
- (29) Sang, S. J.; Jurae, K. Three Distinct Geometries of Surface-adsorbed Carboxylate Groups. *J. Raman Spectrosc.* **1998**, *29*, 143–148.
- (30) Joo, S. W.; Chung, H.; Kim, K.; Noh, J. Conformational Changes of Cyclohexanethiol Adsorbed on Gold Surfaces. *Surf. Sci.* **2007**, *601*, 3196–3201.
- (31) Zhang, Z.; Bando, K.; Mochizuki, K.; Taguchi, A.; Fujita, K.; Kawata, S. Quantitative Evaluation of Surface-Enhanced Raman Scattering Nanoparticles for Intracellular PH Sensing at a Single Particle Level. *Anal. Chem.* **2019**, *91*, 3254–3262.
- (32) Michota, A.; Bukowska, J. Surface-Enhanced Raman Scattering (SERS) of 4-Mercaptobenzoic Acid on Silver and Gold Substrates. *J. Raman Spectrosc.* **2003**, *34*, 21–25.
- (33) Marshall, A. R. L.; Stokes, J.; Viscomi, F. N.; Proctor, J. E.; Gierschner, J.; Bouillard, J. S. G.; Adawi, A. M. Determining Molecular Orientation: Via Single Molecule SERS in a Plasmonic Nano-Gap. *Nanoscale* **2017**, *9*, 17415–17421.
- (34) Ahuja, T.; Ghosh, A.; Mondal, S.; Basuri, P.; Kumar, J. S.; Srikrishnarka, P.; Mohanty, J. S.; Bose, S.; Pradeep, T. Ambient Electrodeposition Raman Spectroscopy (AESD RS) Using Soft Landed Preformed Silver Nanoparticles for Rapid and Sensitive Analysis. *Analyst* **2019**, *144*, 7412–7420.
- (35) Kwon, C. K.; Kim, M. S.; Kim, K. Raman Spectroscopy of Cyclohexanethiol Adsorbed on a Silver Surface. *J. Raman Spectrosc.* **1989**, *20*, 575–580.
- (36) Barthelmes, J.; Plieth, W. SERS Investigations on the Adsorption of Pyridine Carboxylic Acids on Silver-Influence of PH and Supporting Electrolyte. *Electrochim. Acta* **1995**, *40*, 2487–2490.
- (37) Zheng, X.-S.; Hu, P.; Zhong, J.-H.; Zong, C.; Wang, X.; Liu, B.-J.; Ren, B. Laser Power Dependent Surface-Enhanced Raman Spectroscopic Study of 4-Mercaptopyridine on Uniform Gold Nanoparticle-Assembled Substrates. *J. Phys. Chem. C* **2014**, *118*, 3750–3757.
- (38) Kimling, J.; Maier, M.; Okenve, B.; Kotaidis, V.; Ballot, H.; Plech, A. Turkevich Method for Gold Nanoparticle Synthesis Revisited. *J. Phys. Chem. B* **2006**, *110*, 15700–15707.
- (39) Emory, S. R.; Jensen, R. A.; Wenda, T.; Han, M.; Nie, S. Re-Examining the Origins of Spectral Blinking in Single-Molecule and Single-Nanoparticle SERS. *Faraday Discuss.* **2006**, *132*, 249–259.
- (40) Chaudhari, K.; Ahuja, T.; Murugesan, V.; Subramanian, V.; Mohd, A. G.; Thundat, T.; Pradeep, T. Appearance of SERS Activity

in Single Silver Nanoparticles by Laser-Induced Reshaping. *Nanoscale* **2018**, *11*, 321–330.

(41) Kerker, M.; Siman, O.; Bumm, L. A.; Wang, D. S. Surface enhanced Raman scattering (SERS) of citrate ion adsorbed on colloidal silver. *Appl. Opt.* **1980**, *19*, 3253–3255.

(42) Kang, J. F.; Liao, S.; Jordan, R.; Ulman, A. Mixed Self-Assembled Monolayers of Rigid Biphenyl Thiols: Impact of Solvent and Dipole Moment. *J. Am. Chem. Soc.* **1998**, *120*, 9662–9667.

(43) Pool, R.; Schapotschnikow, P.; Vlugt, T. J. H. Solvent Effects in the Adsorption of Alkyl Thiols on Gold Structures: A Molecular Simulation Study. *J. Phys. Chem. C* **2007**, *111*, 10201–10212.

## Supporting Information

# Probing Subtle Changes in Molecular Orientations Using Ambient Electro spray Deposition Raman Spectroscopy (AESD RS)

Atanu Ghosh<sup>‡</sup>, Tripti Ahuja<sup>‡</sup>, Kamalesh Chaudhari and Thalappil Pradeep<sup>\*</sup>

DST Unit on NanoScience (DST UNS) and Thematic Unit of Excellence (TUE), Department of Chemistry, Indian Institute of Technology Madras, Chennai 600 036, India.

Tel: +91044-2257-4208, E-mail: [pradeep@iitm.ac.in](mailto:pradeep@iitm.ac.in)

<sup>‡</sup>Equal contribution

<sup>\*</sup>Corresponding author

### Table of Contents

Sl. No.	Title	Page No.
	Experimental details on SERS spectral collection using AESD RS	S2
Figure S1	Characterization studies of the as-synthesized and electrosprayed AgNPs using UV-Vis absorption spectroscopy, TEM, DFM and plasmonic scattering spectroscopy	S3
Figure S2	Real-time SERS spectra of 10 $\mu$ M p-MBA after electrospray of AgNPs	S3
Figure S3	Real-time SERS spectra of 10 $\mu$ M p-MBA and AgNPs mixture (1:5) drop-casted on ITO	S4
Figure S4	SERS spectra of citrate-capped AgNPs and p-MBA interacted with citrate-capped AgNPs after ES	S4
Figure S5	Gaussian fitting of 1 $\mu$ M p-MBA 1586 and 1380 $\text{cm}^{-1}$ peaks at different time (54 and 62 s)	S5
Figure S6	Gaussian fitting of 1 $\mu$ M CHT 991 $\text{cm}^{-1}$ peak at different time (54	S5



	and 62 s)	
Table S1	Vibrational bands assignments of p-MBA	S6
Table S2	Vibrational bands assignments of BT	S6
Table S3	Vibrational bands assignments of CHT	S7
Ref.	References	S7

### Experimental details on SERS spectral collection using AESD RS

Description about AESD RS set up has been discussed in the experimental section of the main manuscript (AESD RS set-up). We electrospray AgNPs on the analyte drop-casted on ITO glass surface until SERS signal from analyte starts appearing. In all experiments, we observed that roughly 30-40 s of ES of AgNPs was required to get signals from analytes. We positioned the conducting surface of ITO in such a way that the tip of the silica capillary faced the surface and the laser was falling from the exactly opposite side. We started SERS signals collection even before switching on the ES. Then, we switched on the high voltage for ES. We did not observe any signals from analyte till 30-40 s of ES of AgNPs. As soon as we observed the signal from analyte, ES was switched off and spectral collection was continued for 5 minutes (300 s). For real-time SERS spectra collection, an accumulation time of 0.3 s was used throughout all the measurements. Every second spectrum was collected with a time gap of 1s. All the experiments were repeated for three times to check the reproducibility of the results.

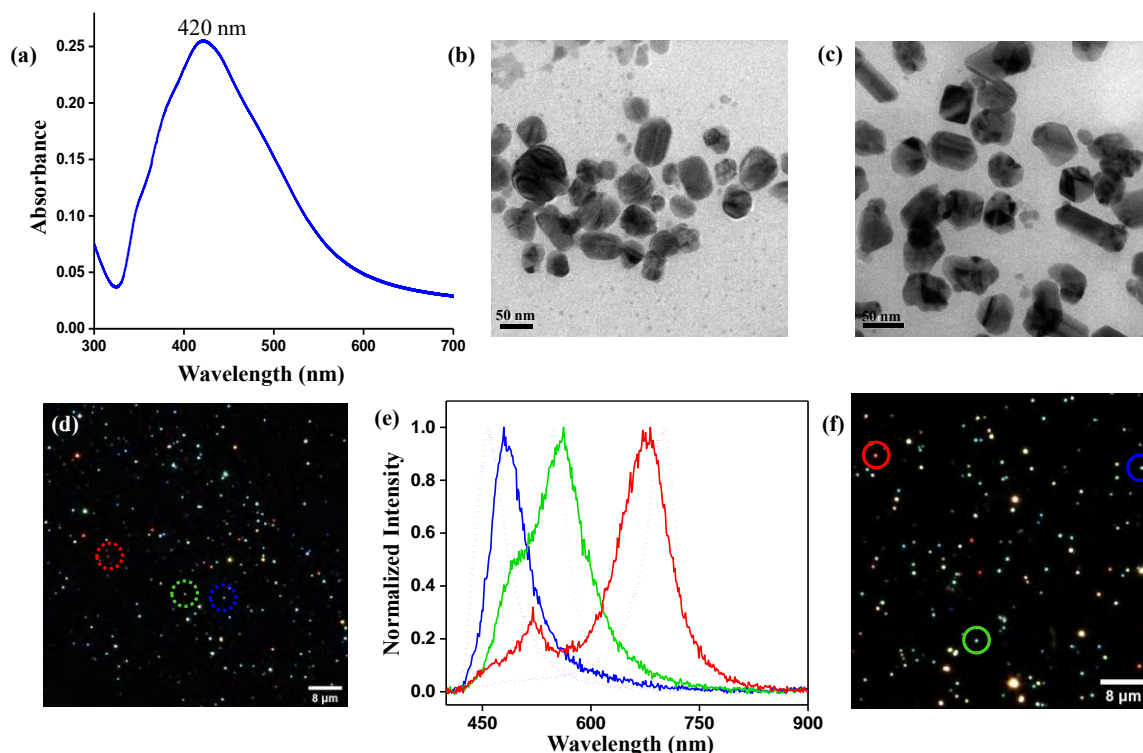


**Figure S1.** Characterization of silver nanoparticles (AgNPs). (a) UV-Vis spectrum of as synthesized AgNPs; TEM images of AgNPs before ES (b) and after ES (c); DFM images of AgNPs before and after ES (d and f); plasmonic scattering spectra of three differently colored NPs (before ES and after ES) are shown in e. The spectra before ES are shown as dotted lines and those after ES are shown as full lines.

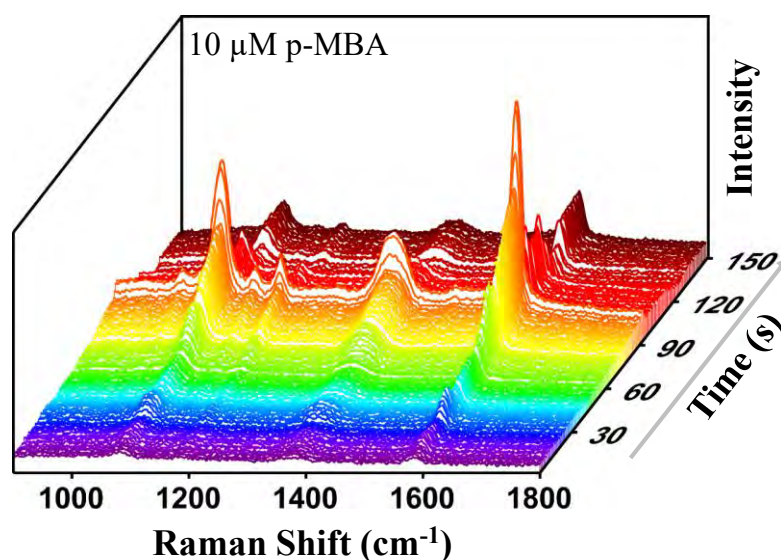


**Figure S2.** Time-dependent SERS waterfall plot of 10  $\mu\text{M}$  p-MBA in the case of electro sprayed AgNPs, showing variations in the intensities of SERS signals.

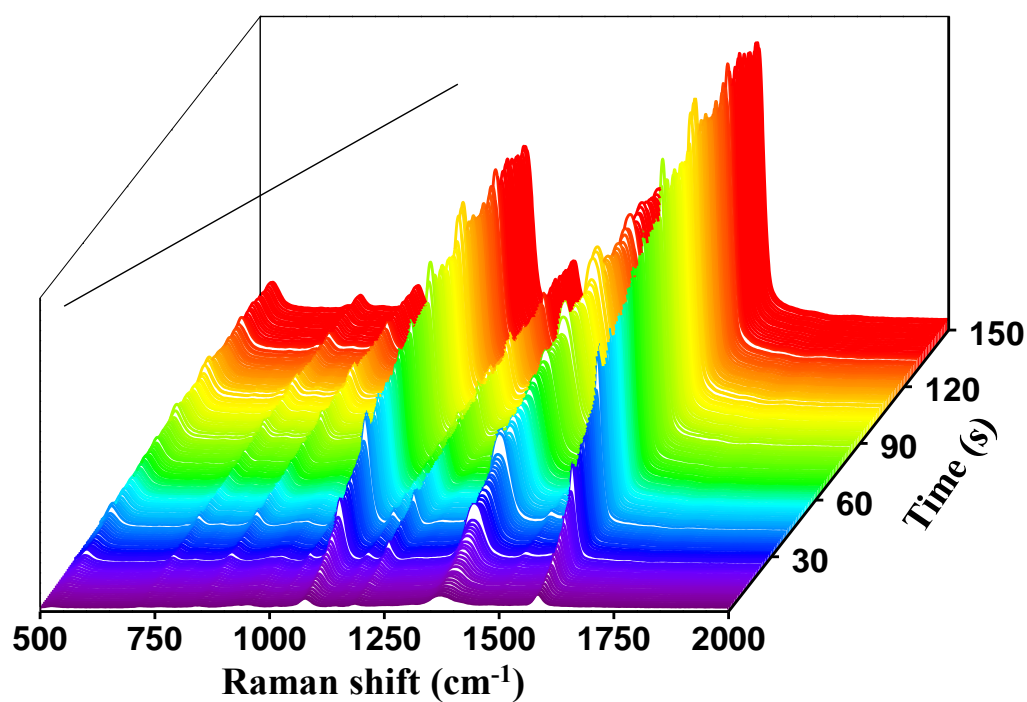


**Figure S3.** Real-time SERS spectra of 10  $\mu\text{M}$  p-MBA mixed with AgNPs (1:5) kept for 2 h for equilibration.

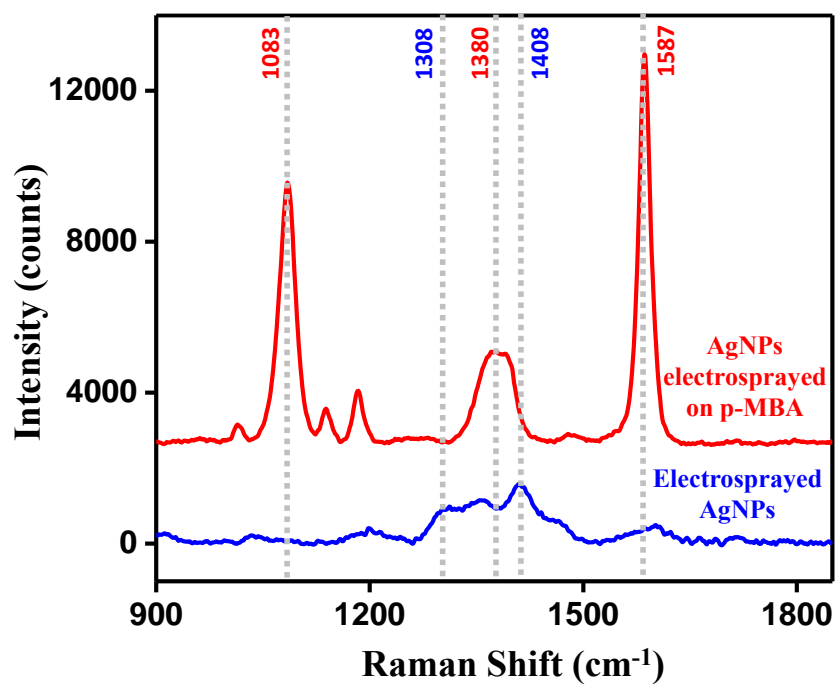


**Figure S4.** SERS spectra of citrate-capped AgNPs (blue) and p-MBA (red) interacted with citrate-capped AgNPs after ES.

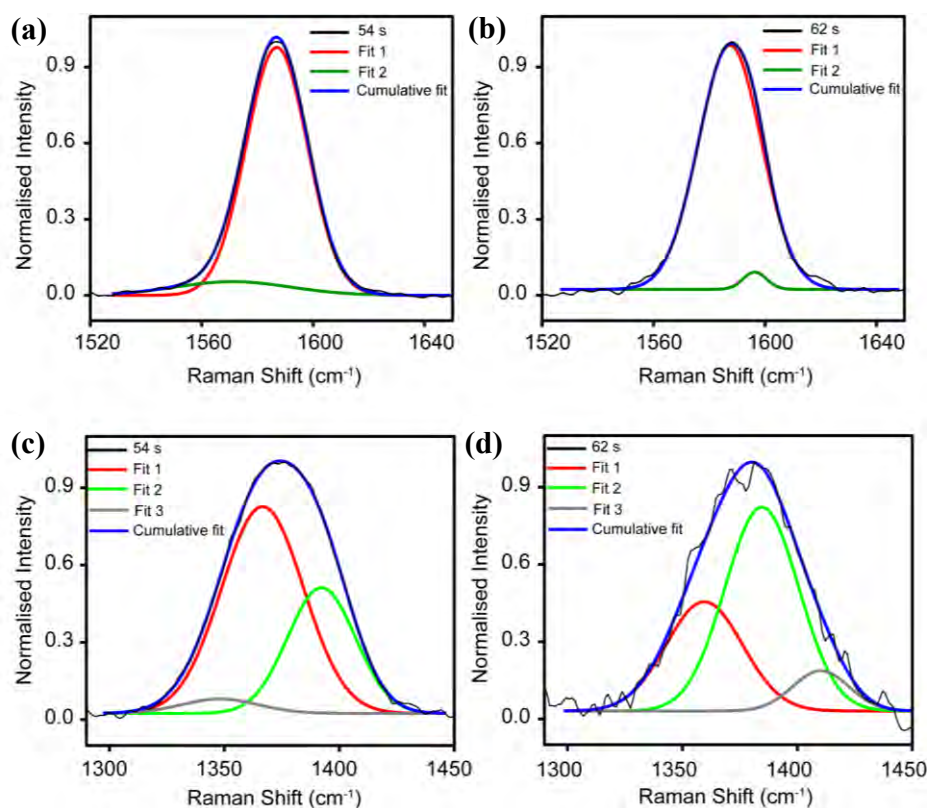


**Figure S5.** Gaussian fitting of  $\nu_{8a}$  phenyl ring (a, b) and  $\nu(\text{COO}^-)$  (c, d) peaks of 1  $\mu\text{M}$  p-MBA at two different time (a, c) 54 s and (b, d) 62s. (All peaks were fitted using multiple Gaussians, and the fitted peak is denoted as cumulative fit in all the cases)

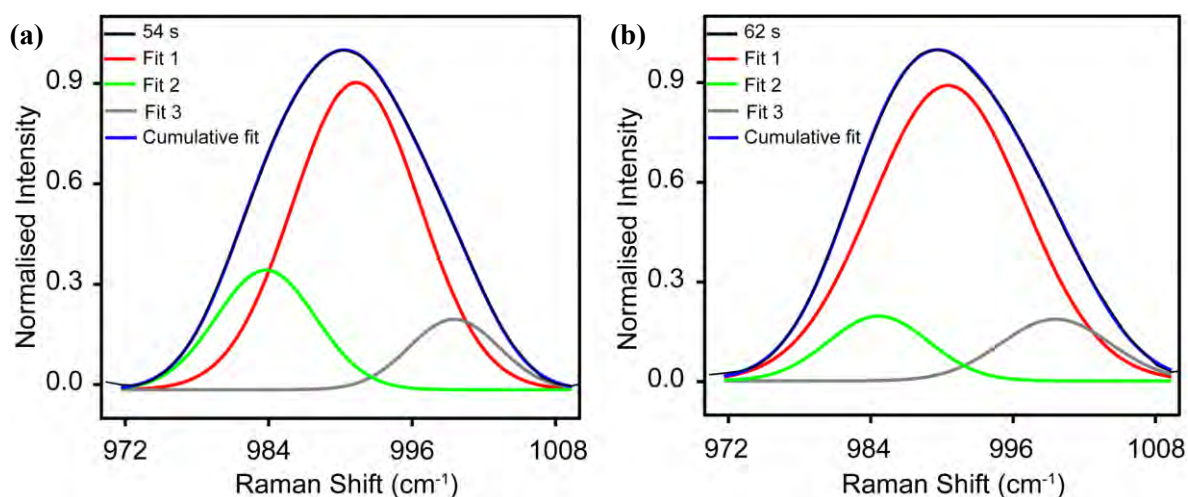


**Figure S6.** Gaussian fitting of 1  $\mu\text{M}$  CHT peak at two different times, (a) 54 s and (b) 62 s. (All peaks were fitted using multiple Gaussians, and the fitted peak is denoted as cumulative fit in all the cases)

**Table S1.** Vibrational band assignments of p-MBA

Peak Position (cm <sup>-1</sup> )	Assignments <sup>(1-2)</sup>
717	$\gamma$ (CCC) (aromatic)
842	$\delta$ (COO <sup>-</sup> )
910 (Absent)	$\delta$ (CSH)
1013	Ring deformation
1078-1086	$\nu_{12}$ (ring)
1136	13 $\beta$ (CCC) + $\nu$ (C-S) + $\nu$ (C-COOH)
1186	$\delta$ (C-H)
1375-1380	$\nu_s$ (COO <sup>-</sup> )
1586	$\nu_{8a}$ (ring)

**Table S2.** Vibrational band assignments of BT

Peak Position (cm <sup>-1</sup> )	Assignments <sup>(3)</sup>
986	12(a <sub>1</sub> ), $\beta_{\text{CCC}}$
1035	18a(a <sub>1</sub> ), $\beta_{\text{CH}}$
1072	1(a <sub>1</sub> ), $\beta_{\text{CCC}}$ + $\nu_{\text{CS}}$
1223	9a(a <sub>1</sub> ), $\beta_{\text{CH}}$
1280	3(b <sub>2</sub> ), $\nu_{\text{CC}}$
1361	14(b <sub>2</sub> ), $\nu_{\text{CC}}$
1579	8a(a <sub>1</sub> ), $\nu_{\text{CC}}$

**Table S3.** Vibrational band assignments of CHT

Peak Position (cm <sup>-1</sup> )	Assignments <sup>(4-5)</sup>
352	$\delta$ (C-S)
510	Ring deformation
711	$\nu$ (C-S)
849	Ring stretch
988	$\delta$ (CH <sub>2</sub> ) rocking
1024	$\nu$ (C-C)
1077	$\delta$ (CH <sub>2</sub> ) twisting
1186	$\delta$ (CH <sub>2</sub> ) wagging
1258	$\delta$ (CH <sub>2</sub> ) wagging

**References:**

- (1) Sang, S. J.; Jurae, K. Three Distinct Geometries of Surface-adsorbed Carboxylate Groups. *J. Raman Spectrosc.* **1998**, *29*, 143–148.
- (2) Ho, C. H.; Lee, S. SERS and DFT Investigation of the Adsorption Behavior of 4-Mercaptobenzoic Acid on Silver Colloids. *Colloids Surfaces A Physicochem. Eng. Asp.* **2015**, *474*, 29–35.
- (3) Carron, K. T.; Hurley, L. G. Axial and Azimuthal Angle Determination with Surface-Enhanced Raman Spectroscopy: Thiophenol on Copper, Silver, and Gold Metal Surfaces. *J. Phys. Chem.* **1991**, *95*, 9979–9984.
- (4) Kwon, C. K.; Kim, M. S.; Kim, K. Raman Spectroscopy of Cyclohexanethiol Adsorbed on a Silver Surface. *J. Raman Spectrosc.* **1989**, *20*, 575–580.
- (5) Joo, S. W.; Chung, H.; Kim, K.; Noh, J. Conformational Changes of Cyclohexanethiol Adsorbed on Gold Surfaces. *Surf. Sci.* **2007**, *601*, 3196–3201.



# Entrapping Atomically Precise Clusters in Cyclodextrin-Functionalized Aminoclay Sheets: Synthesis and Enhanced Luminescence

Mohd Azhardin Ganayee, C. K. Manju, Wakeel Ahmed Dar, Biswajit Mondal, and Thalappil Pradeep\*



Cite This: *Ind. Eng. Chem. Res.* 2020, 59, 12737–12744



Read Online

ACCESS |



Metrics & More

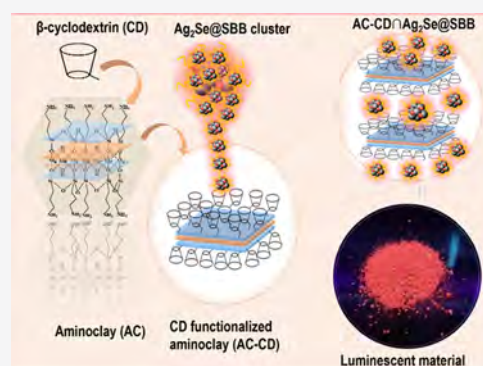


Article Recommendations



Supporting Information

**ABSTRACT:** In this article, a unique covalently linked aminoclay substrate, grafted with  $\beta$ -cyclodextrin (AC-CD), was prepared to entrap luminescent silver nanoclusters. Chemically synthesized aminoclay (AC) sheets grafted with  $\beta$ -cyclodextrins ( $\beta$ -CDs) were used to develop a supramolecular entity. Here, we grafted  $\beta$ -CD onto aminoclays using cyanuric chloride as a linker. The AC-CD material was thoroughly characterized using Fourier transform infrared spectroscopy (FTIR), powder X-ray diffraction (PXRD), and transmission electron microscopy (TEM). The grafting ratio of  $\beta$ -CD onto AC-CD was determined using the phenolphthalein inclusion protocol. The as-prepared functionalized clay (AC-CD) is an effective and attractive material for entrapping a luminescent silver chalcogenide cluster stabilized by 4-(*t*-butyl)benzyl mercaptan ( $\text{Ag}_{56}\text{Se}_{13}\text{S}_{15}@\text{SBB}_{28}$  shortened as  $\text{Ag}_2\text{Se}@\text{SBB}$ ). The cluster AC-CD ( $\text{AC-CD}@\text{Ag}_2\text{Se}@\text{SBB}$ ) supramolecular nanocomposite is based on specific host–guest interactions involving  $\beta$ -CD of AC-CD and SBB of a silver cluster. Entrapment of the cluster into the  $\beta$ -CD cavity was verified using optical absorption, luminescence spectroscopy, XRD, and TEM. The entrapment resulted in enhanced luminescence and stability of the cluster. Such a dispersible nanocomposite system exhibiting intense luminescence will be useful in creating novel materials for various applications such as sensors, optoelectronic devices, etc.



## INTRODUCTION

Atomically precise metal nanoclusters (NCs) are an emerging class of materials and have attracted tremendous attention due to their unique physical and chemical properties.<sup>1–3</sup> NCs having a core size <3 nm possess exceptional geometric and electronic structures and exhibit intriguing properties such as strong photoluminescence, high catalytic activity, facile surface tailorability, and good photostability, which are different from bulk nanoparticles, with diameter >3 nm. Manipulating such functional materials is an important aspect of nanocluster chemistry.<sup>4–12</sup> In view of their exciting properties and applications, a large number of differently sized clusters of noble metals (Ag and Au) have been synthesized although those of silver are of poor stability. Therefore, synthetic modifications are needed to increase the stability of NCs. Mixed chalcogenide silver clusters or alloy NCs composed of more than two metals have gained research interest in recent years.<sup>4–6</sup> Alloying could increase their stability and photophysical properties, which opens up a broader window for their applications.<sup>7</sup> Hybrid nanocomposites have received attention in view of their simple preparation, lightweight, mechanical strength, flexible behavior, layered structures, etc.<sup>13–15</sup> Nanoclusters can also be incorporated in scaffolds such as polymers, 2D materials, etc., and such materials exhibit different physical properties due to additional influences of the matrix on their

electronic structure.<sup>16–18</sup> The important features observed in such clusters are greater stability, strong luminescence, etc., which occur when these clusters are anchored on suitable supports.<sup>19–21</sup> Consequently, such materials are used in fluorescence bioimaging including that of cancer cells, along with the detection of analytes such as ascorbic acid (AA), dopamine (DA), and uric acid (UA).<sup>17,18</sup> For a wide range of applications, there is a need to use tailored or functional clays as supports that would be highly dispersible in water.

One such scaffold is aminoclay (AC). It is a tailored organoclay having smaller micron-sized pieces of single clay sheets, which have a 2:1 trioctahedral phyllosilicate structure (also known as T-O-T structure).<sup>22,23</sup> In this structure, two tetrahedral aminopropyl-functionalized silica sheets sandwich octahedral brucite sheets on both sides by covalent bonding to give an approximate unit cell composition formulated as  $[\text{H}_2\text{N}(\text{CH}_2)_3]_8\text{Si}_8\text{Mg}_6\text{O}_{16}(\text{OH})_4$ .<sup>23</sup> It is protected with amine groups on both sides and is prominently water-soluble. AC has

**Received:** December 23, 2019

**Revised:** June 20, 2020

**Accepted:** June 22, 2020

**Published:** June 22, 2020



multifaceted applications and is utilized for the stabilization of metal NPs,<sup>24</sup> catalysis,<sup>25,26</sup> light harvesting,<sup>27</sup> drug delivery,<sup>28,29</sup> energy devices,<sup>30</sup> and many other applications. It forms nanocomposite hydrogels and films with suitable polymers and macromolecules by acting as a cross-linker.<sup>31</sup> The terminal amine groups in AC can be functionalized with various chemically reactive species. One such functionalization can be performed with cyclodextrins (CDs), resulting in CD-functionalized AC, labeled as AC-CD. CDs are cyclic oligosaccharides, consisting of glucopyranose subunits joined together by  $\alpha$ -1,4 glycosidic bonds. Typical cyclodextrins contain several glucose monomers ranging from six to eight units in a ring and are known as  $\alpha$ -,  $\beta$ -, and  $\gamma$ -cyclodextrins, respectively. CDs have a hydrophobic (lipophilic) central core cavity with hydrophilic outer surfaces.<sup>32</sup> They can form molecular inclusion complexes with hydrophobic compounds of suitable molecular sizes.<sup>33–35</sup> CDs enhance stability,<sup>36</sup> solubility,<sup>37,38</sup> bioavailability,<sup>39</sup> functionality,<sup>40–42</sup> and controlled release of the guest molecules<sup>43,44</sup> and are being used in food,<sup>45,46</sup> essential oils,<sup>47–49</sup> cosmetics,<sup>50</sup> pharmaceuticals,<sup>51–53</sup> and agrochemicals.<sup>54,55</sup>

Recently, we have reported supramolecular interactions between atomically precise clusters and cyclodextrins using specific host–guest interactions.<sup>21,56,57</sup> Strong inclusion interactions between the inner cavity of cyclodextrin and ligand molecules have been probed experimentally using various spectroscopic techniques and have been further analyzed by density functional theory calculations and molecular modeling.

In this work, we have prepared AC-CD $\cap$ Ag<sub>2</sub>Se@SBB through functionalized CDs, where Ag<sub>2</sub>Se@SBB is an atomically precise silver chalcogenide cluster and  $\cap$  symbolizes an inclusion complex (Ag<sub>2</sub>Se@SBB included in AC-CD is symbolized as AC-CD $\cap$ Ag<sub>2</sub>Se@SBB). A mixed chalcogenide silver cluster has been used because of its good stability and efficient luminescence compared to silver clusters. In our approach, we have derivatized AC, first, with CD so that the clay surfaces are effectively functionalized with CDs, rendering them receptive to entities such as the 4-(*t*-butyl)benzyl group, which protects the cluster core. Such incorporation enhances the luminescent property of the cluster. These materials are likely to be biocompatible as both aminoclays and CDs have this property and may be useful for many applications.

## ■ EXPERIMENTAL SECTION

**Materials.** All chemicals were of analytical grade and were used without further purification. Silver acetate (CH<sub>3</sub>COOAg), 4-*tert*-butylbenzyl mercaptan (BBSH), Se powder (100 mesh, 99.5%), octadecene (ODE, 90%), and 3-aminopropyltriethoxysilane (APTES) were purchased from Sigma-Aldrich. Sodium hydroxide (NaOH), sodium bicarbonate (NaHCO<sub>3</sub>), tetrahydrofuran (THF), and cyanuric chloride (CC) were purchased from Rankem. Magnesium chloride hexahydrate (MgCl<sub>2</sub>·6H<sub>2</sub>O; 98%) and toluene were obtained from Merck (India). Absolute ethanol (99.99%) was purchased from Changshu Hongsheng Fine Chemicals (China). Glassware used was cleaned thoroughly in aqua regia, rinsed with distilled water, and dried in an oven prior to use. Millipore deionized water (~18.2 M $\Omega$ ) was used, wherever required.

**Methods.** *Synthesis of Aminoclay (AC).* Aminoclay (AC) was synthesized by previously reported methods.<sup>22,23</sup> In a typical procedure, magnesium chloride (2.52 g, 10.86 mmol) was dissolved in ethanol (60 mL). To this ethanolic solution of

magnesium chloride, 3-aminopropyltriethoxysilane (3.9 mL, 17.55 mmol) was added dropwise, resulting in the formation of a white slurry. This mixture was kept on stirring for 36 h, and the solution was centrifuged at 5000 rpm. The white precipitate obtained was washed several times using ethanol (150 mL) to remove the unreacted moieties. The pure product was dried at room temperature for 12 h and then ground to obtain the product in a powder form.

*Synthesis of Monochlorotriazinyl- $\beta$ -cyclodextrin (MCT- $\beta$ -CD).* MCT- $\beta$ -CD was synthesized as per the conventional method.<sup>40,58</sup> In this case, 5.50 g of cyanuric chloride was dispersed in 30 mL of cold water using sodium dodecyl sulfate (SDS) as an emulsifier and the solution was kept on stirring at 0 °C. To this, 12 mL of sodium hydroxide (5 mol L<sup>-1</sup>) was added dropwise to adjust the pH around 8. Then, 11.35 g of  $\beta$ -CD solution was gradually added to the above solution and the reaction mixture was kept on stirring for 24 h at 10 °C overnight until a transparent solution was obtained. To this, 10 mL of acetone was added for precipitation, desalted by 2 mL of DMF, and again precipitated by 10 mL of acetone. The product was obtained in a powder form by drying at 40 °C.

*Synthesis of Cyclodextrin-Functionalized Aminoclay (AC-CD).* Initially, 3 wt % AC solution was activated using 0.02 w/w NaHCO<sub>3</sub> and was kept on stirring for 1 h. To this solution, 1 wt % MCT- $\beta$ -CD was gradually added and stirred for 24 h at room temperature. The reaction mixture was centrifuged, and the precipitated product obtained was washed several times with ethanol. The final purified product in powder form was obtained by freeze-drying. The weight percentage of AC, sodium bicarbonate concentration, temperature, and reaction time effectively influence the  $\beta$ -CD grafting ratio. The reaction conditions optimum for the synthesis of higher inclusion ratio of  $\beta$ -cyclodextrin-grafted aminoclay (AC-CD) were achieved.

*Synthesis of Luminescent Ag<sub>56</sub>Se<sub>13</sub>S<sub>15</sub>@SBB<sub>28</sub> (Ag<sub>2</sub>Se@SBB) Nanocluster.* The Ag<sub>2</sub>Se@SBB cluster was synthesized by an already reported method by our group.<sup>59</sup> CH<sub>3</sub>COOAg (0.1 mmol) and BBSH (4 mmol) were added to 5 mL of ODE in a 100 mL three-necked round-bottomed flask under argon (Ar) flow at 60 °C. Ar purging was continued for 30 min at this temperature. Then, the reaction mixture was heated to 90 °C, the Se powder (0.05 mmol) was added to this mixture under constant stirring, and the reaction was continued for 2 h. The reaction mixture was then cooled to room temperature and purified by washing with methanol and subsequent centrifugation. The Ag<sub>2</sub>S nanocluster was stable for a week at room temperature, and this stability was enhanced to more than a month by keeping at low temperatures (4 °C).

*Synthesis of Atomically Precise Clusters in Cyclodextrin-Functionalized Aminoclay (AC-CD $\cap$ Ag<sub>2</sub>Se@SBB).* Native Ag<sub>2</sub>Se@SBB (2 mg) was dissolved in 3 mL of THF/H<sub>2</sub>O (3:1) solution, and to this, AC-CD (5 wt %) solution was added. Both the cluster and composite were dispersible in 3:1 THF/H<sub>2</sub>O. The mixture was sonicated for about 10 min. The reaction was allowed to proceed with continuous stirring for 3 h at room temperature with intermittent sonication for 1 min every 30 min intervals. The final product AC-CD $\cap$ Ag<sub>2</sub>Se@SBB hybrid nanostructure was repeatedly washed, purified by decantation, and then dried. Further, the reaction product was washed with ethanol to remove any unbound AC-CD, AC, and CD.

**Characterization.** Ultraviolet–visible (UV–vis) spectra were measured using a PerkinElmer Lambda 25 instrument in the range 200–1100 nm. Fourier transform infrared spectra





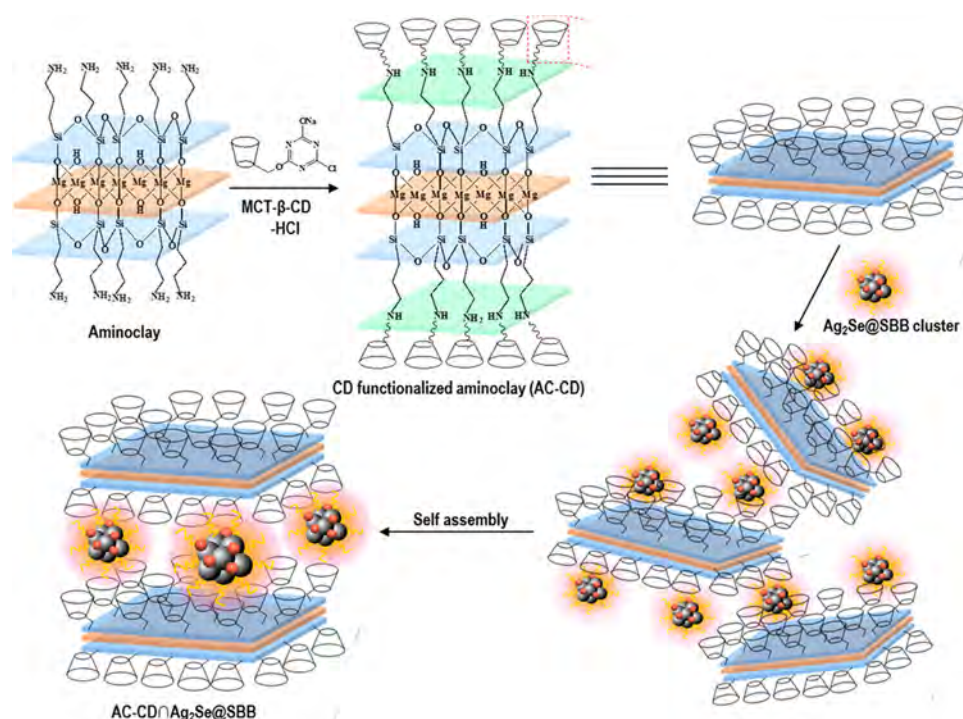


**Figure 2.** Schematic representation of entrapment of atomically precise clusters in cyclodextrin-functionalized aminoclay (AC-CD).

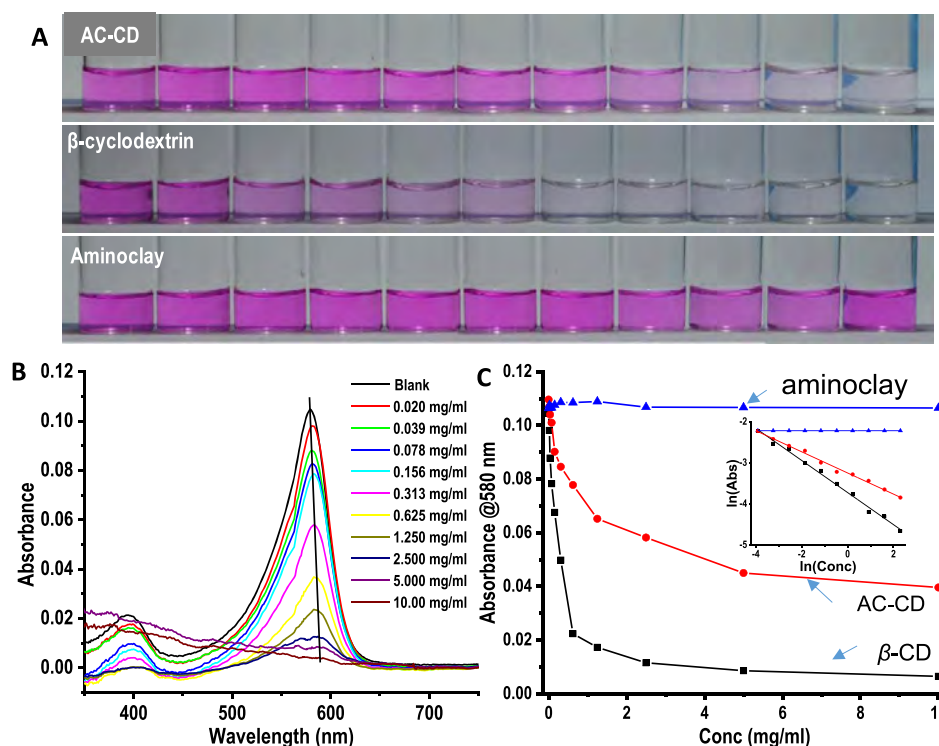


**Figure 3.** (A) Photographs of phenolphthalein solutions with increasing concentrations of AC-CD,  $\beta$ -cyclodextrin, and aminoclay. Color change is observed for AC-CD and  $\beta$ -cyclodextrin. However, no change in color is seen in aminoclay-added solutions. (B) UV absorbance of PHTH/AC-CD solutions with increasing AC-CD concentration. (C) Curves of absorbance vs concentrations of (i)  $\beta$ -CD, (ii) AC-CD, and (iii) aminoclay.

**Grafting Ratio of  $\beta$ -CD.**  $\beta$ -CD is known to form an inclusion complex with phenolphthalein, and this complexation fades the pink color (Figure 3). The grafting ratio of  $\beta$ -CD was measured by the phenolphthalein (PHTH) inclusion method.<sup>60</sup> The PHTH molecule undergoes deprotonation in alkaline media (above a pH of 8.2). This causes an opening

of the lactone ring of the molecule and results in an increase in the delocalization of  $\pi$ -electrons, which changes its color from colorless to pink. PHTH forms a host–guest inclusion complex with  $\beta$ -CD. Binding of PHTH results in the transformation of a pink-colored trigonal  $sp^2$ -conjugated system to a colorless tetrahedral  $sp^3$ -lactonoid form (Figure

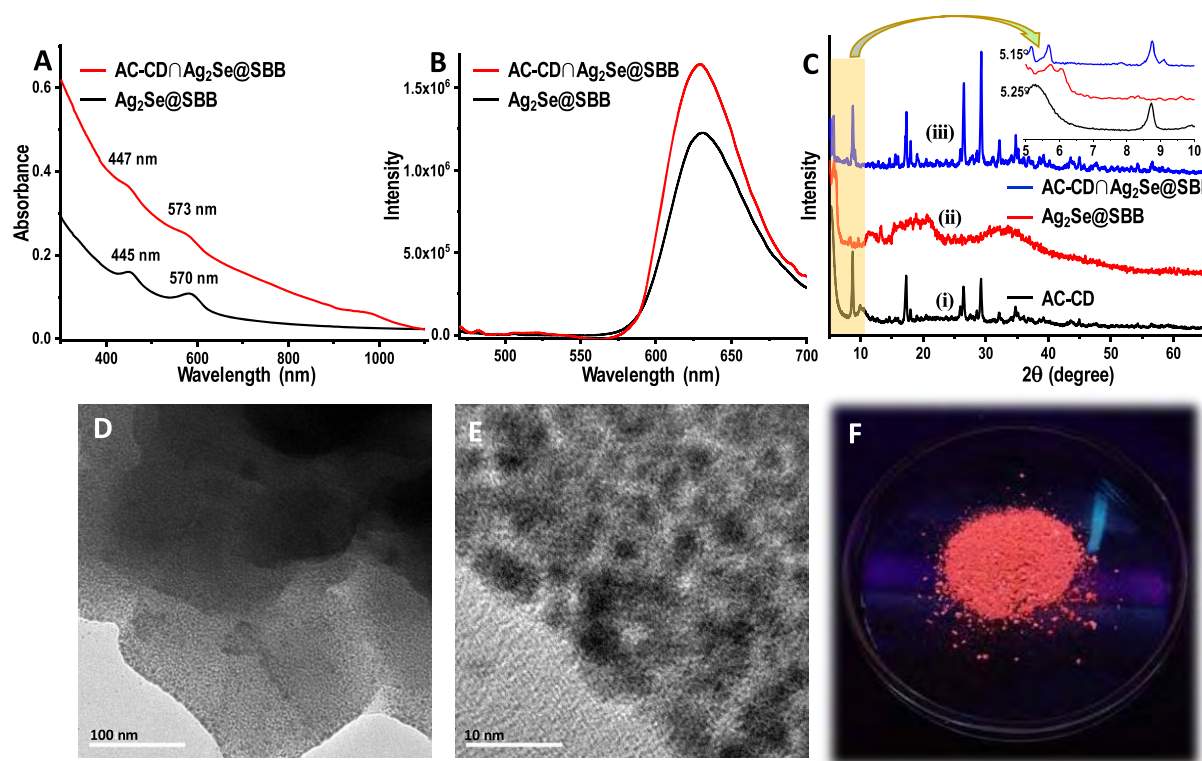


**Figure 4.** (A) UV-vis absorption and (B) emission spectra of the cluster and AC-CD@Ag<sub>2</sub>Se@SBB. (C) XRD pattern of (i) AC-CD, (ii) cluster, and (iii) AC-CD@Ag<sub>2</sub>Se@SBB. (D, E) TEM images and (F) photograph of AC-CD@Ag<sub>2</sub>Se@SBB.

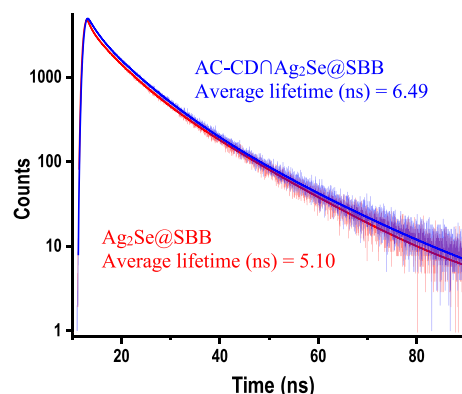


**Figure 5.** Time-resolved fluorescence decay profile of Ag<sub>2</sub>Se@SBB and AC-CD@Ag<sub>2</sub>Se@SBB in a 3:1 THF/H<sub>2</sub>O solution.

S3).<sup>61</sup> In the experiment on the grafting ratio measurement, we have taken a fixed amount of PHTH and different amounts of AC-CD.

A freshly prepared solution of 0.1 mM PHTH in 0.02 M NaHCO<sub>3</sub> buffer was used for all of the measurements. Different concentrations of AC-CD suspensions were mixed with this PHTH solution, and the resulting mixtures were kept for stirring overnight. An alkaline solution of PHTH exhibits an absorption maximum at 580 nm, responsible for the pink color of phenolphthalein (Figure 3A,B).

In the experiment on the grafting ratio measurement, we have taken different amounts of AC-CD. With increasing concentration of AC-CD, the intensity of the pink color decreases as shown in Figure 3A. This is due to its complexation with phenolphthalein. Accordingly, the absorbance intensity at 552 nm decreases (Figure 3B). The decrease in absorbance intensity with an increase in  $\beta$ -CD concentration follows an exponential behavior, which yields a linear relationship between  $\ln(\text{Abs of PHTH})$  and  $\ln(\beta\text{-CD concentration})$  (Figure 3C). PHTH does not interact electrostatically with aminoclay as aminoclay is positively charged due to amine groups on its surface (Figures S4 and S5). Thus, the amount of phenolphthalein anchored in the cavity of  $\beta$ -CD in AC-CD and the average grafting ratio of  $\beta$ -CD in the AC-CD is 4.15 wt %.

**Supramolecular Functionalization of the AC-CD Composite with the Ag<sub>2</sub>Se@SBB Cluster.** The supramolecular interaction between the Au<sub>25</sub> cluster protected by 4-(*t*-butyl)benzyl mercaptan (Au<sub>25</sub>SBB<sub>18</sub>) and CD yielding Au<sub>25</sub>SBB<sub>18</sub>@CD<sub>*n*</sub> (*n* = 1, 2, 3, and 4; @ represents supramolecular inclusion) was reported earlier by our group.<sup>57</sup> To further explore this kind of interaction, we have treated AC-CD, having molecular recognition properties of cyclodextrin, with the Ag<sub>2</sub>Se@SBB cluster to build a luminescent supramolecular structure. Ag<sub>2</sub>Se@SBB is a red luminescent cluster protected with a 4-(*t*-butyl)benzyl mercaptan (SBB) ligand

**Table 1.** Lifetime Values of Ag<sub>2</sub>Se@SBB and AC-CD@Ag<sub>2</sub>Se@SBB

sample	$\tau_1$ (ns)	$\tau_2$ (ns)	$\tau_3$ (ns)	B1	B2	B3	$\chi^2$	average lifetime (ns)
Ag <sub>2</sub> Se@SBB	5.21	0.93	13.13	43.29	5.96	50.75	1.18	5.10
AC-CD@Ag <sub>2</sub> Se@SBB	1.85	6.63	15.23	10.43	54.76	34.81	1.13	6.49

and has been thoroughly characterized. This cluster displays UV–vis absorption features at 445 and 570 nm as shown in Figure S6A. From the MALDI MS of the cluster in negative ion mode, a peak with  $m/z$  12.5 kDa is observed similar to the earlier report.<sup>59</sup> The  $\text{Ag}_2\text{Se}@SBB$  shows red luminescence with an emission maximum at 625 nm, and the TEM image shows that the cluster is monodisperse with an average size of 2 nm as shown in Figure S6C,D. The schematic preparation of the  $\text{AC-CD}\cap\text{Ag}_2\text{Se}@SBB$  supramolecular nanocomposite from AC-CD and  $\text{Ag}_2\text{Se}@SBB$  is shown in Figure 2. It can be seen that the functionalization of AC with MCT- $\beta$ -CD yields AC-CD and its supramolecular self-assembly with the  $\text{Ag}_2\text{Se}@SBB$  cluster results in a highly luminescent  $\text{AC-CD}\cap\text{Ag}_2\text{Se}@SBB$  nanohybrid. AFM images of AC-CD are shown in Figure S7.

The  $\text{AC-CD}\cap\text{Ag}_2\text{Se}@SBB$  nanocomposite is characterized by UV–vis, PXRD, and TEM. UV–vis spectral features of the nanocomposite show absorption bands at 447 and 573 nm, which are blue-shifted by 2 and 3 nm, respectively, as compared to the cluster (Figure 4A). This could be due to the interaction of the cluster with AC-CD. This indicates that the cluster features are retained in the nanocomposite. Photoluminescence (PL) of the cluster and cluster-embedded AC-CD are measured in the solution phase using the following concentration: 5 mg of the sample in 2 mL of the THF and water 3:1 mixture. PL measurements are carried upon exciting the samples at a wavelength of 440 nm. The luminescence profiles of the native cluster and cluster-embedded AC-CD are shown in Figure 4B. The emission spectra marked in black and red correspond to the native cluster and cluster-embedded AC-CD, respectively. The shapes of the emission curves are almost similar having emission maximum at 625 nm; however, cluster-embedded AC-CD shows higher emission intensity and is about 1.4 fold higher as compared to that of the pristine cluster. The origin of luminescence in a nanocomposite is from the cluster as the native AC-CD is nonluminescent. Enhanced luminescence in the nanocomposite could be due to the encapsulation of the cluster in the CD cavities of AC-CD, which provides a rigid support to the cluster and therefore prevents nonradiative energy loss. The powder XRD patterns of AC-CD,  $\text{Ag}_2\text{Se}@SBB$ , and  $\text{AC-CD}\cap\text{Ag}_2\text{Se}@SBB$  are shown in Figure 4C. The XRD pattern of the  $\text{Ag}_2\text{Se}@SBB$  cluster exhibits a broad peak and is similar to the reported one.<sup>59</sup> The powder XRD patterns of  $\text{AC-CD}\cap\text{Ag}_2\text{Se}@SBB$  show the diffraction peaks characteristic of AC-CD. However, the low-angle peak observed for  $\text{AC-CD}\cap\text{Ag}_2\text{Se}@SBB$  splits and gets shifted to a low-angle range from 5.25 to 5.15° as compared to AC-CD (inset of Figure 4C). These results suggest the existence of a layered structure in the  $\text{AC-CD}\cap\text{Ag}_2\text{Se}@SBB$  nanocomposite, which is supported by the TEM micrograph (Figure 4D). TEM micrographs (Figure 4D,E) also show that the cluster is dispersed in  $\text{AC-CD}\cap\text{Ag}_2\text{Se}@SBB$ . The cluster gets incorporated only into the CD of the functionalized aminoclay (AC-CD) as the 4-(*t*-butyl)benzyl group of the SBB ligand on  $\text{Ag}_2\text{Se}@SBB$  acts as a recognition site for a stable host–guest inclusion complex with CD.<sup>57</sup> The photograph of powdered  $\text{AC-CD}\cap\text{Ag}_2\text{Se}@SBB$  shows red luminescence under UV light (Figure 4F). A luminescent  $\text{AC-CD}\cap\text{Ag}_2\text{Se}@SBB$  nanocomposite is obtained in bulk amounts.

**Lifetime Studies.** To study the photoluminescence property of the  $\text{AC-CD}\cap\text{Ag}_2\text{Se}@SBB$  composite, photoluminescence lifetime measurements were recorded using a Horiba Jobin Yvon Fluorocube spectrometer in a time-correlated single-photon-counting (TCSPC) arrangement with a 460 nm LED

having a pulse repetition rate of 1 MHz as the light source. Photoluminescence lifetime curves were investigated by studying the emission wavelength ( $\lambda_{\text{em}}$  625 nm) at an excitation wavelength,  $\lambda_{\text{ex}}$  of 460 nm. Decay curves were investigated by nonlinear least-squares iteration using IBH DAS6 decay analysis software employing the following equation

$$I(t) = A_i \exp(-t/\tau_i)$$

where  $\tau_i$  is the luminescence lifetime and  $A_i$  is the amplitude of the corresponding decay.

Decay curves were fitted triexponentially and are shown in Figure 5. Average lifetimes for the cluster and entrapped cluster-based system ( $\text{AC-CD}\cap\text{Ag}_2\text{Se}@SBB$ ) were found to be 5.10 and 6.49 ns, respectively, as shown in Table 1. The emission expected from the hybrid material arises from the sensitization of  $\text{Ag}_2\text{Se}$  cluster sites, and these clusters possibly occupy the host sites close to the surface of aminoclay and cyclodextrin. Cluster interaction with AC-CD can also be evaluated by lifetime measurements. There are significant changes in the lifetime components, viz.,  $\tau_1$ ,  $\tau_2$ , and  $\tau_3$ . This change suggests a different environment around the  $\text{Ag}_2\text{Se}$  cluster. This is further understood from the decay function  $\tau_3$ , which contributes highest to the total average lifetime. A higher lifetime decay component of the embedded cluster ( $\text{AC-CD}\cap\text{Ag}_2\text{Se}@SBB$ ) compared to the free cluster indicates that the cluster moieties are highly protected to avoid cross-relaxation and vibrational coupling with the SBB ligand.

## CONCLUSIONS

In summary, the grafting of  $\beta$ -cyclodextrin onto the surface of aminoclay was achieved. The as-synthesized AC-CD was shown to be an effective and attractive material for the functionalization of the clay with  $\text{Ag}_2\text{Se}@SBB$ . The interactions between AC-CD and  $\text{Ag}_2\text{Se}@SBB$  resulted in enhanced luminescence of the clusters. These supramolecular interactions were studied in detail by various spectroscopic techniques. We presented a methodology to functionalize AC-CD with luminescent clusters and observed the enhancement in the luminescence for the resulting nanocomposite system. Interlayer spacing between AC-CD layers was determined by various analytical techniques, such as XRD and TEM, and was found to be sufficient enough to accommodate the cluster in it. This material was highly stable. We believe that this stable luminescent material will be useful for various applications such as sensors, optoelectronic devices, etc.

## ASSOCIATED CONTENT

### Supporting Information

The Supporting Information is available free of charge at <https://pubs.acs.org/doi/10.1021/acs.iecr.9b07018>.

XRD pattern of the aminoclay with TEM as the inset; FTIR, ESI MS, and schematic procedure for the synthesis of MCT- $\beta$ -CD, binding of phenolphthalein to cyclodextrin, UV–vis absorbance and calibration curves with different concentrations of  $\beta$ -CD; UV–vis absorbance and calibration curves with different concentrations of aminoclay; characterization of the  $\text{Ag}_2\text{Se}@SBB$  cluster; AFM images of AC-CD (PDF)



## AUTHOR INFORMATION

### Corresponding Author

**Thalappil Pradeep** – DST Unit of Nanoscience, Thematic Unit of Excellence, Department of Chemistry, Indian Institute of Technology Madras, Chennai 600036, India; [orcid.org/0000-0003-3174-534X](https://orcid.org/0000-0003-3174-534X); Email: [pradeep@iitm.ac.in](mailto:pradeep@iitm.ac.in)

### Authors

**Mohd Azhardin Ganayee** – DST Unit of Nanoscience, Thematic Unit of Excellence, Department of Chemistry, Indian Institute of Technology Madras, Chennai 600036, India

**C. K. Manju** – DST Unit of Nanoscience, Thematic Unit of Excellence, Department of Chemistry, Indian Institute of Technology Madras, Chennai 600036, India

**Wakeel Ahmed Dar** – DST Unit of Nanoscience, Thematic Unit of Excellence, Department of Chemistry, Indian Institute of Technology Madras, Chennai 600036, India

**Biswajit Mondal** – DST Unit of Nanoscience, Thematic Unit of Excellence, Department of Chemistry, Indian Institute of Technology Madras, Chennai 600036, India

Complete contact information is available at:  
<https://pubs.acs.org/10.1021/acs.iecr.9b07018>

### Notes

The authors declare no competing financial interest.

## ACKNOWLEDGMENTS

The authors thank the Department of Science and Technology for supporting our research project. M.A.G. thanks U.G.C. for his doctoral fellowship. C.K.M. thanks CSIR for her fellowship. W.A.D. thanks SERB-DST for the award of a National Postdoctoral fellowship, and B.M. thanks IITM for the fellowship.

## REFERENCES

- (1) Jin, R.; Zeng, C.; Zhou, M.; Chen, Y. Atomically Precise Colloidal Metal Nanoclusters and Nanoparticles: Fundamentals and Opportunities. *Chem. Rev.* **2016**, *116*, 10346–10413.
- (2) Chakraborty, I.; Pradeep, T. Atomically Precise Clusters of Noble Metals: Emerging Link between Atoms and Nanoparticles. *Chem. Rev.* **2017**, *117*, 8208–8271.
- (3) Lu, Y.; Chen, W. Sub-Nanometre Sized Metal Clusters: From Synthetic Challenges to the Unique Property Discoveries. *Chem. Soc. Rev.* **2012**, *41*, 3594–3623.
- (4) Khatun, E.; Chakraborty, P.; Jacob, B. R.; Paramasivam, G.; Bodiuzzaman, M.; Dar, W. A.; Pradeep, T. Intercluster Reactions Resulting in Silver-Rich Trimetallic Nanoclusters. *Chem. Mater.* **2020**, *32*, 611–619.
- (5) Kumar, B.; Niihori, Y.; Kurashige, W.; Negishi, Y. Controlled Thiolate-Protected Gold and Alloy Clusters. In *Descriptive Inorganic Chemistry Researches of Metal Compounds*; InTech, 2017; p 13.
- (6) Ferrando, R.; Jellinek, J.; Johnston, R. L. Nanoalloys: From Theory to Applications of Alloy Clusters and Nanoparticles. *Chem. Rev.* **2008**, *108*, 845–910.
- (7) Wang, S.; Li, Q.; Kang, X.; Zhu, M. Customizing the Structure, Composition, and Properties of Alloy Nanoclusters by Metal Exchange. *Acc. Chem. Res.* **2018**, *51*, 2784–2792.
- (8) Wang, G.; Guo, R.; Kalyuzhny, G.; Choi, J.-P.; Murray, R. W. NIR Luminescence Intensities Increase Linearly with Proportion of Polar Thiolate Ligands in Protecting Monolayers of Au<sub>38</sub> and Au<sub>140</sub> Quantum Dots. *J. Phys. Chem. B* **2006**, *110*, 20282–20289.
- (9) Zhang, L.; Wang, E. Metal Nanoclusters: New Fluorescent Probes for Sensors and Bioimaging. *Nano Today* **2014**, *9*, 132–157.
- (10) Díez, I.; Ras, R. H. A. Fluorescent Silver Nanoclusters. *Nanoscale* **2011**, *3*, 1963–1970.

(11) Khatun, E.; Ghosh, A.; Chakraborty, P.; Singh, P.; Bodiuzzaman, M.; Ganesan, P.; Natarajan, G.; Ghosh, J.; Pal, S. K.; Pradeep, T. A Thirty-Fold Photoluminescence Enhancement Induced by Secondary Ligands in Monolayer Protected Silver Clusters. *Nanoscale* **2018**, *10*, 20033–20042.

(12) Ghosh, D.; Baksi, A.; Mudedla, S. K.; Nag, A.; Ganayee, M. A.; Subramanian, V.; Pradeep, T. Gold-Induced Unfolding of Lysozyme: Toward the Formation of Luminescent Clusters. *J. Phys. Chem. C* **2017**, *121*, 13335–13344.

(13) Balazs, A. C.; Emrick, T.; Russell, T. P. Nanoparticle Polymer Composites: Where Two Small Worlds Meet. *Science* **2006**, *314*, 1107–1110.

(14) Bonderer, L. J.; Studart, A. R.; Gauckler, L. J. Bioinspired Design and Assembly of Platelet Reinforced Polymer Films. *Science* **2008**, *319*, 1069–1073.

(15) Munch, E.; Launey, M. E.; Alsem, D. H.; Saiz, E.; Tomsia, A. P.; Ritchie, R. O. Tough, Bio-Inspired Hybrid Materials. *Science* **2008**, *322*, 1516–1520.

(16) Hembury, M.; Beztsinna, N.; Asadi, H.; Van Den Dikkenberg, J. B.; Meeldijk, J. D.; Hennink, W. E.; Vermonden, T. Luminescent Gold Nanocluster-Decorated Polymeric Hybrid Particles with Assembly-Induced Emission. *Biomacromolecules* **2018**, *19*, 2841–2848.

(17) Qiao, J.; Mu, X.; Qi, L.; Deng, J.; Mao, L. Folic Acid-Functionalized Fluorescent Gold Nanoclusters with Polymers as Linkers for Cancer Cell Imaging. *Chem. Commun.* **2013**, *49*, 8030–8032.

(18) Liu, X.; Wei, S.; Chen, S.; Yuan, D.; Zhang, W. Graphene-Multiwall Carbon Nanotube-Gold Nanocluster Composites Modified Electrode for the Simultaneous Determination of Ascorbic Acid, Dopamine, and Uric Acid. *Appl. Biochem. Biotechnol.* **2014**, *173*, 1717–1726.

(19) Ghosh, A.; Jeseentharani, V.; Ganayee, M. A.; Hemalatha, R. G.; Chaudhari, K.; Vijayan, C.; Pradeep, T. Approaching Sensitivity of Tens of Ions Using Atomically Precise Cluster-Nanofiber Composites. *Anal. Chem.* **2014**, *86*, 10996–11001.

(20) Wang, Y.; Chen, J. T.; Yan, X. P. Fabrication of Transferrin Functionalized Gold Nanoclusters/Graphene Oxide Nanocomposite for Turn-on near-Infrared Fluorescent Bioimaging of Cancer Cells and Small Animals. *Anal. Chem.* **2013**, *85*, 2529–2535.

(21) Shibu, E. S.; Pradeep, T. Quantum Clusters in Cavities: Trapped Au<sub>15</sub> in Cyclodextrins. *Chem. Mater.* **2011**, *23*, 989–999.

(22) Burkett, S. L.; Press, A.; Mann, S. Synthesis, Characterization, and Reactivity of Layered Inorganic-Organic Nanocomposites Based on 2:1 Trioctahedral Phyllosilicates. *Chem. Mater.* **1997**, *9*, 1071–1073.

(23) Datta, K. K. R.; Achari, A.; Eswaramoorthy, M. Aminoclay: A Functional Layered Material with Multifaceted Applications. *J. Mater. Chem. A* **2013**, *1*, 6707–6718.

(24) Datta, K. K. R.; Kulkarni, C.; Eswaramoorthy, M. Aminoclay: A Permselective Matrix to Stabilize Copper Nanoparticles. *Chem. Commun.* **2010**, *46*, 616–618.

(25) Kumar, A. S.; Datta, K. K. R.; Rao, T. S.; Raghavan, K. V.; Eswaramoorthy, M.; Reddy, B. V. S. Pd-Aminoclay Nanocomposite as an Efficient Recyclable Catalyst for Hydrogenation and Suzuki Cross Coupling Reactions. *J. Nanosci. Nanotechnol.* **2012**, *12*, 2000–2007.

(26) Ranchani, A. A. J.; Parthasarathy, V.; Devi, A. A.; Meenarathi, B.; Anbarasan, R. Synthesis, Characterization and Catalytic Activity of Nanosized Ni Complexed Aminoclay. *Appl. Nanosci.* **2017**, *7*, 577–588.

(27) Wang, T.; Yu, X.; Li, Z.; Wang, J.; Li, H. Multi-Colored Luminescent Light-Harvesting Hybrids Based on Aminoclay and Lanthanide Complexes. *RSC Adv.* **2015**, *5*, 11570–11576.

(28) Kim, S. Y.; Lee, S. J.; Han, H. K.; Lim, S. J. Aminoclay as a Highly Effective Cationic Vehicle for Enhancing Adenovirus-Mediated Gene Transfer through Nanobiohybrid Complex Formation. *Acta Biomater.* **2017**, *49*, 521–530.

(29) Yang, L.; Shao, Y.; Han, H. K. Aminoclay-Lipid Hybrid Composite as a Novel Drug Carrier of Fenofibrate for the

Enhancement of Drug Release and Oral Absorption. *Int. J. Nanomed.* **2016**, *11*, 1067–1076.

(30) Johnsy, G.; Datta, K. K. R.; Sajeevkumar, V. A.; Sabapathy, S. N.; Bawa, A. S.; Eswaramoorthy, M. Aminoclay: A Designer Filler for the Synthesis of Highly Ductile Polymer-Nanocomposite Film. *ACS Appl. Mater. Interfaces* **2009**, *1*, 2796–2803.

(31) Liu, Y.; Yu, S.-H.; Bergström, L. Transparent and Flexible Nacre-Like Hybrid Films of Aminoclays and Carboxylated Cellulose Nanofibrils. *Adv. Funct. Mater.* **2018**, *28*, No. 1703277.

(32) Szejtli, J. Introduction and General Overview of Cyclodextrin Chemistry. *Chem. Rev.* **1998**, *98*, 1743–1753.

(33) Saenger, W. Cyclodextrin Inclusion Compounds in Research and Industry. *Angew. Chem., Int. Ed.* **1980**, *19*, 344–362.

(34) Messner, M.; Kurkov, S. V.; Flavià-Piera, R.; Brewster, M. E.; Loftsson, T. Self-Assembly of Cyclodextrins: The Effect of the Guest Molecule. *Int. J. Pharm.* **2011**, *408*, 235–247.

(35) Rekharsky, M. V.; Inoue, Y. Complexation Thermodynamics of Cyclodextrins. *Chem. Rev.* **1998**, *98*, 1875–1918.

(36) Connors, K. A. The Stability of Cyclodextrin Complexes in Solution. *Chem. Rev.* **1997**, *97*, 1325–1357.

(37) Song, W.; Li, A.; Xu, X. Water Solubility Enhancement of Phthalates by Cetyltrimethylammonium Bromide and  $\beta$ -Cyclodextrin. *Ind. Eng. Chem. Res.* **2003**, *42*, 949–955.

(38) Păduraru, O. M.; Bosinceanu, A.; Țaintaru, G.; Vasile, C. Effect of Hydroxypropyl- $\beta$ -Cyclodextrin on the Solubility of an Antiarhythmic Agent. *Ind. Eng. Chem. Res.* **2013**, *52*, 2174–2181.

(39) Bardi, L.; Mattei, A.; Steffan, S.; Marzona, M. Hydrocarbon Degradation by a Soil Microbial Population with  $\beta$ -Cyclodextrin as Surfactant to Enhance Bioavailability. *Enzyme Microb. Technol.* **2000**, *27*, 709–713.

(40) Chen, L.; Berry, R. M.; Tam, K. C. Synthesis of  $\beta$ -Cyclodextrin-Modified Cellulose Nanocrystals (CNCs)@Fe<sub>3</sub>O<sub>4</sub>@SiO<sub>2</sub> Superparamagnetic Nanorods. *ACS Sustainable Chem. Eng.* **2014**, *2*, 951–958.

(41) Kang, Y.; Zhou, L.; Li, X.; Yuan, J.  $\beta$ -Cyclodextrin-Modified Hybrid Magnetic Nanoparticles for Catalysis and Adsorption. *J. Mater. Chem.* **2011**, *21*, 3704–3710.

(42) Zhang, F.; Islam, M. S.; Berry, R. M.; Tam, K. C.  $\beta$ -Cyclodextrin-Functionalized Cellulose Nanocrystals and Their Interactions with Surfactants. *ACS Omega* **2019**, *4*, 2102–2110.

(43) Prabakaran, M.; Mano, J. F. Hydroxypropyl Chitosan Bearing  $\beta$ -Cyclodextrin Cavities: Synthesis and Slow Release of Its Inclusion Complex with a Model Hydrophobic Drug. *Macromol. Biosci.* **2005**, *5*, 965–973.

(44) Hirayama, F.; Uekama, K. Cyclodextrin-Based Controlled Drug Release System. *Adv. Drug Delivery Rev.* **1999**, *36*, 125–141.

(45) Szenté, L.; Szejtli, J. Cyclodextrins as Food Ingredients. *Trends Food Sci. Technol.* **2004**, *15*, 137–142.

(46) Cravotto, G.; Binello, A.; Baranelli, E.; Carraro, P.; Trotta, F. Cyclodextrins as Food Additives and in Food Processing. *Curr. Nutr. Food Sci.* **2006**, *2*, 343–350.

(47) Marques, H. M. C. A Review on Cyclodextrin Encapsulation of Essential Oils and Volatiles. *Flavour Fragrance J.* **2010**, *25*, 313–326.

(48) Hill, L. E.; Gomes, C.; Taylor, T. M. Characterization of Beta-Cyclodextrin Inclusion Complexes Containing Essential Oils (Trans-Cinnamaldehyde, Eugenol, Cinnamon Bark, and Clove Bud Extracts) for Antimicrobial Delivery Applications. *LWT - Food Sci. Technol.* **2013**, *51*, 86–93.

(49) Ciobanu, A.; Mallard, I.; Landy, D.; Brabie, G.; Nistor, D.; Fourmentin, S. Retention of Aroma Compounds from Mentha Piperita Essential Oil by Cyclodextrins and Crosslinked Cyclodextrin Polymers. *Food Chem.* **2013**, *138*, 291–297.

(50) Buschmann, H. J.; Schollmeyer, E. Applications of Cyclodextrins in Cosmetic Products: A Review. *J. Cosmet. Sci.* **2002**, *53*, 185–191.

(51) Loftsson, T.; Duchêne, D. Cyclodextrins and Their Pharmaceutical Applications. *Int. J. Pharm.* **2007**, *329*, 1–11.

(52) Brewster, M. E.; Loftsson, T. Pharmaceutical Applications of Cyclodextrins. 1. Drug Solubilization and Stabilization. *J. Pharm. Sci.* **1996**, *85*, 1017–1025.

(53) Zhang, J.; Ma, P. X. Cyclodextrin-Based Supramolecular Systems for Drug Delivery: Recent Progress and Future Perspective. *Adv. Drug Delivery Rev.* **2013**, *65*, 1215–1233.

(54) Wilson, L. D.; Mohamed, M. H.; Guo, R.; Pratt, D. Y.; Kwon, J. H.; Mahmud, S. T. Sorption of Agrochemical Model Compounds by Sorbent Materials Containing  $\beta$ -Cyclodextrin. *J. Agromedicine* **2010**, *15*, 105–116.

(55) König, W. A.; Icheln, D.; Runge, T.; Pfaffenberger, B.; Ludwig, P.; Hühnerfuss, H. Gas Chromatographic Enantiomer Separation of Agrochemicals Using Modified Cyclodextrins. *J. High Resolut. Chromatogr.* **1991**, *14*, 530–536.

(56) Nag, A.; Chakraborty, P.; Paramasivam, G.; Bodiuzzaman, M.; Natarajan, G.; Pradeep, T. Isomerism in Supramolecular Adducts of Atomically Precise Nanoparticles. *J. Am. Chem. Soc.* **2018**, *140*, 13590–13593.

(57) Mathew, A.; Natarajan, G.; Lehtovaara, L.; Häkkinen, H.; Kumar, R. M.; Subramanian, V.; Jaleel, A.; Pradeep, T. Supramolecular Functionalization and Concomitant Enhancement in Properties of Au<sub>25</sub> Clusters. *ACS Nano* **2014**, *8*, 139–152.

(58) Liu, J. H.; Xu, H. C.; Shen, L.; Chen, R. Y.; Yu, Z. C. Synthesis of Monochlorotriazinyl- $\beta$ -Cyclodextrin as a Novel Textile Auxiliary. *Adv. Mater. Res.* **2012**, *441*, 431–435.

(59) Manju, C. K.; Chakraborty, I.; Pradeep, T. Highly Luminescent Monolayer Protected Ag<sub>56</sub>Se<sub>13</sub>S<sub>15</sub> Clusters. *J. Mater. Chem. C* **2016**, *4*, 5572–5577.

(60) Basappa, C.; Rao, P.; Rao, D. N.; Divakar, S. A Modified Colorimetric Method for the Estimation of  $\beta$ -Cyclodextrin Using Phenolphthalein. *Int. J. Food Sci. Technol.* **1998**, 517–520.

(61) Taguchi, K. Transient Binding Mode of Phenolphthalein- $\beta$ -Cyclodextrin Complex: An Example of Induced Geometrical Distortion. *J. Am. Chem. Soc.* **1986**, *108*, 2705–2709.

## Supporting information

### Entrapping Atomically Precise Clusters in Cyclodextrin-Functionalized Aminoclay sheets: Synthesis and Enhanced Luminescence

Mohd Azhardin Ganayee,<sup>†</sup> C. K. Manju,<sup>†</sup> Wakeel Ahmed Dar,<sup>†</sup> Biswajit Mondal,<sup>†</sup> Thalappil Pradeep<sup>\*†</sup>

<sup>†</sup>DST Unit of Nanoscience, Thematic Unit of Excellence, Department of Chemistry, Indian Institute of Technology Madras, Chennai 600036, India.

#### Table of Contents

Particulars	Title	Page No.
Figure S1	XRD pattern of the aminoclay with TEM as inset	1
Figure S2	FTIR, ESI MS and Schematic procedure for the synthesis of MCT- $\beta$ -CD	2
Figure S3	Binding of phenolphthalein to cyclodextrin	3
Figure S4	UV-vis absorbance and calibration curves with different concentrations of $\beta$ -CD	4
Figure S5	UV-vis absorbance and calibration curves with different concentrations of aminoclay	4
Figure S6	Characterization of Ag <sub>2</sub> Se@SBB cluster	5
Figure S7	AFM images of AC-CD	6

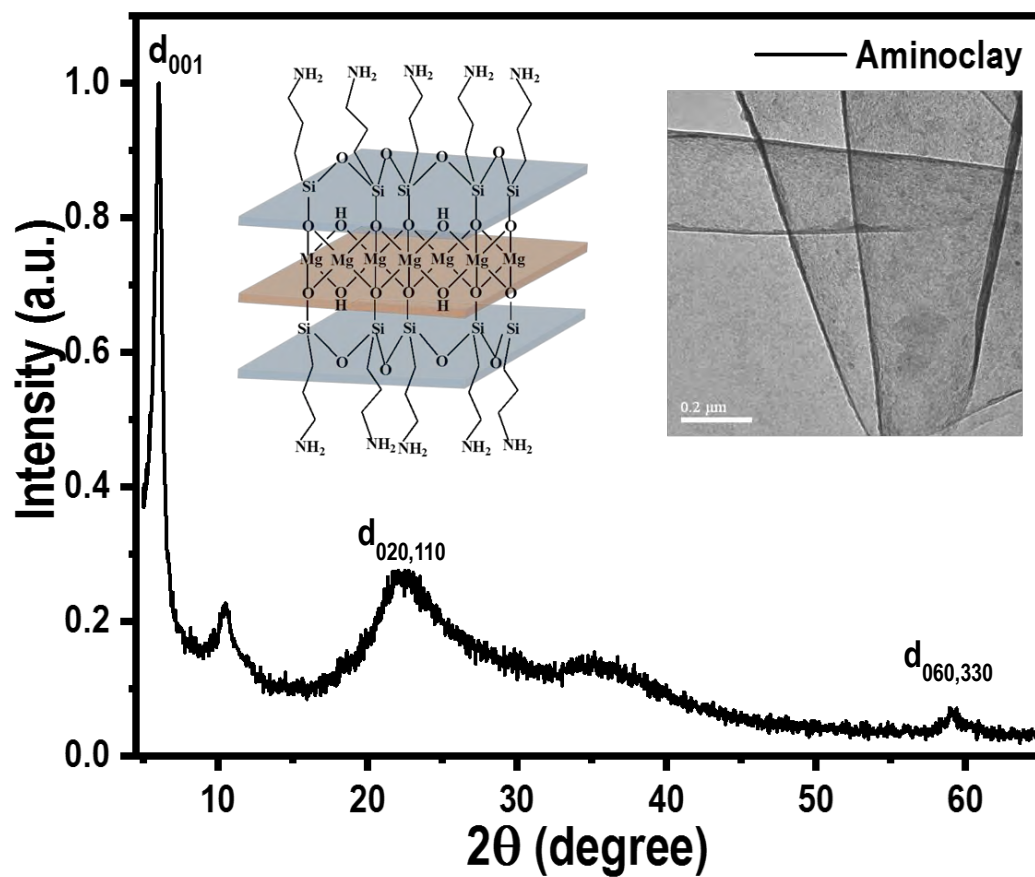


**Figure S1.** XRD pattern of the aminoclay; inset: schematic and corresponding TEM image showing the layered structure.

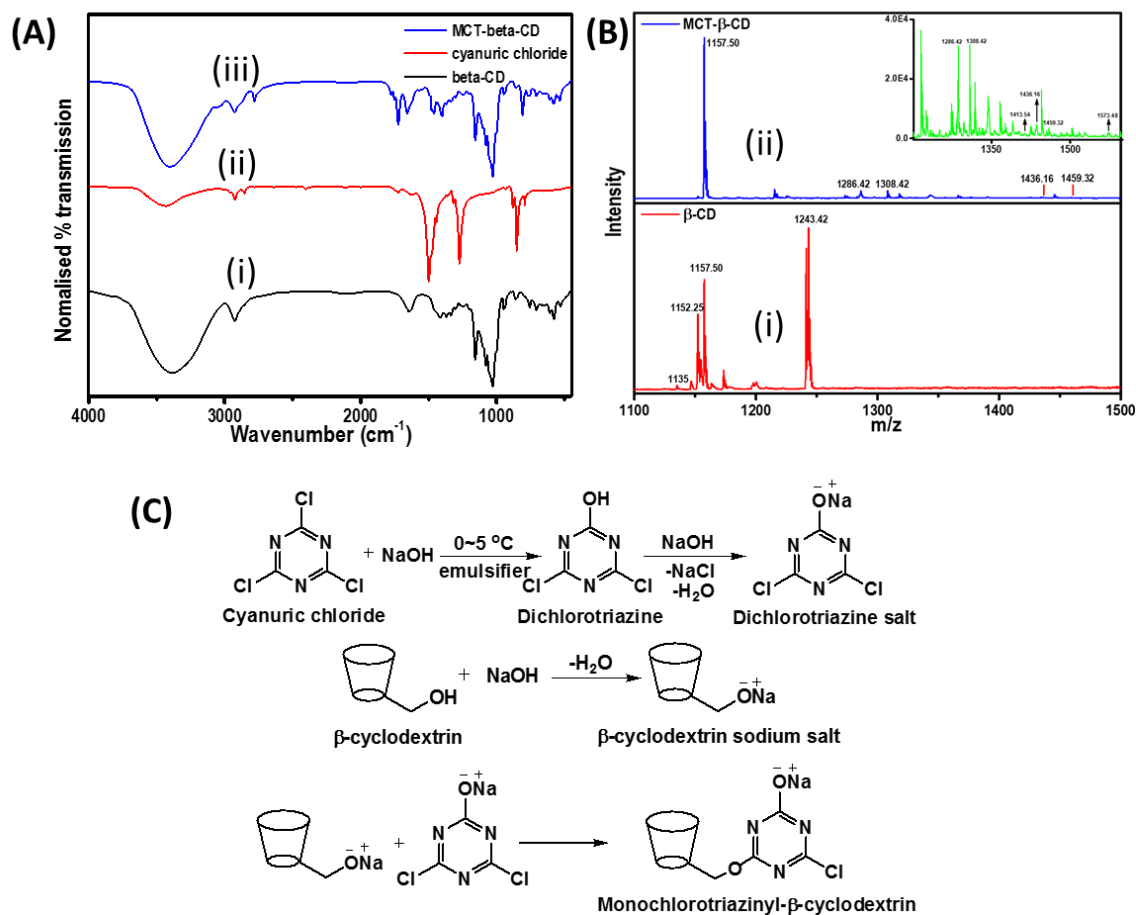


**Figure S2.** (A) FTIR spectra of (i)  $\beta$ -CD (ii) cyanuric chloride and (iii) MCT- $\beta$ -CD. (B) ESI MS of (i)  $\beta$ -CD and (ii) MCT- $\beta$ -CD; inset: corresponding expanded view of ESI MS of MCT- $\beta$ -CD. (C) Schematic procedure for the synthesis of MCT- $\beta$ -CD

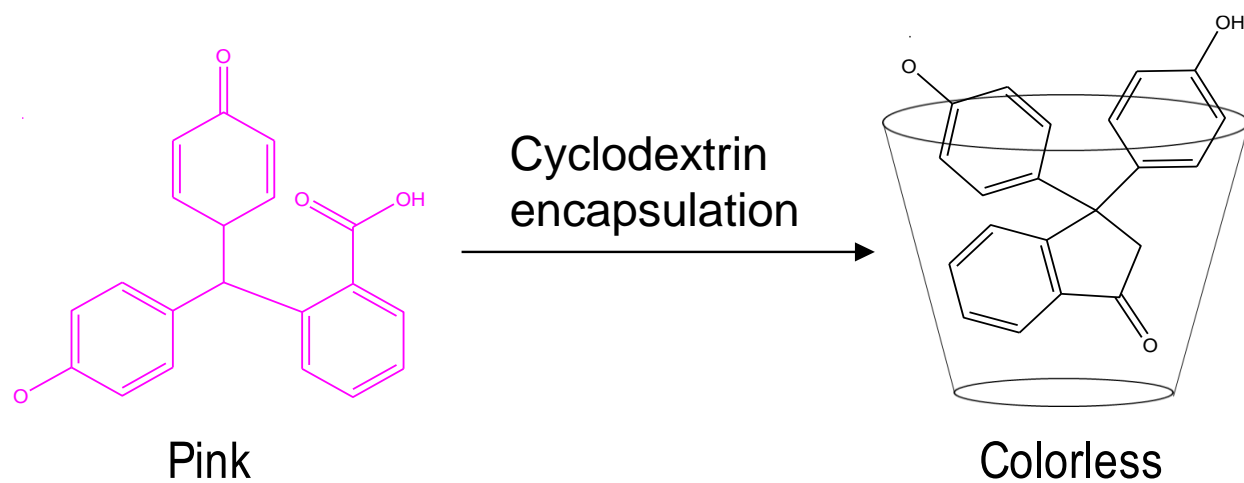


**Figure S3.** Binding of phenolphthalein to cyclodextrin results in the transformation of pink colored dianion of a trigonal  $sp^2$ -conjugated system of phenolphthalein to a colorless lactonoid dianion form having a tetrahedral  $sp^3$  central carbon atom.



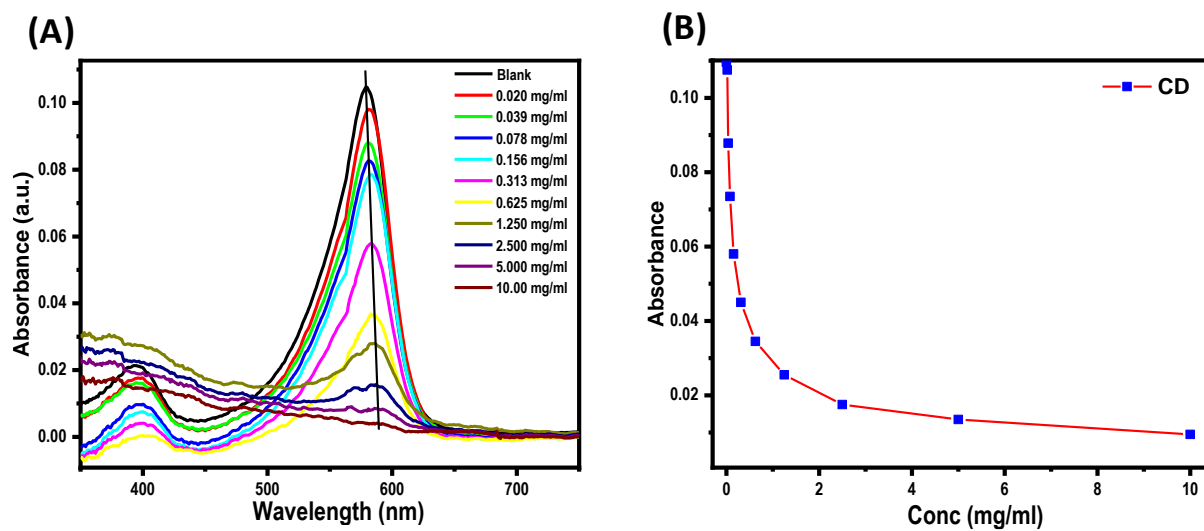


**Figure S4.** (A) UV-vis absorbance of PHTH/CD solutions with increasing CD concentrations. (B) Calibration curve of absorbance and CD concentration

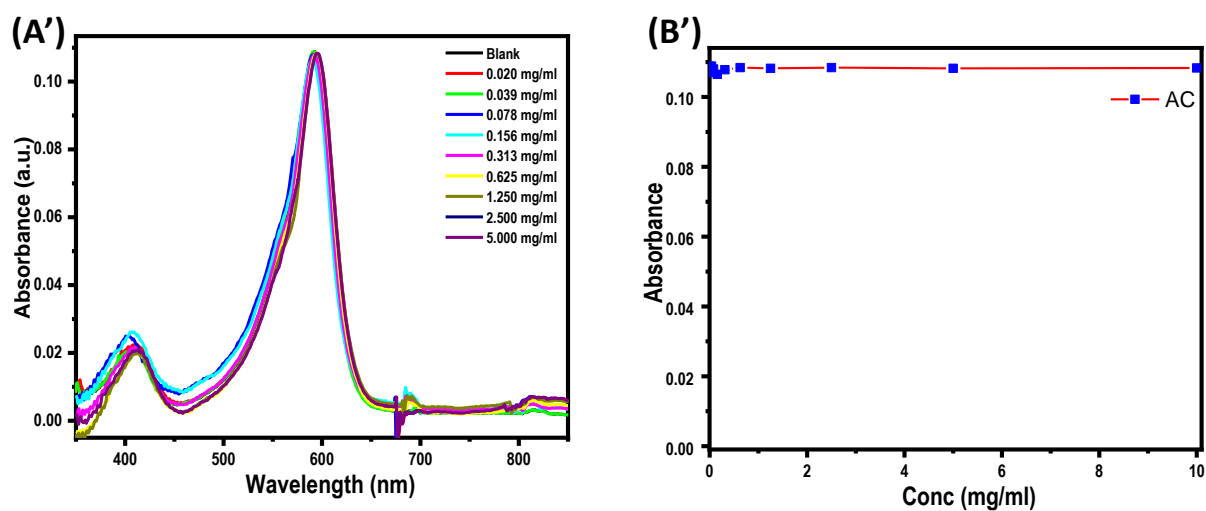


**Figure S5.** (A') UV-vis absorbance of PHTH/AC solutions with increasing AC concentrations. (B') Calibration curve of absorbance and AC concentration.

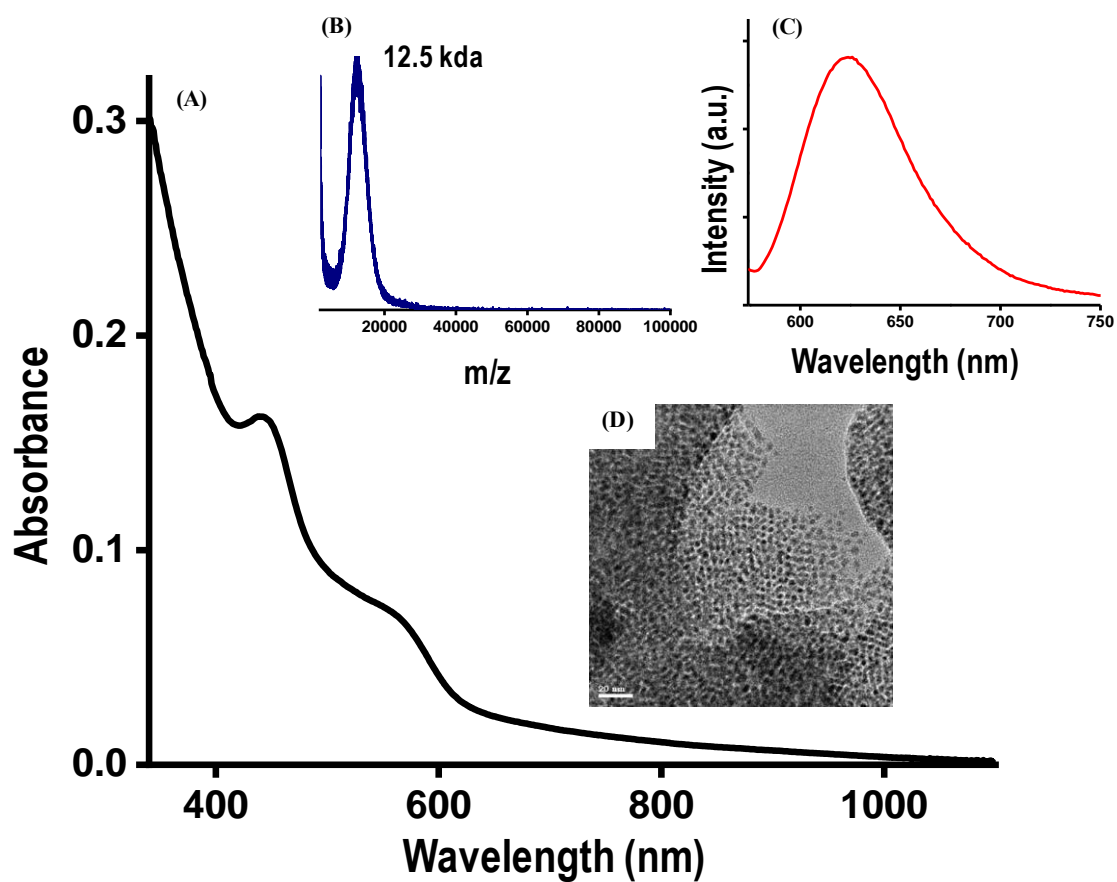


**Figure S6.** (A) UV-vis of Ag<sub>2</sub>Se@SBB cluster (B) MALDI MS measured at threshold laser power in negative mode. (C) Emission spectrum of Ag<sub>2</sub>Se@SBB cluster. (D) TEM image of Ag<sub>2</sub>Se@SBB cluster.

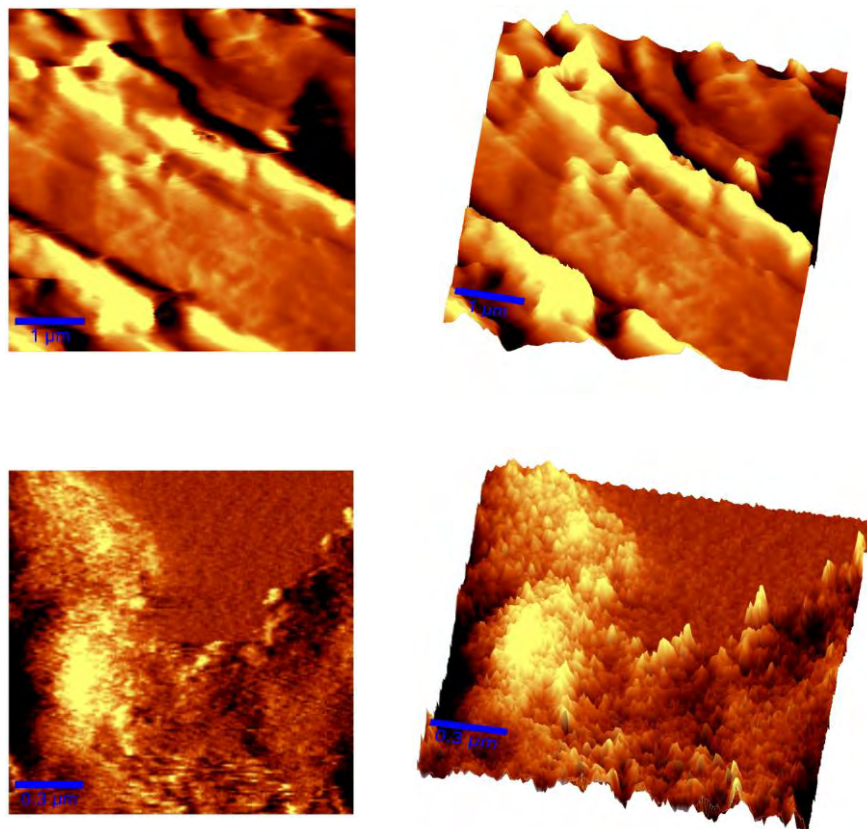


**Figure S7.** AFM images of AC-CD

# Fullerene-Mediated Aggregation of $M_{25}(SR)_{18}^-$ ( $M = Ag, Au$ ) Nanoclusters

Papri Chakraborty, Abhijit Nag, Biswajit Mondal, Esma Khatun, Ganesan Paramasivam, and Thalappil Pradeep\*

Cite This: *J. Phys. Chem. C* 2020, 124, 14891–14900

Read Online

ACCESS |

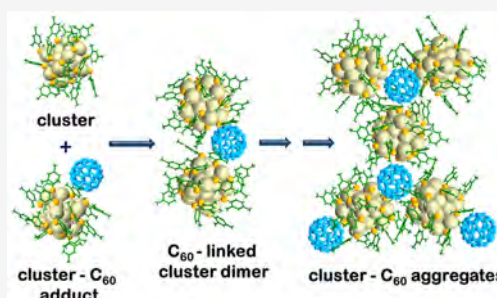
Metrics & More

Article Recommendations

Supporting Information

**ABSTRACT:** We report fullerene ( $C_{60}$  and  $C_{70}$ )-induced aggregation of atomically precise clusters, taking  $M_{25}(SR)_{18}^-$  ( $M = Ag, Au$  and  $-SR$  is a thiolate ligand) clusters as an example. We show that dimers, trimers, tetramers, and even higher aggregates of the clusters can be created by supramolecular interaction with fullerenes. Adducts such as  $[M_{25}(SR)_{18}(C_{60})]^{n-}$  ( $n = 1-5$ ),  $[M_{25}(SR)_{18}(C_{60})_{n-1}]^{n-}$  ( $n = 2-5$ ), and  $[M_{25}(SR)_{18}(C_{60})_n]^{n-}$  ( $n = 1, 2, 3, \dots$ , etc.) were formed, which were studied by electrospray ionization mass spectrometry. Similar adducts with  $C_{70}$  were also observed. Structural insights were obtained from molecular docking and density functional theory calculations. Computational studies predicted the possibility of isomerism in some of these adducts. Fullerenes linked multiple clusters, causing aggregation.

Fullerenes and clusters formed host–guest complexes in such assemblies. The possibilities of coassembly between the clusters and the fullerenes were also studied in the solid state. The nature of adducts observed in the case of  $M_{25}(SR)_{18}^-$  was completely different compared to the previously reported fullerene adducts of  $[Ag_{29}(BDT)_{12}]^{3-}$  (where BDT is 1,3-benzene dithiol), in which multiple fullerenes were attached on the surface of a single cluster. Supramolecular aggregates formed in the case of  $M_{25}(SR)_{18}^-$  were independent of the nature of the metal atoms (Ag or Au). This implied that for an appropriate geometry of the cluster weak interactions with the ligands and ion-induced dipole interactions were more important in controlling the complexation compared to the metallophilic interactions. Exploring the interaction of atomically precise clusters with fullerenes is important, as the resulting adducts can show new properties such as isomerism, chirality, charge transfer, or enhanced optical properties.



## INTRODUCTION

Monolayer protected atomically precise nanoclusters show unique properties and find applications in numerous fields including catalysis, sensing, energy, etc.<sup>1–9</sup> These clusters show molecular behavior which is reflected in their optical absorption features. X-ray crystallography is widely used to determine their structures.<sup>1,10–12</sup> Such clusters are also characterized by using mass spectrometry (MS).<sup>13,14</sup> Monolayers of ligands, capping the metal core of the cluster, can interact with other molecules. This has enabled the possibilities of exploring supramolecular chemistry of such clusters.<sup>15–20</sup> There can be intracuster and intercluster interactions that can form different types of self-assembled structures. These interactions play an active role in their packing in crystals.<sup>16,17,21,22</sup> Nag et al. reported that intercluster interactions were responsible for polymorphism in the crystal packing of  $[Ag_{29}(BDT)_{12}(PPh_3)_4]^{3-}$  (BDT is 1,3-benzene dithiol and  $PPh_3$  is triphenyl phosphine) clusters.<sup>23</sup> Zheng et al. showed how the protecting ligands of  $Au_{246}(p-MBT)_{80}$  ( $p-MBT$  is a *para*-mercapto benzene thiol) formed different patterns on the cluster surface.<sup>21</sup> Intercluster interactions can also result in aggregation of clusters. Dimers and trimers of  $[Au_{25}(SR)_{18}]^-$  ( $-SR$  is a thiolate ligand) were observed in the

gas phase, which were favored due to the aurophilic interactions between the clusters.<sup>24</sup>  $Au_{25}(SBu)_{18}$  ( $SBu$  is *n*-butanethiolate) clusters were also found to be connected by Au–Au bonds and exist as linear polymers in their crystal structure.<sup>25</sup> Recently, Hossain et al. reported one-dimensional structures of  $Au_4Pt_2(SR)_8$  clusters which were also connected via Au–Au bonds.<sup>26</sup> Wen et al. reported one-dimensional polymers of  $[Au_7Ag_9(dppf)_3(CF_3CO_2)_7BF_4]_n$  ( $dppf$  is 1,10-bis(diphenylphosphino)ferrocene), which were connected linearly via Ag–O bonds.<sup>27</sup> Chakraborty et al. reported that dimerization of clusters can also be induced by alkali metal ions, as observed in  $[Ag_{29}(BDT)_{12}(PPh_3)_4]^{3-}$ .<sup>28</sup> Wei et al. further demonstrated that interaction of  $Cs^+$  with  $[Ag_{29}(BDT)_{12}(PPh_3)_4]^{3-}$  modified its geometric structure by stripping off the  $PPh_3$  ligands and induced the formation of intercluster assemblies by arranging the clusters into one-

Received: April 16, 2020

Revised: June 9, 2020

Published: June 10, 2020



dimensional arrays in their crystal lattice.<sup>29</sup> Chandra et al. reported self-assembly of water-soluble Au clusters into spherical colloidal superstructures with high photocatalytic activity and applications in bioimaging by utilizing the interaction of the clusters with  $\text{Sn}^{2+}$  ions.<sup>30</sup> Other cations like  $\text{Zn}^{2+}$  were also used to study phenomena such as aggregation-induced emission in Au clusters.<sup>31,32</sup> Anionic templates like  $\text{CO}_3^{2-}$  were used to link  $\text{Ag}_{17}\text{S}_8$  clusters into a two-dimensional (2D) honeycomb-like structure.<sup>33</sup> Nonappa et al. reported the formation of spherical capsids and 2D monolayer thick sheets of clusters which were formed due to weak hydrogen bonding interactions.<sup>34</sup> Apart from these, aggregates of clusters were also created by covalent linkages.<sup>35–38</sup> Such covalent bonding between clusters was extended to create cluster-based metal–organic frameworks (MOFs).<sup>39–41</sup> Moreover, encapsulation of clusters into common MOFs like ZIF-8 and ZIF-67 occurred due to electrostatic interactions, and such hybrid materials found application in  $\text{CO}_2$  conversion.<sup>42</sup>

Recent studies are also focusing on the interaction of clusters with other molecules like cyclodextrins (CD),<sup>43–46</sup> fullerenes,<sup>47</sup> and crown ethers.<sup>48</sup> Mathew et al. reported host–guest complexes of  $\text{Au}_{25}(\text{SBB})_{18}^-$  (SBB is 4-(*t*-butyl)benzyl thiolate) clusters with CDs,<sup>43</sup> and Nag et al. reported supramolecular complexes of  $[\text{Ag}_{29}(\text{BDT})_{12}]^{3-}$  clusters with CDs.<sup>44</sup> Chakraborty et al. studied the interaction between  $[\text{Ag}_{29}(\text{BDT})_{12}]^{3-}$  and fullerenes.<sup>47</sup> In all these cases, the complexes were primarily stabilized by weak supramolecular forces.<sup>15</sup> Co-crystallization of  $[\text{Ag}_{29}(\text{BDT})_{12}(\text{PPh}_3)_4]^{3-}$  clusters and crown ethers was also achieved.<sup>48</sup> Such supramolecular complexes are particularly interesting due to the additional properties that can be incorporated into the cluster system due to the complexation with the heteromolecules.<sup>15,16</sup> In most cases, such complexation enhanced the stability of the clusters. Isomerism was observed in the host–guest complexes,  $[\text{Ag}_{29}(\text{BDT})_{12}(\text{CD})_n]^{3-}$  ( $n = 1–6$ ).<sup>44</sup> Recently, Muhammad et al. reported pilla[5]arene-capped silver clusters.<sup>49</sup> The pilla[5]arene macrocycles on the surface of the cluster were available for taking part in further host–guest complexation which modified the optical properties of the nanoclusters.<sup>49</sup> Self-assembly of clusters has thus emerged as an effective way to vary their optical and luminescence properties.<sup>50</sup> Due to such possibilities, studies on supramolecular chemistry of atomically precise clusters have attracted researchers in recent times.

Fullerenes are known to form numerous host–guest complexes and can also bring in properties like superconductivity, metallicity, charge transfer, etc., in their hybrid composites.<sup>51–53</sup> Superatomic crystals containing inorganic clusters and fullerenes are particularly important for studying electron transport properties.<sup>54</sup> Several such fullerene-containing superatomic crystals, e.g.,  $[\text{Co}_6\text{Se}_8(\text{PET}_3)_6][\text{C}_{60}]_2$ ,  $[\text{Ni}_9\text{Te}_6(\text{PET}_3)_8][\text{C}_{60}]$ ,  $[\text{Cr}_6\text{Te}_8(\text{PET}_3)_6][\text{C}_{60}]_2$ , etc., have been reported in the literature.<sup>55</sup> However, studies of interaction between ligand-protected noble metal clusters and fullerenes are still limited. One of the reports showed that intercluster compounds,  $[\text{Au}_7(\text{PPh}_3)_7]\text{C}_{60}\cdot\text{THF}$  and  $[\text{Au}_8(\text{PPh}_3)_8](\text{C}_{60})_2$ , were stabilized primarily by  $\pi$ – $\pi$ , C–H $\cdots\pi$ , and Coulomb interactions between the Au clusters and the fullerenes.<sup>56</sup> Earlier, we had reported supramolecular complexes of  $[\text{Ag}_{29}(\text{BDT})_{12}]^{3-}$  with fullerenes.<sup>47</sup> The adducts,  $[\text{Ag}_{29}(\text{BDT})_{12}(\text{C}_{60})_n]^{3-}$  ( $n = 1–9$ ), were formed due to weak supramolecular interactions.  $\text{C}_{60}$  molecules were captured

into appropriate cavities on the surface of the cluster. Thus, the structure of the cluster played a significant role in controlling host–guest complexation. These unfolded the possibilities of studying the interaction of fullerenes with a variety of clusters. Depending on the inherent geometry of the nanocluster, the nature of the metal atoms, and the monolayer of the ligands, the nature of complexation is expected to vary which can produce a wide range of such cluster–fullerene complexes.

In this work, we investigated the interaction of  $\text{C}_{60}$  and  $\text{C}_{70}$  with two archetypical atomically precise clusters,  $[\text{Ag}_{25}(\text{DMBT})_{18}]^-$  (DMBT is 2,4-dimethylbenzene thiol)<sup>57</sup> and  $[\text{Au}_{25}(\text{PET})_{18}]^-$  (PET is 2-phenyl ethanethiol),<sup>10,58</sup> which have the same core structure but protected by different ligands. Fullerene-induced aggregation of the clusters was observed in both cases, and the nature of the complexation was independent of the nature of the metal atoms. Fullerene-mediated dimers, trimers, tetramers, and even higher aggregates of the clusters were formed due to supramolecular interactions between the cluster and the fullerenes. The complexation was studied using electrospray ionization mass spectrometry (ESI MS), and greater insights into the nature of binding were obtained from collision-induced dissociation (CID). We used molecular docking and density functional theory (DFT) to predict the structure of the adducts. The nature of adducts observed in the case of  $[\text{Ag}_{25}(\text{DMBT})_{18}]^-$  and  $[\text{Au}_{25}(\text{PET})_{18}]^-$  was distinct, compared to that of the fullerene adducts of  $[\text{Ag}_{29}(\text{BDT})_{12}]^{3-}$ , reported earlier.<sup>47</sup> In the case of  $[\text{Ag}_{29}(\text{BDT})_{12}]^{3-}$ , the surface of an isolated cluster was functionalized by numerous fullerenes.<sup>47</sup> In contrast, in the case of  $[\text{M}_{25}(\text{SR})_{18}]^-$  ( $\text{M} = \text{Ag}, \text{Au}$ ), multiple clusters self-assembled to form larger aggregates by interaction with fullerene molecules. This study clearly reveals how a variety of cluster–fullerene adducts can be created by choosing the appropriate system of clusters and also how cluster aggregates can be created by supramolecular interaction with heteromolecules.

## ■ EXPERIMENTAL SECTION

**Materials and Methods.** All the reagents used for the synthesis of the clusters were commercially available. Silver nitrate ( $\text{AgNO}_3$ ) was procured from Rankem, India. The thiols 2,4 -DMBT and PET were purchased from Sigma-Aldrich. Sodium borohydride ( $\text{NaBH}_4$ ), tetraphenyl phosphonium bromide ( $\text{PPh}_4\text{Br}$ ), tetrabutyl ammonium bromide ( $\text{TBABr}$ ),  $\text{PPh}_3$ , and fullerenes ( $\text{C}_{60}$  and  $\text{C}_{70}$ ) were obtained from Sigma-Aldrich. Chloroauric acid ( $\text{HAuCl}_4\cdot 3\text{H}_2\text{O}$ ) was synthesized in the laboratory starting from pure metallic gold (24 carat). The solvents used, namely, methanol ( $\text{MeOH}$ ), dichloromethane ( $\text{DCM}$ ), toluene, and acetone, were of HPLC grade.

**Instrumentation.** A PerkinElmer Lambda 25 UV–vis spectrophotometer was used to measure the optical absorption spectra. The ESI MS measurements were done using a Waters Synapt G2 Si mass spectrometer. All the spectra were collected in the negative ion mode. ESI MS measurements were done using the following instrumental parameters: capillary voltage, 3 kV; cone voltage, 0; source offset, 0; trap gas, 8 mL/min; source and desolvation temperature, 150 °C. A JEOL 3010 instrument was used for performing the transmission electron microscopy (TEM) studies.

**Synthetic Protocol of  $[\text{Ag}_{25}(\text{DMBT})_{18}]^-$  Clusters.**  $[\text{Ag}_{25}(\text{DMBT})_{18}]^-$  clusters were synthesized according to the method reported by Joshi et al.<sup>57</sup> About 38 mg of  $\text{AgNO}_3$  and 90  $\mu\text{L}$  of the thiol, 2,4-DMBT, were dissolved in about 18 mL



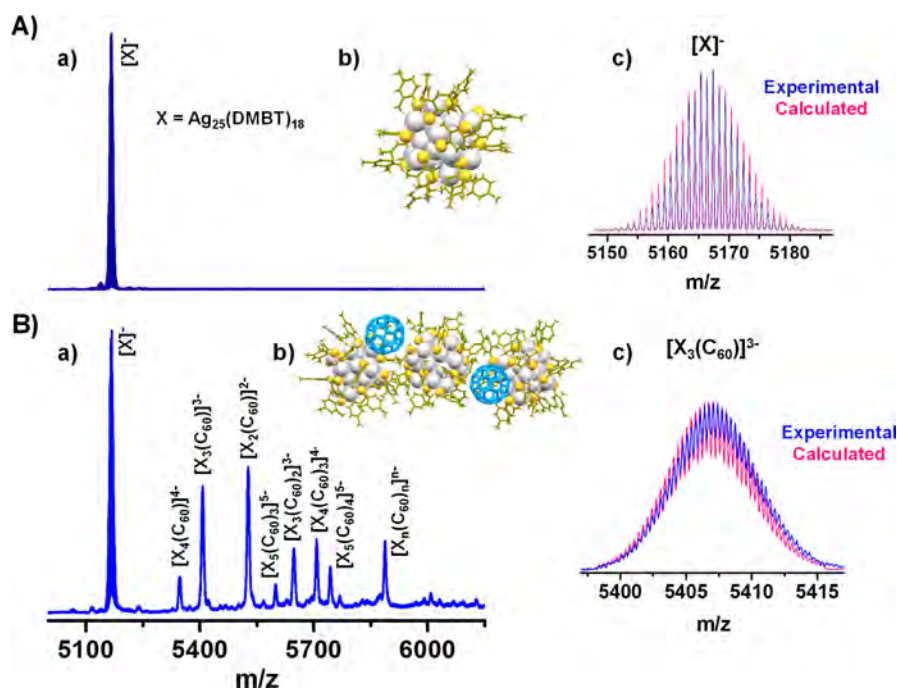


**Figure 1.** (A) (a) ESI MS of  $X^-$ , (b) structure of  $X^-$  (computed using coordinates from the crystal structure), and (c) experimental and theoretical isotopic patterns of  $X^-$ . (B) (a) ESI MS showing the adducts of  $X^-$  and  $C_{60}$ , (b) schematic showing an aggregate of  $X^-$  with  $C_{60}$ , and (c) experimental and theoretical isotopic patterns of one of the adducts,  $[X_3(C_{60})]^{3-}$  [ $X = Ag_{25}(DMBT)_{18}$ ]. Color codes: gray, Ag; yellowish-green, C; yellow, S; white, H; blue, fullerenes.

of a solvent mixture of MeOH and DCM (MeOH:DCM = 1:8) to allow the formation of yellow-colored Ag thiolates. The reaction was maintained at 0 °C and was stirred at 900 rpm. About 15 min later, ~6 mg of  $PPh_4Br$ , dissolved in ~0.5–1 mL of MeOH, was added to the reaction mixture. Next, about 2–3 min later, 15 mg  $NaBH_4$ , dissolved in ~0.5 mL of ice-cold water, was added dropwise. Upon addition of  $NaBH_4$ , the color of the solution changed to brown. The reaction mixture was stirred at 0 °C for about 8 h and then was kept in the freezer at 4 °C for about 2 days. Then, the crude mixture containing the clusters was purified. First, the mixture was centrifuged, and the precipitate was separated. Next, DCM was evaporated from the supernatant, and the resulting solid was cleaned by washing with MeOH. The solid cluster was then dissolved in DCM and centrifuged. The purified clusters were then obtained in powder form by removing DCM by rotary evaporation.

**Synthetic Protocol of  $[Au_{25}(PET)_{18}]^-$  Clusters.**  $[Au_{25}(PET)_{18}]^-$  clusters were made by slightly altering an already reported protocol.<sup>59,60</sup> About 40 mg of the Au precursor,  $HAuCl_4 \cdot 3H_2O$ , was dissolved in ~8 mL of THF and mixed with 65 mg of TOABr. The solution was then stirred for 15–20 min. After about 1 h, ~68  $\mu$ L of PET was introduced into the reaction mixture under stirring conditions, which caused the formation of Au thiolates. Next, about 40 mg of  $NaBH_4$  (in ice-cold water) was added. Then the reaction was kept under stirring for another 5–6 h to allow size-focusing of the clusters. The clusters were then dried by rotary evaporation followed by washing the dried cluster with MeOH. Then, the pure clusters were extracted using acetone and centrifuged, and the precipitate was discarded. The supernatant containing the pure clusters was then vacuum-dried and stored for further use.

**Computational Details.** Molecular docking was done to determine the structure of the cluster–fullerene adducts. The

Lamarckian genetic algorithm in the Autodock 4.2 program<sup>61</sup> was used for this purpose. The lowest energy structures obtained from docking were further optimized using DFT. DFT calculations were done using the grid-based projector-augmented wave (GPAW) method.<sup>62,63</sup> The Perdew–Burke–Ernzerhof (PBE) functional<sup>64</sup> was used in our calculations. Double zeta plus polarization (DZP) was used as the basis set in the linear combination of atomic orbitals (LCAO) method. The crystal structure of  $Ag_{25}(DMBT)_{18}^-$  was used as the initial structure<sup>57</sup> for carrying out the computational work. The binding energies (B.E.s) of the adducts were calculated by deducting the free energies of the isolated clusters and fullerenes from the total energies of the adducts by using the following formula:  $B.E._{adduct} = E_{adduct} - (xE_{cluster} + yE_{fullerene})$ , where  $x$  and  $y$  are the number of clusters and fullerenes in the adduct, respectively.  $E_{adduct}$ ,  $E_{cluster}$ , and  $E_{fullerene}$  are the lowest energies of the DFT-optimized structures of the adduct, isolated clusters, and isolated fullerenes ( $C_{60}/C_{70}$ ), respectively.

## RESULTS AND DISCUSSION

**Supramolecular Interaction of  $Ag_{25}(DMBT)_{18}^-$  with  $C_{60}$ .**  $[Ag_{25}(DMBT)_{18}]^-$  was synthesized according to the method discussed above in the experimental part and further characterized using UV–vis (Figure S1) and ESI MS (Figure 1Aa).<sup>57</sup> As such data have been published before,<sup>57</sup> we are presenting only essential data in the main text.  $Ag_{25}(DMBT)_{18}$  is referred to as X in the subsequent discussion. Fullerene adducts of the cluster were prepared by mixing solutions of  $C_{60}$  (in toluene) and  $X^-$  (in DCM). The parent cluster ion,  $X^-$ , appeared as a peak at  $m/z$  5167 (Figure 1Aa), and its theoretical and experimental isotopic distributions are presented in the inset (c) of Figure 1A. The structure of the cluster is shown in inset (b) of Figure 1A. The structure was



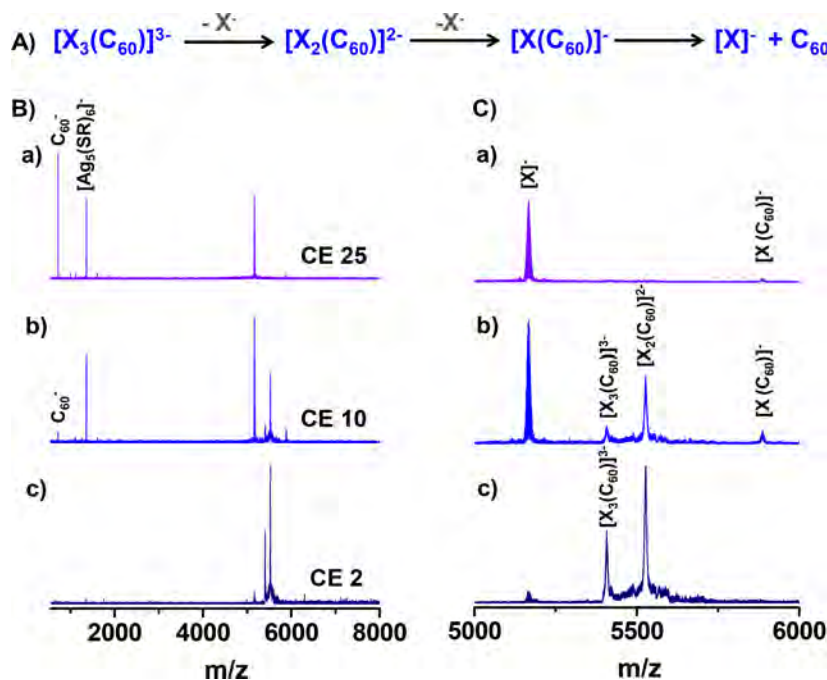


**Figure 2.** (A) Fragmentation pathway of the adduct,  $[X_3(C_{60})]^{3-}$  [ $X = Ag_{25}(DMBT)_{18}$ ]. (B) CID mass spectra of  $[X_3(C_{60})]^{3-}$  and (C) expanded views showing the products of CID in the  $m/z$  range of 5000–6000 at varying C.E.s of 2 (c), 10 (b), and 25 (a). C.E. is in instrumental unit.

optimized using DFT, with initial inputs from the crystal structure.<sup>57</sup> Upon addition of  $C_{60}$ , several new peaks were observed in ESI MS in the  $m/z$  range of 5250–6000 (see Figure 1Ba), which corresponded to the cluster–fullerene complexes. Detailed analysis of the peaks revealed the composition of the adducts as  $[X_4(C_{60})]^{4-}$  ( $m/z$  5347),  $[X_3(C_{60})]^{3-}$  ( $m/z$  5407),  $[X_2(C_{60})]^{2-}$  ( $m/z$  5527),  $[X_5(C_{60})_3]^{5-}$  ( $m/z$  5599),  $[X_3(C_{60})_2]^{3-}$  ( $m/z$  5647),  $[X_4(C_{60})_3]^{4-}$  ( $m/z$  5707), and  $[X_5(C_{60})_4]^{5-}$  ( $m/z$  5743). The composition of some of these adducts may be generalized, such as  $[X_n(C_{60})]^{n-}$  ( $n = 1–4$ ) and  $[X_n(C_{60})_{n-1}]^{n-}$  ( $n = 2–5$ ). Adducts with further higher values of  $n$  were not observed in this case. Probably, such higher adducts were not stable due to Coulombic repulsions between the clusters. The compositions were determined by analyzing the  $m/z$  values, charge states, and isotopic patterns of the peaks. The isotopic distribution of the peak for one of these adducts,  $[X_3(C_{60})]^{3-}$ , is presented in the inset (c) of Figure 1B. The difference between the peaks in the isotopic distribution is  $m/z$  0.33, which confirmed a charge state of 3 $^-$ . The experimental isotopic distribution was comparable to the calculated isotopic distribution of  $[X_3(C_{60})]^{3-}$ , which further confirmed its composition. However, an important aspect to note is the drastic loss of resolution of the adducts, in comparison to the parent cluster, which is partly attributed to the higher charge state of the adducts. ESI MS suggested the attachment of neutral fullerenes to the cluster, but the nature of these adducts was completely different compared to the fullerene adducts of  $[Ag_{29}(BDT)_{12}]^{3-}$ , reported earlier.<sup>47</sup> In the case of  $[Ag_{29}(BDT)_{12}(C_{60})_n]^{3-}$  ( $n = 1–9$ ), the fullerenes covered the surface of a single cluster. For  $X^-$ , in contrast, fullerene-induced aggregation of the clusters occurred. Multiple fullerene attachment to a single cluster was not observed in the case of  $X^-$ . The adduct  $[X_2(C_{60})]^{2-}$  was a fullerene-mediated dimer of the cluster. Similarly, the adducts,  $[X_3(C_{60})]^{3-}$  and  $[X_3(C_{60})_2]^{3-}$ , were trimers, and  $[X_4(C_{60})]^{4-}$  and

$[X_4(C_{60})_3]^{4-}$  were tetramers of the cluster. The peak at  $m/z$  5887 was assigned as  $[X_n(C_{60})_n]^{n-}$  ( $n = 1, 2, 3, \dots$ , etc.). However, due to the poor isotopic resolution of the peak, the limiting value of  $n$  could not be determined accurately. A schematic of aggregate formation between the cluster and  $C_{60}$  is presented in the inset (b) of Figure 1B. Optical absorption showed a slight increase in the absorbance of the cluster upon addition of  $C_{60}$  (Figure S2A), reflecting the effect of such supramolecular complexation in solution. Additional scattering of light by the particulates in the solution may have also resulted in such a phenomenon. However, addition of  $C_{60}$  did not show any significant effect on the emission properties of the cluster (Figure S2B). The cluster–fullerene aggregates were stable when stored under cold conditions at 4 °C, as observed from their optical absorption spectrum, which was almost unaltered even after 7 days (Figure S3).

**CID Studies of the Fullerene Adducts of  $X^-$ .** We performed CID to get further insights into the structure of these adducts. The peak of the adduct,  $[X_3(C_{60})]^{3-}$ , was mass-selected and subjected to collision with Ar gas, confined in the trap chamber of the mass spectrometer. Upon increasing the collision energy (C.E.), stepwise loss of the cluster,  $X^-$ , from the adduct  $[X_3(C_{60})]^{3-}$  (see Figure 2) was observed. The fragmentation pathway is presented in Figure 2A. In the first step, loss of  $X^-$  from  $[X_3(C_{60})]^{3-}$  resulted in the formation of  $[X_2(C_{60})]^{2-}$ . Upon increasing the C.E., further loss of  $X^-$  resulted in the formation of  $[X(C_{60})]^-$ . Finally, at higher C.E.s,  $X^-$  and  $C_{60}^-$  were formed.  $C_{60}^-$  was probably formed by charge transfer from  $X^-$  to  $C_{60}$ .<sup>47</sup> Along with  $C_{60}^-$ ,  $X$  was also formed in this charge transfer process, which being a neutral species was not detected in ESI MS. The CID mass spectra with increasing C.E.s are presented in Figure 2B, and expanded views of the fragment peaks in the  $m/z$  range of 5000–6000 of the corresponding spectra are presented in Figure 2C. At C.E. of 2 also, some extent of fragmentation of  $[X_3(C_{60})]^{3-}$  to  $[X_2(C_{60})]^{2-}$  was observed, as supramolecular adducts are weak

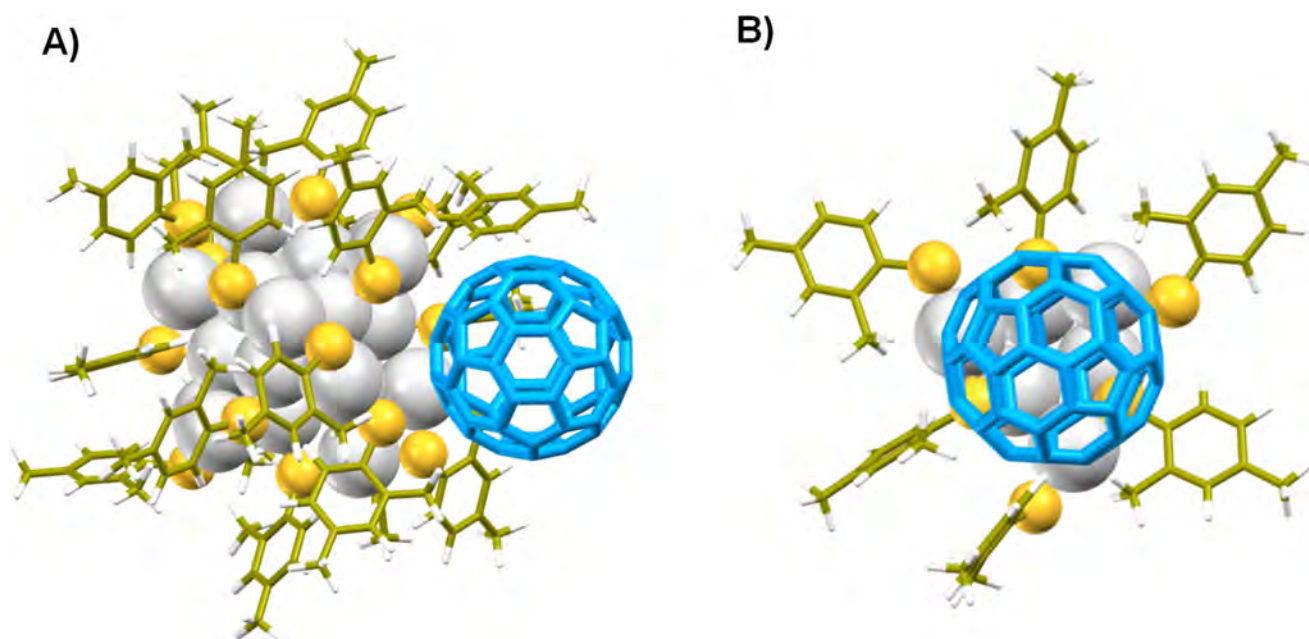


**Figure 3.** (A) Lowest energy structure of the adduct,  $[X(C_{60})]^-$  [ $X = Ag_{25}(DMBT)_{18}$ ], obtained from DFT. (B) Enlarged view of the interaction between  $C_{60}$  attached on the cluster surface and the neighboring DMBT ligands.

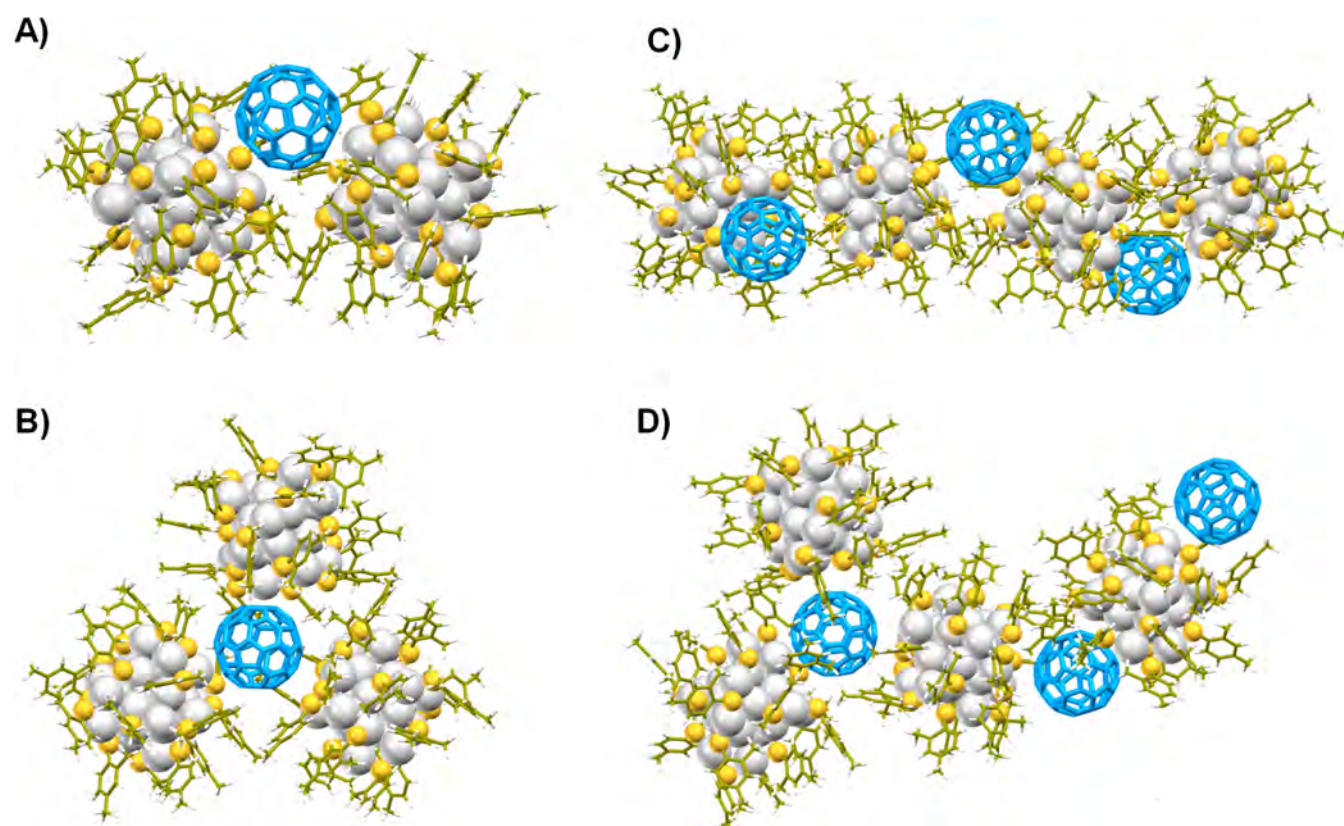


**Figure 4.** Lowest energy structures of (A)  $[X_2(C_{60})]^{2-}$  and (B)  $[X_3(C_{60})]^{3-}$ . Two isomeric structures of  $[X_4(C_{60})_3]^{4-}$  are in (C) and (D) [ $X = Ag_{25}(DMBT)_{18}$ ].

and fragmentation occurs even without any applied C.E. The peak observed for  $Ag_5(SR)_6^-$  was due to the usual fragmentation of the parent cluster.<sup>65</sup> CID studies also revealed the distinct binding modes of complexation of  $C_{60}$  and  $X^-$ , compared to that of the previously reported  $C_{60}$  adducts of  $[Ag_{29}(BDT)_{12}]^{3-}$ .<sup>47</sup> In the case of  $[Ag_{29}(BDT)_{12}(C_{60})_n]^{3-}$  ( $n =$

1–4), where the nanocluster surface was covered by fullerenes, sequential loss of  $C_{60}$  was observed.<sup>47</sup> In contrast, in the case of the adduct  $[X_3(C_{60})]^{3-}$ , sequential loss of the clusters,  $X^-$ , was observed, and  $C_{60}$  was lost only in the final stages. This implied that in the structure of  $[X_3(C_{60})]^{3-}$ ,  $C_{60}$  was probably encapsulated by three clusters. CID of the other adducts like



$[X_4(C_{60})]^{4-}$ , presented in Figure S4, also showed similar fragmentation sequence. Also, at low C.E.,  $[X_4(C_{60})]^{4-}$  showed extensive fragmentation to  $[X_3(C_{60})]^{3-}$ ,  $[X_2(C_{60})]^{2-}$ , and  $[X]^{-}$  indicating that the smaller adducts like  $[X_3(C_{60})]^{3-}$  and  $[X_2(C_{60})]^{2-}$  were probably fragments of the larger adducts.

**Computational Studies to Determine the Structure of Adducts of  $X^{-}$  with  $C_{60}$ .** We carried out molecular docking followed by DFT calculations to investigate the structure of the adducts of  $C_{60}$  and  $X^{-}$ . To determine the lowest energy geometry of the adduct  $[X(C_{60})]^{-}$ ,  $X^{-}$  was used as the receptor, and  $C_{60}$  was used as the free ligand in docking. As molecular docking primarily considers the supramolecular interactions, the lowest energy geometry of  $[X(C_{60})]^{-}$ , obtained from molecular docking, was further optimized using DFT to consider the electronic factors too. The lowest energy structure of  $[X(C_{60})]^{-}$  (Figure 3A) showed that  $C_{60}$  was captured in a cavity on the cluster surface which was enclosed by six 2,4-DMBT ligands. An expanded view of the interactions between the six DMBT ligands and  $C_{60}$ , attached on the cluster surface, is presented in Figure 3B. DFT calculations revealed a binding energy (B.E.) of  $-10.25$  kcal/mol for this adduct. Here, the major forces stabilizing the complex were vdW interactions and  $C-H\cdots\pi$  contacts between the  $-H$  of  $-CH_3$  groups of the ligands and the  $\pi$ -system of  $C_{60}$ . Moreover, it is well-known that metal clusters can also bind to fullerene surfaces.<sup>66</sup> From Figure 3, it is clear that there were strong contacts between the Ag atoms of the cluster and  $C_{60}$ , which contributed ion-induced dipole interactions to the overall stabilization of the complex. Similarly, the structures of the larger adducts were also determined. To determine the structure of  $[X_2(C_{60})]^{2-}$ , the lowest energy structure of  $[X(C_{60})]^{-}$  was chosen as the receptor, and another  $X^{-}$  was chosen as the free ligand in docking. The lowest energy geometry of  $[X_2(C_{60})]^{2-}$  (Figure 4A) showed that  $C_{60}$  interacted with DMBT ligands of two clusters. Similarly, the structure of  $[X_3(C_{60})]^{3-}$  was obtained by docking  $[X_2(C_{60})]^{2-}$  with  $X^{-}$ . The lowest energy structure of  $[X_3(C_{60})]^{3-}$  (Figure 4B) revealed that  $C_{60}$  was indeed encapsulated by three  $X^{-}$  clusters. The surface of  $C_{60}$  was covered by the clusters, and as the clusters remained exposed, they were the first ones to be lost upon increasing C.E. during the CID experiments. The B.E.s for the adducts  $[X_2(C_{60})]^{2-}$  and  $[X_3(C_{60})]^{3-}$  were  $-9.80$  kcal/mol and  $-3.86$  kcal/mol, respectively. The lower B.E. in the case of  $[X_3(C_{60})]^{3-}$  may be attributed to steric factors and an increase in repulsion between the negatively charged clusters, which may reduce the favorable  $C-H\cdots\pi$  interactions.

The structures of the heavier adducts,  $[X_n(C_{60})_{n-1}]^{n-}$  ( $n = 3-4$ ), were obtained only from molecular docking, due to the computational cost involved in DFT. These structures showed two isomeric possibilities in each case. The two isomeric forms of the adduct,  $[X_4(C_{60})_3]^{4-}$ , are presented in Figure 4C and 4D, respectively, where the structure shown in Figure 4D exhibited a greater extent of branching. Similar possibilities of isomerism in the structures of the other adducts like  $[X_3(C_{60})_2]^{3-}$  are presented in Figure S5. In the structures of  $[X_n(C_{60})]^{n-}$  ( $n = 1-3$ ) and  $[X_n(C_{60})_{n-1}]^{n-}$  ( $n = 2-4$ ), some  $C_{60}$ 's were enclosed by the clusters. However, equivalent sites on the cluster surface were free and accessible for the capture of more fullerenes which could further bind more clusters. Thus, these assemblies could extend further, leading to the formation of larger aggregates of such cluster–fullerene complexes.

We further examined the possibilities of such aggregation in the solid state by using TEM. Solutions of cluster–fullerene complexes were drop-casted on TEM grids and examined. TEM studies revealed that the cluster–fullerene adducts were assembled into wire-like structures in the solid state (Figure S6A,B), which was in accordance with the nature of the complexation observed in ESI MS and the structures predicted from theoretical studies. Self-assembly of individual nano-clusters into such a dendritic network of micrometer dimension was recently observed by Musnier et al. by incorporating anisotropic surface charges on atomically precise gold clusters.<sup>67</sup> Here, fullerenes might also act as anisotropic targets, leading to similar assemblies. However, under identical conditions, the parent clusters also assembled into a mixture of wire-like and sheet-like structures (Figure S6C,D). This implied that probably fullerenes enhanced the formation of the linear assemblies of the clusters, resulting in the formation of uniform wire-like structures in the solid state. Specifically, the ion-induced dipole interactions between the Ag atoms of the cluster and  $C_{60}$  might have enhanced the nanowire formation. However, the positions of  $C_{60}$  and the clusters in the assemblies were not resolved from TEM. So, this aspect of assembly formation in the solid state was not probed in further detail in the current study.

**Supramolecular Interaction of  $X^{-}$  with  $C_{70}$ .** We further investigated the interaction of  $X^{-}$  with ellipsoidal-shaped  $C_{70}$ . The similar nature of adducts of  $C_{70}$  with  $X^{-}$  was observed in ESI MS. The adducts,  $[X_4(C_{70})]^{4-}$  ( $m/z$  5376),  $[X_3(C_{70})]^{3-}$  ( $m/z$  5446),  $[X_2(C_{70})]^{2-}$  ( $m/z$  5586),  $[X_5(C_{70})_3]^{5-}$  ( $m/z$  5670),  $[X_3(C_{70})_2]^{3-}$  ( $m/z$  5726),  $[X_4(C_{70})_3]^{4-}$  ( $m/z$  5796),  $[X_5(C_{70})_4]^{5-}$  ( $m/z$  5838), and  $[X_n(C_{70})_n]^{n-}$  ( $m/z$  6006), were formed, as presented in Figure 5(a). Comparison of the

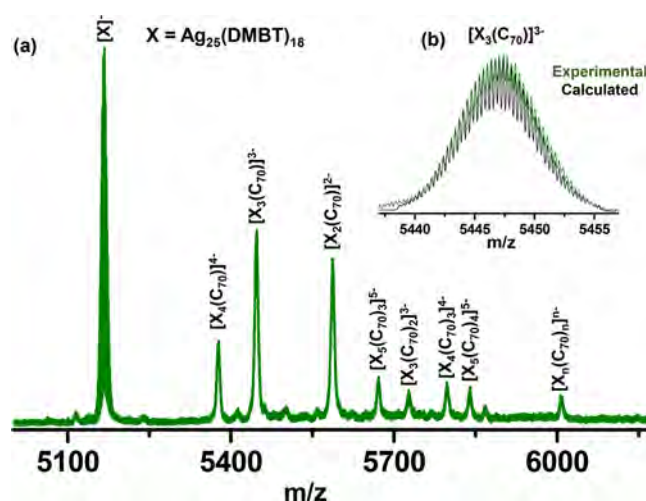


**Figure 5.** ESI MS showing the adducts of  $X^{-}$  and  $C_{70}$  is shown in (a). Inset (b) shows the experimental and theoretical isotopic patterns of one of the adducts,  $[X_3(C_{70})]^{3-}$  [ $X = Ag_{25}(DMBT)_{18}$ ].

experimental and calculated isotopic distributions of one of these adducts,  $[X_3(C_{70})]^{3-}$ , is presented in the inset (b) of Figure 5. We also performed molecular docking followed by DFT calculations to determine the structure of  $[X(C_{70})]^{-}$ . The lowest energy structure, obtained from molecular docking, showed that  $C_{70}$  interacted at a similar site on the cluster surface with its major axis oriented toward the cluster (Figure S7A). The complexation was also stabilized by vdW,  $C-H\cdots\pi$ , and ion-induced dipole interactions. DFT revealed a B.E. value

of  $-7.29$  kcal/mol for the adduct,  $[X(C_{70})]^-$ . However, we also constructed another isomeric structure of  $[X(C_{70})]^-$  with the minor axis of  $C_{70}$  projected toward the cluster and optimized it in DFT (Figure S7B). The B.E. in the case of this isomer was  $-6.15$  kcal/mol, which was slightly lower compared to the B.E. obtained for the lowest energy isomer. The lower B.E.s in the case of  $C_{70}$  compared to that of  $C_{60}$  revealed that larger-sized fullerenes allowed lesser interaction in the case of  $X^-$ .  $C_{70}$  also induced the formation of dendritic assemblies of the cluster in the solid state (Figure S8), but these assemblies were less uniform in their wire-like morphology compared to that of the assemblies of  $C_{60}$ .

**Supramolecular Interaction of  $Au_{25}(PET)_{18}^-$  Cluster with Fullerenes.** We also tried to form similar adducts of fullerene with  $Au_{25}(PET)_{18}^-$ ,<sup>10,58,68</sup> which has a core structure similar to that of  $X^-$  but protected by a different ligand.  $Au_{25}(PET)_{18}$  is referred to as  $Y$  in the subsequent discussion. The  $Y^-$  cluster was synthesized following the method discussed in the Experimental Section and characterized by UV-vis and ESI MS (Figure S9).  $Y^-$  showed the parent cluster ion peak at  $m/z$  7393, as presented in Figure S9B. Upon addition of  $C_{60}$ , several new peaks appeared in ESI MS in the  $m/z$  range 7500–8300, as presented in Figure 6. The fullerene adducts,

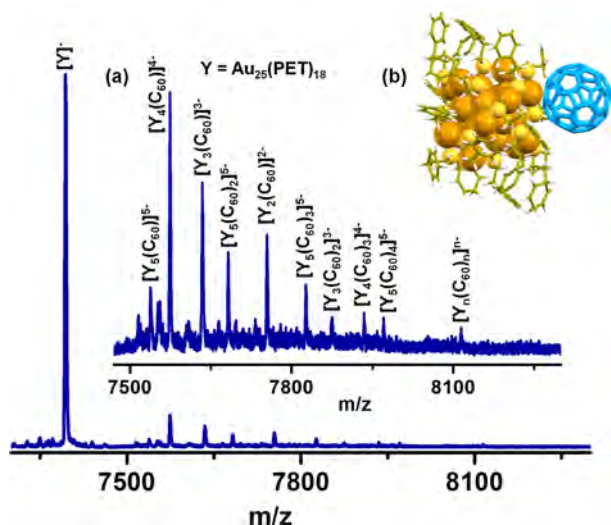


**Figure 6.** ESI MS showing the formation of adducts of  $C_{60}$  with  $Y^-$  ( $Y = Au_{25}(PET)_{18}$ ). Expanded view of adducts in the  $m/z$  range of 7500–8300 is shown in inset (a), and the DFT-optimized lowest energy structure of  $[Y(C_{60})]^-$  is presented in inset (b). Color codes: orange, Au; yellowish-green, C; yellow, S; and white, H.

$[Y_n(C_{60})]^{n-}$  ( $n = 1-5$ ),  $[Y_n(C_{60})_{n-1}]^{n-}$  ( $n = 2-5$ ), and  $[Y_n(C_{60})_n]^{n-}$  ( $n = 1, 2, 3, \dots$ , etc.), observed in the case of  $Y^-$ , were similar to those observed in the case of  $X^-$ . In order to study the nature of complexation and interactions of  $C_{60}$  with  $Y^-$ , we calculated the structure of  $[Y(C_{60})]^-$  using a similar approach used in the case of  $[X(C_{60})]^-$ . The lowest energy structure of  $[Y(C_{60})]^-$  is presented in the inset (b) of Figure 6.  $[Y(C_{60})]^-$  showed a B.E. of  $-12.33$  kcal/mol which was marginally higher compared to the B.E. of  $[X(C_{60})]^-$  ( $-10.25$  kcal/mol). As the nature of complexation in the case of  $[X(C_{60})]^-$  and  $[Y(C_{60})]^-$  was similar and independent of the ligands or the metal atoms, ion-induced dipole interaction was expected to be the major driving force behind this complexation. Similar complexation of  $Y^-$  with  $C_{70}$  was also studied (Figure S10). Our results showed that for an appropriate

geometry of the cluster the complexation was independent of the nature of the metal atoms (Au or Ag), and host–guest complexation was primarily favored by the interaction with the protecting ligands of the cluster and ion-induced dipole interactions.

## CONCLUSIONS

In summary, we demonstrated the assembly of atomically precise clusters with fullerenes,  $C_{60}$  and  $C_{70}$ . Taking  $M_{25}(SR)_{18}^-$  ( $M = Ag, Au$ ) clusters as our model systems of study, we showed that fullerene-mediated dimers and trimers and higher aggregates of the clusters were formed, and the nature of complexation was independent of the nature of metal atoms (Ag or Au). The complexation was favored due to ion-induced dipole interactions between the metal clusters and fullerenes and interaction between the protecting ligands of the cluster and the aromatic surface of the fullerenes. Computational studies also supported the formation of such cluster–fullerene complexes and also predicted the possibility of isomerism in some of these adducts. The present study revealed how variation in the structure of the cluster can induce the formation of a variety of cluster–fullerene adducts. The nature of adducts observed in the case of  $M_{25}(SR)_{18}^-$  ( $M = Ag, Au$ ) was completely different compared to the previously observed adducts of  $[Ag_{29}(BDT)_{12}]^{3-}$  clusters,<sup>47</sup> where multiple fullerenes were attached to an isolated cluster. Also, our work opens up a methodology to create aggregates of clusters by supramolecular interaction with other molecules. Exploring the interaction of a variety of ligand-protected noble metal clusters with fullerenes can bring in more variation in the nature of supramolecular adducts, which will help to create a large family of such cluster–fullerene hybrid systems. Though we have used clusters protected by hydrophobic ligands in this work, these studies may also be extended to water-soluble metal nanoclusters by using suitable phase transfer agents or by using clusters and fullerenes with appropriate functionalization. Moreover, dimers, trimers, and other aggregates with the fullerenes were formed as a mixture in solution, and selective formation of a particular adduct, containing a desired number of clusters, could not be controlled. Future work will involve separating these aggregates to study their physical and chemical properties. The dimers and trimers may show a change in their mechanical or optical properties. Conductivity may also be observed in the fullerene-mediated aggregates of the clusters. Moreover, the chemical properties of these dimers and trimers may also be altered. These aggregates may behave differently in interparticle reactions,<sup>60</sup> compared to the monomers of the clusters. Such cluster–fullerene complexes may find applications in diverse fields such as optoelectronics, solar cells, catalysis, etc.

## ASSOCIATED CONTENT

### Supporting Information

The Supporting Information is available free of charge at <https://pubs.acs.org/doi/10.1021/acs.jpcc.0c03383>.

Optical absorption spectra, additional ESI MS, and computational details (PDF)

## AUTHOR INFORMATION

### Corresponding Author

Thalappil Pradeep – DST Unit of Nanoscience (DST UNS) and Thematic Unit of Excellence (TUE), Department of



Chemistry, Indian Institute of Technology Madras, Chennai 600 036, India; [orcid.org/0000-0003-3174-534X](https://orcid.org/0000-0003-3174-534X);  
Email: [pradeep@iitm.ac.in](mailto:pradeep@iitm.ac.in)

## Authors

**Papri Chakraborty** – DST Unit of Nanoscience (DST UNS) and Thematic Unit of Excellence (TUE), Department of Chemistry, Indian Institute of Technology Madras, Chennai 600 036, India

**Abhijit Nag** – DST Unit of Nanoscience (DST UNS) and Thematic Unit of Excellence (TUE), Department of Chemistry, Indian Institute of Technology Madras, Chennai 600 036, India

**Biswajit Mondal** – DST Unit of Nanoscience (DST UNS) and Thematic Unit of Excellence (TUE), Department of Chemistry, Indian Institute of Technology Madras, Chennai 600 036, India

**Esma Khatun** – DST Unit of Nanoscience (DST UNS) and Thematic Unit of Excellence (TUE), Department of Chemistry, Indian Institute of Technology Madras, Chennai 600 036, India

**Ganesan Paramasivam** – DST Unit of Nanoscience (DST UNS) and Thematic Unit of Excellence (TUE), Department of Chemistry, Indian Institute of Technology Madras, Chennai 600 036, India

Complete contact information is available at:  
<https://pubs.acs.org/10.1021/acs.jpcc.0c03383>

## Notes

The authors declare no competing financial interest.

## ACKNOWLEDGMENTS

Authors thank Dr. Anirban Som, Dr. Ganapati Natarajan, Tripti Ahuja, and Korath Shivan Sugi for their help and suggestions in this work. P.C. thanks the Council of Scientific and Industrial Research (CSIR) for a research fellowship. A.N., B.M., and E.K. thank IIT Madras for their Doctoral fellowship. G.P. thanks IIT Madras for an Institute Postdoctoral fellowship. We thank the Department of Science and Technology, Government of India, for providing funding through the grant SR/NM/NS-05/2014(G).

## REFERENCES

- (1) Chakraborty, P.; Pradeep, T. Atomically Precise Clusters of Noble Metals: Emerging Link between Atoms and Nanoparticles. *Chem. Rev.* **2017**, *117*, 8208–8271.
- (2) Jin, R.; Zeng, C.; Zhou, M.; Chen, Y. Atomically Precise Colloidal Metal Nanoclusters and Nanoparticles: Fundamentals and Opportunities. *Chem. Rev.* **2016**, *116*, 10346–10413.
- (3) Maity, P.; Xie, S.; Yamauchi, M.; Tsukuda, T. Stabilized Gold Clusters: From Isolation Toward Controlled Synthesis. *Nanoscale* **2012**, *4*, 4027–4037.
- (4) Song, X.-R.; Goswami, N.; Yang, H.-H.; Xie, J. Functionalization of Metal Nanoclusters for Biomedical Applications. *Analyst* **2016**, *141*, 3126–3140.
- (5) Du, X.; Jin, R. Atomically Precise Metal Nanoclusters for Catalysis. *ACS Nano* **2019**, *13*, 7383–7387.
- (6) Ghosh, A.; Mohammed, O. F.; Bakr, O. M. Atomic-Level Doping of Metal Clusters. *Acc. Chem. Res.* **2018**, *51*, 3094–3103.
- (7) Kurashige, W.; Niihori, Y.; Sharma, S.; Negishi, Y. Precise Synthesis, Functionalization and Application of Thiolate-Protected Gold Clusters. *Coord. Chem. Rev.* **2016**, *320–321*, 238–250.
- (8) Du, Y.; Sheng, H.; Astruc, D.; Zhu, M. Atomically Precise Noble Metal Nanoclusters as Efficient Catalysts: A Bridge between Structure and Properties. *Chem. Rev.* **2020**, *120*, 526–622.

- (9) Knoppe, S.; Bürgi, T. Chirality in Thiolate-Protected Gold Clusters. *Acc. Chem. Res.* **2014**, *47*, 1318–1326.
- (10) Zhu, M.; Aikens, C. M.; Hollander, F. J.; Schatz, G. C.; Jin, R. Correlating the Crystal Structure of a Thiol-Protected Au<sub>25</sub> Cluster and Optical Properties. *J. Am. Chem. Soc.* **2008**, *130*, 5883–5885.
- (11) Yang, H.; Wang, Y.; Huang, H.; Gell, L.; Lehtovaara, L.; Malola, S.; Häkkinen, H.; Zheng, N. All-Thiol-Stabilized Ag<sub>44</sub> and Au<sub>12</sub>Ag<sub>32</sub> Nanoparticles with Single-Crystal Structures. *Nat. Commun.* **2013**, *4*, 2422.
- (12) Yan, N.; Xia, N.; Liao, L.; Zhu, M.; Jin, F.; Jin, R.; Wu, Z. Unraveling the Long-Pursued Au<sub>144</sub> Structure by X-Ray Crystallography. *Sci. Adv.* **2018**, *4*, eaat7259.
- (13) Chen, T.; Yao, Q.; Nasaruddin, R. R.; Xie, J. Electrospray Ionization Mass Spectrometry: A Powerful Platform for Noble-Metal Nanocluster Analysis. *Angew. Chem., Int. Ed.* **2019**, *58*, 11967–11977.
- (14) Chakraborty, P.; Pradeep, T. The Emerging Interface of Mass Spectrometry with Materials. *NPG Asia Mater.* **2019**, *11*, 48.
- (15) Chakraborty, P.; Nag, A.; Chakraborty, A.; Pradeep, T. Approaching Materials with Atomic Precision Using Supramolecular Cluster Assemblies. *Acc. Chem. Res.* **2019**, *52*, 2–11.
- (16) Kang, X.; Zhu, M. Intra-Cluster Growth Meets Inter-Cluster Assembly: The Molecular and Supramolecular Chemistry of Atomically Precise Nanoclusters. *Coord. Chem. Rev.* **2019**, *394*, 1–38.
- (17) Wu, Z.; Yao, Q.; Zang, S.; Xie, J. Directed Self-Assembly of Ultrasmall Metal Nanoclusters. *ACS Mater. Lett.* **2019**, *1*, 237–248.
- (18) Nonappa; Ikkala, O. Hydrogen Bonding Directed Colloidal Self-Assembly of Nanoparticles into 2D Crystals, Capsids, and Supracolloidal Assemblies. *Adv. Funct. Mater.* **2018**, *28*, 1704328.
- (19) Rival, J. V.; Nonappa; Shibu, E. S. Light-Triggered Reversible Supracolloidal Self-Assembly of Precision Gold Nanoclusters. *ACS Appl. Mater. Interfaces* **2020**, *12*, 14569–14577.
- (20) Shen, J.; Wang, Z.; Sun, D.; Liu, G.; Yuan, S.; Kurmoo, M.; Xin, X. Self-Assembly of Water-Soluble Silver Nanoclusters: Superstructure Formation and Morphological Evolution. *Nanoscale* **2017**, *9*, 19191–19200.
- (21) Zeng, C.; Chen, Y.; Kirschbaum, K.; Lambright, K. J.; Jin, R. Emergence of Hierarchical Structural Complexities in Nanoparticles and their Assembly. *Science* **2016**, *354*, 1580–1584.
- (22) Gan, Z.; Chen, J.; Wang, J.; Wang, C.; Li, M.-B.; Yao, C.; Zhuang, S.; Xu, A.; Li, L.; Wu, Z. The Fourth Crystallographic Closest Packing Unveiled in the Gold Nanocluster Crystal. *Nat. Commun.* **2017**, *8*, 14739.
- (23) Nag, A.; Chakraborty, P.; Bodiuzzaman, M.; Ahuja, T.; Antharjanam, S.; Pradeep, T. Polymorphism of Ag<sub>29</sub>(BDT)<sub>12</sub>(TPP)<sub>4</sub><sup>3−</sup> Cluster: Interactions of Secondary Ligands and Their Effect on Solid State Luminescence. *Nanoscale* **2018**, *10*, 9851–9855.
- (24) Baksi, A.; Chakraborty, P.; Bhat, S.; Natarajan, G.; Pradeep, T. [Au<sub>25</sub>(SR)<sub>18</sub>]<sub>2</sub><sup>2−</sup>: A Noble Metal Cluster Dimer in the Gas Phase. *Chem. Commun.* **2016**, *52*, 8397–8400.
- (25) De Nardi, M.; Antonello, S.; Jiang, D.-e.; Pan, F.; Rissanen, K.; Ruzzi, M.; Venzo, A.; Zoleo, A.; Maran, F. Gold Nanowired: A Linear (Au<sub>25</sub>)<sub>n</sub> Polymer from Au<sub>25</sub> Molecular Clusters. *ACS Nano* **2014**, *8*, 8505–8512.
- (26) Hossain, S.; Imai, Y.; Motohashi, Y.; Chen, Z.; Suzuki, D.; Suzuki, T.; Kataoka, Y.; Hirata, M.; Ono, T.; Kurashige, W.; et al. Understanding and Designing One-Dimensional Assemblies of Ligand-Protected Metal Nanoclusters. *Mater. Horiz.* **2020**, *7*, 796–803.
- (27) Wen, Z.-R.; Guan, Z.-J.; Zhang, Y.; Lin, Y.-M.; Wang, Q.-M. [Au<sub>7</sub>Ag<sub>9</sub>(Dppf)<sub>3</sub>(CF<sub>3</sub>CO<sub>2</sub>)<sub>7</sub>BF<sub>4</sub>]<sub>n</sub>: A Linear Nanocluster Polymer from Molecular Au<sub>7</sub>Ag<sub>8</sub> Clusters Covalently Linked by Silver Atoms. *Chem. Commun.* **2019**, *55*, 12992–12995.
- (28) Chakraborty, P.; Baksi, A.; Mudedla, S. K.; Nag, A.; Paramasivam, G.; Subramanian, V.; Pradeep, T. Understanding Proton Capture and Cation-Induced Dimerization of [Ag<sub>29</sub>(BDT)<sub>12</sub>]<sup>3−</sup> Clusters by Ion Mobility Mass Spectrometry. *Phys. Chem. Chem. Phys.* **2018**, *20*, 7593–7603.

- (29) Wei, X.; Kang, X.; Yuan, Q.; Qin, C.; Jin, S.; Wang, S.; Zhu, M. Capture of Cesium Ions with Nanoclusters: Effects on Inter- and Intramolecular Assembly. *Chem. Mater.* **2019**, *31*, 4945–4952.
- (30) Chandra, S.; Nonappa; Beaune, G.; Som, A.; Zhou, S.; Lahtinen, J.; Jiang, H.; Timonen, J. V. I.; Ikkala, O.; Ras, R. H. A. Highly Luminescent Gold Nanocluster Frameworks. *Adv. Opt. Mater.* **2019**, *7*, 1900620.
- (31) Huang, H.-Y.; Cai, K.-B.; Talite, M. J.; Chou, W.-C.; Chen, P.-W.; Yuan, C.-T. Coordination-Induced Emission Enhancement in Gold Nanoclusters with Solid-State Quantum Yields up to 40% for Eco-Friendly, Low-Reabsorption Nano-Phosphors. *Sci. Rep.* **2019**, *9*, 4053.
- (32) Gayen, C.; Basu, S.; Goswami, U.; Paul, A. Visible Light Excitation-Induced Luminescence from Gold Nanoclusters Following Surface Ligand Complexation with  $\text{Zn}^{2+}$  for Daylight Sensing and Cellular Imaging. *Langmuir* **2019**, *35*, 9037–9043.
- (33) Shi, J.-F.; Gao, X.-L.; Feng, Y.-H.; Zhou, K.; Ji, J.-Y.; Bi, Y.-F. A  $\{\text{Ag}_{17}\text{S}_8\}$  Cluster-Based Coordination Polymer Linked by Bridging  $\text{CO}_3^{2-}$  Ligands. *Inorg. Chim. Acta* **2019**, *497*, 119107.
- (34) Nonappa; Lahtinen, T.; Haataja, J. S.; Tero, T.-R.; Häkkinen, H.; Ikkala, O. Template-Free Supracolloidal Self-Assembly of Atomically Precise Gold Nanoclusters: From 2D Colloidal Crystals to Spherical Capsids. *Angew. Chem., Int. Ed.* **2016**, *55*, 16035–16038.
- (35) Lahtinen, T.; Hulkko, E.; Sokolowska, K.; Tero, T.-R.; Saarnio, V.; Lindgren, J.; Pettersson, M.; Häkkinen, H.; Lehtovaara, L. Covalently Linked Multimers of Gold Nanoclusters  $\text{Au}_{102}(\text{p-MBA})_{44}$  and  $\text{Au}_{250}(\text{p-MBA})_n$ . *Nanoscale* **2016**, *8*, 18665–18674.
- (36) Sokolowska, K.; Luan, Z.; Hulkko, E.; Rameshan, C.; Barrabès, N.; Apkarian, V. A.; Lahtinen, T. Chemically Selective Imaging of Individual Bonds through Scanning Electron Energy-Loss Spectroscopy: Disulfide Bridges Linking Gold Nanoclusters. *J. Phys. Chem. Lett.* **2020**, *11*, 796–799.
- (37) Bodiuzzaman, M.; Nag, A.; Pradeep Narayanan, R.; Chakraborty, A.; Bag, R.; Paramasivam, G.; Natarajan, G.; Sekar, G.; Ghosh, S.; Pradeep, T. A Covalently Linked Dimer of  $[\text{Ag}_{25}(\text{DMBT})_{18}]^-$ . *Chem. Commun.* **2019**, *55*, 5025–5028.
- (38) Sels, A.; Salassa, G.; Cousin, F.; Lee, L.-T.; Bürgi, T. Covalently Bonded Multimers of  $\text{Au}_{25}(\text{SBut})_{18}$  as a Conjugated System. *Nanoscale* **2018**, *10*, 12754–12762.
- (39) Alhilaly, M. J.; Huang, R.-W.; Naphade, R.; Alamer, B.; Hedhili, M. N.; Emwas, A.-H.; Maity, P.; Yin, J.; Shkurenko, A.; Mohammed, O. F.; et al. Assembly of Atomically Precise Silver Nanoclusters into Nanocluster-Based Frameworks. *J. Am. Chem. Soc.* **2019**, *141*, 9585–9592.
- (40) Wu, X.-H.; Luo, P.; Wei, Z.; Li, Y.-Y.; Huang, R.-W.; Dong, X.-Y.; Li, K.; Zang, S.-Q.; Tang, B. Z. Guest-Triggered Aggregation-Induced Emission in Silver Chalcogenolate Cluster Metal–Organic Frameworks. *Adv. Sci.* **2019**, *6*, 1801304.
- (41) Huang, R.-W.; Wei, Y.-S.; Dong, X.-Y.; Wu, X.-H.; Du, C.-X.; Zang, S.-Q.; Mak, T. C. W. Hypersensitive Dual-Function Luminescence Switching of a Silver-Chalcogenolate Cluster-Based Metal–Organic Framework. *Nat. Chem.* **2017**, *9*, 689–697.
- (42) Sun, L.; Yun, Y.; Sheng, H.; Du, Y.; Ding, Y.; Wu, P.; Li, P.; Zhu, M. Rational Encapsulation of Atomically Precise Nanoclusters into Metal–Organic Frameworks by Electrostatic Attraction for  $\text{CO}_2$  Conversion. *J. Mater. Chem. A* **2018**, *6*, 15371–15376.
- (43) Mathew, A.; Natarajan, G.; Lehtovaara, L.; Häkkinen, H.; Kumar, R. M.; Subramanian, V.; Jaleel, A.; Pradeep, T. Supramolecular Functionalization and Concomitant Enhancement in Properties of  $\text{Au}_{25}$  Clusters. *ACS Nano* **2014**, *8*, 139–152.
- (44) Nag, A.; Chakraborty, P.; Paramasivam, G.; Bodiuzzaman, M.; Natarajan, G.; Pradeep, T. Isomerism in Supramolecular Adducts of Atomically Precise Nanoparticles. *J. Am. Chem. Soc.* **2018**, *140*, 13590–13593.
- (45) Bhunia, S.; Kumar, S.; Purkayastha, P. Gold Nanocluster-Grafted Cyclodextrin Suprastructures: Formation of Nanospheres to Nanocubes with Intriguing Photophysics. *ACS Omega* **2018**, *3*, 1492–1497.
- (46) Yan, C.; Liu, C.; Abroshan, H.; Li, Z.; Qiu, R.; Li, G. Surface Modification of Adamantane-Terminated Gold Nanoclusters Using Cyclodextrins. *Phys. Chem. Chem. Phys.* **2016**, *18*, 23358–23364.
- (47) Chakraborty, P.; Nag, A.; Paramasivam, G.; Natarajan, G.; Pradeep, T. Fullerene-Functionalized Monolayer-Protected Silver Clusters:  $[\text{Ag}_{29}(\text{BDT})_{12}(\text{C}_{60})_n]^{3-}$  ( $n = 1–9$ ). *ACS Nano* **2018**, *12*, 2415–2425.
- (48) Chakraborty, P.; Nag, A.; Sugi, K. S.; Ahuja, T.; Varghese, B.; Pradeep, T. Crystallization of a Supramolecular Coassembly of an Atomically Precise Nanoparticle with a Crown Ether. *ACS Mater. Lett.* **2019**, *1*, 534–540.
- (49) Muhammed, M. A. H.; Cruz, L. K.; Emwas, A.-H.; El-Zohry, A. M.; Moosa, B.; Mohammed, O. F.; Khashab, N. M. Pillar[5]Arene-Stabilized Silver Nanoclusters: Extraordinary Stability and Luminescence Enhancement Induced by Host–Guest Interactions. *Angew. Chem., Int. Ed.* **2019**, *58*, 15665–15670.
- (50) Wang, J.; Lin, X.; Shu, T.; Su, L.; Liang, F.; Zhang, X. Self-Assembly of Metal Nanoclusters for Aggregation-Induced Emission. *Int. J. Mol. Sci.* **2019**, *20*, 1891.
- (51) Haddon, R. C. Electronic Structure, Conductivity and Superconductivity of Alkali Metal Doped ( $\text{C}_{60}$ ). *Acc. Chem. Res.* **1992**, *25*, 127–133.
- (52) Wang, Y.; Cheng, L. T. Nonlinear Optical Properties of Fullerenes and Charge-Transfer Complexes of Fullerenes. *J. Phys. Chem.* **1992**, *96*, 1530–1532.
- (53) Holczer, K.; Klein, O.; Huang, S.-m.; Kaner, R. B.; Fu, K.-j.; Whetten, R. L.; Diederich, F. Alkali-Fulleride Superconductors: Synthesis, Composition, and Diamagnetic Shielding. *Science* **1991**, *252*, 1154.
- (54) Pinkard, A.; Champsaur, A. M.; Roy, X. Molecular Clusters: Nanoscale Building Blocks for Solid-State Materials. *Acc. Chem. Res.* **2018**, *51*, 919–929.
- (55) Roy, X.; Lee, C.-H.; Crowther, A. C.; Schenck, C. L.; Besara, T.; Lalancette, R. A.; Siegrist, T.; Stephens, P. W.; Brus, L. E.; Kim, P.; et al. Nanoscale Atoms in Solid-State Chemistry. *Science* **2013**, *341*, 157.
- (56) Schulz-Dobrick, M.; Jansen, M. Intercluster Compounds Consisting of Gold Clusters and Fullerides:  $[\text{Au}_7(\text{PPh}_3)_7]\text{C}_{60}\cdot\text{THF}$  and  $[\text{Au}_8(\text{PPh}_3)_8](\text{C}_{60})_2$ . *Angew. Chem., Int. Ed.* **2008**, *47*, 2256–2259.
- (57) Joshi, C. P.; Bootharaju, M. S.; Alhilaly, M. J.; Bakr, O. M.  $[\text{Ag}_{25}(\text{SR})_{18}]^-$ : The “Golden” Silver Nanoparticle. *J. Am. Chem. Soc.* **2015**, *137*, 11578–11581.
- (58) Heaven, M. W.; Dass, A.; White, P. S.; Holt, K. M.; Murray, R. W. Crystal Structure of the Gold Nanoparticle  $[\text{N}(\text{C}_8\text{H}_{17})_4][\text{Au}_{25}(\text{SCH}_2\text{CH}_2\text{Ph})_{18}]$ . *J. Am. Chem. Soc.* **2008**, *130*, 3754–3755.
- (59) Zhu, M.; Lanni, E.; Garg, N.; Bier, M. E.; Jin, R. Kinetically Controlled, High-Yield Synthesis of  $\text{Au}_{25}$  Clusters. *J. Am. Chem. Soc.* **2008**, *130*, 1138–1139.
- (60) Krishnadas, K. R.; Ghosh, A.; Bakshi, A.; Chakraborty, I.; Natarajan, G.; Pradeep, T. Intercluster Reactions between  $\text{Au}_{25}(\text{SR})_{18}$  and  $\text{Ag}_{44}(\text{SR})_{30}$ . *J. Am. Chem. Soc.* **2016**, *138*, 140–148.
- (61) Morris, G. M.; Huey, R.; Lindstrom, W.; Sanner, M. F.; Belew, R. K.; Goodsell, D. S.; Olson, A. J. Autodock4 and Autodocktools4: Automated Docking with Selective Receptor Flexibility. *J. Comput. Chem.* **2009**, *30*, 2785–2791.
- (62) Mortensen, J. J.; Hansen, L. B.; Jacobsen, K. W. Real-Space Grid Implementation of the Projector Augmented Wave Method. *Phys. Rev. B: Condens. Matter Mater. Phys.* **2005**, *71*, No. 035109.
- (63) Enkovaara, J.; Rostgaard, C.; Mortensen, J. J.; Chen, J.; Dułak, M.; Ferrighi, L.; Gavnholt, J.; Glinosvad, C.; Haikola, V.; Hansen, H. A.; et al. Electronic Structure Calculations with Gpaw: A Real-Space Implementation of the Projector Augmented-Wave Method. *J. Phys.: Condens. Matter* **2010**, *22*, 253202.
- (64) Perdew, J. P.; Burke, K.; Ernzerhof, M. Generalized Gradient Approximation Made Simple. *Phys. Rev. Lett.* **1996**, *77*, 3865–3868.
- (65) Chakraborty, P.; Bakshi, A.; Khatun, E.; Nag, A.; Ghosh, A.; Pradeep, T. Dissociation of Gas Phase Ions of Atomically Precise



Silver Clusters Reflects Their Solution Phase Stability. *J. Phys. Chem. C* **2017**, *121*, 10971–10981.

(66) Dugourd, P.; Antoine, R.; Rayane, D.; Compagnon, I.; Broyer, M. Enhanced Electric Polarizability in Metal  $C_{60}$  Compounds: Formation of a Sodium Droplet on  $C_{60}$ . *J. Chem. Phys.* **2001**, *114*, 1970–1973.

(67) Musnier, B.; Wegner, K. D.; Comby-Zerbino, C.; Trouillet, V.; Jourdan, M.; Häusler, I.; Antoine, R.; Coll, J.-L.; Resch-Genger, U.; Le Guével, X. High Photoluminescence of Shortwave Infrared-Emitting Anisotropic Surface Charged Gold Nanoclusters. *Nanoscale* **2019**, *11*, 12092–12096.

(68) Kang, X.; Chong, H.; Zhu, M.  $Au_{25}(SR)_{18}$ : The Captain of the Great Nanocluster Ship. *Nanoscale* **2018**, *10*, 10758–10834.

## Supporting information

# Fullerene-Mediated Aggregation of $M_{25}(SR)_{18}^-$ (M = Ag, Au) Nanoclusters

*Papri Chakraborty, Abhijit Nag, Biswajit Mondal, Esma Khatun, Ganesan Paramasivam, and Thalappil Pradeep\**

DST Unit of Nanoscience (DST UNS) and Thematic Unit of Excellence (TUE), Department of Chemistry, Indian Institute of Technology Madras, Chennai 600 036, India.

\*E-mail: [pradeep@iitm.ac.in](mailto:pradeep@iitm.ac.in)

## Table of Contents

List of figures	Description	Page no.
Figure S1	UV-vis of $Ag_{25}(DMBT)_{18}^-$	S2
Figure S2	UV-vis and emission spectra of cluster-fullerene mixture	S2
Figure S3	UV-vis spectra of the cluster-fullerene aggregates showing their stability up to 7 days	S3
Figure S4	CID of $[X_4(C_{60})]^{4-}$ [ $X=Ag_{25}(DMBT)_{18}$ ]	S3
Figure S5	Computational structures of $[X_3(C_{60})_2]^{3-}$	S4
Figure S6	TEM images of the assemblies of cluster-fullerene complexes and cluster alone	S5
Figure S7	DFT optimized structures of $[X(C_{70})]^-$ ( $X=Ag_{25}(DMBT)_{18}$ )	S6
Figure S8	TEM images of the assemblies of $Ag_{25}(DMBT)_{18}$ and $C_{70}$	S6
Figure S9	UV-vis and ESI MS of $Au_{25}(PET)_{18}^-$	S7
Figure S10	ESI MS showing adducts of $Au_{25}(PET)_{18}^-$ with $C_{70}$	S7

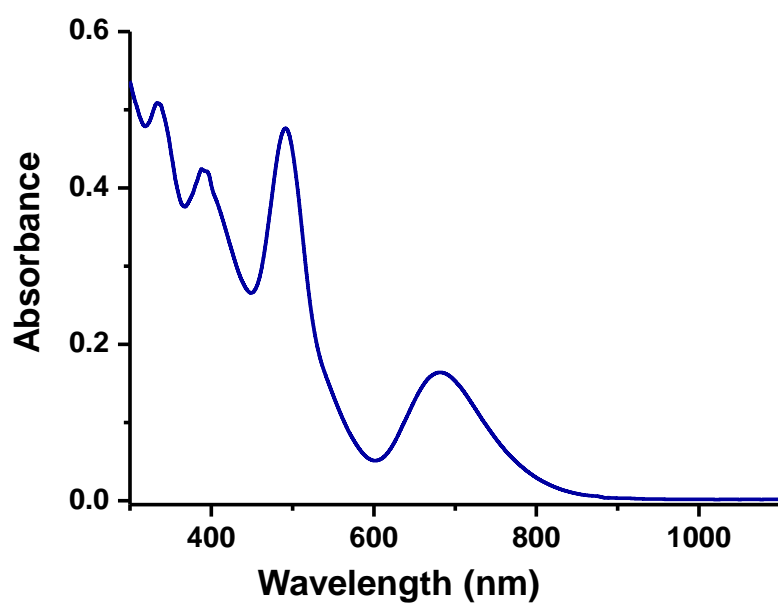


**Figure S1.** UV-vis spectrum of  $[\text{Ag}_{25}(\text{DMBT})_{18}]^-$ .

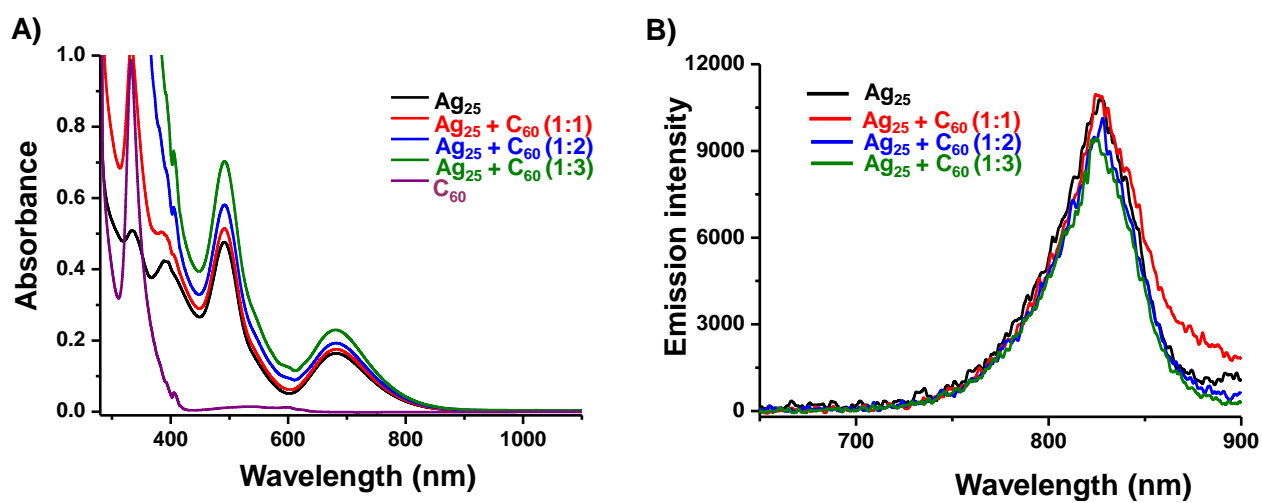


**Figure S2.** (A) UV-vis and (B) emission spectra of the cluster-fullerene mixture at different molar ratios of mixing.

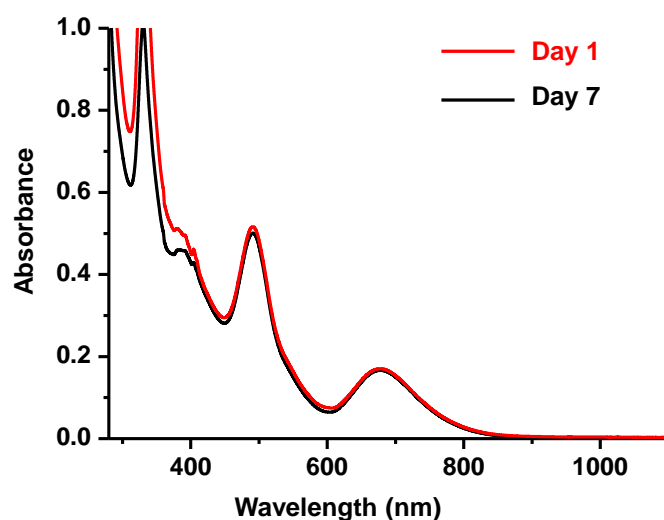


**Figure S3.** UV-vis spectra of the cluster-fullerene aggregates showing their stability up to 7 days.

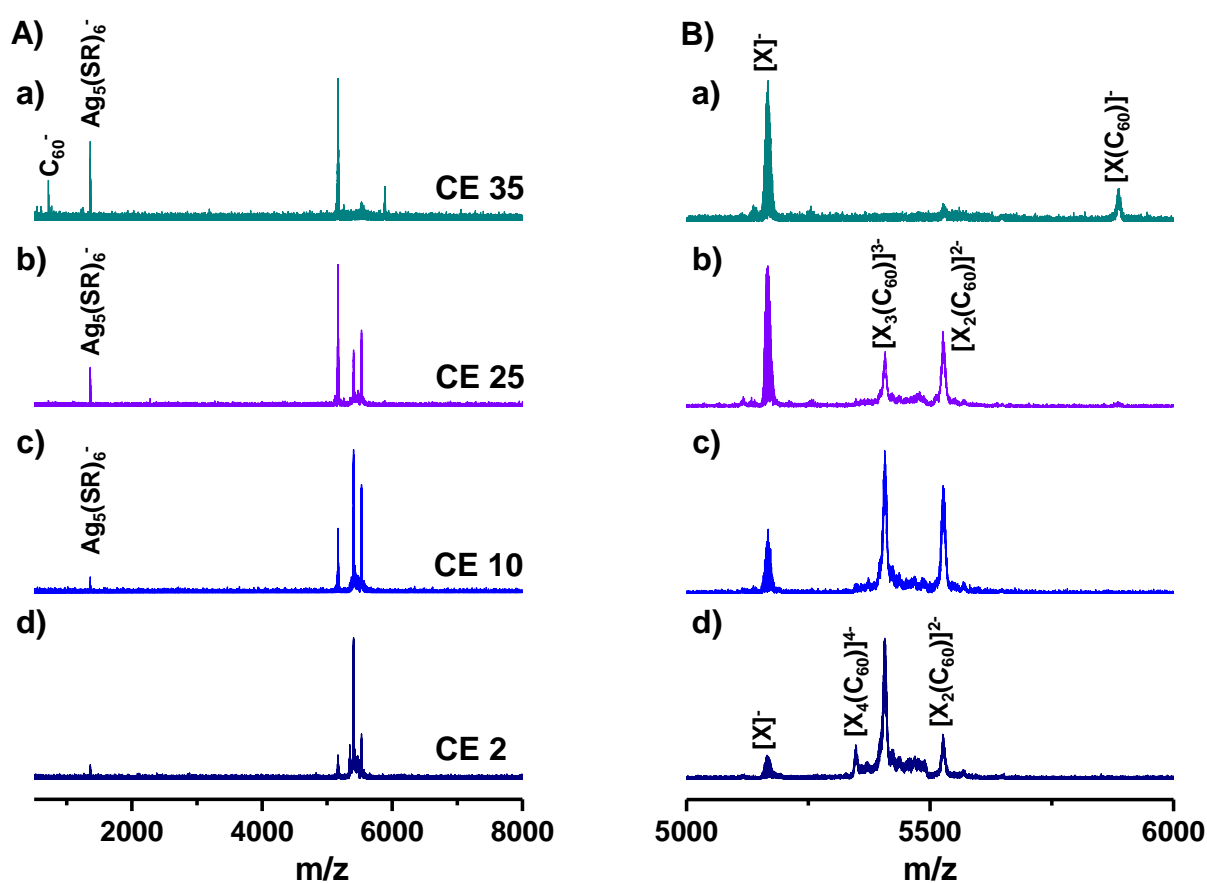


**Figure S4.** (A) CID mass spectra of  $[X_4(C_{60})]^{4-}$  and (B) expanded view showing the products of CID in the  $m/z$  range 5000-6000 at varying C.E.s of 2 (d), 10 (c), 25 (b) and 35 (a) (SR = 2, 4 - DMBT).

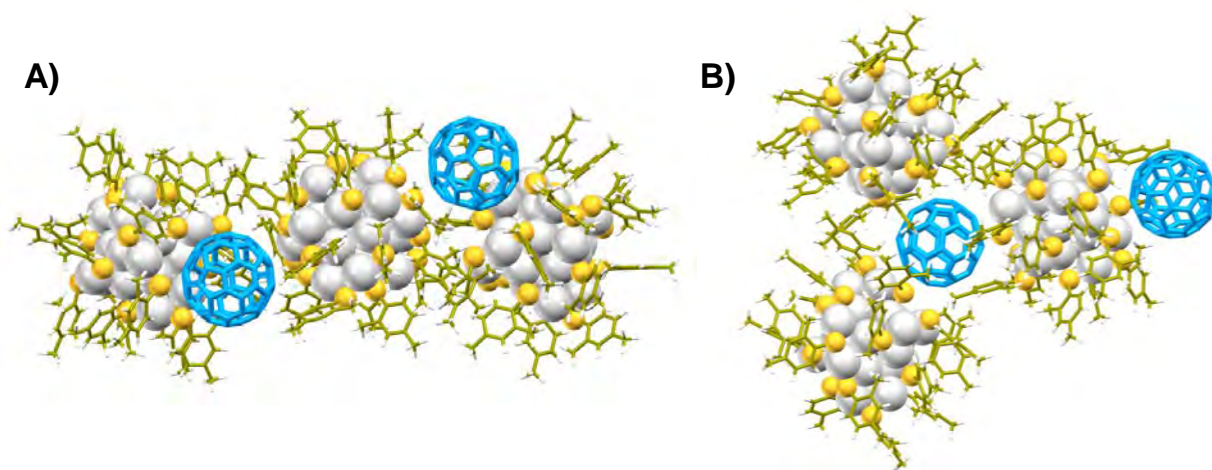


**Figure S5.** Two isomeric structures of  $[X_3(C_{60})_2]^{3-}$  where (A) shows linear structure and (B) shows branched structure of the adduct.  $[X = Ag_{25}(DMBT)_{18}]$

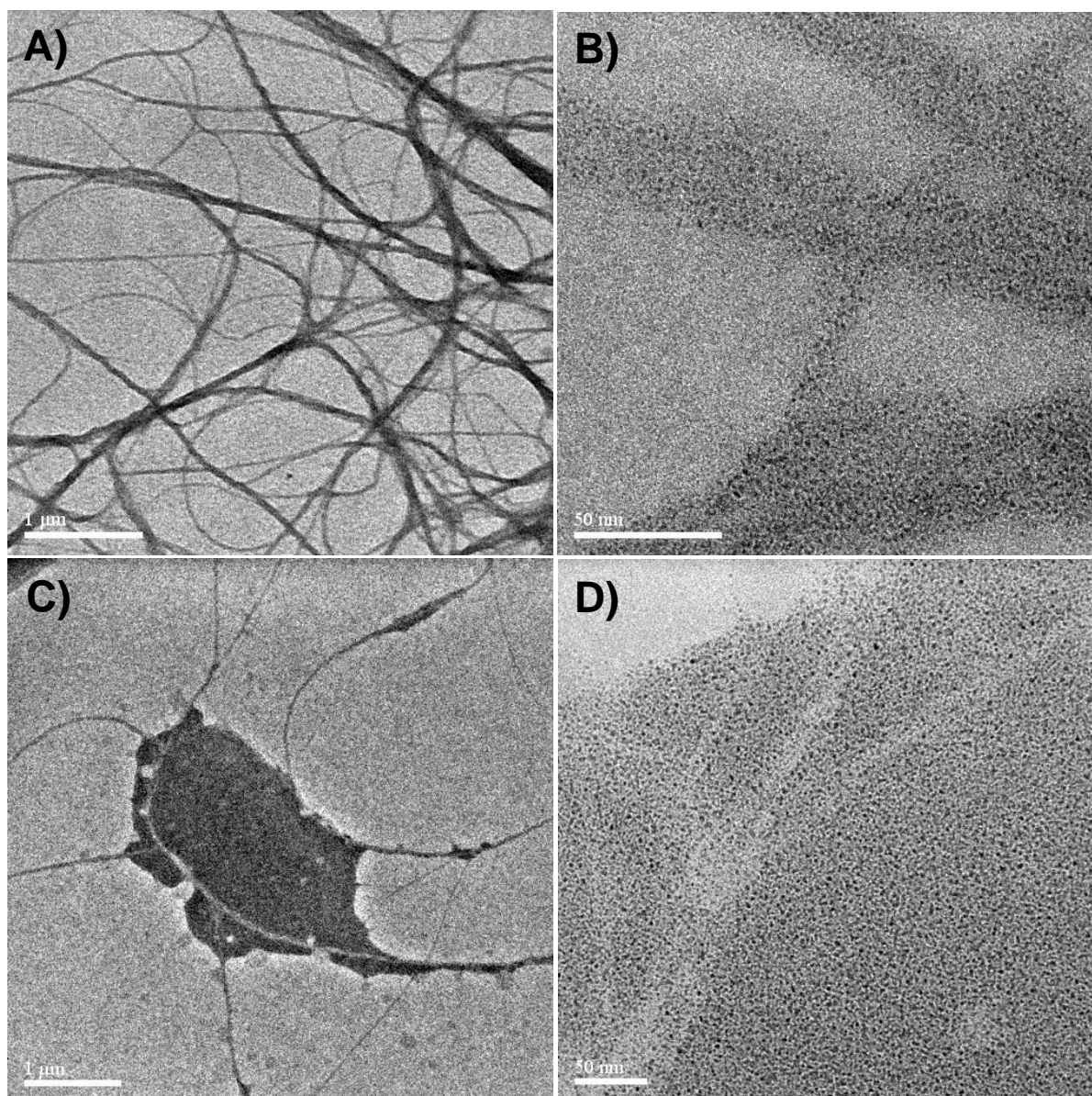


**Figure S6.** TEM image of assemblies of (A, B)  $[\text{Ag}_{25}(\text{DMBT})_{18}]^+$  cluster and  $\text{C}_{60}$  at 1:1 molar ratio of mixing and (C, D)  $[\text{Ag}_{25}(\text{DMBT})_{18}]^+$  cluster alone. B and D are higher magnification images of A and C, showing the cluster- $\text{C}_{60}$  wires and cluster sheets, respectively. The concentrations of the solutions were ~1 mM and the assemblies were studied in DCM-toluene mixture in both the cases.



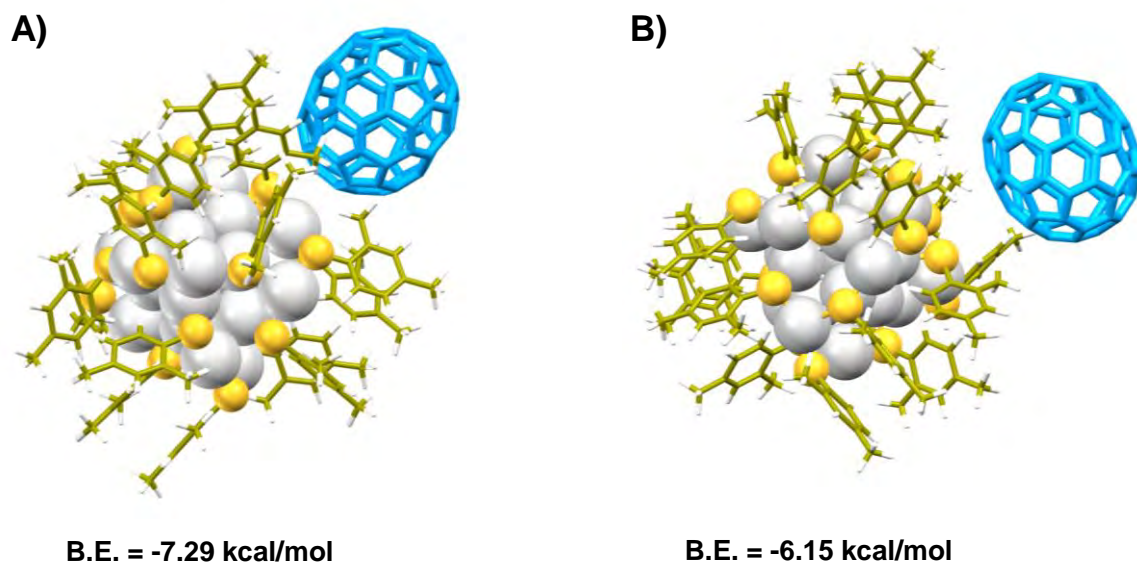


**Figure S7.** DFT optimized structures of  $[X(C_{70})]^-$  ( $X=Ag_{25}(DMBT)_{18}$ ) with A) major axis and B) minor axis of  $C_{70}$  oriented toward the cluster.

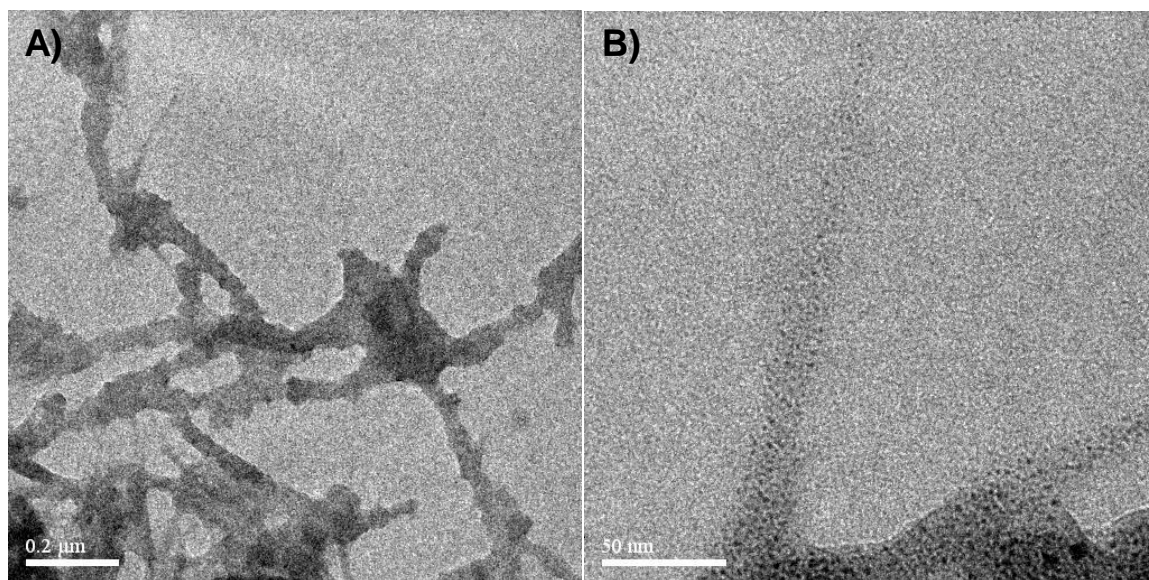


**Figure S8.** A) TEM image of the assemblies of  $[Ag_{25}(DMBT)_{18}]^-$  and  $C_{70}$  and B) is a higher magnification image of the assemblies.

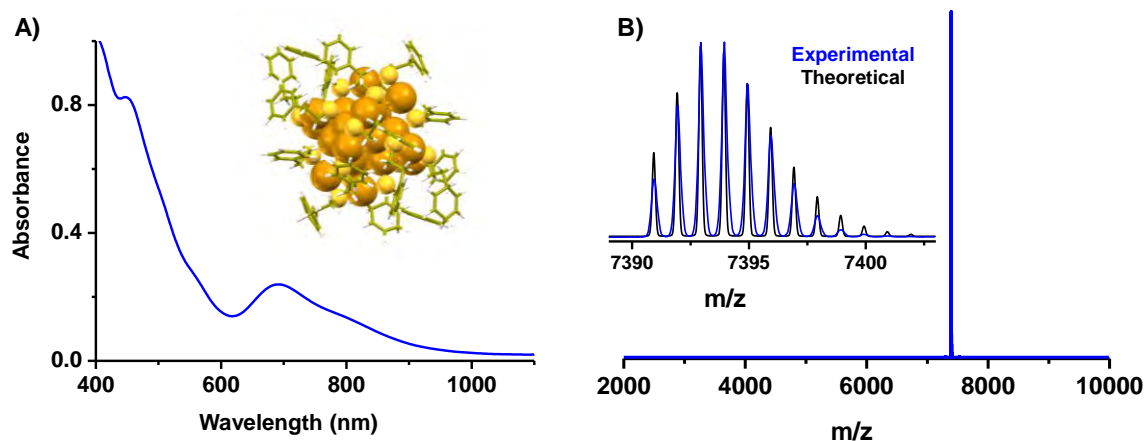


**Figure S9.** (A) UV-vis spectrum of  $[\text{Au}_{25}(\text{PET})_{18}]^-$ . Inset shows the structure of the cluster (modelled using the co-ordinates from its crystal structure). (B) ESI MS of  $\text{Au}_{25}(\text{PET})_{18}^-$  cluster showing molecular ion peak at  $m/z$  7393. Inset shows the comparison of the experimental and theoretical isotope patterns of  $[\text{Au}_{25}(\text{PET})_{18}]^-$ . Color codes: orange: Au, yellow: S, yellowish green: C and white: H.

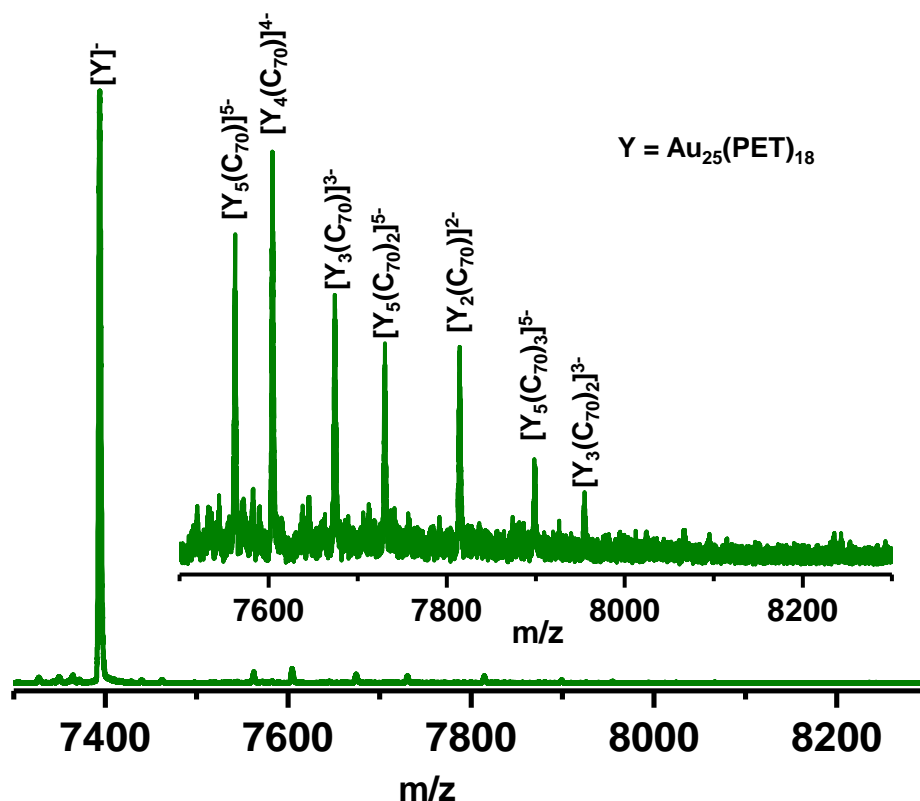


**Figure S10.** ESI MS showing the formation of adducts of  $\text{C}_{70}$  with  $\text{Au}_{25}(\text{PET})_{18}^-$  cluster. Expanded view of the adducts in the  $m/z$  range 7500-8300 is shown in the inset.

# Clean Water through Nanotechnology: Needs, Gaps, and Fulfillment

Ankit Nagar and Thalappil Pradeep\*



Cite This: *ACS Nano* 2020, 14, 6420–6435



Read Online

ACCESS |



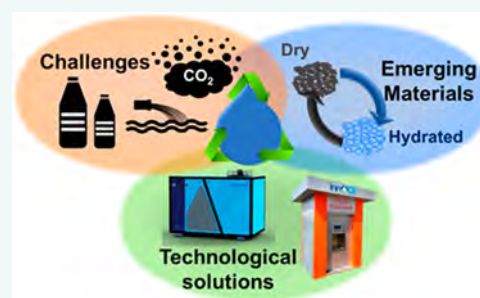
Metrics & More



Article Recommendations

**ABSTRACT:** Sustainable nanotechnology has made substantial contributions in providing contaminant-free water to humanity. In this Review, we present the compelling need for providing access to clean water through nanotechnology-enabled solutions and the large disparities in ensuring their implementation. We also discuss the current nanotechnology frontiers in diverse areas of the clean water space with an emphasis on applications in the field and provide suggestions for future research. Extending the vision of sustainable and affordable clean water to environment in general, we note that cities can live and breathe well by adopting such technologies. By understanding the global environmental challenges and exploring remedies from emerging nanotechnologies, sustainability in clean water can be realized. We suggest specific pointers and quantify the impact of such technologies.

**KEYWORDS:** clean water, nanotechnology, desalination, atmospheric water harvesting, nanosensors, toxicity, smart water purifiers, Internet of Things



Crowded, expanding cities in many parts of the world are experiencing an increased demand for fresh water, and planners are unclear as to how the water needs of tomorrow will be met. In cities such as Bangalore, where data are currently the most valuable commodity, we believe that a data ecosystem could be created for water. Focus on water availability is likely to create businesses, drive the economy, and make the world breathe better. Taking a specific case, India has just 4% of the global freshwater resources but ~18% of the world's population. The country, which was largely rural years ago, has *en masse* become urban in the past two decades. The urban population has risen from 28% in 2000 to 33% in 2016.<sup>1</sup> With a growth rate over 6% in gross domestic product (GDP), the most populous countries, such as India and China, are increasing their chemical, pharmaceutical, agrochemical, automotive, petrochemical, semiconductor, and many other outputs, which will eventually “enrich” our ecosystem materially. Simultaneously, their rapidly declining water resources will be burdened by unprocessed industrial waste. The World Bank has predicted that achieving a growth rate of 8% or above for India will be possible only with a robust water management system.<sup>2</sup> These emerging issues, similar to those existing throughout the world, present a complicated suite of problems that will require technological advances, limits on usage, and collective wisdom, and compassion in order to create sustainable solutions. For instance, the control over carbon emissions by developed

countries is probably not the reason for the globe's survival, but the lack of development in less-developed countries is, according to the Intergovernmental Panel on Climate Change (IPCC).<sup>3</sup> Sustainable economic and technological development for all is needed, although acquiring a quality of life comparable to the United States for the rest of the world would require significant advances in treating, purifying, and assessing toxicity in water. Clean water challenges are highly interdisciplinary, and solutions therefore must cut across boundaries of disciplines. Water in diverse forms is related to climate, food, health, and many other aspects of life, including its origin. The need for urgent, concerted action is clear from just one observation: *ca.* 83% of freshwater species have declined in the last 50 years.<sup>4</sup> Water is and will continue to be one of the most important interdisciplinary subjects of research.

Recent advances in the field of nanoscience provide many solutions to alleviate needs with regard to reducing scarcity or removing contamination. For example, there are filters that remove pesticides from drinking water using nanochemis-

**Received:** March 4, 2019

**Accepted:** May 20, 2020

**Published:** May 20, 2020





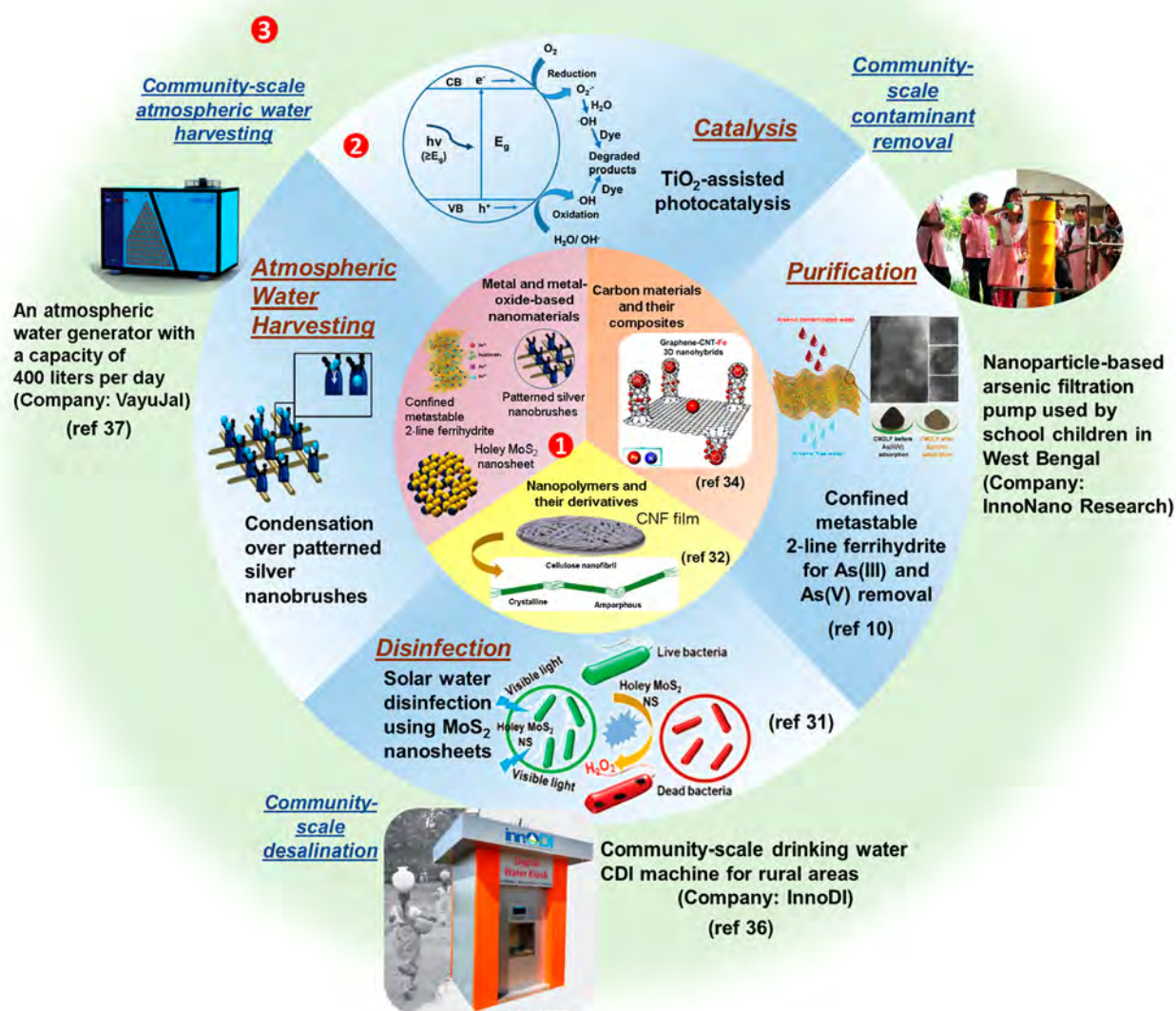


Figure 1. Schematic illustrating translation of materials from lab-scale to market. Innermost circle 1 indicates materials as building blocks; middle circle 2 indicates reported phenomena using such materials; and outermost circle 3 shows products built out of research and their commercialization to create a societal impact. Images containing 2-line ferrihydrite in circles 1 and 2 adapted with permission from ref 10. Copyright 2017 John Wiley and Sons. Images involving holey  $\text{MoS}_2$  in circles 1 and 2 adapted with permission from ref 31. Copyright 2018 John Wiley and Sons. Image in yellow section of circle 1 adapted with permission from ref 32 under Creative Commons Attribution 4.0 International License. Schematic showing graphene-CNT-Fe nanohybrids in circle 1 adapted with permission from ref 34. Copyright 2013 American Chemical Society. Image of a community-scale CDI machine in circle 3 adapted with permission from ref 36. Copyright 2018 Innodi Water Technologies Pvt. Ltd. Image of an atmospheric water generator in circle 3 adapted with permission from ref 37. Copyright 2019 Vayujal Technologies Pvt. Ltd.

try.<sup>5–8</sup> This technology had already reached over 7.5 million people by 2016, when implementation data were last collected, reducing pesticide levels from over 20 times the safety standard to concentrations substantially below it (0.5 parts per billion, ppb, for all pesticides taken together).<sup>9</sup> In another example, a nanostructured material is able to remove arsenic from drinking water affordably and the technology is delivering clean water (CW) to about 1 million people each day, providing hope for another 80 million or so in India, who are affected by this problem.<sup>10–12</sup> The government of India has approved the technology for national implementation.

Such a solution does not require electricity and is affordable, even for those living in the poorest parts of the world. Several alternate solutions to address arsenic as well as other organic and inorganic contaminants are available and are being explored in various parts of the world. Alternate methods of microbial disinfection, desalination, water harvesting, recycling, contaminant sensing, and monitoring are debuting in the marketplace. Scalability and massive implementation of technologies is slow but encouraging. For example, the prospects of nanotechnology (NT) for CW have enthused many researchers, and numerous articles have been published

around the theme of NT and nanomaterials for CW production and wastewater treatment.<sup>13,14</sup> Among several issues of relevance for developing affordable NTs for CW, there are four principal points to be considered: (1) More for less: As constituent materials reduce in dimension and reach the nanoscale regime, their effective capacity to remove contaminants increases due to additional derivatization of the material to increase charge, solubility, affinity, *etc.* Properties of relevance, such as the presence of active surface sites for adsorption, enhanced adsorption enthalpy for specific species, reactivity as a result of activation of specific chemical bonds, size-dependent optical absorption, and emission, are being explored today. All of these properties individually and collectively make it possible to acquire more effective scavenging capacity per unit mass of the material at the nanoscale than the bulk material, making a purifier composed of nanoscale material smaller and more affordable. (2) Decreasing limits of contaminants: The World Health Organization (WHO) set the upper limit on arsenic in drinking water at 50 ppb in 1963,<sup>15</sup> and the U.S. Environmental Protection Agency decreased the limit to 10 ppb in 2002.<sup>16</sup> A primary reason for decreasing contaminant limits has been an enhanced understanding of the effects of contaminants on human health. However, the limited availability and high cost of remedial technologies have kept governments from implementing these standards. Moreover, the actual safe limit is expected to be further below the present WHO limit. This is because the arsenic intake per capita per day through drinking water is much higher than that assumed by the WHO in the arsenic-affected tropical regions of India due to unaccounted sources of arsenic intake, such as food crops.<sup>17</sup> In addition to India, South Asian countries including Vietnam and Bangladesh,<sup>18–21</sup> and Latin American countries including Argentina, Bolivia, Chile, and others including regions of the United States are also prone to alarming levels of arsenic.<sup>21–23</sup> In order to accomplish the already prescribed limits, nanomaterials are essential. (3) What are achievable levels of contaminant removal using advanced materials? Single nanoparticles (NPs) have even shown sensitivity to a few species of contaminants.<sup>24</sup> Thus, even at this level of contaminant concentration, several materials are selective in removing them. (4) Special properties: The unique properties of nanostructures, such as atomically precise pores and thicknesses of desired dimensions,<sup>25</sup> controlled functionalities,<sup>26</sup> maneuverability,<sup>27</sup> *etc.*, offer exciting possibilities for making CW.

In this Review, we discuss nanomaterials and technologies that can be used for water treatment and sensing, highlighting major challenges that need to be addressed through NT in providing sustainable access to CW.

## NANOMATERIALS AND NANOTECHNOLOGIES THROUGH THE AGES

Throughout history and into the present, water filtration and purification components are primarily made of carbon. Using carbon in the form of wood charcoal for water purification was practiced by Egyptians and Sumerians in 3750 BC.<sup>28</sup> Activated carbon, introduced in the 1940s,<sup>29</sup> and its various modifications, including nanostructures such as carbon nanotubes (CNTs), carbon nanofibers (CNFs), and graphene-based materials have been exploited for treatment through mechanisms such as adsorption, catalytic wet air oxidation, membrane-based separation, and disinfection, and

also for sensing and monitoring.<sup>30</sup> Metal and metal oxide NPs have also been reported for adsorption, photocatalysis, oxidation, disinfection, and sensing. Despite being an active research area for decades, nanomaterials-based treatment and sensing technologies are yet to occupy a large share of the market due to unreliability in terms of sensitivity and selectivity, higher cost, and field-level issues during operation. Figure 1 illustrates applications of nanomaterials, such as, MoS<sub>2</sub> nanosheets for disinfection,<sup>31</sup> CNF films for biocidal activity,<sup>32</sup> silver nanobrushes for atmospheric water harvesting,<sup>33</sup> graphene-CNT-iron oxide nanostructures,<sup>34</sup> and ferrihydrite for heavy-metal removal.<sup>10</sup> These have reached people in the form of affordable and easy-to-operate devices such as filtration-incorporated hand pumps,<sup>35</sup> desalination units,<sup>36</sup> and atmospheric water generators.<sup>37</sup> We discuss the future of nanomaterials that can be integrated into these technologies to overcome the existing challenges.

## DESALINATION

Nearly 40% of the global population resides within 100 km of an ocean or a sea, rendering desalination a crucial solution to water scarcity. Presently, there are 19,744 desalination plants operating across 150 countries supplying 100 million m<sup>3</sup> of water per day to 300 million people globally.<sup>38</sup> However, desalination is still energy-intensive and hazardous to the environment. It consumes 0.4% of the global electricity, that is, 75 TWh per year and also produces 76 million tons of CO<sub>2</sub> annually.<sup>39</sup> Therefore, three major challenges for desalination technologies are (1) high specific energy consumption (SEC), (2) CO<sub>2</sub> emissions from burning of fossil fuels, and (3) negative impacts on marine ecosystems due to the discharge of concentrated brine back into the sea. These challenges propelled the development and commercialization of nanomaterials for respective desalination technologies. Desalination technologies are either pressure-driven, temperature-driven, or chemical-driven processes.

**Thermal Desalination.** Thermal distillation is a conventional approach mainly used for treating water with a high level of total dissolved solids (TDS; >45,000 mg/L).<sup>40</sup> Thermal desalination processes such as multistage flash distillation and multiple-effect desalination are energy intensive (overall equivalent electrical energy consumption of ~15–30 kWh<sub>elec</sub>/m<sup>3</sup> for a power plant running at 30% efficiency), costly (cost of produced water ~0.52–1.75 US \$/m<sup>3</sup>), and hazardous to the environment (CO<sub>2</sub> emissions ~15–30 kg/m<sup>3</sup> for standalone operation and 8–16 kg/m<sup>3</sup> for cogeneration operation).<sup>41</sup> An emerging alternative process is membrane distillation, integrated with carbon nanomaterials.<sup>42,43</sup> As an example, a CNF-ceramic nanoporous composite membrane, which has a 10 μm hydrophobic carbon fiber layer with a minimum pore size of ~30 nm on a ceramic substrate, has shown greater than 99% salt rejection and 3–20 times higher water flux than traditional polymeric membranes.<sup>44</sup> Hydrophobicity of the CNF layer ensures smooth permeation of water vapor across nanopores, and thermal conductivity enables more than 80% recovery of the latent heat.

Thermal desalination plants running on solar and geothermal energy sources are being explored. Also, the efficiency of solar-powered thermal desalination is being enhanced by improving the performance of solar concentrators by using nanomaterials that have high photothermal conversion efficiencies and energy storage.<sup>45</sup> Nanofluids with extraordi-



nary thermal conductivity and absorption-emission properties have improved the performance of thermal collectors.<sup>46</sup>

**Membrane-Based Desalination.** Membrane-based separation is adequate for treating water with TDS typically below 45,000 mg/L.<sup>40</sup> Such technologies (RO, reverse osmosis; forward osmosis, FO; electrodialysis, ED; nanofiltration, NF) have gained immense commercial success due to their much lower specific energy requirement ( $3\text{--}8\text{ kWh}_{\text{elec}}/\text{m}^3$ ), cost effectiveness ( $0.26\text{--}0.54\text{ US } \$/\text{m}^3$ ), and low  $\text{CO}_2$  release ( $1.7\text{--}2.8\text{ kg}/\text{m}^3$  for seawater RO) into the atmosphere.<sup>39,41</sup> RO has now surpassed thermal technologies in the desalination market, replacing them as convention. The membrane module is the most energy-intensive part of the desalination process and constitutes nearly 71% ( $2.5\text{--}4\text{ kWh}/\text{m}^3$  for seawater RO) of the SEC.<sup>47</sup> While a majority of RO systems have achieved an SEC of  $2.3\text{ kWh}/\text{m}^3$ , thermodynamic limit stands at  $0.76\text{ kWh}/\text{m}^3$ , for a feed having a TDS of 35,000, indicating scope for improvement. However, taking into account an energy recovery of 50%, the practically achievable SEC limit rises to  $1.06\text{ kWh}/\text{m}^3$ .<sup>48</sup> Reduction in recovery percentage can improve SEC, but will enhance operational and capital costs. The next-generation membranes should therefore focus to overcome the trade-off between permeability and rejection and improve selectivity.

Among membrane materials, nanocomposite polymeric membranes are commercially successful due to their low cost and feasibility for large-scale manufacturing. Polyamide membranes are widely used due to their high selectivity and permeability compared to conventional cellulose acetate-based membranes. Polyamide membranes are composed of an extensively cross-linked nonporous polyamide layer supported by a porous polysulphone layer at the bottom.<sup>49</sup> Progress in the development of membrane materials has been gradual, as permeability and selectivity have to be counterbalanced and fouling probability needs to be decreased. Nanomaterials designed at the molecular level are essential for addressing these challenges. In one such attempt, researchers created a three-dimensional (3D)-printed polyamide membrane prepared by layer-by-layer electrospinning in order to achieve reduced thickness (minimum thickness  $\sim 4\text{ nm}$ ) to maximize permeance and increased smoothness (roughness  $\sim 2\text{ nm}$ ) to decrease the probability of fouling, while maintaining the membrane's strength.<sup>50</sup>

Membranes composed of aligned CNTs are suitable for ultrafiltration. To improve their selective nature, CNT tips are functionalized with zwitterionic species or aliphatic groups such as carboxylic acids.<sup>51</sup> Integration of CNTs with existing membranes has rendered them superhydrophilic, improved their permeation and solute rejection, increased their lifespan, and led to better electrical and mechanical properties.<sup>52</sup> Another promising class of materials includes graphene and two-dimensional (2D)-derived frameworks that physically separate undissolved solids at the nanometer scale.<sup>53</sup> Lab-scale results indicate up to 1000 times better permeability for graphene compared to conventional thin-film composite polymers as RO membranes.<sup>54</sup> However, scaling remains a challenge. Defect-free aquaporin-based membranes, prepared by embedding bacterial aquaporin Z (AqpZ) into a chemically and mechanically stable matrix of a block copolymer or a unilamellar lipid, match the single-channel water permeability coefficient of conventional polyamide membranes ( $5\text{--}36\text{ molecules s}^{-1}\text{ Pa}^{-1}$ ).<sup>55</sup> Aquaporin-based membranes can potentially achieve a permeability of  $601\text{ L}\cdot\text{m}^{-2}\cdot\text{h}^{-1}\cdot\text{bar}^{-1}$ ,

exceeding the performance of commercial RO membranes by 2 orders of magnitude.<sup>56</sup>

Further, Kevlar aramid nanofiber (KANF)-based membranes are an emerging category, constituted of nanoscale form of poly(paraphenylene terephthalamide).<sup>57</sup> Nanomaterials under this class are mechanically robust, flexible, tunable in pore size, electrically conducting, and physically stable. Membranes based on KANFs and their composites have demonstrated over 96% rejection of Rhodamine B dye and Au NPs ( $\sim 6\text{ nm}$ ).<sup>58</sup> They have also shown a desalination efficiency of 99.7% for  $\text{Na}_2\text{SO}_4$  by performing electrodialysis-based ion separation at a constant voltage of  $15.0\text{ V}$ .<sup>59</sup>

RO can also be made operationally efficient by improving the quality of feedwater with FO pretreatment. Using FO in concert with RO reduces the fouling probability of membranes, decreases the consumption of chemicals used for cleaning, and enhances recovery. However, RO-FO hybrids are practical only above a threshold flux of  $30\text{ L}/\text{m}^2/\text{h}$ .<sup>60</sup> Therefore, FO membranes for achieving threshold flux are being developed by incorporating nanomaterials to improve hydrophilicity ( $\text{TiO}_2$ , halloysite nanotubes, graphene oxide, *etc.*), resulting in a faster transport of water molecules. Loading metal-organic frameworks (MOFs) into existing membranes has shown up to 72% improvement in the permeability of pure water for FO desalination.<sup>61</sup> Another aspect of improvement lies in the fabrication process of commercial polyamide membranes. Structural characteristics of the film, such as, morphology, uniformity in chemical composition, and roughness directly affect the membrane's performance.<sup>62–64</sup> Polyamide thin-film composite membranes, created by conventional interfacial polymerization technique, offer a limited scope for optimization of permselectivity. During polymerization, the ultrafast reaction between *m*-phenylenediamine and trimesoyl chloride monomers causes the system to quickly reach the gel point, thereby limiting any further diffusion of the monomers. This creates selective layers with high heterogeneity in depth and restricted control over film thickness. It can be overcome by performing molecular layer-by-layer deposition (mLbL) which results in relatively smooth films, tunable at molecular level.<sup>65–67</sup> Controllably reducing film thickness helps to minimize pressure requirements, ultimately making RO energy efficient. Amidst these advantages, there still remains the challenge of scalability and limited throughput associated with mLbL techniques.<sup>68</sup>

**Chemical Desalination.** Of the chemical-driven desalination technologies (*i.e.*, ion-exchange, liquid-liquid extraction, and precipitation), the ion-exchange process is the most commonly used. Ion-exchange uses only  $7.2\text{ MJ}/\text{m}^3$  of specific energy while producing  $\text{CO}_2$  below  $0.7\text{ kg}/\text{m}^3$ , compared to RO, which uses  $29.5\text{ MJ}/\text{m}^3$  of specific energy and emits  $3.8\text{ kg}/\text{m}^3$  of  $\text{CO}_2$ .<sup>41</sup> Ion-exchange processes are composed of ED and capacitive deionization (CDI).

ED is among the most extensively researched and commercially successful electromembrane desalination method at present. Oxide NPs ( $\text{SiO}_2$ ,  $\text{TiO}_2$ ), carbon nanomaterials (*e.g.*, CNTs, graphene-based nanomaterials), and Ag NPs, zeolites, *etc.*, are examples of nanomaterials that are incorporated into ion-exchange membranes for ED to tune properties such as surface area, ionic conductivity, tensile strength, energy efficiency, thermal stability, *etc.*<sup>69</sup> Fouling, separation efficiency for different types of ions (monovalent, divalent, *etc.*), lifetime, and eco-friendly routes of synthesis are



current performance gaps of ion-exchange membranes that need to be improved.

Discovered more than 50 years ago,<sup>70</sup> capacitive deionization is promising due to its relatively low input capital, high-energy efficiency, scalability, and minimal maintenance requirements, despite being limited by feedwater's TDS and by capacity. Therefore, variable capacity CDI units with nanomaterials incorporated for effective treatment are expected to be an emerging direction for desalination. Currently, commercial CDI units are available for desalination of brackish water (up to 3000 TDS).<sup>71</sup> Further modification of electrode materials has involved integration with ion-exchange membranes (membrane CDI; MCDI), resulting in up to 80% energy recovery during the regeneration step.<sup>72</sup> Researchers have improved the porosity of CDI electrodes by incorporating oxide NPs ( $\text{TiO}_2$ ,  $\text{SiO}_2$ , etc.) and carbon-based nanomaterials (CNTs, CNFs, graphene, etc.), leading to a higher degree of hydrophobicity and enhanced surface area.<sup>73</sup> The MCDI technology utilizing ion-exchange membranes faces challenges of intermittent sequential operation, limited adsorption capacity due to plate electrodes, and expensive CDI cells, which are barriers in scaling up of the technology. Substituting stationary electrodes with flow electrodes consisting of suspended carbon powder in conventional MCDI has enabled researchers to overcome the operational limitation by eliminating the discharging cycle, enabling self-regeneration, and improving the ion adsorption capacity, providing practically unlimited surface area for ion adsorption.<sup>74,75</sup>

## ATMOSPHERIC WATER HARVESTING

The earth's troposphere contains approximately  $1.42 \times 10^{19}$  liters of water in the form of water vapor, and the world population today is about 7.6 billion. Therefore, there is nearly 1.8 billion liters of water available per person in the atmosphere. Atmospheric water harvesting, thus, has vast potential, even if only a miniscule fraction of this resource is used. Note that the oceans of the planet were once dry and were filled by rain.<sup>76</sup> Thermodynamics suggests that for an open water surface to attain maximum entropy and equilibrium, water vapor above the surface has to attain saturation, thereby causing replenishment through greater evaporation. We note that excessive extraction of vapor locally might affect the hydrological cycle negatively.

An early example of fog harvesting practice includes one in 1969 in Mpumalanga, South Africa, where two large ( $\sim 28.0 \text{ m} \times 3.6 \text{ m}$ ) nets made from plastic mesh were used to harvest fog water for South African Air Force personnel. These nets harvested an average of  $11 \text{ L/m}^2/\text{day}$  during the 15-month interval from October 1969 to December 1970.<sup>77</sup> In another instance, implementation of fog collection took place in a village named Chungungo in North Chile in 1987; 75 nets, each of which were  $12 \text{ m} \times 4 \text{ m}$  in size, delivered an average of 33 L of CW per capita per day to 330 villagers. Both of these harvesters were passive as they did not require energy input.

Alongside passive water harvesters, systems of active water harvesting that require external energy to produce CW now exist. Active harvesting mechanisms have been translated to commercial atmospheric water generators (AWGs). These AWGs extract moisture primarily by condensation or adsorption mechanisms, or a combination of both. The energy efficiency of AWGs (amount of energy consumed per

liter of water generated) renders them fit for regions with relative humidity (RH) > 40%. Hence, AWGs have proven to be a viable alternative in coastal regions where a lack of sufficient resources has deterred the installation of desalination plants. However, they are inefficient when RH drops below 40%.<sup>78</sup> Efficient water-capturing mechanisms are being developed and demonstrated by studying natural phenomena and mimicking them at the micro- and nanoscale.

Identifying natural harvesting routes used by several plant and animal species, understanding their harvesting mechanisms, and mimicking them have helped scientists to create a next generation of nanoengineered materials and structures that harvest moisture and efficiently transport the condensed water. Examples of a few successful mimics include those inspired from the elytra of a Namib Desert's beetle,<sup>79</sup> Stenocara, spider's silk,<sup>80</sup> and banana leaf.<sup>81</sup> Successful mimicking of the surface structures of these species followed by systematic water-harvesting experiments have led to a better understanding of the science of dew condensation, involving the nucleation of droplets and their coalescence and subsequent transportation from the surface.<sup>82–86</sup> Most modern-day condensation-based AWG devices are partially or completely based on the vapor compression refrigeration cycle. Implementing nature-mimicking structures in existing and future AWG devices will boost these devices' ability to operate efficiently, even in harsh, hot, and dry climatic conditions. Micro–nano hierarchical structures have been reported to be the most efficient in terms of offering a large number of nucleation sites as well as fast coalescence and transportation of the nucleated droplets from the surface.<sup>87,88</sup> Sarkar *et al.* recently reported further advancement in this direction with a harvesting efficiency of  $56.6 \text{ L/m}^2/\text{day}$  at 87% RH.<sup>33</sup> We expect that the future of surface science and engineering for atmospheric water harvesting will focus on combining nanoengineered structures with unique wetting gradients. Biomimicked structures can particularly help the AWG market flourish in arid North African and Middle East countries, specific regions of which are severely suffering from water scarcity today. Stand-alone AWG systems working on renewable energy sources should prove extremely valuable to societies residing near coastal regions, where the atmosphere is relatively rich in moisture and electricity costs are too high to afford any other water-delivery solution.

Condensation being infeasible below 40% RH has accelerated the development of materials for adsorption-based harvesting. Conventional desiccants have low adsorption capacities (silica gel and zeolites) and slow kinetics (hygroscopic salts) or need energy-intensive regeneration (polymers). An emerging class of MOFs offer high surface area and tunable pore size and hydrophilicity. Their promising performance ( $2.8 \text{ L/day}$  at 20% RH corresponding to a kg of  $\text{Zr}_6\text{O}_4(\text{OH})_4(\text{fumarate})_6$ ) and unique sorption behavior have shown potential for harvesting in deserts.<sup>89</sup> However, substantial work is required on optimizing thermodynamic properties of MOFs and their variants, along with device engineering, before field implementation. For a detailed discussion on all aspects of atmospheric water harvesting, readers are requested to visit ref 78.

## AFFORDABLE NANOSENSORS AND CATALYSTS FOR CLEAN WATER

Although conventional analytical methods such as high-performance liquid chromatography (HPLC) and inductively

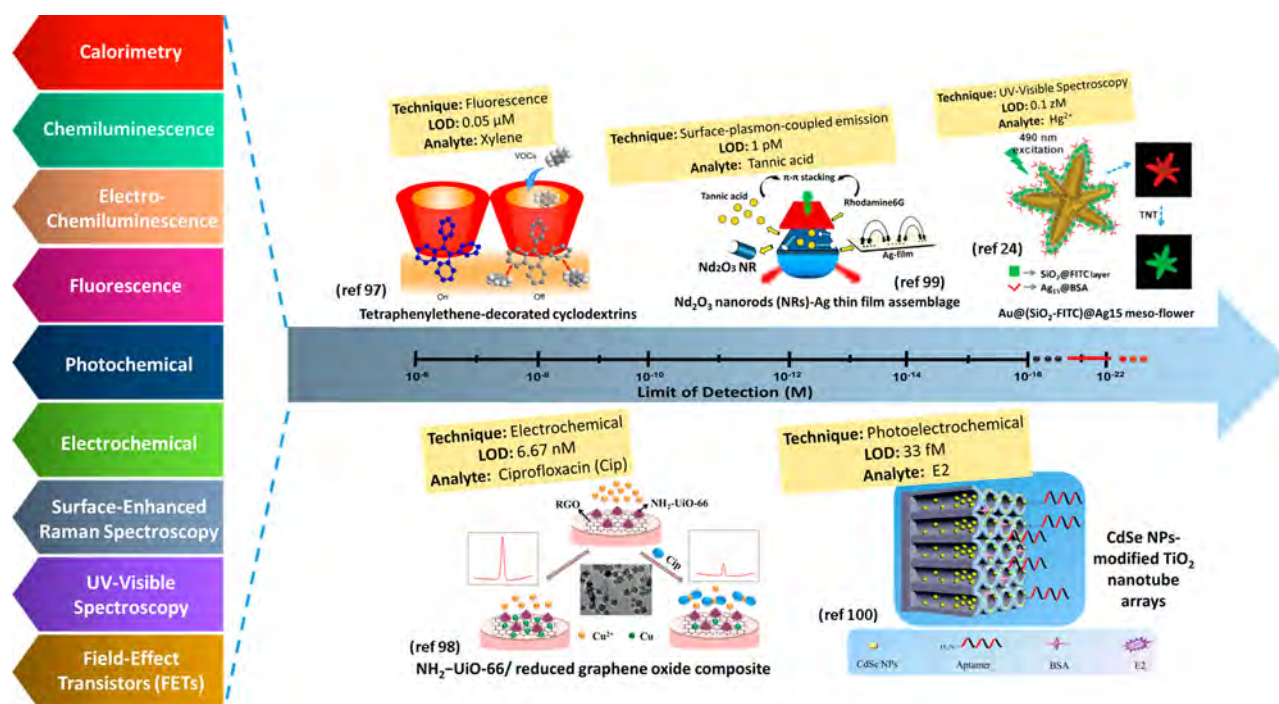


Figure 2. Schematic of the limits of detection (LOD) achieved using nanomaterials. The rightmost part represents detection up to the single-particle/ion level. Reprinted with permissions from ref 24. Copyright 2012 John Wiley & Sons; ref 97. Copyright 2016 American Chemical Society; ref 98. Copyright 2019 American Chemical Society; ref 99. Copyright 2019 American Chemical Society; and ref 100. Copyright 2014 American Chemical Society.

coupled plasma mass spectrometry (ICP-MS) exist for lab-scale testing, high cost, elaborate sample preparation, and unavailability at point-of-use have been limiting factors for their utilization. Nanomaterials are unique in their properties such as optical absorption and emission, which are extremely sensitive to surface functionalization and local environment. These properties have been extensively used in sensing in the context of CW.

An absorbed photon causes several consequences in a semiconducting NP, most important is the creation of a free electron and a hole, both of which can diffuse to the surface of the particle and react with adsorbed water molecules.<sup>90,91</sup> The hole, therefore, can create an oxidizing species such as  $\text{HO}^\bullet$  and the electron can form  $\text{OH}^-$ , particularly for a hydrated particle in water. Other similar species that can arise are  $\text{O}_2^{\bullet-}$ ,  $\text{HO}_2^\bullet$ , and  $\text{O}^\bullet$ , which also appear on hydroxylated particles. A  $\text{TiO}_2$  NP generates reactive species upon photoirradiation, creating an active reaction center that is regenerative in nature, and it becomes the basis for efficient photocatalysis. Consider the following example of photocatalytic sensing of a dye, rhodamine B (RB), using NPs. RB is a contaminant found in wastewater produced from the textile, dyeing, and plastic industries, with proven effects of carcinogenicity, and reproductive and neurotoxicity, thus posing a serious threat to humans and animals upon reaching the groundwater and other water bodies. Photodegradation of an aqueous solution of  $10^{-5}$  M tetraethylated RB in the presence of 100 mg of  $\text{TiO}_2$  NPs in a 50 mL solution can be observed visibly upon solar irradiation, with 560 nm light.<sup>92</sup> The self-photosensitized dye reaches an excited state upon visible light absorption, enabling electron injection from the excited state of the dye to the conduction band of  $\text{TiO}_2$ . Adsorbed  $\text{O}_2$  on the  $\text{TiO}_2$  surface takes up the injected electron to form  $\text{O}_2^{\bullet-}$ . Protonation of  $\text{O}_2^{\bullet-}$  forms  $\text{HOO}^\bullet$ , followed by further

reaction with a trapped electron to form  $\text{HO}^\bullet$ , which ultimately leads to degraded products.

Researchers are actively investigating emerging materials and their properties, such as luminescence and catalysis of noble metal clusters, in the context of sensing. Atomically precise clusters of noble metals are composed of a few tens of atoms, with precise composition.<sup>93</sup> One such example is  $\text{Ag}_{29}(\text{BDT})_{12}(\text{PPh}_3)_4^{3-}$  (where BDT and  $\text{PPh}_3$  are 1,3-benzenedithiol and triphenylphosphine, respectively), which is intensely luminescent in the red region of the electromagnetic spectrum.<sup>94</sup> Luminescence, as in the case of molecular systems, is extremely sensitive to the medium. Such clusters may also be sensitive to the metal core because they are reactive as well. The core, being accessible to ions and molecules in the medium, makes this chemistry fundamental to developing cluster-based molecular sensors. The catalytic processes and their high reactivity can be used for the destruction of refractory organics.

The luminescence of clusters can be enhanced by anchoring them on plasmonic particles through a process called metal-enhanced luminescence.<sup>95</sup> This enhancement is also possible by embedding clusters onto electrospun fibers.<sup>96</sup> In both cases, it is possible to detect and to quantify contaminants such as mercuric ions down to a few ions, at the single-particle or single-fiber level. Such sensor mats could make test strips affordable for ultrasensitive detection. Figure 2 represents illustrations of detection limits achieved using nanomaterials such as tetraphenylethene-decorated cyclodextrins,<sup>97</sup>  $\text{NH}_2\text{-UiO-66}$ /reduced graphene oxide composite,<sup>98</sup>  $\text{Nd}_2\text{O}_3$  nanorod-Ag thin-film assemblage,<sup>99</sup> CdSe NP-modified  $\text{TiO}_2$  nanotubes arrays,<sup>100</sup> and  $\text{Au}@\text{(SiO}_2\text{-FITC)}@\text{Ag}_{15}$  meso-flowers,<sup>24</sup> and their corresponding properties.

Achieving higher sensitivity and creating a compact and cost-effective sensor accessory will enable the integration of

Table 1. Nanotechnology for Clean Water: Status of Implementation<sup>a</sup>

technology umbrella/ref	material	problem addressed	organization	status	cost (cents/gallon)
adsorption/ <sup>110</sup>	FeOOH	arsenic	IIT Madras	commercial	0.14
adsorption/ <sup>111</sup>	nanalumina fibers	submicron and colloidal particles, bacteria, viruses, dissolved salts, endotoxin, pharmaceuticals	Argonide	commercial	0.03
sorption/ <sup>112</sup>	nanocellulose	metal ions	UPM-Kymmene Oy	commercial	—
adsorption and physical separation/ <sup>113</sup>	zeolite	heavy metals and ammonia	KMI Zeolite	commercial	—
FO/ <sup>114</sup>	CNT-based membranes	brines and several industrial salts	Porifera	commercial	—
RO/ <sup>115</sup>	CNT-based membranes	dissolved salts	NanOasis	commercial	—
FO and RO/ <sup>116</sup>	Aquaporin water channels	micropollutants, xenobiotics, organics	Aquaporin	pilot	—
CDI/ <sup>36</sup>	high surface area carbon electrodes	dissolved salts and metals	InnoDI and IIT Madras	commercial	0.5
NF/ <sup>117</sup>	hollow fiber membrane	salts, heavy metals, toxic chemicals	De Mem Ltd. and NTU Singapore	pilot	—
abiotic chemical reduction or anaerobic biodegradation/ <sup>118</sup>	iron nanoparticles	heavy metals, nitrates, phosphates	NANOIRON	commercial	—

<sup>a</sup>Only select technologies and solutions are listed, based on publicly available information. CNT = carbon nanotube; FO = forward osmosis; RO = reverse osmosis.

such devices with smartphones and will facilitate point-of-use applications. A geographical map of contaminants in water could be possible, and it could potentially even be dynamic, like weather maps. An affordable sensor put on all CW sources and service lines will enable continuous monitoring and rectification wherever needed, also verifying the sustainability of the solutions. Upon linking sensors to smartphones, a much-needed in-depth knowledge of global and local water quality will be available as and when needed, which will help to create a rapid action force solving water quality issues. The data generated may provide direction to water quality professionals and help to allocate resources for every region, ensuring the availability of CW for all.

## TOXICITY

The properties that make NPs useful and relevant in CW applications can also make them objects of suspicion.<sup>101</sup> Being in the same size regime as biomolecules, NPs can mimic biomolecules and enter biological systems, such as humans, animals, and plant cells, or organelles. Coupled with the possibility of appropriate functionalization, this probability gets further enhanced. When polystyrene NPs (~40 nm in diameter) are adsorbed on medaka fish eggs (*Oryzias latipes*), the NPs reach the yolk and gall bladder during embryogenesis. Exposing an adult medaka to a 10 mg/L NP solution caused NP accumulation in the gills and intestine, with NPs also propagating to the liver, testes, and eventually to the brain through the blood–brain barrier.<sup>102</sup> In light of such findings, NP release in the CW stream has to be controlled, particularly when loose NPs are used in the process. Even in the case of supported NPs, depending on the strength of anchoring, the particles may get dislodged, especially in forced flow. It is also possible for NPs to enter the medium when the surface binding group or ligand is affected by external stimuli such as light. For example, a hydroxyl radical can react by breaking the bond between the particle and the anchoring ligand. One approach to safety is to ensure that the NPs used are similar to natural materials and that their bulk counterparts are available in nature. The only point of concern will be whether the NPs are released in the processed water stream.<sup>103</sup>

Evaluating the presence of free particles in water at low concentrations may pose a challenge for measurement. However, this challenge can be solved by understanding the dynamics of release, which depend on factors such as water chemistry, size of NPs, surface area, surface functionalization, etc.<sup>104</sup> Particle release may be evaluated using single-particle ICP-MS to track decreasing particle diameters or increasing constituent elements' concentrations as a function of time. One such study highlights the release of silver ions from silver NPs in river and lake water, suggesting more than 80% dissolution for smaller particles (<10 nm), while only 50% dissolution for larger particles (50 nm), over a period of four months.<sup>105</sup>

## COMMERCIALIZATION, BUSINESSES, AND INCUBATION

Globally, the water sector is too broad to estimate its net worth. Over the years, nanotechnology-based businesses have emerged in the CW sector to address global and local needs (Table 1). As an example, a lack of freshwater in rural areas has led to the development of rolling water purifying drums, which purify the water collected from a distant place, as one rolls it home.<sup>106</sup> This local solution would prove extremely valuable to people who walk long distances carrying cans of water over their heads and shoulders. Such drums could contain nanomaterials to enable purification during transport. Later, an oil–water emulsion can be prepared by simple agitation, and nanomaterials can be extracted by trapping them at the oil–water interface.<sup>107</sup> Such simple methods of extraction suggest the possibility of using rolling water purification for contaminant-specific treatment in a particular area, by mixing with a specific nanomaterial.<sup>108,109</sup>

Several limitations still exist in the commercialization of NTs for CW, including low governmental investment in and lack of adequate focus on water-related research activities, especially in developing countries. These limitations have resulted in slow progress in the translation of developed technologies. In many ways, this lack of progress is understandable because water availability and associated issues have been major challenges, and therefore investments for



**Table 2. Examples of Emerging Nanomaterials That Could Translate or Have Already Translated into Nanotechnologies for Clean Water**

material	application	organization	ref
metal–organic framework	atmospheric water harvesting	Massachusetts Institute of Technology, United States	123
organic-templated nanometal oxyhydroxide impregnated with silver nanoparticles	water purification	Indian Institute of Technology Madras, India	124
cationic and anionic membranes	capacitive deionization	Idropan Dell'orto Depuratori Srl, Italy	125
metal oxide nanocomposite heterostructure powder	sensing of hydrogen sulfide	Honeywell Romania SRL, Romania	126
layer-by-layer assembly of graphene oxide membranes	water purification	University of Maryland, United States	127
aromatic diimide chromophores	sensing of volatile organic compounds	Jawaharlal Nehru Centre for Advanced Scientific Research, India	128
doped carbonaceous material	photocatalytic removal of chemical/biological pollutants and micropollutants	University of Arkansas, United States	129
graphene oxide	dehydration using vapor phase separation or pervaporation	The University of Manchester, United Kingdom	130

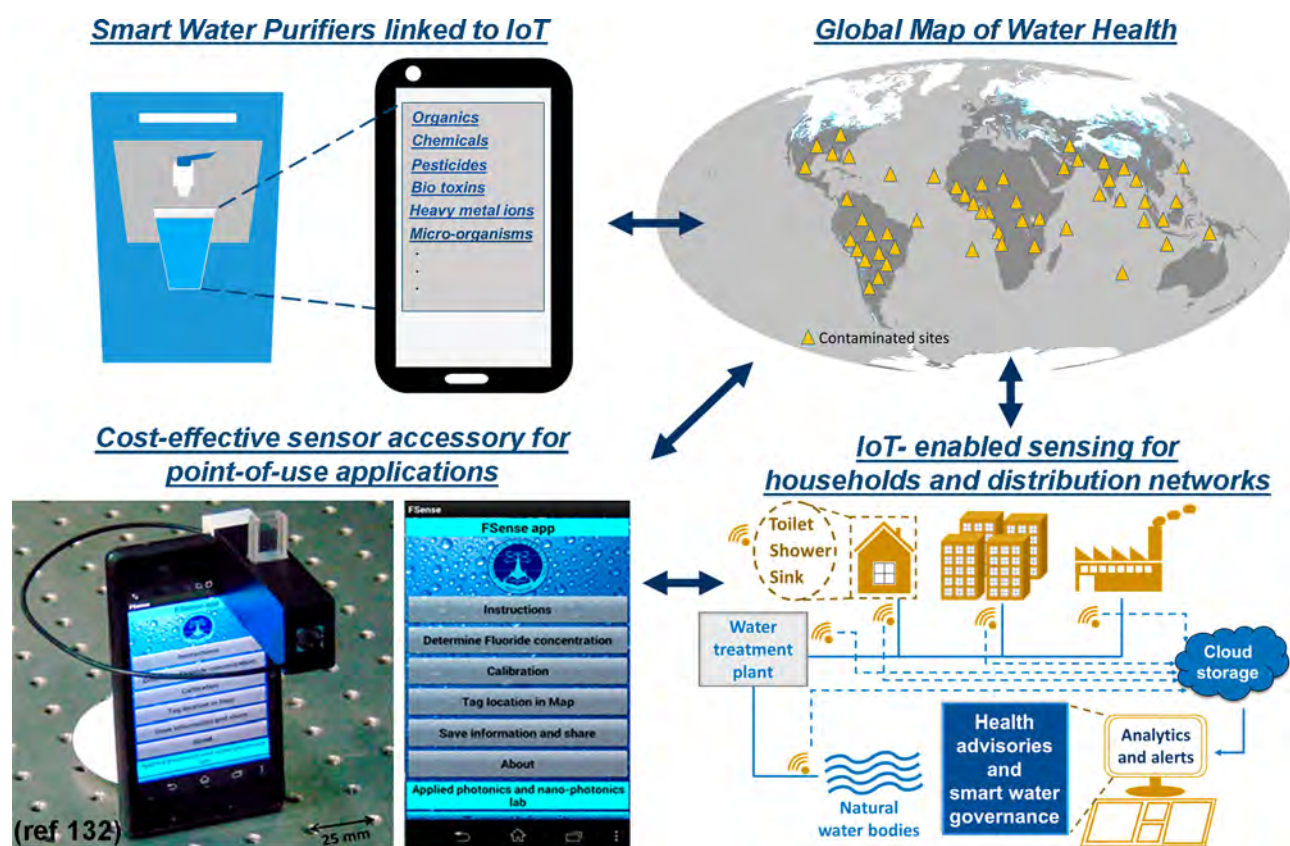


**Figure 3.** Schematic representation of future data on water being collected from water purifiers, field samples, and city infrastructure through nanosensors embedded in smartphones and IoT-enabled domestic water purifying systems and water distribution networks across the world, proving health advisories in the long run. Top-right panel image adapted and modified with permission from NASA Earth Observatory. Copyright 2020 NASA Earth Observatory. Bottom-left panel image reprinted with permission from ref 132. Copyright 2017 American Chemical Society.

them took priority over research on CW. For example, \$0.26 billion were allocated by the Indian government in 2017, under the National Rural Drinking Water Program to provide arsenic- and fluoride-free drinking water to 28,000 habitations in India, which was about 0.007% of the GDP of the country.<sup>119</sup> While allocation to the drinking water segment declined from 87% to 31% in 10 years, the share of rural sanitation increased from 13% to 69%.<sup>120,121</sup> Therefore, 0.1% of the country's GDP, utilized by the ministry in 2018–2019,<sup>122</sup> was majorly expended for combating fundamental challenges of open defecation, improvement in cleanliness, and uniform sanitation coverage, which of course are essential.

However, looking at the long-term challenges, a continuous focus of ministry on research on arsenic and fluoride, and related issues would have partially solved the problem of these persistent contaminants. Currently, research on CW and implementing solutions for CW are subjects of separate ministries and, therefore, are separately budgeted and administered. Similar situations exist in other countries too.

Table 2 provides illustrations of emerging nanomaterials in the diverse areas of CW that are either serving the community or have the potential to do so.

## WATER PURIFIERS OF TOMORROW

Increasing awareness of the need for essential minerals in water and the dangers of harmful ones will necessitate ensuring that optimal mineral content is delivered through drinking water. Next-generation technologies that can retain certain minerals or reject others completely would make it possible for water purifiers to select purification technologies according to need. All of these in conjunction with Internet of Things (IoT)-enabled devices and the proliferation of Internet availability across the world would enable acquisition and transfer of water quality data across time through personal electronic devices.<sup>131–133</sup> Big data analytics would thus help create personal health advisories. The availability of such data across a population would be of use to communities and governments to understand and to plan for the health of their people. Water purifiers may become intelligent devices in the foreseeable future, as shown in Figure 3.

Future CW solutions will need to be implementable both locally and nationally. The decentralization of CW technologies is essential for any country, but especially for emerging economies. Many nations have adequate resources to empower local governments with region-specific solutions. The decentralization and implementation of technologies will also trigger the generation and employment of local manpower, which would help strengthen the economy, if carried out nationwide. It is vital for forthcoming technologies to be environmentally friendly with no net carbon emissions in order to restore the purity of the planet and sustain its natural resources.

## OPPORTUNITIES IN SUSTAINABLE AND AFFORDABLE CLEAN WATER

The global water crisis is being countered today by effective removal of contaminants, creation of robust water networks, real-time monitoring of water quality, and linking these efforts with social, political, and economic action. In this section, we highlight both untapped water resources and major problems in the CW sector where NTs could be useful. We offer a few proposals in the context of Bangalore, India, although any city may be chosen in its place.

- (1) Ideally, the world must run with net-zero carbon emissions, converting CO<sub>2</sub> and H<sub>2</sub>O to fuels and back again to the same amount of CO<sub>2</sub> and H<sub>2</sub>O. This cycle is upset when more CO<sub>2</sub> is produced over time, as we do not know how to fix the imbalance using only sunlight as an energy source. We also do not know how to burn fuels efficiently to produce contaminant-free CW that can be used directly. Perhaps engines of the future can be designed to produce usable liquid water. Note that the unsustainable release of CO<sub>2</sub> into the environment has led to the emergence of CO<sub>2</sub>-conversion techniques such as photo/electrochemical reduction, sequestration, *etc.*,<sup>134</sup> powered by renewable energy sources such as solar energy, although they do not perform as efficiently as plants. The burning of octane, represented by the reaction,  $2\text{C}_8\text{H}_{18} + 25\text{O}_2 \rightarrow 16\text{CO}_2 + 18\text{H}_2\text{O}$  suggests the formation of 162 g of water per 114 g of fuel or 1.42 g of water per gram of fuel. It might be possible to trap this water, similar to trapping CO<sub>2</sub>. India consumed approximately 24 billion kg of petrol in the year 2016–2017,<sup>135</sup> which corresponds to burning nearly 21 billion kg of octane

(considering the octane rating as 87), making 186 billion kg of water in a year. Urban water collected this way could grow vegetables on windowsills, as one of the end uses.

- (2) Bangalore is meeting nearly 52% of its water requirements by exploitation of its groundwater, through borewells that currently reach depths close to 2000 feet in several parts of the city.<sup>136,137</sup> The rest of the water is supplied by the Arkavathy and Cauvery rivers. Dependence on deep borewells will continue to increase with the city's burgeoning population. Hence, restoring groundwater is a serious challenge. Out of the 33 billion cubic feet of rainwater available annually to Greater Bangalore, 5–10 billion cubic feet can be collected and used to replenish depleted groundwater levels.<sup>138</sup> Lakes and ponds can be rejuvenated using rainwater and can be directed for domestic nonpotable usage. Sewage treatment and use of recycled water will also prove to be vital. In a typical residential building in Bangalore having 500 people, 70% of the total domestic water requirement can be reduced through recycling of greywater, saving ~ US \$14,500 annually and also substantially reducing dependence on groundwater.<sup>139</sup> Decentralization of greywater treatment could be a vital measure to reduce the overall water demand. In comparison to conventional centralized treatment systems, which require a large initial investment on infrastructure and technical manpower for maintenance, affordable decentralized treatment systems can be built using nanomaterials-based strategies. As an example, catalytic oxidation processes involving nanomaterials (ZnO, TiO<sub>2</sub>, CNTs, *etc.*) mineralize and partially oxidize organic pollutants into harmless products while also destroying pathogenic micro-organisms to an extent;<sup>140</sup> such processes are scalable toward designing compact decentralized systems. Harvesting atmospheric humidity in highly water-stressed regions of the city will assist as well. Innovative methods of water conservation and recycling which reduce consumption have to be rewarded. Water recycling at the household-level (rapid micro- or "nanorecycling") calls for developing technologies not only in remediation methods but also in enhancing eco-friendliness of materials, in general.
- (3) Every personal activity has an impact on water. Water audits on materials of consumption, such as detergents, clothes, food, packaging, paint, furniture, *etc.*, need to happen, and each of them has to be reinvented to make cities livable. It is worth recalling that cotton became water-intensive due to the dyeing industry, which used synthetic dyes during the process of industrialization. Variants of cotton that did not need dyeing, such as yellow and red, were replaced with white by the 1900s, as it could be dyed better.<sup>141,142</sup> Reintroducing these native varieties would reduce dependence on synthetic dyes and detergents.<sup>143</sup> Nanotechnological solutions in the dyeing and leather industries can reduce water consumption and pollution as well.<sup>144</sup>
- (4) The maintenance of water infrastructure has caused a rise in the price of CW. According to a 2017 water affordability assessment, the percentage of U.S. households that find water services unaffordable is expected to rise from 11.9% in 2017 to 35.6% in 2022.<sup>145</sup>

Atmospheric water harvesting and capacitive deionization integrated with next-generation nanomaterials offer affordable solutions, and such technologies, free from municipal water networks, may be a way forward in select areas. Municipal water systems have to be upgraded too, with reduced resistance to flow using NT-enabled coatings.<sup>146</sup>

- (5) Bottled mineral water sales continue to rise. A report found the presence of microplastics in mineral water samples in glass and poly(ethylene terephthalate) packaged bottles.<sup>147</sup> However, the effect on human health of such microplastics, additives, and pigment particles of sizes below 5  $\mu\text{m}$  remains unexamined. Integration of nanosensors with smart water bottles and linking of water quality and quantity to an individual's physiological information in real-time has the potential to revolutionize personal health. Patients suffering from kidney diseases and congestive heart failure, with recommended protocols on water intake and its quality, could enormously benefit from such sensors. In addition to such nanosensors, biodegradable materials are needed as a replacement for nondisposable plastics, which could bring about another materials revolution.

Among other synthetic matter is an ever-expanding class of per- and polyfluoroalkyl substances, which comprise nearly 4730 commercially available synthetic chemicals and polymers.<sup>148</sup> A majority of them have high water solubility and mobility and are bioaccumulative in nature. Their sources include manufacturing facilities, industrial and domestic wastewater treatment plants, landfills, *etc.* Given their ability to persist indefinitely in the environment due to the presence of strong carbon–fluorine bonds, they pose a serious threat for future generations, if they reach groundwater through one of the sources. Several nanoenabled remediation strategies have been found promising for these contaminants.<sup>149</sup> Techniques such as electrochemical oxidation and hydrolysis using CNTs, photocatalytic decomposition using nanostructured oxides, reductive degradation using nanoscale zerovalent iron, *etc.*, have proven as effective remediation strategies in near-ambient conditions. However, it is imperative that no toxic metal ions should release into the treated water. Immobilization of effective nanosorbents into a matrix could result in a deployable remediation device.

- (6) Providing CW for all citizens drains resources initially, but builds resources in the long run. In countries such as India, old practices and emerging aspirations coexist. Villages live on traditional agricultural practices such as burning harvested fields prior to sowing and flooding them during farming. These practices contribute to smog and reduce water availability in neighboring cities, which in turn respond by conveying water from further away, leaving the farmlands dry and inhabitants hungry. Technologies will need to address imbalances of many kinds.
- (7) Challenges of CW are linked to clean air, clean energy, sustainable agriculture, and a clean environment. As an example, it is possible to harvest energy from natural and wastewater by utilizing salinity gradients. A power of 0.8 kW/m<sup>3</sup> can be generated by utilizing the osmotic pressure difference between river water (0.01 M NaCl) and seawater (0.1 M NaCl).<sup>150</sup> Globally, an untapped

amount of nearly 1000 GW and 18 GW of energy is available, from rivers and wastewaters going into the sea, respectively.<sup>151</sup> Currently, pressure-retarded osmosis and reverse electrodialysis have emerged as membrane-based techniques for osmotic energy harvesting. Existing challenges of having to use expensive materials and the requirement of high power density could be overcome by channelizing energy from complementary sources such as waste heat and brines.

The foregoing suggests that only integrated water management with outside-the-box thinking can make cities breathe better. In the context of overall water balance, we list 10 challenges or opportunities that can be addressed through NT (combined with other technologies) for sustainable cities:

- (1) Global CO<sub>2</sub> emissions due to desalination were nearly 76 million tons (MT) in 2015,<sup>39</sup> and global methanol requirements that year were approximately 75 MT.<sup>152</sup> Nanotechnology-assisted production of methanol from CO<sub>2</sub>, supported by renewable energy sources, is a promising direction to address both concerns simultaneously. One potential pathway is to develop an efficient catalytic system for CO<sub>2</sub>-to-methanol conversion that demonstrates high selectivity, conversion efficiency, and low global-warming impact through the use of renewable energy.<sup>153</sup>
- (2) Efficient water-harvesting mechanisms that do not require additional energy input are needed, such as solar-heat-enabled atmospheric water capture by a porous MOF (801, Zr<sub>6</sub>O<sub>4</sub>(OH)<sub>4</sub>(fumarate)<sub>6</sub>) at a relative humidity as low as 20%.<sup>89</sup>
- (3) Nanomaterials can be used to conserve CW by improving the physicochemical and biological characteristics of soil. For example, the application of biodegradable nanohydrogels enhances the moisture content of soil and its water retention capacity, thereby relieving water stress.<sup>154</sup> Groundwater demand by the irrigation sector in India is expected to increase from 605 billion cubic meters (BCM) in 2000 to 675 BCM in 2025, but may be reduced to 637 BCM by 2050.<sup>155</sup> The projected decline in groundwater consumption beyond 2025 is attributed to NTs that can enhance the efficiency of groundwater-driven irrigation.
- (4) Water audits in developing consumables from food to toiletries are needed. For example, cradle-to-grave life cycle assessments of the process of washing 5 kg of laundry (requiring medium hardness water at 40 °C and consuming 120 g of liquid detergent, 49 L of water, and 0.53 kWh of electricity per washing cycle) reveals a primary energy footprint of 6.57 MJ equivalent, a carbon footprint of 0.54 kg CO<sub>2</sub> equivalent, and an environmental footprint of 3.34  $\times 10^{-2}$  EI99 points (see ref 156 for a detailed description of the units).<sup>156,157</sup> This understanding may change the consumer's choice of detergents, packaging materials, chemicals, building materials, *etc.* (see point 7 below). The “water positive” aspect of nanomaterials in this context, indicating net CW production during a synthesis, was shown when an antimicrobial silver-based composition was synthesized for controlled release of silver ions. The synthesized material consumed only 1 L of water for its production, while it helped to make 500 L of CW.<sup>158</sup>



- (5) Point-of-use water recycling products for personal and local reuse, such as portable, chemical-free, ozone-based disinfection solutions, using hydrodynamic cavitation, acoustic cavitation, and electrochemical oxidation, may lead to energy-efficient water treatment and recycling across oil and gas industries, municipalities, mining industries, *etc.*, at capacities as large as 12,492 L/min.<sup>159</sup> Note that more than 80% of wastewater is discharged into surface water bodies in developing countries today. India alone generates approximately 6.2 million m<sup>3</sup> of untreated industrial water every day.<sup>160</sup> Such solutions will contribute to better wastewater management and preservation of freshwater resources.
- (6) Placing compact nanosensors on water bottles and other water-based beverage containers to monitor water quality (pH, hardness, turbidity, *etc.*) and to create an interconnected network (Internet of Nano Things) will generate opportunities.<sup>133</sup>
- (7) Self-cleaning fabrics lead to reductions in consumption of water, detergent, electricity, or an equivalent amount of CO<sub>2</sub>. Nanomaterials such as SiO<sub>2</sub> NPs, CNTs, TiO<sub>2</sub> NPs, *etc.*, are known to demonstrate photocatalytic self-cleaning through the creation of hierarchical structures, whereas adsorption of organic molecules such as alkanethiols and fluorosilanes imparts water repellency to surfaces by lowering their surface energy. A U.S. study found that a treated, self-cleaning fabric could reduce electricity and water consumption by as much as 84%, compared to an untreated fabric, while undergoing 50 laundry cycles in its lifetime.<sup>161</sup>
- (8) Waterless vacuum toilets with incorporated fecal and urinal waste-repellant nanocoatings are possible at the domestic level.<sup>162</sup> Also, the possibility of nanoenabled nutrient recovery from human feces and urine could be explored for reuse at homes.<sup>163</sup> Overcoming the social stigma is crucial to implement such solutions, particularly in developing countries.
- (9) Next-generation membranes for desalination are needed. At present, production of 1 m<sup>3</sup> of CW through RO desalination consumes approximately 3–5 kWh of electricity, although enhanced efficiency has been demonstrated.<sup>164</sup> Highly selective membranes can filter chlorine and boron from seawater in a single pass, unlike the multiple passes required in RO that currently makes desalination a costly, and energy- and time-intensive process. One possible direction is the development of aquaporin membranes that offer the required selectivity. However, efficient salt rejection and cost-effective upscaling of the process are required. Synthetic water channels, mimicking aquaporins, such as CNTs and several aligned peptides to form pores, is another possibility. Tunability in terms of pore size is required here. Other promising materials include graphene oxide,<sup>164</sup> MoS<sub>2</sub>,<sup>165</sup> *etc.* The development of next-generation membranes could contribute to achieving the set target of reducing desalination costs from US \$2.00 to US \$0.50 per m<sup>3</sup> (as per the U.S. Department of Energy).<sup>166</sup>
- (10) Nanomaterials can enhance oil recovery in oil and gas industries. For instance, oil viscosity can be reduced by use of a suspension of Al<sub>2</sub>O<sub>3</sub> NPs in distilled water or brine, and rock wettability can be modified by the application of silane-treated silicon dioxide NPs. Both of

these modifications improve oil recovery.<sup>167</sup> An oleogelator-impregnated cellulose pulp effectively recovers oil from oil–water mixtures by congealing it within a matrix, thereby offering an eco-friendly, cost-effective, and practical solution to restore the marine ecosystem from oil spills.<sup>168</sup>

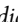
## CONCLUSIONS AND PROSPECTS

CW production presents questions of clean manufacturing, responsible use of materials, equitable distribution, and, ultimately, concern for humanity. Genuine concern for water availability puts limits on reckless growth and consumption. Water, therefore, presents an appropriate subject on which green chemistry and green manufacturing converge for social good. In this Review, we presented directions for materials science and sustainable growth around water, through the eye of NT, which is interlinked with other disciplines. Similar approaches need to be pursued for other areas such as agriculture, energy, housing, and healthcare for a sustainable planet. Nanotechnology can acquire a significant role in all of them as it expands the limits of materials and functions.

For a more comprehensive treatment of the topic with available NTs currently being explored, it is necessary to go through other perspectives and reviews<sup>169–177</sup> as well. Limitations of space and the nature of this review have kept our discussion focused on affordable and sustainable NT. We have taken a significant number of Indian examples in the article with the notion that it is an aspiring country in dire need of generating data on a large number of water-related issues, thereby offering endless opportunities of discussion and work, and the outcomes are applicable across the world.

## AUTHOR INFORMATION

### Corresponding Author

**Thalappil Pradeep** — Department of Chemistry, DST Unit of Nanoscience (DST UNS) and Thematic Unit of Excellence (TUE), Indian Institute of Technology Madras, Chennai 600036, India;  [orcid.org/0000-0003-3174-534X](https://orcid.org/0000-0003-3174-534X); Email: [pradeep@iitm.ac.in](mailto:pradeep@iitm.ac.in)

### Author

**Ankit Nagar** — Department of Chemistry, DST Unit of Nanoscience (DST UNS) and Thematic Unit of Excellence (TUE), Indian Institute of Technology Madras, Chennai 600036, India

Complete contact information is available at:  
<https://pubs.acs.org/10.1021/acsnano.9b01730>

### Notes

The authors declare no competing financial interest.

## ACKNOWLEDGMENTS

T.P. thanks his former and current students and associates whose work enriched his understanding of the subject area. Work in this area has been supported by the Department of Science and Technology, Government of India.

## VOCABULARY

**hydrophobicity**, a physical property in which molecules show absence of affinity toward water and prefer nonpolar interactions with molecules of similar nature, leading to positive change in their free energy, thereby causing

segregation of water molecules; **photocatalysis**, a phenomenon in which a reaction is accelerated due to the presence of a catalyst which generates electron-hole pairs upon irradiation to create active species such as free radicals, enabling secondary pathways and reducing activation energy barrier for the reaction; **desalination**, a process of removal of dissolved minerals and salts from high-salinity water to obtain product freshwater and concentrated brine for disposal; **nanosensors**, a class of devices that utilize unique properties of nanomaterials to detect and quantify events occurring at nanoscale; **specific energy consumption**, a variable defined as amount of energy consumed per unit of production

## REFERENCES

- (1) Urban Population (% of total population). *The World Bank Data*; The World Bank Group: Washington, D.C., 2019 <https://data.worldbank.org/indicator/SP.URB.TOTL.IN.ZS?end=2016&start=2000> (accessed 2019/07/18).
- (2) Gupta, P.; Blum, F.; Jain, D.; John, S.; Seth, S.; Singhi, A. *India Development Update: India's Growth Story*; 123152; The World Bank Group: Washington, D.C., 2018.
- (3) Intergovernmental Panel on Climate Change. *Mitigation Of Climate Change*; Cambridge University Press: New York, 2014.
- (4) Grooten, M.; Almond, R. E. A. *Living Planet Report - 2018: Aiming Higher*; WWF: Switzerland, 2018.
- (5) Sreekumaran Nair, A.; Tom, R. T.; Pradeep, T. Detection and Extraction of Endosulfan by Metal Nanoparticles. *J. Environ. Monit.* **2003**, *5*, 363–365.
- (6) Nair, A.; Pradeep, T. Halocarbon Mineralization and Catalytic Destruction by Metal Nanoparticles. *Curr. Sci.* **2003**, *84*, 1560–1563.
- (7) Pradeep, T.; Nair, A. S. *Method for the Preparation of Adsorption Compositions Including Gold or Silver Nanoparticles*. United States Patent US7968493. June 28, 2011.
- (8) Pradeep, T.; Nair, A. S. *A Method of Preparing Purified Water from Water Containing Pesticides (Chlorpyrifos and Malathion)*. Indian Patent 200767. June 2, 2006.
- (9) Directive 2006/118/EC of the European Parliament and of the Council of 12 December 2006 on the Protection of Groundwater against Pollution and Deterioration. *Official Journal of the European Union*; European Union: Brussels, Belgium, 2006; pp 19–31.
- (10) Kumar, A. A.; Som, A.; Longo, P.; Sudhakar, C.; Bhuin, R. G.; Gupta, S. S.; Anshup; Sankar, M. U.; Chaudhary, A.; Kumar, R.; Pradeep, T. Confined Metastable 2-Line Ferrihydrite for Affordable Point-of-Use Arsenic-Free Drinking Water. *Adv. Mater.* **2017**, *29*, 1604260.
- (11) Maliyekkal, M. S.; Anshup Pradeep, T. *Removal of Fluoride, Alkalinity, Heavy Metals and Suspended Solids Simultaneously Adsorbent Synthesis, Adsorbent Composition and a Device for Affordable Drinking Water*. Indian Patent 313917, 2019.
- (12) Pradeep, T.; Baidya, A.; Rath, B. B.; Kumar, A. A. *Cellulose Nanocrystal Templated Iron Oxyhydroxide Based Adsorbent for Arsenic Removal from Water and a Device Thereof*. Indian Patent Application 201641027660, 2016.
- (13) *Aquananotechnology: Global Prospects*; Reisner, D. E., Pradeep, T., Eds.; CRC Press: Boca Raton, FL, 2014.
- (14) Carpenter, A. W.; de Lannoy, C.-F.; Wiesner, M. R. Cellulose Nanomaterials in Water Treatment Technologies. *Environ. Sci. Technol.* **2015**, *49*, 5277–5287.
- (15) *WHO Guidelines for Drinking-Water Quality*, 3rd ed.; WHO Press: Geneva, Switzerland, 2008, Vol. 1, p 564.
- (16) *Technical Fact Sheet: Final Rule for Arsenic in Drinking Water*; EPA 815-F-00-016; US EPA: Washington, D.C., 2001.
- (17) Rehman, K.; Fatima, F.; Waheed, I.; Akash, M. S. H. Prevalence of Exposure of Heavy Metals and their Impact on Health Consequences. *J. Cell. Biochem.* **2018**, *119*, 157–184.
- (18) Agusa, T.; Kubota, R.; Kunito, T.; Minh, T. B.; Trang, P. T. K.; Chamnan, C.; Iwata, H.; Viet, P. H.; Tana, T. S.; Tanabe, S. Arsenic Pollution in Groundwater of Vietnam and Cambodia: A Review. *Biomed. Res. Trace Elem.* **2007**, *18*, 35–47.
- (19) Pokhrel, D.; Bhandari, B. S.; Viraraghavan, T. Arsenic Contamination of Groundwater in the Terai Region of Nepal: An Overview of Health Concerns and Treatment Options. *Environ. Int.* **2009**, *35*, 157–161.
- (20) Brinkel, J.; Khan, M.; Kraemer, A. A Systematic Review of Arsenic Exposure and Its Social and Mental Health Effects with Special Reference to Bangladesh. *Int. J. Environ. Res. Public Health* **2009**, *6*, 1609–1619.
- (21) Ng, J. C.; Wang, J.; Shraim, A. A. Global Health Problem Caused by Arsenic from Natural Sources. *Chemosphere* **2003**, *52*, 1353–1359.
- (22) McClintock, T. R.; Chen, Y.; Bundschuh, J.; Oliver, J. T.; Navoni, J.; Olmos, V.; Lepori, E. V.; Ahsan, H.; Parvez, F. Arsenic Exposure in Latin America: Biomarkers, Risk Assessments and Related Health Effects. *Sci. Total Environ.* **2012**, *429*, 76–91.
- (23) Mendez, W. M.; Eftim, S.; Cohen, J.; Warren, I.; Cowden, J.; Lee, J. S.; Sams, R. Relationships between Arsenic Concentrations in Drinking Water and Lung and Bladder Cancer Incidence in US Counties. *J. Exposure Sci. Environ. Epidemiol.* **2017**, *27*, 235–243.
- (24) Mathew, A.; Sajanlal, P. R.; Pradeep, T. Selective Visual Detection of TNT at the Sub-zeptomole Level. *Angew. Chem., Int. Ed.* **2012**, *51*, 9596–9600.
- (25) Wang, L.; Boutilier, M. S. H.; Kidambi, P. R.; Jang, D.; Hadjiconstantinou, N. G.; Karnik, R. Fundamental Transport Mechanisms, Fabrication and Potential Applications of Nanoporous Atomically Thin Membranes. *Nat. Nanotechnol.* **2017**, *12*, 509–522.
- (26) Sun, Z.; Liao, T.; Li, W.; Dou, Y.; Liu, K.; Jiang, L.; Kim, S.-W.; Ho Kim, J.; Xue Dou, S. Fish-Scale Bio-Inspired Multifunctional ZnO Nanostructures. *NPG Asia Mater.* **2015**, *7*, No. e232.
- (27) Li, Y.; He, L.; Zhang, X.; Zhang, N.; Tian, D. External-Field-Induced Gradient Wetting for Controllable Liquid Transport: From Movement on the Surface to Penetration into the Surface. *Adv. Mater.* **2017**, *29*, 1703802.
- (28) *Porosity in Carbons: Characterization and Applications*; Patrick, J. W. Ed.; Wiley: London, UK, 1995.
- (29) Pollard, S. J. T.; Fowler, G. D.; Sollars, C. J.; Perry, R. Low-Cost Adsorbents for Waste and Wastewater Treatment: A Review. *Sci. Total Environ.* **1992**, *116*, 31–52.
- (30) Das, R.; Vecitis, C. D.; Schulze, A.; Cao, B.; Ismail, A. F.; Lu, X.; Chen, J.; Ramakrishna, S. Recent Advances in Nanomaterials for Water Protection and Monitoring. *Chem. Soc. Rev.* **2017**, *46*, 6946–7020.
- (31) Sarkar, D.; Mondal, B.; Som, A.; Ravindran, S. J.; Jana, S. K.; Manju, C. K.; Pradeep, T. Holey MoS<sub>2</sub> Nanosheets with Photocatalytic Metal Rich Edges by Ambient Electrospray Deposition for Solar Water Disinfection. *Glob. Challenges* **2018**, *2*, 1800052.
- (32) Tavakolian, M.; Jafari, S. M.; Van de Ven, T. G. A Review on Surface-Functionalized Cellulosic Nanostructures as Biocompatible Antibacterial Materials. *Nano-Micro Lett.* **2020**, *12*, 1–23.
- (33) Sarkar, D.; Mahapatra, A.; Som, A.; Kumar, R.; Nagar, A.; Baidya, A.; Pradeep, T. Patterned Nanobrush Nature Mimics with Unprecedented Water-Harvesting Efficiency. *Adv. Mater. Interfaces* **2018**, *5*, 1800667.
- (34) Vadahanambi, S.; Lee, S. H.; Kim, W. J.; Oh, I. K. Arsenic removal from contaminated water using three-dimensional graphene-carbon nanotube-iron oxide nanostructures. *Environ. Sci. Technol.* **2013**, *47*, 10510–10517.
- (35) *Indian Scientists Develop Low-Cost Arsenic Water Filter*; The Third Pole. <https://www.thethirdpole.net/2016/01/22/indian-scientists-develop-low-cost-arsenic-water-filter/> (accessed 2020/05/01).
- (36) *Inmodi - Innovative Technologies in Water Treatment*. <https://www.inmodi.in/> (accessed 2020/05/12).
- (37) *Vayujal*. <http://www.vayujal.com/> (accessed 2020/05/12).
- (38) *Idadesal*. <https://idadesal.org/> (accessed 2019/07/18).
- (39) Shahzad, M. W.; Burhan, M.; Ang, L.; Ng, K. C. Adsorption Desalination—Principles, Process Design, and Its Hybrids for Future

Sustainable Desalination. *Emerg. Technol. Sustain. Desalin. Handb.* **2018**, 3–34.

(40) Mishra, D. The Cost of Desalination. *Advisian*. <https://www.advisian.com/en/global-perspectives/the-cost-of-desalination> (accessed 2019/07/18).

(41) Shahzad, M. W.; Burhan, M.; Ang, L.; Ng, K. C. Energy-Water-Environment Nexus Underpinning Future Desalination Sustainability. *Desalination* **2017**, 413, 52–64.

(42) Gethard, K.; Sae-Khow, O.; Mitra, S. Water Desalination Using Carbon-Nanotube-Enhanced Membrane Distillation. *ACS Appl. Mater. Interfaces* **2011**, 3, 110–114.

(43) Dudchenko, A. V.; Chen, C.; Cardenas, A.; Rolf, J.; Jassby, D. Frequency-Dependent Stability of CNT Joule Heaters in Ionizable Media and Desalination Processes. *Nat. Nanotechnol.* **2017**, 12, 557–563.

(44) Chen, W.; Chen, S.; Liang, T.; Zhang, Q.; Fan, Z.; Yin, H.; Huang, K.-W.; Zhang, X.; Lai, Z.; Sheng, P. High-Flux Water Desalination with Interfacial Salt Sieving Effect in Nanoporous Carbon Composite Membranes. *Nat. Nanotechnol.* **2018**, 13, 345–350.

(45) Gao, M.; Zhu, L.; Peh, C. K.; Ho, G. W. Solar Absorber Material and System Designs for Photothermal Water Vaporization towards Clean Water and Energy Production. *Energy Environ. Sci.* **2019**, 12, 841–864.

(46) Ghasemi, H.; Ni, G.; Marconnet, A. M.; Loomis, J.; Yerci, S.; Miljkovic, N.; Chen, G. Solar Steam Generation by Heat Localization. *Nat. Commun.* **2014**, 5, 4449.

(47) Qasim, M.; Badrelzaman, M.; Darwish, N. N.; Darwish, N. A.; Hilal, N. Reverse Osmosis Desalination: A State-Of-The-Art Review. *Desalination* **2019**, 459, 59–104.

(48) Elimelech, M.; Phillip, W. A. The Future of Seawater Desalination: Energy, Technology, and the Environment. *Science* **2011**, 333, 712–717.

(49) Tan, Z.; Chen, S.; Peng, X.; Zhang, L.; Gao, C. Polyamide Membranes with Nanoscale Turing Structures for Water Purification. *Science* **2018**, 360, 518–521.

(50) Chowdhury, M. R.; Steffes, J.; Huey, B. D.; McCutcheon, J. R. 3D Printed Polyamide Membranes for Desalination. *Science* **2018**, 361, 682–686.

(51) Majumder, M.; Chopra, N.; Hinds, B. Effect of Tip Functionalization on Transport through Vertically Oriented Carbon Nanotube Membranes. *J. Am. Chem. Soc.* **2005**, 127, 9062–9070.

(52) Das, R.; Ali, M. E.; Hamid, S. B. A.; Ramakrishna, S.; Chowdhury, Z. Z. Carbon Nanotube Membranes for Water Purification: A Bright Future in Water Desalination. *Desalination* **2014**, 336, 97–109.

(53) Dervin, S.; Dionysiou, D. D.; Pillai, S. C. 2D Nanostructures for Water Purification: Graphene and Beyond. *Nanoscale* **2016**, 8, 15115–15131.

(54) Cohen-Tanugi, D.; Grossman, J. C. Nanoporous Graphene as a Reverse Osmosis Membrane: Recent Insights from Theory and Simulation. *Desalination* **2015**, 366, 59–70.

(55) Werber, J. R.; Osuji, C. O.; Elimelech, M. Materials for Next-Generation Desalination and Water Purification Membranes. *Nat. Rev. Mater.* **2016**, 1, 16018.

(56) Tang, C. Y.; Zhao, Y.; Wang, R.; Hélix-Nielsen, C.; Fane, A. G. Desalination by Biomimetic Aquaporin Membranes: Review of Status and Prospects. *Desalination* **2013**, 308, 34–40.

(57) Zhao, Y.; Li, X.; Shen, J.; Gao, C.-J.; Van der Bruggen, B. The Potential of Kevlar Aramid Nanofibers Composite Membranes. *J. Mater. Chem. A* **2020**, 8, 7548.

(58) Li, Y.; Wong, E.; Mai, Z.; Van der Bruggen, B. Fabrication of Composite Polyamide/Kevlar Aramid Nanofiber Nanofiltration Membranes with High Permeability in Water Desalination. *J. Membr. Sci.* **2019**, 592, 117396.

(59) Zhao, Y.; Qiu, Y.; Mai, Z.; Ortega, E.; Shen, J.; Gao, C.; Van der Bruggen, B. Symmetrically Recombined Nanofibers in a High-Selectivity Membrane for Cation Separation in High Temperature and Organic Solvent. *J. Mater. Chem. A* **2019**, 7, 20006–20012.

(60) Blandin, G.; Verliefde, A. R. D.; Tang, C. Y.; Le-Clech, P. Opportunities to Reach Economic Sustainability in Forward Osmosis-Reverse Osmosis Hybrids for Seawater Desalination. *Desalination* **2015**, 363, 26–36.

(61) Zirehpour, A.; Rahimpour, A.; Khoshhal, S.; Firouzjaei, M. D.; Ghoreysy, A. A. The Impact of MOF Feasibility to Improve the Desalination Performance and Antifouling Properties of FO Membranes. *RSC Adv.* **2016**, 6, 70174–70185.

(62) Kwak, S.-Y.; Jung, S. G.; Kim, S. H. Structure-Motion-Performance Relationship of Flux-Enhanced Reverse Osmosis (RO) Membranes Composed of Aromatic Polyamide Thin Films. *Environ. Sci. Technol.* **2001**, 35, 4334–4340.

(63) Kim, H. J.; Choi, K.; Baek, Y.; Kim, D.-G.; Shim, J.; Yoon, J.; Lee, J.-C. High-Performance Reverse Osmosis CNT/Polyamide Nanocomposite Membrane by Controlled Interfacial Interactions. *ACS Appl. Mater. Interfaces* **2014**, 6, 2819–2829.

(64) Freger, V. Nanoscale Heterogeneity of Polyamide Membranes Formed by Interfacial Polymerization. *Langmuir* **2003**, 19, 4791–4797.

(65) Choi, W.; Choi, J.; Bang, J.; Lee, J.-H. Layer-by-Layer Assembly of Graphene Oxide Nanosheets on Polyamide Membranes for Durable Reverse-Osmosis Applications. *ACS Appl. Mater. Interfaces* **2013**, 5, 12510–12519.

(66) Wang, M.; Wang, Z.; Wang, X.; Wang, S.; Ding, W.; Gao, C. Layer-by-Layer Assembly of Aquaporin Z-Incorporated Biomimetic Membranes for Water Purification. *Environ. Sci. Technol.* **2015**, 49, 3761–3768.

(67) Gu, J.; Lee, S.; Stafford, C. M.; Lee, J. S.; Choi, W.; Kim, B.; Baek, K.; Chan, E. P.; Chung, J. Y.; Bang, J.; et al. Molecular Layer-by-layer Assembled Thin-film Composite Membranes for Water Desalination. *Adv. Mater.* **2013**, 25, 4778–4782.

(68) Stafford, C. M. Scalable Manufacturing of Layer-by-Layer Membranes for Water Purification. In *Frontiers of Engineering: Reports on Leading-Edge Engineering from the 2016 Symposium*; National Academies Press: Washington, D.C., 2017; pp 69–74.

(69) Alabi, A.; AlHajaj, A.; Cseri, L.; Szekely, G.; Budd, P.; Zou, L. Review of Nanomaterials-Assisted Ion Exchange Membranes for Electromembrane Desalination. *npj Clean Water* **2018**, 1, 10.

(70) Wood, E. N.; Tucker, J. H.; Papastamatiki, A.; Caudle, D.; Hock, R.; Murphy, G. W. *Electrochemical Demineralization of Water with Carbon Electrodes*; U.S. Department of the Interior: Washington, D.C., 1965.

(71) Gupta, S. S.; Islam, M. R.; Pradeep, T. Capacitive Deionization (CDI): An Alternative Cost-Efficient Desalination Technique. *Adv. Water Purif. Technol.* **2019**, 165–202.

(72) Długolecki, P.; van der Wal, A. Energy Recovery in Membrane Capacitive Deionization. *Environ. Sci. Technol.* **2013**, 47, 4904–4910.

(73) Gaikwad, M. S.; Balomajumder, C. Capacitive Deionization for Desalination Using Nanostructured Electrodes. *Anal. Lett.* **2016**, 49, 1641–1655.

(74) Tang, K.; Yiaccoumi, S.; Li, Y.; Tsouris, C. Enhanced Water Desalination by Increasing the Electroconductivity of Carbon Powders for High-Performance Flow-Electrode Capacitive Deionization. *ACS Sustainable Chem. Eng.* **2019**, 7, 1085–1094.

(75) Jeon, S.; Park, H.; Yeo, J.; Yang, S.; Cho, C. H.; Han, M. H.; Kim, D. K. Desalination via a New Membrane Capacitive Deionization Process Utilizing Flow-Electrodes. *Energy Environ. Sci.* **2013**, 6, 1471.

(76) Abe, Y. Physical State of the Very Early Earth. *Lithos* **1993**, 30, 223–235.

(77) Olivier, J. Fog-Water Harvesting along the West Coast of South Africa: A Feasibility Study. *Water SA* **2002**, 28, 349–360.

(78) Tu, Y.; Wang, R.; Zhang, Y.; Wang, J. Progress and Expectation of Atmospheric Water Harvesting. *Joule* **2018**, 2, 1452–1475.

(79) Nørgaard, T.; Dacke, M. Fog-Basking Behaviour and Water Collection Efficiency in Namib Desert Darkling Beetles. *Front. Zool.* **2010**, 7, 23.



- (80) Zheng, Y.; Bai, H.; Huang, Z.; Tian, X.; Nie, F.-Q.; Zhao, Y.; Zhai, J.; Jiang, L. Directional Water Collection on Wetted Spider Silk. *Nature* **2010**, *463*, 640–643.
- (81) Ghosh, A.; Beaini, S.; Zhang, B. J.; Ganguly, R.; Megaridis, C. M. Enhancing Dropwise Condensation through Bioinspired Wettability Patterning. *Langmuir* **2014**, *30*, 13103–13115.
- (82) Zhu, H.; Yang, F.; Li, J.; Guo, Z. High-Efficiency Water Collection on Biomimetic Material with Superwetable Patterns. *Chem. Commun.* **2016**, *52*, 12415–12417.
- (83) Feng, X. J.; Jiang, L. Design and Creation of Superwetting/Antiwetting Surfaces. *Adv. Mater.* **2006**, *18*, 3063–3078.
- (84) Wen, R.; Li, Q.; Wu, J.; Wu, G.; Wang, W.; Chen, Y.; Ma, X.; Zhao, D.; Yang, R. Hydrophobic Copper Nanowires for Enhancing Condensation Heat Transfer. *Nano Energy* **2017**, *33*, 177–183.
- (85) Attinger, D.; Frankiewicz, C.; Betz, A. R.; Schutzius, T. M.; Ganguly, R.; Das, A.; Kim, C.-J.; Megaridis, C. M. Surface Engineering for Phase Change Heat Transfer: A Review. *MRS Energy Sustain.* **2014**, *1*, E4.
- (86) Zhang, J.; Han, Y. Shape-Gradient Composite Surfaces: Water Droplets Move Uphill. *Langmuir* **2007**, *23*, 6136–6141.
- (87) Hou, Y. P.; Feng, S. L.; Dai, L. M.; Zheng, Y. M. Droplet Manipulation on Wettable Gradient Surfaces with Micro-/Nano-Hierarchical Structure. *Chem. Mater.* **2016**, *28*, 3625–3629.
- (88) Peng, S.; Bhushan, B. Mechanically Durable Superoleophobic Aluminum Surfaces with Microstep and Nanoreticula Hierarchical Structure for Self-Cleaning and Anti-Smudge Properties. *J. Colloid Interface Sci.* **2016**, *461*, 273–284.
- (89) Kim, H.; Yang, S.; Rao, S. R.; Narayanan, S.; Kapustin, E. A.; Furukawa, H.; Umans, A. S.; Yaghi, O. M.; Wang, E. N. Water Harvesting from Air with Metal-Organic Frameworks Powered by Natural Sunlight. *Science* **2017**, *356*, 430–434.
- (90) Fujishima, A.; Honda, K. Electrochemical Photolysis of Water at a Semiconductor Electrode. *Nature* **1972**, *238*, 37–38.
- (91) Hashimoto, K.; Irie, H.; Fujishima, A.  $\text{TiO}_2$  Photocatalysis: A Historical Overview and Future Prospects. *Jpn. J. Appl. Phys.* **2005**, *44*, 8269–8285.
- (92) Wu, T.; Liu, G.; Zhao, J. C.; Hidaka, H.; Serpone, N. Self-Photosensitized Oxidative Transformation of Rhodamine B under Visible Light Irradiation in Aqueous  $\text{TiO}_2$  Dispersions. *J. Phys. Chem. B* **1998**, *102*, 5845–5851.
- (93) Chakraborty, I.; Pradeep, T. Atomically Precise Clusters of Noble Metals: Emerging Link between Atoms and Nanoparticles. *Chem. Rev.* **2017**, *117*, 8208–8271.
- (94) AbdulHalim, L. G.; Bootharaju, M. S.; Tang, Q.; Del Gobbo, S.; AbdulHalim, R. G.; Eddaoudi, M.; Jiang, D.; Bakr, O. M.  $\text{Ag}_{29}(\text{BDT})_{12}(\text{TPP})_4$ : A Tetravalent Nanocluster. *J. Am. Chem. Soc.* **2015**, *137*, 11970–11975.
- (95) Habeeb Muhammed, M. A.; Verma, P. K.; Pal, S. K.; Retnakumari, A.; Koyakutty, M.; Nair, S.; Pradeep, T. Luminescent Quantum Clusters of Gold in Bulk by Albumin-Induced Core Etching of Nanoparticles: Metal Ion Sensing, Metal-Enhanced Luminescence, and Biolabeling. *Chem. - Eur. J.* **2010**, *16*, 10103–10112.
- (96) Ghosh, A.; Jeseentharani, V.; Ganayee, M. A.; Hemalatha, R. G.; Chaudhari, K.; Vijayan, C.; Pradeep, T. Approaching Sensitivity of Tens of Ions Using Atomically Precise Cluster-Nanofiber Composites. *Anal. Chem.* **2014**, *86*, 10996–11001.
- (97) Liang, G.; Ren, F.; Gao, H.; Wu, Q.; Zhu, F.; Tang, B. Z. Bioinspired Fluorescent Nanosheets for Rapid and Sensitive Detection of Organic Pollutants in Water. *ACS Sens.* **2016**, *1*, 1272–1278.
- (98) Fang, X.; Chen, X.; Liu, Y.; Li, Q.; Zeng, Z.; Maiyalagan, T.; Mao, S. Nanocomposites of Zr (IV)-Based Metal-Organic Frameworks and Reduced Graphene Oxide for Electrochemically Sensing Ciprofloxacin in Water. *ACS Appl. Nano Mater.* **2019**, *2*, 2367–2376.
- (99) Bhaskar, S.; Ramamurthy, S. S. Mobile Phone-Based Picomolar Detection of Tannic Acid on  $\text{Nd}_2\text{O}_3$  Nanorod-Metal Thin-Film Interfaces. *ACS Appl. Nano Mater.* **2019**, *2*, 4613–4625.
- (100) Fan, L.; Zhao, G.; Shi, H.; Liu, M.; Wang, Y.; Ke, H. A Femtomolar Level and Highly Selective  $17\beta$ -Estradiol Photoelectrochemical Aptasensor Applied in Environmental Water Samples Analysis. *Environ. Sci. Technol.* **2014**, *48*, 5754–5761.
- (101) Colvin, V. L. The Potential Environmental Impact of Engineered Nanomaterials. *Nat. Biotechnol.* **2003**, *21*, 1166–1170.
- (102) Kashiwada, S. Distribution of Nanoparticles in the See-Through Medaka (*Oryzias Latipes*). *Environ. Health Perspect.* **2006**, *114*, 1697–1702.
- (103) Mauter, M. S.; Zucker, I.; Perreault, F.; Werber, J. R.; Kim, J.-H.; Elimelech, M. The Role of Nanotechnology in Tackling Global Water Challenges. *Nat. Sustain.* **2018**, *1*, 166–175.
- (104) Mitrano, D. M.; Ranville, J. F.; Bednar, A.; Kazor, K.; Hering, A. S.; Higgins, C. P. Tracking Dissolution of Silver Nanoparticles at Environmentally Relevant Concentrations in Laboratory, Natural, and Processed Waters Using Single Particle ICP-MS (SpICP-MS). *Environ. Sci.: Nano* **2014**, *1*, 248–259.
- (105) Dobias, J.; Bernier-Latmani, R. Silver Release from Silver Nanoparticles in Natural Waters. *Environ. Sci. Technol.* **2013**, *47*, 4140–4146.
- (106) Hippo Roller. <https://www.hipporoller.org/> (access April 20, 2020).
- (107) Tiwari, B.; Zhang, D.; Winslow, D.; Lee, C. H.; Hao, B.; Yap, Y. K. A Simple and Universal Technique to Extract One- and Two-Dimensional Nanomaterials from Contaminated Water. *ACS Appl. Mater. Interfaces* **2015**, *7*, 26108–26116.
- (108) Gao, W.; Majumder, M.; Alemany, L. B.; Narayanan, T. N.; Ibarra, M. A.; Pradhan, B. K.; Ajayan, P. M. Engineered Graphite Oxide Materials for Application in Water Purification. *ACS Appl. Mater. Interfaces* **2011**, *3*, 1821–1826.
- (109) Gupta, S. S.; Sreeprasad, T. S.; Maliyekkal, S. M.; Das, S. K.; Pradeep, T. Graphene from Sugar and Its Application in Water Purification. *ACS Appl. Mater. Interfaces* **2012**, *4*, 4156–4163.
- (110) AMRIT - Arsenic and Metal Removal by Indian Technology; IIT Madras: Chennai, 2015.
- (111) Tepper, F.; Kaledin, L. A.; *Drinking Water Filtration Device*. U.S. Patent 7390343. June 24, 2008.
- (112) Hartikainen, H.; Venäläinen, S.; Nuopponen, M.; Meriluoto, A. *Water Treatment*. U.S. Patent 20190039918. February 7, 2019.
- (113) Pure US Sourced and Produced Clinoptilolite Zeolite. KMI Zeolite. <https://www.kmizeolite.com/> (accessed 2019/07/18).
- (114) Revanur, R.; Roh, I.; Klare, J. E.; Noy, A.; Bakajin, O. *Thin Film Composite Membranes for Forward Osmosis, and Their Preparation Methods*. U.S. Patent 8920654. December 30, 2014.
- (115) Ratto, T. V.; Holt, J. K.; Szmodis, A. W. *Membranes with Embedded Nanotubes for Selective Permeability*. U.S. Patent 7993524. August 9, 2011.
- (116) Jensen, P. H.; Keller, D.; Nielsen, C. H.; Aquaporin, A. S. *Membrane for Filtering of Water*. U.S. Patent 7857978. December 28, 2010.
- (117) Modern Systems and Solutions for Clean Water. *De.mem.* <http://demembranes.com/> (accessed 2019/07/18).
- (118) Zero-Valent Iron Nanoparticles. NANOIRON. <http://nanoiron.cz/en/products/zero-valent-iron-nanoparticles> (accessed 2019/07/18).
- (119) *Annual Report 2017–18; Ministry of Drinking Water and Sanitation*; Government of India: New Delhi, 2018.
- (120) *Detailed Demands for Grants of Ministry of Drinking Water and Sanitation for 2018–19*; Government of India: New Delhi, 2018.
- (121) *Demand for Grants 2018–19 Analysis: Drinking Water and Sanitation*; PRS Legislative Research: New Delhi, 2018.
- (122) *Expenditure Profile 2018–19*; Ministry of Finance; Government of India: New Delhi, 2019.
- (123) Kim, H.; Yang, S.; Narayanan, S.; Umans, A. S.; Wang, E. N.; Rao, S. R. *Sorption-Based Atmospheric Water Harvesting Device*. U.S. Patent 20180171604. June 21, 2018.
- (124) Pradeep, T.; Chaudhary, A.; Sankar, M. U.; Rajarajan, G. *Sustained Silver Release Composition for Water Purification*. U.S. Patent 15677618. July 5, 2018.

- (125) Servida, T.; Servida, E. C. I.; *Idropan Dell'orto Depuratori Srl. Apparatus for Purifying a Liquid and Method for Operating Said Apparatus*. U.S. Patent 20180037479. February 8, 2018.
- (126) Cobianu, C. P.; Dumitru, V. G.; Serban, B. C.; Stratulat, A.; Brezeanu, M.; Buiiu, O. *Honeywell Romania SRL. Metal Oxide Nanocomposite Heterostructure Methods and Hydrogen Sulfide Sensors Including the Same*. U.S. Patent 10067107. September 4, 2018.
- (127) Mi, B.; Hu, M.; *University of Maryland, Baltimore. Layer-by-Layer Assembly of Graphene Oxide Membranes via Electrostatic Interaction and Eludication of Water and Solute Transport Mechanisms*. U.S. Patent 9902141. February 27, 2018.
- (128) George, S. J.; Kumar, M.; Jawaharlal Nehru Centre for Advanced Scientific Research. *Chromophores for the Detection of Volatile Organic Compounds*. U.S. Patent 9376435. June 28, 2016.
- (129) Ghosh, A.; Chhetri, B. P.; *University of Arkansas. Doped Carbonaceous Materials for Photocatalytic Removal of Pollutants under Visible Light, Making Methods and Applications of Same*. U.S. Patent 20190015818. January 17, 2019.
- (130) Nair, R. R.; Budd, P.; Geim, A.; *University of Manchester. Separation of Water Using a Membrane*. U.S. Patent 9844758. December 19, 2017.
- (131) Global Pollution Map <https://www.pollution.org/> (accessed 2019/07/19).
- (132) Hussain, I.; Ahamad, K. U.; Nath, P. Low-Cost, Robust, and Field Portable Smartphone Platform Photometric Sensor for Fluoride Level Detection in Drinking Water. *Anal. Chem.* **2017**, *89*, 767–775.
- (133) Vikesland, P. J. Nanosensors for Water Quality Monitoring. *Nat. Nanotechnol.* **2018**, *13*, 651–660.
- (134) Lim, R. J.; Xie, M.; Sk, M. A.; Lee, J.-M.; Fisher, A.; Wang, X.; Lim, K. H. A Review on the Electrochemical Reduction of CO<sub>2</sub> in Fuel Cells, Metal Electrodes and Molecular Catalysts. *Catal. Today* **2014**, *233*, 169–180.
- (135) *Energy Statistics* (25th issue); Central Statistics Office, Ministry of Statistics and Programme Implementation, Government of India, New Delhi, 2018.
- (136) *Census of India. Housing, Household Amenities And Assets*; Government of India: Karnataka; Bangalore, 2011.
- (137) Lele, S.; Srinivasan, V.; Jamwal, P.; Thomas, B. K.; Eswar, M.; Zuhail, T. M. Water Management in Arkavathy Basin: A Situation Analysis. *Environment and Development Discussion Paper No. 1*; Ashoka Trust for Research in Ecology and the Environment: Bengaluru, 2013.
- (138) *Bangalore Water Supply and Sewerage Board*. [https://www.bwssb.gov.in/com\\_content?page=3&info\\_for=3](https://www.bwssb.gov.in/com_content?page=3&info_for=3) (accessed 2019/07/19).
- (139) Parameshwara Murthy, P. M.; Sadashiva Murthy, B. M.; Kavya, S. Qualitative Characterization of Greywater from a Residential Complex in Bengaluru City, Karnataka, India. *Int. J. Eng. Res.* **2016**, *V5*, 194–199.
- (140) Hodges, B. C.; Cates, E. L.; Kim, J.-H. Challenges and Prospects of Advanced Oxidation Water Treatment Processes Using Catalytic Nanomaterials. *Nat. Nanotechnol.* **2018**, *13*, 642–650.
- (141) Vreeland, J. M. The Revival of Colored Cotton. *Sci. Am.* **1999**, *280*, 112–118.
- (142) Singh, A. How Colourful is the Future of Naturally Coloured Cotton?. *Cotton Statistics and News*; Cotton Association of India: Mumbai, India, 2014.
- (143) Boopathi, N. M.; Sathish, S.; Dachinamoorthy, P.; Kavitha, P.; Ravikesavan, R. Usefulness and Utilization of Indian Cotton Germplasm. *World Cotton Germplasm Resources*; InTech: Rijeka, Croatia, 2014.
- (144) Das, S. K.; Khan, M. M. R.; Parandhaman, T.; Laffir, F.; Guha, A. K.; Sekaran, G.; Mandal, A. B. Nano-Silica Fabricated with Silver Nanoparticles: Antifouling Adsorbent for Efficient Dye Removal, Effective Water Disinfection and Biofouling Control. *Nanoscale* **2013**, *5*, 5549.
- (145) Mack, E. A.; Wrase, S. Erratum: Correction: A Burgeoning Crisis? A Nationwide Assessment of the Geography of Water Affordability in the United States (*PloS One* (2017) 12 1 (E0169488)). *PLoS One* **2017**, *12*, No. e0176645.
- (146) Baidya, A.; Das, S. K.; Ras, R. H. A.; Pradeep, T. Fabrication of a Waterborne Durable Superhydrophobic Material Functioning in Air and under Oil. *Adv. Mater. Interfaces* **2018**, *5*, 1701523.
- (147) Oßmann, B. E.; Sarau, G.; Holtmannspötter, H.; Pischetsrieder, M.; Christiansen, S. H.; Dicke, W. Small-Sized Microplastics and Pigmented Particles in Bottled Mineral Water. *Water Res.* **2018**, *141*, 307–316.
- (148) Cordner, A.; De La Rosa, V. Y.; Schaidler, L. A.; Rudel, R. A.; Richter, L.; Brown, P. Guideline Levels for PFOA and PFOS in Drinking Water: The Role of Scientific Uncertainty, Risk Assessment Decisions, and Social Factors. *J. Exposure Sci. Environ. Epidemiol.* **2019**, *29*, 157–171.
- (149) Saleh, N. B.; Khalid, A.; Tian, Y.; Ayres, C.; Sabaraya, I. V.; Pietari, J.; Hanigan, D.; Chowdhury, I.; Apul, O. G. Removal of Poly- and per-Fluoroalkyl Substances from Aqueous Systems by Nano-Enabled Water Treatment Strategies. *Environ. Sci. Water Res. Technol.* **2019**, *5*, 198–208.
- (150) Chen, C.; Liu, D.; He, L.; Qin, S.; Wang, J.; Razal, J. M.; Kotov, N. A.; Lei, W. Bio-Inspired Nanocomposite Membranes for Osmotic Energy Harvesting. *Joule* **2020**, *4*, 247–261.
- (151) Logan, B. E.; Elimelech, M. Membrane-Based Processes for Sustainable Power Generation Using Water. *Nature* **2012**, *488*, 313–319.
- (152) The Methanol Industry. *Methanol Institute*. <https://www.methanol.org/the-methanol-industry/> (accessed 2019/07/19).
- (153) Artz, J.; Müller, T. E.; Thenert, K.; Kleinekorte, J.; Meys, R.; Sternberg, A.; Bardow, A.; Leitner, W. Sustainable Conversion of Carbon Dioxide: An Integrated Review of Catalysis and Life Cycle Assessment. *Chem. Rev.* **2018**, *118*, 434–504.
- (154) Vundavalli, R.; Vundavalli, S.; Nakka, M.; Rao, D. S. Biodegradable Nano-Hydrogels in Agricultural Farming - Alternative Source For Water Resources. *Procedia Mater. Sci.* **2015**, *10*, 548–554.
- (155) Amarasinghe, U. A.; McCornick, P. G.; Shah, T. India's Water Demand Scenarios to 2025 and 2050: A Fresh Look. *Strategic Analyses of the National River Linking Project (NRLP) of India; Series 2*; International Water Management Institute: Bangalore, 2009; pp 23–61.
- (156) Koehler, A.; Wildbolz, C. Comparing the Environmental Footprints of Home-Care and Personal-Hygiene Products: The Relevance of Different Life-Cycle Phases. *Environ. Sci. Technol.* **2009**, *43*, 8643–8651.
- (157) *Eco-Indicator 99 Manual for Designers; Ministry of Housing; Spatial Planning and the Environment: Communications Directorate: The Netherlands, 2000.*
- (158) Sankar, M. U.; Aigal, S.; Maliyekkal, S. M.; Chaudhary, A.; Anshup; Kumar, A. A.; Chaudhari, K.; Pradeep, T. Biopolymer-Reinforced Synthetic Granular Nanocomposites for Affordable Point-of-Use Water Purification. *Proc. Natl. Acad. Sci. U. S. A.* **2013**, *110*, 8459–8464.
- (159) McGuire, D.; Jakhete, S. *Enhanced Water Treatment for Reclamation of Waste Fluids and Increased Efficiency Treatment of Potable Waters*. U.S. Patent 7699994, April 20, 2010.
- (160) Ranade, V. V.; Bhandari, V. M. *Industrial Wastewater Treatment, Recycling and Reuse*; Butterworth-Heinemann: Oxford, U.K., 2014.
- (161) Yun, C.; Islam, M. I.; LeHew, M.; Kim, J. Assessment of Environmental and Economic Impacts Made by the Reduced Laundering of Self-Cleaning Fabrics. *Fibers Polym.* **2016**, *17*, 1296–1304.
- (162) Erdmann, W.; Gienke, T.; Heinrich, H.-J. *Waterless Vacuum Toilet System for Aircraft*. U.S. Patent 6977005, December 20, 2005.
- (163) Simha, P.; Ganesapillai, M. Ecological Sanitation and Nutrient Recovery from Human Urine: How Far Have We Come? A Review. *Sustain. Environ. Res.* **2017**, *27*, 107–116.
- (164) Abraham, J.; Vasu, K. S.; Williams, C. D.; Gopinadhan, K.; Su, Y.; Cherian, C. T.; Dix, J.; Prestat, E.; Haigh, S. J.; Grigorieva, I.

- V.; Carbone, P.; Geim, A. K.; Nair, R. R. Tunable Sieving of Ions Using Graphene Oxide Membranes. *Nat. Nanotechnol.* **2017**, *12*, 546.
- (165) Heiranian, M.; Farimani, A. B.; Aluru, N. R. Water Desalination with a Single-Layer MoS<sub>2</sub> Nanopore. *Nat. Commun.* **2015**, *6*, 8616.
- (166) Patel, P.; Biedermann, L. Will Next-Generation Membranes Rise to the Water Challenge? *MRS Bull.* **2018**, *43*, 406–407.
- (167) Ogolo, N. A.; Olafuyi, O. A.; Onyekonwu, M. O. Enhanced Oil Recovery Using Nanoparticles. SPE 160847-MS. Proceedings from the *SPE Saudi Arabia Section Technical Symposium and Exhibition*, Al-Khobar, Saudi Arabia, April 8–11, 2012; OnePetro: Richardson, Texas, 2012.
- (168) Prathap, A.; Sureshan, K. M. Organogelator-Cellulose Composite for Practical and Eco-Friendly Marine Oil-Spill Recovery. *Angew. Chem.* **2017**, *129*, 9533–9537.
- (169) Alvarez, P. J. J.; Chan, C. K.; Elimelech, M.; Halas, N. J.; Villagrán, D. Emerging Opportunities for Nanotechnology to Enhance Water Security. *Nat. Nanotechnol.* **2018**, *13*, 634.
- (170) Hilal, N.; Wright, C. J. Exploring the Current State of Play for Cost-Effective Water Treatment by Membranes. *npj Clean Water* **2018**, *1*, 8.
- (171) Peng, B.; Tang, J.; Luo, J.; Wang, P.; Ding, B.; Tam, K. C. Applications of Nanotechnology in Oil and Gas Industry: Progress and Perspective. *Can. J. Chem. Eng.* **2018**, *96*, 91–100.
- (172) Lin, S.; Yu, T.; Yu, Z.; Hu, X.; Yin, D. Nanomaterials Safer-by-Design: An Environmental Safety Perspective. *Adv. Mater.* **2018**, *30*, 1705691.
- (173) Ali, I. New Generation Adsorbents for Water Treatment. *Chem. Rev.* **2012**, *112*, 5073–5091.
- (174) Westerhoff, P.; Atkinson, A.; Fortner, J.; Wong, M. S.; Zimmerman, J.; Gardea-Torresdey, J.; Ranville, J.; Herckes, P. Low Risk Posed by Engineered and Incidental Nanoparticles in Drinking Water. *Nat. Nanotechnol.* **2018**, *13*, 661–669.
- (175) Shannon, M. A.; Bohn, P. W.; Elimelech, M.; Georgiadis, J. G.; Mariñas, B. J.; Mayes, A. M. Science and Technology for Water Purification in the Coming Decades. *Nature* **2008**, *452*, 301–310.
- (176) Lu, L.; Guest, J. S.; Peters, C. A.; Zhu, X.; Rau, G. H.; Ren, Z. J. Wastewater Treatment for Carbon Capture and Utilization. *Nat. Sustain.* **2018**, *1*, 750–758.
- (177) Babu, P.; Nambiar, A.; He, T.; Karimi, I. A.; Lee, J. D.; Englezos, P.; Linga, P. A Review of Clathrate Hydrate Based Desalination to Strengthen Energy-Water Nexus. *ACS Sustainable Chem. Eng.* **2018**, *6*, 8093–8107.



# Enhanced Capture of Particulate Matter by Molecularly Charged Electrospun Nanofibers

Pillalamarri Srikrishnarka, Vishal Kumar, Tripti Ahuja, Vidhya Subramanian, Arun Karthick Selvam, Paulami Bose, Shantha Kumar Jenifer, Ananthu Mahendranath, Mohd Azhardin Ganayee, Ramamurthy Nagarajan,\* and Thalappil Pradeep\*



Cite This: *ACS Sustainable Chem. Eng.* 2020, 8, 7762–7773



Read Online

ACCESS |



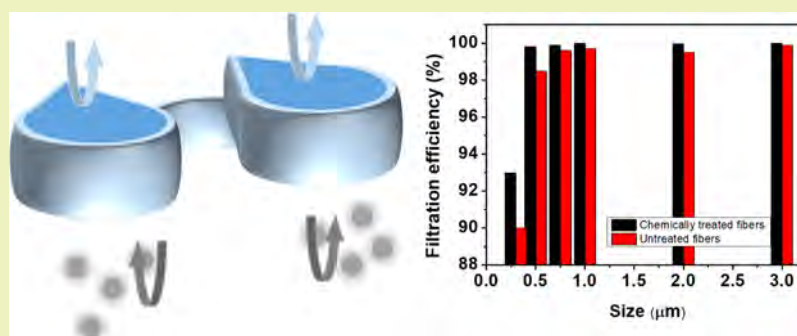
Metrics & More



Article Recommendations



Supporting Information



**ABSTRACT:** We introduce molecularly charged electrospun nanofibers obtained by soft chemical treatment for the capture of particulate matter (PM). These PMs, along with certain volatile organic compounds (VOCs), pose a severe threat not only to human health but also to the environment. As the concentrations of these PMs have been steadily increasing in the Southeast Asian countries, a dire need for protection against these particles is warranted. Filtering out the polluted air using various filtration media, such as face masks and nasal filters, has been the standard method for minimizing exposure to PM. Here, we demonstrate the removal of PM and VOCs by utilizing electrospun nanofibers of polystyrene (PS) and polyacrylonitrile (PAN) with molecular charges imparted on them via chemical treatment. The chemically treated fibers were successful in capturing even particles measuring 300 nm, which are considered to be the most penetrable particles. We report a filtration efficiency of  $\sim 93\%$  for removing such particles, which is  $\sim 3 \pm 1.5\%$  enhancement when compared to the untreated fibers. The fibers have been subjected to extreme haze conditions ( $\sim 1413 \mu\text{g m}^{-3}$ ) of  $\text{PM}_{2.5}$  for a duration of 1 h, and the filtration efficiency was measured to be  $\sim 99.01\%$ . These fibers also possess the capability to capture model VOCs such as aniline, toluene, tetrahydrofuran, and chloroform. When PAN, PS, and their chemically treated counterparts were tested for their antibacterial activity, these filter mats had bactericidal effect on *Escherichia coli*, *Bacillus subtilis*, and *Enterococcus faecalis*. A nasal plug hosting these filter mats has been designed, which can offer personal protection from PM. Enhanced removal of residual particles is extremely important, and this difficult task is made possible with our approach. The efficiency of our approach is due to the charged nature of PM, especially of the smaller size regime.

**KEYWORDS:** electrospun fibers, particulate matter, volatile organic compounds, nasal filters

## INTRODUCTION

An exponential rise in air pollution and its consequences for human health and environment have raised serious concerns, warranting appropriate solutions for remediation. Natural phenomena such as dust storms, volcanic eruptions, forest fires, sea droplet impact on surfaces,<sup>1–3</sup> and man-made sources such as combustion of fossil fuels, agricultural waste, and vehicular emissions are some of the causes for the rise of particulate matter (PM) in air. Polluted air primarily comprises solid particles suspended in air, called PM, and volatile organic compounds (VOCs). These PMs are composed of both organic and inorganic ( $\text{SO}_x$ ,  $\text{NO}_x$ ,  $\text{F}^-$ )<sup>4,5</sup> species, minerals (such as calcite, dolomite, anorthite, and feldspar),<sup>6,7</sup> and soil

dust. Solid particles with diameters,  $d < 2.5 \mu\text{m}$  ( $\text{PM}_{2.5}$ ) and  $< 10 \mu\text{m}$  ( $\text{PM}_{10}$ ), are of prime importance as they can enter lungs,<sup>8</sup> and their prolonged exposure can even cause cancer.<sup>9–11</sup> Adverse health effects pertaining to VOCs are well known: headaches and nausea, damage to the central nervous system, kidney, lung, and liver.<sup>12</sup> Extended exposure to

Received: November 16, 2019

Revised: April 17, 2020

Published: May 5, 2020



high levels of pollution can severely affect the very young and elderly. There is a rise in polluted air in the recent past in different parts of India and other developing nations of Southeast Asia. Rise in PM causes prolonged hazy days, and visibility is highly compromised. Extended deposition of dust can also severely affect the performance of solar panels, among other things.

Utilizing a centralized ventilation system to achieve a controlled indoor environment is the only means of protection against polluted air. Ventilation systems offer high efficiency in removing PM but consume high energy in generating clean air.<sup>13</sup> Use of commercial-grade filter masks as a primary means of protection against PM has been the standard practice. However, many commercial masks provide negligible efficiency for filtering PM<sub>10</sub> and PM<sub>2.5</sub>; in addition, they offer resistance to airflow.<sup>14</sup> PMs are generally captured by impact, interaction, or diffusion of particles on the fiber surface because of their varied chemical, physical, and mechanical properties. Ideally, a good filter needs to remove the maximum amount of PM<sub>2.5</sub> while offering minimum resistance to airflow and also providing high mechanical stability. Electrospinning is one of the versatile routes by which such filter mats can be fabricated. Recently, Cui et al. have made electrospun fibers out of polyacrylonitrile (PAN), polystyrene (PS), polyvinyl pyrrolidone, and polyvinyl alcohol (PVA), which show high efficiency (above 98%) in filtering PM<sub>2.5</sub>.<sup>15</sup> By modifying the surface morphology and increasing the hydrophilicity of PAN, Jing et al. showed a better filtration of soot.<sup>16</sup> Li et al. recently fabricated polytetrafluoroethylene/(PVA) electrospun fibers, and after removing PVA, the resulting fibers had a filtration efficiency of 98.05% for filtering PM<sub>2.5</sub>.<sup>17</sup> Substrates made of textiles have gained significant attention for capturing PM, which is due to their flexibility, minimum resistance to airflow, and low manufacturing cost.<sup>18</sup> Forming hierarchical structures on these electrospun fibers has found multiple applications in air and water purification.<sup>19–21</sup> Huang et al. fabricated hierarchical structures on polycaprolactone/polyethylene oxide nanofibers by exposing the electrospun mat to acetone vapors, which caused physical wrinkles on these fibers creating hierarchical structures, and these modified fibers had a clear ~20% rise in their particulate removal efficiency.<sup>22</sup> These, coupled with the possibility of functionalization by metal–organic frameworks (MOFs), show potential as a washable and reusable medium for capturing soot.<sup>23</sup> However, because of the brittle nature of MOFs, the interactions between MOF and the textile substrate need further attention as they could have poor adhesion and may not be suitable as a personal filter mask. A disposable gelatin electrospun fiber-based multifunctional air filter was fabricated by Souzandeh et al., where the paper towel was used as a substrate to collect these gelatin nanofibers.<sup>24</sup> Other eco-friendly materials such as cellulose nanocrystals,<sup>25</sup> wood pulp,<sup>26</sup> and lignin<sup>27</sup>-based air filters were fabricated and used for obtaining clean air devoid of PM. Apart from PM<sub>10</sub> and PM<sub>2.5</sub>, particles with size <300 nm (PM<sub>0.3</sub>) are generally not captured by common masks, and these are considered to be highly penetrating airborne particles having dire consequences on health.<sup>28</sup> In an urban environment, traffic emissions are considered to be a major source for ultrafine particles.<sup>29</sup> During the combustion of fuels, ion concentrations are generated, wherein the nucleation of ultrafine particles occurs.<sup>30</sup> Because of the ion–particle collision, these particles attain charges, either positive or negative. Charges on these particles greatly affect the coagulation and transport.

Coagulation leads to increase in the particle size, which causes changes to the aggregate geometry and further modifies the diffusion coefficients.<sup>31</sup> For the capture of these extremely small particles, Wang et al. investigated an electret-type nanofiber based on triboelectric nanogenerators obtained from electrospun polyimide and polyvinylidene fluoride (PVDF).<sup>32</sup> PM<sub>0.3</sub> is considered to be the most penetrable particle, and commercial-grade masks cannot capture them.<sup>33</sup> Recently, Li et al. fabricated an anionic surfactant Steiner geometry-based electrospun PVDF fiber for capturing these 300 nm PMs.<sup>34</sup> Parameters such as lower pressure drop, flexibility, high filtration efficiency, and affordability need to be addressed in defining an ideal filter medium.

VOCs constitute a major component of both indoor and outdoor pollutants, the former being a major concern for children.<sup>35</sup> Some of the common health effects are asthma, allergies, and chronic obstructive pulmonary disease, which is primarily caused by increased indoor air pollutants.<sup>36,37</sup> Prolonged exposure to VOCs such as benzene, toluene, xylene, and so forth can lead to cancer. In view of these concerns, developing appropriate materials capable of adsorbing these VOCs is necessary. Usually, activated carbon has been used for the removal of VOCs because of its large surface area and pore volume. However, major limitations are due to high-pressure drop across the bed, minimal mechanical flexibility, and faster saturation. Recent reports suggest that electrospun fibers are capable of adsorbing VOCs and also offer additional features such as flexibility and minimum pressure drop.<sup>38</sup> Scholten et al. demonstrated the capability of electrospun polyurethane fibers for adsorbing VOCs.<sup>39</sup> These fibers show an affinity for adsorbing toluene and chloroform and limited affinity toward hexane.

In this work, we have fabricated a chemically charged filter mat that can be used in diverse situations to filter both PM and VOCs. This mat consists of electrospun PAN and PS fibers that have been chemically treated to increase the surface charge, both negative and positive, which, in turn, improved the filtration efficiency of PM<sub>0.3</sub> by  $\sim 3 \pm 1.5\%$ . In addition, this filter mat was capable of removing model VOCs such as toluene, tetrahydrofuran (THF), aniline, and chloroform. The mat offers a reduced resistance of <60 Pa to airflow. These filters were also effective in filtering under extreme haze conditions ( $\sim 1416 \mu\text{g m}^{-3}$ ) of constant exposure to PM<sub>2.5</sub> when continuously used for 24 h. The fiber mats were also tested for their antibacterial property using Gram-negative bacteria *Escherichia coli* and Gram-positive bacteria *Bacillus subtilis*. In addition, they were also tested on *Enterococcus faecalis*, a pathogenic bacterium commonly found in root canal and saliva. Investigation on *E. faecalis* found in saliva revealed that they possess the highest abundance of virulence genes when compared to the isolates from other parts of the body.<sup>40–42</sup> They are also known to cause nosocomial infections.<sup>43</sup> A nasal plug designed to host this filter mat can serve as a personal protective gear with minimal inconvenience for daily use.

## ■ EXPERIMENTAL METHODS

**Materials.** Commercial-grade PAN and general-purpose PS were purchased from Sandhya Polymer Industries, India, and Vardhaman Acrylics Ltd., India, respectively. Dimethylformamide (DMF), sulfuric acid (H<sub>2</sub>SO<sub>4</sub>), acetonitrile (ACN, HPLC grade), and hydrochloride acid (HCl) were purchased from Sigma-Aldrich. Choline chloride (referred to as ChCl throughout the article), aniline, toluene, ethanol,

chloroform, and THF were purchased from RANKEM, India. Fumed silica particles were purchased from Astra Chemicals, India. Millipore-processed deionized water ( $\sim 18.2$  M $\Omega$ ) was used throughout the experiments, and all chemicals were used without further purification. Nutrient agar, *E. coli* MTCC 739, and *B. subtilis* ATCC 21331 were procured from MTCC and ATCC, respectively. *B. subtilis* (ATCC 21331) was provided by Prof. S. Gummadi (Department of Biotechnology, IITM). *E. faecalis* was obtained as a gift from Dr. A. R. Pradeep Kumar, Thai Moogambigai Dental College and Hospital, Chennai, India.

**Methods. Preparation of Electrospun Fibers.** About 2 g (20 wt %) of PS and 1.4 g (14 wt %) of PAN were dissolved separately in 10 mL of DMF. These two were stirred for 6 h in ambient conditions to obtain uniform solutions. Later, they were loaded into disposable syringes with a flattened 21G needle. The PAN and PS nanofibers were prepared separately using the ESPIN-NANO electrospinning machine. The spinning parameters for PAN were as follows: a flow rate of 0.5 mL h<sup>-1</sup>, a working distance of 14 cm, and a voltage of 15 kV, applied for a period of 30 min. For PS, a flow rate of 1 mL h<sup>-1</sup>, a working distance of 14 cm, and a voltage of 22 kV voltage applied for a period of 30 min were used. These fibers were collected on a nonwoven (NW) polypropylene (PP) mat placed on a rotating drum collector.

**Imparting Surface Charges on the Fibers.** To impart positive charge on the fibers, about 0.6 g of PAN fibers was immersed in 0.1 M HCl solution containing an optimized concentration of 216 mM ChCl. This solution, along with fibers, was left undisturbed for 30 min. Later, these fibers were rinsed with deionized (DI) water repeatedly and finally dried overnight in an oven at 60 °C. This treatment anchors positive charges on PAN fibers. Similarly, PS fibers were immersed in 3 M H<sub>2</sub>SO<sub>4</sub> solution at room temperature for 24 h.<sup>44</sup> Finally, these sulfonated PS (SPS) fibers were rinsed repeatedly to remove the unbound acid moieties and dried overnight in an oven at 60 °C.

**Assembly of the Filtration Mat.** A NW PP mat was cut into dimensions of 13 × 16 cm and placed on a drum collector and used as a substrate for collecting PAN and PS fibers. Subsequently, PAN and PS fibers were placed on top of each other, and the combined fibers were later placed between two NW PP mats, forming the entire filter mat. A similar protocol was followed for the chemically treated counterparts. These PP mats provide structural stability but have negligible efficiency for filtering PM<sub>10</sub>, PM<sub>2.5</sub>, and VOCs.

**Filtration Efficiency of the Fiber Mat.** To determine the filtration efficiency of the fiber mat, we fabricated an aerosol filtration efficiency tester (AFET) based on the ASTM F2299 protocol.<sup>45</sup> Briefly, clean compressed air was obtained from a compressor coupled with a high-efficiency particulate air filter. This compressed-air was split into two streams, with one being used to aerosolize the aqueous NaCl solution and the other being directed to the dilution chamber. These two streams were then combined in the dilution chamber to reduce the concentration of NaCl aerosols, which pass through an 80 cm long cylindrical tube with a face velocity of 5 cm s<sup>-1</sup> and a flow rate of 16 L min<sup>-1</sup>. The pressure drop across the filter was measured using a differential pressure gauge. The input and output aerosol concentrations were measured using a laser particle counter (Lasair III, Particle Measuring System), and the filtration efficiency was calculated. Commercial-grade fumed silica powder was used as model solid aerosols, and their capture was also studied. The filter mat considered for this test had an area of 10 cm<sup>2</sup>. A schematic of the AFET setup is shown in Figure S1. Extreme haze conditions were simulated by using soot obtained from the burning of incense sticks, and an optical image of the experimental setup is shown in Figure S2. The filters were placed between two glass bottles, and soot was introduced into the left chamber. The concentrations of aerosols in the left chamber and the right chamber were counted using a particle counter (Perfect Prime AQ9600). For measuring the efficiency of these filter mats at prolonged exposure to PM, fresh soot was introduced at the end of every hour, and the particulate concentrations were measured for the same sample. The size of the filter sample was 4 cm<sup>2</sup> for testing the soot removal efficiency. A

digital manometer (HTC instrument PM-6105) was used to measure the pressure drop across the mat before and after filtration. The pressure drop was calculated under two flow rates, 5 and 8 L min<sup>-1</sup> using the IPM-191 dust collector. The filtration efficiency was calculated based on the equation of filtration efficiency ( $\eta$ ) =  $(C_0 - C)/C_0 \times 100$ , where  $C_0$  and  $C$  are the PM concentrations without and with a filter mat, respectively. The performance of the filter mats was quantified using a quality factor (QF), where QF is the ratio of penetration of particles  $(1 - \eta)$  to the pressure drop ( $\Delta P$ ) across the filter,  $(QF) = -\ln(1 - \eta)/\Delta P$ .

**Dust Sampling and Processing.** Dust settled on leaves was collected from four residential locations within the campus of Indian Institute of Technology Madras. These particles were collected by scooping them using a nylon-bristled soft brush and storing within a polyethylene bag. The particles were ground using a mortar and pestle and sieved to <100  $\mu$ m. About 500 mg of these particles was dispersed in ethanol, sonicated, and centrifuged thrice for 10 min at 5000 rpm.<sup>46</sup> These particles, after multiple washing, were dried overnight at 70 °C and stored in vials for charge and X-ray diffraction (XRD) analysis. Furthermore, indoor dust was collected onto a 25 mm cellulose filter paper with a pore size of 0.22  $\mu$ m using a dust collector (IMP-191, INSTRUMEX) for 8 h, with a flow rate of 9 L min<sup>-1</sup>. The dust was collected consecutively for 20 days, and the filter paper was back-washed using DI water and stored.

**Uptake of VOCs by the Fiber Mat.** Using chloroform, aniline, THF, and toluene as model VOCs, their uptake by electrospun fibers was studied. Briefly, electrospun mats of 2, 10, and 20 mg were placed at the bottom of a glass desiccator containing a beaker with 40  $\mu$ L of the intended VOC. The desiccator utilized was 30 cm in diameter and height. After exposing the fibers for 1 h, the sample was removed and placed inside a hood for 30 min to remove any excess/unadsorbed VOC. This sample was then immersed in a beaker containing 4 mL of ACN for 2 h. Finally, 0.5 mL of this solution was loaded into high-performance liquid chromatography (HPLC) vials, and chromatography was performed.

**Antibacterial Activity Tests.** The fibers were tested for their antibacterial activity through the zone inhibition method against Gram-negative bacteria *E. coli* and Gram-positive bacteria *B. subtilis* and *E. faecalis*. Fibers of PAN, PP, PS, ChClPAN, and SPS were cut to dimensions of  $\sim 10 \times 10$  mm and placed gently on the nutrient agar plates inoculated with *E. coli*, *B. subtilis*, and *E. faecalis* using the uniform streaking method. The plates were incubated overnight at 37 °C for 24 h, and the bacteria growth inhibition zone around the fiber mats was observed.

**Characterization.** For determining the fiber diameter and morphology, the mats were analyzed using an FEI QUANTA 200 scanning electron microscope coupled with an energy-dispersive spectroscope. The samples were sputtered with gold using a CRESSINGTON sputter-coater. For the confirmation of surface functionalization, the fiber mat was made into a pellet using KBr as the matrix and analyzed using PerkinElmer Spectrum One FTIR. XRD studies for the samples were performed using a Bruker D8 ADVANCE powder X-ray diffractometer. Contact angle measurements were performed using a sessile water droplet of volume 3  $\mu$ L using a Holmarc contact angle meter. Finally, a Shimadzu Prominence Analytical high-performance liquid chromatograph equipped with a photodiode array detector was used to measure the VOC uptake capacity. An injection volume of 5  $\mu$ L on the C18 column with a flow rate of 0.5 mL min<sup>-1</sup> with ACN (100%) as the mobile phase was chosen.

## RESULTS AND DISCUSSION

**Active and Passive Monitoring of Dust.** To determine the physical and chemical nature of dust, ambient dust was captured actively and passively. Indoor dust was collected onto a cellulose-based filter paper using a dust collector, IPM-191. The filter paper, upon washing with DI water, released the trapped particles into the solution, which was then stored in centrifuge vials. This suspension was analyzed to determine the



size and zeta potential of the suspended particles. Dust was collected for 20 days, and the average size and zeta potential from these measurements are shown in Figure S3. The particle size varied from 2 to 18  $\mu\text{m}$ , and they were randomly distributed, as shown in Figure S3a. The zeta potentials of the collected particles on different days are shown in Figure S3b.

To determine the size of the passively monitored dust, particles deposited on leaves were analyzed using a scanning electron microscope. Typically, the leaves were at a height of  $\sim 6$  m from the ground. Micrographs of the dust are shown in Figure S4c,d. The particles were highly irregular and nonuniform. A Faraday cup coupled to a Keithley 6514 electrometer was used to determine their charge in the native environment. The system was stabilized for 300 s, after which about 500 mg of the collected particles was added to it. Upon addition, a steep increase in charge was observed, and the cumulative charge of the particles was  $1.4 \times 10^{-10} \mu\text{C}$ , which was stabilized to  $1.0 \times 10^{-10} \mu\text{C}$ , as shown in Figure S4a. A similar experiment was performed using particles from another location, and the cumulative charge was found to be  $-2.0 \times 10^{-8} \mu\text{C}$ , as shown in Figure S4b. To determine the chemical nature of the dust, XRD analysis of the passively collected samples was performed. Diffraction patterns of the dust samples from four different locations are shown in Figure S5. They were compared with the Inorganic Crystal Structure Database (ICSD) using the X'pert High Score Plus to characterize the composition. The samples were seen to predominantly contain mixtures of quartz and albite, both  $\alpha$  and  $\beta$  forms, in agreement with previous reports.<sup>47–49</sup> The chemical compositions of the minerals that matched with the dust collected from four different locations are shown in Table S1.

**Electrospun Fiber Mats for the Capture of PM.** To efficiently capture PM and VOCs, electrospun fibers of PAN and PS were chosen. These fibers were chemically treated to impart molecular charges on them so as to enhance the filtration efficiency. Owing to its versatility, electrospinning technique was chosen for the fabrication of these polymeric nanofibers. Briefly, it is a technique wherein a high voltage of 15 kV is applied to a syringe containing a polymeric solution. This electrical force overcomes the surface tension of the solution and draws the solution as fibers.<sup>50,51</sup> These fibers can be collected either on a metal plate or on a NW fiber mat or glass. We chose a NW mat, as shown in Figure 1. A molecular model of ChCl-treated PAN is also shown in Figure 1. The calculated dipole moments of untreated PAN and PS were 3.9 D and 0.29 D, respectively, and after chemically treating these fibers, the dipole moment increased to 11 D for choline-treated PAN and 13.86 D for SPS. For this, the structure was initially drawn in Avogadro, and for density functional theory (DFT), we used the B3LYP method with a 6-31G(d) basis set. After initial structure optimization, the coordinates were exported to Gaussian 09 for complete optimization of the structure to obtain the dipole moment.<sup>52</sup> The dipole moment was calculated using the expression  $\mu_{\text{total}} = (\mu_x^2 + \mu_y^2 + \mu_z^2)^{1/2}$ , and the corresponding coordinate file is attached in the Supporting Information. In the present study, PM was generated by three methods: (1) aerosolizing aqueous NaCl droplets (size range of 300 nm to 3  $\mu\text{m}$ ), (2) burning an incense stick (sizes of 2.5 and 10  $\mu\text{m}$ ), and (3) fluidizing fumed silica (size range of 1–30  $\mu\text{m}$ ). We chose aniline, THF, toluene, and chloroform as representative model VOCs present in air, and their uptake by the fibers was studied.

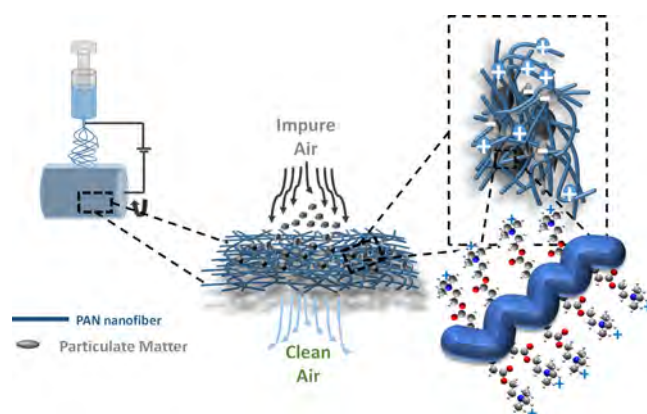


**Figure 1.** (Top left) Schematic representation of the electrospinning technique; fibers were collected on a NW fiber mat placed on a drum collector. These fibers captured PM to provide clean air. (Top right) Enlarged image illustrating the capture of particles because of the positive charge on the fibers. (Centre) Further enlargement to illustrate the molecular model of ChCl-treated PAN. While positive and negative charges are shown, fibers were designed to have only one preferred charge. In the ball and stick model for ChCl, the color code is gray for carbon, blue for nitrogen, and red for oxygen.

**Positively Charged Electrospun Fibers.** PAN has been reported for efficient filtration of PM without offering much resistance to the air flow.<sup>15</sup> In our study, for cost-effectiveness, commercial-grade PAN was chosen to prepare the electrospun fiber mat. The morphology and physical dimensions of the electrospun fibers before and after treatment by ChCl are shown in Figure 2, respectively. The untreated fibers were

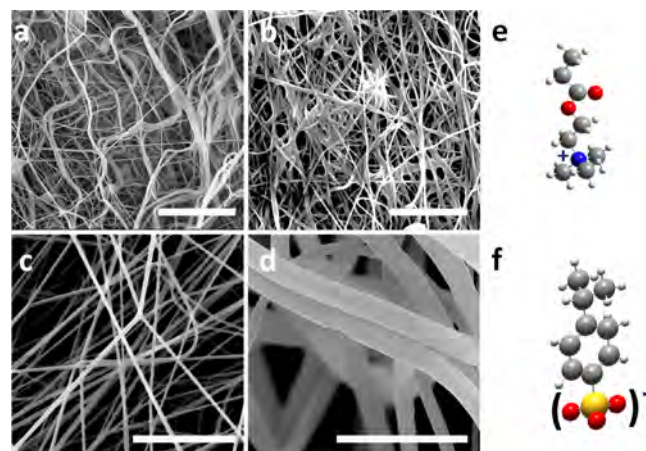


**Figure 2.** Scanning electron micrographs of electrospun PAN [(a) bare and (b) treated fibers] and PS [(c) bare and (d) treated fibers]. Scale bar corresponds to 5  $\mu\text{m}$ . Molecular models of chemically functionalized fibers: (e) ChCl-treated PAN and (f) SPS. In the ball and stick model, the color codes for carbon, oxygen, nitrogen, and sulfur are gray, red, blue, and yellow, respectively.

uniform without any beads, as shown in Figure 2a,b. The fiber diameter of the untreated fiber was  $\sim 300$  nm, while after treatment with ChCl, it increased to  $\sim 450$  nm, as shown in Figure S6a. This increase in fiber diameter might be due to the anchoring of choline moieties on the fiber. Upon treatment, webbing between the fibers was also observed, as shown in Figure 2b. The webbing could be due to interconnections formed between two neighboring fibers, caused by the

anchoring of the choline moiety and subsequent drying-related artifacts. Fourier transform infrared spectroscopy (FTIR) was performed on the untreated and ChCl-treated PAN to confirm the anchoring of choline groups on the fibers. The spectrum of PAN fibers shows several peaks, which are related to the existence of C–H, C≡N, C=O, and C–O bonds and associated groups, as shown in Figure S6b. The peak at 3430  $\text{cm}^{-1}$  corresponds to the N–H stretching frequency.<sup>45</sup> The peaks at 2938, 1453, 1357, and 1249  $\text{cm}^{-1}$  represent the aliphatic stretching C–H vibrations in CH, CH<sub>2</sub>, and CH<sub>3</sub>, while the peaks at 1700–1780  $\text{cm}^{-1}$  indicate the presence of C–O and C=O, possibly because of the presence of monomers of methacrylate found in commercial-grade PAN.<sup>53</sup> The peak at 1070  $\text{cm}^{-1}$  represents the C–N stretching present only in ChCl-treated PAN. The characteristic peak at 2250  $\text{cm}^{-1}$  represents the C≡N bond, and the presence of this bond with a lower intensity in ChCl-PAN, compared to that in bare PAN, suggests the anchoring of the choline moiety on the fiber. Increased intensity of the C=O peak in ChCl-treated PAN and the presence of C–N stretching frequency also confirm the addition of the choline moiety onto PAN.<sup>54</sup> Because of the overall positive charge of the choline moiety, upon anchoring with PAN, ChCl-PAN would attain this positive charge on the PAN fiber passively. Charge of PAN nanofibers before and after chemical treatment was measured by placing 20 mg of the fiber mat inside the Faraday cup, and the data are shown in Figure S7a. The untreated PAN fiber mat was added into the Faraday cup at the end of 10 s, and the charge of this mat was stabilized to  $\sim -8 \times 10^{-10}$  C. The ChCl-treated PAN fiber mat was added to the Faraday cup at the end of 20 s, and the charge of this fiber was stabilized to  $\sim 1 \times 10^{-9}$  C. This confirms a positive charge on the ChCl-PAN fiber mat, relative to the untreated mat.

**Negatively Charged Electrospun Fibers.** Commercial-grade general-purpose PS was utilized for the preparation of negatively charged electrospun fibers. The morphology of the fiber before and after treatment with H<sub>2</sub>SO<sub>4</sub> is shown in Figure 2c,d. The untreated PS fibers displayed a narrow size distribution of around  $\sim 450$  nm, but upon chemical treatment with H<sub>2</sub>SO<sub>4</sub>, the fiber diameter increased without any physical damage, as shown in Figure S4c, and the corresponding scanning electron microscopy (SEM) image is shown in Figure 2d. The fiber diameter after treatment increased to  $\sim 1000$  nm, which could be due to the chemical treatment in the solution phase, causing a polymer chain relaxation. To confirm the presence of sulfonate groups anchored on the fibers, FTIR analysis was performed, as shown in Figure S6d. The presence of peaks at 3060, 2906, and 1460  $\text{cm}^{-1}$  corresponds to C–H aromatic, C–H alkyl, and C=C aromatic stretching modes, respectively.<sup>55</sup> The presence of a peak in the region of 1195–1168  $\text{cm}^{-1}$  is due to S=O stretching.<sup>44</sup> This peak, absent in untreated PS fibers, confirms the anchoring of sulfonate moieties onto PS. The overall charge of the sulfonate moiety is negative, and upon anchoring of this on PS fibers, they impart negative charge. Charge of PS nanofibers before and after chemical treatment was measured by placing 20 mg of the filter mat inside the Faraday cup, and the data are shown in Figure S7b. The untreated PS filter mat was placed inside the Faraday cup at the end of 10 s, and the charge of this mat was stabilized to  $\sim 2 \times 10^{-9}$  C. The SPS nanofiber mat was added to the Faraday cup at the end of 18 s, and the charge of this fiber mat was stabilized to  $\sim -4 \times 10^{-9}$  C. This confirms that the charge of the chemically treated PS fibers became negative.

**Contact Angle Measurements.** To measure the contact angle of the fibers, PAN and PS were electrospun on glass slides for 30 min and subsequently treated with ChCl and sulfuric acid for imparting surface charges. The optical images obtained during the contact angle measurements are shown in Figure S8. The contact angles for untreated PAN and PS fibers were 102 and 98°, respectively, and upon chemical treatment, the contact angles subsequently reduced to 41 and 78°. This decrease in the contact angle could be due to the introduction of surface polarizability caused by chemical functionalization.

**Assembly of the Filtration Mat.** Ideally, the filtration mat should offer zero or negligible resistance to airflow. To obtain a near-ideal filter without compromising filtration efficiency, the electrospinning time for obtaining the fibers, as well as the number of NW mats utilized to make the filtration mat, was varied. Pressure drop across these filters was measured using AFET, and the values are shown in Figure S9a. A pressure gauge was used to measure the resistance offered to airflow. Fibers with 15, 30, 45, and 60 min of electrospinning duration combined with two or four NW mats were considered. The chemically treated fibers offered higher resistance to airflow compared to the untreated ones. The resistance to airflow increased with increase in electrospinning duration and with increasing number of NW mats. The pressure drop across the mats reached a maximum value of  $\sim 56$  Pa chemically treated 4NW60 (four NW mats with the electrospun mat obtained after 60 min of electrospinning) mat. By varying the duration of electrospinning, the amount of fibers deposited on the NW mat was varied, which could affect the air resistance. The NW mat of 13  $\times$  16 cm weighed about 0.8 g, and the weight of the filter mat per fixed area for different electrospinning durations is shown in Figure S9c. We chose to use four NW mats and a spinning time of 30 min, as this combination offered minimal resistance without compromising on the filtration efficiency.

**Filtration of Fumed Silica Particles.** To understand how solid particles are captured, fumed silica was fluidized with a face velocity of 5  $\text{cm s}^{-1}$  using compressed air. These particles were loaded in a chamber, as shown in Figure S1. The particles were seen to be captured by the electrospun mat. SEM images of the bare PAN, PS, and chemically treated PAN and PS after exposure to the silica particles are shown in Figure 3. Figure 3a shows the SEM images of bare PAN fibers after exposure to

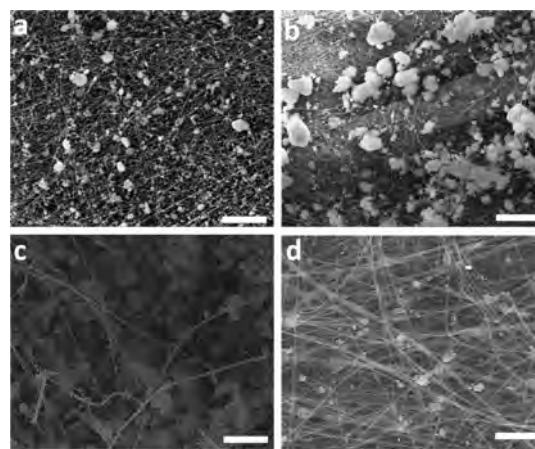


**Figure 3.** Scanning electron micrographs of fibers after exposure to fumed silica: (a) bare PAN, (b) ChCl-PAN, (c) bare PS, and (d) SPS. Scale bar corresponds to 50  $\mu\text{m}$ .



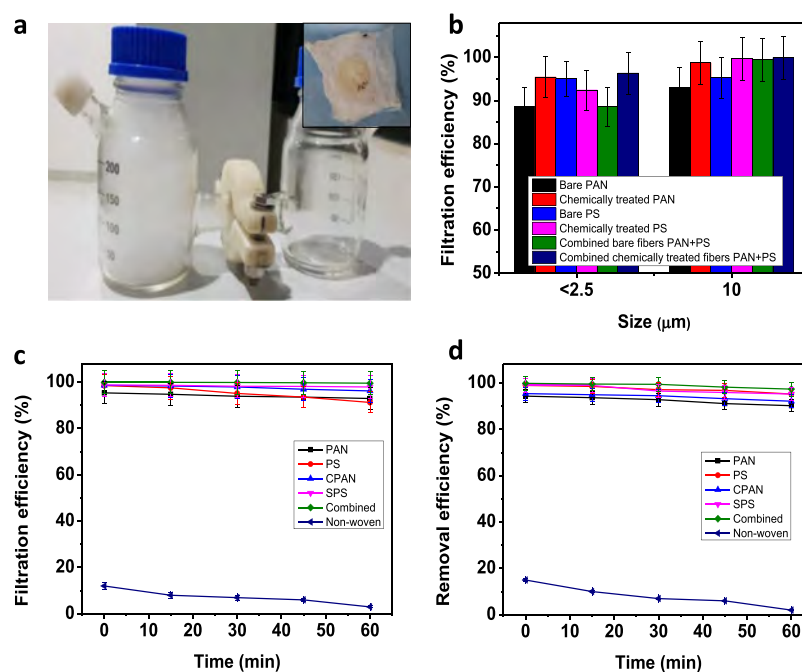


**Figure 4.** Comparison of filtration efficiencies of treated and untreated fibers. (a) Photograph of the filtration setup used for trapping of soot particles (left) using fiber mats; hazy condition is created by the introduction of  $\sim 1413 \mu\text{g m}^{-3}$  of  $\text{PM}_{2.5}$ . (Inset) Photograph of the PS mat; the circular region is due to the contact by soot for 60 min. (b) Comparison of the filtration efficiency in removing  $\text{PM}_{2.5}$  and  $\text{PM}_{10}$  of untreated PAN, PS, and combined (PAN + PS) fiber mats with the treated fibers. (c,d) Comparison of the time-dependent filtration efficiency of  $\text{PM}_{2.5}$  and  $\text{PM}_{10}$ , respectively, of the fibers.

silica particles. As the electrospun fiber mats are densely packed, they restrict the movement of the particles flowing through, thus effectively trapping the particles within. A similar phenomenon of trapping was observed for  $\text{ChCl}$ -PAN, PS, and SPS. Hang et al. reported during the filtration of soil dust that the particles come in contact with the fibers and subsequently get attached and grow as dendrites on the fibers.<sup>56</sup> This adhesion on the single fiber could be due to the presence of enhanced surface charges present because of chemical treatment. In the case of chemically modified PAN, webbing between fibers was observed, and this could enhance the filtration, as shown in Figure 3b, by offering more resistance for easy particle movement. In the case of SPS, upon chemical treatment, the fibers have a larger fiber diameter compared to untreated fibers, and this further restricts the movement of particles (as shown in Figure 3d). Because of this diameter change, webbing between fibers, and surface charges, we believe that the chemically treated fibers offer better filtration efficiency compared to the untreated ones.

**Filtration of Aqueous NaCl Aerosols.** During the generation of aerosols from aqueous NaCl, excess  $\text{Na}^+$  and  $\text{Cl}^-$  species are expected to be present. The input and output concentrations of these aerosols are measured by AFET, as shown in Figure S1. A comparison of the filtration efficiency of chemically treated and bare fibers is presented in the inset of Figure S10. For removing  $\text{PM}_{0.3}$ , the filtration efficiency rose to  $\sim 93 \pm 1.5\%$  with an increment of  $\sim 3\%$ . Similarly, for removing  $\text{PM}_{0.5}$ , the efficiency rose to  $\sim 99.8 \pm 0.6\%$ , and it reached  $\sim 99.92 \pm 0.2\%$  for  $\text{PM}_{0.7}$ ,  $\text{PM}_1$ ,  $\text{PM}_2$ , and  $\text{PM}_3$ . The enhancement in capturing  $\text{PM}_{0.3}$  by the chemically treated fibers is attributed to the presence of molecular charges on these fibers, as shown in Figure S10. This enhancement can also be due to the entanglement and webbing between individual fibers observed after chemical treatment. To

visualize the particles trapped by the fibers, NaCl concentration was increased to 60 wt % by weight, and it was aerosolized. The fibers were placed in AFET under continuous exposure of 10 min. Later, the fibers were dried and analyzed using SEM, as shown in Figure S10a. NaCl crystals trapped by chemically treated PS fibers are shown in the marked region of Figure S8a. The chemical composition of the crystal was determined by spot energy-dispersive spectroscopy (EDS). A semiquantitative view of the elemental composition in both atomic % and weight % is shown in the inset. Note that a slight Na excess is seen, and this is expected for sulfonated fibers as the negatively charged fibers attract positively charged ( $\text{Na}^+$  excess) droplets. Typical bacteria range from 0.3 to  $2 \mu\text{m}$  in size;<sup>57</sup> because of this  $\sim 3\%$  enhancement in removing  $\text{PM}_{0.3}$ , we believe using our filters we can offer protection from bacterial aerosols. For filtering  $\text{PM}_{0.3}$ , the QF was noted to be 0.11 for untreated fibers and  $0.12 \text{ Pa}^{-1}$  for the chemically treated fibers, suggesting that the chemically treated fibers were slightly better compared to the untreated counterparts.

**Filtration of Soot by Fibers.** In the present work, in order to replicate a harsh and hazy environment, soot released from the burning of an incense stick was studied. The setup used for the filtration process of soot is depicted in Figure 4a, and the process is shown in Video S1. The mats which need to be tested were placed between the two bottles, and the smoke from the incense sticks was passed through them. The filtration efficiency was estimated by using a Perfect Prime AQ9600 particle counter. The input concentration of PM was  $\sim 1413 \mu\text{g m}^{-3}$  of  $\text{PM}_{2.5}$ . PS fibers ( $>95\%$ ) showed higher efficiency than PAN ( $>94\%$ ) in removing  $\text{PM}_{2.5}$ , a result that contradicts other reports.<sup>15,58,59</sup> Because of 30 min of electrospinning duration, the fiber packing density increased, which could lead to these high filtration efficiencies. The highest filtration efficiency was observed in a system combining the chemically treated PAN



and PS fibers embedded between the PP membrane, and the efficiency was  $\sim 98.4\%$  for  $PM_{2.5}$  and  $\sim 99.9\%$  for  $PM_{10}$ . By combining the untreated PAN and PS fibers, the filtration efficiency was noted to be  $\sim 98\%$  for  $PM_{2.5}$  and  $\sim 99.3\%$  for  $PM_{10}$ . The filtration efficiency of PP was negligible at 13 and 18% in removing  $PM_{2.5}$  and  $PM_{10}$ , respectively, as shown in Figure 4b. We observed hazy condition in the second bottle as well while using the PP mats alone.

To systematically study the dependence of charge on the filtration efficiency, we have varied the input concentrations of  $ChCl$  and  $H_2SO_4$ . The concentration of  $ChCl$  was optimized to 216 mM. Upon doubling the concentration, there was a loss in the structural integrity, making the fiber mat brittle. The scanning electron micrograph of the 432 mM  $ChCl$ -treated PAN fiber is shown in Figure S11b. The porosity was greatly reduced because of the increased webbing between the neighboring PAN fibers. The pores are highlighted with yellow arrows and are represented in white circles. The charges of the PAN fibers with three different concentrations of  $ChCl$  are shown in Figure S11a. With increasing concentration of  $ChCl$ , we observed higher positive charge, which increased the filtration efficiency of  $ChCl$ -PAN, as shown in Figure S11c. However, this reduction in porosity increases the pressure drop, making it difficult to breathe, and because the mat was brittle, this could lead to easy cracking, eventually decreasing the overall filtration efficiency. To impart negative charges on electrospun PS fibers, these fibers were treated with  $H_2SO_4$ . The concentration of  $H_2SO_4$  was optimized to 3 M, and charges of these fibers at different concentrations are shown in Figure S12a. By doubling the concentration of  $H_2SO_4$ , the amplitude of charge increased marginally. The filtration efficiency shown in Figure S12b showed an increase with doubling concentration of  $H_2SO_4$ . However, the increase was only  $\sim 1\%$ .

To understand the performance of the mat under harsh conditions for longer durations, a time-dependent filtration test was performed by leaving the filters in the harsh condition for 1 and 24 h. The output concentration of soot particles was studied periodically every 15 min to investigate the saturation point. The filtration efficiencies exhibited by untreated and treated fibers in removing  $PM_{2.5}$  and  $PM_{10}$  are shown in Figure 4c,d. We observed a decrease in the filtration efficiency by the untreated fibers as the time progressed. This decrease was from 95.3 to 92.9% for PAN and from 98.5 to 91.2% by PS in removing  $PM_{2.5}$ . For chemically treated PAN and PS fibers, this decrease was minimal. However, by sandwiching the treated PAN and PS fibers between two PP NW mats, the consistent filtration efficiency of  $\sim 99.9\%$  in removing  $PM_{2.5}$  for the entire duration of 1 h was observed. Similar trends were observed during the removal of  $PM_{10}$ . The filtration efficiency saw a decline as the time progressed in the case of untreated fibers. On the other hand, the combined filter mat maintained the efficiency at  $\sim 99.9\%$ .

The SEM images of soot trapped by the bare and chemically treated PAN and PS after exposure to soot for 60 and 86,400 s are shown in Figure 5. The SEM images of bare PAN after exposure to soot for 60 and 86,400 s are shown in Figure 5a(i,ii), respectively. The soot particles were seen to be trapped by the fibers everywhere on the mat. During longer exposure to soot, webbing was observed between adjacent fibers and attributed to soot aggregation, as shown in Figure 5a(ii). Similar phenomena were observed for the  $ChCl$ -PAN, bare PS, and SPS mats. The excessive morphological change observed

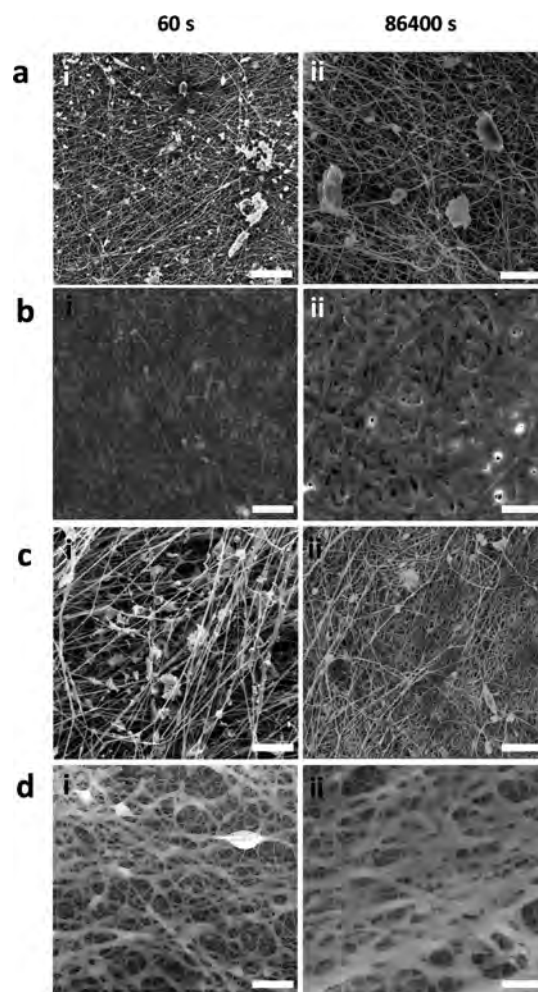


**Figure 5.** Scanning electron micrographs of fibers after soot deposition: (a) bare PAN fibers, (b)  $ChCl$ -PAN, (c) bare PS, and (d) SPS fibers. Scale bar corresponds to 50  $\mu m$ . Images (i,ii) in each correspond to 60 and 86,400 s of exposure.

in  $ChCl$ -PAN and SPS during extended soot deposition is possibly a major reason for the enhancement in filtration efficiency.

**Filtration Efficiency of the Mat.** After studying the performance of individual fibers, we studied the performance of mats prepared using these fibers. A typical mat consists of either treated or untreated PAN and PS fibers sandwiched between four NW PP mats. The average filtration efficiency of six samples of untreated and treated mats under long exposure to soot is shown in Figure 6a,b. In the case of the untreated fiber mat, the filtration efficiencies at the end of 1 h were  $\sim 98.0 \pm 0.5$  and  $99.3 \pm 0.35\%$  for removing  $PM_{2.5}$  and  $PM_{10}$ , respectively, as shown in Figure 6a. This efficiency further increased to  $\sim 99.6 \pm 0.25\%$  ( $PM_{2.5}$ ) and  $\sim 99.8 \pm 0.2\%$  ( $PM_{10}$ ), respectively, after 10 h of exposure. Finally, at the end of 24 h, this efficiency reached a maximum of  $\sim 99.92 \pm 0.07\%$  ( $PM_{2.5}$ ) and  $\sim 99.92 \pm 0.07\%$  ( $PM_{10}$ ), respectively. This enhancement in filtration could be due to the morphological change of fibers caused by extended exposure to soot. The filtration efficiencies for the treated fiber mat are shown in Figure 6b, which at the end of 1 h of exposure were  $\sim 99.07 \pm 0.07\%$  ( $PM_{2.5}$ ) and  $\sim 99.9 \pm 0.07\%$  ( $PM_{10}$ ), respectively. It reached  $\sim 99.92 \pm 0.07\%$  for both  $PM_{2.5}$  and  $PM_{10}$  at the end of 10 h. The capture efficiencies at the end of 24 h were

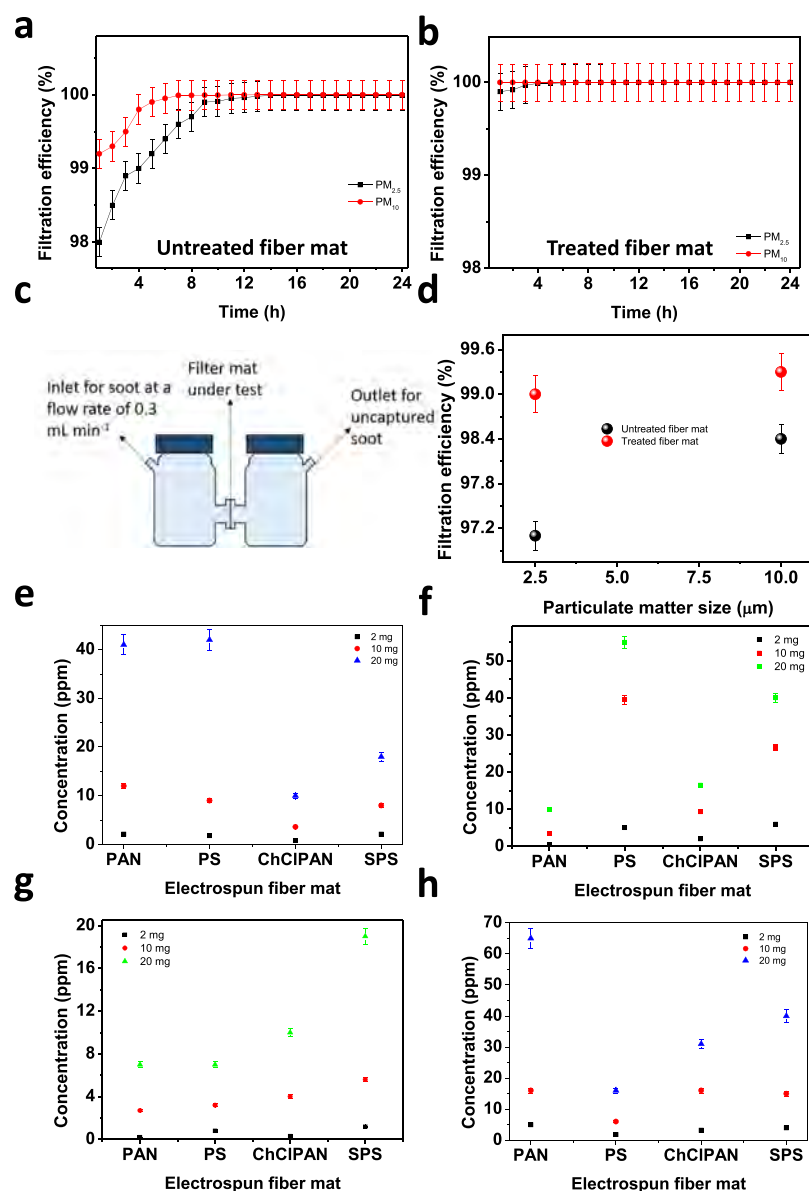


**Figure 6.** (a,b) Long-term filtration efficiencies of  $PM_{2.5}$  and  $PM_{10}$  by the untreated fiber mat and chemically treated fiber mat of different masses, respectively. (c) Schematic of the filtration setup, and filters were placed between two glass bottles wherein the soot particles were introduced in the left bottle. (d) Comparison of the PM removal efficiency between untreated and treated filter mats. VOC uptake by the fiber mat after 1 h of exposure to (e) THF, (f) aniline, (g) toluene, and (h) chloroform.

~99.92  $\pm$  0.07 and ~99.92  $\pm$  0.07% for  $PM_{2.5}$  and  $PM_{10}$ , respectively. The enhanced capture efficiency is due to morphological changes inherent to the treated fibers. However, the fibers were completely enveloped by soot at the end of 24 h in the case of treated fibers. Under extreme harsh and hazy conditions, we believe that the chemically treated fiber mat is preferable over the untreated mat.

While testing the long-term filtration efficiency, soot particles did settle down, forming a yellow colored precipitate. To circumvent the issue of the settling of PM, the chamber was saturated with soot, the particles were fluidized with a face velocity of 0.3 mL min<sup>-1</sup>, and the filtration efficiency was noted. The schematic of this modified setup is shown in Figure 6c. The filtration efficiency under the forced movement of soot is shown in Figure 6d.

The pressure drop across the filter mat before and after filtration is shown in Figure S9b. To measure this pressure

drop, a digital manometer was placed across the filter mat in the soot filtration setup. Here, air flow was created by using the IPM-191 dust collector, which has variable flow rates of 5 and 8 L min<sup>-1</sup>. The fresh untreated filter mat had pressure drops of 82 and 608 Pa at the flow rates of 5 and 8 L min<sup>-1</sup>, respectively. This pressure drop increased when the untreated filter mat was exposed to soot for 24 h and rose to 100 and 690 Pa, respectively. A similar trend was observed in the case of the treated filter mat, where the initial pressure drops were 91 and 651 Pa, which then increased to 131 and 700 Pa, respectively. This increase in pressure drop is predominantly due to the blockage of the pores caused by aggregated soot particles after filtration. The pressure drop across both the untreated and treated filters before exposure to soot is comparable to the pressure drop of the commercial-grade N95 filter mask.<sup>60</sup> The QF, also known as the figure of merit, was used to evaluate the performance of the filter mat. For the flow rates of 0.3, 5 and 8

L min<sup>-1</sup>, the untreated fibers had QFs of 0.07, 0.04, and 0.006 Pa<sup>-1</sup>, respectively. In the case of the treated filter mat, the QFs are 0.08, 0.05, and 0.007 Pa<sup>-1</sup> for the flow rates of 0.3, 5, and 8 L min<sup>-1</sup>, respectively. The QF values indicated that the treated fiber mats performed better under different flow rates compared to the untreated fibers. A comparison of filtration efficiency and pressure drop of the untreated and chemically treated filter mat is shown in Table 1.

**Table 1. Comparison of Different Properties of Untreated and Treated Fibers**

property	untreated filter mat	treated filter mat
pressure drop (Pa) @ 16 L min <sup>-1</sup> flow rate <sup>a</sup>	24	28
Pressure drop (Pa) @ 5 L min <sup>-1</sup> flow rate before soot deposition	82	690
after soot deposition	100	608
pressure drop (Pa) @ 8 L min <sup>-1</sup> flow rate before soot deposition	91	651
after soot deposition	131	700
filtration efficiency (PM <sub>0.3</sub> ) (%)	~89 ± 1.3	~93 ± 1.3
forced soot filtration at a flow rate of 0.3 mL min <sup>-1</sup>		
PM <sub>2.5</sub>	97.2	99
PM <sub>10</sub>	98.4	99.5
natural soot filtration		
PM <sub>2.5</sub>	98	99.8
PM <sub>10</sub>	99.3	99.9
electrospinning time of 30 min		
mass of PAN (g)	0.15	0.21
mass of PS (g)	0.25	0.32
QF (Pa <sup>-1</sup> ) for removing PM <sub>0.3</sub> having a face velocity of 5 cm s <sup>-1</sup>	0.11	0.12

<sup>a</sup>Mat area is 10 cm<sup>2</sup> here, and for others, it is 4 cm<sup>2</sup>.

**VOC Uptake by Electrospun Fibers.** Recent studies have concluded that electrospun polymer fibers and their composites are capable of capturing VOCs. Similar studies were performed to determine the maximum VOC uptake by the fibers. Electrospun fiber mats of different masses—2, 10, and 20 mg were taken, and their uptake capacities for model VOCs such as THF, toluene, chloroform, and aniline were studied for a duration of 1 h. These fibers were later immersed in ACN to leach out adsorbed VOCs. This solution was analyzed using HPLC to determine the analyte concentrations, and the data are shown in Figure 6e–h. From Figure 6e, the maximum uptake of THF was observed for 20 mg of untreated PAN and PS fibers, and this was reduced for the chemically treated ones. A similar trend was also observed for 10 mg mass. However, SPS captured ~3 ppm more than ChCl-PAN, whereas PAN captured ~2 ppm more than PS. We observed that even 2 mg of the electrospun fiber mat captured THF, and the maximum amount captured was ~1 ppm. The uptake of aniline by the electrospun fibers is shown in Figure 6f, where the maximum capture was observed by 20 mg of PS fibers reaching ~55 ppm and the SPS fibers captured ~40 ppm of aniline. For aniline, ChCl-PAN showed a higher capture than PAN fibers. Similar trends were observed for 10 and 2 mg of the material. PS fibers of 2, 10, and 20 mg captured the maximum amount of aniline. Capture of toluene by the electrospun fibers is shown in Figure 6g, and the maximum capture was observed for the chemically treated fibers compared to the bare fibers, SPS > PS, and ChCl-PAN >

PAN. We observed a similar trend for both 2 and 10 mg, and the smallest amount of 0.8 ppm was captured by 2 mg of PAN electrospun fibers. Capture of chloroform by the electrospun fibers is shown in Figure 6h, in which PAN fibers of 20 mg captured the maximum amount compared to PS fibers; however, upon chemical treatment, ChCl-PAN captured lesser. PS fibers also captured lesser amount when compared to their chemically treated counterparts. Similar trends were observed for both 2 and 10 mg of fibers, and the smallest amount of ~1.5 ppm was captured by 2 mg of the fibers. From Figure 6e–h, electrospun fiber mats both treated and untreated are capable of capturing model VOCs, and because of the chemical functionalization, the treated fibers had lower uptake capture when compared to the untreated ones.

**Antibacterial Activity.** Digital photographs of the agar plate containing *E. coli*, *B. subtilis*, and *E. faecalis* with the fiber mats are shown in Figure S13. An agar plate containing *E. coli* with the filter mats is shown in Figure S13a, and a visible zone of inhibition along the filter mat was observed for PAN, PP, ChCl-PAN, and SPS. *E. subtilis* containing an agar plate along with the filter mat is shown in Figure S13b, and similar to *E. coli*, a visible zone of inhibition was observed for PP, PAN, and ChCl-PAN. Finally, the agar plate containing *E. faecalis* along with the filter mats is shown in Figure S13c, and a small zone of inhibition was observable in the case of PAN, ChCl-PAN, and PP mats. It is evident from these zones that PAN, ChCl-PAN, and PP show slight susceptibility for the antibacterial activity; however, the zone of inhibitions is not significant when compared with that of antibiotics. PS fibers did not show any antibacterial activity toward any of the bacteria used. We conclude that these fibers are repulsive to the tested bacteria and thus suitable to be used inside a nasal plug for extended periods of time.

In order to determine the practical applicability of the filtration mat in real-life conditions, a silicone-based nasal plug was procured, and the mat was placed inside this nasal plug. Ten volunteers were asked to use the nasal plug and 90% of them did not experience any discomfort while breathing using the nasal plug. The comfort of breathing was similar to that of a commercial-grade N95 mask.

## CONCLUSIONS

Chemically functionalized PAN and PS fibers offer better filtration efficiency for removing PM compared to the untreated counterparts. They were also capable of adsorbing VOCs. The enhancement in filtration efficiency was suggested to be primarily due to the morphological change observed after chemical treatment and also due to the presence of surface charges. A filtration mat was assembled using four NW PP mats and employing an optimized electrospinning time of 30 min to obtain PAN and PS fibers. The fibers were functionalized with +ve and -ve charges by chemical treatment after electrospinning. Under hazardous environments, these chemically functionalized mats maintained a filtration efficiency of ~99.92 ± 0.07% in removing PM<sub>2.5</sub> and PM<sub>10</sub>. The mats offer minimum resistance to air flow, with the maximum pressure drop across the fibers being <60 Pa. Pressure drop across the untreated and treated filter mats was measured at 5 and 8 L min<sup>-1</sup> air flow. The untreated fibers offered resistances of 82 and 608 Pa, respectively, before exposure to soot. After exposure to soot for 24 h, this resistance increased to 100 and 690 Pa, respectively. The chemically treated filter mats before exposure to soot offered



resistances of 91 and 651 Pa, respectively, which increased to 131 and 700 Pa after exposure to soot for 24 h. The QF indicates that at these flow rates, the chemically treated filter mat offered better filtration efficiency with a lower pressure drop. The untreated and treated fibers were tested for their antibacterial property, and using the zone of inhibition method, *E. coli*, *B. subtilis*, and *E. faecalis* were tested. PP, PAN, and ChCl-PAN presented a visible zone near the mat, suggesting the presence of antibacterial property in these fibers. Because of this antibacterial property, the filters can be used for extended duration. We believe such mats can be used in nasal plugs for personal protection.

## ■ ASSOCIATED CONTENT

### SI Supporting Information

The Supporting Information is available free of charge at <https://pubs.acs.org/doi/10.1021/acssuschemeng.9b06853>.

Schematic of AFET; soot filtration setup; particle size and zeta potential; charge and dust distribution of dust; XRD of dust; FTIR and fiber diameter distribution; filtration efficiency using NaCl aerosol; contact angle measurement; pressure drop measurement; antibacterial testing; and charge distribution on fibers (PDF)

PAN (TXT)

ChCl-PAN (TXT)

PP (TXT)

SPS (TXT)

Soot filtration (MP4)

## ■ AUTHOR INFORMATION

### Corresponding Authors

**Ramamurthy Nagarajan** – Department of Chemical Engineering, Indian Institute of Technology Madras, Chennai 6000036, India; Email: [nag@iitm.ac.in](mailto:nag@iitm.ac.in)

**Thalappil Pradeep** – DST Unit of Nanoscience and Thematic Unit of Excellence, Department of Chemistry, Indian Institute of Technology Madras, Chennai 6000036, India; [orcid.org/0000-0003-3174-534X](https://orcid.org/0000-0003-3174-534X); Email: [pradeep@iitm.ac.in](mailto:pradeep@iitm.ac.in)

### Authors

**Pillalamarri Srikrishnarka** – DST Unit of Nanoscience and Thematic Unit of Excellence, Department of Chemistry and Department of Chemical Engineering, Indian Institute of Technology Madras, Chennai 6000036, India; [orcid.org/0000-0001-5187-6879](https://orcid.org/0000-0001-5187-6879)

**Vishal Kumar** – DST Unit of Nanoscience and Thematic Unit of Excellence, Department of Chemistry and Department of Chemical Engineering, Indian Institute of Technology Madras, Chennai 6000036, India

**Tripti Ahuja** – DST Unit of Nanoscience and Thematic Unit of Excellence, Department of Chemistry, Indian Institute of Technology Madras, Chennai 6000036, India

**Vidhya Subramanian** – DST Unit of Nanoscience and Thematic Unit of Excellence, Department of Chemistry, Indian Institute of Technology Madras, Chennai 6000036, India

**Arun Karthick Selvam** – DST Unit of Nanoscience and Thematic Unit of Excellence, Department of Chemistry, Indian Institute of Technology Madras, Chennai 6000036, India

**Paulami Bose** – DST Unit of Nanoscience and Thematic Unit of Excellence, Department of Chemistry, Indian Institute of Technology Madras, Chennai 6000036, India

**Shantha Kumar Jenifer** – DST Unit of Nanoscience and Thematic Unit of Excellence, Department of Chemistry and Department of Metallurgy and Materials Engineering, Indian Institute of Technology Madras, Chennai 6000036, India

**Ananthu Mahendranath** – DST Unit of Nanoscience and Thematic Unit of Excellence, Department of Chemistry and Department of Metallurgy and Materials Engineering, Indian Institute of Technology Madras, Chennai 6000036, India

**Mohd Azhardin Ganayee** – DST Unit of Nanoscience and Thematic Unit of Excellence, Department of Chemistry, Indian Institute of Technology Madras, Chennai 6000036, India

Complete contact information is available at:

<https://pubs.acs.org/doi/10.1021/acssuschemeng.9b06853>

## Notes

The authors declare no competing financial interest.

## ■ ACKNOWLEDGMENTS

The authors thank the Department of Science and Technology, Government of India, for supporting their research in nanomaterials. P.S., V.K., T.A., V.S., A.K.S., P.B., and A.M. thank IIT Madras for research fellowship. M.A.G. thanks the University Grants Commission (UGC), Government of India, for his fellowship. P.S. acknowledges Sugi K for assistance during HPLC studies. The authors would also like to acknowledge Prof. N. Gopi of the Department of Textile Technology, Anna University, for allowing them to use his filtration efficiency testing facility.

## ■ REFERENCES

- (1) Blanchard, D. C. The Electrification of the Atmosphere by Particles from Bubbles in the Sea. *Prog. Oceanogr.* **1963**, *1*, 73–202.
- (2) Villermaux, E.; Bossa, B. Single-Drop Fragmentation Determines Size Distribution of Raindrops. *Nat. Phys.* **2009**, *5*, 697.
- (3) Blanchard, D. C. The Size and Height to Which Jet Drops Are Ejected from Bursting Bubbles in Seawater. *J. Geophys. Res.: Oceans* **1989**, *94*, 10999–11002.
- (4) Kassotis, C. D.; Hoffman, K.; Stapleton, H. M. Characterization of Adipogenic Activity of House Dust Extracts and Semi-Volatile Indoor Contaminants in 3T3-L1 Cells. *Environ. Sci. Technol.* **2017**, *51*, 8735–8745.
- (5) Kampa, M.; Castanas, E. Human Health Effects of Air Pollution. *Environ. Pollut.* **2008**, *151*, 362–367.
- (6) Badarinath, K. V. S.; Kharol, S. K.; Kaskaoutis, D. G.; Sharma, A. R.; Ramaswamy, V.; Kambezidis, H. D. Long-Range Transport of Dust Aerosols over the Arabian Sea and Indian Region — A Case Study Using Satellite Data and Ground-Based Measurements. *Global Planet. Change* **2010**, *72*, 164–181.
- (7) Ghose, M. K.; Majee, S. R. Characteristics of Hazardous Airborne Dust Around an Indian Surface Coal Mining Area. *Environ. Monit. Assess.* **2007**, *130*, 17–25.
- (8) Lintermann, A.; Schröder, W. Simulation of Aerosol Particle Deposition in the Upper Human Tracheobronchial Tract. *Eur. J. Mech. B* **2017**, *63*, 73–89.
- (9) Betha, R.; Behera, S. N.; Balasubramanian, R. 2013 Southeast Asian Smoke Haze: Fractionation of Particulate-Bound Elements and Associated Health Risk. *Environ. Sci. Technol.* **2014**, *48*, 4327–4335.
- (10) Timonen, K. L.; Vanninen, E.; de Hartog, J.; Ibaldo-Mulli, A.; Brunekreef, B.; Gold, D. R.; Heinrich, J.; Hoek, G.; Lanki, T.; Peters, A.; et al. Effects of Ultrafine and Fine Particulate and Gaseous Air Pollution on Cardiac Autonomic Control in Subjects with Coronary Artery Disease: The ULTRA Study. *J. Expo. Sci. Environ. Epidemiol.* **2006**, *16*, 332–341.
- (11) Wu, S.; Deng, F.; Wei, H.; Huang, J.; Wang, X.; Hao, Y.; Zheng, C.; Qin, Y.; Lv, H.; Shima, M.; et al. Association of Cardiopulmonary

Health Effects with Source-Appointed Ambient Fine Particulate in Beijing, China: A Combined Analysis from the Healthy Volunteer Natural Relocation (HVNLR) Study. *Environ. Sci. Technol.* **2014**, *48*, 3438–3448.

(12) Otto, D. A.; Hudnell, H. K.; House, D. E.; Mølhave, L.; Counts, W. Exposure of Humans to a Volatile Organic Mixture. I. Behavioral Assessment. *Arch. Environ. Health* **1992**, *47*, 23–30.

(13) Valentín, D.; Guardo, A.; Egusquiza, E.; Valero, C.; Alavedra, P. Assessment of the Economic and Environmental Impact of Double Glazed Façade Ventilation Systems in Mediterranean Climates. *Energies* **2013**, *6*, 5069.

(14) Hinds, W. C. *Aerosol Technology: Properties, Behavior, and Measurement of Airborne Particles*; John Wiley & Sons, 1999.

(15) Liu, C.; Hsu, P.-C.; Lee, H.-W.; Ye, M.; Zheng, G.; Liu, N.; Li, W.; Cui, Y. Transparent Air Filter for High-Efficiency PM<sub>2.5</sub> Capture. *Nat. Commun.* **2015**, *6*, 6205.

(16) Jing, L.; Shim, K.; Toe, C. Y.; Fang, T.; Zhao, C.; Amal, R.; Sun, K.-N.; Kim, J. H.; Ng, Y. H. Electrospun Polyacrylonitrile-Ionic Liquid Nanofibers for Superior PM<sub>2.5</sub> Capture Capacity. *ACS Appl. Mater. Interfaces* **2016**, *8*, 7030–7036.

(17) Li, X.; Wang, X.-X.; Yue, T.-T.; Xu, Y.; Zhao, M.-L.; Yu, M.; Ramakrishna, S.; Long, Y.-Z. Waterproof-Breathable PTFE Nano- and Microfiber Membrane as High Efficiency PM<sub>2.5</sub> Filter. *Polymers* **2019**, *11*, 590.

(18) Hu, L.; Cui, Y. Energy and Environmental Nanotechnology in Conductive Paper and Textiles. *Energy Environ. Sci.* **2012**, *5*, 6423–6435.

(19) Huang, X.; Wang, R.; Jiao, T.; Zou, G.; Zhan, F.; Yin, J.; Zhang, L.; Zhou, J.; Peng, Q. Facile Preparation of Hierarchical AgNP-Loaded MXene/Fe<sub>3</sub>O<sub>4</sub>/Polymer Nanocomposites by Electrospinning with Enhanced Catalytic Performance for Wastewater Treatment. *ACS Omega* **2019**, *4*, 1897–1906.

(20) Xing, R.; Wang, W.; Jiao, T.; Ma, K.; Zhang, Q.; Hong, W.; Qiu, H.; Zhou, J.; Zhang, L.; Peng, Q. Bioinspired Polydopamine Sheathed Nanofibers Containing Carboxylate Graphene Oxide Nanosheet for High-Efficient Dyes Scavenger. *ACS Sustain. Chem. Eng.* **2017**, *5*, 4948–4956.

(21) Wang, C.; Yin, J.; Han, S.; Jiao, T.; Bai, Z.; Zhou, J.; Zhang, L.; Peng, Q. Preparation of Palladium Nanoparticles Decorated Polyethyleneimine/Polycaprolactone Composite Fibers Constructed by Electrospinning with Highly Efficient and Recyclable Catalytic Performances. *Catalysts* **2019**, *9*, 559.

(22) Huang, X.; Jiao, T.; Liu, Q.; Zhang, L.; Zhou, J.; Li, B.; Peng, Q. Hierarchical Electrospun Nanofibers Treated by Solvent Vapor Annealing as Air Filtration Mat for High-Efficiency PM<sub>2.5</sub> Capture. *Sci. China Mater.* **2019**, *62*, 423–436.

(23) Zhang, K.; Huo, Q.; Zhou, Y.-Y.; Wang, H.-H.; Li, G.-P.; Wang, Y.-W.; Wang, Y.-Y. Textiles/Metal–Organic Frameworks Composites as Flexible Air Filters for Efficient Particulate Matter Removal. *ACS Appl. Mater. Interfaces* **2019**, *11*, 17368–17374.

(24) Souzandeh, H.; Scudiero, L.; Wang, Y.; Zhong, W.-H. A Disposable Multi-Functional Air Filter: Paper Towel/Protein Nanofibers with Gradient Porous Structures for Capturing Pollutants of Broad Species and Sizes. *ACS Sustain. Chem. Eng.* **2017**, *5*, 6209–6217.

(25) Zhang, Q.; Li, Q.; Young, T. M.; Harper, D. P.; Wang, S. A Novel Method for Fabricating an Electrospun Poly(Vinyl Alcohol)/Cellulose Nanocrystals Composite Nanofibrous Filter with Low Air Resistance for High-Efficiency Filtration of Particulate Matter. *ACS Sustain. Chem. Eng.* **2019**, *7*, 8706–8714.

(26) Fan, X.; Wang, Y.; Kong, L.; Fu, X.; Zheng, M.; Liu, T.; Zhong, W.-H.; Pan, S. A Nanoprotein-Functionalized Hierarchical Composite Air Filter. *ACS Sustain. Chem. Eng.* **2018**, *6*, 11606–11613.

(27) Zeng, Z.; Ma, X. Y. D.; Zhang, Y.; Wang, Z.; Ng, B. F.; Wan, M. P.; Lu, X. Robust Lignin-Based Aerogel Filters: High-Efficiency Capture of Ultrafine Airborne Particulates and the Mechanism. *ACS Sustain. Chem. Eng.* **2019**, *7*, 6959–6968.

(28) Li, D.; Frey, M. W.; Joo, Y. L. Characterization of Nanofibrous Membranes with Capillary Flow Porometry. *J. Membr. Sci.* **2006**, *286*, 104–114.

(29) Lee, E. S.; Xu, B.; Zhu, Y. Measurements of Ultrafine Particles Carrying Different Number of Charges in On- and near-Freeway Environments. *Atmos. Environ.* **2012**, *60*, 564–572.

(30) Leppä, J.; Anttila, T.; Kerminen, V.-M.; Kulmala, M.; Lehtinen, K. E. J. Atmospheric New Particle Formation: Real and Apparent Growth of Neutral and Charged Particles. *Atmos. Chem. Phys.* **2011**, *11*, 4939–4955.

(31) Jacobson, M.; Seinfeld, J. H. Evolution of Nanoparticle Size and Mixing State near the Point of Emission. *Atmos. Environ.* **2004**, *38*, 1839–1850.

(32) Gu, G. Q.; Han, C. B.; Lu, C. X.; He, C.; Jiang, T.; Gao, Z. L.; Li, C. J.; Wang, Z. L. Triboelectric Nanogenerator Enhanced Nanofiber Air Filters for Efficient Particulate Matter Removal. *ACS Nano* **2017**, *11*, 6211–6217.

(33) Xiong, Z.-C.; Yang, R.-L.; Zhu, Y.-J.; Chen, F.-F.; Dong, L.-Y. Flexible Hydroxyapatite Ultralong Nanowire-Based Paper for Highly Efficient and Multifunctional Air Filtration. *J. Mater. Chem. A* **2017**, *5*, 17482–17491.

(34) Li, X.; Wang, C.; Huang, X.; Zhang, T.; Wang, X.; Min, M.; Wang, L.; Huang, H.; Hsiao, B. S. Anionic Surfactant-Triggered Steiner Geometrical Poly(Vinylidene Fluoride) Nanofiber/Nanonet Air Filter for Efficient Particulate Matter Removal. *ACS Appl. Mater. Interfaces* **2018**, *10*, 42891–42904.

(35) Bennett, W. D.; Zeman, K. L.; Jarabek, A. M. Nasal Contribution to Breathing and Fine Particle Deposition in Children Versus Adults. *J. Toxicol. Environ. Health, Part A* **2007**, *71*, 227–237.

(36) Mendell, M. J. Indoor Residential Chemical Emissions as Risk Factors for Respiratory and Allergic Effects in Children: A Review. *Indoor Air* **2007**, *17*, 259–277.

(37) Pawankar, R.; Holgate, S. T.; Rosenwasser, L. J. *Allergy Frontiers: Epigenetics, Allergens and Risk Factors*; Springer, 2009.

(38) Kadam, V. V.; Wang, L.; Padhye, R. Electrospun Nanofibre Materials to Filter Air Pollutants – A Review. *J. Ind. Textil.* **2016**, *47*, 2253–2280.

(39) Scholten, E.; Bromberg, L.; Rutledge, G. C.; Hatton, T. A. Electrospun Polyurethane Fibers for Absorption of Volatile Organic Compounds from Air. *ACS Appl. Mater. Interfaces* **2011**, *3*, 3902–3909.

(40) Anderson, A. C.; Jonas, D.; Huber, I.; Karygianni, L.; Wölber, J.; Hellwig, E.; Arweiler, N.; Vach, K.; Wittmer, A.; Al-Ahmad, A. Enterococcus Faecalis from Food, Clinical Specimens, and Oral Sites: Prevalence of Virulence Factors in Association with Biofilm Formation. *Front. Microbiol.* **2016**, *6*, 1534.

(41) Pinheiro, E. T.; Márcia, P. A. M. *J. Interdiscip. Med. Dent. Sci.* **2014**, *3*, 160.

(42) Wang, Q.-Q.; Zhang, C.-F.; Chu, C.-H.; Zhu, X.-F. Prevalence of Enterococcus Faecalis in Saliva and Filled Root Canals of Teeth Associated with Apical Periodontitis. *Int. J. Oral Sci.* **2012**, *4*, 19–23.

(43) Souto, R.; Colombo, A. P. V. Prevalence of Enterococcus Faecalis in Subgingival Biofilm and Saliva of Subjects with Chronic Periodontal Infection. *Arch. Oral Biol.* **2008**, *53*, 155–160.

(44) Yao, Y.; Ji, L.; Lin, Z.; Li, Y.; Alcoutlabi, M.; Hamouda, H.; Zhang, X. Sulfonated Polystyrene Fiber Network-Induced Hybrid Proton Exchange Membranes. *ACS Appl. Mater. Interfaces* **2011**, *3*, 3732–3737.

(45) Karbownik, I.; Rac-Rumijowska, O.; Fiedot-Toboła, M.; Rybicki, T.; Teterycz, H. The Preparation and Characterization of Polyacrylonitrile-Polyaniline (PAN/PANI) Fibers. *Materials* **2019**, *12*, 664.

(46) Ram, S. S.; Kumar, R. V.; Chaudhuri, P.; Chanda, S.; Santra, S. C.; Sudarshan, M.; Chakraborty, A. Physico-Chemical Characterization of Street Dust and Re-Suspended Dust on Plant Canopies: An Approach for Finger Printing the Urban Environment. *Ecol. Indic.* **2014**, *36*, 334–338.

- (47) Falkovich, A. H.; Ganor, E.; Levin, Z.; Formenti, P.; Rudich, Y. Chemical and Mineralogical Analysis of Individual Mineral Dust Particles. *J. Geophys. Res. Atmos.* **2001**, *106*, 18029–18036.
- (48) Senthil Kumar, R.; Rajkumar, P. Characterization of Minerals in Air Dust Particles in the State of Tamilnadu, India through FTIR, XRD and SEM Analyses. *Infrared Phys. Technol.* **2014**, *67*, 30–41.
- (49) Nowak, S.; Lafon, S.; Caquineau, S.; Journet, E.; Laurent, B. Quantitative Study of the Mineralogical Composition of Mineral Dust Aerosols by X-Ray Diffraction. *Talanta* **2018**, *186*, 133–139.
- (50) Yang, Y.; Jia, Z.; Liu, J.; Li, Q.; Hou, L.; Wang, L.; Guan, Z. Effect of Electric Field Distribution Uniformity on Electrospinning. *J. Appl. Phys.* **2008**, *103*, 104307.
- (51) Ramakrishna, S. *An Introduction to Electrospinning and Nanofibers*; World Scientific, 2005.
- (52) Pereira, F.; Aires-de-Sousa, J. Machine Learning for the Prediction of Molecular Dipole Moments Obtained by Density Functional Theory. *J. Cheminf.* **2018**, *10*, 43.
- (53) Shimada, I.; Takahagi, T.; Fukuhara, M.; Morita, K.; Ishitani, A. FT-IR Study of the Stabilization Reaction of Polyacrylonitrile in the Production of Carbon Fibers. *J. Polym. Sci., Part A: Polym. Chem.* **1986**, *24*, 1989–1995.
- (54) Nakanishi, K. *Infrared Absorption Spectroscopy, Practical*. By Koji Nakanishi. Holden-Day, Inc., 728 Montgomery St., San Francisco 11, Calif, ix + 233pp. 18 × 26cm. Price \$8. *J. Pharm. Sci.* **1963**, *52*, 716.
- (55) Al-Sabagh, A. M.; Moustafa, Y. M.; Hamdy, A.; Killa, H. M.; Ghanem, R. T. M.; Morsi, R. E. Preparation and Characterization of Sulfonated Polystyrene/Magnetite Nanocomposites for Organic Dye Adsorption. *Egypt. J. Pet.* **2018**, *27*, 403–413.
- (56) Zhang, R.; Liu, B.; Yang, A.; Zhu, Y.; Liu, C.; Zhou, G.; Sun, J.; Hsu, P.-C.; Zhao, W.; Lin, D.; et al. In Situ Investigation on the Nanoscale Capture and Evolution of Aerosols on Nanofibers. *Nano Lett.* **2018**, *18*, 1130–1138.
- (57) Levin, P. A.; Angert, E. R. Small but Mighty: Cell Size and Bacteria. *Cold Spring Harbor Perspect. Biol.* **2015**, *7*, a019216.
- (58) Zhao, X.; Wang, S.; Yin, X.; Yu, J.; Ding, B. Slip-Effect Functional Air Filter for Efficient Purification of PM<sub>2.5</sub>. *Sci. Rep.* **2016**, *6*, 35472.
- (59) Wang, Q.; Bai, Y.; Xie, J.; Jiang, Q.; Qiu, Y. Synthesis and Filtration Properties of Polyimide Nanofiber Membrane/Carbon Woven Fabric Sandwiched Hot Gas Filters for Removal of PM<sub>2.5</sub> Particles. *Powder Technol.* **2016**, *292*, 54.
- (60) Kim, J.-H.; Roberge, R. J.; Powell, J. B.; Shaffer, R. E.; Ylitalo, C. M.; Sebastian, J. M. Pressure Drop of Filtering Facepiece Respirators: How Low Should We Go? *Int. J. Occup. Med. Environ. Health* **2015**, *28*, 71–80.



## Supporting information for:

### Enhanced Capture of Particulate Matter by Molecularly Charged Electrospun Nanofibers

Pillalamarri Srikrishnarka,<sup>†,‡</sup> Vishal Kumar,<sup>†,‡</sup> Tripti Ahuja,<sup>†</sup> Vidhya Subramanian,<sup>†</sup> Arun Karthick Selvam,<sup>†</sup> Paulami Bose,<sup>†</sup> Shantha Kumar Jenifer,<sup>†,¶</sup> Ananthu Mahendranath,<sup>†,¶</sup> Mohd Azhardin Ganayee,<sup>†</sup> Ramamurthy Nagarajan<sup>\*,‡</sup> and Thalappil Pradeep<sup>\*,†</sup>

<sup>†</sup>*DST Unit of Nanoscience, Department of Chemistry, Indian Institute of Technology Madras, Chennai, India 6000036.*

<sup>‡</sup>*Department of Chemical Engineering, Indian Institute of Technology Madras, Chennai, India 6000036.*

<sup>¶</sup> *Department of Metallurgy and Materials Engineering, Indian Institute of Technology Madras, Chennai, India 6000036.*

\*E-mail: Thalappil Pradeep [pradeep@iitm.ac.in](mailto:pradeep@iitm.ac.in)

Ramamurthy Nagarajan [nag@iitm.ac.in](mailto:nag@iitm.ac.in)

## SUPPORTING INFORMATION CONTENT

Total number of pages: 15

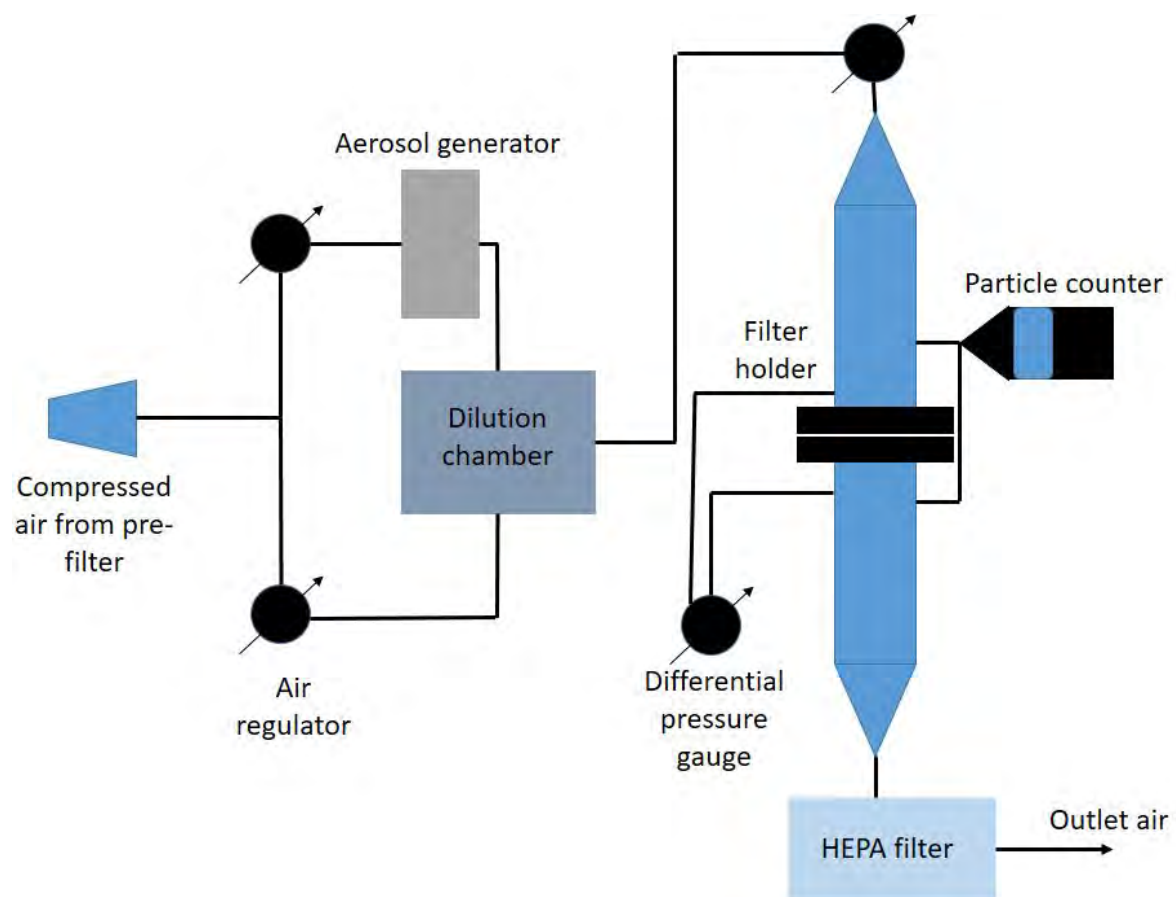
Total number of figures: 13

Total number of tables: 1

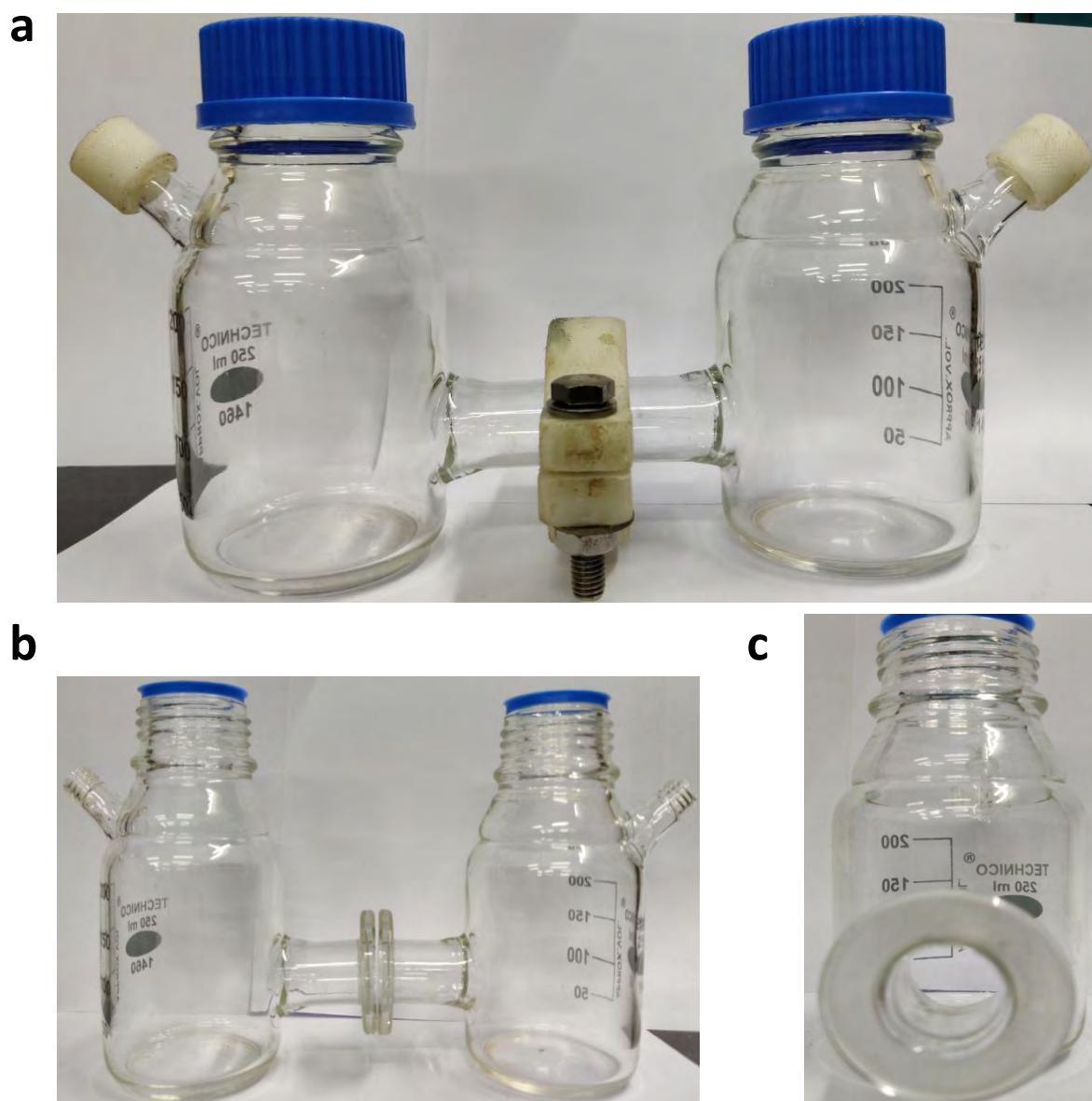
## TABLE OF CONTENTS

Figure No.	Description	Page No.
Figure S1	Illustration of the aerosol filtration efficiency tester set-up	S3
Figure S2	Photograph of the soot filtration set-up	S4
Figure S3	(a) Size distribution of dust particles collected on different days. (b) Zeta potential of the dust collected on different days	S5
Figure S4	(a and b) Charge distribution of dust collected from 2 different locations measured using a Faraday cup. (c and d) Scanning electron micrographs of dust collected from 2 locations. Scale	S5

	bar corresponds to 100 $\mu\text{m}$	
Figure S5	X-ray diffraction patterns of dust collected from 4 different locations matched with the standard ICSD database	S6
Table S1	Chemical composition of dust collected from 4 different locations matched using the ICSD database	S6
Figure S6	(a and c) Fiber diameter distribution comparing the bare and chemically treated PAN and PS. (b and d) fibers FTIR spectra comparing bare, chemically treated PAN and bare, chemically treated PS, respectively	S7
Figure S7	Charge distribution of untreated and treated fibers of (a) PAN and (b) PS	S8
Figure S8	Water contact angle measurements	S9
Figure S9	(a) Pressure drop across various filter mats with different electrospinning time. (b) Pressure drop across untreated and treated filter mat before and after exposure to soot for 24 h. (c) Comparing the mass of fibers collected on the non-woven mat with electrospinning time	S10
Figure S10	(a) Scanning electron micrograph of chemically treated PS fiber with NaCl crystals on them. (b) Spot energy dispersive spectrum (EDS) for the highlighted region with various components presented in the atomic and weight %. Scale bare corresponds to 10 $\mu\text{m}$ . Comparing the filtration efficiencies of the untreated and treated fibers. Expanded view of the filtration efficiency is shown in the inset	S11
Figure S11	(a) Charge distribution of electrospun PAN fibers. Marked region is zone presented in the inset. (b) Scanning electron micrograph of ChCl-PAN fibres. Scale bar corresponds to 5 $\mu\text{m}$ . The pores are highlighted by arrows. (c) Filtration efficiency of ChCl-PAN fibres	S13
Figure S12	(a) Charge distribution of PS fibres before and after chemical treatment with sulfuric acid. The time of addition of material is marked. (b) Soot filtration efficiency of SPS fibres	S14
Figure S13	Antibacterial property of the fiber	S15
Video S1	Capture of soot on the fiber mat	V-S1



**Figure S1.** Illustration of the aerosol filtration efficiency tester set-up.



**Figure S2.** Photograph of soot filtration set-up. (a) The complete set-up with clamps and caps, (b) without the clamps and caps. (c) Side view of one the bottle were the fibers meet the soot particles.

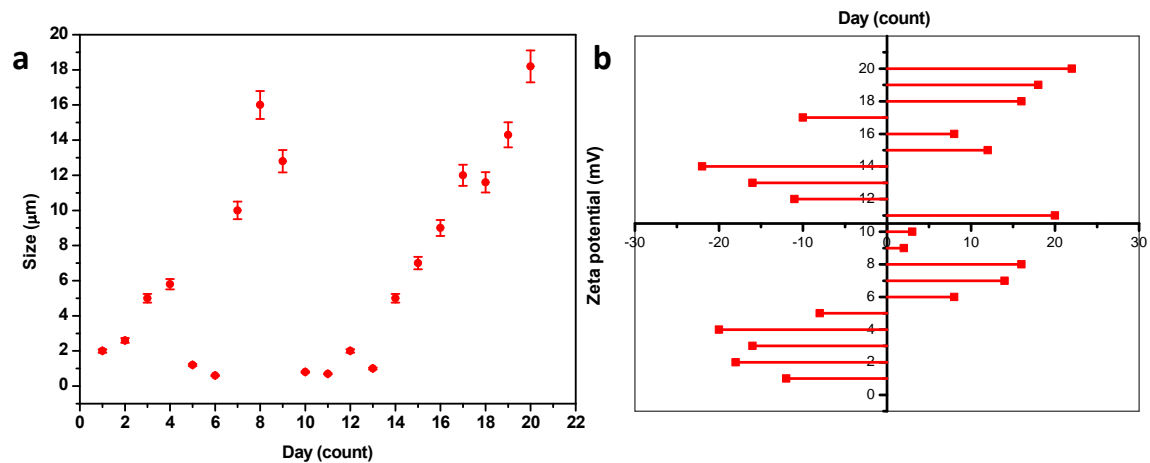


**Figure S3.** (a) Size distribution of dust particles collected on different days. (b) Zeta potential of the dust collected on different days.

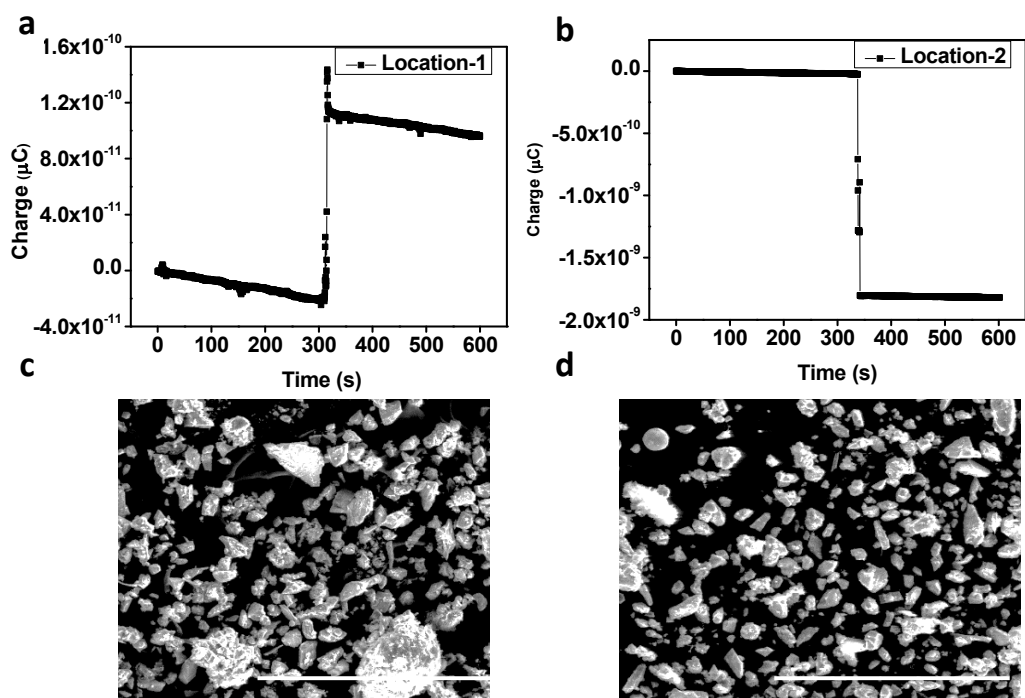


**Figure S4.** (a and b) Charge distribution of dust collected from 2 different locations measured using a Faraday cup. (c and d) Scanning electron micrographs of dust collected from 2 different locations. Scale bar corresponds to 10  $\mu\text{m}$ .



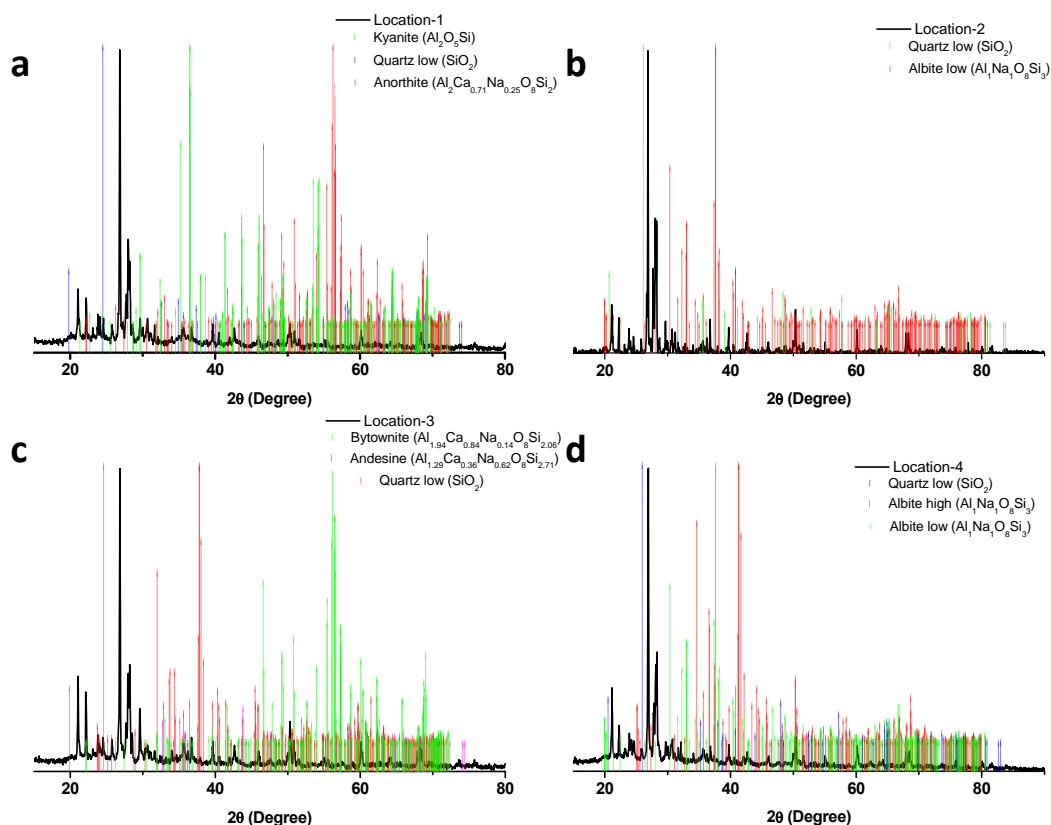


**Figure S5.** (a, b, c and d) X-ray diffraction patterns of dust collected from 4 different locations matched with the ICSD database.

**Table S1.** Chemical composition of dust collected from 4 different locations and matched using ICSD database.

Location	Sample name	Inorganic crystal structure database (ICSD)	Chemical composition
1	Kyanite Quartz low Anorthite	83456 201353 63547	$\text{Al}_2\text{O}_5\text{Si}$ $\text{SiO}_2$ $\text{Al}_2\text{Ca}_{0.71}\text{Na}_{0.25}\text{O}_8\text{Si}_2$
2	Quartz low Albite low	201353 77423	$\text{SiO}_2$ $\text{Al}_1\text{Na}_1\text{O}_8\text{Si}_3$
3	Bytownite Quartz low Lauzurite 4A Andesine	30932 201353 85087 100867	$\text{Al}_{1.94}\text{Ca}_{0.85}\text{Na}_{0.14}\text{O}_8\text{Si}_{2.06}$ $\text{SiO}_2$ $\text{Al}_6\text{Ca}_1\text{Na}_7\text{O}_{30}\text{S}_{2.12}\text{Si}_6$ $\text{Al}_{1.29}\text{Ca}_{0.36}\text{Na}_{0.62}\text{O}_8\text{Si}_{2.7}$
4	Quartz low Albite low Albite high	201353 77423 9829	$\text{SiO}_2$ $\text{Al}_1\text{Na}_1\text{O}_8\text{Si}_3$ $\text{Al}_1\text{Na}_1\text{O}_8\text{Si}_3$

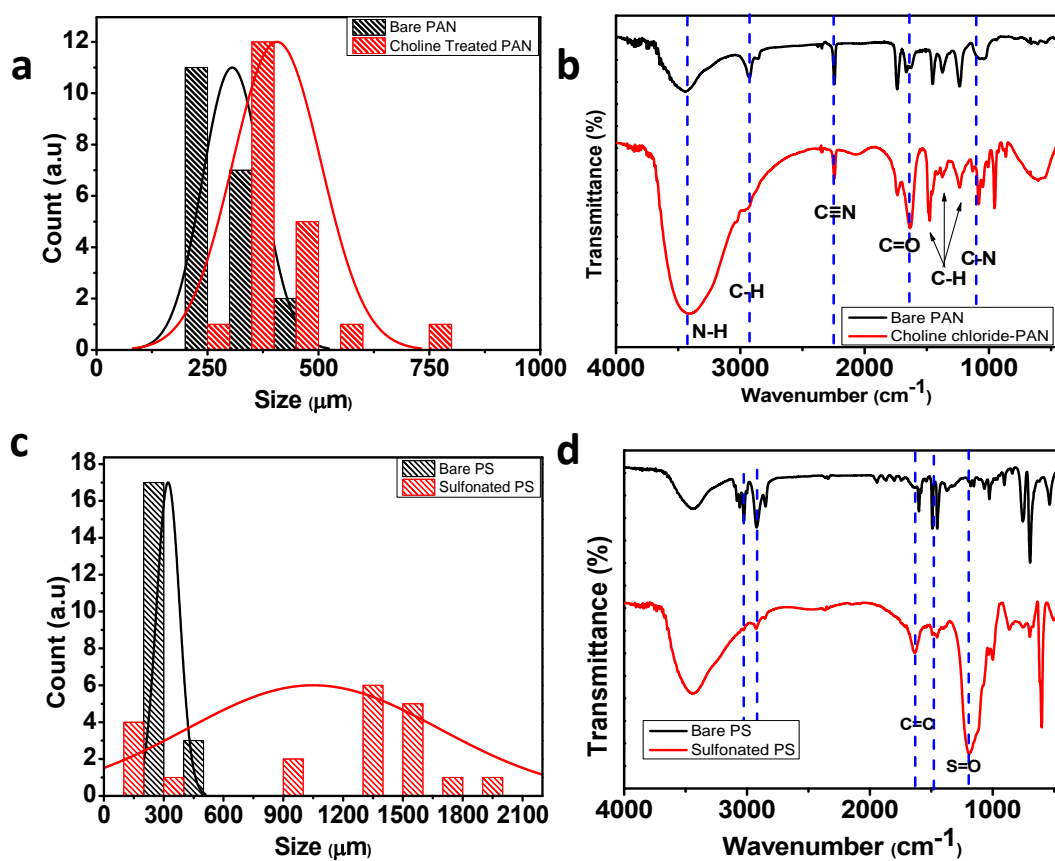


**Figure S6.** (a and c) Fiber diameter distribution comparing the bare and chemically treated PAN and PS. (b and d) fibers FTIR spectra comparing bare, chemically treated PAN and bare, chemically treated PS, respectively.

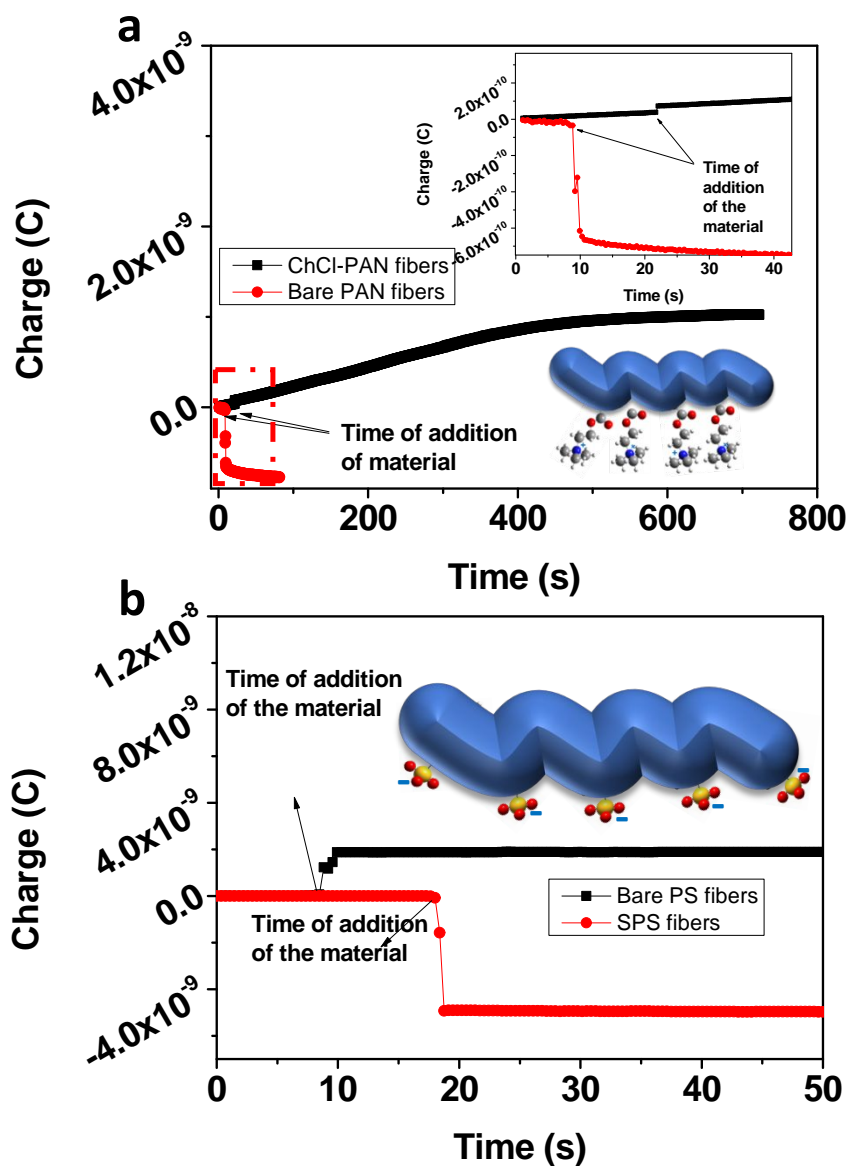


**Figure S7.** Charge distribution of untreated and treated (a) PAN and (b) PS fiber mats. (Inset) (a) Molecular model of ChCl treated PAN where, grey represents carbon, blue represents nitrogen and red represents oxygen. Marked region is enlarged and shown in inset. Marked region of the charge distribution is enlarged and shown in another inset. (b) Molecular model of sulfonated PS where, red represents oxygen and yellow represents sulfur. Time of addition of materials to the Faraday cup is indicated.

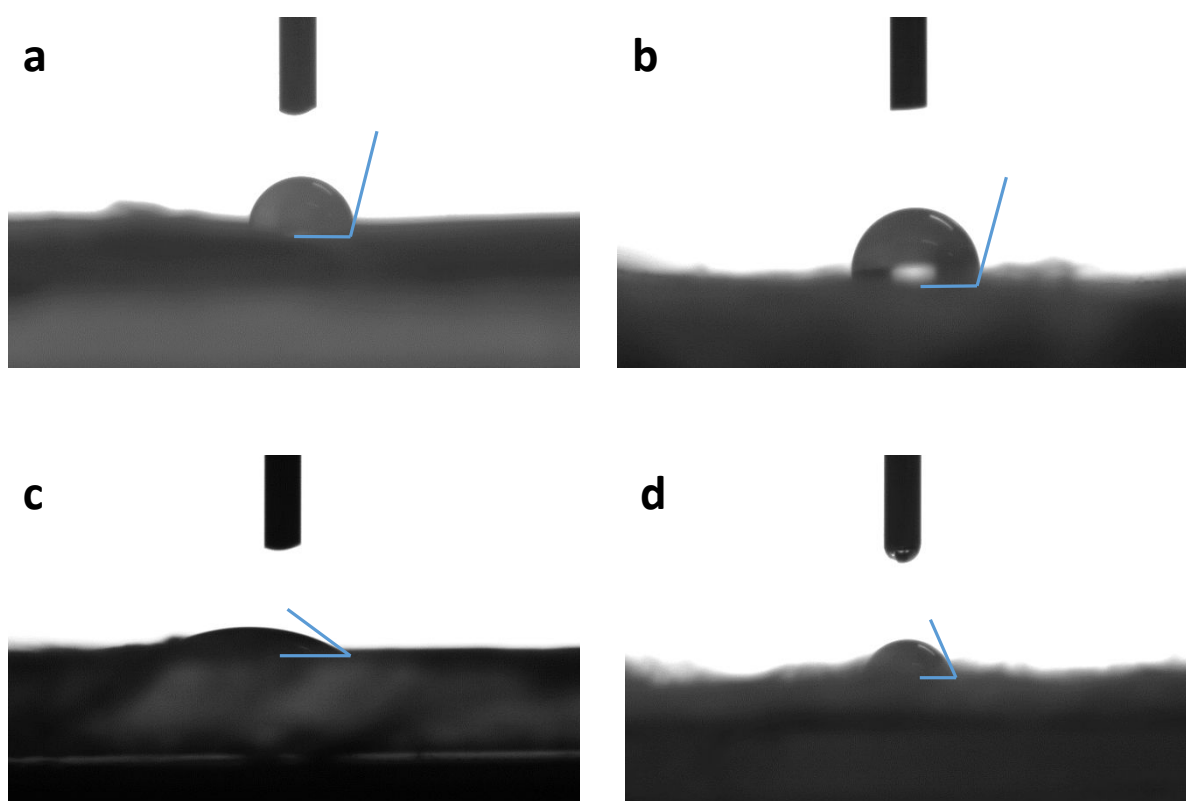


**Figure S8.** Water contact angle measurements performed on (a) PAN, (b) PS, (c) ChClPAN and (d) SPS.

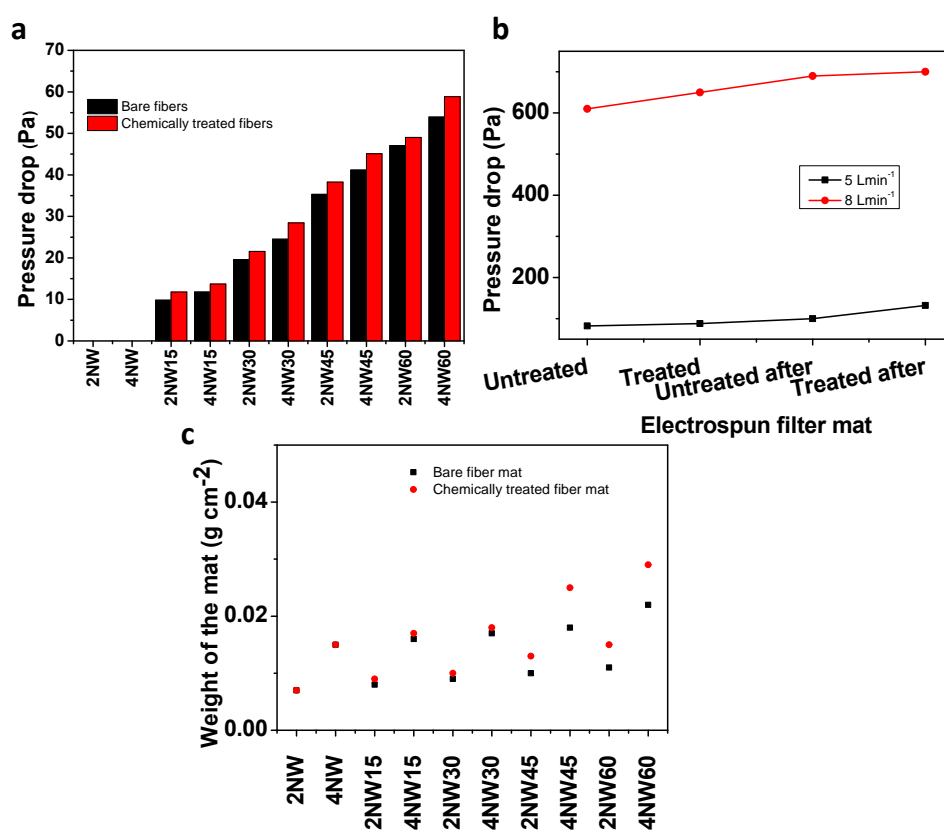


**Figure S9.** (a) Pressure drop across various filter mats with different electrospinning time, Here, 4NW30 indicate 4 NW mats with 30 min of electrospinning time. (b) Pressure drop across untreated and treated filter mat before and after exposure to soot for 24 h. Here, untreated, treated represent the untreated and treated filter mat before exposure to soot, respectively. Untreated after and treated after represent untreated and treated filter mat after exposure to soot, respectively. (c) Comparing the mass of fibers collected on the non-woven mat with electrospinning time.

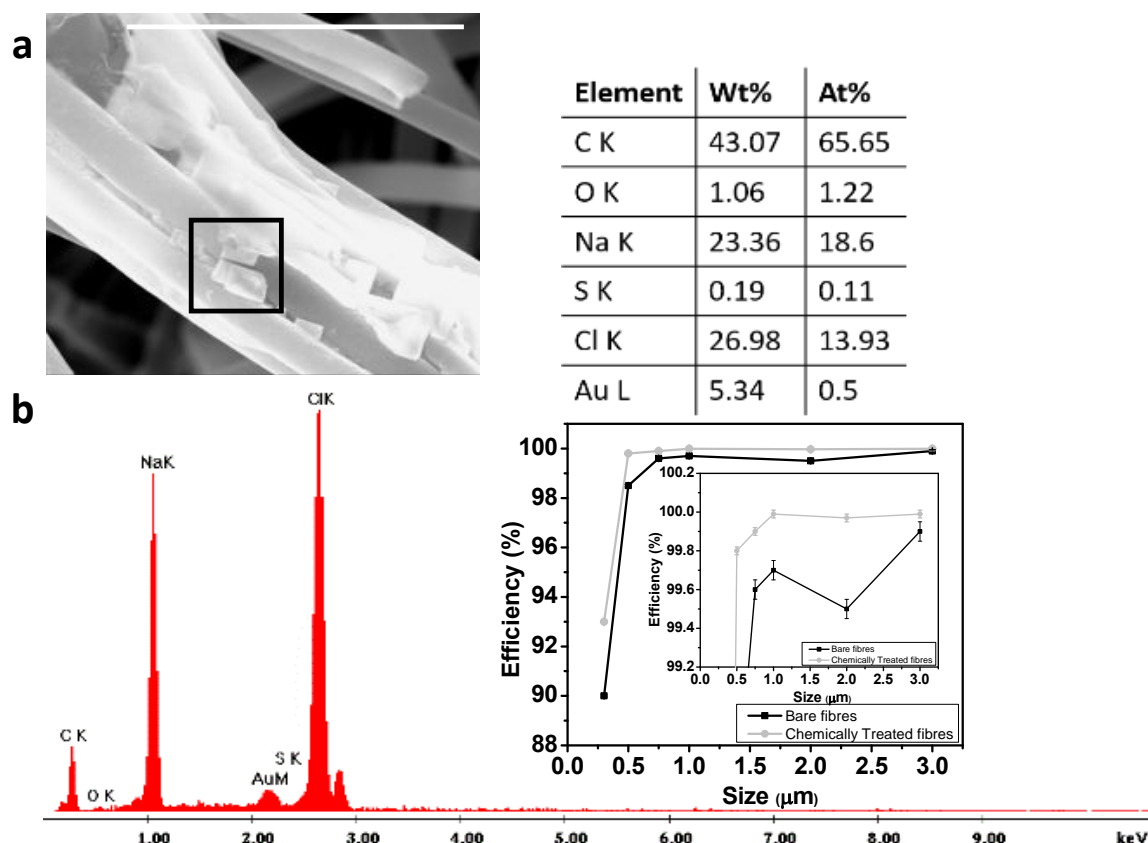


**Figure S10.** (a) Scanning electron micrograph of chemically treated PS fiber with NaCl crystals on them. (b) Spot energy dispersive spectrum (EDS) for the highlighted region with various components presented in the atomic and weight %. Scale bare corresponds to 10  $\mu\text{m}$ . Comparing the filtration efficiencies of the untreated and treated fibers. Expanded view of the filtration efficiency is shown in the inset.



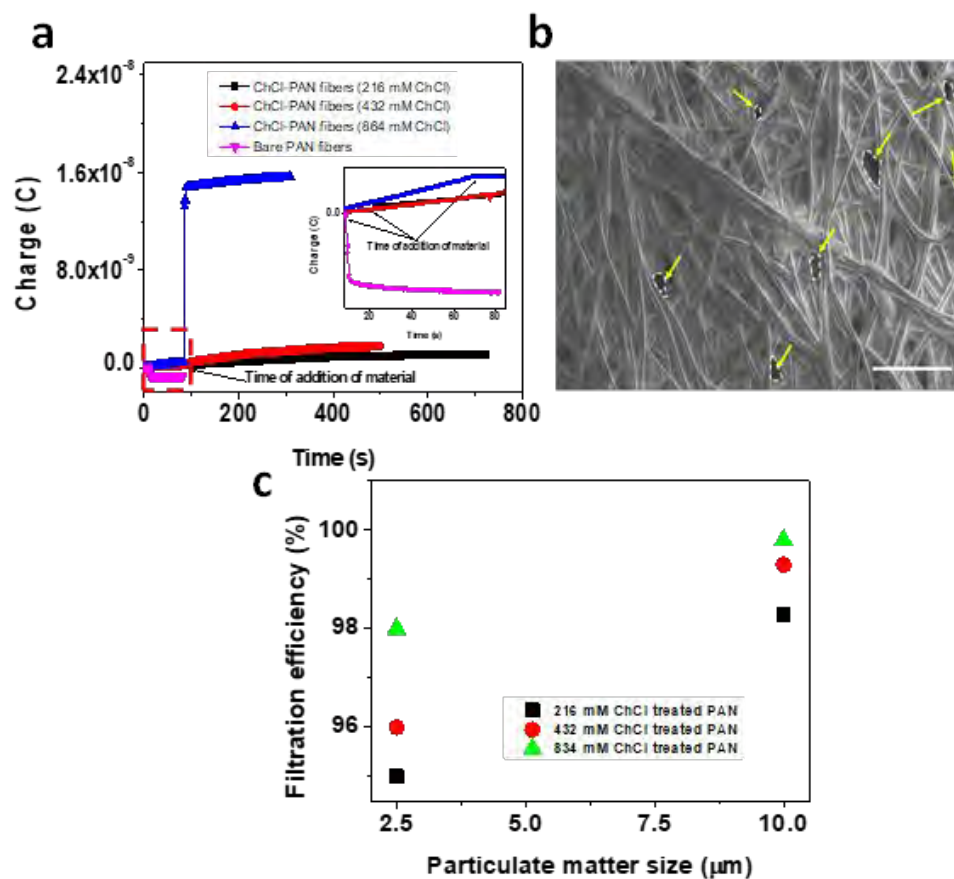


**Figure S11.** (a) Charge distribution of electrospun PAN fibers. Marked region is zone presented in the inset. (b) Scanning electron micrograph of ChCl-PAN fibres. Scale bar corresponds to 5  $\mu\text{m}$ . The pores are highlighted by arrows. (c) Filtration efficiency of ChCl-PAN fibres.

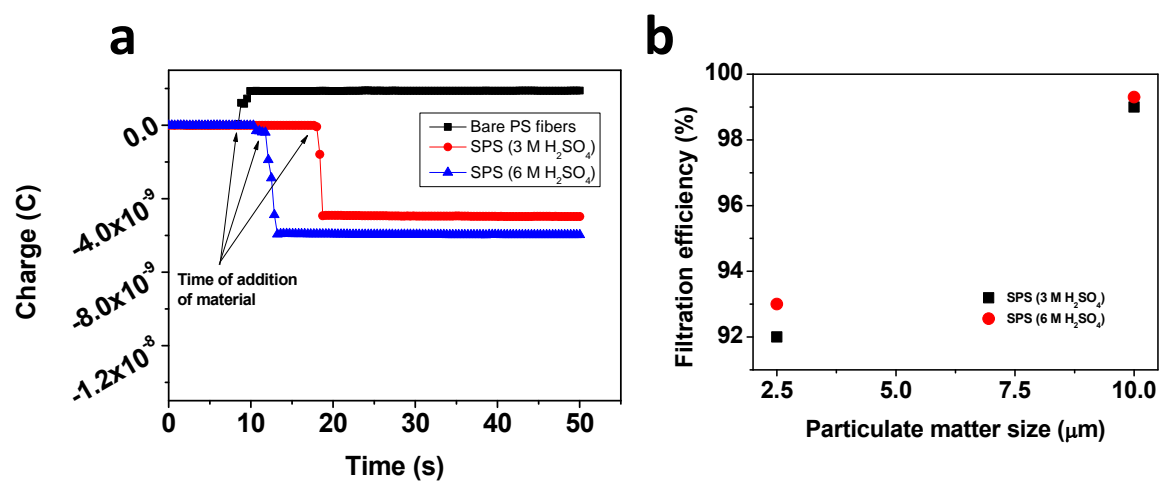


**Figure S12.** (a) Charge distribution of PS fibres before and after chemical treatment with sulfuric acid. The time of addition of material is marked. (b) Soot filtration efficiency of SPS fibres.

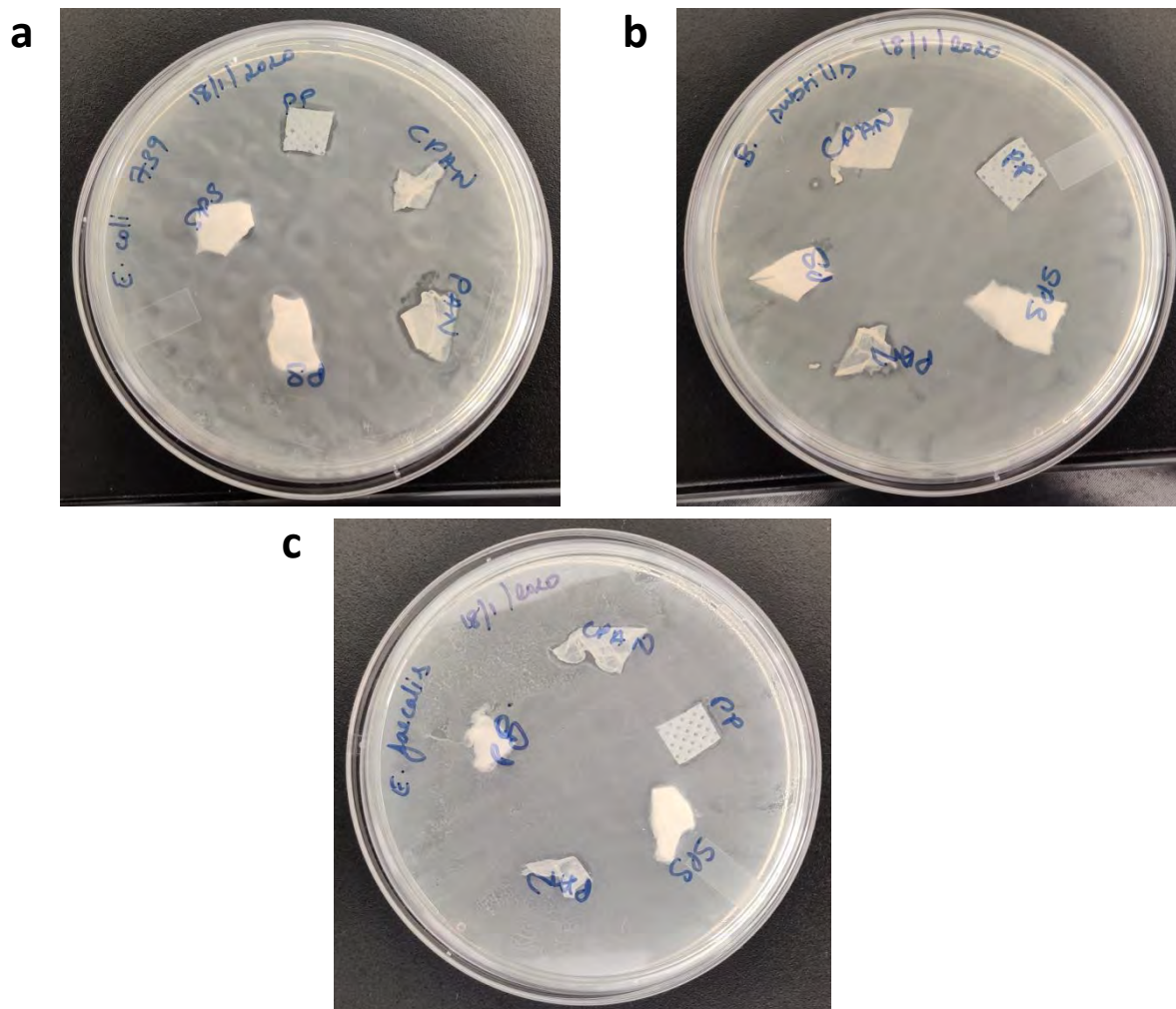







**Figure S13.** Antibacterial property testing of the filter mats using (a) *E. coli*, (b) *B. subtilis* and (c) *E. faecalis*. Here CPAN represent ChCIPAN.



Cite this: *Phys. Chem. Chem. Phys.*,  
2020, 22, 8491

# Iron assisted formation of CO<sub>2</sub> over condensed CO and its relevance to interstellar chemistry†

Rabin Rajan J. Methikkalam,  § Jyotirmoy Ghosh,  ‡ Radha Gobinda Bhui,  ¶  
Soumabha Bag,  || Gopi Ragupathy and Thalappil Pradeep  \*

Catalytic conversion of CO to CO<sub>2</sub> has been investigated in ultrahigh vacuum (UHV) under cryogenic conditions (10 K). This cryogenic oxidation is assisted by iron upon its co-deposition with CO, on a substrate. The study shows that the interaction of Fe and CO results in a Fe–CO complex that reacts in the presence of excess CO at cryogenic conditions leading to CO<sub>2</sub>. Here, the presence of CO on the surface is a prerequisite for the reaction to occur. Different control experiments confirm that the reaction takes place in the condensed phase and not in the gas phase. Surface sensitive reflection absorption infrared spectroscopy (RAIRS), temperature programmed desorption (TPD), and Cs<sup>+</sup> based low energy ion scattering are utilized for this study. The iron assisted formation of CO<sub>2</sub> may be proposed as another pathway relevant in interstellar ices, containing CO. This direct oxidation process, which occurs at extremely low temperatures and pressures, in the presence of a reactive metal species like iron (the most abundant metal in the interstellar medium) may have astrochemical importance. It does not require any external energy in the form of photo-irradiation or thermal processing. Such reactions are highly relevant in cold dense molecular clouds where interactions between neutral species are more favoured.

Received 27th December 2019,  
Accepted 4th April 2020

DOI: 10.1039/c9cp06983f

rsc.li/pccp

## Introduction

Although transition metal assisted catalytic processes/reactions in interstellar space were proposed long ago,<sup>1</sup> they have received consistent attention only in recent years.<sup>2,3</sup> Our knowledge of transition metal assisted catalysis is largely derived from surface science experiments. Many such processes occur at a much higher temperature window than that is possible in the interstellar space. Mechanistic pathways involved in the catalysis for the formation of complex molecular species in the interstellar medium (ISM) and the role of transition metals in them are open questions. Considering the cryogenic conditions present in ISM, this catalysis reaction can be termed as “cryo-catalysis in ISM”, which may be of much importance and can have great relevance in various astrochemical environments. Elements having atomic masses

greater than silicon are found in places like protostars, star-forming regions, and even in diffused and cold dense clouds.<sup>4,5</sup> Among these, iron is observed with higher abundance compared to several other transition metals<sup>5,6</sup> and in fact, iron is the most abundant metal in the universe. These metals are produced and ejected as dust during star formation as well as during the death of stars.<sup>7</sup> Considering the higher abundance of iron in ISM, the possibility of iron assisted catalysis is expected in these conditions.

Iron is known to be a well-known catalyst for the oxidation of CO to CO<sub>2</sub>.<sup>8–11</sup> In the interstellar space, CO and CO<sub>2</sub> have been detected in various environments.<sup>12,13</sup> However, the formation of CO<sub>2</sub> in the gas phase is not efficient to account for its proposed and observed abundance.<sup>14</sup> Several pathways toward the formation of CO<sub>2</sub> in the interstellar space are proposed, such as UV photo-processing of CO ice, high energy ion irradiation of CO ice, oxygenation of CO ice, *etc.*<sup>15–18</sup> Formation of solid CO<sub>2</sub> has also been proposed through CO + O, CO + OH, and H<sub>2</sub>CO + O routes.<sup>19–21</sup> CO is ubiquitous in the ISM and its observed abundance can be explained by the gas phase reactions.<sup>22</sup> In surface science literature, the interaction of CO with iron atoms and iron surfaces is well-studied.<sup>10,11,23</sup> It is one of the model systems, understood in detail with respect to metal–ligand bond formation. CO can undergo dissociative adsorption on iron surfaces.<sup>8,9</sup> Laser ablated iron oxides (clusters) react with CO to produce the carbonyl iron

DST Unit of Nanoscience (DST UNS) and Thematic Unit of Excellence (TUE),  
Department of Chemistry, Indian Institute of Technology Madras, Chennai 600 036,  
India. E-mail: pradeep@iitm.ac.in

† Electronic supplementary information (ESI) available. See DOI: 10.1039/c9cp06983f  
‡ These authors contributed equally.

§ Current address: Department of Chemistry, Mar Ivanios College, Thiruvananthapuram, Kerala, India.

¶ Present address: Lehrstuhl für Physikalische Chemie II, Friedrich-Alexander-Universität Erlangen-Nürnberg, Egerlandstr. 3, 91058 Erlangen, Germany.

|| Current address: Institute of Nanotechnology, Karlsruhe Institute of Technology, 76344 Eggenstein-Leopoldshafen, Germany.

oxides  $\text{FeO}(\text{CO})_n$  ( $n = 1-3$ ) and  $\text{FeO}_2(\text{CO})_m$  ( $m = 1, 2$ ) which can further dissociate to give  $\text{CO}_2$ ; such processes have been investigated using infrared spectroscopy.<sup>24,25</sup> Besides, CO adsorbed on Fe(110) surface undergoes dissociation, and further oxidation in the presence of  $\text{O}_2$  leads to  $\text{CO}_2$  at room temperature and at higher temperatures.<sup>8,9,26</sup>

In this work, we have studied the interaction of neutral iron atoms with CO, which is also abundantly found in ISM.<sup>13</sup> The co-deposition of Fe and CO resulted in Fe + CO complex together with a small amount of  $\text{CO}_2$ . The observed  $\text{CO}_2$  is a product formed due to the reaction of CO with iron atoms as we did not observe any  $\text{CO}_2$  peak during the deposition of CO on the substrate. The Fe + CO band is broad in nature due to the formation of  $\text{Fe}(\text{CO})_x$  (where  $x = 1-5$ ).

The experiments were performed in simulated astrophysical conditions by depositing CO and iron atoms on a surface precooled to 10 K. The formation of  $\text{CO}_2$  was observed just after the deposition, at 10 K. From different control experiments, it was concluded that the formation of  $\text{CO}_2$  occurs on the surface, only in the presence of condensed CO and below the CO residence temperature. To further understand, we have performed a detailed DFT computational study on the electronic structure and vibrational frequency of Fe + CO complexes. The computed vibrational frequency of CO had been compared with our experimental frequency. We have also constructed a free energy map for the formation of  $\text{CO}_2$  from the Fe + CO mixture. The proposed reaction mechanism justified the conversion of CO to  $\text{CO}_2$  in the presence of Fe atoms.

## Experimental

The experiments were performed in a custom-built ultrahigh vacuum instrument with a base pressure of  $< 5 \times 10^{-10}$  mbar. A detailed description of the instrument is given elsewhere.<sup>27</sup> The instrument consists of a Ru(0001) substrate, where the molecular solids or ices are deposited. The substrate is attached to a 10 K closed-cycle helium cryostat with a copper holder. The temperatures are measured using a silicon diode sensor, a thermocouple sensor, and a Pt-sensor attached at three different points and are calibrated with  $\pm 0.1$  K accuracy. Molecular solid's structure, reactivity, *etc.*, can be probed using several spectroscopic probes attached to the instrument chamber.<sup>28-31</sup> In this study, we used reflection absorption infrared (RAIR) spectroscopy and  $\text{Cs}^+$  based low energy ion scattering to probe the surface species and temperature programmed desorption (TPD) to examine the desorbed species. The background pressure before starting the experiment was maintained at  $< 5 \times 10^{-10}$  mbar. We have deposited CO, iron, and the mixture (Fe + CO) on the pre-cooled Ru(0001) substrate at 10 K. CO gas (99.999% purity, RANA GAS) was leaked through an all-metal leak valve and metallic iron was evaporated using an electron beam evaporator (Mantis Deposition, e-beam evaporator). The electron beam evaporator can control the rate of evaporation by monitoring the deposition flux, *via* the ion current of the evaporant. The electron beam evaporator consists of an iron rod (99.99%, GoodFellow Cambridge Limited) which was placed

inside a tungsten crucible and heated using the electron beam, and the flux of the evaporant was monitored using a flux plate electrically isolated and biased at 50 V. We maintained the iron flux current at 3 nA (corresponding to ionized Fe atoms over the crucible) during deposition. The amount of iron atoms vaporized is proportional to the flux current. Nearly all the iron ions are neutralized at the flux plate, and no iron ions are falling on the substrate as no current was measured at the substrate. The thermal evaporator was kept 2 cm away from the substrate during the deposition of iron atoms and there was no increase in substrate temperature due to the evaporator. The UHV chamber was backfilled at  $1 \times 10^{-7}$  mbar of CO (by opening the all-metal leak valve) and was exposed to the surface for 10 minutes which would generate 50 MLs of solid CO on the substrate.<sup>27</sup> The deposition of Fe with 3 nA current (observed on the flux plate) for 10 minutes can give iron atoms of a few monolayers. In different experiments, we have maintained the above ratio of iron (3 nA) and CO (pressure at  $1 \times 10^{-7}$  mbar), constant. This constant ratio ensured that the experiments are similar, and the results could be compared with each other. The mixture (Fe + CO) was generated by switching on the evaporator and exposing the chamber with CO gas at  $1 \times 10^{-7}$  mbar simultaneously. The simultaneous exposure for 10 minutes will lead to iron atoms getting mixed with CO in the gas phase and this mixture was getting deposited slowly on to the precooled Ru(0001) substrate to give multilayers of Fe + CO mixture. This thicker sample mixture (Fe + CO) makes sure that the Ru(0001) substrate does not have any influence on the reaction. We have also performed sequential deposition, where CO gas was backfilled for 10 minutes, followed by Fe (3 nA for 10 minutes) by giving a time gap in between for the background pressure to come down to the initial values.

To confirm further that the substrate is not affecting the reaction, solid argon and later water-ice (both amorphous and crystalline forms of ice) were used to cover the ruthenium substrate. Argon (99.998%, Sigma Aldrich) was used at a pressure (back-filling the chamber) of  $5 \times 10^{-7}$  mbar for 16 minutes to produce  $\sim 500$  MLs coverage.  $\text{H}_2\text{O}$  (99.996%, Millipore), taken in a glass to metal seal adaptor, further purified by several freeze pump thaw cycles, was used to deposit water-ice. Amorphous ice was grown by depositing water vapor by backfilling the chamber at  $1 \times 10^{-7}$  mbar pressure for 16.7 minutes, to give  $\sim 100$  MLs of amorphous ice at 10 K. Crystalline ice was developed by depositing the same amount of water vapor at 120 K, further heated to 145 K and subsequently cooled back to 10 K. A residual gas analyser (RGA) was run throughout the deposition which ensured the purity of the gas getting deposited.

After deposition, the deposited sample was heated resistively, and the substrate temperatures were controlled by a LakeShore temperature controller. A typical RAIR spectrum was collected as an average of 512 scans. Temperature-dependent RAIR spectra were measured by depositing Fe + CO mixtures at 10 K and subsequently heating them to higher temperatures at  $2 \text{ K min}^{-1}$  heating rate and giving a 2 minute equilibration time after reaching the desired temperature, followed by spectral measurement.



Computational quantum chemistry, especially DFT, is well suited for understanding the mechanistic insights of transition-metal-catalysed chemical reactions by providing detailed reaction energy profiles with the geometric and electronic structures of reactants, products, intermediates, and transition states. Single-point DFT calculations, similar to previously performed computational analyses of metal clusters,<sup>32</sup> were likewise carried out *via* the Gaussian 09 computational package.<sup>33</sup> In this study, we chose 6-31+G\*, a double- $\zeta$  Popletype basis set. LANL2DZ (Los Alamos National Laboratory 2 double- $\zeta$ ), which is a widely used, effective core potential (ECP)-type basis set, was used to model the metal atoms.<sup>33</sup> This mixed basis set was created through the use of the GEN keyword in Gaussian 09.

Frequency analysis was performed on each ground state and transition state. We verified that all frequencies are positive for each ground state, and only one imaginary frequency existed (within a computational tolerance of  $30\text{ cm}^{-1}$ ) for each transition state complex. It has been shown that the current DFT method (with B3LYP functional) provides reliable geometries, energies, and vibrational frequencies in related mechanistic studies.<sup>34</sup>

## Results and discussion

The experiment was carried out by depositing CO on a pre-cooled Ru(0001) substrate at 10 K. Subsequently, in a different experiment, CO was deposited along with iron atoms. Fig. 1 shows the RAIR spectrum obtained upon depositing CO at 10 K (bottom trace) and upon co-deposition of CO along with iron (Fe + CO) (top trace) at 10 K. The spectra are shown in a range focussing on the C=O antisymmetric stretching band ( $2142\text{ cm}^{-1}$ ). Solid pure CO shows a C=O stretching peak at

$2142\text{ cm}^{-1}$  and a small peak at  $2092\text{ cm}^{-1}$  arises due to the contribution from  $^{13}\text{CO}$  molecules,<sup>18</sup> present with  $^{12}\text{CO}$  as a natural impurity. When CO was deposited along with iron atoms, we observed three peaks, (i) CO antisymmetric stretching peak ( $2142\text{ cm}^{-1}$ ) with reduced intensity compared to the pure sample, (ii) a broad band in the  $2100$  to  $2000\text{ cm}^{-1}$  range, attributed to the formation of an Fe + CO complex and (iii) a weak peak at  $2343\text{ cm}^{-1}$  due to the antisymmetric (C=O) stretching mode of  $\text{CO}_2$ .

During the deposition, iron can interact with more than one CO molecules to form a range of  $\text{Fe}(\text{CO})_x$  clusters. The C=O stretching positions will be different for all the various combinations of Fe and CO. Previous reports suggest that both thermally evaporated iron atoms, as well as laser-ablated iron atoms, form  $\text{Fe}(\text{CO})_x$  clusters upon reaction with CO in the gas phase.<sup>35,36</sup> The infrared peaks of these  $\text{Fe}(\text{CO})_x$  were already reported in the literature by depositing them in various matrices.<sup>37,38</sup>

Computationally, we calculated the optimized vibrational frequencies for CO,  $\text{CO}_2$ , and  $\text{Fe}(\text{CO})_x$  ( $x = 1-5$ ) complexes. The calculated IR frequencies of the CO and  $\text{Fe}(\text{CO})_x$  are compared with the experimental IR frequencies, as shown in Fig. S1 (ESI<sup>†</sup>). The experimental and calculated spectra are qualitatively similar. Our DFT calculations predicted that the C=O stretching frequency for  $\text{Fe}(\text{CO})_x$  complex shows a lower wave-number value (red-shift) with respect to free CO.

In order to characterise the Fe + CO mixture, temperature-dependent RAIRS measurement of the same was performed by slowly heating the substrate from 10 K to higher temperatures and measuring the RAIR spectrum at each temperature indicated, as shown in Fig. 2a. Enlarged regions from Fig. 2a corresponding to  $\text{CO}_2$  and  $\text{Fe}(\text{CO})_x$  regions are shown in the insets as Fig. 2b and c, respectively. The  $\text{CO}_2$  region is multiplied by a factor of 10 for better visibility. The intensity of the C=O stretching peak ( $2142\text{ cm}^{-1}$ ) goes down completely above 30 K, attributed to CO desorption, whereas the broad  $\text{Fe}(\text{CO})_x$  band stayed till 250 K but its intensity got reduced above 150 K.  $\text{Fe}(\text{CO})_x$  may undergo dissociative desorption upon heating, and it was completely dissociated at  $\sim 250\text{ K}$ . However, this happens very slowly with temperature. This implies that the  $\text{Fe}(\text{CO})_x$  cluster has higher desorption energy. Fig. 2b shows the characteristic peak of solid  $\text{CO}_2$  ( $2342\text{ cm}^{-1}$ ), which eventually gets desorbed above 80 K, in accordance with the desorption temperature of  $\text{CO}_2$  in UHV.<sup>39</sup>

Low energy  $\text{Cs}^+$  collision was also performed on the deposited Fe + CO mixture to check the species formed due to the reaction. These data are shown in Fig. 2d and e.  $\text{Cs}^+$  scattering is a versatile surface analytical technique and is very specific to the top few layers.<sup>40,41</sup> Low energy ( $\sim 40\text{ eV}$ )  $\text{Cs}^+$  upon collision on the surface undergoes reactive ion scattering where  $\text{Cs}^+$  picks up the surface molecules forming an adduct-ion species, which can be detected by a mass spectrometer. During 40 eV  $\text{Cs}^+$  collision (Fig. 2d),  $\text{Cs-CO}^+$  ( $m/z = 161$ ) was observed as the major peak next to  $\text{Cs}^+$  ( $m/z = 133$ ) and  $\text{Cs-CO}_2^+$  ( $m/z = 177$ ) as a minor peak, confirming the presence of  $\text{CO}_2$  molecules on the surface. Upon increasing the kinetic energy of  $\text{Cs}^+$  to 80 eV (Fig. 2e), various peaks related to

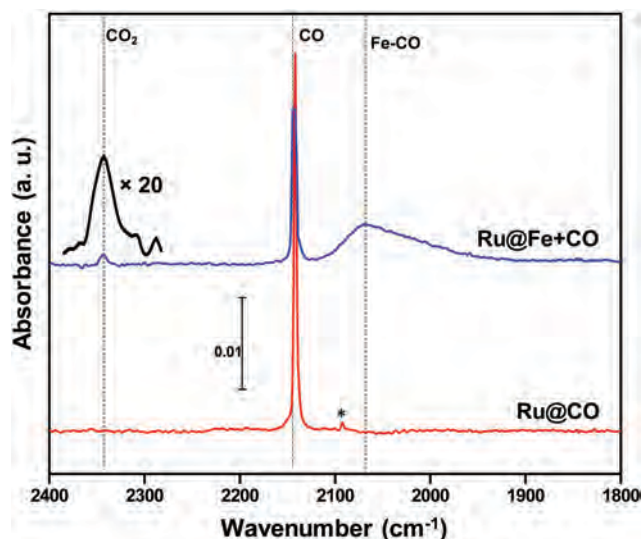


Fig. 1 RAIR spectrum collected upon deposition of CO on top of Ru(0001) substrate (Ru@CO) (bottom trace) and co-deposition of thermally evaporated iron with CO (Ru@Fe + CO) at 10 K (top trace). The  $\text{CO}_2$  peak obtained at  $2343\text{ cm}^{-1}$  is multiplied by a factor of 20. Peak labeled \* is due to the  $^{13}\text{CO}$ .



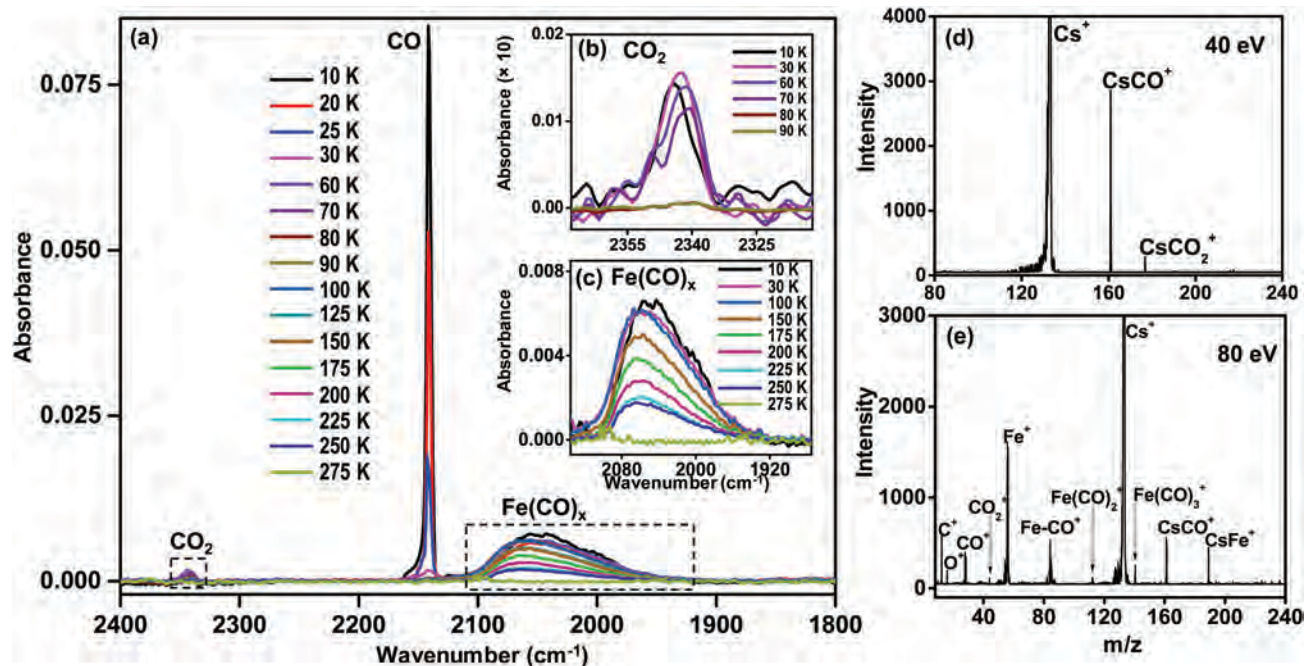


Fig. 2 (a) Temperature-dependent RAIR spectra of Fe + CO deposited mixture. The insets (b) and (c) are enlarged views of the CO<sub>2</sub> and Fe(CO)<sub>x</sub> regions, respectively. Figures (d) and (e) are the Cs<sup>+</sup> scattering spectra of Fe + CO deposited mixture at 40 eV and 80 eV ion kinetic energy, respectively. Various features are marked. The mixture was deposited, and the scattering spectra were collected at 10 K.

Fe(CO)<sub>x</sub> and Fe started to appear. The relatively higher energy of Cs<sup>+</sup> (~80 eV) makes it act mainly as a sputtering source and the deeper monolayers will be probed after knocking out the molecules from the top surface. At higher collision energies of Cs<sup>+</sup>, the product ions (Cs-CO<sub>2</sub><sup>+</sup>, in our case) can also dissociate, explaining the observations. These data suggest that Fe(CO)<sub>x</sub> consists of various combinations of CO bound with iron and the value of *x* can be from 1 to 5.

The Fe + CO deposited mixture was further characterised by temperature programmed desorption (TPD). The obtained TPD spectra of the Fe + CO mixture is shown in Fig. S2a (ESI†). In this experiment, the deposited Fe + CO mixture was heated from 10 K, at a heating rate of 30 K min<sup>-1</sup>. The intensity of the desorbed species of masses 28 (for CO) and 44 (for CO<sub>2</sub>) were plotted as a function of substrate temperature. TPD spectra of mass 28 (Fig. S2a, ESI†) shows the characteristic peak centered at ~30 K, due to the desorption of CO molecules having weak or no interaction with Fe atoms. The observed tail, which continued above 120 K, originated from the CO molecules interacting with the Fe atoms and also from the dissociation of Fe(CO)<sub>x</sub>. Such a dissociation of Fe(CO)<sub>5</sub> upon chemical vapor deposition is already reported at higher temperatures.<sup>42</sup> TPD of mass 44 gave a peak centered at 85 K, which is the characteristic desorption profile of CO<sub>2</sub>.<sup>39</sup> This is very low in intensity and is shown in the inset (Fig. S2b, ESI†). Fig. S2c (ESI†) is the instantaneous mass spectrum obtained at 85 K showing the intensity ratios of CO<sub>2</sub><sup>+</sup> and CO<sup>+</sup> along with C<sup>+</sup> and O<sup>+</sup>.

The gas-phase reactions of CO molecules with Fe atoms are highly feasible, leading to Fe(CO)<sub>x</sub>.<sup>35,37,38</sup> In order to observe whether the reaction is occurring in the gas phase or the

condensed phase and to get a better insight into the formation mechanism of CO<sub>2</sub>, different control experiments were carried out. The Fe + CO mixture was deposited at various temperatures (10 K, 20 K, 30 K, 40 K, 50 K and 60 K). These data are shown in Fig. 3a. Since the desorption temperature of CO is 30 K, the possibility of CO molecule to get deposited above 30 K in the Fe + CO mixture is negligible. The primary observation upon deposition of Fe + CO at various temperatures is that the formation of CO<sub>2</sub> solely depends on the residence of CO at the surface.

We have also calculated the column densities of CO and CO<sub>2</sub> formed at various temperatures from Fig. 3a and the results are plotted together in Fig. 3b. Major observations from the data can be summarized as, (i) the formation of CO<sub>2</sub> decreases substantially with increase in the deposition temperature and follows the column density pattern of CO. Maximum formation of CO<sub>2</sub> was observed when Fe and CO were co-deposited at 10 K. (ii) There is a drastic decrease of CO<sub>2</sub> peak intensity above 30 K, which is the temperature above which CO will not get condensed on the surface. This led us to suggest that an excess or unbound CO molecule is required for the iron assisted CO<sub>2</sub> formation. (iii) The formation of CO<sub>2</sub> stops completely at and above 50 K. This observation suggests that the reaction is occurring in the condensed phase only, and the possibility of the same in the gas phase can be ruled out. If the reaction is feasible in the gas phase, it must have formed at all the above temperatures and the formed CO<sub>2</sub> must have condensed till 80 K, since CO<sub>2</sub> is known to desorb only above 80 K. A small amount of CO<sub>2</sub> was observed at 40 K. It may be explained as follows: CO gets dissociated from Fe(CO)<sub>x</sub> and is also available

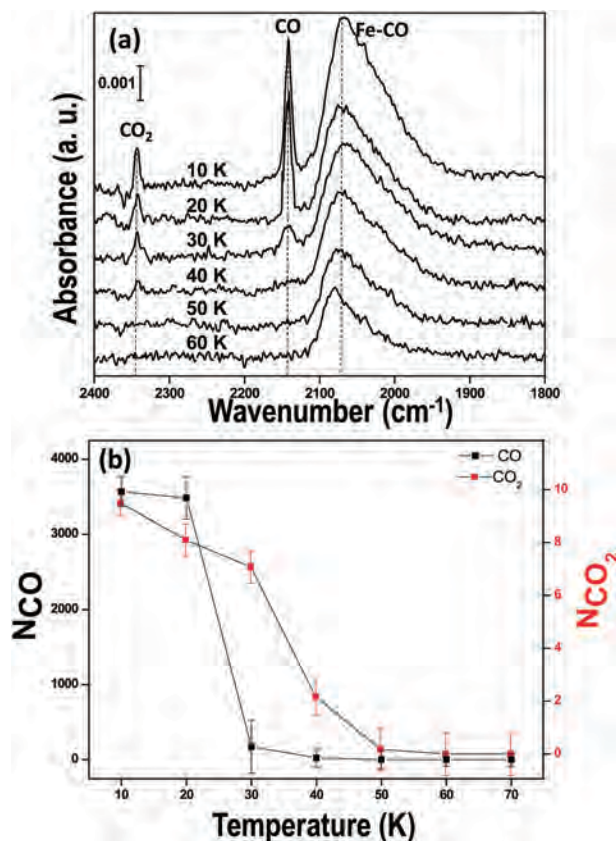


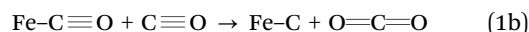
Fig. 3 (a) Iron and CO co-deposited at various temperatures (10–60 K). (b) The column density ratios of CO and CO<sub>2</sub> calculated from the data obtained from the experiments depositing Fe + CO at different temperatures.

from trapped CO, which gets desorbed at a higher temperature than its usual desorption temperature (30 K).<sup>43,44</sup> The trapped CO was observed as a tail in the TPD profile of the CO desorption curve in the Fe + CO mixture in Fig. S2a (ESI†). The intensity of the tail reduces with temperature. Similar trapping of CO (of very less amount) is possible when we deposit Fe + CO at 40 K and we strongly believe that this trapped CO is making the formation of CO<sub>2</sub> feasible at 40 K. The intensity of CO<sub>2</sub> formed at 40 K is much lower than that at 30 K (Fig. 3b). Another observation is that the ratio of CO to CO<sub>2</sub> intensity is also quite less for the 40 K deposition experiment (Fig. 3a). This may be due to an experimental limitation, which can be explained as follows: the formation of CO<sub>2</sub> from Fe + CO mixture is not time dependent. The desorption temperature of CO from different surfaces is higher than 30 K, and ranges up to 40 K.<sup>43–45</sup> We measured the RAIR spectrum after the deposition of Fe + CO mixture (at 40 K) and waiting for the pressure to settle down to the base pressure. The 512 scans used in the spectral collection took around 7 minutes. Throughout this time, the surface was equilibrated at 40 K, which made a significant amount of CO to desorb leading to reduced intensity of CO than CO<sub>2</sub> (at 40 K). Above 40 K, upon deposition of the Fe + CO mixture, the chance of CO getting trapped decreased substantially as it was far above its desorption temperature which restricted the

formation of CO<sub>2</sub> completely as unbound surface CO was required for CO<sub>2</sub> formation.

It may be concluded from the above data that an excess or unbound CO in the condensed phase is essential for the formation of CO<sub>2</sub>. The Fe–CO bond formation weakens the C–O bond resulting in partial dissociation of O. This partially dissociated O in Fe + CO can bind with a free CO molecule leading to CO<sub>2</sub> and the remaining part stays as iron carbide and the entire process occurs in the condensed phase.

The reaction can be explained by the following equations,



The overall reaction mechanism consists of two molecules of CO getting converted to one molecule of CO<sub>2</sub> in the presence of a Fe atom. We have plotted the gas-phase Gibbs free energy ( $\Delta G$ , kcal mol<sup>−1</sup>) and the mechanism with reaction coordinate in Fig. 4.

The reaction mechanism begins with the formation of FeCO, a complex that is 2.73 kcal mol<sup>−1</sup> stable than the reactants. The preferred pathway continues through the insertion of one more CO molecule to form Fe(CO)<sub>2</sub>. The intrinsic reaction coordinate (IRC) revealed that transition state (TS) is actually an O-transfer from one CO to other CO molecule, which occurs with a minimal activation barrier *via* TS (+4.65 kcal mol<sup>−1</sup>). Transition states were confirmed by vibrational frequency calculations yielding a single imaginary frequency along the reaction coordinate. Consequently, the breakage of the C–O bond occurs, which leads to FeC–CO<sub>2</sub>. The final step is the formation of free CO<sub>2</sub> and FeC. The data depicted in Fig. 3 could surely conclude that (i) the formation of CO<sub>2</sub> is highly dependent on the accessibility of free or unbound CO and (ii) the reaction happens in the condensed phase.

The current experiments could not resolve all the observations. For example, the deposition of Fe and CO mixture at 10 K and 20 K is observed to give almost the same intensity of CO (corresponds to the same amount of deposition) while the CO<sub>2</sub> formed at these two temperatures show a linear decrease.

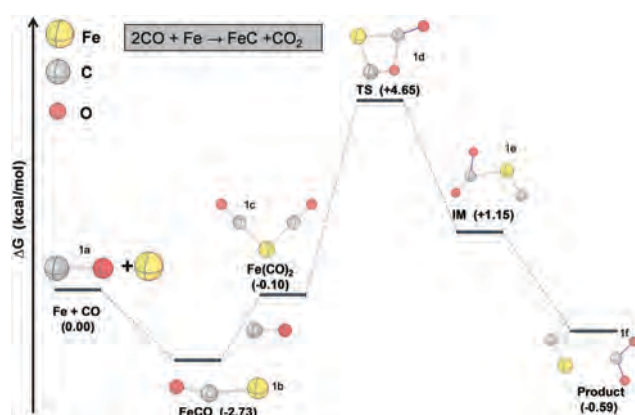


Fig. 4 Proposed reaction mechanism for the formation of CO<sub>2</sub> from CO with Fe atom. The relative energies are given in kcal mol<sup>−1</sup>.



The reason for this could not be explained. The computed mechanism (Fig. 4) serves well to explain our experimental observation, except the temperature dependence of the experiment, that more  $\text{CO}_2$  was observed at 10 K. This could be because the  $\Delta G$  values were computed for gas phase reactions and not considering condensed state of these species. We believe that this difference in the conditions of calculations and experiments is reflected in the discrepancy in the temperature dependence. However, the intermolecular interaction between CO and Fe will be similar in both gaseous and condensed phases. Literature reports<sup>46,47</sup> suggest that disproportionation reactions as depicted in the mechanism could occur at low temperatures.

### Role of substrate in the reaction

All these reactions described above were performed on a Ru(0001) substrate. In order to confirm that the substrate does not have any role in the present reactions, we covered the Ru(0001) substrate by depositing 500 MLs of argon. This was followed by co-deposition of Fe and CO mixture on top of argon. The result obtained was very similar (data are not shown), which makes us conclude that the reaction is substrate independent.

We also performed other sets of experiments by depositing iron on CO and also a reverse experiment; by depositing CO on iron sequentially, both at 10 K. The experiments were performed on Ru(0001) substrate as well as by covering it with 500 MLs of argon. The results were similar and the data

obtained upon deposition on argon covered Ru(0001) substrate are shown in Fig. 5a and b. Here, we observed the IR peak for  $\text{CO}_2$  (at 10 K) when iron was deposited on top of CO (Fig. 5a) while, a similar IR peak of  $\text{CO}_2$  was not observed in the reverse case where CO was deposited on top of iron (Fig. 5b). The observation from Fig. 5 would lead us to suggest that heat of adsorption of iron atoms on solid CO is facilitating this reaction. Neutral iron atoms upon condensation on solid CO would react to give Fe–CO complex and  $\text{CO}_2$ . The observation that  $\text{CO}_2$  was not formed above 40 K from the deposition of the species at various temperature experiment (Fig. 3) clearly confirms that this is a condensed phase reaction and more  $\text{CO}_2$  formed at temperatures lower than 30 K suggests the presence of free or unbound CO is necessary for this ( $\text{CO}_2$  formation) reaction to proceed. The above sequential deposition experiment of Fe atoms on solid CO could be more realistic or a better model for ISM but the product ( $\text{CO}_2$ ) formed was less as compared to co-deposition experiment. We attribute this to the better interaction of Fe and CO possible in a co-deposition method than the sequential deposition. In sequential deposition, iron atoms could interact only with the surface CO molecules while in co-deposition, the interactions are more as CO and Fe are getting mixed during the deposition, which leads to more amount of  $\text{CO}_2$  than the former. However, the observation of the formation of  $\text{CO}_2$  in both cases predicts that the reaction proceeds in a very similar way in both cases.

To give more realistic data pertaining to the interstellar medium, we performed a similar experiment by depositing

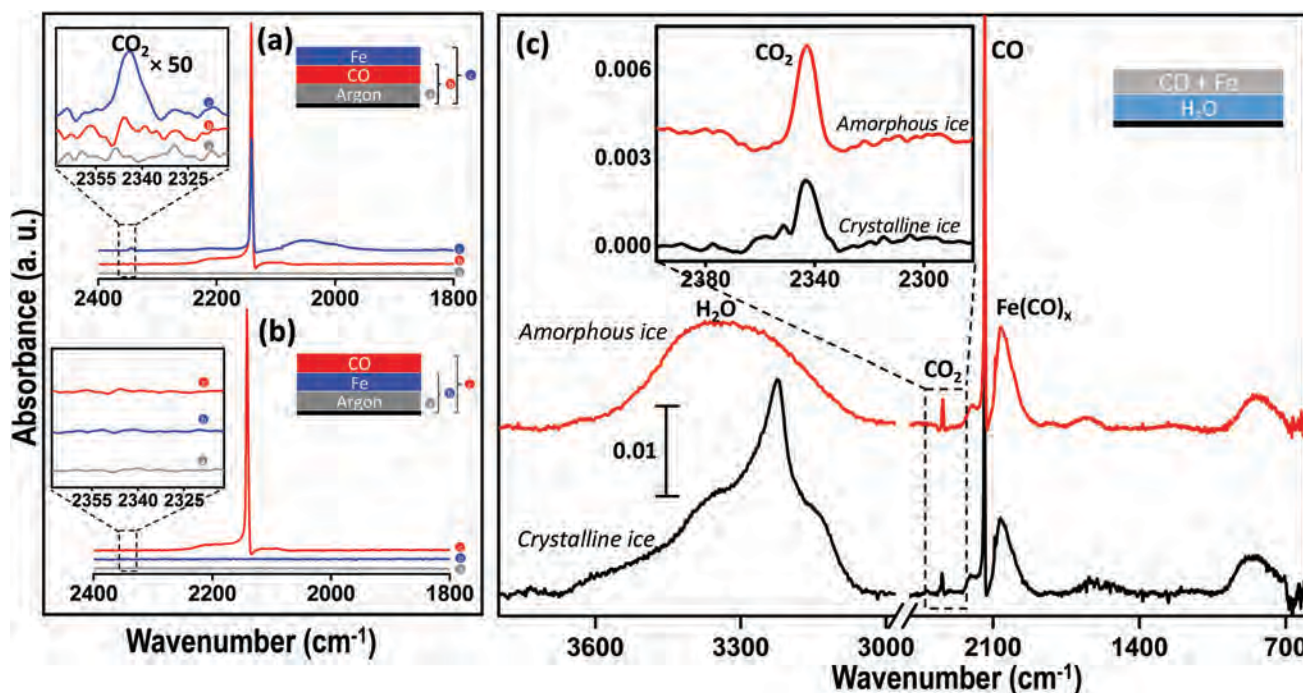


Fig. 5 (a) RAIR spectra collected upon deposition of thermally evaporated iron on top of CO at 10 K. (b) Similar RAIR spectral measurement from the deposition of CO on top of deposited iron. The substrate was initially covered by 500 MLs of argon in order to avoid the interaction and any probable influence of the Ru(0001) substrate. The inset shows the schematic of the sample and the order of deposition. The spectra have corresponding labels. The  $\text{CO}_2$  stretching region is enlarged and multiplied by a factor of 50 for better clarity. (c) RAIR spectra obtained from Fe + CO mixture co-deposited on amorphous and crystalline water at 10 K. The spectral regions of water,  $\text{CO}_2$ , CO, and  $\text{Fe}(\text{CO})_x$  are labeled. The  $\text{CO}_2$  antisymmetric stretching region is enlarged. The inset shows a schematic of the sequence of deposition of molecules under study.

Fe + CO mixture on top of water-ice, both amorphous and crystalline forms. Amorphous ice was formed by depositing water at 10 K followed by Fe + CO deposition as mentioned before. Crystalline ice was developed by depositing water vapor at 120 K and heating the sample ice to 145 K. The crystalline ice sample was subsequently cooled to 10 K and Fe + CO was co-deposited on top. These data are shown in Fig. 5c. We could not find any additional peak due to water molecules interacting with CO or Fe atoms. However, the formation of CO<sub>2</sub> due to the interaction of Fe + CO occurs on the water surface at 10 K. Data from amorphous and crystalline ices also suggest this. The intensity of CO<sub>2</sub> formed is higher on amorphous ice than on the crystalline ice, although this result needs further investigation. Altogether, this proves that the Fe can react with condensed CO leading to CO<sub>2</sub> and this reaction could proceed on the water surface.

## Conclusions

We performed co-deposition of CO and iron atoms on a substrate, pre-cooled to 10 K. Such a deposition gave peaks corresponding to pure CO at 2142 cm<sup>-1</sup>, and a broad band in ~2000 cm<sup>-1</sup> range due to CO bonded with Fe [Fe(CO)<sub>x</sub>] in the infrared spectrum. More importantly, a new peak due to CO<sub>2</sub> (2343 cm<sup>-1</sup>) was observed due to the reaction. The Fe + CO solid mixture was further characterised by temperature-dependent RAIRS, low energy Cs<sup>+</sup> scattering, and TPD, revealing that Fe(CO)<sub>x</sub> is one in which  $x = 1$  to 5. Infrared frequencies were calculated by optimizing different structures and was found to be matching with the experimentally obtained values. This Fe(CO)<sub>x</sub> dissociates to give Fe and CO, which disappears completely above 250 K.

The formation of CO<sub>2</sub> is an instantaneous process upon the deposition of iron atoms on CO (or during co-deposition) and was found to proceed only in the presence of unbound CO, as proven by different control experiments. Based on these experiments, we propose that iron assisted formation of CO<sub>2</sub> is another pathway that can occur in interstellar ices containing condensed CO. The importance of this reaction is that it is a direct oxidation of CO to CO<sub>2</sub> at cryogenic temperatures, made possible by a reactive metal species like iron being condensed on the molecular surface. It does not require any form of photo-irradiation or thermal processing and occurs at lower temperatures (such as 10 K). Such a reaction is a highly favorable one in cold dense molecular clouds where the presence of CO and Fe are detected in abundance. The reaction occurs also on the surface of water ice and CO<sub>2</sub> was detected in more abundance on amorphous ice. Mechanistic details of the CO<sub>2</sub> formation reaction were supported by computational studies.

## Conflicts of interest

There are no conflicts to declare.

## Acknowledgements

T. P. acknowledges the Science and Engineering Research Board (SERB), Department of Science and Technology (DST),

Government of India for research funding. J. G. thanks the University Grants Commission (UGC) for his research fellowship.

## References

- 1 D. K. Bohme, *Chem. Rev.*, 1992, **92**, 1487–1508.
- 2 M. Fioroni, *Phys. Chem. Chem. Phys.*, 2014, **16**, 24312–24322.
- 3 M. Fioroni, *Comput. Theor. Chem.*, 2016, **1084**, 196–212.
- 4 M. J. Adrienne, S. S. Norbert, C. Deepto and W. G. Thomas, *Astrophys. J.*, 2006, **648**, 1066.
- 5 C. M. Walmsley, R. Bachiller, G. Pineau des Forets and P. Schilke, *Astrophys. J.*, 2002, **566**, L109–L112.
- 6 A. P. Jones, *Mon. Not. R. Astron. Soc.*, 1990, **245**, 331–334.
- 7 P. Ventura, M. Di Criscienzo, R. Schneider, R. Carini, R. Valiante, F. D'Antona, S. Gallerani, R. Maiolino and A. Tornambe, *Mon. Not. R. Astron. Soc.*, 2012, **420**, 1442–1456.
- 8 D. E. Jiang and E. A. Carter, *Surf. Sci.*, 2004, **570**, 167–177.
- 9 T. Wang, X.-X. Tian, Y.-W. Li, J. Wang, M. Beller and H. Jiao, *ACS Catal.*, 2014, **4**, 1991–2005.
- 10 Y.-H. Chen, D.-B. Cao, J. Yang, Y.-W. Li, J. Wang and H. Jiao, *Chem. Phys. Lett.*, 2004, **400**, 35–41.
- 11 S. K. Nayak, M. Nooijen, S. L. Bernasek and P. Blaha, *J. Phys. Chem. B*, 2001, **105**, 164–172.
- 12 L. B. D'Hendecourt and M. Jourdain de Muizon, *Astron. Astrophys.*, 1989, **223**, L5–L8.
- 13 A. G. G. M. Tielens, A. T. Tokunaga, T. R. Geballe and F. Baas, *Astrophys. J.*, 1991, **381**, 181–199.
- 14 E. F. Van Dishoeck, F. P. Helmich, T. De Graauw, J. H. Black, A. C. A. Boogert, P. Ehrenfreund, P. A. Gerakines, J. H. Lacy and T. J. Millar, *et al.*, *Astron. Astrophys.*, 1996, **315**, L349–L352.
- 15 C. J. Bennett, C. S. Jamieson and R. I. Kaiser, *Phys. Chem. Chem. Phys.*, 2010, **12**, 4032–4050.
- 16 S. Ioppolo, M. E. Palumbo, G. A. Baratta and V. Mennella, *Astron. Astrophys.*, 2009, **493**, 1017–1028.
- 17 H. Linnartz, S. Ioppolo and G. Fedoseev, *Int. Rev. Phys. Chem.*, 2015, **34**, 205–237.
- 18 M. J. Loeffler, G. A. Baratta, M. E. Palumbo, G. Strazzulla and R. A. Baragiola, *Astron. Astrophys.*, 2005, **435**, 587–594.
- 19 M. Minissale, E. Congiu, G. Manicò, V. Pirronello and F. Dulieu, *Astron. Astrophys.*, 2013, **559**, A49.
- 20 M. Minissale, J.-C. Loison, S. Baouche, H. Chaabouni, E. Congiu and F. Dulieu, *Astron. Astrophys.*, 2015, **577**, A2.
- 21 J. A. Noble, F. Dulieu, E. Congiu and H. J. Fraser, *Astrophys. J.*, 2011, **735**, 121.
- 22 P. M. Solomon and W. Klemperer, *Astrophys. J.*, 1972, **178**, 389–421.
- 23 A. Stibor, G. Kresse, A. Eichler and J. Hafner, *Surf. Sci.*, 2002, **507–510**, 99–102.
- 24 Z.-H. Lu and Q. Xu, *J. Chem. Phys.*, 2011, **134**, 034305.
- 25 W. Xue, Z.-C. Wang, S.-G. He, Y. Xie and E. R. Bernstein, *J. Am. Chem. Soc.*, 2008, **130**, 15879–15888.
- 26 S. Liu, Y.-W. Li, J. Wang and H. Jiao, *J. Phys. Chem. C*, 2015, **119**, 28377–28388.

- 27 S. Bag, R. G. Bhuin, R. R. J. Methikkalam, T. Pradeep, L. Kephart, J. Walker, K. Kuchta, D. Martin and J. Wei, *Rev. Sci. Instrum.*, 2014, **85**, 014103.
- 28 J. Ghosh, R. G. Bhuin, G. Ragupathy and T. Pradeep, *J. Phys. Chem. C*, 2019, **123**, 16300–16307.
- 29 J. Ghosh, A. K. Hariharan, R. G. Bhuin, R. R. J. Methikkalam and T. Pradeep, *Phys. Chem. Chem. Phys.*, 2018, **20**, 1838–1847.
- 30 J. Ghosh, R. R. J. Methikkalam, R. G. Bhuin, G. Ragupathy, N. Choudhary, R. Kumar and T. Pradeep, *Proc. Natl. Acad. Sci. U. S. A.*, 2019, **116**, 1526–1531.
- 31 J. Ghosh, R. G. Bhuin, G. Vishwakarma and T. Pradeep, *J. Phys. Chem. Lett.*, 2020, **11**, 26–32.
- 32 E. G. Mednikov, S. A. Ivanov and L. F. Dahl, *Inorg. Chem.*, 2011, **50**, 11795–11806.
- 33 M. J. Frisch, G. W. Trucks, H. B. Schlegel, G. E. Scuseria, M. A. Robb, J. R. Cheeseman, G. Scalmani, V. Barone, G. A. Petersson, H. Nakatsuji, X. Li, M. Caricato, A. V. Marenich, J. Bloino, B. G. Janesko, R. Gomperts, B. Mennucci, H. P. Hratchian, J. V. Ortiz, A. F. Izmaylov, J. L. Sonnenberg, D. Williams-Young, F. Ding, F. Lipparini, F. Egidi, J. Goings, B. Peng, A. Petrone, T. Henderson, D. Ranasinghe, V. G. Zakrzewski, J. Gao, N. Rega, G. Zheng, W. Liang, M. Hada, M. Ehara, K. Toyota, R. Fukuda, J. Hasegawa, M. Ishida, T. Nakajima, Y. Honda, O. Kitao, H. Nakai, T. Vreven, K. Throssell, J. A. Montgomery, Jr., J. E. Peralta, F. Ogliaro, M. J. Bearpark, J. J. Heyd, E. N. Brothers, K. N. Kudin, V. N. Staroverov, T. A. Keith, R. Kobayashi, J. Normand, K. Raghavachari, A. P. Rendell, J. C. Burant, S. S. Iyengar, J. Tomasi, M. Cossi, J. M. Millam, M. Klene, C. Adamo, R. Cammi, J. W. Ochterski, R. L. Martin, K. Morokuma, O. Farkas, J. B. Foresman and D. J. Fox, *Gaussian 09 Rev. A.1*, Wallingford, CT, 2009.
- 34 Y. Yang, M. N. Weaver and K. M. Merz, *J. Phys. Chem. A*, 2009, **113**, 9843–9851.
- 35 C. H. F. Peden, S. F. Parker, P. H. Barrett and R. G. Pearson, *J. Phys. Chem.*, 1983, **87**, 2329–2336.
- 36 M. Zhou, L. Andrews and C. W. Bauschlicher, *Chem. Rev.*, 2001, **101**, 1931–1962.
- 37 M. Zhou and L. Andrews, *J. Chem. Phys.*, 1999, **110**, 10370–10379.
- 38 M. Zhou, G. V. Chertihin and L. Andrews, *J. Chem. Phys.*, 1998, **109**, 10893–10904.
- 39 R. M. Escribano, G. M. Muñoz Caro, G. A. Cruz-Díaz, Y. Rodríguez-Lazcano and B. Maté, *Proc. Natl. Acad. Sci. U. S. A.*, 2013, **110**, 12899–12904.
- 40 H. Kang, *Acc. Chem. Res.*, 2005, **38**, 893–900.
- 41 H. Kang, *Bull. Korean Chem. Soc.*, 2011, **32**, 389–398.
- 42 F. Zaera, *Langmuir*, 1991, **7**, 1188–1191.
- 43 S. Cazaux, R. Martín-Doménech, Y. J. Chen, G. M. M. Caro and C. G. Díaz, *Astrophys. J.*, 2017, **849**, 80.
- 44 J. A. Noble, E. Congiu, F. Dulieu and H. J. Fraser, *Mon. Not. R. Astron. Soc.*, 2012, **421**, 768–779.
- 45 S. E. Bisschop, H. J. Fraser, K. I. Öberg, E. F. van Dishoeck and S. Schlemmer, *Astron. Astrophys.*, 2006, **449**, 1297–1309.
- 46 H. J. Lee and W. Ho, *Science*, 1999, **286**, 1719–1722.
- 47 J. R. Hahn and W. Ho, *Phys. Rev. Lett.*, 2001, **87**, 166102.

# Iron Assisted Formation of CO<sub>2</sub> over Condensed CO and Its Relevance to Interstellar Chemistry

Rabin Rajan J. Methikkalam, Jyotirmoy Ghosh, Radha Gobinda Bhuin, Soumabha Bag, Gopi Ragupathy and Thalappil Pradeep\*

DST Unit of Nanoscience (DST UNS) and Thematic Unit of Excellence (TUE), Department of Chemistry, Indian Institute of Technology Madras, Chennai 600 036, India

\*Corresponding author: Fax: + 91-44 2257-0545

\*E-mail: [pradeep@iitm.ac.in](mailto:pradeep@iitm.ac.in)

## Supporting Information

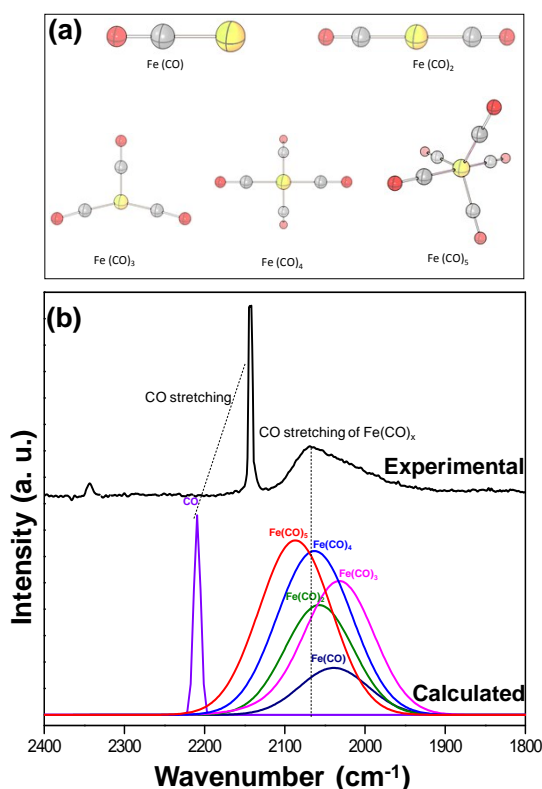


**Fig S1.** (a) Optimized geometry of Fe(CO)<sub>x</sub> (x=1-5) at the B3LYP/LANL2DZ: (Fe)/6-31G\* (C and O) level. Colour code: C: grey; O: red; Fe: yellow (b) Calculated vibration frequencies for CO and Fe(CO)<sub>x</sub> (x=1-5) complexes compared with the experimental spectrum.



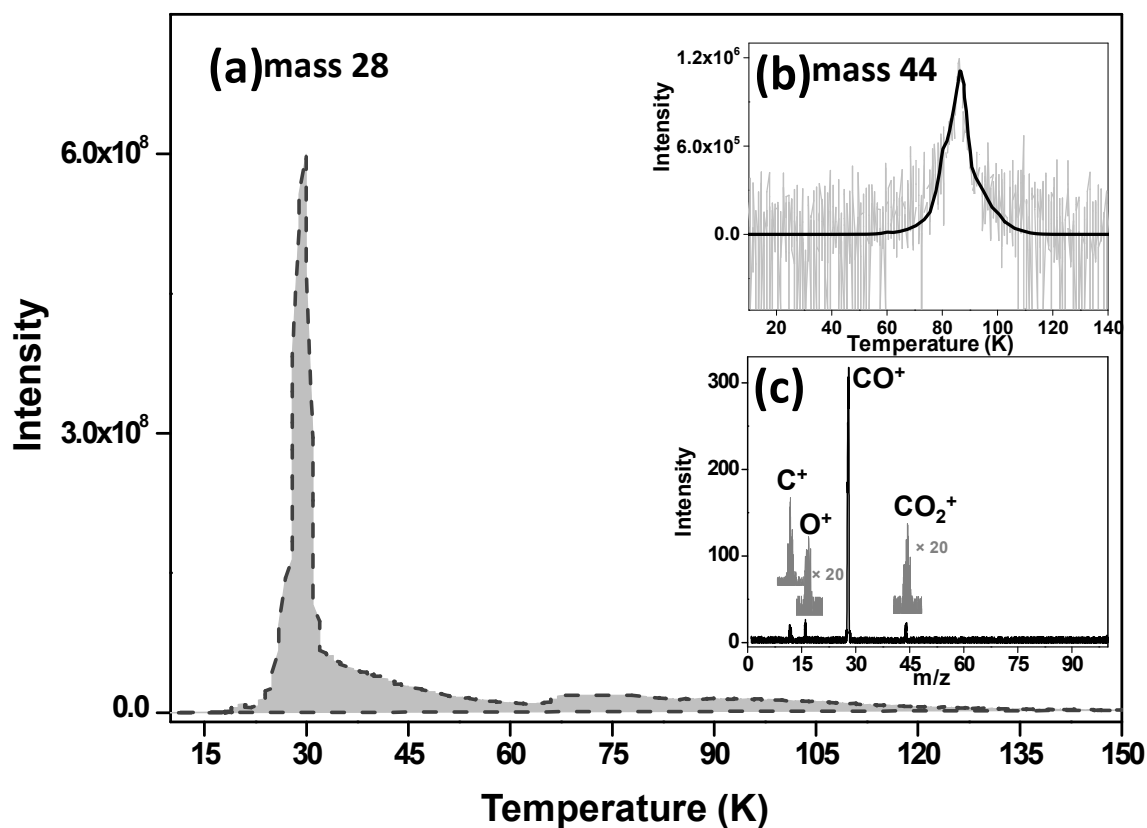


**Fig S2.** (a) Temperature programmed desorption profile of Fe + CO deposited at 10 K at a heating rate of 30 K/min for mass 28 (for CO). (b) The TPD of mass 44 (for CO<sub>2</sub>) and (c) the mass spectrum obtained at 85 K from the TPD profile showing the CO and CO<sub>2</sub> concentration ratio (inset, the peaks are enlarged by multiplying by a factor of 20). CO in spectrum (c) is due to the dissociation of Fe(CO)<sub>x</sub>.

## Arsenic Toxicity: Carbonate's Counteraction Revealed

Swathy Jakka Ravindran, Shantha Kumar Jenifer, Jayashree Balasubramanyam, Sourav Kanti Jana, Subramanian Krishnakumar, Sailaja Elchuri, Ligy Philip, and Thalappil Pradeep\*

Cite This: *ACS Sustainable Chem. Eng.* 2020, 8, 5067–5075

Read Online

ACCESS |



Metrics &amp; More



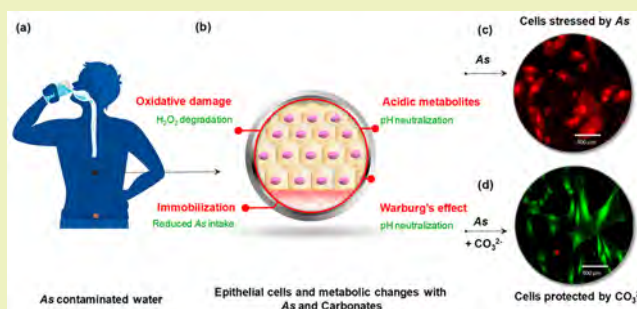
Article Recommendations



Supporting Information

**ABSTRACT:** Well-known purification technologies built for arsenic (As) removal from drinking water are not sustainable, either being unaffordable or inefficient in the elimination of traces of As. In our experiments, we observed that carbonate ion can counteract the effects of As exposure as it efficiently prevented As-induced cytotoxicity on epithelial cell lines of the small intestine (IEC-6). The cotreatment of IEC-6 cells with 40 ppm of carbonates and As ( $\geq 3$  ppm) showed substantial remissions in the As-induced cytotoxicity and increased the viability from 50% to 75%. The production of intracellular reactive oxygen species (ROS) and cellular acidification were also reduced in this process (pH increase from 5 to 6.5). Thus, the present study suggests that the cytoprotective effect of carbonate can involve multiple pathways, such as reduction of extracellular/intracellular acidosis,  $\text{H}_2\text{O}_2$  decomposition, balancing mitochondrial potential, and immobilization of As. We show that As-contaminated drinking water enriched with carbonates up to 40 ppm has a reduced toxic effect on cells in comparison to that of an As-alone sample. Therefore, carbonates can act as an adjunct in addition to the prevailing approaches to tackle mass poisoning by As. We believe that this study is initial evidence for developing an alternative method to tackle the prevailing mass environmental poisoning by As, using locally available, affordable, safe, and sustainable solutions.

**KEYWORDS:** Arsenic toxicity, Cytoprotection, Carbonates in water, Counteraction, Toxicity mitigation



## INTRODUCTION

While arsenic (As) ranks first in the priority list of hazardous substances,<sup>1,2</sup> over 150 million people in 70 countries are estimated to be exposed to unsafe levels of As in drinking water globally.<sup>3,4</sup> In India, it is estimated that about 70.4 million people in 20 states are at risk due to the presence of excess amounts of As in groundwater.<sup>5</sup> With these startling numbers, As poisoning is regarded as the “worst mass poisoning in history”. Thus, intense efforts are taken to reduce As exposure to humans. Most of the water purification plants designed for As removal are failing to reduce below the maximum safe level (10  $\mu\text{g/L}$ ) insisted by the World Health Organization (WHO).<sup>6–8</sup> The cost and energy associated with membrane processing, ion exchange, and adsorption techniques are high while they deliver poor performance and introduce toxic substances, creating secondary pollution.<sup>9–11</sup> Chemical reagents such as chlorine and ozone are used in the oxidation of  $\text{As}^{3+}$  to  $\text{As}^{5+}$ , a widely used As removal technique.<sup>11</sup> Nanomaterials are increasingly researched upon<sup>12</sup> and applied in the field<sup>13</sup> to solve As contamination.<sup>14</sup> Interventional research to alleviate As toxicity is in its early stages and is of unknown effectiveness.<sup>15</sup> In the following, we present the problem of As poisoning and essential background necessary to appreciate this work.

**Arsenic: Toxicity, Oxidative Stress, and Human Disease.** Arsenic in water provides the majority of its daily dose through inorganic As species ( $\text{As}^{3+}$  and  $\text{As}^{5+}$ ) that enter orally. Among the two forms,  $\text{As}^{3+}$  and  $\text{As}^{5+}$ , As exists primarily as  $\text{As}^{5+}$  in water under aerobic conditions.<sup>16</sup> Thus, the effect of carbonate on  $\text{As}^{5+}$  in water was studied in this work. It has been observed that when some of the vital human metabolic pathways are stressed by As, progressive cellular dysfunction results in apoptosis and diverse health effects such as cancer and cardiovascular diseases are manifested.<sup>17–21</sup> It inhibits glucose uptake by cells, oxidation of fatty acids, gluconeogenesis, and further production of acetyl CoA. Experimental evidence shows that the acute toxicity of As is due to the development of a superoxide anion radical ( $\text{O}_2^{\bullet-}$ ), singlet oxygen ( $^1\text{O}_2$ ), peroxide radical ( $\text{ROO}^\bullet$ ), hydroxyl radical ( $^\bullet\text{OH}$ ), dimethylarsenic radical [ $(\text{CH}_3)_2\text{As}^\bullet$ ], oxidant-induced DNA damage, and hydrogen peroxide ( $\text{H}_2\text{O}_2$ ).<sup>22</sup> Arsenic

Received: November 16, 2019

Revised: March 12, 2020

Published: March 17, 2020

exposure leads to an increase in levels of reactive oxygen species (ROS) and reactive nitrogen species produced, which can surpass the antioxidant capacity of the living cells.<sup>23,24</sup> Additionally, the morphology and the integrity of mitochondria are disturbed by As and a rapid decline in the mitochondrial membrane potential occurs. Acidification of growth media that contained cultured cell lines exposed to As at levels below the lethal concentrations has been observed in this work. A possible reason for this increased extracellular acidification is lactate production, generated as a result of the Warburg effect (aerobic glycolysis).<sup>23,25</sup>

**Carbonate's Association with As and its Toxicity.** A broad range of associations have been encountered in the literature between carbonate and various As species.<sup>26</sup> Arsenic discharges from the aquifer rocks into groundwater are strongly related to the concentration of bicarbonate in the leaching solution.<sup>7,27</sup> This release is mainly because of the formation of arseno-carbonate complexes, which are stable in groundwater.<sup>26</sup> In the case of the worm *Caenorhabditis elegans*, the gene *abts-1*, which encodes a sodium ( $\text{Na}^+$ )-dependent  $\text{Cl}^-/\text{HCO}_3^-$  transporter (a bicarbonate transporter), has been reported to protect it from As toxicity. Stronger expression of the *abts-1* gene was observed in the cells of *C. elegans* after exposure to As, and the cells of the worms lacking *abts-1* were found to be hypersensitive to As.<sup>28</sup> In the experiments performed by Ruby et al., the dissolution of As in a stomach environment was found to be strongly pH dependent and the extent of dissolution was observed to decrease by 16% when there was a minimal increase in pH.<sup>29</sup> Arsenic-affected cells produce acidic metabolites and undergo the Warburg effect, an effect also seen in cancer cells.<sup>30</sup> In the case of cancer cells, this acidification is generally treated with systemic buffers and carbonates that can significantly inhibit the development of metastases.<sup>30,31</sup> In the As-affected cells, ROS are the major reason for the intensification of As toxicity, and prior research implies that the carbonate (or bicarbonate) anion has a role in promoting peroxide decomposition, found to be nine times faster than sodium hydroxide.<sup>32</sup> Intracellular pH is a crucial factor that regulates cellular behavior. In the presence of oxygen, pyruvate is imported into mitochondria for the Krebs (or tricarboxylic acid) cycle and oxidative phosphorylation in the cells.<sup>33</sup> Under anaerobic conditions, glucose is converted into pyruvate followed by its transformation into lactate to cope with the low oxygen availability. For unascertained reasons, even during stressed conditions, like As exposure or cancer, cells perform glycolysis, irrespective of oxygen availability. This is termed as the Warburg effect, and it involves the increased uptake of glucose and higher lactate production, shifting the pH of the microenvironment toward an acidic range.<sup>25</sup> At such stressed conditions, aerobic glycolysis is inefficient in generating adenosine 5'-triphosphate (ATP) and its advantage to the cells is unclear.<sup>25</sup>

**Sustainable Counteraction for As Toxicity.** From the discussion above, it is clear that the carbonate anion can counteract the potential risk of As toxicity, following any or all of the possible routes. Here, we have investigated the hypothesis that the increased systemic concentrations of carbonate species can reduce various cellular dysfunctions, namely, extracellular/intracellular acidosis,  $\text{H}_2\text{O}_2$  decomposition, balancing mitochondrial potential, and immobilization of As into the cell. Since the majority of As present in water is absorbed in the gastrointestinal tract (ingestion) and causes a

cascade of cellular dysfunctions, our study was performed using epithelial cell lines of the small intestine (IEC-6).

Even though  $\text{H}_2\text{O}_2$  is not a free radical, it is next to superoxide anion and hydroxyl radical in its toxic effects, which is a key member in the class of ROS. Earlier reports state that increased cellular concentrations of free iron (during overload of iron in the organism) imposes deleterious effects where Fe(II) participates during the decomposition of  $\text{H}_2\text{O}_2$ , known as a Fenton reaction, which generates reactive hydroxyl radicals.<sup>34</sup> Through CV experiments, it was observed that carbonates can reduce the  $\text{H}_2\text{O}_2$  produced by As-exposed cells by 95%.

Following an initial observation of rapid acidification in the culture media that contained As-exposed cells, we show that the buffering capacity of carbonates can regulate the impact of cellular acidification caused by As. The current study shows that the administration of safe levels of carbonate in the form of sodium carbonate or calcium carbonate can counteract the toxicity levels of As. As bolus ingestion of bicarbonates can also lead to metabolic disturbances, we propose that a divided dose of carbonate-balanced water containing sodium carbonate and/or calcium carbonate throughout the day is the best way to compensate the impact of As on human body.

As the chemistry of ions present in the groundwater is complex<sup>35–37</sup> and As-related cellular changes are diverse, this paper stands as a piece of salient preliminary evidence to tackle the mass poisoning due to As, using abundantly available carbonates. The addition of carbonates does not involve complex chemicals or need energy, as may be necessary for the currently practiced arsenic removal techniques, and thus it can contribute to developing a sustainable and effective method for As remediation.

## MATERIALS AND METHODS

**Cell Culture.** Rat small intestinal cells (IEC-6) obtained from National Centre for Cell Science (NCCS, Pune, India) were maintained in Dulbecco's modified Eagles medium (DMEM) supplemented with 10% fetal bovine serum and secured with antibiotics, namely, penicillin and streptomycin (100 IU/100  $\mu\text{g}$ ). IEC-6 intestinal cells were grown in T-75 culture flasks and were maintained at 37 °C at a 5%  $\text{CO}_2$  atmosphere. Upon reaching confluency, the growth medium from the T-75 culture flask was removed and the cells were gently rinsed with 2 mL of phosphate buffered saline (PBS), and then 5 mL of trypsin-EDTA (ethylenediaminetetraacetic acid) solution was added and kept at room temperature (in a laminar hood) for 40 s. Then, the trypsin-EDTA solution was removed and the flask was kept at 37 °C in a  $\text{CO}_2$  incubator for 3 min, and the cells were detached completely from the surface by tapping gently over the flask. The cells were then suspended in a fresh growth medium and then transferred to sterile T-75 flasks. The total volume was made up to 5 mL using the growth medium.

**Cell Viability Assay.** The viability of the cells was assessed by a MTT [3-(4, 5-dimethylthiazol-2-yl)-2,5-diphenyltetrazolium bromide tetrazolium] assay.<sup>38</sup> About  $5 \times 10^3$  cells were plated in 96-well plates with DMEM containing 10% FBS (fetal bovine serum). The cells were incubated for 24 h under 5%  $\text{CO}_2$  and 95%  $\text{O}_2$  at 37 °C. Then the DMEM with FBS was removed and replaced with a serum-free medium. Arsenic and carbonate were given to cells through the DMEM media, and the system was incubated for 24 h. After treatment, the medium was removed and replaced with 500  $\mu\text{L}$  of 0.5% MTT containing DMEM and then incubated at 37 °C for 4 h. After incubation, the MTT containing medium was removed from the plate and 500  $\mu\text{L}$  of dimethyl sulfoxide was added and mixed well, and after 2 h, the color that developed was read at 570 nm in a microplate spectrophotometer (SpectraMax M5Microplate Reader). The un-

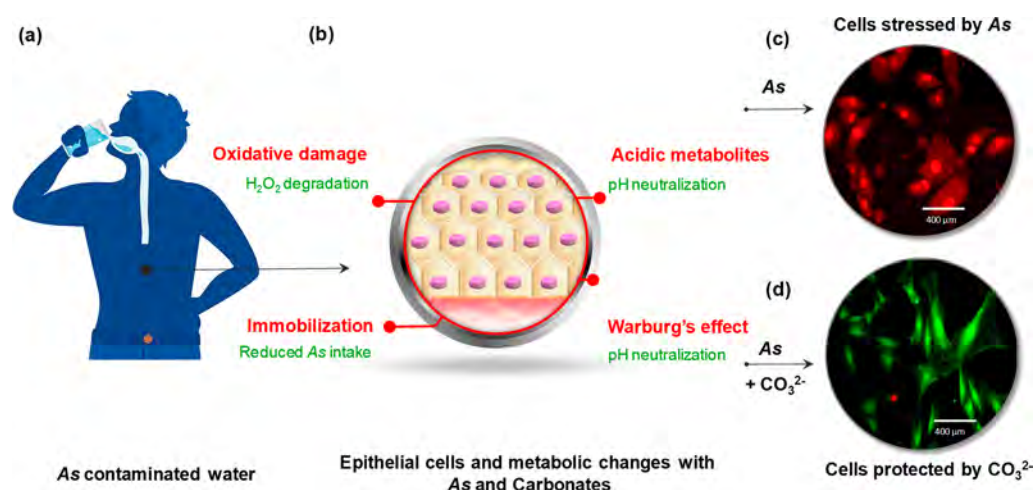


**Figure 1.** Schematic representation of As-induced toxic metabolism and carbonate's cytoprotective action to encounter them.

treated control cells were used for the normalization of absorbance to calculate the changes in cell viability. The cell viability was calculated as the percentage of viable cells and then plotted against time in hours. The total As concentration of the cells was estimated using inductively coupled plasma mass spectrometry (ICP-MS) (PerkinElmer Nex ION 300 ICP-MS).

**Cellular Morphology.** The morphological changes in the cells due to As exposure and the cytoprotective action of  $As^{5+}$  and carbonate were studied under a phase-contrast microscope (EVOS FL auto cell imaging system).

**Live/Dead Staining.** A LIVE/DEAD viability/cytotoxicity kit designed for mammalian cells (Molecular Probes, Invitrogen) was used for differentiating live cells from dead cells. The treated adherent cells, cultured on 24-well plates as confluent monolayers, were washed with 500–1000 volumes of Dulbecco's phosphate-buffered saline (D-PBS) prior to the assay to remove serum, growth media, and other ions added during the studies. About 20  $\mu L$ /10 mL of ethidium homodimer-1 stock solution and 5  $\mu L$ /10 mL of calcein were mixed thoroughly, and the mixture was added directly to cells. Imaging was performed at an excitation/emission wavelength of 494/517 nm for calcein and at 528/617 nm for ethidium homodimer-1 using an EVOS FL auto cell imaging system.

**Determination of ROS.** 2',7'-dichlorodihydrofluorescein diacetate ( $H_2DCFDA$ ) (Molecular Probes, Eugene, OR) is a non-fluorescent dye that is oxidized by intracellular ROS to form highly fluorescent 2',7'-dichlorofluorescein. The cells, after treatment with different concentrations of ions, were washed once with DMEM, stained with 20  $\mu M$   $H_2DCFDA$ , and incubated at 37  $^{\circ}C$  for 30 min. The dye was then removed, and the cells were washed with DMEM. Fluorescence images were taken at 485 nm excitation and 535 nm emission using the EVOS FL auto cell imaging system.

**Cyclic Voltammetry.** Cyclic voltammetry (CV) experiments were performed using an electrochemical analyzer (CHI 600A) to study the  $H_2O_2$  decomposition caused by  $CaCO_3$  and  $Na_2CO_3$ . For CV experiments, a precleaned gold (Au) electrode was chosen as a working electrode, Ag/AgCl was chosen as the reference electrode, and Pt was fixed as the counter electrode. Arsenic-treated cells were separated from the growth media, suspended, and lysed in PBS (pH  $\sim$  7).  $H_2O_2$  produced by the As-treated cells lysed in PBS was exposed to various concentrations of  $CaCO_3$  during voltammetry measurements. This sample was used for  $H_2O_2$  measurement. CV measurements for every sample were performed in a potential window between 0 to +1.2 V with a fixed scan rate of 100 mV  $s^{-1}$  at room temperature. For reference values, CV profiles of Au were performed in a blank solution (only PBS).

**Cellular pH Profiling.** A stock of a pH indicator solution containing 100 mM bromothymol blue (BTB) was prepared in water with 10 mL of 4% sodium hydroxide and 20 mL of absolute alcohol. For the pH profiling of cells through staining, the cell culture medium

was first aspirated and then the washing procedure was completed three times using PBS. Following this step, the cells were treated with the pH indicator solution (1 mg/mL) and removed after 10 min of incubation. Finally, the redundant pH indicator stain sticking to the extracellular lines of the cells were washed using 20% aqueous ethanol solution for three times. Treated cells were observed under the bright field EVOS FL auto cell imaging system.

## RESULTS AND DISCUSSION

The cause and development of As toxicity are complex and have not been fully understood. A cascade of cellular dysfunction occurs in which oxidative stress plays a vital role. The oxidative damage further leads to loss of mitochondrial membrane potential, which complicates the toxicity, leading to cell death. Figure 1 is a schematic representation of As-induced toxic metabolism resulting from the exposure to As contaminated water (Figure 1a) and carbonate's cytoprotective action to counter it. In the present study, a model of rat intestinal cells, IEC-6 in confluent culture, was used. Important analytical studies, namely, cell viability, morphological changes, cell death, ROS generation,  $H_2O_2$  decomposition, As uptake, and cellular pH neutralization, were performed to understand the role of the carbonate ion. Figure 1b shows vital cellular dysfunction as a result of As intake and the carbonate's activity to encounter each of them. Part c and d of Figure 1 represent the cells stressed by As toxicity and the carbonates' cytoprotective action against it.

**Qualitative Assessment of Carbonate's Cytoprotective Action.** It has been reported that As intake leads to a decrease in the efficacy of cellular defense mechanisms (reduced glutathione), and it increases the formation of superoxide derived free radicals. This leads to progressive cellular dysfunction, leading to apoptosis.<sup>21</sup> IEC-6 cells upon treatment with varying concentrations of  $As^{5+}$ , namely, 1, 3, and 5 ppm for 24 h, resulted in a 50% loss of cell viability at 3 and 5 ppm As exposure. At concentrations of As lower than 1 ppm, a longer incubation time was required to achieve cell death with As. In such cases, it was difficult to differentiate natural vs arsenic-induced cell death. The cell viability was studied by differentiating live cells vs dead cells through staining with calcein and ethidium bromide, followed by fluorescence imaging. The intracellular esterase present in live cells hydrolyzes the acetomethoxy group of nonfluorescent calcein AM dye, making it fluorescent. Ethidium bromide is a



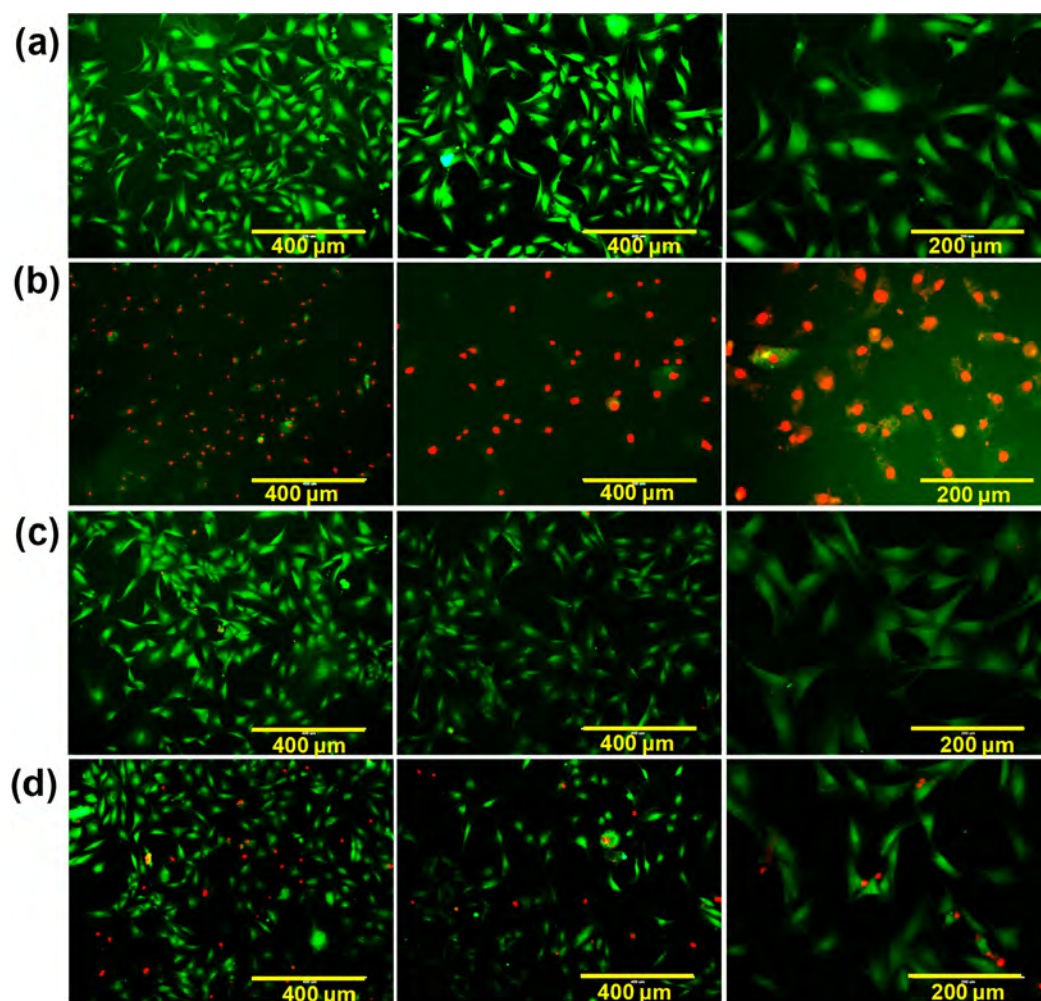


**Figure 2.** Fluorescence microscopy images demonstrating the effect of carbonates on the cytotoxicity produced by arsenate on IEC-6 cells at 3 ppm. Two different magnifications are shown for every type. Line (row) (a) Control cells without any treatment. Line (b) 3 ppm of  $\text{As}^{5+}$  treatment. Line (c) 3 ppm  $\text{As}^{5+}$  + 40 ppm of  $\text{CaCO}_3$ . Line (d) 3 ppm  $\text{As}^{5+}$  + 40 ppm of  $\text{Na}_2\text{CO}_3$ . Calcein stains the live cells green and ethidium bromide stains the dead cells red.

commonly used fluorescent tag that intercalates with nucleic acids and stains dead cells red. Figure 2 shows the effect of As on the IEC-6 cells and the increase in cell viability due to exposure to  $\text{CaCO}_3$  and  $\text{Na}_2\text{CO}_3$ . The control IEC-6 cells showed only green fluorescence (Figure 2a), a characteristic of live cells, whereas 3 ppm  $\text{As}^{5+}$ -treated cells showed significant red fluorescence, which indicated dead cells, as shown in Figure 2b. The cells treated with only 40 ppm of  $\text{CaCO}_3$  or  $\text{Na}_2\text{CO}_3$  showed a negligible number of dead cells (Supporting Information; Figures S1 and S2). Almost 75% of the cells of  $\text{As}^{5+}$   $\text{CaCO}_3$ - or  $\text{As}^{5+}$   $\text{Na}_2\text{CO}_3$ -treated samples were green fluorescent (Figure 2 c,d), indicating that carbonates protected IEC-6 cells from the As-induced cell death. The result was obtained from triplicate experiments. We observed that a cotreatment of carbonate showed effective protection against As-induced cell death. Due to the poor solubility of  $\text{CaCO}_3$ , precipitates were formed on the surface of the treated cells, as seen in the Supporting Information, Figure S1d. In order to understand if  $\text{CaCO}_3$  is involved in As complexation,<sup>26</sup> SEM with EDS spectra and elemental maps of the  $\text{CaCO}_3$  precipitates were studied (Supporting Information; Figure S3). Chemical characterization of the precipitates showed no presence of As on them, and thus, we infer that As–carbonate

complexes might be of concentrations below the detection limit. Cyclic voltammetry experiments to study the effect of  $\text{CaCO}_3$  on  $\text{H}_2\text{O}_2$  concentration in the cells have shown 95% reduction in  $\text{H}_2\text{O}_2$  concentration after incubation of IEC-6 cells with  $\text{As}^{5+}$  and 40 ppm of  $\text{CaCO}_3$ .

**Morphological and Quantitative Assessment of Carbonate's Action.** Morphological criteria have been used to define cell death. Rounded bodies observed in cell tissue culture are distinct morphological features associated with cell death (specifically, apoptosis) and cells under stress or exposed to stressful environments.<sup>39</sup> The untreated IEC-6 control cells were polygonal in shape with more regular dimensions and were grown attached to the substrate in discrete patches. Figure 3A shows the phase-contrast microscopic images of untreated control cells, cells treated with  $\text{As}^{5+}$ ,  $\text{As}^{5+}$  +  $\text{CaCO}_3$ , and  $\text{As}^{5+}$  +  $\text{Na}_2\text{CO}_3$  (Parts a, b, c, and d of Figure 3A, respectively). Morphological changes were observed in As-affected cells, whereas the cotreatment of  $\text{As}^{5+}$  with either calcium carbonate or sodium carbonate acted as a cytoprotectant and preserved the morphology similar to that of the control cells. The morphology of cells treated with 40 ppm of  $\text{CaCO}_3$  or  $\text{Na}_2\text{CO}_3$  was not disrupted (Supporting Information, Figure S4).  $\text{CaCO}_3$ -treated cells show increased

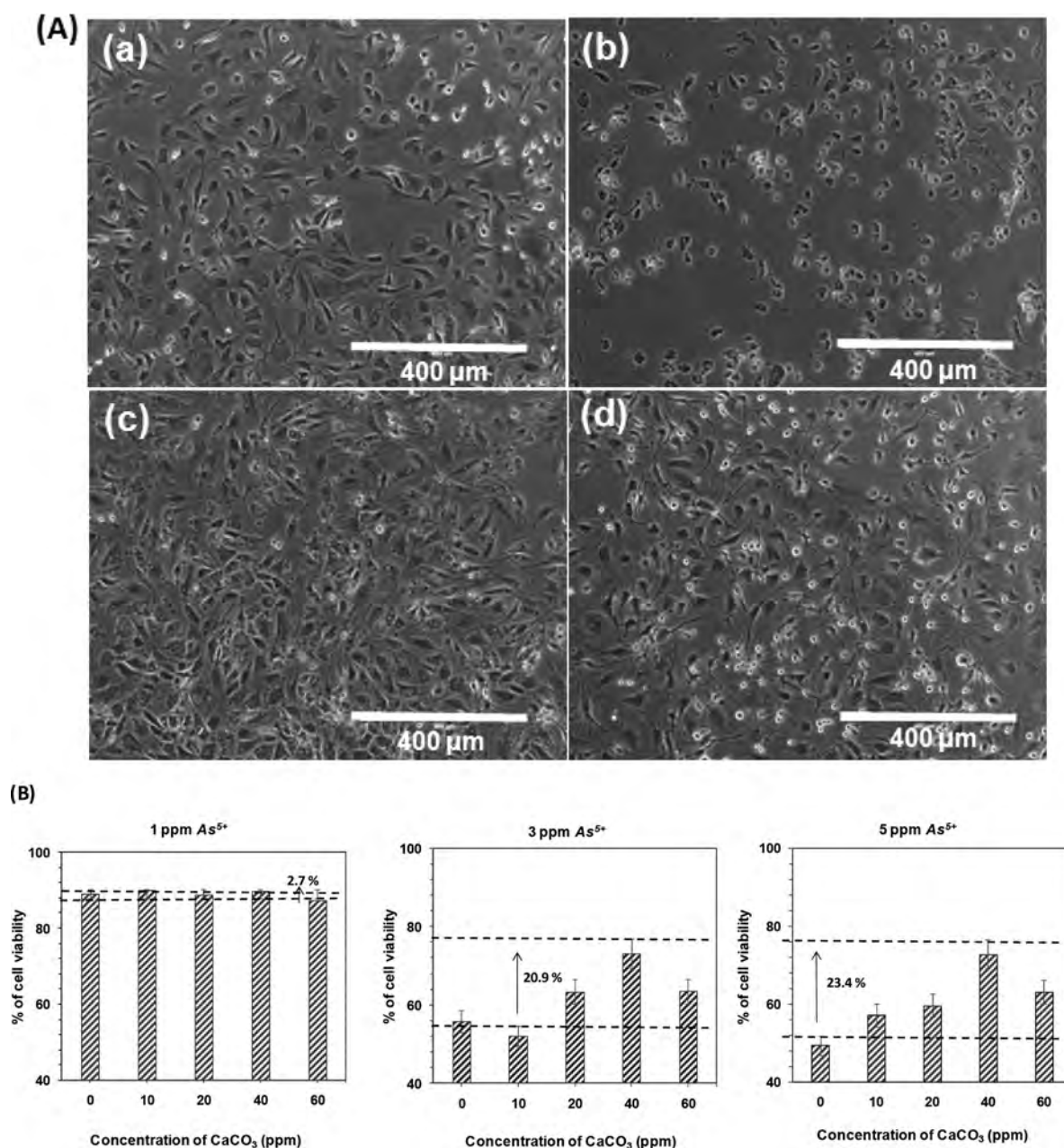


**Figure 3.** (A) Effect of arsenate on the cellular morphology and the cytoprotection by calcium carbonate and sodium carbonate. (a) Untreated control cells, (b) 3 ppm of As<sup>5+</sup> treatment, (c) 3 ppm As<sup>5+</sup> + 40 ppm of CaCO<sub>3</sub>, and (d) 3 ppm As<sup>5+</sup> + 40 ppm of Na<sub>2</sub>CO<sub>3</sub>. (B) Effect of calcium carbonate on the toxicity of varying concentrations of arsenate (As<sup>5+</sup>). The percentage of cell viability was measured using MTT assay. The difference between the heights of dashed lines represents the increase in viability of the cells.

viability than Na<sub>2</sub>CO<sub>3</sub>-treated cells as the buffering capacity, and acid neutralization efficiency of CaCO<sub>3</sub> is higher than that of Na<sub>2</sub>CO<sub>3</sub>.<sup>40</sup>

This difference in viability was measured quantitatively using the MTT colorimetric assay. The cotreatment of the cells with a combination of As<sup>5+</sup> + CaCO<sub>3</sub> (Figure 3B) or As<sup>5+</sup> + Na<sub>2</sub>CO<sub>3</sub> (Supporting Information, Figure S5) resulted in protection against As-induced toxicity in a dose-dependent manner. The cytosolic and mitochondrial dehydrogenases produced by the living cells reduced the yellow tetrazolium salt (MTT) and produced a purple formazan dye that was detected using a spectrophotometer. The viability of As-treated cells was restored to above 75% of the control when they were cotreated with carbonates. This cell viability assay stands as preliminary

data to indicate the protective action of carbonate during As exposure. The total concentration of As in As<sup>5+</sup> + CaCO<sub>3</sub>-cotreated cells reduced by 31.5% when compared with the 3 ppm As<sup>5+</sup>-treated cells (Supporting Information, Figure S6). In this study, we found that the concentration of carbonates above 10 ppm and below 40 ppm is necessary for protection.

**Intracellular ROS Levels.** An important biomarker to indicate oxidative stress caused by As is the intracellular level of ROS. When the ROS concentration increases, it indicates an increase in cellular oxidative stress. Initial experiments were performed with an oxidatively stressed model in which IEC-6 cells were treated with a toxic level of 3 ppm As. For a positive control to represent intracellular ROS production, cells were treated with 1 mM H<sub>2</sub>O<sub>2</sub> for 1 h and were stained subsequently



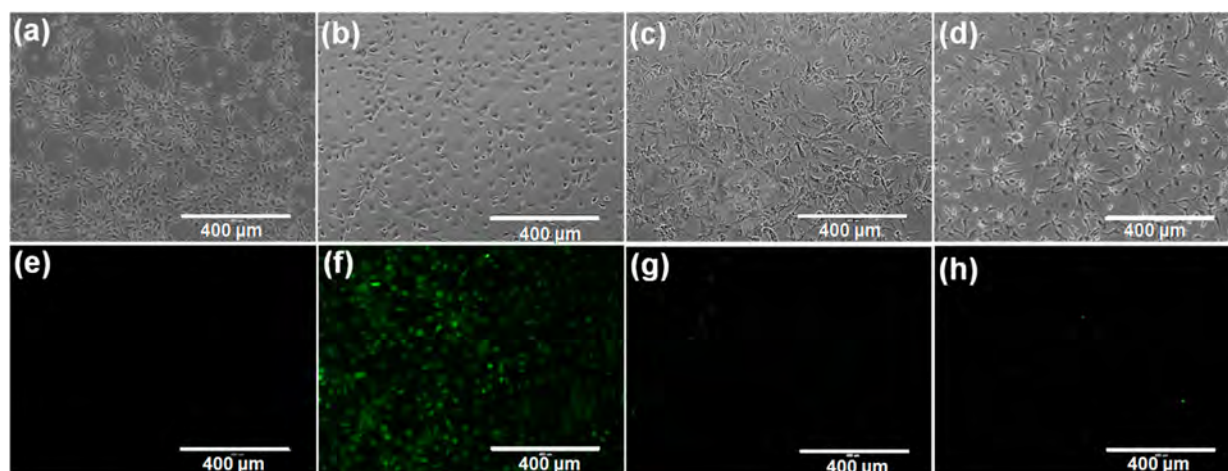


**Figure 4.** Determination of ROS in treated cells. Phase-contrast (top) and fluorescence microscopy (bottom) images demonstrating the effect of carbonates on the ROS produced by cells during 3 ppm  $\text{As}^{5+}$  treatment: (a, e) control, (b, f) 3 ppm  $\text{As}^{5+}$ , (c, g) 3 ppm  $\text{As}^{5+}$  + 40 ppm of  $\text{CaCO}_3$ , and (d, h) 3 ppm  $\text{As}^{5+}$  + 40 ppm of  $\text{Na}_2\text{CO}_3$ .

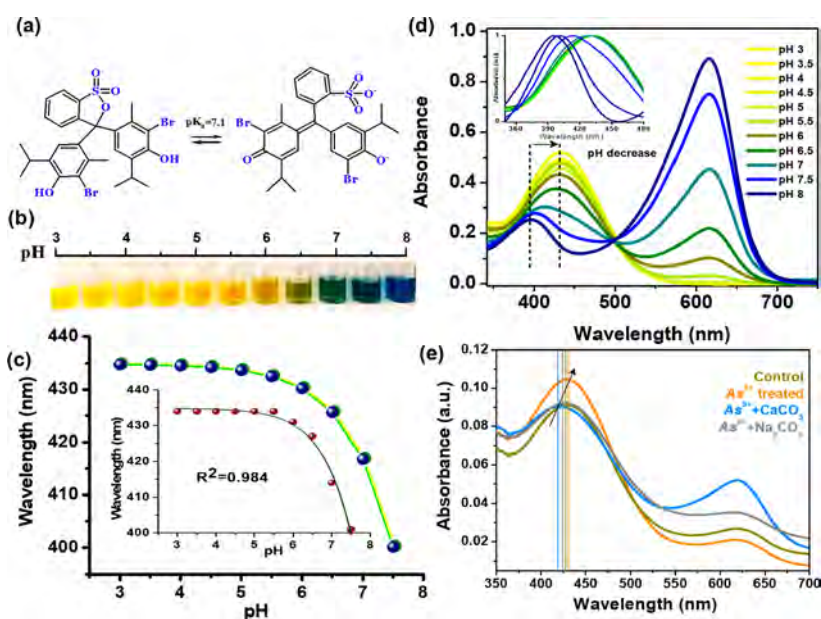


**Figure 5.** (a) Structure of BTB at different pH ranges. (b) Different colors of BTB at marked pH conditions. (c) Calibration curve of UV-vis absorption peak of the dye solutions. The inset shows the calibration curve from pH 4.5 to 7.5. (d) UV-vis absorption spectra of BTB/PBS solutions at different pH. The red shift in acidic solutions at 420 nm is marked. Inset is the normalized UV-vis absorption spectra in the 350–500 nm window at different pH. (e) UV-vis absorption spectra of the treated cells eluted from the culture plate, sonicated, and stained with BTB.

(Supporting Information, Figure S7). The As-treated cells showed green fluorescence depicting excessive oxidative stress (Figure 4f). The data summarized in Figure 4 show that the cotreatment of  $\text{As}^{5+}$   $\text{CaCO}_3$  or  $\text{As}^{5+}$   $\text{Na}_2\text{CO}_3$  (Figure 4g,h) significantly decreased the levels of intracellular ROS in comparison to that produced in As-treated cells. The negative control (untreated healthy cells) and 40 ppm of  $\text{CaCO}_3$ - (Figure 4e) or  $\text{Na}_2\text{CO}_3$ -treated cells showed no significant difference in the intracellular ROS production and showed no fluorescence. Parts a–d of Figure 4 are the phase-contrast images of control cells, cells treated with  $\text{As}^{5+}$ , 3 ppm  $\text{As}^{5+}$  + 40 ppm of  $\text{CaCO}_3$ , and 3 ppm  $\text{As}^{5+}$  + 40 ppm of  $\text{Na}_2\text{CO}_3$ , respectively. This experiment suggested that the protective role of carbonates is mediated, at least in part by direct  $\text{H}_2\text{O}_2$  decomposition. The result was obtained from triplicate experiments for three separate trials. In all the experiments,

treatment with carbonates resulted in a significant reduction in As-induced intracellular ROS production, proving its ability to decrease oxidative damage and subsequent cell death.

**Cellular pH Profiling.** Upon  $\text{As}^{5+}$  exposure, the acidic metabolites of As and the Warburg effect lead to a decreased pH in the cells. This was evident from the change in the color of the growth media (DMEM) in which  $\text{As}^{5+}$ -affected cells were cultured. Although the pH change in a cell is balanced by the buffering activity of the  $\text{CO}_3^{2-}/\text{HCO}_3^-$  system, the acidic metabolites formed due to As-induced toxicity were high in concentration, leading to cell death. Therefore, the effect of external administration of carbonates along with  $\text{As}^{5+}$  on the cellular pH was studied.

The UV-vis absorption spectra of the treated cells that were eluted from the culture plate, sonicated, and stained with BTB are shown in Figure 5. Each condition was tested in triplicate.

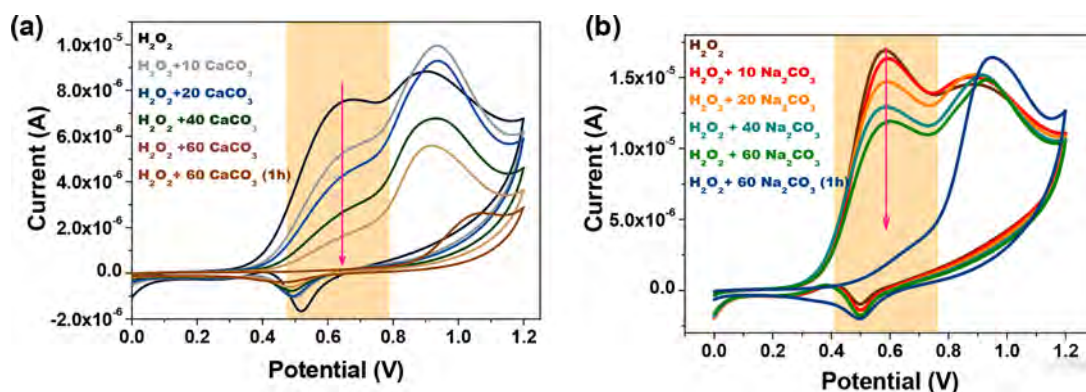


**Figure 6.** Carbonate's role in the decomposition of  $\text{H}_2\text{O}_2$  at varying concentrations of (a)  $\text{CaCO}_3$  and (b)  $\text{Na}_2\text{CO}_3$  by cyclic voltammetry.

BTB can be in its protonated or deprotonated form, indicated by a yellow or blue color, respectively (Figure 5a,b). An intermediate of the deprotonation mechanism is responsible for a greenish color at neutral pH. The absorption spectra of BTB/PBS solution were initially studied at varied pH, and a correlation curve was obtained (Figure 5c) to quantitate and compare the pH of the treated cells. The dye shows two distinct features at 420 and 620 nm (Figure 5d). The protonated form of the dye had its peak absorption at 420 nm, thus transmitting yellow light in  $\text{As}^{5+}$ -treated acidic solutions, and the deprotonated form had its peak absorption at 620 nm, thus transmitting blue light in the control and carbonate-treated basic solutions (Figure 5e). This peak can be attributed to the occurrence of a hydrogen transfer (on the phenolic groups) and intramolecular charge transfer (caused by the conjugate effects of the system).

The color of BTB/PBS varies as an active indication of pH change in the range 6.0–7.6.<sup>41</sup> As the pH decreases in an  $\text{As}^{5+}$ -treated cell solution (the orange trace in Figure 5e), the highly pH-dependent absorption peak centered at 420 nm shows a definite red shift from 420 to 430 nm (inset of Figure 5d). The change in pH can be interpreted by comparing the peak center and the absorbance vs pH calibration curve plotted with standard solutions in the inset of Figure 5c, where the red shift reaches saturation thereafter. Another important feature is the absorption peak centered at 620 nm. This peak shown in the standard solution decreases gradually and finally disappears when the solution turns acidic. The peak intensity of the  $\text{As}^{5+}$ -treated cell solution (orange trace) at 620 nm had decreased significantly in comparison to that of the control cells. Whereas, there was an increase in the intensity of  $\text{As}^{5+}$  +  $\text{CaCO}_3$ -treated cells (blue trace) as the solution was neutralized.

A colorimetric imaging method with bright-field microscopy using a pH indicator, BTB, was used also to demonstrate the change in cellular pH. Upon optical microscopic observation, cells, when treated with 3 ppm of  $\text{As}^{5+}$ , stained yellow due to lowering of the cellular pH, whereas the color turned darker when treated with 3 ppm  $\text{As}^{5+}$  + 40 ppm of  $\text{CaCO}_3$  and 3 ppm  $\text{As}^{5+}$  + 40 ppm of  $\text{Na}_2\text{CO}_3$  (Figure S8a of Supporting Information). The pH distribution of treated cells was calculated from the calibration curve, which showed a decrease in the intensity of the 620 nm peak for  $\text{As}$ -treated cells, whereas the carbonate-treated cells retained the intensity similar to that of the control cells (Figure S8b of Supporting Information). The pH change of cotreated cells was 5–6.5, which was significant although being small. Treatment with

carbonates balanced the cellular pH to the neutral range and prevented acid-promoted cellular stress.

**$\text{H}_2\text{O}_2$  Decomposition.** To prove that carbonates are efficient in decomposing  $\text{H}_2\text{O}_2$  produced during oxidative stress induced by  $\text{As}^{5+}$ , a set of CV experiments were performed on  $\text{As}^{5+}$ -treated cells lysed in PBS. The CV curve of PBS (pH = 7) used in the experiment is shown in the Supporting Information, Figure S9. Figure 6 (a and b) shows the concentration-dependent decomposition of  $\text{H}_2\text{O}_2$  through voltammogram when the cells were incubated for 1 min with calcium carbonate and sodium carbonate, respectively. In the potential window ( $0 \pm 1.4$  V), we observed a broad oxidation peak of  $\text{H}_2\text{O}_2$  at 0.4–0.8 V. However, this peak gradually decreases with lowering of the concentration of  $\text{H}_2\text{O}_2$  in the presence of carbonate in the sample. When the incubation time was increased, a complete decomposition was observed, which lead to the disappearance of the  $\text{H}_2\text{O}_2$  peak. More than 95% reduction in  $\text{H}_2\text{O}_2$  concentration was observed within an incubation period of 1 h. Studies on several different systems have demonstrated significant decomposition of  $\text{H}_2\text{O}_2$  by carbonates.<sup>42</sup> It is reported that oxidative cell death in the presence of iron involves Fenton-type reactions, and peroxidative damage to the cell may be prevented by the decomposition caused by carbonates.<sup>43</sup>

In view of the above, the carbonate-mediated protection can be suggested due to one or more of the following mechanisms: (1) direct decomposition of ROS produced and (2) action as a buffering agent in neutralizing the acidic byproducts formed in the cell. The formation of  $\text{As}$ –carbonate complexes can be another mechanism, as reported in the literature.<sup>44</sup> Carbonated water may be a prudent solution in preventing the slow impairment caused by continuous intake of  $\text{As}$  from the contaminated water. The counteraction of carbonates on  $\text{As}$  toxicity has to be studied using animal models, and the influence of other metal ions in the digestive system on the effect of carbonate has to be investigated. Additional investigations on the impact of such measures on the overall well-being of individuals are necessary before proposing such methods as remedial measures.

## CONCLUSION

Carbonates are nonhazardous, abundantly available in the earth's crust, and are affordable to all the communities present throughout the world. The current study shows that the administration of safe levels of carbonate in the form of calcium carbonate or sodium carbonate can counteract the toxicity levels of  $\text{As}$ . A cascade of cellular dysfunction that



occurs as a result of As toxicity results in cellular acidification and excessive ROS generation in IEC-6 cells. While acidification is neutralized by the buffering action of carbonates, the oxidative stress created inside the cell is counteracted by its  $\text{H}_2\text{O}_2$  decomposing activity. Any mineral intake in living organisms through fluids plays a key role in maintaining its balance in comparison to food. We propose that a divided dose of mineral balanced water containing sodium carbonate and/or calcium carbonate at concentrations adjusted according to the As content can be the best way to compensate for the multiplex complications caused by As in the human system. While developing advanced materials to create an affordable drinking water purifier,<sup>45</sup> we have reported in our earlier work that 20–50 ppm of carbonates and other essential minerals can be released continuously and sustainably from confined scaffolds.<sup>46,47</sup> The use of such sustainable carbonate releasing encapsulations can provide cytoprotection against As toxicity at an affordable cost, without any energy demand. This paper stands as preliminary evidence to tackle the mass poisoning scenario by using this sustainable and affordable solution. Although the effective route of administration of carbonates in order to tackle  $\text{As}^{5+}$  contamination in living systems is not clearly understood in this study, this may be evaluated in the future by detailed clinical analysis.

## ■ ASSOCIATED CONTENT

### ■ Supporting Information

The Supporting Information is available free of charge at <https://pubs.acs.org/doi/10.1021/acssuschemeng.9b06850>.

Figures of fluorescence microscopy, phase-contrast microscopy, SEM, and bright-field optical microscopy images, EDS spectra, effects of  $\text{Na}_2\text{CO}_3$  on the toxicity induced by varying concentrations, comparative analysis of  $\text{As}^{5+}$  concentration in cells, histograms of pH distribution, and CV curves (PDF)

## ■ AUTHOR INFORMATION

### Corresponding Author

**Thalappil Pradeep** – DST Unit of Nanoscience (DST UNS) and Thematic Unit of Excellence (TUE), Department of Chemistry, Indian Institute of Technology Madras, Chennai, Tamil Nadu 600036, India; [orcid.org/0000-0003-3174-534X](https://orcid.org/0000-0003-3174-534X); Email: [pradeep@iitm.ac.in](mailto:pradeep@iitm.ac.in); Fax: +91-44-2257-0545

### Authors

**Swathy Jakka Ravindran** – DST Unit of Nanoscience (DST UNS) and Thematic Unit of Excellence (TUE), Department of Chemistry and Environmental and Water Resources Engineering (EWRE) Division, Department of Civil Engineering, Indian Institute of Technology Madras, Chennai, Tamil Nadu 600036, India; [orcid.org/0000-0002-7882-7871](https://orcid.org/0000-0002-7882-7871)

**Shantha Kumar Jenifer** – DST Unit of Nanoscience (DST UNS) and Thematic Unit of Excellence (TUE), Department of Chemistry, Indian Institute of Technology Madras, Chennai, Tamil Nadu 600036, India

**Jayashree Balasubramanyam** – Department of Nanobiotechnology, Vision Research Foundation, Sankara Nethralaya, Chennai, Tamil Nadu 600006, India

**Sourav Kanti Jana** – DST Unit of Nanoscience (DST UNS) and Thematic Unit of Excellence (TUE), Department of Chemistry, Indian Institute of Technology Madras, Chennai,

Tamil Nadu 600036, India; [orcid.org/0000-0001-5772-7022](https://orcid.org/0000-0001-5772-7022)

**Subramanian Krishnakumar** – Department of Nanobiotechnology, Vision Research Foundation, Sankara Nethralaya, Chennai, Tamil Nadu 600006, India

**Sailaja Elchuri** – Department of Nanobiotechnology, Vision Research Foundation, Sankara Nethralaya, Chennai, Tamil Nadu 600006, India; [orcid.org/0000-0002-9780-2717](https://orcid.org/0000-0002-9780-2717)

**Ligy Philip** – Environmental and Water Resources Engineering (EWRE) Division, Department of Civil Engineering, Indian Institute of Technology Madras, Chennai 600036, India; [orcid.org/0000-0001-8838-2135](https://orcid.org/0000-0001-8838-2135)

Complete contact information is available at: <https://pubs.acs.org/doi/10.1021/acssuschemeng.9b06850>

## Author Contributions

T.P. and S.J.R. designed the experiments. S.J.R. and J.B. performed the experiments. T.P., L.P., S.E., S.J.R. and S.K.J. analyzed the data and wrote the paper.

## Notes

The authors declare no competing financial interest.

## ■ ACKNOWLEDGMENTS

The authors thank Mr. Ranjith and Mrs. Lakshmi for their timely support in cell culture, Mr. Srikrishnarka Pillalamarri for his technical support in SEM analysis, and the Science and Engineering Research Board (Government of India) for supporting this work through the grant, EMR/2015/000607, which made this research possible.

## ■ REFERENCES

- (1) Straif, K.; Benbrahim-Tallaa, L.; Baan, R.; Grosse, Y.; Secretan, B.; El Ghissassi, F.; Bouvard, V.; Guha, N.; Freeman, C.; Galichet, L. A Review of Human Carcinogens-Part C: Metals, Arsenic, Dusts, and Fibres. *Lancet Oncol.* **2009**, *10* (5), 453–454.
- (2) Toxicological Profile for Arsenic. Agency for Toxic Substances and Disease Registry. <https://www.atsdr.cdc.gov/toxprofiles> (accessed 2019-12-12).
- (3) Paul, S.; Das, N.; Bhattacharjee, P.; Banerjee, M.; Das, J. K.; Sarma, N.; Sarkar, A.; Bandyopadhyay, A. K.; Sau, T. J.; Basu, S.; et al. Arsenic-Induced Toxicity and Carcinogenicity: A Two-Wave Cross-Sectional Study in Arsenicosis Individuals in West Bengal, India. *J. Exposure Sci. Environ. Epidemiol.* **2013**, *23* (2), 156–162.
- (4) Ravenscroft, P.; Brammer, H.; Richards, K. *Arsenic Pollution: A Global Synthesis*; RGS-IBG Book Series; Wiley-Blackwell: UK, 2009.
- (5) Occurrence of high arsenic content in groundwater. India Environmental portal. <http://www.indiaenvironmentportal.org.in> (accessed 2019-12-23).
- (6) Arsenic. WHO news room. <https://www.who.int/news-room/fact-sheets/detail/arsenic> (accessed 2019-11-05).
- (7) Zhu, Y.-G.; Yoshinaga, M.; Zhao, F.-J.; Rosen, B. P. Earth Abides Arsenic Biotransformations. *Annu. Rev. Earth Planet. Sci.* **2014**, *42*, 443–467.
- (8) Sreepasad, T. S.; Maliyekkal, S. M.; Lisha, K. P.; Pradeep, T. Reduced Graphene Oxide–Metal/Metal Oxide Composites: Facile Synthesis and Application in Water Purification. *J. Hazard. Mater.* **2011**, *186* (1), 921–931.
- (9) Yang, Q.; Lau, C. H.; Ge, Q. Novel Ionic Grafts That Enhance Arsenic Removal via Forward Osmosis. *ACS Appl. Mater. Interfaces* **2019**, *11* (19), 17828–17835.
- (10) Hossain, M. A.; Sengupta, M. K.; Ahamed, S.; Rahman, M. M.; Mondal, D.; Lodh, D.; Das, B.; Nayak, B.; Roy, B. K.; Mukherjee, A.; et al. Ineffectiveness and Poor Reliability of Arsenic Removal Plants in West Bengal, India. *Environ. Sci. Technol.* **2005**, *39* (11), 4300–4306.

- (11) Wang, J. S.; Wai, C. M. Arsenic in Drinking Water—A Global Environmental Problem. *J. Chem. Educ.* **2004**, *81* (2), 207–213.
- (12) Sankar, M. U.; Aigal, S.; Maliyekkal, S. M.; Chaudhary, A.; Anshup Kumar, A. A.; Chaudhari, K.; Pradeep, T. Biopolymer-Reinforced Synthetic Granular Nanocomposites for Affordable Point-of-Use Water Purification. *Proc. Natl. Acad. Sci. U. S. A.* **2013**, *110* (21), 8459–8464.
- (13) Kumar, A. A.; Som, A.; Longo, P.; Sudhakar, C.; Bhuin, R. G.; Gupta, S. S.; Anshup; Sankar, M. U.; Chaudhary, A.; Kumar, R.; et al. Confined Metastable 2-Line Ferrihydrite for Affordable Point-of-Use Arsenic-Free Drinking Water. *Adv. Mater.* **2017**, *29* (7), 1604260.
- (14) Sudhakar, C.; Anil Kumar, A.; Bhuin, R. G.; Sen Gupta, S.; Natarajan, G.; Pradeep, T. Species-Specific Uptake of Arsenic on Confined Metastable 2-Line Ferrihydrite: A Combined Raman-X-Ray Photoelectron Spectroscopy Investigation of the Adsorption Mechanism. *ACS Sustainable Chem. Eng.* **2018**, *6* (8), 9990–10000.
- (15) Ball, P. Arsenic-Free Water Still a Pipedream. *Nature* **2005**, *436* (7049), 313.
- (16) Dixit, S.; Hering, J. G. Comparison of Arsenic(V) and Arsenic(III) Sorption onto Iron Oxide Minerals: Implications for Arsenic Mobility. *Environ. Sci. Technol.* **2003**, *37* (18), 4182–4189.
- (17) Oberoi, S.; Barchowsky, A.; Wu, F. The Global Burden of Disease for Skin, Lung, and Bladder Cancer Caused by Arsenic in Food. *Cancer Epidemiol. Biomarkers Prev.* **2014**, *23* (7), 1187–1194.
- (18) Vrijenhoek, E. M.; Waypa, J. J. Arsenic Removal from Drinking Water by a “Loose” Nanofiltration Membrane. *Desalination* **2000**, *130* (3), 265–277.
- (19) Guo, H.-R.; Wang, N.-S.; Hu, H.; Monson, R. R. Cell Type Specificity of Lung Cancer Associated with Arsenic Ingestion. *Cancer Epidemiol. Biomarkers Prev.* **2004**, *13* (4), 638–643.
- (20) Hughes, M. F. Arsenic Toxicity and Potential Mechanisms of Action. *Toxicol. Lett.* **2002**, *133* (1), 1–16.
- (21) Jomova, K.; Jenisova, Z.; Feszterova, M.; Baros, S.; Liska, J.; Hudecova, D.; Rhodes, C. J.; Valko, M. Arsenic: Toxicity, Oxidative Stress and Human Disease. *J. Appl. Toxicol.* **2011**, *31* (2), 95–107.
- (22) Flora, S. J. S.; Bhadauria, S.; Kannan, G. M.; Nutan, S. Arsenic Induced Oxidative Stress and the Role of Antioxidant Supplementation during Chelation: A Review. *J. Environ. Biol.* **2007**, *28* (2), 333–347.
- (23) Liu, S. X.; Athar, M.; Lippai, I.; Waldren, C.; Hei, T. K. Induction of Oxyradicals by Arsenic: Implication for Mechanism of Genotoxicity. *Proc. Natl. Acad. Sci. U. S. A.* **2001**, *98* (4), 1643–1648.
- (24) Shi, H.; Shi, X.; Liu, K. J. Oxidative Mechanism of Arsenic Toxicity and Carcinogenesis. *Mol. Cell. Biochem.* **2004**, *255* (1), 67–78.
- (25) Vander Heiden, M. G.; Cantley, L. C.; Thompson, C. B. Understanding the Warburg Effect: The Metabolic Requirements of Cell Proliferation. *Science* **2009**, *324* (5930), 1029–1033.
- (26) Kim, M.-J.; Nriagu, J.; Haack, S. Carbonate Ions and Arsenic Dissolution by Groundwater. *Environ. Sci. Technol.* **2000**, *34* (15), 3094–3100.
- (27) Hochella, M. F.; Lower, S. K.; Maurice, P. A.; Penn, R. L.; Sahai, N.; Sparks, D. L.; Twining, B. S. Nanominerals, Mineral Nanoparticles, and Earth Systems. *Science (Washington, DC, U. S.)* **2008**, *319* (5870), 1631–1635.
- (28) Sherman, T.; Chernova, M. N.; Clark, J. S.; Jiang, L.; Alper, S. L.; Nehrke, K. The Abts and Sulp Families of Anion Transporters from *Caenorhabditis Elegans*. *Am. J. Physiol. Physiol.* **2005**, *289* (2), C341–C351.
- (29) Ruby, M. V.; Davis, A.; Schoof, R.; Eberle, S.; Sellstone, C. M. Estimation of Lead and Arsenic Bioavailability Using a Physiologically Based Extraction Test. *Environ. Sci. Technol.* **1996**, *30* (2), 422–430.
- (30) Zhao, F.; Severson, P.; Pacheco, S.; Futscher, B. W.; Klimecki, W. T. Arsenic Exposure Induces the Warburg Effect in Cultured Human Cells. *Toxicol. Appl. Pharmacol.* **2013**, *271* (1), 72–77.
- (31) Robey, I. F.; Baggett, B. K.; Kirkpatrick, N. D.; Roe, D. J.; Donescu, J.; Sloane, B. F.; Hashim, A. I.; Morse, D. L.; Raghunand, N.; Gatenby, R. A.; et al. Bicarbonate Increases Tumor pH and Inhibits Spontaneous Metastases. *Cancer Res.* **2009**, *69* (6), 2260–2268.
- (32) Navarro, J. A.; de la Rosa, M. A.; Roncel, M.; de la Rosa, F. F. Carbon Dioxide-Mediated Decomposition of Hydrogen Peroxide in Alkaline Solutions. *J. Chem. Soc., Faraday Trans. 1* **1984**, *80*, 249–253.
- (33) Lithaw, P. N. *Glycolysis Regulation, Processes and Diseases*; Nova Biomedical Books: NY, 2009.
- (34) Florence, T. M. The Production of Hydroxyl Radical from Hydrogen Peroxide. *J. Inorg. Biochem.* **1984**, *22* (4), 221–230.
- (35) Maliyekkal, S. M.; Philip, L.; Pradeep, T. As(III) Removal from Drinking Water Using Manganese Oxide-Coated-Alumina: Performance Evaluation and Mechanistic Details of Surface Binding. *Chem. Eng. J.* **2009**, *153*, 101–107.
- (36) Cumbal, L.; SenGupta, A. K. Arsenic Removal Using Polymer-Supported Hydrated Iron(III) Oxide Nanoparticles: Role of Donnan Membrane Effect. *Environ. Sci. Technol.* **2005**, *39* (17), 6508–6515.
- (37) Litter, M. I.; Ingallinella, A. M.; Olmos, V.; Savio, M.; Difeo, G.; Botto, L.; Torres, E. M. F.; Taylor, S.; Frangie, S.; Herkovits, J.; et al. Arsenic in Argentina: Technologies for Arsenic Removal from Groundwater Sources, Investment Costs and Waste Management Practices. *Sci. Total Environ.* **2019**, *690*, 778–789.
- (38) Mosmann, T. Rapid Colorimetric Assay for Cellular Growth and Survival: Application to Proliferation and Cytotoxicity Assays. *J. Immunol. Methods* **1983**, *65* (1), 55–63.
- (39) Malek, A. M.; Izumo, S. Mechanism of Endothelial Cell Shape Change and Cytoskeletal Remodeling in Response to Fluid Shear Stress. *J. Cell Sci.* **1996**, *109* (4), 713–726.
- (40) Kapil, N.; Bhattacharyya, K. G. A Comparison of Neutralization Efficiency of Chemicals with Respect to Acidic Kopili River Water. *Appl. Water Sci.* **2017**, *7* (5), 2209–2214.
- (41) Hou, H.; Zhao, Y.; Li, C.; Wang, M.; Xu, X.; Jin, Y. Single-Cell PH Imaging and Detection for PH Profiling and Label-Free Rapid Identification of Cancer-Cells. *Sci. Rep.* **2017**, *7* (1759), 1–8.
- (42) Cota, H. M.; Katan, T.; Chin, M.; Schoenweis, F. J. Decomposition of Dilute Hydrogen Peroxide in Alkaline Solutions. *Nature* **1964**, *203* (4951), 1281.
- (43) Burg, A.; Shamir, D.; Shusterman, I.; Kornweitz, H.; Meyerstein, D. The Role of Carbonate as a Catalyst of Fenton-like Reactions in AOP Processes: CO<sub>3</sub><sup>2-</sup> as the Active Intermediate. *Chem. Commun.* **2014**, *50* (86), 13096–13099.
- (44) Han, M.-J.; Hao, J.; Christodoulatos, C.; Korfiatis, G. P.; Wan, L.-J.; Meng, X. Direct Evidence of Arsenic(III)-Carbonate Complexes Obtained Using Electrochemical Scanning Tunneling Microscopy. *Anal. Chem.* **2007**, *79* (10), 3615–3622.
- (45) Swathy, J. R.; Udhaya, M. S.; Amrita, C.; Aigal, S.; Anshup; Pradeep, T. Antimicrobial Silver: An Unprecedented Anion Effect. *Sci. Rep.* **2015**, *4* (1), 1–5.
- (46) Jakka Ravindran, S.; Mahendranath, A.; Srikrishnarka, P.; Anil Kumar, A.; Islam, M. R.; Mukherjee, S.; Philip, L.; Pradeep, T. Geologically Inspired Monoliths for Sustainable Release of Essential Minerals into Drinking Water. *ACS Sustainable Chem. Eng.* **2019**, *7* (13), 11735–11744.
- (47) Swathy, J. R.; Pugazhenthiran, N.; Sudhakar, C.; Anil Kumar, A.; Pradeep, T. Sparingly Soluble Constant Carbonate Releasing Inert Monolith for Enhancement of Antimicrobial Silver Action and Sustainable Utilization. *ACS Sustainable Chem. Eng.* **2016**, *4* (7), 4043–4049.

# SUPPORTING INFORMATION

## Arsenic Toxicity: Carbonate's Counteraction Revealed

Swathy Jakka Ravindran<sup>†‡</sup>, Shantha Kumar Jenifer<sup>†</sup>, Jayashree Balasubramanyam<sup>§</sup>, Sourav Kanti Jana<sup>†</sup>, Subramanian Krishnakumar<sup>§</sup>, Sailaja Elchuri<sup>§</sup>, Ligy Philip<sup>‡</sup>, and Thalappil Pradeep<sup>†\*</sup>

<sup>†</sup>DST Unit of Nanoscience (DST UNS) and Thematic Unit of Excellence (TUE), Department of Chemistry, Indian Institute of Technology Madras, Chennai, Tamil Nadu 600036, India

<sup>§</sup>Department of Nanobiotechnology, Vision Research Foundation, Sankara Nethralaya, Chennai, Tamil Nadu 600006, India

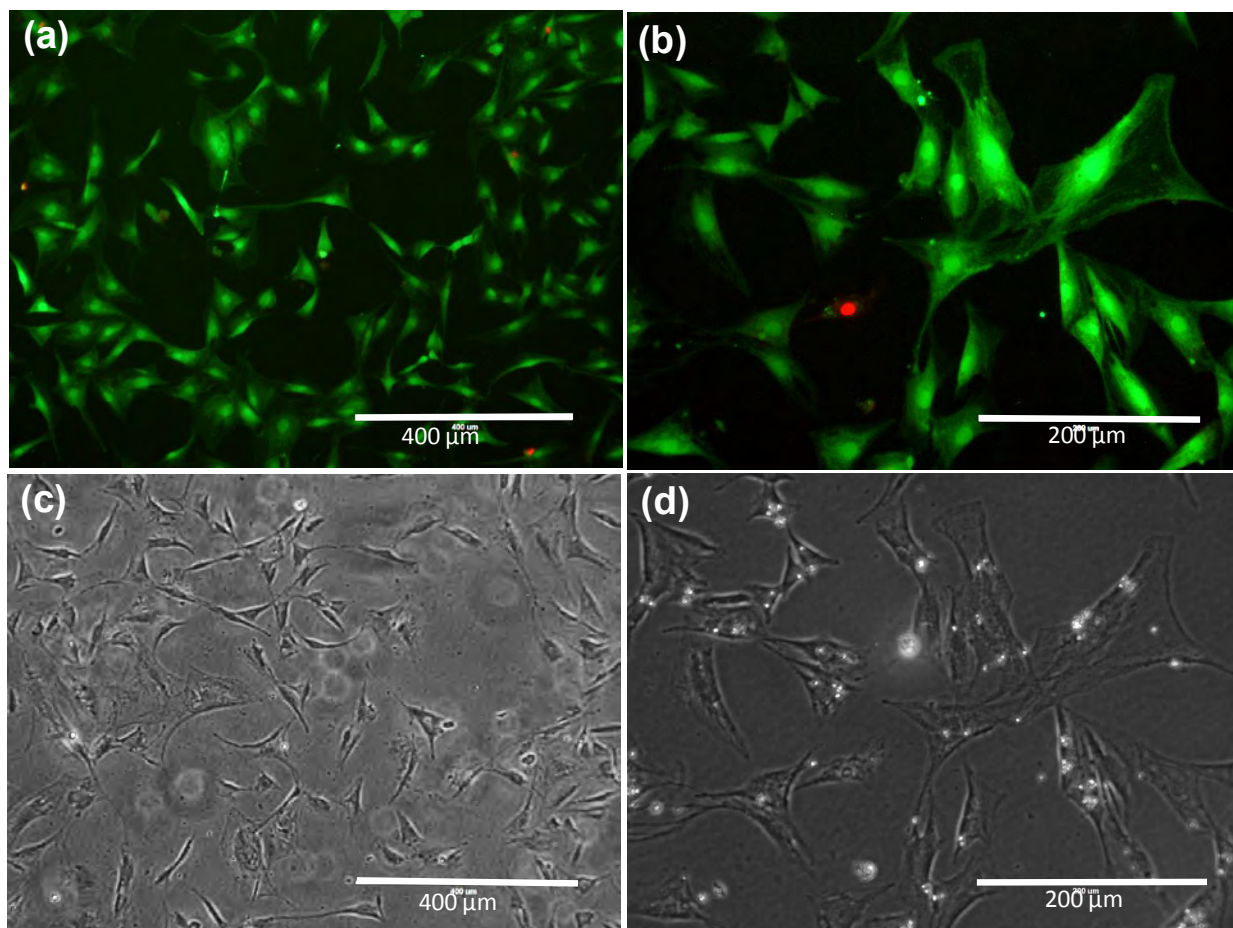
<sup>‡</sup>Environmental and Water Resources Engineering (EWRE) Division, Department of Civil Engineering, Indian Institute of Technology Madras, Chennai 600 036, India.

\* Corresponding Author: (T.P.) E-mail: pradeep@iitm.ac.in. Fax: +91-44-2257-0545.

## TABLE OF CONTENTS

Supporting Figure	Title	Page No.
Figure S1	Control experiment for live dead staining assay – CaCO <sub>3</sub> treatment	S2
Figure S2	Control experiment for live dead staining assay – Na <sub>2</sub> CO <sub>3</sub> treatment	S3
Figure S3	Characterization and chemical composition of the precipitates formed on cells during CaCO <sub>3</sub> treatment	S4
Figure S4	Control experiment for morphological study - 40 ppm of calcium carbonate and sodium carbonate	S5
Figure S5	Effect of Na <sub>2</sub> CO <sub>3</sub> on the toxicity	S6
Figure S6	A comparative analysis of Arsenate uptake by cells in the presence of carbonates	S7
Figure S7	Control experiment for ROS staining – H <sub>2</sub> O <sub>2</sub> stressed cells	S8
Figure S8	pH profiling of treated cells using bromothymol blue	S9
Figure S9	CV curve of PBS	S10

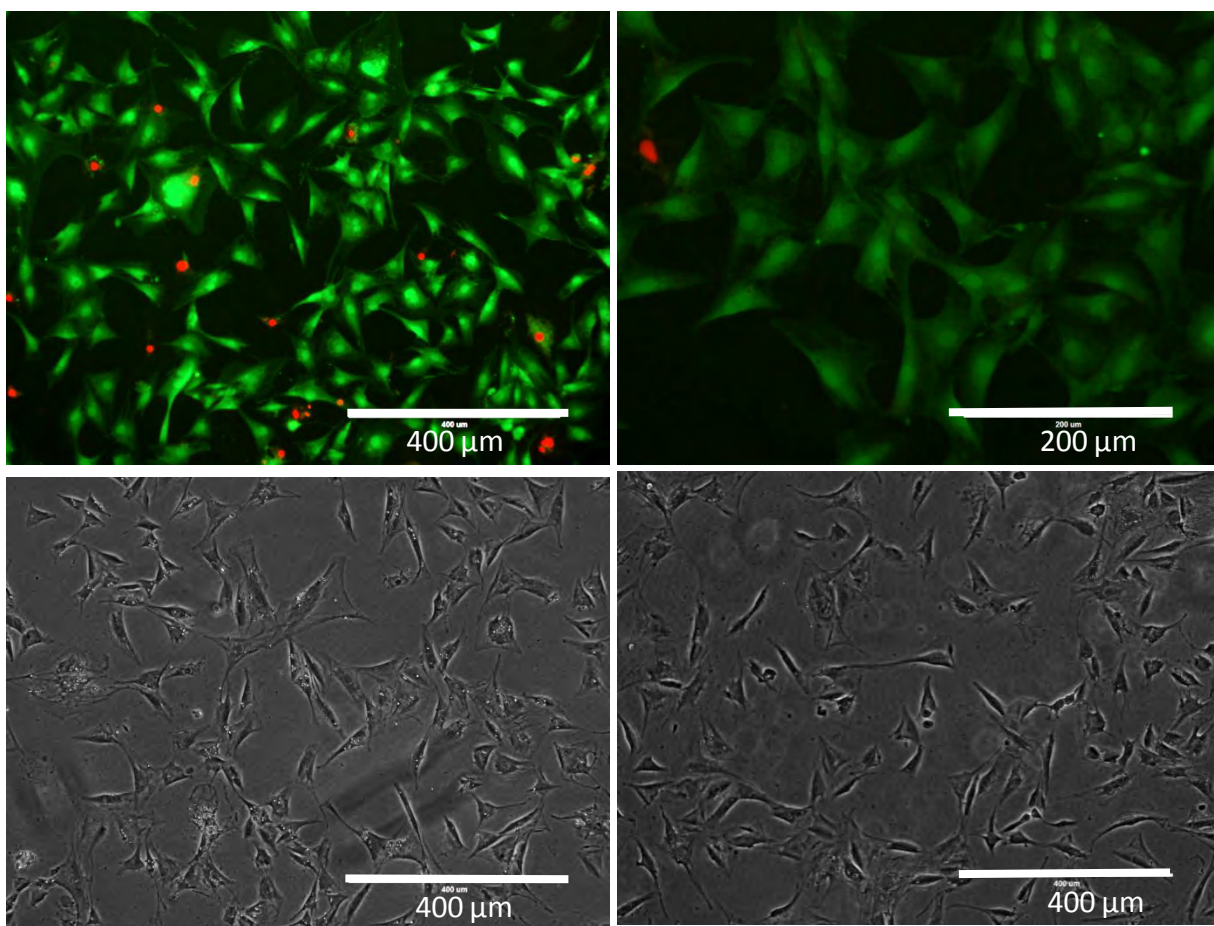
15    **Supporting information 1**



16  
17    **Figure S1.** Control experiment for live dead staining assay – CaCO<sub>3</sub> treatment. (a) and (b)  
18    Fluorescence microscopy image of IEC-6 cells treated with 40 ppm of calcium carbonate at two  
19    different magnifications. 40 ppm of CaCO<sub>3</sub> used for the studies was found to be non-toxic to the  
20    cells. (c) and (d) Phase contrast microscopy images showing precipitates of CaCO<sub>3</sub> on the surface  
21    of the cells.



22    **Supporting information 2**



23  
24    **Figure S2.** Control experiment for live dead staining assay –  $\text{Na}_2\text{CO}_3$  treatment. Fluorescence  
25    microscopy images (a and b) and phase contrast microscopy image (c and d) of IEC-6 cells with  
26    40 ppm of sodium carbonate. 40 ppm of sodium carbonate used for the studies was found to be  
27    non-toxic to the cells.

Supporting information 3

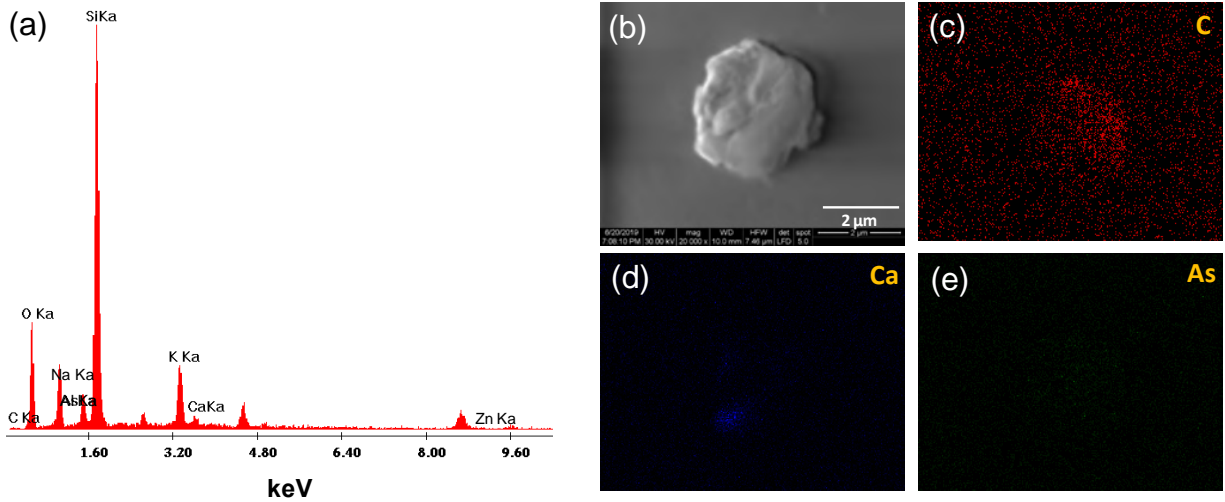
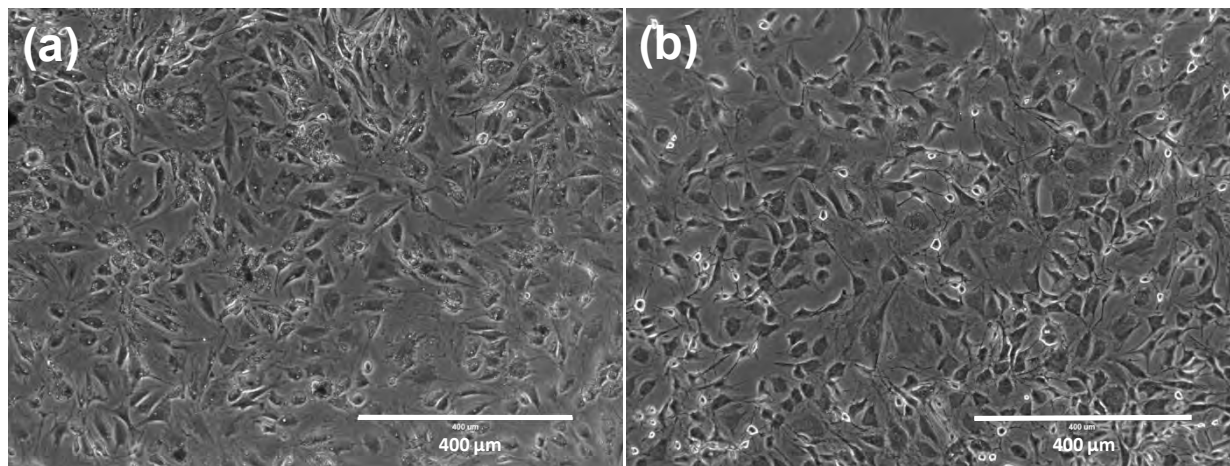


**Figure S3.** Characterization and chemical composition of the precipitates formed on cells during  $\text{CaCO}_3$  treatment. EDS spectrum (a) and the SEM image (b) of the precipitate along with (c-e) elemental maps are shown. No complexes of arsenic were formed as *As* is absent. Scale bars in c-e are the same as in b.

34 **Supporting information 4**



35  
36 **Figure S4.** Phase-contrast images of control experiment for morphological study - 40 ppm of  
37 calcium carbonate and sodium carbonate. Treatment of IEC-6 cells with (a) 40 ppm of calcium  
38 carbonate and (b) 40 ppm of sodium carbonate (control experiments). Precipitates of  $\text{CaCO}_3$   
39 were found on the surface of the cells. 40 ppm of  $\text{CaCO}_3$  and  $\text{Na}_2\text{CO}_3$  used for the studies did not  
40 alter the cellular morphology.

Supporting information 5

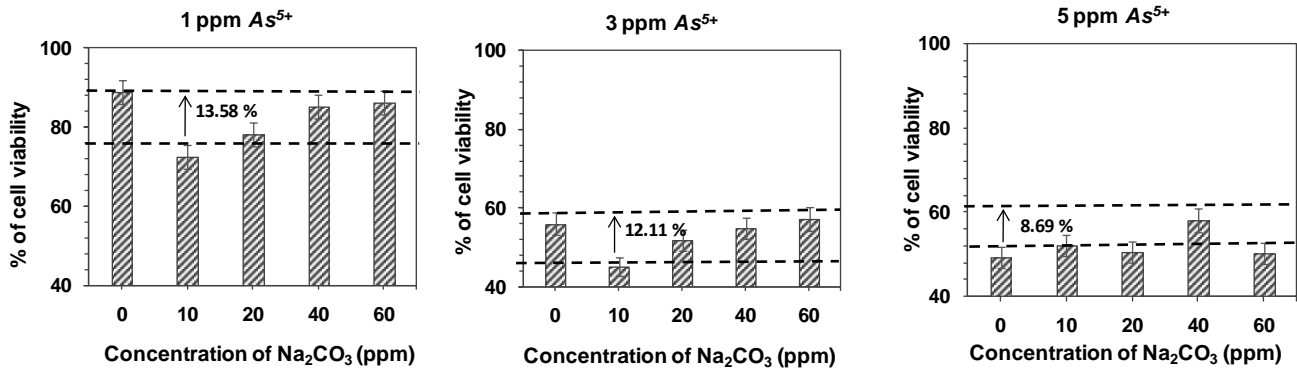
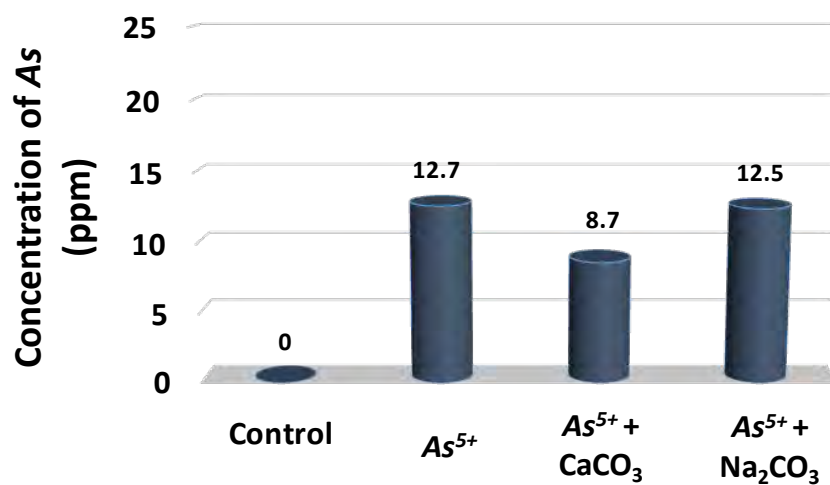


**Figure S5.** Effect of  $\text{Na}_2\text{CO}_3$  on the toxicity induced by varying concentrations (1 ppm, 3 ppm and 5 ppm) of arsenate ( $\text{As}^{5+}$ ). The percentage of cell viability was measured using the MTT assay. The difference between the heights of dashed lines represent the percentage of increase in viability of the cells.



48  
 49 **Figure S6.** A comparative analysis of  $As^{5+}$  concentration in cells in presence of 40 ppm of  
 50  $CaCO_3$  and  $Na_2CO_3$ .



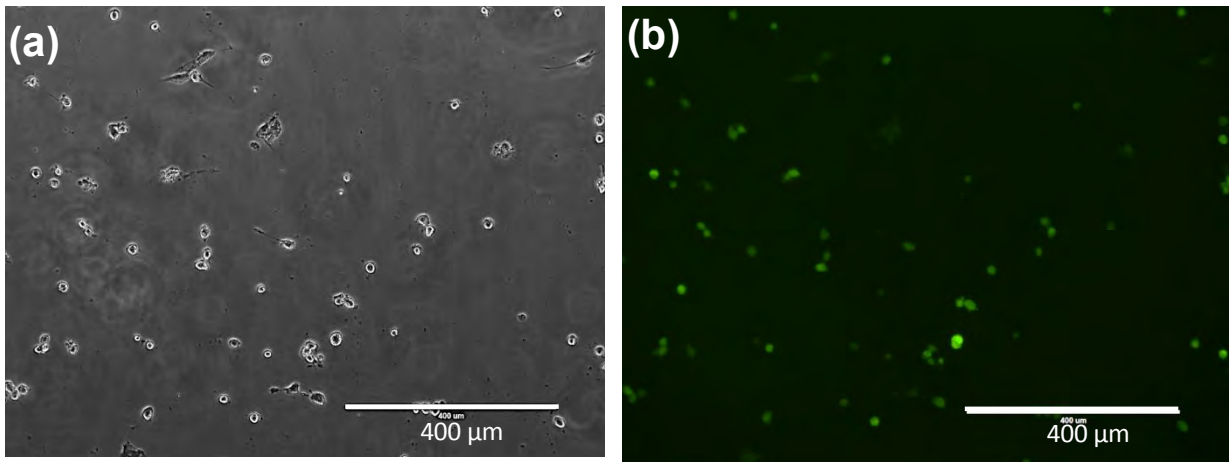


**Figure S7.** Control experiment for ROS staining. IEC – 6 cells treated with 1 mM hydrogen peroxide for 1 h induced ROS production and showed fluorescence on staining. (a) Phase contrast microscopy image. (b) Fluorescence microscopy image.

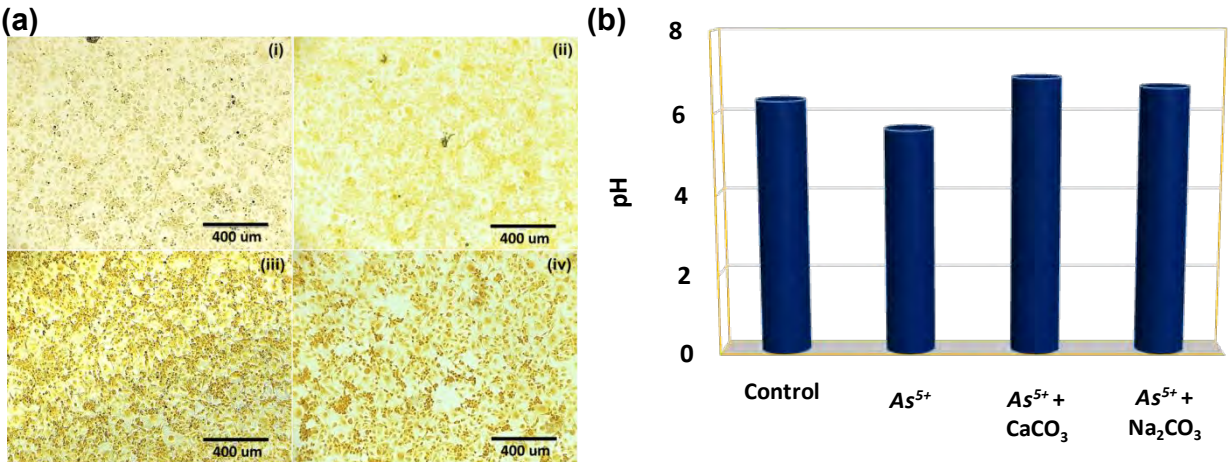
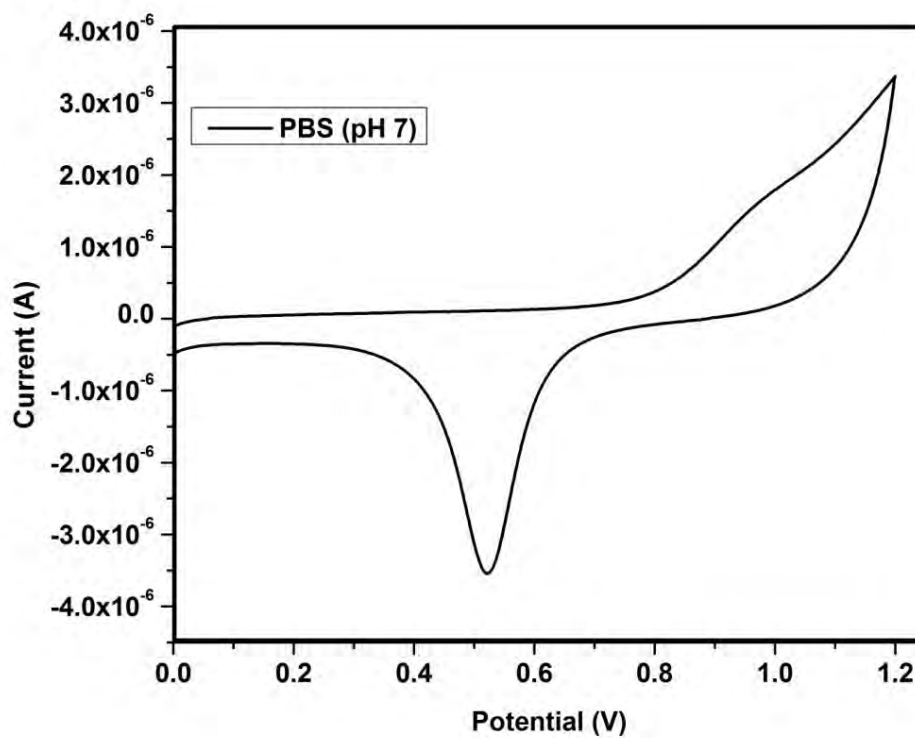


**Figure S8.** pH profiling of treated cells using bromothymol blue (a) Bright-field optical microscopy images of cells stained with BTB; (i) Control (ii) 3 ppm  $As^{5+}$  (iii) 3 ppm  $As^{5+}$  + 40 ppm  $CaCO_3$  (iv) 3 ppm  $As^{5+}$  + 40 ppm  $Na_2CO_3$ . (b) Histogram of the pH distribution for treated cells.



63

64 **Figure S9.** CV curve of PBS (pH=7) used in the cyclic voltammetry experiment demonstrating  
65  $\text{H}_2\text{O}_2$  decomposition by  $\text{CaCO}_3$ .



Cite this: DOI: 10.1039/c9an02043h

# Ligand structure and charge state-dependent separation of monolayer protected Au<sub>25</sub> clusters using non-aqueous reversed-phase HPLC†

Korath Shivan Sugi,<sup>a</sup> Shridevi Bhat,<sup>a</sup> Abhijit Nag,<sup>a</sup> Paramasivam Ganesan,<sup>a</sup> Ananthu Mahendranath<sup>a,b</sup> and Thalappil Pradeep<sup>a\*</sup>

The synthesis of atomically precise noble metal clusters using various protocols often results in a mixture of clusters with different cores. Hence, it is important to isolate such clusters in their pure form in terms of composition especially for crystallization. High-performance liquid chromatography (HPLC) is a powerful tool to achieve this. The interaction of ligands with column functionalities determine the extent of separation and their stability under conditions used. We demonstrate a systematic flow rate dependent study of three different aliphatic ligand protected Au<sub>25</sub> clusters, with three commercially available alkyl and aryl functionalized reversed-phase HPLC columns, as they represent the variations encountered commonly. Molecular docking simulations were carried out to understand the interactions between the stationary phase and the cluster surface. These investigations enabled the selection of an appropriate column for better separation of structurally different ligand protected clusters. High-resolution separation of anionic and neutral Au<sub>25</sub> clusters was achieved with a selectivity ( $\alpha$ ) of 1.2 by tuning the chromatographic conditions. This study would provide new insights in developing better methods for the efficient separation of monolayer protected clusters.

Received 11th October 2019,  
Accepted 3rd January 2020

DOI: 10.1039/c9an02043h

rsc.li/analyst

## Introduction

Atomically precise monolayer-protected clusters (MPCs)<sup>1,2</sup> of noble metals are attractive due to their unique size and ligand-dependent properties. Several properties of clusters can be tuned by varying their protecting ligands. Their unique optical absorption,<sup>3</sup> luminescence,<sup>4,5</sup> mechanical,<sup>6</sup> nonlinear,<sup>7,8</sup> and catalytic<sup>9,10</sup> properties can be tailored significantly by using different ligands such as phosphines,<sup>11,12</sup> thiols,<sup>13</sup> alkynyls,<sup>14</sup> and mixed ligands.<sup>15</sup> Among them, the thiolate ligands are widely used, and their structures play a pivotal role in controlling the clusters; in terms of the inner metal core, metal-ligand interfaces having staple motifs. An investigation of three structurally different ligands resulted in clusters having different core and staple motifs with unique optical pro-

perties.<sup>16</sup> In this context, knowledge of their total structure is essential to bridge the gap in understanding their properties in detail. The purity of MPCs is a crucial factor affecting the growth of single crystals of clusters and their applications in sensing,<sup>17</sup> imaging,<sup>18</sup> and catalysis.<sup>10,19</sup> There are several methods to purify and isolate MPCs which include fractional precipitation,<sup>20</sup> ultracentrifugation,<sup>21</sup> gel electrophoresis,<sup>22</sup> thin layer chromatography (TLC),<sup>23</sup> size-exclusion chromatography (SEC),<sup>24</sup> and capillary electrophoresis.<sup>25</sup> However, these techniques have certain limitations. In the case of SEC and electrophoresis, selectivity is a major issue.<sup>26</sup>

The reversed-phase high-performance liquid chromatography (RP-HPLC) is an established technique for the high-resolution separation of organic molecules.<sup>27</sup> In 2003, Murray and co-workers separated gold clusters protected with hexane thiol, *N*-acetyl-L-cysteine and tiopronin by RP-HPLC.<sup>28,29</sup> In recent years, Negishi and co-workers have been working extensively on developing new RP-HPLC methodologies for the separation of clusters. They have designed several methods to achieve the separation of clusters according to the number of constituent atoms,<sup>30–32</sup> chemical composition,<sup>33</sup> structural isomers,<sup>19</sup> and coordination isomers.<sup>34</sup> Recently, Knoppe *et al.*, successfully isolated and characterized mass spectrometrically silent Au<sub>40</sub>(DDT)<sub>24</sub> clusters<sup>26</sup> using RP-HPLC but, they were not successful in isolating phenylethane thiol protected

<sup>a</sup>DST Unit of Nanoscience (DST UNS) and Thematic Unit of Excellence (TUE), Department of Chemistry, Indian Institute of Technology Madras, Chennai 600 036, India. E-mail: pradeep@iitm.ac.in

<sup>b</sup>Department of Metallurgical and Materials Engineering, Indian Institute of Technology Madras, Chennai 600036, India

†Electronic supplementary information (ESI) available: Computational details, online UV-vis spectra of clusters in different columns, docked energy minimum conformers of clusters, concentration dependent studies and peak fitting parameters. See DOI: 10.1039/c9an02043h

clusters. Important issues in HPLC based separation of clusters are their solubility and stability, which are predominantly controlled by the protecting ligands. Due to enhanced stability the separation of  $\text{Au}_{24}\text{Pd}$  clusters has been studied extensively.<sup>19,34</sup> Irreversible adsorption of the clusters to column due to the high surface area of the stationary phase can complicate cluster separation.<sup>35</sup> This issue can limit the use of different types of columns for cluster separation. Moreover, the use of buffer solution in the mobile phase can result complications in preparing the mobile phase and shorten the lifetime of the chromatographic columns.<sup>35</sup> However, to achieve higher resolution and better separation, a deeper understanding of the interactions between the stationary phase and the cluster surface is required.

In this work, we have performed a flow rate dependent elution study of three different and commonly used ligand protected  $\text{Au}_{25}$  clusters, over three standard RP-HPLC columns. We have chosen  $\text{Au}_{25}$  clusters as model system for our experiments due to their exceptional stability and robustness towards different ligands. The alkyl functionalized  $\text{C}_{18}$ ,  $\text{C}_8$ , and aryl functionalized phenylhexyl RP-HPLC columns were used. We have also performed molecular docking simulations to understand the noncovalent interactions between the cluster surface and the stationary phase. This study reveals deep insights into the interaction of cluster surfaces having different polarities with alkyl and aryl stationary phases. It also provides helpful information in choosing appropriate columns for the separation of clusters protected with structurally different ligands. We have successfully separated the anionic and neutral  $\text{Au}_{25}$  clusters from the mixture by optimising the chromatographic parameters.

## Experimental

### Chemicals

Chloroauric acid trihydrate ( $\text{HAuCl}_4 \cdot 3\text{H}_2\text{O}$ ), dodecanethiol (DDT), octanethiol (OT), phenylethanethiol (PET), tetraoctylammonium bromide (TOAB), and sodium borohydride ( $\text{NaBH}_4$ ) were purchased from Sigma Aldrich. The solvents such as tetrahydrofuran (THF), dichloromethane (DCM), and methanol (MeOH) were purchased from Merck and were of HPLC grade. All the chemicals were used as such without any further purification.

### Synthesis of $[\text{Au}_{25}(\text{SR})_{18}]^-$ clusters

The  $\text{Au}_{25}(\text{DDT})_{18}$ ,  $\text{Au}_{25}(\text{OT})_{18}$ , and  $\text{Au}_{25}(\text{PET})_{18}$  clusters were synthesized according to reported methods.<sup>36</sup> Briefly, 2 mL of 50 mM  $\text{HAuCl}_4 \cdot 3\text{H}_2\text{O}$  in THF was diluted to 7.5 mL using THF. To this, about 65 mg of TOAB was added and stirred for 30 min at room temperature. A yellow to deep red color change was observed. About 0.5 mmol of thiol was added to this solution. The deep red color slowly turned to yellow and eventually became colorless after about 45 min. After 2 h, 2.5 mL of ice-cold aqueous  $\text{NaBH}_4$  (0.2 M) was added. The solution turned black immediately and the reaction was continued for 6 h. The

obtained crude cluster solution was evaporated and washed with MeOH repeatedly. After MeOH wash they are extracted in acetone. The acetone fraction was vacuum-dried, and the pure nanocluster was extracted in DCM.

### Conversion of $[\text{Au}_{25}(\text{SR})_{18}]^-$ clusters to $[\text{Au}_{25}(\text{SR})_{18}]^0$

The purified cluster solution in DCM was kept under  $\text{O}_2$  environment for 1 h. The oxygen environment was created by an  $\text{O}_2$ -filled balloon.<sup>37</sup> The oxidation of the clusters was confirmed by monitoring the UV-vis spectrum of the clusters.

### Instrumentation

**UV-Vis spectroscopy.** UV-vis spectra of cluster samples were recorded using a Perkin Elmer Lambda 365 instrument in the range of 200–1100 nm.

**MALDI MS measurements.** Matrix-assisted laser desorption ionization mass spectrometry (MALDI MS) studies were conducted using an Applied Biosystems Voyager-DE PRO Biospectrometry Workstation. For MALDI MS measurements we have used *trans*-2-[3-(4-tertbutylphenyl)-2-methyl-2-propenylidene] malononitrile (DCTB, >98%) as matrix. Appropriate volumes of the sample and DCTB in DCM were mixed thoroughly, and spotted on the sample plate and allowed to dry at ambient conditions. All the measurements were carried out at the threshold laser fluence in order to minimize fragmentation.

**HPLC experiments.** HPLC experiments were conducted on a Shimadzu instrument consisting of a CBM-20A controller, DGU-20AR online degasser, LC20AD pump, SIL-20A autosampler, CTO-20A column oven, and SPD-M20A photodiode array (PDA) detector. The stainless-steel columns packed with 5- $\mu\text{m}$   $\text{C}_{18}$  bonded silica, (250  $\times$  4.6 mm i.d.)  $\text{C}_8$  bonded silica, (250  $\times$  4.6 mm i.d.) and phenylhexyl bonded silica (150  $\times$  4.6 mm i.d.) with a 120 Å pore size (Enable) were used for above experiments. The column temperature was maintained at 28 °C. The absorbance chromatogram was monitored by the photodiode array (PDA) and extracted at 400 nm. The UV-vis spectrum of the eluted peaks was collected over 190–800 nm by the PDA detector. Each sample was dissolved in DCM, *i.e.*, 1.0 mg of the neutral cluster in 1.0 mL of DCM. Then, 30  $\mu\text{L}$  of the sample was injected into the instrument with a mobile phase of 100% MeOH at flow rate varying from 0.5  $\text{mL min}^{-1}$  to 2.0  $\text{mL min}^{-1}$ . After sample injection, the amount of THF in the mobile phase was continuously increased using a gradient program [10] that increased the  $[\text{THF}]/[\text{MeOH}]$  ratio of the mobile phase from 0% to 100%. The experiments were performed with  $\text{Au}_{25}(\text{DDT})_{18}$ ,  $\text{Au}_{25}(\text{OT})_{18}$  and  $\text{Au}_{25}(\text{PET})_{18}$  clusters.

## Results and discussion

Reversed-phase HPLC is emerging as a widely used technique for the separation of gold clusters. Generally, atomically precise clusters are separated in RP-HPLC by non-aqueous solvents due to their insolubility in aqueous solvents. However, the interaction of the column functionalities with protecting ligands of the clusters, and its effects on their separation and



stability within the column are not adequately known. To understand this aspect, we have investigated the separation of atomically precise gold clusters protected with dodecanethiol, octanethiol, and phenylethanethiol in analytical  $C_{18}$ ,  $C_8$ , and phenylhexyl columns (Fig. S1, ESI†). We will denote them as clusters I, II, and III, respectively in the following discussion. The synthesis of clusters I, II, and III are carried out according to the published procedures<sup>36</sup> and characterized by MALDI mass spectrometry (Fig. S2, ESI†) and UV-vis spectroscopy (Fig. 1a). We have used neutral clusters in our study as anions do not interact actively with the stationary phase.<sup>38</sup> The oxidation of clusters was carried out by keeping them in  $O_2$  environment<sup>37</sup> and the conversion was confirmed from the UV-vis spectrum (Fig. 1a). The neutral cluster solution was injected into the column in DCM and eluted with MeOH-THF as the mobile phase.<sup>19</sup> We have used a linear gradient [10] program as described in Fig. S3† to elute the clusters.<sup>19</sup> In our method, the separation was accomplished in two steps. First, upon injection, the clusters were adsorbed onto the stationary phase (the column) when MeOH was passed, thereby enhancing the interaction of the clusters with the stationary phase.

Next, the adsorbed clusters were eluted slowly from the stationary phase depending on their surface polarity. This was accomplished by gradually adjusting the mobile phase from pure MeOH to THF using a linear gradient [10] program. We have used the linear gradient [10] program as increasing the gradient time resulted in peak broadening. In this elution process, the injection solvent was eluted in the initial stage,<sup>19</sup> whose effect was unlikely in the retention process of the clusters. The peaks in the chromatogram were analysed from the online UV-vis spectrum recorded by the PDA detector. The strength of the interaction with the stationary phase is reflected in the retention time ( $t_R$ ). Scheme 1 shows the schematic representation of the separation process. We have varied the flow rate to understand its dependency on cluster separation. The flow rate was varied from  $0.5 \text{ mL min}^{-1}$  to  $2.0 \text{ mL min}^{-1}$ . We haven't used flow rate below  $0.5 \text{ mL min}^{-1}$  as our interest has been relatively faster isolation. The variation in flow rate can change the eluent volume in a linear gradient [10] program (Fig. S4, ESI†). Fig. 1a shows the UV-visible spectra of anionic and neutral cluster I. The oxidation of cluster I was evident from the increase in the intensity of the 400 nm peak and the dis-

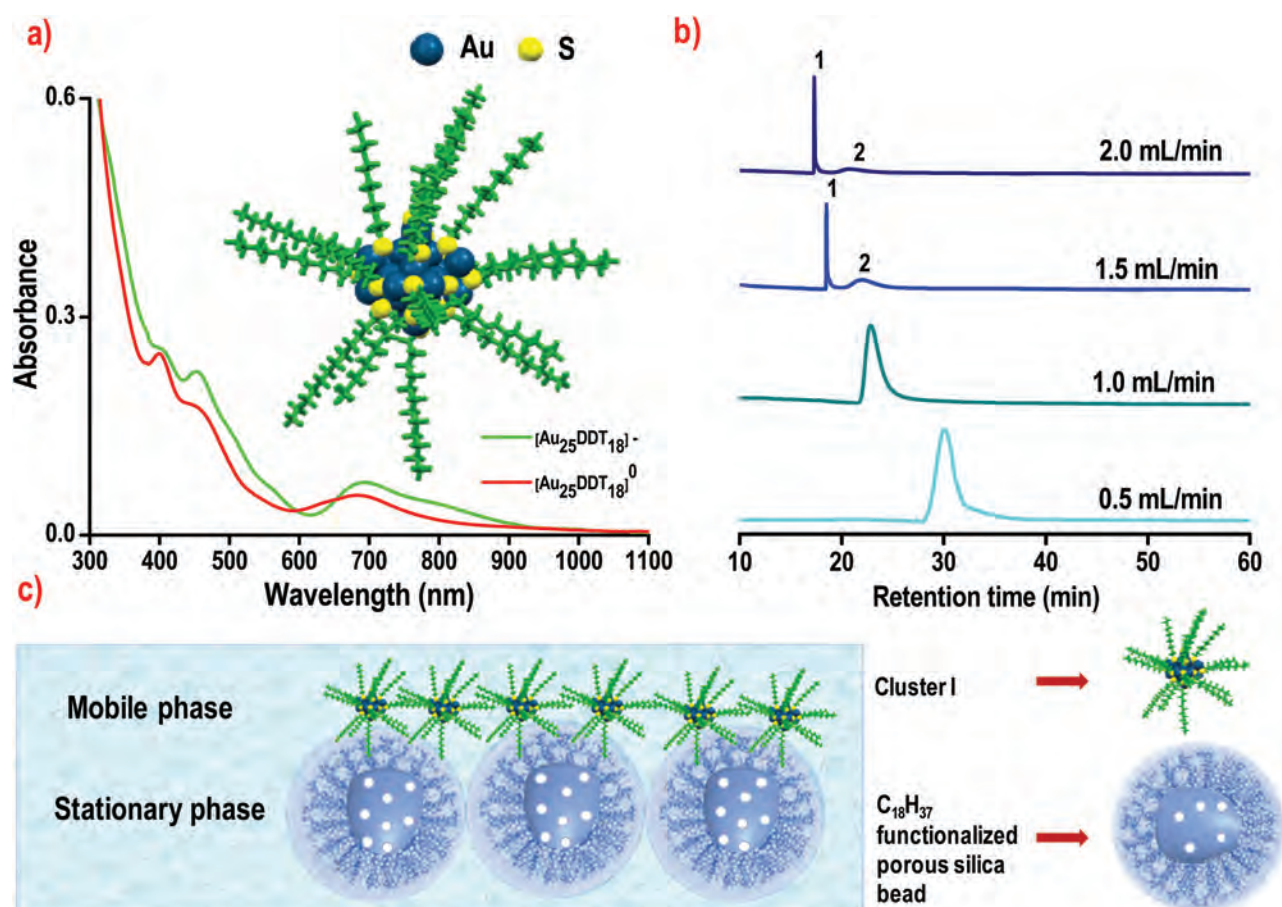
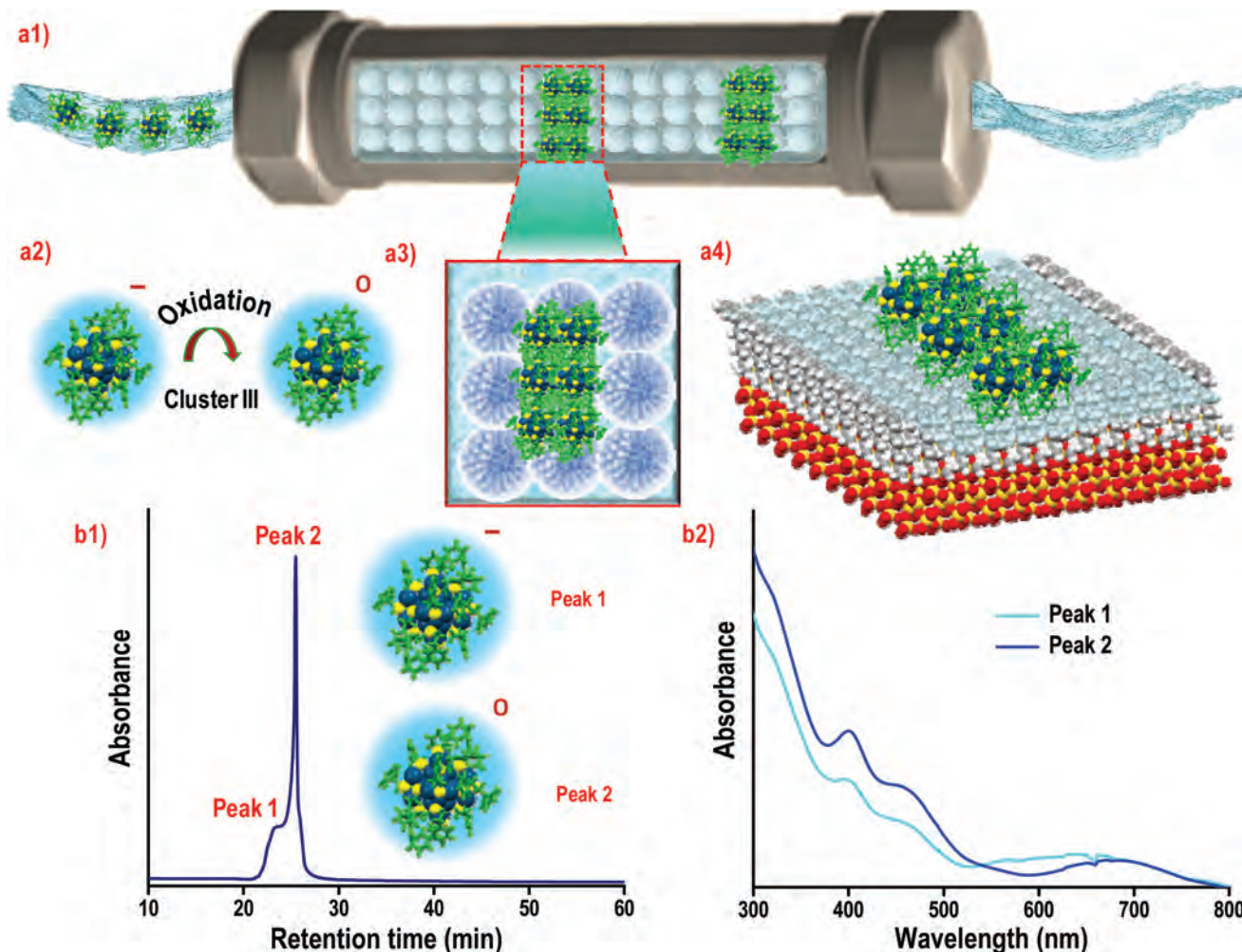


**Fig. 1** (a) The UV-vis spectra of anionic (green trace) and neutral (red trace) cluster I. Inset shows the DFT optimized structure of cluster I. (b) Chromatograms of cluster I over  $C_{18}$  column, by varying the flow rate. The mobile phase used was MeOH-THF with a linear gradient [10] program. (c) Schematic representation of the strong hydrophobic interaction between the  $C_{18}$  functionalized silica beads and the ligands of cluster I. Color labels: teal, Au; yellow, S; green, DDT ligands.



**Scheme 1** Separation of Au<sub>25</sub> clusters in RP-HPLC column. Image a1 is the schematic representation of the separation of Au<sub>25</sub> clusters over an RP-HPLC column, based on their interaction with the stationary phase. Image a2 represents the oxidation of cluster III. Images a3 and a4 are the enlarged views of silica functionality and clusters. The b1 and b2 are the chromatogram and corresponding UV-vis spectra of the separated bands, respectively.

appearance of the hump at 800 nm. The chromatograms of neutral cluster I eluted at different flow rates are shown in Fig. 1b. The  $t_R$  of cluster I at  $0.5 \text{ mL min}^{-1}$  was 32.28 min. At this flow rate, significant peak broadening and tailing were observed. The characteristic features of Au<sub>25</sub> clusters was observed in the corresponding online UV-vis spectrum (Fig. S5, ESI†). When flow rate is increased to  $1.0 \text{ mL min}^{-1}$ , the peak broadening was reduced as compared to the previous case and the clusters were eluted well. At  $1.5 \text{ mL min}^{-1}$  flow rate, the chromatogram exhibited two peaks which are labelled as peak 1 and 2 (Fig. 1b). The  $t_R$  of peak 1 and 2 are at 21.56 and 24.78 min, respectively. The online UV-vis spectrum of peak 2 doesn't show any features of clusters except a broad feature at 680 nm. This could be a decomposed fraction of cluster I which was strongly adsorbed on the column. Similar decomposition was observed in the case of  $2.0 \text{ mL min}^{-1}$  flow rate. We hypothesize that the strong hydrophobic interaction between long alkyl chain of cluster I and C<sub>18</sub> functionality of

the column (Fig. 1c) might resulted in the decomposition of a small fraction of the cluster. It also indicated that separation was better at an optimum flow rate *i.e.*,  $1.0 \text{ mL min}^{-1}$ . The peak 2 was observed only at higher flow rates which further confirmed that they were decomposed clusters rather than impurities and the peak purity index of peak 1 at  $1.5 \text{ mL min}^{-1}$  flow rate was 0.96. We have further performed the flow rate dependent elution experiments of other two clusters, *i.e.*, II and III in C<sub>18</sub> column by keeping all conditions the same. In the case of cluster II, we have observed two peaks up to  $1.5 \text{ mL min}^{-1}$  flow rate (Fig. 2). The online UV-vis spectra of peak 2 didn't show any characteristic features of the cluster (Fig. S6, ESI†), and this peak was not observed at  $2.0 \text{ mL min}^{-1}$  flow rate. This indicates that peak 2 may be due to minor impurities<sup>39</sup> present in the cluster as this peak was observed only at lower flow rates. At  $2.0 \text{ mL min}^{-1}$  flow rate, the elution was very fast and the impurities might be co-eluted along with the clusters which was evident from the reduction in peak purity index to



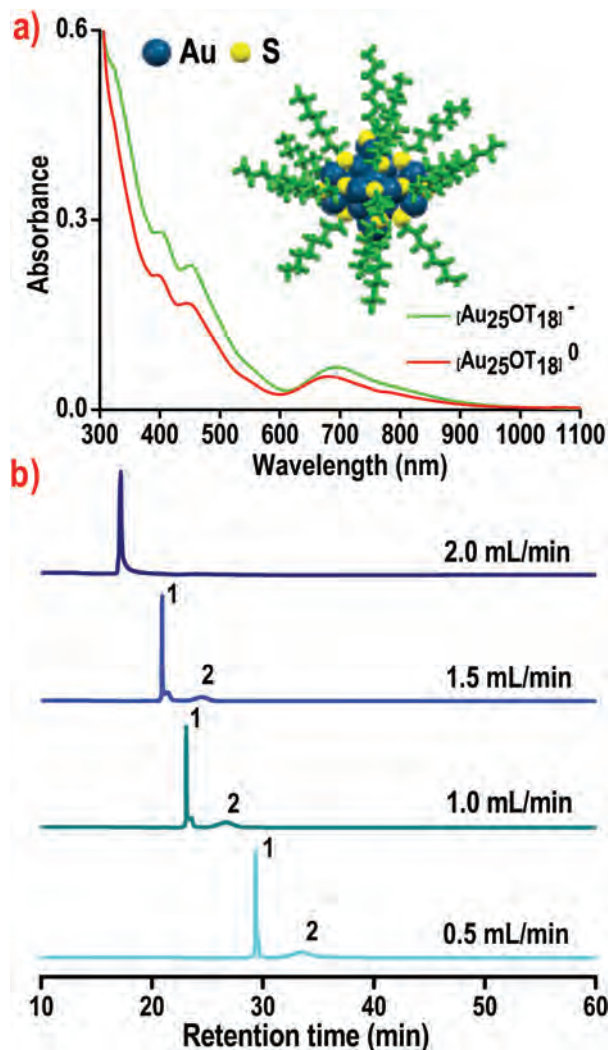


**Fig. 2** (a) The UV-vis spectra of anionic (green trace) and neutral (red trace) cluster II. The inset shows the DFT optimized structure of cluster II. (b) Chromatograms of cluster II over  $C_{18}$  column by varying the flow rate. Color labels: teal, Au; yellow, S; green, OT ligands.

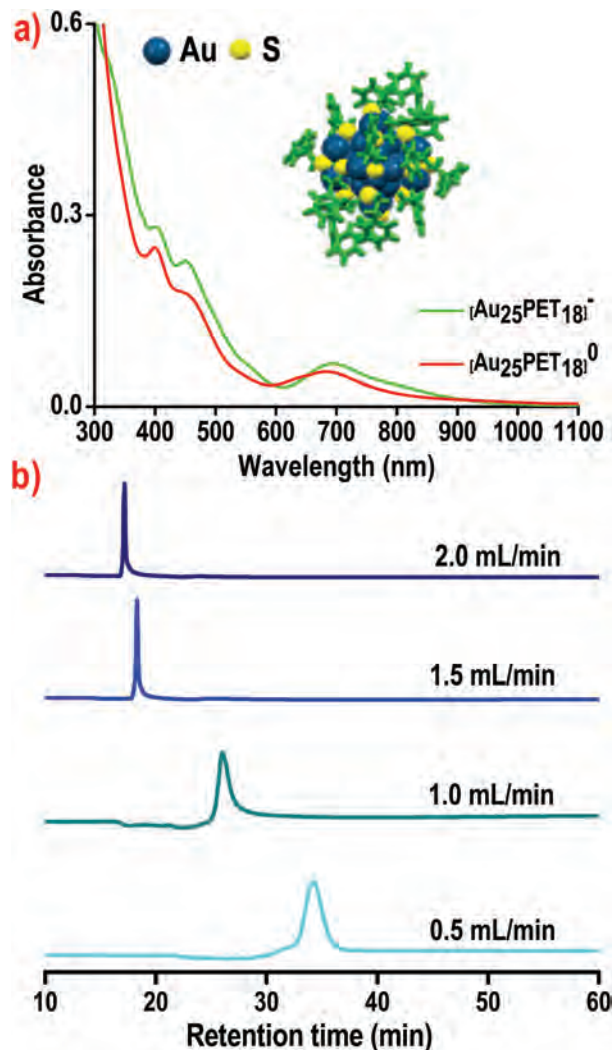


**Fig. 3** (a) The UV-vis spectra of anionic (green trace) and neutral (red trace) cluster III. The inset shows the X-ray crystal structure of cluster III. (b) Chromatograms of cluster III over  $C_{18}$  column by varying the flow rate. Color labels: teal, Au; yellow, S; green, PET ligands.

0.95. The flow rate dependent study of cluster III in  $C_{18}$  column is presented in Fig. 3. We haven't observed any decomposition/impurities of clusters in the chromatograms with increasing flow rate. Also, the peak purity index was 0.98 at  $1.5 \text{ mL min}^{-1}$ . This observation indicates that the DDT and OT protected clusters bind strongly than that of PET in a  $C_{18}$  column (Fig. S7, ESI†). We have carefully analyzed the peak width of each cluster in the  $C_{18}$  column. The  $t_R$  and peak width (Fig. S8, ESI†) decreases with increase in flow rate. We have conducted similar elution experiments of these clusters with  $C_8$  column under same conditions. All the three clusters were separated well through  $C_8$  column (Fig. S9, ESI†). We didn't observe any flow rate dependent decomposition/impurities, which was further confirmed from the corresponding online UV-vis spectra (Fig. S10, ESI†). But peak broadening was observed in case of cluster III (Fig. S11, ESI†). In our investigation we have explored that the aryl ligand protected clusters

are eluting well in all the tested flow rates without decomposition in  $C_{18}$  and  $C_8$  columns. So, we extended our flow rate dependent experiments to aryl functionalized phenylhexyl column to understand its effect on cluster separation. We observed that clusters I and II are eluted well (Fig. 4) in all the tested flow rates without any decomposition on this column (Fig. S12, ESI†). In the case of cluster III, the chromatogram of  $0.5 \text{ mL min}^{-1}$  flow rate shows two peaks, i.e., a small hump at 23.08 min and a peak at 25.47 min which are labelled as peak 1 and 2 in Fig. 5. The online UV-vis spectra of peaks 1 and 2 show features at 400, 450, and 680 nm, but in case of peak 1 the intensity of 400 nm feature was very less compared to that of peak 2. This observation implies that peak 1 and 2 are anionic and neutral cluster III (Fig. 5b). With increasing the flow rate, the small fraction of anionic cluster III present in the solution was transformed entirely into the neutral cluster which was evident from the disappearance of peak 1 in the

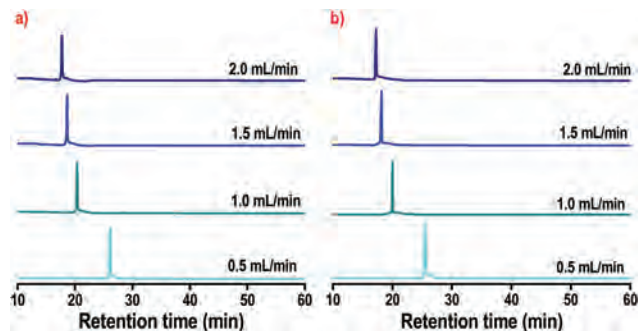


Fig. 4 Chromatograms of cluster (a) I and (b) II at different flow rates over phenylhexyl column.

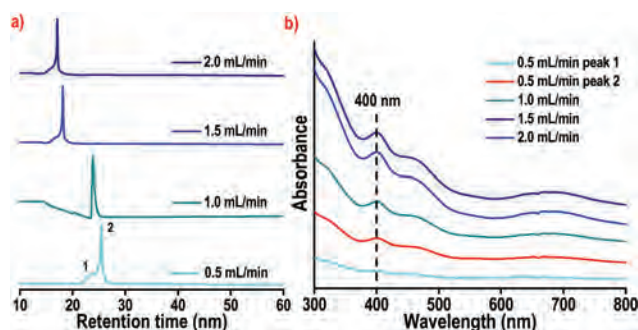


Fig. 5 (a) Flow rate dependent chromatograms of cluster III over phenylhexyl column. (b) The corresponding online UV-vis spectra.

chromatograms at higher flow rates (Fig. 5). Such change in the oxidation state was not observed in the chromatograms of clusters, I and II. This observation implies that the alkyl thiol protected  $\text{Au}_{25}$  clusters oxidizes fast compared to the PET protected clusters.<sup>40</sup> The peak width analysis of the chromatogram reveals that the peak widths of clusters I and II are lesser than that of cluster III (Fig. S13, ESI†). A plot of the  $t_R$  vs. flow rate of all the three clusters are shown in Fig. 6. The  $t_R$  decreases exponentially with the flow rate, and the data could be fitted with a function of the form  $t_R = A \cdot (\exp(-x/b) + c)$  where 'x' is the flow rate in  $\text{mL min}^{-1}$ . The fitting parameters A, b, and c are listed in Table S1.† This plot provides insights

into the interaction of the three structurally different ligand protected clusters with different columns. It is evident from the plot that  $t_R$  of clusters I, II, and III in phenylhexyl column are similar, which indicates that the phenylhexyl column separates alkyl and aryl ligand protected clusters with the same efficiency.

We have also tried to separate neutral and anionic  $\text{Au}_{25}$  clusters from their mixture. For this, a mixture containing 0.5 mg of anionic (labelled as cluster IIIa) and 0.5 mg of neutral cluster (III) in 1 mL DCM was prepared and eluted at  $1 \text{ mL min}^{-1}$  flow rate. The chromatogram (Fig. 7) shows the high-resolution separation of anionic and neutral cluster which eluted according to their affinity towards the stationary phase (Fig. S14, ESI†). The ratio of retention factor (K) between

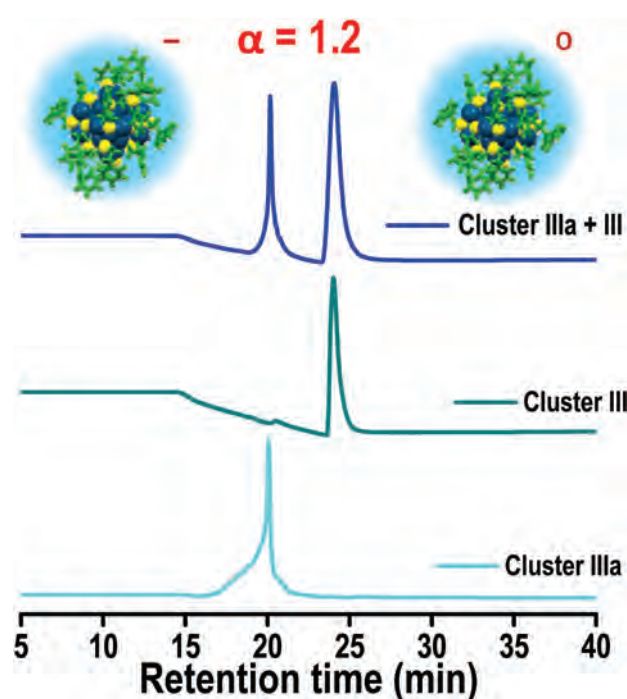


Fig. 7 High-resolution separation of anionic and neutral cluster III over phenylhexyl column at  $1 \text{ mL min}^{-1}$  flow rate using linear gradient [10] program.

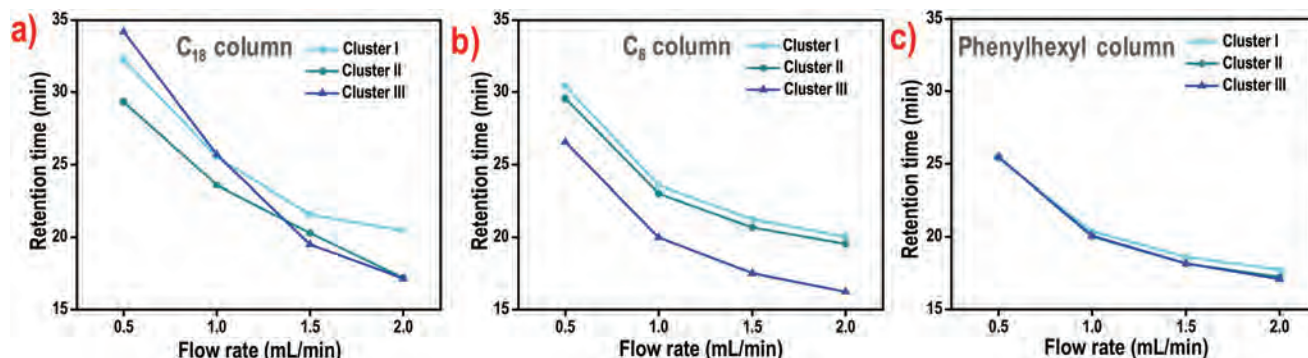


Fig. 6 Variation of the  $t_R$  with flow rate of clusters I, II, and III in (a)  $\text{C}_{18}$ , (b)  $\text{C}_8$ , and (c) phenylhexyl columns.



**Table 1** The binding energies of clusters I, II, and III on C<sub>18</sub>, C<sub>8</sub>, and phenylhexyl columns

Column	Cluster I (kcal mol <sup>-1</sup> )	Cluster II (kcal mol <sup>-1</sup> )	Cluster III (kcal mol <sup>-1</sup> )
C <sub>18</sub>	-6.09	-2.35	-3.83
C <sub>8</sub>	-6.09	-5.99	-10.67
Phenylhexyl	-6.55	-6.02	-8.53

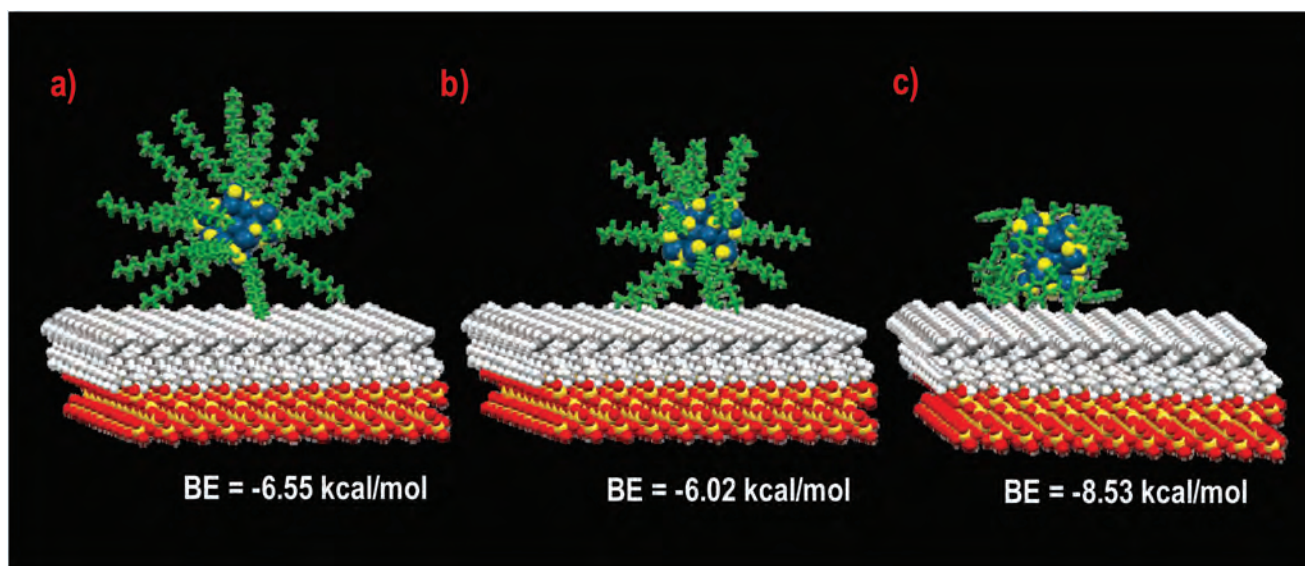
the two peaks is the selectivity 'α' of the HPLC method and it was found to be 1.2.

Molecular docking studies were carried out to understand the interaction of structurally different ligands with the stationary phases used. The docking was performed using the Autodock 4.2 and AutoDock Tools programs.<sup>41</sup> We used the cluster as "ligand", and stationary phase as "receptor" and only the noncovalent interactions were taken into account. The docking study provides information about the binding energies (BE) and the low energy conformations of the stationary phase-analyte complexes. However, the molecular docking study was performed without taking into account the effect of solvent and flow rate used in the real separation. The binding energy values are presented in Table 1. The BE values were negative for all clusters in the RP columns used, revealing that the interaction between stationary phase and cluster are an enthalpy-driven and spontaneous process.<sup>42</sup> The BE of cluster I with C<sub>18</sub> column was higher compared to that of II and III. The stable low energy confirmations between octadecyl silyl functionality and clusters I, II, and III are shown in Fig. S15.† With C<sub>8</sub> column the BEs of clusters I and II show a similar trend as that of the *t<sub>R</sub>* (Fig. S16, ESI†). In the case of cluster III, the BE is -10.67 kcal mol<sup>-1</sup> whereas, the *t<sub>R</sub>* is very less for the same. This indicates that the contributions of other factors such as solvent, flow rate, and entropy are inevitable. In

phenylhexyl column BEs of clusters I, II, and III are -6.55, -6.02, -8.53 kcal mol<sup>-1</sup> (Fig. 8). The slightly higher BE value in the case of cluster III could be due to the π-π interactions between the aryl stationary phase and the PET ligand. The BEs (without solvent) obtained by molecular docking were expected to be higher than the experimental results obtained from the HPLC (with solvent) analyse because docking considers enthalpic contribution alone. Nevertheless, a good qualitative agreement was observed, and the docking results may significantly contribute to the understanding of the nature of intermolecular forces responsible for the separation. The factors such as solvent, entropy, and flow rate contributions had to be taken into consideration to obtain the separation quantitatively, which were thought to reduce the differential interaction energy predicted by the simulation study.<sup>43,44</sup> As all the three clusters retain identically in phenylhexyl column, a concentration-dependent elution studies were carried out with cluster III. We have used three different concentrations, *i.e.*, 0.8, 4.0, and 8.0 mg of neutral cluster III, in 1.0 mL DCM by keeping 1.0 mL min<sup>-1</sup>, as optimum flow rate (Fig. S17, ESI†). The peak area *vs.* concentration shows a linear relationship (Fig. S18, ESI†). With regard to the values of BE and *t<sub>R</sub>*, the aliphatic ligands such as DDT and OT protected clusters bind strongly to long chain alkyl functionalised columns which allows the separation of small fractions of decomposed products/impurities whereas, aryl columns are better to separate clusters protected with PET where π-π interactions are involved.

## Conclusions

Flow rate dependent elution studies were carried out with three Au<sub>25</sub> clusters protected with aliphatic ligands using C<sub>18</sub>, C<sub>8</sub>, and phenylhexyl RP-HPLC columns. We observed that the

**Fig. 8** The energy minimum conformers of phenylhexyl silyl functionality docked with clusters; (a) I, (b) II, and (c) III. Color labels: golden yellow, Si; red, O; grey, C; white, H; teal, Au; yellow, S; green, DDT, OT, and PET ligands.

aliphatic ligands such as DDT and OT protected clusters bind strongly to long chain alkyl functionalised columns which allows the separation of small fractions of decomposed products/impurities whereas, aryl columns are better to separate aryl ligand protected clusters. By tuning the chromatographic conditions, we were able to isolate the neutral and anionic PET protected clusters over the phenylhexyl column with a selectivity of 1.2. The interactions between three clusters and three alkyl and aryl stationary phases were simulated by molecular docking. The experimental findings were corroborated with the binding energy values from the docked structures. We believe that the results of this study provide new insights into the high-resolution separation of structurally different ligand protected metal clusters, and the outcome will help in developing highly efficient cluster separation methods.

## Conflicts of interest

There are no conflicts to declare.

## Acknowledgements

We thank the Department of Science and Technology, Government of India for constantly supporting our research program on nanomaterials. K. S. S. thanks the University Grants Commission (UGC), Govt. of India for a research fellowship. S. B., A. N. and A. M. thanks IIT Madras for their research fellowships. P.G. thanks IIT Madras for institute post-doctoral fellowship.

## References

- R. Jin, C. Zeng, M. Zhou and Y. Chen, *Chem. Rev.*, 2016, **116**, 10346–10413.
- I. Chakraborty and T. Pradeep, *Chem. Rev.*, 2017, **117**, 8208–8271.
- M. Zhu, C. M. Aikens, F. J. Hollander, G. C. Schatz and R. Jin, *J. Am. Chem. Soc.*, 2008, **130**, 5883–5885.
- A. Mathew, E. Varghese, S. Choudhury, S. K. Pal and T. Pradeep, *Nanoscale*, 2015, **7**, 14305–14315.
- E. Khatun, A. Ghosh, P. Chakraborty, P. Singh, M. Bodiuzzaman, P. Ganesan, G. Natarajan, J. Ghosh, S. K. Pal and T. Pradeep, *Nanoscale*, 2018, **10**, 20033–20042.
- K. S. Sugi, G. Mallikarjunachari, A. Som, P. Ghosh and T. Pradeep, *ChemNanoMat*, 2018, **4**, 401–408.
- G. Ramakrishna, O. Varnavski, J. Kim, D. Lee and T. Goodson, *J. Am. Chem. Soc.*, 2008, **130**, 5032–5033.
- S. Knoppe, M. Vanbel, S. van Cleuvenbergen, L. Vanpraet, T. Bürgi and T. Verbiest, *J. Phys. Chem. C*, 2015, **119**, 6221–6226.
- X.-K. Wan, J.-Q. Wang, Z.-A. Nan and Q.-M. Wang, *Sci. Adv.*, 2017, **3**, e1701823.
- S. Yamazoe, K. Koyasu and T. Tsukuda, *Acc. Chem. Res.*, 2014, **47**, 816–824.
- M. S. Bootharaju, R. Dey, L. E. Gevers, M. N. Hedhili, J.-M. Basset and O. M. Bakr, *J. Am. Chem. Soc.*, 2016, **138**, 13770–13773.
- Y. Shichibu, M. Zhang, Y. Kamei and K. Konishi, *J. Am. Chem. Soc.*, 2014, **136**, 12892–12895.
- R. Jin, *Nanoscale*, 2015, **7**, 1549–1565.
- Z. Lei, X.-K. Wan, S.-F. Yuan, Z.-J. Guan and Q.-M. Wang, *Acc. Chem. Res.*, 2018, **51**, 2465–2474.
- A. Das, T. Li, K. Nobusada, Q. Zeng, N. L. Rosi and R. Jin, *J. Am. Chem. Soc.*, 2012, **134**, 20286–20289.
- M. Rambukwella, N. A. Sakthivel, J. H. Delcamp, L. Sementa, A. Fortunelli and A. Dass, *Front. Chem.*, 2018, **6**, 330.
- L.-Y. Chen, C.-W. Wang, Z. Yuan and H.-T. Chang, *Anal. Chem.*, 2015, **87**, 216–229.
- L. Polavarapu, M. Manna and Q.-H. Xu, *Nanoscale*, 2011, **3**, 429–434.
- Y. Niihori, M. Matsuzaki, T. Pradeep and Y. Negishi, *J. Am. Chem. Soc.*, 2013, **135**, 4946–4949.
- P. R. Nimmala, B. Yoon, R. L. Whetten, U. Landman and A. Dass, *J. Phys. Chem. A*, 2013, **117**, 504–517.
- R. P. Carney, J. Y. Kim, H. Qian, R. Jin, H. Mehenni, F. Stellacci and O. M. Bakr, *Nat. Commun.*, 2011, **2**, 335.
- T. G. Schaaff and R. L. Whetten, *J. Phys. Chem. B*, 2000, **104**, 2630–2641.
- A. Ghosh, J. Hassinen, P. Pulkkinen, H. Tenhu, R. H. A. Ras and T. Pradeep, *Anal. Chem.*, 2014, **86**, 12185–12190.
- S. Knoppe, J. Boudon, I. Dolamic, A. Dass and T. Bürgi, *Anal. Chem.*, 2011, **83**, 5056–5061.
- C. K. Lo, M. C. Paau, D. Xiao and M. M. F. Choi, *Electrophoresis*, 2008, **29**, 2330–2339.
- S. Knoppe and P. Vogt, *Anal. Chem.*, 2019, **91**, 1603–1609.
- I. A. Haidar Ahmad, W. Chen, H. M. Halsey, A. Klapars, J. Limanto, G. F. Pirrone, T. Nowak, R. Bennett, R. Hartman, A. A. Makarov, I. Mangion and E. L. Regalado, *Analyst*, 2019, **144**, 2872–2880.
- M. M. F. Choi, A. D. Douglas and R. W. Murray, *Anal. Chem.*, 2006, **78**, 2779–2785.
- V. L. Jimenez, M. C. Leopold, C. Mazzitelli, J. W. Jorgenson and R. W. Murray, *Anal. Chem.*, 2003, **75**, 199–206.
- Y. Negishi, T. Nakazaki, S. Malola, S. Takano, Y. Niihori, W. Kurashige, S. Yamazoe, T. Tsukuda and H. Häkkinen, *J. Am. Chem. Soc.*, 2015, **137**, 1206–1212.
- Y. Niihori, D. Shima, K. Yoshida, K. Hamada, L. V. Nair, S. Hossain, W. Kurashige and Y. Negishi, *Nanoscale*, 2018, **10**, 1641–1649.
- Y. Niihori, C. Uchida, W. Kurashige and Y. Negishi, *Phys. Chem. Chem. Phys.*, 2016, **18**, 4251–4265.
- Y. Negishi, W. Kurashige, Y. Niihori, T. Iwasa and K. Nobusada, *Phys. Chem. Chem. Phys.*, 2010, **12**, 6219–6225.
- Y. Niihori, Y. Kikuchi, A. Kato, M. Matsuzaki and Y. Negishi, *ACS Nano*, 2015, **9**, 9347–9356.
- Y. Zhang, S. Shuang, C. Dong, C. K. Lo, M. C. Paau and M. M. F. Choi, *Anal. Chem.*, 2009, **81**, 1676–1685.



- 36 Z. Wu, J. Suhan and R. Jin, *J. Mater. Chem.*, 2009, **19**, 622–626.
- 37 S. Bhat, R. P. Narayanan, A. Baksi, P. Chakraborty, G. Paramasivam, R. R. J. Methikkalam, A. Nag, G. Natarajan and T. Pradeep, *J. Phys. Chem. C*, 2018, **122**, 19455–19462.
- 38 Y. Niihori, Y. Koyama, S. Watanabe, S. Hashimoto, S. Hossain, L. V. Nair, B. Kumar, W. Kurashige and Y. Negishi, *J. Phys. Chem. Lett.*, 2018, **9**, 4930–4934.
- 39 M. Galchenko, R. Schuster, A. Black, M. Riedner and C. Klinke, *Nanoscale*, 2019, **11**, 1988–1994.
- 40 J. Jung, S. Kang and Y.-K. Han, *Nanoscale*, 2012, **4**, 4206–4210.
- 41 G. M. Morris, R. Huey, W. Lindstrom, M. F. Sanner, R. K. Belew, D. S. Goodsell and A. J. Olson, *J. Comput. Chem.*, 2009, **30**, 2785–2791.
- 42 Y. Li, D. Liu, P. Wang and Z. Zhou, *J. Sep. Sci.*, 2010, **33**, 3245–3255.
- 43 H.-W. Tsui, N. H. L. Wang and E. I. Franses, *J. Phys. Chem. B*, 2013, **117**, 9203–9216.
- 44 B. Zhu, F. Zhao, J. Yu, Z. Wang, Y. Song and Q. Li, *New J. Chem.*, 2018, **42**, 13421–13429.

## Electronic Supplementary Information

### Ligand structure and charge state-dependent separation of monolayer protected Au<sub>25</sub> clusters using non-aqueous reversed-phase HPLC

Korath Shivan Sugi,<sup>a</sup> Shridevi Bhat,<sup>a</sup> Abhijit Nag,<sup>a</sup> Ganesan Paramasivam,<sup>a</sup> Ananthu Mahendranath,<sup>a,b</sup> and Thalappil Pradeep<sup>\*a</sup>

<sup>a</sup> *DST Unit of Nanoscience (DST UNS) and Thematic Unit of Excellence (TUE), Department of Chemistry, Indian Institute of Technology Madras, Chennai 600 036, India*

<sup>b</sup> *Department of Metallurgical and Materials Engineering, Indian Institute of Technology Madras, Chennai 600036, India.*

\*E-mail: [pradeep@iitm.ac.in](mailto:pradeep@iitm.ac.in)

#### Table of contents

SL. No.	Description	Page No.
	Calculation of selectivity ( $\alpha$ )	3
	Computational methods	3
Fig. S1	Schematic representation of functionalized silica beads of reversed-phase columns	5
Fig. S2	Negative ion MALDI MS of cluster I, II, and III.	5
Fig. S3	Linear gradient program used for the separation	6
Fig. S4	Flow rate vs. eluent volume required in linear gradient [10] program	6
Fig. S5	Online UV-vis spectra of cluster I in C <sub>18</sub> column with different flow rates	7
Fig. S6	Online UV-vis spectra of cluster II in C <sub>18</sub> column with different flow rates	8
Fig. S7	Online UV-vis spectra of cluster III in C <sub>18</sub> column with different flow rates	9
Fig. S8	Variation of peak width of half maxima at different	10

	flow rates of cluster I, II, and III in C <sub>18</sub> column	
Fig. S9	Chromatograms of cluster a) I, b) II, and c) III at different flow rates in C <sub>8</sub> column	10
Fig. S10	Online UV-vis spectra of cluster I, II, and III in C <sub>8</sub> column with different flow rates	11
Fig. S11	Variation of peak width of half maxima at different flow rates of cluster I, II, and III in C <sub>8</sub> column	12
Fig. S12	Online UV-vis spectra of cluster I and II in a phenylhexyl column with different flow rates	12
Fig. S13	Variation of peak width of half maxima at different flow rates of cluster I, II, and III in phenylhexyl column	13
Table S1	Fitting parameters for the exponential fits	14
Fig. S14	Online UV-vis spectra of cluster IIIa, III, and mixture of both eluted in phenylhexyl column with 1.0 mL/min flow rate	15
Fig. S15	The energy minimum structures of octadecyl silyl functionality docked with cluster I, II, and III	15
Fig. S16	The energy minimum structures of octyl silyl functionality docked with cluster I, II, and III	16
Fig. S17	Concentration-dependent chromatograms of cluster III in the phenylhexyl column at 1.0 mL/min flow rate	16
Fig. S18	Peak area vs. concentration of cluster III in the phenylhexyl column at 1mL/min flow rate	17

### Calculation of selectivity ( $\alpha$ )

The selectivity ( $\alpha$ ) of the method is estimated using equation (1).

$$\alpha = \frac{K_2}{K_1} = \frac{t_{R2} - t_0}{t_{R1} - t_0} \quad (1)$$

Here,  $K$  = retention factor of the separation

$t_R$  = retention time of the peak

$t_0$  = dead time

### Computational methods

#### DFT calculations

The structures of Au<sub>25</sub> cluster protected with different thiols such as dodecanethiol (DDT) and octanethiol (OT) were built from the crystal structure of Au<sub>25</sub>(PET)<sub>18</sub> cluster by replacing the phenylethanethiol (PET) ligands. All the geometries were optimized using density functional theory (DFT) with projector augmented waves (PAW) as implemented in the GPAW software package.<sup>1</sup> The atomic PAW setup was used as Au(5d<sup>10</sup>6s<sup>1</sup>), S(3s<sup>2</sup>3p<sup>4</sup>), C(2s<sup>2</sup>2p<sup>2</sup>) and H(1s<sup>1</sup>), with scalar-relativistic effects included for Au. Further, these atomic orbitals were described by the DZP (double zeta plus polarization) basis set with the Perdew-Burke-Ernzerhof (PBE) exchange-correlation functional<sup>2</sup> in LCAO mode<sup>3</sup> to effectively include the interactions in the considered clusters. The geometries were relaxed with a grid spacing of 0.2 Å, and the convergence was set to minimize the residual forces without any symmetry constraints by 0.05 eV/Å.

#### Molecular docking calculations

Molecular docking studies were performed using AutoDock4.2 and its associated tools.<sup>4</sup> DFT-optimized geometries of clusters I, II, and III were used for the study. The different columns were computationally modeled by constructing a SiO<sub>2</sub> surface of ~ 5 nm by cutting out from

its crystal structure,<sup>5</sup> and the column functionalities such as octadecyl silyl, octyl silyl, and phenylhexyl silyl were attached to the silicon atoms on the SiO<sub>2</sub> surface. All the structures were built using Avogadro software package.<sup>6</sup> We used the cluster as “ligand” and stationary phase as “receptor”. Receptor grids were generated using 126 × 126 × 126 grid points in XYZ, with a grid spacing of 0.375 Å, and map types were created using AutoGrid-4.2. The grid parameter file (.gpf) was saved using MGL Tools-1.4.6.50. The docking parameter files (.dpf) were generated using MGLTools-1.4.6.50. The results of AutoDock generated an output file (.dlg), and the generated conformers were scored and ranked as per the interaction energy. Ten lowest-energy conformers were obtained. We used the Lamarckian genetic algorithm for the output file using MGLTools-1.4.6.

## Supplementary information 1

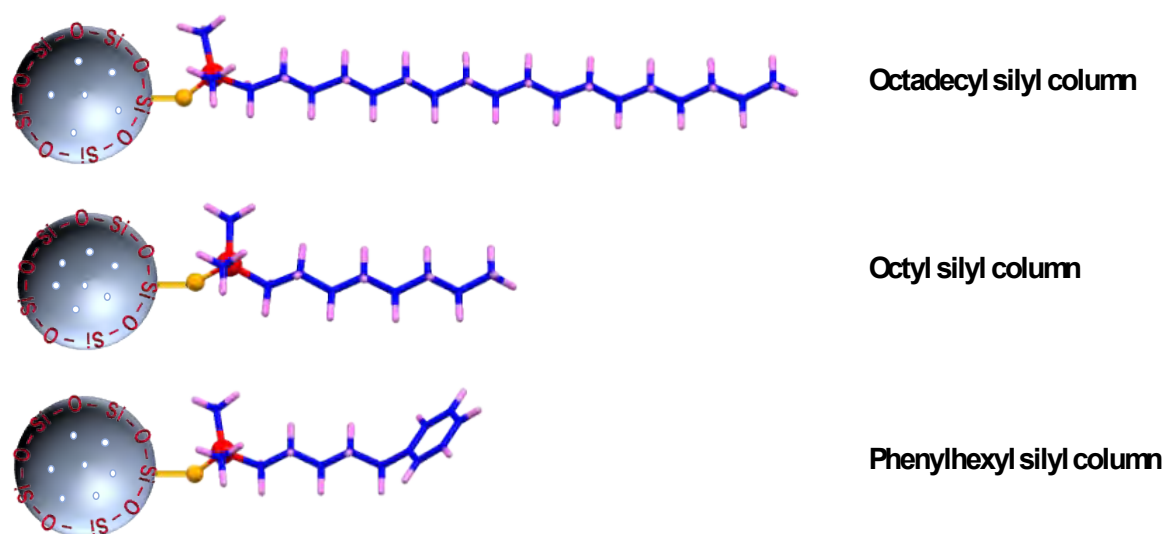


**Fig. S1** Schematic representation of three different silica beads of reversed-phase HPLC columns. Color labels: blue, C; pink, H; red, Si; yellow, O.

## Supplementary information 2

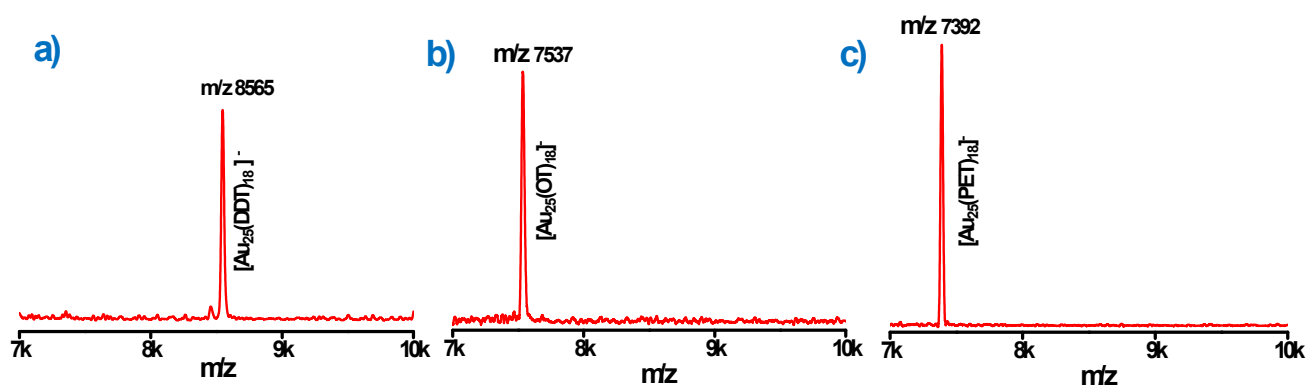


**Fig. S2** Negative ion MALDI MS of clusters a) I, b) II, and c) III.



### Supplementary information 3

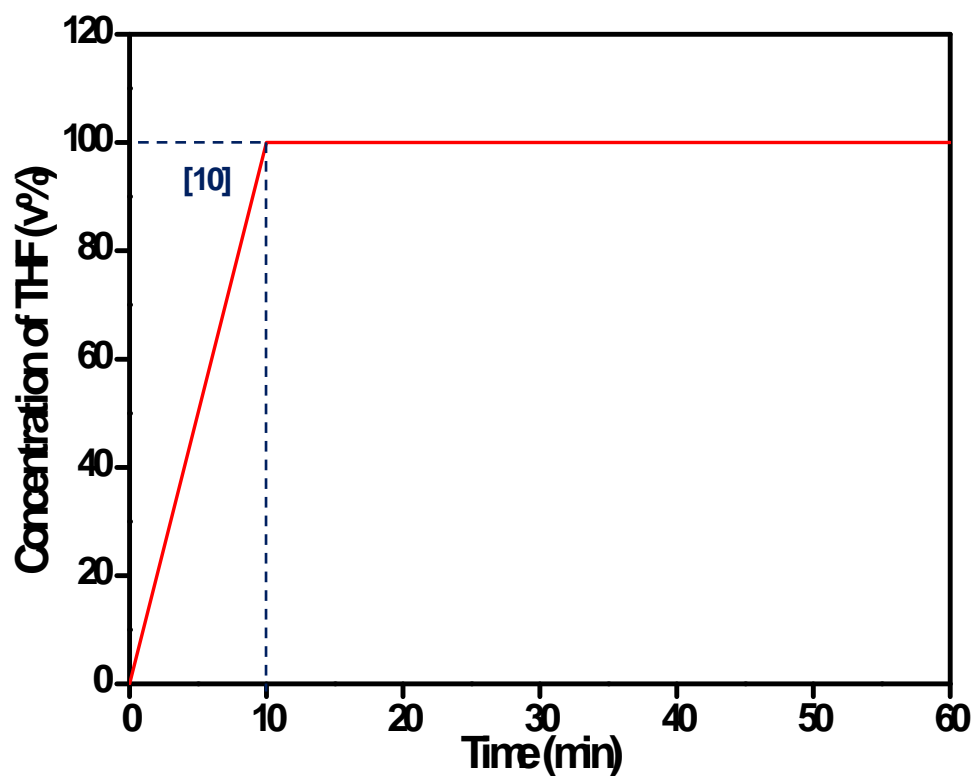


**Fig. S3** Linear gradient program used for the separation of clusters. The label (e.g., [10]) indicates the time (in minutes) taken to replace the mobile phase fully with THF.

### Supplementary information 4

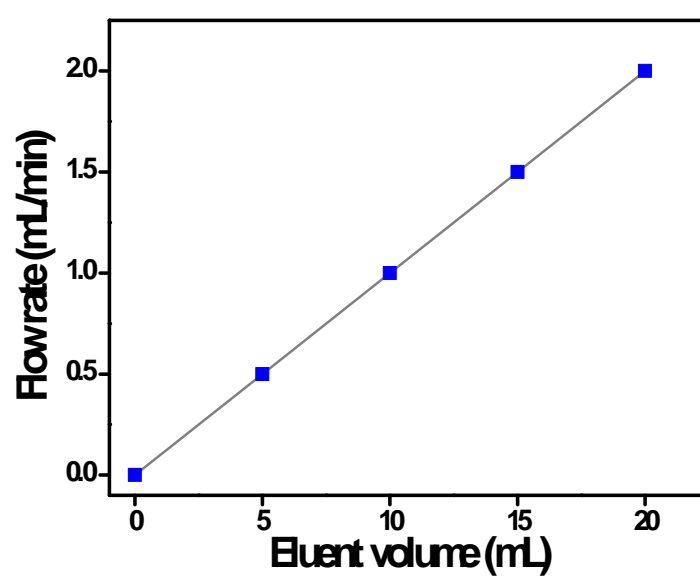


**Fig. S4** Eluent volume required to replace 100% MeOH to 100% THF in a linear gradient [10] program with varying flow rate.

Supplementary information 5

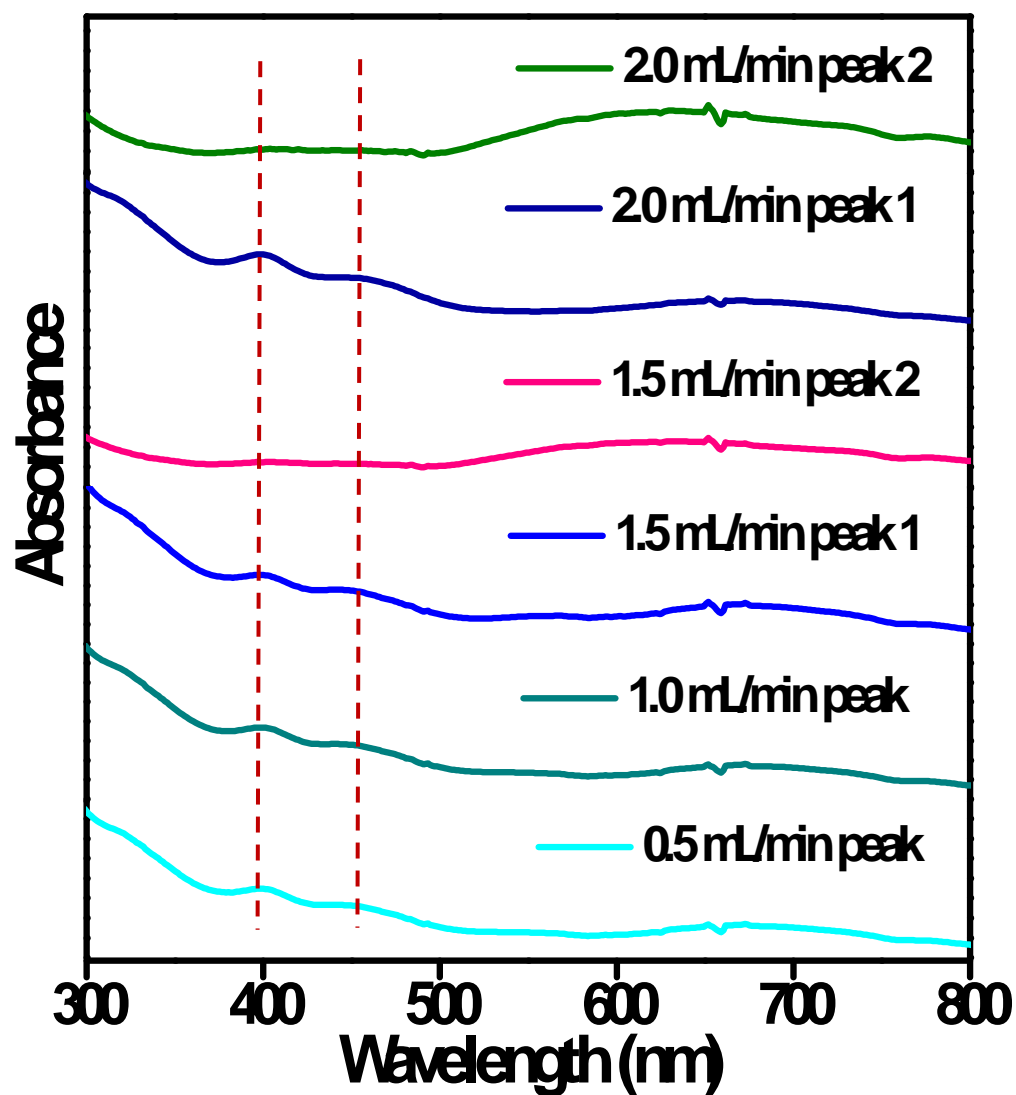


**Fig. S5** Online UV-vis spectra of cluster I in C<sub>18</sub> column at different flow rates, extracted at 400 nm wavelength obtained by PDA detector.

Supplementary information 6

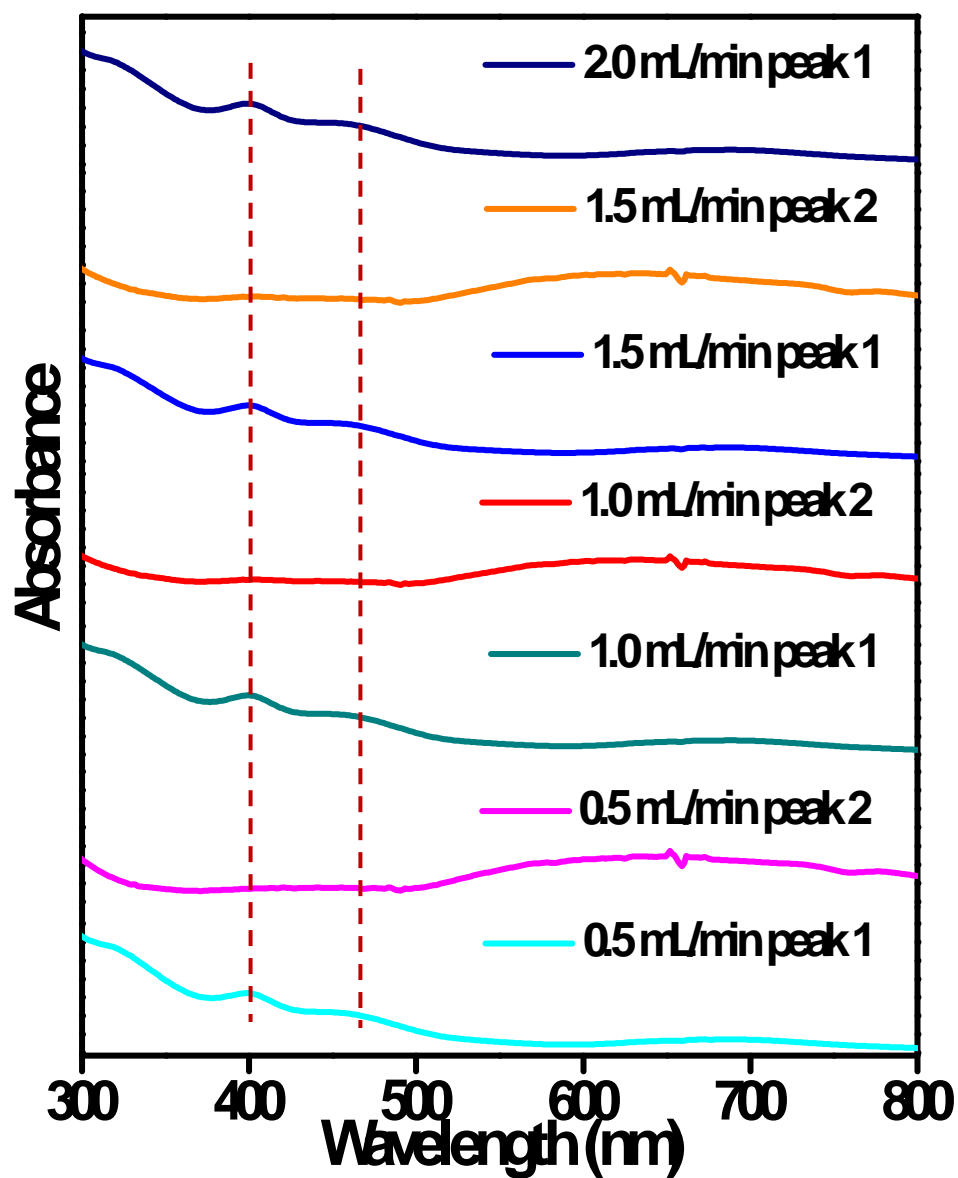


**Fig. S6** Online UV-vis spectra of cluster II in C<sub>18</sub> column at different flow rates, extracted at 400 nm wavelength obtained by PDA detector.

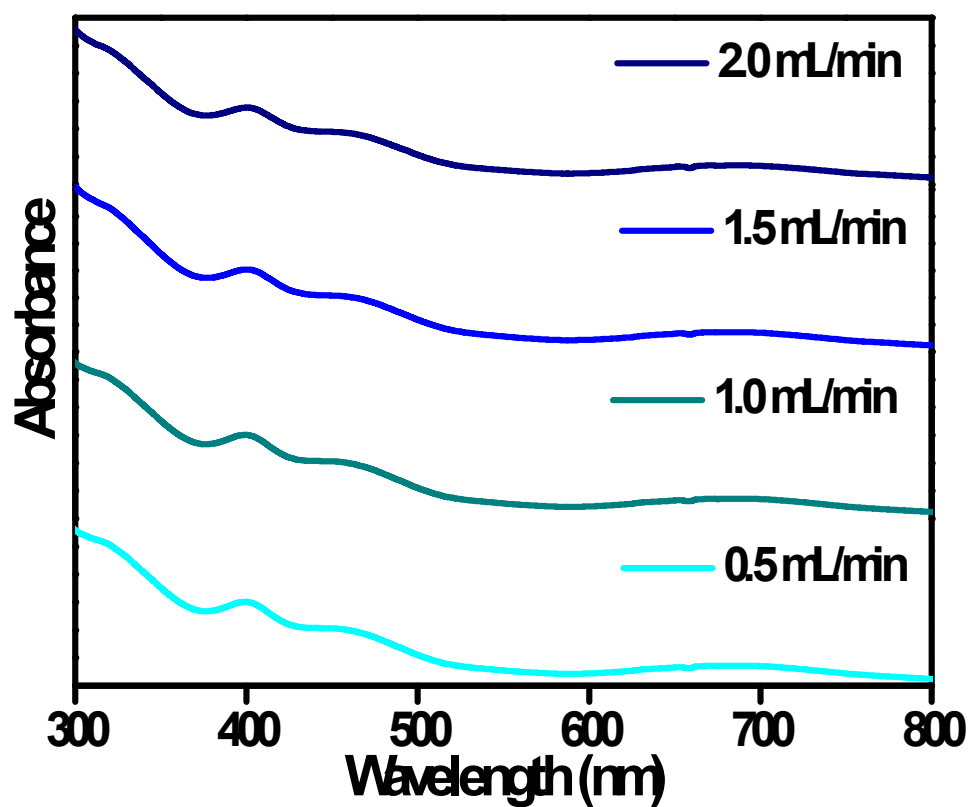


**Fig. S7** Online UV-vis spectra of cluster III in  $C_{18}$  column at different flow rates, extracted at 400 nm wavelength obtained by PDA detector.

# Supplementary information 8

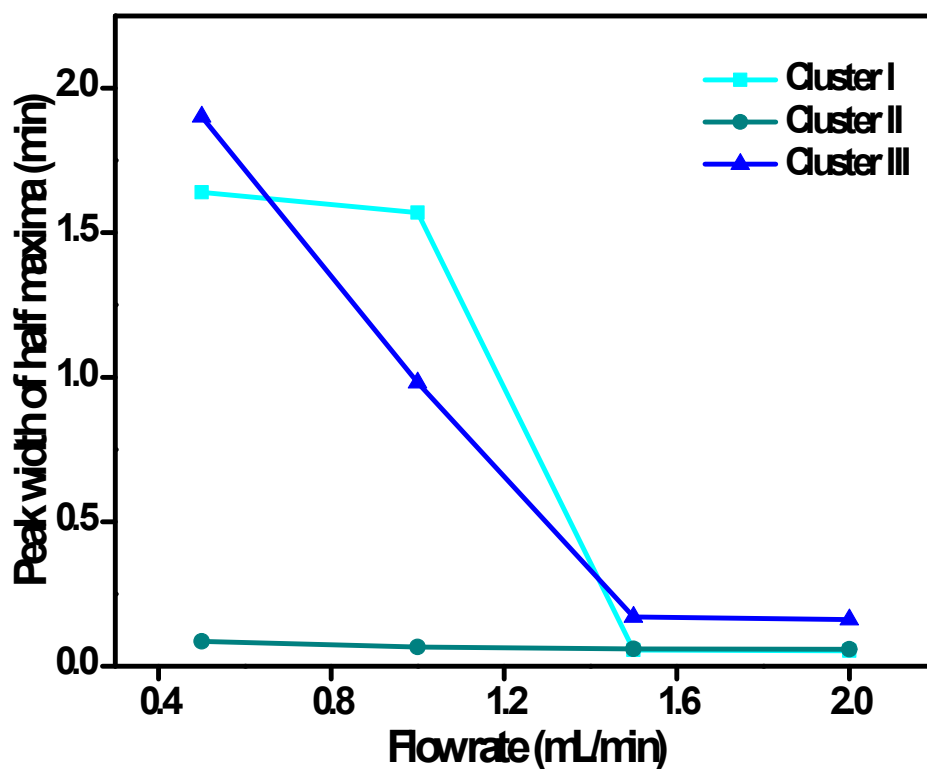


**Fig. S8** Variation of peak width of half maxima with different flow rates of cluster I, II, and III in C<sub>18</sub> column.

# Supplementary information 9

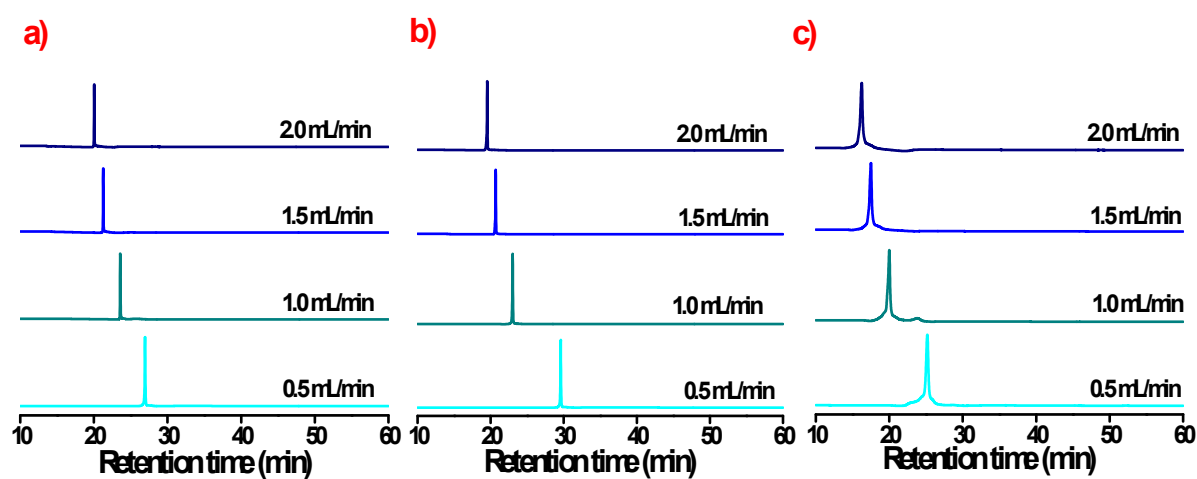


**Fig. S9** Chromatograms of cluster a) I, b) II, and c) III at different flow rates in C<sub>8</sub> column.

## Supplementary information 10

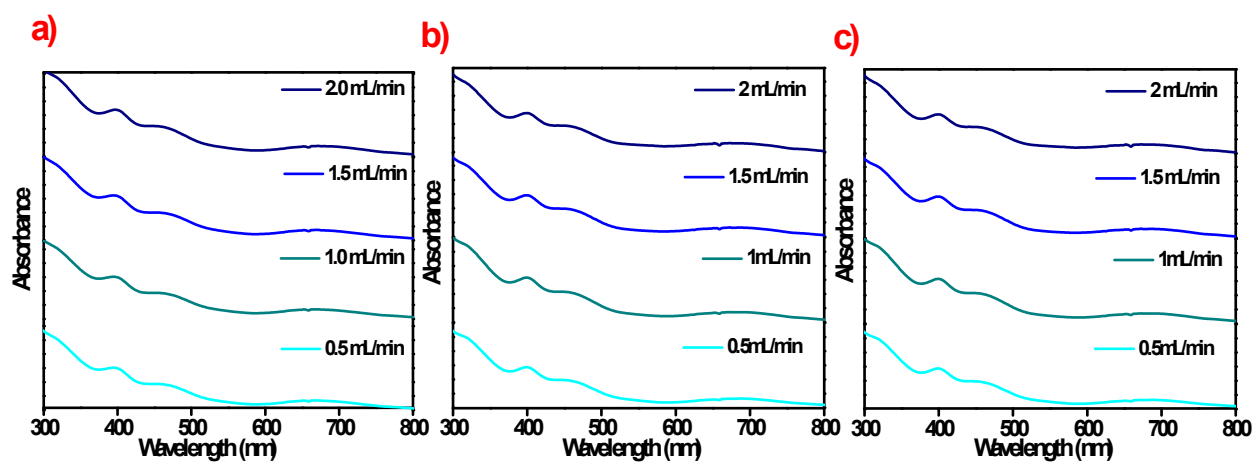


**Fig. S10** Online UV-vis spectra of clusters a) I, b) II, and c) III in  $C_8$  column with different flow rate obtained by PDA detector.



### Supplementary information 11

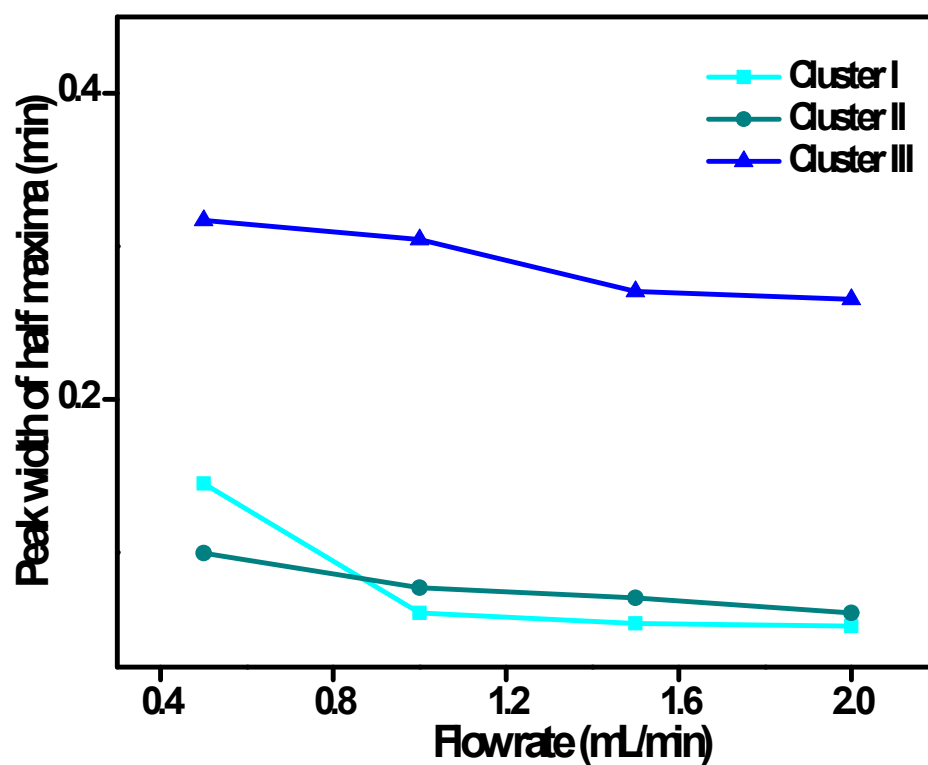


**Fig. S11** Variation of peak width half maxima with different flow rates of cluster I, II, and III in C<sub>8</sub> column.

### Supplementary information 12

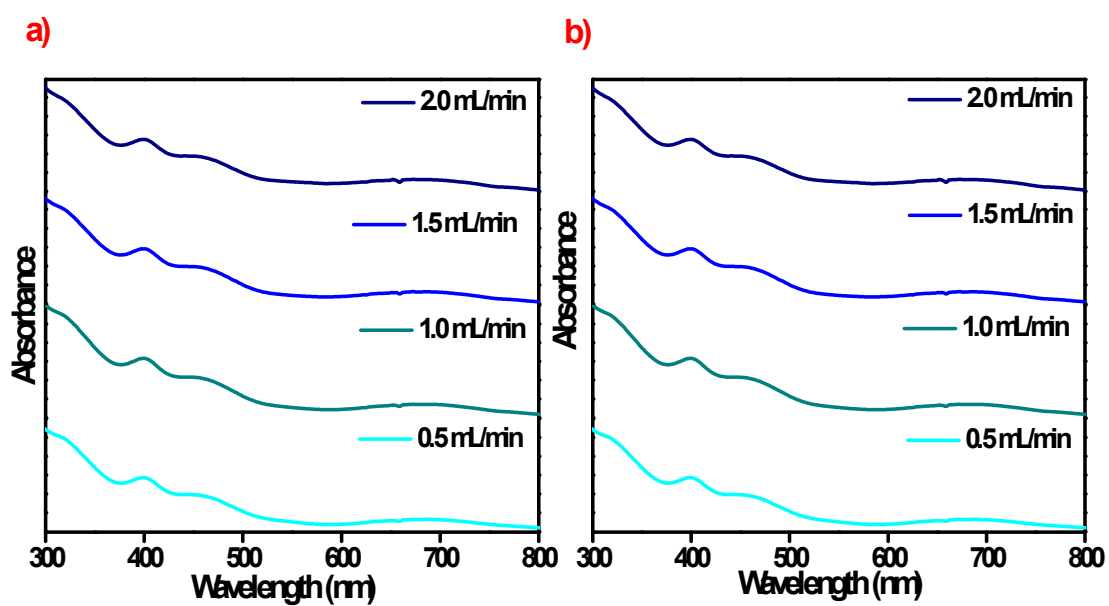


**Fig.S12** a) and b) are the online UV-vis spectra of cluster I and II in a phenylhexyl column with different flow rates obtained by PDA detector.

### Supplementary information 13

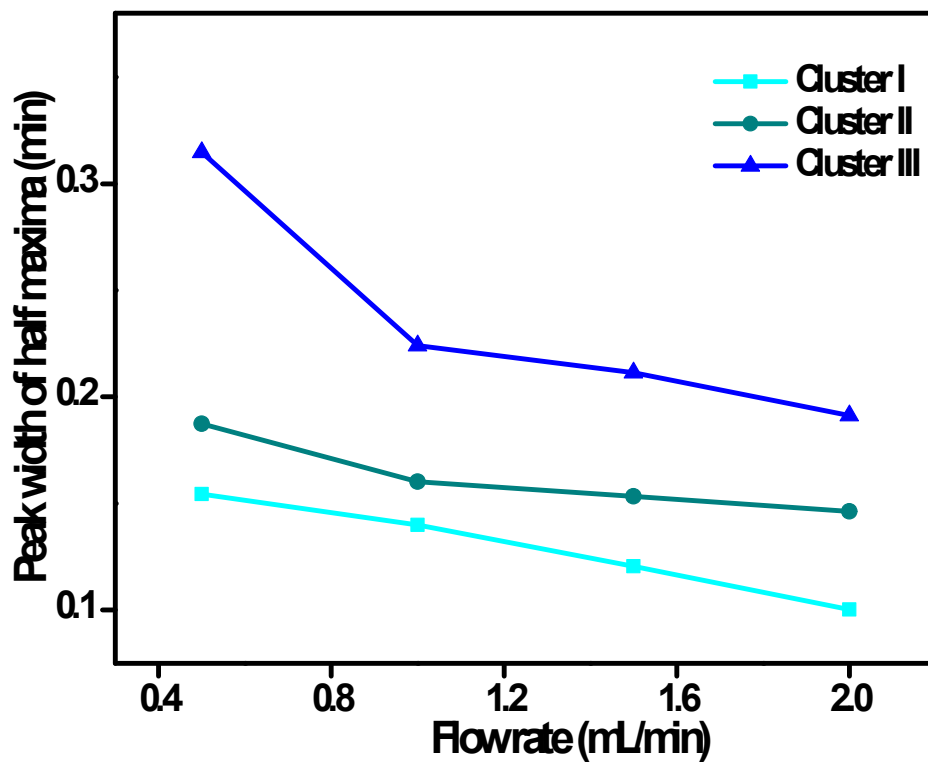


**Fig. S13** Variation of peak width of half maxima with different flow rates of cluster I, II, and III in the phenylhexyl column.

**Table S1** Fitting parameters for the exponential fits shown in Figure 7.

The fitting function has the form  $t_R = A \cdot (\exp(-x/b) + c)$  where 'x' is flow rate in mL/min

Column	Cluster	A (in min)	b	c	R <sup>2</sup>
C <sub>18</sub>	Au <sub>25</sub> (DDT) <sub>18</sub>	28.136	0.687	18.74	0.992
C <sub>18</sub>	Au <sub>25</sub> (OT) <sub>18</sub>	26.055	1.407	11.013	0.993
C <sub>18</sub>	Au <sub>25</sub> (PET) <sub>18</sub>	37.033	0.951	12.380	0.991
C <sub>8</sub>	Au <sub>25</sub> (DDT) <sub>18</sub>	28.680	0.515	19.530	0.997
C <sub>8</sub>	Au <sub>25</sub> (OT) <sub>18</sub>	27.498	0.523	18.990	0.998
C <sub>8</sub>	Au <sub>25</sub> (PET) <sub>18</sub>	26.914	0.559	15.55	0.998
Phenylhexyl	Au <sub>25</sub> (DDT) <sub>18</sub>	20.980	0.520	17.328	0.998
Phenylhexyl	Au <sub>25</sub> (OT) <sub>18</sub>	22.960	0.5118	16.815	0.998
Phenylhexyl	Au <sub>25</sub> (PET) <sub>18</sub>	22.151	0.545	16.597	0.997

#### Supplementary information 14

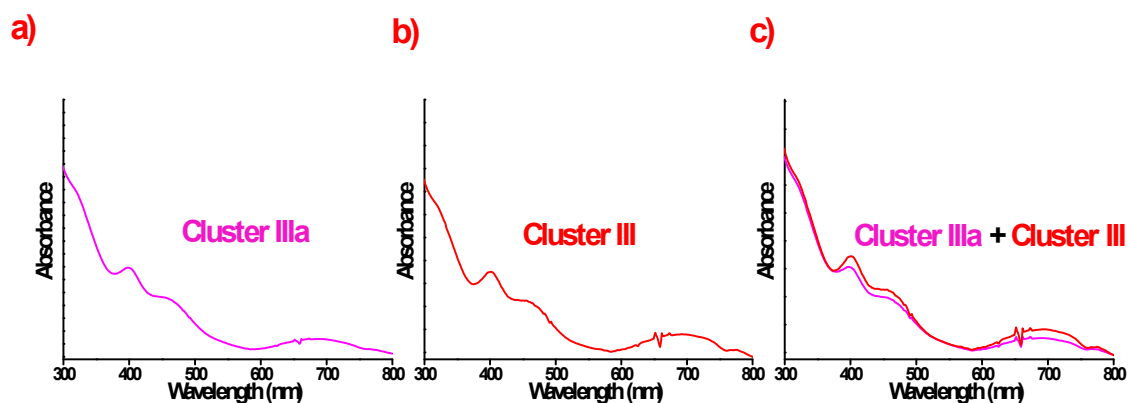


**Fig.S14** a), b), and c) are the online UV-vis spectra of cluster IIIa, III, and mixture of both eluted in phenylhexyl column with 1.0 mL/min flow rate obtained by PDA detector.

#### Supplementary information 15

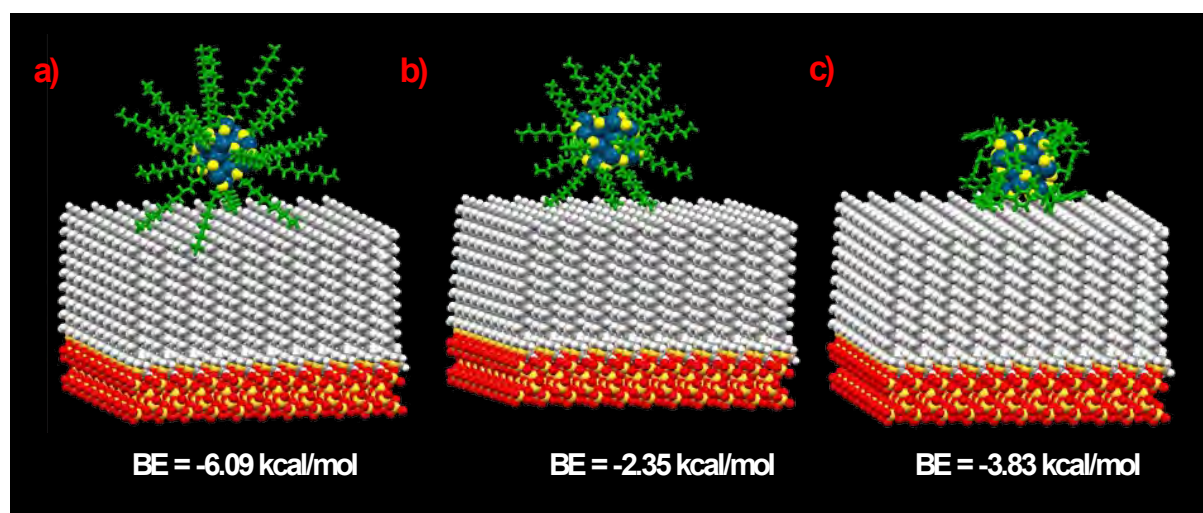


**Fig. S15** Energy minimum conformers of octadecyl functionality docked with clusters; a) I, b) II, and c) III. Color labels: golden yellow, Si; red, O; grey, C; white, H; teal, Au; yellow, S; green, DDT, OT, and PET ligands.

### Supplementary information 16

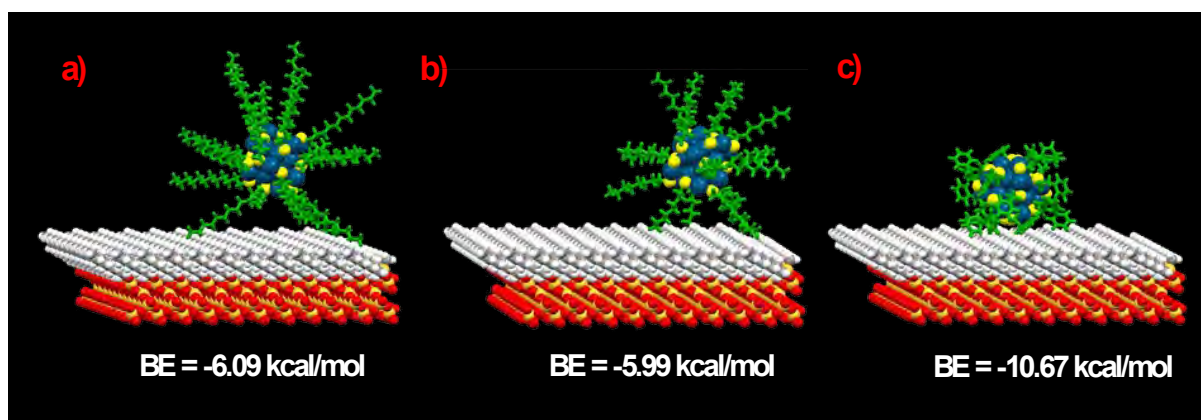


**Fig. S16** Energy minimum conformers of octyl functionality docked with clusters; a) I, b) II, and c) III. Color labels: golden yellow, Si; red, O; grey, C; white, H; teal, Au; yellow, S; green, DDT, OT, and PET ligands.

### Supplementary information 17

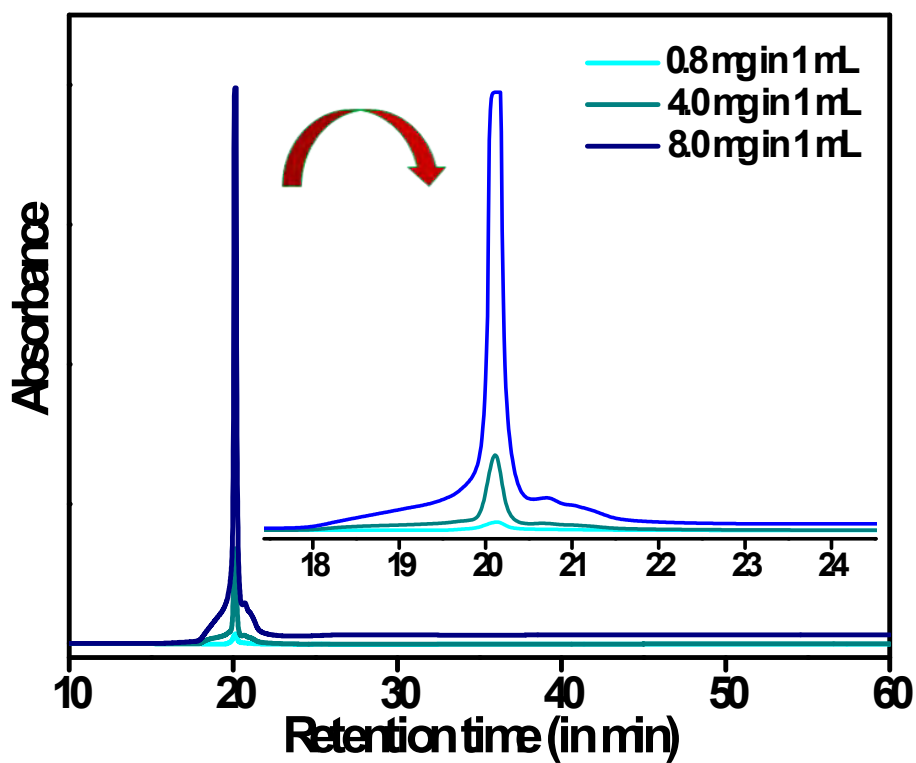


**Fig. S17** Concentration-dependent chromatograms of cluster III in the phenylhexyl column at 1.0 mL/min flow rate.

## Supplementary information 18

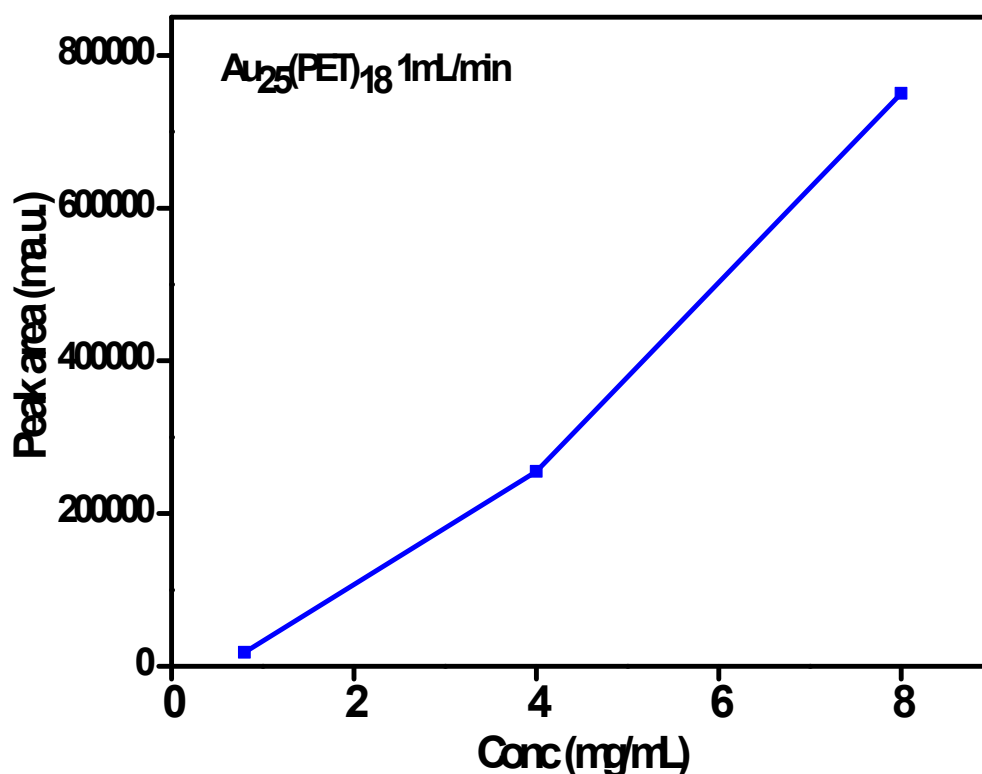


**Fig. S18** Peak area vs. concentration of cluster III in the phenylhexyl column at 1.0 mL/min flow rate.

## References

1. Enkovaara, J.; Rostgaard, C.; Mortensen, J. J.; Chen, J.; Duřak, M.; Ferrighi, L.; Gavnholt, J.; Glinsvad, C.; Haikola, V.; Hansen, H. A.; Kristoffersen, H. H.; Kuisma, M.; Larsen, A. H.; Lehtovaara, L.; Ljungberg, M.; Lopez-Acevedo, O.; Moses, P. G.; Ojanen, J.; Olsen, T.; Petzold, V.; Romero, N. A.; Stausholm-Møller, J.; Strange, M.; Tritsarlis, G. A.; Vanin, M.; Walter, M.; Hammer, B.; Häkkinen, H.; Madsen, G. K. H.; Nieminen, R. M.; Nørskov, J. K.; Puska, M.; Rantala, T. T.; Schiøtz, J.; Thygesen, K. S.; Jacobsen, K. W., Electronic structure calculations with GPAW: a real-space implementation of the projector augmented-wave method. *Journal of Physics: Condensed Matter* **2010**, *22* (25), 253202.
2. Perdew, J. P.; Burke, K.; Ernzerhof, M., Generalized Gradient Approximation Made Simple [Phys. Rev. Lett. 77, 3865 (1996)]. *Physical Review Letters* **1997**, *78* (7), 1396-1396.
3. Larsen, A. H.; Vanin, M.; Mortensen, J. J.; Thygesen, K. S.; Jacobsen, K. W., Localized atomic basis set in the projector augmented wave method. *Physical Review B* **2009**, *80* (19), 195112.
4. Morris, G. M.; Huey, R.; Lindstrom, W.; Sanner, M. F.; Belew, R. K.; Goodsell, D. S.; Olson, A. J., AutoDock4 and AutoDockTools4: Automated docking with selective receptor flexibility. *Journal of Computational Chemistry* **2009**, *30* (16), 2785-2791.
5. Prewitt, C. T.; Weidner, D. J.; Levien, L., Structure and elastic properties of quartz at pressure. *American Mineralogist* **1980**, *65* (9-10), 920-930.
6. Hanwell, M. D.; Curtis, D. E.; Lonie, D. C.; Vandermeersch, T.; Zurek, E.; Hutchison, G. R., Avogadro: an advanced semantic chemical editor, visualization, and analysis platform. *Journal of Cheminformatics* **2012**, *4* (1), 17.



Publications with  
other groups

# Ferrofluid Microdroplet Splitting for Population-Based Microfluidics and Interfacial Tensiometry

Mika Latikka, Matilda Backholm, Avijit Baidya, Alberto Ballesio, Amandine Serve, Grégory Beaune, Jaakko V. I. Timonen, Thalappil Pradeep, and Robin H. A. Ras\*

Ferrofluids exhibit a unique combination of liquid properties and strong magnetic response, which leads to a rich variety of interesting functional properties. Here, the magnetic-field-induced splitting of ferrofluid droplets immersed in an immiscible liquid is presented, and related fascinating dynamics and applications are discussed. A magnetic field created by a permanent magnet induces instability on a mother droplet, which divides into two daughter droplets in less than 0.1 s. During the splitting process, the droplet undergoes a Plateau–Rayleigh-like instability, which is investigated using high-speed imaging. The dynamics of the resulting satellite droplet formation is shown to depend on the roughness of the supporting surface. Further increasing the field results in additional splitting events and self-assembly of microdroplet populations, which can be magnetically actuated. The effects of magnetization and interfacial tension are systematically investigated by varying magnetic nanoparticles and surfactant concentrations, and a variety of outcomes from labyrinthine patterns to discrete droplets are observed. As the splitting process depends on interfacial tension, the droplet splitting can be used as a measure for interfacial tension as low as  $0.1 \text{ mN m}^{-1}$ . Finally, a population-based digital microfluidics concept based on the self-assembled microdroplets is presented.


Ferrofluids are remarkably controllable materials allowing for magnetic manipulation of their shape, viscosity, flow, and heat transfer properties.<sup>[1–5]</sup> Also magnetic properties can be tuned; a ferrofluid droplet can be reversibly switched from superparamagnetic to ferromagnetic by interfacial jamming of nanoparticles.<sup>[6]</sup> Due to their versatility, ferrofluids find use in a range of applications from simple magnetically retained seals and lubricants to microfluidics and biomedical devices.<sup>[2,7–13]</sup> Recently, they have shown potential as multifunctional<sup>[14]</sup> and anti-icing surfaces,<sup>[15]</sup> wearable sensors,<sup>[16]</sup> probes for wetting characterization,<sup>[17]</sup> and even liquid robotics.<sup>[18,19]</sup> Ferrofluids can also undergo fascinating ferrohydrodynamic instabilities, where a small variation of a control parameter (such as external magnetic field) causes an abrupt change in the ferrofluid configuration.<sup>[1]</sup> These are interesting from a physics point of view, but also useful for applications, such as ferrofluid molding<sup>[20]</sup> and field-induced mixing in

microfluidics.<sup>[21]</sup> Here we present the magnetic-field-induced instability leading to splitting and self-assembly of ferrofluid microdroplets immersed in immiscible liquid (**Figure 1a**) as well as related potential applications. The ferrofluid we use is a colloidal suspension of citrate-stabilized magnetite nanoparticles in water (synthesis procedure and in-depth analysis are presented in ref. [22]). The aqueous ferrofluid droplet is placed in an immiscible solvent (e.g., octane or silicone oil) and subjected to an increasing magnetic field created by a permanent magnet underneath (see the text and Figure S1 in the Supporting Information for details). At a critical field strength and gradient, the droplet becomes unstable and splits into two daughter droplets, which has not been previously shown for ferrofluid droplets immersed in another liquid. The splitting process gives rise to another instability; as the ferrofluid bridge connecting the two daughter droplets gets thinner, it breaks up into satellite droplets with orders of magnitude smaller volumes than the daughter droplets. This phenomenon is similar to Plateau–Rayleigh instability, which leads to breakup of a falling liquid stream.<sup>[23]</sup> We investigated the satellite droplet formation in detail using high-speed imaging and found that the dynamics depends on the roughness of the supporting substrate. Numerous subsequent splitting events can be triggered by increasing the external field further after the first splitting, creating

M. Latikka, Dr. M. Backholm, Dr. A. Baidya, A. Ballesio, A. Serve, Dr. G. Beaune, Prof. J. V. I. Timonen, Prof. R. H. A. Ras  
Department of Applied Physics  
Aalto University School of Science  
Puumiehenkuja 2, Espoo 02150, Finland  
E-mail: robin.ras@aalto.fi

Dr. A. Baidya, Prof. T. Pradeep  
Department of Chemistry  
Indian Institute of Technology Madras  
Chennai 600036, India

Prof. R. H. A. Ras  
Department of Bioproducts and Biosystems  
Aalto University School of Chemical Engineering  
Kemistintie 1, Espoo 02150, Finland

 The ORCID identification number(s) for the author(s) of this article can be found under <https://doi.org/10.1002/advs.202000359>

© 2020 The Authors. Published by WILEY-VCH Verlag GmbH & Co. KGaA, Weinheim. This is an open access article under the terms of the Creative Commons Attribution License, which permits use, distribution and reproduction in any medium, provided the original work is properly cited.

DOI: 10.1002/advs.202000359

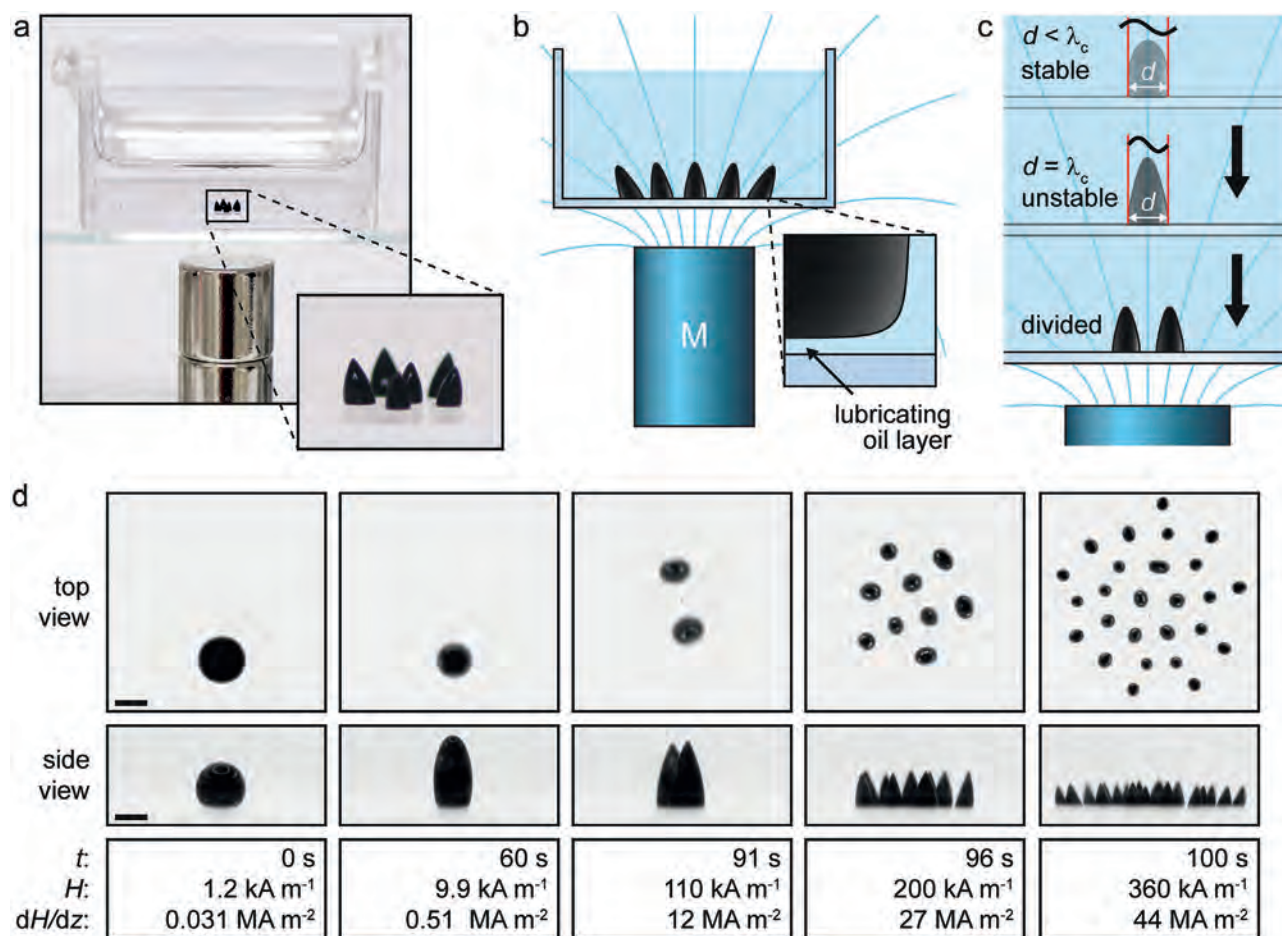


**Figure 1.** Magnetic-field-induced ferrofluid droplet splitting in an immiscible liquid. a) Photo of ferrofluid droplets in a polystyrene container filled with silicone oil and a stack of two cylindrical magnets (diameter and height = 9.5 mm) underneath. b) Schematic of a droplet population in a magnetic field (field lines in cyan) created by a permanent magnet. Inset shows a lubricating oil layer between the droplet and the substrate. c) Schematic of droplet splitting in an increasing magnetic field ( $\lambda_c$ : critical wavelength,  $d$ : droplet diameter). d) Top and side views of ferrofluid droplet splitting in silicone oil ( $t$ : time,  $H$ : external magnetic field, and  $dH/dz$ : vertical field gradient). The distance between the magnet (diameter = 20 mm, height = 42 mm) and the droplets is reduced from 102.8 to 2.8 mm at a speed of  $1 \text{ mm s}^{-1}$ . Scale bar: 1 mm.

multiple generations of daughter droplets, which self-assemble into well-defined mobile patterns as guided by their mutual magnetic repulsion and attraction toward the permanent magnet. The shape and number of droplets depend on the ferrofluid magnetization and interfacial tension (IFT), which we varied by controlling the volume percentage of the superparamagnetic iron oxide nanoparticles (SPIONs), surfactant type, and surfactant concentration. As the field-induced instability is governed by the IFT in addition to the magnetic field, the size of the split droplets can be used to determine IFTs as low as  $0.1 \text{ mN m}^{-1}$  with a simple theoretical model, well below the sensitivity limit of the commonly used pendant drop method. Finally, we demonstrate how the self-assembled droplet patterns can be magnetically actuated and used in population-based digital microfluidics, which allows switching between population-level and droplet-level controls.

The shape of a ferrofluid droplet is determined by magnetic, gravitational, and interfacial tension forces (when forces related to wetting are assumed negligible).<sup>[24–26]</sup> The interfacial free energy is minimized when the droplet is spherical, while

gravitational and magnetic forces deform this shape. Ferrofluid magnetization elongates the droplet along the field direction, and the strength of this effect compared to interfacial tension can be quantified with a dimensionless parameter  $S = \mu_0 M^2 V^{\frac{1}{3}} \sigma^{-1}$ , where  $\mu_0$  is the vacuum permeability,  $M$  is the magnetization of the ferrofluid,  $V$  is the volume of the droplet, and  $\sigma$  is the interfacial tension between ferrofluid and surrounding fluid.<sup>[27]</sup> In our work, we use a permanent magnet underneath the ferrofluid, which creates a nonuniform magnetic field affecting the droplets with a vertical magnetic force density  $f_M = \mu_0 (\vec{M} \cdot \nabla) \vec{H} = \mu_0 M dH/dz$ ,<sup>[1]</sup> where  $H$  is the external magnetic field. We approximate  $M$  and vertical field gradient  $dH/dz$  as constant over droplet volume, calculated at the center of the droplet. Together with the gravitational force density  $f_G = \Delta \rho g$  ( $\Delta \rho$  is the density difference between ferrofluid and the surrounding fluid, and  $g$  is the gravitational acceleration) the normal force density  $f_N = f_G + f_M$  pulls the droplet against the substrate, flattening it. This can be quantified relative to the interfacial tension using the effective Bond number  $B_e = f_N V^{\frac{2}{3}} \sigma^{-1}$ .<sup>[27]</sup>

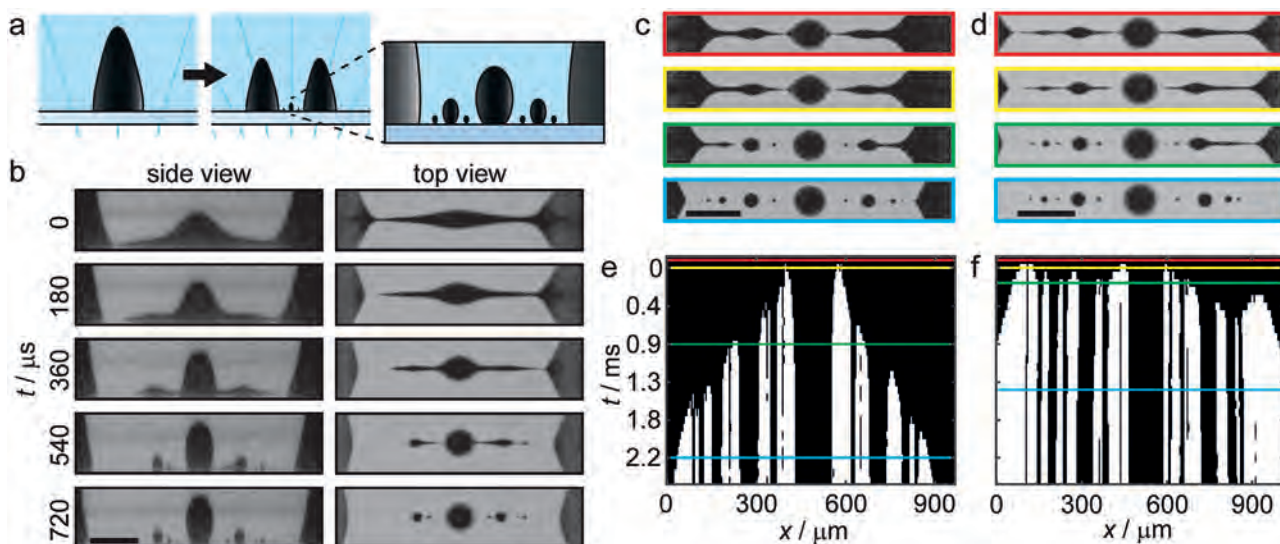


**Figure 2.** Dynamics of satellite droplet formation. a) Schematic of a mother droplet splitting into two daughter droplets. The zoomed inset shows small satellite and subsatellite droplets, which are formed during the splitting process due to the Plateau–Rayleigh-like instability. b) Side- and top-view snapshots of the breakup of the capillary bridge between two splitting daughter droplets on the Glaco-coated substrate (SPION concentration 22 vol%, Movie S2, Supporting Information). The time between each picture is 180  $\mu$ s. c,d) Top-view snapshots of the capillary bridge breakup on the PS and Glaco surfaces, respectively (SPION concentration 24 vol%; see the colored lines in the graphs below for time stamp information). e,f) Corresponding graphs showing the detailed time evolution of the bridge breakup (black corresponds to the ferrofluid and white the surrounding oil). Before  $t = 0$  ms, the bridge is still intact (red lines and boxes) and at  $t = 0$  ms, the first pinch-off occurs (yellow lines and boxes). On the smooth PS surface, the breakup starts around the largest satellite droplet in the center and continues outward in a symmetric manner (green and cyan lines and boxes). The entire breakup event takes several milliseconds. In comparison, on the rough Glaco-coated surface, the breakup starts almost simultaneously at the center and the edge of the bridge, and evolves then quickly inward from both sides in a total breakup time of 0.5 ms. All scale bars: 0.2 mm.

The interplay between interfacial, gravitational, and magnetic forces gives rise to interesting phenomena, including field-induced instabilities. A classic example is the Rosensweig instability, where a uniform vertical magnetic field creates a macroscopic array of spikes on a horizontal ferrofluid surface.<sup>[1]</sup> The periodicity of the array is determined by the critical wavelength  $\lambda_c^{\text{Rosenweig}} = 2\pi\sqrt{\sigma/f_G}$ . In case of a nonuniform magnetic field created by a permanent magnet, the critical wavelength can be written analogously as<sup>[24]</sup>

$$\lambda_c = 2\pi\sqrt{\frac{\sigma}{f_N}} \quad (1)$$

If the ferrofluid volume is small, the spikes can continue all the way down to the substrate. On a sufficiently liquid-repellent surface, there is no ferrofluid film connecting the spikes, and individual droplets are created instead. This was first experimentally demonstrated by using superhydrophobic surfaces, where a thin air layer separates the droplet from the substrate (Cassie state of wetting) allowing droplets to move with little friction.<sup>[24]</sup> Contrary to the previous experiments done in air,<sup>[24,26,28]</sup> we achieve here repellency by immersing the ferrofluid droplets in an immiscible liquid, which creates a lubricating liquid film between the droplets and the substrate (Figure 1b; Figure S2, Supporting Information).<sup>[29,30]</sup> When the ferrofluid droplet diameter  $d$  is smaller than  $\lambda_c$ , the droplet remains stable and is only deformed by the field (Figure 1c, top image). However, when  $d = \lambda_c$ , the droplet becomes unstable and splits into two daughter droplets (Figure 1c, bottom image). A comprehensive theoretical discus-

sion about the phenomena has recently been presented by Vieu and Walter.<sup>[26]</sup> The splitting event takes less than 0.1 s, depending on the viscosities of the ferrofluid and the surrounding liquid. The split droplets are magnetized by the external field and are attracted to the global field maximum at the magnet's axis. Since the droplets are magnetized in the same direction, there is also dipolar interdroplet repulsion, leading to a symmetric, self-assembled droplet pattern.<sup>[24]</sup>

As can be seen in the top view images of a splitting experiment (Figure 1d; Movie S1, Supporting Information), small satellite droplets are formed between the daughter droplets during the splitting event (Figure 2a). To study the formation dynamics of these satellite droplets, we performed high-speed imaging of a single splitting event at high spatial resolution (Figure 2b) in a polystyrene (PS) container filled with 5 cSt silicone oil. A rectangular magnet was used to induce splitting along the direction of the long side of the magnet, which allowed for side-view imaging where both daughter droplets and all satellite droplets remained in focus during the entire splitting event.

Toward the end of each splitting event, a capillary bridge is formed between the two daughter droplets (Figure 2b). This capillary bridge undergoes an interfacial-tension-driven Plateau–Rayleigh-like instability,<sup>[31–33]</sup> where a disturbance of a specific wavelength is amplified, leading to the breakup of the bridge. The creation of satellite droplets during the breakup process is a highly nonlinear phenomenon and has been carefully studied by Tjahjadi et al.,<sup>[23]</sup> combining experiments with boundary-integral calculations to investigate the time evolution of a capillary oil bridge suspended in corn syrup. In our system, however, the



liquid bridge consists of non-Newtonian magnetic fluid, whose viscosity changes with the external magnetic field, thus requiring complicated magnetohydrodynamics for it to be fully modeled.<sup>[2]</sup> Furthermore, our ferrofluid droplets are substrate-supported, and the added drag effect can influence the fluid dynamics of the satellite droplet formation. For these reasons, we made a purely qualitative investigation on the satellite droplet formation using two substrates of different roughness (Figure S3a,b, Supporting Information): a smooth PS surface (RMS roughness =  $6.2 \pm 0.2$  nm), and a PS surface coated with the commercial superhydrophobic Glaco coating (RMS roughness =  $43 \pm 3$  nm).

In Figure 2b, the satellite droplet formation process on the Glaco-coated surface is shown as time-lapse images from the side and from the top (Movie S2, Supporting Information). The top view shows the ferrofluid bridge breaking up in a repeated, self-similar fashion into a single large satellite droplet surrounded by  $\approx 10$  tiny subsatellite droplets. The resulting droplet size distribution is fractal like, similar to a droplet population resulting from a breakup of a Newtonian capillary bridge in a viscous, infinite medium.<sup>[23]</sup> From the side view, however, our magnetic system is very different since the height of the bridge is affected by the external magnetic field, rendering ellipsoidal rather than spherical satellite droplets. Within the spatial sensitivity of our experiments, we find no clear difference between the two substrates in the final number, size, or spacing between the satellite droplets (Figure 2c,d). However, a strong effect is seen in the dynamics of the breakup and satellite droplet formation on the PS and Glaco-coated substrates (Figure 2e,f). The fractal-like time evolution graphs show the breakup as viewed along the horizontal symmetry axis, where black corresponds to the ferrofluid and white shows the surrounding media. On the PS substrate, the breakup starts at the center and moves symmetrically outward as a function of time, while on the Glaco-coated substrate the breakup starts almost simultaneously at the center and the edge of the ferrofluid bridge and continues at a much faster pace than on the PS substrate. We hypothesize the greater roughness of the Glaco-coated surface allows increased oil flow between the surface asperities compared to the smooth PS surface (Figure S2b,c, Supporting Information). This reduces shear stress in the lubricating layer and enhances droplet mobility, leading to faster splitting dynamics. Supporting Information contains more detailed discussion on the experiments and the effect of ferrofluid density on the time-evolution dynamics on the two different substrates (Figure S3c,d, Supporting Information).

Further increasing the magnetic field after the first droplet splitting leads to numerous sequential splitting events, which were investigated using a cylindrical permanent magnet to create radially symmetric self-assembled droplet populations. Here we focused on the self-assembly of the daughter droplets and ignored the small satellite droplets due to limitations in imaging resolution. We investigated three liquid–liquid systems: aqueous ferrofluid/oil, aqueous ferrofluid/oil with the anionic surfactant sodium dodecyl sulfate (SDS), and aqueous ferrofluid/oil with the nonionic surfactant pentaethylene glycol monododecyl ether ( $C_{12}E_5$ ). In addition to PS substrates, we also tested two superhydrophobic surfaces: a copper surface coated with nanorough silver and fluorinated thiol, and a glass slide coated with the commercial coating Glaco. Despite the differences in satellite droplet

formation dynamics on different surfaces, we did not observe any change in the number of split daughter droplets in a given magnetic field. This is further discussed in the Supporting Information, while the experiments described here were performed in PS containers.

To investigate the effect of ferrofluid magnetization and interfacial tension systematically, we varied  $c_{\text{SPION}}$  from 8 to 25 vol% (corresponding to  $\approx 0.8$ – $2.4$  mmol L<sup>−1</sup> of SPIONs, calculated from the size distribution of the nanoparticles)<sup>[22]</sup> and surfactant concentrations  $c$  from 0 to 17 mmol L<sup>−1</sup> (Figure 3a,b). At a low  $c_{\text{SPION}}$  of 8 vol% with no surfactant,  $B_e$  dominates over  $S$  leading to flattened droplets, and splitting does not occur (Figure S4, Supporting Information). Increasing  $c_{\text{SPION}}$  to 12 vol% results in four splitting events, but the resulting droplets are still flattened due to  $f_N$ , leading to a labyrinthine pattern. Further increasing  $c_{\text{SPION}}$  to 17 vol% results in discrete, conical droplets. On the other hand, addition of surfactant (SDS) allows droplet splitting even with a low  $c_{\text{SPION}}$  of 8 vol%. However, the droplets adopt a dumbbell-like shape due to droplet flattening. For high  $c_{\text{SPION}}$  (17 vol%), increasing the SDS concentration  $c_{\text{SDS}}$  from 0 to 17 mmol L<sup>−1</sup> leads to almost a sevenfold increase in the number of split, conical droplets. Nonionic surfactant  $C_{12}E_5$  allows reaching very low IFT values without adding a co-surfactant or salt in the system (Figures S5 and S6, Supporting Information).<sup>[34]</sup> This not only leads to smaller, but also deformed droplets (Figure 3b), as the droplets become more and more elongated in the lateral direction. At  $c_{\text{C}_{12}\text{E}_5} = 17$  mmol L<sup>−1</sup>, ribbons and complex shapes are created instead of well-defined droplets with narrow size distribution (Figure 3b, top image).

The simple approximation of the critical wavelength (Equation (1)) holds well for a wide range of magnetic field strengths as well as SPION and surfactant concentrations. As an example, Figure 3c presents experimental cross-sectional major axes  $d$  of unstable droplets (dots) and theoretically calculated critical wavelengths  $\lambda_c$  (solid curves) as a function of external magnetic field  $H$ . The shaded area corresponds to the uncertainty of the theoretical prediction ( $\pm 1$  standard deviation) arising from the uncertainty of the IFTs measured with pendant droplet and micro-pipette aspiration techniques (see the Supporting Information for more details on these measurements). The theory holds for a system A) without surfactant, B) with SDS, and C) with  $C_{12}E_5$ . However, Equation (1) does not describe the appearance of dumbbell-shaped droplets or labyrinthine patterns, which are typical for confined films of ferrofluids.<sup>[1]</sup> In our experiments, the ferrofluid is not mechanically confined, and we instead hypothesize that  $f_N$  is sufficiently strong to cause a similar effect.

An increase in surfactant concentration leads to a decrease in  $d$  as predicted by Equation (1), as shown in Figure 3d for droplets affected by  $f_N = 2$  MN m<sup>−3</sup>. As mentioned earlier,  $C_{12}E_5$  allows for the creation of smaller droplets ( $d \approx 50$   $\mu\text{m}$ ) than SDS ( $d \approx 200$   $\mu\text{m}$ ). With SDS  $d$  plateaus for  $c_{\text{SDS}} > 1.7$  mmol L<sup>−1</sup>, but becomes ill-defined with  $C_{12}E_5$ , for  $c_{\text{C}_{12}\text{E}_5} > 17$  mmol L<sup>−1</sup>, as the droplet shapes and sizes are no longer uniform. After this limit, the theory presented by Equation (1) is no longer sufficient to describe the system. This limit corresponds to an IFT of  $\approx 0.1$  mN m<sup>−1</sup>. For higher IFTs, Equation (1) holds and  $d$  can be used to determine the interfacial tension between the ferrofluid and the surrounding liquid, when the magnetization and field properties are known. This is demonstrated in Figure 3e, where the

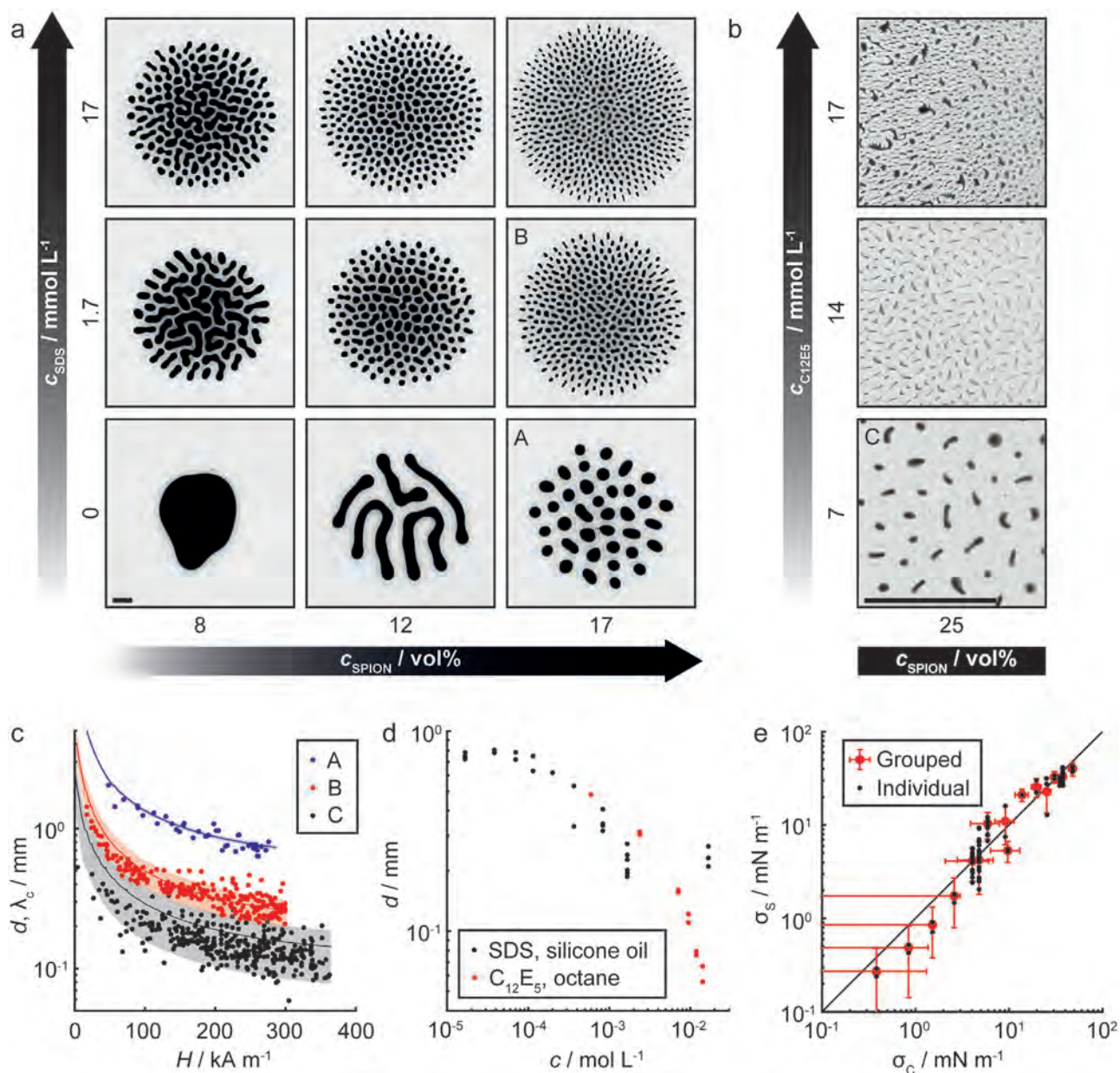


**Figure 3.** Droplet populations. a) Droplet populations created by field-induced splitting for different SDS and SPION concentrations ( $c_{\text{SDS}}$  and  $c_{\text{SPION}}$ ) in silicone oil. Initial droplet volume  $V_0 = 5 \mu\text{L}$  and external magnetic field  $H = 290 \text{ kA m}^{-1}$ . SDS lowers the IFT between ferrofluid and silicone oil, leading to smaller droplets. Low SPION concentration leads to dumbbell-shaped droplets and labyrinthine patterns, whereas high concentration allows formation of distinct droplets. Scale bar: 1 mm. b) Split ferrofluid droplets in octane with different concentrations of  $\text{C}_{12}\text{E}_5$  ( $c_{\text{C}_{12}\text{E}_5}$  ( $V_0 = 0.2 \mu\text{L}$ ,  $H = 300 \text{ kA m}^{-1}$ )).  $\text{C}_{12}\text{E}_5$  lowers IFT, leading to droplets with elongated cross sections. At  $17 \text{ mmol L}^{-1}$ , ribbons are formed in addition to irregular droplets (top photo). Scale bar: 1 mm. c) Theoretically calculated critical wavelengths  $\lambda_c$  (lines) and droplet cross-sectional major axes  $d$  (dots) for experimentally observed splitting events as a function of  $H$ . Shaded area represents uncertainty of the theoretical prediction ( $\pm 1$  standard deviation). A) 17 vol% SPIONs (droplet population shown in panel (a)); B) 17 vol% SPIONs,  $1.7 \text{ mmol L}^{-1}$  SDS (panel (a)); and C) 25 vol% SPIONs,  $7.1 \text{ mmol L}^{-1}$   $\text{C}_{12}\text{E}_5$  (panel (b)). d)  $d$  as a function of surfactant concentration  $c$  (17–25 vol% SPIONs, normal force density  $f_N = 2 \text{ MN m}^{-3}$ ). e) IFT measured using splitting experiments  $\sigma_s$  as a function of IFT measured with control methods  $\sigma_c$  (pendant droplet and micropipette aspiration). The solid line has a slope of one. Black dots: individual experiments; red circles: experiments grouped based on control method IFT ( $n = 2$ –23). Error bars represent uncertainty ( $\pm 1$  standard deviation).

IFT as measured using splitting experiments is compared to values measured with micropipette aspiration (verified with the pendant droplet method for IFTs  $> 3 \text{ mN m}^{-1}$ ). The method presented here can also be employed by simply calculating the number of droplets at different magnetic field strengths, if the shape

of each droplet is assumed identical, making the technique optically less demanding. This is further described in the Supporting Information (Figure S7, Supporting Information). It is important to note that SPIONs themselves also affect the IFT (Figure S6, Supporting Information), which needs to be taken into account



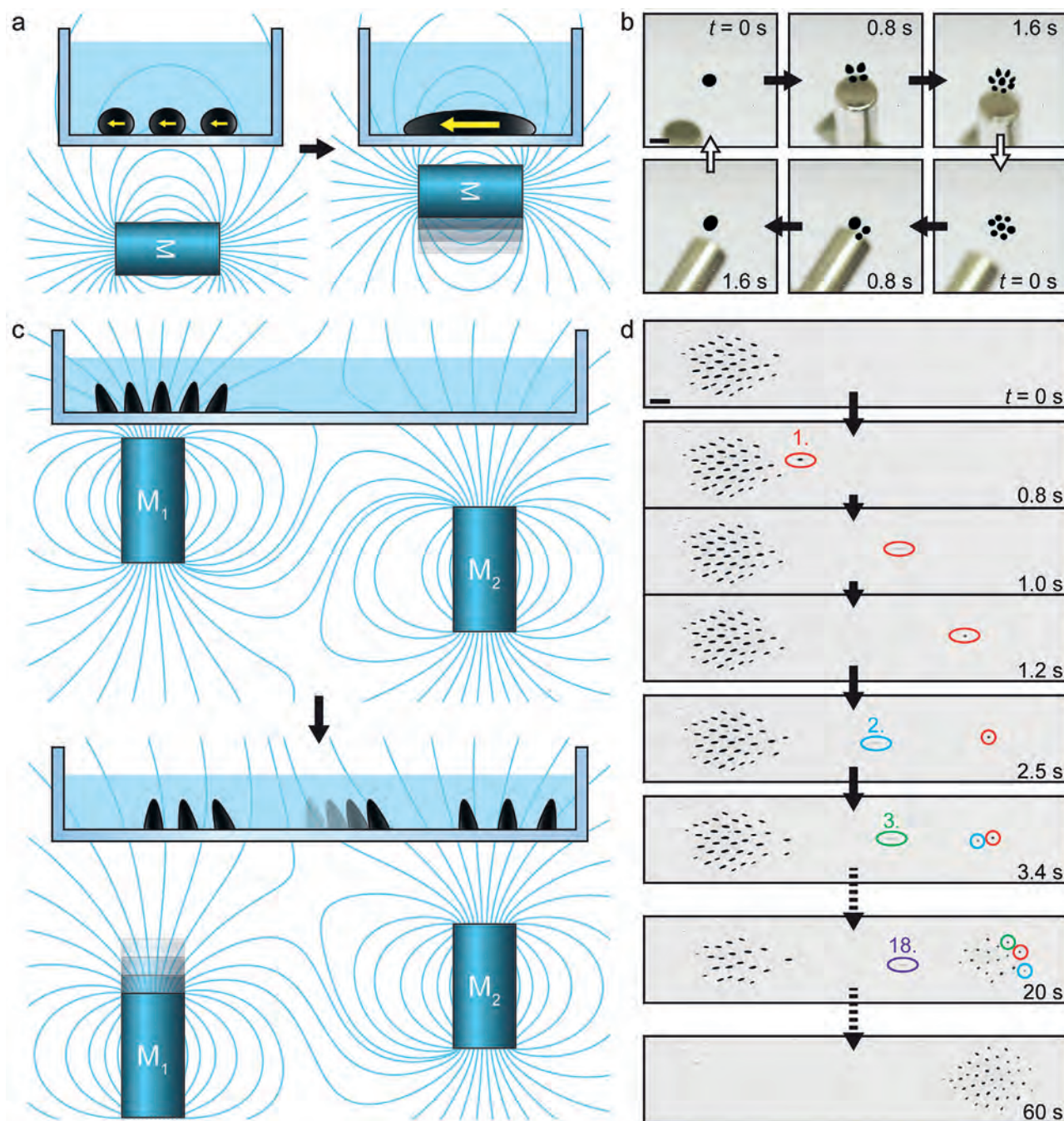


**Figure 4.** Microfluidics operations. a) Schematic of field-induced droplet combination. As a horizontally oriented magnet is brought closer, the ferrofluid droplets magnetize horizontally (yellow arrows) and combine due to their mutual attraction. b) Image series of splitting (top row) and combining (bottom row) a ferrofluid droplet with a magnetic field (Movie S3, Supporting Information). Scale bar: 2 mm. c) Schematic of sequential transport of droplets between populations. As magnet  $M_1$  is lowered away from the droplets, they are increasingly pulled toward  $M_2$  due to the magnetic field (cyan lines), until they slide one by one from above  $M_1$  to above  $M_2$ . d) Top-view image series of sequential transport of ferrofluid droplets (numbered in the order of movement) with two magnets (Movie S6, Supporting Information). Scale bar: 1 mm.

if the method is used to quantify surfactant concentrations, for example.

Understanding the role of SPION concentration and interfacial tension in field-induced splitting allows for the creation of self-assembled droplet populations in a controlled manner.

These could serve as a platform for a new kind of population-based digital microfluidics. Droplet division is difficult to achieve in conventional magnetic digital microfluidics without irreversibly pinning the droplet,<sup>[10]</sup> but is easy using the field-induced droplet splitting. Droplet combination is possible by rotating the

magnet by 90°, which induces horizontal magnetization and mutual attraction between the droplets (Figure 4a,b; Movie S3, Supporting Information). The self-assembled population can be transported as a whole with a single vertical magnet, while keeping the droplets separate due to their mutual repulsion. The lubricating layer of immiscible liquid prevents pinning and allows moving the droplets with little friction (Figure S2, and Movies S4 and S5, Supporting Information). Individual droplets can be extracted from the population as needed with the help of another magnet (Figure 4c,d; Movie S6, Supporting Information). Thus, it is possible to switch between traditional droplet-based microfluidics scheme, where all the droplets are addressed simultaneously via flow control, and digital microfluidics scheme, where droplets are addressed individually. Combining these concepts would allow developing more flexible droplet manipulation solutions. Since the population-based digital microfluidics concept is based on permanent magnets, manual devices working without electricity could also be designed for field operations in remote locations.

In this work, we investigated magnetic-field-induced splitting of aqueous ferrofluid microdroplets immersed in an immiscible liquid. The formation of satellite droplets during the splitting process was studied using high-speed imaging, and while the surface roughness affected splitting dynamics, it did not have a strong effect on the final droplet size and number. The mother droplet stability was shown to follow a simple theory (Equation (1)) over a wide range of interfacial tension and magnetization values, which were investigated by varying surfactant and magnetic nanoparticle concentrations. Self-assembled droplet populations created by sequential splitting events were systematically studied, and regimes of labyrinthine patterns, dumbbell shaped, and conical droplets were identified. These results can be used to develop methods for measuring interfacial tension in liquid–liquid systems as well as novel digital microfluidics concepts using magnetically controlled ferrofluid droplet populations.

## Experimental Section

**Splitting Experiments:** A typical splitting experiment was performed as follows: a PS Petri dish (10 cm diameter, VWR) or a transparent, flat-sided container (25 × 25 × 16 mm<sup>3</sup>, Ted Pella, Inc.) was filled with ≈3 mL of 5 cSt silicone oil or octane. Low interfacial tension experiments were done by adding either SDS to the ferrofluid or C<sub>12</sub>E<sub>5</sub> to the outer phase (octane). All chemicals were purchased from Sigma–Aldrich. A neodymium magnet (diameter = 20 mm, height = 42 mm; Supermagnete) was attached to a computer-controlled linear stage (Zaber X-LSQ300B) underneath the container. At the beginning of the experiment, the magnet was far away (>100 mm) from the container, creating a field of ≈1.2 kA m<sup>−1</sup> at the container bottom. A ferrofluid droplet (0.5–5 μL when using SDS, 0.2 μL when using C<sub>12</sub>E<sub>5</sub>) was pipetted in the filled container. To avoid the effect of electrostatic charging on the droplet, an electrostatic gate was passed around the sample. The droplet was left to equilibrate for 3 min, after which the magnet was lifted toward the ferrofluid at a velocity of 1 mm s<sup>−1</sup> until a minimum distance (2–5 mm, creating a field of 280–410 kA m<sup>−1</sup> at the container bottom) was reached. The increasing magnetic field and gradient induced droplet splitting, which was captured by recording a video with a digital single-lens reflex camera (Canon EOS 60D). The videos were analyzed with custom Matlab functions to extract droplet positions and cross sections, which were fitted with ellipses. The beginning of an individual splitting event was identified by a decrease in minor axis length of the droplet cross section (Movie S7, Supporting Information). The corre-

sponding major axis length was used as the experimental critical wavelength.

**High-Speed Imaging:** Top- and side-view high-speed imaging were performed using two synchronized high-speed cameras (Phantom Miro M310 and Phantom v1610) at a frame rate of 11 200 fps using two macrolenses (with a resolution of ≈4.3 μm pixel<sup>−1</sup>). To make the side-view imaging easier to analyze, a rectangular magnet (100 × 13 × 6 mm<sup>3</sup>) was used, which induces splitting along the direction of the longest magnet side. More information can be found in the Supporting information.

**Statistical Analysis:** In splitting experiments, video data were preprocessed with automatic thresholding; droplets were resolved with image recognition; and incorrectly identified droplets were removed using custom Matlab functions. All data were presented as mean ± standard deviation. In grouped splitting experiments presented in Figure 3c, sample size  $n = 2–23$ . All statistical analyses were calculated with Matlab.

## Supporting Information

Supporting Information is available from the Wiley Online Library or from the author.

## Acknowledgements

The authors acknowledge the support from the European Research Council ERC-2016-CoG (725513-SuperRepel) and the Academy of Finland (Centres of Excellence Programme (2014–2019, Grant Agreement No. 272361), Academy Key Project (Grant Agreement No. 304174), and postdoctoral researcher project (Grant Agreement No. 309237)). The authors thank M. Junaid (Aalto University) for performing the atomic force microscopy measurements and M. Vuckovac (Aalto University) for preparing the superhydrophobic samples. Work at IIT Madras was supported by the Nano Mission, Government of India. The authors appreciate discussions with Prof. Ulf Olsson (Lund University) on the C<sub>12</sub>E<sub>5</sub> surfactant.

## Conflict of Interest

The authors declare no conflict of interest.

## Keywords

ferrofluids, fluid dynamics, interfacial tension, magnetic fields, magnetic nanoparticles, microfluidics

Received: January 30, 2020

Revised: May 17, 2020

Published online:

- [1] R. E. Rosensweig, *Ferrohydrodynamics*, Courier Corporation, North Chelmsford, MA 2013.
- [2] *Colloidal Magnetic Fluids: Basics, Development and Application of Ferrofluids* (Ed: S. Odenbach), Springer, Berlin 2009.
- [3] I. Nkurikiyimfura, Y. Wang, Z. Pan, *Renewable Sustainable Energy Rev.* **2013**, 21, 548.
- [4] M. Bahiraei, M. Hangi, J. Magn. Mater. **2015**, 374, 125.
- [5] M. Backholm, M. Vuckovac, J. Schreier, M. Latikka, M. Hummel, M. B. Linder, R. H. A. Ras, *Langmuir* **2017**, 33, 6300.

- [6] X. Liu, N. Kent, A. Ceballos, R. Streubel, Y. Jiang, Y. Chai, P. Y. Kim, J. Forth, F. Hellman, S. Shi, D. Wang, B. A. Helms, P. D. Ashby, P. Fischer, T. P. Russell, *Science* **2019**, 365, 264.
- [7] I. Torres-Díaz, C. Rinaldi, *Soft Matter* **2014**, 10, 8584.
- [8] R.-J. Yang, H.-H. Hou, Y.-N. Wang, L.-M. Fu, *Sens. Actuators, B* **2016**, 224, 1.
- [9] N.-T. Nguyen, *Microfluid. Nanofluid.* **2012**, 12, 1.
- [10] Y. Zhang, N.-T. Nguyen, *Lab Chip* **2017**, 17, 994.
- [11] G. Huang, M. Li, Q. Yang, Y. Li, H. Liu, H. Yang, F. Xu, *ACS Appl. Mater. Interfaces* **2017**, 9, 1155.
- [12] X. Zhang, L. Sun, Y. Yu, Y. Zhao, *Adv. Mater.* **2019**, 31, 1903497.
- [13] J. Philip, J. M. Laskar, *J. Nanofluids* **2012**, 1, 3.
- [14] W. Wang, J. V. I. Timonen, A. Carlson, D.-M. Drotlef, C. T. Zhang, S. Kolle, A. Grinthal, T.-S. Wong, B. Hatton, S. H. Kang, S. Kennedy, J. Chi, R. T. Blough, M. Sitti, L. Mahadevan, J. Aizenberg, *Nature* **2018**, 559, 77.
- [15] P. Irajizad, M. Hasnain, N. Farokhnia, S. M. Sajadi, H. Ghasemi, *Nat. Commun.* **2016**, 7, 13395.
- [16] A. Ahmed, I. Hassan, I. M. Mosa, E. Elsanadidy, M. Sharafeldin, J. F. Rusling, S. Ren, *Adv. Mater.* **2019**, 31, 1807201.
- [17] A. Al-Azawi, M. Latikka, V. Jokinen, S. Franssila, R. H. A. Ras, *Small* **2017**, 13, 1700860.
- [18] A. Chiolerio, M. B. Quadrelli, *Adv. Sci.* **2017**, 4, 1700036.
- [19] A. Chiolerio, M. B. Quadrelli, *Energy Technol.* **2019**, 7, 1800580.
- [20] C. P. Lee, Y. H. Chen, M. F. Lai, *Microfluid. Nanofluid.* **2014**, 16, 179.
- [21] G. Kitenbergs, K. Ērglis, R. Perzynski, A. Cēbers, *J. Magn. Magn. Mater.* **2015**, 380, 227.
- [22] C. Vasilescu, M. Latikka, K. D. Knudsen, V. M. Garamus, V. Socoliuc, R. Turcu, E. Tombácz, D. Susan-Resiga, R. H. A. Ras, L. Vékás, *Soft Matter* **2018**, 14, 6648.
- [23] M. Tjahjadi, H. A. Stone, J. M. Ottino, *J. Fluid Mech.* **1992**, 243, 297.
- [24] J. V. I. Timonen, M. Latikka, L. Leibler, R. H. A. Ras, O. Ikkala, *Science* **2013**, 341, 253.
- [25] M. Latikka, M. Backholm, J. V. I. Timonen, R. H. A. Ras, *Curr. Opin. Colloid Interface Sci.* **2018**, 36, 118.
- [26] T. Vieu, C. Walter, *J. Fluid Mech.* **2018**, 840, 455.
- [27] C. Rigoni, M. Pierno, G. Mistura, D. Talbot, R. Massart, J.-C. Bacri, A. Abou-Hassan, *Langmuir* **2016**, 32, 7639.
- [28] C. Rigoni, S. Bertoldo, M. Pierno, D. Talbot, A. Abou-Hassan, G. Mistura, *Langmuir* **2018**, 34, 9762.
- [29] D. Daniel, J. V. I. Timonen, R. Li, S. J. Velling, J. Aizenberg, *Nat. Phys.* **2017**, 13, 1020.
- [30] P. Zhang, S. Wang, S. Wang, L. Jiang, *Small* **2015**, 11, 1939.
- [31] L. Rayleigh, *Proc. Lond. Math. Soc.* **1878**, s1–10, 4.
- [32] F. D. Rumscheidt, S. G. Mason, *J. Colloid Sci.* **1962**, 17, 260.
- [33] H. A. Stone, L. G. Leal, *J. Fluid Mech.* **1989**, 198, 399.
- [34] J. Balogh, U. Olsson, *J. Dispersion Sci. Technol.* **2007**, 28, 223.

Copyright WILEY-VCH Verlag GmbH & Co. KGaA, 69469 Weinheim, Germany, 2020.

## Supporting Information

### **Ferrofluid microdroplet splitting for population-based microfluidics and interfacial tensiometry**

Mika Latikka, Matilda Backholm, Avijit Baidya, Alberto Ballesio, Amandine Serve, Gregory Beaune, Jaakko Timonen, Thalappil Pradeep and Robin Ras\*

**Supplementary movies**

- Movie S1: Magnetic field induced splitting. A) 5  $\mu\text{L}$  aqueous ferrofluid droplet with SDS in silicone oil (top view analysis). B) 1  $\mu\text{L}$  aqueous ferrofluid droplet in octane (top and side views).
- Movie S2: High-speed videos of a field-induced splitting of a 5  $\mu\text{L}$  ferrofluid droplet in 5 cSt silicone oil on a Glaco-coated substrate. The videos were recorded at 11200 fps.
- Movie S3: Sequential splitting and combination of 1.5  $\mu\text{L}$  ferrofluid droplet in 5 cSt silicone oil with a small cylindrical magnet (diameter 4.5, length 9 mm).
- Movie S4: Ferrofluid droplet population (initial volume 5  $\mu\text{L}$ ) immersed in 5 cSt silicone oil moved around on a polystyrene surface with a permanent magnet.
- Movie S5: Ferrofluid droplet population (initial volume 5  $\mu\text{L}$ ) in air moved around on a polystyrene surface with a permanent magnet. The droplets pin to the surface, leaving behind small sessile droplets.
- Movie S6: Sequential droplet transport from one ferrofluid droplet population to another with two magnets in 5 cSt silicone oil.
- Movie S7: Analysis of magnetic field induced splitting of a 2  $\mu\text{L}$  ferrofluid droplet in octane. When a ferrofluid droplet becomes unstable, its minor axis (top view) starts to decrease, and corresponding major axis is the maximum droplet diameter.

## Properties of the permanent magnets and the ferrofluids

### *Magnets*

Most of the splitting experiments were performed using a cylindrical neodymium permanent magnet (diameter 20 mm, height 42 mm, Supermagnete, **Figure S1a**). Investigation of the satellite droplet formation using high-speed imaging was done with a rectangular magnet (100 x 13 x 6 mm<sup>3</sup>, K&J Magnetics), which induces splitting along the direction of the longest magnet side. Predictable splitting direction made the side view imaging easier.

During data analysis the magnetic field affecting the droplets was evaluated based on the field profile of the magnet measured with a gaussmeter (Lakeshore 410), magnet's vertical distance from the ferrofluid and droplet shapes. Droplets' horizontal distance from the magnet axis was assumed small, and the field value was calculated at the magnet axis. The field was calculated at the approximate height of the mass center of the droplets, which was estimated based on total ferrofluid volume and cross-sectional area of the droplets assuming the droplet shape to be half of an ellipsoid. Demagnetizing field was calculated assuming ellipsoidal droplets.<sup>[1]</sup>

### *Ferrofluid synthesis*

Aqueous ferrofluid was synthesized using the co-precipitation method<sup>[2]</sup> and stabilized with citric acid near pH 7, as described earlier.<sup>[3]</sup> The excess water was evaporated in room temperature until the ferrofluid contained up to 25 vol% of nanoparticles. Ferrofluid was diluted with ultrapure water for the experiments as needed. Approximate superparamagnetic iron oxide nanoparticle (SPION) volume percent  $c_{\text{SPION}}$  is calculated from ferrofluid density assuming that ferrofluid consists only of water and SPIONs (SPION density is assumed 5175 kg m<sup>-3</sup>). According to XPS and FTIR spectra the nanoparticles consist of magnetite.<sup>[3]</sup>

### *Ferrofluid characterization*

Ferrofluid samples (7  $\mu$ l) were sealed in polypropylene powder cups with vacuum grease and Parafilm. Hysteresis loops were measured with vibrating sample magnetometer (Quantum Design PPMS Dynacool) using field values of -9 – 9 T (Figure S1b-d).



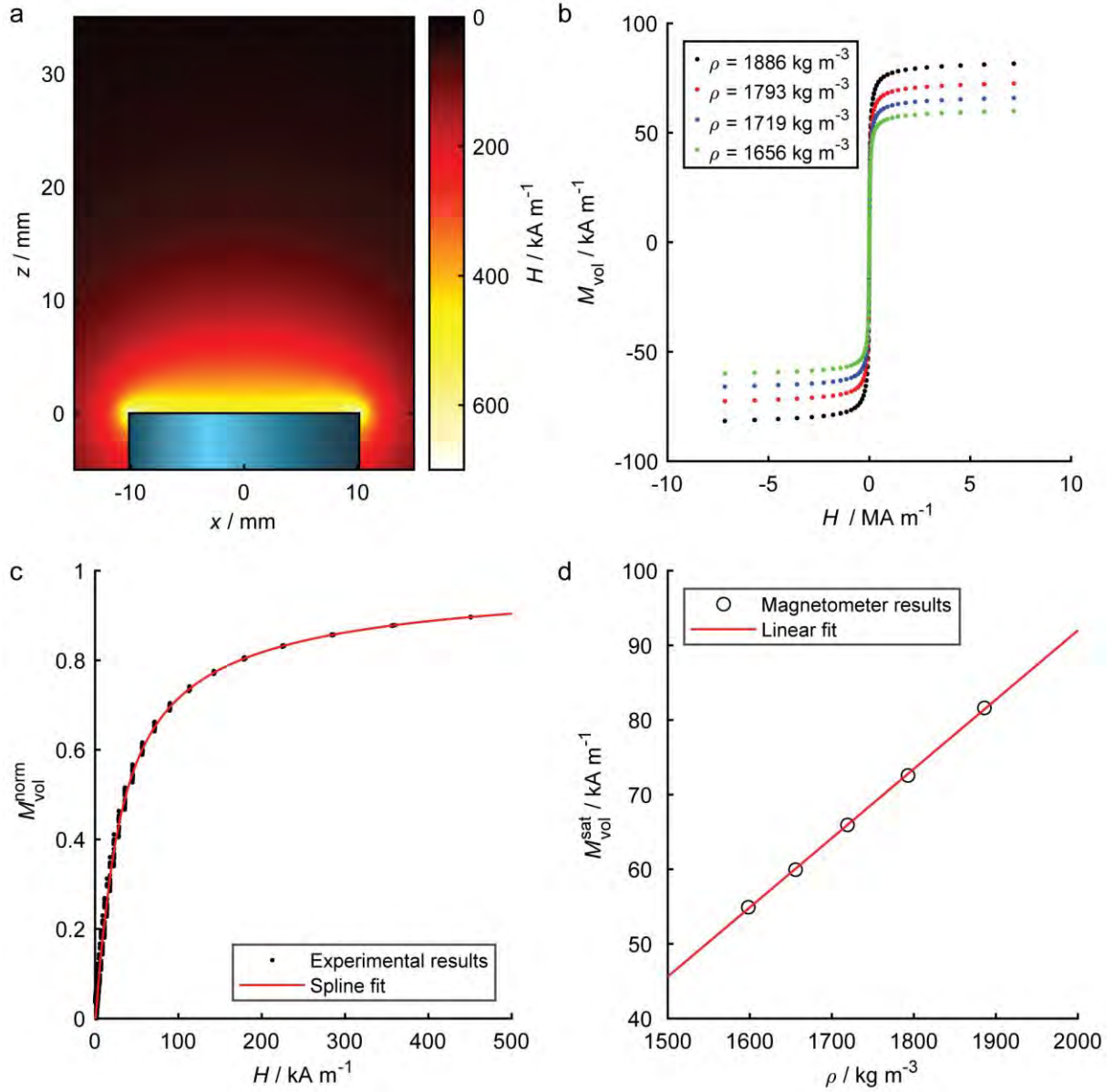


**Figure S1: Magnetic properties of the permanent magnet and the ferrofluids.** a) Magnetic field  $H$  created by the cylindrical permanent magnet used in most of the splitting experiments. b) Magnetic hysteresis loops with different ferrofluid densities. c) Normalized magnetization  $M_{\text{vol}}^{\text{norm}} = M_{\text{vol}}/M_{\text{vol}}^{\text{sat}}$  as a function of applied magnetic field. d) Saturation magnetization  $M_{\text{vol}}^{\text{sat}}$  as a function of ferrofluid density  $\rho$ .

### Low-friction surfaces

In order to achieve individual, highly mobile droplets via magnetic field induced splitting, the surface supporting the droplets has to be sufficiently repellent to the aqueous ferrofluid. This can be achieved by using a superhydrophobic surface<sup>[4]</sup> or a lubricating layer of immiscible liquid (**Figure S2**). In case of lubricated surface the splitting dynamics depend on the surface roughness. On a rough surface (Figure S2c) the increased flow in the roughness reduces the viscous dissipation when the droplet moves compared to a flat surface (Figure S2b), which leads to faster splitting dynamics (**Figure S3**).

When ferrofluid droplets in air are actuated on a smooth polystyrene (PS) surface by horizontally moving the permanent magnet below the substrate, the droplets pin to the surface, leaving behind small immobile droplets (Figure S3d, **Movie S5**). However, when the droplets are immersed in silicone oil, they can be moved without pinning (Figure S3e, **Movie S4**).

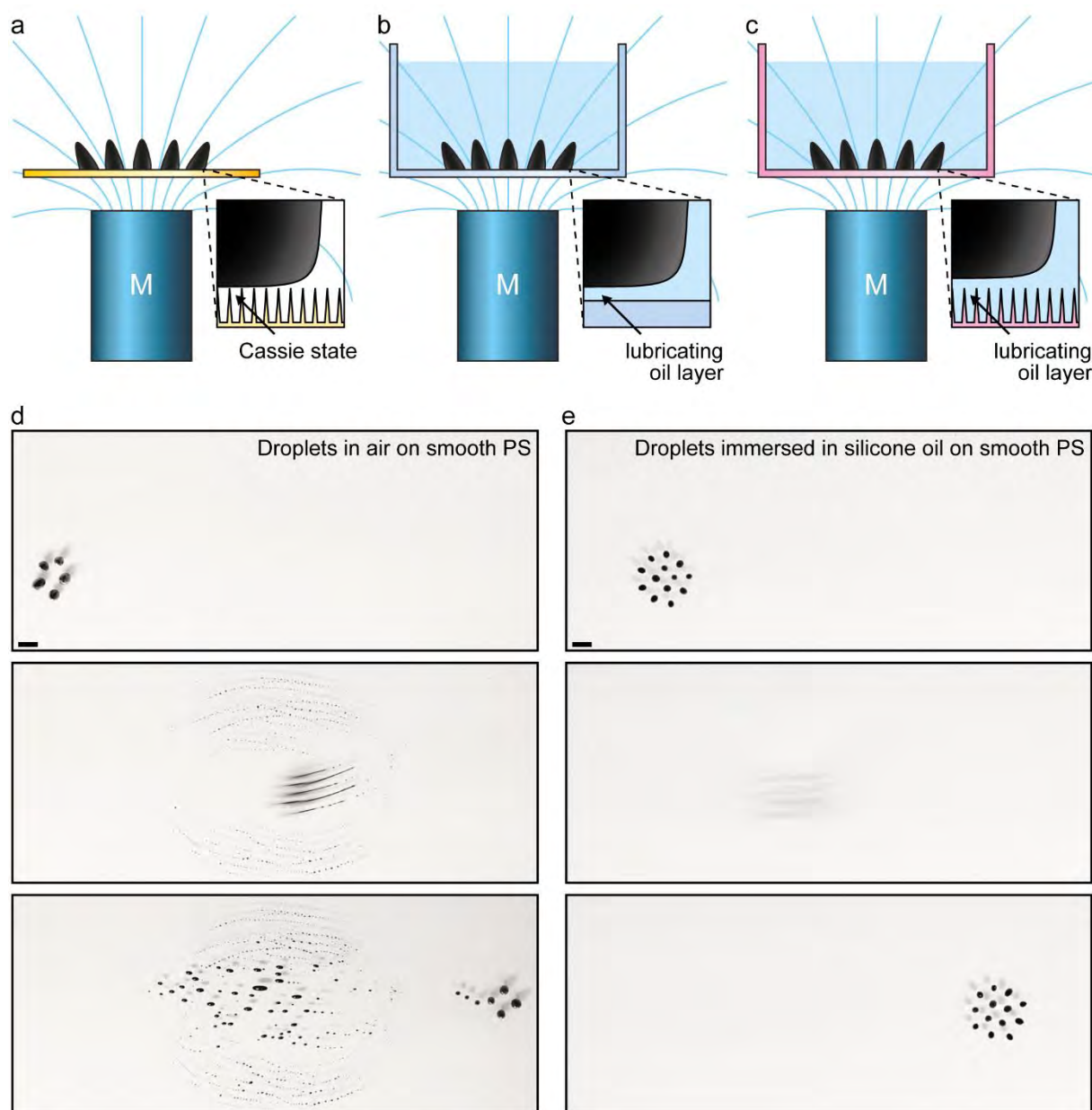


**Figure S2: Schematic of droplet populations on different low-friction water-repellent surfaces.** Adhesion between the droplets and the surface is reduced by the Cassie state on a superhydrophobic surface (a) and a lubricating oil layer for droplets immersed in immiscible liquid (b and c). Splitting dynamics are slower on flat lubricated surfaces (b) compared to rough lubricated surfaces (c). Magnetic field lines created by the permanent magnet below the droplets are shown in cyan. d) Droplet population (initial ferrofluid volume 5  $\mu\text{L}$ ) in air moved around on a PS surface with a permanent magnet below the substrate. The droplets pin to the surface during transport, leaving behind small sessile droplets (Movie S5). e) As (d), but the droplets are immersed in 5 cSt silicone oil, which prevents pinning to the surface (Movie S4). Scale bars 2 mm.

## Field-induced splitting on different surfaces

### *Atomic force microscopy*

The effect of surface roughness on splitting dynamics was investigated using a PS surface and a PS surface coated with the commercial superhydrophobic spray Glaco. To assess the roughness of the two surfaces, atomic force microscopy (AFM) imaging was performed in air by using Dimension icon (Bruker instrument). The images were acquired in ScanAsyst Peak force tapping mode by using rectangular shaped silicon cantilevers (OTESPA-R3 Bruker) with a nominal spring constant of  $26 \text{ N m}^{-1}$ , resonance frequency in air 300 KHz and typical tip curvature radius of 8 nm. Images of  $(50 \times 50 \text{ }\mu\text{m}^2)$  were collected with 256 data points per line at the rate of 1 Hz with the peak force amplitude of 150 nm. RMS roughness values were  $6.2 \pm 0.2 \text{ nm}$  for PS and  $43 \pm 3 \text{ nm}$  for Glaco-coated PS surface (Figure S3a-b). The values are mean and standard deviations of three measurements on different parts of the samples.

### *High-speed imaging on different surfaces*

Satellite droplet formation on the two surfaces was investigated using high-speed imaging. At the beginning of the experiment, the rectangular magnet was located 8 cm below the container to keep the magnetic field affecting the droplets small. The magnet was then moved up with a motorized stage at a speed of  $1 \text{ mm s}^{-1}$  until it almost touched the container. The experiments were performed with a  $5 \text{ }\mu\text{L}$  ferrofluid mother droplet with SPION volume percent  $c_{\text{SPION}} = 22 - 25 \text{ vol\%}$ , which corresponds to ferrofluid densities  $\rho = 1.938 - 2.060 \text{ g mL}^{-1}$  (Figure S3c-d). Lower SPION concentrations could not be investigated, as the magnet was not powerful enough to split a  $5 \text{ }\mu\text{L}$  droplet of less concentrated ferrofluid.

When viewed from the top the breakup process looks very similar to the breakup of a viscous, Newtonian capillary bridge in a viscous, infinite medium,<sup>[5]</sup> where a thickening of the middle of the bridge can be seen at early times (Figure 2b). As the largest satellite droplet is being formed in the center, the narrow side bridges protruding from its sides evolve and break up in a repeated, self-similar fashion into several tiny subsatellite droplets. Interestingly, the W-shape of the time evolution on the Glaco-coated substrate is qualitatively very similar to what was found in the work by Tjahjadi et al.,<sup>[5]</sup> where the breakup first started at the edges of the bridge and then continued from the center after a short time. The pure PS substrate seems to render stronger drag between the ferrofluid and the solid substrate, leading to slower breakup dynamics that, furthermore, proceeds in the opposite direction as compared to rougher Glaco-coated substrate.

### *Splitting-based IFT measurements on different surfaces*

We used three different substrates to measure interfacial tension (IFT) between the ferrofluid and 5 cSt silicone oil. No significant difference in the measured IFT was observed between different substrates: a PS container ( $\text{IFT } 33 \pm 7 \text{ mN m}^{-1}$ ), a glass surface coated with Glaco ( $\text{IFT } 32 \pm 8 \text{ mN m}^{-1}$ ) and a copper substrate coated with nanorough silver and fluorinated thiol to make it superhydrophobic ( $\text{IFT } 30 \pm 8 \text{ mN m}^{-1}$ ).<sup>[6]</sup> Pendant droplet method was used as a control technique, and results obtained with splitting experiments agree with it within experimental accuracy ( $\text{IFT } 38 \pm 2 \text{ mN m}^{-1}$ ). Uncertainties represent standard deviation.

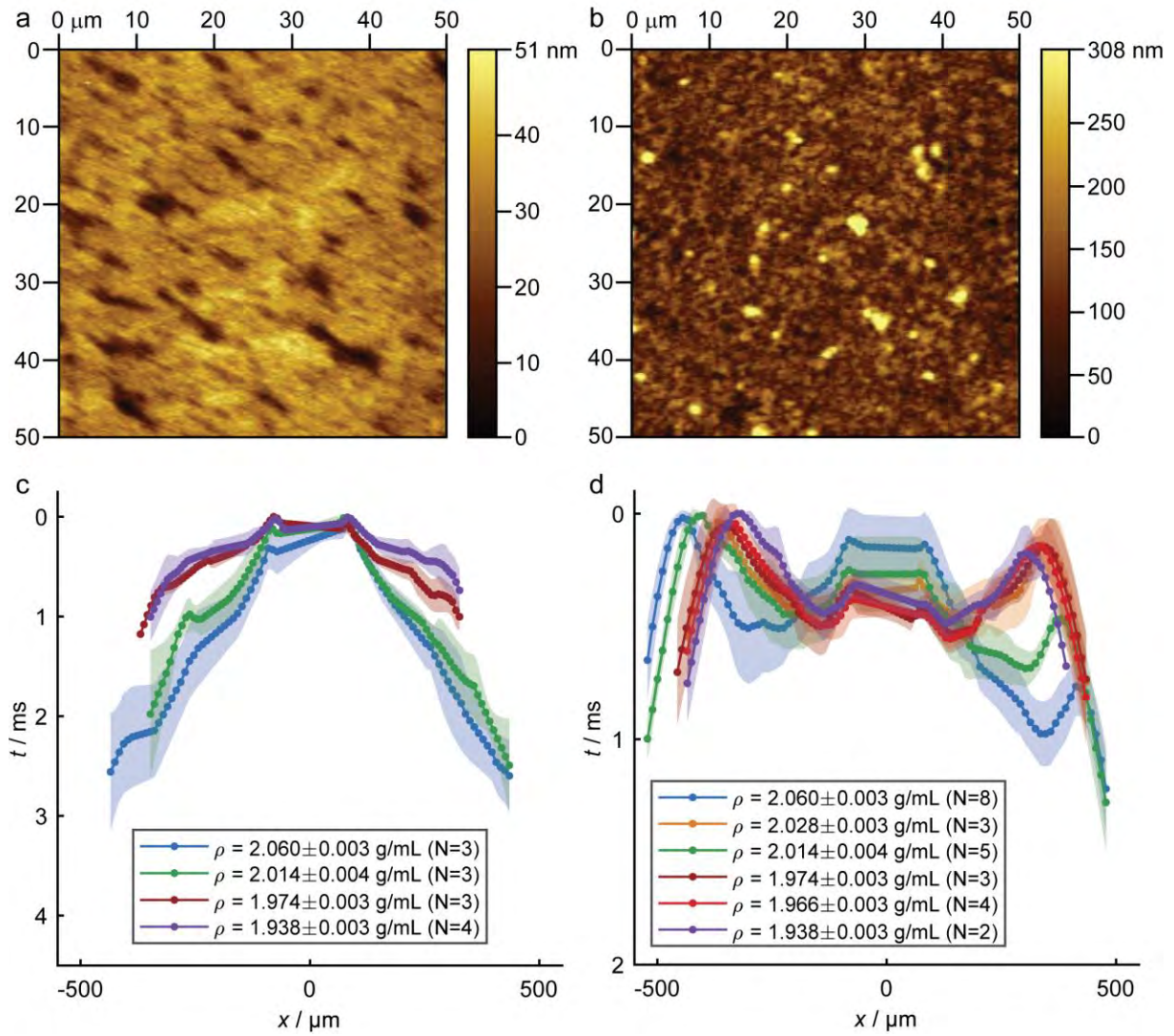


**Figure S3: Satellite droplet formation dynamics on different surfaces.** a-b) AFM measurements of a) PS container and b) Glaco-coated PS container. c-d) Averaged time evolution of the satellite droplet formation dynamics on c) PS container and d) Glaco-coated PS container for different ferrofluid densities  $\rho$ . The shaded area shows the standard deviation of multiple (N) experiments.

**Ferrofluid droplet shape in a magnetic field**

As the cylindrical permanent magnet underneath the ferrofluid is brought closer, magnetic field and vertical field gradient are increased. However, the field gradient increases more rapidly than the field strength and magnetization (**Figure S4a**). Consequently, as the magnet is brought closer to the ferrofluid the effective Bond number  $B_e$ , which is related to droplet flattening, increases compared to the dimensionless number  $S$ , which is related to droplet elongation. As a result, the droplets are typically first elongated and then flattened during splitting experiment. The droplet shape depends also on the SPION concentration and IFT (**Figure S4b-d**).



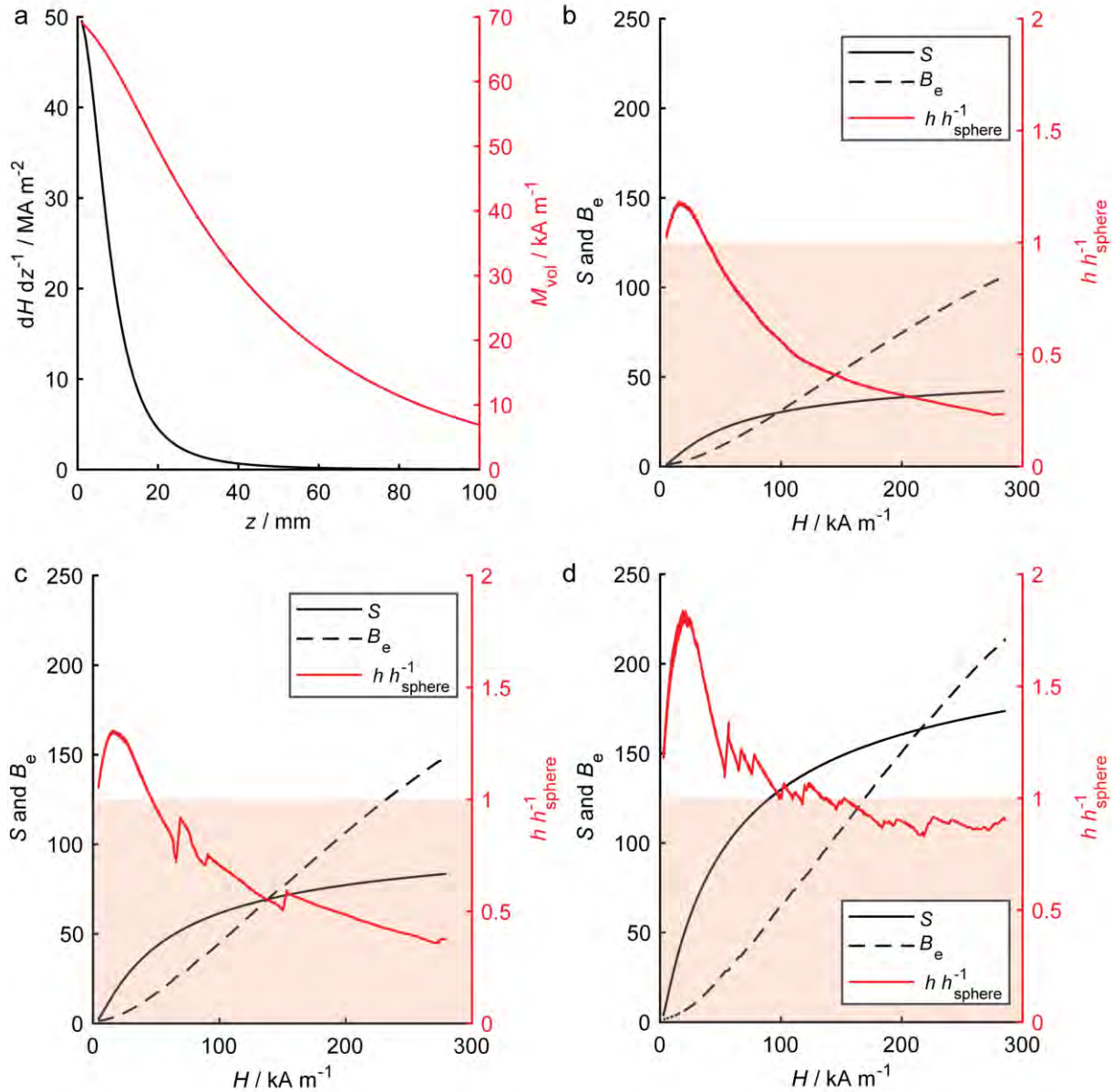


**Figure S4: Ferrofluid droplet shape in magnetic field.** a) Field gradient  $dH/dz$  and ferrofluid magnetization  $M_{\text{vol}}$  ( $c_{\text{SPION}} = 20$  vol%, with no demagnetizing field) as a function of the vertical distance  $z$  from the surface of the cylindrical magnet.  $dH/dz$  grows more rapidly than  $M_{\text{vol}}$  when  $z$  is small. b-d) show the relative magnitudes of  $S$  and  $B_e$ , and the height of the droplets  $h$  compared to a height of a sphere with equal volume  $h_{\text{sphere}}$ . Red shaded area corresponds to flattened droplets.  $h$  is calculated from the top view images using the total ferrofluid volume and cross-sectional droplet areas by assuming ellipsoidal droplet shape. As  $S$ ,  $B_e$  and  $h$  are approximations, only a qualitative agreement is expected. b) With  $c_{\text{SPION}} = 8$  vol%  $B_e$  dominates  $S$  already at relatively small magnetic fields and droplet is flattened. c) Higher  $c_{\text{SPION}}$  (12 vol%) leads to a smaller difference between  $B_e$  and  $S$ , and less flattened droplets. d) With  $c_{\text{SPION}} = 17$  vol%  $S$  is significantly larger than  $B_e$  and droplets are elongated at low magnetic fields. At high fields  $B_e$  is approximately equal to  $S$ , and the droplet heights remains close to that of corresponding spheres.

#### Droplet self-assembly

Ferrofluid droplets self-assemble due to their attraction to the magnet axis and their mutual dipolar repulsion. The magnetic field  $H_{\text{mag}}$  created by the permanent magnet near the magnet axis is approximately parabolic:<sup>[4]</sup>

$$H_{\text{mag}} = H_0(z) - \frac{1}{2}cl^2$$

where  $H_0$  is the field at the magnet axis at distance  $z$  from magnet surface,  $c = -d^2H/dl^2$  is the radial field curvature and  $l$  is distance from the magnet axis. Magnetized ferrofluid droplet creates a dipolar field:<sup>[7]</sup>

$$H_{\text{drop}}(\vec{r}) = \frac{1}{4\pi} \left( \frac{3\vec{r}(\vec{m} \cdot \vec{r})}{|\vec{r}|^5} - \frac{\vec{m}}{|\vec{r}|^3} \right)$$

where  $r$  is the location vector and  $m$  is the magnetic dipole moment of the droplet. The energy  $U$  of a magnetic dipole in a magnetic field  $H$  is:<sup>[7]</sup>

$$U = -\mu_0 \vec{m} \cdot \vec{H}$$

The droplets are confined to (x,y)-plane, while the dipolar moments  $m_i$  are approximately parallel to z-direction, and as a result  $\vec{m}_i \cdot (\vec{r}_i - \vec{r}_j) \approx 0$  and  $\vec{m}_i \cdot \vec{m}_j \approx m_i m_j$ . The interdroplet dipolar interaction energy  $U_{\text{dipolar}}$  of the droplet population is then:

$$U_{\text{dipolar}} = \frac{\mu_0}{4\pi} \sum_{i=1}^N \sum_{j=i+1}^N \frac{m_i m_j}{|\vec{r}_i - \vec{r}_j|^3}$$

The potential energy increases as the distance  $|\vec{r}_i - \vec{r}_j|$  between the droplet decreases, leading to interdroplet repulsion.

The total energy  $U$  of the droplet population in the magnetic field created by the permanent magnet is:<sup>[4]</sup>

$$U = \frac{\mu_0}{4\pi} \sum_{i=1}^N \sum_{j=i+1}^N \frac{m_i m_j}{|\vec{r}_i - \vec{r}_j|^3} - \mu_0 \sum_{i=1}^N m_i \left( H_0 - \frac{1}{2} c |\vec{r}_i|^2 \right)$$

## Interfacial tension measurements

### *Pendant droplet measurements*

IFTs between ferrofluid and surrounding media were measured with the pendant droplet method using Attension Theta tensiometer (Biolin Scientific). IFT value was recorded after equilibration time of 3 minutes, as with splitting experiments. Measurements were repeated using water instead of ferrofluid for comparison (**Figure S5**).

### *Micropipette aspiration measurements*

Micropipettes were prepared by pulling borosilicate capillaries (WPI, 1 mm, 0.58 mm o.d./i.d.) using a flaming/brown type puller (P-97, Sutter Instrument Company). Afterward, the pipettes were sized to about 20  $\mu\text{m}$  in inner diameter by using a microforge (MF-900, Narishige). To introduce pipettes horizontally into sample holders, they were bent by heating the pipette on a flame. Micropipettes were made hydrophobic by incubation for at least 1 h in an organic solution made of dichlorodimethylsilane (Sigma-Aldrich) diluted 20 times in cyclohexane. Pipettes were then filled with octane and connected to an octane reservoir attached to a piezoelectric pressure controller unit (Elveflow). The pressure was controlled with a precision of about 10 microbars using the instrument software during the measurements. Aspirated droplets of ferrofluid were visualized with an inverted microscope (Nikon Eclipse Ti) equipped with various objectives (from  $1\times$  to  $60\times$ ) associated with a  $1.5\times$  magnification device. Droplets inside micropipettes were observed using a CCD camera (Andor Zyla Scmos). All experiments were performed at ambient pressure using an in-house built observation chamber. A 1-10  $\mu\text{L}$  pipette tip connected to the corresponding pipette was filled with successive “layers” of the octane – surfactant solution, ferrofluid, air and ferrofluid (**Figure S6a**). This strategy was used in order to limit the evaporation of the solvents during the experiments. The tip was then removed from the pipette and cut with a razor. The tip, which was our observation chamber, was placed on a microscopy slide on the stage of the microscope and the micropipette was inserted in the octane phase from the larger aperture. A pressure  $P_0$  was applied by the pressure controller to compensate for the high between the octane tank and the sample. There was no flow in the observation chamber when  $\Delta P_0$  was applied. The micropipette was put in contact with the ferrofluid and a pressure  $\Delta P > \Delta P_0$  was applied to aspirate the ferrofluid in the micropipette (**Figure S6b**). The pressure was decreased until the penetration length of the ferrofluid inside the pipette was equal to the radius of the micropipette  $R_p$ . This pressure was called the critical pressure  $\Delta P_c$ . If we continued to decrease the pressure, a large volume of ferrofluid was aspirated in the micropipette.

Knowing  $\Delta P_c$ , the interfacial tension  $\sigma$  between the ferrofluid and octane – surfactant solution could be determine using the Laplace law  $\left( - \frac{\Delta P_c}{2R_0} \right)$ , where  $R_0$  is the radius of curvature of the ferrofluid – octane interface.

Three sets of experiments were performed using octane solutions containing different concentrations of  $\text{C}_{12}\text{E}_5$  surfactant (0, 0.6, 2, 5, 7, 9, 12 and 14  $\text{mmol L}^{-1}$ ) (**Figure S6c**).

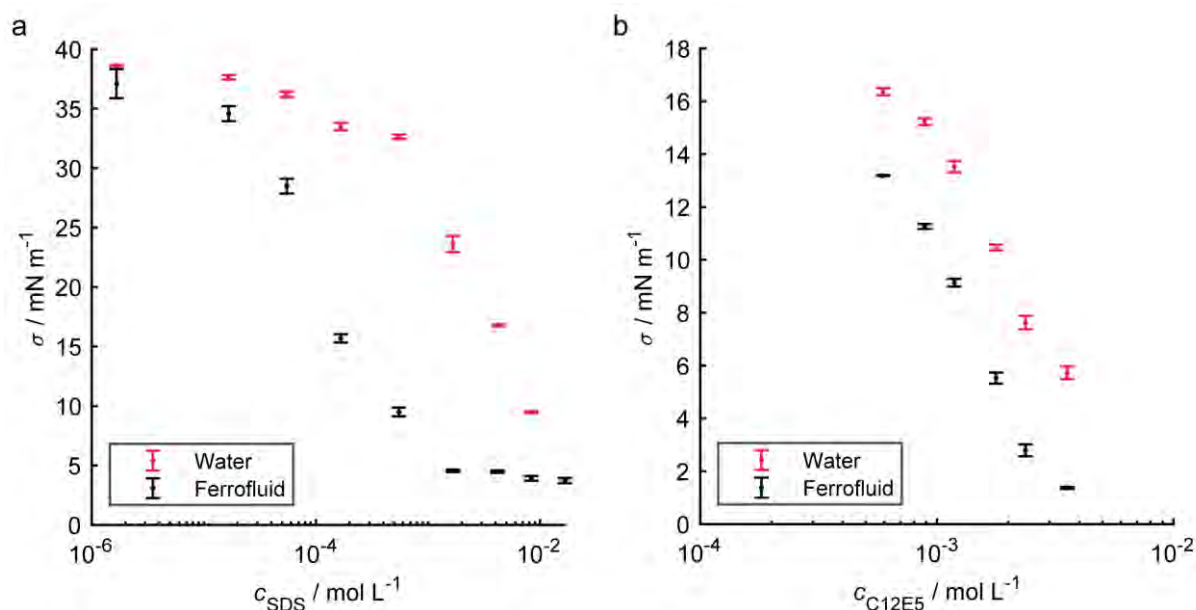


**Figure S5: Effect of SPIONs to IFT.** IFT was measured for one minute after equilibration time of three minutes. The values are mean values of 2 – 5 measurements and error bars represent standard deviation. a) IFT of water and ferrofluid droplets in silicone oil with sodium dodecyl sulfate (SDS) as a function of SDS concentration  $c_{\text{SDS}}$ . b) IFT of water and ferrofluid droplets with pentaethylene glycol monododecyl ether ( $\text{C}_{12}\text{E}_5$ ) in octane as a function of  $\text{C}_{12}\text{E}_5$  concentration  $c_{\text{C}_{12}\text{E}_5}$ .

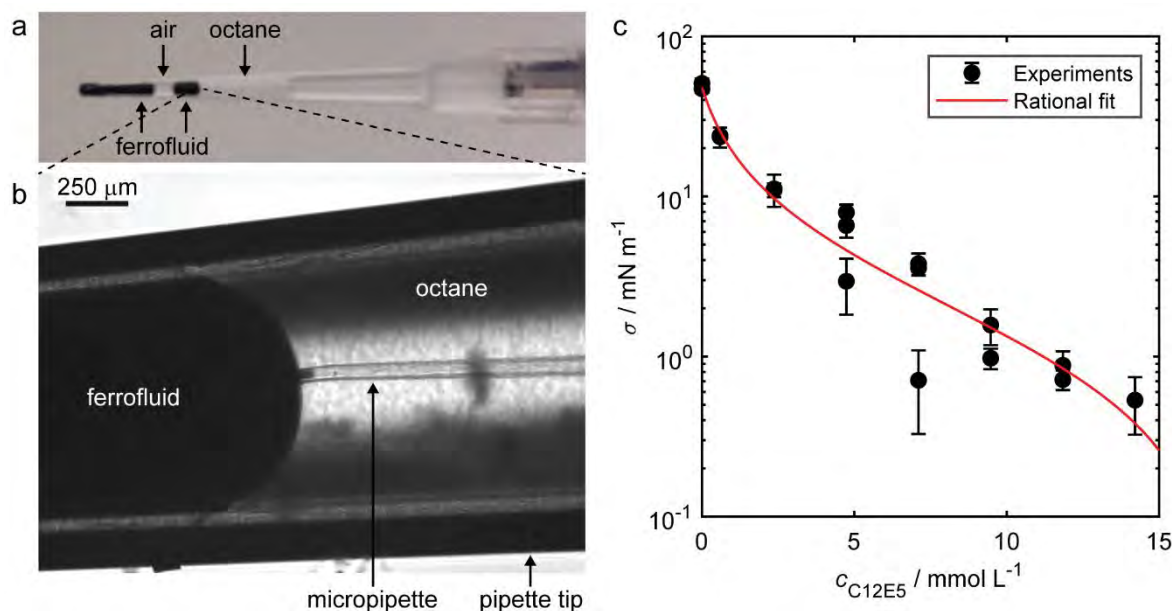


**Figure S6: Micropipette aspiration measurements.** a) Typical pipette tip in which the micropipette experiments were performed. b) Aspiration of the ferrofluid inside a micropipette at the ferrofluid/octane interface. c) IFT of ferrofluid in octane with  $\text{C}_{12}\text{E}_5$  as a function of  $c_{\text{C}_{12}\text{E}_5}$ . The black circles are mean values of 3 to 10 measurements and error bars represent standard deviation. The data was fitted with a rational function  $(p_1 x + p_2)/(x + q_1)$  (red line) weighted by the inverse of standard deviations of the data

points. The two outlying data points with lower IFT ( $c_{\text{C}_{12}\text{E}_5} = 4.7$  and  $7.1 \text{ mmol L}^{-1}$ ) are probably due to evaporation of the octane during the experiments.

### IFT measurements based on number of droplets

Instead of optically measuring the droplet diameters  $d$  as they split due to the field-induced instability, the critical wavelength  $\lambda_c$  can be approximated with the help of the total ferrofluid volume  $V_0$  and assuming the droplets are identical half ellipsoids. Volume of a single droplet  $V = V_0/n = 2/3 \pi (d/2)^2 h$ , where  $n$  is the number of droplets and  $h$  is the droplet height.

Right before splitting event  $\sigma_c = d = \sqrt[3]{6V_0/(\pi n a)}$ , where  $a = h d^{-1}$  is the droplet aspect ratio, which can be treated as a free parameter. When analyzing all the splitting experiments,  $a = 1.15$  minimizes the cumulative relative errors compared to control IFT measurements using pendant droplet and micropipette aspiration techniques (**Figure S7**).

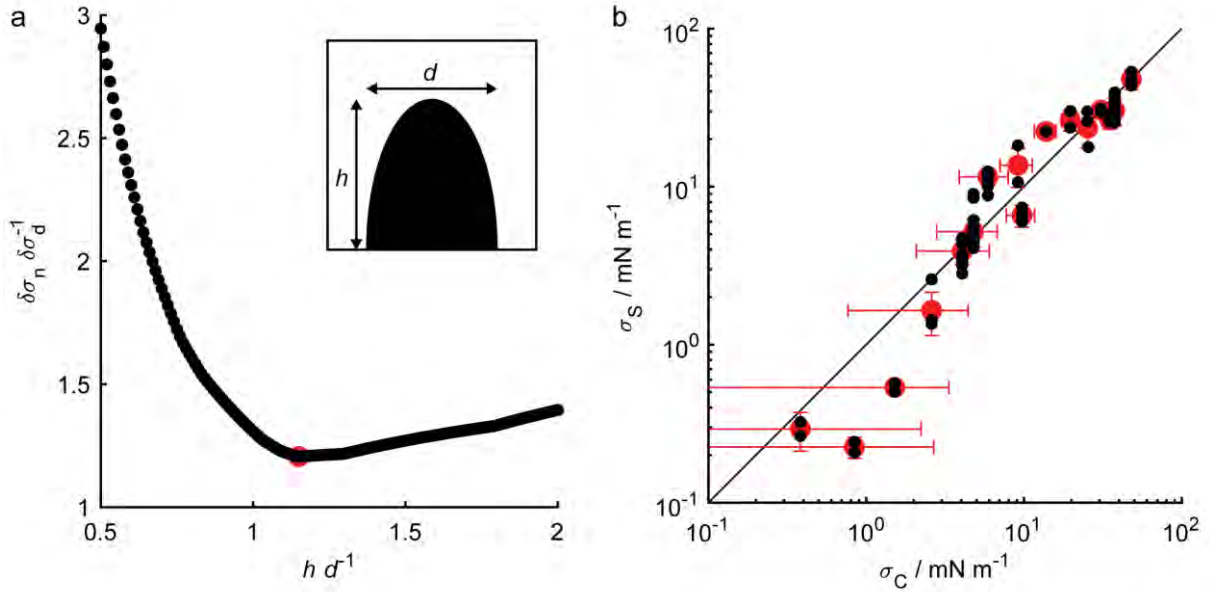


**Figure S7: IFT measurement based on number of split droplets.** a) Comparison of errors in measured IFT for different analysis methods:  $\sigma_n$  is based on number of split droplets and  $\sigma_d$  is based on droplet diameters.  $\delta\sigma_n$  and  $\delta\sigma_d$  are cumulative relative errors compared to control method  $\delta\sigma_C$  (pendant droplet and micropipette aspiration) over all measurements:  $\delta\sigma_n = \sum |\sigma_n - \sigma_C|/\sigma_C$ . The relative error is plotted as a function of droplet aspect ratio  $h d^{-1}$ , where  $h$  is the height of the droplet and  $d$  is the diameter of droplet base. Droplet is assumed a half of an ellipsoid. Inset shows the droplet shape, which minimizes the error ( $h d^{-1} = 1.15$ , red circle in the main figure). b) IFT based on number of droplets in splitting experiments  $\sigma_S$  as a function of IFT measured with control methods  $\sigma_C$  (pendant droplet and micropipette aspiration). Black dots: individual experiments, red circles: experiments grouped based on control method IFT. Error bars represent uncertainty ( $\pm 1$  standard deviation).



## Image processing

Brightness and contrast of the photographs and image series in Figures 1-4 were adjusted with Photoshop. In addition, photographs in Figure 1d and 3a-b were converted to grayscale and white balance of Figure 4b was adjusted.

## References

- [1] T. Vieu, C. Walter, *J. Fluid Mech.* **2018**, 840, 455.
- [2] R. Massart, *IEEE Trans. Magn.* **1981**, 17, 1247.
- [3] C. Vasilescu, M. Latikka, K. D. Knudsen, V. M. Garamus, V. Socoliuc, R. Turcu, E. Tombácz, D. Susan-Resiga, R. H. A. Ras, L. Vékás, *Soft Matter* **2018**, 14, 6648.
- [4] J. V. I. Timonen, M. Latikka, L. Leibler, R. H. A. Ras, O. Ikkala, *Science* **2013**, 341, 253.
- [5] M. Tjahjadi, H. A. Stone, J. M. Ottino, *J. Fluid Mech.* **1992**, 243, 297.
- [6] I. A. Larmour, S. E. J. Bell, G. C. Saunders, *Angew. Chem. Int. Ed.* **2007**, 46, 1710.
- [7] J. M. D. Coey, *Magnetism and Magnetic Materials*, Cambridge University Press, **2009**.

# Nonenzymatic Glucose Sensing Using $\text{Ni}_{60}\text{Nb}_{40}$ Nanoglass

Soumabha Bag,<sup>\*,#</sup> Ananya Baksi,<sup>\*,#</sup> Sree Harsha Nandam, Di Wang, Xinglong Ye, Jyotirmoy Ghosh, Thalappil Pradeep, and Horst Hahn<sup>\*</sup>



Cite This: *ACS Nano* 2020, 14, 5543–5552



Read Online

ACCESS |



Metrics & More



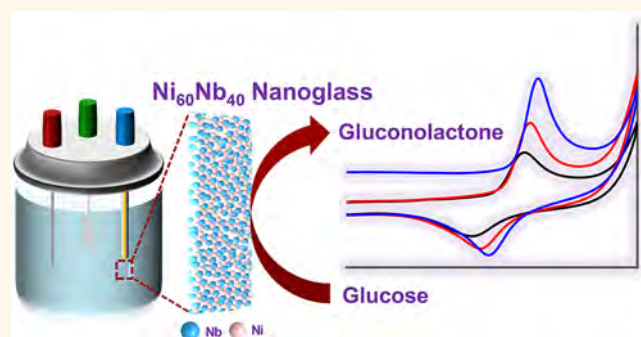
Article Recommendations



Supporting Information

**ABSTRACT:** Despite being researched for nearly five decades, chemical application of metallic glass is scarcely explored. Here we show electrochemical nonenzymatic glucose-sensing ability of nickel–niobium ( $\text{Ni}_{60}\text{Nb}_{40}$ ) amorphous alloys in alkaline medium. Three different  $\text{Ni}_{60}\text{Nb}_{40}$  systems with the same elemental composition, but varying microstructures are created following different synthetic routes and tested for their glucose-sensing performance. Among melt-spun ribbon, nanoglass, and amorphous–crystalline nanocomposite materials, nanoglass showed the best performance in terms of high anodic current density, sensitivity ( $20 \text{ mA cm}^{-2} \text{ mM}^{-1}$ ), limit of detection (100 nM glucose), stability, reproducibility (above 5000 cycles), and sensing accuracy among nonenzymatic glucose sensors involving amorphous alloys. When annealed under vacuum, only the heat-treated nanoglass retained a similar electrochemical-sensing property, while the other materials failed to yield desired results. In nanoglass, a network of glassy interfaces, compared to melt-spun ribbon, is plausibly responsible for the enhanced sensitivity.

**KEYWORDS:** nanoglass, nonenzymatic glucose sensor, nickel–niobium alloy, cyclic voltammetry, electrochemistry



Accurate glucose detection ability is essential to capture small changes in concentration in order to design advanced clinical diagnostic devices<sup>1,2</sup> (blood sugar analysis apparatus<sup>1–5</sup> and other personal health care devices<sup>6</sup>). Besides clinical applications, environmental,<sup>7,8</sup> food<sup>9–11</sup> and drug quality inspection,<sup>12,13</sup> and bioprocesses<sup>14</sup> monitoring is carried out upon evaluating glucose reactivity. In order to accommodate all the above-mentioned requirements, constant efforts are made to develop a universal sensor, which will be fast, selective, reliable, cost-effective, user-friendly, and efficient. Initially, Clark and Lyons<sup>15</sup> designed an enzyme-based electrode using the specific biocatalytic property of glucose oxidase, or GOx. This was further improved, leading to the development of redox electrodes<sup>16,17</sup> toward clinical diagnosis aimed for point of use in diabetes control. Despite its success, enzymatic glucose sensors possess several problems to address, such as immobilization of GOx on electrodes,<sup>18,19</sup> long-time stability,<sup>20</sup> thermal and chemical stability,<sup>21</sup> handling, and repeated use of the same sensor. Besides clinical diagnostics, a limited range of thermal stability<sup>21,22</sup> (until 44 °C) of GOx-based sensors along with their unstable nature in lower (below 2) and higher (above 8) pH values<sup>18</sup> makes it a poor choice for sensors for commercial use in agriculture and food quality monitoring.<sup>23</sup> In order to address the above-

mentioned problems, immense efforts are made to develop effective nonenzymatic glucose-sensing technology based on metals and nanomaterials.

Among different diagnostic patterns invented to monitor glucose concentrations, such as transdermal technology,<sup>24,25</sup> optical<sup>14,26,27</sup> and acoustic,<sup>28</sup> and electrochemistry<sup>29–33</sup> based diagnostic tools have been found to be the most efficient and user-friendly. Generally, electrodes made of noble metals, such as gold,<sup>34</sup> silver,<sup>35</sup> palladium,<sup>36,37</sup> and platinum,<sup>38,39</sup> are used to produce enzyme-free glucose sensors in spite of their high cost. But, all these emerging sensors have been unable to demonstrate sensitivity comparable to GOx-based detectors mainly due to poor electro-oxidation kinetics, despite introducing anisotropic nanostructured electrodes<sup>40–42</sup> or alloying<sup>20,43,44</sup> during the design of the electrode. Therefore, readily available, cost-effective transition metal<sup>3,20</sup> catalysts are

**Received:** December 12, 2019

**Accepted:** April 8, 2020

**Published:** April 8, 2020



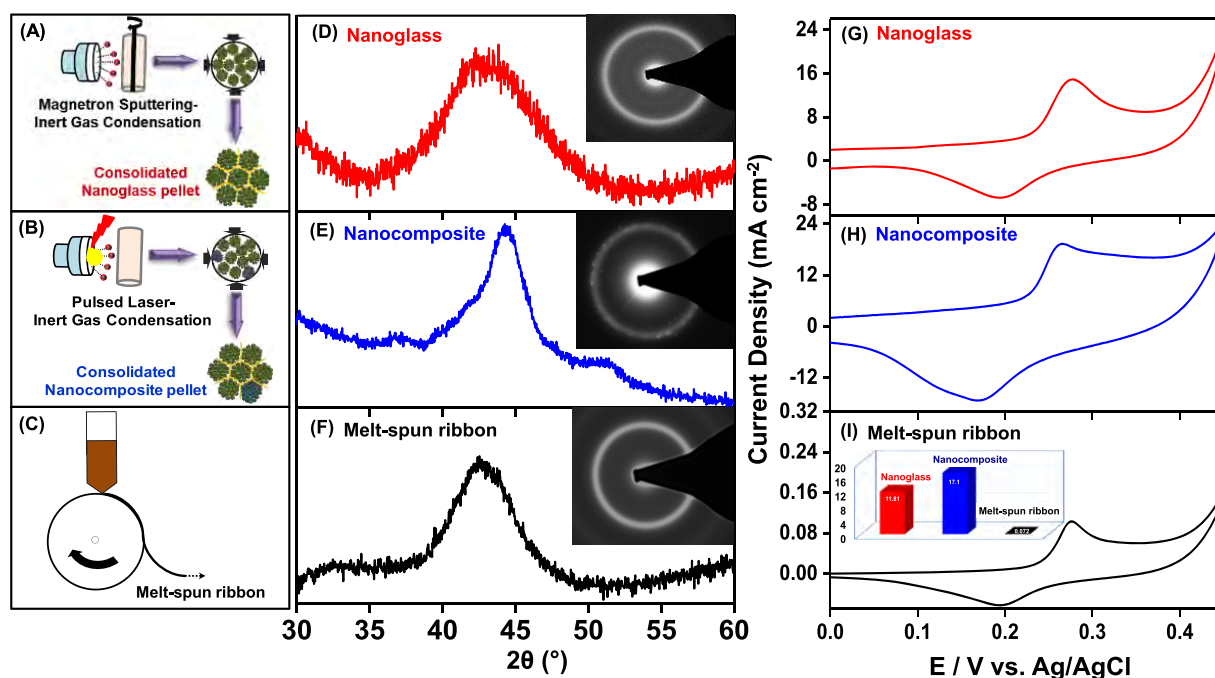


Figure 1. Nonenzymatic glucose sensor based on  $\text{Ni}_{60}\text{Nb}_{40}$  glassy alloy materials is illustrated. Schematics in A to C show preparation methods of nanoglass, nanocomposite, and melt-spun ribbon, respectively. XRD analysis indicates the amorphous phase of the sample (D and F), which are further confirmed through SAED patterns shown in the insets. Cyclic voltammograms of 0.10 mM glucose in 0.1 M sodium hydroxide solution are shown in G–I. Variation of anodic peak current density of all the materials is shown in the inset of I.

selected to design a futuristic enzymeless glucose sensor. Among known metals, nickel-based materials (nickel nanoparticle decorated substrate,<sup>45</sup> anisotropic Ni-structures,<sup>20</sup> multicomponent alloys,<sup>18,46</sup> or hybrid structures<sup>47,48</sup> containing nickel) are chosen because of the stable and reversible  $\text{Ni(III)/Ni(II)}$  redox system<sup>20,49–51</sup> activity known in alkaline conditions. However, during electrochemical oxidation of glucose, such Ni-based sensors' performance and stability decline over time. The above-mentioned challenges can be addressed by designing a new type of ligand-free Ni-based sensor that is able to survive several electrochemical cycles, easy to handle, and able to detect very low concentrations of glucose reproducibly.

Nanostructured metallic glasses (nanoglasses) gained popularity for their different properties<sup>52–58</sup> compared to bulk metallic glassy<sup>59</sup> analogues. The recent introduction of nanoglass<sup>55</sup> in the family of glassy alloys further improved the mechanical strength,<sup>54</sup> enhanced magnetic properties,<sup>53</sup> etc., compared to bulk metallic glasses. Typically, a nanoglass is prepared by consolidating amorphous alloy nanoparticles at high uniaxial pressures (2–6 GPa),<sup>60</sup> creating a large number of glass–glass interfaces, which are responsible for the distinct properties<sup>61</sup> compared to bulk metallic glass of similar or identical composition. While stable amorphous alloys are being used in several places,<sup>62</sup> only a few attempts are made (organic catalyst,<sup>63</sup> electrocatalysis,<sup>64</sup> and sensor<sup>65</sup>) to utilize the chemical reactivity of such amorphous systems as a replacement for crystalline metals. Nickel-based glassy alloys such as  $\text{Ni}_{60}\text{Nb}_{40}$ ,<sup>66,67</sup>  $\text{Ni}_{60}\text{Zr}_{40}$ ,<sup>68,69</sup>  $\text{Ni}_{60}\text{Ag}_{40}$ ,<sup>70,71</sup> and  $\text{Ni}_{50}\text{Ti}_{50}$ <sup>72,73</sup> are well known for their distinct thermal stability and mechanical strength, but they have not been used for unconventional chemical applications.<sup>74</sup> These nickel-based glasses could be an excellent choice to develop futuristic nonenzymatic glucose sensors.

In this paper, we synthesized  $\text{Ni}_{60}\text{Nb}_{40}$  nanoglass and demonstrated its electro-oxidation ability in terms of sensitivity and selectivity in glucose sensing. For comparison, melt-spun ribbon and a nanocomposite of amorphous and crystalline alloy with identical compositions ( $\text{Ni}_{60}\text{Nb}_{40}$ ) have been investigated for their electrochemical activity. The results from the investigations reveal that all three  $\text{Ni}_{60}\text{Nb}_{40}$  alloys can effectively be used to detect glucose electrochemically in the absence of any enzyme. Among them, the nanoglass showed the highest sensitivity ( $20 \text{ mA cm}^{-2} \text{ mM}^{-1}$ ) reported so far for any nonenzymatic glucose sensor based on Ni-based nanomaterials.

## RESULTS AND DISCUSSION

**Structural Analysis of the Alloys.** Three different  $\text{Ni}_{60}\text{Nb}_{40}$  alloys, namely, nanoglass, a mixture of an amorphous–crystalline nanocomposite alloy, and melt-spun ribbon (MSR), were synthesized following different routes shown in Figure 1A–C (details are in the Experimental Section). Structural characterization of the as-prepared samples was performed using X-ray diffraction (XRD) immediately after each synthesis. Corresponding diffractograms associated with each material are shown in Figure 1D to F. Both nanoglass and MSR show a typical halo peak, indicating an amorphous phase in the samples. Detailed microstructural analysis using FESEM (Figure S1A to C) and TEM was carried out. The amorphous nature of the samples was confirmed during a TEM-selected area electron diffraction (SAED) study, which exhibited broad diffuse rings as shown in the insets of Figure 1D and F. Although there was no clear crystalline peak in the XRD pattern (amorphous–crystalline composite or nanocomposite), the halo was sharper for the nanocomposite materials, suggesting nanocrystallinity (Figure 1E) in the sample. Additionally, distinguished spots identified in the

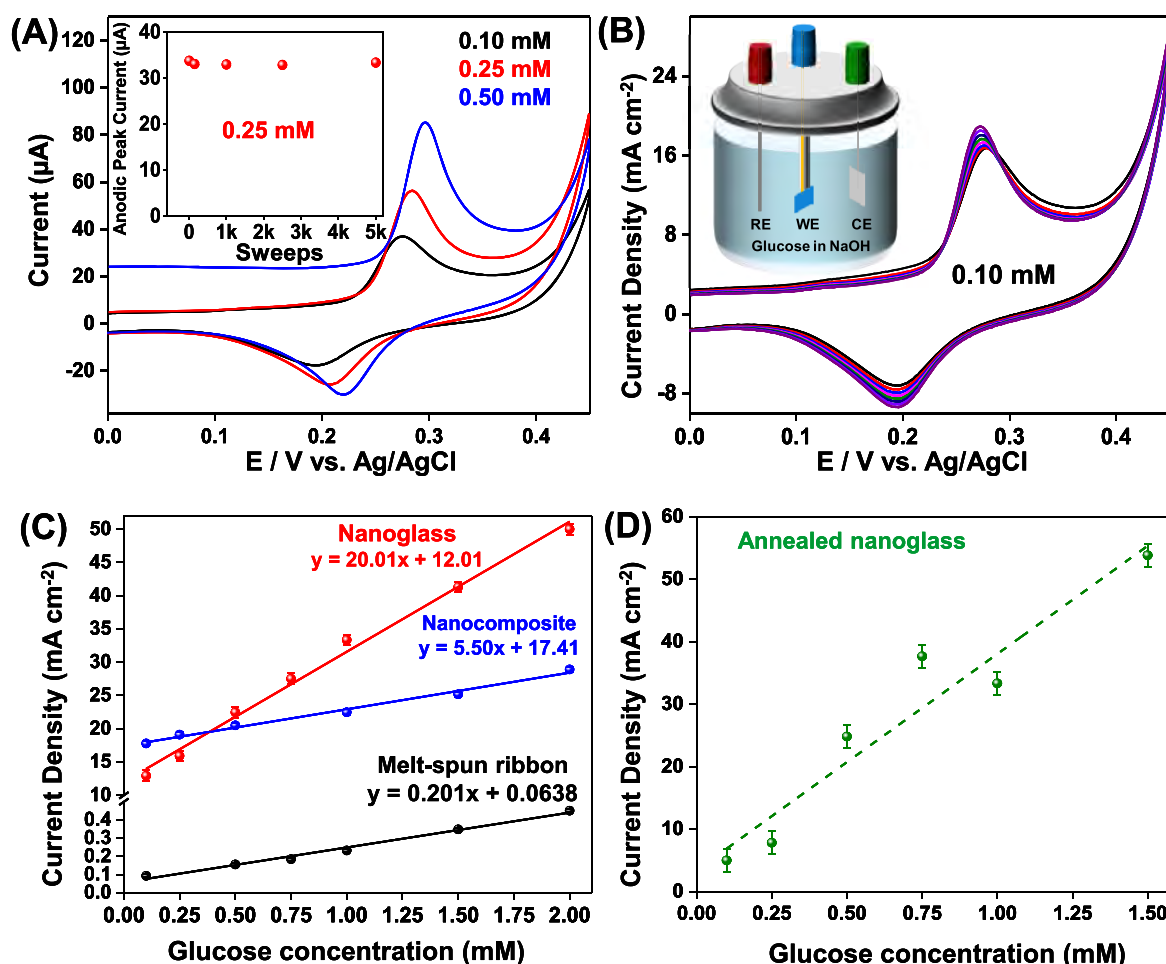
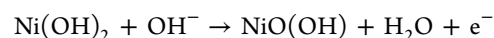
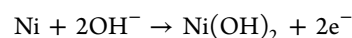


Figure 2. Concentration-dependent (0.10, 0.25, and 0.50 mM glucose) cyclic voltammograms with the nanoglass are shown in A. Stable anodic peak current of a 0.25 mM glucose solution over 5000 cycles is shown in the inset. In B, eight sweeps in a 0.10 mM glucose solution demonstrate stable anodic peak current density. Schematic of the electrochemical cell is shown in the inset of B. In alkaline (NaOH) glucose solution, the reference electrode (Ag/AgCl), working electrode (alloy materials), and counter electrode (platinum foil) are represented by RE, WE, and CE, respectively. Linear dependence on the glucose concentration was found for all three systems, as shown in C, including the equations. Only the annealed nanoglass retained its detection ability and its response, which is captured in D.

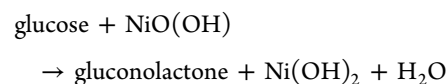
SAED (inset of Figure 1E) pattern indicate some extent of nanocrystallinity in the sample.

**Electrochemical Stability of the Alloys.** After the initial microstructural characterization, these three samples were tested for their electrochemical responses as working electrode (WE) toward glucose in cyclic voltammetry (CV) experiments in the presence of Ag/AgCl as a reference electrode (RE) and platinum as counter electrode (CE) in alkaline medium. The scan rate dependent stability of the alloy electrodes has been checked before initiating any experiment. With the polished glassy electrode, during sweeping from  $-0.1$  to  $+0.45$  V at  $10$  mV s<sup>-1</sup> scan rate, oxidative peak in the first cycle indicate the formation of Ni(II) oxide layers.<sup>46</sup> At repeated sweeps using  $10$  to  $100$  mV s<sup>-1</sup> rates the nanoglass electrode produced well-defined and reproducible voltammograms in  $0.1$  M NaOH solution as shown in Figure S2. Other alloy electrodes also generate a similar voltammetric response. The anodic peak voltage shifts to more positive value with an increase in the scan rate, while reductive peak voltage moves to more negative potential as found in previous studies.<sup>20</sup> During sweeping at a  $20$  mV s<sup>-1</sup> rate, the current response was found to be  $0.64$  μA for the anodic peak at  $+0.266$  V. For a direct comparison

between the three materials, the scan rate was fixed at  $20$  mV s<sup>-1</sup> for the rest of the experiments. The chemical reactions are as follows<sup>3,20</sup>



**Glucose-Sensing Using Cyclic Voltammetry.** In the identical potential regime for nanoglass, upon addition of  $0.10$  mM glucose solutions into the alkaline medium, a substantial increase in the oxidative peak current was identified in the resultant CV curve, as evident in Figure 1G, and the anodic peak potential shifts to higher voltage. Notable enhancement in anodic peak current is due to the electrochemical oxidation of glucose in the presence of NiO(OH) on the electrode surface. The chemical reaction can be described as



A comparable sensitivity was measured when the electrode was replaced with the nanocomposite (shown in Figure 1H). Although MSR was able to detect  $0.10$  mM glucose in solution,



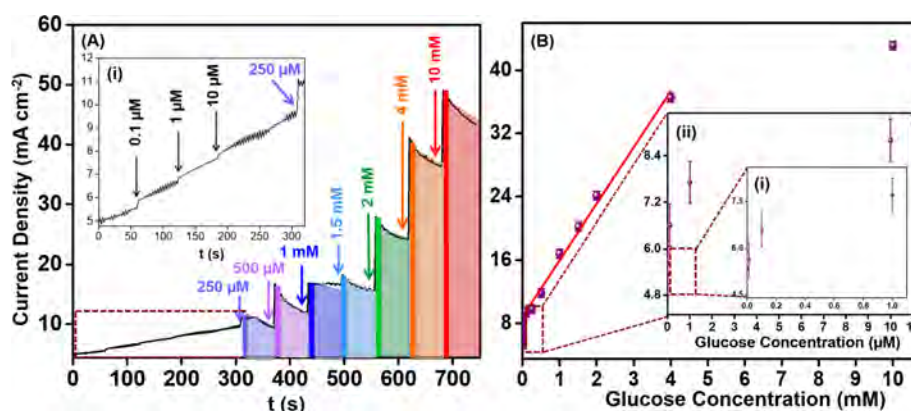


Figure 3. (A) Chronoamperometric response from the nanoglass electrode upon sequential addition of glucose solutions. Inset (i) shows the expanded view of the red dotted region. (B) Distribution of current densities with respect to glucose concentration. A linear increase of current density is established from 0.25 to 4 mM. Current densities at lower concentration are given in insets (i) and (ii).

a weaker oxidative peak current response (inset of Figure 1I) makes it unsuitable for a glucose sensor at the low concentration window (Figure 1I). Appropriate glucose diagnosis is formulated with further CV experiments with different batches of solutions. The gradual increase in the values of the oxidative peak current with increase in glucose concentrations (0.10 to 0.50 mM) clearly indicates the proper sensing response of the nanoglass (Figure 2A). All the CV experiments also produced a very stable anodic peak current. In the inset of Figure 2A, the anodic peak current value of the 0.25 mM glucose solution is shown above 5000 cycles, showing insignificant variation. Additionally, eight replicates of voltammograms from a 0.10 mM glucose solution, shown in Figure 2B, confirm the reproducible nature of every measurement with stable anodic peak current density. Identical measurements were performed on the nanocomposite and MSR, and the sensitivity of these materials was checked with varying glucose concentrations. A linear relationship was found when the anodic peak current density is plotted *vs* glucose concentration (0.10 to 2 mM), and the sensor performance is evaluated for all three alloys (Figure 2C).

The sensitivity values of the alloy sensors are calculated from the slopes shown in Figure 2C, and it is evident that the responses of the nanoglass and the nanocomposite are higher compared to MSR. Although the nanocomposite material shows comparatively higher current density for lower glucose concentration, the current density does not increase tremendously with higher glucose concentration, and hence the overall sensitivity of the nanocomposite materials is lower than the nanoglass (Figure 2C).

**Sensitivity of the Nanoglass.** Sensitivity of the nanoglass is found to be  $20 \text{ mA cm}^{-2} \text{ mM}^{-1}$  (Figure 2C), which is substantially higher compared to other reported nickel-based glucose sensors.<sup>18</sup> The sensitivity of the nanocomposite materials and MSR are 5.5 and  $0.2 \text{ mA cm}^{-2} \text{ mM}^{-1}$ , respectively. The current density as well as sensitivity is found to be the lowest for the MSR among all three alloys examined here. It is interesting to note that all three materials showed nearly linear behavior in terms of current response with respect to glucose concentration.

**Response from the Annealed Nanoglass.** In order to gain more insight into the phase-dependent sensitivity of the materials; all sensors were first annealed at  $700^\circ\text{C}$  [above its glass transition temperature ( $T_g$ ),  $622^\circ\text{C}$ ] for 2 h in a vacuum furnace. Upon crystallization (Figure S3), a mixture of

intermetallic compounds of nickel and niobium ( $\text{Ni}_3\text{Nb}$ ,  $\text{Ni}_6\text{Nb}_7$ ) appears from a single-phase  $\text{Ni}_{60}\text{Nb}_{40}$  nanoglass.<sup>75</sup> When the CVs of all the annealed (crystallized) electrodes are tested, only the annealed nanoglass showed reproducible current density comparable to the parent nanoglass. However, the high sensitivity is lost (Figure 2D) in the crystallized nanoglass, while other materials do not respond at all and fail to produce any anodic peak current. Although the current density is higher for the annealed nanoglass (with respect to the parent nanoglass), the linear behavior is no more perfect [adj.  $R^2 = 0.905$  compared to adj.  $R^2 = 0.992$  for pristine nanoglass, 0.986 for the nanocomposite, and 0.986 for MSR, respectively (adj. = adjusted)]. This study clearly proves the weak sensitivity of the crystalline materials in nonenzymatic glucose-sensing applications in alkaline medium. Due to the higher sensitivity of the pristine and the annealed samples, further studies are focused on the nanoglass only.

**Chronoamperometric Detection Ability of Glucose with Nanoglass.** To identify the limit of detection of the nanoglass, chronoamperometric experiments were performed from the lowest to highest concentration ( $0.1 \mu\text{M}$  to 10 mM) of glucose, and the results are shown in Figure 3. During the measurement, the potential was held constant at  $+0.45 \text{ V}$  while the solution is stirred constantly (200 rpm rate), and the current is monitored upon successive addition of glucose solutions into 0.1 M NaOH medium. The well-defined stepwise current increase upon sequential addition of glucose proves the accurate electro-oxidation response of the nanoglass as a working electrode. Above 10 mM glucose concentration, a negligible increase of current is identified; therefore, the concentration range of the present investigation is chosen until 10 mM (see later). Based on signal-to-noise ratio (S/N) calculation, the nanoglass offers 100 nM glucose as the limit of detection (LOD), as shown in the inset of Figure 3A. A linear increase of the current density with respect to glucose concentration has been established between 0.25 and 4 mM when chronoamperometric current densities are plotted against glucose concentration (Figure 3B). Due to high current density, a few nanomolar glucose concentration is also detectable as shown in Figure 3Bi and ii, which also supports proper detection ability of the nanoglass at a lower concentration range.

**Selectivity of the Nanoglass Electrode.** In order to demonstrate the ability of the nanoglass as an enzyme-free glucose sensor for future applications, the selectivity is another

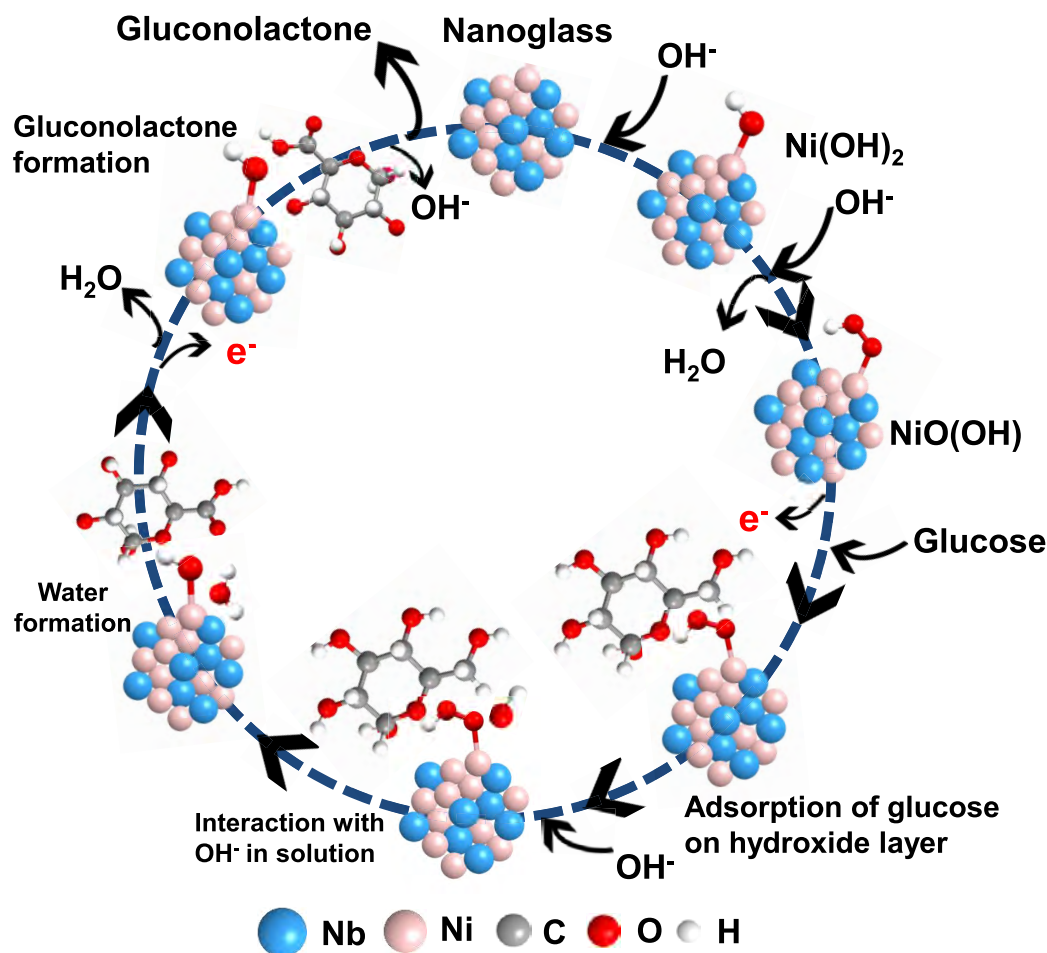


Figure 4. Proposed mechanism of electrochemical glucose oxidation process at the surfaces of the  $\text{Ni}_{60}\text{Nb}_{40}$  nanoglass based on the IHOAM model.

important factor alongside sensitivity, which has to be taken into consideration. Glucose detection is hampered mostly by the presence of sucrose, ascorbic acid, and other solutes in the bloodstream. To perform this test, 0.25 mM ascorbic acid, sodium chloride (NaCl), and a sucrose solutions are added in succession (Figure S4A) in a 0.25 mM glucose solution. A marginal current change upon the addition of other solutes confirms the good selectivity of the nanoglass for glucose. This control test reveals that the nanoglass has potential for accurate glucose detection, and it can be used as a nonenzymatic glucose sensor in future applications. In addition to its selectivity toward glucose detection, the chronoamperometric response of the nanoglass for the sensing of higher glucose concentrations (2 to 38 mM) has also been tested independently (Figure S4B). In identical chronoamperometric experiments (applied potential +0.50 V), the current increases linearly (adj.  $R^2 = 0.996$ ) with infusion of a higher concentration of glucose until 38 mM. However, above 10 mM, continuous cleaning of the electrodes has been carried out before additional infusion of glucose solution. This problem can be avoided by using a suitable reference electrode, replacing Ag/AgCl.

**Post-Experiment Structural Analysis of the Nanoglass.** Following the electrochemical studies, structural analysis of the nanoglass electrode was carried out using GAXRD to understand the active phase present on its surface. The resultant diffractograms before (Figure S5A) and after (Figure

S5B) the reaction showed identical featureless broad peaks, indicating retention of the amorphous phase in the alloy even after electro-oxidation experiments. XRD patterns shown in Figure 1D and Figure S5A were collected from the same sample. The stable nature of the anodic peak current (in the inset of Figure 2A) during the glucose-sensing experiments indicated that chemical composition at the nanoglass surface did not undergo a significant change. Subsequently, surface characterization of the nanoglass was carried out using XPS to determine the chemical composition. The results are summarized in Figure S6. While Figure S6A1, A2, and A3 represent Ni ( $2p_{3/2}$ ), O (1s), and Nb (3d) regions, respectively, of the unreacted nanoglass samples, the same regions of the reacted samples are shown in Figure S6B1, B2, and B3. Nearly the same features are found upon deconvoluting the Ni  $2p_{3/2}$  regions (in Figure S6A1 and B1), which also indicates the unaltered surface of the electrode. Careful analysis of the O 1s region points toward different metal–oxygen bonding possibilities at the nanoglass surface (Figure S6A2 and B2), which also do not change significantly following the electro-oxidation process. These features appear mainly due to the presence of amorphous niobium oxide at the surface of the sample, recognized by XPS analysis in the Nb 3d region (Figure S6A3 and B3). Two oxidation states of Nb are found upon deconvoluting two indistinguishable (Figure S6A3 and B3) spectra (dashed lines) measured before and after sensing experiments, respectively. The peak at 203.86 eV is



attributed to the NbO, while the Nb<sub>2</sub>O<sub>5</sub> 3d<sub>5/2</sub> signal appears at 207.62 eV. It should be noted that the presence of niobium oxide at the surfaces of the nanoglass has not been identified either by XRD or during TEM/SAED analysis (Figure 1D). The appearance of Ni, Nb, and O peaks from metallic nanoglass suggests the presence of a niobium oxide layer at the surface, which also maintains metallic bonding with Ni<sup>76</sup> but protects underlying Ni–Nb layers from further oxidation. As a result of metallic bonding between Ni and NbO<sub>x</sub> at the surface, the oxide layer and the sample remain conducting. This niobium oxide not only facilitates the electrochemical sensing but also shields underlying Ni-excess regions of the sample.

**Mechanism.** In view of all experimental evidence produced by the electrochemical oxidation process and subsequent spectroscopic characterization of the materials, the nanoglass has emerged as a stable, sensitive, reliable, and robust glucose detector. However, all the studied Ni<sub>60</sub>Nb<sub>40</sub> alloy materials have the potential for glucose sensing. The principle reason for such activity is the presence of amorphous nickel with noninterfering and noncompeting niobium in the material. Together these elements produce a stable yet reactive alloy electrode surface for electrochemical glucose sensing. The incipient hydrous oxide adatom mediator (IHOAM)<sup>29,30</sup> model can be used to explain the plausible mechanism (Figure 4) of the oxidation process. According to the reaction mentioned before and this model, a thin layer of nickel hydroxide [Ni(OH)<sub>2</sub>] forms on the electrode surface in the first sweep of electro-oxidation.<sup>46</sup> Ni(OH)<sub>2</sub> subsequently oxidized to nickel oxohydroxide [NiO(OH)] in the alkaline medium, which adsorbs a glucose molecule and gradually converts it to gluconolactone in alkaline conditions. In the process, NiO(OH) reduces to Ni(OH)<sub>2</sub> (see Figure 4 for details). Considering the experimental evidence provided here, every working electrode in the current investigations seems to be following the common mechanism formulated using the IHOAM model as shown in Figure 4. In the case of annealed glasses, probably the presence of several intermetallic compounds simultaneously do not help in glucose sensing. Their presence also reduces the metallic bonding between Ni–NbO<sub>x</sub> significantly and transforms into a less conducting electrode, which is inefficient for the electrochemical sensing process. The difference in microstructure in the nanoglass and nanocomposite alloy compared to MSR can be another reason for the better electrochemical response among the three materials. In contrast to the melt-spun ribbons, nanoglasses exhibit a network of interfaces. The atomic structure of nanoglasses has been described on the basis of many experiments as to consist of nanometer-sized glassy core regions, *i.e.*, the remnant of the former nanoparticles prior to compaction, and of glassy interfacial regions, which clearly only appear during compaction.<sup>60</sup> The experimental results suggest that the combined reactivity of the two glassy regions, which are characterized by different atomic structures, affects the overall performance of the nanoglass in the sensing application. This is clearly seen in the change of the slope of the current density *vs* the glucose concentration curve (in Figure 2C). The nanoglasses behave distinctively different than the rapidly quenched glass and the nanocomposite materials, both in absolute intensity and in the slope. Both these effects hint toward a different behavior of the interfacial regions present in nanoglasses. Previously, increased mechanical strength (CuZr<sup>54</sup>), altered magnetic properties (FeSc,<sup>53</sup> NiTi<sup>77</sup>), and even enhanced biocompatibility<sup>78</sup> of nanoglasses were

correlated with the interfacial regions. The glassy core regions in nanoglasses have similar electrochemical reactivity to that of the melt-spun ribbons. But, the interfacial reactivity in nanoglasses seems to be the main difference, which is reflected as higher current density and sensitivity compared to melt-spun ribbons. On the other hand, the nanocomposite sample consists of glassy, glass–nanocrystalline, and nanocrystalline grains as well as similar interfaces, a combination that might be responsible for the high current density at the lowest glucose concentration. Between nanoglasses and nanocomposite samples, the presence of a larger fraction of glass–glass interfaces is mainly responsible for the higher sensitivity considering the larger concentration range. However, as pointed out above, the change of the slope as seen in Figure 2C indicates additional effects, which cannot be identified based on the present research results.

## CONCLUSION

In this report, electrochemical detection of glucose has been demonstrated using nickel-based glassy alloys. Fast, reproducible responses from different Ni<sub>60</sub>Nb<sub>40</sub> metallic alloys (nanoglass, nanocomposite, and melt-spun ribbon) are compared for the sensing of glucose solutions. Exceptional response from the nanoglass sample is determined, which retains its partial sensitivity even after annealing and subsequent crystallization. Due to high current density, a few nanomolar glucose is still detectable using a nanoglass electrode. Besides the contribution of metallic nickel, the special nano/microstructure of the nanoglass with interfacial regions of enhanced free volume (interfaces) also seems to play a role in the electrochemical response. A conducting niobium oxide layer coating creates a protection for the Ni-rich alloy but maintains chemical reactivity toward glucose. Based on the IHOAM model, a glucose oxidation mechanism is provided, but further structural insights are necessary to establish it. With a detection limit of 100 nM, the nanoglass has been shown to be an unconventional, nanostructured and ligand-free material to design a futuristic nonenzymatic glucose sensor. An impressive performance of this type of unconventional yet responsive alloy-based sensor has great potential toward the development of diagnostic apparatus and technology to monitor glucose concentrations in challenging application fields.

## EXPERIMENTAL SECTION

**Chemicals.** Ni<sub>60</sub>Nb<sub>40</sub> target (99.9% purity) was purchased from MaTeck GmbH. Glucose (99% purity) was procured from VWR GmbH. Sodium hydroxide (NaOH), ascorbic acid, sodium chloride (NaCl), and sucrose with 99.9% purity were purchased from Sigma-Aldrich. Deoxygenated Milli-Q water (18.3 MΩ) was used throughout the experiments.

**Synthesis.** Synthetic schemes are illustrated in Figure 1 (A to C). Briefly, melt-spun ribbons were prepared by rapid quenching of a molten alloy of Ni and Nb with a 60:40 atomic ratio on a rotating Cu disk. The other samples were synthesized using inert gas condensation (IGC) techniques using two custom-built instruments followed by uniaxial compaction. Ni<sub>60</sub>Nb<sub>40</sub> nanoglass was prepared by using magnetron sputtering-IGC (MS-IGC) followed by compaction at 1.4 GPa under vacuum.<sup>54</sup> Here, the Ni<sub>60</sub>Nb<sub>40</sub> alloy target was sputtered at an aggregation pressure of 0.3 mbar, which leads to the formation of very fine nanoparticles of the same composition. The nanoparticles were then collected and pressed *in situ* at a pressure of 1.4 GPa to make a disc-shaped pellet. The sample was further consolidated at 6 GPa and polished mechanically (pellet diameter 8 mm, thickness 0.21

mm, weight ~100 mg from 90 min of sputtering) at ambient conditions before studying its electro-oxidation property. The amorphous–crystalline nanocomposite sample was prepared using pulsed laser (20 W laser power) ablation (on the same  $\text{Ni}_{60}\text{Nb}_{40}$  alloy target) setup coupled to an IGC instrument followed by successive consolidation at 1.8 and 6 GPa.<sup>79</sup> A disc-shaped pellet was prepared and polished similar to the previous nanoglass sample. The use of pulsed laser ablation instead of magnetron sputtering in the IGC system induced nanocrystallinity in the compacted pellet.

**Electrochemical Cell Configuration.** All the electrochemical (cyclic voltammetry and chronoamperometry) experiments were performed in a general-purpose electrochemical system (from  $\mu\text{Autolab}$  Type III) coupled with a three-electrode electrochemical cell, where  $\text{Ni}_{60}\text{Nb}_{40}$  alloys were used as working electrode, platinum foil as counter electrode, and saturated Ag/AgCl as reference electrode. A gold wire of 0.10 mm thickness was used to connect working electrodes (pellets of nanoglass, nanocomposite, or melt-spun ribbon).

**Cyclic Voltammetry and Chronoamperometry.** Cyclic voltammetric and chronoamperometric studies were performed with different concentrations of glucose solutions (100 nM to 38 mM, generated more than a few thousand sensing experiments with a single nanoglass electrode) prepared in 0.1 M NaOH at room temperature (25 °C) in a 50 mL cell (schematically shown in the inset of Figure 2B). Scan voltage was fixed between  $-0.1$  and  $+0.45$  V to avoid any interference emerging from niobium. During chronoamperometric measurement, glucose, ascorbic acid, sodium chloride (NaCl), and sucrose solutions were added into a 0.1 M NaOH solution sequentially with constant stirring at 200 rpm. The geometric surface area of the working electrodes (alloys) was used to calculate the current density values reported here. All the potential values described in this paper were determined with respect to the saturated Ag/AgCl electrode.

**Characterization.** Conventional characterization techniques were used to determine the phase and composition of the as-prepared materials. Structural characterization (XRD) of the metallic alloys was carried out using a Bruker X-ray diffractometer equipped with a Cu  $K\alpha$  X-ray source before attempting electrochemical studies. A STOE Stadi P diffractometer with a Ga  $K\beta$  source was used for Ga-jet XRD characterization of the reacted electrode. Microstructure analysis was performed using a Zeiss LEO 1530 scanning electron microscope and an image aberration-corrected FEI Titan 80-300 transmission electron microscope operated at 300 kV. Elemental analysis and chemical compositions ( $\text{Ni}_{60}\text{Nb}_{40}$ ) were determined with an energy dispersive X-ray spectroscopy detector attached to the SEM and TEM instruments. X-ray photoelectron spectroscopy (XPS) measurement was carried out in an ECSA probe TPD spectrometer from Omicron Nanotechnology with polychromatic Al  $K\alpha$  ( $h\nu = 1486.6$  eV) as X-ray source. All XPS spectra were deconvoluted and analyzed using CasaXPS software.

## ASSOCIATED CONTENT

### Supporting Information

The Supporting Information is available free of charge at <https://pubs.acs.org/doi/10.1021/acsnano.9b09778>.

FESEM, CV, selectivity test of the nanoglass, and additional characterization before and after the electro-oxidation reaction such as XRD and XPS (PDF)

## AUTHOR INFORMATION

### Corresponding Authors

**Soumabha Bag** – *Institute of Nanotechnology, Karlsruhe Institute of Technology, 76344 Eggenstein-Leopoldshafen, Germany*; [orcid.org/0000-0002-0932-105X](https://orcid.org/0000-0002-0932-105X);  
Email: [soumabha.bag@kit.edu](mailto:soumabha.bag@kit.edu)

**Ananya Bakshi** – *Institute of Nanotechnology, Karlsruhe Institute of Technology, 76344 Eggenstein-Leopoldshafen, Germany*;

[orcid.org/0000-0003-3328-4399](https://orcid.org/0000-0003-3328-4399); Email: [ananya.bakshi@kit.edu](mailto:ananya.bakshi@kit.edu)

**Horst Hahn** – *Institute of Nanotechnology, Karlsruhe Institute of Technology, 76344 Eggenstein-Leopoldshafen, Germany*; KIT-TUD Joint Research Laboratory Nanomaterials, 64206 Darmstadt, Germany; [orcid.org/0000-0001-9901-3861](https://orcid.org/0000-0001-9901-3861);  
Email: [horst.hahn@kit.edu](mailto:horst.hahn@kit.edu)

## Authors

**Sree Harsha Nandam** – *Institute of Nanotechnology, Karlsruhe Institute of Technology, 76344 Eggenstein-Leopoldshafen, Germany*

**Di Wang** – *Institute of Nanotechnology and Karlsruhe Nano Micro Facility, Karlsruhe Institute of Technology, 76344 Eggenstein-Leopoldshafen, Germany*; [orcid.org/0000-0001-9817-7047](https://orcid.org/0000-0001-9817-7047)

**Xinglong Ye** – *Institute of Nanotechnology, Karlsruhe Institute of Technology, 76344 Eggenstein-Leopoldshafen, Germany*

**Jyotirmoy Ghosh** – *Department of Science and Technology (DST) Unit of Nanoscience and Thematic Unit of Excellence (TUE), Department of Chemistry, Indian Institute of Technology Madras, Chennai 600036, India*

**Thalappil Pradeep** – *Department of Science and Technology (DST) Unit of Nanoscience and Thematic Unit of Excellence (TUE), Department of Chemistry, Indian Institute of Technology Madras, Chennai 600036, India*; [orcid.org/0000-0003-3174-534X](https://orcid.org/0000-0003-3174-534X)

Complete contact information is available at:  
<https://pubs.acs.org/doi/10.1021/acsnano.9b09778>

## Author Contributions

#S. Bag and A. Bakshi contributed equally.

## Author Contributions

A.B. and S.B. jointly planned and performed the experiments and interpreted the results. S.H.N. helped in magnetron sputtering experiments. D.W. performed the TEM characterization and helped in microstructure analysis. X.L.Y. helped to design initial electrochemical experiments. The XPS was done in collaboration with T.P. and his group. J.G. carried out XPS measurement and analysis. H.H. supervised the entire project. A.B., S.B., and H.H. wrote the manuscript with contributions from other authors.

## Notes

The authors declare no competing financial interest.

## ACKNOWLEDGMENTS

S.B. and A.B. gratefully acknowledge Karlsruhe Institute of Technology for guest scientist fellowships. H.H. and S.H.N. acknowledge the financial support provided by the Deutsche Forschungsgemeinschaft under grant HA 1344/30-2. S.B. and A.B. thank Dr. Robert Kruk for scientific support. J.G. thanks the University Grants Commission (UGC), India, for his research fellowship. T.P. thanks Department of Science and Technology (DST), India, for the research support. The authors would like to thank Dr. Zbigniew Śniadecki from Institute of Molecular Physics, Polish Academy of Sciences, Poland, for the melt-spun ribbon sample. Dr. Ben Breitung is gratefully acknowledged for the Ga-jet XRD measurements.

## REFERENCES

- (1) Heller, A.; Feldman, B. Electrochemical Glucose Sensors and Their Applications in Diabetes Management. *Chem. Rev.* **2008**, *108*, 2482–2505.
- (2) Harper, A.; Anderson, M. R. Electrochemical Glucose Sensors - Developments Using Electrostatic Assembly and Carbon Nanotubes for Biosensor Construction. *Sensors* **2010**, *10*, 8248–8274.
- (3) Tian, K.; Prestgard, M.; Tiwari, A. A Review of Recent Advances in Nonenzymatic Glucose Sensors. *Mater. Sci. Eng., C* **2014**, *41*, 100–118.
- (4) Ahmad, R.; Tripathy, N.; Park, J.-H.; Hahn, Y.-B. A Comprehensive Biosensor Integrated with a ZnO Nanorod FET Array for Selective Detection of Glucose, Cholesterol and Urea. *Chem. Commun.* **2015**, *51*, 11968–11971.
- (5) Ahmad, R.; Ahn, M.-S.; Hahn, Y.-B. Fabrication of a Non-Enzymatic Glucose Sensor Field-Effect Transistor Based on Vertically-Oriented ZnO Nanorods Modified with Fe<sub>2</sub>O<sub>3</sub>. *Electrochem. Commun.* **2017**, *77*, 107–111.
- (6) Alfian, G.; Syafrudin, M.; Ijaz, M. F.; Syaekhoni, M. A.; Fitriyani, N. L.; Rhee, J. A Personalized Healthcare Monitoring System for Diabetic Patients by Utilizing BLE-Based Sensors and Real-Time Data Processing. *Sensors* **2018**, *18*, 2183.
- (7) Bandiello, E.; Sessolo, M.; Bolink, H. J. Aqueous Electrolyte-Gated ZnO Transistors for Environmental and Biological Sensing. *J. Mater. Chem. C* **2014**, *2*, 10277–10281.
- (8) Sardesai, N. P.; Karimi, A.; Andreescu, S. Engineered Pt-Doped Nanoceria for Oxidase-Based Bioelectrodes Operating in Oxygen-Deficient Environments. *ChemElectroChem* **2014**, *1*, 2082–2088.
- (9) Amor-Gutierrez, O.; Costa Rama, E.; Costa-Garcia, A.; Fernandez-Abedul, M. T. Paper-Based Maskless Enzymatic Sensor for Glucose Determination Combining Ink and Wire Electrodes. *Biosens. Bioelectron.* **2017**, *93*, 40–45.
- (10) Liu, Y.; Javvaji, V.; Raghavan, S. R.; Bentley, W. E.; Payne, G. F. Glucose Oxidase-Mediated Gelation: A Simple Test to Detect Glucose in Food Products. *J. Agric. Food Chem.* **2012**, *60*, 8963–8967.
- (11) Baksi, A.; Gandhi, M.; Chaudhari, S.; Bag, S.; Sen Gupta, S.; Pradeep, T. Extraction of Silver by Glucose. *Angew. Chem., Int. Ed.* **2016**, *55*, 7777–7781.
- (12) Balaconis, M. K.; Billingsley, K.; Dubach, M. J.; Cash, K. J.; Clark, H. A. The Design and Development of Fluorescent Nano-Optodes for *In Vivo* Glucose Monitoring. *J. Diabetes Sci. Technol.* **2011**, *5*, 68–75.
- (13) Elshaarani, T.; Yu, H.; Wang, L.; Zain ul, A.; Ullah, R. S.; Haroon, M.; Ullah Khan, R.; Fahad, S.; Khan, A.; Nazir, A.; Usman, M.; Naveed, K.-u.-R. Synthesis of Hydrogel-Bearing Phenylboronic Acid Moieties and Their Applications in Glucose Sensing and Insulin Delivery. *J. Mater. Chem. B* **2018**, *6*, 3831–3854.
- (14) Steiner, M.-S.; Duerkop, A.; Wolfbeis, O. S. Optical Methods for Sensing Glucose. *Chem. Soc. Rev.* **2011**, *40*, 4805–4839.
- (15) Clark, L. C., Jr.; Lyons, C. Electrode Systems for Continuous Monitoring in Cardiovascular Surgery. *Ann. N. Y. Acad. Sci.* **1962**, *102*, 29–45.
- (16) Updike, S. J.; Hicks, G. P. Enzyme Electrode. *Nature* **1967**, *214*, 986–988.
- (17) Updike, S. J.; Hicks, G. P. Reagentless Substrate Analysis with Immobilized Enzymes. *Science* **1967**, *158*, 270–272.
- (18) Toghiani, K. E.; Compton, R. G. Electrochemical Non-Enzymatic Glucose Sensors: A Perspective and An Evaluation. *Int. J. Electrochem. Sci.* **2010**, *5*, 1246–1301.
- (19) Park, S.; Boo, H.; Chung, T. D. Electrochemical Non-Enzymatic Glucose Sensors. *Anal. Chim. Acta* **2006**, *556*, 46–57.
- (20) Niu, X.; Lan, M.; Zhao, H.; Chen, C. Highly Sensitive and Selective Nonenzymatic Detection of Glucose Using Three-Dimensional Porous Nickel Nanostructures. *Anal. Chem.* **2013**, *85*, 3561–3569.
- (21) Li, J.; Lin, X. Glucose Biosensor Based on Immobilization of Glucose Oxidase in Poly(*o*-Aminophenol) Film on Polypyrrole-Pt Nanocomposite Modified Glassy Carbon Electrode. *Biosens. Bioelectron.* **2007**, *22*, 2898–2905.
- (22) Wilson, R.; Turner, A. P. F. Glucose Oxidase: An Ideal Enzyme. *Biosens. Bioelectron.* **1992**, *7*, 165–185.
- (23) Niu, X. H.; Shi, L. B.; Zhao, H. L.; Lan, M. B. Advanced Strategies for Improving the Analytical Performance of Pt-Based Nonenzymatic Electrochemical Glucose Sensors: A Minireview. *Anal. Methods* **2016**, *8*, 1755–1764.
- (24) Kost, J.; Mitragotri, S.; Gabbay, R. A.; Pishko, M.; Langer, R. Transdermal Monitoring of Glucose and Other Analytes Using Ultrasound. *Nat. Med.* **2000**, *6*, 347–350.
- (25) Lee, H.; Song, C.; Hong, Y. S.; Kim, M. S.; Cho, H. R.; Kang, T.; Shin, K.; Choi, S. H.; Hyeon, T.; Kim, D.-H. Wearable/Disposable Sweat-Based Glucose Monitoring Device with Multistage Transdermal Drug Delivery Module. *Sci. Adv.* **2017**, *3*, e1601314/1–e1601314/8.
- (26) Larin, K. V.; Eledrisi, M. S.; Motamedi, M.; Esenaliev, R. O. Noninvasive Blood Glucose Monitoring with Optical Coherence Tomography. A Pilot Study in Human Subjects. *Diabetes Care* **2002**, *25*, 2263–2267.
- (27) Zhang, C.; Cano, G. G.; Braun, P. V. Linear and Fast Hydrogel Glucose Sensor Materials Enabled by Volume Resetting Agents. *Adv. Mater.* **2014**, *26*, 5678–5683.
- (28) Weiss, R.; Yegorchikov, Y.; Shusterman, A.; Raz, I. Noninvasive Continuous Glucose Monitoring Using Photoacoustic Technology - Results from the First 62 Subjects. *Diabetes Technol. Ther.* **2007**, *9*, 68–74.
- (29) Burke, L. D. Premonolayer Oxidation and Its Role in Electrocatalysis. *Electrochim. Acta* **1994**, *39*, 1841–1848.
- (30) Rahman, M. M.; Ahammad, A. J. S.; Jin, J.-H.; Ahn, S. J.; Lee, J.-J. A Comprehensive Review of Glucose Biosensors Based on Nanostructured Metal-Oxides. *Sensors* **2010**, *10*, 4855–4886.
- (31) Ahmad, R.; Ahn, M.-S.; Bhat, K. S.; Mahmoudi, T.; Wang, Y.; Yoo, J.-Y.; Kwon, D.-W.; Yang, H.-Y.; Hahn, Y.-B.; Tripathy, N. Highly Efficient Non-Enzymatic Glucose Sensor Based on CuO Modified Vertically-Grown ZnO Nanorods on Electrode. *Sci. Rep.* **2017**, *7* (1–10), 5715.
- (32) Ahmad, R.; Vaseem, M.; Tripathy, N.; Hahn, Y.-B. Wide Linear-Range Detecting Nonenzymatic Glucose Biosensor Based on CuO Nanoparticles Inkjet-Printed on Electrodes. *Anal. Chem.* **2013**, *85*, 10448–10454.
- (33) Bhat, K. S.; Ahmad, R.; Yoo, J.-Y.; Hahn, Y.-B. Nozzle-Jet Printed Flexible Field-Effect Transistor Biosensor for High Performance Glucose Detection. *J. Colloid Interface Sci.* **2017**, *506*, 188–196.
- (34) Xie, F.; Huang, Z.; Chen, C.; Xie, Q.; Huang, Y.; Qin, C.; Liu, Y.; Su, Z.; Yao, S. Preparation of Au-Film Electrodes in Glucose-Containing Au-Electroplating Aqueous Bath for High-Performance Nonenzymatic Glucose Sensor and Glucose/O<sub>2</sub> Fuel Cell. *Electrochem. Commun.* **2012**, *18*, 108–111.
- (35) Baci, A.; Pop, A.; Remes, A.; Manea, F.; Burtica, G. Non-Enzymatic Electrochemical Determination of Glucose on Silver-Doped Zeolite-CNT Composite Electrode. *Adv. Sci., Eng. Med.* **2011**, *3*, 13–19.
- (36) Lu, J.; Do, I.; Drzal, L. T.; Worden, R. M.; Lee, I. Nanometal-Decorated Exfoliated Graphite Nanoplatelet Based Glucose Biosensors with High Sensitivity and Fast Response. *ACS Nano* **2008**, *2*, 1825–1832.
- (37) Zhong, X.; Yuan, R.; Chai, Y. *In Situ* Spontaneous Reduction Synthesis of Spherical Pd@Cys-C<sub>60</sub> Nanoparticles and Its Application in Nonenzymatic Glucose Biosensors. *Chem. Commun.* **2012**, *48*, 597–599.
- (38) Yuan, J.; Wang, K.; Xia, X. Highly Ordered Platinum-Nanotubule Arrays for Amperometric Glucose Sensing. *Adv. Funct. Mater.* **2005**, *15*, 803–809.
- (39) Park, S.; Chung, T. D.; Kim, H. C. Nonenzymatic Glucose Detection Using Mesoporous Platinum. *Anal. Chem.* **2003**, *75*, 3046–3049.
- (40) Song, Y.-Y.; Zhang, D.; Gao, W.; Xia, X.-H. Nonenzymatic Glucose Detection by Using a Three-Dimensionally Ordered, Macroporous Platinum Template. *Chem. - Eur. J.* **2005**, *11*, 2177–2182.



- (41) Dawson, K.; Baudequin, M.; O'Riordan, A. Single On-Chip Gold Nanowires for Electrochemical Biosensing of Glucose. *Analyst* **2011**, *136*, 4507–4513.
- (42) Jung, D.-U.-J.; Ahmad, R.; Hahn, Y.-B. Nonenzymatic Flexible Field-Effect Transistor Based Glucose Sensor Fabricated Using NiO Quantum Dots Modified ZnO Nanorods. *J. Colloid Interface Sci.* **2018**, *512*, 21–28.
- (43) Zhu, C.; Guo, S.; Dong, S. PdM (M = Pt, Au) Bimetallic Alloy Nanowires with Enhanced Electrocatalytic Activity for Electro-Oxidation of Small Molecules. *Adv. Mater.* **2012**, *24*, 2326–2331.
- (44) Gao, H.; Xiao, F.; Ching, C. B.; Duan, H. One-Step Electrochemical Synthesis of PtNi Nanoparticle-Graphene Nanocomposites for Nonenzymatic Amperometric Glucose Detection. *ACS Appl. Mater. Interfaces* **2011**, *3*, 3049–3057.
- (45) You, T.; Niwa, O.; Chen, Z.; Hayashi, K.; Tomita, M.; Hirono, S. An Amperometric Detector Formed of Highly Dispersed Ni Nanoparticles Embedded in a Graphite-Like Carbon Film Electrode for Sugar Determination. *Anal. Chem.* **2003**, *75*, 5191–5196.
- (46) Luo, P. F.; Kuwana, T. Nickel-Titanium Alloy Electrode as a Sensitive and Stable LCEC Detector for Carbohydrates. *Anal. Chem.* **1994**, *66*, 2775–2782.
- (47) Wang, C.; Yin, L.; Zhang, L.; Gao, R. Ti/TiO<sub>2</sub> Nanotube Array/Ni Composite Electrodes for Nonenzymatic Amperometric Glucose Sensing. *J. Phys. Chem. C* **2010**, *114*, 4408–4413.
- (48) Hui, S.; Zhang, J.; Chen, X.; Xu, H.; Ma, D.; Liu, Y.; Tao, B. Study of an Amperometric Glucose Sensor Based on Pd-Ni/SiNW Electrode. *Sens. Actuators, B* **2011**, *155*, 592–597.
- (49) Karikalan, N.; Velmurugan, M.; Chen, S.-M.; Karuppiiah, C. Modern Approach to the Synthesis of Ni(OH)<sub>2</sub> Decorated Sulfur Doped Carbon Nanoparticles for the Nonenzymatic Glucose Sensor. *ACS Appl. Mater. Interfaces* **2016**, *8*, 22545–22553.
- (50) Chen, T.; Liu, D.; Lu, W.; Wang, K.; Du, G.; Asiri, A. M.; Sun, X. Three-Dimensional Ni<sub>2</sub>P Nanoarray: An Efficient Catalyst Electrode for Sensitive and Selective Nonenzymatic Glucose Sensing with High Specificity. *Anal. Chem.* **2016**, *88*, 7885–7889.
- (51) Urgunde, A. B.; Kumar, A. R.; Shejale, K. P.; Sharma, R. K.; Gupta, R. Metal Wire Networks Functionalized with Nickel Alkanethiolate for Transparent and Enzymeless Glucose Sensors. *ACS Appl. Nano Mater.* **2018**, *1*, 5571–5580.
- (52) Fang, J. X.; Vainio, U.; Puff, W.; Wuerschum, R.; Wang, X. L.; Wang, D.; Ghafari, M.; Jiang, F.; Sun, J.; Hahn, H.; Gleiter, H. Atomic Structure and Structural Stability of Sc<sub>75</sub>Fe<sub>25</sub> Nanoglasses. *Nano Lett.* **2012**, *12*, 458–463.
- (53) Witte, R.; Feng, T.; Fang, J. X.; Fischer, A.; Ghafari, M.; Kruk, R.; Brand, R. A.; Wang, D.; Hahn, H.; Gleiter, H. Evidence for Enhanced Ferromagnetism in an Iron-Based Nanoglass. *Appl. Phys. Lett.* **2013**, *103*, 073106/1–073106/5.
- (54) Nandam, S. H.; Ivanisenko, Y.; Schwaiger, R.; Sniadecki, Z.; Mu, X.; Wang, D.; Chellali, R.; Boll, T.; Kilmametov, A.; Bergfeldt, T.; Gleiter, H.; Hahn, H. Cu-Zr Nanoglasses: Atomic Structure, Thermal Stability and Indentation Properties. *Acta Mater.* **2017**, *136*, 181–189.
- (55) Gleiter, H. Nanoglasses: A New Kind of Noncrystalline Materials. *Beilstein J. Nanotechnol.* **2013**, *4*, 517–533.
- (56) Chen, N.; Louzguine-Luzgin, D. V.; Yao, K. A New Class of Non-Crystalline Materials: Nanogranular Metallic Glasses. *J. Alloys Compd.* **2017**, *707*, 371–378.
- (57) Ghafari, M.; Hahn, H.; Gleiter, H.; Sakurai, Y.; Itou, M.; Kamali, S. Evidence of Itinerant Magnetism in a Metallic Nanoglass. *Appl. Phys. Lett.* **2012**, *101*, 243104/1–243104/4.
- (58) Singh, S. P.; Chellali, M. R.; Velasco, L.; Ivanisenko, Y.; Boltynjuk, E.; Gleiter, H.; Hahn, H. Deformation-Induced Atomic Rearrangements and Crystallization in the Shear Bands of a Tb<sub>75</sub>Fe<sub>25</sub> Nanoglass. *J. Alloys Compd.* **2020**, *821*, 153486.
- (59) Wang, W. H.; Dong, C.; Shek, C. H. Bulk Metallic Glasses. *Mater. Sci. Eng., R* **2004**, *R44*, 45–89.
- (60) Danilov, D.; Hahn, H.; Gleiter, H.; Wenzel, W. Mechanisms of Nanoglass Ultrastability. *ACS Nano* **2016**, *10*, 3241–3247.
- (61) Wang, J. Q.; Chen, N.; Liu, P.; Wang, Z.; Louzguine-Luzgin, D. V.; Chen, M. W.; Perepezko, J. H. The Ultrastable Kinetic Behavior of an Au-Based Nanoglass. *Acta Mater.* **2014**, *79*, 30–36.
- (62) Li, J.; Doubek, G.; McMillon-Brown, L.; Taylor, A. D. Recent Advances in Metallic Glass Nanostructures: Synthesis Strategies and Electrocatalytic Applications. *Adv. Mater.* **2019**, *31*, 1802120.
- (63) Kaneko, T.; Tanaka, S.; Asao, N.; Yamamoto, Y.; Chen, M.; Zhang, W.; Inoue, A. Reusable and Sustainable Nanostructured Skeleton Catalyst: Heck Reaction with Nanoporous Metallic Glass Pd (PdNPore) as a Support, Stabilizer and Ligand-Free Catalyst. *Adv. Synth. Catal.* **2011**, *353*, 2927–2932.
- (64) Doubek, G.; Sekol, R. C.; Li, J.; Ryu, W.-H.; Gittleson, F. S.; Nejati, S.; Moy, E.; Reid, C.; Carmo, M.; Linardi, M.; Bordeenithikaseem, P.; Kinser, E.; Liu, Y.; Tong, X.; Osuji, C. O.; Schroers, J.; Mukherjee, S.; Taylor, A. D. Guided Evolution of Bulk Metallic Glass Nanostructures: A Platform for Designing 3D Electrocatalytic Surfaces. *Adv. Mater.* **2016**, *28*, 1940–1949.
- (65) Kinser, E. R.; Padmanabhan, J.; Yu, R.; Corona, S. L.; Li, J.; Vaddiraju, S.; Legassey, A.; Loye, A.; Balestrini, J.; Solly, D. A.; Schroers, J.; Taylor, A. D.; Papadimitrakopoulos, F.; Herzog, R. I.; Kyriakides, T. R. Nanopatterned Bulk Metallic Glass Biosensors. *ACS Sens* **2017**, *2*, 1779–1787.
- (66) Zhang, P.; Wang, Z.; Perepezko, J. H.; Voyles, P. M. Vittrification, Crystallization, and Atomic Structure of Deformed and Quenched Ni<sub>60</sub>Nb<sub>40</sub> Metallic Glass. *J. Non-Cryst. Solids* **2018**, *491*, 133–140.
- (67) Yang, L.; Meng, X.-f.; Guo, G.-q. Structural Origin of the Pinpoint-Composition Effect on the Glass-Forming Ability in the NiNb Alloy System. *J. Mater. Res.* **2013**, *28*, 3170–3176.
- (68) Enayati, M. H.; Dastanpoor, E. Comparative Study of Mechanical Alloying Induced Nanocrystallization and Amorphization in Ni-Nb and Ni-Zr Systems. *Metall. Mater. Trans. A* **2013**, *44*, 3984–3998.
- (69) Enayati, M. H.; Schumacher, P.; Cantor, B. The Structure and Thermal Stability of Mechanically Alloyed Ni-Nb-Zr Amorphous Alloys. *J. Mater. Sci.* **2002**, *37*, 5255–5259.
- (70) Luo, W. K.; Sheng, H. W.; Alamgir, F. M.; Bai, J. M.; He, J. H.; Ma, E. Icosahedral Short-Range Order in Amorphous Alloys. *Phys. Rev. Lett.* **2004**, *92*, 145502/1–145502/4.
- (71) Sun, L.; He, J. H.; Sheng, H. W.; Searson, P. C.; Chien, C. L.; Ma, E. Magnetic Properties of Amorphous Ni<sub>60</sub>Ag<sub>40</sub> Films. *J. Non-Cryst. Solids* **2003**, *317*, 164–168.
- (72) Lee, W. S.; Kim, S. C.; Yoon, W. Y.; Kwun, S. I. Mechanical Alloying Behaviors of the Ni<sub>50</sub>Ti<sub>50</sub> System by Pulverization. *Taehan Kumsok Hakhoechi* **1996**, *34*, 886–896.
- (73) Twohig, E.; Tiernan, P.; Butler, J.; Dickinson, C.; Tofail, S. A. M. Mechanical, microstructural and thermal properties of a 50:50 at.% nickel-titanium alloy subjected to a dieless drawing process. *Acta Mater.* **2014**, *68*, 140–149.
- (74) Plummer, J. Is Metallic Glass Poised to Come of Age? *Nat. Mater.* **2015**, *14*, 553–555.
- (75) Collins, L. E.; Grant, N. J.; Vander Sande, J. B. Crystallization of Amorphous Nickel-Niobium (Ni<sub>60</sub>Nb<sub>40</sub>). *J. Mater. Sci.* **1983**, *18*, 804–814.
- (76) Trifonov, A. S.; Lubchenko, A. V.; Polkin, V. I.; Pavolotsky, A. B.; Ketov, S. V.; Louzguine-Luzgin, D. V. Difference in Charge Transport Properties of Ni-Nb Thin Films with Native and Artificial Oxide. *J. Appl. Phys.* **2015**, *117*, 125704/1–125704/5.
- (77) Chellali, M. R.; Nandam, S. H.; Li, S.; Fawey, M. H.; Moreno-Pineda, E.; Velasco, L.; Boll, T.; Pastewka, L.; Kruk, R.; Gumbsch, P.; Hahn, H. Amorphous Nickel Nanophases Inducing Ferromagnetism in Equiatomic Ni-Ti Alloy. *Acta Mater.* **2018**, *161*, 47–53.
- (78) Chen, N.; Shi, X.; Witte, R.; Nakayama, K. S.; Ohmura, K.; Wu, H.; Takeuchi, A.; Hahn, H.; Esashi, M.; Gleiter, H.; Inoue, A.; Louzguine, D. V. A Novel Ti-Based Nanoglass Composite with Submicron-Nanometer-Sized Hierarchical Structures to Modulate Osteoblast Behaviors. *J. Mater. Chem. B* **2013**, *1*, 2568–2574.
- (79) Bag, S.; Baksi, A.; Wang, D.; Kruk, R.; Benel, C.; Chellali, M. R.; Hahn, H. Combination of Pulsed Laser Ablation and Inert Gas

Condensation for the Synthesis of Nanostructured Nanocrystalline, Amorphous and Composite Materials. *Nanoscale Adv.* **2019**, *1*, 4513–4521.

# Supporting Information

## Nonenzymatic Glucose Sensing Using Ni<sub>60</sub>Nb<sub>40</sub> Nanoglass

Soumabha Bag,<sup>1,\*,#</sup> Ananya Baksi,<sup>1,\*,#</sup> Sree Harsha Nandam,<sup>1</sup> Di Wang,<sup>1,2</sup> Xinglong Ye,<sup>1</sup>

Jyotirmoy Ghosh,<sup>3</sup> Thalappil Pradeep,<sup>3</sup> and Horst Hahn<sup>1,4,\*</sup>

<sup>1</sup>Institute of Nanotechnology, Karlsruhe Institute of Technology, 76344 Eggenstein-Leopoldshafen, Germany

<sup>2</sup>Karlsruhe Nano Micro Facility, Karlsruhe Institute of Technology, 76344 Eggenstein-Leopoldshafen, Germany

<sup>3</sup>Department of Science and Technology (DST) Unit of Nanoscience and Thematic Unit of Excellence (TUE), Department of Chemistry, Indian Institute of Technology Madras, Chennai 600036, India

<sup>4</sup>KIT-TUD Joint Research Laboratory Nanomaterials, FB 11, TU Darmstadt, 64206 Darmstadt, Germany

<sup>#</sup>These authors contributed equally

Email: Soumabha Bag - [soumabha.bag@kit.edu](mailto:soumabha.bag@kit.edu)

Ananya Baksi - [ananya.baksi@kit.edu](mailto:ananya.baksi@kit.edu) and

Horst Hahn - [horst.hahn@kit.edu](mailto:horst.hahn@kit.edu)

\*Corresponding author

### Table of Content

Name	Description	Page number
Figure S1	FESEM images of <i>nanoglass</i> , nanocomposite and melt-spun ribbon	S2
Figure S2	Scan rate dependent CV of <i>nanoglass</i> sample	S3
Figure S3	XRD of the annealed <i>nanoglass</i> sample	S4
Figure S4	Selectivity and long range chronoamperometric sensitivity of the <i>nanoglass</i> electrode	S5
Figure S5	Structural analysis of <i>nanoglass</i> sample following electrochemical oxidation	S6
Figure S6	XPS analysis of the <i>nanoglass</i> before and after sensing experiment	S7



**Supporting Information 1:**

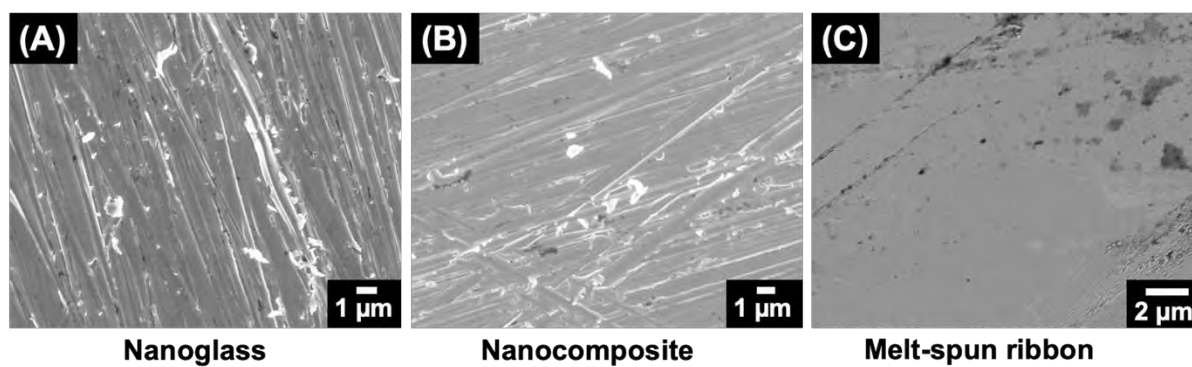


**Figure S1.** FESEM images of the (A) *nanoglass*, (B) nanocomposite and (C) melt-spun ribbon samples before the electrochemical experiments.

Supporting Information 2:

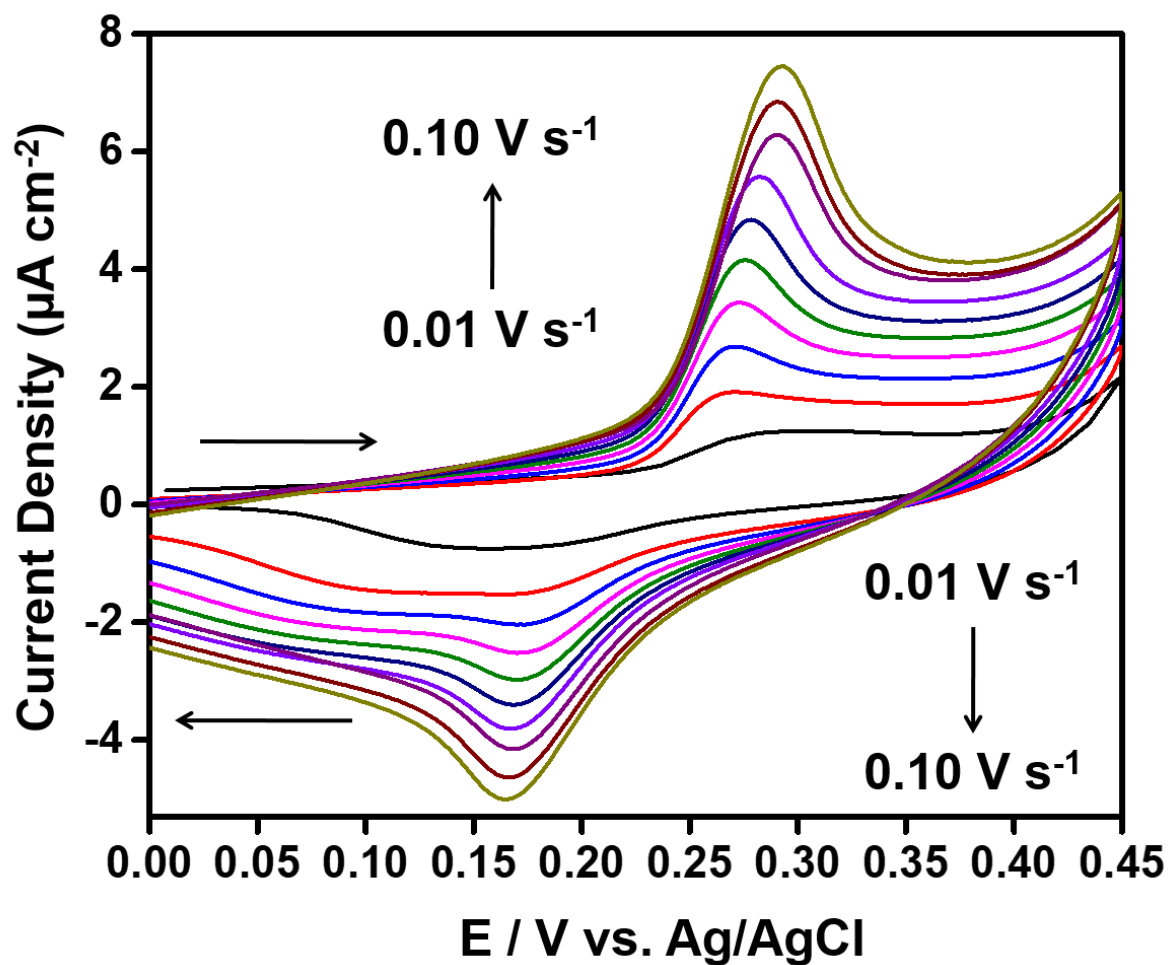


**Figure S2.** Performance of  $\text{Ni}_{60}\text{Nb}_{40}$  nanoglass as working electrode (WE). Cyclic voltammetric scans in the potential window -0.1 to +0.45 V are conducted with scan rate from 10 to 100  $\text{mV s}^{-1}$  in 0.1 M NaOH solution.

Supporting Information 3:

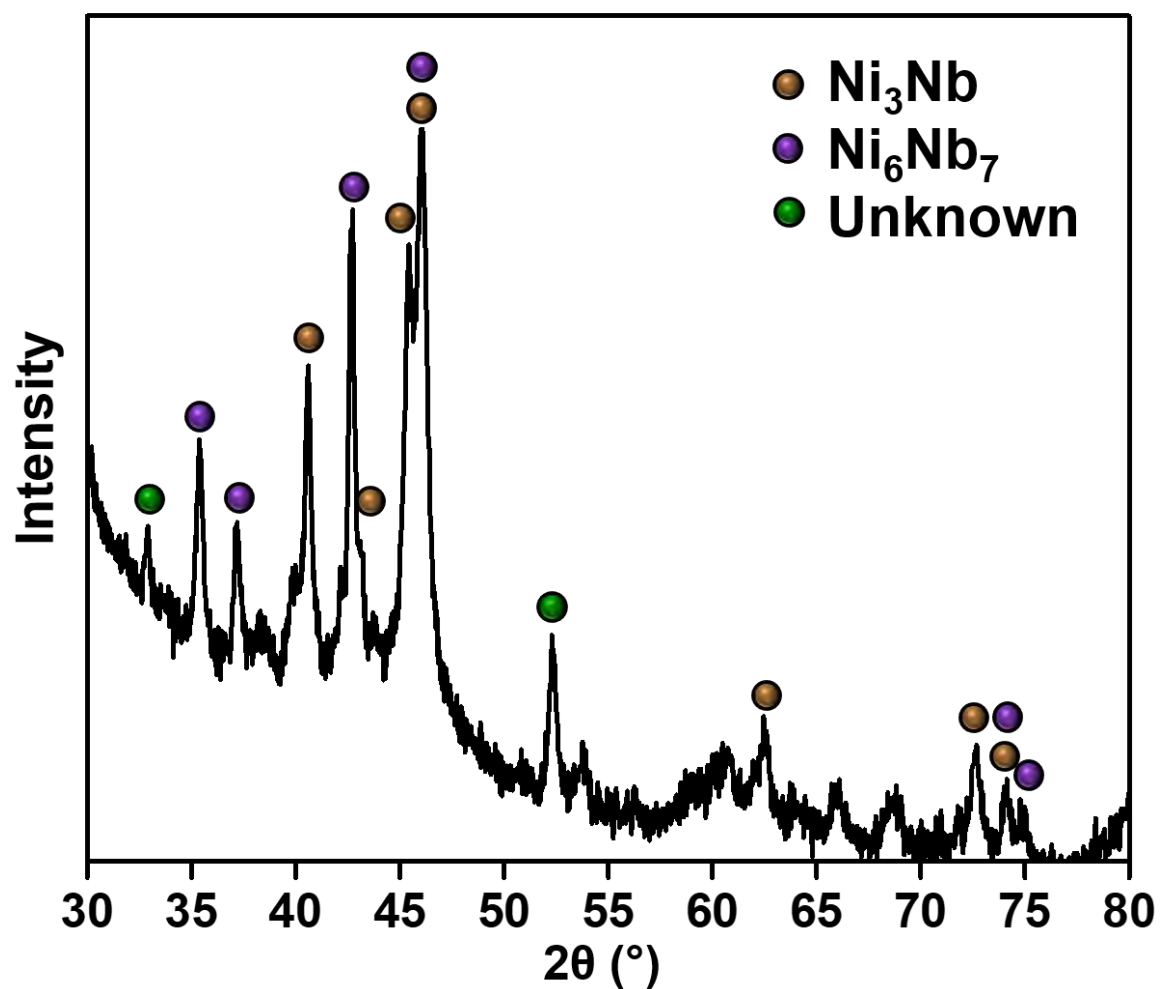


**Figure S3.** Cu-XRD patterns of annealed *nanoglass* sample. Mixtures of different intermetallic compounds ( $\text{Ni}_3\text{Nb}$ ,  $\text{Ni}_6\text{Nb}_7$ ) are identified in the annealed sample.

#### Supporting Information 4:

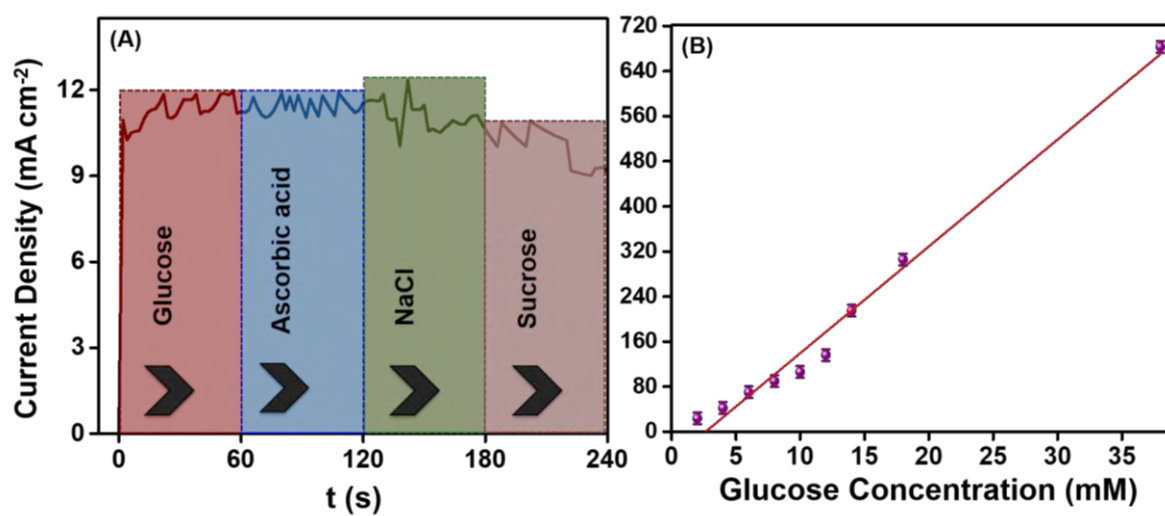


**Figure S4.** (A) Stable chronoamperometric current response are identified with infusion of 0.25 mM ascorbic acid, NaCl and sucrose solutions in succession into 0.25 mM glucose solution prepared in 0.1 M NaOH solution. (B) Linear increase in current density is found chronoamperometrically as glucose concentration enhanced from 2 mM to 38 mM.

Supporting Information 5:

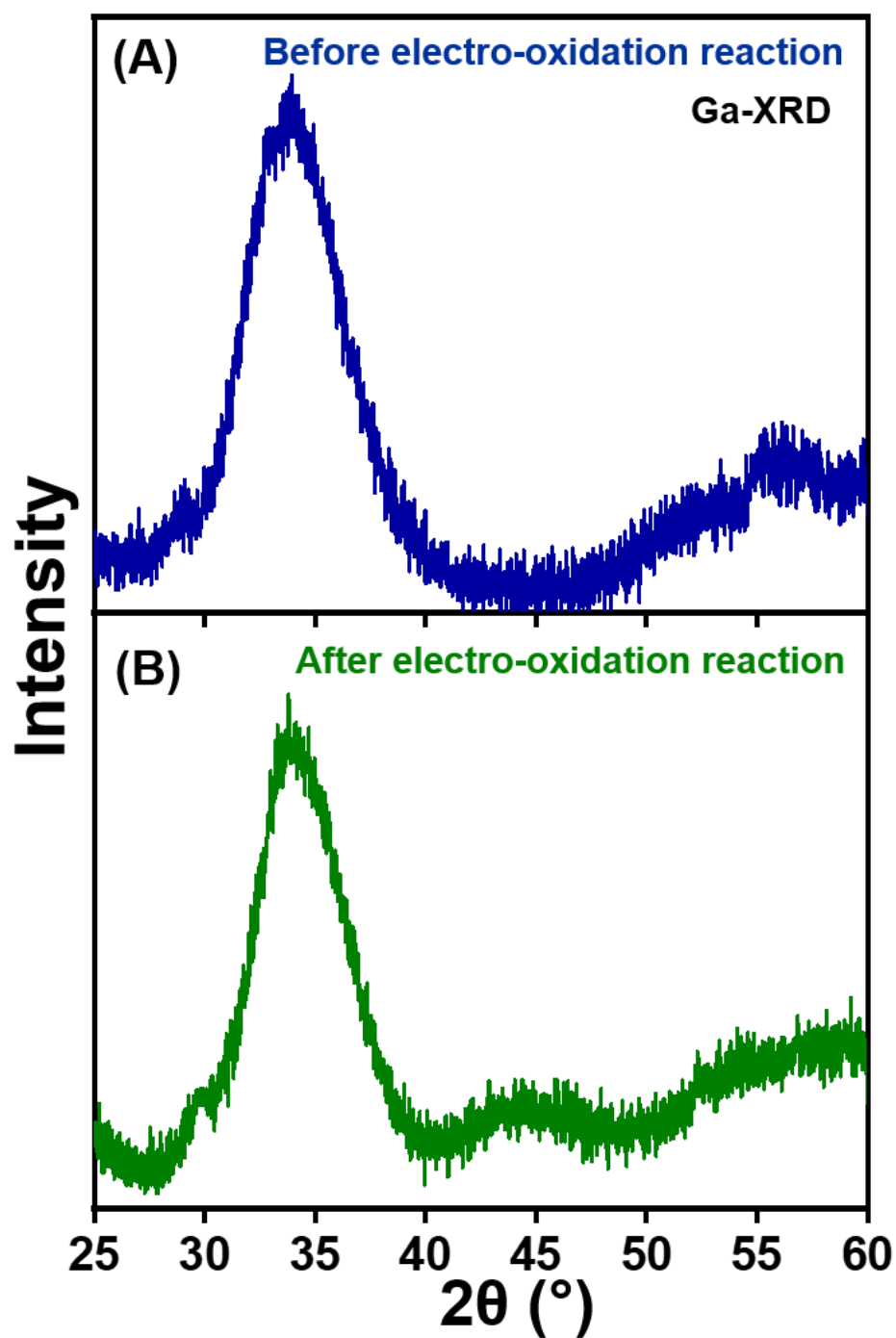


**Figure S5.** Structural analysis of the  $\text{Ni}_{60}\text{Nb}_{40}$  *nanoglass* electrode before and after sensing experiments. Ga-XRD confirms amorphous phase in the material before sensing experiments given in (A), which remains indistinguishable after the experiment as shown in (B).

## Supporting Information 6:

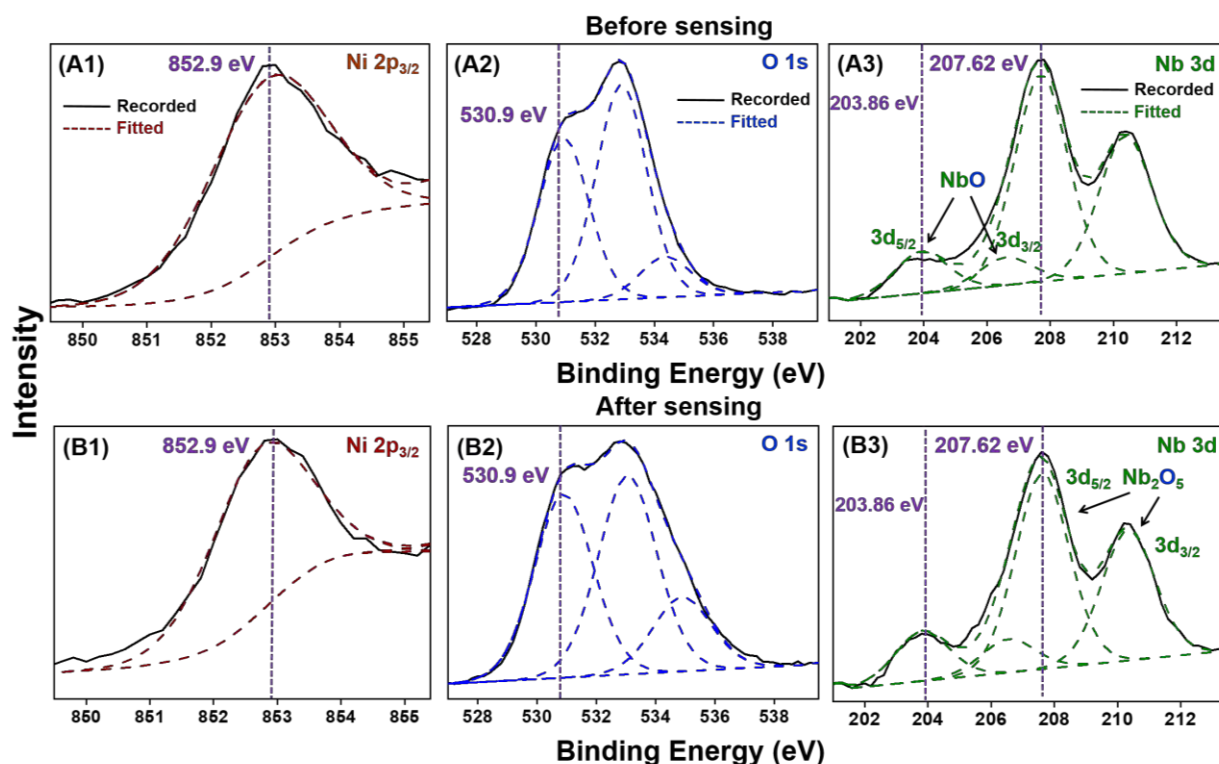


**Figure S6.** Photoelectron spectra (XPS) of the *nanoglass* sample before (A1 to A3) and after (B1 to B3) electrochemical studies. Ni (2p<sub>3/2</sub>), O (1s) and Nb (3d) regions are highlighted for the current investigations. Nearly indistinguishable spectra of the sample before and after sensing experiments indicate unaltered surface of the *nanoglass* electrode. Fitted and deconvoluted spectra (dashed lines) points out different niobium oxides present at the surface (A3 and B3).



# Ultrafast Intersystem Crossing in Isolated $\text{Ag}_{29}(\text{BDT})_{12}^{3-}$ Probed by Time-Resolved Pump–Probe Photoelectron Spectroscopy

Aron P. Veenstra,\* Laurenz Monzel, Ananya Baksi, Joseph Czekner, Sergei Lebedkin, Erik K. Schneider, Thalappil Pradeep, Andreas-Neil Unterreiner, and Manfred M. Kappes



Cite This: *J. Phys. Chem. Lett.* 2020, 11, 2675–2681



Read Online

ACCESS |



Metrics & More

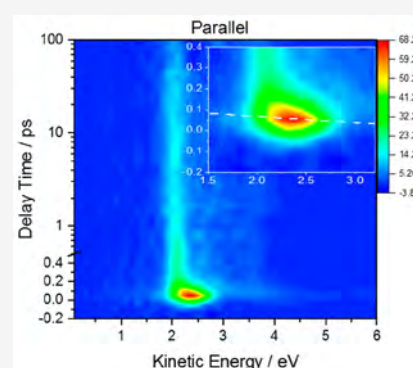


Article Recommendations



Supporting Information

**ABSTRACT:** The photophysics of the isolated trianion  $\text{Ag}_{29}(\text{BDT})_{12}^{3-}$  (BDT = benzenedithiolate), a ligand-protected cluster comprising BDT-based ligands, terminating a shell of silver thiolates and a core of silver atoms, was studied in the gas phase by femtosecond time-resolved, pump–probe photoelectron spectroscopy. UV excitation at 490 nm populates one or more singlet excited states with significant charge transfer (CT) character in which electron density is shifted from shell to core. These CT states relax on an average time scale of several hundred femtoseconds by charge recombination to yield either the vibrationally excited singlet ground state (internal conversion) or a long-lived triplet (intersystem crossing). Our study is the first ultrafast spectroscopic probe of a ligand-protected coinage metal cluster in isolation. In the future, it will be interesting to study how cluster size, overall charge state, or heteroatom doping can be used to tune the corresponding relaxation dynamics in the absence of solvent.



Atomically precise, ligand-stabilized (“protected”) coinage metal clusters are of great present interest due to their size-tunable electronic structure, which has stimulated applications in fields ranging from electrocatalysis to optical sensing.<sup>1–13</sup> While protected gold clusters have been explored most extensively, there has also been much recent interest in preparing and characterizing ligand-stabilized silver clusters<sup>14</sup> as well as protected nanoalloy clusters comprising mixed coinage metal cores.<sup>15</sup> Several thiolate-protected silver clusters ranging up to  $\text{Ag}_{374}$  have been crystallized.<sup>16</sup>

Like some thiolated organosoluble gold clusters, many silver clusters show visible and near-infrared (NIR) emission. A prototypical ligand-protected silver cluster with known X-ray crystal structure is  $\text{Ag}_{29}(\text{BDT})_{12}(\text{TPP})_4$ , first prepared and characterized in solid state and liquid solution by Bakr et al. (BDT, 1,3-benzenedithiolate; TPP, triphenylphosphine).<sup>17</sup> Upon near-UV excitation of  $\text{Ag}_{29}(\text{BDT})_{12}(\text{TPP})_4$ , long-lived near-IR photoluminescence (PL) has been observed, which is attributed to phosphorescence. It has also been reported that this PL can be efficiently quenched by codissolved molecular oxygen.<sup>10</sup> Also, ultrafast intermolecular electron transfer occurs upon UV photoexcitation of  $\text{Ag}_{29}(\text{BDT})_{12}(\text{TPP})_4$  when methylviologen is added to the solution.<sup>18</sup>

Electrospray mass spectrometry of  $\text{Ag}_{29}(\text{BDT})_{12}(\text{TPP})_4$  solutions yields *trianions* as the predominant negative charge state in isolation ( $\text{Ag}_{29}(\text{BDT})_{12}(\text{TPP})_{4-x}^{3-}$ , where  $x = 0–4$ ). Bakr et al. have proposed that these trianions all reflect eight valence electron species in a closed-shell  $1s^21p^6$  superatom configuration ( $29 - (12 \times 2) + 3 = 8$ ).<sup>17</sup> Density functional theory (DFT) calculations have established that such a

“superatom” grouping of valence orbitals is a characteristic of particularly stable coinage metal clusters.<sup>7</sup> Correspondingly, solid  $\text{Ag}_{29}(\text{BDT})_{12}(\text{TPP})_4$  has been proposed to consist of  $\text{Ag}_{29}(\text{BDT})_{12}(\text{TPP})_4^{3-}$  units surrounded by counteranions (which remain to be assigned)<sup>19</sup> and as a corollary, the corresponding solutions are thought to comprise predominantly solvated  $\text{Ag}_{29}(\text{BDT})_{12}(\text{TPP})_4^{3-}$ .

Time-dependent density-functional theory (TDDFT) calculations of the  $\text{Ag}_{29}(\text{BDT})_{12}(\text{TPP})_4$  cluster suggested that the UV excitation giving rise to photoluminescence is of charge transfer type—transferring negative charge from the shell toward empty d-like superatom orbitals mainly associated with the silver cluster core.<sup>17</sup> A more recent linear response (LR)-TDDFT calculation of  $\text{Ag}_{29}(\text{BDT})_{12}(\text{TPP})_4^{3-}$  comes to the conclusion that UV excitation mainly involves ligand-to-metal charge transfer.<sup>10</sup> At this stage, the accuracy of TDDFT excited-state predictions for this compound class, the relaxation mechanism following photoexcitation (in particular, the route to the PL emitting state) and the role of the molecular environment in modulating these processes all remain unclear.

We therefore studied this problem by removing the solvent entirely. Specifically, we used femtosecond time-resolved, two-

**Received:** February 13, 2020

**Accepted:** March 13, 2020

**Published:** March 13, 2020

color, pump–probe photoelectron spectroscopy (tr-PES) to examine the corresponding isolated multianions. These are the first ultrafast spectroscopic measurements of ligand stabilized coinage metal clusters in the gas phase. Previously, one-photon PES of isolated multianionic ligand-protected coinage metal clusters with pulsed nanosecond lasers has yielded information on electron affinities (EA), repulsive Coulomb barrier heights (RCB), as well as overall electronic structure.<sup>12,13,20,21</sup> However, accessing fast decay dynamics following electronic excitation requires tr-PES.

Specifically, we generated isolated  $\text{Ag}_{29}(\text{BDT})_{12}^{3-}$  as the system for tr-PES study by electrospray ionization of  $\text{Ag}_{29}(\text{BDT})_{12}(\text{TPP})_4$  solutions (with associated loss of all four weakly bound monodentate phosphines). The probable  $\text{Ag}_{29}(\text{BDT})_{12}^{3-}$  molecular structure (based on the X-ray structure of  $\text{Ag}_{29}(\text{BDT})_{12}(\text{TPP})_4$  and DFT calculations—see the Supporting Information) is illustrated in Figure 1. Using tr-

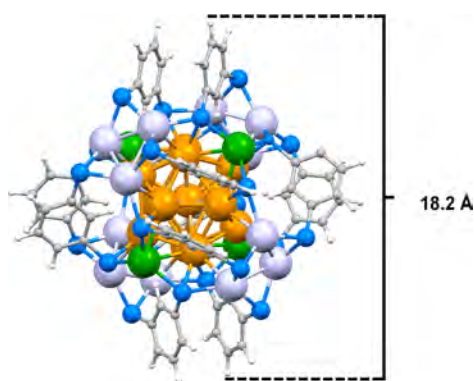


**Figure 1.** Molecular structure of  $\text{Ag}_{29}(\text{BDT})_{12}^{3-}$  based on the X-ray crystal structure of  $\text{Ag}_{29}(\text{BDT})_{12}(\text{TPP})_4$  as reported in ref 17 (after removal of four TPP ligands and DFT structure reoptimization of  $\text{Ag}_{29}(\text{BDT})_{12}^{3-}$  without symmetry constraints (see the Supporting Information)). Color scheme: **core** comprising 13 silver atoms (orange); **shell** comprising 12 fully coordinated (light purple) and 4 partially coordinated silver atoms (green—after TPP removal), 24 sulfur atoms (blue), and 12 terminating benzyl-derived **ligands** (gray).

PES we find that resonant pulsed laser excitation of this species at 490 nm (2.53 eV) can lead to rapid population of a long-

lived excited state, which we identify as the carrier of the photoluminescence observed under similar irradiation conditions in solution.

The  $\text{Ag}_{29}(\text{BDT})_{12}(\text{TPP})_4$  solid was synthesized following a previously reported method and used without further purification.<sup>22</sup> Approximately 5  $\mu\text{M}$  of clusters in dimethylformamide (DMF) was electrosprayed and probed using an ion beam apparatus—parts of which have been previously described.<sup>23–25</sup> It has recently been modified to incorporate a velocity map imaging (VMI) setup and a new femtosecond laser system.

In brief, after transfer into the high-vacuum machine, electrosprayed multianions were accelerated into a time-of-flight (TOF) mass spectrometer and selected therein by their mass-to-charge ratio. The selected ions entered a perpendicularly oriented VMI spectrometer mounted within the TOF flight tube. There the trianions interacted with either one (one-color) or two femtosecond laser pulses (two color pump–probe) leading to photoelectron detachment. Three open electrodes in an Eppink-Parker like<sup>26</sup> design (pulsed) accelerated the photoelectrons toward an imaging micro-channel plate detector (MCP) equipped with a phosphor screen. The corresponding electron impacts were recorded with a charge-coupled device (CCD) camera. Angle-resolved one-color photoelectron (PE) spectra (as well as two-color, time-resolved pump–probe PE spectra (tr-PES)) were obtained from these raw data using the polar onion peeling algorithm developed by the Verlet group.<sup>27</sup> The VMI setup was calibrated using one-color, one-photon photodetachment of  $\text{I}^-$  at several different wavelengths.

The femtosecond laser system consisted of a Ti:sapphire pump laser (Astrella, Coherent) with a fundamental output wavelength of 800 nm (1.55 eV), generating 35 fs pulses at a repetition rate of 1 kHz and pulse energy of 7 mJ. This pumped a wavelength tunable TOPAS Prime (Light Conversion) optical parametric amplifier (OPA), which delivered the 490 nm pump pulses (and also UV wavelengths for one-photon detachment). We used an optical delay line to vary the pump–probe timing. The instrument response function in the vacuum chamber was  $50 \pm 5$  fs. The full width at half-maximum (fwhm) bandwidths of pump and probe pulses were  $\sim 56$  and  $\sim 51$  meV, respectively. Further details, including laser pulse energies, polarization and focusing

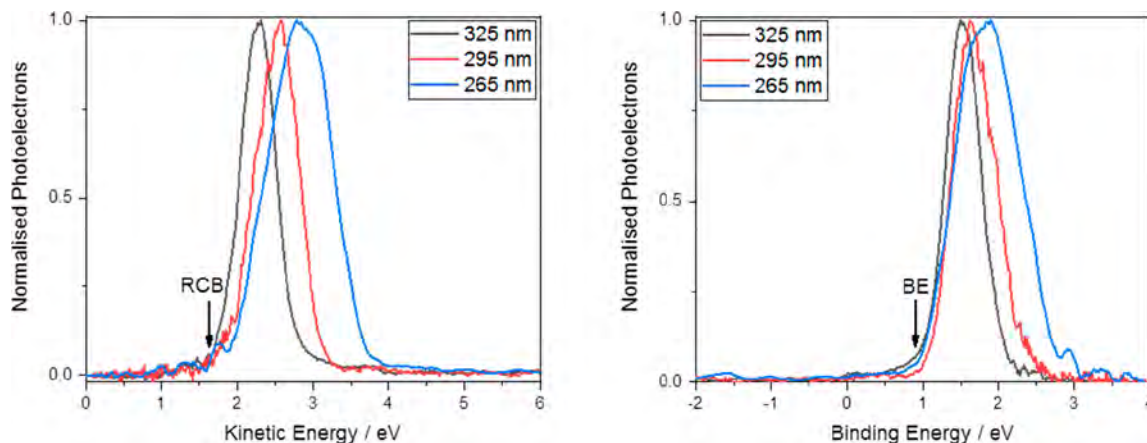


**Figure 2.** One-photon PES spectra of  $\text{Ag}_{29}(\text{BDT})_{12}^{3-}$  at various UV detachment wavelengths as indicated (at photon energies of 3.81 (black), 4.20 (red), and 4.68 (blue) eV). Normalized photoelectron counts are plotted vs EKE for determination of the RCB height and vs electron BE toward determination of the third electron affinity, EA(3).

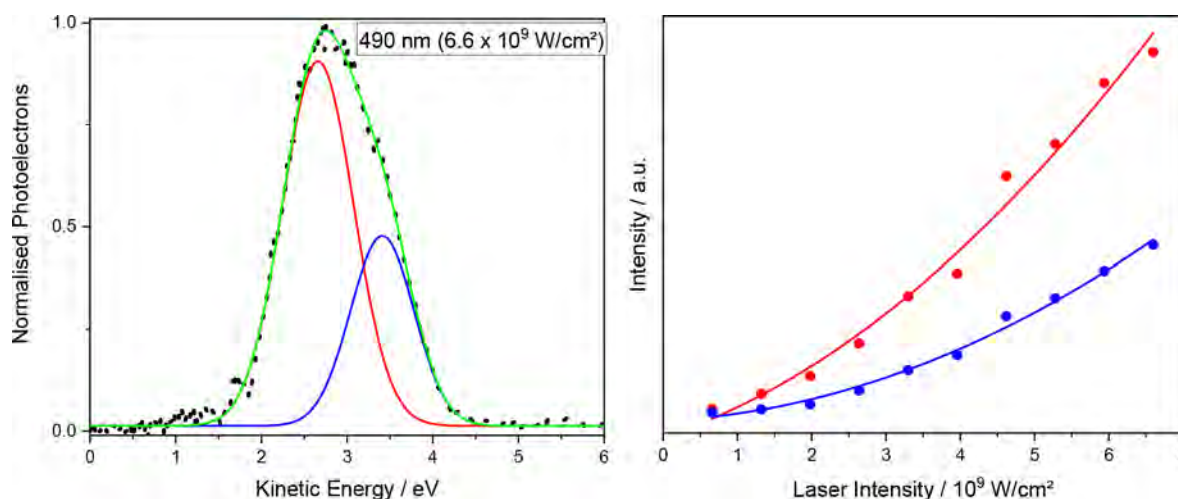


**Figure 3.** (left) One-color PE spectrum recorded at a detachment wavelength of 490 nm (2.53 eV). Note the presence of two EKE components. Gaussian deconvolution yields features centered at EKEs of  $2.66 \pm 0.02$  and  $3.41 \pm 0.02$  eV. (right) The integral intensities of these features scale quadratically with laser intensity indicating that both originate from two-photon processes taking place within the same laser pulse.

conditions, OPA wavelength range, data acquisition, and deconvolution procedures used to obtain either “stationary” one-photon spectra or time-resolved pump–probe PES measurements are described in the [Supporting Information](#).

We begin with the stationary measurements (one-color photodetachment with fs laser pulses), which were recorded at detachment wavelengths of 325, 295, and 265 nm as indicated in [Figure 2](#) (corresponding to photon energies of 3.81, 4.20, and 4.68 eV, respectively). In all cases, isotropic angular distributions were observed. The corresponding PE spectra show essentially only one component. Plotted versus electron binding energy (BE), the data allow to determine the third electron affinity (EA(3)) of  $\text{Ag}_{29}(\text{BDT})_{12}^{3-}$  as  $0.9 \pm 0.1$  eV (with  $h\nu - \text{EA}(3) = \text{electron kinetic energy (EKE)}$ ). The estimated error is a result of the experimental noise, the extrapolation procedure used to determine EA(3), and the spectral width of the laser pulses. Plotted versus electron kinetic energy, the spectra also allow to determine the repulsive Coulomb barrier (RCB) height (as measured from the dianion ground state) to be  $1.7 \pm 0.1$  eV.

It is of interest to compare RCB and EA(3) with the predictions of classical electrostatics for charging a metallic sphere of radius corresponding roughly to that of the molecule in question (see structure in [Figure 1](#)).  $\text{Ag}_{29}(\text{BDT})_{12}^{3-}$  can be thought of as consisting of a central 13-atom silver icosahedron (of radius ca. 2.8 Å), surrounded by a silver sulfide shell (of outside radius ca. 5.1 Å), which is capped by terminating ligands (to yield a total radius of 9.1 Å). Assuming a polycrystalline silver work function (WF) of 4.26 eV, classical electrostatics predicts that a third electron affinity of 0.9 eV is obtained for a conducting sphere of radius  $R = 10.7$  Å ( $\text{WF} - 2.5 e^2/4\pi\epsilon_0 R = 0.9$  eV), that is, larger than the actual molecular dimensions.

Similarly, the RCB height can be contrasted with a classical electrostatic calculation of the Coulomb repulsion between a single negative and a twofold negative point charge at distance  $R$ . This reaches a value of 1.7 eV at a separation of 17 Å—well outside the actual molecule. The RCB can also be compared to the height of a Coulomb barrier associated with charging a metallic sphere of radius  $R$ , from  $2^-$  to  $3^-$ . According to eq 5 in [ref 28](#) an RCB of height 1.7 eV requires an  $R$  of ca. 16 Å, that

is, again a radius significantly outside the perimeter of  $\text{Ag}_{29}(\text{BDT})_{12}^{3-}$ .

We conclude that the electronic ground state of  $\text{Ag}_{29}(\text{BDT})_{12}^{3-}$  is not well-described by a classical metallic sphere, implying that “metallic” valence electron delocalization does not extend uniformly throughout the ligand-stabilized cluster. This is consistent with the previous TDDFT calculation<sup>17</sup> already alluded to. This ascribes the first strong UV absorption band at ca. 450 nm (see solution absorption and PL excitation spectra in the [Supporting Information](#)) to a charge-transfer excitation from *localized* electron orbitals on the silver sulfide shell to D-like, superatom lowest unoccupied molecular orbital (LUMO+1) orbitals on the silver cluster core.

We next explored the relaxation dynamics associated with 490 nm (2.53 eV) excitation. This wavelength was chosen as a compromise between TOPAS emission intensity and cluster absorption cross section in an overall range attributable to charge transfer excitations.<sup>17</sup> We first performed one-color photoelectron spectroscopy (PES) measurements at 490 nm at a number of different laser intensities. A typical PE spectrum (at an intermediate laser intensity of  $5 \times 10^9$  W/cm<sup>2</sup>) is shown in [Figure 3](#). Again, the corresponding velocity map image on which it is based was found to be isotropic (over the full intensity range probed). In contrast to the UV measurements shown in [Figure 2](#), the PE spectrum now manifests at least *two* components. This is highlighted by a corresponding two-component Gaussian deconvolution. Systematically varying the laser intensity and recording the corresponding PE spectra shows that both Gaussian components (centered at  $2.66 \pm 0.02$  and  $3.41 \pm 0.02$  eV, respectively) manifest a two-photon intensity dependence. This is consistent with the above determination of EA(3) and RCB. One 490 nm photon (2.53 eV) alone cannot surmount the RCB, which lies at  $2.6 \pm 0.2$  eV ( $\text{RCB} + \text{EA}(3)$ ) when referred to the trianion ground state.

The two different electron kinetic energy (EKE) components that are fit to the 490 nm one-color PE spectra can be interpreted as deriving from two separate excited electronic states, each of which is accessed *during the same* ca.  $54 \pm 5$  fs wide laser pulse (ion packets spend ca. 50 ns in the VMI extraction zone; the next laser pulse arrives 1 ms later). Most



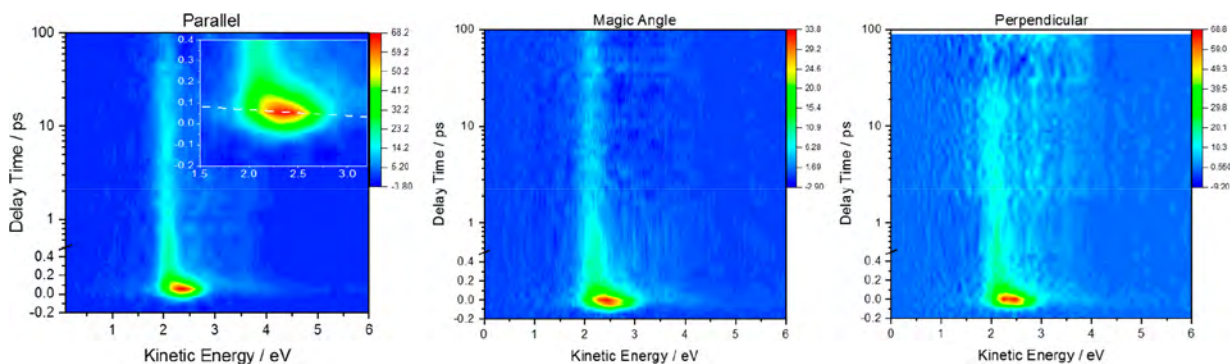


**Figure 4.** Two-color pump probe measurements (490 nm (2.53 eV)/800 nm (1.55 eV)) recorded for parallel (a), magic angle (b), and perpendicular (c) relative (linear) laser polarizations as indicated. Shown are contour plots of the transient photoelectron counts vs electron kinetic energy and pump–probe delay. The three data sets look very similar indicating that they are not influenced by rotational dephasing. The expanded scale insert in (a) highlights the dynamics during the first 400 fs following 490 nm excitation.

likely, only the higher-lying state is initially (photo)-populated and can relax very rapidly to the lower state within the laser pulse. The lower electron kinetic energy component then results upon electron detachment from this state with an additional photon. By contrast, the higher electron kinetic energy feature derives from direct photoionization of the initially populated excited state.

Interestingly, there is no clear indication of excited-state electron tunneling detachment (ESETD) in this multianion system. ESETD has been previously observed by some of us and others in tr-PES measurements of a wide variety of different organic and inorganic multianions (having both negative and positive electron affinities).<sup>23–25,29–32</sup> For  $\text{Ag}_{29}(\text{BDT})_{12}^{3-}$ , ESETD should give rise to PE spectral features at  $\text{EKE} \leq 1.63$  eV ( $=2.53 - 0.9$  eV), which are not observed. Perhaps, tunneling barriers (also contributed to by the ligands) are so wide that ESETD in this system occurs on much longer time scales that are inaccessible by our tr-PES setup.<sup>33</sup>

To further explore the ultrafast decay implied by the 490 nm one-color PES data, we performed time-resolved pump–probe measurements (490 (2.53 eV pump) and 800 nm (1.55 eV probe)). The results are shown in Figure 4, which plots pump–probe transients (i.e., after subtraction of the pure pump contributions to the corresponding PE spectra). Specifically, we present contour plots of electron signal versus electron kinetic energy as a function of pump–probe delay for three different relative laser polarizations: perpendicular, parallel, and magic angle. Again, the corresponding velocity map images showed no significant anisotropy, that is, all three contour maps show essentially the same time-dependent behavior. Consequently, the transients are not significantly contributed to by rotational dephasing.<sup>34</sup> Note that the free-rotor orientational correlation time of  $\text{Ag}_{29}(\text{BDT})_{12}^{3-}$  at 300 K is expected to be  $\sim 13$  ps based on the DFT-derived ground-state structure.<sup>35</sup> Apparently, excitation anisotropy is not conserved over this time scale.

Two further qualitative observations from the pump–probe measurements are also noteworthy. (i) Consistent with the 490 nm (2.53 eV) one-color PE spectra, we observe ultrafast decay of the initially populated state on an average time scale of less than 100 fs. This is associated with a systematic decrease in EKE during the course of this decay from 3.0 to ca. 2.1 eV (slope of ca. 0.01 eV/fs; see inset in Figure 4a). (ii) Within less than 150 fs after the initial 490 nm excitation, we clearly see a

long-lived state with characteristic EKE of 2.1 eV, which remains populated at probe delay times greater than 100 ps—that is, beyond the delay time range accessible to our experiment. Given the EA(3) determination, this translates to an excitation energy of ca. 1.45 eV ( $2.1 + 0.9 - 1.55$  eV) relative to the trianion ground state. This is roughly consistent with the photoluminescence spectroscopy of  $\text{Ag}_{29}(\text{BDT})_{12}(\text{TPP})_4$  in condensed phase, which shows an NIR emission maximum at ca. 1.61 eV for the room-temperature solid, which has been assigned as phosphorescence on the basis of its greater than microsecond lifetime (see also the Supporting Information). Conceivably, the long-lived pump–probe feature observed in tr-PES can be assigned to detachment from a vibrationally excited triplet state.

The gas-phase absorption spectrum of  $\text{Ag}_{29}(\text{BDT})_{12}^{3-}$  is not (yet) available. However, on the basis of our inference that triplet-state energies are comparable in gaseous and condensed phases we also expect comparable absorption spectra. The solution measurement (see the Supporting Information) in DMF shows an absorption peak at 450 nm and a shoulder at 520 nm. Bakr et al. have performed TDDFT calculations of  $\text{Ag}_{29}(\text{BDT})_{12}(\text{TPP})_4$  in an attempt to assign these features. They come to the conclusion, that there are *nine separate singlet excited states* in this (unscaled) absorption energy range from 1.87 (663 nm) to 2.60 eV (480 nm), all of which have significant charge-transfer character (with corresponding shifts of electron density from shell to core). The systematic temporal decay of EKE from ca. 3.0 to 2.1 eV observed over several hundred femtoseconds following photoexcitation may reflect a cascade of rapid internal conversion (IC) (also involving intramolecular vibrational redistribution) *through several such states*. Note that our tr-PES transients show no clear indication of “mechanical” low-frequency breathing-like vibrational modes (observed in many time-resolved pump–probe transient absorption spectroscopic probes of gold nanoparticles and clusters<sup>36</sup>), which for  $\text{Ag}_{29}(\text{BDT})_{12}^{3-}$  are calculated by DFT to have a period of ca. 400 fs.

We deconvoluted the transient PES measurements using the Glotaran global analysis package<sup>37</sup> assuming sequential decay of the initially excited state through a detectable intermediate to a detectable long-lived final state. This yields rate constants of greater than 10,  $\sim 2$ , and less than  $0.01$  ps<sup>−1</sup>, respectively. The corresponding decay-associated difference spectra are shown in the Supporting Information. Such a sequential decay process would, for example, correspond to population of one

or more singlet excited states, which can rapidly decay ( $>10$  ps $^{-1}$ ) to a “doorway” singlet state (presumably  $S_1$ ) from which intersystem crossing ( $\sim 2$  ps $^{-1}$ ) to the long-lived triplet can occur—as indicated schematically in the Jablonski diagram shown in Figure 5.

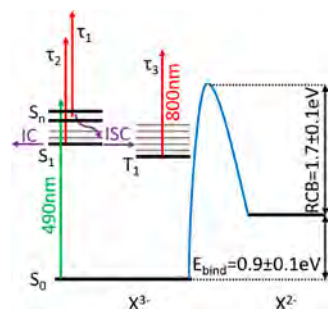


**Figure 5.** Jablonski diagram illustrating the proposed relaxation mechanism. The 490 nm (2.53 eV) irradiation populates a singlet charge transfer state,  $S_n$ , which rapidly relaxes via a cascade of IC steps to  $S_1$  (also involving intramolecular vibrational redistribution). From there, either rapid ISC to a long-lived triplet state ( $T_1$ ), or internal conversion to the vibrationally excited ground state can occur—mediated by charge recombination. Singlet excited states ( $S_1 - S_n$ ) as well as the triplet state  $T_1$  are selectively detected via their characteristic EKE features in the transient pump–probe PES measurements (using 800 nm (1.55 eV) probe photons). For a brief discussion of final state energetics see the [Supporting Information](#).

In the absence of higher-level calculations, we speculate that the triplet state is localized near the “surface” of the cluster. PL in solution can be quenched by  $O_2$  (which is expected to be able to diffuse within the ligand shell).<sup>10</sup> This would imply that the initial excitation involving charge transfer from shell to the cluster core is rapidly followed by charge recombination to yield either a vibrationally hot ground state or a triplet state localized on the cluster shell. Charge recombination induced intersystem crossing is known for coupled organic chromophores photoexcited to a charge transfer state.<sup>38,39</sup> Charge recombination is also thought to mediate ultrafast ISC in certain transition-metal complexes.<sup>23,40–46</sup> However, in such cases the sequential relaxation steps usually invoked following singlet excitation are (symmetry breaking) charge transfer and then charge recombination to either triplet or ground states. For the silver clusters studied here, the initial singlet excitation is already of charge transfer type; no further symmetry breaking step is needed to rationalize the observations.

Previous ultrafast spectroscopy of protected coinage metal clusters—comprising almost exclusively gold clusters—has been confined only to condensed phase. Such studies are subject to environmental effects, which cannot occur in isolation (e.g., quenching of cluster-surface localized excitations by the solvent).<sup>47–49</sup> Here we have for the first time measured what we interpret to be an intrinsic ISC rate for free  $Ag_{29}(BDT)_{12}^{3-}$ . Should ultrafast ISC via charge transfer excitation followed by charge recombination be a common relaxation mechanism for other protected coinage metal clusters in gas-phase, it will be of interest to see how tuning cluster size, overall excess charge, and composition can affect the corresponding triplet quantum yields.

In summary, we have studied the photophysics of isolated  $Ag_{29}(BDT)_{12}^{3-}$  by pump–probe photoelectron spectroscopy. UV excitation (at 490 nm) populates one or more singlet

charge transfer states in which electron density is shifted from silver sulfide moieties on the shell to the silver cluster core. We suggest that the charge transfer states can relax very rapidly (on an overall time scale of several hundred fs) by charge recombination mediated intersystem crossing to yield a long-lived triplet state on the cluster shell.

## ■ ASSOCIATED CONTENT

### Supporting Information

The Supporting Information is available free of charge at <https://pubs.acs.org/doi/10.1021/acs.jpcllett.0c00482>.

Discussion of pump–probe photoelectron spectroscopy, schematic diagram of experimental apparatus, DFT calculations, condensed-phase spectroscopy, electronic absorption spectrum, photoluminescence emission and excitation spectra, global analysis of tr-PES measurements, dianion state energetics (PDF)

## ■ AUTHOR INFORMATION

### Corresponding Author

Aron P. Veenstra — Institute of Physical Chemistry, Karlsruhe Institute of Technology, 76128 Karlsruhe, Germany; [orcid.org/0000-0002-7658-102X](https://orcid.org/0000-0002-7658-102X)

### Authors

Laurenz Monzel — Institute of Physical Chemistry, Karlsruhe Institute of Technology, 76128 Karlsruhe, Germany

Ananya Bakshi — Institute of Nanotechnology, Karlsruhe Institute of Technology, 76344 Eggenstein-Leopoldshafen, Germany; [orcid.org/0000-0003-3328-4399](https://orcid.org/0000-0003-3328-4399)

Joseph Czekner — Institute of Physical Chemistry, Karlsruhe Institute of Technology, 76128 Karlsruhe, Germany; [orcid.org/0000-0002-7013-8334](https://orcid.org/0000-0002-7013-8334)

Sergei Lebedkin — Institute of Nanotechnology, Karlsruhe Institute of Technology, 76344 Eggenstein-Leopoldshafen, Germany

Erik K. Schneider — Institute of Physical Chemistry, Karlsruhe Institute of Technology, 76128 Karlsruhe, Germany

Thalappil Pradeep — DST Unit of Nanoscience and Thematic Unit of Excellence, Indian Institute of Technology Madras, 600036 Chennai, Tamil Nadu, India; [orcid.org/0000-0003-3174-534X](https://orcid.org/0000-0003-3174-534X)

Andreas-Neil Unterreiner — Institute of Physical Chemistry, Karlsruhe Institute of Technology, 76128 Karlsruhe, Germany; [orcid.org/0000-0002-1225-5460](https://orcid.org/0000-0002-1225-5460)

Manfred M. Kappes — Institute of Physical Chemistry, Institute of Nanotechnology, and Institute of Quantum Materials and Technology, Karlsruhe Institute of Technology, 76128 Karlsruhe, Germany; [orcid.org/0000-0002-1199-1730](https://orcid.org/0000-0002-1199-1730)

Complete contact information is available at: <https://pubs.acs.org/doi/10.1021/acs.jpcllett.0c00482>

### Notes

The authors declare no competing financial interest.

## ■ ACKNOWLEDGMENTS

M.K. acknowledges support by the DFG-funded collaborative research center TRR 88 “3MET” (Project C6). M.K. and A.N.U. also thank DFG for funding the femtosecond laser system under INST 121384/133-1FUGG. T.P. thanks the Department of Science and Technology, India, for funding.

J.C. thanks the Alexander von Humboldt Stiftung for additional support with a Postdoctoral Fellowship.

## REFERENCES

- (1) Brust, M.; Walker, M.; Bethell, D.; Schiffrin, D. J.; Whyman, R. Synthesis of Thiol-Derivatized Gold Nanoparticles in a 2-Phase Liquid-Liquid System. *J. Chem. Soc., Chem. Commun.* **1994**, 0 (7), 801–802.
- (2) Chen, S. W.; Ingram, R. S.; Hostetler, M. J.; Pietron, J. J.; Murray, R. W.; Schaaff, T. G.; Khoury, J. T.; Alvarez, M. M.; Whetten, R. L. Gold nanoelectrodes of varied size: Transition to molecule-like charging. *Science* **1998**, 280 (5372), 2098–2101.
- (3) Negishi, Y.; Nobusada, K.; Tsukuda, T. Glutathione-protected gold clusters revisited: Bridging the gap between gold(I)-thiolate complexes and thiolate-protected gold nanocrystals. *J. Am. Chem. Soc.* **2005**, 127 (14), 5261–5270.
- (4) Gautier, C.; Burgi, T. Chiral Gold Nanoparticles. *ChemPhysChem* **2009**, 10 (3), 483–492.
- (5) Natarajan, G.; Mathew, A.; Negishi, Y.; Whetten, R. L.; Pradeep, T. A Unified Framework for Understanding the Structure and Modifications of Atomically Precise Monolayer Protected Gold Clusters. *J. Phys. Chem. C* **2015**, 119 (49), 27768–27785.
- (6) Tlahuice-Flores, A.; Whetten, R. L.; Jose-Yacamán, M. Ligand Effects on the Structure and the Electronic Optical Properties of Anionic  $\text{Au}_{25}(\text{SR})_{18}$  Clusters. *J. Phys. Chem. C* **2013**, 117 (40), 20867–20875.
- (7) Walter, M.; Akola, J.; Lopez-Acevedo, O.; Jadzinsky, P. D.; Calero, G.; Ackerson, C. J.; Whetten, R. L.; Gronbeck, H.; Hakkinen, H. A unified view of ligand-protected gold clusters as superatom complexes. *Proc. Natl. Acad. Sci. U. S. A.* **2008**, 105 (27), 9157–9162.
- (8) Chakraborty, A.; Fernandez, A. C.; Som, A.; Mondal, B.; Natarajan, G.; Paramasivam, G.; Lahtinen, T.; Hakkinen, H.; Nonappa, Pradeep, T. Atomically Precise Nanocluster Assemblies Encapsulating Plasmonic Gold Nanorods. *Angew. Chem., Int. Ed.* **2018**, 57 (22), 6522–6526.
- (9) Chakraborty, P.; Nag, A.; Paramasivam, G.; Natarajan, G.; Pradeep, T. Fullerene-Functionalized Monolayer-Protected Silver Clusters:  $[\text{Ag}_{29}(\text{BDT})_{12}(\text{C}_{60})_n]^{3-}$  ( $n = 1-9$ ). *ACS Nano* **2018**, 12 (3), 2415–2425.
- (10) Khatun, E.; Ghosh, A.; Chakraborty, P.; Singh, P.; Boduazzaman, M.; Ganesan, P.; Natarajan, G.; Ghosh, J.; Pal, S. K.; Pradeep, T. A thirty-fold photoluminescence enhancement induced by secondary ligands in monolayer protected silver clusters. *Nanoscale* **2018**, 10 (42), 20033–20042.
- (11) Zhang, B.; Garcia, C.; Sels, A.; Salassa, G.; Rameshan, C.; Llorca, J.; Hradil, K.; Rupprechter, G.; Barrabes, N.; Burgi, T. Ligand and support effects on the reactivity and stability of  $\text{Au}_{38}(\text{SR})_{24}$  catalysts in oxidation reactions. *Catal. Commun.* **2019**, 130, 105768.
- (12) Hirata, K.; Tomihara, R.; Kim, K.; Koyasu, K.; Tsukuda, T. Characterization of chemically modified gold and silver clusters in gas phase. *Phys. Chem. Chem. Phys.* **2019**, 21 (32), 17463–17474.
- (13) Kim, K.; Hirata, K.; Nakamura, K.; Kitazawa, H.; Hayashi, S.; Koyasu, K.; Tsukuda, T. Elucidating the Doping Effect on the Electronic Structure of Thiolate-Protected Silver Superatoms by Photoelectron Spectroscopy. *Angew. Chem., Int. Ed.* **2019**, 58 (34), 11637–11641.
- (14) Jin, R. C.; Zeng, C. J.; Zhou, M.; Chen, Y. X. Atomically Precise Colloidal Metal Nanoclusters and Nanoparticles: Fundamentals and Opportunities. *Chem. Rev.* **2016**, 116 (18), 10346–10413.
- (15) Bakshi, A.; Schneider, E. K.; Weis, P.; Krishnadas, K. R.; Ghosh, D.; Hahn, H.; Pradeep, T.; Kappes, M. M. Nanogymnastics: Visualization of Intercluster Reactions by High-Resolution Trapped Ion Mobility Mass Spectrometry. *J. Phys. Chem. C* **2019**, 123 (46), 28477–28485.
- (16) Yang, H. Y.; Wang, Y.; Chen, X.; Zhao, X. J.; Gu, L.; Huang, H. Q.; Yan, J. Z.; Xu, C. F.; Li, G.; Wu, J. C.; Edwards, A. J.; Dittrich, B.; Tang, Z. C.; Wang, D. D.; Lehtovaara, L.; Hakkinen, H.; Zheng, N. F. Plasmonic twinned silver nanoparticles with molecular precision. *Nat. Commun.* **2016**, 7. DOI: 10.1038/ncomms12809
- (17) AbdulHalim, L. G.; Bootharaju, M. S.; Tang, Q.; Del Gobbo, S.; AbdulHalim, R. G.; Eddaoudi, M.; Jiang, D. E.; Bakr, O. M.  $\text{Ag}_{29}(\text{BDT})_{12}(\text{TPP})_4$ : A Tetravalent Nanocluster. *J. Am. Chem. Soc.* **2015**, 137 (37), 11970–11975.
- (18) Aly, S. M.; AbdulHalim, L. G.; Besong, T. M. D.; Soldan, G.; Bakr, O. M.; Mohammed, O. F. Ultrafast static and diffusion-controlled electron transfer at  $\text{Ag}_{29}$  nanocluster/molecular acceptor interfaces. *Nanoscale* **2016**, 8 (10), 5412–5416.
- (19) Soldan, G.; Aljuhani, M. A.; Bootharaju, M. S.; AbdulHalim, L. G.; Parida, M. R.; Emwas, A. H.; Mohammed, O. F.; Bakr, O. M. Gold Doping of Silver Nanoclusters: A 26-Fold Enhancement in the Luminescence Quantum Yield. *Angew. Chem., Int. Ed.* **2016**, 55 (19), 5749–5753.
- (20) Hirata, K.; Kim, K.; Nakamura, K.; Kitazawa, H.; Hayashi, S.; Koyasu, K.; Tsukuda, T. Photoinduced Thermionic Emission from  $[\text{M}_{25}(\text{SR})_{18}]^{-}$  ( $\text{M} = \text{Au}, \text{Ag}$ ) Revealed by Anion Photoelectron Spectroscopy. *J. Phys. Chem. C* **2019**, 123 (20), 13174–13179.
- (21) Hirata, K.; Yamashita, K.; Muramatsu, S.; Takano, S.; Ohshimo, K.; Azuma, T.; Nakanishi, R.; Nagata, T.; Yamazoe, S.; Koyasu, K.; Tsukuda, T. Anion photoelectron spectroscopy of free  $[\text{Au}_{25}(\text{SC}_{12}\text{H}_{25})_{18}]^{-}$ . *Nanoscale* **2017**, 9 (36), 13409–13412.
- (22) Bakshi, A.; Ghosh, A.; Mudedla, S. K.; Chakraborty, P.; Bhat, S.; Mondal, B.; Krishnadas, K. R.; Subramanian, V.; Pradeep, T. Isomerism in Monolayer Protected Silver Cluster Ions: An Ion Mobility-Mass Spectrometry Approach. *J. Phys. Chem. C* **2017**, 121 (24), 13421–13427.
- (23) Winghart, M. O.; Yang, J. P.; Vonderach, M.; Unterreiner, A. N.; Huang, D. L.; Wang, L. S.; Kruppa, S.; Riehn, C.; Kappes, M. M. Time-resolved photoelectron spectroscopy of a dinuclear  $\text{Pt}(\text{II})$  complex: Tunneling autodetachment from both singlet and triplet excited states of a molecular dianion. *J. Chem. Phys.* **2016**, 144 (5), 054305.
- (24) Winghart, M. O.; Yang, J. P.; Kuhn, M.; Unterreiner, A. N.; Wolf, T. J. A.; Dau, P. D.; Liu, H. T.; Huang, D. L.; Kloppe, W.; Wang, L. S.; Kappes, M. M. Electron tunneling from electronically excited states of isolated bisdisulizole-derived trianion chromophores following UV absorption. *Phys. Chem. Chem. Phys.* **2013**, 15 (18), 6726–6736.
- (25) Dau, P. D.; Liu, H. T.; Yang, J. P.; Winghart, M. O.; Wolf, T. J. A.; Unterreiner, A. N.; Weis, P.; Miao, Y. R.; Ning, C. G.; Kappes, M. M.; Wang, L. S. Resonant tunneling through the repulsive Coulomb barrier of a quadruply charged molecular anion. *Phys. Rev. A: At., Mol., Opt. Phys.* **2012**, 85 (6). DOI: 10.1103/PhysRevA.85.064503
- (26) Eppink, A. T. J. B.; Parker, D. H. Velocity map imaging of ions and electrons using electrostatic lenses: Application in photoelectron and photofragment ion imaging of molecular oxygen. *Rev. Sci. Instrum.* **1997**, 68 (9), 3477–3484.
- (27) Roberts, G. M.; Nixon, J. L.; Lecointre, J.; Wrede, E.; Verlet, J. R. R. Toward real-time charged-particle image reconstruction using polar onion-peeling. *Rev. Sci. Instrum.* **2009**, 80 (5), 053104.
- (28) Stoermer, C.; Friedrich, J.; Kappes, M. M. Observation of multiply charged cluster anions upon pulsed UV laser ablation of metal surfaces under high vacuum. *Int. J. Mass Spectrom.* **2001**, 206 (1–2), 63–78.
- (29) Ehrler, O. T.; Yang, J. P.; Sugiharto, A. B.; Unterreiner, A. N.; Kappes, M. M. Excited state dynamics of metastable phthalocyanine-tetrasulfonate tetra-anions probed by pump/probe photoelectron spectroscopy. *J. Chem. Phys.* **2007**, 127 (18), 184301.
- (30) Verlet, J. R. R.; Horke, D. A.; Chatterley, A. S. Excited states of multiply-charged anions probed by photoelectron imaging: riding the repulsive Coulomb barrier. *Phys. Chem. Chem. Phys.* **2014**, 16 (29), 15043–15052.
- (31) Horke, D. A.; Chatterley, A. S.; Verlet, J. R. R. Effect of Internal Energy on the Repulsive Coulomb Barrier of Polyanions. *Phys. Rev. Lett.* **2012**, 108 (8). DOI: 10.1103/PhysRevLett.108.083003
- (32) Horke, D. A.; Chatterley, A. S.; Verlet, J. R. R. Femtosecond Photoelectron Imaging of Aligned Polyanions: Probing Molecular Dynamics through the Electron-Anion Coulomb Repulsion. *J. Phys. Chem. Lett.* **2012**, 3 (7), 834–838.



- (33) Jager, P.; Brendle, K.; Schwarz, U.; Himmelsbach, M.; Armbruster, M. K.; Fink, K.; Weis, P.; Kappes, M. M. Q and Soret Band Photoexcitation of Isolated Palladium Porphyrin Tetraanions Leads to Delayed Emission of Nonthermal Electrons over Microsecond Time Scales. *J. Phys. Chem. Lett.* **2016**, *7* (7), 1167–1172.
- (34) Horke, D. A.; Chatterley, A. S.; Bull, J. N.; Verlet, J. R. R. Time-Resolved Photodetachment Anisotropy: Gas-Phase Rotational and Vibrational Dynamics of the Fluorescein Anion. *J. Phys. Chem. Lett.* **2015**, *6* (1), 189–194.
- (35) Schalk, O.; Unterreiner, A. N. The influence of rotational diffusion on transient anisotropy in ultrafast experiments. *Phys. Chem. Chem. Phys.* **2010**, *12* (3), 655–666.
- (36) Jung, Y.; Shen, J.; Liu, Y. H.; Woods, J. M.; Sun, Y.; Cha, J. J. Metal Seed Layer Thickness-Induced Transition From Vertical to Horizontal Growth of MoS<sub>2</sub> and WS<sub>2</sub>. *Nano Lett.* **2014**, *14* (12), 6842–6849.
- (37) Snellenburg, J. J.; Liptonok, S. P.; Seger, R.; Mullen, K. M.; van Stokkum, I. H. M. Glotaran: A Java-Based Graphical User Interface for the R Package TIMP. *J. Stat. Softw.* **2012**, *49* (3), 1–22.
- (38) Wiederrecht, G. P.; Svec, W. A.; Wasielewski, M. R.; Galili, T.; Levanon, H. Novel mechanism for triplet state formation in short distance covalently linked radical ion pairs. *J. Am. Chem. Soc.* **2000**, *122* (40), 9715–9722.
- (39) Hou, Y. Q.; Biskup, T.; Rein, S.; Wang, Z. J.; Bussotti, L.; Russo, N.; Foggi, P.; Zhao, J. Z.; Di Donato, M.; Mazzone, G.; Weber, S. Spin-Orbit Charge Recombination Intersystem Crossing in Phenothiazine-Anthracene Compact Dyads: Effect of Molecular Conformation on Electronic Coupling, Electronic Transitions, and Electron Spin Polarizations of the Triplet States. *J. Phys. Chem. C* **2018**, *122* (49), 27850–27865.
- (40) Ha-Thi, M. H.; Shafizadeh, N.; Poisson, L.; Soep, B. An Efficient Indirect Mechanism for the Ultrafast Intersystem Crossing in Copper Porphyrins. *J. Phys. Chem. A* **2013**, *117* (34), 8111–8118.
- (41) Trinh, C.; Kirlikovali, K.; Das, S.; Ener, M. E.; Gray, H. B.; Djurovich, P.; Bradforth, S. E.; Thompson, M. E. Symmetry-Breaking Charge Transfer of Visible Light Absorbing Systems: Zinc Dipyrrins. *J. Phys. Chem. C* **2014**, *118* (38), 21834–21845.
- (42) Pomarico, E.; Pospisil, P.; Bouduban, M. E. F.; Vestfrid, J.; Gross, Z.; Zalis, S.; Chergui, M.; Vlcek, A. Photophysical Heavy-Atom Effect in Iodinated Metalloporphyrins: Spin-Orbit Coupling and Density of States. *J. Phys. Chem. A* **2018**, *122* (37), 7256–7266.
- (43) Frei, F.; Rondi, A.; Espa, D.; Mercuri, M. L.; Pilia, L.; Serpe, A.; Odeh, A.; Van Mourik, F.; Chergui, M.; Feurer, T.; Deplano, P.; Vlcek, A.; Cannizzo, A. Ultrafast electronic and vibrational relaxations in mixed-ligand dithione-dithiolato Ni, Pd, and Pt complexes. *Dalton T* **2014**, *43* (47), 17666–17676.
- (44) Chergui, M. On the interplay between charge, spin and structural dynamics in transition metal complexes. *Dalton T* **2012**, *41* (42), 13022–13029.
- (45) El Nahhas, A.; Consani, C.; Blanco-Rodriguez, A. M.; Lancaster, K. M.; Braem, O.; Cannizzo, A.; Towrie, M.; Clark, I. P.; Zalis, S.; Chergui, M.; Vlcek, A. Ultrafast Excited-State Dynamics of Rhenium(I) Photosensitizers [Re(Cl)(CO)<sub>3</sub>(N, N)] and [Re(imidazole)(CO)<sub>3</sub>(N, N)]<sup>+</sup>: Diimine Effects. *Inorg. Chem.* **2011**, *50* (7), 2932–2943.
- (46) Cannizzo, A.; Blanco-Rodriguez, A. M.; El Nahhas, A.; Sebera, J.; Zalis, S.; Vlcek, A.; Chergui, M. Femtosecond fluorescence and intersystem crossing in Rhenium(I) Carbonyl-Bipyridine Complexes. *J. Am. Chem. Soc.* **2008**, *130* (28), 8967–8974.
- (47) Zhou, M.; Higaki, T.; Li, Y. W.; Zeng, C. J.; Li, Q.; Sfeir, M. Y.; Jin, R. C. Three-Stage Evolution from Non-scalable to Scalable Optical Properties of Thiolate-Protected Gold Nanoclusters. *J. Am. Chem. Soc.* **2019**, *141* (50), 19754–19764.
- (48) Hartland, G. V. Optical Studies of Dynamics in Noble Metal Nanostructures. *Chem. Rev.* **2011**, *111* (6), 3858–3887.
- (49) Jin, R. C.; Cao, Y. C.; Hao, E. C.; Metraux, G. S.; Schatz, G. C.; Mirkin, C. A. Controlling anisotropic nanoparticle growth through plasmon excitation. *Nature* **2003**, *425* (6957), 487–490.

## Supporting Information

### Ultrafast Intersystem Crossing in Isolated $\text{Ag}_{29}(\text{BDT})_{12}^{3-}$ Probed by Time-Resolved Pump-Probe Photoelectron Spectroscopy

Aron P. Veenstra<sup>a</sup>, Laurenz Monzel<sup>a</sup>, Ananya Baksi<sup>b</sup>, Joseph Czekner<sup>a</sup>, Sergei Lebedkin<sup>b</sup>, Erik K. Schneider, Thalappil Pradeep<sup>d</sup>, Andreas-Neil Unterreiner<sup>a</sup> and Manfred M. Kappes<sup>a,b,c</sup>

<sup>a</sup>Institute of Physical Chemistry (IPC), KIT, 76131 Karlsruhe, Germany

<sup>b</sup>Institute of Nanotechnology (INT), KIT, 76344 Eggenstein-Leopoldshafen, Germany

<sup>c</sup>Institute of Quantum Materials and Technology (IQMT), KIT, 76344 Eggenstein-Leopoldshafen, Karlsruhe, Germany

<sup>d</sup>DST Unit of Nanoscience and Thematic Unit of Excellence, Indian Institute of Technology Madras, Chennai, Tamil Nadu 600036, India

- A. Details of experimental methods: pump-probe photoelectron spectroscopy
- B. DFT Calculations
- C. Condensed phase spectroscopy of  $\text{Ag}_{29}(\text{BDT})_{12}(\text{TPP})_4$
- D. Glotoran global analysis of tr-PES measurements
- E. Final (dianion) state energetics

## **A. Details of Experimental Methods: Pump-Probe Photoelectron Spectroscopy**

A schematic of the setup used is shown in figure S1. Ions were generated with a nano-ESI source. The glass needles used were 5 cm long with a tip diameter of a few  $\mu\text{m}$  and a capacity of ca. 50  $\mu\text{l}$ . The spray voltage was between 7 and 8 kV. Ions were transferred through a 20 cm long and resistively heated capillary into the first vacuum chamber with a pressure of 1 mbar. There the ions are focused and guided to the TOF mass spectrometer with an ion funnel. The last electrode of the funnel was pulsed with a higher potential to trap and accumulate ions before being released into the TOF mass spectrometer. Ions were then accelerated to 4 kV by pulsed Wiley-McLaren acceleration grids (1 kHz, 15  $\mu\text{s}$ ) into a 3 m long flight tube and then detected with an MCP. The mass spectrometer has a mass resolution of 200  $m/\Delta m$ . The ion beam is collimated with Einzel lenses and steered with deflection plates immediately after the acceleration region.

The perpendicularly oriented VMI photoelectron spectrometer is located 15 cm before the TOF ion detector. Three acceleration electrodes made of 1 mm thick stainless steel plates and a diameter of 7.75 cm are arranged in an Eppink-Parker like setup. They are mounted on insulating ceramic rods and separated by 12.7 mm with ceramic spacers. To avoid deflecting the ions prior to photodetachment, the voltages of the VMI setup (-5 kV for the repeller and -3.45 kV for the extractor at 1 kHz) were only applied for 200 ns coinciding with the interaction of the laser with the ions. The photoelectron cloud is accelerated through holes in the extractor and ground plate, 15 mm and 20 mm respectively towards the detector through the 60 cm long electron flight tube. The detector is composed of a position sensitive MCP, phosphor screen and CCD camera. The impact of an electron is then recorded by a high resolution CCD-camera with a repetition rate of 32 Hz. Thus ca. 31 laser shots are recorded in 1 image. For reconstruction of the convoluted image, a polar onion peeling algorithm from the Verlet-group is used.

The femtosecond laser system used (Astrella, Coherent) operates at 1 kHz and provides 34 fs pulses with 7 mJ pulse energies at 800 nm. UV and 490 nm pulses were generated by a TOPAS Prime (Light conversion). The TOPAS is pumped with 800 nm (3 mJ) and generates an output energy of 100  $\mu\text{J}$  at 490 nm and ca. 10  $\mu\text{J}$  in the UV-region. All pulses enter the spectrometer unfocused with a beam diameter of ca. 6 mm through a 3 mm thick  $\text{CaF}_2$ -window.

For the pump-probe experiment the 490 nm laser beam (100  $\mu\text{J}$ ) was aligned collinearly with the fundamental 800 nm beam (400  $\mu\text{J}$ ) by a dichroic combiner mirror. The variable delay times were realized by a computer controlled delay stage. The 490 nm radiation was perpendicularly polarized relative to the ion beam direction. To change the polarization between pump and probe pulse, a  $\lambda/2$  waveplate (800 nm, mica, B. Halle Nachfl. GmbH) was used. For the power dependency, measurements the laser intensity was controlled by a 1 mm thick variable metallic neutral density filter.

Both, pump and probe pulses, are assumed to have a Gaussian beam shape with a diameter of 6 mm. The ions are focused by an Einzel lens through a 5 mm hole into the VMI setup. Thus, the laser beam is slightly bigger than the ion cloud. The laser is aligned to get maximal electron signal.

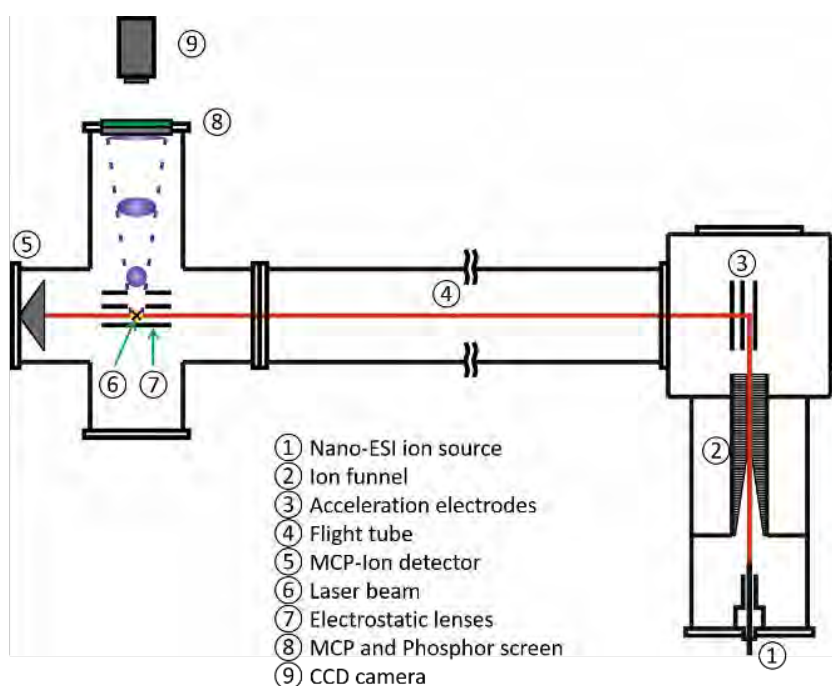


**Figure S1.** Schematic diagram (not to scale) of the apparatus used in the current experiments

## B. DFT Calculations

$\text{Ag}_{29}(\text{BDT})_{12}^{3-}$  geometries were obtained from DFT calculations with the BP-86 functional and the def-SV(P) basis set as implemented in the TURBOMOLE package.<sup>50</sup> We used the experimental geometry (X-ray structure) of  $\text{Ag}_{29}(\text{BDT})_{12}(\text{TPP})_4$  as the starting point and removed the four TPP neutral phosphine ligands to obtain a  $\text{Ag}_{29}(\text{BDT})_{12}^{3-}$  structure which was taken as the starting for geometry optimization without any symmetry restrictions.

### C. Condensed phase spectroscopy of $\text{Ag}_{29}(\text{BDT})_{12}(\text{TPP})_4$

(a) The electronic absorption spectrum in DMF solution was taken using a Varian Cary 500 UV-Vis-NIR spectrophotometer at room temperature. The spectrum was measured in the range of 250-800 nm with 1 nm resolution.

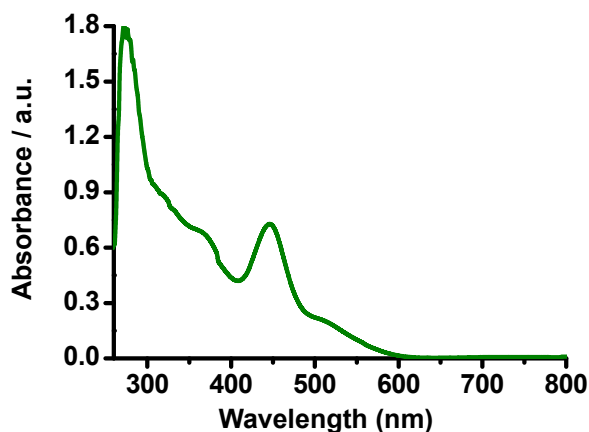


**Figure S2.** Electronic absorption spectrum of  $\text{Ag}_{29}(\text{BDT})_{12}(\text{TPP})_4$  in DMF solution

(b) Photoluminescence measurements were performed on a Horiba Jobin Yvon Fluorolog-322 spectrometer equipped with a closed-cycle optical cryostat operating within a temperature range of 15-300 K. A Hamamatsu R9910 photomultiplier was used as detector for the emission spectral range of ~300-850 nm. All emission spectra were corrected for the wavelength-dependent response of the spectrometer and detector (in relative photon flux units). A solid sample (crystalline powder) of  $\text{Ag}_{29}(\text{BDT})_{12}(\text{TPP})_4$  was measured dispersed in a thin layer of viscous perfluorocarbon oil between two 1 mm quartz plates. This sample holder was mounted on the cold finger of the cryostat. PL decay traces were recorded by connecting the photomultiplier to a 500 MHz LeCroy LT322 oscilloscope (via a 50 or 500  $\Omega$  load depending on the decay time scale) and using a nitrogen laser (~2 ns, ~5  $\mu\text{J}$  per pulse) for pulsed excitation at 337 nm. The PL quantum yield of crystalline  $\text{Ag}_{29}(\text{BDT})_{12}(\text{TPP})_4$  at ambient temperature was determined using an integrating sphere which was installed into the sample chamber of the spectrometer. The uncertainty of this measurement was estimated to be  $\pm 10\%$ .

Figure S3 shows PL emission and excitation (PLE) spectra of  $\text{Ag}_{29}(\text{BDT})_{12}(\text{TPP})_4$  in a DMF solution (saturated with argon gas) and in the solid state. In room temperature DMF, the cluster emits relatively weak PL with a maximum at ca. 670 nm (1.85 eV) and a lifetime of 70 ns. In contrast, the solid compound demonstrates a bright, broad NIR emission at ca. 770 nm (1.61 eV) with a quantum yield of 11 % (excitation at 450 nm). At low temperatures, the emission band shifts to ca. 740 nm (1.68 eV) and increases in efficiency up to 40 % as estimated from the temperature-dependent PL spectra (Figure S3). The PL decay of solid  $\text{Ag}_{29}(\text{BDT})_{12}(\text{TPP})_4$  follows biexponential curves with the following times and relative weights:  $\tau_1 = 31 \mu\text{s}$  (45%) and  $\tau_2 = 130$

$\mu\text{s}$  (55%) at  $T = 17\text{ K}$  and  $\tau_1 = 1.0\text{ }\mu\text{s}$  (57%) and  $\tau_2 = 5.3\text{ }\mu\text{s}$  (43%) at  $T = 295\text{ K}$ . The relatively slow decay clearly indicates that the emission of the silver cluster is phosphorescence.

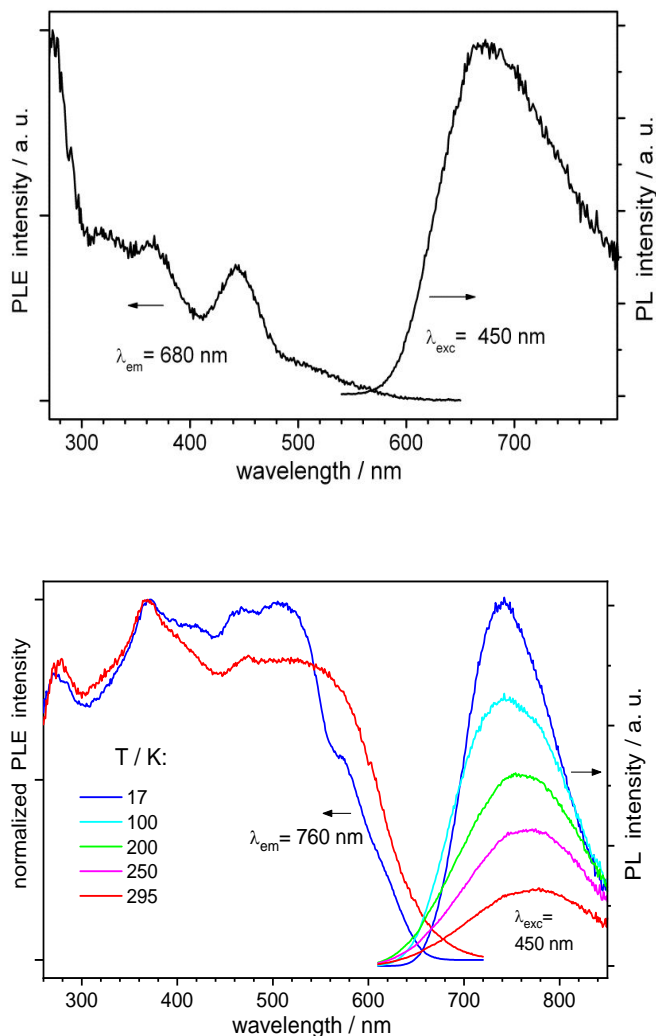


**Figure S3.** Photoluminescence emission (PL) and excitation (PLE) spectra for  $\text{Ag}_{29}(\text{BDT})_{12}(\text{TPP})_4$  dissolved in DMF and measured at room temperature and as a solid (polycrystalline) sample at various temperatures between 17 and 295 K (top and bottom panels, respectively). Note, that at room temperature for an excitation wavelength of 450 nm, the maximum of the solid photoluminescence spectrum is observed at ca. 770 nm (1.61 eV) whereas in DMF solution it is seen at ca. 670 nm. By comparison, Bakr et al.<sup>17</sup> report an emission maximum of 670 nm (1.85 eV) in solution and at 715 nm (1.73 eV) for the solid – both measurements presumably carried out at room temperature.



#### D. Glotaran global analysis of tr-PES measurements

Glotaran (**G**lobal and **t**arget **a**nalysis) is a software package specially designed for analysis of data obtained by time-resolved spectroscopy. It allows users to analyze the whole data set at once with a user-given kinetic model, i.e. a series of sequential decays or parallel decays. The model used here is a Gaussian type instrument response function (IRF) and a sequence of three exponential decays corresponding to the observable states: (i) the first excited CT-states; (ii) the “doorway” state for ISC; (iii) the long-living triplet-state.

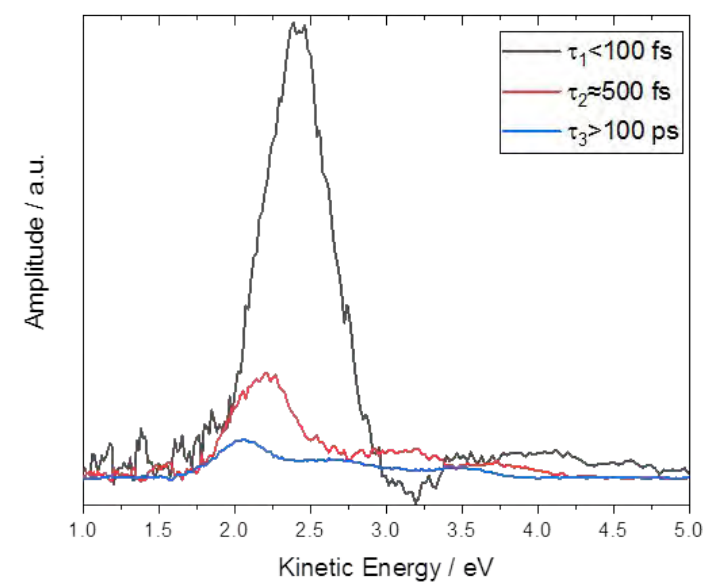


**Figure S4.** Glotaran global analysis of the 490 /800 nm pump-probe transient measurements (parallel polarization) shown in the contour plot of Fig. 4. The analysis assumes sequential kinetics: fast decay to an intermediate state followed by fast decay to a long lived state. This results in best fitting unimolecular decay rates of  $>10$ ,  $\sim 2$  and  $<0.01$  ps $^{-1}$  respectively. Shown are resulting decay associated difference spectra which correspond roughly to the PE spectra of the initially populated (black), the intermediate (red) and the long-lived state (blue) which we assign as a triplet.

### **E. Final (dianion) state energetics**

The one-color measurements of Figure 3 indicate that interaction with two photons (490 nm, 2.53 eV) leads to two resolvable detachment features. The higher EKE singlet detachment feature at 3.41 eV implies that ca. 0.65 eV of excess energy ( $2 \times 2.53 - 1 - 3.41 = 0.65$  eV) must be going into final state vibrational excitation. We have rationalized the lower EKE feature at 2.66 eV as corresponding to triplet detachment within the same laser pulse, i.e, a comparable inelasticity of ca. 0.4 eV must pertain ( $1.53 + 2.53 - 1 - 2.66 = 0.4$  eV). Note further, that in the one-color measurement the triplet feature is significantly more intense than the singlet component. By contrast, the triplet is much weaker than the singlet signal in the pump-probe measurement. Presumably, this reflects the RCB barrier height which at  $2.6 \pm 0.2$  eV (as measured from the trianion ground state) is comparable to the sum of triplet state and probe pulse energies ( $1.53 + 1.55 = 3.06$  eV). Therefore, the relative triplet detachment cross section is expected to be much higher at the 490 nm pump photon wavelength.



# Association of co-accumulation of arsenic and organophosphate insecticides with diabetes and atherosclerosis in a rural agricultural community: KMCH-NNCD-I study

Ganesan Velmurugan<sup>1,2</sup> · Krishnan Swaminathan<sup>1,2</sup> · Sundaresan Mohanraj<sup>2</sup> · Mani Dhivakar<sup>1</sup> · Ganesh Veerasekar<sup>2</sup> · Thomas Alexander<sup>2</sup> · Mathew Cherian<sup>2</sup> · Nalla G. Palaniswami<sup>2</sup> · Thalappil Pradeep<sup>1</sup>

Received: 15 November 2019 / Accepted: 10 March 2020  
© Springer-Verlag Italia S.r.l., part of Springer Nature 2020

## Abstract

**Aims** In last few decades, the prevalence of diabetes and vascular diseases has intensified concurrently with increased use of synthetic chemicals in agriculture. This study is aimed to evaluate the association of co-accumulation of arsenic and organophosphate (OP) insecticides with diabetes and atherosclerosis prevalence in a rural Indian population.

**Methods** This study included observations from KMCH-NNCD-I (2015) cross-sectional study ( $n = 865$ ) from an Indian farming village. The participants had assessment of clinical parameters including HbA<sub>1c</sub> and carotid intima-media thickness and urinary heavy metals. Serum OP residues were extracted and quantified by GC-MS. Statistical analyses were performed to unravel the co-association of arsenic and OPs on prevalence of diabetes and atherosclerosis.

**Results** On multivariate regression analyses, total organophosphate level and arsenic accumulation showed association with diabetes and atherosclerosis. Higher odds ratio with significant trends were observed for the sub-quartiles formed by the combination of higher quartiles of arsenic and total organophosphates in association with diabetes and atherosclerosis.

**Conclusions** We observed evidence of possible synergism between arsenic and OPs in association with prevalence of diabetes, pre-diabetes and atherosclerosis in the study population. Our findings highlight the importance of understanding health effects of mixed exposures and raises vital questions on the role of these agrochemicals in the etiology of diabetes and vascular diseases.

**Keywords** Rural health · Organophosphates · Arsenic · Endocrine-disrupting chemicals · Diabetes · Atherosclerosis

---

Managed by Massimo Federici.

---

Ganesan Velmurugan and Krishnan Swaminathan have contributed equally to this work.

---

**Electronic supplementary material** The online version of this article (<https://doi.org/10.1007/s00592-020-01516-6>) contains supplementary material, which is available to authorized users.

---

✉ Ganesan Velmurugan  
vel@kmchr.org

✉ Thalappil Pradeep  
pradeep@iitm.ac.in

<sup>1</sup> DST Unit of Nanoscience and Thematic Unit of Excellence in Water Research, Department of Chemistry, Indian Institute of Technology, Chennai, Tamil Nadu 600 036, India

<sup>2</sup> Chemomicrobiomics Laboratory, KMCH Research Foundation, Kovai Medical Centre and Hospital, Coimbatore, Tamil Nadu 641 014, India

## Abbreviations

As	Arsenic
AsQ	Quartiles based on arsenic values
CIMT	Carotid intima-media thickness
EDC	Endocrine disrupting chemicals
HbA <sub>1c</sub>	Glycated hemoglobin
LOD	Limit of detection
LOQ	Limit of quantification
OP	Organophosphates
OPQ	Quartiles based on total organophosphate levels

## Introduction

The prevalence of diabetes has increased alarmingly and today represents one of the largest global health emergencies of the twenty-first century. Diabetes confers a twofold increased risk of a wide range of vascular diseases including myocardial infarction and stroke. As per WHO estimation

[1], the prevalence of diabetes has increased from 4.7% (108 million adults) in 1980 to 8.5% (422 million adults) in 2014. This sudden increase in diabetes rate was higher particularly in middle- and low-income countries and the rural world [2]. South Asia, specifically India houses 15.3% of global diabetic population and frequently referred as the diabetic capital of the world. It is an interesting corollary that though India witnessed adoubling in diabetes rate during 1980–2014, there was no significant increase in the incidence of traditional risk factors like obesity, hypertension, hypercholesterolemia and smoking during the same period [2]. On the other hand, this same period witnessed a massive production and release of toxic chemicals into environment, which are potent endocrine-disrupting chemicals (EDC) [2, 3]. There is now a growing body of evidence for the role of environmental chemicals in the etiology of diabetes [2, 3] and vascular diseases [4, 5].

We noticed increasing number of farmers with minimal traditional risk factors around our catchment areas seeking medical management for diabetes and vascular diseases. In our KMCH-NNCD-I (2015) cross-sectional study, executed in Nallampatti, a farming village in South India, we observed 42%, 16.2% and 10.3% prevalence of pre-diabetes (as per ADA criteria), diabetes and atherosclerosis [6]. There was no association of traditional risk factors with diabetes in this rural population, Velmurugan et al. [7] indicating the probable role of non-traditional risk factors particularly environmental chemicals. The major source of environmental chemicals in a farming village are chemicals (synthetic fertilizers and pesticides) used for agriculture. The phosphate fertilizers are a rich source of heavy metals including arsenic. Urine heavy metal analyses in this population suggested a significant association between arsenic and prevalence of pre-diabetes, diabetes and atherosclerosis [7].

The other important EDC in rural environment are insecticides used for pest control. Organophosphates (OPs) are the largely used group of insecticides in the world, accounting for more than 40% of insecticide usage. Our interest in the role of OPs and diabetes was sparked by a case of insecticide poisoning in a 15-year-old girl masquerading as diabetic ketoacidosis [8]. Studies done by our study group raised vital questions on this intriguing link between OPs and human diabetes in rural India [8–10]. Except for a few, all studies focused on a single environmental chemical that does not reflect the real-world scenario where humans are exposed to multiple chemicals. Therefore, the aim of this study is to understand the combined effect of co-accumulation of arsenic and OP insecticides on prevalence of pre-diabetes, diabetes and atherosclerosis among the participants of KMCH-NNCD-I study performed in rural India.

## Materials and methods

### Chemicals

All the organophosphate insecticides used are of analytical pure grade purchased from Sigma-Aldrich Inc., (PEST-NAL). The solvents used were of chromatographic grade. Glassware was cleaned thoroughly with aqua regia (HCl/HNO<sub>3</sub>, 3:1 vol%), rinsed with distilled water, and dried in oven prior to use. Deionized water was used throughout the experiments.

### Study population

KMCH-NNCD-I is a cross-sectional study designed to be representative of farming rural population in South India. The study was performed in Nallampatti, an agricultural village in South India (latitude: 11°21'2.39" N; longitude: 77°32'4.79" E; Figure S1) during March–April 2015. The details of this study have been described previously [6]. Inclusion criteria included all those native to the village and ≥ 20 and ≤ 85 years of age. Pregnant ladies, people outside of this age criteria and those not native to Nallampatti were excluded. The study design and protocol were approved by KMCH Ethics Committee, Kovai Medical Center and Hospital Limited, Coimbatore (Approval no EC/AP/02/2015 dated 16 February 2015).

### Data retrieval

All the demographic, clinical and heavy metal data of the 865 participants of KMCH—Nallampatti non-communicable disease—I (NNCD-I) study were retrieved from our database and used for the study. The variables included basic demographic details, life style, disease history, medications, body weight, height, waist circumference, blood pressure and carotid intima-media thickness (CIMT). CIMT was measured using two high resolution B-mode ultrasound machines (GE Healthcare, Venue 40, USA). Blood investigations included a random glucose (Hexokinase/GOD-POD/endpoint method), HbA<sub>1c</sub> (Automated HPLC method), cystatin-c (Nephelometric method-BN Prospec), non-fasting lipid profile, uric acid (Uricase Endpoint method) and hemoglobin (SLS method). Fasting and post-meal glucose were not considered due to logistical issues. Urinary arsenic was determined by ICP-MS (NHANES, 2011–2012) and normalized to urinary creatinine level and expressed as µg/mg creatinine [7].

## Diabetes and atherosclerosis

People with glycated hemoglobin (HbA<sub>1c</sub>) of  $\geq 6.5\%$  or under diabetic medications were considered as diabetic. People with no history of diabetes and HbA<sub>1c</sub> ranging between 5.7 and 6.4% were defined as pre-diabetic as per American Diabetic Association guidelines (2017). People with CIMT  $\geq 1$  mm in either left or right arteries were considered atherosclerosis [7, 11].

## Survey on use of insecticides

A survey on name, type and frequency of insecticides being used was conducted among the insecticide sellers, insecticide applicators and land owners in Nallampatti and other villages within five kilometers circumference of study village. Based on this survey, the insecticides were selected for the study.

## Standards calibration

Primary stock solutions of each insecticide (1 mg/l) were prepared in methanol. Working standard solutions of the compounds were prepared by combining the aliquots of each primary solution and diluting with hexane. The stock solutions were stored at  $-20^{\circ}\text{C}$  in the dark when not in use.

## Sample preparation

Serum samples were extracted by dispersive liquid–liquid microextraction technique [10] for insecticide assay. The extraction method was optimized for extraction solvent, dispersive solvent, its volume and pH. Briefly, 200  $\mu\text{l}$  of serum sample was spiked with 1 ppm of azobenzene as internal standard. 20  $\mu\text{l}$  of 5 N HCl was added and made up to 1 ml with deionized water. Subsequently, the sample was incubated at 70 min for 30 min to avoid protein interaction with insecticides. 150  $\mu\text{l}$  of acetonitrile (dispersive solvent) and 50  $\mu\text{l}$  of chloroform (extraction solvent) mixture was forcibly added to the sample using syringe and sonicated for 3 min followed by centrifugation at 10,000 rpm for 5 min. The organic phase at the bottom of the tube was carefully collected and dried under a gentle stream of nitrogen gas and dissolved in 20  $\mu\text{l}$  of hexane.

## GC–MS conditions

The GC injector temperature was set at  $200^{\circ}\text{C}$ . The oven temperature program was optimized to hold at  $120^{\circ}\text{C}$  for 1 min and then to increase by  $10^{\circ}\text{C min}^{-1}$  up to  $290^{\circ}\text{C}$  [12]. Helium gas was used as carrier gas. The transfer line temperature was adjusted to  $280^{\circ}\text{C}$ . Mass spectrometry conditions were as follows: electron ionization source set to 70 eV,

emission current 500 IA, MS Quad 150 C, MS Source  $200^{\circ}\text{C}$ . The mass spectrometer was run in full-scan mode and in single ion monitoring mode for the fragments specific to each insecticide [10, 12].

## Calibration, LOD, LOQ and recoveries

The standards were run at different concentrations, and peak area was calculated and subsequently, linearity was established. Limit of detection (LOD) and limit of quantification (LOQ) were determined by standard methods. The recovery efficiencies for each individual insecticide were determined by spiking known concentration of insecticide and measurement by GC–MS.

## Statistical analysis

All statistical analyses were performed using the statistical software SPSS version 20.0. We calculated mean and percentage of participant characteristics by diabetic and pre-diabetic status. The cumulative sum of the level of all organophosphates studied was expressed as total organophosphates. Linear regression was performed to study the strength of association of serum organophosphate residues with HbA<sub>1c</sub> and CIMT. Based on detection level, the participants were categorized as below and above detectable limit, and the odds ratio was calculated by logistic regression. We included likely or suspected confounders in models based on previously published data. Our logistic regression models were fitted with appropriate degrees of adjustment. We adjusted for age, sex, family diabetic history, education, occupation, smoking, smoking frequency, alcohol consumption, frequency of alcohol usage, tobacco usage and frequency of tobacco usage, waist circumference, obesity, hypertension and hypercholesterolemia. For total organophosphates and arsenic, we used logistic regression to estimate odds ratios and confidence interval (CI) levels for diabetes, pre-diabetes and atherosclerosis by comparing each quartile with the lowest quartile. Subsequently, we tested for linear trends across quartiles of insecticide by including the median of each quartile as a continuous variable in logistic regression models. The Spearman correlation coefficient was calculated between insecticides with HbA<sub>1c</sub> and CIMT. Statistical significance was determined on the basis of two-sided tests at a 5% significance level. In addition, linear regression analysis was performed to understand the relation between arsenic accumulation and corresponding serum insecticide residues. To understand the relationship between arsenic and total organophosphates, 16 sub-quartiles were created by combining the quartiles of arsenic and total organophosphates. Subsequently, logistic regression with adjustment for above-mentioned confounding factors was performed for pre-diabetic, diabetic and atherosclerosis populations.

**Table 1** Characteristics of the study population (KMCH-NNCD-I Study) [ $n = 865$ ]

KMCH-NNCD, 2015		Whole population ( $n = 865$ )	Pre-diabetes ( $n = 371$ )	Diabetes ( $n = 142$ )	Carotid Atherosclerosis ( $n = 90$ )
		Percent	Percent	Percent	Percent
Sex	Male	48.0	43.1	59.6	67.5
	Female	52.0	56.9	40.4	32.5
Age (years)	20–40	32.9	25.3	5.7	2.3
	41–60	46.6	53.7	57.4	46.1
	Above 60	20.5	21.0	36.9	51.7
Alcohol intake (only males)	Daily	2.7	2.0	3.8	1.8
	Occasionally	50.4	47.3	58.2	64.9
	Never	47.0	50.7	38.0	33.3
Smoking (only males)	Daily	31.2	20.5	32.8	35.7
	Occasionally	25.0	14.0	30.3	34.0
	Never	43.8	55.5	36.8	30.3
Tobacco use	Daily	14.2	17.5	16.2	12.2
	Occasionally	11.5	11.0	8.5	20.8
	Never	74.3	71.5	75.4	67.1
BMI ( $\text{kg}/\text{m}^2$ )	Obese ( $\geq 25$ )	31.6	34.2	36.2	32.6
	Underweight ( $\leq 18.5$ )	13.2	11.2	6.4	18
HbA1c (%)	Diabetes ( $\geq 6.5$ )	16.2	–	–	32.6
	Pre-diabetes (5.7–6.4)	43.4	–	–	48.4
Blood pressure (mm Hg)	Hypertension ( $\geq 140/90$ )	37.8	33.0	49.6	54.0
Total cholesterol (mg/dL)	Hypercholesterolemia ( $\geq 200$ )	33.4	40.4	34.6	39.4
CIMT (mm)	Atherosclerosis ( $\geq 1$ )	10.3	11.6	20.5	–

## Results

The characteristics of the study population are summarized in Table 1. 82.5% of the participants were involved in farming occupation. Based on our survey with farmers, pesticide applicators and pesticide vendors, we identified no organochlorine or any other persistent insecticides are being used in the study community and surrounding regions. The insecticides being used are largely dominated by organophosphates followed by carbamates, pyrethroids and neonicotinoids. We noticed 12 insecticides as commonly used that includes ten organophosphates (dichlorvos, acephate, monocrotophos, phorate, dimethoate, methyl parathion, malathion, chlorpyrifos, quinalphos and profenofos) a carbamate (carbofuran) and a pyrethroid ( $\lambda$ -cyhalothrin) (Table S1). Among them, methyl parathion is classified as extremely hazardous (Class Ia), malathion as slightly hazardous (Class III) and others fall within highly (Class Ib) and moderately (Class II) hazardous classes. As organophosphates occupies the 70% of insecticide usage in the study community, we focused on these group of insecticides.

The mass fragments scanned for each organophosphate under single ion monitoring mode in GC–MS are provided in Table S2. The LOD and LOQ for each organophosphate

were calculated (Table S3), and the recovery efficiencies ranges from 57.8 to 102.7% (Table S4). Monocrotophos, methyl parathion, malathion and chlorpyrifos were detected in more than 70% of the samples analyzed, while detection rate for other organophosphates ranges between 38 and 65% (Table S5). We observed a strong correlation between the insecticides irrespective of the disease status of the participants (data not shown). Relatively high levels of acephate, monocrotophos, methyl parathion, malathion and chlorpyrifos residues were detected in among diabetes population (Table S6). We observed a significant linear trend between serum organophosphate residues level and of urinary arsenic accumulation by regression analysis (Table S7).

The prevalence of diabetes and pre-diabetes were determined by HbA<sub>1c</sub> levels. We noticed a significant positive correlation between all the organophosphate residue levels and HbA<sub>1c</sub> (Table S8) indicating the role of insecticides in glucose homeostasis. Based on detection of insecticide residue level, the population was categorized as “detected below LOD” and “detected above LOD”. On multivariate regression analysis between these two groups, significant odds ratio was obtained for monocrotophos, methyl parathion, malathion, chlorpyrifos and profenofos for pre-diabetes



**Table 2** Association of organophosphate insecticide residues with prevalence of pre-diabetes

	Total no. of samples above LOD (%)	Samples above LOD		Samples below LOD		Odds ratio (95% CI)
		No. of pre-diabetes	Percentage of pre-diabetes	No. of pre-diabetes	Percentage of pre-diabetes	
Dichlorvos	274 (38%)	81	29.6	290	49.1	0.44 (0.32–0.59)
Acephate	339 (47%)	152	44.8	219	41.6	1.14 (0.87–1.50)
Monocrotophos	563 (78%)	298	43.7	73	39.7	<b>1.18***</b> <b>(1.08–1.65)</b>
Phorate	312 (41%)	152	48.7	219	39.6	1.45 (1.10–1.92)
Dimethoate	469 (65%)	161	28.5	210	70	0.17 (0.12–0.23)
Methyl parathion	491 (68%)	320	54.7	51	18.2	<b>1.42***</b> <b>(1.12–1.65)</b>
Malathion	548 (76%)	333	50.4	38	18.6	<b>1.44**</b> <b>(1.02–1.81)</b>
Chlorpyrifos	527 (73%)	351	55.9	20	8.4	<b>1.75**</b> <b>(1.47–2.31)</b>
Quinalphos	259 (36%)	122	34.7	249	48.5	0.562 (0.42–0.74)
Profenofos	296 (41%)	185	62.5	186	32.6	<b>1.43*</b> <b>(1.26–2.60)</b>

The odds ratio values showed in boldness indicates the statistical significance (\*\*\* $p < 0.001$ ; \*\* $p < 0.01$ ; \* $p < 0.05$ ). Multivariate adjustment included age, sex, familial diabetic history, education, occupation, smoking, smoking frequency, alcohol consumption, frequency of alcohol usage, tobacco usage, frequency of tobacco usage, waist circumference, obesity, hypertension and hypercholesterolemia

(Table 2), while for diabetes, all the above except profenofos showed significant association (Table 3).

The level of all the ten organophosphates residues detected was added and expressed as total organophosphates. On multivariate regression analysis with the total organophosphates level, significance was observed for only diabetes and not for pre-diabetes (ADA) (Fig. 1a), but urinary arsenic levels showed significant trends with higher odds ratio for both pre-diabetes and diabetes (Fig. 1b). For every unit increase in the level of serum organophosphates residues, a corresponding increase in HbA<sub>1c</sub> value was found by linear regression analysis. For all the organophosphates analyzed, the regression coefficient for highest arsenic quartiles was relatively higher on comparison with lower quartiles of arsenic (Table S9). By combining the quartiles of arsenic (AsQ) and total organophosphates (OPQ), 16 sub-quartiles were formed, and inter-quartile multiple regression analysis was performed. Higher odds ratio with significant trends was observed for the sub-quartiles formed by the combination of higher quartiles of arsenic and total organophosphates [AsQ3 × OPQ3, AsQ3 × OPQ4, AsQ4 × OPQ3, AsQ4 × OPQ4] for both pre-diabetes and diabetes (Table 5; Fig. S2). The sub-quartiles [AsQ3 × OPQ2, AsQ4 × OPQ2] formed by highest quartile of arsenic and relatively lower

quartile of organophosphates showed association for only diabetes and not for pre-diabetes.

On multivariate regression analysis in atherosclerotic population, significant odds ratio was observed for monocrotophos, methyl parathion, chlorpyrifos and (Table 4) total organophosphates (Fig. 1a). The urinary arsenic levels also exhibited higher odds ratio and significant trend in atherosclerotic population (Fig. 1b). Higher regression coefficient for CIMT on analysis with serum insecticide residues was observed for all organophosphates (Table S10). Higher odds ratio with significant trends was observed for the sub-quartiles formed by the combination of higher quartiles of arsenic and total organophosphates [AsQ3 × OPQ3, AsQ3 × OPQ4, AsQ4 × OPQ3, AsQ4 × OPQ4] for atherosclerosis (Table 5, Fig. S2). In addition, the sub-quartile [AsQ3 × OPQ2] formed by highest quartile of arsenic and relatively lower quartile of organophosphates also showed association for atherosclerosis (Table 5, Fig. S2). Thus, this study revealed the association of agrochemicals with diabetes and cardiovascular diseases in rural communities.

**Table 3** Association of organophosphate insecticide residues with prevalence of diabetes

	Total no. of samples above LOD (%)	Samples above LOD		Samples below LOD		Odds ratio (95% CI)
		No. of diabetes	Percentage of diabetes	No. of diabetes	Percentage of diabetes	
Dichlorvos	274 (38%)	25	9.1	116	19.6	0.41 (0.26–0.65)
Acephate	339 (47%)	62	18.3	79	15	0.66 (0.42–1.01)
Monocrotophos	563 (78%)	125	18.4	16	8.7	<b>2.36*</b> <b>(1.37–4.09)</b>
Phorate	312 (41%)	58	18.5	83	15	1.29 (0.90–1.87)
Dimethoate	469 (65%)	88	15.6	53	17.7	0.860 (0.59–1.25)
Methyl parathion	491 (68%)	112	19.1	29	10.4	<b>1.25***</b> <b>(1.18–1.52)</b>
Malathion	548 (76%)	135	20.4	6	2.9	<b>1.47**</b> <b>(1.18–2.55)</b>
Chlorpyrifos	527 (73%)	124	19.7	17	7.2	<b>1.18***</b> <b>(1.07–1.42)</b>
Quinalphos	259 (36%)	45	12.8	96	18.7	0.64 (0.43–0.93)
Profenofos	296 (41%)	45	15.2	96	16.8	0.88 (0.60–1.30)

The odds ratio values showed in boldness indicates the statistical significance (\*\* $p < 0.001$ ; \*\* $p < 0.01$ ; \* $p < 0.05$ ). Multivariate adjustment included age, sex, familial diabetic history, education, occupation, smoking, smoking frequency, alcohol consumption, frequency of alcohol usage, tobacco usage, frequency of tobacco usage, waist circumference, obesity, hypertension and hypercholesterolemia

**Table 4** Association of organophosphate insecticide residues with prevalence of atherosclerosis

	Total no. of samples above LOD (%)	Samples above LOD		Samples below LOD		Odds ratio (95% CI)
		No. of atherosclerosis	Percentage of atherosclerosis	No. of atherosclerosis	Percentage of atherosclerosis	
Dichlorvos	274 (38%)	12	4.4	77	13.0	0.31 (0.16–0.57)
Acephate	339 (47%)	22	6.5	67	12.7	0.48 (0.29–0.79)
Monocrotophos	563 (78%)	80	11.7	9	4.9	<b>2.59***</b> <b>(1.27–3.26)</b>
Phorate	312 (41%)	21	6.7	68	12.3	0.51 (0.31–0.86)
Dimethoate	469 (65%)	18	3.2	71	23.7	0.11 (0.06–0.18)
Methyl parathion	491 (68%)	65	11.1	24	8.6	<b>1.33*</b> <b>(1.02–3.22)</b>
Malathion	548 (76%)	56	8.5	33	16.2	0.48 (0.30–0.76)
Chlorpyrifos	527 (73%)	78	12.4	11	4.6	<b>1.91*</b> <b>(1.52–2.58)</b>
Quinalphos	259 (36%)	33	9.4	56	10.9	0.84 (0.54–1.32)
Profenofos	296 (41%)	40	13.5	49	8.6	<b>1.66*</b> <b>(1.07–2.58)</b>

The odds ratio values showed in boldness indicates the statistical significance (\*\* $p < 0.001$ ; \*\* $p < 0.01$ ; \* $p < 0.05$ ). Multivariate adjustment included age, sex, familial diabetic history, education, occupation, smoking, smoking frequency, alcohol consumption, frequency of alcohol usage, tobacco usage, frequency of tobacco usage, waist circumference, obesity, hypertension and hypercholesterolemia

## Discussion

We were particularly concerned that nearly more than 10% of our rural participants in the KMCH-NNCD-I study had diabetes (Table 1), higher than previous studies done in India [13]. The non-association of traditional risk factors with incidence of diabetes and atherosclerosis [7] in this study population led us to question whether traditional risk factors alone were enough to explain the huge prevalence of NCDs in this rural population. Two areas that interested us were insecticides and heavy metals. Our previous study indicated the association of urinary heavy metals particularly arsenic with diabetes and atherosclerosis [7]. The pesticide scene in India is a cause for huge concern with more than 100 pesticides registered for use. There has been a more than 15-fold increase in the production of insecticides, from a mere 5000 tons in 1952 to 85,000 tons in 2004 [14]. Rampant injudicious use of such insecticides may be a one “cog in the wheel” that explains the increase in metabolic disorders, cancers, neurodegenerative disorders and reproductive abnormalities [15]. In this study, we noticed withdrawal of usage of persistent insecticides like endosulfan, DDT in the study area indicating development of awareness on their toxicity by government and non-governmental agencies. Organophosphates are christened as one of the most poisonous chemicals in the world by Carson [16]. They are largely used along with carbamates and pyrethroids due to their short half-life. Irrespective of their non-persistent nature, these insecticides pose a heavy risk on human health. Though these organophosphate groups of insecticide possess short half-life, they are detected in large populations in this study and in other previous studies [10, 17]. The probable explanation is these insecticides are being exposed to the farming people day-to-day continuously, and hence, they are under detectable limits.

Organophosphate insecticides seem to affect multiple glucose homeostatic pathways that can lead to hyperglycemia. Physiological stress, oxidative stress, inhibition of paraoxonase, nitrosative stress, pancreatitis, inhibition of cholinesterase, stimulation of adrenal gland and disturbed metabolism of liver tryptophan and gut microbiota were enlisted as proposed mechanisms behind OP-induced disruption of glucose homeostasis [10, 17]. We observed farmers and workers mixing and spraying insecticides without using personal protective equipment [6, 9, 10]. It is well recognized that insecticides can not only get avidly absorbed through layers of epidermis and mucosa but can remain in the skin which acts as a reservoir for release in future [18]. The other possibility is the metabolic effects of chronic exposure through food commodities that is being used by both rural and urban populations. Studies have shown that 20% of food commodities in India have

insecticides residue levels above the maximal permissible levels on a worldwide basis [14]. Chronic exposure of mice to organophosphates-induced glucose intolerance was mediated by the gut microbial degradation of organophosphates [10]. Our previous studies with rats showed that prolonged exposure of monocrotophos leads to cardiac oxidative stress and myocardial damage [19]. In addition, organophosphate insecticides have been implicated in hypertension, abnormal geometry of left ventricle, peripheral arterial disease, obesity, atherosclerosis and end-stage renal disease [20–22].

Arsenic exposure is a global public health problem and labeled by WHO as the largest mass poisoning of the world.

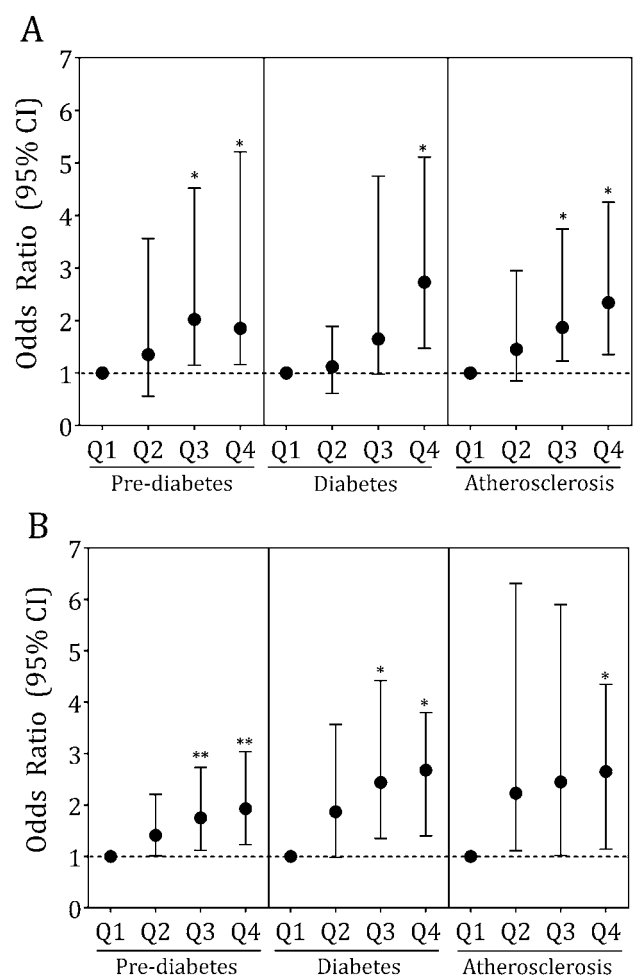


**Fig. 1** Odds ratio (95% CI) for pre-diabetes, diabetes and atherosclerosis associated with the quartiles of total organophosphates (a) and total arsenic (b). \*indicates statistical significance (\*\* $p < 0.01$ ; \* $p < 0.05$ ). Multivariate adjustment included age, sex, education, occupation, waist circumference, BMI, diastolic and systolic blood pressure, LDL-cholesterol, familial diabetic history, smoking, alcohol and tobacco usage for pre-diabetes and diabetes. Besides the above mentioned, familial ischemic heart disease history and glycated hemoglobin are also included for atherosclerosis

**Table 5** Association of co-accumulation of arsenic and total organophosphate insecticide residues with prevalence of diabetes, pre-diabetes and atherosclerosis

Sub-quartile (SQ) (AsQ×OPQ)	Odds ratio (95% CI)		
	Pre-diabetes	Diabetes	Atherosclerosis
SQ1 (AsQ1×OPQ1)	1.00	1.00	1.00
SQ2 (AsQ1×OPQ2)	1.25 (0.72–2.17)	1.60 (0.91–2.79)	1.46 (0.98–1.72)
SQ3 (AsQ1×OPQ3)	0.91 (0.59–1.43)	1.17 (0.77–1.77)	1.19 (0.78–1.80)
SQ4 (AsQ1×OPQ4)	0.92 (0.47–1.70)	0.82 (0.41–1.63)	0.87 (0.43–1.76)
SQ5 (AsQ2×OPQ1)	2.03 (0.85–3.74)	1.80 (0.52–2.25)	0.86 (0.44–1.67)
SQ6 (AsQ2×OPQ2)	1.10 (0.71–1.72)	1.48 (0.95–2.02)	1.47 (0.97–2.24)
SQ7 (AsQ2×OPQ3)	1.89 (0.88–4.04)	1.92 (0.86–2.12)	0.87 (0.43–1.76)
SQ8 (AsQ2×OPQ4)	1.29 (0.35–1.56)	1.95 (0.85–2.86)	0.76 (0.38–1.52)
SQ9 (AsQ3×OPQ1)	1.08 (0.52–2.27)	1.84 (0.92–3.72)	1.77 (0.87–3.61)
SQ10 (AsQ3×OPQ2)	0.87 (0.43–1.76)	<b>2.86 (1.33–4.02)*</b>	0.99 (0.50–1.98)
SQ11 (AsQ3×OPQ3)	<b>3.54 (1.87–5.34)*</b>	<b>2.15 (1.14–3.52)*</b>	<b>2.19 (1.16–4.12)*</b>
SQ12 (AsQ3×OPQ4)	<b>1.48 (1.05–4.82)*</b>	<b>2.02 (1.82–5.01)*</b>	1.21 (0.84–3.87)
SQ13 (AsQ4×OPQ1)	1.25 (0.72–2.17)	0.99 (0.55–1.84)	1.46 (0.76–2.75)
SQ14 (AsQ4×OPQ2)	1.04 (0.58–1.89)	<b>2.46 (1.10–3.50)*</b>	<b>2.70 (1.16–3.77)*</b>
SQ15 (AsQ4×OPQ3)	<b>3.20 (2.25–5.20)*</b>	<b>2.86 (1.25–4.52)*</b>	<b>2.45 (1.34–3.75)*</b>
SQ16 (AsQ4×OPQ4)	<b>1.86 (3.54–1.15)*</b>	<b>2.10 (1.56–4.56)*</b>	<b>1.56 (1.03–2.98)*</b>

The odds ratio values showed in boldness indicates the statistical significance (\*\*\* $p < 0.001$ ; \*\* $p < 0.01$ ; \* $p < 0.05$ ). Multivariate adjustment included age, sex, familial diabetic history, education, occupation, smoking, smoking frequency, alcohol consumption, frequency of alcohol usage, tobacco usage, frequency of tobacco usage, waist circumference, obesity, hypertension and hypercholesterolemia

The heavy use of synthetic phosphate fertilizers leads to extension of arsenic problem to the different regions of the world that are not previously identified as natural arsenic-rich regions. Arsenic has been implicated in beta-cell dysfunction and atherogenesis with higher risk of diabetes and vascular diseases [23]. Our interest in the synergistic co-exposure hypothesis of arsenic and insecticides in the development of diabetes and atherosclerosis was stimulated by reports of Sri Lankan Agricultural Nephropathy, a new form of nephropathy in paddy farmers in Sri Lanka attributed to synergistic effect of heavy metals like arsenic and glyphosate, an organophosphate herbicide [24]. In an animal study, combined exposure of arsenic and dichlorvos to rats led to changes in glutathione metabolism, neurological and hepatic damage [25, 26]. Higher odds ratio in the sub-quartiles dominated by higher quartiles of arsenic and lower quartile of total organophosphates [AsQ3×OPQ2, AsQ4×OPQ2] indicate that arsenic may be the strongest player on comparison with organophosphates (Table 5). Significant regression coefficient for the insecticides in the highest quartile of arsenic in our study suggests that it may promote the accumulation of insecticide residues in blood (Table S7). Arsenic is known to cause hepatic damage with increase in serum aminotransferases, hepatic fibrosis due to progressive reduction in hepatic glutathione, oxidative stress and fatty infiltration [27]. Both metals and insecticides, in the presence of hepatic impairment, can potentially act in concert to produce reactive oxygen species with depletion of antioxidant systems

[28]. We hypothesize that arsenic-induced hepatic damage results in impairment of hepatic detoxification mechanisms that may lead to higher accumulation of organophosphate residues. The role of gut microbiota in this process is not ignorable as both arsenic and organophosphates are proven to be metabolized by gut microbiota [2, 10, 29]. There are also possibilities that interaction of arsenic and organophosphates produce a new arsenic species that may have more detrimental effect on the system leading to metabolic and vascular dysregulation. NMR-based studies [30] showed the interaction of cadmium with chlorpyrifos yields a new complex that confers increased hepatotoxicity. Future studies focusing on computational and experimental studies are needed to prove these hypotheses.

## Limitations

There are some limitations to our study. Being a cross-sectional study, it is difficult to infer causality of any kind, and this study is mere hypothesis generating at this point. Due to practical issues and ethical guidelines, we had participation from two-third of the village population indicating that the prevalence rates reported will have small margin of error (3.3%). Due to logistics and manpower issues, we were not able to have an independent review of carotid intima thickness nor could we do quality assurance on measurement readings. A single arsenic or insecticide measurement at one time point may not represent

cumulative exposure. Finally, we cannot rule out confounding effects by other potentially harmful substances in the environment that we could not measure.

## Conclusion

In summary, findings from this study highlight the importance of possible synergistic detrimental metabolic and cardiovascular effects of arsenic and organophosphates in a rural population. The results of this study raise vital research questions on the role of these agrochemicals in the etiology of diabetes and vascular diseases.

**Acknowledgements** This study was funded by Nano Mission, Department of Science and Technology, Government of India (TP) and KMCH Research Foundation (GV & KS). GV acknowledges Indian Institute of Technology Madras for Institute Post-doctoral fellowship. Authors acknowledge the KMCH Radiology and Nursing team for their assistance in sample collection process. We also acknowledge M/s. MicroLabs, Coimbatore for their assistance in analyzing blood samples. We are thankful to the village heads, volunteers and participants of this study.

**Author contributions** GV<sup>1</sup>, KS, GV<sup>2</sup>, MC, TA, NGP and TP conceived and designed the experiments. GV<sup>1</sup>, KS, GV<sup>2</sup>, MC and NGP are involved in sample collection. GV<sup>1</sup> and KS performed the experiments. GV<sup>1</sup>, KS, SM, MD and TP analyzed the data. KS, MC, TA, NGP and TP have contributed reagents/materials/analysis tools. GV<sup>1</sup> and KS wrote the manuscript. All the authors read and approved the final manuscript.

**Funding** This study was funded by KMCH Research Foundation (NNCD-I, 2015) and supported by Nano Mission, Department of Science and Technology, Government of India (DST UNS).

**Availability of data and materials** Complete data, clinical details and samples are available for researchers on reasonable request to corresponding author. But providing of data or samples will depend on the approval of Institute ethical committee.

## Compliance with ethical standards

**Conflict of interest** The authors declare that they have no conflict of interest.

**Informed consent** Informed consent was obtained from all participants of this study for publication of this data as per the guidelines of institute's ethical committee.

**Ethics approval** The study design and protocol were approved by KMCH Ethics Committee, Kovai Medical Center and Hospital Limited, Coimbatore (Approval No. EC/AP/02/2015 dated 16 February 2015).

## References

1. World Health Organization (2016) Global report on diabetes. World Health Organization. <https://apps.who.int/iris/handle/10665/204871>
2. Velmurugan G, Ramprasath T, Gilles M, Swaminathan K, Ramasamy S (2017) Gut microbiota, endocrine-disrupting chemicals and the diabetes epidemic. *Trends Endocrinol Metab* 28:612–625
3. Neel BA, Sargis RM (2011) The paradox of progress: environmental disruption of metabolism and the diabetes epidemic. *Diabetes* 60:1838–1848
4. Sekhota MM, Monyeki KD, Sibuyi ME (2016) Exposure to agrochemicals and cardiovascular disease: a review. *Int J Environ Res Public Health* 13:229
5. Cosselman KE, Navas-Acien A, Kaufman JD (2015) Environmental factors in cardiovascular disease. *Nat Rev Cardiol* 12:627–642
6. Swaminathan K, Veerasekar G, Kuppusamy S et al (2017) Non-communicable disease in rural India: are we seriously underestimating the risk? The Nallampatti noncommunicable disease study. *Ind J Endocrinol Metab* 21:90–95
7. Velmurugan G, Swaminathan K, Veerasekar G et al (2018) Metals in urine in relation to prevalence of pre-diabetes, diabetes and atherosclerosis in rural. *India J Occup Environ Med* 75:661–667
8. Swaminathan K, Sundaram M, Prakash P, Subbiah S (2013) Diabetic ketoacidosis: an uncommon manifestation of pesticide poisoning. *Diabetes Care* 36:e4
9. Swaminathan K (2013) Pesticides and human diabetes: a link worth exploring. *Diabetes Med* 30:1268–1271
10. Velmurugan G, Ramprasath T, Swaminathan K et al (2017) Gut microbial degradation of organophosphate insecticides induces glucose intolerance via gluconeogenesis. *Genome Biol* 18:8
11. Jacoby DS, Mohler ER III, Rader DJ (2004) Noninvasive atherosclerosis imaging for predicting cardiovascular events and assessing therapeutic interventions. *Curr Atheroscler Rep* 6:20–26
12. Musshoff F, Junker H, Madea B (2002) Simple determination of 22 organophosphorous pesticides in human serum using head-space solid-phase microextraction and gas chromatography with mass spectrometric detection. *J Chromatogr Sci* 40:29–34
13. Anjana RM, Deepa M, Pradeepa R et al (2017) Prevalence of diabetes and pre-diabetes in 15 states of India: results from the ICMR-INDIAB population-based cross-sectional study. *Lancet Diabetes Endocrinol* 5:585–596
14. Gupta PK (2004) Pesticide exposure—Indian scene. *Toxicology* 198(1–3):83–90
15. Mostafalou S, Abdollahi M (2013) Pesticides and human chronic diseases: evidences, mechanisms, and perspectives. *Toxicol Appl Pharmacol* 268(2):157–177
16. Carson R (1962) Silent spring. Houghton Mifflin, Boston
17. Rahimi R, Abdollahi M (2007) A review on the mechanisms involved in hyperglycemia induced by organophosphorous pesticides. *Pestic Biochem Physiol* 88:115–121
18. Macfarlane E, Carey R, Keegel T, El-Zaemay S, Fritschi L (2013) Dermal exposure associated with occupational end use of pesticides and the role of protective measures. *Saf Health Work* 4(3):136–141
19. Velmurugan G, Babu DDV, Ramasamy S (2012) Prolonged intake of monocrotophos induces cardiac oxidative stress and myocardial damage in rats. *Toxicology* 307:103–108
20. Lee DH, Steffes MW, Sjödin A, Jones RS, Needham LL, Jacobs DR Jr (2011) Low dose organochlorine pesticides and polychlorinated biphenyls predict obesity, dyslipidemia, and insulin resistance among people free of diabetes. *PLoS ONE* 6(1):e15977

21. Sjöberg Lind Y, Lind L, Salihovic S, van Bavel B, Lind PM (2013) Persistent organic pollutants and abnormal geometry of the left ventricle in the elderly. *J Hypertens* 31(8):1547–1553
22. Lebov JF, Engel LS, Richardson D, Hogan SL, Hoppin JA, Sandler DP (2016) Pesticide use and risk of end-stage renal disease among licensed pesticide applicators in the Agricultural Health Study. *Occup Environ Med* 73:3–12
23. Seldenrich N (2018) Arsenic and diabetes: assessing risk at low-to-moderate exposures. *Environ Health Perspect.* <https://doi.org/10.1289/EHP3257>
24. Jayasumana C, Gunatilake S, Siribaddana S (2015) Simultaneous exposure to multiple heavy metals and glyphosate may contribute to Sri Lankan agricultural nephropathy. *BMC Nephrol* 11(16):103
25. Flora SJ (2016) Arsenic and dichlorvos: possible interaction between two environmental contaminants. *J Trace Elem Med Biol* 35:43–60
26. Flora SJS, Dwivedi N, Deb U, Kushwaha P, Lomah V (2014) Effects of co-exposure to arsenic and dichlorvos on glutathione metabolism, neurological, hepatic variables and tissue histopathology in rats. *Toxicol Res* 3:23–31
27. Mazumder DN (2005) Effect of chronic intake of arsenic-contaminated water on liver. *Toxicol Appl Pharmacol* 206(2):169–175
28. Rouimi P, Zucchini-Pascal N, Dupont G et al (2012) Impacts of low doses of pesticide mixtures on liver cell defence systems. *Toxicol In Vitro* 26(5):718–726
29. Velmurugan G (2018) Gut microbiota in toxicological risk assessment of drugs and chemicals: the need of hour. *Gut Microbes.* <https://doi.org/10.1080/19490976.2018.1445955>
30. Chen L, Qu G, Sun X et al (2013) Characterization of the Interaction between cadmium and chlorpyrifos with integrative techniques in incurring synergistic hepatotoxicity. *PLoS ONE* 8:e59553

**Publisher's Note** Springer Nature remains neutral with regard to jurisdictional claims in published maps and institutional affiliations.



## **Supplementary Information**

### **Association of Co-accumulation of Arsenic and Organophosphate Insecticides with Diabetes and Atherosclerosis in a Rural Agricultural Community: KMCH-NNCD-I Study**

Ganesan Velmurugan Ph.D<sup>1,2\*#</sup>, Krishnan Swaminathan MD FRCP<sup>1,2\*</sup>, Sundaresan Mohanraj  
PhD<sup>2</sup>, Mani Dhivakar PhD<sup>1</sup>, Ganesh Veerasekar MPH<sup>2</sup>, Thomas Alexander MD., DM.,  
FACC., FICC., FCSI<sup>2</sup>, Mathew Cherian MD PDCC<sup>2</sup>, Nalla G Palaniswami MD<sup>2</sup> and  
Thalappil Pradeep PhD FRSC<sup>1\*#</sup>

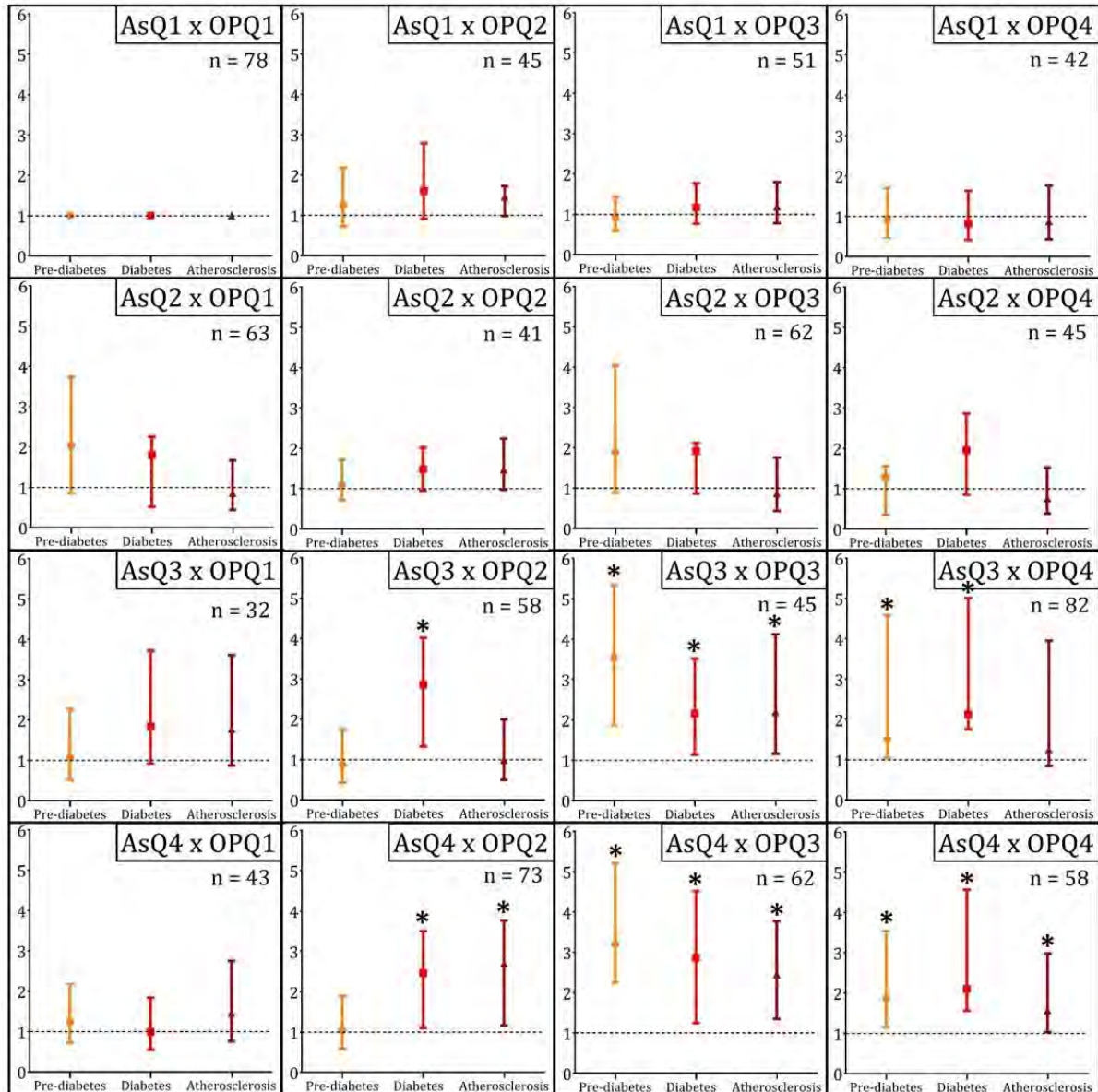
<sup>1</sup>DST Unit of Nanoscience & Thematic Unit of Excellence in Water Research, Department of  
Chemistry, Indian Institute of Technology, Chennai 600 036, Tamilnadu, India.

<sup>2</sup>KMCH Research Foundation, Kovai Medical Centre & Hospital, Coimbatore 641 014,  
Tamilnadu, India.

## Nallampatti – Noncommunicable Disease Study



**Supplementary Fig. S1:** Geographic location of the study village - Nallampatti. The red dot indicates the study village. (Latitude: 11°21'2.39" N; Longitude: 77°32'4.79" E).



**Supplementary Fig. S2:** Odds ratio (95% CI) for pre-diabetes (orange), diabetes (red) and atherosclerosis (meroon) associated with sub-quartiles of arsenic (As) and total organophosphates (OP). The each box represents a sub-quartile formed by the combination of quartile of arsenic and total organophosphate. \*indicates statistical significance ( $p < 0.05$ ). Multivariate adjustment included age, sex, education, occupation, waist circumference, BMI, diastolic and systolic blood pressure, LDL-cholesterol, familial diabetic history, smoking, alcohol and tobacco usage for pre-diabetes and diabetes. Besides the above mentioned familial ischemic heart disease history and glycated hemoglobin are also included for atherosclerosis.

**Table S1:** List of commonly and largely used insecticides in study village and surrounding areas.

	<b>Type</b>	<b>WHO Classification</b>
Dichlorvos	OP	Class Ib
Acephate	OP	Class II
Monocrotophos	OP	Class Ib
Phorate	OP	Class Ia
Dimethoate	OP	Class II
Carbofuran	Carbamate	Class Ib
Methyl parathion	OP	Class Ia
Malathion	OP	Class III
Chlorpyrifos	OP	Class II
Quinalophos	OP	Class II
Profenofos	OP	Class II
Cyhalothrin	Pyrethroid	Class II

OP – Organophosphate. WHO Classification: Class Ia – Extremely hazardous; Class Ib – Highly hazardous; Class II – Moderately hazardous; Class III – Slightly hazardous.

**Table S2:** Mass fragments for each insecticide monitored under single ion monitoring (SIM) mode.

<b>Insecticide</b>	<b>Retention Time</b>	<b>Mass Fragments</b>
Dichlorvos	3.59	79,109,145,185
Acephate	5.57	42,94,136,183
Monocrotophos	8.20	67,97,109,127,192
Phorate	8.29	181,197,208,141
Dimethoate	8.63	124,9,87,93
Methyl parathion	10.31	79,109,125,263
Malathion	10.96	93,127,173,285
Chlorpyrifos	11.11	97,197,286,314
Quinalophos	12.04	90,118,146,157
Profenofos	12.92	337,208,139,97
Azobenzene	7.67	51, 77, 105. 152
(Internal Standard)		

**Table S3:** Descriptive statistics of the organophosphate insecticides and arsenic

	LOD (µg/ l)	LOQ (µg/ l)	No. of Samples detected (%)	Percentile				
				5 <sup>th</sup>	25 <sup>th</sup>	50 <sup>th</sup>	75 <sup>th</sup>	95 <sup>th</sup>
Dichlorvos	0.1	10	331 (38%)	BDL	BDL	BDL	11.52	48.58
Acephate	1	10	339 (39%)	BDL	BDL	BDL	28.5	70.23
Monocrotophos	1	10	681 (78%)	BDL	45.6	112.2	152.2	285.25
Phorate	100	100	312 (41%)	BDL	BDL	BDL	8.52	39.95
Dimethoate	0.1	10	565 (65%)	BDL	BDL	11.23	23.59	33.58
Methyl parathion	0.1	10	585 (68%)	BDL	BDL	18.52	38.45	98.56
Malathion	1	10	661 (76%)	BDL	1.54	28.18	54.68	202.54
Chlorpyrifos	1	10	628 (73%)	BDL	BDL	45.85	78.15	112.56
Quinalophos	100	1000	352 (36%)	BDL	BDL	BDL	1.23	19.56
Profenofos	100	1000	296 (41%)	BDL	BDL	BDL	8.88	29.49
<b>Total organophosphate<sup>#</sup></b>	-	-	-	142.8	352.20	456.21	584.20	1153.24
<b>Arsenic<sup>*</sup></b>	0.1	1	865 (100%)	4.10	18.92	39.79	63.30	8.23

<sup>#</sup>Total organophosphate is the cumulative of the ten organophosphates studied. <sup>\*</sup>Arsenic was detected in urine and provided in µg/ mg creatinine units.



**Table S4:** Limit of detection, limit of quantification and recovery efficiency for each insecticide

	LOD (µg/ l)	LOQ (µg/ l)	Recovery (%)
Dichlorvos	0.1	10	70.10
Acephate	1	10	84.62
Monocrotophos	1	10	79.21
Phorate	100	100	102.70
Dimethoate	0.1	10	57.80
Methyl parathion	0.1	10	86.30
Malathion	1	10	77.82
Chlorpyrifos	1	10	64.67
Quinalophos	100	1000	72.89
Profenofos	100	1000	79.15

**Table S5:** The number of samples in which insecticide detected and its mean value.

	<b>No. of Samples detected (%)</b>	<b>Mean <math>\pm</math> SEM (<math>\mu\text{g/l}</math>)</b>
Dichlorvos	274 (38%)	41.93 $\pm$ 8.2
Acephate	339 (47%)	67.47 $\pm$ 12.5
Monocrotophos	563 (78%)	62.97 $\pm$ 9.8
Phorate	312 (41%)	37.8 $\pm$ 8.6
Dimethoate	469 (65%)	43.20 $\pm$ 6.5
Methyl parathion	491 (68%)	45.10 $\pm$ 3.4
Malathion	548 (76%)	42.93 $\pm$ 12.5
Chlorpyrifos	527 (73%)	49.57 $\pm$ 6.8
Quinalophos	259 (36%)	38.43 $\pm$ 5.1
Profenofos	296 (41%)	35.40 $\pm$ 7.9

**Table S6:** Mean  $\pm$  SEM value of insecticides detected in diabetic, pre-diabetic and non-diabetic groups.

	Mean $\pm$ SEM ( $\mu\text{g/l}$ )		
	Diabetes	Pre-diabetes	No diabetes
Dichlorvos	43.4 $\pm$ 5.6	44.0 $\pm$ 7.5	38.4 $\pm$ 7.9
Acephate	72.7 $\pm$ 12.5	68.9 $\pm$ 6.8	64.8 $\pm$ 8.5
Monocrotophos	80.8 $\pm$ 5.6	58.6 $\pm$ 3.4	49.5 $\pm$ 4.9
Phorate	37.5 $\pm$ 5.0	40.5 $\pm$ 5.4	35.4 $\pm$ 5.8
Dimethoate	45.6 $\pm$ 4.8	39.4 $\pm$ 8.0	44.6 $\pm$ 4.9
Methyl parathion	52.4 $\pm$ 15.5	40.5 $\pm$ 6.5	42.4 $\pm$ 11.2
Malathion	44.7 $\pm$ 9.8	45.5 $\pm$ 2.9	35.6 $\pm$ 9.4
Chlorpyrifos	60.8 $\pm$ 11.2	44.3 $\pm$ 8.1	43.6 $\pm$ 6.8
Quinalophos	90.6 $\pm$ 13.6	86.4 $\pm$ 9.1	88.3 $\pm$ 10.8
Profenofos	100.5 $\pm$ 20.5	98.3 $\pm$ 11.2	87.4 $\pm$ 15.8

**Table S7:** Linear regression between the urinary arsenic and serum insecticide residues

<b>OP</b>	<b>Samples above LOD</b>	<b><math>\beta</math></b>
Dichlorvos	274	0.534
Acephate	339	0.245
Monocrotophos	563	0.954
Phorate	312	0.651
Dimethoate	469	0.015
Methyl parathion	491	0.213
Malathion	548	0.111
Chlorpyrifos	527	0.154
Quinalophos	259	0.056
Profenofos	296	0.215

**Table S8:** Correlation analyses between insecticides and HbA1c values

OP	r
Dichlorvos	0.091*
Acephate	0.058**
Monocrotophos	0.221***
Phorate	0.182**
Dimethoate	0.118**
Methyl parathion	0.112***
Malathion	0.014*
Chlorpyrifos	0.087**
Quinalophos	0.028**
Profenofos	0.082**

Spearman correlation, two-tailed. \*\*\* $p < 0.001$ ; \*\* $p < 0.01$ ; \* $p < 0.05$

**Table S9:** Linear regression analysis of HbA1c between quartiles of arsenic and insecticide residues.

	Regression co-efficient ( $\beta$ ) for HbA1c				
	As (Q1)	As (Q2)	As (Q3)	As (Q4)	All quartiles
Dichlorvos	$2.8 \times 10^{-6}$	$7.7 \times 10^{-5}$	$6.6 \times 10^{-4*}$	$1.2 \times 10^{-4*}$	$2.1 \times 10^{-4*}$
Acephate	$3.7 \times 10^{-7}$	$6.7 \times 10^{-7}$	$6.9 \times 10^{-5*}$	$2.6 \times 10^{-5*}$	$2.4 \times 10^{-4*}$
Monocrotophos	$9.1 \times 10^{-6}$	$1.1 \times 10^{-4*}$	$8.6 \times 10^{-4*}$	$3.5 \times 10^{-3*}$	$1.1 \times 10^{-3*}$
Phorate	$9.7 \times 10^{-5}$	$2.7 \times 10^{-5}$	$2.9 \times 10^{-5*}$	$2.2 \times 10^{-4*}$	$9.3 \times 10^{-5*}$
Dimethoate	$2.9 \times 10^{-6}$	$1.1 \times 10^{-6*}$	$7.9 \times 10^{-5*}$	$1.9 \times 10^{-4*}$	$6.8 \times 10^{-5*}$
Methyl parathion	$2.8 \times 10^{-6}$	$0.9 \times 10^{-5}$	$6.8 \times 10^{-5*}$	$9.2 \times 10^{-4*}$	$2.5 \times 10^{-4*}$
Malathion	$9.7 \times 10^{-7}$	$5.4 \times 10^{-6}$	$3.1 \times 10^{-5*}$	$2.8 \times 10^{-5*}$	$1.6 \times 10^{-5*}$
Chlorpyrifos	$7.6 \times 10^{-6}$	$0.6 \times 10^{-6*}$	$3.8 \times 10^{-5*}$	$7.5 \times 10^{-4*}$	$1.9 \times 10^{-4*}$
Quinalophos	$1.9 \times 10^{-7}$	$2.9 \times 10^{-7}$	$6.6 \times 10^{-6*}$	$3.6 \times 10^{-5*}$	$1.1 \times 10^{-5*}$
Profenofos	$2.8 \times 10^{-8}$	$8.0 \times 10^{-6}$	$6.9 \times 10^{-6*}$	$1.2 \times 10^{-6*}$	$4.0 \times 10^{-6*}$

Adjusted for the variables enlisted in Table 2. \* indicates statistical significance with  $p < 0.05$ .



**Table S10:** Linear regression analysis of CIMT between quartiles of arsenic and insecticide residues.

	Regression co-efficient ( $\beta$ ) for CIMT				
	As (Q1)	As (Q2)	As (Q3)	As (Q4)	All quartiles
Dichlorvos	$1.1 \times 10^{-10}$	$1.7 \times 10^{-9}$	$7.6 \times 10^{-8*}$	$5.1 \times 10^{-7*}$	$1.5 \times 10^{-7}$
Acephate	$5.4 \times 10^{-10}$	$2.8 \times 10^{-8}$	$5.5 \times 10^{-7}$	$4.5 \times 10^{-6*}$	$1.3 \times 10^{-6}$
Monocrotophos	$6.4 \times 10^{-10}$	$4.5 \times 10^{-7*}$	$6.4 \times 10^{-6*}$	$7.5 \times 10^{-5*}$	$2.0 \times 10^{-5*}$
Phorate	$8.2 \times 10^{-8}$	$8.2 \times 10^{-7}$	$6.2 \times 10^{-6}$	$8.6 \times 10^{-6*}$	$4.0 \times 10^{-6*}$
Dimethoate	$4.4 \times 10^{-9}$	$9.2 \times 10^{-8}$	$2.4 \times 10^{-7*}$	$5.2 \times 10^{-6*}$	$1.4 \times 10^{-6*}$
Methyl parathion	$1.8 \times 10^{-10}$	$9.8 \times 10^{-8}$	$8.5 \times 10^{-8*}$	$5.2 \times 10^{-7*}$	$1.8 \times 10^{-7*}$
Malathion	$1.3 \times 10^{-11}$	$1.3 \times 10^{-10}$	$2.5 \times 10^{-9}$	$4.8 \times 10^{-8*}$	$1.3 \times 10^{-8*}$
Chlorpyrifos	$3.4 \times 10^{-9}$	$7.5 \times 10^{-8*}$	$5.4 \times 10^{-8*}$	$1.3 \times 10^{-7*}$	$6.6 \times 10^{-8*}$
Quinalophos	$3.8 \times 10^{-12}$	$5.8 \times 10^{-10}$	$2.8 \times 10^{-10*}$	$3.3 \times 10^{-9*}$	$1.0 \times 10^{-9}$
Profenofos	$2.9 \times 10^{-11}$	$9.8 \times 10^{-10}$	$1.8 \times 10^{-10}$	$3.7 \times 10^{-8*}$	$1.2 \times 10^{-9*}$

Adjusted for the variables enlisted in Table 3. . \* indicates statistical significance with  $p < 0.05$ .



# Phosphorylated cellulose nanofibers exhibit exceptional capacity for uranium capture

Janika Lehtonen · Jukka Hassinen · Avula Anil Kumar · Leena-Sisko Johansson ·  
Roni Mäenpää · Nikolaos Pahimanolis · Thalappil Pradeep · Olli Ikkala ·  
Orlando J. Rojas

Received: 30 November 2019 / Accepted: 2 January 2020 / Published online: 13 January 2020  
© The Author(s) 2020

**Abstract** We investigate the adsorption of hexavalent uranium, U(VI), on phosphorylated cellulose nanofibers (PHO-CNF) and compare the results with those for native and TEMPO-oxidized nanocelluloses. Batch adsorption experiments in aqueous media show that PHO-CNF is highly efficient in removing U(VI) in the pH range between 3 and 6. Gelling of nanofiber hydrogels is observed at U(VI) concentration of 500 mg/L. Structural changes in the nanofiber network (scanning and transmission electron microscopy) and the surface chemical composition (X-ray photoelectron spectroscopy) gave insights on the mechanism of adsorption. The results from batch adsorption experiments are fitted to Langmuir,

Freundlich, and Sips isotherm models, which indicate a maximum adsorption capacity of 1550 mg/g, the highest value reported so far for any bioadsorbent. Compared to other metals (Zn, Mn, and Cu) and typical ions present in natural aqueous matrices the phosphorylated nanofibers are shown to be remarkably selective to U(VI). The results suggest a solution for the capture of uranium, which is of interest given its health and toxic impacts when present in aqueous matrices.

**Keywords** Cellulose nanofibers · Phosphorylated · Uranium · U(VI) · Adsorption · Heavy metal

**Electronic supplementary material** The online version of this article (<https://doi.org/10.1007/s10570-020-02971-8>) contains supplementary material, which is available to authorized users.

J. Lehtonen · J. Hassinen (✉) · L.-S. Johansson ·  
O. J. Rojas (✉)  
Department of Bioproducts and Biosystems, School of  
Chemical Engineering, Aalto University, P.O. Box 16300,  
00076 Aalto, Espoo, Finland  
e-mail: jukka.hassinen@aalto.fi

O. J. Rojas  
e-mail: orlando.rojas@aalto.fi

J. Hassinen · R. Mäenpää · O. Ikkala  
Department of Applied Physics, School of Science, Aalto  
University, P.O. Box 16300, 00076 Aalto, Espoo, Finland

A. A. Kumar · T. Pradeep  
DST Unit of Nanoscience (DST UNS) and Thematic Unit  
of Excellence (TUE), Department of Chemistry, Indian  
Institute of Technology Madras, Chennai 600036, India

N. Pahimanolis  
Betulium Ltd., Tekniikantie 2, 02150 Espoo, Finland

O. J. Rojas  
Departments of Chemical and Biological Engineering,  
Chemistry and Wood Science, The University of British  
Columbia, 2360 East Mall, Vancouver, BC V6T 1Z3,  
Canada

## Introduction

Cellulose has been considered in the development of eco-friendly materials. Particularly, cellulose nanofibers (CNF) have raised interest for their suitability for water purification and heavy metal removal (Voisin et al. 2017). Chemical pretreatments have been used to reduce the energy consumed in CNF production and to introduce functional groups and charges on its surface. Such pretreatments include TEMPO oxidation, sulfonation, cationization, and phosphorylation (Klemm et al. 2018). The nanoscopic dimensions of CNF result in materials with a high surface area, which enhances interaction with metal ions (Bethke et al. 2018). Consequently, anionic CNF has been studied for removal of several heavy metals (Ma et al. 2012; Liu et al. 2015a). In this application, uranium is highly relevant given its occurrence in natural water as a result of leaching from mineral deposits and industrial processes, e.g., mining waters and nuclear fuel cycle facilities (WHO 2011; Kapnisti et al. 2018). In Finland, for example, concentrations as high as  $\sim 15$  mg/L have been determined for uranium in water obtained from drilled wells (Asikainen and Kahlos 1979). Uranium removal from these waters is important since it is both hazardous to the environment and toxic to humans. It can cause a kidney failure due to its chemical toxicity, which is typically of greater concern compared to its radioactivity (Kapnisti et al. 2018).

In aqueous media, two stable oxidation states are common for uranium, U(IV) and U(VI) (Aly and Hamza 2013; Xie et al. 2019). Under aerobic conditions, uranium is present in aqueous solutions in its hexavalent form as uranyl ions ( $\text{UO}_2^{2+}$ ) (Sylwester et al. 2000; Cai et al. 2017; Sarafraz et al. 2017), which predominate in acidic environments (Riegel and Schlitt 2017). As pH increases, hydrolysis of uranyl leads to the formation of  $(\text{UO}_2)_p(\text{OH})_q^{(2p-q)}$  species (Berto et al. 2012). The uranyl ion can also form various complexes with carbonates present in groundwater (Xie et al. 2019). Due to uranyl complexation, in this manuscript U(VI) is discussed instead of  $\text{UO}_2^{2+}$  since we consider conditions where various  $\text{UO}_2^{2+}$  complexes are present.

The presented information points to the urgent need of technologies that are effective for uranium removal or to prevent the release of toxic concentrations of uranium into the environment (Ghasemi Torkabad

et al. 2017). Common techniques used for heavy metal extraction include membrane processes, ion exchange, adsorption, precipitation, and solvent extraction (Chen et al. 2017; Xue et al. 2017; Sarafraz et al. 2017). As a low-cost, easily applicable alternative, adsorption has been considered promising for the removal of U(VI) from aqueous solutions (Su et al. 2018). In such application, bioadsorbents are sought after given a number of advantages including costs, geographical availability and the possibility of metal recovery after incineration.

Due to the high affinity of phosphoryl groups to uranium (Zhou et al. 2015), phosphorylated materials such as lignin (Bykov and Ershov 2009), pine wood sawdust (Zhou et al. 2015), graphene oxide (Liu et al. 2015b; Chen et al. 2017), carbon spheres (Yu et al. 2014), chitosan (Sakaguchi et al. 1981; Morsy 2015), cactus fibers (Prodromou and Pashalidis 2013), polyethylene (Shao et al. 2017), zirconium (Um et al. 2007), and mesoporous silica (Sarafraz et al. 2017; Xue et al. 2017), have been demonstrated for uranium removal. Phosphorous-based functional groups act as chelating agents and thus favor binding of uranyl species (Xie et al. 2019). Phosphorylated cellulose nanomaterials have been studied for adsorption of  $\text{Fe}^{3+}$  (Božič et al. 2014),  $\text{Cu}^{2+}$ , and  $\text{Ag}^+$  (Liu et al. 2015a). In addition, CNF bearing bisphosphonate has been shown to be efficient for vanadium removal (Sirviö et al. 2016) while phosphorylated CNF nanopapers have been prepared for the removal of copper (Mautner et al. 2016). The removal of U(VI) has been studied with TEMPO oxidized CNF (TO-CNF), which achieved an adsorption capacity of 167 mg/g (Ma et al. 2012), and with carboxycellulose nanofibers prepared by nitro-oxidation, presenting a maximum adsorption capacity of 1470 mg/g (Sharma et al. 2017). However, to the best of our knowledge, there are no reports on the removal of U(VI) using phosphorylated CNF (PHO-CNF), which is surprising given the prospects indicated for other metals in the earlier studies.

In addition to chemical chelation, surface sorption mechanisms occur at the solid–liquid interface, such as physisorption, complexation, ion exchange, and precipitation, all of which play a crucial role for uranium removal (Xie et al. 2019). In this work, we study the removal of uranium with PHO-CNF using several batch adsorption approaches. Furthermore, we compare the uranium removal efficiency of PHO-CNF

with different phosphorylation degrees with that determined for native CNF and TO-CNF. The nanocelluloses are characterized by Fourier transform infrared spectroscopy (FT-IR), zeta potential measurements, and transmission electron microscopy (TEM) imaging. Results from the scanning electron microscopy (SEM), TEM, and X-ray photoelectron spectroscopy (XPS) after adsorption are found to give insights into the adsorption mechanism of U(VI). The effect of pH on the adsorption of U(VI) and selectivity against other metals are also studied. Adsorption data at pH 6 are fitted to the Langmuir, Freundlich, and Sips isotherm models. The data was found to fit best with the Sips isotherm, demonstrating a maximum adsorption capacity of 1550 mg/g, the highest among the values reported so far for organic adsorbents.

## Experimental

### Materials

Native CNF was produced at Aalto University from bleached birch pulp by a method reported previously (Rajala et al. 2016). PHO-CNF and TO-CNF were obtained from Betulium Oy, Finland. The concentrations of phosphoryl groups provided by the manufacturer were 0.66 and 1 mmol/g for the PHO-CNF samples referred to as PHO-CNF<sub>0.66</sub> and PHO-CNF<sub>1.00</sub>, respectively. The concentration of carboxylate groups in TO-CNF was 1 mmol/g. Uranyl acetate, Arsenazo III, ascorbic acid, perchloric acid, and nitric acid were all obtained from Sigma Aldrich. Milli-Q water (Millipore) was used for the preparation of all solutions.

### Characterization of CNF

The electrostatic charge of CNF was determined with a Zetasizer Nano-ZS90 (Malvern), reported as zeta potential, and measured at pH 3, 5, 7, and 9 (adjusted by using 1 M HCl and NaOH) from 0.05 wt% CNF suspensions. The different types of CNF were imaged with a FEI Tecnai 12 TEM operating at 120 kV. For sample preparation, 3  $\mu$ L of 0.01 wt% CNF suspension was drop casted on a copper grid with an ultrathin carbon support film and the excess solution was blotted with filter paper after 1 min of contact time, followed by drying under ambient conditions.

Thereafter, 3  $\mu$ L of 2% uranyl acetate was drop casted onto the dried CNF sample in order to stain the sample. The excess solution was blotted with filter paper after 1 min of contact time, followed by drying under ambient conditions. FT-IR spectra of freeze-dried CNF samples were recorded with Nicolet 380 FT-IR Spectrometer using an ATR accessory. The spectra were recorded in the region of 400–4000  $\text{cm}^{-1}$  with 0.5  $\text{cm}^{-1}$  intervals.

### Adsorption experiments

A dry mass of 5 mg of the respective nanocellulose and a total volume of 15 mL of solution were used in the adsorption experiments, unless otherwise mentioned. Experiments were conducted at room temperature (21–22 °C), which remained stable throughout the experiments. A stock solution of 2000 mg/L uranyl acetate was used to prepare the solutions. The adsorption isotherm studies were conducted with initial uranium concentrations of 10, 25, 50, 100, 200, 300, 400, and 500 mg/L. Experiments at different pH and with different CNF types were performed using an initial concentration of 100 mg/L uranium. For the isotherm study, for the comparison between CNF types, and for the selectivity study, the pH was adjusted to 6 using 2 M HCl and NaOH. In all experiments, glass vials were filled with 15 mL of the suspension containing uranium and CNF and sonicated to disperse the fibrils in an ultrasonic bath at 37 kHz for 5 min. The samples were then left in a shaker at 200 rpm for 55 min to reach the equilibrium. After the adsorption process, samples were taken from the solutions and filtered with 0.1  $\mu$ m filters (Whatman). Samples without CNF having similar initial U(VI) concentrations were used as controls to analyze any possible adsorption of U(VI) onto the filters. Based on this analysis, the adsorption of uranium onto the filters was found to be negligible. Uranium concentrations were determined spectrophotometrically with Arsenazo III method (Khan et al. 2006) using a microplate reader (Synergy H1) to determine the absorbance of the solutions at 651 nm. Briefly, 25  $\mu$ L of ascorbic acid (100 g/L), 175  $\mu$ L of Arsenazo III (0.07 w/v% in 3 M perchloric acid) and 50  $\mu$ L of sample were added to the wells of a microwell plate. If necessary, the samples were diluted to reach a maximum U(VI) concentration of 10 mg/L before mixing with ascorbic acid and Arsenazo III. For each

sample, two parallel measurements were conducted with the plate reader and the average of these values reported.

Selectivity experiments were conducted using a concentration of 10 mg/L for all the metals tested (U, Zn, Mn, and Cu). Other typical ions present in natural waters were also added to the solution according to Table S1 (adapted from Sankar et al. 2013). In the selectivity tests, two different amounts of PHO-CNF<sub>1.00</sub> were used, 5 mg and 0.25 mg (values given as dry mass in 15 mL solution). Metal concentrations in the samples used in the selectivity tests were analyzed with inductively coupled plasma mass spectrometry (ICP-MS) (PerkinElmer, NexION 300X). For ICP-MS analysis, the samples were diluted to a maximum concentration of 1 mg/L and digested with 5% (vol.) concentrated HNO<sub>3</sub> (68–70%) before analysis.

The percentage of U(VI) removed in adsorption studies was calculated based on Eq. (1):

$$U \text{ removal } (\%) = \frac{C_0 - C_f}{C_0} \times 100\% \quad (1)$$

and the equilibrium adsorption capacities ( $q_e$ ) were calculated using Eq. (2):

$$q_e = \frac{(C_0 - C_e)V}{m} \quad (2)$$

where  $C_0$ ,  $C_f$ , and  $C_e$  are the initial, final and equilibrium concentrations (mg/L) of U(VI), respectively,  $V$  is the volume (L) and  $m$  is the mass of adsorbent (g) used.

Langmuir, Freundlich, and Sips isotherm models were used for fitting the experimental adsorption data. The Langmuir and Freundlich isotherm models are shown in Eqs. (3) and (4), respectively:

$$\frac{C_e}{q_e} = \frac{C_e}{q_{\max}} + \frac{1}{q_{\max}K_L} \quad (3)$$

$$\ln q_e = \ln K_F + \frac{1}{n} \ln C_e \quad (4)$$

where  $q_{\max}$  is the maximum adsorption capacity (mg/g) and  $K_L$  is the Langmuir adsorption constant (L/mg).  $K_F$  is the Freundlich isotherm constant and  $n$  is the dimensionless heterogeneity factor.

The Sips isotherm model, a combination of the Langmuir and Freundlich isotherms, is expressed as Eq. (5):

$$\ln \left( \frac{q_e}{q_m - q_e} \right) = \frac{1}{n} \ln C_e + \ln K_s \quad (5)$$

where  $q_m$  is the maximum adsorption capacity (mg/g) and  $K_s$  is the median association constant.

#### Characterization of PHO-CNF<sub>1.00</sub> after adsorption

The uranium stock solution was diluted to reach final concentrations of 50, 100, 250, and 500 mg/L. After mixing with PHO-CNF<sub>1.00</sub>, sonication and shaking as described earlier, a 10  $\mu$ L drop of the PHO-CNF<sub>1.00</sub> uranium suspension was drop casted onto the carbon tape on aluminum stubs and the stubs were placed in a -80 °C freezer overnight and freeze dried at -50 °C. For SEM imaging, the samples were sputter-coated with 3 nm of platinum-palladium and observed using an acceleration voltage of 1.6 kV with a scanning electron microscope (Zeiss Sigma VP). TEM samples for imaging after U(VI) adsorption were prepared by drop casting from the suspension with initial U(VI) concentration of 100 mg/L similarly as described in the characterization section without additional uranium staining.

#### X-ray photoelectron spectroscopy

Samples for XPS were prepared by vacuum filtration of PHO-CNF<sub>1.00</sub> onto 0.1  $\mu$ m filters after adsorption of U(VI) from the initial concentrations of 0, 100 mg/L, and 500 mg/L. After vacuum filtration, the filter cakes were frozen at -80 °C and freeze-dried to obtain dry films. An electron spectrometer (AXIS Ultra, Kratos Analytical, UK) with monochromatic Al K $\alpha$  irradiation at 100 W under neutralization was used for the measurements. Three different spots from each film were scanned and elemental surface compositions of the films were determined from low resolution survey scans. High resolution measurements of uranium U 4f, carbon C1s and oxygen O1s were also conducted. Pure cellulose filter paper (Whatman) was used as an in situ reference in all measurements. Data analysis was performed with CasaXPS software, using fitting parameters customized for celluloses and the C–O component of the high resolution C1s at 286.7 eV as

the energy reference for all the spectra (Beamson and Briggs 1992; Johansson and Campbell 2004).

### Uranium speciation

An ion speciation software (PHREEQC) was used to determine the uranyl speciation at pH range 3–7, and in the simulated drinking water used for selectivity experiments (Tables S2 and S3). The U(VI) concentration used for the calculations was 100 mg/L.

## Results and discussion

### Native and modified CNF

FT-IR was used to confirm the functional groups on the TO-CNF and PHO-CNF (Fig. 1a). The characteristic bands of cellulose were observed in all the samples (broad band at  $3340\text{ cm}^{-1}$  due to O–H stretching vibrations, peak at around  $1640\text{ cm}^{-1}$  corresponding to the O–H bending of adsorbed water and peaks at around  $1030$  and  $2900\text{ cm}^{-1}$  corresponding to the C–O and C–H stretching vibrations, respectively). For the PHO-CNF samples, additional peaks were detected at around  $820\text{ cm}^{-1}$ ,  $930\text{ cm}^{-1}$ , and  $1230\text{ cm}^{-1}$  which are assigned to P–O–C, P–OH, and P=O stretching vibrations, respectively (Suflet et al. 2006). For the TO-CNF, a peak at around  $1600\text{ cm}^{-1}$  was detected corresponding to the C=O

stretching vibration of the  $\text{COO}^-$  group. The zeta potentials of all the CNFs were negative in the pH range tested (Fig. 1b). The zeta potential values for PHO-CNF and TO-CNF decreased as the pH increased. This can be explained by the deprotonation of carboxyl or phosphoryl groups. The zeta potentials of the native CNF indicate that it is negatively charged owing to the residual hemicelluloses (containing carboxyl groups) and other impurities originating from the fibers used to prepare the material.

TEM images of the CNFs used in the study are shown in Fig. 2. The images show a clear difference in the size of the native fibrils (Fig. 2a) compared to TO-CNF, PHO-CNF<sub>0.66</sub>, and PHO-CNF<sub>1.00</sub> (Fig. 2b–d). The native CNF consists of long fibrils, while much shorter fibrils are present in TO-CNF and PHO-CNF, due to the chemical treatment used in the respective preparation.

### Adsorption studies

Batch U(VI) adsorption experiments were conducted with the nanocelluloses. U(VI) adsorption was observed to happen within minutes but to ensure that equilibrium was reached, a contact time of 1 h was used in all adsorption tests.

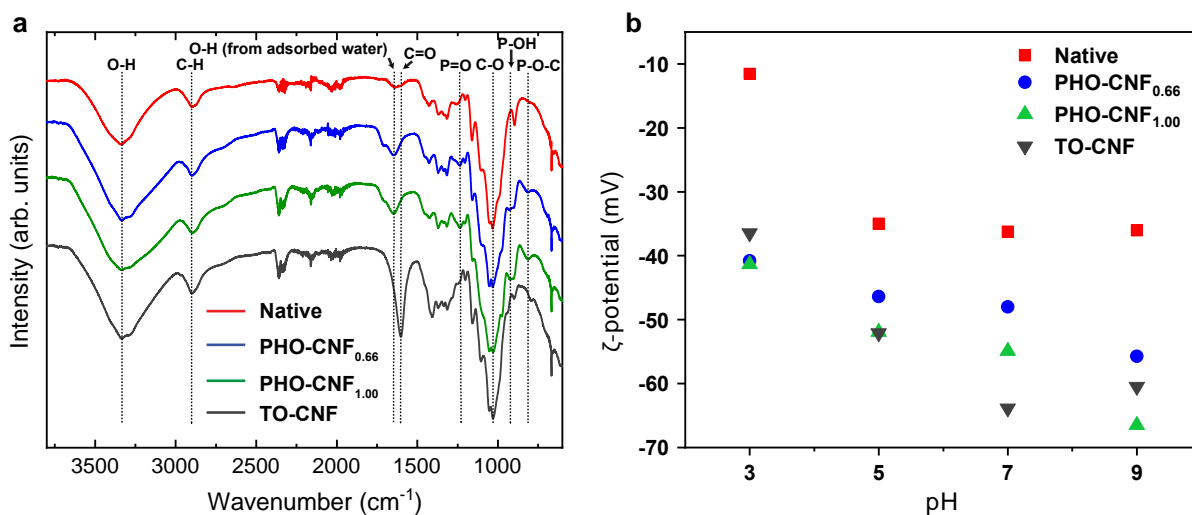


**Fig. 1** a FT-IR spectra and b zeta potentials in the pH range 3–9 of native CNF, PHO-CNF<sub>0.66</sub>, PHO-CNF<sub>1.00</sub>, and TO-CNF



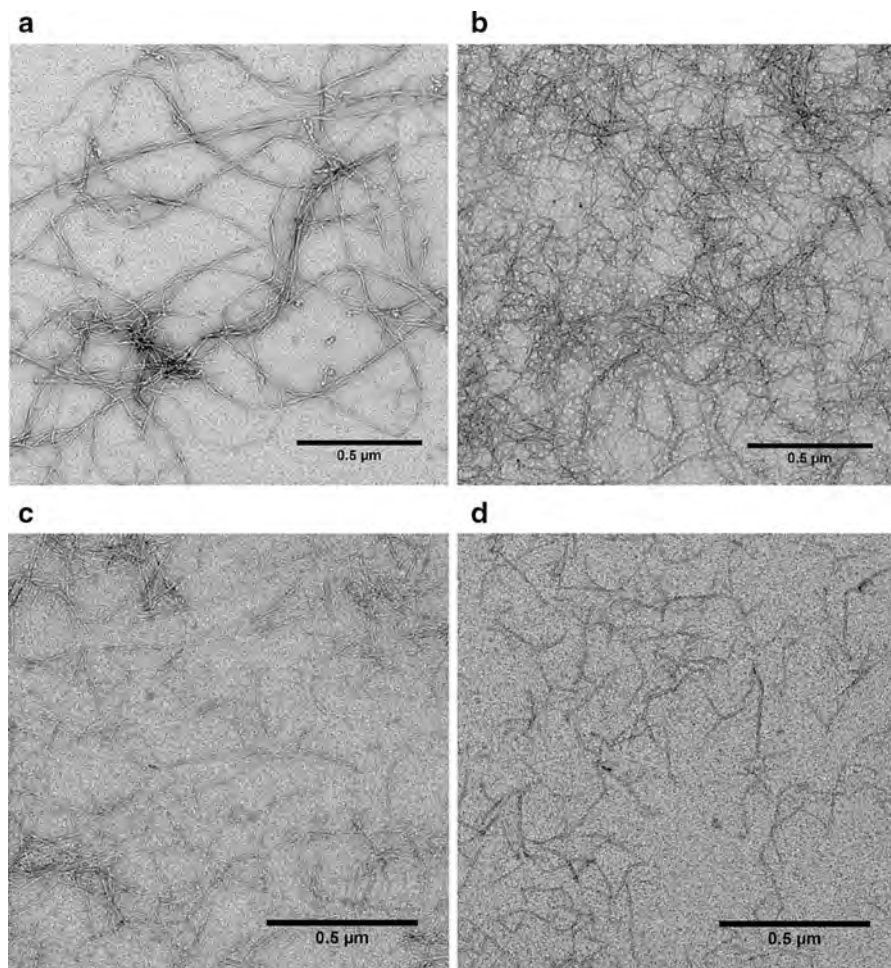


**Fig. 2** TEM images of **a** Native CNF, **b** TO-CNF, **c** PHO-CNF<sub>0.66</sub>, and **d** PHO-CNF<sub>1.00</sub>

#### *Comparison of adsorption on different types of CNF*

First, the removal of U(VI) with the four different types of CNF was compared using an initial U(VI) concentration of 100 mg/L (Fig. 3). The results indicate that the PHO-CNF<sub>1.00</sub> was the most efficient of the nanocelluloses for uranium removal. The degree of phosphorylation was found to affect the removal of uranium only slightly, since 94% and 92% removal was observed with 1 mmol/g and 0.66 mmol/g phosphorylation degrees, respectively. However, the removal was significantly higher with PHO-CNF in comparison to TO-CNF (77%) or native CNF (7%). Based on the results, it can be concluded that the anionic charge of the CNF is an important factor in the adsorption of U(VI). The removal of U(VI) with PHO-CNF and TO-CNF can be mainly attributed to the

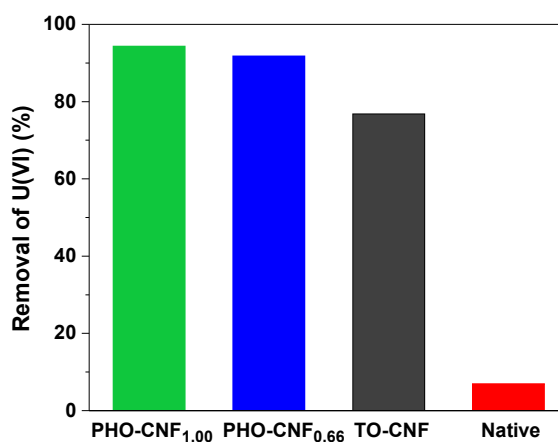


**Fig. 3** Removal of U(VI) with PHO-CNF with varying degree of phosphorylation (1 mmol/g and 0.66 mmol/g), TEMPO oxidized CNF, and native fibrils

phosphoryl and carboxyl groups present on the fibrils. In the case of native CNF, the adsorption is most likely explained by the slight negative charge on the fibrils, as confirmed by the zeta potential measurements. However, the higher removal degree achieved with PHO-CNF compared to TO-CNF indicate the higher affinity between phosphoryl groups and U(VI). In addition, the smaller dimensions of the PHO-CNF and TO-CNF compared to native CNF lead to higher surface area, thus enabling higher adsorption capacities. Based on the results of the comparison study, adsorption tests were further continued with PHO-CNF<sub>1.00</sub>.

#### *Characterization of PHO-CNF<sub>1.00</sub> after adsorption*

In batch adsorption experiments, we observed gelling of the nanocellulose at high initial uranium concentrations, e.g. 500 mg/L (Fig. S1). Thus, the interaction of the fibrils with U(VI) was studied by SEM imaging of the PHO-CNF<sub>1.00</sub> after adsorption using given initial U(VI) concentrations (Fig. 4). It can be observed that the adsorption at initial uranium concentrations of 50 and 100 mg/L did not affect the fibrillar morphology and thus the colloidal stability of PHO-CNF<sub>1.00</sub>. However, an initial concentration of 250 mg/L led to the formation of sheet-like structures, and at 500 mg/L, also precipitate-like material was observed. In order to gain more insights on the formation of these structures, TEM images from samples that used an initial U(VI) concentration of 100 mg/L were taken after adsorption with PHO-CNF<sub>1.00</sub> (Fig. 5). The onset of aggregation can be observed in the images, as evidenced by the formation of fibril bundles, ultimately converging to sheet-like structures. It has been reported that due to the linear geometry of uranyl ion, sheet-like or chain-like structures can form upon complexation (Hu et al. 2018). The individual fibrils observed in the images were surprisingly uniform in width, indicating uniform coverage of phosphoryl groups which led to a spatially homogeneous adsorption of U(VI). Distinctively, the width of the fibrils was measured to be  $15 \pm 2$  nm based on image analysis, which is larger than the width measured for the fibrils before adsorption ( $12 \pm 2$  nm).

These results indicate that crosslinking occurred between the fibrils and U(VI) at high initial U(VI) concentrations, which leads to aggregation of the fibrils. A similar gelling effect has been reported for

CNF containing anionic functional groups and reports are available on the hydrogelation of carboxylated CNF with monovalent ( $\text{Ag}^+$ ) (Dong et al. 2013a), divalent ( $\text{Ca}^{2+}$ ,  $\text{Zn}^{2+}$ ,  $\text{Cu}^{2+}$ ), and trivalent cations ( $\text{Al}^{3+}$  and  $\text{Fe}^{3+}$ ) (Dong et al. 2013b). Gelation was suspected to initiate from the screening of repulsive charges caused by cation-carboxylate interactions (Dong et al. 2013b). Moreover,  $\text{UO}_2^{2+}$  has been found to cause the gelation of TO-CNF. 150 mg/L was reported as the threshold concentration of  $\text{UO}_2^{2+}$  for gel formation in a 0.05 wt% CNF suspension (Ma et al. 2012). Formation of gels through ionic cross-linking has also been reported with TO-CNF and  $\text{Al}^{3+}$  cations (Masruchin et al. 2015). In this study, the gelling effect is likely due to the reduction of electrostatic repulsion between the nanofibers after the adsorption of U(VI).

Results of XPS analysis of PHO-CNF<sub>1.00</sub> after U(VI) adsorption (Fig. 6 and Table S4) confirmed the presence of uranium in its hexavalent state on the fibers, based on the position of the  $\text{U}4f_{7/2}$  peak ( $382.5 \pm 0.5$  eV) which was detected after adsorption from both 100 mg/L and 500 mg/L samples (Moulder et al. 1995). The XPS results are summarized in Table 1, where the amounts of phosphorous, sodium, and uranium were calculated in relation to the nominal surface cellulose content of the respective sample, in order to remove the effect of adventitious carbon from the results. The nominal surface cellulose content was calculated from the total carbon and the C–O component of  $\text{C}1s$ . The decrease in surface cellulose upon increasing uranium content is mainly due to the increase of adventitious carbon (Fig. 6 inset, C–C peak at 285 eV), indicating changes in the surface energy of cellulose surfaces (Johansson et al. 2011) upon uranium adsorption.

The amount of sodium, which is present as a counterion of phosphoryl groups in the PHO-CNF, was found to decrease as the amount of uranium increased, indicating the occurrence of ion exchange. The amount of phosphorous remained stable in 0 mg/L and 100 mg/L samples, and decreased slightly in the 500 mg/L sample. This is likely due to the increased coverage of uranium on the PHO-CNF<sub>1.00</sub>. High-resolution spectra of O 1s and U 4f with superimposed spectra from 100 to 500 mg/L samples are shown in Fig. S2. The similar shape of the superimposed U 4f spectra of 100 and 500 mg/L samples clearly indicates that uranium was adsorbed in both cases in a similar chemical form.

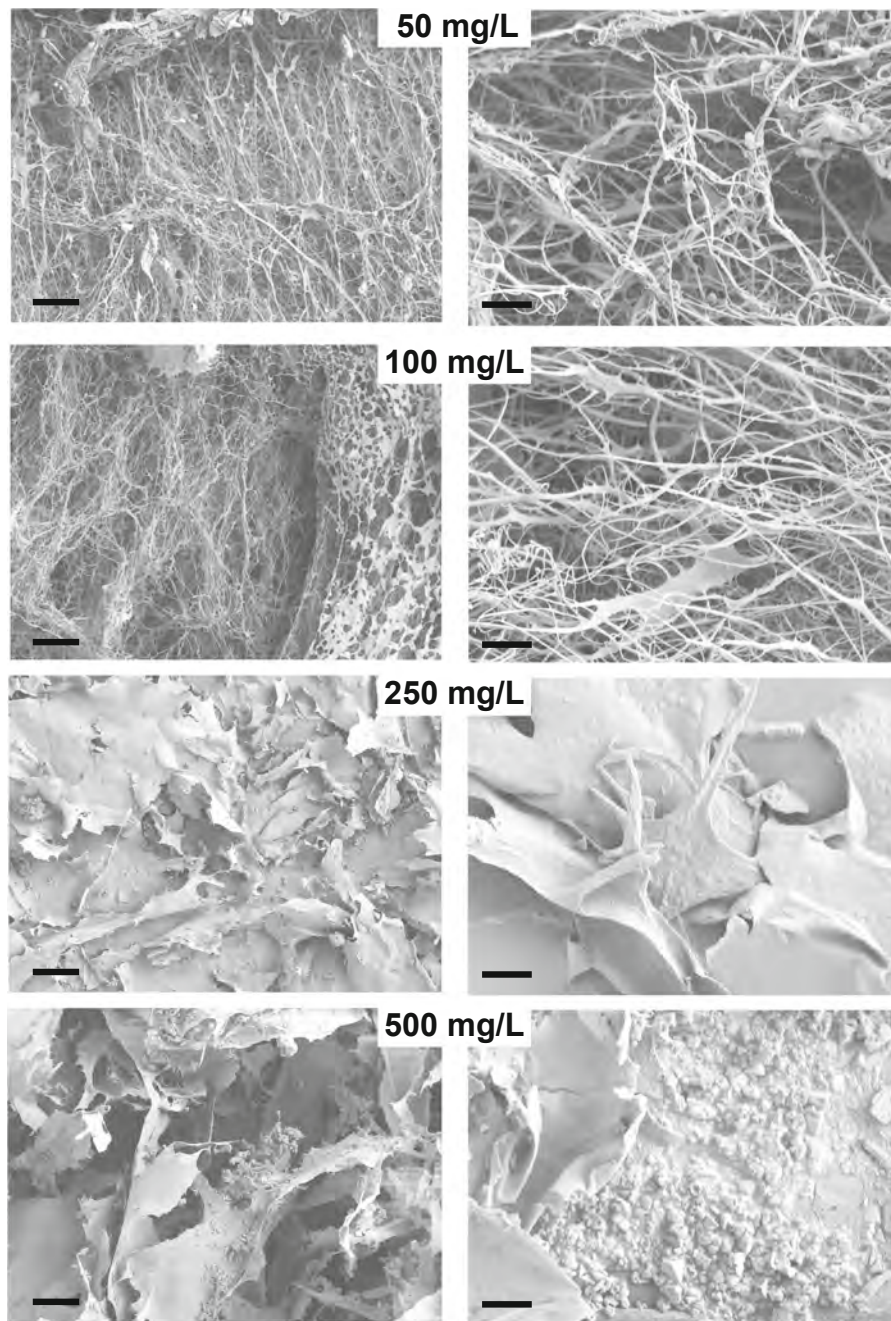


**Fig. 4** SEM images of PHO-CNF<sub>1.00</sub> after 1 h contact with solutions with initial U(VI) concentration of 50, 100, 250, and 500 mg/L. Scale bars are 20  $\mu\text{m}$  (left) and 3  $\mu\text{m}$  (right)

Apart from elemental information within the top-most few nanometers, XPS survey spectra also yield information on elemental depth distributions within the surface region (Tougaard 1998; Johansson et al. 2004). According to the background shapes of carbon,

oxygen, and uranium (see Fig. 6 and Fig. S2), it is clear that uranium species observed in both treated samples were present as islands or open films with similar thicknesses (at least 3–5 nm).



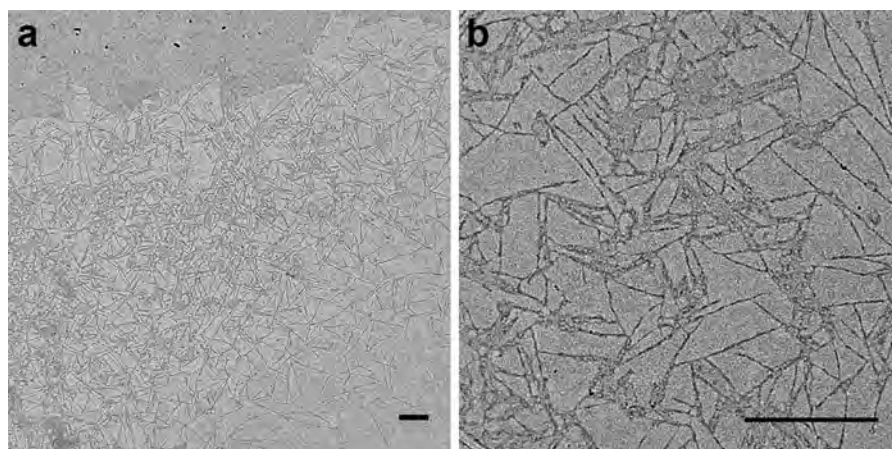


**Fig. 5** TEM images showing **a** overview and **b** magnified view of PHO-CNF<sub>1.00</sub> after adsorption of U(VI) from initial U(VI) concentration of 100 mg/L. The scale bars correspond to 1  $\mu$ m

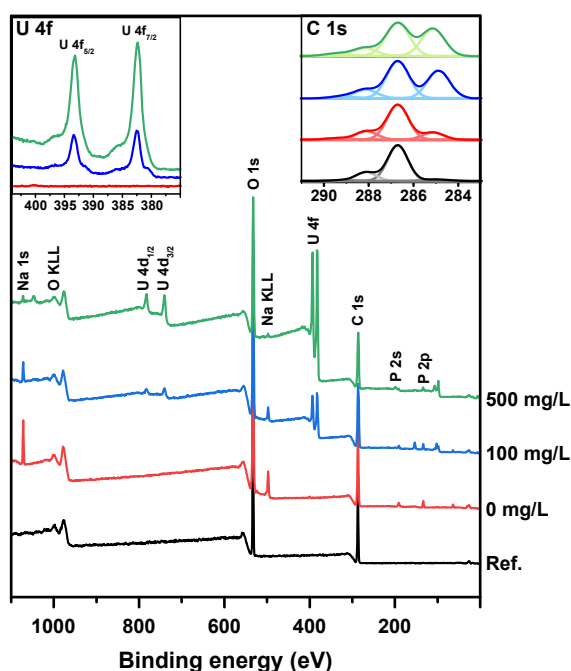


**Fig. 6** Survey spectra from XPS measurements of PHO-CNF<sub>1.00</sub> after U(VI) adsorption from initial concentrations of 0, 100, and 500 mg/L and the in situ cellulose reference sample. High-resolution U 4f and C 1s spectra are included in the insets, as indicated

#### Effect of pH on U(VI) adsorption

Both the adsorbent charge and the speciation of U(VI) are influenced by pH (Guo et al. 2018). The optimum pH for heavy metal adsorption is typically acidic, around 4–6. At around neutral pH and higher, heavy

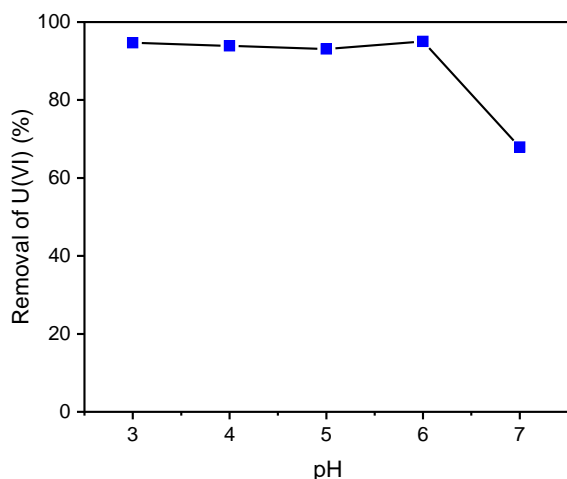
metals often tend to precipitate into hydroxides (Hokkanen et al. 2014). The removal of uranium did not vary significantly in the pH range 3–6, as shown in Fig. 7. However, when pH was increased to 7, a  $\sim 30\%$  reduction in the uranium removal was observed.  $\text{UO}_2^{2+}$  speciation is dependent on pH, temperature and composition of the water. At pH values below 5, uranium mainly exists as  $\text{UO}_2^{2+}$  in solution. At pH values between 5–7, neutral and anionic uranium species can also form in addition to cationic uranyl complexes (Aly and Hamza 2013). At  $\text{pH} > 6$ ,  $\text{UO}_2^{2+}$  forms complexes in the presence of carbonate causing reduction in U(VI) removal as reported for nanocrystalline titanium dioxide (Wazne et al. 2006) and iron oxyhydroxide (Wazne et al. 2003).

#### Adsorption capacity

In order to quantify the maximum adsorption capacity of PHO-NFC<sub>1.00</sub>, adsorption experiments were performed with varying initial U(VI) concentration. The results were fitted to the Langmuir, Freundlich, and Sips adsorption isotherm models (Fig. 8). As expected, the adsorbed uranium amount increases with the equilibrium concentration ( $C_e$ ) and eventually stabilizes at high  $C_e$  values. Table S5 shows the isotherm parameters calculated based on Eqs. (3), (4), and (5). Based on the  $R^2$  values, the Sips isotherm was found to fit best with the experimental data. This model is, in fact, a combination of the Langmuir and Freundlich isotherms. The Langmuir isotherm

**Table 1** Summary of XPS results

Sample	Nominal surface cellulose content (%)	P (at%) in relation to cellulose content (%)	Na (at%) in relation to cellulose content (%)	U (at%) in relation to cellulose content (%)
Reference Whatman paper	98	0.0	0.0	0.0
0 mg/L	77	4.1	3.2	0.0
100 mg/L	60	4.1	1.9	2.0
500 mg/L	57	3.3	0.6	6.8

**Fig. 7** Effect of pH on U(VI) removal with PHO-CNF<sub>1.00</sub>

assumes monolayer adsorption with a homogeneous surface while the Freundlich isotherm takes into account multilayer adsorption on heterogeneous surfaces (Lombardo and Thielemans 2019). However, in practical terms, the isotherm models do not fully reveal the actual mechanisms of adsorption.

Table 2 presents  $q_{max}$  values of uranium for adsorbents based on different cellulose nanomaterials or phosphorylated biomaterials. Typical maximum adsorption capacities reported for uranium are between 100 and 1000 mg/g. In addition to the high selectivity of the phosphoryl groups to U(VI), the high adsorption capacity achieved in this study is attributed to the high surface area provided by the nanosized fibrils and surface charge density of the PHO-CNF<sub>1.00</sub>.

An estimation of the theoretical maximum adsorption capacity of PHO-CNF<sub>1.00</sub> at pH 6 can be made assuming that all the U(VI) in the solution occurs as  $(\text{UO}_2)_3(\text{OH})_5^+$  species. This is reasonable since according to the speciation analysis presented in Table S2,

96% of the uranium is in this form. Considering a coordination ratio of 2:1 between this species and phosphoryl groups, the maximum adsorption capacity of the PHO-CNF<sub>1.00</sub> is calculated to be 1430 mg/g, which is very close to the value derived from the Sips isotherm based on the experimental data (1550 mg/g). Taken any uncertainty on the speciation and the exact form of adsorbed uranium, the results indicate extensive capturing of uranium by PHO-CNF.

### Selectivity

Figure 9 shows the selectivity of PHO-CNF<sub>1.00</sub> to U(VI) compared to selected divalent metals (Cu, Zn, and Mn) in the presence of other ions typically present in natural waters (Table S1). The removal percentages were found to be in the order of  $\text{U} > \text{Cu} > \text{Zn} > \text{Mn}$  with 5 mg PHO-CNF<sub>1.00</sub>, corresponding to a metal/adsorbent weight ratio of 0.03. When the amount of CNF was decreased, at a metal/adsorbent weight ratio of 0.6, the selectivity of the PHO-CNF<sub>1.00</sub> to U(VI) is clearly demonstrated. The results also indicate that high removal rates for uranium could be achieved with PHO-CNF<sub>1.00</sub> in the presence of competing divalent ions at similar concentrations. Another interesting observation from the results is that the removal of U(VI) increased from 95 to 99% in the presence of competing ions when the initial uranium concentration was 10 mg/L. A similar result has been reported for uranium removal by magnesium ferrite loaded carbon nanosheets (Li et al. 2019). The removal percentage achieved here is comparable to the high removal efficiency reported for uranyl acetate using an amyloid-carbon membrane (99.35%) (Bolisetty and Mezzenga 2016).

The selectivity of PHO-CNF<sub>1.00</sub> to U(VI) can be explained by the high affinity of the phosphoryl groups

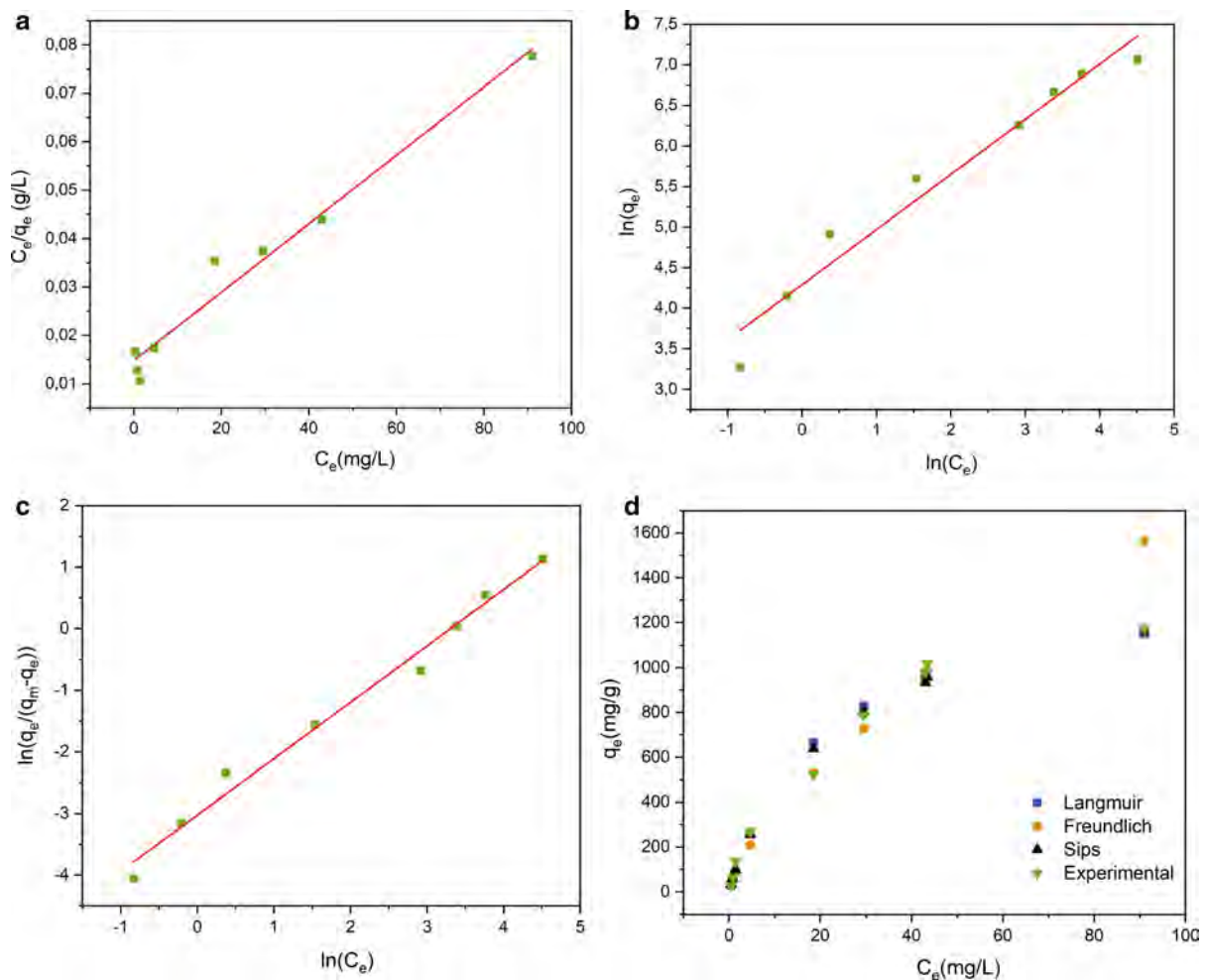


**Fig. 8** Effect of initial concentration of U(VI) on adsorption. Adsorption data fitted to **a** Langmuir isotherm, **b** Freundlich isotherm, and **c** Sips isotherm. **d** Adsorption data for PHO-CNF<sub>1.00</sub> compared to the theoretical Langmuir, Freundlich, and Sips isotherm models

**Table 2** Maximum adsorption capacity of uranium on different organic adsorbents

Adsorbent	$q_{\max}$ (mg/g)	References
TEMPO CNF	167 (at pH 6.5)	Ma et al. (2012)
Phosphorylated cactus fibers	107 (at pH 4.5)	Prodromou and Pashalidis (2013)
Phosphorylated chitosan	55 (pH not reported)	Morsy (2015)
Carboxycellulose nanofibers	1467 (at pH 7)	Sharma et al. (2017)
Phosphorylated GO-chitosan	779 (at pH 5)	Cai et al. (2017)
Phosphorylated chitosan CMC	978 (at pH 5)	Cai et al. (2019)
Phosphorylated CNF	1550 (at pH 6)	This work

to uranium. Based on the XPS and batch adsorption studies, it is proposed that the phosphoryl groups play a significant role in the adsorption process. Other factors that can contribute to the high selectivity are the high oxidation state, charge-to-radius ratio and the

likelihood of U(VI) to hydrolyze, since solid surfaces typically have a higher affinity to the hydrolyzed species (Cai et al. 2019). Mesoporous silica with phosphonic groups has been found to have high selectivity to uranium against interfering elements



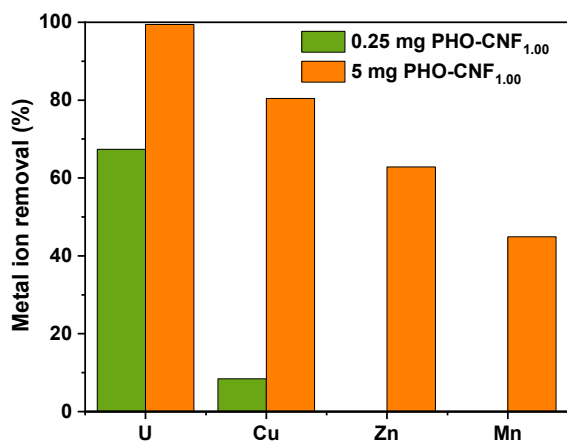


**Fig. 9** Selectivity of PHO-CNF<sub>1.00</sub> to U(VI). Removal of heavy metals by PHO-CNF<sub>1.00</sub> was studied from solutions containing U, Cu, Zn, and Mn (initial concentrations were 10 mg/L)

such as As, K Ni, Mo, Cu, and Pb (Sarafriz et al. 2017). High selectivity of phosphate-functionalized polyethylene towards uranium compared to Cu<sup>2+</sup>, Al<sup>3+</sup>, Fe<sup>3+</sup>, and V<sup>4+</sup> has also been reported (Shao et al. 2017).

## Conclusions

This work demonstrates that PHO-CNF can efficiently remove U(VI) from aqueous solutions with an unprecedented maximum bioadsorption capacity of 1550 mg/g. Over 90% removal of U(VI) was achieved in a pH range of 3–6. The efficiency of PHO-CNF can be attributed to the high surface area, anionic charge and the affinity of the phosphoryl groups to U(VI). The morphology of the substrates was studied after adsorption by SEM, TEM, and XPS, which indicated that U(VI) forms sheet-like aggregates with PHO-CNF at high initial U(VI) concentrations. The high selectivity of the PHO-CNF against other metals and ions present in natural waters is demonstrated, which is critical in application of the material for U(VI) removal. Overall, this study shows that PHO-NFC has great potential as an environmentally friendly bioadsorbent for U(VI) removal from highly contaminated waters.

**Acknowledgments** Open access funding provided by Aalto University. The Academy of Finland Center of Excellence on Molecular Engineering of Biosynthetic Hybrid Materials

Research (HYBER) and the H2020-ERC-2017-Advanced Grant “BioELCell” (788489) are acknowledged for funding this work. We are also grateful for support of the FinnCERES Materials Bioeconomy Ecosystem. Dr. Joseph Campbell is acknowledged for the XPS measurements. The facilities and technical assistance of Aalto University’s OtaNano Nanomicroscopy center (Aalto-NMC) are gratefully acknowledged.

**Open Access** This article is licensed under a Creative Commons Attribution 4.0 International License, which permits use, sharing, adaptation, distribution and reproduction in any medium or format, as long as you give appropriate credit to the original author(s) and the source, provide a link to the Creative Commons licence, and indicate if changes were made. The images or other third party material in this article are included in the article’s Creative Commons licence, unless indicated otherwise in a credit line to the material. If material is not included in the article’s Creative Commons licence and your intended use is not permitted by statutory regulation or exceeds the permitted use, you will need to obtain permission directly from the copyright holder. To view a copy of this licence, visit <http://creativecommons.org/licenses/by/4.0/>.

## References

- Aly MM, Hamza MF (2013) A review: studies on uranium removal using different techniques: overview. *J Disper Sci Technol* 34:182–213. <https://doi.org/10.1080/01932691.2012.657954>
- Asikainen A, Kahlos H (1979) Anomalous high concentrations of uranium, radium and radon in water from drilled wells in the Helsinki region. *Geochim Cosmochim Acta* 43:1681–1686. [https://doi.org/10.1016/0016-7037\(79\)90187-X](https://doi.org/10.1016/0016-7037(79)90187-X)
- Beamson G, Briggs D (1992) High resolution XPS of organic polymers. In: *The Scienta ESCA 300 Database*. Wiley, Chichester, p 56
- Berto S, Crea F, Daniele PG, Gianguzza A, Pettignano A, Sammartano S (2012) Advances in the investigation of dioxouranium(VI) complexes of interest for natural fluids. *Coord Chem Rev* 256:63–81. <https://doi.org/10.1016/j.ccr.2011.08.015>
- Bethke K, Palantöken S, Andrei V, Roß M, Raghuvanshi VS, Kettemann F, Greis K, Ingber TTK, Stückrath JB, Valiyaveetil S, Rademann K (2018) Functionalized cellulose for water purification, antimicrobial applications, and sensors. *Adv Funct Mater* 28(1800409):1–14. <https://doi.org/10.1002/adfm.201800409>
- Bolisetty S, Mezzenga R (2016) Amyloid-carbon hybrid membranes for universal water purification. *Nat Nanotechnol* 11:365–372. <https://doi.org/10.1038/NNANO.2015.310>
- Božič M, Liu P, Mathew AP, Kokol V (2014) Enzymatic phosphorylation of cellulose nanofibers to new highly-ions adsorbing, flame-retardant and hydroxyapatite-growth induced natural nanoparticles. *Cellulose* 21:2713–2726. <https://doi.org/10.1007/s10570-014-0281-8>

- Bykov GL, Ershov BG (2009) Sorption of uranyl ions on phosphorylated lignin. *Radiochemistry* 51:292–294. <https://doi.org/10.1134/S1066362209030138>
- Cai Y, Wu C, Liu Z, Zhang L, Chen L, Wang J, Wang X, Yang S, Wang S (2017) Fabrication of a phosphorylated graphene oxide-chitosan composite for highly effective and selective capture of U(VI). *Environ Sci Nano* 4:1876–1886. <https://doi.org/10.1039/c7en00412e>
- Cai Y, Chen L, Yang S, Xu L, Qin H, Liu Z, Chen L, Wang X, Wang S (2019) Rational synthesis of novel phosphorylated chitosan-carboxymethyl cellulose composite for highly effective decontamination of U(VI). *ACS Sustain Chem Eng* 7:5393–5403. <https://doi.org/10.1021/acssuschemeng.8b06416>
- Chen H, Wang Y, Zhao W, Xiong G, Cao X, Dai Y, Le Z, Zhang Z, Liu Y (2017) Phosphorylation of graphene oxide to improve adsorption of U(VI) from aqueous solutions. *J Radioanal Nucl Chem* 313:175–189. <https://doi.org/10.1007/s10967-017-5274-2>
- Dong H, Snyder JF, Tran DT, Leadore JL (2013a) Hydrogel, aerogel and film of cellulose nanofibrils functionalized with silver nanoparticles. *Carbohydr Polym* 95:760–767. <https://doi.org/10.1016/j.carbpol.2013.03.041>
- Dong H, Snyder JF, Williams KS, Andzelm JW (2013b) Cation-induced hydrogels of cellulose nano fibrils with tunable moduli. *Biomacromolecules* 14:3338–3345. <https://doi.org/10.1021/bm400993f>
- Ghasemi Torkabad M, Keshtkar AR, Safdari SJ (2017) Comparison of polyethersulfone and polyamide nanofiltration membranes for uranium removal from aqueous solution. *Prog Nucl Energy* 94:93–100. <https://doi.org/10.1016/j.pnucene.2016.10.005>
- Guo X, Feng Y, Ma L, Yu J, Jing J, Gao D, Khan AS, Gong H, Zhang Y (2018) Uranyl ion adsorption studies on synthesized phosphoryl functionalised MWCNTs: a mechanistic approach. *J Radioanal Nucl Chem* 316:397–409. <https://doi.org/10.1007/s10967-018-5761-0>
- Hokkanen S, Repo E, Suopajarvi T, Liimatainen H, Niinimaa J, Sillanpää M (2014) Adsorption of Ni(II), Cu(II) and Cd(II) from aqueous solutions by amino modified nanostructured microfibrillated cellulose. *Cellulose* 21:1471–1487. <https://doi.org/10.1007/s10570-014-0240-4>
- Hu F, Di Z, Lin P, Huang P, Wu M, Jiang F, Hong M (2018) An anionic uranium-base metal-organic framework with ultralarge nanocages for selective dye adsorption. *Cryst Growth Des* 18:576–580. <https://doi.org/10.1021/acs.cgd.7b01525>
- Johansson L-S, Campbell J (2004) Reproducible XPS on biopolymers: cellulose studies. *Surf Int Anal* 36:1018–1022. <https://doi.org/10.1002/sia.1827>
- Johansson L-S, Campbell J, Koljonen K, Kleen M, Buchert J (2004) On surface distributions in natural cellulosic fibres. *Surf Int Anal* 36:706–710. <https://doi.org/10.1002/sia.1741>
- Johansson L-S, Tammelinn T, Campbell JM, Setälä H, Österberg M (2011) Experimental evidence on medium driven cellulose surface adaptation demonstrated using nanofibrillated cellulose. *Soft Matter* 7:10917–10924. <https://doi.org/10.1039/C1SM06073B>
- Kapnisti M, Noli F, Misaelides P, Vourlias G, Karfaridis D, Hatzidimitriou A (2018) Enhanced sorption capacities for lead and uranium using titanium phosphates; sorption, kinetics, equilibrium studies and mechanism implication. *Chem Eng J* 342:184–195. <https://doi.org/10.1016/j.cej.2018.02.066>
- Khan MH, Warwick P, Evans N (2006) Spectrophotometric determination of uranium with arsenazo-III in perchloric acid. *Chemosphere* 63:1165–1169. <https://doi.org/10.1016/j.chemosphere.2005.09.060>
- Klemm D, Cranston ED, Fischer D, Gama M, Kedzior SA, Kralisch D, Kramer F, Kondo T, Lindström T, Nietzsche S, Petzold-Welcke K, Rauchfuß F (2018) Nanocellulose as a natural source for groundbreaking applications in materials science: today's state. *Mater Today* 21:720–748. <https://doi.org/10.1016/j.mattod.2018.02.001>
- Li X, Li Y, Wu Q, Zhang M, Guo X, Li X, Ma L, Li S (2019) Ultrahigh uranium uptake by magnetic magnesium ferrite loaded hydrothermal carbon nanosheets under acidic condition. *Chem Eng J* 365:70–79. <https://doi.org/10.1016/j.cej.2019.02.002>
- Liu P, Borrell PF, Božić M, Kokol V, Oksman K, Mathew AJ (2015a) Nanocelluloses and their phosphorylated derivatives for selective adsorption of Ag<sup>+</sup>, Cu<sup>2+</sup> and Fe<sup>3+</sup> from industrial effluents. *J Hazard Mater* 294:177–185. <https://doi.org/10.1016/j.jhazmat.2015.04.001>
- Liu X, Li J, Wang X, Chen C, Wang X (2015b) High performance of phosphate-functionalized graphene oxide for the selective adsorption of U(VI) from acidic solution. *J Nucl Mater* 466:56–64. <https://doi.org/10.1016/j.jnucmat.2015.07.027>
- Lombardo S, Thielemans W (2019) Thermodynamics of adsorption on nanocellulose surfaces. *Cellulose* 26:249–279. <https://doi.org/10.1007/s10570-018-02239-2>
- Ma H, Hsiao BS, Chu B (2012) Ultrafine cellulose nanofibers as efficient adsorbents for removal of UO<sub>2</sub><sup>2+</sup> in water. *ACS Macro Lett* 1:213–216. <https://doi.org/10.1021/mz200047q>
- Masruchin N, Park B, Causin V, Um IC (2015) Characteristics of TEMPO-oxidized cellulose fibril-based hydrogels induced by cationic ions and their properties. *Cellulose* 22:1993–2010. <https://doi.org/10.1007/s10570-015-0624-0>
- Mautner A, Maples HA, Kobkeathawin T, Kokol V, Karim Z, Li K, Bismarck A (2016) Phosphorylated nanocellulose papers for copper adsorption from aqueous solutions. *Int J Environ Sci Technol* 13:1861–1872. <https://doi.org/10.1007/s13762-016-1026-z>
- Morsy AMA (2015) Adsorptive removal of uranium ions from liquid waste solutions by phosphorylated chitosan. *Environ Technol Innov* 4:299–310. <https://doi.org/10.1016/j.eti.2015.10.002>
- Moulder JF, Stickle WF, Sobol PE, Bomben KD (1995) Handbook of X-ray photoelectron spectroscopy: a reference book of standard spectra for identification and interpretation of XPS data. Perkin-Elmer Corp., Physical Electronics Division, Eden Prairie
- Prodromou M, Pashalidis I (2013) Uranium adsorption by non-treated and chemically modified cactus fibres in aqueous solutions. *J Radioanal Nucl Chem* 298:1587–1595. <https://doi.org/10.1007/s10967-013-2565-0>
- Rajala S, Siponkoski T, Sarlin E, Mettänen M, Vuoriluoto M, Pammo A, Juuti J, Rojas OJ, Franssila S, Tuukkanen S (2016) Cellulose nanofibril film as a piezoelectric sensor

- material. *ACS Appl Mater Interfaces* 8:15607–15614. <https://doi.org/10.1021/acsami.6b03597>
- Riegel M, Schlitt V (2017) Sorption dynamics of uranium onto anion exchangers. *Water* 9(268):1–17. <https://doi.org/10.3390/w9040268>
- Sakaguchi T, Horikoshi T, Nakajima A (1981) Adsorption of uranium by chitin phosphate and chitosan phosphate. *Agric Biol Chem* 45:2191–2195. <https://doi.org/10.1080/00021369.1981.10864862>
- Sankar MU, Aigal S, Maliyekkal SM, Chaudhary A, Anshup KA, Chaudhari K, Pradeep T (2013) Biopolymer-reinforced synthetic granular nanocomposites for affordable point-of-use water purification. *Proc Natl Acad Sci* 110:8459–8464. <https://doi.org/10.1073/pnas.1220222110>
- Sarafraz H, Minuchehr A, Alahyarizadeh G, Rahimi Z (2017) Synthesis of enhanced phosphonic functional groups mesoporous silica for uranium selective adsorption from aqueous solutions. *Sci Rep* 7:1–12. <https://doi.org/10.1038/s41598-017-11993-5>
- Shao D, Li Y, Wang X, Hu S, Wen J, Xiong J, Asiri AM, Marwani HM (2017) Phosphate-functionalized polyethylene with high adsorption of uranium(VI). *ACS Omega* 2:3267–3275. <https://doi.org/10.1021/acsomega.7b00375>
- Sharma PR, Chattopadhyay A, Sharma SK, Hsiao BS (2017) Efficient removal of  $\text{UO}_2^{2+}$  from water using carboxycellulose nanofibers prepared by the nitro-oxidation method. *Ind Eng Chem Res* 56:13885–13893. <https://doi.org/10.1021/acs.iecr.7b03659>
- Sirviö JA, Hasa T, Leiviskä T, Liimatainen H, Hormi O (2016) Bisphosphonate nanocellulose in the removal of vanadium(V) from water. *Cellulose* 23:689–697. <https://doi.org/10.1007/s10570-015-0819-4>
- Su S, Liu Q, Liu J, Zhang H, Li R, Jing X, Wang J (2018) Functionalized sugarcane bagasse for U(VI) adsorption from acid and alkaline conditions. *Sci Rep* 8:1–10. <https://doi.org/10.1038/s41598-017-18698-9>
- Suflet DM, Chitanu GC, Popa VI (2006) Phosphorylation of polysaccharides: new results on synthesis and characterisation of phosphorylated cellulose. *React Funct Polym* 66:1240–1249. <https://doi.org/10.1016/j.reactfunctpolym.2006.03.006>
- Sylwester ER, Hudson EA, Allen PG (2000) The structure of uranium(VI) sorption complexes on silica, alumina, and montmorillonite. *Geochim Cosmochim Acta* 64:2431–2438. [https://doi.org/10.1016/S0016-7037\(00\)00376-8](https://doi.org/10.1016/S0016-7037(00)00376-8)
- Tougaard S (1998) Accuracy of the non-destructive surface nanostructure quantification technique based on analysis of the XPS or AES peak shape. *Surf Int Anal* 24:249–269. [https://doi.org/10.1002/\(SICI\)1096-9918\(199804\)26:4<249::AID-SIA368>3.0.CO;2-A](https://doi.org/10.1002/(SICI)1096-9918(199804)26:4<249::AID-SIA368>3.0.CO;2-A)
- Um W, Mattigod S, Serne RJ, Fryxell GE, Kim DH, Troyer LD (2007) Synthesis of nanoporous zirconium oxophosphate and application for removal of U(VI). *Water Res* 41:3217–3226. <https://doi.org/10.1016/j.watres.2007.05.030>
- Voisin H, Bergström L, Liu P, Mathew AP (2017) Nanocellulose-based materials for water purification. *Nanomaterials* 7:57. <https://doi.org/10.3390/nano7030057>
- Wazne M, Korfiatis GP, Meng X (2003) Carbonate effects on hexavalent uranium adsorption by iron oxyhydroxide. *Environ Sci Technol* 37:3619–3624. <https://doi.org/10.1021/es034166m>
- Wazne M, Meng X, Korfiatis GP, Christodoulatos C (2006) Carbonate effects on hexavalent uranium removal from water by nanocrystalline titanium dioxide. *J Hazard Mater* 136:47–52. <https://doi.org/10.1016/j.jhazmat.2005.11.010>
- World Health Organization WHO (2011) Guidelines for drinking-water quality, 4th edn
- Xie Y, Chen C, Ren X, Wang X, Wang H, Wang X (2019) Emerging natural and tailored materials for uranium-contaminated water treatment and environmental remediation. *Prog Mater Sci* 103:180–234. <https://doi.org/10.1016/j.pmatsci.2019.01.005>
- Xue G, Feng Y, Ma L, Gao D, Jing J, Yu J, Sun H, Gong H, Zhang Y (2017) Phosphoryl functionalized mesoporous silica for uranium adsorption. *Appl Surf Sci* 402:53–60. <https://doi.org/10.1016/j.apsusc.2017.01.050>
- Yu XF, Liu YH, Zhou ZW, Xiong GX, Cao XH, Li M, Zhang ZB (2014) Adsorptive removal of U(VI) from aqueous solution by hydrothermal carbon spheres with phosphate group. *J Radioanal Nucl Chem* 300:1235–1244. <https://doi.org/10.1007/s10967-014-3081-6>
- Zhou L, Huang Z, Luo T, Jia Y, Liu Z, Adesina AA (2015) Biosorption of uranium(VI) from aqueous solution using phosphate-modified pine wood sawdust. *J Radioanal Nucl Chem* 303:1917–1925. <https://doi.org/10.1007/s10967-014-3725-6>

**Publisher's Note** Springer Nature remains neutral with regard to jurisdictional claims in published maps and institutional affiliations.

## Supporting information

### Phosphorylated cellulose nanofibers exhibit exceptional capacity for uranium capture

Janika Lehtonen<sup>a</sup>, Jukka Hassinen<sup>b,\*</sup>, Avula Anil Kumar<sup>c</sup>, Roni Mäenpää<sup>b</sup>, Leena-Sisko Johansson<sup>a</sup>, Nikolaos Pahimanolis<sup>d</sup>, Thalappil Pradeep<sup>c</sup>, Olli Ikkala<sup>b</sup>, Orlando J. Rojas<sup>a,c,\*</sup>

<sup>a</sup> Department of Bioproducts and Biosystems, School of Chemical Engineering, Aalto University, P. O. Box 16300, FI-00076 Aalto, Espoo, Finland; <sup>b</sup> Department of Applied Physics, School of Science, Aalto University, P. O. Box 16300, FI-00076 Aalto, Espoo, Finland; <sup>c</sup> DST Unit of Nanoscience (DST UNS) and Thematic Unit of Excellence (TUE), Department of Chemistry, Indian Institute of Technology Madras, Chennai 600036, India; <sup>d</sup> Betulium Ltd., Tekniikantie 2, FI-02150, Espoo, Finland. <sup>e</sup> Departments of Chemical & Biological Engineering, Chemistry and, Wood Science, 2360 East Mall, The University of British Columbia, Vancouver, BC V6T 1Z3, Canada.

e-mail: [orlando.rojas@aalto.fi](mailto:orlando.rojas@aalto.fi)

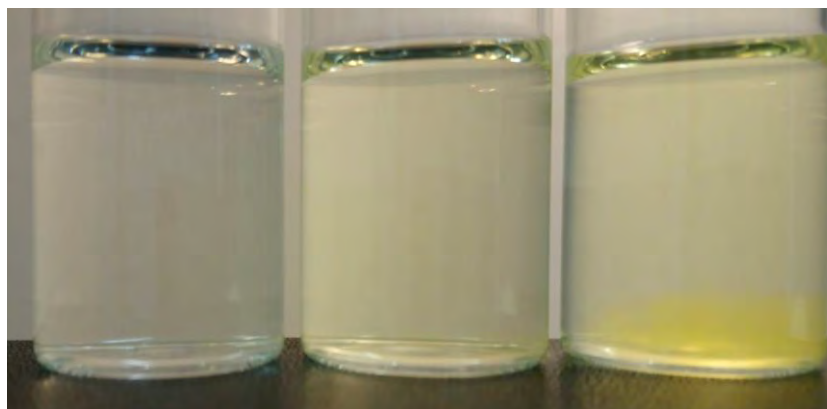


**Fig. S1.** Gelling of PHO-CNF<sub>1.00</sub> as initial uranium concentration increases. The photos were taken after 1 h contact of PHO-CNF<sub>1.00</sub> with uranium solutions of initial concentrations of 100, 300 and 500 mg/L (vials from left to right, respectively)

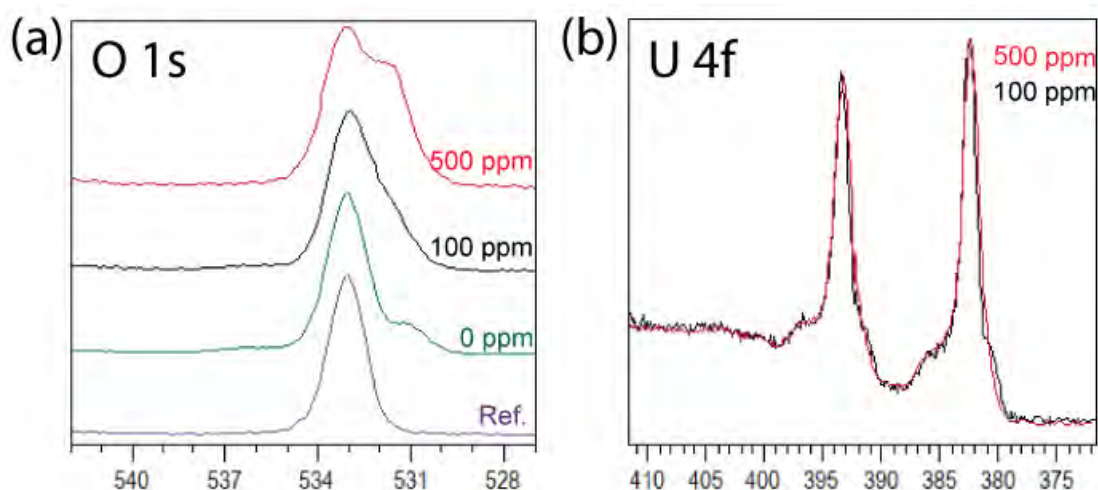


**Fig. S2.** High-resolution XPS spectra of (a) oxygen for PHO-CNF<sub>1.00</sub> samples with initial U(VI) concentrations of 0, 100 and 500 mg/L and for the in situ cellulose reference and (b) uranium for PHO-CNF<sub>1.00</sub> samples with initial U(VI) concentrations of 100 and 500 mg/L

**Table S1.** The ionic composition of water used for selectivity studies

Ion	mg/L
Cl <sup>-</sup>	89
SO <sub>4</sub> <sup>2-</sup>	33
NO <sub>3</sub> <sup>-</sup>	1.8
Carbonates	54
Na <sup>+</sup>	46
Mg <sup>2+</sup>	8.3
K <sup>+</sup>	1.2
Ca <sup>2+</sup>	28

**Table S2.** Uranyl speciation with initial uranium concentration of 100 mg/L at pH 3-7

	pH 3		pH 4		pH 5		pH 6		pH 7	
	<i>m</i> (mol/kg)	%*	<i>m</i> (mol/kg)	%*	<i>m</i> (mol/kg)	%*	<i>m</i> (mol/kg)	%*	<i>m</i> (mol/kg)	%*
(UO <sub>2</sub> ) <sub>3</sub> (OH) <sub>5</sub> <sup>+</sup>	1.21E-11	0.00	8.03E-07	0.57	1.04E-04	73.96	1.38E-04	98.60	1.40E-04	99.88
(UO <sub>2</sub> ) <sub>2</sub> (OH) <sub>2</sub> <sup>+2</sup>	4.00E-07	0.19	2.95E-05	14.04	3.39E-05	16.12	1.97E-06	0.94	8.93E-08	0.04
UO <sub>2</sub> OH <sup>+</sup>	4.70E-07	0.11	4.07E-06	0.97	4.40E-06	1.05	1.05E-06	0.25	2.26E-07	0.05
UO <sub>2</sub> <sup>+2</sup>	4.19E-04	99.69	3.55E-04	84.41	3.74E-05	8.90	9.19E-07	0.22	1.92E-08	0.00

\* Percent of total uranium in the indicated form

**Table S3.** Uranyl speciation in simulated drinking water at pH 6

	<i>m</i> (mol/kg)	%*
$(\text{UO}_2)_3(\text{OH})_5^+$	8.40E-06	53.10
$\text{UO}_2\text{CO}_3$	1.56E-05	32.88
$\text{UO}_2(\text{CO}_3)_2^{-2}$	4.89E-06	10.31
$(\text{UO}_2)_2(\text{OH})_2^{+2}$	3.89E-07	1.64
$\text{UO}_2^{+2}$	4.64E-07	0.98
$\text{UO}_2\text{OH}^+$	4.14E-07	0.87
$\text{UO}_2\text{SO}_4$	1.09E-07	0.23
$\text{UO}_2(\text{CO}_3)_3^{-4}$	9.07E-09	0.02

\* Percent of total uranium in the indicated form

**Table S4.** XPS surface elemental concentrations, in at-%

Sample	C 1s	O 1s	U 4f <sub>7/2</sub>	Na 1s	P 2p	Si 2s
Whatman	59.2	40.8	b.d.l.	b.d.l.	b.d.l.	b.d.l.
0 ppm	52.8	41.0	b.d.l.	2.5	3.2	0.6
100 ppm	53.8	36.8	1.2	1.1	2.5	4.6
500 ppm	55.1	37.9	3.8	0.3	1.9	0.9

**Table S5.** Langmuir, Freundlich and Sips isotherm parameters

<b>Langmuir</b>	$q_m$ (mg/g)	1413
	$K_L$ (L/g)	0.048
	$R^2$	0.972
<b>Freundlich</b>	$K_F$ (mg/g)	72.86
	$n$	1.47
	$R^2$	0.962
<b>Sips</b>	$q_m$ (mg/g)	1550
	$n$	1.09
	$K_s$ (L/mg)	0.0485
	$R^2$	0.986



# Lectures delivered

## Offline lectures

1. Nanomaterials to clean water: Science, technology and industry, PSG College of Technology, Coimbatore, January 9, 2020.
2. Nanoparticles with atomic precision, international conference on advances in chemistry with specific reference to catalysis, sensors, drug delivery and energy materials (ICACSEM – 2020), University of Madras, January 9-10, 2020.
3. Atomically precise nanoparticles, Biodesign Institute, Arizona State University, Tempe, February 7, 2020.
4. Reactions of clusters, Gordon Research Conference on Atomically Precise Nanochemistry, February 9-14, 2020.
5. Atom exchange in nanoparticles, Department of Chemistry, Purdue University, February 17, 2020.
6. Affordable clean water using advanced materials, Brick Nanotechnology Centre, Purdue University, February 18, 2020.
7. Affordable clean water using advanced materials, DWWS, Government of Punjab, February 27, 2020.
8. Nanoparticles are molecules, ICONSAT Kolkata, March 5, 2020.

## Online lectures (Virtual)

9. Nanoparticles are molecules, ACS Virtual Talk: Science Lecture Series, April 9, 2020.
10. Advanced Nanomaterials- emerging opportunities, HPCL, April 16, 2020.
11. Innovations in academic institutions during and after the pandemic, National Technology Day Lecture, CSIR-IITR, Lucknow, May 11, 2020.
12. Clean water: How can science make a difference? IIT Madras, May 15, 2020.
13. Doing science with roots intact, St. Thomas College, Thrissur, May 25, 2020.
14. Clean water through nanotechnology, UKIERI SPARC Webinars, June 24, 2020.

15. Clean water using nanotechnology: Current status, 2nd International Symposium on Functional Nanomaterials in Industrial and Clinical Applications, University of Central Lancashire, July 14-16, 2020.
16. New Molecules, IIT Tirupati, Welcoming the first batch of M.Sc. students, August 31, 2020.
17. Chemistry for clean air, blue skies and clean water, International Day of Clean Air for blue skies, Govt. Madhav Science P. G. College Ujjain (M.P.), September 7, 2020.
18. Atom exchange in nanoparticles, Manipal Academy of Higher Education, September 26, 2020.
19. Affordable Excellence: Doing Science in Indian Universities, University of Calicut, September 28, 2020.
20. Affordable Excellence: Doing Science in India, IISER Bhopal, October 16, 2020.
21. How to build academic – industry linkage in colleges, Farook College, October 22, 2020.
22. Nanoparticles are molecules, IIT Jammu, October 23, 2020.
23. Future of our universities, 11<sup>th</sup> P. T. Bhaskara Panicker Memorial Lecture, 57<sup>th</sup> KSSP Annual Meet, October 22-26, 2020.
24. Clean water using nanotechnology: Science, technology and entrepreneurship, BESE Student-led seminar series, King Abdullah University of Science and Technology, October 28, 2020.
25. Atomically precise clusters, National Chemistry Week Lecture, CRSI NE Chapter, November 4, 2020.
26. Clean water using nanotechnology, EFCS 2020, Farook College, December 4-5, 2020.
27. Harvesting humidity for clean water, National Water Mission, Technology Talk, Ministry of Jal Shakti, December 11, 2020.

# Patents/Technology

## Indian patents (granted)

1. A method for preparing cellulose microstructures-templated nanocomposites with enhanced arsenic removal capacity, Thalappil Pradeep, Sritama Mukherjee, 201641044817, December 26, 2016, granted as patent no. 337979 on June 4, 2020.
2. Method for preparing crossed bilayer assembly of 1D nanowires using an atomically precise clusters, T. Pradeep, Anirban Som, Indranath Chakraborty and Tuhina Adit Maark, 6993/CHE/2015, December 28, 2015, granted as patent no. 340305 on July 3, 2020.
3. An enhanced carbon dioxide sorbent nanofiber membrane and a device thereof, T. Pradeep, Anangha Yatheendran, Ramesh Kumar and Arun Karthik, 201841031076, August 20, 2018, granted as patent no. 323314 on August 4, 2020.
4. Cellulose nanocrystal templated iron oxyhydroxide based adsorbent for arsenic removal from water and a device thereof, T. Pradeep, Avijit Baidya, Bibhuti Bhusan Rath and A. Anil Kumar, 201641027660, filed on August 12, 2016, granted as patent no. 343818 on August 10, 2020.
5. An integrated CDI electrode, T. Pradeep, Md. Rabiul Islam, Soujit Sengupta, Srikrishnarka Pillalamarri, 201741047400, filed on December 30, 2017, granted as patent no 345270 on August 27, 2020.
6. Methods of making alloys of precise composition in solution by inter-cluster reactions in solution, T. Pradeep, K. R. Krishnadas, Atanu Ghosh, Ananya Baksi, Indranath Chakrabarti and Ganapathy Natarajan, 6907/CHE/2015, filed on December 14, 2015, granted as patent no. 345596 on August 29, 2020.
7. Organic-templated-boehmite-nanoarchitecture: An adsorbent composition to remove arsenic and fluoride from drinking water, T. Pradeep, Shihabudheen M. Maliyekkal, Anshup, M. Udhaya Sankar and Amrita Chaudhary, 1529/CHE/2010, granted as patent no 346000 on September 3, 2020.
8. Chitosan reinforced mixed oxide nanocomposite for fluoride removal from water and a device thereof, T. Pradeep, Anil Kumar Avula, Bibhuti Bhusan Rath, filed as application number 201641045048, December 30, 2016, granted as patent no. 354374 on December 23, 2020.

9. Multilayer multifunctional nasal filter by T. Pradeep, Arun Karthick, Pillalamarri Srikrishnarka, Vishal Kumar, Sathvik Ajay Iyengar and Ramesh Kumar Soni, filed as application on March 2, 2017, granted as patent no. 351038 on November 6, 2020.

## Indian patents (applied)

1. A point-of-care (POC) amperometric device for selective arsenic sensing, Thalappil Pradeep, Sourav Kanti Jana, Kamalesh Chaudhari, 202041023576, June 5, 2020.
2. A smartphone based fluoride-specific sensor for rapid and affordable colorimetric detection and precise quantification at sub-ppm levels for field applications, Thalappil Pradeep, Sritama Mukerjee, Manav Shah and Kamalesh Chaudhari, 202041026054, June 20, 2020.
3. Method for selective extraction of gold by niacin, Thalappil Pradeep and Abhijit Nag, 202041047984, November 3, 2020.
4. Cluster-assisted antiviral medications, Thalappil Pradeep, G Velmurugan, Esma Khatun, Krishnan Swaminathan, S Krishnakumar, 202041012975, March 25, 2020.
5. Multi-charged nanodroplets of water for microbial disinfection, Thalappil Pradeep, Jenifer Shantha Kumar, Tripti Ahuja, Depanjan Sarkar, Pallab Basuri and Sandeep Bose, 202041015937, April 13, 2020.
6. Ambient microdroplet annealing method for converting polydispersed nanoparticles to their monodispersed analogues, Thalappil Pradeep, Angshuman Ray Chowdhuri, Spoorthi Bhat, 202041056735, December 28, 2020.

## PCT patents (applied)

1. URD-119/00US: Methods for coupling a carbon containing moiety to an amine containing moiety, PRF ref: 69066, R. G. Cooks, Thalappil Pradeep, Nicolas Mauricio Morato Gutierrez and Pallab Basuri, filed on May 26, 2020.
2. Method for creating nanopores in MoS<sub>2</sub> nanosheets by chemical drilling for disinfection of water under visible light. Thalappil Pradeep, Depanjan Sarkar, Anirban Som, Biswajit Mondal, Swathy Jakka Ravindran, US Patent App. 16/757411, November 30, 2020.

# Media reports

## THE HINDU

### Seven unique achievers bring laurels for State

N.R. Madhava Menon, father of modern Indian legal education, and spiritual Guru Sri M get Padma Bhushan

SPECIAL CORRESPONDENT  
THIRUVANANTHAPURAM

Seven Keralites whose achievements have remained relatively unsung have been conferred Padma awards on the occasion of Republic Day this year.

N.R. Madhava Menon, the father of modern Indian legal education, will be awarded Padma Bhushan posthumously. Spiritual guru Sri M is the other Keralites selected for Padma Bhushan this year.

Five other Keralites, including puppetry artist Moozhikkal Pankajakshi, social activist Sathyannarayanan Mundayoor, and botanist and taxonomist K.S. Manilal will be conferred with Padma Shri.

Born in Thiruvananthapuram, Madhava Menon was founder director of the National Law School of India University (NLSIU) and the National Judicial Academy, Bhopal. He was honoured



K.S. Manilal, N. Chandrasekharan Nair, Sathyannarayanan Mundayoor, M. Pankajakshi, Thalapiti Pradeep

with Padma Shri in 2003. Madhava Menon passed away in May 2019.

Hailing from Thiruvananthapuram, Sri M (M. Mumtaz Ali) heads the Satsang Foundation. Growing up listening to Sufi tales, Mumtaz Ali had embarked upon a spiritual quest. He later became the disciple of Maheshwaramath Babaji.

Mr. Manilal is the botanist who opened the monumental *Herbarium* to

English and Malayalam readers. He has discovered many new plant species.

#### M.C. Kunjil

The other Keralites selected for the Padma Shri are M. K. Kunjil (social work), N. Chandrasekharan Nair (literature and education), Sathyannarayanan Mundayoor and Moozhikkal Pankajakshi.

Mr. Chandrasekharan Nair is a noted Hindi scholar and founder of the Kerala Hindi

Sahitya Academy.

#### Sathyannarayanan

Mundayoor, aka Uncle Moosa from Thrissur, has been recognised for developing libraries as part of a social movement in Arunachal Pradesh. Mr. Mundayoor, who reached Arunachal Pradesh in 1979 at the age of 25 as a 'life worker' for the Vivekananda Kendra, opened schools to educate tribal chil-

dren. He went from 'life worker' to a teacher and then an education officer. He took the name Uncle Moosa while writing a column for children in a local newspaper.

In 1998, he decided to place the school libraries of the Vivekananda Kendra in the midst of tribal communities. Tribal girls and boys discovered the joy of reading and also learnt to express themselves through storytelling, skits, and recitation.

#### Moozhikkal Pankajakshi

Moozhikkal Pankajakshi is the sole practitioner of a fading form of puppetry called Kolkvidiya Paava Kali. She has been balancing the entire Ramayana and Mahabharata on the tip of her lips for almost her entire life.

She had performed the art form, in which a stick puppet is balanced on the upper lip, for a living. Even after with-

drawing from the scene, the 81-year-old has kept the passion for the art alive.

Pankajakshi learnt it from her parents, who used to perform in houses and temples. She started training at the age of 12. Soon, she became the art form's sole exponent.

Assisted by her family, Pankajakshi has visited many places in the country and abroad, showcasing her unique art form.

Having lost her front teeth, which rendered her unable to balance the puppet, she stopped performing some six years ago.

The artist is recuperating from a massive stroke she suffered a few years ago.

An eighth Keralite, Thalapiti Pradeep, nanotechnology expert who works at IIT, Madras, in Tamil Nadu also gets Padma Shri.

SEE ALSO • PAGE 8

An article was published in The Hindu newspaper on 26th January 2020, congratulating Padma Shri awardees of 2020.

### Plight of doctoral students during the pandemic

T. Pradeep

May 30, 2020 07:39 pm IST

Updated: May 30, 2020 07:37 pm IST



Fallout: COVID-19 will take away at least six months from the productive life of PhD students.

*This crisis will most severely affect those who have just finished, or are finishing, their PhD degrees*

An article on the plight of the doctoral students during the COVID pandemic by Prof. T Pradeep was published in The Hindu. It was posted on 30th May 2020.



A short documentary titled 'Hawa se Pani' featured in History channel, YouTube. This documentary shows the capacitive deionization technology developed by our group.

VayuJal Technologies features in the HISTORY for its commendable OMG innovation.

VayuJal Technologies, a Startup initiative by Pradeep Thalappil, Ram... See More



An interview in Malayalam about 'Digital divide due to COVID pandemic' on Asianet news, 3<sup>rd</sup> June 2020.



# Providing safe drinking water is his mission

*In the last five years, five companies have been incubated, whose technologies are providing nearly 10 million people across India with clean drinking water.*

Published: 26th January 2020 05:50 AM | Last Updated: 26th January 2020 05:50 AM

CHENNAI: Over more than two decades, an IIT-Madras professor T Pradeep and his research group have systematically developed advanced yet affordable technologies to solve major water-related problems in the country.

His efforts were recognised by Union government, which bestowed Padma Shri, under Science and Engineering category. Over 450 papers have been published and 110-plus patents have been filed or granted. In the last five years, five companies have been incubated, whose technologies are providing nearly 10 million people across India with clean drinking water.

Pradeep told Express “I am happy that my team’s work has been recognised. Developing affordable and safe drinking water solutions using nanomaterials, from bench-scale science to commercial products, creating knowledge, technology and wealth for social good simultaneously was very satisfying.

We have demonstrated that completely home-grown nanotechnology, from excellent science to relevant technology is possible in our institutions, with limited resources available from research grants, in the process transforming students to entrepreneurs.”

An article on providing affordable and safe drinking water using nanomaterials was published in The New Indian Express on 26th of January, 2020.

## Covid: Lockdown leaves research scholars in a lurch

T. SUDHEESH | DC  
CHENNAI, JULY 7

While Covid is spreading its tentacles, forcing governments to come up with relief packages for various sectors in the society to save life and livelihood, the struggle of the young research community in various institutions in the country continues to be unheard by the authorities.

Highlighting the plight of research scholars, Rohit Jhunjhunwala, a research scholar with Indian Institute of Technology-Madras (IIT-M), has started an online petition campaign a couple of days back, grabbing the eyeballs of over 2,000 research scholars across the country.

The petition has requested the Ministry of Human Resource Development (MHRD) for an extension of the research period as well as the fellowship to all scholars as their works are affected by the pandemic and subsequent lockdowns.

"Due to the lockdown, all institutes were shut down and the scholars had been asked to vacate the campus in March 2020. Due to the urgency and short duration of the notice by institute authorities, scholars left their valuables, laptops and research notes behind in

the hope that they would be able to return soon and restart their research.

"The educational institutes remained shut making scholars unable to access the research infrastructures. This has resulted in a lot of anxiety among scholars about the status of their research work, experiments and the expiry of their fellowship.

All experimental setups have already been degraded or unusable due to the long delay. The fellowships of scholars have expired in the middle of the lockdown leaving them without any means to survive. The financial pressure is a huge mental stress for us along with health and future uncertainties," the petition says.

As per the procedure, it takes five years to finish a PhD degree in institutions. During the research period, a doctoral fellow in a national institution will get a fellowship of Rs 31,000 per month for the first two years and Rs 35,000 per month for the remaining three years or till they submit their theses, whichever is earlier.

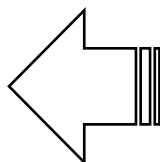
T. Pradeep, professor, the department of chemistry at IIT-M, told Deccan Chronicle that the MHRD should extend the tenure of research by at least six months along with the fel-

lowship.

The pandemic has created an unprecedented situation in the education sector especially among the research community. Many who had been pursuing research programmes abroad have now returned without completing their work. They do not have new assignments, and even if they do, there is no way to proceed with them. They too remain unpaid.

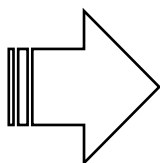
Research fellows after completing the PhD programme often go for post-doctoral fellowships (PDF) for higher studies and independent research. Many of them are now stuck even if they have postdoctoral offers. They have no support from parent laboratories as institutional resources are limited.

In order to deal with the situation, the government must announce a package of Rs 200 crores to help the young scientific community. In addition to this, the MHRD must fast-track the filling up of scientist posts vacant in various institutions. "The government has also to come up with the decision to create favourable atmosphere in research institutes lifting the restriction imposed due to the pandemic," said Prof Pradeep



An article published in Deccan Chronicle on 7<sup>th</sup> of July, 2020.

An article in Times of India where Prof. T. Pradeep expresses his views on the importance of interdisciplinary research, was published on the 13th of August, 2020.



## Chemistry has become central to every discipline

Avik.Das1@timesgroup.com

T Pradeep, professor of chemistry at IIT Madras, says many have an aversion to chemistry, thinking it is something smelly and toxic. But chemistry, he says, has undergone a drastic change and is no more just a science of molecules, "not just something that happens in reaction bottles or in a laboratory with colourful solutions." It is a central subject, he says.

He says part of the problem has also been that educational institutions teach the subject in a silo, with little interaction with other departments like biology, biotechnology or engineering. To make the subject more interesting, he says more interdisciplinary studies is required.

### HEAR THE PROF

Pradeep is a Padma Shri awardee and an Institute professor in IIT Madras, the highest title a professor can earn in a university. He is the second such professor among the institute's long list of 600 faculty.

The professor, who specialises in molecular and nanoscale materials, says that the time has come to reinvent the face of the subject. "If it was not so important, all the 16 departments of IIT Madras, barring mathematics and management, would not have published their papers in journals of American Chemical Society," he says.

The larger reason, he says, is that the world around has become hugely molecular in nature. "Anything that matters to people, whether it is energy, transportation, electronics, environment, or health, all of them have become molecular. Energy is about molecules, plastics is about molecules, medicines is about molecules," he says.

Chemistry is also continuing to offer new solutions to problems of the planet. New materials are needed for fast and clean energy. New materials are needed to protect the environment. New sensors, pesticides, dyes, pharmaceuticals, etc, are needed. "There is an infinite ocean in all of these," says Pradeep.

Pradeep has been working on affordable clean water technology and has devised an eco-friendly method to degrade the physically stable and chemically inert plastic fluoropolymer — polytetrafluoroethylene (PTFE). Plastics are resistant to degradation. PTFE is used in making Teflon, best known for its use in coating non-stick frying pans and other cookware, as it is hydrophobic (repels water) and possesses fairly high heat resistance.

Opportunities are enormous, Pradeep says, with research areas such as how new polymers can be degraded, how new forms of plastics can be created and other material sciences. But industry leaders like GE and BASF are not just looking for good chemists but also those who have the knowledge of products.

"A student of chemistry has to understand processing, testing, data management. If he is joining the tyre industry, he will have to research nano-scale additives in tyres for new product development. Material chemistry has expanded by leaps and bounds over the years," Pradeep says.

Pradeep's views are similar to that of IIT Delhi director Ramgopal Rao, who told TOI last month that chemistry has become more important than ever as finding new materials has become the elixir of life for the nano and micro-electronics world. Researchers are looking for newer materials like molybdenum disulfide and graphene for use in integrated circuits to boost the performance of devices.

“Students have to pursue a subject for some time to appreciate it. Go after that for some time. After some years in chemistry, one may find it interesting in biology or materials or electronics or computing. All these options are now possible

T Pradeep |  
INSTITUTE PROFESSOR,  
IIT MADRAS





# Pradeep Research Group 2020



**From Left: 1<sup>st</sup> Row:** Gaurav Vishwakarma, Kannan M. P., Devaraj Krishnan, Sooraj B. S., Sritama Mukherjee, **Prof. T. Pradeep**, Tanvi Gupte. **2<sup>nd</sup> Row:** Abhijit Nag, Esma Khatun, Swetashree Acharya, Anil Kumar Avula, Subrata Duary, Paulami Bose, Priya K., Sugi K. S. **3<sup>rd</sup> Row:** Asish Kurian, Bijesh Malla, Anagha Jose, B. K. Spoorthi, Arijit Jana, Vishal Kumar, Tripti Ahuja, A. Suganya. **4<sup>th</sup> Row:** Amrita Chakraborty, Dhivyaraja K., Angshuman Ray Chowdhuri, Pallab Basuri, Vivek Yadav, Madhuri Jash, Sandeep Bose, S. Jenifer. **5<sup>th</sup> Row:** Ananthu Mahendranath, Srikrishnarka Pillalamarri, Kartheek Joshua, Mohd. Azhardin Ganayee, Tanmayaa Nayak, Sujan Manna, Biswajit Mondal, Jayoti Roy. **6<sup>th</sup> Row:** Sudhakar Chennu, Md. Rabiul Islam, Ankit Nagar, Sourav Kanti Jana, Sundar Raj, Ganesan Paramasivam, Amoghavarsha R. Kini, and Ramesh Kumar Soni.

# Acknowledgements

Students and Collaborators

Funding



Department of Science and Technology

Government of India